

IFMBE Proceedings

Peng · Weng (Eds.)

Volume 19

7th Asian-Pacific Conference
on Medical and Biological
Engineering

APCMBE 2008, 22–25 April 2008,
Beijing, China



 Springer

Series Editors: R. Magjarevic and J. H. Nagel

The International Federation for Medical and Biological Engineering, IFMBE, is a federation of national and transnational organizations representing internationally the interests of medical and biological engineering and sciences. The IFMBE is a non-profit organization fostering the creation, dissemination and application of medical and biological engineering knowledge and the management of technology for improved health and quality of life. Its activities include participation in the formulation of public policy and the dissemination of information through publications and forums. Within the field of medical, clinical, and biological engineering, IFMBE's aims are to encourage research and the application of knowledge, and to disseminate information and promote collaboration. The objectives of the IFMBE are scientific, technological, literary, and educational.

The IFMBE is a WHO accredited NGO covering the full range of biomedical and clinical engineering, healthcare, healthcare technology and management. It is representing through its 58 member societies some 120.000 professionals involved in the various issues of improved health and health care delivery.

IFMBE Officers

President: Makoto Kikuchi, Vice-President: Herbert Voigt, Former-President: Joachim H. Nagel

Treasurer: Shankar M. Krishnan, Secretary-General: Ratko Magjarevic

<http://www.ifmbe.org>

Previous Editions:

IFMBE Proceedings APCMBE 2008 “7th Asian-Pacific Conference on Medical and Biological Engineering”, Vol. 19, 2008, Beijing, China, CD

IFMBE Proceedings CLAIB 2007 “IV Latin American Congress on Biomedical Engineering 2007, Bioengineering Solution for Latin America Health”, Vol. 18, 2007, Margarita Island, Venezuela, CD

IFMBE Proceedings ICEBI 2007 “13th International Conference on Electrical Bioimpedance and the 8th Conference on Electrical Impedance Tomography”, Vol. 17, 2007, Graz, Austria, CD

IFMBE Proceedings MEDICON 2007 “11th Mediterranean Conference on Medical and Biological Engineering and Computing 2007”, Vol. 16, 2007, Ljubljana, Slovenia, CD

IFMBE Proceedings BIOMED 2006 “Kuala Lumpur International Conference on Biomedical Engineering”, Vol. 15, 2004, Kuala Lumpur, Malaysia, CD

IFMBE Proceedings WC 2006 “World Congress on Medical Physics and Biomedical Engineering”, Vol. 14, 2006, Seoul, Korea, DVD

IFMBE Proceedings BSN 2007 “4th International Workshop on Wearable and Implantable Body Sensor Networks”, Vol. 13, 2006, Aachen, Germany

IFMBE Proceedings ICBMEC 2005 “The 12th International Conference on Biomedical Engineering”, Vol. 12, 2005, Singapore, CD

IFMBE Proceedings EMBEC'05 “3rd European Medical & Biological Engineering Conference, IFMBE European Conference on Biomedical Engineering”, Vol. 11, 2005, Prague, Czech Republic, CD

IFMBE Proceedings ICCE 2005 “The 7th International Conference on Cellular Engineering”, Vol. 10, 2005, Seoul, Korea, CD

IFMBE Proceedings NBC 2005 “13th Nordic Baltic Conference on Biomedical Engineering and Medical Physics”, Vol. 9, 2005, Umeå, Sweden

IFMBE Proceedings APCMBE 2005 “6th Asian-Pacific Conference on Medical and Biological Engineering”, Vol. 8, 2005, Tsukuba, Japan, CD

IFMBE Proceedings BIOMED 2004 “Kuala Lumpur International Conference on Biomedical Engineering”, Vol. 7, 2004, Kuala Lumpur, Malaysia

IFMBE Proceedings MEDICON and HEALTH TELEMATICS 2004 “X Mediterranean Conference on Medical and Biological Engineering”, Vol. 6, 2004, Ischia, Italy, CD

IFMBE Proceedings 3rd Latin – American Congress on Biomedical Engineering “III CLAEB 2004”, Vol. 5, 2004, Joao Pessoa, Brazil, CD

IFMBE Proceedings WC2003 “World Congress on Medical Physics and Biomedical Engineering”, Vol. 4, 2003, Sydney, Australia, CD

IFMBE Proceedings EMBEC'02 “2nd European Medical and Biological Engineering Conference”, Vol. 3, Parts 1 & 2, 2002, H. Hutten and P. Kroesl (Eds.), Vienna, Austria

IFMBE Proceedings 12NBC “12th Nordic Baltic Conference on Biomedical Engineering and Medical Physics”, Vol. 2, 2002, Stefan Sigurdsson (Ed.) Reykjavik, Iceland

IFMBE Proceedings Vol. 19
Yi Peng, Xiaohong Weng (Eds.)

7th Asian-Pacific Conference on Medical and Biological Engineering

APCMBE 2008
22–25 April 2008
Beijing, China

Editors

Yi Peng
Institute of Basic Medical Sciences
Chinese Academy of Medical Sciences
5 Dong Dan San Tiao
Beijing 100005
China

Xiaohong Weng
Chinese Society of Biomedical Engineering
5 Dong Dan San Tiao
Beijing 100005
China

ISSN 1680-0737

ISBN-13 978-3-540-79038-9

e-ISBN-13 978-3-540-79039-6

DOI 10.1007/978-3-540-79039-6

Library of Congress Control Number: 2008924060

© International Federation of Medical and Biological Engineering 2008

This work is subject to copyright. All rights are reserved, whether the whole or part of the material is concerned, specifically the rights of translation, reprinting, reuse of illustrations, recitation, broadcasting, reproduction on microfilm or in any other way, and storage in data banks. Duplication of this publication or parts thereof is permitted only under the provisions of the German Copyright Law of September 9, 1965, in its current version, and permissions for use must always be obtained from Springer. Violations are liable to prosecution under the German Copyright Law.

The use of general descriptive names, registered names, trademarks, etc. in this publication does not imply, even in the absence of a specific statement, that such names are exempt from the relevant protective laws and regulations and therefore free for general use.

The IFMBE Proceedings is an Official Publication of the International Federation for Medical and Biological Engineering (IFMBE)

Typesetting: Data supplied by the authors

Production: le-tex publishing services oHG, Leipzig

Cover design: deblik, Berlin

Printed on acid-free paper

9 8 7 6 5 4 3 2 1

springer.com

About IFMBE

The International Federation for Medical and Biological Engineering (IFMBE) was established in 1959 to provide medical and biological engineering with a vehicle for international collaboration in research and practice of the profession. The Federation has a long history of encouraging and promoting international cooperation and collaboration in the use of science and engineering for improving health and quality of life.

The IFMBE is an organization with membership of national and transnational societies and an International Academy. At present there are 52 national members and 5 transnational members representing a total membership in excess of 120 000 worldwide. An observer category is provided to groups or organizations considering formal affiliation. Personal membership is possible for individuals living in countries without a member society. The International Academy includes individuals who have been recognized by the IFMBE for their outstanding contributions to biomedical engineering.

Objectives

The objectives of the International Federation for Medical and Biological Engineering are scientific, technological, literary, and educational. Within the field of medical, clinical and biological engineering its aims are to encourage research and the application of knowledge, and to disseminate information and promote collaboration.

In pursuit of these aims the Federation engages in the following activities: sponsorship of national and international meetings, publication of official journals, cooperation with other societies and organizations, appointment of commissions on special problems, awarding of prizes and distinctions, establishment of professional standards and ethics within the field, as well as other activities which in the opinion of the General Assembly or the Administrative Council would further the cause of medical, clinical or biological engineering. It promotes the formation of regional, national, international or specialized societies, groups or boards, the coordination of bibliographic or informational services and the improvement of standards in terminology, equipment, methods and safety practices, and the delivery of health care.

The Federation works to promote improved communication and understanding in the world community of engineering, medicine and biology.

Activities

Publications of IFMBE include: the journal *Medical and Biological Engineering and Computing*, the electronic magazine *IFMBE News*, and the Book Series on Biomedical Engineering. In cooperation with its international and regional conferences, IFMBE also publishes the IFMBE Proceedings Series. All publications of the IFMBE are published by Springer Verlag. The Federation has two divisions: Clinical Engineering and Health Care Technology Assessment.

Every three years the IFMBE holds a World Congress on Medical Physics and Biomedical Engineering, organized in cooperation with the IOMP and the IUPESM. In addition, annual, milestone and regional conferences are organized in different regions of the world, such as Asia Pacific, Europe, the Nordic-Baltic and Mediterranean regions, Africa and Latin America.

The administrative council of the IFMBE meets once a year and is the steering body for the IFMBE: The council is subject to the rulings of the General Assembly, which meets every three years.

Information on the activities of the IFMBE can be found on the web site at: <http://www.ifmbe.org>.

The Seventh Asian-Pacific Conference on Medical and Biological Engineering (APCMBE 2008)

Foreword

Chinese Society of Biomedical Engineering (CSBME) has the great honor to organize the Seventh Asian-Pacific Conference on Medical and Biological Engineering (APCMBE 2008) at the agreement and invitation of IFMBE. APCMBE 2008 takes place together with the Seventh National Annual Meeting of Chinese Society of Biomedical Engineering in Beijing from April 22 to 25, 2008.

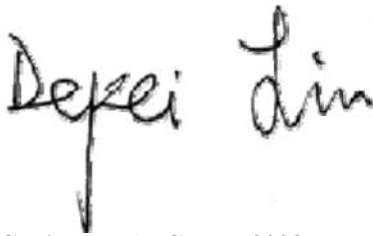
The theme of the conference is “Biomedical Engineering — Promoting Sustainable Development of Modern Medicine”. The conference provides a most appropriate platform for medical and biological engineering professionals to interact and exchange their ideas and experiences on the application of modern biomedical engineering to medical diagnosis, treatment and health promotion. The conference consists of plenary lectures delivered by leading scientists in the field, and organized sessions in important areas in biomedical engineering. I am very pleased that a strong program has been developed from a large number of submitted papers.

I would like to thank the members of Advisory Committee for their instructive suggestions, to thank the members of Scientific Program Committee and reviewers for their hard work to provide review comments and select the papers for inclusion in the program and conduct additional review for the papers involved in the Young Investigators Competition, to thank the members of Organizing Committee for their hard work to handle numerous arrangement affairs.

Participants from the Asian-Pacific countries have the opportunity of coming together to meet with the researchers and engineers on medical and biological engineering, from China in the world famous capital city of Beijing.

I hope you will enjoy the stimulating scientific program, and enjoy Beijing.

Dr. Depei Liu

A handwritten signature in black ink that reads "Depei Liu". The signature is written in a cursive style with a long vertical stroke extending downwards from the letter 'i'.

**Chairman, APCMBE 2008
President, Chinese Society of Biomedical Engineering**

Conference details

Name

The Seventh Asian-Pacific Conference on Medical and Biological Engineering

Short name

APCMBE 2008

Venue

Beijing, China
April 22 to 25, 2008

Organizer

Chinese Society of Biomedical Engineering (CSBME), China

Cosponsor

International Federation for Medical and Biological Engineering (IFMBE)

Endorser

China Association for Science & Technology (CAST), China

Conference Chairman

Depei LIU, China

Conference Co-Chairmen

James GOH, Singapore
Mengsun YU, China

Advisory Committee

Denian BA, China
Dov JARON, USA
Yazhu CHEN, China
Weiqi WANG, China
Kerong DAI, China
Shibi LU, China

Scientific Program Committee

Zulai TAO, China (Chairman)
Shangkai GAO, China (Co-Chairman)

Barry ALLEN, Australia
Yilin CAO, China
Walter CHANG, Taiwan, China
Wufan CHEN, China

Xiuzhen DONG, China

Yubo FAN, China

Jing FANG, China

Zuxiang FANG, China

James GOH, Singapore

Ning GU, China

Hanqing GU, China

Dayi HU, China

Dov JARON, USA

Zonglai JIANG, China

Makoto KIKUCHI, Japan

Sun I. KIM, Korea

Mian LONG, China

Ratko MAGJAREVIC, Croatia

Peter ROLFE, USA

Mingxi WAN, China

Zhibiao WANG, China

James WEAR, USA

Tingfei XI, China

Zhengping XU, China

Jiren ZHANG, China

Ming ZHANG, Hong Kong, China

Xiaoxiang ZHENG, China

Organizing Committee

Yimin HU, China (Chairman, Secretary General)

Arthur F.T. MAK, Hong Kong, China (Co-Chairman)

Yubo FAN, China

Hanqing GU, China

Hua KONG, China

Xigang LENG, China

Tao LI, China

Zhicheng LIU, China

Yi PENG, China

Zhongjie PU, China

Jinxin WANG, China

Xitai WANG, China

Xiaohong WENG, China

Tingfei XI, China

Haiyan XU, China

Guozhong YANG, China

Hu YANG, China

Hongli YU, China

Jiwu ZHANG, China

Quanlu ZHENG, China

Content

Part 1

Pedorthic care of the arthritic foot.....	1
<i>Peng Hu</i>	
Development and Biocompatibility evaluation of silk fibroin-based nerve grafts for peripheral nerve regeneration	4
<i>Yumin Yang, Fei Ding, Jian Wu, Xuemei Chen, Jie Liu, Xiaosong Gu</i>	
Synthesis and Gene Transfection Efficiency of PEG-chitosan-PEI copolymers	9
<i>Wei Zhang, Shi-rong Pan, Yu-ting Wen and Xin Luo</i>	
Preparation and physicochemical characteristics of self-assembled nanoparticles of cholesterol succinate modified pullulan conjugates.....	13
<i>Wen-Zhi Yang, Qi-Qing Zhang, Hong-Li Chen, Xue-Ming Li, Qian Jiang, Min-Mao Chen, Fu-Ping Gao, Hui-Zhu Zhang</i>	
Structural investigations of novel triblock cationic copolymer/DNA complexes	18
<i>Yuting Wen, Shirong Pan, Xuan Zhang, Xin Luo, Wei Zhang</i>	
Alginate/hydroxyapatite hydrogel as biodegradable in situ forming scaffold.....	22
<i>Lu Lu, Yusha Qi, Jinhuan Tian and Changren Zhou</i>	
Drug controlled release of novel alginate/poly-L-arginine microcapsules.....	26
<i>Wenguo Wu, Wei Liu, Shibin Wang and Yuangang Liu</i>	
Targeted and Controlled Release of Indomethacin from a Prodrug of Amylose.....	29
<i>Xiang Cai, Liqun Yang, Yifu Huang, Ningfu Peng, Li-Ming Zhang, Qing Wu, Rufu Chen</i>	
<i>In Vitro</i> Study of Alginate/Poly-L-Arginine Microcapsules as a Protein or Anticancer Drug Carrier.....	32
<i>Qi Lan, Ying Wang, Shibin Wang, Yuangang Liu</i>	
Study of Solanine on Mitochondrion in HepG₂ Cell.....	36
<i>Shiyong Gao, Yubin Ji, Chenfeng Ji, Xiang Zou</i>	
Preparation and Biocompatibility of a Novel Scaffold Made from Small Intestinal Submucosa Powders	40
<i>Juhui Qiu, Guixue Wang and Tao Jiang</i>	

Part 2

Performance Comparison between Two Types of Miniature Axial Flow Pumps for Children.....	44
<i>Ningning Chen, Yu Chang, Bin Gao, Linxi Shi, Ling Li, Xinrui Ma</i>	
Invasive Blood Pressure Monitoring System for Artificial Heart Surgery.....	47
<i>Bin Gao, Linxi Shi, Yu Chang, Xinrui Ma, Ling Li, Ningning Chen</i>	
A Speed Controller Design to a Heart Pump	50
<i>Linxi Shi, Bin Gao, Yu Chang</i>	
A visual prosthesis based on Optic Nerve Stimulation: In vivo Electrophysiological Study in Rabbits.....	54
<i>Liming Li, Mingjie Sun, Pengjia Cao, Changsi Cai, Xinyu Chai, Xiaoliang Li, Panpan Chen, and Qiushi Ren</i>	
A Circuit System Design for Implantable Multi-channel neural stimulator	58
<i>Yan Xi, Qian Du, Hanyan Gong, Nan Tang, Lei Cao, Jinhai Niu, Qiushi Ren</i>	

Implementation of the Natural Heartbeat Synchronize Control for the Undulation Pump Ventricular Assist Device Using the Inflow Pressure	62
<i>I. Saito, T. Chinzei, T. Isoyama, H. Miura, A. Kouno, T. Ono, H. Nakagawa, S. Yamaguchi-Sekine, W. Shi, Y. Inoue, A. Kishi and Y. Abe</i>	
Development of an Auto Calibration Method for the Implantable Blood Pressure Sensor in the Undulation pump ventricular assist device (UPVAD)	66
<i>W. Shi, I. Saito, T. Chinzei, T. Isoyama, H. Miura, A. Kouno, T. Ono, H. Nakagawa, S. Yamaguchi, Y. Inoue, A. Kishi, Y. Abe</i>	
 Part 3	
Coating preparation and drug delayed release of dexamethasone-eluting intravascular stents <i>in vitro</i> and <i>in vivo</i>	70
<i>Yongpeng Chen, Guixue Wang, Xianchun Jin, Lailong Luo, Gang Zhang, Laichun Lu</i>	
 Part 4	
A Comparative Study on the Expression of Telomerase Reverse Transcriptase in Different Development Stages of Human Epidermal Stem Cells <i>in vitro</i>	73
<i>Dewu Liu, Peixin Huang, Yuangui Mao, Jianping Chen, Wei Lan, Lianqun Wang</i>	
The Location and the Telomerase Expression of the Different Development Stages of Human Skin Epidermal Stem Cells <i>in vivo</i>.....	76
<i>Dewu Liu, Wei Lan, Peixin Huang, Yuangui Mao, Jianping Chen, Lianqun Wang</i>	
Differentiation of the Human Marrow Mesenchymal Stem Cells into Vascular Endothelium-like Cells <i>in vitro</i>	80
<i>Dewu Liu, Xiangrong Zhang, Xiaoliang Li, Zhian Zhang, Guanghua Guo</i>	
Effect of microstructure on the mechanical properties and biology performance of bone tissue scaffolds using selective laser sintering.....	84
<i>Liulan Lin, Jiafeng Zhang, Li Zhao, Aili Tong, Jian Sun and Qingxi Hu</i>	
Fabrication of porous β-TCP scaffolds by combination of rapid prototyping and freeze drying technology	88
<i>Liulan Lin, Shaohua Ju, Lian Cen, Huicun Zhang, Qingxi Hu</i>	
The property of ion current in human amniotic mesenchymal stem cell (hAMSC).....	92
<i>Bo-jiang Liu, Xue Lin, Lian-feng Chen, Quan Fang</i>	
 Part 5	
Power density spectra of the velocity waveforms in Artificial heart valves.....	95
<i>A.A. Sakhaeimanesh</i>	
Mechanotransduction of mandibular condylar chondrocytes under pressure	99
<i>Min Zhang, Yong-Jin Chen, Xin Lv, Jing-Jie Wang, Han-Guo Wang</i>	
Effect of femoral tunnel angle on tunnel enlargement in anterior cruciate ligament reconstructions.....	103
<i>Guang-si Shen, You-jia Xu, Hai-bin Zhou, Wen-xin Niu, Xia Guo, Ming Yin, Zu-quan Ding</i>	
Optimization of Anastomotic Configuration in CABG Surgery	107
<i>Y. Sui, B. Ma, A. Qiao</i>	
Nmerical Simulation of Blood Flow in Stented Aneurysm using Lattice Boltzmann Method.....	113
<i>X.J. Zhang, X.Y. Li and F. He</i>	
Improved Experimental System for Analyzing Biomechanical Properties of Iris Tissue	117
<i>Xuefeng Bo, Haiying Quan, Zhicheng Liu</i>	

Effect of Dynamic Stabilization Device Stiffness on Disc Loading under Compression	119
<i>Q.H. Zhang, E.C. Teo</i>	
An AAA-ICT Used to the Single Trial of SEP	123
<i>Y. Wang, Z.X. Xie, Z.F. Wang, H. Liu and Y.H. Liu</i>	
A Finite Element Study of The Response of Thoracolumbar Junction to Accidental Mine Blast Scenario	129
<i>Q.H. Zhang, J.Z. Li, H.N. Serena Tan, E.C. Teo</i>	
Experimental modeling and biomechanical measurement of flatfoot deformity	133
<i>Wenxin Niu, Yunfeng Yang, Yubo Fan, Zuquan Ding, Guangrong Yu</i>	
Numerical Simulation of A Bidirectional Cavopulmonary Anastomosis Connection with Antegrade Pulmonary Blood Flow	139
<i>Qi Sun, Dawei Wan, Jinfen Liu, Yingzheng Liu, Ming Zhu, Haifa Hong, Qian Wang</i>	
Numerical Study on the Changes of the Pressure Waveform in a Large Artery	143
<i>F. He and X.Y. Li</i>	
A Lumped Parameters Dynamic Model for Cerebral Circulation.....	147
<i>Shengzhang Wang</i>	
The Motion Simulation of Human Lower Extremity Based on Dynamics	151
<i>Jin Li, Qiuju Cheng, Hong Liang, Zhuwei Guo</i>	
Design of Active Artificial Knee Joint.....	155
<i>Liang Song, Xitai Wang, Siyuan Gong, Zengguang Shi, Lingling Chen</i>	
Importance of Anterior Mitral Basal Stay Chords for Left Ventricular Outflow Hemodynamics: A Computational Study.....	159
<i>F. Xiong, J.H. Yeo, K.H. Lim, P. Zhang, Y.L. Chua and W.A. Goetz</i>	
A Theoretical Model for Binary Adhesion of Cells in Flows	164
<i>Ying Fang, Yonghua Lao, Quhuan Li, Cheng Zhu, Jianhua Wu</i>	
A New Structure-Activity Relationship of Linear Cationic α-helical Antimicrobial Peptides	167
<i>Li Liu, Ying Fang, Qingsheng Huang, Qiaoling Pan, Jianhua Wu</i>	
Numerical Simulations of Colliding Particle Distribution in Flow Chamber	171
<i>Yonghua Lao, Jiangguo Lin, Ying Fang, Quhuang Li, Cheng Zhu, Jianhua Wu</i>	
Analysing the effect of gas press's little wave in measuring result of velocity of ultra-sound	174
<i>Xiaoning Wang, Mengsun Yu</i>	
A new respiratory training system for astronauts	179
<i>Chunhua Hu, Hongwei Hao, Bozhi Ma, Yuan Yuan, Fangjun Liu, Luming Li</i>	
Computational Simulation for Osteoporosis at the Basic Multicellular Unit Level	182
<i>H. Gong, Y.B. Fan and M. Zhang</i>	

Part 6

Synthesis, Characterization and Cell-uptake of Porphyrin-capped Gold Nanoparticle	186
<i>Lü Feng, Liu Tianjun, Wu Li</i>	
Preparation of nanoparticle of methoxy poly(ethylene glycol)/ poly(ϵ-caprolactone)/ methoxy poly(ethylene glycol) triblock copolymer for drug delivery applications.....	190
<i>N.V. Cuong, C.H. Chen, Y.T. Chen and M.F. Hsieh</i>	
Biological responses of endothelial cells to aligned nanofibers of MWNT/PU by electrospinning.....	194
<i>Z.Z. Han, H. Kong, J. Meng, C.Y. Wang, S.S. Xie, H.Y. Xu</i>	

Preparation, Characterization and Cellular Biological Impact of Water Soluble Multiwalled Carbon Nanotubes.....	198
<i>J. Meng, M. Yang, L. Song, H. Kong, C.Y. Wang, R. Wang, C. Wang, S.S. Xie, H.Y. Xu</i>	

Hapten-Modified Tumor Vaccines Enhance Lymphocytes' Cytotoxicity Against Human Breast Cancer Cells.....	202
<i>W. Wang, Y. Hu, Z. Sun, J.H. Duan, S.C. Chen and X.-D. Yang</i>	

Part 7

A New Heuristic Weighting Function for FDK-based reconstruction of Cone Beam Tomography	206
<i>Han Zheng, Zikuan Chen, Yan Kang, Jiren Liu</i>	

Elementary Design and Implementation of Liver Treatment Planning System	210
<i>Hong-jian Gao, Shui-cai Wu, Yan-ping Bai and Chun-lan Yang</i>	

Deformation-Based Morphometric study on Blind men's brain structures.....	213
<i>Chunlan Yang, Shuicai Wu, Yanping Bai, Hongjian Gao</i>	

Automated detection of exudates on color fundus image using region merging by k-NN graph.....	216
<i>Wei Lin, Hongzhi Liu, Mantao Xu and Jiwu Zhang</i>	

An Investigation of Interpolation Methods in Rebinning Circular Cone-beam data into Parallel-fan-beam Data.....	221
<i>Feng Han, Nianming Zuo, Jiwu Zhang, Xiaochuan Pan</i>	

A Novel Fast Marching Segmentation Algorithm for Pulmonary Nodules in Chest Radiographs	225
<i>Qiyong Guo, Mantao Xu and Jiwu Zhang</i>	

Approximate algorithms for $2N+1$ sources cone-beam CT along saddle trajectories	229
<i>Yang Lu, Jun Zhao</i>	

Using Fast Marching in Automatic Segmentation of Retinal Blood Vessels	233
<i>Chao Liu, Huihai Lu and Jiwu Zhang</i>	

A Robust Fiber Tracking Method in Diffusion Tensor Imaging.....	237
<i>Lifeng Song, Zikuan Chen and Wei Xing</i>	

Detection of blood vessels in retinal images using improved iterative threshold probing of a matched filter response	241
<i>Yongli Wang, Huihai Lu, Mantao Xu and Jiwu Zhang</i>	

An Auto-Reference, Auto-Correlation and Adaptive Interference Cancellation Theories and Techniques (AAA-ICT) Used to the Single Trial of Slow Cortical Auditory Evoked Potentials	245
<i>Zhengxiang Xie, Hong Li, Zhifang Wang, Ying Wang, Yuhong Liu</i>	

Study on the Algorithm of Surface Reconstruction of Defective Bone Based on Delaunay Triangulation	250
<i>Fei You, Qingxi Hu, Qi Lu and Yuan Yao</i>	

An Anisotropic Diffusion Model for Medical Image Smoothing by Using the Lattice Boltzmann Method	255
<i>Yu Chen, Zhuangzhi Yan and YueHong Qian</i>	

Lung region segmentation based on multi-resolution Active Shape Model.....	260
<i>Chunyan Wang, Shengwen Guo, Jianbo Wu, Qiong Liu, Xiaoming Wu</i>	

A Fast Doppler Ultrasound Simulator Based on RF Beamlines.....	264
<i>Minghui Zhen and Dong C. Liu</i>	

Volumetric Non-rigid Registration via Thin-plate Spline Model	269
<i>F. Babapour, A. Abbaspour, R. Zoroofi, S.H. Akhlaghpour</i>	

Interactive Display Methods for Ultrasound Strain Imaging	273
<i>Fei Luo and Dong C. Liu</i>	

Adaptive Spatial Processing for Autocorrelation-based Ultrasound Color Flow Imaging	278
<i>Qiang Wang and Dong C. Liu</i>	
Rationalized Gain Compensation for Ultrasound Imaging	282
<i>Mingwang Tang and Dong C. Liu</i>	
Interactive Frequency Compounding to Medical Ultrasound Images	286
<i>Xiaoming Zhou and Dong C. Liu</i>	
Study on a novel tumor cell recognition system based on orthogonal image moments	290
<i>Haiping Ren, Aizhen Liu, Ziliang Ping and Dongting Bai</i>	
Deformable Mesh based Motion Tracking for Ultrasound Strain Imaging	293
<i>Zhiqiang Jiang and Dong C. Liu</i>	

Part 8

Development of a noninvasive glucose measurement system based on orthogonal twin polarized lights and its primary experimental investigation.....	298
<i>Hong Wang, Baoming Wu</i>	
Effect of Interface Characteristics of Substrates on Performance of Biosensors Based on Supported Mimetic Biomembranes	302
<i>Shengping Liu, Yongbo Wu, Yunlong Wei</i>	
A Novel Taste Sensor Based on Ion Channels Incorporated in Nano-lipid Bilayer Membranes	306
<i>Qingjun Liu, Jinjiang Yu, Zongbin Liu, Wei Zhang, Ping Wang and Mo Yang</i>	
Micro-Electrode Cell-Based Biosensor Using Electrochemical Impedance Spectroscopy for Cancer Research.....	309
<i>Qingjun Liu, Jinjiang Yu, Hui Yu, Lidan Xiao, Ping Wang and Mo Yang</i>	
Piezoelectric Biosensor Based on Olfactory Receptor Expressed in a Heterologous Cell System for Drug Discovery	313
<i>Chunsheng Wu, Haimin Tan, Hui Yu, Luhang Zhao, Ping Wang</i>	
A Flexible Thin-film Microelectrode for Optic-Nerve Visual Prosthesis.....	317
<i>Xiaohong Sui, Yinghui Li, Yijing Xie, Ting Liang, Wei Chen, Yiliang Lu, Gang Li, Kai Wang, Qiushi Ren</i>	
Study of enzyme biosensor for monitoring carbamate pesticides in seawater	323
<i>Shu-ping Zhang, Lian-gang Shan, Yi Zheng, Lli-yi Shi</i>	

Part 9

Spectral analysis of heart rate variability applied in the exercise of professional shooting athletes.....	326
<i>J.J. Zhuang, X.L. Huang, X.B. Ning, M. Zou and B. Sun</i>	
Using EMG to Evaluate Muscular Fatigue Induced during Video Display Terminal Keyboard Use Task.....	329
<i>Haijun Niu, Ran Li, Guanglei Liu, Fang Pu, Deyu Li, Yubo Fan</i>	
The ERP Signal Analysis of Visual Influences on Auditory Intensity Perception	333
<i>R. Cai, Z. Li, Y. Li, Y. Qiu, Y. Zhu, S. Tong</i>	
Dipole Analysis of Eye Movement Artifacts from the EEG	337
<i>Weidong Zhou</i>	
BLDA Approach for Classifying P300 Potential.....	341
<i>Anhu Huang, Weidong Zhou</i>	

A GPRS-based Wrist Type Pulse Wave and Body Temperature Monitor for Children Healthcare.....	344
<i>Yanhui Chen, Junnan Han, Kai Wu, Xiaoming Wu, Jing Zhou</i>	
Design of Physiological Parameter Acquisition and Communication Module Based on CC2430.....	348
<i>Qi Zhao, Kai Wu, Jianbo Wu, Xiaoming Wu</i>	
Improved System of Artificial Heart Valve Detector Based on Windows XP.....	352
<i>Cheng Lu, Xiaogang Hu, Xi Zhang, Jianyu Wang, Shuo Wang</i>	
Wireless monitoring system via ZigBee in ICUs.....	357
<i>Shaojie Lin, Qiong Liu, Xiaoming Wu, Shanglin Li and Zhicong Zhao</i>	
Largest Lyapunov index of EHRV for analyzing status of cardiovascular system.....	361
<i>Xia Li, Tianliang Kang, Jinghua Liu, Xin Tian</i>	
Wavelet transform for on-off switching BCI device.....	363
<i>C.S. Li and H. Wang</i>	
Optimization of the Coil to Focalize the Electrical Field Induced by Magnetic Stimulation in the Human Brain.....	366
<i>Lina Pu, Tao Yin, Hao An, Song Li, Zhipeng Liu</i>	
A miniature telemetric system base on chip nRF24E1for recording EEG activity in freely moving rat.....	373
<i>Zhanping Wang, Chong Luo, Chunpeng Zhang, Yang Xia</i>	
Spatial Sensitivity of NIRS Tissue Oxygenation Measurement using a Simplified Instrument.....	377
<i>R. Liu, X. Liu, F. Scopesi, G. Serra, J.W. Sun, P. Rolfe</i>	
Adaptive Liver Segmentation from Multi-slice CT Scans.....	381
<i>J. Liu, Q. Hu, Z. Chen and P. Heng</i>	
Investigation of multifunctional cell physiological analysis instrument based on integrated chip.....	385
<i>Hua Cai, Shi Zhu, Hui Yu, Lidan Xiao, Zhaoying Hu, Wei Zhang, Ping Wang</i>	
AMS Based Spectrum Subtraction Algorithm with Confidence Interval Test.....	389
<i>Xin Ma, Weidong Zhou</i>	
System of magnetic coupled PPM transcutaneous wireless communication.....	392
<i>Weiming Wang, Bozhi Ma, Hongwei Hao, Luming Li</i>	
SPME-GC analysis of alkanes and aromatic hydrocarbons in human breath to screen lung cancer.....	396
<i>Hao Yu, Ping Wang</i>	
Application of Independent Component Analysis on Artifacts Removal in the Time-Frequency Analysis of Transient Evoked Otoacoustic Emissions.....	399
<i>Ying Zhao, Liang Dong, Qiushi Ren, Xinyu Chai</i>	
Based on the FPIA of high-throughput gene and protein detection analysis system.....	404
<i>Ni Yuan, Ju Zhang, Lihong Yang, Yanhai Guo, Zhili Chen, Guoshao Chen</i>	
Thresholding-based Wavelet Packet Methods for Doppler Ultrasound Signal Denoising.....	408
<i>Jiangfeng Yu, Dong C. Liu</i>	
Physiological Monitoring in the Ventilated Neonate: A Rationale.....	413
<i>P. Rolfe, F. Scopesi, J.W. Sun, G. Serra</i>	
Research on Multi-Parameter Physiological Monitor Based on CAN Bus.....	417
<i>Le Yang, Peng Yang, Aiying Tian, Xin Guo</i>	
The Study of C0 Complexity on Epileptic Absence Seizure.....	420
<i>Yi Zhou, Lingli Xie, Gaohang Yu, Fang Liu, Yi Zhao, Yu Huang</i>	

Research of Virtual Nerve Induce Electrical Signal Auto-check Technology 426
Min Wu, Zhi-hui Wei, Li-ming Tang, Yu-bao Sun, Tie-bing Liu

Development of Implantable Neuro-Stimulator Used for Brain and Nerve Stimulation 430
L.M. Li, H.W. Hao, B.Z. Ma, X.W. Wen, F.J. Liu, C.H. Hu

Part 11

3D Vessel Tree Reconstruction from Rotational C-arm Projections by Multi-view Stereo Reconstruction 434
Wei Zhang, Zikuan Chen and Xuefeng Zhang

Implementation of Convolution/Superposition Model of Photon Dose Calculation 442
Jiandong Li, Tie Zhang

Quality assurance of helical tomotherapy intensity modulated radiation therapy 447
Shouping Xu, Xiaowu Deng, Xiangkun Dai, Lianyuan Wang, Yunlai Wang, Chuanbin Xie, Ruigang Ge, Hanshun Gong

Electron spectrum reconstruction as nonlinear programming model using micro-adjusting algorithm 451
Gui Li, Aidong Wu, Hui Lin, Yican Wu

Part 12

Effect of EMP on Superoxide Dismutase and Malondialdehyde in K562 cells 455
Xue-Jun Xie, Gui-Ying Zeng, Yao Guo, Guo-Zheng Guo, Li-Hua Zeng, Dong-Qing Ren

Hsps expression in three human glioma cell lines after radio-frequency field exposure 458
G.R. Ding, X.W. Wang, K.C. Li, J. Miyakoshi and G.Z. Guo

Effects of Electromagnetic Pulses on the Rat Testis 461
Lihua Zeng, Chang-xu Zou, Jie Zhang, Xiao-Wu Wang, Dong-Qin Ren, Yu-Rong Li, Guo-zhen Guo

Effect of EMP on lipid peroxidation of human gastric cancer cells MKN28 466
Yongbin Chen, Guozhen Guo

Effects of electromagnetic pulse on the vimentin of mice testes 469
Xiao-Wu Wang, Chang-Hong Shi, Gui-Rong Ding, Tao Zhao, Li-Hua Zeng, Jie Zhang, Xue-Jun Xie, Guo-Zhen Guo

Study on behavior of male rat 3 months after electromagnetic pulse irradiation 473
Yu-Hong Qi, Dong-Qing Ren, Xiao-Ming Su, Li Zhang, Kai-Dong Liu, Guo-Zhen Guo

Part 13

Research of Environmental Control systems for Disabled people 476
Chunjing Tao, Xiaoyu Zhang and Xitai Wang

The reference research of exercise therapy of residual limb in post-operative of lower limb amputation 480
Xiaoyu Zhang, Qidong Liu, Chunjing Tao and Huiru Gu

Analysis of Emotional Expression of Finger Braille 484
Y. Matsuda, I. Sakuma, Y. Jimbo, E. Kobayashi, T. Arafune and T. Isomura

A Research on EMG Signal and Plantar Pressure Information for AK Prosthetic Control 488
Tengyu Zhang, Peng Yang, Qidong Liu, Lingling Chen and Jie Liu

Pixelized Images Recognition in Simulated Prosthetic Vision 492
Ying Zhao, Yukun Tian, Huwei Liu, Qiushi Ren, Xinyu Chai

Artificial Horse for Rehabilitation	497
<i>C.Y. Li, H.T. Gao, Y.B. Ma, C. Liu and H. Wang</i>	
Effect of Shank Curve of High-heeled Shoe on the Plantar Pressure Distribution.....	500
<i>Y. Cong, Y. Luximon and M. Zhang</i>	

Part 14

Effects of Qinglongyi Polysaccharide on complex biochemistry function with the core of Band 3 on Erythrocyte	503
<i>Chenfeng Ji, Yubin Ji, Xiang Zou, Feng Xiao</i>	
Studies on Effect of Saponins of Asparagus on Tumor Cell Apoptosis and its Mechanisms of Action.....	507
<i>Yu-Bin Ji, Lei Yu, Lang Lang, Chen-Feng Ji</i>	
Effects of electric pulses on apoptosis induction and mitochondrial transmembrane potential of cancer cells.....	511
<i>Fang-Yi Jiang, Li-Ling Tang, Chao Zeng, Huan Liu, Ke-Dao Liang, Yan Mi, Cai-Xin Sun</i>	
Preparation and Release Efficiency of Poly (lactic-co-glycolic) Acid Nanoparticles for Drug Loaded Paclitaxel	514
<i>You Ling, Yueshan Huang</i>	
Effects of Paclitaxel on human lung cancer cell lines in vitro and in vivo	518
<i>Lihua Zeng, Changxu Zou, Xuejun Xie, S. Kizaka-Kondoh, M. Hiraoka, GuoZhen Guo</i>	
Magnetoviscous Effect of Magnetic Fluid Targeting Drug Delivery System.....	524
<i>Dong Cao, Jun Yi, Hui Cao, Wei Liu, Shi Ying Yuan</i>	
Effects of Asparagus Polysaccharide on GPA and Band 3 from Erythrocyte Membrane of S₁₈₀ Mice	528
<i>Yubin Ji, Chenfeng Ji, Xuejun Chen</i>	
Study on S180 Tumor Mice Erythrocyte Membrane Function of Sargassum Fusiform Polysaccharides.....	531
<i>Yubin Ji, Chenfeng Ji, Chong Wang</i>	

Part 15

Enhancement of Liposome Delivery Efficiency Via Cell Membrane Permeability by ultrasound exposure	534
<i>Fang Yang, Ning Gu, Di Chen, Junru Wu, Xiaoyu Xi, Dong Zhang</i>	
Numerical Analysis of a Deformable Model for Ultrasound Border Detection	537
<i>Xiaoyan Liao and Dong C. Liu</i>	
Noninvasive Temperature Estimation Using B-Scan Image For Thermal Therapy	542
<i>Wei Li, Tao Kan, Xiangling Xiao, Jinghai Niu</i>	
The design of noninvasive temperature measure system and software	546
<i>Kan Tao, Wei Li, Xianglin Xiao and Jinghai Niu</i>	
Doppler US Nutrient Artery Waveform Change in Assessment of Non-pregnant Uterus Response to Oxytocin	551
<i>Li-qun Sun, Jian-zhong Zou, Wen-zhi Chen, Zhi-biao Wang</i>	
The Effects of Acoustic Interface Layer on Biological Focal Region By High Intensity Focused Ultrasound	555
<i>Quanyi Li, Liyuan Fu, Faqi Li</i>	

Part 16

Certification of Biomedical Engineering Technicians and Clinical Engineers: Important or Not.....	558
<i>James O. Wear</i>	

Part 17

- The Computer Model in View of Hemodynamic Effects of Electro Ventilation Double Pump CPR..... 562**
Xiaoming Wu, Yanru Zhang, Lin Xu, Hengxin Yuan

Part 18

- The research of the community healthcare network based on ZigBee technology 567**
Jihong Chai, Hongli Yang
- A Design of Mobile Monitoring System Based on Tradition Chinese Medicine 571**
Zhicong Zhao, Qiong Liu, Xiaoming Wu, Shaojie Lin and Jumei Zhang
- A ZigBee-based wearable Cardio-Pulmonary Monitor for Mobile Health Care..... 574**
Junnan Han, Yanhui Chen, Dongsheng Xiong, Xiaoming Wu
- Development of telemonitoring system for PCG by telephone transmission..... 577**
Dong Wang, Xingming Guo, Shouzhong Xiao and Ming Ke
- Research in Development on Wireless Health Care of Infants..... 580**
Lili Zhang, Li Lao, Kai Wu, Qiong Liu and Xiaoming Wu
- The research of medical services sharing platform base on semantic web services..... 584**
Yuan Yao, Hai Wang, Qing-xi Hu, Gao-chun Xu, Di Wu
- HealthED: An Opened Integrate Healthcare IT Architecture 588**
Y. Yao, Q. Wang, Z. Sun and Q.X. Hu

Part 19

- Study of the Ballistocardiogram signal in non-contact life detection system based on radar 594**
Jianqi Wang, Guohua Lu, Xijing Jing, Yang Zhang, Hao Lv
- Research and application of physical protection technology and equipment against biological contamination
in mainland of China 598**
Z. Wang, J.Q. Yang, J.C. Qi, Y.D. Wang, S.Q. Chen, S. Xia
- PI3K-Mediated Epithelial Sodium Channel Activity by Regulating the Apical Membrane Morphology
of Renal Epithelial Cells..... 603**
Yanjun Zhang, Liying Ma, Bo Xu, J. Gorelik, D. Klenerman, M. Lab, C. Edwards, Y. Korchev
- A Novel Method of Prokaryotic Promoter Regions Prediction with Feature Selection: Quadratic Discriminant
Analysis Approach..... 608**
Yaohua Du, Taihu Wu
- The vitro and vivo study of Poly (3-hydroxybutyrate) microspheres 615**
Feng Tian, Yong-Liang Zhao, Chang-Jun Liu, Fan Li, Nan Xing

Part 20

- Designing “Diagnostic ultrasound device” course in high-vocation education of BME 623**
Hao Yu, Rong Song, Quan Su, Hongli Yang, Jun Han, Jihong Chai, Qingping Zhang
- ECG-Analyzing Experimental System Based on Virtual Instrument..... 626**
Jun Han, Hao Yu, Hongli Yang

Undergraduate Education on Biomedical Engineering of Comprehensive University in China.....	629
<i>Xiaohong Weng</i>	
Bioinformatics Education in Medical College.....	633
<i>Xiaolin Yang, Zhengguo Zhang</i>	
Exploring Teaching Methods on Biomedical Courses in Engineering Universities.....	636
<i>Zhuowei Guo, Jin Li, Hong Liang, Guang Tang, Keshen Li, Liwei Zhang, Kuan Luan, Liang Guo</i>	
Build a Characteristic Specialty to Cultivate Persons with Ability in Biomedical Engineering.....	639
<i>Ling Li, Huafu Chen and Nini Rao</i>	
Integrated Training Model on Biomedical Engineering Undergraduates' Innovation Ability	641
<i>Ting Liu, Xin Tian</i>	
Biomedical Engineering Characteristics of Training Model of Education and Training Programme of Reform and Practice	645
<i>Xu Zhang, Zhicheng Liu, Yalin Ye, Xiaopeng Han, Anyu Chen</i>	
Prosthetics and Orthotics Engineering Professionals Training Mode and Curriculum Research and Development	648
<i>Zhicheng Liu, Xu Zhang, Yalin Ye, Anyu Chen, Xueqian Guo</i>	
 Part 22	
The Effect of Acupuncture at Point Neiguan on the Pulse Picture for Patients with Arrhythmia.....	651
<i>Jialiang Chen, Tao Wang and Yuebo Wu</i>	
Primary Study on the Parameters and Methods to Evaluate Needling Sensation and Maneuvers in Acupuncture	655
<i>Ying Li, Yu Zhang, Zhipeng Liu, Tao Yin</i>	
Development of Implantable stimulating system used for electroacupuncture	660
<i>C.S. Niu, Y. Yu, H.W. Hao and L.M. Li</i>	
Study of Acupuncture Manipulation Parameter Based on Data Mining Technique.....	663
<i>Yin-e Hu, Hua-yuan Yang</i>	
A fMRI Study on Electroacupuncture Intervening Heroin Abstainers' Cognitive Attention	668
<i>Ping Xu, Yingping Jiang, Daoying Geng, Yan Wang, Guanghua Lu</i>	
Effects of Acupuncture On Mitochondria of Muscle Cell In Rats of Acute Swimming Exercise.....	678
<i>Ming Gao, Huayuan Yang, Tangyi Liu, Le Kuai</i>	
Determination of Indirect Moxibustion's Temperature and Research on Thermal Conduction Model.....	681
<i>Huayuan Yang, Hu Yine, Zhuicheng Hu</i>	
Quantitative Analysis of Different Consciousness Process Based on Multi-index Dynamic BEAM Technology	685
<i>Yihe Zhang, Chi Chen, Yafei Liu and Jianfen Xu</i>	
Study of the urinary metabolite profile associated with osteoarthritis and the correlation with its TCM syndromes.....	691
<i>Li-Xi Chu, Song-Bin Yang, Wei Jia, Yun-Ping Qiu, Ming-Ming Su</i>	
Research on the Cun-Guan-Chi Pulse Detecting System	697
<i>Wei-chang Tang, Cong-ying Liu, Yu-ping Zhao</i>	
Traditional Chinese Medical Informatics and Virtual Body	700
<i>Shi Cheng, ChangYue Li, Shiqi Fang</i>	

Study on Brain FMRI of the Mechanism of Tuina Analgesia	703
<i>Zhengyu Li, Xiwen Sun and Juntao Yan</i>	
Qualitative Frequency Response Calibration of Sonocardiography System to Sense Wrist Pulse	707
<i>Yih-Nen Jeng and Shang-Yin Lee</i>	
The Effect of Electric Acupuncture on the Retinal Ganglion Cells in Rabbits with Acute High Intraocular Pressure	711
<i>Wenxin Zhou, Jingying Yang, Yong Xia, Hongwei Wang, Genying Guo, Jing Zhang</i>	
Quantitative Research on Analgesic Effects of Electroacupuncture at Multiple Factors Parameters in Rats of Adjuvant-Induced Arthritis	715
<i>Le Kuai, Huayuan Yang, Jie Jiang</i>	
 Part 23	
Computer-Aided analyzing system in root canal therapy	720
<i>Hu Qingxi, Song Chenxia, Yao Yuan, Lu Qi</i>	
The Research of an Optimized Boolean Operation Algorithm for Skull Defect Mending	725
<i>Yuan Yao, Fu Wu, Qing-xi Hu, Gao-chun Xu, Fei You</i>	
Study on the Application of Rapid Prototyping in Assistant Surgical Planning	729
<i>Di Wu, Qingxi Hu, Qi Lu, Gaochun Xu</i>	
Augmented Reality Interactive Interface for Defective Bone Repair System	733
<i>Yuan Yao, Xiu-xiang Pang, Qi Lu, Qing-xi Hu</i>	
Computer Aided Analysis in Maxillary Sinus Surgery	737
<i>Qing-xi Hu, Qin Xu, Yuan Yao, Qi Lu, Yuan-zhi Xu, Jiao-jiao Wang, Qi-xiang Yang</i>	
MRI Compatible Rigid-flexible Outer Sheath Device Using Pneumatic Locking Mechanism for Endoscopic Treatment	741
<i>Siyang Zuo, N. Ymanaka, K. Masamune, H. Liao, K. Matsumiya, T. Dohi</i>	
Development of interactive three-dimensional autostereoscopic image for surgical navigation system using Integral Videography	745
<i>Tran Huy Hoang, Hongen Liao, K. Matsumiya, K. Masamune, T. Dohi</i>	
Distortion Correction of Wedge Prism 3D Endoscopic Images	750
<i>Y. Takata, T. Torigoe, E. Kobayashi, I. Sakuma</i>	
Intraoperative Local Demarcation System of Brain Tumor Based on 5-Aminolaevulinic Acid Induced Porphyrin Fluorescence	754
<i>T. Ando, M. Noguch, K. Shimaya, K. Wang, E. Kobayashi, H. Liao, T. Maruyama, Y. Mulagaki, H. Iseki and I. Sakuma</i>	
Author Index	759
Subject Index	765

Pedorthic care of the arthritic foot

Peng Hu

National Research Center For Rehabilitation Technical Aids, Beijing, China

Abstract — Pedorthic care of the arthritic foot is very important and tough problem. an elastic midfoot bandage may provide limited support for patients with mild midfoot arthritis. More rigid thermoplastics can also play a role in supporting the midfoot. Pedorthic management can dramatically improve the quality of life for individuals who have arthritis. The majority of adults over the age of 50 have been diagnosed with arthritis in at least one joint in their lower extremity. Many of these adult will be referred to a pedorthist for conservative care. Pedorthists, therefore, must realize that arthritic takes many forms and that symptoms and treatment plans vary. A rocker-bottom modification effectively reduces motion in the midfoot and yet simulates lost motion in the hindfoot. Last, we talk about Pedorthic management plays an important role in preserving the arthritic foot.

Keywords — Pedorthic care arthritic foot save

I. INTRODUCTION

Pedorthic care of the arthritic foot is very important and tough problem. Now lots of people think an elastic midfoot bandage may provide limited support for patients with mild midfoot arthritis. The UCBL orthosis stabilizes and supports the midfoot and has higher trim lines and is thinner than a multidensity orthosis. Pedorthic management can dramatically improve the quality of life for individuals who have arthritis. The majority of adults over the age of 50 have been diagnosed with arthritis in at least one joint in their lower extremity. Many of these adult will be referred to a pedorthist for conservative care. In a less severe case of metatarsalgia, supportive footwear in combination with an off-the-shelf orthosis that includes a metatarsal pad may be sufficient to reduce weight on the painful metatarsal heads. The metatarsal pad should be centered on the plantar surface of the shelf orthosis. A rocker-bottom modification effectively reduces motion in the midfoot and yet simulates lost motion in the hindfoot. The apex may be placed closer to the midfoot to increase the rocker motion in more severe cases. However, this increased rocker motion may be unsuitable for patients with poor balance. If the stock shank does not provide enough rigidity, an extended rigid shank may be added to the rocker sole to further reduce motion. An external metatarsal bar placed proximal to the affected metatarsal heads significantly reduces pressure during walking.

A solid ankle cushion heel modification to the out-sole of the shoe significantly reduces the amount of force transmitted through the hindfoot at heel strike. Combining a solid ankle cushion heel with a rocker bottom can affect the entire gait cycle. The solid ankle cushion heel reduces force and the rocker bottom allows the foot to roll through foot-flat to toe-off. However, placing the apex of the rocker bottom too far posterior or allowing it to dorsiflex the foot increases pressure on the hindfoot. If midfoot or forefoot involvement is minor hindfoot pressure may be relieved with a slight increase in heel height, heel and sole flares may also be added to broaden the base of support and increase the area of pressure distribution. Pedorthic management plays an important role in preserving the arthritic foot. Whether the patient was just diagnosed or has undergone surgery to reconstruct or stabilize a painful joint, pedorthists are responsible for providing the highest level of care available.

II. WRITING THE PAPER

Pedorthic care of the arthritic foot is very important and tough problem. Now lots of people think an elastic midfoot bandage may provide limited support for patients with mild midfoot arthritis. A firm multidensity total contact foot orthosis is another option for supporting a flexible collapsed midfoot. When placed in a supportive shoe this type of orthosis will support the decompensated arch and also help prevent further collapse of the joints. Patients with a fixed midfoot deformity can also benefit from a multidensity total contact foot orthosis; however, care should be taken to accommodate the deformity and not try to change it. An attempted change could result in great discomfort and possible foot injury. Accommodation of a fixed deformity relieves high pressure areas and reduces the risk of ulceration. More rigid thermoplastics can also play a role in supporting the midfoot.

The UCBL orthosis stabilizes and supports the midfoot and has higher trim lines and is thinner than a multidensity orthosis. Many patients with midfoot arthritis are unable to tolerate aggressive pressure or support in the longitudinal arch. For these patients, the arch can be supported passively, and a medial forefoot may be added to a multidensity total contact or a UCBL orthosis.

Pedorthic management can dramatically improve the quality of life for individuals who have arthritis. The majority of adults over the age of 50 have been diagnosed with arthritis in at least one joint in their lower extremity. Many of these adults will be referred to a pedorthist for conservative care. Pedorthists, therefore, must realize that arthritis takes many forms and that symptoms and treatment plans vary. The objective is to provide the patient with conservative care that: The first one discourages progressive destruction of the joint involved. The second redistributes pressure to reduce the risk of ulceration and reduce pain. The third allows the patient to ambulate more comfortably. Include hindfoot arthritis and footwear and footwear modifications and orthoses. It can control of the hindfoot is the key to dealing successfully with hindfoot arthritis. A solid ankle cushion heel modification to the out-sole of the shoe significantly reduces the amount of force through the hindfoot at heel strike.

In a less severe case of metatarsalgia, supportive footwear in combination with an off-the-shelf orthosis that includes a metatarsal pad may be sufficient to reduce weight on the painful metatarsal heads. The metatarsal pad should be centered on the plantar surface of the off-the-shelf orthosis. A custom-molded orthosis may be fabricated from multidensity layers of materials for a total contact fit that provides support and relief in specific areas.

A rocker-bottom modification effectively reduces motion in the midfoot and yet simulates lost motion in the hindfoot. The apex may be placed closer to the midfoot to increase the rocker motion in more severe cases. However, this increased rocker motion may be unsuitable for patients with poor balance. If the stock shank does not provide enough rigidity, an extended rigid shank may be added to the rocker sole to further reduce motion. An external metatarsal bar placed proximal to the affected metatarsal heads significantly reduces pressure during walking. A rocker-bottom modification with the apex placed proximal to the metatarsal heads performs a similar function. Care should be taken to place the apex of either modification in the proper location. Normally the metatarsophalangeal joints are not positioned straight across the foot; therefore it is important that the apex be placed proximal to the first and fifth metatarsal heads. Allowing the proximal edge of a metatarsal bar to follow the contour of the metatarsal heads increases relief for the second, third, and fourth metatarsal heads.

Next we research something about footwear modifications. A solid ankle cushion heel modification to the out-sole of the shoe significantly reduces the amount of force transmitted through the hindfoot at heel strike. Combining a solid ankle cushion heel with a rocker bottom can affect the entire gait cycle. The solid ankle cushion heel reduces force

and the rocker bottom allows the foot to roll through foot-flat to toe-off. However, placing the apex of the rocker bottom too far posterior or allowing it to dorsiflex the foot increases pressure on the hindfoot. If midfoot or forefoot involvement is minor hindfoot pressure may be relieved with a slight increase in heel height, heel and sole flares may also be added to broaden the base of support and increase the area of pressure distribution. Control of the hindfoot is the key to dealing successfully with hindfoot arthritis. A multidentate total contact foot orthosis with a high medial flange may be used to accommodate the deformity. If combined with supportive footwear this method provides adequate support and is comfortable.

Sometimes we also talk about midfoot arthritis. Pedorthic objectives in treating midfoot arthritis include relieving painful motion in the joint, providing plantar support to the midfoot, and reducing pressure on the dorsal aspect of the painful joint.

Hallux rigidus and lesser toe deformities is a usual problem of the foot, pedorthic objectives in treating hallux rigidus include limiting motion of the painful metatarsophalangeal joint, providing support proximal to the first metatarsal head to reduce dorsiflexion, and reducing pressure on the dorsal aspect of the joint. Lesser toe deformities include hammer toes, claw toes, mallet toes, and crossover toes, pedorthic objectives in treating. Lesser toe deformities include unloading the metatarsal heads and reducing pressure on the dorsal aspect of the interphalangeal joints and the distal tip of the digit.

Pedorthic management plays an important role in preserving the arthritic foot. Whether the patient was just diagnosed or has undergone surgery to reconstruct or stabilize a painful joint, pedorthists are responsible for providing the highest level of care available. As with arthritis begins with a thorough examination and knowledge of all the implications and complications of the disease, such as neuropathy, or painful and stiff hands that cannot manage a D-ring shoe closure. The patient's height, weight and activity level are also important considerations in selecting materials; the density of material used for extrinsic shoe modifications will vary on the basis of this information. Pedorthists must also educate all patients and help them to make better decisions about their footwear.

More than just personal viewpoint related comments, if not accuracy of the correction also invited criticism please.

III. CONCLUSIONS

Pedorthic care of the arthritic foot is very important and tough problem surely. The UCBL orthosis stabilizes and supports the midfoot and has higher trim lines and is thinner

than a multidensity orthosis. Many patients with midfoot arthritis are unable to tolerate aggressive pressure or support in the longitudinal arch. For these patients, the arch can be supported passively, and a medial forefoot may be added to a multidensity total contact or a UCBL orthosis.

REFERENCES

1. sun guofeng (2001) pedorthic and orthosis, Japan
2. liu zhiquan (2001) orthosis , China
3. sun lei (2000) modern orthosis application , China

Development and Biocompatibility evaluation of silk fibroin-based nerve grafts for peripheral nerve regeneration

Yumin Yang, Fei Ding, Jian Wu, Xuemei Chen, Jie Liu, Xiaosong Gu*

Jiangsu Key Laboratory of Neuroregeneration, Nantong University

Abstract — Silk fibroin (SF) have been used in the field of bone or ligament tissue engineering. We developed a novel biomimetic design of the SF-based nerve graft (SF graft) which was composed of a SF-nerve guidance conduit (NGC). The SF-NGC prepared via well-established procedures exhibits an eggshell-like microstructure that is responsible for its superior mechanical and permeable properties beneficial to nerve regeneration. The inner wall displays a 100- μm -thick netted structure formed by SF fibers of 10 μm diameter, which were spread out as a stiffener. The data also indicate that the cumulative release of vitamin B12 is almost 100% after 75 min of release. MTT assay was performed to determine the in vitro cytotoxicity of the SF-NGC extract fluid on the cultured L929 cells derived from an immortalized mouse fibroblast cell line. The adult rat was subjected to implantation of the SF graft for bridging a 10-mm long sciatic nerve defect. Then the following-up experiments at initial stage (1- 4 weeks) of nerve regeneration including routine blood tests and histochemical investigation were used to evaluate the in vivo biocompatibility of the SF graft with peripheral nerve. The results suggested the non-cytotoxicity of the SF-NGC with grade 0 as per the U.S. Pharmacopeia guidelines. The outcome of peripheral nerve repair at six months post-implantation was evaluated by a combination of electrophysiological assessment, FluoroGold retrograde tracing and histological investigation. The examined functional and morphological parameters show that SF grafts could promote peripheral nerve regeneration. Collectively, these data indicate that SF graft raised a potential possibility of using these newly developed nerve grafts as a promising alternative to nerve autografts.

Keywords — Silk fibroin; Schwann cell; Biocompatibility; Nerve conduit; Nerve regeneration

I. INTRODUCTION

The discovery of silk production by the silkworm *Bombyx mori* can be traced back to a mysterious and romantic legend from ancient China [1]. Natural silk has long been used as fabric materials in textile industry and also as surgical sutures in medical field [2], but only recently has it found rapidly increasing applications in biomedical fields including the generation of tissue-engineered bones, skins and cartilages [3-5].

Peripheral nerve repair represents a common clinical challenge, and the current gold standard for treating large

nerve defects involves the implantation of nerve autografts that is limited by graft availability, secondary deformities, and potential differences in tissue structure and size [6-8]. For the development of artificial nerve grafts as a promising alternative to nerve autografts, a diverse array of synthetic and natural biopolymers such as polyglycolic acid, polylactic acid, collagen, chitosan, alginate and their composites or derivatives, has been tried showing varying levels of success and flaws [9-11]. And seeking new biomaterials with more favorable properties and more flexible processing methods remains an active area of intense research.

Natural silkworm silk consists of a core structural protein called silk fibroin (SF) which is coated with a glue-like protein called sericin. The identification of contaminating sericin as the source of unwanted immunological responses sparks renewed interest in purified SF (instead of natural silk) used for biomedical applications. We have previously reported on good in vitro biocompatibility of SF fibers with peripheral nerve tissues and cells [12]. Here we show a new, biomimetic design of the SF-based nerve graft (SF graft) the main component of which biomimicks the eggshell microstructure, and evaluate bridge implantation of SF grafts across a 10-mm long defect in the rat sciatic nerve with regards to the commonly adopted parameters of peripheral nerve regeneration by using a variety of histological and electrophysiological techniques.

II. MATERIALS AND METHODS

2.1. Preparation of SF grafts

Raw silk fibers (from *Bombyx mori* cocoons) were bought from Xinyuan sericulture company, Hai'an, Jiangsu, China. Their sericin coating was removed via degumming process of boiling in aqueous Na_2CO_3 solution as previously described [12]. The resulting SF aqueous solution was concentrated with a rotary evaporator under vacuum at 40°C and ready for preparing the SF-nerve guidance conduit (NGC). A stainless-steel casting mold was used consisting of an inner pillar and an outer tube, both of which were fixed on the mold bottom and which determined the diameter and thickness of SF-NGCs. After SF fibers had been enwound evenly around its inner pillar, the SF solution was

injected into the mold, followed by demolding under lyophilization in a stepwise manner. The resulting SF-NGC was further treated in 80% (v/v) methanol solution for 15 min to achieve SF insolubility in water.

2.2. Preparation of SF-NGC extracts fluid and MTT assay

The SF-NGC, as the extract phase, was placed in DMEM medium (Gibco, Gaithersburg, MD, USA) supplemented with 10% fetal bovine serum (FBS) that served as the extract medium, according to the ratio of 6 cm² of extract phase surface area in 1ml of extract medium. And the extraction was allowed to proceed at 37°C for 72±0.5 h. MTT assay was used to investigate SF-NGC's cytotoxicity evaluation

2.3. Animals and surgical procedures

Adult male Sprague-Dawley (SD) rats, weighing 200~230 g, were randomized into 4 groups (n=24): a SF graft group, an autograft group (served as positive control), a non-grafted group (as negative control) and a normal group.

All animals except those in normal group were anaesthetized by an intraperitoneal injection of 3% sodium pentobarbital solution (30mg/kg body weight) before the sciatic nerve was exposed by making a skin incision and splitting the underlying muscles in the left lateral thigh. A segment of sciatic nerve was resected, leaving a 10-mm long defect following retraction of the nerve ends. In the SF graft group the nerve defect was bridged with the SF graft; in the autograft group the resected nerve segment was reversed 180° and re-implanted as an autologous nerve graft across the nerve defect. After either implant was sutured to both the proximal and distal nerve stumps with 9/0 nylon suture, surgical incisions closed in routine fashion. As to the non-grafted group, the nerve defect was left unbridged. And animals of the normal group underwent no surgery. After surgery all animals were housed and fed routinely.

2.4. Electrophysiological assessment and fluoroGold retrograde tracing

Six months post-implantation, the rat sciatic nerve of the operated side was re-exposed under anaesthesia with sodium phenobarbital. Electrical stimuli were applied to the nerve trunk at its proximal portion and CMAPs were recorded on the gastrocnemius belly at the ipsilateral side. Normal CMAPs were measured at the contralateral unoperated side [13].

2.5. Meyer's trichrome staining, immunohistochemistry and electron microscopy

Six months post-implantation, the regenerated nerve in the place of the graft was harvested, post-fixed and sectioned. A part of nerve sections was subjected to Meyer's trichrome staining. The other sections were allowed to incubate with rabbit anti-NF polyclonal antibody (1:150 dilution, Sigma) at 4°C for 12 hr and were further reacted with the FITC labeled secondary antibody goat anti-rabbit IgG (1:200, Gibco, Grand Island, NY) at room temperature for 6 hr. Different nerve sections were processed for observation and morphometric examination either under a fluorescent microscope (DMR, Leica) after staining or under a transmission electron microscope after pre-treatments.

2.6. Statistics

The data were expressed as means ± SEM and analyzed by using one-way ANOVA with a SPSS13.0 software package (SPSS Inc, Chicago, IL). If there was a significant overall difference existing among groups, pair-wise comparisons were legitimately conducted by using Scheffe's post hoc test. Values of p<0.05 were considered statistically significant.

III. RESULTS AND CONCLUSIONS

3.1. Cytotoxicity evaluation

After the L929 cells were cultivated in the SF-NGC extract fluid and plain medium, respectively, for 48 and 72 hrs, light microscopic visualization revealed that the L929 cells cultured in the two mediums were not obviously different in their morphological appearance throughout the culture process, namely, the L929 cells showed clear edges and shiny, transparent bodies in either medium.

MTT assay results indicated that the viability of the L929 cells cultured in the SF-NGC extract fluid was significantly higher than that in the plain medium at 48 hr after culture initiation, while no significant difference in the cell viability was observed between the two mediums at 72 hr after culture initiation (Figure 1).

The data of MTT assay indicated that after 48 and 72 hrs of culture the relative viability of L929 cells in the SF-NGC extract fluid, as compared to the control, was larger than 100%, suggesting the non-cytotoxicity of the SF-NGC (grade 0) in accordance with the U.S. Pharmacopeia (USP) guidelines.

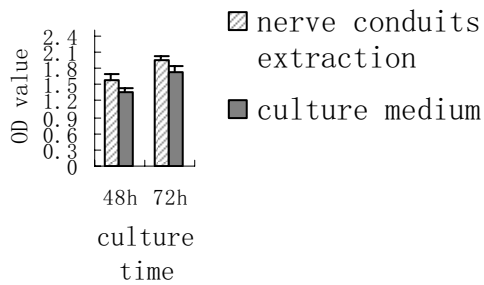


Figure 1 The changes in the cell viability of the L929 cells after they were cultured in the plain DMEM medium or silk nerve conduits extraction fluid for 48 or 72 hrs, respectively. * $p < 0.05$.

3.2. Unique microstructure and performance of SF-NGC

In order to prepare a SF-NGC that accords with the requirements of nerve regeneration in the aspects of mechanical property, permeability, biocompatibility and biodegradability, it is necessary, to design and adopt suitable processing procedures despite two conventional tubulation techniques available for choice. One technique is to inject the SF solution into a casting mold followed by demolding through lyophilization, but the resulting conduit is very fragile with poor mechanical properties, especially minimal compressive and tensile strength under wet conditions, despite their good shape. Another technique is to prepare conduits from the SF fibers by using the technique of hollow fabric weaving, but the resulting conduit is flat in shape, easily crushed and difficultly degraded in the body despite their quite good tensile strength. After having tried these two processing techniques with respective limitations, we drew the inspiration from the unique microstructure of eggshells, which provides a special mechanical protection and a controlled material exchange medium in favor of embryonic development. The uncanny anti-compression feature of spherical eggshells, which benefits from natural selection in biological evolution, can probably be understood by analogy with the thin-shell roof (self-supporting dome) that are more stable than the flat or pointed roof, especially for large-span roof buildings. The layered and micro-porous structure of eggshells, on the other hand, is responsible for their respiration process by which the exchange of materials is conducted for delivering nutrients and oxygen to and carrying away wastes and carbon dioxide from the developing embryo. Therefore, in order to address the coexistence of rigidness and permeability we developed a biomimetic design of SF grafts by biomimicking the eggshell structure. In brief, a little number of SF fibers was pre-introduced into the mold, exerting the function of a stiffener. Then SF aqueous solution was injected into the mold

followed by shaping and demolding under lyophilization to obtain the SF composite conduits.

SF-NGCs shows a comparison of SEM photographs of SF-NGCs (a) and eggshells (b). The two structures exhibit a significant similarity. The SF-NGC presents a hollow, composite channel with a white color of native silk and having an inner diameter of 1.6 mm and a wall thick of 0.75 mm. The inner wall displays a 100- μm -thick netted structure formed by SF fibers of 10 μm diameter, which were spread out as a stiffener (Fig. 1a-A). The outer wall displays a porous structure composed of micropores of 5 to 15 μm diameter (Fig. 1a-B). The size of the micropores within the outer wall is appropriate for material exchange between inside and outside the channel, and also capable of blocking the growth of tissue cells from outside the channel into inside.

The mechanical measurement results indicate that the maximum fracture strength and compressive strength of the SF-NGC are 10.9 ± 0.3 MPa and 27.7 ± 0.8 g respectively under dry conditions, or 5.5 ± 0.4 MPa and 2.5 ± 0.5 g respectively under wet conditions. The animal tests have demonstrated that such good mechanical properties, which benefit from the eggshell-like microstructure, render it possible for the SF-NGC to resist the muscular contraction and keep its cylindrical shape unchanged within a considerable periods after implantation into the body.

3.3. Evaluation of implantation with SF grafts into the rat sciatic nerve defect

In this study, the SF graft consisting of a SF-NGC inserted with SF filaments was used to bridge a 10-mm long sciatic nerve defect of the rats in the SF graft group, and the effects of nerve regeneration were investigated by a range of morphologic and functional assessments as compared to the autograft group and non-grafted group which were served as positive and negative controls respectively. The general observation during 6-month after implantation revealed that there were no conspicuous signs of systematic or regional inflammation observed in the rats of the SF graft group and the locomotor function of their injured limbs was gradually recovered. Blood routine tests indicated that the total and differential leucocyte counts for the SF graft group were not significantly different from either control animals. These results suggest good in vivo biocompatibility of the SF grafts in virtue of poor immunogenic response and little immune rejection elicited following their implantation into the body, which is in agreement with the previous reports on foreign body response to silk-based materials [14].

The peripheral nerve defect treated in this study was from sciatic nerve, the largest single nerve trunk of the animal. At 6 months after implantation, the SF graft was

replaced by a tissue with nerve-like appearance, which passed through the 10-cm long sciatic nerve defect and linked up both stumps, and no infiltration of inflammatory cells was seen in both ends of the graft. Intriguingly, the graft was about to start degradation after 6 months. In our work, SF was first dissolved into an aqueous solution, thus inducing the lowering of its molecular weight and the change in protein conformation with the protease cutting sites partially exposed and microporous spatial structure formed. An accelerated degradation of the graft might probably be ascribed to an increase in the susceptibility of SF to proteolytic enzymes and an enhancement in the moderate foreign body response which is required as the main mechanism for degeneration and absorption *in vivo* [14, 15].

For the SF graft group, Meyer's trichrome staining indicated the formation of many small, thin myelin sheaths for the regenerated nerve; anti-neurofilament immunocytochemistry confirmed the co-existence of myelinated and un-myelinated nerve fibers; and transmission electron microscopy further described the morphometric features of regenerated myelinated fibers. This suggests reconstruction of the sciatic nerve defect in rats at 6 months post implantation.

Since the amplitude of the compound muscle action potential (CMAP) is directly proportional to the number of nerve fibers innervating the target muscle and allows the conduction velocity of motor nerve to be calculated, CMAP examinations offer an important index for the conduction function of peripheral nerve. In this study, the recorded CMAP amplitudes for the animals in the SF graft and autograft groups are 4.68 ± 2.92 and 6.10 ± 2.39 mV, respectively, showing no significant difference between them despite a significantly decrease when both of them are compared to the normal CMAP amplitude value (11.94 ± 3.52 mV) recorded at the contralateral unoperated side. This suggests that the recovery level of electrophysiological properties in the SF graft-implanted rat was close to that in the autograft-implanted rat.

For the SF graft group, the FluoroGold (FG) retrograde tracing revealed that the FG labeled neuron cell bodies were found within both dorsal root ganglions (DRGs) and anterior horn of gray matter in the spinal cord ipsilateral to the operated side at 6 months post-implantation. This confirms a completeness of the regenerated nerve pathway and axonal transport function of regenerated nerve fibers, and there is no significant difference found either in the percentage of retrogradely labelled DRG sensory neurons or in the number of retrogradely labelled anterior horn motoneurons between the SF graft and autograft groups.

3.4. Conclusion

On the basis of our previous work that shows a high neuro-biocompatibility of SF materials *in vitro* [36], here we developed a novel biomimetic design of the SF graft which was composed of a SF-nerve guidance conduit (NGC) inserted with oriented SF fibers. The SF-NGC prepared via well-established procedures exhibits an eggshell-like microstructure that is responsible for its favorable mechanical and permeable properties. The results suggested the non-cytotoxicity of the SF-NGC with grade 0 as per the U.S. Pharmacopeia guidelines, and indicated that the SF graft was quite biocompatible with the surrounding tissues and cells. The SF graft was implanted into the rat sciatic nerve injury across a 10-mm long defect. The morphological and functional investigation after 6 months has given a positive evaluation on the nerve repair outcome elicited by SF grafts which is approaching that by nerve autografts. The further work on improving the design of SF grafts such as an introduction of neurotrophic factors or seeding cells will be attempted in order to establish a possibility of using SF grafts as a suitable alternative to nerve autografts for peripheral nerve regeneration.

ACKNOWLEDGMENT

The financial supports of the Hi-Tech Research and Development Program of China (863 Program, Grant no. 2006AA02A128), the Nature Science Foundation of china (Grant no. 30770585), Basic Research Program of Jiangsu Education Department (Grant no. 07KJA31025) and Program for New Century Excellent Talents in University are gratefully acknowledged (Grant no. NCET-07-0466).

REFERENCES

1. Wurm FM. (2003) Human therapeutic proteins from silkworms. *Nat Biotechnol* 22:34-35.
2. Postlethwait RW. (1970) Long-term comparative study of nonabsorbable sutures. *Ann Surg* 171:892-898.
3. Sofia S, McCarthy M, Gronowicz G, et al. (2001) Functionalized silk-based biomaterials for bone formation. *J. Biomed Mater Res A* 54(1):139-148.
4. Altman GH, Horan RL, Lu HH, et al. (2002) Silk matrix for tissue engineered anterior cruciate ligaments. *Biomaterials* 23(20):4131-41.
5. Altman GH, Diaz F, Jakuba C, et al. (2003) Silk-based biomaterials. *Biomaterials* 24(3):401-16.
6. Ducker TB, Hayes G.J. (1970) Peripheral nerve grafts: experimental studies in the dog and chimpanzee to define homograft limitations. *J Neurosurg* 32:236-43.
7. Madison RD, Silva C, Dikkes P, et al. (1987) Peripheral nerve regeneration with entubulation repair: Comparison of biodegradable nerve guides versus polyethylene tubes and the effects of a laminin-containing gel. *Exp Neurol* 95:378-390.

8. Beris A, Lykissas M, Korompilias A, et al. (2007) End-to-Side Nerve Repair in Peripheral Nerve Injury. *J Neurotrauma* 24:909-916.
9. Wang X, Hu W, Cao Y, et al. (2005) Dog sciatic nerve regeneration across a 30-mm defect bridged by a chitosan/PGA artificial nerve graft. *Brain* 128:1897-1910.
10. Bellamkonda RV. (2006) Peripheral nerve regeneration: An opinion on channels scaffolds and anisotropy. *Biomaterials* 27:3515-3518.
11. Jiang BG, Yin XF, Zhang DY, et al. (2007) Maximum number of collaterals developed by one axon during peripheral nerve regeneration and the influence of that number on reinnervation effects. *Eur Neurol* 58:12-20.
12. Yang Y, Chen X, Ding F, et al. (2007) Biocompatibility evaluation of silk fibroin with peripheral nerve tissues and cells in vitro. *Biomaterials* 28:1643-1652.
13. Suzuki Y, Tanihara M, Ohnishi K, et al. (1999) Cat peripheral nerve regeneration across 50 mm defect repaired with a novel nerve guide composed of freeze-dried alginate gel. *Neurosci Lett* 259: 75-8.
14. Lorenz M, Hofmann S, Karageorgiou V, et al. (2005) The inflammatory responses to silk films in vitro and in vivo. *Biomaterials* 26, 147-155.
15. Panilaitis B, Altman GH, Chen J, et al. (2003) Macrophage responses to silk. *Biomaterials* 24:3079-3085.

Author: Xiaosong Gu
Institute: Nantong University
Street: 19 Qixiu Road, Nantongcity China
Email: neurongu@public.nt.js.cn

Synthesis and Gene Transfection Efficiency of PEG-chitosan-PEI copolymers

Wei Zhang¹, Shi-rong Pan¹, Yu-ting Wen² and Xin Luo²

¹ First Affiliated Hospital, Sun Yat-Sen University, Guangzhou, China

² School of Pharmaceutical Science, Sun Yat-Sen University, Guangzhou, China

Abstract — PEG-chitosan-PEI copolymer was synthesized by ring-opening reaction of ethylenimine monomers with PEG-chitosan. PEG-chitosan was prepared before by an imine reaction between chitosan and mPEG-CHO. With the aim to investigate the gene transfection properties of PEG-chitosan-PEI, we investigated its cytotoxicity by MTT assay, DNA compaction ability by agarose gel retardation, and transfection efficiency of pEGFP in vitro. The results showed higher transfection efficiency and lower cytotoxicity of PEG-chitosan-PEI than PEI(25k) which is a popular gene vector.

Keywords — Chitosan, PEI, PEG, Gene vector, Gene delivery

I. INTRODUCTION

Chitosan, a kind of natural polysaccharide, has been proposed as a biocompatible material and to be suitable for gene delivery[1,2]. However, its low solubility at physical condition and relatively low transfection efficiency among cationic polymers hindered its application. Poly(ethylene glycol) (PEG) is a hydrophilic and biocompatible polymer used widely in biomaterials. Modification of PEG can help enhance water solubility, decrease aggregation, and decrease hemolytic activity[3]. Polyethylenimine(PEI), has been extensively studied as non-viral gene delivery system[4,5], for its efficiency gene transfection efficiency. Copolymer PEG-chitosan-PEI as a gene vector has not been reported before.

II. MATERIALS AND METHODS

A. Materials:

Chitosan (molecular weight 5k and 20kDa, degree of acetylation 90%) was a gift from Golden-Shell Co., LTD., Zhejiang, China. mPEG (monomethoxy polyethylene glycol, molecular weight 5kDa) was purchased from FLUKA. TCCA (Trichlorisocyanuric acid, 97%), and TEMPO (2,2,6,6-Tetramethylpiperidin-1-yloxy, free radical, 98%) from ALDRICH. Other reagents were from Guangzhou Chemical reagent factory, China. Plasmid pEGFP(4.7kb) encoding green fluorescent protein (a gift from West China

Center of Medical Science) was propagated in Escherichia coli and purified by a QIAGEN(Chatsworth, Calif) kit.

B. Synthesis and characterization of PEG-chitosan-PEI copolymer:

Firstly, mPEG was oxidated by TCCA in the presence of TEMPO, to reduce mPEG-CHO. Then mPEG-CHO was reacting with chitosan in an acid solution for the combination of amino groups on chitosan and aldehyde groups of mPEG-CHO. The product was dialyzed in water (MWCO=12,000) to remove unreacted PEG molecules. Secondly, mPEG-chitosan copolymer was dissolved in a slightly acidic solution and was added in freshly prepared ethylenimine monomers[6]. The ethylenimine monomers were ring-opened and polymerized from the amino groups on chitosan chains and resulted in a PEG-chitosan-PEI copolymer. The resulting solution was dialyzed in water (MWCO=12,000) to remove low molecular weight PEI and some other micromolecules. Copolymers PEG-chitosan and PEG-chitosan-PEI were characterized by ¹HNMR.

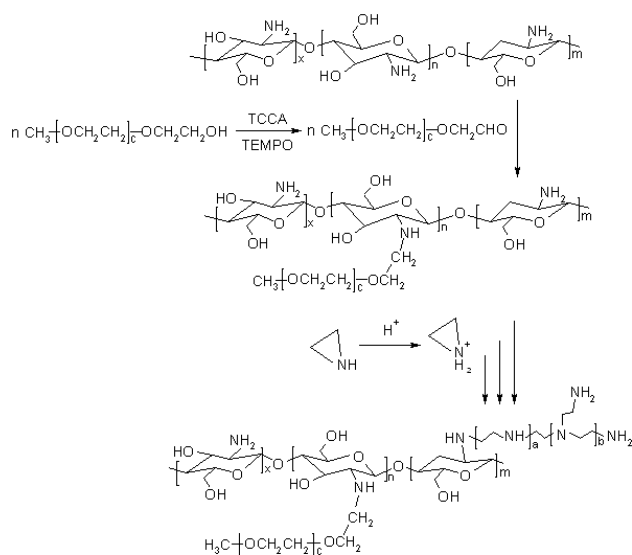


Fig. 1 Schematic Representation of the Preparation of PEG-chitosan-PEI

C. Cytotoxicity of PEG-chitosan-PEI copolymers by MTT assay:

The cytotoxicity of PEG-chitosan-PEI on HeLa cells was carried out on the basis of an MTT assay. HeLa cells were seeded in 96-well plates at an initial density of 10,000 cells per well. Cells were incubated with RPMI 1640 complete medium for 24h. The PEG-chitosan, PEG-chitosan-PEI or PEI(25k) solution was added to the media at different concentrations and incubated with HeLa cells for 24h. Each dosage was replicated in 4 wells. MTT reagent(in PBS, 5mg/ml) was added 20 μ L to each well, and the cells were incubated for another 4h. DMSO (150 μ L/well) was added, and the plate was slightly vibrated until all purple crystals dissolved in DMSO. The absorbance at 620nm of the solution in each well was recorded by a Microplate Reader (Bio-Rad). Cell viability was calculated according to the following equation:

$$\text{Cell viability (\%)} = (\text{OD}_{\text{sample}} / \text{OD}_{\text{control}}) \times 100$$

OD_{sample} is the absorbance of the solution of the cells cultured with polymers, and OD_{control} is the absorbance of the solution of the cells with the medium only.

D. Preparation of PEG-chitosan-PEI/DNA polyplexes:

PEG-chitosan-PEI copolymers and DNA were diluted in deionized water to a chosen concentration. The two solutions were mixed and vortex for several seconds and standing for at least 30 minutes. A 9 μ L sample of the polyplexes solution mixed with 1 μ L of 10 \times loading buffer was loaded to a 0.9% agarose gel. The electrophoresis was performed in a Tris-acetate (TAE) running buffer at 80V for 50min. DNA bands were visualized by an UV(254nm) illuminator and photographed.

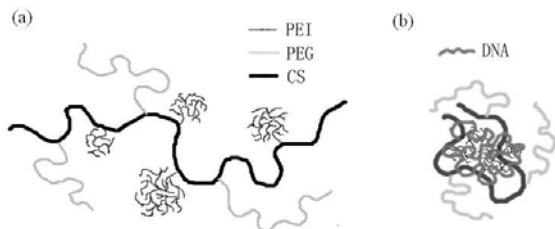


Fig. 2 Structure of (a) PEG-chitosan-PEI and (b) PEG-chitosan-PEI/DNA polyplex

E. Transfection efficiency of PEG-chitosan-PEI copolymers on HeLa cells:

The transfection efficiency of pEGFP mediated by PEG-chitosan-PEI on HeLa cells was visualized by fluorescence microscope (Olympus) and detected by flow cytometry. HeLa cells were seeded in 12-well plates at an initial density of 1.8×10^5 per well. Cells were incubated with RPMI 1640 complete medium for 24h in order to get a confluence of about 70%. Then the medium was replaced with 1ml of fresh complete 1640 medium. The polyplexes of PEG-chitosan-PEI/DNA prepared as described above were added and incubated for 48h. The transfection medium was replaced with 1ml of fresh complete medium, and the cells were incubated for another 48h to make sure a total expression of GFP.

III. RESULTS AND DISCUSSION

Successful synthesis of PEG-chitosan and PEG-chitosan-PEI copolymer were improved by ^1H NMR, as Fig.2 shows.

The cytotoxicity of PEG-chitosan-PEI was compared with that of PEG-chitosan and PEI(25k Da). As illustrated in Fig. 3, the toxicity of the polymers was concentration dependent. While PEI reduced cell viability dramatically, PEG-chitosan-PEI copolymer showed less cytotoxicity on cells. PEG-chitosan had slightly influence on cell viability, indicating that the toxicity of PEG-chitosan-PEI was mainly due to its PEI moiety.

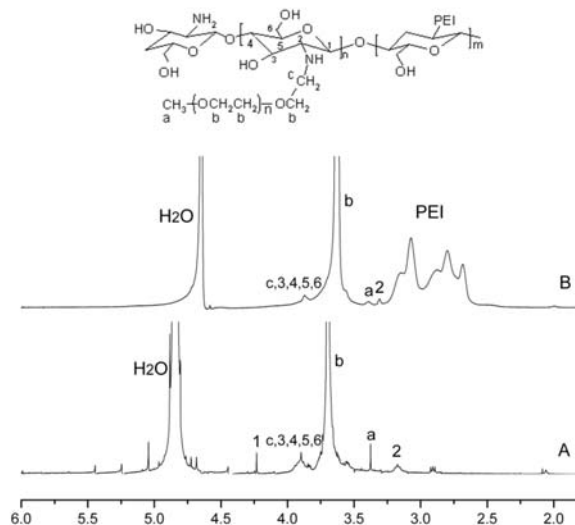


Fig. 3 ^1H NMR spectra of (A) PEG-chitosan and (B) PEG-chitosan-PEI in D_2O .

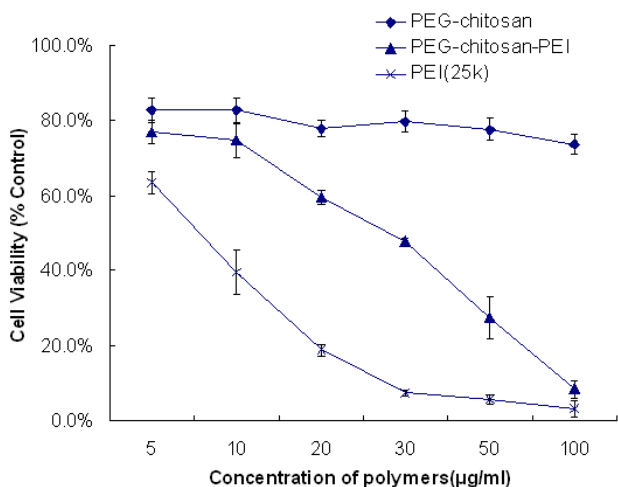


Fig. 4 Cell viability of 24h incubation with PEG-chitosan-PEI, PEG-chitosan, and PEI(25k Da).

The agarose gel electrophoresis was performed to detect the formation of PEG-chitosan/DNA or PEG-chitosan-PEI/DNA polyplexes and at which N/P ratio (the ratio of the number of primary amines on chitosan to the number of phosphate groups on DNA) the plasmid DNA was totally encapsulated by the copolymer.

As Fig.4 shows, both PEG-chitosan and PEG-chitosan-PEI had the ability to compact plasmid DNA. PEG-chitosan-PEI copolymer could totally encapsulate DNA at N/P ratio ≥ 3 . To compare with, PEG-chitosan could totally encapsulate DNA at N/P ratio ≥ 7 . The addition of PEI efficiently enhanced DNA compaction ability of PEG-chitosan.

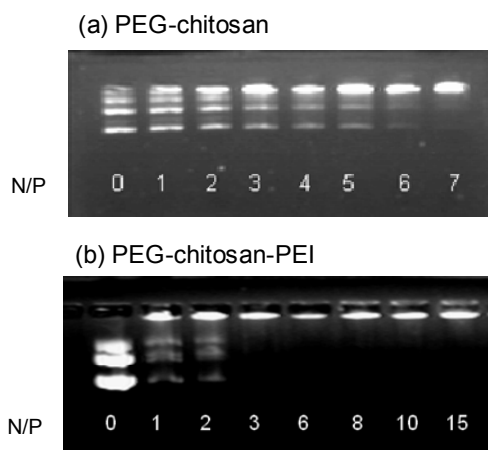


Fig. 5 Agarose gel retardation assay of (a)PEG-chitosan/DNA and (b)PEG-chitosan-PEI/DNA polyplexes

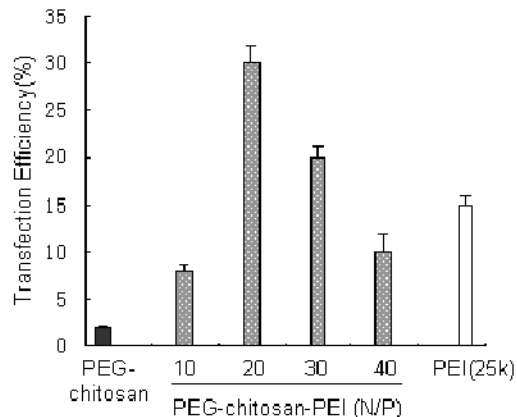


Fig. 6 Gene transfection efficiency of PEG-chitosan-PEI, PEG-chitosan and PEI(25k) for HeLa cells.

Gene transfection efficiency of PEI(25k) was always used as a positive control to evaluate a novel gene vector[7,8], for the reason that PEI(25k) was one of the most efficient and popular gene vector.

Fig.6 shows the efficient transfection ability of PEG-chitosan-PEI, comparing with PEI(25k) and PEG-chitosan. The highest transfection efficiency achieved was PEG-chitosan-PEI at N/P ratio 20. However, at N/P ratio 30 and 40 the transfection efficiency of PEG-chitosan-PEI decreased, due to the dosage dependent cytotoxicity. The transfection efficiency of PEI(25k) or PEG-chitosan showed in this figure was its optimal transfection efficiency in this experiment. It was much less than the optimal one of PEG-chitosan-PEI(at N/P 20).

IV. CONCLUSIONS

In this study, we prepared copolymer PEG-chitosan-PEI, and investigated its cytotoxicity, DNA compaction ability, and gene transfection efficiency. It was found that PEG-chitosan-PEI was more cytotoxic than PEG-chitosan, but had enhanced DNA compaction ability and raised gene transfection efficiency. To compare with PEI(25k), PEG-chitosan-PEI showed less cytotoxicity but higher gene transfection efficiency. It was concluded that PEG-chitosan-PEI was an efficient and promising gene vector.

ACKNOWLEDGMENT

This work was financially supported by National Natural Science Foundation of China (30570500).

REFERENCES

1. Sato T, Ishii T, Okahata Y (2001) In vitro gene delivery mediated by chitosan. *Biomaterials* 22:2075-2080
2. Hashimoto M, Morimoto M, Saimoto H. et al. (2006) Lactosylated chitosan for DNA delivery into hepatocytes. *Bioconjugate Chem* 17:309-316
3. Petersen H, Fechner P M, Fischer D. et al. (2002) Synthesis, characterization, and biocompatibility of polyethylenimine-graft-poly(ethylene glycol) block copolymers. *Macromolecules* 35:6867-6874
4. Boussif O, Lezoualc'h F, Zanta M A. et al. (1995) A versatile vector for gene and oligonucleotide transfer into cells in culture and in vivo: polyethylenimine. *Proc Natl Acad Sci* 92:7297-7301
5. Neu M, Fischer T, Kissel T (2005) Recent advances in rational gene transfer vector design based on poly(ethylene imine) and its derivatives. *J Gene Med* 7:992-1009
6. Wenker H. (1935) The preparation of ethylene imine from monoethanolamine. *J Am Chem Soc* 57:2328
7. Neu M, Germershaus O, Behe M. et al. (2007) Bioreversibly crosslinked polyplexes of PEI and high molecular weight PEG show extended circulation times in vivo. *J Control Release* 124:69-80
8. Hong W J, Park J H, Huh K M. et al. (2004) PEGylated polyethylenimine for in vivo local gene delivery based on lipidolized emulsion system. *J Control Release* 99:167-176

Author: Shi-rong Pan
Institute: First Affiliated Hospital, Sun Yat-Sen University
Street: Zhongshan Rd II
City: Guangzhou
Country: China
Email: gzpshr@163.com

Preparation and physicochemical characteristics of self-assembled nanoparticles of cholesterol succinate modified pullulan conjugates

Wen-Zhi Yang¹, Qi-Qing Zhang^{1,2*}, Hong-Li Chen¹, Xue-Ming Li¹, Qian Jiang¹, Min-Mao Chen¹, Fu-Ping Gao¹, Hui-Zhu Zhang¹

¹Institute of Biomedical Engineering, Chinese Academy of Medical Science & Peking Union Medical College, 236 Baidi Road, Tianjin 300192, PR China

²Research Center of Biomedical Engineering, Xiamen University, 168 DaXue Road, Xiamen 361005, PR China

Abstract — A series of cholesterol-modified pullulan (CHSP) conjugates with different degrees of substitution (DS) of cholesterol moiety were synthesized by the succinyl linkages and characterized by Fourier transform infrared (FTIR) and proton nuclear magnetic resonance (¹H NMR). CHSP conjugates were amphiphilic in nature and their self-aggregation behavior in aqueous media was evaluated by the fluorescence probe technique. CHSP self-aggregated nanoparticles were prepared by dialyzed in water and analyzed by dynamic laser light-scattering (DLS), zeta potential and transmission electron microscopy (TEM) technologies.

Keywords — cholesterol succinate modified pullulan; Self-assembled nanoparticle

I. INTRODUCTION

The nanoparticles prepared from amphiphilic polymers find significant applications in life sciences as clinical diagnostic assays, drug delivery systems and so forth [1,2]. The formation of self-assembled nanoparticles is theorized by a free energy-minimized structure in the aqueous media, which consists of a polycore of hydrophobic moieties and an outer shell of hydrophilic groups [3,4]. These polymeric micelles or micelle like aggregates have been recognized as a promising drug carrier, because their hydrophobic domain, surrounded by hydrophilic outer shell, can serve as a preservatory for various hydrophobic drugs [5,6]. Therefore, many efforts have been made for the past decades to develop some novel polymeric amphiphiles such as amphiphilic block copolymers [7-11] and hydrophobically modified water-soluble polymers [12,13] which can self assemble to form compact micellar structure in the aqueous media.

In recent years, natural polysaccharides, such as chitosan, dextran and pullulan, have been hydrophobically modified with the long alkyl chains or cholesteryl groups, to form micelles or nanoparticles for being used as the controlled drug delivery systems or gene carriers[14-23].

Pullulan, a biodegradable polysaccharide first described in 1959, is a water-soluble extra cellular neutral glucan synthesized by a fungus *Aureobasidium pullulans* [24]. The structure of pullulan predominantly consists of maltotriose units linked via α -1,6 glycosidic bonds and mainly used as a food additive now. Pullulan has several advantages as a macromolecular drug carrier. It is highly water-soluble and non-toxic, has multiple hydroxyl groups that can readily be chemically modified, lacks immunogenicity, and is useful as a plasma expander.

Several researchers have modified the pullulan with palmitoyl or cholesteryl moieties [25-28]. In the past investigation, pullulan was modified with cholesterol moiety by the hexamethylene diisocyanate as a arm and in this reaction 1,4-diazabicyclo(2,2,2)octane was used as a catalyst. It had been known that cholesterol and succinic acid are natural compound existing in the human body and cholesterol has the hydrophobic property due to the presence of hydrophobic moieties such as cyclopentenophenanthrene nucleus in its molecule. Our purpose was to synthesize hydrophobically modified pullulans with a properly hydrophobic modification ratio, and with hydrophobic chains grafted through ester linkages to favor degradability. It was expected that the introduction of cholesterol succinate (CHS) moieties into the pullulan molecule would induce association to form self-assembled nanoparticles.

II. MATERIALS AND METHODS

2.1. Materials

pullulan (Mw 200 000) was purchased from Hayashibara Tokyo. (Japan). 4-dimethylaminopyridine (DMAP) and 1-ethyl-3-[3-(dimethylamino) propyl] carbodiimide (EDC) were purchased from Sigma Co. (St. Louis, MO, USA); pyrene were purchased from Aldrich Co. (Milwaukee, WI). All other chemical reagents were of analytical grade and obtained from commercial sources.

2.2. Synthesis of cholesterol succinate

Synthesis was carried out according to the method reported by Shaikh VAE [29]. Briefly, cholesterol (5.0 g, 13.0 mmol) was mixed with succinic anhydride (3.6 g, 36.0 mmol) in 20 mL of pyridine. After reaction for 48 h at 50°C, the mixture was precipitated in the ice dilute hydrochloric acid solution. The white powder of CHS (4.8 g, 9.8 mmol) was obtained by recrystallization in tetrahydrofuran (THF) and ethanol.

2.3. Cholesterol succinate modified pullulan (CHSP)

The pullulan power (0.5 g) was dispersed in 30 mL dried DMSO by sonication in ultrasonic bath. The cholesterol succinate (CHS) in dried DMSO were activated by addition EDC (1.5 equiv CS) and DMAP (1 equiv CS). Different amounts of activated CHS (0.05-0.30 mol/mol sugar residues of pullulan) were added into the dried DMSO solution containing pullulan. The mixture was reacted by stirring for 48 h at 45°C. Then, the reactant mixture was poured into ethanol and the precipitate was collected by filtration and washed with ethanol, THF and acetone, respectively. Then, the sample was vacuum drying to obtain CHSP conjugates. The chemical structure of CHSPs was confirmed using ¹H NMR (DMSO-d₆), 500 MHz.

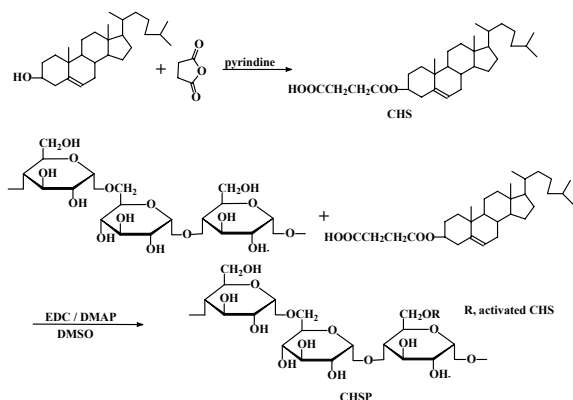


Figure 1. Synthetic route of CHSP

Figure 1. Synthetic route of CHSP

2.4. Determination of CHSP degree of substitution

The degree of substitute (DS) of cholesterol residues per 100 glucose units in pullulan could be calculated by proton nuclear magnetic resonance (VARINA INOVA 500 MHz, USA) using DMSO-d₆ as the solvent.

2.5. Preparation of self-assembled nanoparticles

CHSP self-aggregated nanoparticles were prepared by dialysis method. Briefly, CHSP was dissolved in DMSO, then the solution injected in dialysis bag and repeat changing the distilled water every 8h in 3days. followed by sonication using a probe type sonifier (Automatic Ultrasonic Processor UH-500A, China) at 100W for 1 min.

To observe the morphology of CHSP self-aggregated nanoparticles, sample solutions (1 mg/mL) were dropped onto the carbon-coated 300 mesh copper grids. Then, the grids were air-dried and imaged using a transmission electron microscope (TEM; JEM-100C XII, Japan) at an accelerating voltage of 80 kV. The particle size of the polymeric micelles was measured with dynamic laser light scattering (DLS; BI-90US, Japan).

2.6. Measurement of fluorescence spectroscopy

The self-aggregate property of CHSP conjugates and their critical aggregation concentration (cac) were estimated by the probe fluorescence technique in which pyrene was used as a hydrophobic probe. Briefly, a known amount of pyrene solutions (3×10^{-4}) in acetone were added to a series of vials, and followed evaporation to remove the acetone. Then, various concentrations of CHSP conjugate suspension were added to each vial and sonicated in an ultrasonic bath (AS5150A, China) for 1 h to equilibrate the pyrene and the nanoparticles. The final concentration of pyrene was 6.0×10^{-7} mol/L. The emission spectra of pyrene were recorded in the range of 350–480 nm using a fluorescence spectrophotometer (Shimadzu RF-4500, Japan) at the excitation wavelength (kex) of 334 nm and an integration time of 1 s/nm and the slit opening for excitation and emission was set at 5 and 2.5 nm, respectively.

III. RESULTS AND DISCUSSION

3.1. Synthesis and characterization of CHSP

The cholesterol moieties were grafted onto pullulan molecule by succinic anhydride as a linker. Succinic anhydride reacted with the hydroxyl group of cholesterol to produce cholesterol succinate. Then, the primary hydroxyl of pullulan reacted with cholesterol succinate to obtain CHSP. Degree of substitute of cholesterol could be controlled by the feed ratio of CHS to pullulan.

3.2. Synthesis and characterization of CHS

The FTIR spectra of cholesterol and CHS, the characteristic absorption bands of cholesterol, which appeared at 3380 cm⁻¹, is assigned to -OH groups. For the cholesterol succinate, as compared with cholesterol, two new absorption bands at 1730 cm⁻¹ and 1709 cm⁻¹ were observed and one absorption bands at 3380 cm⁻¹ was disappeared. The former was ascribed to C=O stretch of succinyl group, and the latter was assigned to no -OH group in CHS. These results are evidence of the synthesis of CHS.

¹H NMR (CDCl₃ with TMS, ppm): 0.67 (3H, s, cholesterol 18-H3), 0.8–2.4 (28H, cholesterol 1-H2, 2-H2, 4-H2, 7-H2, 8-H1, 9-H1, 11-H2, 12-H2, 14-H1, 15-H2, 16-H2, 17-H1, 20-H1, 22-H2, 23-H2, 24-H2 and 25-H1), 0.86 (6H, d, J = 9 Hz, cholesterol 26-H3 and 27-H3), 0.91 (3H, d, J = 7 Hz, cholesterol 21-H3), 1.02 (3H, s, cholesterol 19-H3), 2.60 (2H, m, COCH₂), 2.68 (2H, m, CH₂CO), 4.63 (1H, m, cholesterol 3-H1), 5.37 (1H, m, cholesterol 6-H1).

3.3. Synthesis and characterization of CHSP

The ¹H-NMR spectra of pullulan and CHSP, the signals displayed at 4.68 and 5.00 ppm correspond to the protons of C1 position of α-1,6 and α-1,4 glycosidic bonds, respectively. The identification of the protons corresponding to the pullulan chain at: 0.40-2.40 (the H signal of cholesterol), 2.49 (DMSO-d₆) and 2.53 (2 methylene groups, -OCH₂CH₂O-) ppm. Therefore, the degree of substitute (DS) of cholesterol residues per 100 glucose units in pullulan could be calculated by comparing the ratio of methylene groups protons (2.53 ppm) to sugar protons (C1 position of α-1,6 and α-1,4 glycosidic bonds, 4.678 and 5.001 ppm). The DS could be determined calculated by follows:

$$DS = \frac{I_{2.53 \text{ ppm}}}{4(I_{\alpha-1,4, 5.00 \text{ ppm}} + I_{\alpha-1,6, 4.68 \text{ ppm}})} \times 100\%$$

3.4. Self-aggregation of CHSP

The sizes and size distributions of self-assembled nanoparticles of CHSP conjugates in the aqueous media with different DS were measured by DLS. The mean sizes of self-assembled nanoparticles were in the range of 62~74 nm, which depending on the DS value. The size of self-assembled nanoparticles increased as the DS increasing.

Table 1 Characterization of CHSP conjugates in distilled water

sample	Ratio	DS	d(nm)	variance	cac (mg/mL)
CHSP1	1/10	5.37	62	0.272	0.038
CHSP2	3/20	5.40	69	0.312	0.018
CHSP3	1/5	5.70	74	0.281	0.0076

Ratio, The mmol ratio of CHS and pullulan.

DS, Degree of substitution of cholesterol, determined by ¹H NMR.

d, Mean diameter and variance in distilled water determined by dynamic light scattering (θ = 90°).

cac, Critical aggregation concentration in distilled water determined from pyrene emission spectra.

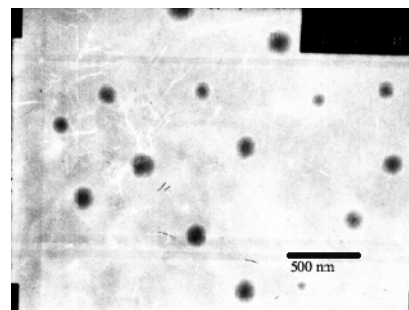


Figure 2. TEM images of self-aggregated nanoparticles prepared from CHSP2 by probe sonication in water.

3.5. Critical aggregation concentration of self-assembled nanoparticles

The fluorescence emission spectra of pyrene in CHSP self-assembled nanoparticles incorporated into various concentrations of in distilled water after dialysis. When pyrene coexists with self-aggregates in the aqueous media, the total emission intensity increases with the increase of CHSP concentration, especially the intensity of the third highest vibrational band at 383 nm (I₃) starts to drastically increase at a certain concentration of polymeric amphiphiles. The critical aggregation concentration (cac), defined as the threshold concentration of selfaggregation of polymeric amphiphiles by intra- and/or intermolecular association, can be determined by measuring the intensity ratio (I₁/I₃) of the first and the third highest energy bands in the emission spectra of

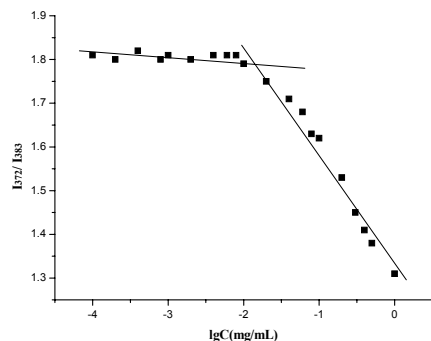


Figure 3. Intensity ratio (I1/I3) from emission spectra vs. logC of CHSP1 self-aggregates.

pyrene. Fig. 3 illustrates the changes of the I1/I3 values as a function of CHSP1 concentration. At low concentration of polymeric amphiphiles, the I1/I3 values are close to the value (1.80) for pyrene in water, and followed by a linear decrease with the addition of polymeric amphiphiles. The cac values of the CHSPs conjugates decreased with the increase in the content of hydrophobic CHS because of enhanced hydrophobicity (Table 1).

IV. CONCLUSIONS

Cholesterol modified pullulan conjugates, a novel kind of polymer amphiphiles, were synthesized and characterized by FTIR and ^1H NMR. CHSP self-assembled nanoparticles were prepared by the probe sonication method and their physicochemical properties in the aqueous media were investigated. The mean diameters of CHSP self-assembled nanoparticles were in the range of 62–74 nm with a unimodal size distribution. The zeta potentials of CHSPs self-assembled nanoparticles were nearly neutral in distilled water. The TEM images of self-aggregates showed a spherical shape. The critical aggregation concentration of CHSP conjugates depended on the DS of cholesterol over a range of 0.0067–0.038 mg/mL. This novel nanoparticle system may be useful in the pharmaceutical and biomedical fields, especially being used as the delivery of anti-tumor drugs, and the further investigations are in progress.

ACKNOWLEDGMENT

This project was supported by the Major State Basic Research Program of China (grant no. 2006 CB 933300) and the Doctoral Fund of Ministry of Education of China (grant no. 96002323).

REFERENCES

- Gref, R., minamitake, Y., Peracchia, M. T., Trubetskoy, V., Torchilin, V., & Langer, R. (1994). Biodegradable long-circulating polymeric nanospheres. *Science*, 263, 1600-1603.
- Kataoka, K., Harada, A., & Nagasaki, Y. (2001). Block copolymer micelles for drug delivery: Design, characterization and biological significance. *Advance Drug Delivery Review*, 47, 113-131.
- Mortensen, K. (2001). Structural properties of self-assembled polymeric aggregates in aqueous solutions. *Polymer Advance Technology*, 12(1-2), 2-22.
- Nagasaki, Y., Yasugi, K., Yamamoto, Y., Harada, A., & Kataoka, K. (2001). Sugar-installed block copolymer micelles: Their preparation and specific interaction with lectin molecules. *Biomacromolecules*, 2, 1067-1070.
- Kataoka, K., Harada, A., & Nagasaki, Y. (2001). Block copolymer micelles for drug delivery: Design, characterization and biological significance. *Advance Drug Delivery Review*, 47, 113-131.
- Nakanishi, T., Fukushima, S., Okamoto, K., Suzuki, M., Matsumura, Y., Yokoyama, M., et al. (2001). Development of the polymer micelle-carrier system for doxorubicin. *Journal of Controlled Release*, 74, 295-302.
- Nakanishi, T., Fukushima, S., Okamoto, K., Suzuki, M., Matsumura, Y., Yokoyama, M., et al. (2001). Development of the polymer micelle carrier system for doxorubicin. *Journal of Controlled Release*, 74, 295-302.
- Gref, R., minamitake, Y., Peracchia, M. T., Trubetskoy, V., Torchilin, V., & Langer, R. (1994). Biodegradable long-circulating polymeric nanospheres. *Science*, 263, 1600-1603.
- Kabanov, A. V., Nazarova, I. R., Astafieva, I. V., Batrakova, E. V., Alakhov, V. Y., Yaroslavov, A. A., et al. (1995). Micelle formation and solubilization of fluorescent probes in poly (oxyethylene-b-oxypropylene-b-oxyethylene) solutions. *Macromolecules*, 28, 2303-2314.
- Lee, S. C., Chang, Y., Yoon, J., Kim, C., Kwon, I. C., Kim, Y., et al. (1999). Synthesis and micellar characterization of amphiphilic diblock copolymers based on poly (2-ethyl-2-oxazoline) and aliphatic polyesters I. *Macromolecules*, 32, 1847-1852.
- Poppe, A., Willner, L., Allgaier, J., Stellbrink, J., & Richter, D. (1997). Structural investigation of micelles formed by an amphiphilic PEP-PEO block copolymer in water. *Macromolecules*, 30, 7462-7471.
- Huh, K. M., Lee, K. Y., Kwon, I. C., Kim, Y., Kim, C., & Jeong, S. Y. (2000). Synthesis of triarmed poly(ethyleneoxide)-deoxycholic acid conjugate and its micellar characteristics. *Langmuir*, 16, 10566-10568.
- Kim, C., Lee, S. C., Kang, S. W., Kwon, I. C., Kim, Y., & Jeong, S. Y. (2000). Synthesis and the micellar characteristics of poly (ethylene oxide)-deoxycholic acid conjugates. *Langmuir*, 16, 4792-4797
- Miwa, A., Ishibe, A., Nakano, M., Yamahira, T., Itai, S., Jinno, S., et al. (1998). Development of novel chitosan derivatives as micellar carriers of taxol. *Pharmaceutical Research*, 15, 1844-1850.
- Zhang, C., Ping, Q. N., & Zhang, H. (2004). Self-assembly and characterization of paclitaxel-loaded N-octyl-O-sulfate chitosan micellar system. *Colloids and Surfaces B: Biointerfaces*, 39, 69-75.
- Jiang, G. B., Quan, D. P., Liao, K. R., & Wang, H. H. (2006). Preparation of polymeric micelles based on chitosan bearing a small amount of highly hydrophobic groups. *Carbohydrate Polymers*, 66, 514-520.
- Lee, K. Y., Kim, J.-H., Kwon, I. C., & Jeong, S. Y. (2000). Self-aggregates of deoxycholic acid-modified chitosan as a novel carrier of adriamycin. *Colloids Polymer Science*, 278, 1216-1219.

18. Yuan, X. B., Li, H., & Yuan, Y. B. (2006). Preparation of cholesterol-modified chitosan self-aggregates for delivery of drugs to ocular surface. *Carbohydrate Polymers*, 65, 337-345.
 19. Yuan, X. B., Li, H., Zhu, X. X., & Woo, H. G. (2006). Self-aggregated nanoparticles composed of periodate-oxidized dextran and cholic acid: Preparation, stabilization and in vitro drug release. *Journal of Chemical Technology and Biotechnology*, 81, 746-754.
 20. Nichifor, M., & Carpov, A. (1999). Bile acids covalently bound to polysaccharides. I. Esters of bile acids with dextran. *European Polymer Journal*, 35, 2125-2129.
 21. Na, K., & Bae, Y. H. (2002). Self-assembled hydrogel nanoparticles responsive to tumor extracellular pH from pullulan derivative/sulfonamide conjugate: Characterization, aggregation, and adriamycin release in vitro. *Pharmaceutical Research*, 19, 681-688.
 22. Kim, Y. H., Gihm, S. H., & Park, C. R. (2001). Structural characteristics of size-controlled self-assembly nanoparticles of deoxycholic acid-modified chitosan and their application as a DNA delivery carrier. *Bioconjugate Chemical*, 12, 932-938.
 23. Lee, K. Y., Kwon, I. C., Kim, Y.-H., Jo, W. H., & Jeong, S. Y. (1998). Preparation of chitosan self-aggregates as a gene delivery system. *Journal of Controlled Release*, 51, 213-220.
 24. McCarthy, S. P. (1993). Biodegradable polymers for packaging. In C. G. Gebelein (Ed.), *Biotechnological polymers: Medical, pharmaceutical and industrial applications* (pp. 214-222). Lancaster: Technomic Publishing.
 25. P.A. Sivakumar, K. Panduranga Rao. The use of cholesteryl pullulan for the preparation of stable vincristine liposomes. *Carbohydrate Polymers* 51 (2003) 327-332
 26. Kang, E. C., Akiyoshi, K., & Sunamoto, J. (1997). Surface coating of liposomes with hydrophobized polysaccharides. *Journal of Bioactive and Compatible Polymers*, 12, 14-26.
 27. Moreira, J. N., Almeida, L. M., Geraldes, C. F., Madeira, V. M. C., & Costa, M. L. (1997). Carboplatin liposomes with O-palmitoyl pullulan: In vitro characterization. *International Journal of Pharmaceutics*, 147, 153-164.
 28. Sunamoto, J., Sato, T., Hirota, M., Fukushima, K., Hiratani, K., & Hara, K. (1987). A newly developed immunoliposomes-an egg phosphatidylcholine liposomes coated with pullulan bearing both a cholesterol moiety and an IgMs fragment. *Biochimica et Biophysica Acta*, 898, 323-330.
 29. Shaikh, V. A. E., Maldar, N. N., Lonikar, S. V., Rajan, C. R., & Ponrathnam, S. (1998). Thermotropic behavior of cholesterol-linked polysaccharides. *Journal of Applied Polymer Science*, 7, 195-201.
- Author: Wen-Zhi Yang, Qi-Qing Zhang*
Institute: Institute of Biomedical Engineering, Chinese Academy of Medical Science & Peking Union Medical College
Street: 236 Baidi Road
City: Tianjin 300192
Country: PR China
Email: wenzhi_yang@sina.com; zhangqiq@xmu.edu.cn.

Structural investigations of novel triblock cationic copolymer/DNA complexes

Yuting Wen¹, Shirong Pan^{1,2}, Xuan Zhang², Xin Luo^{1,2}, Wei Zhang²

¹ School of Pharmaceutical Sciences, Sun Yat-Sen University, Guangzhou, China

² The First Affiliated Hospital, Sun Yat-Sen University, Guangzhou, China

Abstract — A series of biodegradable triblock copolymers poly (ethylene glycol)-g-polyethylenimine-b-poly (dimethylaminoethyl l-glutamine) (PEG-g-PEI-b-PDMAEG) as novel vectors for gene therapy were synthesized and evaluated. Poly (ethylene glycol)-g-polyethylenimine (PEG-g-PEI) was firstly obtained by linking of PEG and PEI using isophorone diisocyanate (IPDI) as coupling reagent. The anionic copolymerization of γ -benzyl l-glutamate N-carboxyanhydride (BLG-NCA) using PEG-g-PEI as a macroinitiator was carried out, followed by aminolysis with 2-dimethylaminoethylamine to obtain the target water soluble triblock copolymer. The structures from PEG-g-PEI precursor to the triblock copolymers were confirmed by FT-IR. The particle sizes, zeta potentials of polyplexes were evaluated. All polyethylenimine derivatives were revealed to compact plasmid DNA effectively to give polyplexes with suitable size (~100 nm) and moderate ζ -potentials (10-15 mV) at N/P ratios of 30. The relationship between the composition of PEG-g-PEI-b-PDMAEG and the size, the ζ -potentials of corresponding copolymer/DNA complexes were also investigated.

Keywords — Polyethylenimine, poly (ethylene glycol, cationic polymer, cytotoxicity, gene delivery.

I. INTRODUCTION

Gene therapy has been regarded as the promising and ultimate cure for many life-threatening diseases, acquired and inherited, such as AIDS, cancer, genetic disorders etc [1] and [2]. To achieve successful gene therapy, development of proper gene delivery systems should be one of the most significant factors [3] and [4].

Among non-viral carriers, polyethylenimine (PEI) has been one of the most widely studied synthetic cationic gene vectors due to its superior transfection efficiency [3] and [4]. The high transfection efficiency of PEI/DNA complexes is attributed to the unique capacity of PEI to buffer endosomes according to “proton sponge hypothesis”. Nevertheless, the use of PEI both in vitro and vivo remains limited due to its low colloidal stability and considerable cytotoxic effects [4].

In the past several years, many studies attempted to modify PEI with poly(ethylene glycol) (PEG) to decrease its cytotoxicity due to the shielding effect of the high positive charges of PEI [8] and [9]. However, the “stealth” effect of PEG often leads to a diminished transfection ascribing to

decreased cellular association and internalization. Additionally, PEGylated PEI complex is incapable to compress DNA effectively into small particles [4]. It is reported that large complex particles are difficult to be cellular uptake resulting in low transfection efficiency [6]. Recently, employing new block to PEI to improve its transfection efficiency has been actively pursued. Tian and co-workers designed novel gene vector by introducing hydrophobic amino acid segment poly(γ -benzyl l-glutamate) at the PEI chain ends for enhancement of gene transfer [6]. M.P. Xiong et al successfully synthesized poly(aspartate-g-PEI800) for gene delivery, displaying low toxicity and high transfection [5]. In light of these results, we speculated that incorporation of biocompatible and biodegradable block in a delivery system might have a promoting effect on gene transportation without increased cytotoxicity. In this paper, we synthesized poly(ethylene glycol)-g-polyethylenimine-b-poly(dimethylaminoethyl l-glutamine) (PEG-g-PEI-b-PDMAEG) triblock copolymers for in vitro gene transfection. The influence of the copolymer structure on DNA binding properties were investigated by electrophoresis and dynamic light scattering. The relationship between the composition of PEG-g-PEI-PDMAEG and the size, the ζ -potentials of corresponding copolymer/DNA complexes were also investigated.

II. MATERIALS AND METHODS

A. Materials

PEG-monomethyl ether (mPEG) 5k was purchased from Fluka (Buchs, Switzerland). Branched polyethylenimine (PEI) with MW of 423, 10k, and 25k were purchased from Sigma-Aldrich (St. Louis, Mo, U.S.A) and were dried in vacuo at 40°C for 48h before use. Isophorone diisocyanate (IPDI) was purchased from Huicai coating material limited company (Guangzhou, China). 2-dimethylaminoethylamine and 2-hydroxypyridine were from Fluka (Buchs, Switzerland). Plasmid pEGFP-C1, driven by an early promoter of CMV and enhanced green fluorescent protein (EGFP) gene, was a gift kindly from West China University of Medical Sciences (Chengdu China). The plasmid was amplified in *Escherichia coli*. and purified by the EndoFree Plasmid Mega Kit (Qiagen Chatsworth, CA, USA).

B. Synthesis of block copolymer PEG-g-PEI

The block copolymers PEG-g-PEI were prepared by the method of Hogler et al [7].

C. Synthesis of the *N*-carboxyanhydride of γ -benzyl *L*-glutamate (BLG-NCA)

γ -benzyl *L*-glutamate was synthesized according to the reported method [8].

D. Synthesis of poly(ethylene glycol)-*g*-polyethylenimine-*b*-poly(γ -benzyl *L*-glutamate) (PEG-g-PEI-*b*-PBLG)

PEG-g-PEI-*b*-PBLG was prepared by ring opening polymerization of the BLG-NCA using synthesized PEG-g-PEI as a macromolecule initiator in benzene/dioxane (v/v 1/4) according to a similar procedure [9] and [10].

E. Synthesis of PEG-g-PEI-*b*-poly(dimethylaminoethyl *L*-glutamine) (PEG-g-PEI-*b*-PDMAEG)

Synthesis of PEG-g-PEI-*b*-PDMAEG was conducted by aminolysis of PEG-g-PEI-*b*-PBLG using 2-Dimethylaminoethylamine in a flask equipped with a magnetic stir bar and a programmable temperature controller. Briefly, certain amount of PEG-g-PEI-*b*-PBLG was dissolved in dimethylformamide (DMF) (w/v 1/20). 2-Dimethylaminoethylamine (20-fold mol of the ester groups of PBLG segment of PEG-g-PEI-*b*-PBLG) and 2-hydroxypyridine (5-fold mol of the ester groups of PBLG segment of PEG-g-PEI-*b*-PBLG) were added, the solution was stirred at 40°C for 48h. Finally, the target copolymer was received by precipitation in cold diethyl ether, followed by dialysis against water (2 days), and lyophilization.

F. Characterizations

The chemical structures of the obtained copolymers were confirmed by FT-IR spectra. FT-IR spectra were recorded on EQUINOX55 spectrometer.

G. Gel retardation assay

Polymer/DNA complexes were prepared at varying N/P ratios: 0.5, 1.0, 1.5, 2.0, 3.0, 4.0 and 5.0. The formed complex solution (9 μ L) was mixed with 1 μ L of loading dye and loaded onto a 0.9% agarose gel containing 0.5 μ g/ml EtBr. Electrophoresis was carried out at 90V for 30 min in TBE buffer solution. The gel was visualized on a UV transilluminator.

H. Measurements of particle size and zeta potential

Particle size and zeta potential of prepared polymer/DNA complex were measured by a Zetasizer Nano Series 90 at 25°C. Complexes formed by polymers with different composition and DNA were prepared in deionized water as described above and diluted to 1 ml in final volume.

III. RESULTS AND CONCLUSION

A. Copolymer analysis

The content of monomeric units and the molecular weights of copolymers were calculated from ^1H NMR were listed in Table 1.

Spectrometric methods were employed to characterize intermediate polymer (i.e. NCO-terminated PEG, PEG-g-PEI, and PEG-g-PEI-*b*-PBLG) and final copolymer PEG-g-PEI-*b*-PDMAEG. Fig. 1 showed the FT-IR spectra of PEG 5k, PEI 10k, the intermediates and the corresponding triblock copolymer. PEG and PEI blocks were characterized by absorptions at **A** 2888 cm^{-1} for C-H, **B** 1111 cm^{-1} for ether C-O and **C** 3300 cm^{-1} for amine N-H respectively. Obviously, both PEG and PEI blocks were present in all intermediate polymers and the final product. The activation of PEG with IPDI, was confirmed by the strong absorption **D** for the isocyanate at 2267 cm^{-1} and **E** for the urethane at 1719 cm^{-1} (Fig. 1 c). After grafting the activated PEG onto PEI, the absorption **D** at 2267 cm^{-1} for the isocyanate disappeared completely and absorption **F** at 1650 cm^{-1} appeared for the urea bond appeared (Fig. 1 d.). That the BLG-NCA polymerization was carried out was confirmed by Fig. 1 e. The absorption **H** at 1652 cm^{-1} (amide I) and **I** 1546 cm^{-1} (amide II) were assigned to the amide group, indicating the formation of the PBLG block. The peaks **G** at 1735 cm^{-1} for the ester group and **J** at 698 cm^{-1} and 747 cm^{-1} for the phenyl group were the characteristics of the PBLG block with the protection group. Fig. 1 f demonstrated that the protective

Table 1 Characterization of synthesized PEG-g-PEI-*b*-PDMAEG copolymers molecular weight and composition determined by ^1H NMR measurement.

Sample number	Composition of PEG, PEI, PDMAEG (content %) ^a			Molecular weight of copolymer ^a
	PEI	PEG	PDMAEG	
PPP-1	34.5	2.4	61.1	1.8k
PPP-2	26	1.8	72.2	2.3k
PPP-3	28	26	46	3.9k
PPP-4	21	19	60	5.2k
PPP-5	24	26	50	9.6k
PPP-6	20	21	59	11.7k

^a Determined by NMR.

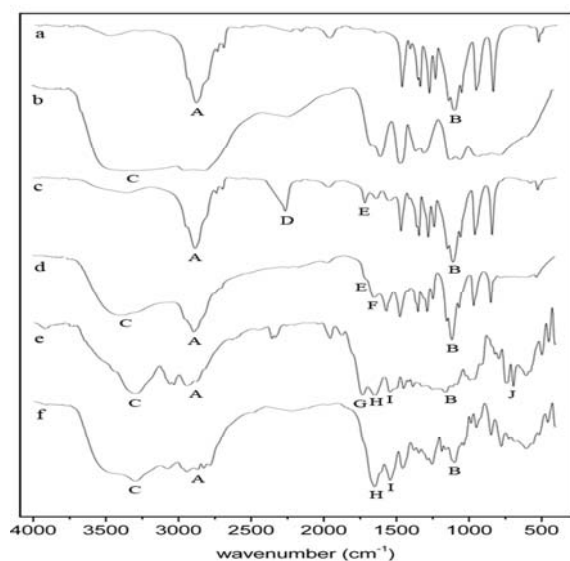


Fig. 1 IR spectra of (a) PEG 5k, (b) PEI 10k, (c) PEG-NCO, (d) PEG-g-PEI (10k), (e) PEG-g-PEI (10k)-b-PBLG, (f) PEG-g-PEI (10k)-b-PDMAEG (PPP-4).

groups in the PBLG block transferred to dimethylaninoethylamine group completely after the reaction of aminolysis. The C-H vibration of the benzyl **J** at 698cm^{-1} and 747cm^{-1} disappeared and the ester group **G** at 1735cm^{-1} disappeared, which clearly illuminated the benzyl group had been removed out completely after aminolysis.

B. Gel retardation assay

The capacity for polymers to interact and condense with plasmid DNA was judged by gel agarose electrophoresis. All the synthesized triblock copolymers were capable to retard DNA migration completely, as depicted in Fig. 2. For homogeneous PEI, two times higher N/P ratio was needed to form stable complexes with DNA for PEI 10k as compare to PEI 25k. More, no ability of PEI 423 to form complexes with DNA even at N/P ratio 100 was found (data not shown), suggesting that DNA mobility was not retarded completely by PEI 423. It was found that mediated copolymers PEG-g-PEI (10k), PEG-g-PEI (25k) completely retarded DNA migration at N/P ratio 4.0 and 2.0 respectively, indicating that a further excess of polycation was needed for complete condensation comparing to corresponding PEI. We believed that when PEI was grafted with PEG block, the complexation was hindered slightly, suggesting that high proportion of the hydrophilic PEG component interfered with the particle formation process and reduced the positive surface charge of polycations. Thus, the DNA condensation ability of the PEG grafted PEI was reduced. However, after

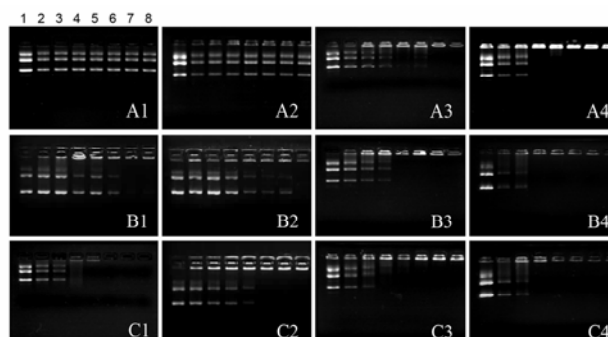


Fig. 2 Agarose gel electrophoresis retardation of DNA by copolymers (A1) PEI 423, (A2) PEG-g-PEI (423), (A3) PPP-1, (A4) PPP-2, (B1) PEI 10K, (B2) PEG-g-PEI (10K), (B3) PPP-3, (B4) PPP-4, (C1) PEI 25K, (C2) PEG-g-PEI (25K), (C3) PPP-5, (C4) PPP-6. Lane numbers corresponded to different N/P ratios of polymer/DNA as follows: (1) 0:1 (DNA only), (2) 0.5:1, (3) 1:1, (4) 1.5:1, (5) 2:1, (6) 3:1, (7) 4:1, (8) 5:1.

the introduction of PDMAEG block, the ability to condense DNA was significantly enhanced. The particle formation activity of PPP-1, PPP-2, PPP-3, PPP-4, PPP-5 and PPP-6 even better than that of the equivalent free PEI 25k, achieving complete gel shift at a charge ratio of 1.5, 1.0, 1.5, 1.0, 1.5, 1.0 respectively. Furthermore, we found that the ability of PEG-g-PEI-b-PDMAEG copolymers to mediate DNA gel shift was influenced by the length of the PDMAEG block, copolymers with longer PDMAEG block was more effective than that with shorter block.

C. Particle size measurements

Various copolymer/DNA complexes formed at an N/P ratio of 30 were assessed in order to get insight into the relationship between copolymer composition and particle size of formed complex. As shown in Table. 2, for homogeneous PEI, PEI 10k, PEI 25k formed small particles of 160nm, 140nm in diameter respectively, suggesting high molecular weight PEI possessed effective DNA compaction and condensation capacity. In contrast, PEI 423 formed large unstable particles of 600nm, indicating that poor complexation between DNA and low molecular PEI. The particle size of PEG-g-PEI/DNA complex was increased comparing to corresponding PEI/DNA complex. It was thought that high proportion of PEG would shield the positive charge of PEI and weaken the ability of DNA compaction. It was worth to note that after introduction of PDMAEG chain, the size of complexes decreased markedly. In this case, we presumed that the long cationic PDMAEG block surrounding the PEI head might intensely enhanced the access and binding of DNA in spite of existence of high proportion of hydrophilic PEG, leading to a sufficient condensation of DNA.

Table 2 Detailed particle size and ζ -potentials of polymer/DNA complex at N/P ratio of 30

Sample	Complex	
	Size (nm) (\pm SD) ^a	ζ -potential (mV) ^a
PEI 423	603.2 \pm 33.7	-22.4 \pm 7.1
PEI 10k	163.5 \pm 12.3	26.0 \pm 3.2
PEI 25k	138.1 \pm 8.0	35.8 \pm 2.1
PEG-g-PEI 423	588.6 \pm 19.2	-24.0 \pm 2.6
PEG-g-PEI 10k	205.5 \pm 11.3	6.5 \pm 0.4
PEG-g-PEI 25k	197.8 \pm 12.4	7.3 \pm 0.9
PPP-1	73.7 \pm 8.4	9.7 \pm 2.3
PPP-2	65.7 \pm 3.6	10.2 \pm 1.9
PPP-3	64.4 \pm 6.8	12.7 \pm 2.6
PPP-4	71.4 \pm 6.2	13.1 \pm 0.7
PPP-5	75.9 \pm 3.9	13.6 \pm 1.9
PPP-6	78.2 \pm 4.9	15.7 \pm 0.3

^a Detected with dynamic light scattering.

D. ζ -potentials determination

ζ -potentials was a key prerequisite for cellular uptake, and also correlated to the cytotoxicity of the complex. The correlation between polymer composition and ζ -potentials of complexes was also discussed here, using various copolymer/DNA complexes formed at an N/P ratio of 30. As revealed in Table. 2, the ζ -potentials of PEI 25k was particular high, indicating that high positive charge on the surface of polyplexes. On the contrary, PEI 423 formed particles with negatively charged surfaces. The ζ -potentials decreased remarkably after grafting hydrophilic PEG block, ascribing to the shielding effect of PEG. As indicated in introduction, PEG here was employed to reduce the cytotoxicity of PEI homopolymers, while the PEGylated PEIs had a ζ -potentials close to zero, which would result in low transfection efficiencies. Interestingly, the ζ -potentials enhanced when the complexes were formed by PEG-g-PEI-b-PDMAEG. It was speculated that only part of positive charged PDMAEG block involved in the compaction of DNA and some long cationic PDMAEG blocks were available at the outer surface of PEG shielded complexes (Fig. 3).

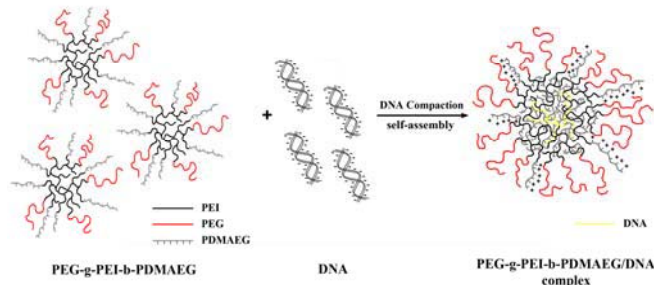


Fig. 3 Possible structure of PEG-g-PEI-b-PDMAEG/DNA complex.

IV. CONCLUSIONS

In conclusion, a new series of polymers PEG-g-PEI-b-PDMAEG were synthesized in light of an efficient approach. Each block length of the prepared triblock copolymers can be designed on the base of their monomer ratios. The molecular weight of PEI segments, the length of PDMAEG chains in copolymers and N/P ratio in the polyplex system were critical factors influencing on the condensation capability, particle size and surface charge.

ACKNOWLEDGMENT

The financial support of the National Nature Science Foundation of China (Project No. 30570500) is gratefully acknowledged.

REFERENCES

- Ahn C, Chae S, Bae Y et al. (2002) Biodegradable poly(ethylenimine) for plasmid DNA delivery. *J. Control. Release.* 80:273-282
- Merdan T, Kopecek J, Kissel T. (2002) Prospects for cationic polymers in gene and oligonucleotide therapy against cancer. *Adv. Drug. Deliv. Rev.* 54:715-758
- Godbey WT, Wu KK, Mikos AG. (1999) Poly(ethylenimine) and its role in gene delivery. *J Control. Release* 60:149-160.
- Neu N, Fischer D, Kissel T. (2005) Recent advances in rational gene transfer vector design based on poly(ethylene imine) and its derivatives. *J. Gene Med.* 7: 992-1009.
- Shuai X, Merdan T, Unger F, et al. (2003) Novel biodegradable ternary copolymers *hy*-PEI-g-PCL-b-PEG: Synthesis, Characterization, and potential as efficient noviral gene delivery vectors. *Macromolecules* 36:5751-5759.
- Zhong Z, Feijen J, Lok MC, et al. (2005) Low Molecular Weight Linear Polyethylenimine-b-poly(ethylene glycol)-b-polyethylenimine triblock copolymers: Synthesis, characterization, and in vitro gene transfer properties. *Biomacromolecules* 6:3440-3448.
- Petersen H, Fechner PM, Fischer D, Kissel T. (2002) Synthesis, characterization, and biocompatibility of polyethylenimine-graft-poly(ethylene glycol) block copolymers, *Macromolecules* 35: 6867-6874.
- Blout ER, Karlson KH. (1956) Polypeptides. III. The synthesis of high molecular weight poly- γ -benzyl-L glutamates. *J. Am. Chem. Soc.* 78: 941.
- Tian TH, Deng C, Lin H, et al. (2005) Biodegradable cationic PEG-PEI-PBLG hyperbranched block copolymer: synthesis and micelle characterization. *Biomaterials* 26: 4209-4217.
- Deng N, Wang R, Rong G, et al. (2004) Synthesis of a novel structural triblock copolymer of poly(γ -benzyl-L-glutamic acid)-b-poly(ethylene oxide)-b-poly(ϵ -caprolactone). *Biomaterials* 25: 3553-3558.

Author: Shirong Pan
 Institute: The First Affiliated Hospital, Sun Yat-Sen University
 Street: No. 58, Zhongshan Er Road
 City: Guangzhou
 Country: China
 Email: gzpshr@hotmail.com

Alginate/hydroxyapatite hydrogel as biodegradable in situ forming scaffold

Lu Lu, Yusha Qi, Jinhuan Tian and Changren Zhou

Department of Materials Science and Engineering, Jinan University, Guangzhou 510632, China
Engineering Research Center of Artificial Organs and Materials, Ministry of Education

Abstract — The injectable polymer scaffolds are important biomaterials for tissue engineering and drug delivery. Hydrogels derived from natural proteins and polysaccharides are ideal tissue engineering scaffolds since they resemble the extracellular matrices of the tissue comprised of various amino acids and sugar based macromolecules. This work present an injectable system from partially oxidized alginate and HA (hydroxyapatite) for tissue engineering and drug delivery applications. In situ release of calcium cations from nano HA particles was adopted through lowering the pH with slow hydrolysis of GDL (D-glucono- δ -lactone) and homogeneous alginate gels were formulated as scaffolds with defined dimensions. The gelation time and the mechanical properties of the system can be controlled by the compositional variables. The SEM observations confirmed a porous 3D hydrogel structure with interconnected pores ranging from 20 to 100 μm and the nano HA particles dispersed in the scaffolds uniformly. The potential applications such as injectable drug delivery vehicle and tissue engineering scaffold are envisaged for this polymer scaffold.

Keywords — Hydrogel, Biodegradable, Injectable, Alginate, Hydroxyapatite

I. INTRODUCTION

Hydrogels are appealing scaffold materials due to their high water content, good biocompatibility and consistency similar to soft tissue. They play important role in several applications including tissue engineering and controlled delivery of therapeutic agents. The simplest and the most convenient approach in these applications will be to inject the polymer-cell or drug entity into the body in a minimally invasive manner. Naturally derived hydrogels resemble the nature extracellular matrix and thus have the potential to direct the migration, growth and organization of cells during tissue regeneration and wound healing and for stabilization of encapsulated and transplanted cells.

Alginate is a natural biomacromolecule isolated from seaweed and bacteria. It is consisting of (1 \rightarrow 4) linked β -D-mannuronate (M) and its C-5 epimer α -L-guluronate (G) residues arranged in blocks of M fragments, G fragments, and alternating G and M fragments [1]. It is an important naturally produced material which can forms well-characterized hydrogels by adding divalent cations (except

Mg^{2+}) under physiological conditions [2]. The use of alginate scaffolds in tissue-engineering applications is limited owing to their weak mechanical properties, lack of cellular interactions, and uncontrollable degradation [3]. For these reasons, covalent crosslinking has been investigated in order to impart controlled mechanical properties to the alginate hydrogels [4]. However almost of the synthetic processes include using toxic reagents.

The present study shows an injectable, nontoxic, biodegradable hydrogel scaffold prepared by crosslinking of oxidized alginate and Hydroxyapatite (HA), in the presence of small concentrations of D-glucono- δ -lactone (GDL). Partially oxidized alginate is degradable and still capable of being ionically cross-linked with calcium ions to form hydrogel [5]. HA ($\text{Ca}_{10}(\text{PO}_4)_6(\text{OH})_2$) is a calcium phosphate salt and being used as an artificial bone material due to its biocompatibility, bioactivity, osteoconductivity, nontoxicity, noninflammatory behavior. Some investigators have reported that HA may bond directly with host bone [6]. GDL is the oxidation product of gluconic acid and widely used as a coagulation, acidulant, leavening agent and sequestrant in human food. Up to now, GDL does not seem to have any obvious toxic effects on human body, and some investigators have reported that GDL showed inhibitory effects on common pathogen icorganisms[7].

II. MATERIALS AND METHODS

A. Alginate/hydroxyapatite hydrogel preparation

Sodium alginate sample (Crystal Rock Biology Development Company, China) was purified by precipitating with absolute ethanol. Partially oxidized alginate sample with 3% degree of oxidation was prepared by adding sodium metaperiodate solutions into the alginate/ethanol suspension and stirred in the dark magnetically at 25°C for 10 hours[8]. After reaction, the solutions were dialyzed against distilled water using cellulose tubular membranes (cut-off molecular weight is \sim 12000) until the dialyzate was periodate free indicated by the absence of any precipitate after adding silver nitrate solution. The dialyzate was then freeze dried and the yield of the products was about 60%.

HA nanocrystal were synthesized based on wet chemical precipitation method with the calcium nitrate and ammonium phosphate dibasic used as Ca and P precursors respectively. To precipitate stoichiometric HA, 0.3M aqueous solution of $(\text{NH}_4)_2\text{HPO}_4$ was slowly added drop by drop to 0.5M aqueous solution of $\text{Ca}(\text{NO}_3)_2$. The rotation speed of stirrer was adjusted to 400 rpm and the pH was adjusted to 10.5 by adding concentrated NH_4OH . The resultant precipitate was aged for 24 hours and the obtained white precipitate was filtered and washed with distilled water followed by drying in a vacuum oven at 80°C . Transmission Electron Microscope and X-ray Diffraction were used to characterize the particles.

In order to prepare homogeneous alginate/hydroxyapatite hydrogel, the method of in situ release of calcium cations from HA was adopted with slow hydrolysis of GDL. Hydrogels were prepared by blending concentrated alginate stock solution with required amount of hydroxyapatite nanoparticles, followed by adding GDL freshly dissolved in distilled water. We define the stoichiometric mole ratio $f = [\text{Ca}^{2+}]/[\text{COO}^-]$ in alginate as a structure parameter. And the pH of the gel extracts is controlled between 7 and 7.4 by the mol ratio of GDL and HA.

B. Viscosity measurement

The degradability of the alginate and oxidation alginate were studied by monitoring the change of molecular weight with time. Sample solutions were prepared in PBS and incubated at 37°C . The viscosity of the samples were measured by an Ubbelohde viscometer with internal dilution. The intrinsic viscosity $[\eta]$ were determined by the Fedors equation[9]

$$\frac{1}{2(\eta_r^{1/2} - 1)} = \frac{1}{[\eta]C} - \frac{1}{[\eta]C_m} \quad (1)$$

where η_r is the solution viscosity relative to the solvent and C_m is a polymer concentration parameter.

C. Gelation time

The method of tilt test tube were exploited to determine the gelation time as the time of the system transition from the fluid to the gel state, which is detected by monitoring the position of the meniscus in the test tube at 37°C . For this purpose, the test samples were mixed in the glass test tube and the tube were tilted every thirty seconds and inverted every minute until the meniscus does not change its position relative to the test tube axis for 15s, the relevant period of time is recorded.

D. Mechanical properties

Cylindrical specimens of the gels with 15mm height and 15mm diameter were made in a plastic mould. Compressive strength of the specimens after immersed in SBF at 37°C for 24 hours were determined by a Universal Testing Machine (SHIMADZUAG-I, Hitachi S-520).

E. Morphology

Morphology of the gel was examined by scanning electron microscopy (SEM). The lyophilized gel samples were placed on double-side tape, sputter coated with gold and examined in the SEM (Philips, ESEM XL-30).

III. RESULTS AND DISCUSSION

A. HA crystals

The HA powder obtained by the wet chemical precipitation appears as white color, bouncy and free flowing powders. The XRD pattern of HA sample (Fig. 1.) shows broad and overlap peaks with poor crystallinity around the characteristic region near to 32° (2θ). Actually it should be as three individual peaks each at 31.83° , 32.10° and 32.90° (2θ) as in the well crystalline HA [10]. The crystallographic structure of our nanocrystals is more identical with natural bone mineral (biological apatite).

TEM images of the HA sample is shown in Fig. 2. The needle-like HA crystallite with almost uniform particle size is about 50~100nm in length and 20nm in width, being in agreement with the above XRD result.

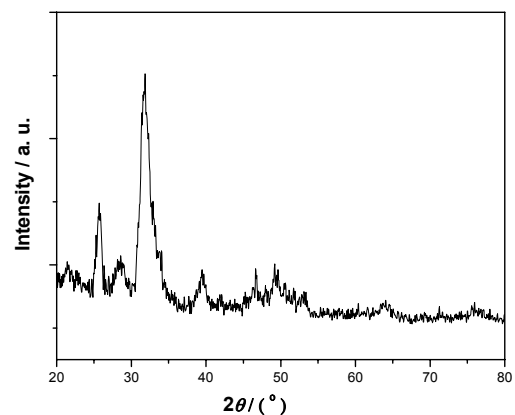


Fig. 1 XRD pattern of HA sample

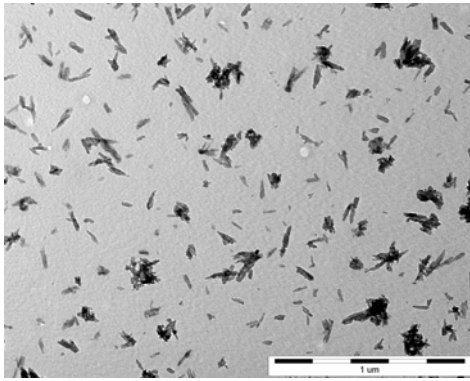


Fig. 2 TEM image of HA powders prepared by wet chemical precipitation

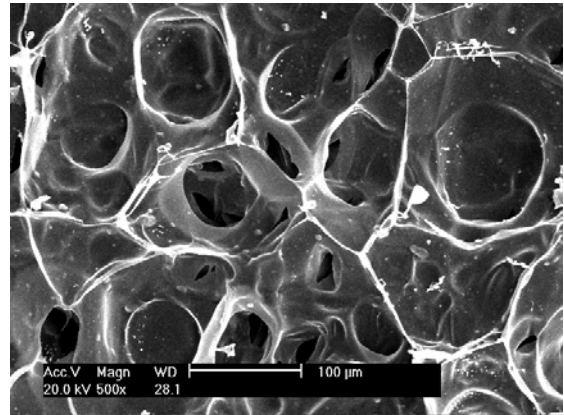


Fig. 5 SEM image of alginate/hydroxyapatite hydrogel

B. Hydrogel characterization

The effect of concentration of oxidized alginate and HA on gelation time and mechanical properties were systematically examined. And the results are shown in Fig. 3 and Fig. 4. As a general rule, with the increase in alginate and HA content, the compressive strength of the gel increased.

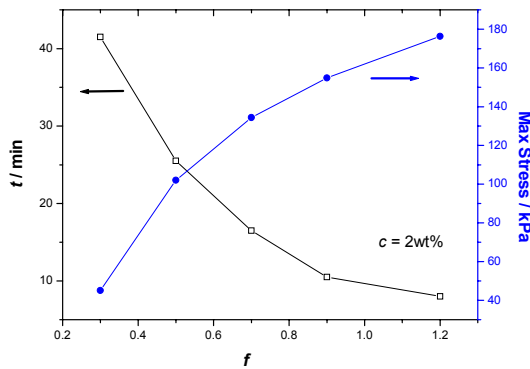


Fig. 3 Gelation time and max stress at different HA content

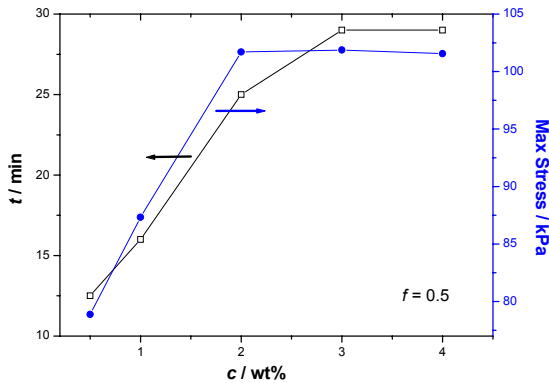


Fig. 4 Gelation time and max stress at different concentration of alginate

The increase in component density increased the density of the crosslink point, and the strength of the hydrogel increased. The increased content of HA stimulate the release rate of Ca^{2+} from HA. As the result the gelation time decreased. On the other hand, when the alginate concentration increased, the viscosity of the system increased rapidly. So the diffusion of Ca^{2+} was restricted and the gelation time increased. From the discussion above we can draw the conclusion that the gelation time and the mechanical properties of the system can be controlled by the compositional variables. So according to the different purpose we can prepare samples with different properties using the same hydrogel system.

SEM image showed interconnecting pores in the gel matrix and the pore size analysis gave an average pore diameter of $50\mu m \sim 100\mu m$, demonstrating the suitability of the matrix for cell encapsulation.

C. Degradation

Mark Houwink equation

$$[\eta] = KM^\alpha \tag{2}$$

is generally employed for the estimation of molecular weight of linear polymers where K and α values are constant for a particular polymer/solvent/temperature system. For alginate the values of K and α are [11]

$$[\eta] = 2.0 \times 10^{-5} M^{1.0} \tag{3}$$

The molecular weight ratio (M/M_0) vs. time were shown in Fig. 6.

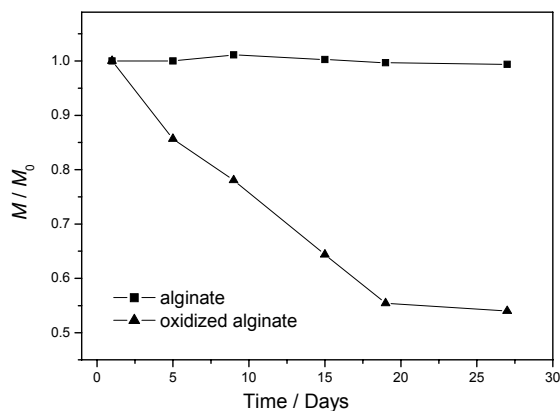


Fig. 6 Degradation profile of alginate and partially oxidized alginate(3%)

During the test period the alginate sample almost kept the same molecular weight. On the other hand, the oxidation alginate molecular weight was linearly decreased with time. The aldehyde groups of oxidized uronic acid residues altered the chair conformation to an open-chain adduct and infers a free rotation about the three bonds adjoining C-4, C-5, the original ring-oxygen atom, and C-1 of the oxidized alginate residues. And this creates hydrolytically labile bonds in the polysaccharide [12,13]. The molecular weight of the oxidized samples decreased to the 50% of the initial values in one month. Therefore the reversible chelation between Ca^{2+} and oxidized alginate and the degradability of oxidized alginate would make the gel fully biodegradable with time in the body.

IV. CONCLUSIONS

We have shown here an injectable biodegradable polymer scaffold constructed from biopolymers of well-known biocompatibility. The use of nona HA crystal has beneficial effect of increasing the compatibility and bioactivity of the system. Potential applications such as injectable drug deliv-

ery vehicle and tissue engineering scaffold are envisaged for this polymer scaffold.

ACKNOWLEDGMENT

The authors are grateful for the financial support from the National High Technology Research and Development Program of China (2007AA091603) and the Science Foundation for Jinan University (51207042).

REFERENCES

1. Moe S T, Dragel K I, Smidsrød O. (1995) Alginates In: Stephen, A. M., (Eds), Food polysaccharides and their applications. New York: Marcel Dekker
2. Ji M. (1997) The chemistry of seaweed. Beijing: Science Publishing House
3. Bouhadir K H, Mooney D J. (2002) Synthesis of hydrogels: alginate hydrogels. In: Atala A, Lanza RP, editors. Methods of tissue engineering. New York: Academic Press
4. Eiselt P, Lee K Y, Mooney D J. (1999) *Macromolecules* 32: 5561-5566
5. Bouhadir K H, Lee K Y, Alsberg E. et al. (2001) *Biotechnol Prog.* 17: 945-950
6. LeGeros R Z. (1991) Calcium phosphates in oral biology and medicine, Karger, Basel, Switzerland
7. SHI Y, HOU F, GENG Z. et al. (2001) *J N Bethune Univ Med Sci.* 27: 603-605
8. Balakrishnan B, Jayakrishnan A. (2005) *Biomaterials* 26: 3941-3951
9. Dragan S, Ghimici L. (2001) *Polymer* 42: 2887-2891
10. Murugan R, Ramakrishna S. (2004) *Biomaterials* 25: 3829-3835
11. Smidsrød O, Haug A, (1968) *Acta. Chem. Scand* 22: 797-810
12. Smidsrød O, Painter T. (1973) *Carbohydr Res.* 26:125-132
13. Boonthedul T, Kong H, Mooney D. (2005) *Biomaterials* 26: 2455

Author: Changren Zhou
 Institute: Department of Materials Science and Engineering, Jinan University
 Street: Huangpu Road
 City: Guangzhou
 Country: China
 Email: tcrz9@jnu.edu.cn

Drug controlled release of novel alginate/poly-L-arginine microcapsules

Wenguo Wu¹, Wei Liu¹, Shibin Wang^{1,2*} and Yuangang Liu¹

¹ college of Materials Science & Engineering, Huaqiao University, Quanzhou, China

² Research Institute of Pharmaceutical Engineering, Quanzhou, China

Abstract— a novel alginate/poly-L-arginine microcapsules were prepared by emulsification using bovine hemoglobin (Hb) as the model drug, and the impact of the release properties such as the molecular weight of poly-L-arginine, the concentration of sodium alginate and calcium chloride were investigated. The microcapsules made from middle molecular weight of poly-L-arginine (PLA) had obviously sustained release profile. The impact of sodium alginate concentration on the release properties was not obviously, the release rate of microcapsules made with 12% (w/v) CaCl₂ were slightly faster, but the accumulative release rate were nearly the same. The microcapsules had so obviously sustained drug release that this novel microcapsules may be used as a promising drug delivery system for hydrophilic proteins and peptides.

Keywords— microcapsule, poly-L-arginine, alginate, emulsification, controlled release

I. INTRODUCTION

Alginate is a non-toxic, biodegradable, natural occurring polysaccharide obtained from marine brown algae. It is a linear copolymer composed of mannuronic acid and guluronic acid residues that gels in the presence of divalent cations, such as calcium, due to the stacking of guluronic acid (G) blocks with the formation of “egg-box” calcium linked junctions^[1]. Alginate microspheres have been used for the encapsulation of a wide variety of biologically active agents, including proteins^[2], enzymes^[3], antibodies^[4], cells^[5] and DNA^[6].

Poly amino acid has attracted considerable attentions due to its nontoxicity, excellent biocompatibility, nutritional function and pharmacological efficacy. For example, poly-arginine and arginine can inhibit tumor growth, enhance the drug delivery across biological membranes and tissues, and possess antimicrobial activity. Researches also reported that poly-arginine can enter into cells more efficiently than other polycationic homopolymers^[7,8,9].

Since the concept of biodegradable polymers for sustained release parenteral DDS (drug delivery systems) began to develop in early 1970s, drug delivery systems for proteins and peptides have been extensively investigated for decades. Poly amino acids make them ideal candidates for applications in drug delivery systems due to their biocompatibility and biodegradability. In this study, we investi-

gated the controlled release of the drug-loaded poly-L-arginine/calcium alginate microcapsules prepared by emulsification.

II. MATERIALS AND METHODS

A. Materials

Alginate sodium and poly-L-arginine were purchased from Sigma(USA). Calcium chloride, isooctane, tween80 and alcohol were obtained from Xilong Chemical Co.(China). Span80 was purchased from Damao Chemical Co.(China) and Bovine hemoglobin (Hb) was obtained from Kejie Biotechnology Co.(China). All other chemicals were of analytical grade.

B. Methods

1. Preparation of poly-L-arginine/calcium alginate microcapsules

Hb was dispersed into the sodium alginate solution and the mixture was slowly added into isooctane containing span80 by high stirring using a digital mixer with a marine impeller. After 10 min emulsification, tween80 was added to adjust the HLB value, then CaCl₂ solution was added to solidify, the drug-loaded calcium alginate microspheres were washed by adding alcohol and distilled water followed by orbital agitation, then transferred into aqueous poly-L-arginine to form microcapsules for 20 min. Microcapsules were separated by centrifugation and lyophilized.

2. In vitro release studies

An amount of drug-loaded poly-L-arginine/calcium alginate microcapsules were resuspended in phosphate buffered saline (PBS) pH 6.8 at 37 °C under magnetic stirring at 150 rpm. Samples were withdrawn and replaced by fresh buffer at different time intervals, the absorbance of centrifugated supernatant was measured at 405 nm by UV-vis spectrophotometer. After sufficient release, microcapsules separated by centrifugation were resuspended in PBS pH 6.8 and completely degraded by ultrasonicator. After centrifugation, the concentration of residual Hb was measured by spectrophotometer as previously mentioned.

III. RESULTS

1. The molecular weight of poly-L-arginine

The microcapsules have an obviously sustained drug release and is far lower than the specified value given in the ‘‘Pharmacopoeia of People’s Republic of China’’ (2005) for the burst release of microcapsules. The microcapsules made with 35.5 kD poly-L-arginine have a better sustained release rate than the microcapsules with a molecular weight of poly-L-arginine at 13.3 kD and 125 kD that had the similar release properties.

2. The concentration of sodium alginate

The microcapsules made with 0.5% (w/v) alginate sodium had the similar release curve with the microcapsules that made from 1.0% (w/v) alginate sodium at the initial stages and 1.5% (w/v) alginate sodium at the last phase respectively. However, the cumulative release rate of microcapsules made with 1.5% (w/v) alginate sodium was higher than the microcapsules made with 1.0% (w/v) alginate sodium.

3. The concentration of calcium chloride

The cumulative release rate of microcapsules under different CaCl_2 concentration of 4% (w/v) and 8% (w/v) were 46.4% and 47.5% respectively. Comparatively, the cumulative release of microcapsules made with 12% (w/v) CaCl_2 was slightly faster than the accumulative release rate within 12h was 42.2% and achieved to 52.7% after 48h.

IV. DISCUSSION

As shown in Fig. 1, The microcapsules with different PLA molecular weight have different cumulative release rate of Hb at different phases, the drug-release in different stage were shown in Table 1. Table 1 showed that the cumulative release rate of Hb is the fast at 0-12 h, as the release time increases, the cumulative release rate decreases. As shown in Table 1, the cumulative release rate is only 45% after 48 h. The main reason is that drugs combine with alginate tightly through molecular effect and entanglement, but Hb has high molecular weight that diffuses very slowly. The other reason is that according to Fick’s second law when substance diffuses from one system to another system, the difference of the concentration between the two systems higher, the diffuse rate higher. As the prepared microcapsules have low drug loading, the electrochemical potential energy in and out of microcapsule all are low that not have enough impetus to promote diffusion^[10].

The microcapsules made with low molecule poly-L-arginine have incompact films because of low amido in molecule structure, although low molecule poly-L-arginine may enter the deep fragment of microspheres; High molecule

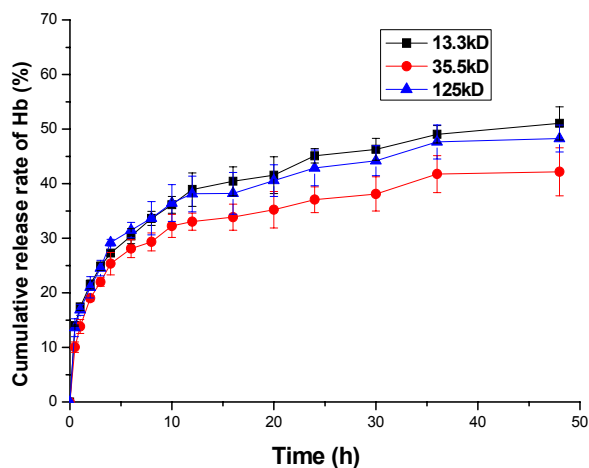


Fig. 1 Release profiles of microcapsules with different PLA molecule weight

Table 1 Drug-release in different stage

Release stage	0-12h	12-24h	24-48h
13.3kD	38.9%	6.1%	6.0%
35.5kD	33.1%	4.0%	5.1%
125kD	38.1%	4.8%	5.4%

poly-L-arginine have more amido to combine with more carboxyl of alginate to form compact film. However, higher molecule poly-L-arginine can only combine to the exterior of microspheres to form incompact films. So the microcapsules made with 35.5 kD poly-L-arginine have a better sustained release properties than the microcapsules with a molecular weight of poly-L-arginine at 13.3 kD and 125 kD.

The cumulative release rate of microcapsules made with low concentration of sodium alginate is higher and decreases as the concentration of sodium alginate increases (Fig. 2). For one reason, the sodium alginate with low concentration form incompact hydrogel like network with big mesh, so Hb can have a fast diffuse rate. The other reason is that low concentration of sodium alginate provides few carboxyl to combine with amido of poly-L-arginine, then form an incompact polyelectrolyte membrane. However, the cumulative release rate of microcapsules made with 1.5% sodium alginate increases, it is because alginate hydrogel is so compact that the poly-L-arginine molecule can not enter deeper into the network to combine interior carboxyl so the polyelectrolyte membrane formed is incompact^[11].

Calcium ions is an important parameter to the formation of sodium alginate hydrogel, the concentration has great effects to the structure of hydrogel. When the concentration of calcium ions is low, the hydrogel gridding dimension is great and decreases as the concentration of calcium increases. On the other hand, the proportion of calcium ions

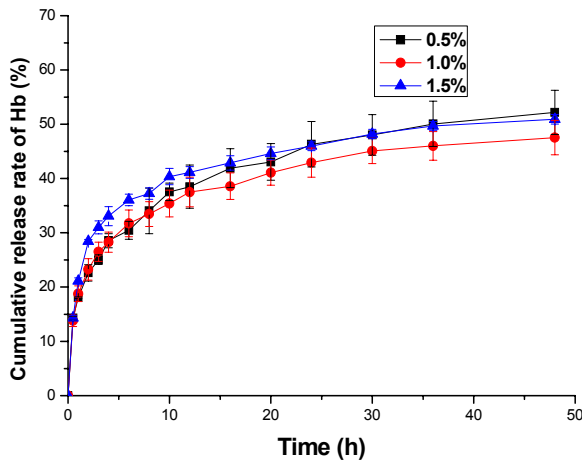


Fig. 2 Release profiles of microcapsules with different Na-Alg concentration

and carboxyl on the alginate molecular chains also affects the rest of carboxyl on the chains^[11]. As shown in Fig. 3, the cumulative release rate of microcapsules under different CaCl_2 concentration of 4% (w/v) and 8% (w/v) were 46.4% and 47.5% respectively. Comparatively, the cumulative release of microcapsules made with 12% (w/v) CaCl_2 was slightly faster that the accumulative release rate within 12 h was 42.2% and achieved to 52.7% after 48h. The reason is that as the concentration of calcium increases, the hydrogel network dimension decreases, then poly-L-arginine can not enter the hydrogel network deeper, so the membrane of microcapsules is thin. In addition, as the concentration of calcium ions increases, the carboxyl on the alginate molecular chains combines with it largely, which leads to the decrease of the combination with amido of poly-L-arginine and then the polyelectrolyte membrane formed is incompact.

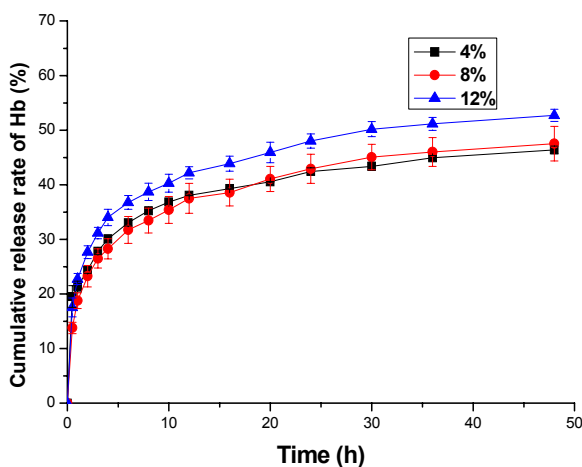


Fig. 3 Release profiles of microcapsules with different CaCl_2 concentration

V. CONCLUSIONS

The microcapsules made from middle molecular weight of poly-L-arginine have obviously sustained release profile. The impact of sodium alginate concentration on the release properties is not obviously, the release rate of microcapsules made with 12% (w/v) CaCl_2 are slightly faster, but the accumulative release rate are nearly the same.

The microcapsules have so obviously sustained drug release that this novel microcapsules may be used as a promising drug delivery system for hydrophilic proteins and peptides.

ACKNOWLEDGMENT

This paper was supported by National 863 Project (2006AA02A118), National Nature Science Foudation of China (30370415), Nature Science Foudation of Fujian Province of China (C0710034).

REFERENCES

- Martinsen A, Skjak Braek G, Smidsrod O. (1989) Alginate as immobilization material: I. Correlation between chemical and physical properties of alginate beads. *Biotechnol. Bioeng.* 33, 79–89.
- Coppi G, Iannuccelli V, Leo E et al. (2002) Protein immobilization in crosslinked alginate microparticles. *J. Microencapsul.* 19, 37–44.
- Boadi DK, Neufeld RJ. (2001) Encapsulation of tannase for the hydrolysis of tea tannins. *Enz. Microbial Technol.* 28, 590–595.
- Albarghouthi M, Fara DA, Saleem M et al. (2000) Immobilization of antibodies on alginate-chitosan beads. *Int. J. Pharm.* 206, 23–34.
- Klinkenberg G, Lystad KQ, Levine TDW et al. (2001) Cell release from alginate immobilized *Lactococcus lactis ssp. lactis* in chitosan and alginate coated beads. *J. Dairy Sci.* 84, 1118–1127.
- Quong D, Neufeld, RJ. (1998) DNA protection from extracapsular nucleases, within chitosan or poly-L-lysine-coated alginate beads. *Biotechnol Bioeng.* 60, 124–134.
- Mitchell DJ, Kim DT, Steinman L et al. (2000) Polyarginine enters cells more efficiently than other polycationic homopolymers. *J. Pept. Res.*, 56:318-325.
- Ragin AD, Chmielewski J. (2004) Probing essential residues for cellular uptake with a cationic nuclear localization signal sequence. *J. Peptide Res.*, 63:155-160.
- Fernández-Carneado J, Kogan MJ, Van Mau N et al. (2005) Fatty acyl moieties: improving Pro-rich peptide uptake inside HeLa cells. *J. Peptide Res.*, 65:580-590.
- Wang LY, Ma GH, Su ZG. (2005) Preparation of uniform sized chitosan microspheres by membrane emulsification technique and application as a carrier of protein drug. *J Control Release*, 106: 62-75.
- Cho NH, Seong SY, Chun KH et al. (1998) Novel mucosal immunization with polysaccharide–proteinconjugates entrapped in alginate microspheres. *J Control Release*, 53:215-224.

Targeted and Controlled Release of Indomethacin from a Prodrug of Amylose

Xiang Cai¹, Liqun Yang¹, Yifu Huang¹, Ningfu Peng², Li-Ming Zhang¹, Qing Wu¹, Rufu Chen²

¹Institute of Polymer Science, School of Chemistry and Chemical Engineering, Sun Yat-Sen University, Guangzhou, P. R. China

²Department of Hepatobiliary Surgery, Second Affiliated Hospital of Sun Yat-sen University, Guangzhou, P. R. China

Abstract— A series of prodrugs of amylose grafted with indomethacin (IND) were mildly synthesized at room temperature and their chemical structures were characterized by FTIR and ¹H NMR spectroscopy. The results showed that IND was conjugated with amylose through the ester bond. The loaded IND content in each prodrug was determined to be 1.8, 2.7, 4.8, 12.0, 15.6 and 21.6 mg/g from UV spectroscopy. For *in vitro* experiment, the simulated medium for stomach and small intestine was a chloric acid solution (pH 1.2), and a sodium phosphate buffer solution (pH 6.8) containing porcine pancreatin. A culture fermentation system was used to simulate the colonic condition. The results indicated that IND was hardly released in the simulated stomach medium, but could be controlled released by hydrolysis of the prodrug through α -amylase and lipase in the simulated small intestine and colonic conditions. The pharmacokinetic analysis indicated that T_{max} , the time at which a maximum concentration of drug in the plasma, was 2.1 h for free IND. But it was prolonged to 5.2 - 8.8 h for the prodrugs. Meanwhile, the maximum drug concentration in the plasma (C_{max}) decreased from 25.8 μ g/mL for free IND to 0.5 - 7.0 μ g/mL for the prodrugs. It further proved that the prodrug could realize controlled release IND.

Keywords— Prodrug, Amylose, Indomethacin, Release

I. INTRODUCTION

Indomethacin (IND) known as a typical model drug in non-steroidal anti-inflammatory drugs (NSAIDs), is widely used for the treatments of rheumatoid arthritis, spondylitis, and osteoarthritis. But IND usually generates gastrointestinal side effects clinically, such as gastric ulcers and gastric perforation [1]. Thus it is important to realize the intestine targeted and controlled release of IND in order to decrease the gastric damage and achieve sustained medication clinically, especially for alleviating the pain during sleeping at night [2,3]. Drug design in recent years has attempted to use a prodrug strategy as a chemical/biochemical approach to overcome various barriers which hinder drug delivery, such as the damage of tissue and mucous membrane, poor water solubility, and too rapid absorption or too rapid excretion [4,5]. In this work, the release of IND from a prodrug of amylose grafted with indomethacin (IND-Am) was investigated. Amylose is an important polysaccharide with low toxicity, good biocompatibility and biodegradability. It is

stable in the stomach and can be hydrolyzed by α -amylase in the intestine. Thus it is anticipated that amylose is used a carrier for the intestine targeted delivery of IND.

II. MATERIALS AND METHODS

Materials

Amylose, *N,N'*-dicyclohexylcarbodiimide (DCC), 4-dimethylaminopyridine (DMAP) and IND were bought from Fluka. Pancreatin (from porcine pancreas, P1500) was purchased from Sigma-Aldrich (Poole, UK). All other reagents were used without further purification.

Synthesis and characterization of IND-Am prodrugs

Amylose (1.0 g) was dissolved in 50 mL of dried dimethyl sulfoxide (DMSO). Then, IND, DCC and of DMAP with different amounts were added. After the reaction was allowed to proceed at room temperature for 24 h, the reaction mixture was filtrated. 200 mL of ethanol was dropped into the filtrate and centrifuged. The precipitate was dried under vacuum at 70°C for 24 h to obtain a solid product. The chemical structures of IND-Am prodrugs were characterized by FTIR and ¹H NMR analyses. The loaded IND content in each prodrug was determined from UV analysis.

In vitro IND release

The simulated medium for stomach and small intestine was a chloric acid solution (pH 1.2), and a sodium phosphate buffer solution (pH 6.8) containing porcine pancreatin, respectively. A culture fermentation system was used to simulate the colonic condition. The IND-Am prodrugs were incubated and protected by nitrogen gas in the different media by slowly stirring at 37°C. At predetermined time intervals, the released IND content was determined by UV analysis.

Pharmacokinetic studies

25 Male Sprague-Dawley mouse, 300-350 g in weight, were divided into five groups ($n = 5$). IND-Am prodrug and free IND were administered to the stomach of mice with a single bolus using feeding needles at doses of 3.6 mg/kg of IND equivalent. At predetermined time intervals, the blood was collected from the tail vein using a heparinized syringe.

Plasma was harvested by centrifugation. Samples were stored at -20°C until analysis.

Analysis methods

FTIR measurement was carried out with a FTIR Analyzer (Nicolet/Nexus 670, USA) at a 4 cm^{-1} resolution using the KBr method. ^1H NMR experiment was carried out on a Nuclear Magnetic Resonance Spectrometer (Mercury-Plus 300, Varian, USA) at room temperature, using DMSO- d_6 as a solvent. UV measurement was performed on a UV-Vis spectrophotometer (UV-3150, Shimadzu, Japan) at 318 nm. A high performance liquid chromatography (HPLC) system (Agilent HP 1100, USA) was used for determining the concentration of IND in the plasma.

III. RESULTS AND DISCUSSION

Structural analysis of IND-Am prodrugs

The chemical structures of IND-Am prodrugs were characterized by FTIR and ^1H NMR spectroscopy. The absorption peak at 1736 cm^{-1} in the FTIR spectra (not shown) is a characteristic of ester bond, giving evidence that IND was conjugated with amylose. In the ^1H NMR spectra (Fig. 1), it was obvious that the signals from 6.0 to 8.0 ppm assigned to the residues of IND increased with increasing the added amount of IND monomer. The loaded IND content, defined as the weight ratio of loaded IND and amylose (mg/g), was determined from UV spectroscopy. Consequently, six prodrugs were named IND-Am-1.8, IND-Am-2.7, IND-Am-4.8, IND-Am-12.0, IND-Am-15.6 and IND-Am-21.6, respectively. The number behind the sample code of IND-Am indicated the loaded IND content.

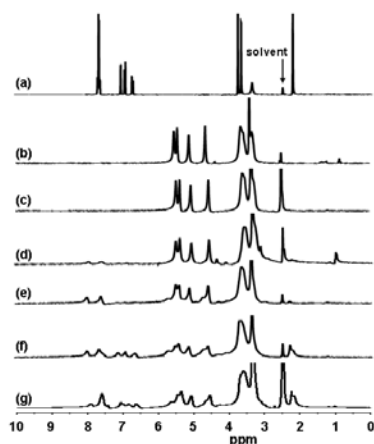


Fig. 1 ^1H NMR spectra of: (a) IND, (b) amylose, (c) IND-Am-2, (d) IND-Am-3, (e) IND-Am-4, (f) IND-Am-5 and (g) IND-Am-6.

In vitro IND release

After the prodrugs were added and slowly stirred in the simulated stomach medium at 37°C for 3 h, the accumulative release of IND for all prodrugs was less than 2% (Fig. 2). On the other hand, IND was slowly released from the prodrugs in the simulative medium of small intestine and colon at 37°C for 6 and 36 h (Fig. 3 and 4), respectively. The accumulative release of IND for the prodrugs except IND-Am-21.6 was 30-90% and 10-65% in both simulated conditions. These results indicated that IND was hardly released in the simulated stomach medium, but could be

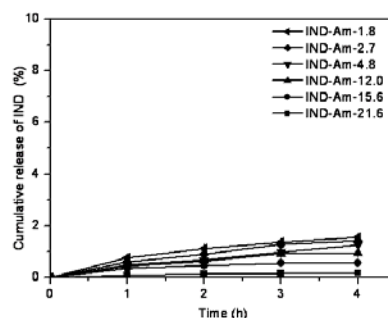


Fig. 2 *In vitro* release of IND from IND-Am prodrugs in the simulated medium of stomach.

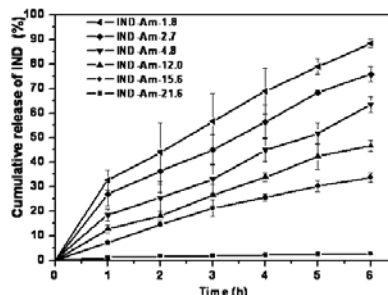


Fig. 3 *In vitro* release of IND from IND-Am prodrugs in the simulated medium of small intestine.

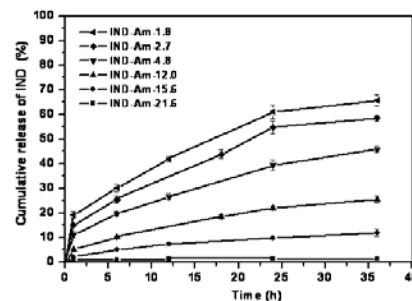


Fig. 4 *In vitro* release of IND from IND-Am prodrugs in the simulated medium of colon.

controlled released by hydrolysis of the prodrug through α -amylase and lipase in the simulated small intestine and colonic conditions. This is not only beneficial to decrease the gastric damage, but also helpful for achievement of sustained medication clinically. On the other hand, it illustrated that the release of IND was dependent on the degree of swelling of the prodrugs, owing to the very low water solubility of IND. The result showed that the prodrug with good swelling property was easily attacked by α -amylase and lipase, and then released IND.

Pharmacokinetic studies

Pharmacokinetic studies were performed to correlate the toxicity and efficacy results obtained for the IND-Am prodrugs and free IND with plasma. The pharmacokinetic curves were shown in Fig. 5, and some pharmacokinetic parameters were listed in Table 1. The results indicated that the value of T_{max} was 2.1 h for free IND. It was prolonged to 5.3, 6.1, 8.8 and 5.2 h for the prodrugs of IND-Am-1.8, IND-Am-2.7, IND-Am-4.8 and IND-Am-12.0. Meanwhile, the value of C_{max} decreased from 25.8 $\mu\text{g}/\text{mL}$ for free IND to 7.0, 3.6, 2.2 and 0.5 $\mu\text{g}/\text{mL}$ for the IND-Am prodrugs. It

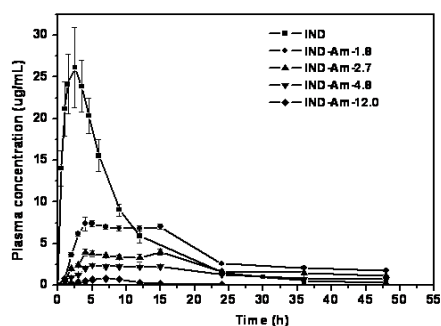


Fig. 5 Variation of IND plasma concentration as a function of time (mean \pm S.D., $n = 5$).

Table 1 Pharmacokinetic parameters after oral administration of the IND-Am prodrugs and free IND at a dose of 3.6 mg/kg of IND equivalent in mice

	Free IND	IND-Am-1.8	IND-Am-2.7	IND-Am-4.8	IND-Am-12.0
T_{max} (h)	2.1	5.3	6.1	8.8	5.2
C_{max} ($\mu\text{g}/\text{mL}$)	25.8	7.0	3.6	2.2	0.5
AUC (h $\mu\text{g}/\text{mL}$)	238.6	209.9	131.9	78.5	8.7

Values presented as mean, $n = 5$ in all groups.

T_{max} : time at which a maximum concentration of drug in the plasma.

C_{max} : maximum drug concentration in the plasma.

AUC: area under plasma concentration vs. time curve.

further proved that the prodrug could realize controlled release of IND. The AUC value of IND-Am-1.8 prodrug with good swelling property closed to that of the free IND, implying that their bioavailability is almost the same.

IV. CONCLUSIONS

A series of IND-Am prodrugs were mildly synthesized at room temperature. IND was conjugated with amylose through ester bond characterized by FTIR and ^1H NMR spectroscopy. The loaded IND content in each prodrug was determined to be 1.8, 2.7, 4.8, 12.0, 15.6 and 21.6 mg/g from UV spectroscopy. The results of *in vitro* experiment indicated that IND was hardly released in the simulated stomach medium, but could be controlled released in the simulated small intestine and colonic conditions. The pharmacokinetic analysis further proved that the prodrug could realize controlled release of IND. Therefore IND-Am prodrug is suitable for the intestine targeted and controlled release of IND.

ACKNOWLEDGMENT

This work was supported by the National Natural Science Foundation of China (20574089, 20676155) and the Scientific Research Foundation for the Returned Overseas Chinese Scholars from the State Education Ministry.

REFERENCES

1. Hardman J G, Gilman A G, Limbird L E (1996) The pharmaceutical basis of therapeutics. McGraw-Hill, New York
2. Zhang Y, Chu C C (2002) Biodegradable dextran-poly(lactide) hydrogel networks: Their swelling, morphology and the controlled release of indomethacin. *J Biomed Mater Res* 59: 318-328
3. Ye S, Wang C, Liu X, Tong Z (2005) Deposition temperature effect on release rate of indomethacin microcrystals from microcapsules of layer-by-layer assembled chitosan and alginate multilayer films. *J Control Release* 106: 319-328
4. Stella V J, Himmelstein K J (1980) Prodrugs and site-specific drug delivery. *J Med Chem* 23: 1275-1282
5. Lambert D M (2000) Rationale and applications of lipids as prodrug carriers. *Eur J Pharm Sci* 11: S15-S27

Author: Liqun Yang

Institute: Institute of Polymer Science, School of Chemistry and Chemical Engineering, Sun Yat-Sen University

Street: Xin-Gang West road 135

City: Guangzhou

Country: P. R. China

Email: yanglq@mail.sysu.edu.cn

***In Vitro* Study of Alginate/Poly-*L*-Arginine Microcapsules as a Protein or Anticancer Drug Carrier**

Qi Lan¹, Ying Wang¹, Shibin Wang^{1,2*}, Yuangang Liu¹

1 College of Materials Science & Engineering, Huaqiao University, Quanzhou, China

2 Research Institute of Pharmaceutical Engineering, Quanzhou, China

Abstract — It is known that drug carriers are widely used for controlling the administration of drugs *in vivo*. Since Lim and Sun invented the first APA microcapsule in 1980s, different microencapsulating crafts have been developed for the application of drug delivery. However, the search of new materials for the preparation of biocompatible, stable, biodegradable microcapsules with high pharmacological efficacy and well release behavior is still ongoing. Poly amino acids have attracted considerable attentions in recent years due to their non-toxicity, biocompatibility, and nutritional function. Poly-*L*-arginine, whose degradation product can inhibit tumor growth, enhance drug delivery across biological membranes and possess antimicrobial activity, has come into our sight.

In this present work, we attempted to prepare a biodegradable and intervening therapeutic drug carrier and focused on its *in vitro* slow-release capacity of protein and anticancer drug.

Keywords — poly-*L*-arginine, microcapsules, protein, anticancer drug, slow-release

I. INTRODUCTION

Due to their biocompatibility and biodegradability, Poly amino acids have been the ideal candidates for applications in drug delivery systems [1]. In this study, poly-*L*-arginine microcapsules were studied as drug carriers for its nutritional function and therapeutic efficacy [2-4]. Cytarabine (Ara-C) and Fluorouracil (5-Fu) were selected as the model drugs in this study because they are widely used in the clinical anticancer treatment while Hemoglobin (Hb) has already been screened out as the modal protein drug in the previous research [5-12]. We managed to manufacture Alginate/Poly-*L*-Arginine Microcapsules and proved them as a potential protein or anticancer drug carrier.

II. MATERIALS

Hemoglobin (Hb)	BR	Cytarabine (Ara-C)	AR
Fluorouracil (5-Fu)	BR	Sodium alginate	AR
Calcium chloride	AR	poly- <i>L</i> -arginine(PLA)	AR

III. METHODS

Microcapsules Formation

Sodium alginate was dissolved in distilled water and filtered through 0.22 μm membrane filters. Alginate solution under certain concentration was then pumped through a syringe into an aqueous solution of calcium chloride. The calcium alginate beads were formed, collected, washed with distilled water and then transferred to aqueous solution of the bovine hemoglobin, cytarabine, fluorouracil for drug loading. The microcapsules were finally obtained by suspending the beads in an aqueous solution of poly-*L*-arginine to form the polymeric membrane.

In Vitro Release Studies

Experiments were performed in a dissolution apparatus at 37°C. The drug loaded alginate/poly-*L*-arginine microcapsules were suspended in 200mL of a phosphate buffered saline solution (PBS, pH 6.8) under a stirring speed of 50rpm. The amount of drug releasing from the microcapsules was indirectly measured under the wavelength of 405nm (Hb), 272nm (Ara-C) and 265nm (5-Fu) by UV-visible spectrophotometer.

IV. RESULTS AND DISCUSSION

Optimized Condition of Beads Formation

The alginate beads were prepared using a high voltage electrostatic droplet generator. The optimized experimental conditions for the preparation of beads with a narrow size distribution were as follows: electric voltage 6.3 kV; pump rate 50 mm/h; distance between needle tip and gelling solution 20 mm; 7[#] flat needle.

Calcified alginate Beads with different sizes were obtained by changing the concentration of alginate or calcium chloride. When the concentration of alginate was too low (<1.8%), only fragments were formed; a higher concentration (>2.6%) resulted in nothing more than oval particles. The ultimate spherical and homogeneous beads

were obtained when the concentration of alginate was 1.8% and with the corresponding 4.5% (w/v) concentration of calcium chloride.

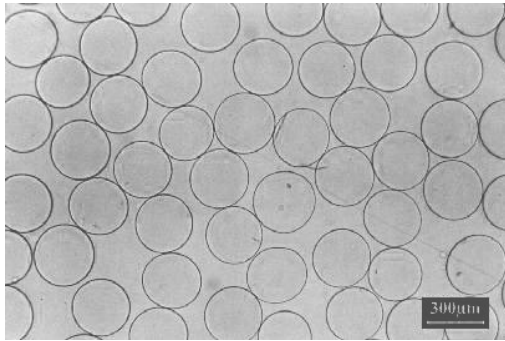


Fig.1 Morphology of Ca-Alginate beads (×40)

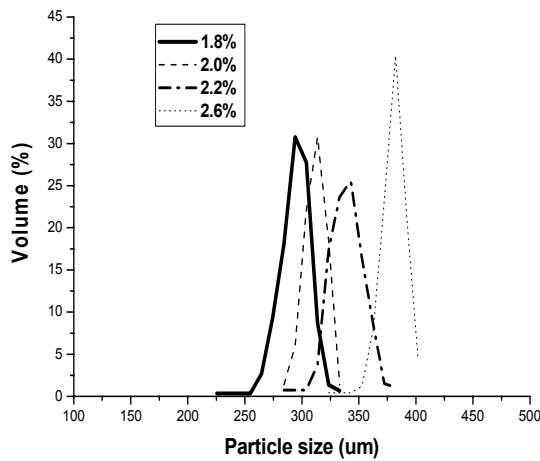


Fig.2 Particle size distribution with different concentrations of Na-Alginate

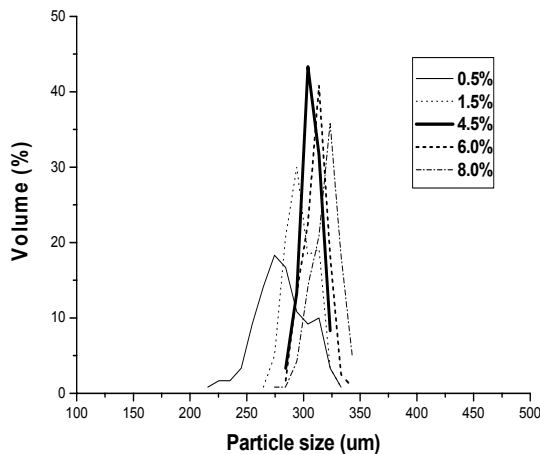


Fig.3 Particle size distribution with different concentrations of CaCl₂

Encapsulation Efficiency of microcapsules

Hb was loaded into the microcapsules by the suspension of beads in Hb solution under a shaking speed of 200rpm for 16h and successful encapsulation at 10°C in a shaking container for 10 minutes to accomplish the electrostatic interaction sufficiently. Effects of molecular weights and concentrations of poly-L-arginine on encapsulation efficiency were considered dissectively, so did the effect of membrane-forming time. Results showed encapsulation efficiency were all beyond the specified value given in the “Pharmacopoeia of People’s Republic of China” (2005).

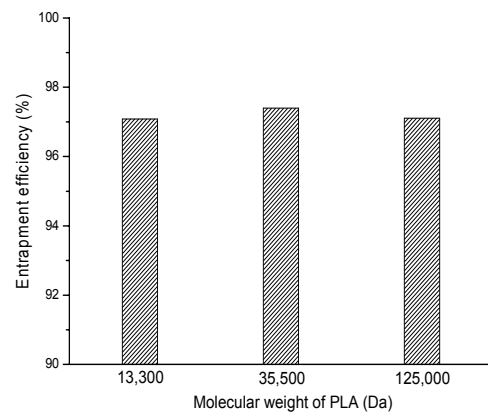


Fig.4 Entrapment efficiency of microcapsules with different molecular weights of PLA

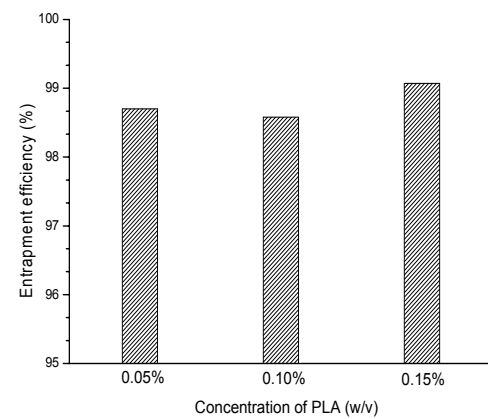


Fig.5 Entrapment efficiency of microcapsules with different concentrations of PLA

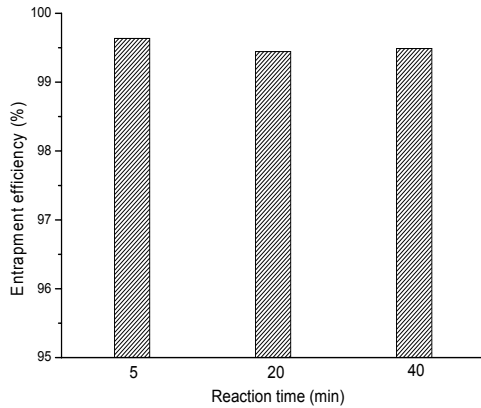


Fig.6 Entrapment efficiency of microcapsules with different reaction time of PLA

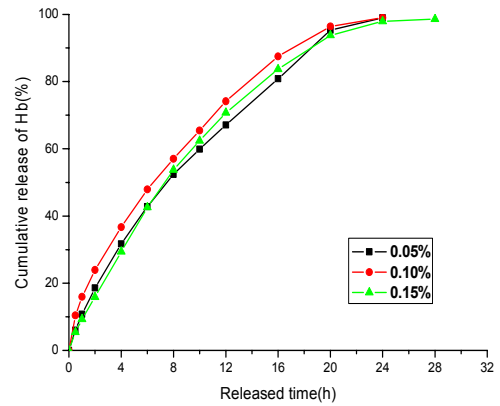


Fig.8 The cumulative released of Hb from microcapsules with different concentrations of PLA

In Vitro Release Studies

In vitro release behavior of Hb from the microcapsules was studied. The release profile of microcapsules based on different molecular weights and concentrations of poly-L-arginine shared the same trend, Hb was slowly released from the microcapsules and the final cumulative release reached 98% and 95% respectively. However, the profile also showed microcapsules prepared under 5 minutes membrane-forming time got a preferable slow-release performance.

In vitro release behaviors of Ara-C and 5-Fu from the microcapsules were not so ideal. Cumulative release of Ara-C and 5-Fu reached 63% and 68% at the end of 0.5h, both were far higher than the specified value given in the ‘‘Pharmacopoeia of People’s Republic of China’’ (2005) of microcapsules and indicated an obvious burst release.

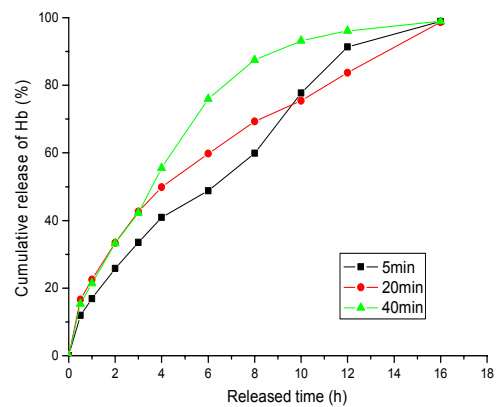


Fig.9 The cumulative released of Hb from microcapsules with different reaction time of PLA

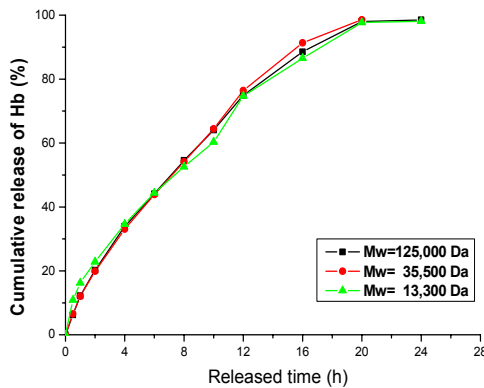


Fig.7 The cumulative released of Hb from microcapsules with different molecular weights of PLA

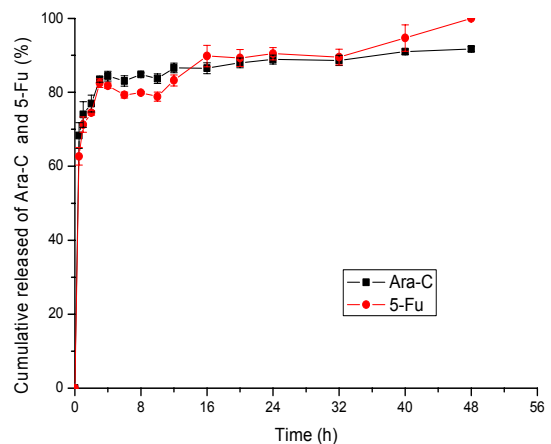


Fig.10 The cumulative released of Ara-C and 5-Fu from microcapsules

V. CONCLUSIONS

We reached a conclusion that the protein Hb was encapsulated with a high efficiency (>90%), *in vitro* release profiles showed that Hb was slowly and completely released from the microcapsules at pH 6.8 within 16 to 28h. Due to the molecular weights and chemical structures, the anticancer Ara-C and 5-Fu contained in alginate/poly-L-arginine microcapsules bursted out at first and turned to slow diffuse after.

These results implied that the alginate/poly-L-arginine microcapsules may be used for some further applications in the encapsulation of protein-based drugs since their stable and complete release *in vitro* studies. We also believe through better crafts, they can be a potential carrier of anticancer drugs as well.

ACKNOWLEDGEMENTS

Financial supports from National 863 Project (2006AA02A118), National Nature Science Foundation of China (30370415), and National Nature Science Foundation of Fujian Province of China (C0710034) were gratefully acknowledged.

REFERENCES

- [1] Wang S B, Xu F H, He H S. *et al.* Novel alginate-poly(L-histidine) microcapsules as drug carriers: in vitro protein release and short term stability [J]. *Macromol. Biosci.* 2005, 5, 408–414
- [2] Tang G P, Chen Q Q. Application of Poly-amino-acid in Drug Controlled Release Systems [J]. *Biomed Engi*, 2001, 18 (2): 169-172
- [3] Tung C H, Weissleder R. Arginine containing peptides as delivery vectors [J]. *Adv Drug Deliver Rev*, 2003, 55: 281-294
- [4] Wang S B, Chen A Z, Weng L J. *et al.* Effect of drug-loading methods on drug load, encapsulation efficiency and release properties of alginate/poly-L-arginine/chitosan ternary complex microcapsules [J]. *Macromol. Biosci.* 2004, 4, 27–30
- [5] Sinha V R, Trehan A. Biodegradable microspheres for protein delivery [J]. *J Control Release*, 2003, 90 (3): 261-280
- [6] Leonarda M, Rastello D B M, Huberta P. Hydrophobically modified alginate hydrogels as protein carriers with specific controlled release properties [J]. *J Control Release*, 2004, 98 (3): 395-405
- [7] George M, Abraham T E. pH sensitive alginate–gaur gum hydrogel for the controlled delivery of protein drugs [J]. *Int J Pharm*, 2006, In press
- [8] Whittlesey K J, Shea L D. Delivery systems for small molecule drugs, proteins and DNA: the neuroscience/biomaterial interface [J]. *Exp Neurol*, 2004, 190 (1): 1-16
- [9] Ruckmani K, Jayakar B, Ghosal S K. Nonionic surfactant vesicles (niosomes) of cytarabine hydrochloride for effective treatment of leukemias: encapsulation, storage and in vitro release[J]. *Drug Dev Ind Pharm*, 2000, 26 (2): 217-222
- [10] Sastre R L, Blanco M D, Go´mez C. Cytarabine trapping in poly (2-hydroxyethylmethacrylate-co-acrylamide) hydrogels: drug delivery studies [J]. *Polym Int*, 1999, 48 (9): 843-850
- [11] Gómez C, Blanco MD, Bernardo MV, et al. Cytarabine release from comatrices of albumin microspheres in a poly (lactide–co–glycolide) film: in vitro and in vivo studies [J]. *Eur J Pharm Biopharm*, 2004, 57 (2):225–233
- [12] Li W, Huang M, Liu XA. Preparation of 5-Fluorouracil-loaded Nanocapsules [J]. *Chemical World*, 2004, (1): 35-38

Study of Solanine on Mitochondrion in HepG₂ Cell

Shiyong Gao, Yubin Ji, Chenfeng Ji, Xiang Zou

Postdoctoral Research Station, The Institute of Materia Medica, Harbin University of Commerce, Harbin 150076, Heilongjiang Province, P.R. of China

Abstract — Objective: To observe the effect of solanine on the membrane potential of mitochondria in HepG₂ cells and [Ca²⁺]_i in the cells, and to uncover the mechanism by which solanine induces apoptosis. **Methods:** HepG₂ cells are double stained with AO/EB, and morphological changes of the cells are observed using laser confocal scanning microscopy (LCSM). HepG₂ cells are stained with TMRE, and change in the membrane potential of mitochondria in the cells are observed using LCSM. HepG₂ cells are double stained with Fluo-3/AM, and change of [Ca²⁺]_i in the cells are observed using LCSM. HepG₂ cells are double stained with TMRE and Fluo-3/AM, and both the change in membrane potential of mitochondria and that of [Ca²⁺]_i in the cells are observed using LCSM. **Results:** Cells in treated groups show typical signs of apoptosis. The results of staining with TMRE show that solanine can lower membrane potential; those of staining with Fluo-3/AM show that solanine can increase the concentration of Ca²⁺ in tumor cells; and those of double staining with TMRE and Fluo-3/AM show that solanine can lower membrane potential; those of staining with TMRE show that solanine can increase the concentration of Ca²⁺ in the cells at the same time as it lowers the membrane potential of mitochondria. **Conclusions:** Solanine opens up the PT channels in the membrane by lowering the membrane potential, leading to Ca²⁺ being transported down its concentration gradient, which in turn leads to the rise of the concentration of Ca²⁺ in the cell, turning on the mechanism for apoptosis.

Keywords — Solanine; Hepatocarcinomatic cell; Ca²⁺ in the cell; Membrane potential; Laser confocal scanning microscopy (LCSM)

I. INTRODUCTION

Solanine is found mainly in the tuber of the potato (*Solanum tuberosum* L.)^[1] and in the whole plant of the nightshade (*Solanum nigrum* Linn.) of the family Solanaceae.

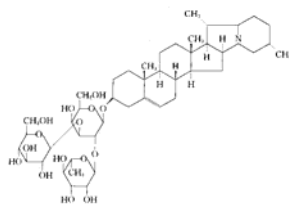


Fig.1 molecular structure of solanine

The whole plant of the nightshade contains many steroid alkaloids, including solamargine, solasonine, and solanine, as well as saponin and other substances. It can be used for anti-tumor purposes, with a strong inhibitory effect on tumors in animals and a clearly toxic effect on tumor cells^[2]. Its ethanol extract is capable of inhibiting the growth of breast cancer and induce apoptosis in tumor cells^[3]. The anti-tumor effect of solamargine has been reported^[4], but there is as yet no report about any anti-tumor effect of solanine. From our past experience in both in vivo and in vitro experiments, we have found that solanine is cytotoxic to cells, especially for the hepatocarcinomatic cell HepG₂. Through morphological observation and observation using the DNA Ladder and flow cytometry, we discovered that solanine exerts its anti-tumor effect by inducing apoptosis in HepG₂. Membrane potential of mitochondria^[5,6] and [Ca²⁺]_i in the cells^[7,8], two factors closely associated with apoptosis, are themselves supplementary to and closely related with each other. In the present study, we try to explicate the mechanism by which solanine induces apoptosis of tumor cells by focusing on the mitochondria and by observing the effect of solanine on the membrane potential of HepG₂ and [Ca²⁺]_i in the cell.

II. METHODS

A. Cell Culture and Treatment

HepG₂ cell is incubated in RPMI1640 medium containing 10% fetal serum at 5%CO₂ and 37°C, and transfer of culture is performed once every 3-4 days. When the cells are growing steadily in the phase of logistic growth, 0.25% pancreatin is used to digest the cells. Digested cells are re-suspended using RPMI 1640 medium containing 10% fetal serum and counted, and the concentration of cells is adjusted to 1×10⁴/mL. Cell suspension is added to the round troughs of 35mm Petri dishes at 200μL/dish, and the dishes are divided into 2, 0.4, 0.08, 0.016, 0.0032μg/mL treatment groups, the control, and the positive control (to be treated with camptothecine). After being incubated for 24h at 5% CO₂ and 37°C, the treatment groups are treated with solanine of different concentrations so that their final concentrations are 2, 0.4, 0.08, 0.016, 0.0032μg/mL, respectively;

an equal volume of RPMI1640 is added to the control, while the positive control is treated with camptothecine, with a final concentration of 0.08 $\mu\text{g}/\text{mL}$. The dishes are then incubated for 48h more at 5% CO_2 and 37°C in CO_2 incubator.

B. Observation of Solanine-Induced Morphological Changes of HepG₂ Nuclei Using LCSM

After 48h, the culture solution in the Petri dishes is sucked out, and the cells are rinsed 3 times with PBS, double stained with 200 μl of AO/ EB so that the final concentration is 5 $\mu\text{g}/\text{mL}$, incubated for 5-10min at 37°C, and rinsed 3 times with PBS, 5min/time. Then 200 μl of PBS is added, and LCSM is used to observe the morphology of the cells. Dual-channel activation is used, with an excitation wavelength of 488nm and a emission wavelength of 500-520nm for PMT1(AO) and an excitation wavelength of 543nm and a emission wavelength of 600-700nm for PMT2(EB).

C. Observation of Solanine-Induced Change in $[\text{Ca}^{2+}]_i$ in HepG₂ Cells Using LCSM

After 48h, the cells are taken out of the incubator. The culture solution in the Petri dishes is sucked out, the cells are rinsed 3 times with HEPES, and 4 $\mu\text{g}/\text{mL}$ Fluo-3/AM is added, 200 $\mu\text{l}/\text{dish}$. After the cells are incubated at 37°C for 50min and rinsed with HEPES 3 times, 200 μl of HEPES culture medium is used to cover all the cells in the troughs, and then LCSM is used to observe the fluorescence intensity (FI) of the cells, with an excitation wavelength of 488nm and a emission wavelength of 555 \pm 15nm.

D. Observation of Solanine-Induced Change in the Membrane Potential of the Mitochondria in the Cells Using LCSM

After 48h, the cells are taken out of the incubator. The culture solution in the Petri dishes is sucked out, the cells are rinsed 2-3 times with PBS, and 200 μl of tetramethyl rhodamine ethyl ester (TMRE) is gently added to the dishes, so that the final concentration is 2 $\mu\text{mol}/\text{L}$. The cells are then incubated for 30min and, after the staining solution is sucked out, gently rinsed 3 times with PBS. 200 μl PBS is used to cover all the cells in the troughs, and then LCSM is used to observe the fluorescence intensity of the cells, with an excitation wavelength of 543nm and a emission wavelength of 570 \pm 20nm.

E. Statistical analysis

t test was performed on data obtained from the experiments, with the results expressed in the format mean \pm SD.

III. RESULTS

A. Effect of Solanine on the Morphology of HepG₂ Cells

After the DNA-specific fluorochromes AO and EB are used to stain HepG₂ cells, LCSM is used to observe the morphological changes of HepG₂ cells treated with solanine. From Figure 2-1A, it can be seen that the control is morphologically normal. The nuclei of different cells are of similar sizes, regularly shaped. With solanine treatment, however, the cells show marked morphological changes. In the groups treated with 0.0032 $\mu\text{g}/\text{mL}$ and 0.016 $\mu\text{g}/\text{mL}$ of solanine (Fig.2-1 B and C), the cells are wrinkled, and the chromatin is concentrated and marginalized. In the group treated with 0.08 $\mu\text{g}/\text{mL}$ of solanine (Fig.2-1D), cells with fragments and apoptotic bodies appear, a typical sign for apoptosis. In the groups treated with 0.4 $\mu\text{g}/\text{mL}$ and 2 $\mu\text{g}/\text{mL}$ of solanine (Fig.2-1E and F), the number of cells containing apoptotic bodies shows significant increase. At the same time, it can be seen that high dosage of solanine is lethal to tumor cells, for with increasing dosage, the number of cells in sight decreases significantly. Apoptotic bodies obviously also appear in the positive control treated with camptothecin with 0.08 $\mu\text{g}/\text{mL}$ as the final concentration.

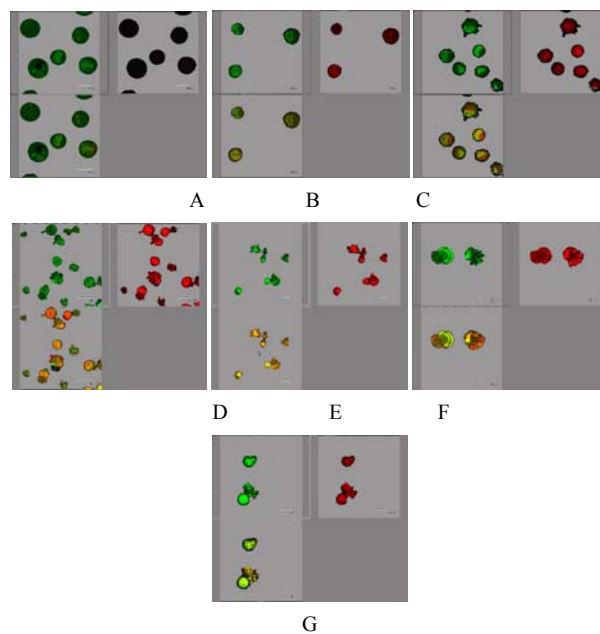


Fig.2 Effect of Solanine on the Morphology of HepG₂

Table 1 Effect of solanine on $[Ca^{2+}]_i$ in HepG₂ cells

Group	Final concentration (μg/mL)	Number of cells(n)	FI
control	—	18	23.98±10.06
CAM	0.08	16	26.92±8.20
solanine	0.0032	25	40.31±10.15 ^b
	0.016	37	59.31±17.56 ^b
	0.08	17	91.01±23.19 ^b
	0.4	19	158.75±14.52 ^b
	2	20	209.85±10.86 ^b

^bP<0.01 vs control

B. Change Induced by Solanine in $[Ca^{2+}]_i$ in HepG₂ Cells in the Process of Apoptosis

Figure 3 shows the effect of different dosages of solanine (0.0032, 0.016, 0.08, 0.4, 2 μg/mL) on $[Ca^{2+}]_i$ in HepG₂ cells observed using LCSM with staining with the fluorescent probe Fluo-3/AM. On the left side of each group is the photograph (green) showing $[Ca^{2+}]_i$ taken with the confocal microscope, with the depth of the color representing the fluorescence intensity (FI). On the right is the 3D configuration reconstructed using LCSM for the group, with different colors reflecting different FI values, which indirectly reflect the concentrations of $[Ca^{2+}]_i$ for the test group in question. From these photographs, we can see that the $[Ca^{2+}]_i$ for the control in Figure 3A is very low, while those for the groups treated with solanine (Figures 3B-F) have all been increased, with the degree of increase being dependent on the dosage of solanine administered. The positive control camptothecin does not increase $[Ca^{2+}]_i$. Statistics on FI obtained through LCSM for the various groups in Table 1 show the same results.

C. Change Induced by Solanine in the Membrane Potential of Mitochondria in HepG₂ Cells in the Process of Apoptosis

Figure 4 shows the effect of different dosages of solanine (0.0032, 0.016, 0.08, 0.4, 2 μg/mL) on the membrane potential of mitochondria in HepG₂ cells observed using LCSM with staining by the fluorescent probe TMRE. The brightness of the coloration reflects different values of FI, thus indirectly reflecting the membrane potential of mitochondria in the cells for these different groups. From these photographs, we can see the membrane potential of mitochondria in the cells is relatively high for the blank in Figure 4A, while those for the groups treated with solanine (Figures 4B-F) have all been increased, with the degree of increase being dependent on the dosage of solanine administered. Statistics on FI obtained through LCSM for the various groups in Table 2 show that the membrane potential of mitochondria in the cells is significantly lowered (p<0.01) in groups treated with 0.016, 0.08, 0.4, and 2 μg/mL

Table 2 Effect of solanine on the membrane potential of mitochondria in HepG₂ cells

Group	Final concentration (μg/mL)	Number of cells (n)	FI
control	—	53	75.70± 8.25
CAM	0.08	16	47.17±15.98
Solanine	0.0032	66	70.04±4.83
	0.016	90	63.21±6.36 ^b
	0.08	144	52.26±6.46 ^b
	0.4	37	32.50±10.00 ^b
	2	33	28.49±9.71 ^b

^bP<0.01 vs control

of solanine. The membrane potential in the 0.0032 μg/mL group is also lowered, but the difference from the blank is not statistically significantly. The membrane potential of mitochondria in HepG₂ cells of the group treated with 0.08 μg/mL of camptothecin is also significantly lowered.

IV. DISCUSSION

In recent years, reports have been made that the dissipation of the membrane potential of mitochondria precedes the activation of nuclease^[9], and that it precedes the exposure of phosphatidylserine on the surface of the cell. When the transmembrane potential of mitochondria is dissipated, the cell would enter the irreversible apoptotic process. The uncoupled respiratory chain of the mitochondrion would produce a large amount of active oxygen, oxidizing the cardiolipin on the inner membrane of the mitochondrion. Experiments have shown that the decoupling reagent mCICCP can lead to the apoptosis of lymphocytes^[10], whereas if the transmembrane potential of mitochondria can be stabilized, apoptosis would be prevented. Therefore, the dissipation of transmembrane potential of mitochondria is closely related to apoptosis.

Results from earlier experiments show that solanine can induce the apoptosis of HepG₂ cells. In the present study, double staining with AO/EB and solanine (0.0032, 0.016, 0.08, 0.4, 2 μg/mL) carried by TMRE are used to treat HepG₂ cells, and LCSM is used to observe changes in the membrane potential of mitochondria as solanine induces the appearance of apoptotic bodies^[11]. The results are shown in Figure 2, Figure 4, and Table 2. As solanine induces the appearance of apoptotic bodies and causes the apoptosis of cells, the membrane potential of mitochondria in cells in groups treated with different dosages of solanine (0.0032, 0.016, 0.08, 0.4, 2 μg/mL) is all decreased in comparison with the control. The amount of decrease is dosage-dependent, and the difference from that of the control is statistically significant for the groups treated with 0.016, 0.08, 0.4, 2 μg/mL of solanine, respectively, suggesting that solanine

can lead to the lowering of the membrane potential of mitochondria in HepG₂ cells. But the lowering of the membrane potential of mitochondria is a manifestation of the opening of the PT pores of the mitochondria^[12], so solanine can lead to the opening of the PT pores of the mitochondria.

The opening of PT pores can lead to the occurrence of two events^[13]: 1) the intra-membrane and extra-membrane ion concentration tend toward equilibrium, the transmembrane H⁺ gradient disappears, and the respiratory chain is uncoupled; 2) the flow of intra- and extra-membrane ions toward equilibrium leads to a hypertonic mitochondrial matrix, resulting in change in the volume of the mitochondrion. Since the surface area of the folded inner membrane of mitochondrion is larger than that of the outer membrane, this would lead to the rupture of the outer membrane.

These two events lead respectively to two consequences. Since a large number of Ca²⁺ have accumulated in mitochondria, the concentration of Ca²⁺ in mitochondria is much higher than that in the cytoplasm. The occurrence of the first event would lead directly to the flow of Ca²⁺ from the mitochondria to the cytoplasm, resulting in rapid increase in the concentration of Ca²⁺ in the cytoplasm. In the present study, the Ca²⁺-specific molecular probe Fluo-3/AM is used to carry solanine in different concentrations to treat HepG₂ cells, and LCSM is used to observe changes in [Ca²⁺]_i in the cells after the treatment. Results of the experiment are shown in Figure 3 and Table 1. In groups treated with different dosages of solanine (0.0032, 0.016, 0.08, 0.4, 2μg/mL), the concentration of Ca²⁺ in HepG₂ cells is all increased in a dosage-dependent way. This verifies the inference we have drawn, namely, by opening up PT channels, solanine leads to the release of Ca²⁺ from the mitochondria, resulting in the increase of [Ca²⁺]_i in the cell.

Through the analysis above, we conclude the following: solanine can facilitate the opening of the PT channels in mitochondria, releasing Ca²⁺ from these organelles. This leads to an increase in the concentration of Ca²⁺ in the cell, thus starting the mechanism for apoptosis and inducing the occurrence of apoptosis. But further research is needed to uncover how the PT channels are opened and which enzymes and genes are involved in this process.

ACKNOWLEDGMENT

The project was supported by the National Natural Science Foundation of China, No.30400591; the Heilongjiang Province Natural Science Foundation, No.D2004-13, D200505; Harbin City Young Scientist Foundation, No.2004AFQXJ035

REFERENCES

- [1] Zywicki B, Catchpole G, Draper J, et al. (2005) Comparison of rapid liquid chromatography-electrospray ionization-tandem mass spectrometry methods for determination of glycoalkaloids in transgenic field-grown potatoes. *Anal Biochem* 336:178-186.
- [2] Ji YB. (1995) *Pharmacological Action and Application of Available Composition of Traditional Chinese Medicine*. Heilongjiang, China.
- [3] Y.O. Sona, J. K imb, J.C. Lima, et al. (2003) Ripe fruits of *Solanum nigrum* L. inhibits cell growth and induces apoptosis in MCF-7 cells. *Food and Chemical Toxicology* 41:1421-1428.
- [4] Liu LF, Liang CH, Shiu LY, et al. (2004) Action of solamargine on human lung cancer cells-enhancement of the susceptibility of cancer cells to TNFs. *FEBS Lett* 577:67-74.
- [5] Hwang JM, Kuo HC, Tseng TH, et al. (2006) Berberine induces apoptosis through a mitochondria/caspases pathway in human hepatoma cells. *Arch Toxicol* 80:62-73.
- [6] Lugli E, Troiano L, Ferraresi R, et al. (2005) Characterization of cells with different mitochondrial membrane potential during apoptosis. *Cytometry A* 68:28-35.
- [7] Lepine S, Sulpice JC, Giraud F. (2005) Signaling pathways involved in glucocorticoid-induced apoptosis of thymocytes. *Crit Rev Immunol* 25:263-88.
- [8] Pretorius E, Bornman MS. (2005) Calcium-mediated apoptosis plays a central role in the pathogenesis of estrogenic chemical-induced neurotoxicity. *Med Hypotheses* 65:893-904.
- [9] Zhang M, Li Y, Zhang H, et al. (2001) BAPTA blocks DNA fragmentation and chromatin condensation downstream of caspase-3 and DFF activation in HT-induced apoptosis in HL-60 cells. *Apoptosis* 6:291-297.
- [10] O'Brien KA, Muscarella DE, Bloom SE. (2001) Differential induction of apoptosis and MAP kinase signaling by mitochondrial toxicants in drug-sensitive compared to drug-resistant B-lineage lymphoid cell lines. *Toxicol Appl Pharmacol* 174:245-256.
- [11] Ning N, Peng ZF, Yuan L, et al. (2005) Realgar nano-particles induce apoptosis and necrosis in leukemia cell lines K562 and HL-60. *Zhongguo Zhong Yao Za Zhi* 30:136-140.
- [12] Ly JD, Grubb DR, Lawen A. (2003) The mitochondrial membrane potential (Δψ_m) in apoptosis; an update. *Apoptosis* 8:115-128.
- [13] Di Lisa F, Bernardi P. (2005) Mitochondrial function and myocardial aging. A critical analysis of the role of permeability transition. *Cardiovasc Res* 66:222-232.

Author: Gao Shiyong
 Institute: Postdoctoral Research Station, The Institute of Materia Medica, Harbin University of Commerce
 Street: 138 Tongda Street Daoli District
 City: Harbin
 Country: P.R. of China
 Email: sygao2002@163.com

Preparation and Biocompatibility of a Novel Scaffold Made from Small Intestinal Submucosa Powders

Juhui Qiu¹, Guixue Wang^{1,*} and Tao Jiang^{1,2}

¹Bioengineering College and “111 Project” Laboratory of Biomechanics and Tissue Repair, Chongqing University, Chongqing, China;

²Histology and Embryology Department, Medicine Academy of China People Armed Police Faculty, Tianjin, China

*Corresponding author, Email: guixue_wang@126.com

Abstract — Three-dimensional porous scaffolds play a critical role in both cell targeting and cell transplantation strategies. Small intestine submucosa (SIS) has been recommended as a cell-free, biocompatible and with minimum immune response biomaterial. However, the three-dimensional structure of SIS isn't very suit for tissue regeneration and tissue engineering. So, we tried to prepare SIS sponges and got a kind of novel scaffold. Scanning electron microscope showed that SIS sponge had interconnected network structure and comparably regular pore. The pore diameter was around 100–150 μ m. In vivo implantation test, the sponges were implanted in dorsal muscle of rats for 4 weeks and the results suggest that the SIS sponges had good biocompatibility and also could completely degrade in vivo. So we conclude that the SIS sponges maybe are available scaffolds for injury repair.

Keywords — Scaffold, Small intestine submucosa, Sponge, biocompatibility

I. INTRODUCTION

Three-dimensional porous scaffolds play a critical role in both cell targeting and cell transplantation strategies. Scaffold matrices serve as space-holders to prevent encroachment of surrounding tissues into the graft site. They provide surfaces that facilitate the attachment, survival, migration, proliferation, and differentiation of stem cells and progenitors. They also provide a void volume in which vascularization, new tissue formation, and remodeling can occur [1-3]. A broad range of scaffolds is already available for clinical use, and many new scaffolds are under development. Small intestine submucosa (SIS) derived from the submucosal layer of porcine intestine has been widely used as biomaterial with minimum immune response [4-6]. SIS consists of types I and III collagens above 90% and small amounts of types IV, V, and VI collagens [7]. SIS contains a wide variety of cytokines as well as glycosaminoglycans, fibronectins, chondroitin sulfates, heparins, heparin sulfates, and hyaluronic acids [8, 9]. These constituents are well known to play an important role for tissue remodeling and wound healing. SIS has been used in practical biomedical fields, such as the repair of numerous body tissues, including musculotendinous structures, lower urinary tract recon-

struction, dura mater replacement, vascular reconstruction, and the repair of full and partial thickness skin wounds [10–12]. However, there are no three-dimensional porous structures in SIS and it isn't very suit for tissue regeneration and tissue engineering. In this paper, we designed three-dimensional porous structures SIS sponge by using chemical to get a kind of novel tissue engineering scaffold.

II. METHODS

A. Materials

Porcine jejunum was purchased from Tianjin Food Company (China). 1-Ethyl-3-(3-dimethylaminopropyl) carbodiimide hydrochloride (EDC) and pepsin were purchased from Sigma Chemical Co. (St. Louis, MO, USA) and used as received.

B. Preparation of SIS powder

To separate SIS in porcine jejunum, fat firstly removed from porcine jejunum, followed by carefully washing with water. The porcine jejunum cut in lengths of approximately 10 cm and then washed with a saline solution. SIS was obtained by mechanical removal of the tunica serosa and tunica muscularis externa. Finally, the obtained SIS washed again with a saline solution and freeze-dried at -55°C . SIS fine powders in the size of approximate 20 μ m were obtained by freeze mill (LGJ-10C, China) after pulverizing using mixer (JFC-1500, Japan).

C. Preparation of SIS sponges

The obtained SIS powders (0.15g) were added in 10 ml vial with aqueous solution consisting of 3% acetic acid and 0.1% pepsin, and then dissolved for 48 h. The SIS solution was carefully poured into homemade silicone mold to give SIS sponge shape, followed by freeze-drying. SIS sponges were crosslinked with EDC (50mM) using a mixture of deionized water and ethanol (5/95 v/v) for 24 h. The crosslinked SIS sponges in the mold were dipped in water at

40°C for 1 h to remove unreacted SIS, followed by freeze-drying to give finally SIS sponges. The SIS sponges prepared for rat model were sterilized by EO gas.

D. Measurement of scanning electron microscope

Scanning electron microscope (SEM, VegaII, Tescan, Czech.) was used to examine the pore structure of the SIS sponges crosslinked with EDC. SIS sponges cut in vertical and horizontal section. The sample was mounted on metal stubs and coated with a thin layer of platinum using plasmasputtering apparatus for 2 min under argon atmosphere.

E. In Vivo Implantation Tests

Twelve healthy rats weighing 200g were divided into four groups (three in each group) randomly and then anesthetized by pentobarbital. The dorsal surface hairs of the rats were shaved. The dorsal muscles were exposed and the muscle pockets were made. A rectangular SIS sponge (1×0.5cm) was implanted. Implants with surrounding tissue were carefully dissected from the muscles site at weeks 1, 2, 3, 4 after implantation. The specimens were fixed with 10% (v/v) formalin for 24h at 4°C. After dehydration in a graded series of ethanol, the samples were embedded in paraffin wax. The sections (5µm) were stained with hematoxylin-eosin (HE) for light microscopy evaluation.

III. RESULT AND DISCUSSION

A. Preparation of SIS sponges

SIS fine powder ranging of approximately 20µm was prepared by freeze-milling. The SIS powder was only swelling but insoluble in water, including biologic solution. To construct a certain structure-remolded sponge shape, SIS powder should be dissolved in an aqueous mixture of 3% acetic acid and 0.1% pepsin, and stirred for 48 h. The suspension of SIS powder was changed to swelled form after 24 h and finally made a SIS solution after 48 h. Various SIS sponge shapes formed in various mold after freeze-drying, but the sponge did not maintained the shape in water because it dissipated in water.

Therefore, the crosslinking reaction of SIS to maintain the shape in water was carried out with EDC (50 mM) as crosslinking agent at room temperature for 24 h, since EDC can be easily removed from the SIS sponge crosslinked after crosslinking [13]. SIS sponges were crosslinked by the intra- and inter-reaction of carboxylic acid group with the amine group on SIS chain via activation reaction of carboxylic acid by EDC. After crosslinking, the crosslinked SIS

sponges keep the shape in water even at 40°C. The SIS sponges prepared by 1.5% SIS concentration exhibited elastic and soft property on touch. In addition, the SIS sponges were ease to handle.

B. Structure of SIS sponges

Figure 1, 2 showed the morphologic SEM image of SIS sponge crosslinked with EDC (50 mM) for 1.5% SIS concentrations. The cross section of SIS sponge seemed to have interconnected network structure and comparably regular pore. The SIS sponge prepared by 1.5% SIS concentration showed pore diameter around 150–200µm. Most scaffolds are designed to have an internal porous structure of void spaces that are interconnected through pores or channels on the scale of 50 to 1000 µm [14]. The pore size of SIS sponges is around 150–200µm, which is just large enough to support ingrowth of parenchymal cells and vascular tissues.

C. In Vivo Implantation Tests

To evaluate the tissue response to the SIS sponges, the sponges were implanted in dorsal muscles of rats for time periods up to 4 weeks. One week after implantation, all samples showed typical acute inflammatory tissue responses. The SIS sponges maintained their porous structure and wrapped with a layer of inflammatory cells. The in-

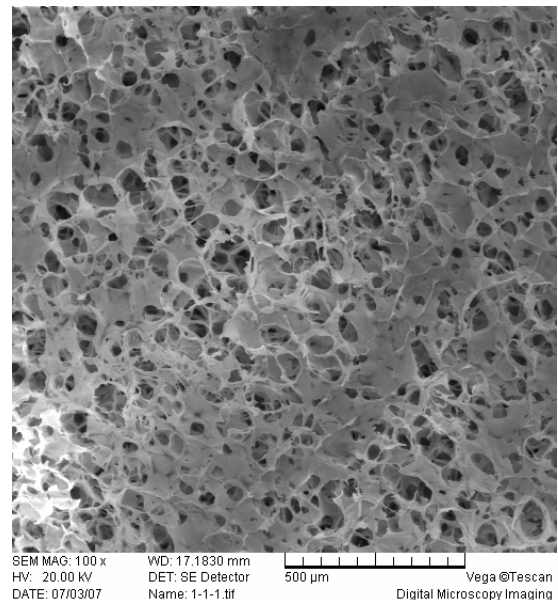


Fig.1 SEM pictures of 1.5% SIS sponges(cross section; magnification, 100×; scale bar, 500µm)

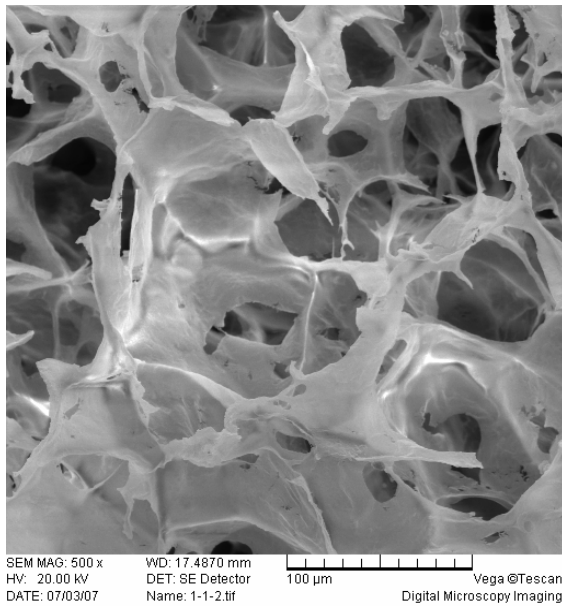


Fig.2 SEM pictures of 1.5% SIS sponges(cross section; magnification, 500 \times ; scale bar, 100 μ m). The cross section of SIS sponge had interconnected network structure and comparably regular pore.

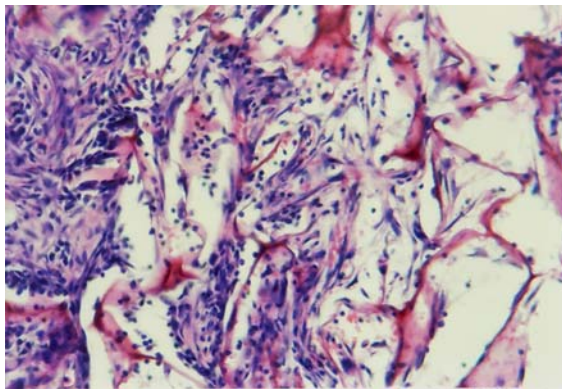


fig.3 hematoxylin-eosin (HE) stain of SIS sponge implanted in rat dorsal muscles (1week; magnification, 200 \times). The SIS sponges maintained their porous structure and wrapped with a layer of inflammatory cells.

flammatory cells had already infiltrated the outside SIS sponges (figure3). Three weeks after operation, slight inflammation with some lymphocytes, progenitor-like cells were observed and the samples became thinner. Four weeks after implantation, there were no inflammation responses and the sponges were almost substituted by muscle cells(figure4).. These results suggest that the SIS sponges had good biocompatibility and it also could completely degrade in vivo.

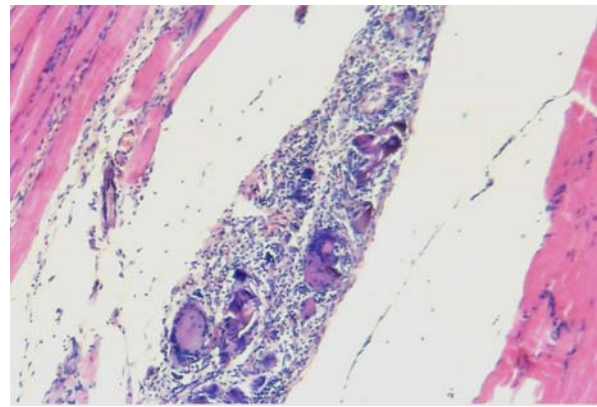


Fig.4 hematoxylin-eosin (HE) stain of SIS sponge implanted in rat dorsal muscles (3week; magnification, 100 \times). There light inflammation and The SIS sponges became thinner.

IV. CONCLUSION

SIS sponge was prepared by crosslinking via the intra- and inter-reaction of carboxylic acid group activated by EDC with the amine group on SIS chain. The crosslinked SIS sponges showed sponge structure with interconnective pore. The pore diameter is around 150–200 μ m. SIS sponges possessed relatively good physical properties and were easily handle. The results of implantation tests in vivo showed the SIS sponges had good biocompatibility and it also could completely degrade in vivo. So we conclude that SIS is a good biocompatibility material and is worthy of continued investigation. It may serve as a structural framework for the application of tissue engineering technologies.

ACKNOWLEDGMENT

This study was supported by grants from the MOST of China(2004DFA06400), the MOE of China (B06023) as well as Chongqing University (200706A1B0140234).

REFERENCES

1. Bauer TW, Muschler GF.(2000) Bone graft materials. An overview of the basic science.Clin Orthop Relat Res371:10-27.
2. Griffith LG.(2002) Emerging design principles in biomaterials and scaffolds for tissue engineering. Ann N Y Acad Sci.961:83-95.
3. Hubbell JA. (1999) Bioactive biomaterials. Curr Opin Biotechnol.10:123-9.
4. Palmer EM, Beilfuss BA, Nagai T et al.(2002)Human helper T cell activation and differentiation is suppressed by porcine small intestinal submucosa. Tissue Eng. 8:893-900.
5. Allman AJ, McPherson TB, Badylak SF et al.(2001) Xenogeneic extracellular matrix grafts elicit a TH2-restricted immune response. Transplantation. 71:1631-40.

6. Kropp BP. (1998) Small-intestinal submucosa for bladder augmentation: a review of preclinical studies. *World J Urol.* 16:262-7.
7. Graham MF, Diegelmann RF, Elson CO et al (1988) Collagen content and types in the intestinal strictures of Crohn's disease. *Gastroenterology.* 94:257-65.
8. Voytik-Harbin SL, Brightman AO, Kraine MR et al (1997) Identification of extractable growth factors from small intestinal submucosa. *J Cell Biochem.* 67:478-91
9. Hodde J. (2002) Naturally occurring scaffolds for soft tissue repair and regeneration. *Tissue Eng.* 8:295-308.
10. Bello YM, Falabella AF, Eaglstein WH. (2001) Tissue-engineered skin. Current status in wound healing *Am J Clin Dermatol.* 2:305-13.
11. Zhang Y, Kropp BP, Moore P et al (2000) Coculture of bladder urothelial and smooth muscle cells on small intestinal submucosa: potential applications for tissue engineering technology. *J Urol.* Sep;164(3 Pt 2):928-34; discussion 934-5.
12. Gastel JA, Muirhead WR, Lifrak JT et al (2001) Meniscal tissue regeneration using a collagenous biomaterial derived from porcine small intestine submucosa. *Arthroscopy.* 17:151-9.
13. Hermanson G.T., (1996) *Bioconjugate Techniques*, Academic Press, San Diego..
14. Muschler GF, Nakamoto C, Griffith LG. (2004) Engineering principles of clinical cell-based tissue engineering. *J Bone Joint Surg Am.* 86-A:1541-58

Performance Comparison between Two Types of Miniature Axial Flow Pumps for Children

Ningning Chen, Yu Chang*, Bin Gao, Linxi Shi, Ling Li, Xinrui Ma

School of Life Science and Bioengineering, Beijing University of Technology, Beijing, China

Abstract— Miniature axial flow pump (M-AFP) is a ventricular assist device that supports the failing ventricle in advanced stage heart failure. In the past several years, we have developed two types of M-AFP aiming for children. In this paper, mechanical performance of them are tested and analyzed in order to help us find out their differences in nature. A simulative circulative apparatus is designed that can be used to quantitatively predict the mechanical characteristic parameters of the pumps and their relationship. Under the condition of load pressure invariance, we mainly test the change of blood flow with these two pumps respectively. The type A has a volume of 47ml; with external diameter of 26mm and length of 72mm. The simulative cardiac flow attains 3–4L/min under the pressure of 100mmHg, which is enough to assist the left ventricular of children. In all the two pumps, rotate speed of impeller and flow rate of blood present positive mutuality with pressure invariance. Besides, comparing with type A, the type B has smaller volume, and it is much easier for type B to increase rotate speed of the pump and comparably reduce energy consumption. Apart from the characters of smaller volume and simpler configuration, the output of miniature axial blood pump has achieved required pressure and blood flow. We still have the possibility to improve the blood pump by reducing energy consumption and increasing efficiency. The performance test and comparison in simulative circulation apparatus that is out of body is very important for improvement of blood pump. It can accelerate the development of mechanical assistant therapy and increase the cure rate of heart failure for children.

Keywords— M-AFP, pump, performance, children, simulative circulation apparatus.

I. INTRODUCTION

Heart failing (HF) is one of the leading causes of death in the world, and children in the patients suffering from heart disease possess a certain proportion. Miniature axial flow pump (M-AFP) is a ventricular assist device that supports the failing ventricle in advanced stage heart failure. Today, with the development of modern medicine and technology, therapy based on mechanical assistant has been paid more and more attention. In the past several years, we have developed two types of M-AFP aiming for children, which require particular smaller volume and blood flow than the standard of the adults. In this paper, mechanical perform-

ance of them are tested and analyzed in order to help us find out their differences in nature, and, based on which, we can seek optical ways for better enhancement. A simulative circulative apparatus is designed that can be used to quantitatively predict the mechanical characteristic parameters (including volume, diameter and length) and performance parameters (including input voltage, input power, blood pump, burthen pressure and amount of blood flow) of the pumps and their relationship. Apart from the characters of smaller volume and simpler configuration, the output of the two types of M-AFP has achieved required pressure and blood flow.

II. MATERIALS AND METHODS

A. Materials

M-AFP that was studied firstly by us is type A axial flow pump. It mainly includes guide blade, impeller, electric motor stator and shell, as is shown in Fig1. Impeller adopts axial helical profile, and curve of special profile is designed in the guide blade. Direction of rotation of guide blade is opposite to the one of impeller. In the result that the power which is generated by rotating of impeller can translate to energy of motion which drive liquid to move forwards along axial. The electric motor stator rings around the impeller, and it drive impeller rotator to rotate. In order to improve able implantation of type A, impeller and guide blade was optimized continuously, and based on which, we developed type B of M-AFP. Mechanical parameters of the two types are shown in Table1.

B. Methods

In order to test the mechanical performance of the two types of M-AFP, a simulative circulative apparatus was conducted to generate data. The simulative circulative apparatus, shown in Fig.1, consisted of a blood pump, a box of reserving liquid, a resistance valve, a manometer, a flowmeter, power resource and silicone tube as simulative vessels. The box of reserving liquid is used to simulate left ventricular. The left orifice of the simulative box is in-flow export of the liquid, and the right one is the outflow

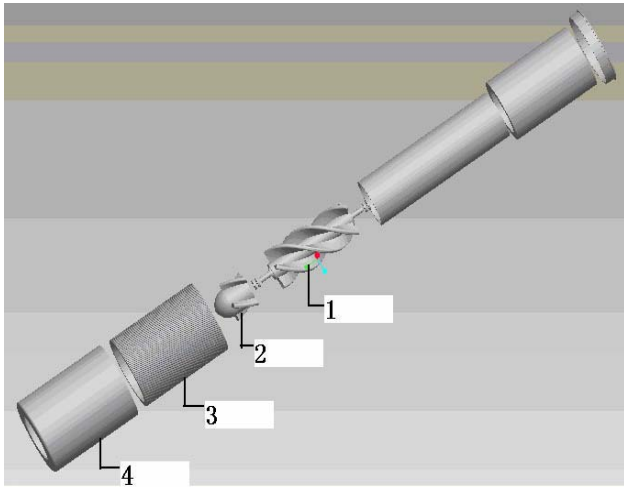


Fig.1 Diagrammatic sketch of M-AFP's structure. The term, 1 is impeller; 2 is guide blade; 3 is electric motor stator; 4 is shell.

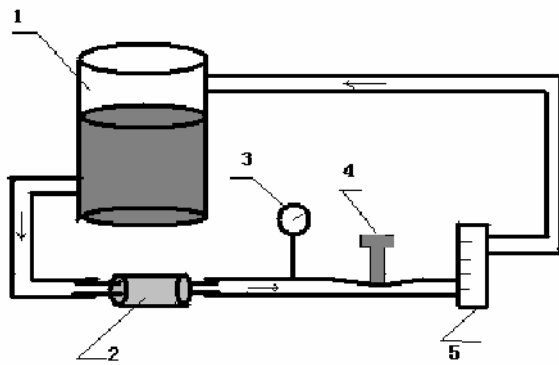


Fig.2 Diagrammatic sketch of simulative circulative apparatus. The term, 1 is box of reserving liquid; 2 is M-AFP; 3 is manometer; 4 is resistance valve; 5 is flowmeter.

export. We adopt solution of 30% glycerol that used to be the circulation transmitter substance, because its concentration resembles the one of blood.

Axial flow pump began to work when a certain input voltage and input current were given, then the pump could drive the liquid to run from inflow export to outflow one. By adjusting resistance valve, pressure difference of 100mmHg generated between the two terminals of the pump. Under the condition of load pressure invariance, by regulating the input voltage of the driving system of the pump, we mainly test the data of rotate speed and blood flow and analyze the changing trends of these parameters with these two pumps respectively. Then relationship curves of “pressure—blood flow—rotate speed” were given. Additional, we can measure and compare the translation ratio of two types of pump according the relationships of input quantities and output ones.

III. RESULTS

By testing, a series of measurement data were obtained. Some of them were shown in Table 1.

Table 1 Mechanical and performance parameters

	Type A	Type B
Diameter(mm)	26	20
Volume(ml)	47	30
Weight(g)	60	50
Power(w)	20	15
Flow(L/min)	3	2,3,4

The volume and weight affect directly the characteristics of dissection consistent of implantation, so according to the data of table, the configuration and size of the two types of M-AFP has achieved the requirements of implantation. Besides, comparing with type A, the type B has smaller volume and weight, and it is much easier to transplant.

The simulative cardiac flow of type A attains 3L/min under the pressure of 100mmHg, and type B attains 4L/min under the same pressure, which is enough to assist the left ventricular of children. In all the two pumps, rotation speeds

of impeller and flow rate of blood present positive mutuality with pressure invariance, which illustrate that advancement of rotation speed can create augment of flow within certain range. Comparing with type A, the efficiency of type B increases apparently because of augment of flow and reduction of input power.

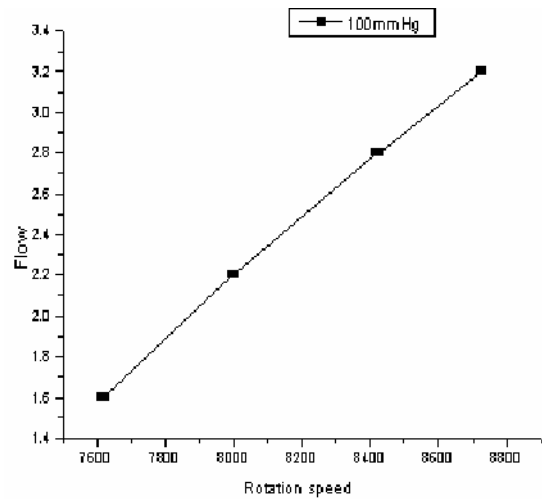


Fig.3 Type A: Grape of “Flow—Rotation speed”

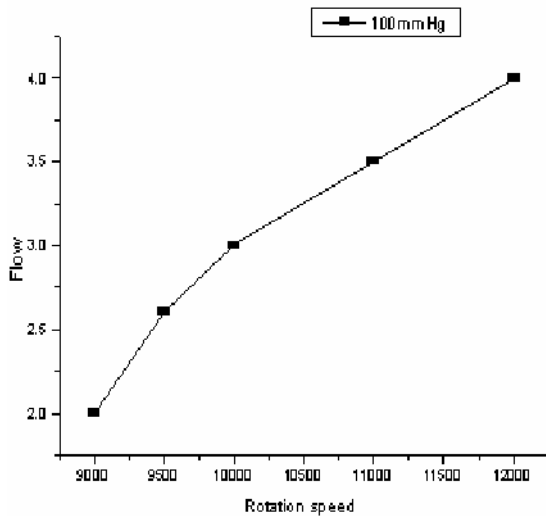


Fig.4 Type B: Grape of “Flow—Rotation speed”

IV. DISCUSSION

Many difficulties need to be solved if we want to research a blood pump that can be transplant long-term. At first, the blood pump should be small and proper possible configuration and size, and adopt natural space of human cavity, which can reduce the affection at the adjacent organs. Moreover, the performance of M-AFP is required to have enough pressure and output flow, as well as higher efficiency. In human, the pressure of circulative system is changing all the time; and we hope that the working performance of the blood pump can keep in favorable stable characteristic when the load pressure vibrates in a certain range. So, the performance test and comparison in simulative circulation apparatus that is out of body is very important for improvement of blood pump.

V. CONCLUSION

Apart from the characters of smaller volume and simpler configuration, the output of miniature axial blood pump has achieved required pressure and blood flow. These merits make M-ABP be paid more and more attention. We still have the possibility to improve the blood pump by reducing energy consumption and increasing efficiency. Further more, if M-ABP can be used in long-term implantation, we should also consider the working stability and longevity.

ACKNOWLEDGMENT

This work partly sponsored by the Beijing Novel Project (33015998200701), and Scientific Research of Beijing Municipal Commission of Education (05015999200701).

REFERENCES

1. Tomonori Tsukiya. Application of indirect flow rate measurement using motor driving signals to a centrifugal blood pump with an integrated motor. *Artificial Organ*, 25(9):692–696, 2001.
2. Akio Funakubo. Flow rate and pressure head estimation in a centrifugal blood pump. *Artificial Organ*, 26(11):985–990, 2002.
3. Tadashi Kitamura. Physical model-based indirect measurements of blood pressure and flow using a centrifugal pump. *Artificial Organ*, 24(8):589–593, 2000.
4. P. J. Ayre. Non-invasive flow estimation in an implantable rotary blood pump: a study considering non-pulsatile and pulsatile flows. *Physiol Meas.*, 24(1):179–189, 2003.
5. Makoto Yoshizawa. Sensorless estimation of pressure head and flow of a continuous flow artificial heart based on input power and rotational speed. *ASAIO J.*, 48(4):443–448, 2002.
6. Akira Tanaka. In vivo test of pressure head and flow rate estimation in a continuous-flow artificial heart. *Artificial Organ*, 27(1):99–103, 2003.
7. K. Takahashi. Estimation of left ventricular recovery level based on the motor current waveform analysis on circulatory support with centrifugal blood pump. *Artificial Organ*, 25(9):713–718, 2001.
8. George Endo. The index of motor current amplitude has feasibility in control for continuous flow pumps and evaluation of left ventricular function. *Artificial Organ*, 25(9):697–702, 2001.

Invasive Blood Pressure Monitoring System for Artificial Heart Surgery

Bin Gao, Linxi Shi, Yu Chang, Xinrui Ma, Ling Li, Ningning Chen

Department Of Life Science & Bioengineering, Beijing Univ. of Technology, Beijing, China

Abstract—Studies of cardiovascular system and cardiac assistance devices are key research direction in our laboratory, a challenging project requires conducting physiological experiments on animal constantly. In an operation, It is significant to detect small changes in important physiological parameters for ensuring the integrity of animal. As a result, in order to detect and acquire accurate parameter variation, a simple monitoring module is quite required as an adjunct to experiments. Directing the widely applied invasive blood pressure monitoring system, a typical block of it is introduced here. Sensor of this system applied has been used in present medical field whose superiorities embody in its continuity, high sensitivity and hygiene. A simulated experiment was established to functionally calibrate the performance of this module to ensure signals can be recorded by the data acquisition system. The result showed a high linear relationship between pressure and output. That the serial output can be used to interface to a computer for further analysis serves a function as continuous monitor during experiment.

Keywords—invasive blood pressure sensor, measurement system.

I. INTRODUCTION

There are two widely used methods in the field of nvasive blood presssure monitoring: fluid coupling method, in which the blood pressure was transferred by a catheter filling with fluid to the sensor outside body, and another method is to put an intravascular pressure sensor against the wall of vessel, in which the blood pressure can be detected more dertectly without transmission of the catheter . Both of them are direct measurement based on fluid transmission and pressure sensor. Normally, during the surgery, fluid coupling method is widely applied. And the installation of intravascular pressure sensor are applied in post-surgery period as a significant feedback to cardiac assistance devices control system, often implanted for long term and required more rigidly in the standard of size and sensitivity.

II. METHODOLOGY

We applied fluid coupling method as our experimental concept. In simulated experiment, A tank of 2:1 mixed water-glycerol functions as blood ^[1-2], on each side of the tank, there connects a tube, which are then connected by

rotary blood pump ^[1-2] to ensure a circulation of blood flow, see Fig.1; a flowmeter installed at the pump outlet detect differentiated fluid pressure. By controlling the fluid pressure, data representing the corresponding pressure are recorded by collection system from sensor output as well as amplifier output.

In this experiment, the pressure sensor is a fundamental factor to sense the blood pressure. For accurately detect abnormal variation of blood pressure, its selection has to be rigid; standard pressure sensor requires high sensitivity and hygiene. The Model 1620 ^[3] (Fig.2) is a fully piezoresistive silicon pressure sensor for use in invasive blood pressure monitoring. The sensor is designed to be used with automated assembly equipment including several three-way stopcocks tubes controlling flow of blood, and irrigation syringe preventing clotting of blood.

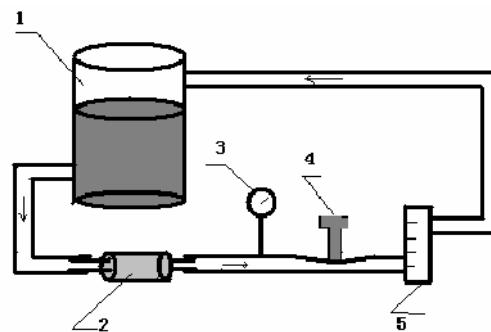
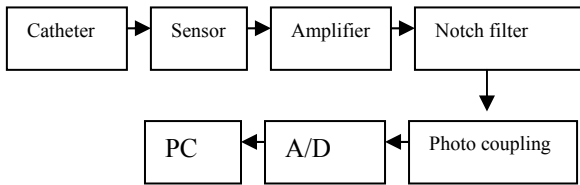


Fig.1 Experiment table. 1. a tank of reserving liquid; 2. blood pump; 3. manometer; 4 is resistance valve; 5 flow meter.



Fig.2 Model 1620

After an extraction device is completed, physiological signals will be converted into electric signals, which are a series of faint alternating signals need to be further processed by active filters, amplifier, as well as photocoupler [4] to ensure that the extracted signals won't be interfered by outer environment(Block. 1). Finally, amplified blood pressure values access to monitor system, which has a rich computer command set for programming data collection and analysis.



Block1.Flow Chart

The following Fig.3 is the sampling circuit of this system.

III. RESULT

According to simulated experiment, with a sensitivity of 5 uV/V/mmHg and a standard range from -30 to 140 mmHg, the outputs of sensor show ascending linear increase (approximate 0.6mV every 20 mmHg). With an amplification of 500, outputs of amplifier show ascending linear increase. The Fig.4 presents high linear correlation between the outputs of the sensor and the pressure imposed (testing from -30mmHg to 140mmH).

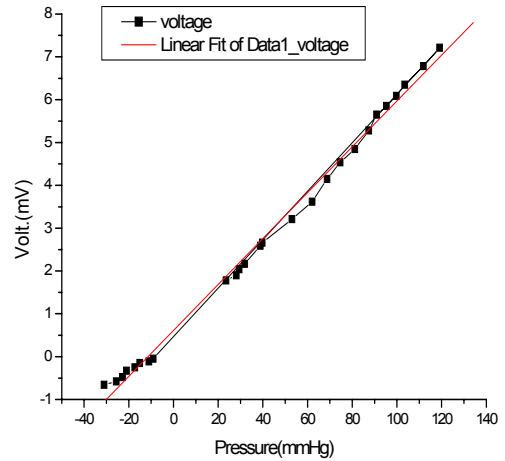


Fig.4 Linear output of Sensor

IV. SIGNIFICANCE

The blood pressure monitoring system is intended for use in experiments of cardiovascular assist devices transplant, in which it was designed for ease of use in monitoring variation of arterial and venous pressure as an adjunct to physiological experiments requiring such a system to ensure the integrity of the animal. Our initial design specification is to gain initial pressure signals and amplify them with a range from -5V to 5V which can be collected by supporting data acquisition software. The sensor performed good linear property. That the serial output of the sensor can be used to interface to a computer for further analysis serves a function as continuous monitor during experiment. With monitoring system, it not only ensures experiment subjects in most

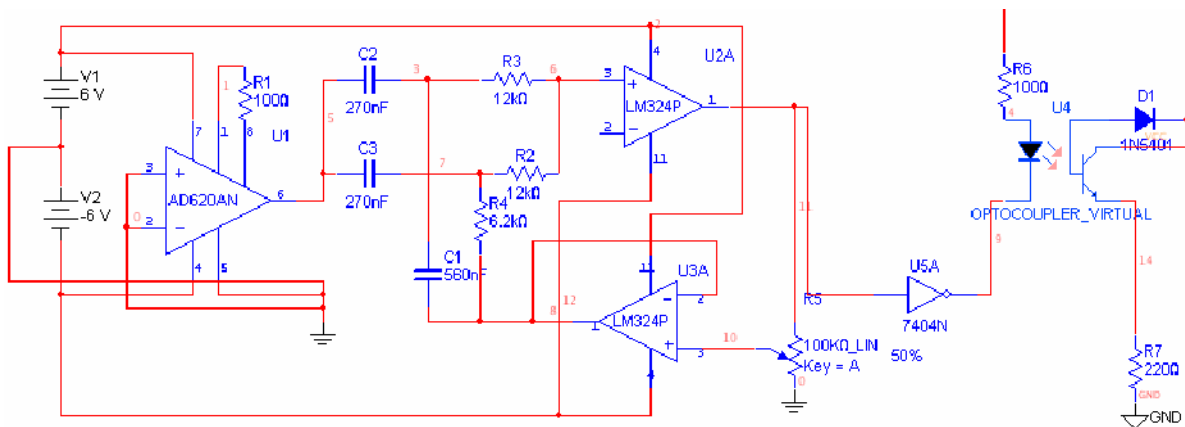


Fig.3 Circuit Diagram

optimal condition, but also enhance success ratio of the physiological operation.

3. DataSheet: Model1620
4. S Buso, S Fasolo. Uninterruptable power supply multiloop control employing digital predictive

REFERENCE

1. Chang Y, Feng FZ, Qiao AK, et al, A Study on a LVAD of a Wear-free Heart Pump, Proceedings of the 2005 IEEE Engineering in Medicine and Biology 27th Annual Conference, 7365-7368
2. Chang Y, Wu SC, Liu YJ, et al, A modeling and linear control to a rotor in a heart pump, Proceedings of the World Engineers' Convention 2004, Vol. B - Biological Engineering and Health Care : 145-150, 2004

Author: Chang Yu
Institute: Beijing Univ. of Technology
Street: No.100 Pingle Yuan, Chao Yang District, Beijing, China
City: Beijing
Country: China
Email: changyu@bjut.edu.cn

A Speed Controller Design to a Heart Pump

Linxi Shi, Bin Gao, Yu Chang

Department of Life Science and Bioengineering, Beijing Univ. of Technology, Beijing, China

Abstract — Objective: This paper introduces a comparable optimized PWM ML4428 control chip, which provides all the functions necessary for controlling a Blood Pump. The Blood Pump is based on an Active magnetic Bearing (AMB) system. **Methodology:** Directing to the dual-loop speed control system in the chip, which has a confined range of speed-modulate voltage, A speed-modulate design is introduced for the purpose of allowing off-range modulate voltages to work. This module serves a function that can transform the off-range modulate voltage into within-range modulate voltage through a digital electrical network as an AD converter to implement PWM.

Conclusion: and Discussion Based on this module, we made experiments to test rev of the Blood Pump under the condition of invariable control voltage and invariable inlet pressure respectively. The result shows, with inlet pressure of 22mmHg and control voltage of 22V, the rev of pump can be up to 8000rpm, outlet pressure with 100mmHg, and flux with 5L/min. The result meets our initial expectation.

Keyword — ABM, Blood Pump, ML4428 chip; PWM; dual-loop speed control; speed-modulate design

I. INTRODUCTION

A. AMB heart pump

The role of left ventricular assist device (LVAD) in treatment options of congestive heart failure is becoming more important and the widespread application is imminent. There are, however, some serious complications associated with LVAD, such as mechanical wear^[1], clot^[2] as well as blood contamination, which make patient management more challenging. The third generation of the artificial heart system will apply an Active magnetic Bearing (AMB) system to overcome these problems mentioned above^[3]. The AMB heart pump^[4], as a non-wearing one, whose life-span will be largely extended; meanwhile, for the patients suffering from congestive heart failure, it will become a permanent replacement for native heart. This article introduces a controller system, which directs to test the performance of AMB heart pump in our lab to see whether this heart pump could supply sufficient blood in different physiological condition.

B. PWM motor controller to heart pump

The ML4428 motor controller produced by MicroLinear is a sensorless Smart-start BLDC PWM controller. It contains particular patented Back-EMF^[1] voltage sensing circuit, start-up and communication logic, PWM current control and one shot as well as the protective circuit, all of which serve the function simplifying BLDC control mechanism. the controller can rotate both forward and reverse, meanwhile ensure no reverse rotation at start-up. Additionally, Utilizing PWM can gain maximum efficiency or linear control for minimum noise. Basing on all features mentioned above, A dual-loop speed control system^[1-3] can be implemented. (Fig.1)

The control system is consist of a three direction H bridge inverter, whose working principle was based on complementarities between P MOSFET and N MOSFET. This P-N complementary approach simplify the power-switch based driving system, then the system will sense the back-EMF to determine which working type should be selected among the total 6 (Fig. 2).

The ML4428 contains a patented back-EMF sensing technique which samples the phase non-energized and finds midpoint of this phase, and then determines when to commute phase (30° after the midpoint) or whether to increase or decrease the commutator frequency.

Two adjustors set in this system, regulating speed rotation and current, respectively. In such a closed dual-loop system, it ensures a stable function so that some errors could be prevented.

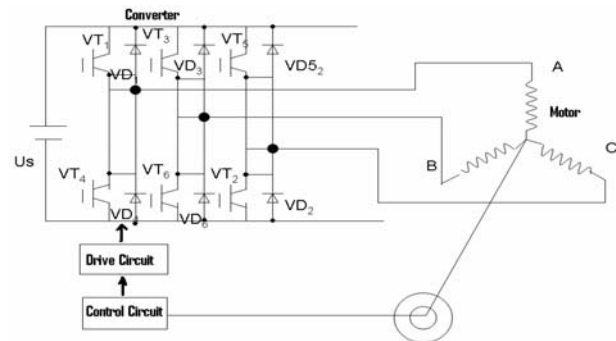


Fig. 1 Closed-loop control system for a Blood Pump

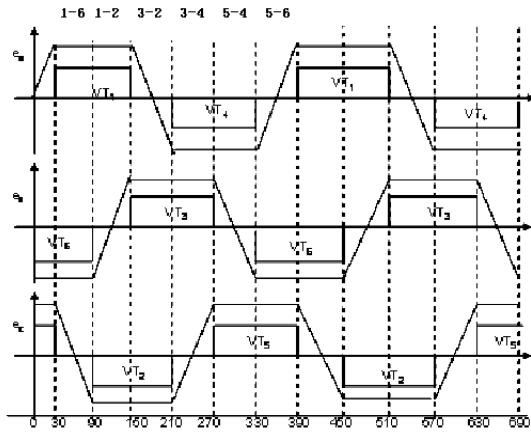


Fig. 2 Back-EMF waveform of each winding and corresponding working of the converter

II. METHODOLOGY

A. Speed control design

Cpwm set notch wave: A capacitor to ground sets the PWM oscillator frequency. Cpwm is the pin to the setting capacitor. in order to change the PWM wave.

Speed regulation plan: Vspeed to the speed loop amplifier controls the speed target of the motor. Thus, changing

Vspeed modulate rotating speed control. However, the modulating range of this pin is only from 0 to 8V, and actual available value only starts at 3V. In experiment, this constraint inevitably brings troubles in that, in some condition, the stated ranged can not be available. When dealing with off-range signals, a mechanism will divide it into eight categories; then transfer each category to the corresponding voltage within stated range (3V-8V). After dividing off-range reference signals into several categories, a set of comparators will be used to compare the actual reference voltage with each separated voltage; then digital output will be gained: For example, proposing the actual reference voltage is within 10V~18V, and then a series of 8 separated Voltages will be set as 10V, 11V, 12V, 13V, 14V, 15V, 16V, 17V. Each of them is the reference voltage to corresponding comparator. When the actual signal is changing from 10V~18V, the outputs of these comparators, in consequence, starts with LLLLLLLH, and then phase into HHHHHHHH; thus, the digital relationship has been gained, and then a 8 line -3 line encoder is needed to process binary encoding. After encoding, it comes to the final step, according to the output of encoder; data selector will select one of the categorized within-range voltages as an output which finally accomplishes the purpose to quantify certain unwanted parameters to qualified range. Specific relationship between input voltages and their corresponding output of encoder can be consulted in Table1.

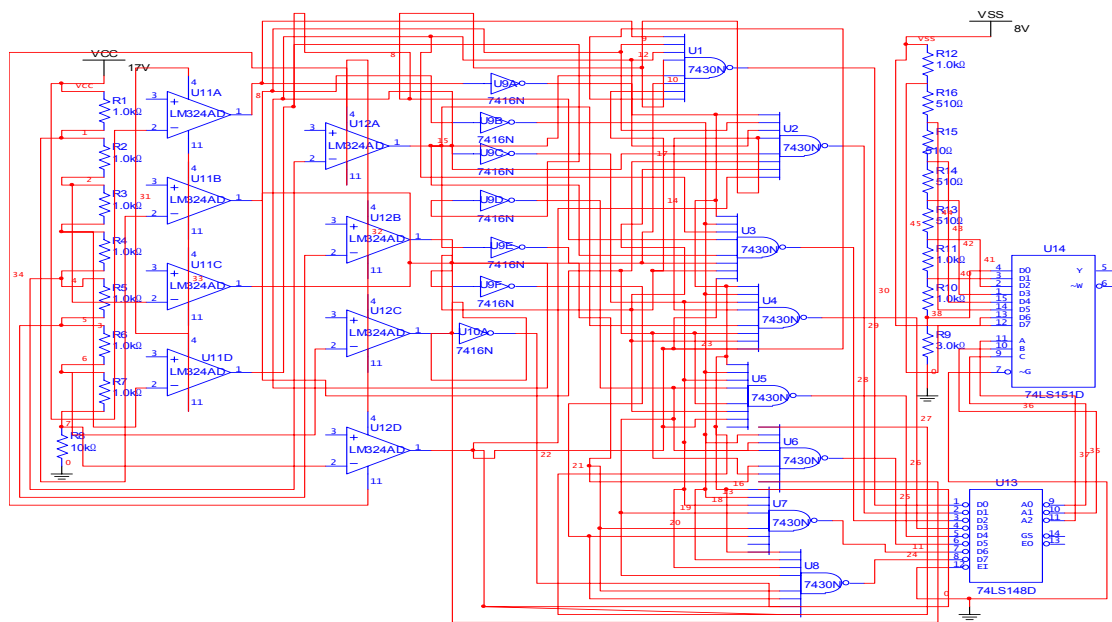


Fig. 3 Implementation of speed modulation

Table1 Corresponding data conversion

Input	Encode	Volt.
10V~11V	000	3.00V
11V~12V	001	4.00V
12V~13V	010	5.00V
13V~14V	011	5.50V
14V~15V	100	6.00V
15V~16V	101	6.50V
16V~17V	110	7.00V
17V~18V	111	8.00V

III. RESULT

In order to test the driving performance of this system, we established a series of experiments, in which the controller aforementioned was applied:

Test of invariable inlet pressure: The inlet pressure of our heart pump was set in a fixed value of 22mmHg (normal afferent value of native heart). According to pump flow rate, outlet pressure of the heart pump, as well as the varia-

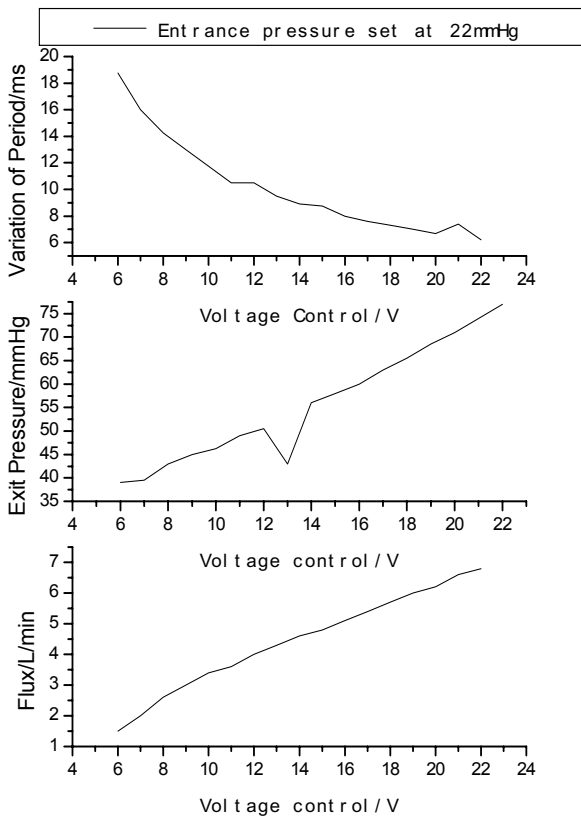


Fig. 4. Variations of the pump-parameters under the condition of invariable inlet pressure

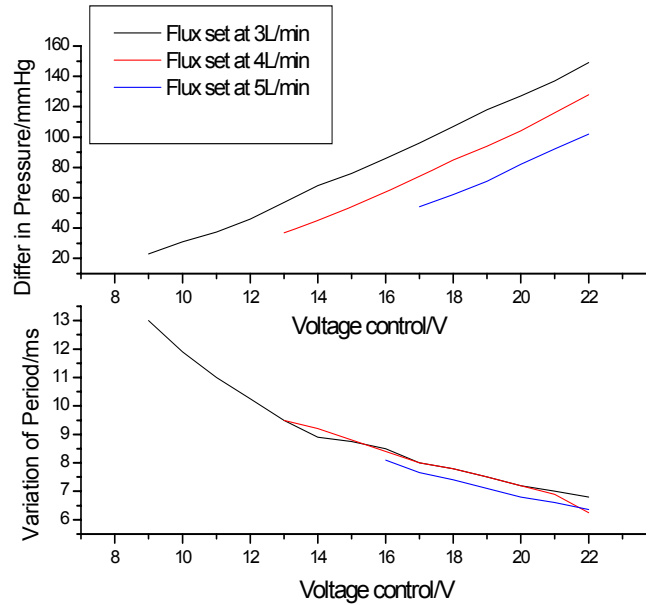


Fig. 5. Variations of the pump-parameters under the condition of invariable flux

tion of the pump rotation changing with the Control Volt, We found a correlation between these parameters. (Fig.4)

Test of invariable flow rate: Setting the pump flow rate in a fixed value in order to observe the relationship between the pump rotation speed and the inlet/ outlet pressure with the change of control volt. (Fig.5)

IV. CONCLUSION

According to the experiment, this controller system can drive blood pump with differentiated control voltage. The driving voltage is ranging from 5V to 24V. Pointing to the driving voltage from 6V to 22V, we made a record of numerical measurement: When the inlet pressure of heart pump is set at 20mmHg (inlet pressure of left ventricle in normal people), we got a coincidence relation of revolution: 8000rpm, exit pressure: 102mmHg, flux: 5L/min and voltage: 22V. The result basically met initial design specification

ACKNOWLEDGEMENT

This work partly sponsored by the Beijing Novel Project (33015998200701), and Scientific Research of Beijing Municipal Commission of Education (05015999200701).

REFERENCES

- [1] DataSheet: *ML4428 Sensorless Smart-Start™ BLDC PWM Motor Controller*.
- [2] J. S. Gui, J. W. Mckeever. *Low cost sensorless control of brush less DC motors with improved speed range [J].Applied Power Electronics Conference and Exposition, Seventeenth Annual IEEE (1): 286-292, 2002.*
- [3] S Buso, S Fasolo. *Uninterruptable power supply multiloop control employing digital predictive voltage and current regulators [J] . IEEE Trans. On Power Electronics 37(11) : 1846-1854, 2001.*
- [4] Chang Y, Feng FZ, Qiao AK, et al, *A Study on a LVAD of a Wear-free Heart Pump, Proceedings of the 2005 IEEE Engineering in Medicine and Biology 27th Annual Conference, 7365-7368*
- [5] Chang Y, Wu SC, Liu YJ, et al, *A modeling and linear control to a rotor in a heart pump, Proceedings of the World Engineers' Convention 2004, Vol. B - Biological Engineering and Health Care : 145-150, 2004*

Author: Chang Yu
Institute: Beijing Univ. of Technology
Street: Ping LeYuan 100, Chaoyang District, Beijing, China
City: Beijing
Country: China
Email: changyu@bjut.edu

A visual prosthesis based on Optic Nerve Stimulation: In vivo Electrophysiological Study in Rabbits

Liming Li, Mingjie Sun, Pengjia Cao, Changsi Cai, Xinyu Chai,
Xiaoliang Li, Panpan Chen, and Qiushi Ren*

Department of Biomedical Engineering, School of Life Science and Technology,
Shanghai Jiao Tong University, Shanghai, China.

Abstract — A visual prosthesis based on optic nerve stimulation has been suggested as a possible way to restore functional vision for the blind. In this study, we investigated the feasibility and basic spatiotemporal properties of cortical responses evoked by optic nerve stimulation with penetrating electrodes, using multi-channel recording electrode array positioned at the visual cortex area in rabbits.

Keywords — visual prosthesis; optic nerve; penetrating electrodes; electrically evoked potentials; visual cortex

I. INTRODUCTION

As a potential way to restore vision of blind patients suffering from degenerative retinal diseases such as retinitis pigmentosa (RP) and age-related macular degeneration (AMD), research and development of visual prosthesis based on electrical stimulation has received continued world-wide interest in the last two decades [1-6].

Visual prosthesis based on optical nerve stimulation was first proposed by Veraart et al. using a spiral cuff surface electrode [6]. Recently, we proposed a new visual prosthesis based on optic nerve stimulation with penetrating electrode array to elicit phosphenes. By applying a penetrating electrode array in the optic nerve, the axons of the ganglion cells local to each electrode could be stimulated. This approach may potentially increase the spatial resolution of the visual prosthesis while lowering the thresholds of the stimulating current when compared to the surface cuff electrodes. In this study, we investigated the feasibility and basic spatiotemporal properties of cortical responses evoked by optic nerve stimulation with penetrating electrodes, using multi-channel recording electrode array positioned at the visual cortex area in rabbits.

II. MATERIALS AND METHODS

A. Subjects

Thirty-six healthy adult Chinese albino rabbits, weighting about 2.0~3.0 kg, were used in this study. After intravenous

anesthetization with 5% Pentobarbital Sodium, orbital surgery was performed to expose the intra-orbital optic nerve of the rabbits. Electrically evoked potentials (EEPs) elicited by optic nerve stimulation with penetrating electrodes was recorded at the contra-lateral visual cortex sub-durally and epi-durally to investigate the temporal and spatial properties of EEPs.

B. Temporal properties

1) Stimulations:

To investigate the temporal properties of EEP evoked by optic nerve stimulation with penetrating electrodes, two micro-electrodes ($\Phi=100\ \mu\text{m}$, a $300\ \mu\text{m}$ exposure) were used to stimulate the optic nerve of rabbits. The impedance of the electrode ranged from 2.5 - 3.5 k Ω at 1 kHz, 50 mV sinusoidal wave. The insertion site of the stimulating and return electrodes was about 1 mm and 2 mm, respectively, posterior to the eyeball (Fig. 1).

A single charge-balanced biphasic pulse of current was applied between the stimulating and return electrodes. Pulse amplitude and pulse duration of the current stimuli were varied to study their effects on EEPs. By holding the charge as a constant, the effects of varying pulse duration and correspondingly varying pulse amplitude on EEPs were also examined. For the above experiments, charge-balanced symmetrical cathode-first biphasic pulses were used with the frequency of 1 Hz.

For evaluating the effects of inter-stimulus interval on EEPs, paired pulses with different inter-stimulus intervals (30ms to 1000ms) were used as stimulation.

The anode-first and cathode-first electrical stimuli with varied pulse amplitudes were applied to the pairs of stimulating electrodes to investigate the effect of the stimuli polarities.

2) Recordings:

A nine-recording-electrode array was placed over the visual cortex area (Fig. 1). The skull was exposed through a skin incision at the top of the head along the midline, and 9 holes arranged by 3 \times 3 with 2 mm spacing were drilled over the visual cortex contralateral to the stimulated eye. EEPs

from the visual cortex contralateral to the stimulated eye were recorded by a multi-channel neurophysiology workstation (System 3, Tucker-Davis Technologies, Alachua, FL, USA). Fifty consecutive evoked responses were averaged and analyzed.

C. Spatial properties

1) Stimulations:

To investigate the spatial properties of cortical responses, triangularly or linearly configured three micro-electrodes were inserted into the optic nerves of the rabbits. The home-made needle-type electrodes were fabricated by micro-electric wires with Platinum-Iridium alloy insulated by Teflon ($\Phi=80 \mu\text{m}$, a $100 \mu\text{m}$ exposure). The uncoated area was about $2.7 \times 10^{-4} \text{cm}^2$ and the impedance was $5 \sim 12 \text{k}\Omega$.

Electrical stimulation was applied to the different pairs of three stimulating electrodes (Fig. 1). Biphasic charge-balanced rectangular stimuli with the cathode-first or anode-first pulse were used. The pulse duration was fixed at 0.5 ms, while the pulse amplitude varied from $10 \mu\text{A}$ to $100 \mu\text{A}$, with the frequency of 1 Hz.

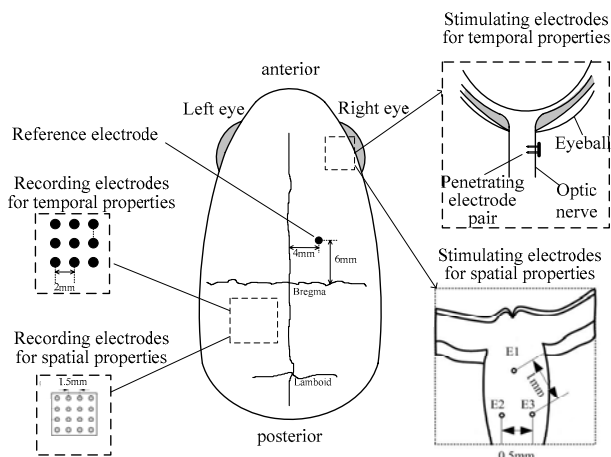


Fig. 1 The electrical stimulation and recording strategy in rabbits.

2) Recordings:

The recording electrode-array was made up of 4×4 silver-ball electrodes (Fig. 1) with $0.3 \sim 0.4 \text{mm}$ in diameter. The silver wire ($\Phi = 0.2 \text{mm}$) behind the silver ball was insulated by glass tube. The impedance of the silver-ball electrodes ranged from $500 \sim 800 \Omega$ measured at 1kHz , 50mV sinusoidal wave.

The EEP responses of 16 channels at the contra-lateral visual cortex to the stimulated eye were recorded to investigate the spatial properties of EEPs. EEPs of each channel were recorded and analyzed.

D. Assessment of the Damage to the Optic Nerve

Electroretinograms (ERG) and visual evoked potentials (VEP) were monitored as a control at the different stages of all the experiments. Histological analysis of the optic nerve was performed after the experiments.

III. RESULTS

A. Temporal properties of the EEPs

Electrical stimulation of the optic nerve induced EEPs in the visual cortex of all the rabbits. The waveform of the induced EEPs was similar to that of VEPs. However, the amplitude of P1 was smaller and the latency of P1 was much shorter than that of VEPs.

1) Threshold for Intraorbital Optic Nerve Stimulation

The current threshold for eliciting reproducible EEPs in the visual cortex was $32.08 \pm 8.44 \mu\text{A}$ when the stimulus pulse duration was 0.5 ms ($n = 5$), and the corresponding charge density threshold was $20.99 \pm 5.52 \mu\text{C}/\text{cm}^2$.

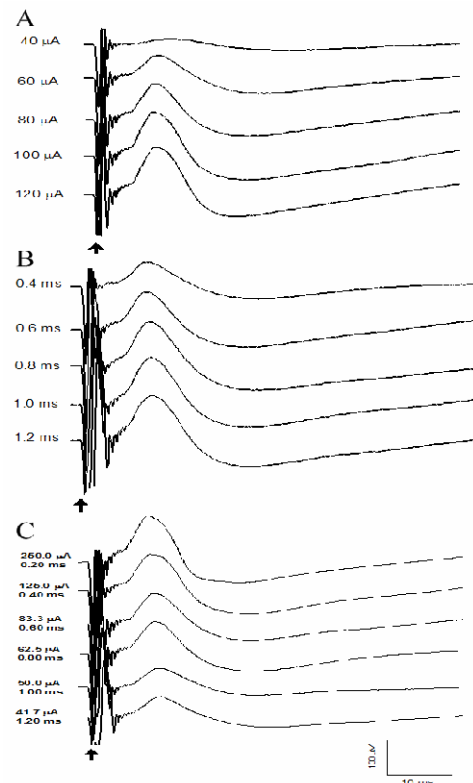


Fig. 2 EEP waveforms to stimuli with A) varying pulse amplitude (pulse duration=0.5ms), B) varying pulse duration (pulse amplitude=100 μA), C) fixed charge.

2) EEPs to Stimuli with Variable Pulse Amplitudes

Fig. 2. A depicts the EEP waveforms to stimuli with varying pulse amplitude and fixed pulse duration. The amplitude of P1 increased with increasing stimulus pulse amplitude while the latency of P1 decreased.

3) EEPs to Stimuli with Variable Pulse Durations

The EEP waveforms to stimuli with varying pulse duration and fixed pulse amplitude are shown in Fig. 2. B. As can be seen, the amplitude of P1 increased when the pulse duration increased from 0.4 to 1.0 ms. But the latency of P1 changed little with increasing stimulus pulse duration.

4) EEPs to Stimuli with Fixed Charge

The effects of cortical responses to stimuli with fixed charge were explored by stepping up the pulse duration gradually and adjusting the pulse amplitude correspondingly to keep the charge fixed (50 μC). Fig. 2. C. displays the EEP waveforms elicited by stimuli with an identical charge per pulse, but different pulse amplitude and duration. The amplitude of P1 decreased and the latency increased when the pulse duration increased with the pulse amplitude decreased accordingly.

5) Effects of inter-stimulus interval

Intervals of 30, 40, 50, 200, 500 or 1000 ms were applied to investigate the effects of inter- *stimulus* interval on the EEPs. The second P1 amplitude depressed while the interval decreased. Fig. 3 shows the EEP waveforms elicited by stimuli with different inter- *stimulus* intervals.

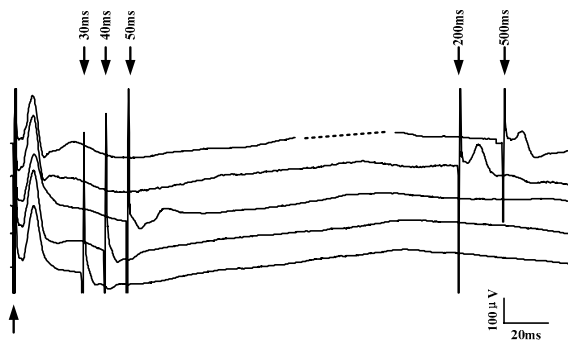


Fig. 3 EEP waveforms elicited by stimuli with different inter-*stimulus* intervals.

6) Effects of stimuli polarities

Under nearly all the current intensity used in this study, the stimulation with cathode-first pulses elicited larger cortical responses than that of anode-first pulses ($n=8$). As the current intensity increases, the difference between the two types of stimulation increases (Fig. 4. A) and the latency of P1 decreased remarkably (Fig. 4. B).

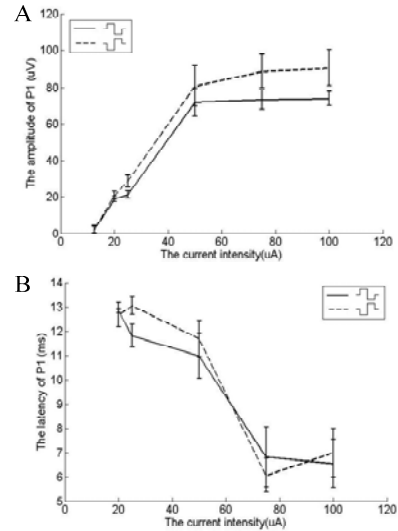


Fig. 4 Comparison of cortical responses under different polarity of stimulation.

B. The Spatial Responses to the Optic Nerve Stimulation

Our experimental results showed that the extent of EEPs increased as the stimulating intensity increased ($n=5$). When stimulating current of 100 μA at 0.5ms of pulse duration was applied in the optic nerve, EEP in nearly all the areas could be detected.

We investigated the spatial distribution of EEPs as the optic nerve was stimulated by different stimulating electrode pairs ($n=5$). Different distribution maps of EEPs were elicited by different pairs of stimulating electrodes. Stimulating electrode pair along the axis of the optic nerve could elicit cortical responses much easier than that perpendicular to the axis of the optic nerve.

C. Assessment of the Damage to the Optic Nerve

The experimental results showed that ERG didn't vary significantly, but the P1 amplitude of VEP declined after the orbital surgery to expose optic nerve. Histological analysis showed mild damage to the optic nerve tissue induced by the electrical stimulation.

IV. DISCUSSION

In our experiment, visual cortex responses were successfully evoked by intraorbital optic nerve stimulation with penetrating electrodes in rabbits. The EEP waveforms were similar to the VEP waveforms. Compared with VEPs, the shortened latency of P1 of EEPs is due to the fact that the direct electrical stimulation of axons of ganglion cells saves

the time that is needed for retinally processing the visual input. The charge density threshold in our study was $20.99 \pm 5.52 \mu\text{C}/\text{cm}^2$, which was much lower compared with surface electrode stimulation.

A. Temporal properties of the EEPs

One of the most important parameters in designing visual prosthesis is the optimal stimulating charge and its dynamic range. From our results, we note that the amplitude of P1 increased linearly with increments of the stimulus charge up to around 60 nC at which stage saturation occurred. These results suggest that phosphenes with different brightness could be activated by intraorbital optic nerve stimulation within a dynamic charge range. It has been reported that charge and charge density are important factors in inducing neural damage.

The duration of the stimulating pulses is another important factor to be considered in visual prosthesis design. From our results, the stimulus with a shorter pulse duration induced a larger amplitude P1 than that with a longer pulse duration, which indicate that stimuli with shorter pulse durations are more efficacious for eliciting EEPs than that with longer pulse durations. This strongly suggests that stimuli with shorter pulse durations should be applied to stimulate the optic nerve to minimize the total charge injected into the neural tissue.

When paired pulses with different inter-stimulus intervals were applied to the optic nerve, we found that the second P1 amplitude depressed while the interval decreased. These results support the finding that ganglion cell responses to a stimulation pulse applied after a preceding one were depressed when the interval between the two pulses decreased.

B. The Spatial Responses to the Optic Nerve Stimulation

As the stimulating intensity increased, the responding area in visual cortex became larger. It was probably due to an increase in the number of recruited fibers of the optic nerves and therefore induced boarder and stronger activation of the visual cortex. The results indicated that as the stimulating intensity increased, larger and brighter phosphenes could be induced in the visual field, which was in agreement with the human phosphenes electrically elicited by optic nerve cuff electrodes.

One of the crucial questions in this study is whether electrical stimulations on different sites of optic nerve can elicit different distributions of cortical responses. Our experimental results showed that while the electrodes were arranged linearly along the axis of the optic nerve, the EEP distribution elicited by different combination of the

stimulating electrodes was not different significantly. This was probably due to the linearly arranged electrodes covered similar axon bundles of the optic nerve. However, when the stimulating electrodes were arranged triangularly in the optic nerve, multi-channel responses elicited by different electrode pairs were quite different. The possible explanation was the electrode pair parallel to the optic nerve produced larger depolarization within the axons of the ganglion cells and therefore resulted in lower threshold than the one perpendicular to the optic nerve.

V. CONCLUSION

Our study has shown that the electrical stimulation in rabbit optic nerve through penetrating electrodes can elicit cortical responses in rabbit visual cortex. The intensity (amplitude of P1) and extend of EEPs increased as the stimulating current amplitude increased, while the latency of P1 decreased. Different responding maps of EEPs were elicited by different stimulating electrode pairs when inserted appropriately in the optic nerve. Stimulating electrode pair along the axis of the optic nerve could elicit cortical responses much easier than that perpendicular to the axis of the optic nerve.

ACKNOWLEDGMENT

This research is supported by the National Basic Research Program of China (973 Program, 2005CB724302), National Science Fund for Distinguished Young Scholars from The National Natural Science Foundation of China (60588101), Shanghai Pujiang Program (07PJ14050), Shanghai Commission of Science and Technology (05DZ22318, 05DZ22325, 04DZ05114).

REFERENCES

- Schmidt EM, Bak MJ, Hambrecht FT, Kufta CV, O'Rourke DK, Vallabhanath P, Feasibility of a visual prosthesis for the blind based on intracortical microstimulation of the visual cortex. *Brain*, 1996, 119: 507-522.
- Zrenner E, Will Retinal Implants Restore Vision. *Science*, 2002, 295: 1022-1025.
- Humayun MS, Weiland JD, Fujii GY, Greenberg R, Williamson R, Little J, Mech B, Cimmarusti V, Van Boemel G, Dagnelie G, de Juan E, Visual perception in a blind subject with a chronic microelectronic retinal prosthesis. *Vision Res*, 2003, 43: 2573-2581.
- Rizzo JF, Wyatt J, Prospects for a Visual Prosthesis. *Neuroscientist*, 1997, 3: 251-262.
- Eckmiller R, Learning retina implants with epiretinal contacts. *Ophthalmic Res*, 1997, 29: 281-9.
- Veraart C, Raftopoulos C, Mortimer JT, Delbeke J, Pins D, Michaux G, Vanlierde A, Parrini S, Wanet-Defalque M, Visual sensations produced by optic nerve stimulation using an implanted self-sizing spiral cuff electrode. *Brain Res*, 1998, 813: 181-186.

A Circuit System Design for Implantable Multi-channel neural stimulator

Yan Xi, Qian Du, Hanyan Gong, Nan Tang, Lei Cao, Jinhai Niu, Qiushi Ren

Institute for Laser Medicine & Bio-photonics, Biomedical Engineering Department of Shanghai Jiao Tong University

Abstract — More than 161 million people worldwide are suffering from ablesia [1], and among them, ten million are blind result from the photoreceptor loss due to degenerative retinal diseases. For these patients, neural stimulating proved to be an effective method of rehabilitation. This method is based on conceive of substituting an artificial device for the defective photoreceptor in patients functionally [2]. Multi-channel neural stimulator is a part of the device. In the design of multi-channel neural stimulator, the kernel problems are concerning the output stimulating current. Micro, bipolar, and steady output current is required to protect guarantee safety and effectiveness of this stimulator [3]. Furthermore, a simple and tiny structure is essential for the stimulator to implanting into human bodies. This paper focused on the design of a circuit serves as the DA converter and stimulation generator, which is made up of a Micro Controller Unit (MCU), a Digital to Analog Convectore (DAC) and Amplifiers. The results of simulation made by Multisim shows that this circuit can put out bi-phasic micro and steady current whose precision of the current is $5\mu\text{A}$. The size of all the intraocular part of the whole device is $36\text{mm}\times 28\text{mm}$.

Keywords — artificial vision, neural stimulator, micro current, bipolar current

I. INTRODUCTION

Artificial vision based on a rehabilitative device replacing defective photoreceptors in blind people appears in many aspects a most reliable choice for us to achieve the patients a better vision, and optical nerve prosthesis with penetrating multi-electrode arrays [4]. This device includes three major modules: Radio Frequency Module, Wireless Power Providing Module and Neural Stimulation Module (Figure 1). The Radio Frequency Module includes CCD camera, Image Acquisition & Processing Unit and Communication Unit. The Neural Stimulation Module includes Multi-channel neural stimulator, and Communication Unit. First, the CCD camera receives stimulations from light, and then information is processed via a image processing unit. A communication module transports visual data from extra ocular modules to intraocular modules via RF technique. Neural stimulation module first converts digital signals to analogy signals and then generates stimulation current on optic afferent nerves.

Wireless Power Providing Module offers energy for intraocular modules. Multi-channel neural stimulator visual data are transmitted by RF inductively to the intraocular unit which in turn recovers the data and sets the charge balanced bipolarity stimulation for the retina via electrodes. MCU receives the signal and passes it with particular format to the DAC. When the 8-channel signals are stored in the registers of DAC, the MCU controls the DAC to perform to drive the after circuits to generate 8-channels currents at the same time.

There are several formidable challenges in designing an implantable, safe, efficient multi-channel neural stimulator. To meet the need of these requirements, the system owns four salient characters. First of all, the size must be small enough to be implantable. To balance the quality and the dimension, we decide the dimension of our design at $36\text{mm}\times 28\text{mm}$ finally. Secondly, to protect the body implanted with the neural stimulator from assembling excessive charge, we use bipolarity (anodic and cathodic) and symmetrical current as our stimulating current. Thirdly, the normal neural potential is at the level of μA , so the current that the circuit generates is limited at the level of μA too. To generate stable and accurate current, we choose exact amplifiers and ADC to perform the current generation. At last, we use 8-channel currents to stimulate the retinal nerve simultaneously to get more efficient result.

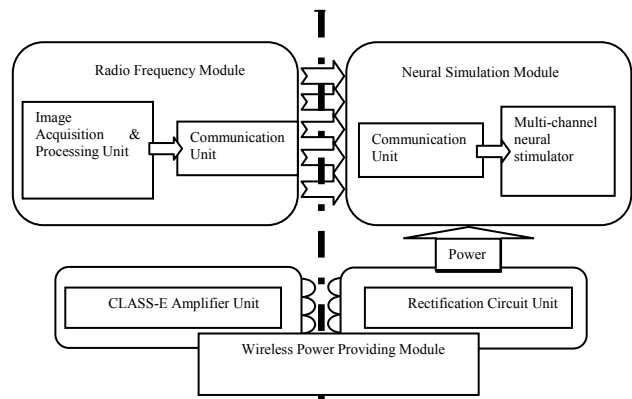


Fig. 1 schematic figure of artificial vision

II. THE CIRCUIT OF IMPLANTABLE MULTI-CHANNEL NEURAL STIMULATOR

A. The architecture and working process of implantable multi-channel neural stimulator

The stimulator is made up of STC12LE5412AD microcontroller, AD530 and AD8608. Data is first transmitted to p1.3 to p1.7 of STC12LE5412AD, and then digital data is sent to AD530 and becomes analogy data. Further, voltage signals are transferred to current signals by AD8608.

B. MCU-DA

Figure 2 shows a serial interface between the AD5308 and the STC12LE5412AD microcontroller. The setup for interface is as following: TxD of the STC12LE5412AD drives SCLK of the AD5308, while RxD drives the serial data line of that part. The #SYNC signal is again derived from a bit programmable pin on the port. In this case, port line P3.3 is used. When data is transmitted to the AD5308, P3.3 is taken low. The 80C51/80L51 transmits data only in 8-bit bytes; thus, only eight falling clock edges occur in the transmit cycle. To load data to the DAC, P3.3 is left low after the first eight bits are transmitted, and a second write cycle is initiated to transmit the second byte of data. P3.3 is taken high following the completion of the cycle.

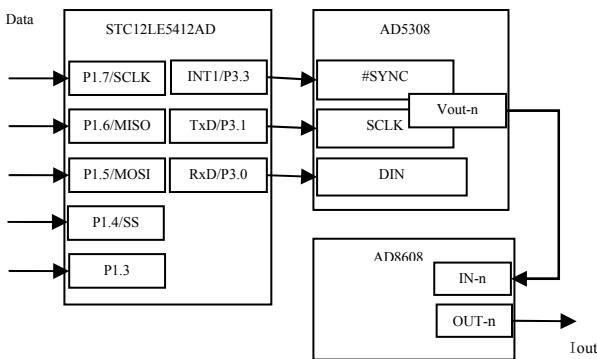


Fig. 2 architecture of the neural stimulator

C. DA-V/I

Circuit design

The unipolar voltage generated by the D/A convertor need to be converted by amplifier to bipolar voltage and be further converted to current. Amplifier with bipolar voltage output, low noise, high speed and quick response are needed. We choose AD8608 (produced by ADI Corporation) as

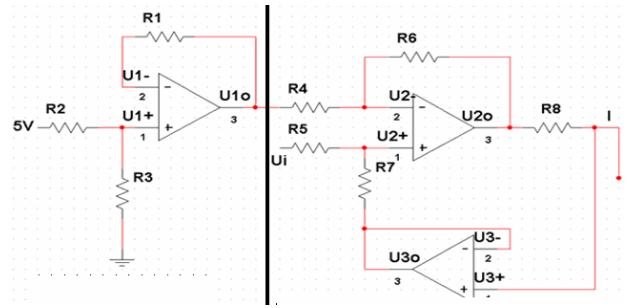


Fig. 3 circuit of the neural stimulator

amplifiers in our circuit. AD8608 contains four amplifier implements converting of unipolar voltage to bipolar voltage and voltage to current. The structure of this unit is shown as Figure 3.

Simulation with MultiSim

Figure5 shows the output when input is a rectangular and the load is 10kΩ. As is shown in figure5, this circuit puts out bipolar current which achieves our goal.

Figure 6 shows output of the stimulator with input changing from 0 to 5V. The curve appears to be nearly a line indicating the linear relationship between input and output.

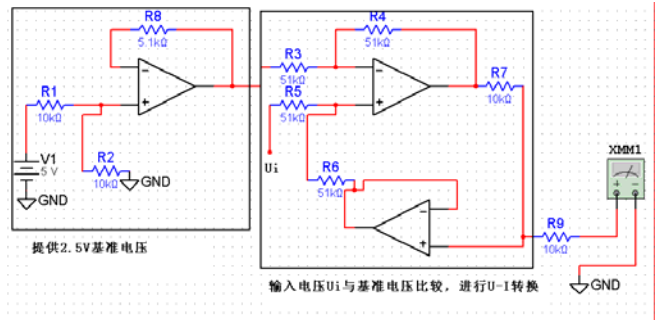


Fig. 4 circuit structure of V/I unit drawn in Mutisim

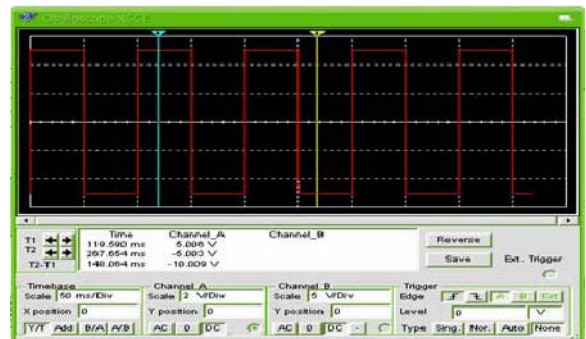


Fig. 5 simulative output of stimulating circuit

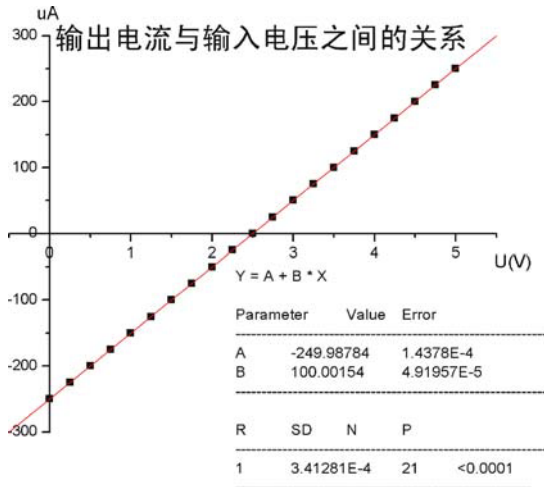


Fig. 6 output current values with changing input voltage

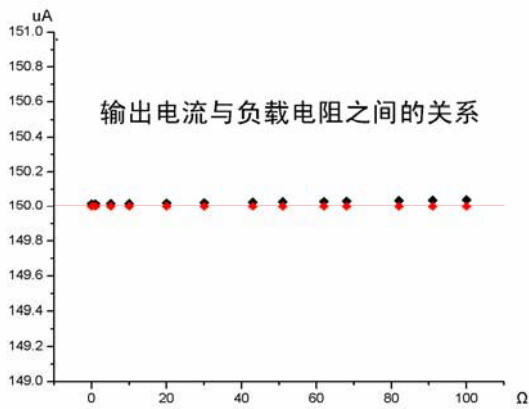


Fig. 7 output current values with changing load resistance

Figure 7 shows ($U_{in}=4V$) output of the stimulator with load changing from 1Ω to 100Ω . It indicates that the stimulator is a satisfying current supply providing stable output. Black points are simulation data and red points are theoretical values.

Results of simulation of the stimulator proves that the designed circuit generally could meet the need of putting out a micro, bi-phasic and steady current.

Design of PCB

The Schematic Document and PCB Document drawn by the software of Protel (Figure 8).

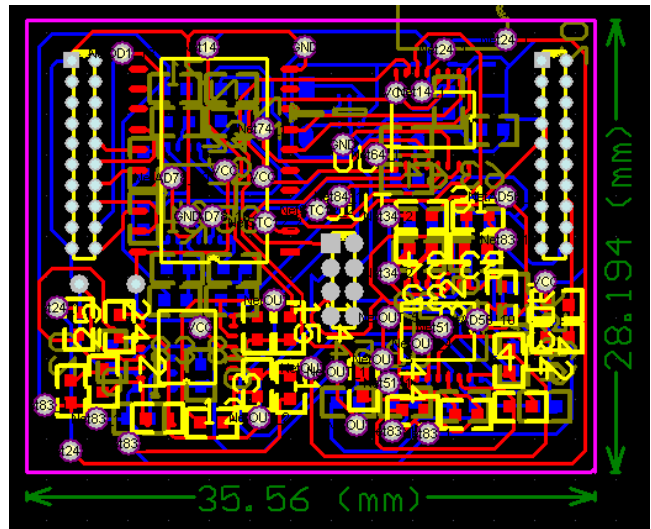


Fig. 8 design of printed circuit board

III. CONCLUSIONS

The circuit of the neural stimulator is made up of a Micro Controller Unit (MCU), a Digital to Analog Converter (DAC) and Amplifiers. And we choose STC12LE5412AD microcontroller to be the MCU, AD530 to be DAC and AD8608 to be Amplifier. As the result shows we get from simulation made by Multisim, the circuit can generate bi-phasic (anodic and cathodic) current and precision of the current is $5\mu A$. The size of all the intraocular part of the whole device is $36mm \times 28mm$. Thus, the circuit system we design for implantable multi-channel neural stimulator is feasible to combine with other parts of this artificial vision system to function in patients who are suffering from retinal diseases.

ACKNOWLEDGMENT

The research is supported by the National Basic Research Program of China (973): Basic Research on the Key Issues of Visual Function Recovery for Blindness (No. G2005CB724302) and the (PRP) PRP-C07040 of Shanghai Jiaotong University.

REFERENCES

1. Blindness: magnitude and causes of visual impairment. World Health Organization (WHO) Fact Sheet No282, November 2004.
2. Weiland J D, Liu W T, Humayun M S. (2005) Retinal prosthesis. *Annu Rev Biomed Eng*, 7: 361–401
3. Weiland J D, Liu W T, Humayun M S. (2005) Retinal prosthesis. *Annu Rev Biomed Eng*, 7: 361–401
4. NIU JinHai et al, (2007) Vision implants: An electrical device will bring light to the blind, *Sci China Ser F-Inf Sci*,101–110

Author: niu jinhai
Institute: Institute for Laser Medicine & Bio-photonics, Biomedical
Engineering Department of Shanghai Jiao Tong University
Street: 800 Dong-Chuan Road, Min-Hang Distr
City: Shanghai
Country: China
Email: jhniu@sjtu.edu.cn

Implementation of the Natural Heartbeat Synchronize Control for the Undulation Pump Ventricular Assist Device Using the Inflow Pressure

I. Saito¹, T. Chinzei¹, T. Isoyama², H. Miura¹, A. Kouno², T. Ono², H. Nakagawa¹, S. Yamaguchi-Sekine², W. Shi², Y. Inoue², A. Kishi² and Y. Abe²

¹Research Center for Advanced Science and Technology, The University of Tokyo, Tokyo, Tokyo, Japan

²Department of Biomedical Engineering, Graduate School of Medicine, The University of Tokyo, Tokyo, Japan

Abstract — The undulation pump ventricular assist device (UPVAD) is a small implantable ventricular assist device using an undulation pump. The UPVAD can produce not only continuous flow but also pulsatile flow by changing the motor rotational speed of the UPVAD. Because the undulation pump is a volume displacement type pump in which the inflow action and outflow action both start at the same phase, the inflow sucking occurs easily. The purpose of this study is to develop a suitable control method for the UPVAD. The UPVAD inflow cannula equipped with an implantable blood pressure sensor is inserted into the ventricular. Therefore, pressure fluctuation that synchronizes with the natural heartbeat is observed in the inflow cannula. By changing the motor rotational speed that responds to the inflow pressure, the UPVAD can synchronize with the natural heartbeat and the UPVAD can generate either a co-pulse assist flow or a counter pulse assist flow. The newly developed control method exhibited superior characteristics than existing ones due to high immunity against pressure sensor drift. The improved control method is implemented into the microcontroller. The UPVAD generated 5.3 l/min co-pulse assist flow without inflow cannula sucking using this control method. The assist flow can be increased more than 15% with this control method. This control was implemented one-chip microcontroller without extra peripheral device. It can reduce the UPVAD controller size. The UPVAD can generate the suitable assist flow with the developed control method.

Keywords — UPVAD, implantable pressure sensor, natural heartbeat synchronization, undulation pump, control method

I. INTRODUCTION

The undulation pump ventricular assist device (UPVAD) is a small implantable motor driven ventricular assist device using an undulation pump [1-3]. The UPVAD can produce arbitrary flow patterns: continuous flow, pulsatile flow based on continuous flow and complete pulsatile flow, by changing the motor rotational speed of the UPVAD.

Because the undulation pump is a volume displacement type pump, the inflow action and outflow action both start at the same phase and the inflow volume and the outflow volume is same in any time. Therefore, high inflow is required to gain the high assist flow by UPVAD and the inflow sucking occurs easily. An unique character of the

UPVAD demands to synchronize with the natural heartbeat to prevent the sucking of inflow cannula.

Most popular method to synchronize with natural heartbeat is ECG R-wave detection method. The start of systolic phase of the natural heartbeat can be detected with ECG R-wave detection method. However, the start of diastolic phase of natural heartbeat can not be detected with ECG R-wave detection method. Also, lifetime of the electrode which detects the ECG is limited and it is difficult to detect ECG R-wave over a year.

The purpose of this study is to develop heartbeat synchronization for the UPVAD and to implement the control method into a microcontroller for reducing the UPVAD controller size and implanting the UPVAD controller.

II. MATERIALS and METHODS

The inflow cannula of the UPVAD is implanted in the ventricular. Therefore, pressure fluctuation that synchronizes with the natural heartbeat is observed in the inflow cannula. By changing the motor rotational speed that responds to the inflow pressure, the UPVAD can synchronize with the natural heartbeat and the UPVAD can generate either a co-pulse assist flow or a counter pulse assist flow.

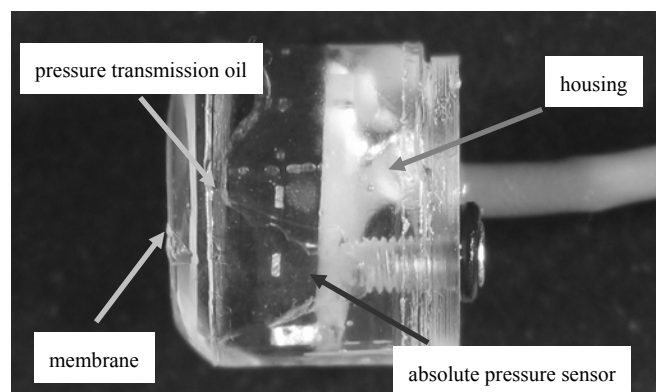


Fig. 1 implantable pressure sensor

The UPVAD inflow cannula equipped with an implantable pressure sensor (IPS) for measuring the inflow cannula pressure. The IPS is composed of a housing, a pressure sensor, a membrane and pressure transmission oil (Fig. 1). Shape of the housing is a cylinder. Length and diameter of the housing are 11.5 mm and 12 mm respectively. The pressure sensor is used absolute pressure sensor (XFAM-115KPASR, Fujikura, Tokyo, JAPAN). This sensor is pre-amplified, pre-calibrated and pre-compensated sensor. The pressure sensor is located bottom side of the housing. The membrane is a thin segmented polyurethane film which thickness is about 50 μm . The membrane is located top side of the housing and it contacts with the blood. Inside of the housing is filled with the pressure transmission oil that is silicone oil. The blood and the pressure transmission oil are separated with the membrane. The blood pressure is transmitted to the pressure sensor through the membrane and pressure transmission oil. The response speed of the IPS is less than 5ms.

Although, many implantable blood pressure sensors were developed, no pressure sensor was succeeded to measure the true blood pressure over a year because of its offset time drift. The IPS also can not measure true inflow cannula pressure

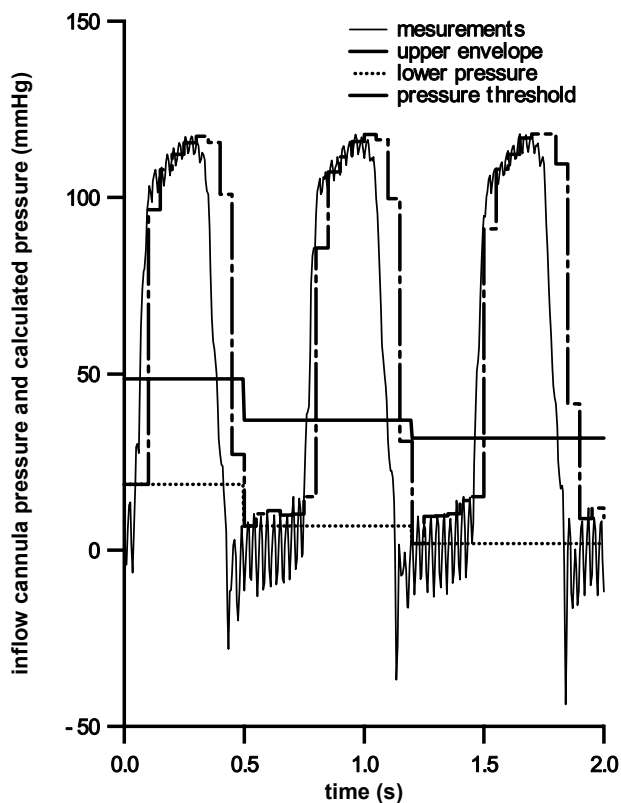


Fig. 2 inflow cannula pressure wave form and calculated pressure wave form

over a year. However, the IPS can measure inflow cannula pressure wave form, because the gain time drift of the IPS is almost zero. We developed the natural heartbeat phase detection algorithm by using the inflow cannula pressure wave form.

The ventricular pressure is high during the systolic phase of natural heartbeat and is low during the diastolic phase of natural heartbeat. Therefore, it is easy to detect the natural heartbeat phase by comparing with the ventricular pressure and a threshold. The threshold is higher than the diastolic phase ventricular pressure and is lower than the systolic phase ventricular pressure.

The inflow cannula pressure that is measured with the IPS is almost same the ventricular pressure except the inflow sucking condition. During the inflow sucking condition, the inflow cannula pressure is over 50 mmHg lower than the ventricular pressure. The UPVAD is driven to prevent the inflow sucking and the UPVAD controller would release the inflow sucking by sucking control if the sucking condition is occurred. However, the inflow sucking has been occurred some time. Therefore, the minimum pressure of the inflow cannula pressure is not reflected the diastolic ventricular pressure.

The systolic ventricular pressure is almost equal to the aortic pressure. The diastolic ventricular pressure is almost equal to the atrium pressure. The aortic pressure is largely changed with the body condition and the atrium pressure is almost constant. Therefore, the difference between the systolic ventricular pressure and the diastolic ventricular pressure is indefinite and it is impossible to estimate the diastolic ventricular pressure from the systolic ventricular pressure.

It is easy to know the systolic ventricular pressure, because the systolic ventricular pressure is almost equal to the maximum pressure of the inflow cannula pressure. However, it is difficult to know the diastolic ventricular pressure. We developed the calculation algorithm of the diastolic ventricular pressure and the threshold for detecting the natural heartbeat phase from the inflow cannular pressure wave form. The calculation algorithm has 4 steps: sucking elimination step, systolic phase elimination step, definition of detecting threshold step and phase detection step.

Assumptions of calculating algorithm are following. The heart rate of the natural heart is greater than 30 bpm (beat per minute) and less than 240 bpm. The percent systole of the natural heart is greater than 20% and less than 40%. Therefore, the systolic duration time of the natural heartbeat is longer than 50 ms and shorter than 800 ms. The diastolic duration time is longer than 150 ms and shorter than 1600 ms. The sucking duration time is shorter than 30 ms by sucking control. The inflow cannula pressure is measured in 200 Hz sampling rate. The mean aortic pressure is over 40 mmHg.

The Measurements of the inflow cannula pressure are divided into 50 ms time slots. One time slot has 10 measurements. A maximum pressure measurement that is named as upper envelope is taken from the measurements of every time slot. The upper envelope is shown as a long dashed line in Fig.2. The upper envelope eliminates the inflow cannula pressure on the inflow sucking condition, because the one time slot duration is longer than the sucking duration time. This is the first step of the calculation algorithm.

A minimum of the upper envelope that is named as lower pressure is taken from the upper envelope over the most recent on second. The lower pressure is shown as a short dashed line in Fig.2. The lower pressure eliminates the systolic pressure from the upper envelope, because the systolic duration is shorter than 800 ms. The lower pressure is nearly equal to the envelope of the diastolic ventricular pressure. This is the second step of the calculation algorithm.

A pressure threshold for detecting of the natural heartbeat phase is defined as sum of the lower pressure and constant. Value of the constant was set to 30 mmHg. This is the third step of the calculation algorithm.

Basic phase detection method is following: the natural heartbeat phase is systolic phase on condition that the inflow cannula pressure is higher than the pressure threshold and the natural heartbeat phase is diastolic phase on condition that the inflow cannula pressure is lower than the pressure threshold. To make a hysteresis for the phase detection stabilization, dead time is made before switching from diastolic to systolic phase and after switching from systolic to diastolic phase. On condition that the inflow cannula pressure is higher than the pressure threshold over the most recent 100 ms, the calculation algorithm sense as the natural heartbeat phase is changed from diastolic to systolic phase. On condition that the inflow cannula pressure is lower than the pressure threshold, the calculation algorithm sense as the natural heartbeat phase is changed from systolic to diastolic phase and keeps the diastolic phase at least 50 ms. This is the final step of the calculation algorithm.

The driving condition of the UPVAD is switched according to the natural hear beat phase: the UPVAD is high output in systolic phase, the UPVAD is low output in diastolic phase.

An implantable UPVAD driver was developed using one-chip microcontroller and motor driver (Fig. 3). The developed natural heartbeat detection algorithm and UPVAD control programs were implemented into the microcontroller. An animal experiment that implanted the UPVAD and the implantable UPVAD driver was performed.

III. RESULTS

This control method could be implemented one-chip microcontroller without extra peripheral devices. Diameter and thickness of the implantable UPVAD driver are 64 mm and 10 mm respectively. The UPVAD and the UPVAD driver was implanted into goat weighing 51 kg and the goat survived more than 2 months successfully.

The UPVAD generated 5.3 l/min. co-pulse assist flow without inflow cannula sucking using this control method. By the implementation of the present method, 15% increase in the assist flow was obtained.

IV. DISCUSSION

This calculation algorithm requires only 40-50 bytes of memory and 30 comparison processes every time slot (50 ms). This means that this algorithm is enough simple for implementing to microcontroller. The use of the microcontroller makes for reducing the size and power to the implantable UPVAD driver.

During animal experiment, the measurements of the IPS observed an error according to the offset time drift. However, phase detection algorithm worked well during animal experiment without calibration of the IPS and the error of the IPS is not affected to this algorithm.

The developed algorithm will be sense the natural heartbeat diastolic phase on the cardiac arrest condition. Although, this sensing is true, it is better to switch to the systolic phase for making the cardiac flow by the UPVAD on cardiac arrest condition. This mechanism can be implemented to make systolic phase timer like a watch dog timer of the

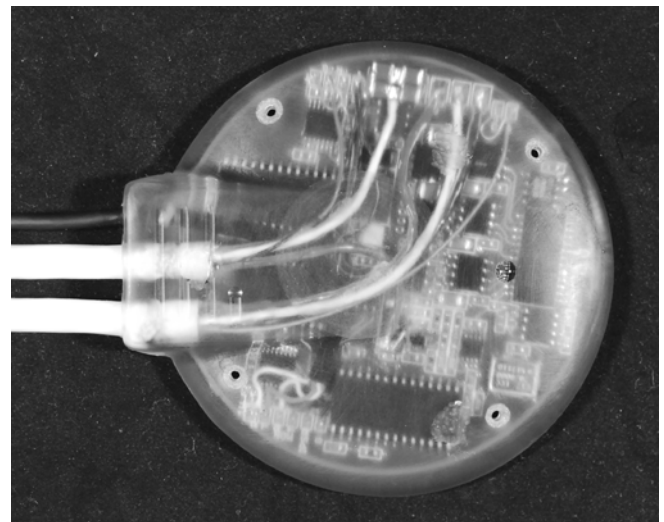


Fig. 3 implantable UPVAD driver

microcontroller. Because the diastolic duration is shorter than 1600 ms, if the diastolic phase keeps more than 2000 ms, the UPVAD output is switched high output and keeps 500 ms during diastolic phase. The pulse rate of the UPVAD is 24 bpm and % systole of the UPVAD is 20% on this condition.

V. CONCLUSIONS

The UPVAD can generate the suitable assist flow with the developed control method. The control method characteristic that is enough simple for implementing to one-chip microcontroller can reduce the UPVAD controller size and power.

ACKNOWLEDGMENT

This work was supported by JSPS KAKENHI (17209046) and MEXT KAKENHI (18689034).

REFERENCES

1. Abe Y, Chinzei T, Isoyama T, Ono T, Mabuchi K, Imanishi K, Kouno A, Atsumi K, Fujimasa I, Imachi K (1995) Basic study to develop the undulation pump for practical use: antithrombogenicity, hemolysis, and flow patterns inside the pump. *Artificial Organs* 19:691-693
2. Abe Y, Chinzei T, Isoyama T, Ono T, Mochizuki S, Mabuchi K, Baba K, Matuura H, Sun Y P, Kouno A, Atsumi K, Fujimasa I, Imachi K (1997) Development of the undulation pump total artificial heart. *Artificial Organs* 21:665-669
3. Abe Y, Chinzei T, Isoyama T, Ono T, Mochizuki S, Saito I, Guba P, Karita T, Sun Y P, Kouno A, Suzuki T, Baba K, Mabuchi K, Imachi K (1999) Present status of the total artificial heart at the University of Tokyo. *Artificial Organs* 23:221-228

Author: Itsuro Saito

Institute: Artificial Biomechanism, Research Center for Advanced Science and Technology, The University of Tokyo

Street: 4-6-1 Komaba Meguro-ku

City: Tokyo

Country: JAPAN

Email: saito@bme.rcast.u-tokyo.ac.jp

Development of an Auto Calibration Method for the Implantable Blood Pressure Sensor in the Undulation pump ventricular assist device (UPVAD)

W. Shi¹, I. Saito², T. Chinzei², T. Isoyama¹, H. Miura², A. Kouno¹, T. Ono¹,
H. Nakagawa², S. Yamaguchi¹, Y. Inoue¹, A. Kishi², Y. Abe¹

¹ Graduate School of Medicine, the University of Tokyo, Tokyo, JAPAN

² Research Center for Advanced Science and Technology, the University of Tokyo, Tokyo, JAPAN

Abstract — Development of an implantable artificial heart is very important to save cardiac disease patients. An undulation pump ventricular assist device (UPVAD) could be a good candidate because of the compact size. Although the implantation improves patient's quality of life (QOL) considerably, several implications hamper the development of an implantable artificial heart. The difficulty in blood pressure measurement is the one of the implications to be solved. We have developed the implantable absolute pressure sensor to be integrated into a UPVAD and the algorithm to infer the blood pressure referred to gauge pressure. Noble feature of the algorithm is autonomous compensation of the offset drift with the pressure sensor in time. Thus the blood pressure could be controlled precisely with the implantable UPVAD even if the pressure sensor exhibited certain drift characteristics. Animal experiment demonstrated the effectiveness in compensating the offset drift.

Keywords — absolute pressure sensor, undulation pump, UPVAD, automatic calibration method

I. INTRODUCTION

The mechanical circulatory support device has been demonstrated as an effective therapeutic strategy in clinical application. Especially, a device that can be implanted into a patient's body, has strong potential. An implantable ventricular assist device (VAD) can sustain not only patient's life, but also improves the quality of life (QOL). There exists, however, several major obstacles to overcome, for the wide usage of an implantable VAD. Autonomous control of a VAD that can harmonize with patient's physiological condition could be the one. The control could be achieved either by a regulation of blood flow, or of blood pressure. For the blood pressure control, one has to measure the pressure accurately, and an implantable pressure sensor is a prerequisite. An implantable pressure sensor that is highly resistive to thrombosis was developed and integrated into a VAD. Important requirements for implantable devices are durability and maintenance-free nature, since they have to be taken out, should the maintenance be required. The implantable pressure sensor is no exception. Unfortunately the pressure sensor that is sensitive enough to measure the blood pressure tends to exhibit certain drift in offset and

gain characteristics. Further the blood pressure is measured as gauge pressure, whereas most of the pressure sensors measure absolute pressure. The purpose of the present study is to develop an automatic calibration method to induce the drift-free gauge pressure using an absolute pressure sensor. The algorithm to evaluate the base pressure (~intrathoracic pressure) by the sensor waveform is induced. The animal experiment justified the validity.

II. MATERIALS

A. Undulation pump and UPVAD

The undulation pump is a unique continuous-flow pump invented by our group(1). A rotary disk divides the pump chamber into two compartments and the wobbling motion of the disk displaces liquid from an inlet to an outlet. It is a volume displacement pump and the response speed is fast. It has relatively large pumping capacity despite the small size. The undulation pump ventricular assist device (UPVAD) utilizes the undulation pump as show as Fig.1, and is appropriate for implant because of compact size. Unlike the VAD of other type, UPVAD can operate in a pulsatile flow mode to synchronize the heartbeat.



Fig. 1 UPVAD

B. Pressure measurement

The pressure measurement is desirable for better control of a VAD. Blood pressure is measured in terms of gauge pressure, where a reading of 0 refers to the environmental atmospheric pressure. In absolute pressure measurement the reference side of the sensing device could be sealed and only measuring side should be connected to the measuring point. On the contrary, one has to measure the pressure difference between the measuring point and the atmospheric point in gauge pressure measurement. For the implantable pressure sensor, the gauge pressure measurement is not feasible in a strict sense, but intrathoracic pressure could be considered as “pseudo atmospheric pressure”. In the present research, we opt to choose an absolute pressure sensor because of easiness in implantation.

III. METHODS

A. Implantable sensor

An implantable blood pressure sensor was developed using an absolute pressure-sensing device (XFAM-115KPASR FUJIKURA). The device was piezo-resistive type manufactured by micromachining technique. It is worth to mention that the sensor of this type is believed to have long-term stability, especially in gain characteristics. The device was contained in a small cylindrical capsule filled with silicone oil to avoid the direct contact to blood (Fig. 2 (a)). The capsule was sealed by anti-thrombotic segmented-polyurethane film. The capsule was attached to ventricular apex cannula to measure the inlet pressure of the UPVAD (Fig. 2 (b)). Since the UPVAD is connected to the left ventricle, the inlet pressure is more or less identical to the ventricular pressure and is always higher than atmospheric pressure in normal condition. The inlet pressure,

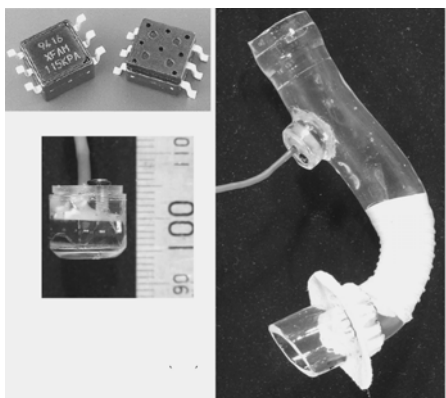


Fig. 2 (a) Pressure sensor, (b) Cannula

however, deviates to a large negative value (< -50 mmHg in gauge unit) under sucking condition (clogging of blood passage).

B. Sensing waveform

Figure 3 shows the pressure waveform obtained by the present sensor during the animal (goat) experiment. During the diastolic phase of the ventricle, the pressure is rather low. Sudden pressure increase would be observed, as ventricle movement switches from the diastolic to systolic phase. During systolic phase the pressure stays high. And sudden decrease in pressure would be observed as the ventricle movement switches from systolic to diastolic phase. A large and sharp negative impulse is also observed at this timing (marked as sucking point in Fig. 3). Clogging of the blood flow (likely the inlet cannula sucking) is believed to be the reason. As new blood flows into the ventricle, ventricle starts to inflate, and the sucking condition will be released. Then the pressure immediately returns to normal value from negative pressure. After the sucking release, the increase rate of the pressure is small, since the ventricle continuously inflates during diastolic period. We believe that the pressure at the start of diastolic phase (inflection point from the sucking condition to slow increase) is almost intrathoracic pressure. If one assumes that the intrathoracic pressure is equivalent to the atmospheric pressure, the inflection point could be a good measure for zero in gauge unit. Since this inflection point is observed in every heartbeat, one can always infer zero in gauge pressure even if the measurement system generates the offset error. This pressure was named as “Calibration pressure”

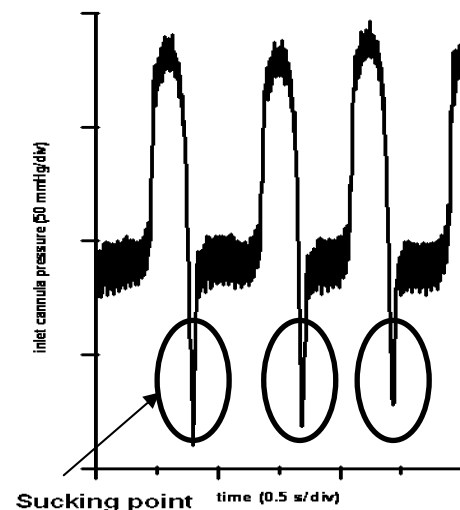


Fig. 3 Observed waveform

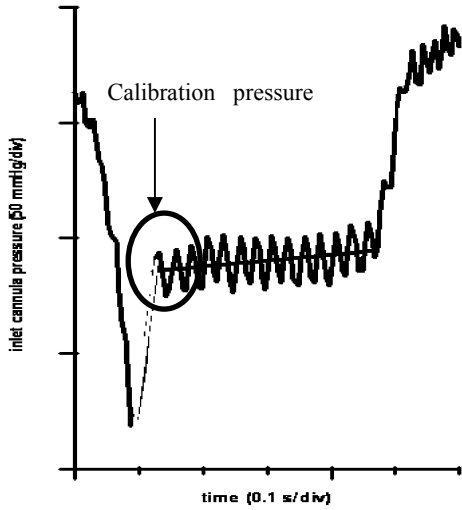


Fig. 4 Expanded waveform

To see inflection part in detail, the pressure waveform for sucking and diastolic phase was expanded in Fig. 4. Small pressure fluctuations (~20 mmHg) in the entire period might be attributed to the pumping characteristics of the UPVAD. Because of this fluctuation, simple derivation of intersection point would not be easy and may introduce significant error if forced to do so.

To eliminate the UPVAD pressure fluctuation, linear curve fitting calculation was performed. First, transient recovery portion from the sucking minimum to the release point was assumed to be linear, and this line was calculated by least-square fitting. Similarly, diastolic period was assumed to be linear and the best-fit linear line was derived by least-square fitting. Calibration pressure is the pressure at the intersection of two fitted lines as shown in Fig. 4.

C. Animal experiment

Actual implantation of the UPVAD with the present sensor was performed to investigate the effectiveness. The UPVAD and the sensor was implanted into an experimental animal (a goat) for 5 months. The sensor was attached to the inlet cannula as shown in Fig. 2 (b). Also the side-tube catheter (not shown in Fig. 2) was attached to monitor the inlet cannula pressure externally. During the experiment, the waveform of the implantable sensor and that of external sensor agrees basically. It should be mentioned that the transient response of the external sensor was slow because of the catheter line resistance and signal of the external sensor tended to be dull.

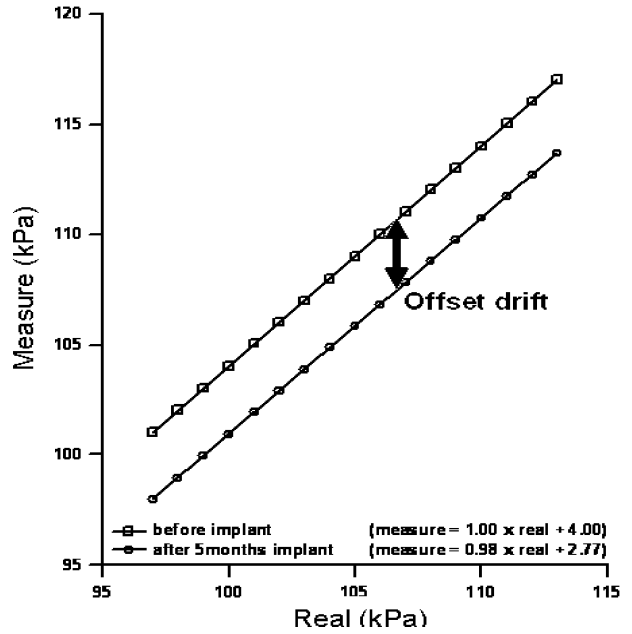


Fig. 6 Sensing characteristics of the implanted sensor before and after the animal experiment

IV. RESULTS

The sensing characteristics of the sensor before and after the implantation is presented in Fig. 5. Two lines did not coincide due to drift. But the two lines are almost parallel. Therefore the gain drift of the sensor is negligible in the measured range, whereas offset drift is noticeable. The sensor drifted about 3.2 kPa. (~24 mmHg) during the ex-

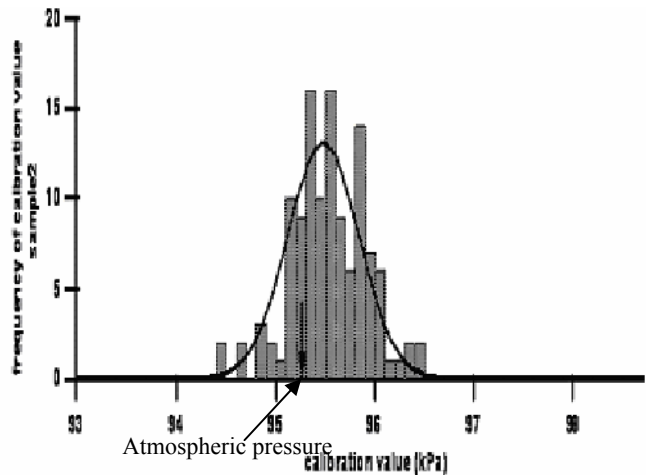


Fig. 5 Histogram of calibration value

periment, which cannot be afforded for the usage in artificial heart control.

Figure 6 shows histogram of the calibration values. The calibration value was calculated for every heartbeat for 2 minutes. Calibration value varied with 0.5 kPa (3.8 mmHg) mean S.D. The mean of calibration value has a discrepancy 0.22 kPa, (1.6 mmHg) from the atmospheric pressure. The implantable pressure sensor could be calibrated. In the short-term pressure measurement (two minutes) errors were no greater than 2 mmHg.

V. DISCUSSION

From the animal experiment, we found histogram of calibration value is close to normal distribution function, the variance was no greater than 3.8 mmHg. The distribution of calibration value might be attributed to the intrathoracic pressure change due to respiration.

In the short-term pressure measurement (two minutes) errors were no greater than 2 mmHg. Therefore it can be concluded that the blood pressure may be inferred from the signal of implanted absolute pressure sensor.

The slight discrepancy between the calibration value and the atmospheric pressure might be originated from the intrathoracic pressure, which is slightly higher than atmospheric pressure.

VI. CONCLUSIONS

The algorithm to induce the left ventricular blood pressure of the UPVAD device using the implanted pressure sensor is presented. The algorithm evaluates the blood pressure from the waveform of the sensor and automatically

compensates offset drift. The five months implantation of animal experiment demonstrated the validity.

Implementation of the present algorithm to an implanted UPVAD enables the reliable blood pressure measurement even with the sensor of long-term offset drift. With the result of this study, further development in UPVAD control method to improve the patient's quality of life (QOL) is expected.

ACKNOWLEDGMENT

This study was supported in part by the JSPS KAKENHI (17209046), and in part by MEXT KAKENHI (18689034). Their financial aids are greatly acknowledged.

REFERENCES

1. Abe Y, Chinzei T, Isoyama T, Ono T, Mabuchi K, Imanishi K, Kouno A, Atsumi K, Fujimasa I, Imachi K (1995) Basic study to develop the undulation pump for practical use: antithrombogenicity, hemolysis, and flow patterns inside the pump. *Artificial Organs* 19:691-693
2. Abe Y, Chinzei T, Isoyama T, Ono T, Mochizuki S, Mabuchi K, Baba K, Matuura H, Sun Y P, Kouno A, Atsumi K, Fujimasa I, Imachi K (1997) Development of the undulation pump total artificial heart. *Artificial Organs* 21:665-669
3. Abe Y, Chinzei T, Isoyama T, Ono T, Mochizuki S, Saito I, Guba P, Karita T, Sun Y P, Kouno A, Suzuki T, Baba K, Mabuchi K, Imachi K (1999) Present status of the total artificial heart at the University of Tokyo. *Artificial Organs* 23:221-228

Author: Wei Shi

Institute: Department of Biomedical Engineering, Graduate School of Medicine, The University of Tokyo

Street: 7-3-1 Hongo, Bunkyo-ku

City: Tokyo

Country: JAPAN

Email: shi@bme.rcast.u-tokyo.ac.jp

Coating preparation and drug delayed release of dexamethasone-eluting intravascular stents *in vitro* and *in vivo*

Yongpeng Chen^{1,2}, Guixue Wang^{1*}, Xianchun Jin², Lailong Luo¹, Gang Zhang², Laichun Lu²

¹College of Bioengineering, Chongqing University, Chongqing, China

²Xinqiao Hospital, Third Military Medical University, Chongqing, China

*Corresponding author, Email: guixue_wang@126.com

Abstract — To prepare the dexamethasone-eluting intravascular stents by dip coating and then to observe the character of drug delayed release *in vitro* and *in vivo* in the stents. Methods Stents were prepared by dip coating. High performance liquid chromatography (HPLC) was used to detect the drug loading of the stents. The weight of bare stents and drug eluting stents was determined in order to know the weight percentage of drugs in the coating. Thermal analyzer was used to analyse the melting point of dexamethasone. The drug slow-release rate *in vitro* was detected with the flow chamber. The buffer solution was taken out at the scheduled time. The dexamethasone-eluting intravascular stents were implanted into the rabbit abdominal aorta. The tissues of the vessel wall and liver were employed for the detection of the drug slow-release properties *in vivo*. The data collected were analyzed by using SPSS 12.0. **Results** The drug loading level increased in a time-dependent manner and peaked 93.15 μg at 4 d. The level of the loaded drug in the coating was (13.70 \pm 0.84)%. Differential scanning calorimetry (DSC) indicated that the melting point was 259.3°C, accordant with the related literatures. Drugs were released slowly and the release rate reached 84% at 15 d. The drug concentration was detected after stent implantation. **Conclusion** Drugs remained 16% of the total loaded drug at 15 d and the drug concentration in the vessel wall and liver tissues was detected after stent implantation, suggesting that the prepared stents may be helpful for the slow-release of dexamethasone.

Keywords — Dexamethasone, Stents, *In vitro*, Slow-release

I. INTRODUCTION

Coronary heart disease is one of the important reasons for human deaths. The drug-eluting stents (DES) combine the advantages of a stainless steel scaffold with controlled release of an agent to prevent restenosis^[1]. They allow to achieve appropriate drug concentration at the treatment site while avoiding systemic toxic effects. DES have been called the third revolution in percutaneous coronary intervention following the introduction of balloon angioplasty and stents^[2]. Dexamethasone is very poorly soluble in water and has the effectiveness of anti-inflammatory and inhibiting restenosis. In this study, dexamethasone-eluting intravascu-

lar stents were prepared by dipping the stents. And then the drug slow-release *in vitro* was determined.

II. MATERIALS AND METHODS

2.1. Reagents and instruments

Dexamethasone (DXM): Sigma corporation, purity \geq 98% (HPLC); L-poly(lactic acid (PLLA): Sigma Corporation, Mw 250,000; 316L coronary artery bare stent: Beijing Am-sino Medical Co., Ltd.; High performance liquid chromatography (HPLC): Agilent1100; Constant flow pump: Baoding Longerpump Co., Ltd.; Electronic balance: Shenyang Longteng Electronic Co., Ltd.; Electric blast drying oven: Chongqing Yinhe Experimental Instrument Co., Ltd.; NETZSCH STA 449C: NETZSCH Instruments Co., Ltd.; Ultrasonic spray device: homemade, national invention patent application NO: 200610054046.7, public NO: CN1827178; Flow chamber: homemade, patent NO: ZL 200620163943.7.

2.2. Methods

2.2.1. Chromatographic condition and standard curve of HPLC

Chromatographic condition of high performance liquid chromatography (HPLC) included C₁₈ column, acetonitrile and water (4:6) as mobile phases and detection wavelength (240 nm). Standard curve of HPLC was $y = 48.10x + 11.96$, $R^2 = 0.9997$. Linear range was 0.2~25 $\mu\text{g}/\text{ml}$.

2.2.2. Preparation of coating

The ratio of DXM to PLLA weight was 2:1. They were added to the chloroform solution. The containers having stents and solution were put into the 80 r/min air shower shaker during dip coating in order to keep the homogeneity of coating. The stents were taken out at the day 1, 2, 3, 4 and 5 and then the PLLA solution was sprayed to the stents at 12 h after the stents dried. Five milliliter tetrahydrofuran was used to elute stents by shake-flask method. The drug concentration was detected by HPLC.

2.2.3 The weight of bare stents was measured by the scale. The dexamethasone-eluting intravascular stents were prepared, and the weight of drug eluting stents was measured. Five milliliter tetrahydrofuran was used to elute stents by shake-flask method. The drug concentration was detected by HPLC and the drug loading of stents was calculated.

2.2.4. NETZSCH thermal analyzer was used for the analysis of the physical properties of dexamethasone(5 mg). Sample was heated from 10°C to 400°C at a rate of 10°C per minute.

2.2.5. Drug slow-release *in vitro*

The drug slow-release rate *in vitro* was detected with the home-made flow chamber, which could simulate the blood vessels and hence could optimize the detection of slow-release of drugs on the stents. Then, the stents were placed in the flow chamber containing 50 ml phosphate buffered solution at 37°C. The velocity of constant flow pump was 20 ml/min. The buffer solution (0.5 ml) was taken out at the time points of 6 h, and 1, 2, 4, 6, 8, 10, 12 and 15 d, respectively, and then was replenished with fresh buffer. The drug concentration was detected by HPLC.

2.2.6. The dexamethasone-eluting intravascular stents were implanted into rabbit abdominal aorta. The vessel wall and liver tissues were taken out at 1 and 10 d after operation, respectively. The extract from the vessel wall and liver tissues was analyzed by HPLC on a C₁₈ column with ultraviolet absorbance detection at the wavelength of 240 nm.

2.3. Statistics analysis

The collected data were analyzed by using variance analysis approach and T-test (SPSS 12.0).

III. RESULTS

3.1. The levels of the drugs loaded on the stents with dip coating (41.77±7.25), (67.64±6.45), (84.71±4.20), (93.15±7.83) and (95.38±7.94) µg at 1, 2, 3, 4 and 5 d, respectively. Compared with that at 1 d, the drug loading at 2, 3, 4 and 5 d increased significantly. Compared with that at 2 d, the drug loading at 4 and 5 d increased significantly, too.

3.2. The weight of coating was the weight of the drug eluting stents subtracted by that of the bare stents. The weight percentage of drugs in the coating was the ratio of the drug loading of stents to the weight of coating. The weight of drug load was (13.70±0.84)% in the coating.

3.3. Differential scanning calorimetry (DSC), as shown in Figure 1, indicated that the melting point was 259.3°C, accordant with 254°C-264°C in the pharmacopoeia of the People's Republic of China. The thermogravimetry (TG) curve indicated the rate of weight loss of dexamethasone was 76.67% from 250°C to 400°C. DSC and TG curves

revealed the course of evaporation and sublimation of dexamethasone within the range of 250°C to 400°C.

3.4. The drug concentrations *in vitro* were detected at the preset time points. As shown in Figure 2 and 3, burst release *in vitro* was detected at 6 h, and the released amount was 9.75% of the total. Then drugs kept releasing slowly and reached 84% at 15 d.

3.5. The drug levels in the vessel wall and liver tissues were 4.59 µg/g and 1.91 µg/g at 1 d, and 0.22 µg/g and 0.73 µg/g at 10 d after stent implantation, respectively.

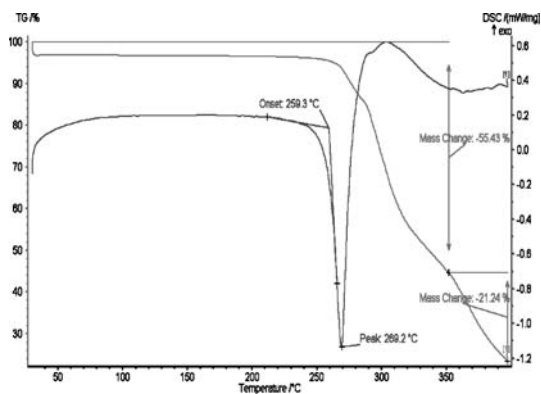


Fig. 1. DSC thermograms and TG of DXM

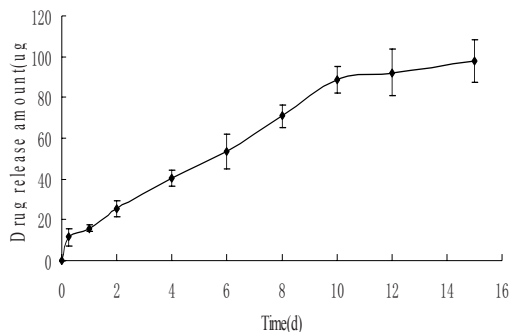


Fig. 2. Drug release amount *in vitro*

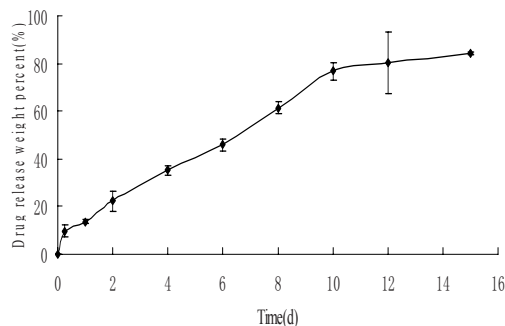


Fig. 3. Drug release weight percent *in vitro*

IV. DISCUSSION

The implantation of DES is the commonly used interventional therapy for coronary heart disease. Dexamethasone significantly inhibited the proliferations of lymphocytes and smooth muscle cells *in vitro*^[3].

The ultrasonic spray coating reduces roughness of stent surface and makes the coating uniform. The drug loading increased in a time-dependent manner and peaked at 93.15 μg at 4 d. The stents prepared by the previously described way were used in the experiment of drug slow-release *in vitro*. The weight of drug load was $(13.70\pm 0.84)\%$ in the coating. DSC indicated that the melting point was 259.3°C, accordant with the related literatures.

The drug slow-release rate *in vitro* was detected with the home-made flow chamber, which could simulate the blood vessels and hence could optimize the detection of slow-release of drugs on the stents. Burst release *in vitro* was detected at 6 h, which may be relevant to the drug diffusion, and then drugs were released slowly. Drugs remained 16% at 15 d. The drug concentrations in the vessel wall and liver

tissues were detected at 1 and 10 d after stent implantation, suggesting that the prepared stents may be helpful for the slow-release of dexamethasone.

ACKNOWLEDGEMENTS

This research was funded by the MOST of China(2004DFA06400), the Scientific Research Foundation of Third Military Medical University (06XG030) and Chongqing Municipality of China (CSTC2006AA5014-3, DRC2005-1006)

REFERENCES

- [1] Sousa J.E., Serruys P.W., Costa M.A., (2003) New frontiers in cardiology: drug-eluting stents: Part I, *Circulation* 107(17): 2274-2279.
- [2] Saia F., Marzocchi A., Serruys P.W., (2005) Drug-eluting stents. The third revolution in percutaneous coronary intervention, *Ital Heart J* 6(4): 289-303.
- [3] Yoon J.J., Kim J.H., Park T.G., (2003) Dexamethasone-releasing biodegradable polymer scaffolds fabricated by a gas-foaming/salt-leaching method, *Biomaterials* 24(13): 2323-2329.

A Comparative Study on the Expression of Telomerase Reverse Transcriptase in Different Development Stages of Human Epidermal Stem Cells in vitro

Dewu Liu¹, Peixin Huang^{1,2}, Yuanguai Mao¹, Jianping Chen¹, Wei Lan¹, Lianqun Wang¹

¹Burn center, The first affiliated hospital of Nanchang University, Nanchang 330006, Jiangxi Province, P.R.China

²Burn and plastic department of the first affiliated hospital of Henan University of Science and Technology, Luoyang 471003, P.R China

Abstract — Aim: The main reasons for limiting the replication and expansion ability of the adult stem cells in vitro are the loss of telomerase activity and the changes of related proliferation gene expression, in which telomerase reverse transcriptase(TERT) plays a key role. In this chapter, we focus on the isolation, culture and identification of the epidermal stem cells derived from human fetus, child and adult skins, and compare the TERT expression of the different developmental periods of the epidermal stem cells. **Methods:** The skin samples of child, adult and fetus were disposed with Trypsin-EDTA respectively. The epidermal stem cells were isolated and purified by means of the type IV collagen rapid adhering method and cultured in vitro using keratinocyte serum free medium contained epidermal growth factor and fetal bovine serum. The keratinocytes were used as the control groups. The colony forming efficiency were calculated. The $\beta 1$ integrin, keratin19 and p63 transcription factor were detected by the immunocytochemical stain and the image quantitative analysis. **Results:** The cultured cells revealed colony growth, the colony forming efficiency of the epidermal stem cell is higher than the keratinocyte. The $\beta 1$ integrin, k19 and p63 had positive expression in the epidermal stem cells but not the keratinocyte cells. The TERT expression level of the fetus epidermal stem cells was higher than that of the adult and the child. The detection of the average value of absorbance and positive area of each group exhibited that the value decreased with the age. **Conclusion:** The expression of TERT in the cultured human epidermal stem cells derived from human fetus, child and adult skins were all positive. And the expression intensity level was followed as the period of the fetus, the child and the adult. It showed that the induction and the reinforcement of the telomerase reverse transcriptase activity may have important influence in the maintenance of the self-renewal and proliferation ability of the epidermal stem cell.

Keywords — epidermal stem cell, telomerase reverse transcriptase, in vitro, tissue engineering.

I. INTRODUCTION

Recently study revealed that the proliferation ability of the epidermal stem cell has great difference between vitro and vivo, that's to say the difficulty of replication and loss of stem cell characteristics iv vitro of the epidermal stem cell restrict the further study and research. The loss of te-

lomerase activity and the changes of related proliferation gene expression are the main reasons for limiting the replication and expansion ability of the adult stem cells in vitro, but whether it had the same expression in the epidermal stem cell is not clear. In this chapter, we focus on the isolation, culture and identification of the epidermal stem cells derived from human fetus, child and adult skins, and to compare the telomerase reverse transcriptase expression of the different developmental periods of the epidermal stem cells, to make a foundation for the application of the epidermal stem cell in the skin tissue engineering.

II. MATERIALS AND METHODS

A. Materials

The experiment was performed at Institute of Burn, the first affiliated hospital of Nanchang University. The skin samples of fetus were taken from the accidental abortion(24 ~ 26 week gestational age)and provided by Department of Maternity, the first affiliated hospital of Nanchang University. The skin samples of child(4 ~ 12 year)and adult(25 ~ 45 year) came from the operation of burn and plastic and provided by Department of Burn, the first affiliated hospital of Nanchang University. The use of these samples were obtained with consent from parturients and patients and approved by Medical Ethics Committee of the Hospital. The main reagents and equipments: serm free medium of keratinocyte(Gibco), fetal bovine serum(Gibco),0.25% Trypsin-0.02% EDTA(Gibco), $\beta 1$ -integrin, keratin-19, p63 monoclonal antibody, collagen IV(Sigma), TERT monoclonal antibody,cx40 commom optical microscope(Olympus), cx40 inverted phase contrast microscope(Olympus), SW-CJ-1F superclean bench(sujing Co.Ltd.),IT-41CO2 incubator (Yamato).

B. Methods

The sample was disposed with Trypsin-EDTA respectively and got the epidermis, and then we digested the epidermis and harvested the epidermal cells. The type IV col-

lagen was used to isolate and purify the human epidermal stem cells, and the epidermal growth factor and the keratinocyte serum free medium were used to culture the cells. The keratinocyte cells were used as the control groups. The $\beta 1$ integrin, keratin19 and p63 transcription factor were identified by the immunocytochemical stain. The colony forming efficiency were calculated. The expressions of the telomerase reverse transcriptase in the different developmental periods of epidermal stem cells were detected by the immunocytochemistry stain and the image quantitative analysis.

III. RESULTS

The cultured cells revealed colony growth, the colony forming efficiency of the epidermal stem cell is higher than the epidermal cell, $P < 0.05$ (Table 1). The $\beta 1$ integrin, k19 and p63 had positive expression in the epidermal stem cells but not the epidermal cells. the TERT immunohistochemistry stain revealed that the expression level of the fetus epidermal stem cells was higher than that of the adult and the child. The detection of the average value of A and S of each group exhibited that the value decreased with the age. Statistics analysis showed that there were statistic differences among them, $P < 0.05$ (Table 2).

Table 1 the determination of the colony forming efficiency of the epidermal stem cell ($\bar{X} \pm s$)

group	Cell mount	Colon mount	Colony forming efficiency (%)
Epidermal stem cell	200	20.5 \pm 1.4 ^a	10.25 ^a
keratinocyte	200	9.0 \pm 1.7	4.50

Compare with the keratinocyte , $aP < 0.05$

Table 2 the quantitation analysis of the tert of human epidermal stem cell ($\bar{X} \pm s$, $n=25$)

Sources of the skin	Average value of A	Average value of S
the fetus	0.1545 \pm 0.0031a	2815.31 \pm 245.36a
child	0.1426 \pm 0.0039ab	1982.45 \pm 273.24ab
adult	0.1216 \pm 0.0043b	1030.26 \pm 304.31b

Compare with the adult , $aP < 0.05$; with the fetal , $bP < 0.05$

IV. DISCUSSIONS

In the normal huamn skin tissue, the epidermal stem cell keeps relative quiescence, the 1%-10% of the basement cells are epidermal stem cells. They have strong proliferation and amplication and play an important role in the skin refreshment, wound healing, tumor formation and the maintance of the skin internal environment^[1,2]. Recently study revealed that the proliferation ability of the epidermal stem cell has great difference between vitro and vivo, that's to say the difficulty of replication and loss of stem cell characteristics iv vitro of the epidermal stem cell restrict the further study and research^[3-5]. How to obtain more epidermal stem cell from the skin and maintain the stem cell character in vitro culture are the precondition of application in the skin tissue engineering.

There are many methods to separate and purify epidermal stem cell at present^[6-12]. In this chapter, the epidermal stem cells separated and purified by the Trypsin-EDTA and type IV collagen revealed colony formation, the $\beta 1$ integrin, k19 and p63 had positive expression , the epidermal stem cell had the stem cell traits. The results demonstrate that the method is pretty good in separating and purifying the epidermal stem cell.

The aging of the cell is believed that it is concerned with the loss of telomere's TTAGGG. With the cell segmentation, the telomere loses 50-200bp, until a extent the cell segmentation will stop and enter aging process. The maintance of the length of the telomere is catalysed by the telomerase. The telomerase contains the RNA section(hTR), the telomerase related protein(TEP) and the telomerase reverse transcriptase(TERT). The TERT play a key role in the telomerase activity. In huamn, the telomerase exists in the stem cell, the germinal cell and most tumor tissues. It's strong activity is necessary for the tumor growth, but the moderate expression is helpful to prolong the cell life^[13-20]. Proper up-regulation and maintain the telomerase activity of the stem cell are helpful to boost the replication and amplication ability and reveal the aging mechanisms. recently study revealed that the expression exists in the basement of epidermis and the growth phase hair follicle, but less is known about the expression of telomerase reverse transcriptase in different development stages of human epidermal stem cells in vitro. To know the rule and expression difference in the epidermal stem cell is useful to acquire more knowledge about the regulation and application of the epidermal stem cell.

On the basement of the culture of the human epidermal stem cell, the expression characteristics of the human epidermal stem cell in the different developmental period are comparaed, the results showed that the different periods of the skin samples had the telomerase activity, the intensity level was followed as the period of the fetus, the child and

the adult. It showed that the induction and the reinforcement of the telomerase activity may have important influence in the maintenance of the self-renewal and proliferation ability of the epidermal stem cell.

ACKNOWLEDGMENT

This work was supported by the National Natural Science Foundation of China (30560058), the Great Invited Tenders Foundation of Jiangxi Science and Technology Bureau (200604), and the Science Research Foundation of Jiangxi Education Bureau(2005-187).

REFERENCES

1. Tumber T, Guasch G, Greco V, et al. Defining the Epithelial Stem Cell Niche in Skin. *Science* 2004;303(5656): 359-363
2. Webb A, Li A, Kaur P. Location and phenotype of human adult keratinocyte stem cells of the skin. *Differentiation* 2004; 72(8):387-395
3. Youn SW, Kim DS, Cho HJ, et al. Cellular senescence induced loss of stem cell proportion in the skin in vitro. *J Dermatol Sci* 2004;35(2):113-123
4. Liu DW, Hu X, Liu DM. Construction and application for skin defect repair of tissue engineered skin with human epidermal stem cells induced by *Radix Astragalus*. *Tissue Eng* 2006;12(4):1109
5. Liu DW, Li GH, Zou P, et al. Construction of tissue-engineered skin by epidermal cells and fibroblasts combined with acellular dermal matrix in vitro. *Journal of Clinical Rehabilitative* 2004,8(8):1439-1441
6. Pellegrini G, Bondanza S, Guerral L, et al. Cultivation of human keratinocyte stem cells: current and future clinical applications. *Med Biol Eng Comput* 1998; 36(6):778-790
7. Wan H, Stone MG, Simpson C, et al. Desmosomal proteins, including desmoglein 3, serve as novel negative markers for epidermal stem cell-containing population of keratinocytes. *J Cell Sci* 2003;116(pt20):4239-4248
8. Nakamura Y, Muguruma Y, Yahata T, et al. Expression of CD90 on keratinocyte stem/progenitor cells. *Br J Dermatol* 2006;154(6):1062-1070
9. Zhou JX, Chen SY, Liu WM, et al. Enrichment and identification of human 'fetal' epidermal stem cells. *Hum Reprod* 2004;19(4):968-974
10. Webb A, Li A, Kaur P. Location and phenotype of human adult keratinocyte stem cells of the skin. *Differentiation* 2004;72(8):387-395
11. Kurata S, Okuyama T, Osada M, et al. p51/p63 Controls subunit alpha3 of the major epidermis integrin anchoring the stem cells to the niche. *J Biol Chem* 2004;279(48):50069-50077
12. Terunuma A, Kapoor V, Yee C, et al. Stem cell activity of human side population and alpha6 integrin-bright keratinocytes defined by a quantitative in vivo assay. *Stem Cells* 2007;25(3):664-669
13. Mokbel K. The role of telomerase in breast cancer. *Eur J Surg Oncol* 2000; 26(5): 509-514
14. Wu A, Ichihashi M, Ueda M. Correlation of the Expression of Human Telomerase Subunits With telomerase activity in Normal Skin and Skin Tumors. *Cancer* 1999;86(10): 2038-2044
15. Boukamp P. Skin aging: a role for telomerase and telomere dynamics? *Curr Mol Med* 2005;5(2):171-177
16. Flores I, Cayuela ML, Blasco MA. Effects of telomerase and telomere length on epidermal stem cell behavior. *Science* 2005;309(5738):1253-1256
17. Meyerson M, Counte CM, Eaton EN, et al. hEST2, the putative human telomerase catalytic subunit gene, is up-regulated in tumor cells and during immortalization. *Cell* 1997;90(4):785-795
18. Kirkpatrick KL, Mokbel K. The significance of human telomerase reverse transcriptase (hTERT) in cancer. *Eur J Surg Oncol* 2001;27(8):754-760
19. Siegl-Cachedenier I, Flores I, Klatt P, et al. Telomerase reverses epidermal hair follicle stem cell defects and loss of long-term survival associated with critically short telomeres. *J Cell Biol* 2007 ;179(2):277-290
20. Sarin KY, Cheung P, Gilson D, et al. Conditional telomerase induction causes proliferation of hair follicle stem cells. *Nature* 2005;436(7053):1048-1052

Correspondence to: Dewu Liu
E-mail: dewuliu@126.com

The Location and the Telomerase Expression of the Different Development Stages of Human Skin Epidermal Stem Cells *in vivo*

Dewu Liu¹, Wei Lan¹, Peixin Huang^{1,2}, Yuangui Mao¹, Jianping Chen¹, Lianqun Wang¹

¹ Burn center, The first affiliated hospital of Nanchang University, Nanchang 330006, Jiangxi Province, P.R.China

² The affiliated hospital, Henan University of Science and Technology, Luoyang 471003, Henan Province, P.R.China

Abstract — **Aim:** To study the characteristics of the location and the telomerase expression of the different developmental periods of human skin epidermal stem cells, to illuminate the significance of these characteristics to the burn wound repair. **Methods:** The skin samples of child and adult that came from the operation of burn and plastic, the samples of fetus came from the accidental abortion. The samples were fixed by 10% formalin at once, then were made into paraffin sections. Integrin β 1, keratin19, p63 transcription factor and telomerase reverse transcriptase (TERT) were detected by the immunohistochemistry stain. **Results:** The β 1 integrin, K19, p63 and TERT positive cells were mainly located in the epidermal basement membrane, and the expression levels of those indexes were highest in the fetus skin, lower in the skins of the child and adult, the distribution was uniformity in the fetus and adult samples. Lowest expression in the adult sample. The expression amount of the β 1 integrin, K19, p63 and TERT in the different development periods revealed decreasing with the age increasing ($P < 0.01$). **Conclusion:** The epidermal stem cell of the fetus, child and adult were mainly located in the epidermal basement membrane, the positive expression sector and the expression levels of the telomerase had a same level with the location and positive expression level of the epidermal stem cells. It showed that the quantity and the expression level of the telomerase of the epidermal stem cell may have a relation with the repair ability of the different developmental periods of the skin tissue.

Keywords — epidermal stem cell, telomerase, skin, tissue engineering

I. INTRODUCTION

The epidermal stem cell is a specific stem cell in human skin. It has powerful potency of proliferation and multi-directional differentiation. Not only sustain the daily metabolism of epidermis, but also positively participate the reparation after skin destruction. Skin destruction caused by severe burn or wounds, injured area healing ability increases along with the age reduces gradually. The reasons involve many aspects, epidermal stem cell's quantity and the potential's difference of multiplication and differentiation is possibly one of its substantial clauses. The research indicated that the cell's senility and the aging were related with the sequence of chromosome terminal end grain loss which

is composed of redundant DNA (TTAGGG). The length of telomere's maintenance namely repetitive sequence catalyzes to the chromosome terminal's increase by telomerase (TLMA), but TERT plays the crucial role to telomerase's activity. This experiment uses the immunohistochemical method to observe the differential expression of keratin 19 (K19), integrin β 1, the p63 transcription factor, telomerase reverse transcriptase catalytic subunit (TERT), which in the person fetal stage, the children time and the adulthood skin specimen, discusses the clinical significances of these differences to the burn injured area's reparation.

II. MATERIALS AND METHODS

A. Specimen origin and preparation

The pregnancy 24~26 week age embryo skin samples came from the accidental abortion, provides by OG (department of gynaecology and obstetrics) of our hospital. The skin samples of child (4~12 years) and adult (25~45 years) that came from the operation of burn and plastic, provides by burns department of our hospital. All of it solicits the patient to agree. The samples were fixed by 10% formalin at once, then were made into paraffin sections, conserved in 4°C and waited to detect.

B. Main reagent and instrument

Mouse anti-person β 1 integrin, K19, p63 monoclonal antibody, EnVision™ reagent box, Mouse anti-person TERT monoclonal antibody, CX40 ordinary optical microscope, Manual rotary microtome, DK-8D electric heating thermostatic water bath.

C. Immunohistochemistry stain

All specimens after serial section, takes mouse anti-person keratin19, p63, TERT and integrin β 1 monoclonal antibody separately as first antibody, were detected by the immunohistochemistry stain (EnVision). The experiment operates according to the reagent box instruction booklet. Simultaneously establishes negative control which replaces by PBS.

D. β 1integrin, K19, p63 and TERT positive expression rate detection

Under 200 times of optical microscope, observes the immunohistochemistry stain result and photographs. Select 20 fields of vision stochastically in each specimen, observes 100 basal cells continuously in each field of vision, record the positive cell number and figures out the positive rate.

E. Statistics processing

All of data express by mean value \pm standard deviation ($X \pm s$). The multi-sample mean value comparison uses the variance analysis and the group comparison uses the q analysis. $P < 0.05$ the difference has significance. $P < 0.01$ the difference has highly significant.

III. RESULTS

A. Integrin β 1, K19, p63 and TERT expression properties in person epidermal tissues of different developmental stage.

The person skin of the fetus, child and adult, in each group, around the epidermal basilar part and the hair-follicle cells, β 1integrin, K19, p63 and TERT have buffy positive expression. In embryo epidermis, under the optical microscope, the cuticular layer has 3~5 layer cells. The cell is the cubic epithelium cell and the size is uniform. The epidermal foot not yet grows. β 1integrin, K19 and p63 are the strong positive in its epidermal basement membrane cells. In the children epidermal basement membrane cells, the majority of cells express β 1integrin, K19 and p63, the distribution of positive cell was uniformity. In adult epidermal basement membrane, the expression levels of β 1integrin, K19 and p63 were lower. The positive cell's distribution was diffused and relatively centralized lamellar, the positive cell expression levels compares the embryo group and the children group to be low.

The embryo skin, the children skin, the adult skin's telomerase immunohistochemistry stain were positive. The positive cells mainly located in the epidermal basement membrane. And positive cell expression level was highest in the fetus skin, lower in the skins of the child, and lowest in the adult skin.

B. Integrin β 1, K19, p63 and TERT positive expression rate detection in person epidermal tissues of different developmental stage.

Integrin β 1, K19, p63 and TERT in the embryo skin, the children skin and in the adult skin's expression increases along with the age reduces gradually, the result in Table 1.

Table 1 Integrin β 1, K19, p63 and TERT positive expression rate in person epidermal tissues of different developmental stage (n= 20 ,%, x \pm s)

Groups	β 1integrin	K19	p63	TERT
Embryo skin	98.3 \pm 1.9*	98.9 \pm 1.1*	97.4 \pm 2.0	99.0 \pm 1.7
Children skin	53.4 \pm 11.3* Δ	50.3 \pm 11.4* Δ	51.5 \pm 10.6* Δ	50.3 \pm 10.4* Δ
Adult skin	11.2 \pm 8.3 Δ	9.5 \pm 8.9 Δ	9.1 \pm 7.9 Δ	5.1 \pm 1.2 Δ

Note: Compares with the adult skin * $P < 0.01$, Compares with the embryo skin $\Delta P < 0.01$

IV. DISCUSSIONS

The skin epidermis differentiates from the embryo surface's ectoderm. In vivo, the epidermal stem cells first differentiate to the transient expansion cells, after splits many times, oriented differentiate to postmitotic cells and terminally differentiated cells, then keratinizing fall off from the skin surface, complete the epidermal metabolism process. Although in vivo epidermal stem cell quantity is few (approximately composes stratum basale cell 1%-10%), but because it has the strong differentiation and reproductive activity, it plays the influential role in the skin renews, wound healing, tumour generation as well as in the maintenance of the skin stable internal environment and so on aspects ^[1]. Although currently surface markers have many, which use in the cell detachment and the identification of epidermal stem cell, but not yet discovers one kind of absolute specificity marker. To clear about the epidermal stem cell's identification and the localization is important prerequisite and foundation to further studies it's proliferative and differentiated regulation mechanism and the application in the skin tissue engineering.

At present epidermal stem cell markers were β 1integrin, K19, p63, PCNA, CD71 and so on which is often used. The integrin not only regulates the epidermal cell and extracellular matrix adhering, but also regulates the initiation of the terminal differentiation, and plays the role in the epidermal differentiation and the morphogenesis. The different of function or expression of the integrin possibly provides the markers to keratinocyte subgroup which have the reproductive activity. Jones and the Watt ^[2], according to the integrin expression level's difference on the surface of keratinocyte in stratum basale, using the fluorescence active cell sorter to classify the cells. The research discovered that the cell with the high expression α 2 β 1 integrin has a higher clonality than the cell without. And the cell with high expression α 3 β 1 and α 5 β 1 integrin also has the similar characteristic. When the

keratinocyte puts in the extracellular matrix protein like IV collagen and fibronectin, it will present gradual adhering, the speed of the cell adhering and the clonality is related. Keratinocytes with the low expression of β 1 integrin will form the small clone shape, and will develop to terminal differentiation^[3-5]. The epidermal stem cells must through the integrin and basal membrane adhering to maintain the stem cell characteristic and the position at the niche. Because the integrin expression level of the transient expansion cell is not to be indefinite, that limits it to do for the application as marker. Moreover, Jones and the Watt^[2] discovered cell's integrin expression level is higher, and then it's clonality to be also stronger.

Keratinocytes have the distinctive keratin intermediate filament. Michel^[6] discovered the mouse hair follicle label-retaining cells which mark with 3H-T, examine K19 to express with immunoblotting. And the K19 positive expressed cells are also the tritium-thymidine (3H-TdR) label-retaining cells. K19 expresses in the skin hair-follicle of person and mouse, and does not express in the interfollicular epidermis of the pilosity area. In depilous area, K19 positive expressed cells located at epidermal cutaneous ridge, its $\alpha_3\beta_1$ integrin expression is also positive. In the newborn praeputium, the number of the K19 positive expressed cells is more than in the adult, showed that it concerns with the keratinocyte's cultural cycle. These results showed that K19 is an epidermal stem cell's valuable marker, or is auxiliary marker at least^[7, 8].

The p63 transcription factor is the homolog of the p53 tumor-suppressing gene. It belongs to the same family with p53 and p73. Pellegrini^[9] obtains the cornea and skin's epidermal cells through in vitro separation, and detects its p63 expression and the clonality, and then discovers the p63 high express in holoclone cells, but does not express in subclone cells. And thought that p63 is the first gene until now which can distinguish the epidermal stem cells and the transient expansion cells. The research of the mouse epidermal embryogeny which removes the gene p63 confirms that the absence of p63 may cause the epidermal basement membrane stem cells to lack, which maintains own quantity constant through the asymmetrical fission^[10]. The p63 high expresses in the epidermal stem cells of mature epidermal basal membrane, along with the terminal differentiation of keratinocytes, the expression of p63 declines finally^[11-13]. P63 can not identify the epidermal stem cell completely in vivo independent expression, because at the full-thickness basal membrane, it expresses in the basal upper stratum cells and hair follicle's outer root sheath department. Therefore, it needs to identify the epidermal stem cell together with other markers.

This experiment synthesizes integrin β 1, K19 and the p63, the epidermal stem cell surface markers to locate and observe the skin epidermal stem cells of different developmental stage, the result showed that the person skin of the fetus, child and adult around the epidermal basilar part and the hair-follicle cells, β 1 integrin, K19, p63 and TERT have buffy positive expression. In embryo epidermal basement membrane cells, β 1 integrin, K19 and p63 are the strong positive. In the children epidermal basement membrane cells, the majority of cells express β 1 integrin, K19 and p63, the distribution of positive cell was uniformity. In adult epidermal basement membrane, the expression levels of β 1 integrin, K19 and p63 were lower. The positive cell's distribution was diffused and relatively centralized lamellar, the positive cell expression levels compares the embryo group and the children group to be low. The embryo skin, the children skin, the adult skin's telomerase immunohistochemistry stain were positive. The positive cells mainly located in the epidermal basement membrane. And positive cell expression level was highest in the fetus skin, lower in the skins of the child, and lowest in the adult skin. Integrin β 1, K19, p63 and TERT in the embryo skin, the children skin and in the adult skin's expression increases along with the age reduces gradually, the difference of the groups has highly significant ($P < 0.01$).

This experimental result also showed that the embryo skin, the children skin and the adult skin, each group of the telomerase immunohistochemistry stain is positive, the positive cells mainly concentrate in the epidermal stratum basale. In the embryo skin, the children skin and in the adult skin, the telomerase positive expression rate increases along with the age reduces gradually. The clinical observation, burn wound healing ability increases along with the age reduces; this result is consistent with it. It showed that the quantity, the localization and the expression level of the telomerase of the epidermal stem cell may have a relation with the repair ability of the different developmental periods of the skin tissue.

ACKNOWLEDGMENT

This work was supported by the National Natural Science Foundation of China (30560058), the Great Invited Tenders Foundation of Jiangxi Science and Technology Bureau (200604), and the Science Research Foundation of Jiangxi Education Bureau(2005-187).

REFERENCES

1. Raja, Sivamani K, Garcia MS et al. Wound re-epithelialization: modulating keratinocyte migration in wound healing. *Front Biosci*, 2007, 12:2849-2868.
2. Jones PH, Watt FM. Separation of human epidermal stem cells from transit amplifying cells on the basis of differences in integrin function and expression. *Cell*, 1993, 73(4):713-724.
3. Lopez-Rovira T, Silva-Vargas V, Watt FM. Different consequences of beta1 integrin deletion in neonatal and adult mouse epidermis reveal a context-dependent role of integrins in regulating proliferation, differentiation, and intercellular communication. *J Invest Dermatol*, 2005, 125(6):1215-1227.
4. Raghavan S, Bauer C, Mundschau G et al. Conditional ablation of beta1 integrin in skin. Severe defects in epidermal proliferation, basement membrane formation, and hair follicle invagination. *J Cell Biol*, 2000, 150(5):1149-1160.
5. Brakebusch C, Grose R, Quondamatteo F et al. Skin and hair follicle integrity is crucially dependent on beta 1 integrin expression on keratinocytes. *EMBO J*, 2000, 19(15):3990-4003.
6. Michel M, Torok N, Goodbout MJ et al. Keratin 19 as a biochemical marker of skin stem cells in vivo and in vitro: keratin 19 expressing cells are differentially localized in function of anatomic sites, and their number varies with donor age and culture stage. *J Cell Sci*, 1996, 109(Pt5):1017-1028.
7. Ma DR, Yang EN, Lee ST. A review: the location, molecular characterisation and multipotency of hair follicle epidermal stem cells. *Ann Acad Med Singapore*. 2004, 33(6):784-788.
8. Larouche D, Hayward C, Cuffley K, et al. Keratin 19 as a stem cell marker in vivo and in vitro. *Methods Mol Biol*, 2005, 289:103-110.
9. Pellegrini G, Dellambra E, Golisano O, et al. p63 identifies keratinocyte stem cells. *Proc Natl Acad Sci USA*, 2001, 98(6):3156-61.
10. Yang A, Schweitzer R, Sun D, et al. p63 is essential for regenerative proliferation in limb, craniofacial and epithelial development. *Nature*, 1999, 398 (6729) : 714-718.
11. Truong AB, Kretz M, Ridky TW et al. p63 regulates proliferation and differentiation of developmentally mature keratinocytes. *Genes*, 2006, 20(22):3185-3197.
12. Koster MI, Kim S, Roop DR. P63 deficiency: a failure of lineage commitment or stem cell maintenance? *J Invest Dermatol Symp Proc*, 2005, 10(2):118-123.
13. Kai-Hong J, Jun X, Kai-Meng H et al. P63 expression pattern during rat epidermis morphogenesis and the role of p63 as a marker for epidermal stem cells. *J Cutan Pathol*, 2007, 34(2):154-159.

Correspondence to: Dewu Liu
E-mail: dewuliu@126.com

Differentiation of the Human Marrow Mesenchymal Stem Cells into Vascular Endothelium-like Cells in vitro

Dewu Liu¹, Xiangrong Zhang¹, Xiaoliang Li^{1,2}, Zhian Zhang¹, Guanghua Guo¹

¹Burn center, The first affiliated hospital of Nanchang University, Nanchang 330006, Jiangxi Province, P.R.China

²First people's hospital of Zhengzhou city, Zhengzhou 450004, Henan Province, P.R.China

Abstract — **Aim:** The two main obstacles of successfully grafting tissue engineered skin are the shortage of the resource of the seed cell and the long process of vascularization of grafted skin. This article investigates the feasibility and condition of differentiation of the human marrow mesenchymal stem cells (MSCs) into the vascular endothelial-like cells in vitro. **Methods:** The MSCs were harvested, isolated and purified by combining density gradient centrifugation with adhering method. The cultured cells in induce group were treated with 10 μ g/L vascular endothelial growth factor(VEGF) and 5 μ g/L basic fibroblast growth factor(bFGF). No VEGF and bFGF were added in control group. The morphological changes of the cells were observed with inverted phase contrast microscope. The expression of CD34, VIII factor were determined by the immunocytochemistry methods. The transmission electron microscope was used to further explore the ultra-structure characteristics of the cultered cells. **Results:** The cells induced by VEGF and bFGF showed the morphological changes from long fusiform-shaped to short fusiform or flat shape, which was consistent with the significant characteristic of endothelium cells. The expression of CD34, VIII factor were positive in the induced cells, which were negative in the control group. The Weibel-Palade body could be found in the cytoplasm of some induced cells. **Conclusion:** Combined VEGF with bFGF can induce MSCs differentiate into vascular endothelial-like cells in vitro, which may be unfold the potential applied prospects for vascularization and application of tissue engineered skin.

Keywords — mesenchymal stem cells, vascular endothelial-like cells, vascular endothelial growth factor, basic fibroblast growth factor.

I. INTRODUCTION

Bone marrow mesenchymal stem cells (MSCs) are pluripotent stem cells present in bone marrow mesenchymal tissues. These cells have the capacity to differentiate into cells of multiple mesoderm-type lineages, including bone, fat, cartilage and muscle. MSCs seem to be the ideal candidates for tissue engineering, as they can be rapidly amplified and maintain pluripotent differentiation capabilities. The aim of our study was to test if MSCs were capable of being the new seed-cells for tissue engineering skin. In the present study, we have induced human MSCs to be differen-

tiated into vascular endothelium-like cells in vitro in the presence of vascular endothelial growth factor (VEGF) and basic fibroblast growth factor(bFGF). This is significant in that it prepares us for future clinical application.

II. MATERIALS AND METHODS

A. Isolation and culture of bone marrow-derived human MSC

The experiment was carried out in the institute of burn, the first affiliated hospital of Nanchang University. Bone marrow aspiration samples in this study were obtained sterilely from human donors without severe hematopietic and genetic diseases. All samples were collected with informed consent. The human bone marrow mesenchymal stem cells were harvested, isolated and purified by combining Ficoll density gradient centrifugation with adhering method and cultured in Low-glucose Dulbecco's Modified Eagle's Medium(L-DMEM) containing 10% fetal bovine serum. After approximately 3 days nonadherent cells were removed by replacing the medium. Once the adherent cells reached 80% confluence, MSCs were passaged further. The MSCs used in the present induce study were cultured at 3th passage.

B. Differentiation of MSCs

The cultured cells in induce group were treated with L-DMEM supplemented with 10 μ g/L vascular endothelial growth factor(VEGF) and 5 μ g/L basic fibroblast growth factor(bFGF). No VEGF and bFGF were added in control group. The morphological changes of the cells were observed with inverted phase contrast microscope.

C. Immunohistochemistry analyses

The expression of CD34, VIII factor were determined by the immunocytochemistry methods.

D. Ultrastructure observation

Cells were routinely collected. Specimens were prepared for transmission electron microscopy by fixing with 2% pre-cold glutaraldehyde for 2h, post-fixing with 1% osmic acid, dehydrating in a graded series of acetone, and then embedding in epoxide resin. Thin sections were cut and double-stained with uranyl acetate and lead citrate. The sections were examined with transmission electron microscope.

III. RESULTS

By Ficoll density gradient centrifuge and monolayer cultured MSCs can successfully be isolated from bone marrow blood in vitro. When inoculating, the modalities of cells maybe round, triangle or virgulate; and began to be adhesive for 48h; and formation of colony could be formed on day 4-5; Many cells grew in clonal manner on day 7, and the cultured cells were characterized by large spindle-shaped appearance by the time of 10 days. After 2 weeks, the 80% confluence could be observed. The passaging cells were homogeneous spindle-shaped and there were no suspending cells in the mediums on the whole. The cells induced by VEGF and bFGF showed the morphological



Fig. 1 The expression of CD34 were positive in the induced cells

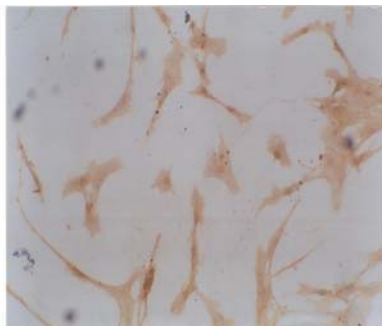


Fig. 2 The expression of VIII factor were positive in the induced cells

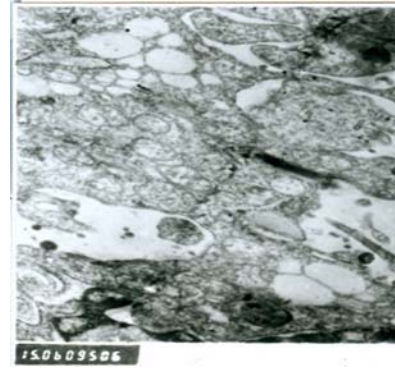


Fig. 3 Weibel-Palade body found in the cytoplasm of some induced cells

changes from long fusiform-shaped to short fusiform or flat shape, which was consistent with the significant characteristic of endothelium cells. The expression of CD34, VIII factor were positive in the induced cells, which were negative in the control group.

The Weibel-Palade body could be found in the cytoplasm of some induced cells by the transmission electron microscope.

IV. DISCUSSION

Mesenchymal stem cells (MSCs) are pluripotent precursor cells that localize to the stromal compartment of the bone marrow, where they support hematopoiesis and differentiate into mesenchymal lineages. The potential of MSCs to form bone, cartilage, and adipose tissues both in vivo and in vitro has been well documented. Their plasticity, however, is not limited to those mesenchymal derivatives. Recent reports have suggested that MSCs can differentiate into neurons, myoblasts, and cardiomyocytes. Because of the ability of MSCs to proliferate extensively ex vivo while maintaining their pluripotent differentiation capabilities (in vivo and in vitro), they are regarded as a particularly attractive seed cell for cell-based therapies in humans. These cells have a high expansion potential, genetic stability, can be easily collected and shipped from the laboratory to the bedside and are compatible with different delivery methods and formulations. In addition, MSCs have one extraordinary characteristics: they have strong immunosuppressive properties that can be exploited for successful autologous as well as heterologous transplantations.

At the present time at least three explanations exist for the differentiation of MSCs into endothelial-like cell. First, MSCs were pluripotent cells rooted in early phase mesoderm and ectoderm, Theoretically they can differentiate into all lineages come from mesoderm and ectoderm, endothe-

lial cell is belong to mesoderm, so there is possibility that MSCs differentiation into endothelial cells. Second, MSCs are pluripotent precursor cells that localize to the stromal compartment of the bone marrow, where they support hematopoiesis and differentiate into mesenchymal lineages. Although they belong to stromal system, MSCs show expression of endothelial-specific phenotype characteristic which is closely related to differentiation and development of endothelial cell. Third, Recent reports have suggested that MSCs cultured and differentiated in vitro express the same gene, surface molecule and phenotype characteristic. Serial analysis of gene expression (SAGE) revealed that single cell-derived colonies of MSCs expressed mRNAs of multiple cell lineages, including characteristic endothelial molecules like Epican and Keratins8 and 10^[1]. These data suggest that the in vitro differentiation potential of MSCs is not restricted to lineages but also transdifferentiation of MSCs into other lineages like endothelial. In addition, a few vWF expression—a typical endothelial cell markers is discovered in MSCs. And the surface adhesion molecules such as VCAM-1, HCAM, integrin are involved in angiogenesis. These data illustrate the possibility of that MSCs differentiation into endothelial cells.

The induce conditions is the critical point for MSCs differentiating into endothelial cells. In vivo differentiation of stem cells is regulated by some structural protein and polypeptide factor. In vitro the mechanism about differentiation is still not clear. Bin F^[2] constructed tissue-engineered homograft bioprosthetic heart valves in vitro by inducing MSCs into mature endothelial cells by VEGF. Oswald J^[3] showed the differentiation of expanded adult human MSCs into cells with phenotypic and functional features of endothelial cells. In our study we induced MSCs in the presence of VEGF and bFGF and observed the feasibility of MSCs differentiating into endothelial cells. Some cells induced by VEGF and bFGF showed the morphological changes from long fusiform-shaped to short fusiform or flat shape, the expression of CD34, VIII factor were positive in the induced cells which was consistent with the significant characteristic of endothelium cells. By transmission electron microscope the Weibel-Palade body could be found in the cytoplasm of some induced cells.

VEGF plays a fundamental role in the growth and differentiation of vascular as well as lymphatic endothelial cells. The Flt-1 (*fms*-like tyrosine kinase) and KDR (kinase domain region) receptors bind VEGF with high affinity. Flt-1 has the highest affinity for recombinant human VEGF and is a positive modulator of vascular sprout formation and branching morphogenesis. In the present researches show that Flt-1 modulates the Flk-1 signal at early point in the pathway^[4-8]. bFGF is a member of a family of growth factors with a complex network of receptors. The predominant-

signaling cascade(s) activated by a particular FGF depend on the cell type and its receptor expression, as well as its immediate environment and stage of development. This complexity accounts for the diverse outcomes of FGF signaling on cell division and migration, affecting developmental processes, angiogenesis, wound healing^[9], and bFGF is related to the chemoattractant of some cells. By change the chemotactic of cells, bFGF induces or inhibits cells synthesizing or secreting special proteins thus regulate internal secretion or nerve function^[10,11]. Mayer H^[12] deduced that VEGF induce MSCs differentiating into endothelial cells by self-secretion or by-secretion. Okuyama H^[13] implicated MSCs autocrine VEGF signaling through VEGF receptor 1 (VEGFR1) promotes cell survival under hypoxic conditions. In the process of vasculogenesis microenvironment may promote recruitment of MSC by increasing expression of VEGFR1 and may also stimulate angiogenesis in ischemic tissue by increasing expression of VEGF. And being a hormonal pleio-peptide bFGF could cooperate with VEGF to promote the clone formation and proliferation^[14-16]. Further studies are needed to carry out to define the mechanism of MSCs differentiating into endothelial cells.

ACKNOWLEDGMENT

This work was supported by the Great Invited Tenders Foundation of Jiangxi Science and Technology Bureau (200604), the Great Invited Tenders Foundation of Jiangxi Health Bureau (200502), the Natural Science Foundation of Jiangxi (0540056), and the Science Research Foundation of Jiangxi Science and Technology Bureau (2006).

REFERENCES

1. Tremain N, Korkko J, Ibberson D, et al. MicroSAGE analysis of 2,353 expressed genes in a single cell-derived colony of undifferentiated human mesenchymal stem cells reveals mRNAs of multiple cell lineages. *Stem Cells*, 2001, 19(5): 408-418
2. Bin F, Yinglong L, Nin X, et al. Construction of tissue-engineered homograft bioprosthetic heart valves in vitro. *ASAIOJ*, 2006, 52(3): 303-309
3. Oswald J, Boxberger S, Jorgensen B. Mesenchymal stem cells can be differentiated into endothelial cells in vitro. *Stem Cells*, 2004, 22: 377-384
4. Roberts DM, Kearney JB, Johnson JH, et al. The vascular endothelial growth factor (VEGF) receptor Flt-1 (VEGFR-1) modulates Flk-1 (VEGFR-2) signaling during blood vessel formation. *Am J Pathol*, 2004, 164(5): 1531-1535
5. Kearney JB, Kappas NC, Ellerstrom C, et al. The VEGF receptor flt-1 (VEGFR-1) is a positive modulator of vascular sprout formation and branching morphogenesis. *Blood*, 2004, 103(12): 4527-4535

6. Wang M, Crisostomo PR, Herring C, et al. Human progenitor cells from bone marrow or adipose tissue produce VEGF, HGF, and IGF-I in response to TNF by a p38 MAPK-dependent mechanism. *Am J Physiol Regul Integr Comp Physiol*, 2006,291(4):R880-884
7. Zeng Q, Li X, Beck G, et al. Growth and differentiation factor-5 (GDF-5) stimulates osteogenic differentiation and increases vascular endothelial growth factor (VEGF) levels in fat-derived stromal cells in vitro. *Bone*.2007,40(2):374-381
8. Crisostomo PR, Wang M, Herring CM, et al. Gender differences in injury induced mesenchymal stem cell apoptosis and VEGF, TNF, IL-6 expression: Role of the 55 kDa TNF receptor (TNFR1). *J Mol Cell Cardiol*. 2007,42(1):142-149
9. Kim S, Honmou O, Kato K, et al. Neural differentiation potential of peripheral blood- and bone-marrow-derived precursor cells. *Brain Res*,2006,1123(1):27-33
10. Schmidt A, Ladage D, Schinkothe T, et al. Basic fibroblast growth factor controls migration in human mesenchymal stem cells. *Stem Cells*,2006,24(7):1750-1758
11. Ong SY, Dai H, Leong KW. Inducing hepatic differentiation of human mesenchymal stem cells in pellet culture. *Biomaterials*,2006,27(22):4087-4097
12. Mayer H, Bertram H, Lindenmaier W, et al. Vascular endothelial growth factor (VEGF-A) expression in human mesenchymal stem cells: autocrine and paracrine role on osteoblastic and endothelial differentiation. *J Cell Biochem*,2005, 95(4):827-839
13. Okuyama H, Krishnamachary B, Zhou YF, et al. Expression of vascular endothelial growth factor receptor 1 in bone marrow-derived mesenchymal cells is dependent on hypoxia-inducible factor. *J Biol Chem*,2006,281(22):15554-15563
14. Hideshima T, Podar K, Chauhan D, et al. Cytokines and signal transduction. *Best Pract Res Clin Haematol*, 2005,18(4):509-524
15. Jiang W, Ma A, Wang T, et al. Intravenous transplantation of mesenchymal stem cells improves cardiac performance after acute myocardial ischemia in female rats. *Transpl Int*,2006,19(7):570-580
16. Miyahara Y, Nagaya N, Kataoka M, et al. Monolayered mesenchymal stem cells repair scarred myocardium after myocardial infarction. *Nat Med*,2006,12(4):459-465

Correspondence to: Dewu Liu
E-mail: dewuliu@126.com

Effect of microstructure on the mechanical properties and biology performance of bone tissue scaffolds using selective laser sintering

Liulan Lin¹, Jiafeng Zhang¹, Li Zhao², Aili Tong¹, Jian Sun² and Qingxi Hu¹

¹Rapid Manufacturing Engineering Center, Shanghai University, Shanghai 200444, China

²Shanghai Tissue Engineering Research and Development Center, Shanghai, 200233, China

Abstract — Porous β -tricalcium phosphate (β -TCP) ceramic scaffolds with axially oriented macropore and random micropore were produced by selective laser sintering (SLS) process. Microstructure parameters including pore size, pore size distribution and interconnectivity were quantified by microcomputed tomography. Compressive mechanical properties were tested. The porosity of sintered scaffolds was over 60%. The range of average compressive modulus and ultimate strength was 24.38–30.64MPa and 1.64–2.35MPa, respectively. Dog bone marrow stromal cells (BMSCs) were seeded in the prepared scaffolds. Cell proliferation and osteogenic differentiation on the scaffolds were evaluated with the alkaline phosphatase (ALP) activity and osteocalcin (OCN) content.

Keywords — Bone tissue engineering; β -tricalcium phosphate; Selective laser sintering; Porous scaffold.

I. INTRODUCTION

Tissue engineering offers a promising new approach to restore and reconstruct the function of impaired tissues. There are three key ingredients in tissue engineering: harvested cells, recombinant signaling molecules, and three-dimensional (3D) scaffold^[1-3]. Biodegradable scaffolds play an important role in tissue engineering by supplying a 3D substrate for cell attachment, proliferation, and guidance of new bone tissue formation. In bone tissue engineering view, the necessary characteristics of an ideal scaffold may be summarized as the following^[4]: (1)Have appropriate surface to favor cellular attachment, differentiation and proliferation; (2)Degradation property : biocompatible and biore-sorbable with a controllable degradation rate to match tissue growth with no undesirable byproducts, so that tissue will eventually replace the scaffold; (3)Possess adequate mechanical properties to temporarily withstand functional loading in vivo or cell traction forces in vitro; (4)Be easily fabricated into a variety of shapes and sizes; (5)Acts as template for tissue growth in three dimensions;(6)Possess interconnecting porosity so as to favor tissue integration and vascularisation.

In this study, porous β -tricalcium phosphate (β -TCP) ceramic scaffolds with axially oriented macropore and random micropore were produced by selective laser sintering (SLS)

process, one of rapid prototyping (RP) techniques. These porous scaffolds were characterized for their use as bone grafts in terms of mechanical and biological properties.

II. MATERIALS AND METHODS

A. Preparation of β -TCP/binder mixture

Mixtures of β -TCP and binder powders were produced by physically blending with a mixing roller (4 Tank Mixer, MTI Corporation) with 3 hours.

B. Porous scaffold design and fabrication

Cylindrical porous scaffolds ($\Phi 20 \times 10$ mm) were designed with UG NX4 (UGS PLM Solution), as showed Fig.1A. The file was converted into STL format before it was exported to a sinterstation machine (HPRS-III A, BinHu Co., Wuhan, China). Scaffolds were fabricated layer by layer with powder layer thickness 0.1mm (Fig.1B). Then the excess powder surrounding the scaffolds was brushed off. Finally, the green parts were calcined with high temperature forming bone tissue engineering scaffolds (Fig.1C).

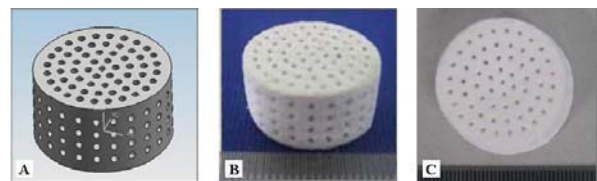


Fig. 1 Scaffold pictures (A) 3D solid modeling, (B) scaffold after laser sintered, (C) scaffold after calcined

C. Porosity analysis

The Archimedes method was used to analyze the porosity of scaffold. The measured values were used to calculate the porosity value with Equation (1):

$$\text{Porosity} = (M_{\text{wet}} - M_{\text{dry}}) / (M_{\text{wet}} - M_{\text{sub}}) \quad (1)$$

Where M_{wet} was the wet mass, M_{dry} was the dry mass and M_{sub} was the submerged mass.

D. Mechanical property assessment

The mechanical properties of the scaffold specimens were measured with an Instron Uniaxial Testing System (Instron 5542, UK). Load and displacement was noted and converted to stress and stain, from which the slope was used to calculate elastic modulus.

E. Micro CT analysis

μ CT-40 (Scanco Medical, Switzerland) was used to analyze microstructure characterization and the pore size distribution of β -TCP scaffold. The μ CT data can be used to define the best processing parameters.

F. Cell culture in vitro

Prior to seeding, scaffolds were incubated in complete culture medium overnight at 37°C. Dog bone marrow stromal cells (BMSCs) with a density of 7×10^4 cells/ml were seeded onto the scaffolds, and incubated for 12 days. Media was changed every 3~4 days. Following seeding, scaffolds were fixed and subsequently dehydrated in graded ethanol concentrations (25%, 50%, 75%, 90%, 95% and 100% v/v in dH₂O), followed by chemical drying with hexamethyldisilazane (HMDS). Cell proliferation and osteogenic differentiation on the scaffolds were evaluated with the alkaline phosphatase (ALP) activity and osteocalcin (OCN) content. To check the cell morphology on the scaffold, samples were taken for SEM (JEOL JSM- 6700F).

III. RESULTS

A. Microstructure analysis

The macro and micro pores were discussed by the diameter of design hole and the binder powder. Fig.2 showed the pore size distribution of scaffold assessed by the Micro-CT.

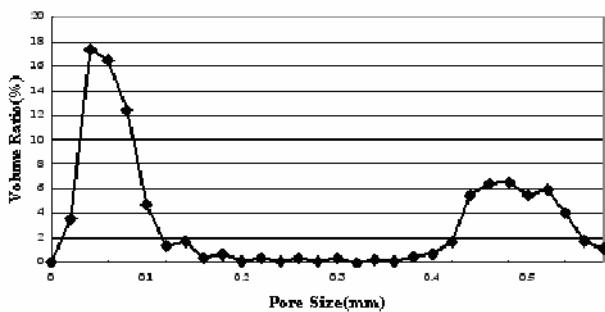


Fig. 2 Pore distribute and volume ratio of calcined β -TCP scaffold.

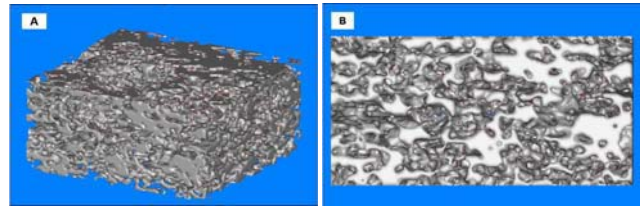


Fig. 3 Micro CT images (A) scaffold reconstructed model, (B) scaffold cross section

The design holes ($D=800\mu\text{m}$) were shrunk to the latter range ($400\sim 560\mu\text{m}$) and the distribution range of micropore became to be $20\sim 100\mu\text{m}$ because the scaffold shrunk and distorted in the high temperature calcination processing.

Fig.3A showed the 3D reconstructed model of sintered scaffold. Fig.3B showed the pore in the scaffold cross section. These pores were highly open and well-interconnected. It was that the binders were burned off and created micropores in calcination processing.

B. Porosity analysis

Table 1 presented the porosity of the scaffolds, which was measured as described in Equation (1). The table showed that the porosity ranged from 73.24% to 74.95%. The porosity of 60% or above was suitable for the bone regeneration [9]. It means that the sintered scaffolds had enough porosity.

Table 1 Porosity of the scaffolds

Specimen number	Porosity (%)
1	73.24
2	73.86
3	74.0
4	74.54
5	74.95

C. Experimental mechanical property assessment

Fig.4 A showed the stress strain curve from compression testing. The Young's modulus of samples respectively is 15.38MPa, 28.57MPa and 48.7MPa with different porosity. The porosity and strength behaviors of the porous β -TCP scaffold with pore volume fraction 60.7%, 70.8% and 75.8% were illustrated in Fig.4B. The compressive strength of the porous β -TCP ceramic appeared to be sensitive to the pore volume, and the difference in the porosity and strength behaviors became pronounce as the porosity volume decreased.

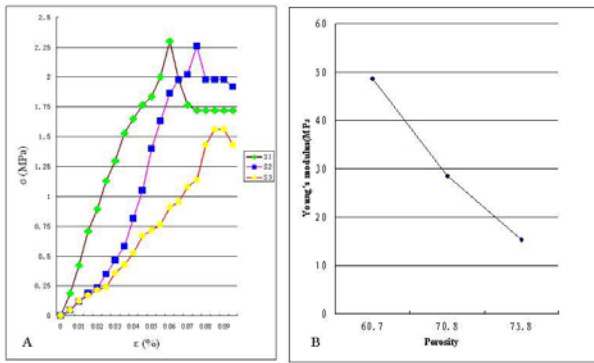


Fig.4 Mechanical property to porosity curves (A) Stress-strain curves (porosity of S1, S2 and S3 were 60.7%, 70.8% and 75.8%), (B)Young's modulus curve

D. Cell culture

Fig. 5 showed the number of cells after 1, 4, 7 and 14 day cultured on β-TCP ceramic scaffolds. At the early time point (1, 4 and 7d), the number of cells had no obvious change in these cultivable time nodes. By 14d, cell number on β-TCP ceramic scaffolds was fast growing to 5 times of the early time point.

Fig. 6 showed the SEM micrographs of cells after 4, 7 and 14d cultured on β-TCP ceramic scaffolds. Fig. 6A and B showed the high cellular density on the surface of the β-TCP porous layer, which indicated that cells adhered favorably. Fig. 6C and Fig. 6D showed that cells did not obstruct the macropores of the scaffold at the surface. Fig. 6F showed that cell spread actively and well distribute in the β-TCP porous scaffolds. Fig. 6E also indicated that cells were able to penetrate deeper into the scaffold.

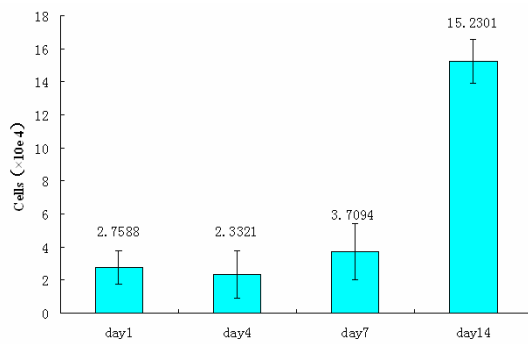


Fig.5 Cell proliferation at 1, 4, 7 and 14d

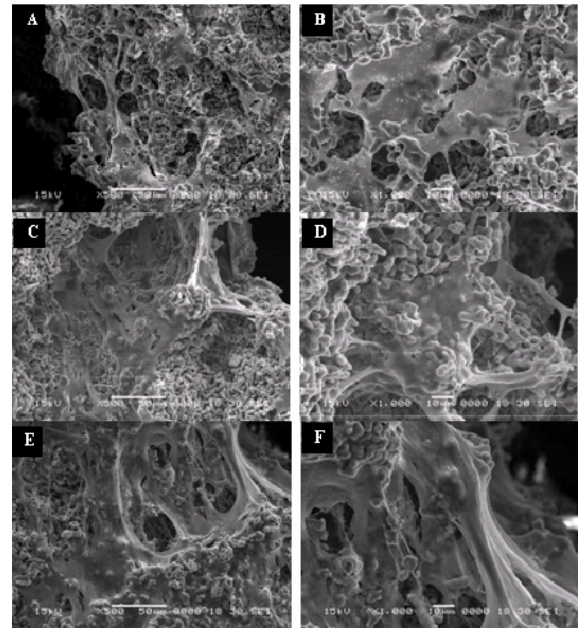


Fig. 6 SEM images of cells after 4, 7 and 14d cultured (A, B) cell proliferation at day 4(500×, 1000×), (C, D) cell proliferation at day 7(500×, 1000×), (E, F) cell proliferation at day 14 (500×, 1000×)

The phenotypic expression of cells cultured on scaffolds was evaluated by monitoring ALP activity of the cells. Fig. 7 showed the ALP activity of BMSCs cells after 4, 7 and 14d cultured on β-TCP scaffolds. At early time point the activity of ALP continued to rise while activity achieved a peak value at 7d. Then it decreased gradually. Fig. 8 showed the expression of the OCN on β-TCP ceramic at 4, 7 and 14d. The value of OCN increased gradually in cultivable time nodes.

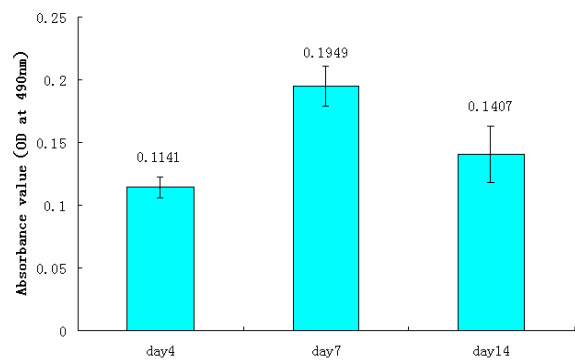


Fig. 7 ALP activity of BMSCs cells after 4, 7 and 14d cultured

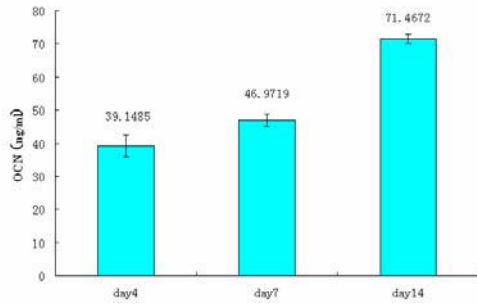


Fig. 8 OCN activity of BMSCs cells after 4, 7 and 14d cultured

IV. CONCLUSIONS

The research showed β -TCP ceramics porosity increased with compressive strength decreased and found a suitable range of β -TCP ceramic scaffolds porosity. In vitro cell culture study demonstrated that β -TCP scaffolds provide an adequate 3D support for the attachment, proliferation and differentiation of BMSCs into osteoblasts medium. This study confirmed that the scaffolds fabricated with SLS processing were suitable for the bone regeneration. However, there is still a lot of work worthy of in-depth study, especially, implantation experiment should be done to observe scaffold biodegradation in vivo and the enhancement of the mechanical properties for the bearing bone repair.

ACKNOWLEDGMENT

The authors would like to acknowledge Shanghai Academic Excellent Youth Instructor Special Fund (No 17014) and Post Doctor Science Fund of China (No.20070410715).

REFERENCES

1. Patrick Jr CW, Mikos AG, Mcintire LV. (1998) *Frontiers in tissue engineering*. Oxford, UK and New York: Pergamon
2. Vacanti JP, Vacanti CA. (2000) *The history and scope of tissue engineering*, in *principles of tissue engineering*. Academic Press, New York
3. S.-S. Kim et al. (2006) Poly (lactide-co-glycolide)/hydroxyapatite composite scaffolds for bone tissue engineering. *Biomaterials* 27 :1399–1409
4. Hutmacher DW. (2001) Scaffold design and fabrication technologies for engineering tissues: state of the art and future perspectives. *J Biomater Sci Polym Ed* 21:107–24
5. F.E.Wiria, K.F.Leong, C.K.Chua et al. (2007) Poly- ϵ -caprolactone/hydroxyapatite for tissue engineering scaffold fabrication via selective laser sintering *Acta Biomaterialia* 3:1–12
6. Saey Tuan Ho, DW. Hutmacher. (2006) A comparison of micro CT with other techniques used in the characterization of scaffolds. *Biomaterials* 27: 1362–1376
7. Ho Saey Tuan, Dietmar W. Hutmacher. (2005) Application of micro CT and computation modeling in bone tissue engineering. *Computer-Aided Design* 37:1151–1161
8. C.K.CHUA, K.F.LEONG, K.H.TAN et al. (2004) Development of tissue scaffolds using selective laser sintering of polyvinyl alcohol/hydroxyapatite biocomposite for craniofacial and joint defects. *Materials in Medicine* 15:1113-1121
9. Chen Zhongzhong, Li Dichen, Lu Bingheng et al. (2005) Fabrication of osteo-structure analogous scaffolds via fused deposition modeling. *Scripta Materialia*, 52: 157–161
10. Joseph R. Woodard, Amanda J. Hilldore, Sheeny K. Lan. (2007) The mechanical properties and osteoconductivity of hydroxyapatite bone scaffolds with multi-scale porosity. *Biomaterials* 28:45–54

Author: Liulan Lin

Institute: Rapid Manufacturing Engineering Center, Shanghai University

Street: 99 Shangda Rd

City: Shanghai

Country: China

Email: linliulan@staff.shu.edu.cn

Fabrication of porous β -TCP scaffolds by combination of rapid prototyping and freeze drying technology

Liulan Lin¹, Shaohua Ju¹, Lian Cen², Huicun Zhang¹, Qingxi Hu¹

¹Rapid Manufacturing Engineering Center, Shanghai University, China

²Shanghai Tissue Engineering Research and Development Center, China

Abstract — The scaffold with exact shape and polygradient inner structure was necessary for bone tissue engineering scaffolds to facilitate cells infiltration and proliferation. A novel method of designing and preparing bone tissue engineering scaffolds with polygradient controllable structure of both macro and micro pores was proposed in this paper. By integrating rapid prototyping and freeze drying technology, the macro and micro pores were formed respectively. The size, shape and quantity of micropores were controlled by slurry concentration. The sintered β -TCP porous scaffolds were with connective macropores of approximately 400 μ m and micropores of 50~300 μ m. The chemical composition, porosity and mechanical properties of scaffolds were measured and analyzed. The detected results indicated that the β -TCP scaffolds could fulfill the requirements of tissue engineering.

Keywords — scaffolds; Tissue engineering; FDM; Freeze drying; β -TCP

I. INTRODUCTION

In tissue engineering, temporary 3D bionic scaffolds are essential to guide cell proliferation and maintain native phenotypes in regenerating biologic tissues or organs^[1]. The shape and inner microstructure are the two critical properties of bionic scaffolds for repairing defective bone. To satisfy tissue engineering's requirement, bionic bone scaffolds must have exact shape with the defects, polygradient porous configuration with characteristics and properties such as porosity, surface area to volume ratio, pore size, pore interconnectivity, shape, structural strength and biocompatibility. These characteristics and properties are often considered to be critical factors in their designing and fabrication^[2].

Traditional methods of scaffold fabrication are mainly based on manual work and lack of corresponding designing process^[3-4], so extra procedure was needed to obtain suitable shape and the microstructure wasn't able to be controlled well. To overcome the limitations of conventional techniques, rapid prototyping fabrication techniques are being explored. Using RP technologies in bionic scaffolds preparation^[5-6] could fully performs the significance of designing and improves the bionic scaffolds' properties.

However, it's difficult to obtain and control the micropores because of the limited manufacturing accuracy of RP technologies.

In this study, medical images processing software Mimics, 3D CAD modeling software UG NX3.0 were used in the scaffolds reconstruction and design. Bone tissue engineering scaffolds with β -TCP bioceramic as the material were prepared through the integrated method based on fused deposition modeling (FDM) and freeze drying technology. A group of scaffolds with cylinder shape were prepared and the chemical composition, microstructure, porosity and mechanical properties of these scaffolds were measured and analyzed.

II. MATERIALS AND METHODS

A. CAD model construction

The patient's CT data of defective skull were imported into Mimics 9.11 (The Materialise Group, Leuven, Belgium) and the 3D STL model of the skull was created through image processing and 3D reconstruction technologies. Then the restoration's 3D STL model of defect was constructed by the symmetrically repairing operation in Mimics, as shown in Fig. 1.

The models of negative mould with strut were designed in 3D CAD software UG NX 3.0(UGS PLM Solutions, USA). As shown in Fig. 2, the 3D connective channels with diameter of 0.8mm and distance of 2.5mm between adjacent channels, the X-axis pores and Y-axis pores were not in the same horizontal plane, and the strut of negative mould with the equal sizes.

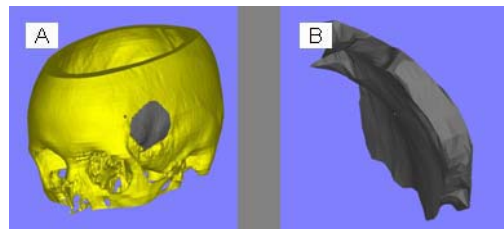


Fig. 1 Defective skull repairing (A) skull model,, (B) restoration model

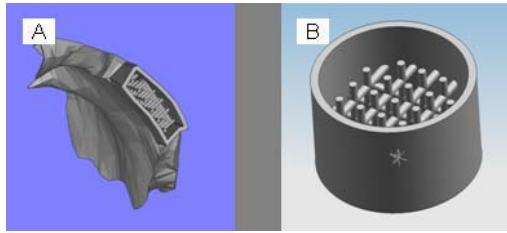


Fig. 2 Scaffold models designed (A) negative model with channel, (B) cylinder negative mould with strut

B. Preparation of the scaffolds

The bioceramic slurry used in this work was prepared by mixing distilled water with β -TCP particulate (provided by Shanghai Tissue Engineering Center), a small amount of high-temperature binder and dispersant. The slurry was ball-milled for 12h to be homogeneous. Three kinds of slurries were prepared respectively with the β -TCP ratio was 40.0%, 50.0% and 60.0% by weight.

The negative moulds of scaffolds were fabricated through FDM (Stratasys Corp. USA), and the cylinder negative moulds were fabricated through SLA (Shanghai Union Ltd. China), as shown in Fig. 3.

There were three steps included by the whole preparation process: filling slurry into the mould, freeze drying and high temperature treatment. After filled with the slurry, the moulds were put in vacuum environment for 10 minutes to remove the gas that was interfused when filling slurry into the mould.

Freeze drying was to make the water of the slurry sublimate^[7] while the slurry was kept at solid state. The moulds filled with slurry were kept at -75°C in a refrigeratory for 3 hours in order to freeze the slurry. Then the moulds were kept in a freeze drier (Anke FDC 5506, Anke Corp. China) for 24 hours. The micropores were formed by the sublimation of ice.

The negative moulds were put into an experimental stove (SX2-1013, Zufa Ltd., China) and the β -TCP ceramic was

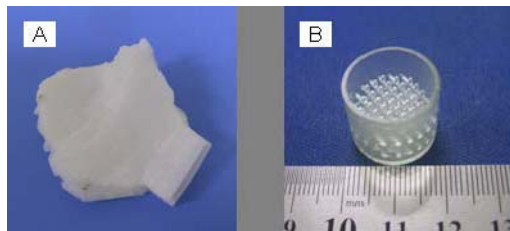


Fig. 3 Scaffolds fabricated (A) ABS part fabricated by FDM, (B) resin part fabricated by SLA

sintered. Below 550°C , the heating rate should be slow to make thermal decomposition of the ABS moulds as smoothly as possible. Above 550°C , a moderate heating with $100^{\circ}\text{C}/\text{h}$ was adopted and kept at 1100°C for 3 hours to sinter β -TCP ceramic thoroughly and avoid grow into coarse grain.

C. Characterization of β -TCP scaffolds

Four groups of porous β -TCP scaffolds were prepared through the process based on rapid prototyping and freeze drying technology. The chemical composition, microstructure, porosity and mechanical properties of scaffolds were measured and analyzed.

• Chemical composition

Samples were analyzed using a Rigaku diffractometer with using $\text{CuK}\alpha$ radiation at $40\text{kV}/200\text{mA}$. Scan was performed with 2θ values from 10deg to 90deg at a rate of $4.8\text{deg}/\text{min}$.

• Microstructure

Microstructural characterization of the scaffolds were carried out with a scanning electron microscope (SEM, JEOL JSM-6700F) to observe the surface morphology and microstructure characterization of the scaffolds after high temperature treatment specimens.

• Porosity measurement

The Archimedes method was used to assess the porosity of the β -TCP scaffolds. Measured values were used to calculate the porosity value with Equation (1):

$$\text{Porosity} = (M_{\text{wet}} - M_{\text{dry}}) / (M_{\text{wet}} - M_{\text{sub}}) \quad (1)$$

Where M_{wet} was the wet mass, M_{dry} was the dry mass and M_{sub} was the submerged mass.

• Mechanical properties

The compressive properties of the β -TCP scaffolds were evaluated using a Zwick BZ2.5/TS1S material testing machine (Zwick/Roell Co. Germany) with speed $0.5\text{ mm}/\text{min}$.

III. RESULTS

A. General features

The porous β -TCP scaffolds with both macropores and micropores were prepared using slurries with β -TCP ratio 40.0wt%. The sintered scaffolds were with diameter of 9.1mm and height of 11.2mm . The horizontal linear

shrinkage was about 7.1% and the vertical linear shrinkage 6.7%, corresponding to a volumetric decrease in by 19.5%. Scaffolds formed the exact shape and polygradient porous configuration with designed, as shown in Fig. 4.

B. Chemical composition

Fig. 5 showed the XRD comparison of the high temperature treatment specimens and the β -TCP standard pattern. There were six highest peaks occurred at 2θ angle of 26.20° , 28.04° , 30.92° , 34.47° , 48.37° , and 53.21° , and these peaks matched with pure β -tricalcium phosphate's.

C. morphology

The micro-morphology of β -TCP scaffolds with macro channels was observed with SEM, as shown in Fig. 6. The sizes of micropores were between $50\mu\text{m}$ and $300\mu\text{m}$. The morphology of micropores was almost crack and the ceramic is lamellar, with long parallel pores aligned in the movement direction of ice front.

D. Influence of slurry concentration

- Porosity

In order to evaluate the effect of slurry concentration on the porosity obtained, the porosity of the samples with different slurry concentration were assessed. The relationship between the final porosity and the initial slurry concentration was linear, provided sintering conditions was constant, as shown in Fig. 7. To these sintered β -TCP scaffolds, the porosity caused by macropores was the same as the designed model by UG NX. The porosity caused by micropores was determined by the concentration of slurry used to prepare the scaffolds.

- Compressive strength tests

The compressive strength of the samples with different slurry concentration were tested. The compressive strength of the three kinds of scaffolds was 1.13Mpa, 0.66MPa and 0.31MPa with β -TCP ratio of 40wt%, 50wt% and 60wt%. As water ratio increasing, the compressive strength of scaffolds became lower. The porosity of scaffolds was higher and micropores connectivity was better with β -TCP ratio decreasing, that the scaffolds' mechanical properties were weakened.

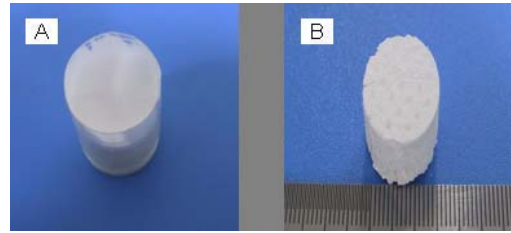


Fig. 4 Scaffold samples (A) before sintered, (B) after sintered

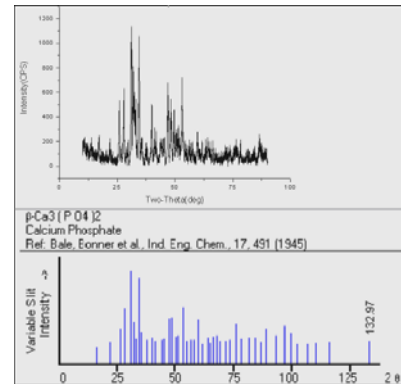


Fig. 5 The XRD spectrum compared specimens with pure β -TCP

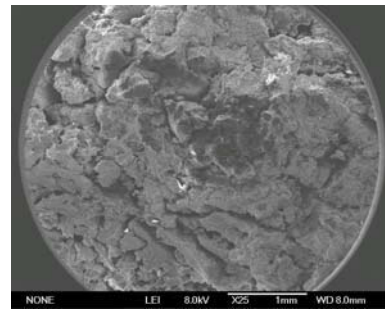


Fig. 6 SEM micrographs of β -TCP scaffolds ($\times 25$)

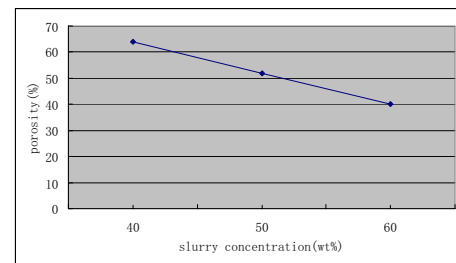


Fig. 7 Porosity of sintered scaffolds vs. slurry concentration.

IV. CONCLUSIONS

A novel method of designing and preparing bone tissue engineering scaffolds with complex shape and controllable structure of macro and micro pores was proposed in this paper. The integration of medical image processing system and RP technologies prove highly useful for design and fabrication of complex bone defects. The application of CT and the medical image processing system make the CAD model of bone defects flexibly and accurately.

A strategy of designing scaffolds of polygradient controllable interior structure with both macro and micro pores was proposed. By integrating RP and freeze drying technology, β -TCP scaffolds of polygradient interior structure with both macro and micro pores were prepared. The micropores were formed by freeze drying. Freeze drying was to make the ice of the slurry sublimate in low temperature and pressure environment while the slurry was kept at solid state. The microstructure obtained was a replica of entangled dendrites of ice crystals. The diameter, shape and interconnectivity of the pores were regulated by the control of ice crystal growth. The relationship between the final porosity and the initial slurry concentration could be used for microstructure controlling. Next step research, the cell culture experiments will be studied to test the biology performance of scaffolds.

ACKNOWLEDGEMENTS

The authors would like to acknowledge Academic Excellent Youth Instructor Special Fund. of Shanghai (No. 17014) and Post Doctor Science Fund of China (No.20070410715).

REFERENCES

1. K.H. Tan, C.K. Chua, K.F. Leong, C.M. Cheah. (2005) Scaffold development using selective laser sintering polyetheretherketone-hydroxyapatite biocomposite blends. *Biomaterials* 26: 4281-4289
2. SF Yang, KF Leong, ZH Du, CK Chua. (2001) The design of scaffolds for use in tissue engineering: Part 1-Traditional factors. *Tissue Engineering* 7(6): 679-690
3. Wu Linbo, Ding Jiandong. (2005) Compression Molding of PCL Porous Scaffolds with complicated shape for Tissue Engineering, *Polymer Material Science and Engineering Vol.25 No.1*: 296-299
4. A. Woesz, M. Rumpler, J. Stampfl, F. Varga. (2005) Towards bone replacement materials from calcium phosphates via rapid prototyping and ceramic gelcasting, *Materials Science and Engineering C* 25: 181-186
5. Li Xiang, Li Dichen, Su Yanping, lu Bingheng, (2005) Structure Design and Fabrication of B-tricalcium Phosphate Artificial Bone Based on Rapid Prototyping Technique, *Journal of Xi'an Jiantong University Vol.39 No.1*: 13-16
6. Shi Pujiang, Li Yubao, Zhang Li. (2006) Fabrication and characterization of n-HA/CS porous scaffold containing ALG/CS microspheres, *Journal of Functional Materials Vol.37*: 1798-1800
7. Sylvain Deville, Eduardo Saiz, Antoni P. Tomsia.(2006) Freeze casting of hydroxyapatite scaffolds for bone tissue engineering, *Biomaterials* 27: 5480-5489

Author: Liulan Lin
Institute: Rapid Manufacturing Engineering Center
Street: 99 Shangda Rd
City: Shanghai
Country: China
Email: linliulan@staff.shu.edu.cn

The property of ion current in human amniotic mesenchymal stem cell (hAMSC)

Bo-jiang Liu, Xue Lin, Lian-feng Chen, Quan Fang

Chinese Academy of Medical Sciences & Peking Union Medical College. Department of Cardiology, Peking Union Medical College Hospital, 100730 China

Abstract — The study is to determine the distribution of ion channel and property of ion current in human amniotic mesenchymal stem cell (hAMSC). The amniotic membrane was gathered from the healthy and mature newborn after delivery. The hAMSCs were isolated and cultured in DMEM with 10% FBS for 2 weeks. The mRNA of hAMSC was collected after 2 week, and the Reverse transcriptase-polymerase chain reaction (RT-PCR) were then performed to detect the mRNA expression of ion channel. The ion current of hAMSC were recorded under the whole cell mode with patch clamp. Most of the hAMSCs (76/82) cells showed outward current during the patch clamp test. The membranes potential of the hAMSC is $-3.89 \pm 7.14 \text{ mV}$ ($-25 \sim -13.9 \text{ mV}$), the membranes capacity offset is 300.06 ± 189.81 ($0 \sim 780 \text{ pF}$). There were 3 types of outward current presented in the hAMSC, including the delayed rectifier potassium current (IkDR), Calcium-activated-potassium current (IkCa) and transient outward current (Ito). The current of IkDR can present in most hAMSCs (93.4%), and half of the cells show a slow activating delayed rectifier K current (Iks). The noisy oscillation like IkCa current was observed in 35.5% hAMSCs, and Ito present in 14.5% hAMSCs. The inward currents such as sodium currents, calcium currents, inward rectifier K current (Ik1) and funny current (If) were absent in our study. The expression of mRNA of certain ion channel subunit of MaxIK (for IkCa), Kir2.1, Kv1.4 (for Ito), HminK (for IkDR) can be detected. This is the first study of the electrophysiology property in hAMSCs. The hAMSC can express a distinct pattern of ion channel mRNA and functional ion channels. The ion current of IkDR, IkCa and Ito can present in the hAMSCs.

Keyword — human amniotic mesenchymal stem cell, ion channel, patch clamp

I. INTRODUCTION

The amnion is a tissue of fetal origin and is composed of epithelial cells on a thicker basement membrane containing collagen and layers of spongy tissues containing cells of the mesenchymal lineage. The amniotic membrane contain a high number of mesenchymal stem cells with bi-potential osteogenic and adipogenic differentiation [1]. Recently, Zhao [2] reported the human amniotic mesenchymal cells (hAMC) possess some characteristics of cardiomyocytes. The high-yield of stem cell makes amniotic membrane a truly exciting alternative source for cell therapy [3]. Ion channels are extensively expressed in different types of

cells, and they have important roles in maintaining physiological homeostasis. However, expression of ion channels is not well documented in hAMSCs.

II. MATERIALS AND METHODS

A. Isolation and culture of hAMSC

Human amnions from both sexes were collected with informed consent of the mothers and prove of Peking Union Medical College Hospital ethnic committee. The amnions were minced and digested with 0.25% trypsin-EDTA (Invitrogen) three times 10 mins each time, and then the supernatant fluid were disposed. The remaining mixture would further digested by 1% collagenase (Roche company), after that, the cells were triturated and passed through a 100 μm filter mesh, centrifuged and resuspended in DMEM supplemented with 20% fetal bovine serum, glutamine, penicillin in a 95% humidified, 5% CO_2 incubator at 37°C . After achieving 70-80% confluence, cell passages are initiated.

B. Reverse Transcription-Polymerase Chain Reaction

Total RNA was extracted from hAMSCs using trizol reagent according to the manufacture's introduction. The cDNA was synthesized using 1 μg of total RNA and in further RT-PCR reaction, 0.4 μg of cDNA were used. Expression of various cell markers were assessed using a one-Step RT-PCR kit (Takara) and gene specific primers. The primer sequence is:

HCN2(F:GCTGTCCGATGGCTCCTACTTC;R:TCTCCTGGATGATGGCGTTCT), **HCN4**(F:CGCCTCATTGCGATA TATTCAC;R:CGCGTAGGAGTACTGCTTC), **KIR2.1**(F:GACCTGGAGACGGACGAC;R:AGCCTGGAGTCTGTCAAAGTC), **MaxiK**(F:ACAACATCTCCCCCAACC;R:TCATCACCTTCTTTCCAATTC); **a-ACTIN**(F:CGCACCCTGGCATTGTGCAT;R:TTCTCCTTGATGTCACGCAC), **Kv1.4**(F:AACAGTCACATGCCTTAG;R:TAGTAAAACCTTCCCTCCTC), **Kv4.2**(F:CTTCAC TATCCCCGCCAT;R:GTTTCCACCACATTCGCG), **Kv4.3**(F:GAAGAGGAGCACATGGGC;R:GTGATCTGGGATGTTTGC), **HminK**(F:ACGCCCTTTCTGACCAAGC;R:ATCGGACTCGATGTAGACG), **Herg1**(F:TCGCCGTCCACT

ACTTCAA;R:AGAGCGCCGTCACATACTT),**HKvLQT1** (F:CCACCATTAAGGTCATTTCG;R:CCTTGTCTTCTAC TCGGTTCA),**SCN5A**(F:CCTAATCATCTTCCGCATCC; R:GGTTGTTTGCATCAGGGTCT) **α 1c**(F:TGAGACCGA GTCCGTCA AA;R:GAAAATCAGCAGCCAGTAGAAGA).F: Forward primer sequence(5'-3'),R: Reverse primer sequence (3'-5'). T, temperature; HCN2/4, hyperpolarization-activated cyclic nucleotide-gated cation channel2/4; Kir2.1, inward rectifiers K channel; MaxiK, human large-conductance, voltage and calcium activated K channel; Heag, human ether-à-go-go K channel; SCN5A, human cardiac tetrodotoxin-insensitive voltage-dependent Na⁺ channel, α -subunit; α 1c, human voltage-dependent L-type Ca²⁺ channel, alpha 1C subunit; Kv1.4-4.3, voltage-gated K channel subunits; HminK, human minK gene; HKvLQT1, human KvLQT1 gene; LQT1, long QT syndrome 1.

C. Electrophysiological Recordings

Electrophysiological recording was performed in the whole-cell configuration using a patch clamp amplifier (EPC-7, HEKA). All recordings were performed at room temperature. Acquired whole cell current data were analyzed with the pCLAMP program (version 10.0). The bath solution (Tyrode's solution) of patch clamp study contained (mmol/L) : NaCl 140; KCl 5.4; MgCl₂ 1.0; HEPES 5.0; Glucose 10.0; CaCl₂ 1.8; the pH was adjusted to 7.35 with NaOH. The pipette solution contained (mmol/L) K-aspartate 120; KCl 20; KH₂PO₄ 5; HEPES 10; MgCl₂ 1; EGTA 0.05; Na₂ATP 5; GTP 0.1; the pH was adjusted to 7.20 with KOH.

III. RESULT

A. The ion current distribution in hAMSCs

The ion current of hAMSC were recorded under the whole cell mode with patch clamp. There are 82 cells can get giga-seal and make a recording during patch clamp study. Most of the hAMSC (92.68%, 76/82) can show outward current during the patch clamp test. The membrane potential of these hAMSC is -389 ± 7.14 mV ($-25 \sim -13.9$ mV), the membranes capacity offset was 300.06 ± 189.81 (0~780 pF).

Figure 1 illustrate the families of membrane current elicited by 1.5s depolarizing steps from -50 mV to $+70$ mV in 10 mV step. There were 3 types of outward current presented in the hAMSC.

The most prevalent outward current of hAMSCs showed a gradually activating current which were hardly demon-

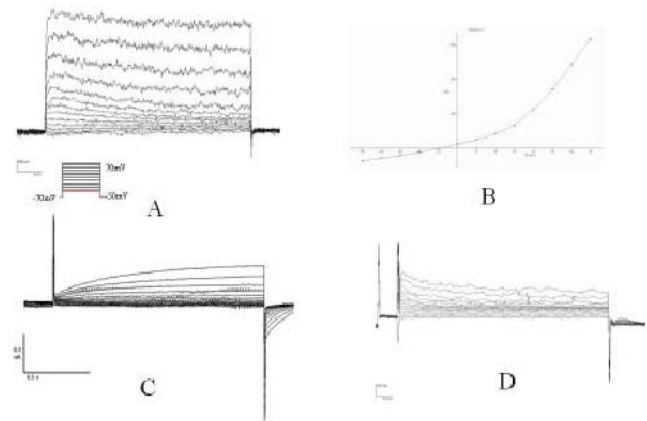


Figure 1: Different patterns of membrane currents recorded in hAMSCs. (A): Membrane currents were activated. The outward membrane currents were elicited in a 1.5s depolarizing steps from -50 mV to $+70$ mV in 10 mV step after a holding potential of -70 mV (as shown in the inset of [A]), showing that two components of outward currents are present; one is a slowly activating current similar to delayed rectifier K current (IKDR), and the other is a rapidly activating current with noisy oscillation, similar to Ca²⁺-activated K current (IKCa). (B): Current-voltage (I-V) relationship of the cell in fig-A, which show a rectifier characterization. (C): Another type of IKDR, show a much slower activate kinetic like slow activating delayed rectifier K current (Iks). (D): another hAMSC show transient outward current coexisted with IKCa.

strated any inactivation (figure 1 A). The relationship of I-V show a rectifier characteristic, which presume to be a delayed rectifier K current (IKDR). The current of I_{KDR} can present in most hAMSCs (93.4%), and half of the cells show a slow activation kinetic like slow activating delayed rectifier K current (Iks). (figure 1 C)

The other kind of outward current showed rapid activation with noisy oscillation between $+20$ mV to 70 mV, which were presented in 35.5% hAMSCs. This rapidly activating component with noisy oscillation was similar to a Ca²⁺-activated K current (IKCa) reported in previous documents. (figure 1 A).

We also found another type of outward current show a transient outward current, which similar to Ca²⁺-resistant transient outward K⁺ current (Ito) in cardiac and neuronal cells named a transient outward current (Ito) (Fig 1 D).

The inward currents such as sodium currents, calcium currents, inward rectifier K current (Ik1) and funny current (If) can't be recorded in our study.

B. mRNA expression of functional ion channel in hAMSCs

The mRNA expression pattern of functional ion channel in hAMSCs was investigated in our study, including the MaxIK, Kv1.4, Kv4.2, Kv4.3, HminK, HERG, HKVLQT1, Kir2.1, α 1c, SCN5A, HCN2 and HN4. Figure 2 displays the

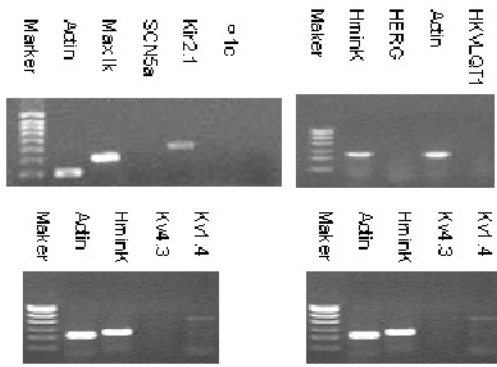


Figure 2: the Message RNA (mRNA) of different ion channel subunits related to the functional ionic currents was amplified by reverse transcription polymerase chain reaction (RT-PCR). The Original gels were shown. The figure show the mRNA expression of MaxiK, SCN5A, Kir2.1, $\alpha 1c$ of Ca-L, HminK, Kv4.3, Kv1.4, HCN2, HCN4, Herg, KvLQT1. The β -actin mRNA as the internal standard

mRNA expression (mRNA) for ion channel related to functional outward and inward ionic currents. The results show high mRNA levels of MaxiK, Kir2.1, Kv1.4, HminK can be detected in the hAMSCs, which provide the molecular basis of functional ionic current in hAMSCs.

IV. DISCUSSION

The hAMSC, unlike bone marrow stem cell, are easily to get in large amount of numbers, and have a multipotent. So the hAMSCs were thought as a new ideal cell sources for cardiomyoplasty. But the knowledge of electrophysical property of hAMSCs were not well understood. This is the first study of the electrophysiology property in hAMSCs.

Ion channels have important roles in maintaining physiological homeostasis in different types of cells. The study of ion channel in MSC from bone marrow in human, rat, mouse and rabbit had demonstrated that multiple functional ion channel currents are expressed, including IKCa, Ito, IKDR, IK1, INa, and ICa-L[4,5]. In our study, there were no inward currents can be recorded, and the mRNA of SCN5A and $\alpha 1c$ of Ca-L can not be detected in hAMSCs also. The mRNA expression of Kir2.1 was detected, but it can not show a functional ion channel current in our study.

Ito was first observed in hMSCs through mRNA expression analysis by Heubach et al[5], and then it was detected in a small population of hMSCs (8%) by another group[4]. In our study to hAMSC, Ito was recorded in 14.5% of hUCMSCs. During development of embryonic stem cell-derived

cardiomyocytes, inhibition of Ito can changed the duration and frequency of action potentials in the early stage but not in the late stage, suggesting that the Ito of early-stage cardiomyocytes plays an important role. Voltage-gated K⁺ currents are found to modulate the progression through the cell cycle in proliferating cells. MaxiK channels are usually believed to be sensors of intracellular Ca²⁺ and are found to regulate membrane potential in an intracellular Ca²⁺-dependent manner in hMSCs. These results suggest that MaxiK current could, be an effector of trophic factors within the body fluids or cell culture medium.

In summary, the multiple expression of ion channels would suggest possible differential roles of these channels in the cellular physiological activity.

V. CONCLUSION

The present study demonstrates for the first time that three distinct ion channel currents are expressed in hAMSCs, including three types of outward currents (IKCa, Ito, and IKDR), which provides a strong basis for a study of physiological roles of these functional ionic currents in proliferation and differentiation of hMSCs in the future for a further investigate the human biology. The physiology roles of these ion channels in cell development and differentiation were remained study in the further.

ACKNOWLEDGMENT

This study was supported by the fund of Janssen Research Council China (JRCC).

REFERENCE

1. In 't Anker PS, Scherjon SA, Kleijburg-van der Keur C, et al. (2004) Isolation of mesenchymal stem cells of fetal or maternal origin from human placenta. *Stem Cells* 22:1338-1345.
2. Zhao. P., Ise. H.; Hongo. M, et al. (2005) Human amniotic mesenchymal cells have some characteristics of cardiomyocytes. *Transplantation*. 79:528-535.
3. Alviano. F, Fossati. V, Marchionni. C, et al.(2007) Term Amniotic membrane is a high throughput source for multipotent Mesenchymal Stem Cells with the ability to differentiate into endothelial cells in vitro. *BMC Dev Biol*. 7:11.
4. Li G, Sun H, Deng X, et al. (2005) Characterization of ionic currents in human mesenchymal stem cells from bone marrow. *Stem Cells* 23: 371--382.
5. Heubach J.F, Graf EM, Leutheuser J, et al (2004) Electrophysiological properties of human mesenchymal stem cells. *J Physiol* 554: 659--672.

Power density spectra of the velocity waveforms in Artificial heart valves

A.A. Sakhaeimanesh

Biomedical Engineering Group, Faculty of Engineering, University of Isfahan, Isfahan, Iran

Abstract — To find the possible frequencies induced by the vibration of the flexible membrane of the Jellyfish valve, power density spectra of the the valvular velocity waveforms were carried out.

Most of the spectral energy was contained in frequencies lower than 11 Hz and all spectra exhibited pronounced peaks which implied wave motions in the preferred frequency range.

Two distinct peak frequencies, 1.2 and 2.4 Hz, were observed downstream of the Jellyfish valve which qualified as the frequencies of fundamental harmony of the waveform velocity and one of its sub harmonics.

Effect of oscillation on elevating turbulent shear stresses through the jellyfish and St.Vincent valves has also been investigated. Laser Doppler Anemometry (LDA) was employed to determine the velocity and shear stress distributions at various locations downstream of the valves. Comparison between two valves revealed that at 0.5D downstream of the valves the magnitude of shear stresses in the Jellyfish valve were much higher than those of the St. Vincent valve at cardiac outputs of 4, 5.5 and 7 l/min.

The cause of high shear stresses in close proximity to the Jellyfish valve could be attributed to the oscillation of the membrane which in turn generated a wake downstream of the valve (in the core of valve chamber) and produced a wide region of disturbance further downstream. This resulted in further pressure drag and consequently, higher pressure drops across the valve and higher shear stresses downstream of the valve.

Keywords — Power density spectra, Heart valves, shear stresses, oscillation, LDA technique

I. INTRODUCTION

Prosthetic heart valves are commonly used for replacement of natural valves, in ventricular assist devices (VADs) and total artificial hearts (TAHs). In artificial heart valves, the problems of haemolysis, platelet destruction, thrombus formation, perivalvular leakage, tissue over growth and endothelial damages are directly related to the fluid dynamic characteristics of flow past artificial heart valves ([1], [2], [3]). The presence of the prosthetic valve as a stenosis disturbs the blood flow and produces regions of high turbulent shear stresses, jetting and flow stagnation which, in turn cause pathological problems such as haemolysis and thrombosis. Blood cells in the region of high shear stresses are exposed to a distribution of shear

stresses over their entire membrane which causes the blood-cell membrane to be stretched and cause harmful changes to its essential function and eventually rupture the cells. Therefore, haematologically, it is highly desirable that a valve design shouldn't produce excessive turbulence, which may cause haemolysis ([2], [3], [4], [5]). In this study power density spectra of the valvular velocity waveforms were carried out and the effect of oscillation on elevating turbulent shear stresses and pressure drops through the jellyfish and St.Vincent valves has been investigated. Laser Doppler Anemometry (LDA) was employed to determine the velocity and shear stress distributions at various locations downstream of the valves.

II. METHOD

Power density spectra of the valvular velocity waveforms were carried out. The fast Fourier transform (FFT) was implemented by FLOWare to calculate spectral estimate of the valvular velocity waveforms over the entire cycle to produce the power spectra density.

Mean spectral or power spectral density can be estimated as:

$$S_T(f)_{FFT} = \frac{T}{N^2} \left\{ \left| \sum_{i=1}^N u_i e^{j2\pi f t_i} \right|^2 \right\} \quad \& \quad \bar{S}_T = \frac{1}{M} \sum_{m=1}^M S_{Tm}$$

where $S_T(f)$ is spectral estimate, $\bar{S}_T(f)$ is mean spectral estimate or power spectral density, S_{Tm} is the spectral estimate S_T calculated from the mth blocks of data, M is the total number of blocks, T is duration of block during which N spherical samples occur and u_i is axial velocity component of i^{th} particle.

Two valves namely Jellyfish and St.Vincent valves were selected. Jellyfish valve consist of a thin flexible membranous occluder made of Polyurethane and attached centrally to a rigid frame which have several spokes to protect against prolapse of the membrane.

A blood analogue fluid of water-saline solution was contained inside the ventricle chamber and was separated from the piston pump by the polymeric flexible ventricle. Blood analogue fluid provided a transparent and easy

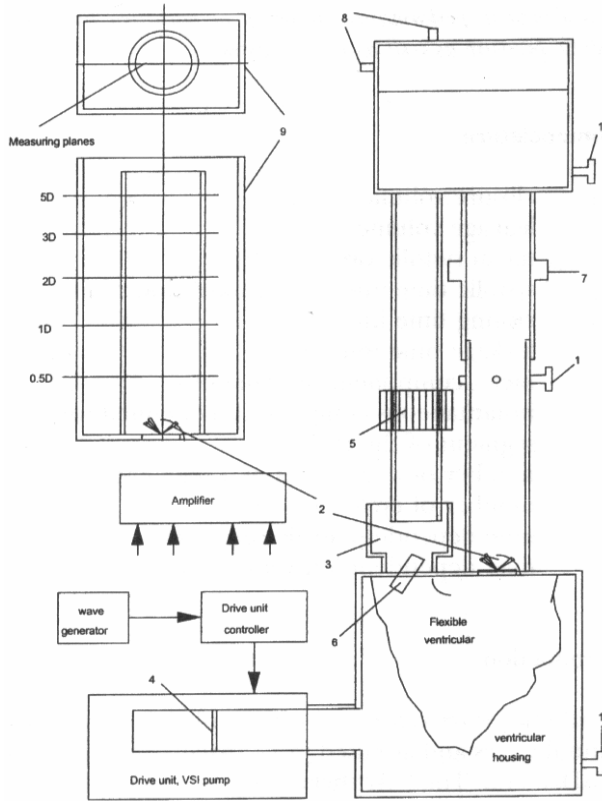


Fig. 1: Diagram of the pulse duplicator used in this study (not in scale), (1) ventricular, aortic and compliance pressure taps; (2) aortic valves; (3) mitral chamber; (4) pump piston; (5) adjustable resistance; (6) mitral valve; (7) electromagnetic flow meter probe; (8) air releaser and air pump; (9) index matching box.

handling situation for velocity measurements with Laser Doppler Anemometry. In the inlet of the flexible ventricle chamber (mitral position) a Björk-Shiley tilting disc valve was installed.

An electromagnetic square-wave flowmeter, which was calibrated before measurement, was installed 8D downstream of the valve so that the instantaneous flow rates could be determined.

The pressure pulses were measured by three disposable and physiological blood pressure transducers in the left ventricle, downstream of the aortic valve and in the compliance chamber. Flow measurements were done at cardiac outputs of 4, 5.5 and 7 l/min.

A Dantec (Skovlunde, Denmark) two-component LDA system was used to determine the flow field at various locations downstream of the valve.

Data was collected in continuous mode over 100 to 200 cycles, depending on the collected data rate to ensure that at least 1000 samples would be collected during every 5 ms of

the forward flow phase. After collecting data over complete cycles, data from each cycle is divided into 168 sample windows, each 5 ms duration. Then data belong to n th sample window of each cycle was compiled into n th bin and averaged to yield fluctuating and mean components. Mean components over 100 to 200 cycles (depending on data rate collection) can be manipulated into one representative cycle as follows:

$$S_n = \frac{\sum_{i=1}^n \sum_{j=1}^m S_{ij}}{nm}$$

where S_n is the mean component of n th sample window, S_i are the instantaneous components contained within a sample window, n is the number of data points in a sample window and m is the number of cycles measured.

All possible sources of error were carefully examined and having ensured that all recommendations concerning optical component alignment, seeding, filtering, signal processing, and calibration were carried out, the estimated measurement error of the mean velocity is $\sim 3\%$ and that in the rms is $\sim 7\%$.

Diagram of mock circulatory system is shown in Figure 1 and more details of it and LDA technique are given somewhere else ([6] and [7]).

III. RESULTS AND DISCUSSION

A Spectrum analysis

To find the possible frequencies induced by the vibrations of the flexible membrane of the Jellyfish valve, power density spectra of the valvular velocity waveforms were carried out. The random nature of the LDA prohibits sampling at regular and equi-spaced intervals which presents additional variability of the spectral estimator. In order to reduce this variability, spectral analysis of data was performed according to the method of direct Fourier transform of short blocks of data by FLOWare by implementing the re-sampling of the signals for data that were not collected in the dead time mode.

Important and useful information about dominant frequency peaks and preferred mode which exists in the flow can be derived from the spectral information. Figures 2 and 3 show typical energy spectra measured at downstream locations of the Jellyfish and St. Vincent valves in the regions of stagnation and jetting at cardiac output of 6.5 l/min.

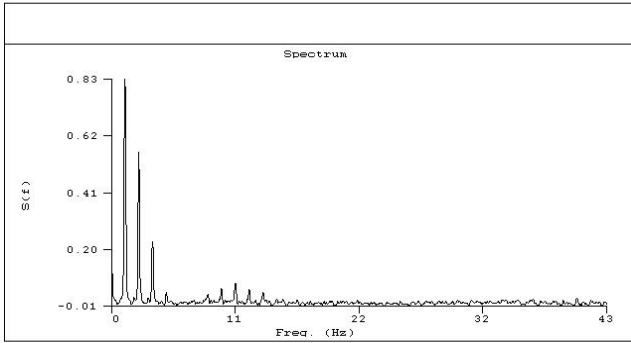


Fig. 2: power density spectra of waveform velocity estimated at 0.5D downstream of the Jellyfish valve in the region of Jetting at cardiac output of 6.5 l/min under pulsatile flow condition.

Most of the spectral energy was contained in frequencies lower than 11 Hz and all spectra exhibited pronounced peaks which implied wave motions in the preferred frequency range.

Two distinct peak frequencies, 1.2 and 2.4 Hz, were observed downstream of the Jellyfish valve which qualified as the frequencies of fundamental harmony of the waveform velocity and one of its sub harmonics.

Another distinct peak, between 3 and 4 Hz, with the power of 0.2 was observed at 0.5D of the jellyfish valve (Figure 2). This frequency peak may qualify as the second sub harmonic frequency of the velocity waveform or, together with other higher frequency peaks, may qualify as the product of the membrane induced vibration peaks. The same results were found downstream of the Jellyfish valve at the other cardiac outputs. These are not presented here due to similarity in the results.

Behind the occluder and in the jetting region of the St. Vincent valve, two distinct peak frequencies of the fundamental and its sub harmonics of the velocity waveform motion were observed (Figure 3). A third distinct peak frequency, between 3 and 4 Hz, which was observed at

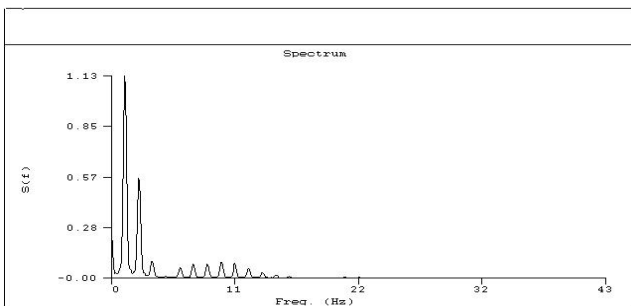


Fig. 3: power density spectra of waveform velocity estimated at 0.5D downstream of the St. Vincent valve in the region of Jetting at cardiac output of 6.5 l/min under pulsatile flow condition.

downstream of the Jellyfish valve did not exist at downstream of the St. Vincent valve. This can be described in terms of solidarity of the occluder of the St. Vincent valve, which does not induce vibration in the flow.

Comparison between two valves revealed that at 0.5D downstream of the valves the magnitude of shear stresses in the Jellyfish valve were much higher than those of the St. Vincent valve at cardiac outputs of 4, 5.5 and 7 l/min. Furthermore, at 3D and 5D downstream of the Jellyfish valve the magnitudes of shear stresses reduced dramatically to 6 and 1 N/m² respectively at cardiac output of 7 l/min. At 3 and 5D downstream of the St. Vincent valve, on the other hand, showed maximum shear stresses of the values of 49 and 17 N/m² respectively at the same cardiac output

It is hypothesized that the cause of high shear stresses in close proximity to the Jellyfish valve was due to the oscillation of the membrane which in turn generated a wake downstream of the valve (in the core of valve chamber) and produced a wide region of disturbance further downstream. This resulted in further pressure drag and consequently, higher pressure drops across the valve and higher shear stresses downstream of the valve.

This idea was supported by the results of shear stress (Table 1) and pressure drop measurements (Figure 7). Maximum and mean shear stresses at 0.5D downstream of the Jellyfish valve were about twice those of the St. Vincent valve and pressure drops across the Jellyfish valve were up to 93 % higher than those of the St. Vincent valve under steady flow rates between 10 to 26 l/min.

The effect of oscillation can also be seen from the results of turbulence intensities. Maximum and mean turbulent intensities 0.5D downstream of the Jellyfish valve were as high as 781 and 273 % respectively at cardiac output of 7 l/min (605 and 212% at cardiac output of 5.5 l/min and 440 and 145 % at cardiac output of 4 l/min respectively). At 3D downstream of the valve, maximum and mean turbulent intensities reduced dramatically to 19 and 8 % respectively at cardiac output of 7 l/min (Table 3 and Figure 6). Reduction in turbulence, and consequently in shear stress estimation in the 3D and 5D downstream measuring planes of the Jellyfish valve, indicated that the effect of the membrane oscillation decayed beyond 1D at all cardiac outputs. The consequence of such a reduction in turbulence was low shear stress estimations in these measuring planes (less than 5 N/m²) at cardiac output of 7 l/min.

Despite the eccentricity of the flow at downstream of the St. Vincent valve, turbulent intensities at close vicinity of the St. Vincent valve (0.5D) were much less than those of the Jellyfish valve (Table 1). This can be attributed to the fact that solid occluder of the St. Vincent valve did not produce vibration in the downstream flow field which consequently resulted in low shear stress estimations.

Table 1: Mean and maximum values of shear stresses, turbulent intensities and r.m.s of axial velocities of the Jellyfish and St. Vincent valves at cardiac outputs of 7 l/min at different downstream locations.

Distance, in diameter	Jellyfish valve			St. Vincent valve		
	0.5D	3D	5D	0.5D	3D	5D
Max shear stress, N/m ²	155	5	1	88	49	21
Mean shear stress, N/m ²	62	1	0.3	19.4	18.5	5.5
Max turbulent intensity, U %	781	19	17.7	118	37.8	33
Mean turbulent intensity, U %	273	8	6	47	24.5	17

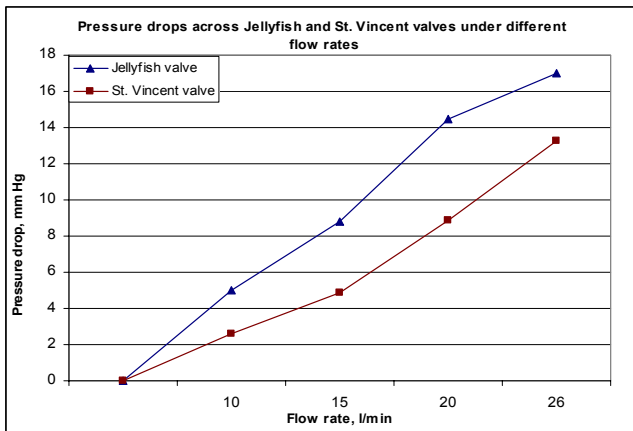


Fig. 7: pressure drops across the Jellyfish and St. Vincent valves under different flow rates.

At 3 and 5D downstream of the St. Vincent valve, eccentricity of flow still existed. This meant that flow become a fully developed beyond 5D. Maximum and mean turbulent intensities of the values of 33 and 17 % respectively were found 5D downstream of the St. Vincent valve. These were twice the values found at 5D downstream of the Jellyfish valve (17 and 6 %) at cardiac output of 7 l/min. Such a disturbed flow at 3 and 5D downstream of the St. Vincent valve produced maximum shear stresses in the range of 21-49 N/m² (compare to 1-5 N/m² in The Jellyfish valve). A summary of the data are presented in Table 1 for cardiac outputs of 7 l/min. Similar trends and results were

found at mid acceleration and deceleration but are not presented here due to their similarity with the peak systole results.

REFERENCES

1. Hanle D.D., Harrison E.C., Yoganathan, A.P., et al. (1989), In vitro flow dynamics of four prosthetic valves, a comparative analysis, *J. Biomechanics*, 22: 597-607.
2. Reul H., Van Son Jaques A.M, et al. (1993), In vitro comparison of bileaflet aortic heart valve prostheses- St. Jude Medical, CarboMedics, Modified Edwards-Durmedics and Sorin-Bicarbon valves. *J of Thoracic and Cardiovascular Surgery*, 106: 412-420.
3. Yoganathan A.P. (1995) Cardiac Valve prostheses, In: J.D. Bronzino (ed), *The Biomedical Engineering Handbook* (CRC and IEEE presses, 1847-1870).
4. Ruel H. (1983), In vitro evaluation of artificial heart valves., In: D.N. Ghista, O. Hamilton, (eds). *Advance in Cardiovascular physics* (Basel New York, Karger, 5)
5. Shim H.S., Lenker J. A. (1988) Heart valve prostheses, In: Webster J.G., (ed), *Encyclopedia of Medical device and instrumentation* (John Wiley and sons, Inc., 3: 1457-1473)
6. Sakhaeimanesh A.A., Morsi Y.S. (1999) Analysis of regurgitation, mean systolic pressure drops and energy losses for two artificial aortic valves. *Journal of Medical Engineering and Technology*, 23(2): 63-68.
7. Morsi Y. S., Sakhaeimanesh A. A (2000) Flow characteristics past jellyfish and St. Vincent valves in the aortic position under physiological pulsatile flow conditions. *Artificial Organs*, Volume 24(7): 564-574.
8. Bluestein D, Einav S (1994) A modified stability diagram of pulsatile flow through heart valves based on improved spectral estimations of LDA data, *American Society of Mechanical Engineers: Laser Anemometry, Advance and Application*, Volume 191: 125-133.

Author: A. A. Sakhaeimanesh
 Institute: Biomedical Engineering Group, Faculty of Engineering,
 University of Isfahan
 Street: Hezar Jarib Street
 City: Isfahan
 Country: Iran
 Email: sakhaei@eng.ui.ac.ir

Mechanotransduction of mandibular condylar chondrocytes under pressure

Min Zhang, Yong-Jin Chen, Xin Lv, Jing-Jie Wang, Han-Guo Wang

Department of General Dentistry & Emergency, School of Stomatology, Fourth Military Medical University, Xi'an China.

Abstract — To investigate the possible involved signal molecules in the mechanotransduction of mandibular condylar chondrocytes (MCCs) under pressure, *in vitro* cultured rabbit MCCs were incubated and pressed under continuous pressure of 90 KPa for 1 h and 6 h by hydraulic pressure controlled cellular strain unit. The signal molecules of integrin pathway and G protein pathway were detected step by step. The results showed that expression of all the signal molecules investigated here, including integrin $\alpha_5\beta_1$, F-actin, G protein, intracellular calcium, PKC, ERK $_1$, JNK $_1$, IL-4 and IL-6 increased under the pressure. At the same time, series of membrane or cytoplasmic proteins, such as F-actin, PKC and ERK $_1$ and JNK $_1$ showed characteristic translocation from cytoplasm to the membrane, to the nuclei, or to the perinuclear region, and underwent reversible binding interactions. There were only integrin β_1 , JNK $_1$ and IL-4 in the long-term pressure group showed all the more higher than that of short-term pressure group. It was suggested that integrin $\alpha_5\beta_1$, F-actin, G protein, intracellular calcium, PKC, ERK $_1$, JNK $_1$, IL-4 and IL-6 all participated in the mechanotransduction of mandibular condylar cartilage under continuous pressure. Mechanotransduction under long-term and short-term pressure may involve different dominant signal molecules.

Keywords — Mechanotransduction, mandibular condylar chondrocytes, pressure, signal molecules

I. INTRODUCTION

Mechanotransduction is the process of translating mechanical stimulation into cellular reaction, by which the live tissues adapt to the mechanical environment all around and obtain extensive physiological functions[1]. It is now well recognized that mechanical forces play a fundamental role in the function regulation of many cells[2-7], with the cells and mechanical stimulations differed, the varied pathway for mechanotransduction will be activated which are essential to maintain tissue homeostasis[8].

Temporomandibular joint (TMJ) is the only joint that keeps relatively active remodeling ability for all one's life[9,10]. Condylar cartilage is one of the important parts of TMJ with mechanical sensitivity and biomechanical reconstruction potential. By animal experiments, Papachristou et al had reported that Runx2 and AP-1 family participated into the signal transduction pathway of mechanical loading of condylar cartilage[11-13]. Our previous researches found that mechanical pressure caused

changes on the ultrastructure, up-regulation of aggrecan synthesis, increase of nitric oxide secretion and decrease of PGF $_2$ composition in mandibular condylar chondrocytes (MCCs) [14,15]. However, mechanotransduction in MCCs, similar to other cell systems, is not well understood and appears to be equally complex.

Although the precise mechanisms and signaling pathways involved in MCCs mechanotransduction are not fully elucidated, there is an increasing evidence for roles of integrins as mechanoreceptors, regulating the cellular response to both changes in the ECM and mechanical stresses that cells are subjected to[16, 17]. As an important family of membrane proteins, G proteins are also closely involved in modulating the mechanotransduction pathways [18], which could trigger a cascade of downstream signaling events. However, till now, specific roles for these signaling molecules in the mechanotransduction pathway of MCCs have yet to be defined.

This study aimed to characterize the role of them in the mechanotransduction process of MCCs under pressure and to test the hypothesis that static pressure signals could be transferred into the nuclei of MCCs either by integrin-cytoskeleton pathway and its relative molecules or by the membrane G protein pathway as well as its downstream protein phosphatase.

II. MATERIALS AND METHODS

A. Source of cartilage and basic culture procedure

For this study, mandibular condylar cartilages of New Zealand white rabbits, (1 or 2 weeks old) were dissected under a microscope. MCCs were cultured according to the method of Engel et al. [19] Then, the cells were identified by type II collagen immunocytochemical reaction.

B. Mechanical pressure of the cell culture and mechanical pressure condition selection

To apply compressive stress to cultured MCCs, a hydraulic pressure-controlled cellular strain unit similar to the model developed by Yousefian et al. was used [20]. The pressure was generated by continuously compressing the gas phase (2% CO $_2$ in air) in a closed culture chamber (humidity 98%), which was placed in a 37°C incubator. It can

exert accurate, adjustable and identical hydraulic pressure upon cells and can fairly well mimic the mechanical environment of MCCs *in vivo*. Optimizing the treatment conditions were reported elsewhere in detail [14,15]. In short, the alkaline phosphatase (ALP) activity, the maturation indicator of MCCs from prechondrocytes to hypertrophic chondrocytes, and cell proliferation capability were adopted for investigation. 90 KPa pressure for 1 h was selected as short-term treatment condition, under which ALP activity of the cells could be promoted without affecting cell proliferation. In addition, 90 KPa pressure for 6 h was selected as long-term treatment condition, under which cell proliferation was inhibited.

C. Signal molecules detection

In situ hybridization (ISH) was used for integrin $\alpha_5\beta_1$ mRNA detection. Digoxigenin UTP-labeled single-stranded RNA probes: integrin α_5 5' TGA TGA TCC ACA GTG GGA CGC CAT AGC T 3' and integrin β_1 5' CGA GAC TCT TGA CGT TCT CCA GAT CAT C 3' were synthesized by using a DIG RNA Labeling Kit (Roche Diagnostics, Mannheim, Germany) according to the manufacturer's instructions. Immunofluorescence (IF) study was adopted for detecting F-actin and intracellular calcium. Primary mouse monoclonal rabbit polyclonal antibody against G $\alpha_q/11$ (Santa Cruz), antibody against F-actin (Sigma) and fluorescein-isothiocyanate-conjugated goat anti-mouse IgG secondary antibody (Sigma-Aldrich, Auckland, New Zealand) were used for F-actin staining, and propidium iodide tripolidine was used for nuclear staining. For intracellular calcium monitoring, the cells were loaded with 10 μ mol/L fluo-3/AM. Then cell images were taken using Leica SP2 laser scanning confocal microscope (LSCM, Leica; Heidelberg, Germany). Immunohistochemistry (IHC) method was used for PKC, ERK $_1$, JNK $_1$, IL-4 and IL-6 protein detection. Antibodies adopted here were monoclonal antibody against PKC (Sigma), goat polyclonal antibody against extracellular signal-regulated kinases (ERK $_1$), mouse monoclonal antibody against the Jun N-terminal kinase (JNK $_1$) (Santa Cruz), and mouse monoclonal antibody against interleukin-4 and 6 (Sigma). Western blot (WB) analysis was adopted for the protein volume detection of ERK $_1$ and JNK $_1$.

D. Statistical analysis

High power image analysis system (HPIAS) 1000 (Tongji University, China) was used for analyzing the ISH and immunohistochemistry staining results, which was corrected by the same visual field of the same slide as the blank. The semi-quantitative analysis method was described elsewhere [15]. The data from image analysis were from the

results of three repetitive experiments. Comparison between the control and experimental groups was evaluated by one-way analysis of variance (ANOVA) followed by Scheffe's post-hoc test. A *p* value smaller than 0.05 was considered statistically significant.

III. RESULTS

All of the signal molecules investigated here showed distinct increased intracellular expressions under both 90KPa/1h and 90KPa/6h pressure condition (*p*<0.05). The staining intensity increments to that of the control were showed as Fig.1. Most of the molecules were expressed stronger under short-term pressure than long-term pressure, except integrin β_1 , JNK $_1$ and IL-4, which showed continuous increase during pressure stimulation period till 6 hours.

In addition to variations in expression intensity, there were still some characteristic changes in the cellular distribution of some signal molecules. As we can see from the Fig.2, the F-actin staining of cultured MCCs was revealed uniform in the cytoplasm, while under pressure, there are distinct stress fibers assembled in the cytoplasm. Besides, The distribution of PKC in the cells showed character of translocation to the plasma membrane and perinuclear region of the cells and, partly, nuclei under the 90KPa/1h pressure. When the pressure extended to 6 h, the PKC signal resumed uniform distribution in the cytoplasm. Again, ERK $_1$ and JNK $_1$ distributed uniformly in both the cytoplasm and nuclei of control cells, while after being pressed for 1 h, distribution of both proteins showed distinct translocation from cytoplasm to nuclei. When the pressure extended to 6 h, ERK $_1$ distributed uniformly again in the cytoplasm and nuclei. But the translocation of JNK $_1$ from cytoplasm to nuclei continued (Fig.2).

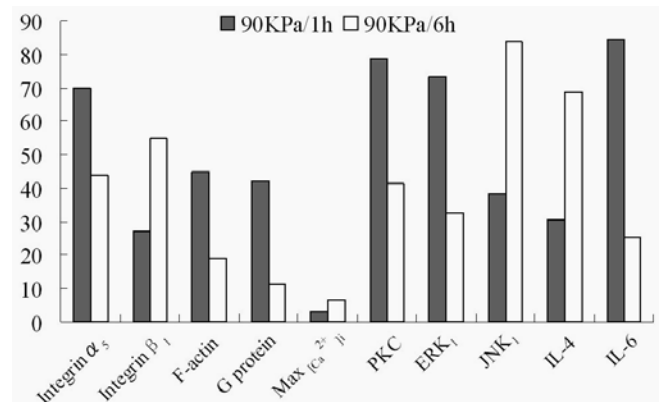


Fig. 1 Increments of expression intensity of each signal molecule in the cells of two different pressure groups compared with those of the control.

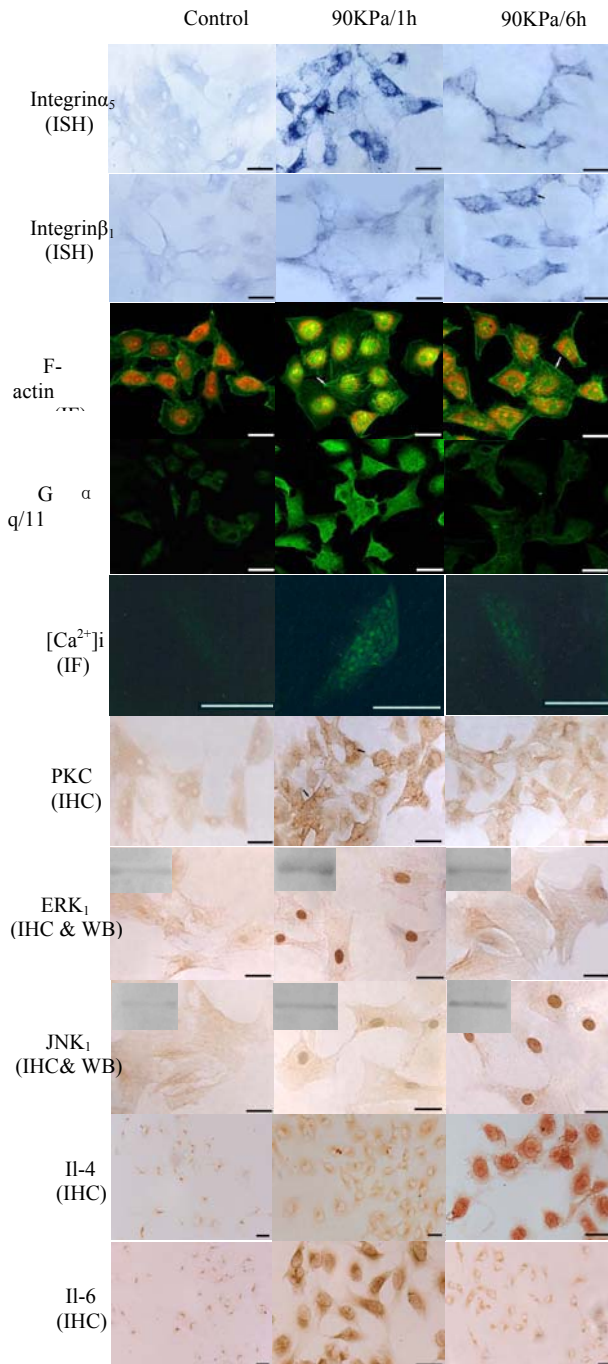


Fig. 2 Cellular distribution of each signal molecule showed that in addition to their increased expression under pressure, the translocation of several signal molecules i.e. PKC, ERK₁, and JNK₁ were observed (Bar=10μm)

IV. DISCUSSIONS

A. Mechanotransduction pathway of MCCs

From the aspect of mechanotransduction mechanism, we got two different signal pathway in MCC under pressure (Fig.3). One was transmission process initiated by integrin-cytoskeleton system. The $\alpha_5\beta_1$ integrin was proved by the present study to function as a mechanoreceptor and participate into the launching of mechanotransduction process of MCCs under the static pressure. Then, the cytoskeleton and F-actin expression strengthened and stress fibers assembled. The other pathway was transduction process initiated by G protein locating on cellular membrane, which is a major cog in the machinery that a cell uses to transduce signals from activated transmembrane receptors to intracellular effectors[3,21,22]. The result of the present study confirmed the participation of $G\alpha_{q/11}$ proteins in the mechanoreception of mechanical pressure in MCCs. Along with that, the intracellular calcium increased and the protein kinase C was activated and translocated to the cytomembrane and nuclei. After that, the mitogen-activated protein kinases (MAPK) access was activated and the mechanical signal was transduced further into the nuclei.

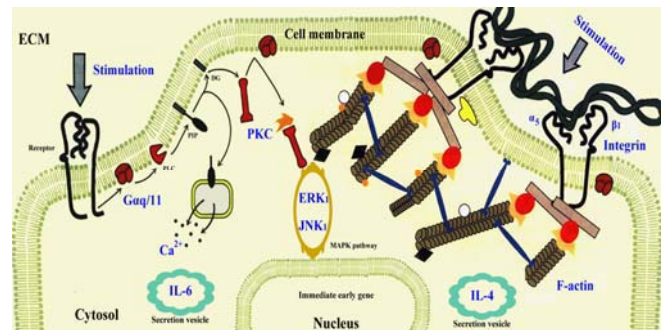


Fig. 3 Mechanotransduction pathway of MCCs under static pressure.

B. Softwired signaling modulations in mechanotransduction of MCCs

The current “softwired signaling concept” is built on the idea that signaling proteins translocate and undergo reversible binding interactions as key steps of the signal transmission process[23]. The results of the present study manifested that mechanical pressure could activate the membrane mechanotransducer, integrin $\alpha_5\beta_1$ or G protein, and launch the mechanotransduction process in MCCs. Further by the softwired signaling modulations of series of membrane or cytoplasmic proteins, including F-actin, G protein, PKC and MAPK molecules, the mechanical signal was conducted into the nuclei. However, the mechanism

underlying effects of activation and translocation of the cytoplasm proteins and the interactions between the signal molecules in MCCs still need further study.

C. Temporal variation character of mechanotransduction signal molecules

We have previously reported that continuous 90KPa/1h pressure condition provided a feasible physiological mechanical environment for the *in vitro* cultured MCCs. Continuous pressure for 6 h caused inhibition of cell proliferation, reduced cellular secretion ability and some signs of cell apoptosis, which suggested that 90KPa/6h was excessive for the cells. Together with the results of the present study[14,15], we found that in the short-term pressure groups, all the signal molecules we have investigated, including integrin $\alpha_3\beta_1$, F-actin, G protein, intracellular Ca^{2+} , PKC, ERK₁, JNK₁, IL-4 and 6 increased, which meant that all of these molecules were involved in the mechanotransduction process of physiological reconstruction of condylar cartilage under feasible pressure. As to the long-term pressure group, there were only integrin β_1 IL-4 and JNK₁ showed all the more higher than that of short-term pressure group, which suggested that these molecules might especially related with pathological reconstruction process of condylar cartilage under excessive pressure.

ACKNOWLEDGEMENT

This work was sponsored by Nature Science Foundation of China (No.30000035; No.30670518). We thank the Dept. Oral Anatomy and Physiology of School of Stomatology of Fourth Military Medical University for support in research works.

REFERENCES

1. Wang N, Butler JP, Ingber DE. (1993) Mechanotransduction across the cell surface and through the cytoskeleton. *Science* 260:1124–1127.
2. Duncan RL, Turner CH. (1995) Mechanotransduction and the Functional Response of Bone to Mechanical Strain. *Calcif Tissue Int* 57: 344–358.
3. Gudi SR, Lee AA, Clark CB, Frangos JA. (1998) Equibiaxial strain and strain rate stimulate early activation of G proteins in cardiac fibroblasts. *Am J Physiol* 274: C1424–8.
4. Zhao XH, Laschinger C, Arora P, Szász K, Kapus A, McCulloch CA. (2007) Force activates smooth muscle alpha-actin promoter activity through the Rho signaling pathway. *J Cell Sci* 120:1801–9.
5. Howdhury TT, Appleby RN, Salter DM, Bader DA, Lee DA. (2006) Integrin-mediated mechanotransduction in IL-1 beta stimulated chondrocytes. *Biomech Model Mechanobiol* 5: 192–201.
6. Knight MM, Bomzon Z, Kimmel E, Sharma AM, Lee DA, Bader DL. (2006) Chondrocyte deformation induces mitochondrial distortion and heterogeneous intracellular strain fields. *Biomech Model Mechanobiol* 5: 180–91.
7. Millward-Sadler SJ, Khan NS, Bracher MG, Wright MO, Salter DM. (2006) Roles for the interleukin-4 receptor and associated JAK/STAT proteins in human articular chondrocyte mechanotransduction. *Osteoarthritis Cartilage* 14: 991–1001.
8. Wang JHC, Thampatty BP. (2006) An introductory review of cell mechanobiology. *Biomechan Model Mechanobiol* 5: 1–16.
9. Blackwood HJJ. (1966) Growth of the mandibular condyle of the rat studied with tritiated thymidine. *Arch Oral Biol* 11: 493–8
10. Zarb GA, Carlsson GE. (1979) Temporomandibular function and dysfunction. pp. 155–172. 1st ed.. St. Louis. Washington, D. C.. Toronto: The C.V. Mosby Company.
11. Teramoto M, Kaneko S, Shibata S, Yanagishita M, Soma K. (2003) Effect of compressive forces on extracellular matrix in rat mandibular condylar cartilage. *J Bone Miner Metab* 21: 276–86.
12. Papachristou DJ, Pirttiniemi P, Kantomaa T, Agnantis N, Basdra EK. (2006) Fos- and Jun-related transcription factors are involved in the signal transduction pathway of mechanical loading in condylar chondrocytes. *Eur J Orthod* 28: 20–6.
13. Papadopoulou AK, Papachristou DJ, Chatzopoulou SA, Pirttiniemi P, Papavassiliou AG., Basdra EK. (2007) Load application induces changes in the expression levels of Sox-9, FGFR-3 and VEGF in condylar chondrocytes. *FEBS Lett* 581: 2041–6.
14. Zhang M, Wang JJ, Chen YJ. (2006) Effects of mechanical pressure on intracellular calcium release channel and cytoskeletal structure in rabbit mandibular condylar chondrocytes. *Life Sci* 78: 2480–7.
15. Chen YJ, Zhang M, Wang JJ. (2007) Study on the effects of mechanical pressure to the ultrastructure and secretion ability of mandibular condylar chondrocytes. *J Oral Bio* 52: 173–81.
16. Millward-Sadler SJ, Salter DM. (2004) Integrin-dependent signal cascades in chondrocyte mechanotransduction. *Annals of Biomedical Engineering* 32: 435–46.
17. Lucchinetti E, Bhargava MM, Torzilli PA. (2004) The effect of mechanical load on integrin subunits α_5 and β_1 in chondrocytes from mature and immature cartilage explants. *Cell Tissue Res* 315: 385–91.
18. Hansen CA, Schroering AG, Carey DJ, Robishaw JD. (1994) Localization of a heterotrimeric G protein gamma subunit to focal adhesions and associated stress fibers. *J Cell Biol* 126: 811–9.
19. Engel FE, Khare AG., Boyan BD. (1990) Phenotypic changes of rabbit mandibular condylar cartilage cells in culture. *J Dent Res* 69: 1753–1758
20. Yousefian J, Firouzian F. (1995) A new experimental model for studying the response of periodontal ligament cells to hydrostatic pressure. *Am J Orthod Dentofacial Orthop* 108: 402–409
21. Gudi SR, Clark CB, Frangos JA. (1996) Fluid flow rapidly activates G proteins in human endothelial cells. *Circ Res* 79: 834–9.
22. Erickson GR, Alexopoulos LG, Guilak F. (2001) Hyper-osmotic stress induces volume change and calcium transients in chondrocytes by transmembrane, phospholipid, and G-protein pathways. *J Biomech* 34:1527–35.
23. Teruel MN, Meyer T. (2000) Translocation and reversible localization of signaling proteins: a dynamic future for signal transduction. *Cell* 103: 181–4.

Corresponding author:

Author: Min Zhang
 Institute: Dept. General Dentistry & Emergency
 Street: West Changle Road No.145
 City: Xi'an
 Country: China
 Email: zhangmin@fmmu.edu.cn;
 cherryzhangmin@126.com

Effect of femoral tunnel angle on tunnel enlargement in anterior cruciate ligament reconstructions

Guang-si Shen¹, You-jia Xu¹, Hai-bin Zhou¹, Wen-xin Niu², Xia Guo³, Ming Yin¹, Zu-quan Ding²

¹ Department of Orthopedics, The Second Affiliated Hospital of Soochow University, Jiangsu, People's Republic of China.

² School of Life Science & Technology Engineering, Tongji University, Shanghai 200092, People's Republic of China.

³ Department of Rehabilitation Sciences, Hong Kong Polytechnique University, Hong Kong, People's Republic of China.

Abstract — Introduction The aims of this study were to explore whether the angle of the femoral tunnel had effect on the contact pressure of the graft in the femoral tunnel and to find the best femoral tunnel with the aim of minimizing bone tunnel enlargement after anterior cruciate ligament (ACL) reconstruction.

Materials and methods A three-dimensional (3D) finite element (FE) model of a healthy human knee which comprised proximal tibia, distal femur, ligaments, menisci and articular cartilages was developed. Besides, five FE models of femoral tunnels which were 10°, 20°, 25°, 30° and 40° relative to the midcoronal plane respectively and each FE model of tibial tunnel and Ligament Advanced Reinforcement System (LARS) were constructed. A load of 40N was applied to the quadriceps and each load of 10N was applied to the biceps femoris and semitendinosus tendons of the FE model. The contact pressures of the simulated graft in the femoral tunnel wall were measured at 0°, 30°, 60°, 90° and 120° of knee flexion.

Results The contact pressure at anterior portion of 40° femoral tunnel was significantly higher than those of 10°, 20°, 25° and 30° femoral tunnels. The contact pressure at posterior portion of 10° femoral tunnel was significantly higher than those of the other four tunnels. The contact pressure at posterior portion of 20° femoral tunnel was higher than that of 25° femoral tunnels. The contact pressure at anterior portion of 30° femoral tunnel was significantly higher than that of 25° femoral tunnel.

Conclusion The results obtained showed that the femoral tunnel angle had noticeable effect on the contact pressure in the femoral tunnel which could lead to femoral tunnel enlargement and the 25° femoral tunnel was the best femoral tunnel minimizing the femoral tunnel enlargement after ACL reconstruction.

Keywords — Finite element method, Anterior cruciate ligament reconstruction, Bone tunnel enlargement, Knee biomechanics, Tunnel angle

I. INTRODUCTION

Bone tunnel enlargement is a common phenomenon after ACL reconstruction^[1, 2]. The vast majority of previous studies showed that bone tunnel enlargement did not have effect on clinical outcome^[1]. However, bone tunnel enlargement

often complicates revision ACL reconstruction^[3] and increases its cost. A proper understanding of the etiology of bone tunnel enlargement is therefore essential to prevent its occurrence. Despite that many studies have been performed to find out the exact causes of bone tunnel enlargement, the causes are not completely known yet. Biological and mechanical factors have been reported as potential causes of this phenomenon^[4]. The mechanical factors consist of stress deprivation of bone within the tunnel wall, graft-tunnel motion, an accelerated rehabilitation, as well as improper tunnel placement^[5]. Segawa et al.^[2, 6] concluded that the contact pressure in the femoral tunnel was influenced by the angle of the femoral tunnel. However, Kobayashi^[1] reviewed retrospectively thirty ACL reconstructions performed with hamstring tendons, and believed that the femoral tunnel angle had no clear effect on the prevalence of bone enlargement. Here we presented a complete 3D FE model of a healthy human knee joint to the effect of femoral tunnel angle on tunnel enlargement in anterior cruciate ligament reconstructions.

II. MATERIALS AND METHODS

The geometrical data of the knee model was acquired from a healthy young volunteer by nuclear magnetic resonance (MRI) scan. The contours of bones, articular cartilages, ligaments and menisci were identified by automatic contouring software (Mimics10.0), and used to construct the solid models with the help of Geomagic, a reverse engineering software. The IGES files of solid models were transferred into the ANSYS software of FE analysis to mesh the solid models.

Models of bone tunnels whose diameters were 7.5 mm were created through Boolean operation. Tibial tunnel was centered at the location described by the literature^[7], and with an angle of 30° relative to the midsagittal plane and 65° relative to the tibial plateau from the lateral view^[7, 8]. The isometric point of femoral tunnel located 6mm anterior to the over-the-top point. The femoral tunnels were created 30° relative to the midsagittal plane, and 10°, 20°, 25°, 30° and 40° relative to midcoronal plane respectively (Fig. 2).

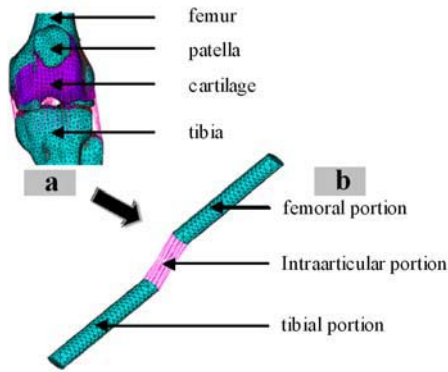


Fig. 1 finite element models: (a) knee joint; (b) LARS artificial ligament

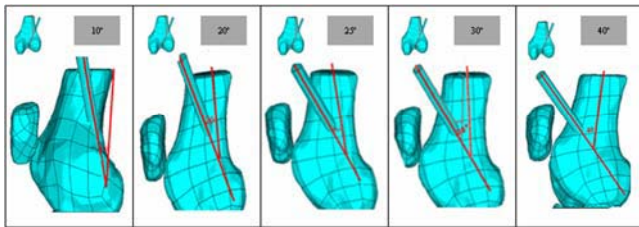


Fig. 2 solid models of femoral tunnel: 30° relative to the midsagittal plane, 10°, 20°, 25°, 30° and 40° relative to the midcoronal plane respectively.

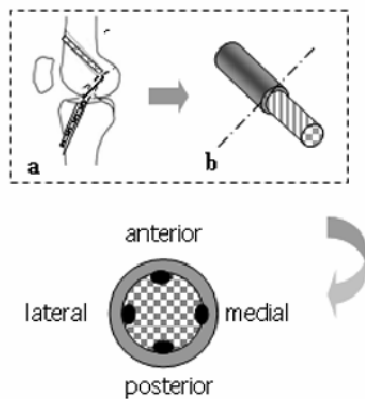


Fig. 3 schematic diagram of the contact pressure of the graft in the femoral tunnel. The grids represent the graft, the grey ring represents the femoral tunnel wall and the four black points represent the direction of contact pressure. (a) schematic diagram of LARS ligament in the tunnels (b) schematic diagram of femoral tunnel and intraarticular portion of LARS ligament.

The models of intraarticular and extraarticular portions of LARS ligament formed a nunchaku-type FE model (Fig.1 b).

A load of 40N was applied to the quadriceps and each load of 10N was applied to the biceps femoris and semitendinosus tendons. The contact pressures of the simulated grafts in the walls of the femoral tunnel models which were 10°, 20°, 25°, 30° and 40° relative to midcoronal plane respectively were measured at 0°, 30°, 60°, 90° and 120° of knee flexion(Fig. 3).

III. RESULTS

The graphs in Fig4. showed the values and dynamic changes of contact pressures of the grafts in each portion of the 5 femoral tunnels. The values and dynamic changes of contact pressures at the anterior and posterior portions of the femoral tunnel were evident throughout the knee flexion, while those of the contact pressures at the medial and lateral portions of the femoral tunnels were minimal. Peak contact pressures appeared in the anterior portion of the 40° femoral tunnel at 0° of flexion and in the posterior portion of 10° femoral tunnel at 120° of flexion. When the knee was in full extension, the contact pressure was the highest at the anterior portion and the lowest at the posterior portion. As flexion progressed, the contact pressure at anterior portion gradually decreased but increased at posterior portion.

The contact pressures of graft in the femoral tunnel varied with the femoral tunnel angle. The contact pressure at anterior portion of 40° femoral tunnel was significantly higher than those of 10°, 20°, 25° and 30° femoral tunnels. The contact pressure at posterior portion of 10° femoral tunnel was significantly higher than those of the other four tunnels. Differences of the contact pressure at anterior portion between 20° and 25° femoral tunnel were not evident. But the contact pressure at posterior portion of 20° femoral tunnel was higher than that of 25° femoral tunnels. The contact pressure at anterior portion of 30° femoral tunnel was significantly higher than that of 25° femoral tunnels, while that at posterior portion of the two tunnels were almost the same.

IV. DISCUSSION

Stress deprivation of bone within the tunnel wall is one of the most important mechanical factors that contribute to bone tunnel enlargement. A graft in a malposition tunnel might be shifted to the physiological position, leads to the occurrence of the contact pressure of the graft in the tunnel wall and finally results in bone tunnel enlargement^[9]. We here presented a FE model to analyze the effect of the femoral tunnel angle on the contact pressure of the graft in the bone tunnel wall, and to find a femoral tunnel with a certain angle minimizing bone tunnel enlargement after ACL reconstruction. The finite element method is a useful tool for biomechanical research which can overcome the inherent limitations of cadaveric experiment such as the difficulties of accurate measures of stresses and strains and sometimes impossible reproduction of the natural or pathological situations.

As shown in Fig.4, the contact stress at anterior portion of 40° femoral tunnel was significantly higher than that of the 10°, 20°, 25°, and 30° femoral tunnels. As the angle of the femoral tunnel decreased from 40° to 10°, the contact pressures in the anterior portion decreased too. Therefore, the anterior portion of the 40° femoral tunnel was more likely to be widened because of the stress deprivation of the femoral tunnel bone. For the same reason, bone tunnel enlargement occurred at the posterior portion of 10° femoral tunnel more likely than the other four. The contact pressure at posterior portion of 20° femoral tunnel was higher than that of 25° femoral tunnels. The contact pressure at anterior portion of 30° femoral tunnel was significantly higher than that of 25° femoral tunnels at 0°, 60° and 90° of knee flexion, while that at posterior portion between the two tunnels were almost the same. Based on these analysis, we conclude that among the five different femoral tunnels, the contact pressures of the graft in 25° femoral tunnel was the most minimal. Thus considering only from the mechanical view, the 25° femoral tunnel was the best femoral tunnel with the aim of minimizing the bone tunnel enlargement.

The obtained results were close to the result from the experimental, demonstrating that this FE models can effectively simulate the influence of the femoral tunnel angle on the contact pressure of the graft in the femoral tunnels. We conclude that the femoral tunnel angle has much effect on the contact pressure of the graft in the femoral tunnels which could lead to femoral tunnel enlargement, and that from the mechanical view, the 25° femoral tunnel is the best femoral tunnel which could minimize the femoral tunnel enlargement.

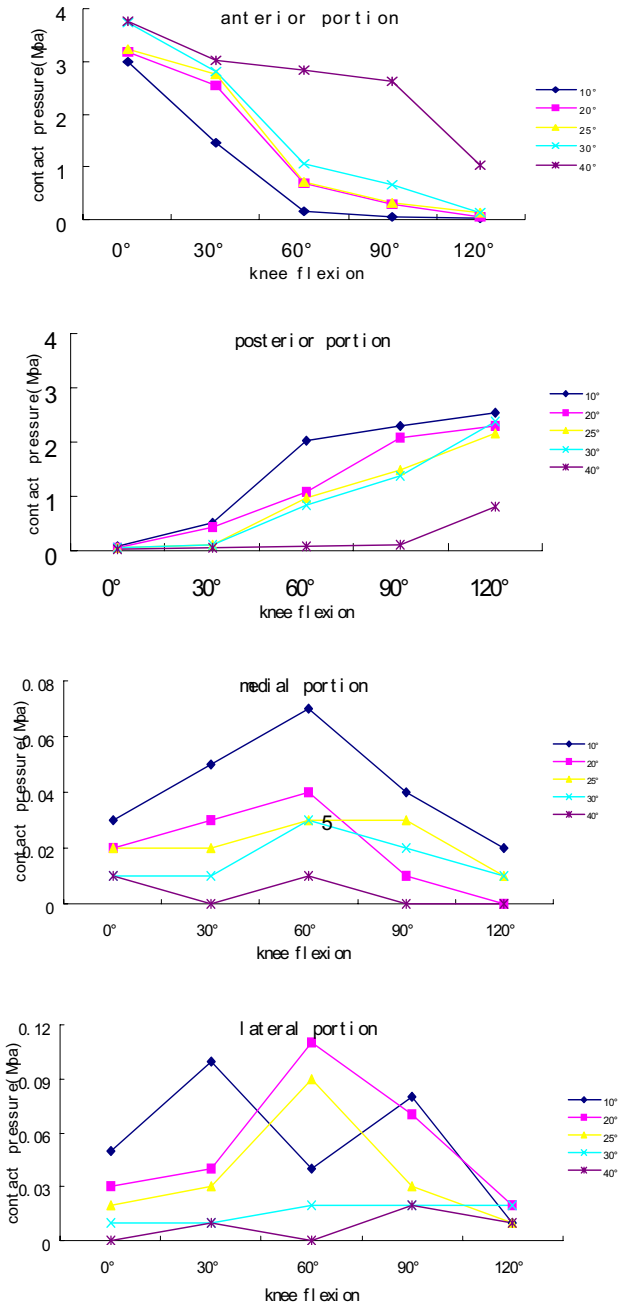


Fig. 4 The contact pressures of the LARS ligament at the walls of the five femoral tunnels at different knee flexion angle.

REFERENCES

1. Kobayashi M, Nakagawa Y, Suzuki T, Okudaira S, Nakamura T (2006) A retrospective review of bone tunnel enlargement after anterior cruciate ligament reconstruction with hamstring tendons fixed with a metal round cannulated interference screw in the femur. *Arthroscopy* 22:1093-1099
2. Segawa H, Omori G, Tomita S, Koga Y (2001) Bone tunnel enlargement after anterior cruciate ligament reconstruction using hamstring tendons. *Knee Surg Sports Traumatol Arthrosc* 9:206-210
3. Getelman MH, Friedman MJ (1999) Revision anterior cruciate ligament reconstruction surgery. *J Am Acad Orthop Surg* 7:189-198
4. Höher J, Möller HD, Fu FH (1998) Bone tunnel enlargement after anterior cruciate ligament reconstruction: fact or fiction? *Knee Surg Sports Traumatol Arthrosc* 6:231-240
5. Wilson TC, Kantaras A, Atay A, Johnson DL (2004) Tunnel enlargement after anterior cruciate ligament surgery. *Am J Sports Med* 32:543-549
6. Segawa H, Koga Y, Omori G, Sakamoto M, Hara T (2003) Influence of the femoral tunnel location and angle on the contact pressure in the femoral tunnel in anterior cruciate ligament reconstruction. *Am J Sports Med* 31: 444-448
7. Morgan CD, Kalman VR, Grawl DM (1995) Definitive landmarks for reproducible tibial tunnel placement in anterior cruciate ligament reconstruction. *Arthroscopy* 11:275-288
8. Shirazi-Adl A, Mesfar W (2007) Effect of tibial tubercle elevation on biomechanics of the entire knee joint under muscle loads. *Clinical Biomechanics* 22:344-351
9. Linn RM, Fischer DA, Smith JP, Burstein DB, Quick DC (1993) Achilles tendon allograft reconstruction of the anterior cruciate ligament-deficient knee. *Am J Sports Med* 21:825-831

Author: You-jia Xu
Institute: The Second Affiliated Hospital of Soochow University
Street: 1055Sanxiang Road
City: Suzhou 215004
Country: People's republic of China
Email: xuyoujia@medmail.com.cn

Optimization of Anastomotic Configuration in CABG Surgery

Y. Sui¹, B. Ma¹, A. Qiao²

¹College of Mechanical Engineering & Applied Electronics Technology, ²College of Life Science & Bioengineering, Beijing University of Technology, Beijing, 100022, P. R. China

Abstract — The geometric factors have prominent impacts on the success rate of coronary artery bypass graft (CABG). In order to clarify how to choose suitable graft-host diameter ratio and junction angle, ANSYS9.0 was used to simulate CABG, then response surface methodology was applied to construct mathematical model, finally theory of optimization was performed to determine the optimum graft-host diameter ratio and junction angle which could make the main factor influencing the success rate of CABG, i.e. wall shear stress gradients, smallest. The result indicates that the model of large graft-host diameter ratio and small junction angle has better hemodynamics. It can be concluded that adopting large graft-host diameter ratio and small junction angle with the help of clinical experiences is advisable in CABG surgery.

Keywords — Hemodynamics, CABG, Optimization, Response surface methodology, Numerical simulation

I. INTRODUCTION

The success rate of CABG is influenced by hemodynamics which is closely correlated with postoperative intimal hyperplasia and restenosis at the distal anastomosis [1-2]. Some geometric parameters, such as the lumen diameter of graft and the technique of anastomosis etc., distinctly influence the hemodynamics [3-4], such as flow patterns, pressure distribution, Wall Shear Stress (WSS), and Wall Shear Stress Gradients (WSSG).

The graft-host diameter ratio (shortened as: diameter ratio) and junction angle are important geometric parameters in Coronary Artery Bypass Graft (CABG). How on earth do they influence the hemodynamics under certain condition? Nobody has explicit answer so far.

The diameter ratio plays a complicated role in the hemodynamics and pathogenesis of CABG. Relationship between graft diameter and the postoperative patency rate was studied by Schneider et al., whose results showed that the graft diameter did not influence life-table patency when the graft was appropriately matched to native vessel size [5]. Yet Bonert et al. concluded that large diameter ratio can result in better hemodynamics while small one corresponds to

high rate of postoperative occlusion [6]. Abbott et al. found the high success rate in the femoral up the knee artery bypass graft was associated with the large graft diameter [7]. Stonebridge et al. considered the reason of high unsuccessful rate in artery bypass graft below the knee was enlarging the graft diameter, which made hemodynamics deteriorate, at least part of the reasons it plays [8]. Numerical simulation with different graft diameter was done by Qiao et al. in the femoral bypass graft [9, 10].

Small junction angle has more prominent advantage for the hemodynamics in CABG [11]. It is believed that 20° is the smallest angle at which surgeons can suture graft to the artery due to physical constrictions [12]. But in reality, the junction angle of 45° is adopted popularly for the simplicity of suturing.

In order to improve the success rate in CABG, it is very necessary to investigate how diameter ratio and junction angle influence the hemodynamics. As a numerical study, hemodynamics of CABG was simulated using ANSYS9.0 in this paper, response surface methodology (RSM) was applied to construct the mathematical model, and theory of optimization was employed to determine the best diameter ratio and junction angle which could make the WSSG at the downstream of the host artery smallest. It is conformed that reducing the WSSG can obtain approximately uniform hemodynamics and prominently debase the occurrence of pathological changes after bypass grafting [13,14].

II. NUMERICAL SIMULATION

The following assumptions were made in the numerical simulation: (a) The host artery and the graft are impermeable rigid circular tubes. (b) The blood is supposed to be symmetrical, homogenous and incompressible Newtonian fluid. (c) Blood flows are iso-thermal, pulsatile and laminar flows with the gravity of blood ignored.

A 2-dimensional model was adopted for the simulation. The geometry model of CABG was shown in Fig.1. The host artery is assumed to be straight conduit with medial stenosis which is described by a sine curve [13]. The diameter of host artery is $d_1=0.26\text{cm}$. The thickness of intimal hyperplasia at the neck of stenosis is a quarter of d_1 (i.e. the stenosis rate of cross-section is 75%). The diameter of graft

This work was supported by National Natural Science Foundation of China (10472003, 10772010) and Scientific Research Foundation of Doctoral Subjects in Chinese Universities(20060005010)

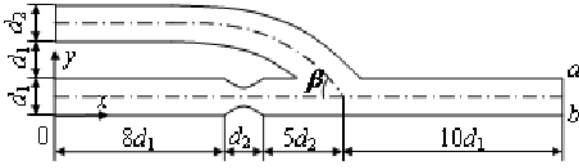


Fig.1 The geometry model

Tab.1 Characteristic parameters of blood

$\mu(\text{Pa} \cdot \text{s})$	$\rho(\text{g}/\text{cm}^3)$	$T(\text{s})$	Re	α
0.00424	1.06	0.8	111.7	1.82

is $d_2 = \gamma d_1$ (γ is the graft-host diameter ratio, $0.5 \leq \gamma \leq 2.0$). The graft meets the host artery with a side-to-end anastomosis at a junction angle of β ($20^\circ \leq \beta \leq 45^\circ$). When $\gamma \geq 0.8$, the circular cross-section of graft turns into an ellipse whose short axis is 80% of the diameter of host artery. This configuration approximates the Taylor patch model which is commonly considered to be effective for improving the hemodynamics of bypass graft [12].

The main characteristic parameters of blood flow include the viscosity of blood μ , the density of blood ρ , the period of pulsatile cardiac cycle T , the Reynolds number Re and the Womersley number α . The values of these parameters are depicted in table.1.

Boundary conditions for the computation are: (a) On all rigid vessel walls, all velocity components are constant zero according to the no-slip condition. (b) Uniform entrance velocities, which are computed according to the flow-rate measured in the body (Fig.2), are applied to the inlet of graft and host artery. (c) At the distal end of the host artery, a traction-free condition was imposed in accordance with the fully developed flow condition.

Hemodynamics is complex near the vessel wall, so finer and finer meshes were used from the central point to the wall in a cross-section. In the direction of longitudinal axis, the graft and host arteries were divided into some sections for the convenience of obtaining necessary mesh quality according to importance and computing the hemodynamic parameters in the post-process procedure. Symmetrical and the finest meshes were imposed to the section downstream from the distal anastomosis in the host artery where will be deeply concerned. Table 2 shows the numbers of node and element.

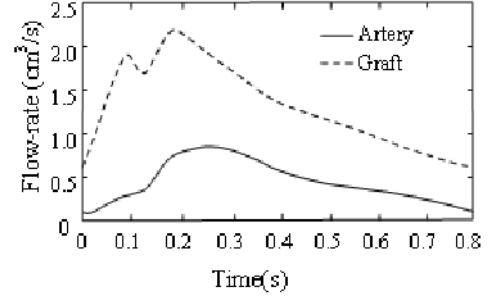


Fig.2 Entrance flow-rate

Tab.2 Numbers of node and element

diameter ratio	Node number	Element number
$0.5 \leq \gamma \leq 0.8$	33901	32031
$0.8 < \gamma \leq 2.0$	33300	31400

The simulation was performed using FLOTTRAN module of the commercial software ANSYS9.0. For quickening the convergence of numerical calculations, the same relaxation factors of 0.5 were imposed on the velocity and the pressure during the iteration. The convergence precision of the velocity field and the pressure field was limited to $1\text{E-}6$ during the calculation.

A 16-exponent polynomial function of nodal WSSs was constructed to compute spatial WSSG.

III. MATHEMATICAL MODELS

RSM was used during the process of constructing mathematical model. Two models with different constrictions were constructed to evaluate the hemodynamics of optimization.

A. Model 1

1. Description of mathematical model

$$\begin{cases} \text{search: } \gamma, \beta \\ \text{make: } W_{\max}^b(\gamma, \beta) \rightarrow \min \\ \text{s.t. } 0.5 \leq \gamma \leq 2.0; \\ \quad 20^\circ \leq \beta \leq 45^\circ; \end{cases}$$

Searching optimum geometric parameter γ and β in the given constrictions, which can make the largest WSSG of the line b in the downstream of host artery, $W_{\max}^b(\gamma, \beta)$, smallest.

2. RSM of objective function

Construct the RSM:

$$W_{\max}^b(\gamma, \beta) = a_1 + a_2\gamma + a_3\beta + a_4\gamma^2 + a_5\gamma\beta + a_6\beta^2 \quad (1)$$

For a set of experimental parameter $\gamma^{(i)}$, $\beta^{(i)}$ ($i=1, \dots, 7$) which is selected according to the modified RSM [15], geometry model was simulated and then WSS of M nodes in the line $b - \tau^{(m)}$ ($m=1, \dots, M$) were obtained through analysis. $\tau(x)$ is the function of WSS, which can be fitted by $\tau^{(m)}$ and the corresponding coordinate $x^{(m)}$. So the function of WSSG is $W(x) = \partial\tau^{(i)}/\partial x$,

then response point $W_{\max}^b = W_{\max}^{(i)}$ can be computed, where $W_{\max}^{(i)}$ is the large one of $|W(x)|$, extremum. Finally, the function of objective $W_{\max}^b(\gamma, \beta)$ is constructed according to $\gamma^{(i)}$, $\beta^{(i)}$ and W_{\max}^b .

(1) From $\gamma^{(i)}$ and $\beta^{(i)}$ to W_{\max}^b

For a certain geometric parameter $\gamma^{(i)}$ and $\beta^{(i)}$, hemodynamics of CABG can be simulated and WSS value $\tau^{(m)}$ of M nodes in line b obtained using ANSYS9.0, and the corresponding ordinate is $x^{(m)}$.

Construct the fitted function of WSS:

$$\tau(x) = \sum_j b_j x^{j-1} \quad (j=1, \dots, 17) \quad (2)$$

According to the principle of least-squares methodology, make $\sum_m [\tau^{(m)} - \tau(x_m)]^2 \rightarrow \min$, then:

$$\mathbf{b} = \mathbf{X}^{-1} \mathbf{d} \quad (3)$$

where $\mathbf{b} = [b_1, \dots, b_{17}]^T$, $\mathbf{d} = [d_1, \dots, d_{17}]^T$ and \mathbf{X} are respectively a matrix with the dimensions of 17×17 .

$$d_k = (\tau^{(m)}, \phi_k(x_m)) = \sum_m \tau^{(m)} \phi_k(x_m), \quad \phi_k(x) = x^{k-1}$$

$$X_{nk} = (\phi_n(x_m), \phi_k(x_m)) = \sum_m \phi_n(x_m) \phi_k(x_m) \quad (n=1, \dots, 17; k=1, \dots, 17)$$

From equation (2) above, WSSG is as follows:

$$W(x) = \sum_j (j-1) b_j x^{j-2} \quad (j=2, \dots, 17) \quad (4)$$

Computing W_{\max} which is the largest value of $|W(x)|$, extremum, then the response point W_{\max}^b is obtained.

(2) Response surface of objective

According to the $\gamma^{(i)}$, $\beta^{(i)}$ and W_{\max}^b , the coefficients of equation (1) are computed with modified RSM.

$$\mathbf{a} = (\mathbf{Y}^T \mathbf{Y})^{-1} \mathbf{Y}^T \mathbf{Z} \quad (5)$$

where $\mathbf{a} = [a_2, \dots, a_6]^T$, \mathbf{Y} is a matrix with dimension of 6×5 and \mathbf{Z} is a column vector with 6 dimensions.

$$Y_{nk} = y_k^{(n+1)} - y_k^{(1)}$$

$$y_1^{(i)} = \gamma^{(i)}, \quad y_2^{(i)} = \beta^{(i)}, \quad y_3^{(i)} = (\gamma^{(i)})^2$$

$$y_4^{(i)} = \gamma^{(i)} \beta^{(i)}, \quad y_5^{(i)} = (\beta^{(i)})^2$$

$$Z_n = W_{\max}^{(n+1)} - W_{\max}^{(1)}$$

and then:

$$a_1 = W_{\max}^{(1)} - \sum_k a_{k+1} y_k^{(1)}$$

$$(i=1, \dots, 7; k=1, \dots, 5; n=1, \dots, 6) \quad (6)$$

So far, the mathematical model 1 is constructed.

3. Result of optimization

The optimum diameter ratio is $\gamma^* = 2.0$ and the optimum junction angle $\beta^* = 20^\circ$.

B. Model 2

1. Description of mathematical model

$$\left\{ \begin{array}{l} \text{search : } \gamma, \beta \\ \text{make : } W_{\max}^b(\gamma, \beta) \rightarrow \min \\ \text{s.t.} \quad 0.5 \leq \gamma \leq 2.0; \\ \quad 20^\circ \leq \beta \leq 45^\circ; \\ \quad W_{\max}^a(\gamma, \beta) - W_{\max}^b(\gamma, \beta) \leq 0; \\ \quad -\underline{\tau} \leq \tau_{ave}^a(\gamma, \beta) - \tau_{ave}^b(\gamma, \beta) \leq \underline{\tau}; \end{array} \right.$$

Searching optimum geometric parameter γ and β in the given constrictions, which can make the largest WSSG of the line b in the downstream of host artery, $W_{\max}^b(\gamma, \beta)$, smallest.

2. Description of constrictions

Model 2 has another two constrictions compared with model 1. The construction method of RSM in models 2 is same as that in model 1. The reasons why the additional constrictions are added to model 2 are two folds: (a) $W_{\max}^a(\gamma, \beta) - W_{\max}^b(\gamma, \beta) \leq 0$. $W_{\max}^a(\gamma, \beta)$ is the RSM of

largest WSSG of line *a*. Adding this constrictions can avoid appearance of the phenomenon: $W_{\max}^b(\gamma, \beta)$ is becoming smaller, yet $W_{\max}^a(\gamma, \beta)$'s extremum is already larger than $W_{\max}^b(\gamma, \beta)$. (b) $-\underline{\tau} \leq \tau_{\text{ave}}^a(\gamma, \beta) - \tau_{\text{ave}}^b(\gamma, \beta) \leq \underline{\tau}$. $\tau_{\text{ave}}^a(\gamma, \beta)$, $\tau_{\text{ave}}^b(\gamma, \beta)$ are average WSSs of line *a* and *b*. Adding $-\underline{\tau} \leq \tau_{\text{ave}}^a(\gamma, \beta) - \tau_{\text{ave}}^b(\gamma, \beta) \leq \underline{\tau}$ to model 2 can control the WSSG of host artery to some extent.

So far, the mathematical model 2 is constructed.

3. Result of optimization

The optimum diameter ratio is $\gamma^* = 2.0$ and optimum junction angle $\beta^* = 25.71^\circ$.

Fig.3, Fig.4 and Fig.5 are iterative histories of objectives, variables in model 1 and model 2 respectively.

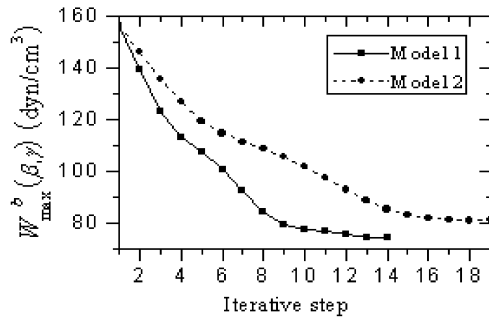


Fig.3 Iterative history of object

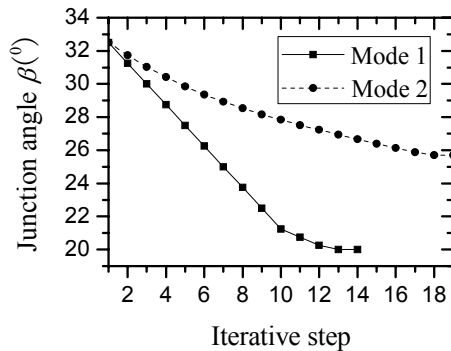


Fig.4 Iterative history of junction angle

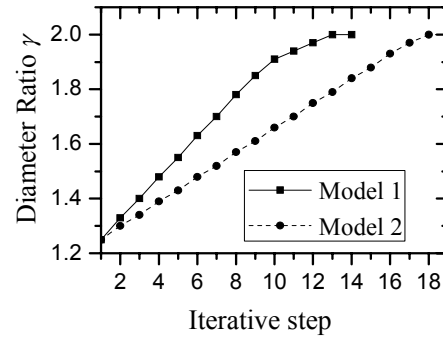


Fig.5 Iterative history of diameter ratio

IV. ANALYSIS OF RESULT AND DISCUSSION

The optimization result of model 1 shows that large diameter ratio and small junction angle may reduce WSSG along line *b* in the downstream of anastomosis and effectively improve the hemodynamics in CABG. Three typical cases of CABG were simulated in the present study. Figure 6 is the comparison of WSSG in these cases. Just as it shows: the model with parameter $\gamma = 2.0$ and $\beta = 20^\circ$ has the smallest and symmetrical WSSG along line *b* in CABG.

As concluded above, the model with large diameter ratio and small junction angle may improve the hemodynamics, however, model with the smallest junction angle is not the best choice in the CABG when synthetic factors are taken into account according to the result of model 2. It's reasonable to believe that model with the largest diameter ratio is not the best choice either, because the large thin venous graft may bring the distort transfiguration and large diameter ratio also means the large suture region and long seam [16], all those phenomenon ultimately lead more intimal hyperplasia damnification etc.[17] In addition, large diameter ratio may lead the sink of graft. Fig.7 and Fig.8 show

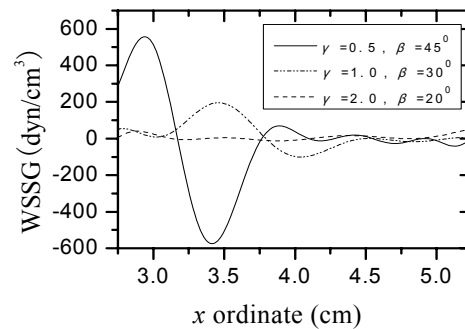


Fig.6 Comparison of WSSG

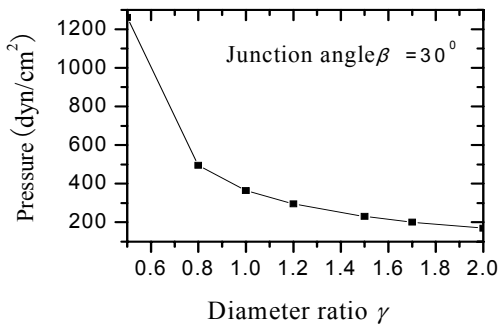


Fig.7 Influence of diameter ratio on the bypass graft

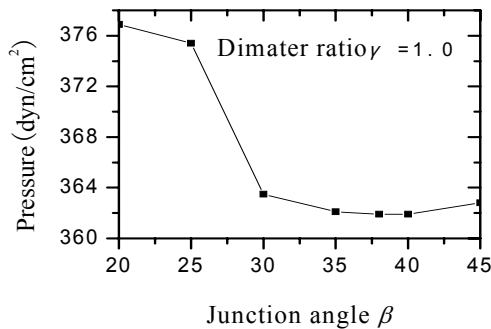


Fig.8 Influence of junction angle to the bypass graft

that graft-host diameter ratio and junction angle prominently influence the pressure of blood vessel. It is believed that the better result of optimization would be obtained with deep knowledge of the sink graft, when constrictions of pressure can be added. In this way, the success rate of CABG can also be improved remarkably. The reason influencing the success rate of CABG is complicated, so it is necessary to investigate the optimum result when all factors are taken into account.

The study is based on the rigid circular tube, so there are some errors compared with the real physical condition. Steinman's research shows that the largest WSS will slightly decrease in the distensible blood vessel, but difference of average WSS in time is unobvious between the rigid tube and distensible one. So the conclusion is acceptable [18].

V. CONCLUSION

There are many reasons influencing the success rate of CABG. Numerical simulation is a powerful tool to study the influence of geometrical factors, such as graft-host diameter

ratio and junction angle, on the hemodynamics of CABG. It is believed that structural optimization is an effective method in this field. The result of the optimization simulation in the present study indicates that the model of large graft-host diameter ratio and small junction angle has better hemodynamics. It is advisable to adopt large diameter ratio and small junction angle with help of clinical experiences in CABG surgery.

REFERENCES

1. Pedrini L, Pisano E, Donato DPM, et al. (1994) Late occlusion of aortofemoral bypass graft: surgical treatment. *Cardiovasc Surg* 2:763-766.
2. Glagov S. (1994) Intimal hyperplasia, vascular modeling and the restenosis problem. *Circulation* 89: 2888-2891
3. Bonert M, Myers JG, Fremes SE, et al. (2000) Influence of graft/host diameter ratio on the hemodynamics in sequential ITA anastomoses[A]. In: Conway TA. 2000 *Advances in Bioengineering*[C]. New York: American Society of Mechanical Engineers, 48: 269-270
4. Bassiouny HS, White S, Glagov S, Choi E, Giddens DP, Zarins CK. (1992) Anastomotic intimal hyperplasia: mechanical injury or flow induced. *J Vasc Surg* 15:708-717
5. Longest PW, Kleinstreuer C. Particle- hemodynamics modeling of the distal end-to-side femoral bypass: effects of graft caliber and graft-end cut. *Med Eng Phys*, 2003; 25: 843-858
6. Schneider JR, Zwolak RM, Walsh DB, Mcdanniel MD, Cronenwett, JL. (1991) Lack of diameter effect on short-term patency of size-matched Dacron aortobifemoral grafts. *J Vasc Surg* 13:785-791
7. Bonert M, Myers JG, Fremes S, et al. (2002) A numerical study of blood flow in coronary artery bypass graft side-to-side anastomoses. *Ann Biomed Eng* 30:599-611
8. Abbott WM, Green RM, Matsumoto T, et al. (1997) Prosthetic above-knee femoropopliteal bypass grafting: results of a multi-center randomized prospective trial. *J Vasc Surg* 25:19-28
9. Stonebridge PA, Prescott RJ, Ruckley CV. (1997) Randomized trial comparing infrainguinal polytetrafluoroethylene bypass grafting with and without vein interposition cuff at the distal anastomosis. *J Vasc Surg* 26: 543-550
10. Qiao A, Liu Y. (2006) Influence of Graft-Host Diameter Ratio on the Hemodynamics of CABG. *Bio-medical Materials and Engineering* 16: 189-201
11. Qiao A, Liu Y, Guo Z. (2006) Wall Shear Stresses in Small and Large 2-way Bypass Grafts. *Medical Engineering & Physics* 28: 251-258
12. Inzoli F, Migliavacca F, Pennati G. (1996) Numerical analysis of steady flow in aorto-coronary bypass 3-D model. *J Biomech Eng* 118:172-179
13. Cole JS, Watterson JK, O'Reilly MJG. (2002) Numerical investigation of the haemodynamics at a patched arterial bypass anastomosis. *Med Eng Phys* 24:393-401
14. Buchanan JR, Kleinstreuer C, Truskey GA, et al. (1999) Relation between non-uniform hemodynamics and sites of altered permeability and lesion growth at the rabbit aorto-celiac junction. *Atherosclerosis* 143:27-40
15. Yunkang Sui, Haibo Bai. (2005) Simulation Center of Engineering Numerical Value. *Journal of Machine Design* 22:10-11
16. Philip BD, David H, Thomas C, et al. (2001) Mechanical determinants of graft kinking. *Ann Vasc Surg* 15: 343-349

17. Loth F, Jones SA, Zarins CK, et al. (2002) Bassiouny. Relative contribution of wall shear stress and injury in experimental intimal thickening at PTFE end-to-side arterial anastomoses. *J Biomech Eng* 24:44-51
18. Steinman DA, Ethier CR. (1994) The effect of wall distensibility on flow in a two-dimensional end-to-side anastomosis. *J Biomech Eng* 116: 294-301

Author: Aike Qiao
Institute: College of Life Science & Bioengineering, Beijing University of Technology
Street: Pingleyuan 100, Chaoyang District
City: Beijing
Country: P. R. China
Email: qak@bjut.edu.cn

Numerical Simulation of Blood Flow in Stented Aneurysm using Lattice Boltzmann Method

X.J. Zhang, X.Y. Li and F. He

School of Mechanical Engineering and Applied Electronics Technology,
Beijing University of Technology, Beijing 100022, CHINA

Abstract — Hemodynamics are thought to play an important role in the creation, thrombosis, recanalization, regrowth and re-bleeding of cerebral aneurysms treated by endovascular means. Recently, the stents for cerebral aneurysms are expected to be flexible enough to prevent injuries in small diameters and intricate vessels. And the lattice Boltzmann method has received considerable interest as an efficient method of computing a variety of fluid flows, especially with complex geometrical configurations. Therefore, 2-dimensional mathematical model of cerebral aneurysm with stent were created. Furthermore, CFD calculations were performed by using lattice BGK model with the assumption of Newtonian fluid property for blood and the rigid wall property for the vessel and the aneurysm. The results suggest that stent prevents vortices driven directly by the parent vessel flow and that the ratio of the stent pore size to the aneurysm orifice size plays an important role in the formation of stented flow pattern, and small pore size is preferable for the aneurysm with large orifice though it causes a kind of orifice effect and prevents the flow reduction in the stented aneurysm with small orifice.

Keywords — Cerebral aneurysm, Stent, Lattice Boltzmann method, Hemodynamics.

I. INTRODUCTION

Blood flow dynamics are thought to be an important factor in the pathogenesis and treatment of cerebral aneurysms. Hemodynamic factors, such as pressure distribution, impingement force and wall shear stress, have been implicated in aneurysm growth and rupture [1]. And appropriate control of these hemodynamic factors in clinic may also govern the outcomes of endovascular therapies. Especially, stents have been used in minimally invasive treatments of aneurysms, as an alternative to heavy by-pass surgery. Stents are a tubular mesh made of some metal alloys weaved filaments. They are inserted with a guiding catheter into the supporting vessels and released right at the aneurysm location. However, their complex hemodynamics mechanisms involved in promotion of thrombosis are not yet well understood. The first experimental and clinical studies of this occlusion technique using stents in carotid aneurysms have been done in 1994 [2, 3], and several experimental and

numerical studies on stented flows have been reported. They emphasize the existence of large coherent vortex structures within lateral aneurysm models. However, they do not discuss the flow reduction mechanism (i.e. the total reduction of the flux through the stent) well. So this study is aim to investigate the mechanism of flow reduction by the stent implantation in aneurysm.

It has been demonstrated that advanced computational fluid dynamics (CFD) methods have the ability to predict velocity fields and other hemodynamic parameters on the aneurysms [4]. Furthermore, CFD methods are able to simulate conditions that do not currently exist and can, therefore, be used to predict the hemodynamic consequences of a surgical intervention [5]. Recently, the lattice Boltzmann method (LBM) [6] has received considerable interest in the last decade as an efficient method of computing a variety of fluid flows, especially, with complex geometrical configurations [7,8]. The solution of the lattice Boltzmann equation converges to the Navier-Stokes solution in the continuum limit (small Knudsen number). Thus, two-dimensional numerical analysis of local hemodynamics flow-reduction mechanism by stent implantation in cerebral aneurysms is presented, and the corresponding flow phenomena around the aneurysm are simulated using lattice BGK model.

II. LATTICE BOLTZMANN METHOD

A. Principles of lattice Boltzmann method

In traditional numerical methods normally partial differential equations (PDEs) are used to simulate fluid flow. These PDEs are discretized by finite differences, finite volumes or finite elements. The resulting algebraic equations or systems of ordinary differential equations are solved by standard numerical methods. Traditional Numerical simulations have serious drawbacks like long computation times, poor convergence and numerical instabilities.

LBM is developed as another computational method that is more efficient and it uses simple rules to represent the fluid flow rather than partial differential equations. LBM is a discrete computational method based upon the Boltzmann

equation. It considers a typical volume element of fluid to be composed of a collection of particles that are represented by a particle velocity distribution function at each grid point. In discrete time steps the fluid particles can collide with each other as they move.

B. Lattice Boltzmann BGK model

In the LBM, the state quantity or particle density is described as a continuous distribution function, and the evolution of the original lattice Boltzmann model consists of two steps: relaxation and streaming (Seen in Fig.1). In the relaxation step, distributions $f_\alpha(x, t)$ at grid node x relax to the equilibrium state $f_\alpha^0(x, t)$ according to the Bhatnagar-Gross-Krook (BGK) [9] rule. In the streaming process, distributions advect freely at their characteristic velocities e_α to the next site $x + e_\alpha \delta_t$. The evolution equation for the incompressible lattice BGK model can be described by

$$f_\alpha(x + e_\alpha \delta_t, t + \delta_t) - f_\alpha(x, t) = -\frac{1}{\tau} (f_\alpha(x, t) - f_\alpha^0(x, t)) \quad (1)$$

Where τ is the dimensionless collision relaxation time, and δ_t is the time step, respectively.

The fluid density ρ and velocity \mathbf{u} are obtained from the density distribution function $f_\alpha(x, t)$:

$$\rho = \sum_\alpha f_\alpha(x, t) \quad (2)$$

$$\mathbf{u} = \sum_\alpha e_\alpha f_\alpha(x, t) / \sum_\alpha f_\alpha(x, t) \quad (3)$$

Furthermore, applying to the Eq.(1) a second order Chapman-Enskog expansion, continuous equation for mass and momentum can be obtained. Precisely, mass conservation leads to the continuity equation:

$$\partial_t \rho + \nabla \cdot (\rho \mathbf{u}) = 0 \quad (4)$$

Moreover, the momentum conservation is expressed as a Navier-Stokes "like" equation [10]:

$$\rho \partial_t (\mathbf{u}) + \rho (\mathbf{u} \cdot \nabla) \mathbf{u} = -\nabla p + \nu \nabla^2 (\rho \mathbf{u}) \quad (5)$$

And the macroscopic pressure p can be calculated as

$$p = c_s^2 \rho \quad (6)$$

Where the c_s is the sound velocity, and the kinematic viscosity are defined by the equation

$$\nu = (2\tau - 1) \delta_x^2 / 6\delta_t \quad (7)$$

Where δ_x is the lattice constant size.

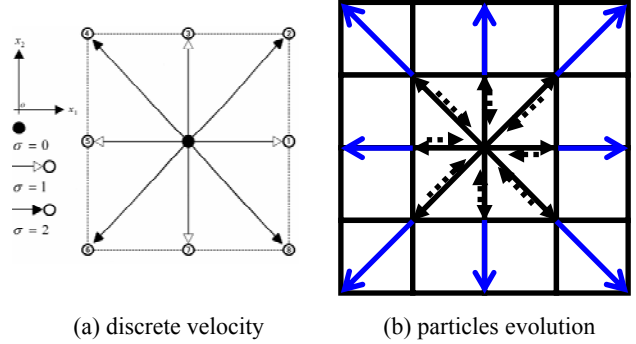


Fig. 1 Sketch of discrete velocity and evolution lattice in LBM (D2Q9)

Moreover, the density distribution functions in equilibrium state $f_\alpha^0(x, t)$ are designed so that the time averaged motion of the particles is consistent with the Navier-Stokes equation. And LBM could be applied to both two- and three-dimensional flows.

D2Q9 lattice BGK model is popular in 2-dimensional fluid flow. The discrete velocity (Seen in Fig.1) matrix of D2Q9 BGK model is

$$e_\alpha = \begin{bmatrix} 0 & 1 & 1 & 0 & -1 & -1 & -1 & 0 & 1 \\ 0 & 0 & 0 & 1 & 1 & 1 & 0 & -1 & -1 \end{bmatrix} \quad (8)$$

And corresponding equilibrium distribution function is

$$\begin{cases} f_0^0 = \frac{4}{9} \rho \left[1 - \frac{3}{2} u^2 \right] (\alpha = 0) \\ f_\alpha^0 = \frac{1}{9} \rho \left[1 + 3(e_\alpha \cdot u) + \frac{9}{2} (e_\alpha \cdot u)^2 - \frac{3}{2} u^2 \right] (\alpha = 1, 3, 5, 7) \\ f_\alpha^0 = \frac{1}{36} \rho \left[1 + 3(e_\alpha \cdot u) + \frac{9}{2} (e_\alpha \cdot u)^2 - \frac{3}{2} u^2 \right] (\alpha = 2, 4, 6, 8) \end{cases} \quad (9)$$

Thus the sound velocity c_s is equal to $\sqrt{3}/3$.

C. Computing methodology

For simplicity, blood flow in aneurysm is considered to be incompressible, homogeneous and pulsatile. Body forces such as gravity, boundary forces such as pressure in the brain and the wall elasticity are neglected. The fluid is assumed to be Newtonian. And corresponding boundary condition with a known pressure difference is used at inlet and outlet of the fracture aperture, where all fluid densities are propagated from non-occupied nodes along the lattice-connection lines to their next neighbors. The physical boundary condition at solid-fluid interfaces is the no-slip boundary condition, which in LBM is usually realized as bounce-back rule [11]. This is physically appropriate whenever the solid wall has a sufficient rigidity to prevent any net fluid motion at the wall. The complete bounce-back scheme is used to simulate the no-slip boundary condition,

which requires that when a particle distribution streams to a solid boundary node, it scatters back to the node it came from. The velocity vector of all fluid densities is inverted, so all the fluid densities will be sent back to the node where they were located before the last propagation step, but with opposite velocity vector.

Furthermore, we mainly consider two types of saccular aneurysms with different neck size in order to investigate the influence of the neck size on the velocity reduction based on the experimental observation [12]. The Reynolds number range in parent vessels 2-4 mm in diameter is between 100 and 300 and within the aneurysms is less or about 30 [12].

III. SIMULATIONS

Send your papers only in electronic form. Papers *must be uploaded* before the deadline. After a paper is accepted for oral or poster presentation, one of the authors must complete a registration form and pay the appropriate fees before the paper can be published in the Proceedings. Please pay attention to the registration deadline.

We have carried out two different benchmark simulations. The first benchmark considers unsteady flow in aneurysm without stent and validates the results against a conventional Navier-Stokes solver. The second benchmark uses this lattice Boltzmann model to simulate the blood flow in stented aneurysm. The general aim of these benchmark simulations is to demonstrate that the lattice Boltzmann yields accurate and robust results for applications related to hemodynamics and biomedical engineering.

Firstly, the effect of the inlet blood velocity waveform in human was mainly investigated. For the inlet condition, a pulsatile flow with a Womersley velocity profile, seen in Fig.3(a), was obtained with transcranial Doppler measurement (0.6 m/s at peak systole, 0.24 m/s at end diastole, and 57 bpm). This inlet velocity condition was applied to all aneurysms (mean Reynolds number, 400; mean Womersley number, 3.90). In order to confirm numerical stability, the calculation was performed for 50 cardiac cycles and the result at the last cardiac cycle was used for the analysis.

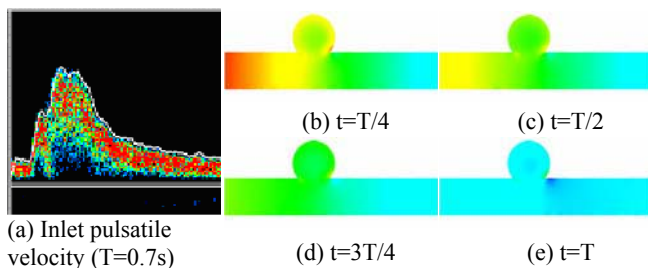


Fig. 2 Evolution of pressure with time in central plane of straight vessels with aneurysm

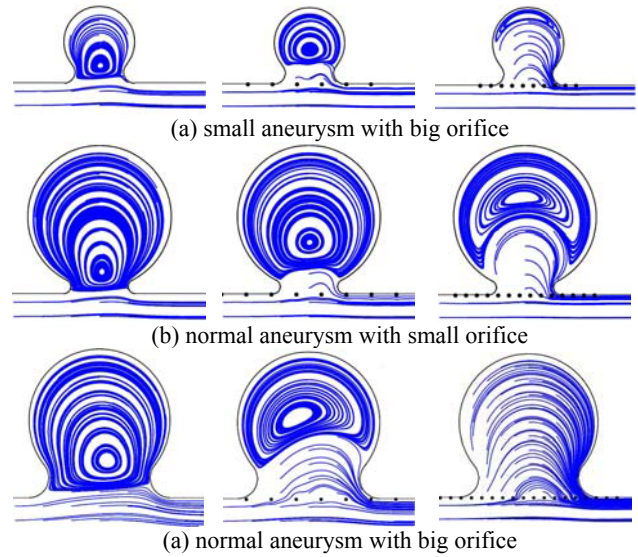


Fig. 3 Streamlines in stented aneurysm flow

The pressure distributions of the central plane with four cross-sectional times during the cardiac cycle are presented in Fig.2. With the change of pressure in the inlet, the corresponding pressure distribution in the straight vessel with aneurysm transformed with time, but the position with the relative maximum pressure in the aneurysm is nearly stationary. In other words, it is fixed on the local spot of bloodstream impact, which is consistent to traditional Navier-Stokes results [13].

Secondly, the hemodynamic effects of stent implantation on aneurysms with different orifices were investigated. Fig.3 shows the variation of the flow patterns in different stented aneurysms with the large orifice and the small orifice using the streamline.

Compared with the vortex in the nonstented aneurysm which is driven directly by the flow in the parent vessel, as seen in Fig.3, the vortex in the stented aneurysm is not driven by the orifice flow directly because the velocity at the orifice does not have the enough magnitude to drive it. It can be thought that this stented vortex is driven by the existence of the pressure difference in the aneurysm where the percolation dominant velocity, which is the velocity at the no-vortex part in the aneurysm, is small in comparison with the magnitude of the pressure difference.

Furthermore, Fig.3 shows that not only the stent pore size but also the aneurysm orifice size determines the vortex evolution in the aneurysm, thus the ratio of the stent pore size to the aneurysm orifice size is the critical value, which makes the flow reduction effect in aneurysm with small orifice size smaller than that with big orifice size. This insufficient reduction is due to the small number of stent

struts at the aneurysm orifice. This numerical analysis confirms well the experimental observations [12].

IV. CONCLUSION

Two-dimensional numerical simulation results using the lattice BGK model of D2Q9 are presented. The results show that stent prevents vortices driven directly by the parent vessel flow and that the ratio of the stent pore size to the aneurysm orifice size plays an important role in the formation of stented flow pattern. We need to consider aneurysm size when we choose the suitable stent for flow reduction. The desirable stent should be designed to decrease the direct influence of the main flow. We need the sufficient number of stent struts at the aneurysm orifice, therefore small pore size is preferable for the stented aneurysm with large orifice, and however it causes a kind of orifice effect and prevents the flow reduction in the small orifice aneurysm. These numerical observations can explain well the experimental results [12]. This conclusion suggests that lattice BGK model has the potential to be a useful clinical tool for the prediction of the hemodynamics in cerebral aneurysm.

ACKNOWLEDGMENT

This work was supported by the National Natural Scientific Foundation of China (Grant No: 10372010).

REFERENCES

- Molyneux KR, Yu LM, Clarke M et al. (2005) International subarachnoid aneurysm trial (ISAT) of neurosurgical clipping versus endovascular coiling in 2143 patients with ruptured intracranial aneurysms: a randomised comparison of effects on survival, dependency, seizures, rebleeding, subgroups, and aneurysm occlusion. *Lancet* 366:809-817.
- Marks MP, Dake MD, Steinberg GK et al. (1994) Stent placement for arterial and venous cerebrovascular disease: preliminary clinical experience. *Radiology* 191:441-446.
- Wakhloo AK, Schellhammer F, Vries J de. et al. (1994) Self-expanding and balloon-expandable stents in the treatment of carotid aneurysms: an experimental study in a canine model. *AJNR Am J Neuroradiol* 15:493-502
- Choi IS, David C (2003) Giant intracranial aneurysms: development, clinical presentation and treatment. *European Journal of Radiology* 46:178-194.
- Hassan T, Ezura M, Timofeev EV et al. (2004) Computational simulation of therapeutic parent artery occlusion to treat giant vertebrobasilar aneurysm. *AJNR Am J Neuroradiol* 25:63-68.
- McNamara GR, Zanetti G. (1988) Use of the lattice Boltzmann equation to simulate lattice-gas automata. *Phys Rev Lett* 61:2331-2335.
- Hirabayashi M, Ohta M, Rüfenacht DA et al. (2003) Lattice Boltzmann analysis of the flow reduction mechanism in stented cerebral aneurysms for the endovascular treatment. *ICCS LCNS 2657:1044-1053*
- Chopard B, Ouedraoui R, Daniel AR (2006) A lattice Boltzmann simulation of clotting in stented aneurysms and comparison with velocity or shear rate reductions. *Mathematics and Computers in Simulation* 72:108-112
- Bhatnagar PL, Gross EP, Krook MA (1954) Model for collision processes in gases. I. Small amplitude processes in charged and neutral one-component system. *Phys Rev* 94:511-525.
- Qian YH, Orszag SA (1993) Lattice BGK models for the Navier-Stokes equation: nonlinear deviation in compressible regimes. *Euophys Lett* 21:255-259.
- Gallivan MA, Noble DR, Georgiadis JG et al. (1997) An evaluation of the bounce-back boundary condition for lattice Boltzmann simulations. *Int J Num Meth Fluids* 25:249-263.
- Lieber BB, Stancampiano AP, Wakhloo AK (1997) Alteration of hemodynamics in aneurism models by stenting: influence on stent porosity. *Ann Biomed Eng* 25: 460-469.
- Aenis M, Stancampiano AP, Wakhloo AK et al. (1997) Modeling of flow in a straight stented and nonstented side wall aneurysm model. *J Biomech Eng* 119:206-212

[Corresponding author address]:

Author: Xiao-jun ZHANG
 Institute: Beijing University of Technology
 Street: Pingleyuan 100, Chaoyang District
 City: Beijing
 Country: CHINA
 Email: xjzhang@bjut.edu.cn

Improved Experimental System for Analyzing Biomechanical Properties of Iris Tissue

Xuefeng Bo, Haiying Quan*, Zhicheng Liu*

Institute of Biomedical Engineering, Capital Medical University, Beijing, China

Abstract — We designed a experimental system based on stereo vision in order to analyze quantitatively biomechanical properties of iris tissue without destroying the structure and function of iris. This experimental system, which was designed and improved upon the primary experimental device, consists of three vidicons assembled with tripod, a circular desk scaled from one degree to 360 degrees, a signal generator, a special lamp-house, a pupil-blocking simulating device, a negative pressure device, a constant temperature trough assembled with a fixed bracket, a load-pressure trough and a small electric elevator. The new experimental system could simulate the pupil-blocking phenomena. The animal research was proved that the results were consistent with the clinical observation. The new experimental system could also obtain continuous pressure data and corresponding 2D image of iris from three different degrees in the course of load-pressure. The experimental system not only is an ideal experimental system to measure biomechanical properties of iris tissue and pupil-blocking force quantitatively, but also can be used to research small distortion characteristic of other biologic material.

Keywords — biomechanical properties of iris, pupil-blocking phenomenon, experimental system.

I. INTRODUCTION

The pupil-blocking force is deemed to the important factor of causing primary angle-closure glaucoma[1]. But there wasn't optical simulating device, which simulates the course of causing primary angle-closure glaucoma, and precise method of measuring pupil-blocking force. So scientific researchers couldn't adequately know the function of pupil-blocking force and the change of iris' structure and function in the course of causing primary angle-closure glaucoma.

According to the principle of causing pupil-blocking and the anatomical structure of eyeball, Zhicheng Liu, Ding Lin, etc^[2,3,4,5] devised a simulating device and simulated the course of causing primary angle-closure glaucoma through simulating pupil-blocking force and stated a method of quantitative researching biomechanical properties iris tissue.

But primary experimental device had single angle of view to acquire images. It caused shelter phenomenon of iris when pressure was increased and iris was inflated. The

experimental device of single visual angle couldn't acquire images in detail. We couldn't obtain exact 3D data during passive iris deformation and couldn't construct a appropriate model of iris and analyze biomechanical properties of iris using the finite element method. So we designed a experimental system based on stereo vision. This experimental system, which was designed and improved upon the primary experimental device, can analyze quantitatively biomechanical properties of iris tissue without destroying the structure and function of iris.

II. EXPERIMENTAL SYSTEM

The experimental system consists of three vidicons assembled with tripod, a circular desk scaled from one degree to 360 degrees, a signal generator, a special shadowless lamp-house, a pupil-blocking simulating device, a negative pressure device, a constant temperature trough assembled with a fixed bracket, a load-pressure trough and a small electric elevator.

A. Sampling image system

Three vidicons were fixed symmetrical upon the circular desk and each couple vidicons form 120 degrees angle. The height and the vertical gradient of the vidicons can be adjusted in order to avoid shelter phenomenon of iris and obtain clear images of passive iris deformation. The signal generator, which offers a synchronous signal to achieve picture synchronization, was connected to three vidicons by trigger line. We can adjust frequency of obtaining images through setting the output of the signal generator. Above-mentioned sampling image system was demonstrated according to Fig. 1.

We use shadowless lamp in order to avoiding accumulation of heat because high temperature can affect active characteristics of iris sample. At the same time, several lamp-houses irradiate the sample from different position so that we can reduce shelter area due to experimenter, equipment and passive iris deformation. Furthermore, we can adjust brightness according to demand of the experiment.

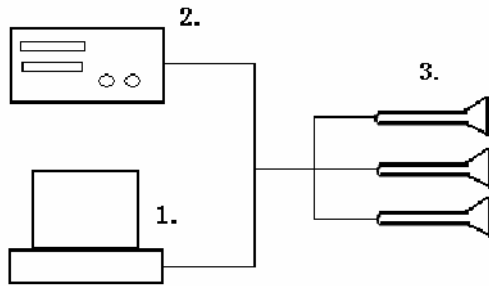


Fig.1 Sampling image system: 1. computer, 2. signal generator, 3. vidicons

B. Experimental device

The pupil-blocking simulating device, which simulates anatomical structure of eyeball according to the principle of causing pupil-blocking force, was fixed inside the constant temperature trough using the fixed bracket. At the same time, the negative pressure device was used to suck the iris through some small laser-hole of the pupil-blocking simulating device in order to simulate the pupil-blocking phenomena. We connected the pupil-blocking simulating device to the load-pressure trough using the tube. Then we hoisted the load-pressure trough using the electric elevator. According to the principle of connected vessels, we can calculate different pressure between the constant temperature trough and the load-pressure trough. We simulate the anterior chamber and using the liquid of the constant temperature trough and simulate the posterior chamber and using the liquid of the load-pressure trough. Then we can simulate and compute different pressure between the anterior and posterior chamber. Above-mentioned devices were demonstrated according to Fig. 2.

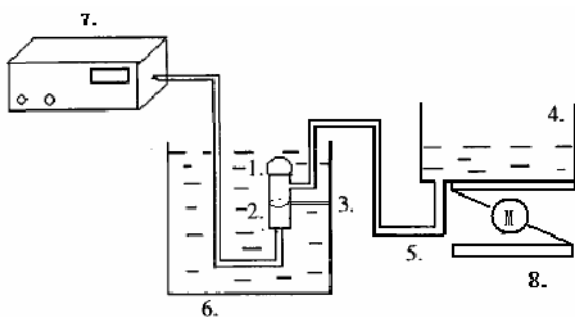


Fig.2 Experimental device: 1. sample of rabbit's iris, 2. pupil-blocking simulating device, 3. fixed bracket, 4. load-pressure trough, 5. tube, 6. constant temperature trough, 7. negative pressure device, 8. small electric elevator

III. CONCLUSIONS

We could obtain serial image list. An image of experiment is displayed in Fig. 3.



Fig.3 Image of experiment

We select character from 2D image of iris and stereo match these corresponding characters. After traditional camera calibrating, we can computer the parallax of corresponding characters and obtain the depth of dimensional characters. Then we interpolate depth based on primary sparse depth and obtain 3D data of iris during the passive iris distortion. We could obtain the iris' biomechanical property with the pupil-blocking force quantitatively using the finite element method.

REFERENCES

1. Chul H,Ki Ho. Evaluation of papillary block component in angle-closure glaucoma. *Jpn J Ophthalmol*,1996,40:239-243.
2. Zhicheng Liu, Ding Lin, Yuhui Wang, etc. A study of experiment method to measure mechanical property of iris tissue. *Chinese Journal of Medical Physics*, 2001, Vol. 18, No.4: 234-248.
3. Zhicheng Liu, Ding Lin, Yuhui Wang, etc. An experimental research on biomechanical properties of iris tissue of rabbits. *Chinese Journal of Medical Physics*, 2002, Vol. 19, No.1: 40-42.
4. Xiaohua Liu, Chen Chen, Kunya Zhang, etc. An Experimental Method to Measure Mechanical Properties and Pupil-blocking Force of Iris Tissue Quantificationlly. *Chinese Journal of Medical Physics*, 2005, Vol. 22, No.1: 382-403.
5. Chen Chen, Xiaohua Liu, Ding Lin, etc. Design of a device for measuring biomechanical properties of iris tissue and pupil-blocking force. *Clinical Ophthalmia Research*, 2006, Vol24, No.2: 206-208.

Effect of Dynamic Stabilization Device Stiffness on Disc Loading under Compression

Q.H. Zhang, E.C. Teo

School of Mechanical & Aerospace Engineering, Nanyang Technological University, Singapore

Abstract — An anatomically realistic three-dimensional (3D) finite element (FE) model of L4-L5 motion segment was created. The intact model was further modified to simulate two different disc degeneration grades, slight and moderate, at the L4-L5 segment. The implanted models were accordingly developed by incorporating a pair of 6mm diameter straight longitudinal rods position bilaterally into the degenerated models. In order to study the effect of implant stiffness on disc loading under compression, the stiffness of the longitudinal rod was varied between 1 and 83,000 N/mm in discrete steps. The intact, degenerated and implanted models were then exercised by applying 3,000N compressive force on the superior surface of L4 vertebra to investigate the load transmission characteristics of different implants. The results showed that the side effect of a degenerated disc is obvious for the lumbar segment load bearing capacity. The stiffness of the segment was increased due to the stiffer disc, which is caused by the severity of disc degeneration. The implant stiffness of lower than 2,000N/m has greater effect on disc loading and segment behavior. For an implanted model, the predicted annulus stress is close to the intact model when the implant stiffness is around 2000N/m. In addition, the effect of stiffness became less significant beyond this value. For dynamic stabilization purpose, the stiffness implant is suggested to be lower than 2000N/m.

Keywords — Finite element, Dynamic stabilization, Disc, Compression.

I. INTRODUCTION

For a relatively slight degeneration patient, the new concept of dynamic stabilization becomes more and more popular since it was introduced in 1980s. Dynamic stabilization devices may be defined as a system, which would favorably alter the movement and load transmission of a spinal motion segment, without the intention of fusing segment. The hypothesis behind such a system is that the control of abnormal motions and more physiological load transmission would relieve pain, and prevent adjacent segment degeneration, and a remote expectation for dynamic stabilization is that, once normal motion and load transmission is achieved, the damaged disc may repair itself, unless the degeneration is too advanced [1]. Based on this concept, some dynamic stabilization devices, such as Graf ligament and Dynesis device, etc., have been designed and put into clinical application.

The previous studies investigating the dynamic stabilization devices generally examine the effect of specific device on the load-displacement response of implanted segment under the rotational moment [2-4]. Few studies investigate the load relief capability of the devices for the implanted segment under compression. Different from the totally load bearing implants, such as fusion and disc replacement device, the nature of dynamic stabilization device is the load sharing for the degenerated disc. During tasks of daily living, the lumbar spine withstands compressive loads of very high magnitude due to muscle activation along with significant amounts of motion. Compressive loads can easily approach several thousand newtons during some lifting tasks [5]. Accordingly, it is important to study the load transmission characteristics of the dynamic stabilization device under compressive force. In the current study, a geometrically accurate FE model of L4-L5 lumbar motion segment was developed and validated under axial compressive loading. The biomechanical effect of the stiffness of posterior implanted dynamic stabilization device was accordingly investigated by examine the responses of healthy, degenerated and implanted models under compressive force.

II. MATERIALS AND METHODS

An anatomically realistic three-dimensional (3D) FE model of L4-L5 motion segment was created based on embalmed vertebral specimens from a 56-year-old male subject. In the current model, the vertebral body was modeled as a cancellous core with a cortical shell whose thickness was assumed to be 1.0mm. One cartilaginous endplate with a thickness of 0.5mm was assumed at the superior and inferior surfaces of each intervertebral disc, respectively. For the intervertebral disc, the nucleus pulposus portion was assumed to occupy approximately 48 percent of the disc's cross sectional area, which fell in the range reported in the literature [6] and simulated to be nearly incompressible with a poisson's ratio of 0.4999 and Young's modulus of 1MPa. The annulus fibrous was modeled as a composite with a matrix of homogeneous ground substance reinforced by annulus fibers. To create the lordosis of the lumbar-sacral spine, different values were assigned to anterior and posterior disc heights according to the range reported in literature [7].

Table 1 Material properties used for various components in current model.

Components	Young's Modulus (MPa)	Poisson's Ratio
Spine		
Cortical Bone	12,000.0	0.29
Cancellous Bone	100.0	0.29
Endplates	500.0	0.30
Posterior Element	3,500.0	0.29
Annulus	4.2	0.45
Nucleus	1.0	0.499
Annulus fiber	500	0.30
Implants		
Cap & Wires	110,000.0	0.30
PCU	8.6	0.47
Pedicle Screw	110,000.0	0.30

The ligaments groups were not incorporated in the model since only compressive force was considered in current study. The material properties used in this study are listed in Table 1 [8-10]. The intact L4-L5 model was validated against experimental results in terms of load-displacement response under axial compression. As for the loading and boundary conditions, all nodes pertaining to the bottom surface of the L5 vertebral body were fixed. An axial compressive force of 3,000N, which represents the lower limit of the range of load at fracture of lumbar spine [10], was applied to the top surface of the L4 vertebral body.

Subsequently, the validated intact model was further modified to simulate two different disc degeneration grades, slight and moderate, at the L4-L5 segment, corresponding to the general scope of dynamic stabilization device application. For Grade I, the elastic modulus of the disc nucleus was two times the elastic modulus of the annulus in the intact model and the Poisson's ratio was adopted to be the same as that of the annulus [11-13]. The Grade II included Grade I changes, in addition, the elastic modulus of disk annulus was assigned two times the value of disk annulus in the intact model, and the annulus fiber volume was reduced by 25% from the value of the intact model [13]. The implanted models were accordingly developed by incorporating a pair of straight longitudinal rods with a diameter of 6mm (Fig.1) bilaterally into the degenerated models. In order to study the effect of implant stiffness on disc loading under compression, the stiffness of the longitudinal rod was varied between 1 and 83,000 N/mm in discrete steps. The latter value represents titanium alloy. The two end of each rod were connected with the pedicle using solid element to simplify the screw fixation of the implant into pedicle. Fig.1 showed the completed implanted L4-L5 motion segment with paired posterior dynamic stabilization implants.

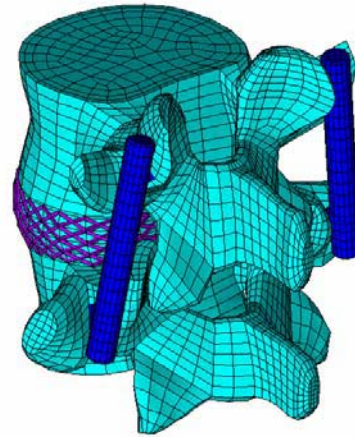


Fig. 1 Finite element model of the implanted L4-L5 motion segment.

The degenerated and implanted models were then exercised under the same loading configuration as that applied to the healthy model of L4-L5 in validation study to investigate the load transmission characteristics of different implants by comparison of the load-displacement curves and the compressive stress distribution of annulus from various models.

III. RESULTS & DISCUSSIONS

The comparison of the predicted load-displacement relationships of the intact L4-L5 segment under axial compression against experimental data was shown in Fig.2. It can be found that the FE predicted displacement-force curve appeared to possess the general nonlinear character of the experimental results [14-16] and fell within the mid-range of the experimental scatter, which testified that the current L4-L5 model was justified for further biomechanical analysis.

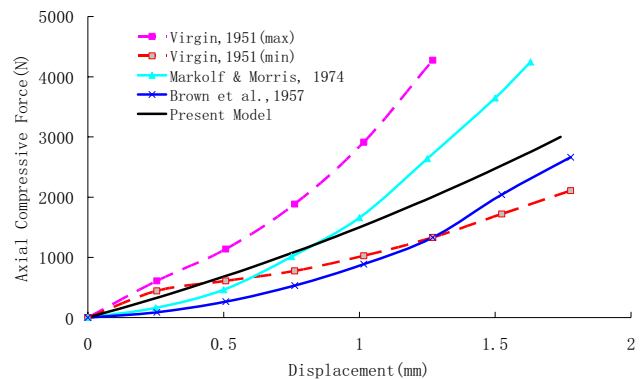


Fig. 2 Comparison of predicted load-displacement curve of normal L4-L5 segment under compression versus experimental results.

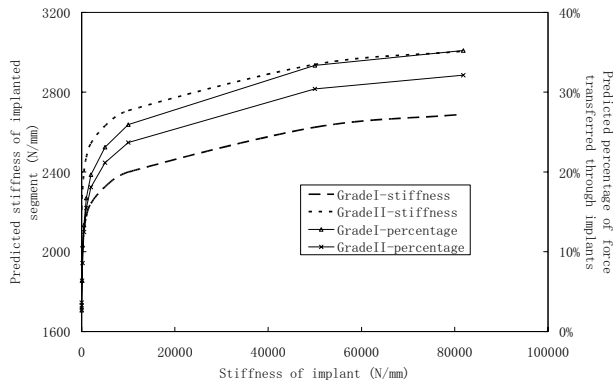


Fig. 3 Effect of implant stiffness on the predicted overall segment stiffness and the percentage of compressive force transferred through implants under 2000N compressive force.

The simulated degenerated models were stiffer than the normal segment. The predicted stiffness of the simulated Grade I and II degenerated segment were 5% and 21% higher than that of intact model, respectively. The implants further increased the stiffness of the implanted L4-L5 segment. As shown in Fig.3, the percentage of compressive force shared by the implants increase with the increment of implant stiffness, which resulted in the increase of the predicted overall segment stiffness. It can be found that the increase of segment stiffness and force shared by implants were most obvious among the implants with lower stiffness value. For any specific curve, the calculated slope of the part corresponding to implants stiffness below 2,000N/mm can be around 35 times of that obtained from the part beyond 5,000N/mm. It is obvious that the force transferred through implant was related with the stiffness of the implant and degeneration grade of the disc. The stiffer of the implant or the lower severity of the disc degeneration, the implant will share more load.

The goal of dynamic stabilization is to stabilize the motion segment with motion preservation. But the definition of spinal instability and the ideal mechanism of dynamic stabilization are not clear as yet. It has not been clearly defined in the literature how much restriction of motion and how much disc unloading are optimum. Fig.4 further examined the effect of implant stiffness on the disc stress. As shown in Fig.4a, a circular path was chosen along the middle layer of the disc, which begins from a node at the posterior part and goes through left lateral, anterior, right lateral and back to the node closest to the beginning node. Along the circular path, the compressive stress values variation of the normal model, Grade II degenerated model and implanted models with implant stiffness of 200N/mm, 2000N/mm and 50,000N/mm under 2,000N were shown in Fig.4b. It can be seen that, for the intact model, the highest stress occurred at

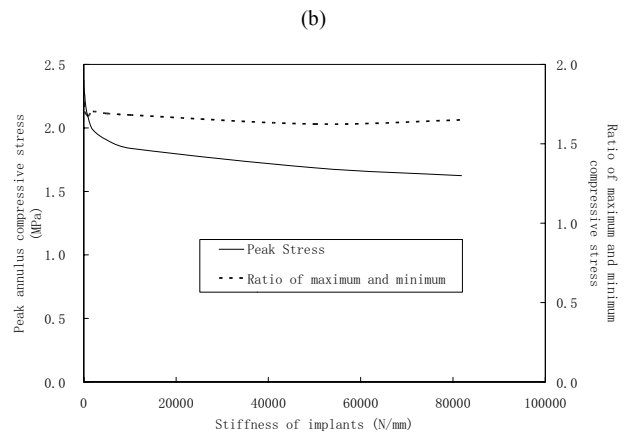
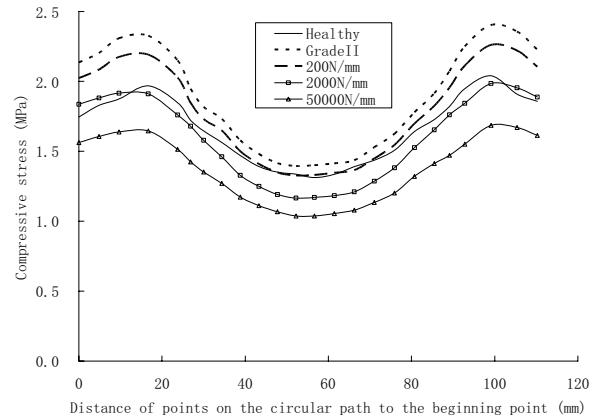
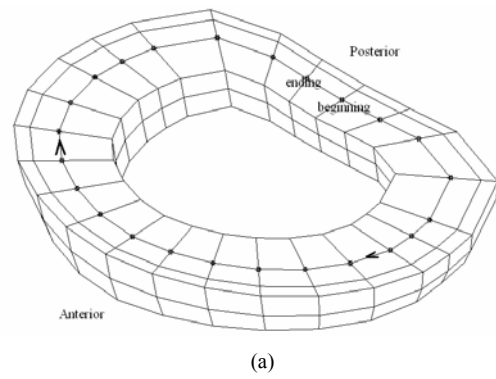


Fig. 4 Comparison of predicted annulus compressive stress distribution under 2000N compressive force from different models. (a) Plot to show the path chosen for compressive stress value extraction. (b) Comparison of predicted annulus stress along the path among healthy, grade II degeneration and some chosen implanted grade II degenerated models under 2000N force; (c) Effect of implant stiffness on the maximum annulus compressive stress and ratio of maximum and minimum compressive stress under 2000N force.

the posterior-lateral part of the disc, which was predicted as 2.0MPa, followed by the posterior and anterior parts. The ratio of the maximum stress to minimum one was less than 1.3. The overall stress distribution pattern was not changed in the degenerated and implanted models, but the stress magnitude and uniformity of stress distribution was significantly altered. The maximum annulus stress of Grade II degeneration model was increased to 2.4MPa, while the ratio of maximum to minimum stresses was increased to 1.8. Such prediction is consistent with the observations obtained from previous *in vivo* studies [17]. Such irregular load distribution may lead to accelerated degeneration of the annulus, further decreasing its ability to resist shear forces, which will ultimately place additional stress on the facet joints and may lead to progressive degenerative changes. Combine with Fig.4c, it is obvious that the implants can effectively reduce the overall stress magnitude in disc annulus. In addition, the effect of implant stiffness on maximum disc stress presents similar trend with those shown in Fig.3. However, the non-uniformity of the disc stress distribution was hardly improved with the implantation. Even for the implanted model with rigid rod (83,000N/mm), the ratio of maximum and minimum stress was only 5% lower than that of degenerated model.

IV. CONCLUSIONS

The side effect of a degenerated disc is obvious for the lumbar segment load bearing capacity. The stiffness of the segment was increased due to the stiffer disc, which is caused by the severity of disc degeneration. The implant stiffness of lower than 2,000N/m has greater effect on disc loading and segment behavior. For an implanted model, the predicted annulus stress is close to the intact model when the implant stiffness is around 2000N/m. In addition, the effect of stiffness became less significant beyond this value. For dynamic stabilization purpose, the stiffness implant is suggested to be lower than 2000N/m.

REFERENCES

1. Smith J, Sengupta, D. (2005) Dynamic stabilization device in the treatment of low back pain. *Neurol India* 53(4), 466-474.
2. Quint U, Wilke HJ, Loer F. et al (1998) Laminectomy and functional impairment of the lumbar spine: the importance of muscle forces in flexible and rigid instrumented stabilization—a biomechanical study *in vitro*. *Eur Spine J* 7:229-238.
3. Niosi CA, Zhu QA, Wilson DC. et al (2006) Biomechanical characterization of the three-dimensional kinematic behavior of the Dynesys dynamic stabilization system: an *in vitro* study. *Eur Spine J* 15:913-922.
4. Rohlmann A., Burra NK, Zander T. et al (2007) Comparison of the effects of bilateral posterior dynamic and rigid fixation devices on the loads in the lumbar spine: a finite element analysis. *Eur Spine J* Aug;16(8):1223-31.
5. Rohlmann A, Bergman G, Graichen F. et al (1997) Comparison of internal spinal fixation devices measured *in vitro* and *in vivo*. *Med Eng Phys* 19 (6), 539-546.
6. Panjabi MM, White AA (1990) *Clinical biomechanics of the spine*. 2th ed. Lippincott-Raven.
7. Brinckmann P, Grootenboer H. (1991) Change of disc height, radial disc bulge, and intradiscal pressure from discectomy. *Spine*16:641-6.
8. Goel VK, Kim YE, Lim TH et al (1988) An analytical investigation of the mechanics of spinal instrumentation. *Spine* 13:1003-1011.
9. Lavaste F, Skalli W, Robin S. et al (1992) Three-dimensional geometrical and mechanical modelling of the lumbar spine. *J. Biomechanics* 25(10):1153-1164.
10. Shirazi-Adl A, Shrivastava SC, Ahmed AM. (1984). Stress analysis of the lumbar disc-body unit in compression: a three-dimensional nonlinear finite element study. *Spine* 9(2), 120-134.
11. Kim YE, Goel VK, Weinstein JN et al (1991) Effect of disc degeneration at one level on the adjacent level in axial mode. *Spine* 16:331-335.
12. Iatridis JC, Setton LA, Weidenbaum M et al (1997) Alterations in the mechanical behavior of the human lumbar nucleus pulposus with degeneration and aging. *J Orthop Res* 15:318-22.
13. Kumaresan S, Yoganandan N, Pintar FA et al (2001) Contribution of disc degeneration to osteophyte formation in the cervical spine: a biomechanical investigation. *J Orthop Res*. 19(5):977-84.
14. Brown T, Hansen RJ, Yorra AJ. (1957) Some mechanical tests on the lumbosacral spine with particular reference to the intervertebral discs. *J Bone Joint Surg* 39-A(5), 1135-1164.
15. Markolf KL, Morris JM. (1974) The structural components of the intervertebral disc. *J Bone Joint Surg* 56-A(4), 675-687.
16. Virgin WJ (1951) Experimental investigations into the physical properties of the intervertebral disc. *J Bone Joint Surg* 33B(4), 607-611.
17. McNally DS, Shackelford IM, Goodship AE et al (1996) *In vivo* stress measurement can predict pain on discography. *Spine* 21:2580-7.

An AAA-ICT Used to the Single Trial of SEP

Y. Wang, Z.X. Xie, Z.F. Wang, H. Liu and Y.H. Liu

Department of Biomedical Engineering in Chongqing Medical University, Chongqing, China

Abstract — A traditional method to extract human somatosensory evoked potential (SEP) is commonly averaging theory. Due to the defects of traditional averaging theory, what's more, extracting SEP usually needs tens or hundreds times for averaging, we proposed an auto-reference, auto-correlative and adaptive interference cancellation theories and techniques (AAA-ICT) used in the single trial of somatosensory evoked potential (SEP) on the basis of analyzing the character of the spontaneous electroencephalo-signal (S-EES) and the special environment of extracting evoked potential (EP). This method avoids the defects of the traditional averaging theory for extracting SEP. The extracted SEP of single trial does not contain the averaging component and direct current component. Meanwhile the single trial of SEP describes more exactly about the differences of the latency and amplitude of SEP in detail.

Keywords — SEP, single trial, AAA-ICT.

I. INTRODUCTION

Somatosensory evoked potential (SEP) is an electric reaction of superior center which is caused by the stimulation to peripheral nerve (PN) [1]. It stands for the bioelectric changes of superior center on the particular functional status. Through this noninvasive technique of SEP, it can show the conduction and functional status of corresponding neuraxon at different level to a certain degree. Also it can provide exactly quantitative information about the conduction function of certain nerves.

SEP is the bioelectric changes which is caused by special stimulation to the human sensing system in encephalic region [2]. But the amplitude of SEP is very small. It is covered in background electroencephalo-signal which is much bigger than SEP. Because the signal to ratio is very low, we need special method to exact SEP from the background electroencephalo-signal. At present, averaging technique is usually used in clinical medicine. But this averaging theory has defects. The exacted SEP is the combination of tens or even hundreds times evoked potentials. It lost the details of every single SEP.

Some work of single trial belongs to few trials [7]. Some work depends on the averaging results [8]. What's more, some theory formula is not proved rigorously [9].

On the basis of analyzing the defects of traditional averaging theory for extracting SEP and the works of extracting evoked potential, knowing of the characteristic of spontane-

ous electroencephalo-signal (S-EES) and the special environment of extracting evoked potential (EP), we proposed an auto-reference, auto-correlative and adaptive interference cancellation theories and techniques (AAA-ICT) used in single trial of SEP

II. INSTRUMENT AND METHOD

2.1 AAA- ICT

AAA-ICT: Auto-reference and Autocorrelation and Adaptation Interference Cancellation Theories and Techniques.

2.1.1 The defects of traditional averaging theory for extracting SEP

(1) Since the S-EES include some deterministic waveform components used in clinic diagnosis [3] such as δ wave: 0.5~3Hz, θ wave: 4~7Hz, α wave: 8~13Hz, β wave: 14~31Hz and so on, It does not meet the condition that the average value is zero. Therefore, the SEP contains the averaging component and direct current (DC) component [10] in S-EES. Especially the DC component can not be canceled by averaging technique and can only be canceled by interference cancellation technique.

(2) The average of SEP cancels the differences of the latency and amplitude of SEP among every single stimulation. Thus the averaging result can not provide exact, short-duration and detailed information.

2.1.2 The basic hypothesis of AAA- ICT

(1) The S-EES, considered as the background interference, bears the chaotic characteristics of self-similarity and infinite circle and incomplete repetition. Therefore we can always find a certain segment in S-EES which have enough similarity to the evoked potential so that we can cancel the background electroencephalo-signal (B-EES) concluded in the evoked electroencephalo-signal (E-EES) as much as possible. Only residual, for example, evoked component SEP, is related to the stimulation.

(2) The relationship between SEP and B-EES is additive.

(3) It does not need any prophetic hypothesis to the character of SEP.

2.1.3 The particular circumstance of exacting SEP

The environment of SEP has the following features: The stimulus (evoked) signal is controllable and successively generated. Electroencephalo-signal(EES) is always generated continuously. The EES which does not send stimulus signal is called spontaneous electroencephalo-signal (S-EES). The EES that is generated after sending stimulus signal is called evoked electroencephalo-signal(E-EES). EES is acquired from the scalp by the specially made electrode. As the reference signal, the S-EES and E-EES can be acquired time-sharing. This promises that we can acquire enough time reference signal at the same electrode position where we acquired the E-EES. Therefore, we call the reference signal that acquired at the same electrode the auto-reference signal. The key point to be successful of this technique is to acquire the auto-reference in the same environment as the E-EES.

2.1.4 The basic theory of AAA-ICT

The basic principle of AAA-ICT is shown in Fig.1. In Fig.1, the dashed line of acquiring reference signal represents that in E-EES X(n), they are from the same set of electrodes. It mainly has three steps. I. From the starting point (q=0) of REF(q), the moving correlation between X(n) and REF_i(n) in REF(q) are calculated point by point. And then we choose and output the most correlative reference signal segment REF_m(n) between X(n) and REF(q); II. According to the rule of the minimum power, the cancellation factor W is computed and output W*REF_m(n); III. Completing the cancellation between X(n) and W*REF_m(n) and outputting EP(n) at last. In order to make this technique has general significance, we did not use individual symbol of EPs.

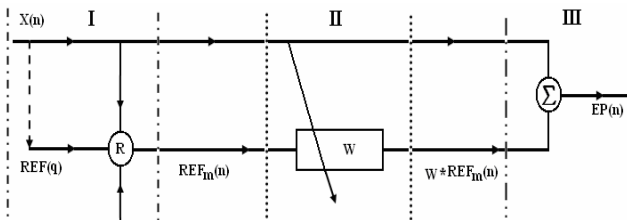


Fig. 1 The scheme of AAA-ICT

2.1.5 The basic calculation of AAA-ICT

(1)Auto-reference: we call the reference signal that is acquired from the same electrode system the auto-reference signal.

(2)Auto-correlation: Calculating and finding the signal segment of reference signal REF(q), which has the best

correlation with the E-EES[4]. Supposing that the length of REF(q) is Q, the length of X(n) is N, where Q>>N, shown in Fig.2. From the starting point(q=0) of REF(q), each time we compute a correlation coefficient, R(i) by a correlation operation between X(n) and the same length sequence REF_i(q) as X(n) in order to obtain a correlative coefficient sequence R(p), where i=p=0,1,2,...,P-1,

$$P=1+(Q-N) \tag{1}$$

The correlation coefficient sequence is

$$R(p)= \text{SUM}(X(n)*\text{REF}_i(n)), i=0,1,2,\dots,P-1 \tag{2}$$

The maximal correlation coefficient is

$$R(m)=\text{MAX}(R(p)) \tag{3}$$

Where m is the starting point of the signal segment REF_m(n) which has the maximum correlation coefficient to X(n) in REF(q). This moving correlation between signals which are obtained from the same electrode system is called moving auto-correlation.

(3)Auto-adaptation: According to the principle of the minimum power, we calculate the cancellation factor W from REF_m(n) and X(n).

The maximal correlation insures that the waveform of REF_m(n) has the statistically similarity with the waveform of X(n). But it cannot guarantee that it has the minimum variance between them. In order to cancel the background EEG to the largest extent, we use the minimum error power principle to calculate the cancellation factor W[6], Suppose

$$\text{EP}(n)= X(n)-W* \text{REF}_m(n) \tag{4}$$

Then the error power is

$$\text{SUM}(\text{EP}^2(n))=\text{SUM}((X(n)-W* \text{REF}_m(n))^2) \tag{5}$$

According to the minimum error power principle computing the derivative of the right side in the above formula to W and let the result equals zero, we have

$$\frac{d[\text{SUM}(\text{EP}^2(n))]}{dw}=\frac{d\{\text{SUM}((X(n)-W* \text{REF}_m(n))^2)\}}{dw}=0 \tag{6}$$

we can get

$$W= \frac{\text{SUM}(X(n)-W* \text{REF}_m(n))}{\text{SUM}[\text{REF}_m^2(n)]} \tag{7}$$

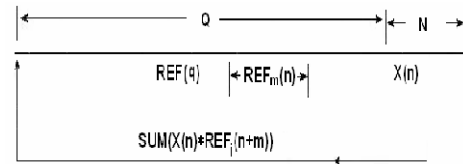


Fig. 2 The scheme for finding maximal correlation sequence REF_m(n)

(4) Interference cancellation: Putting the cancellation factor W which is calculated from the formula (7) into formula (4), we can cancel the interference signal including B-EES to the largest extent and get the evoked potential signal $EP(n)$.

2.2 The stimulator based on the multi-media sound resources of computer

At present, in clinical medicine the electricity stimulation is usually used to be the stimulus style to extract SEP [5]. The stimulator that our lab has developed is based on the multi-media sound resources of modern computer. It can generate stimulus signals used to extract SEP by amplifier and voltage-constancy circuit. This stimulator makes full use of D/A converting function of the sound card in computer which replaces the traditional D/A converter so that it saves devices and it is easy to be integrated. It meets the developmental tendency of modern equipments. Furthermore, since there are abundant multi-media sound resources in the computer, the stimulus signals are more affluent so that the stimulator guarantees to extract different kinds of SEPs. It is also a part of components to single trail of SEP.

2.3 The methods of experiment

This study chose the subjects whose somatosensory paths are normal and used the modified Bio-2000 electrophysiology hardware platform of Chongqing Bio company. We use the software based on AAA-ICT of single trial SEP to extract SLSEP (short-latency SEP) and LLSEP (long-latency SEP). The software is designed by means of Delphi. In the experiment, the subject is sitting with his eyes closed. The stimulus electrodes are Ag/AgCl cotyloideus and electrodes. They are put on skin of the body surface of wrist median nerve. The stimulus voltage can be changed from 0 to 100V according to different persons and different experimental needs. The constant-electricity levels have 3mA, 2.7mA, 2mA, 1.8mA, 1.4mA and 1mA levels to be chose. The stimulus signals are square wave [5] whose width are 0.1ms~0.9ms. Each stimulation contains 20 square waves. The stimulus time interval for SLSEP is 2000ms and 100ms for LLSEP.

When recording SLSEP, the recording electrode should be put on C3' or C4' of the head. When recording LLSEP, the recording electrode should be put on Cz of the head. The reference electrodes are both put on the ear lobes. The ground electrode is on the forehead [2].

Among the total, the sampling frequency for acquiring SLSEP are 5120Hz. The gain is 100k. The band-pass is 0.1~1.5kHz. The sampling frequency for acquiring LLSEP are 512Hz. The gain is 20k and the band-pass is 0.1~75Hz.

The scalp where put the electrodes on should be degeased with alcohol. The electrodes should be smeared with electrode cream so that the impedance between electrode and skin is lower than $5K\Omega$. The subject should relax and close his eyes. After 15 minutes, we start to collect the evoked potentials. During the process of sampling signals, the surrounding environment should be kept quiet. The sampled subject should not have any limbs' activities.

III. CONCLUSIONS

We compared the waveforms of averaging 20 times of SEP, the single trial waveforms and the averaging 20 times single trial waveforms of eighty healthy subjects. In all figures, B-EES stands for the reference background electroencephalo-signal. E-EES stands for evoked electroencephalo-signal. SSLSEP stands for single extraction short latency SEP. SLLSEP stands for single extraction long latency SEP. ASLSEP stands for averaging SLSEP. ALLSEP stands for averaging LLSEP. ASSLSEP stands for averaging single extraction SLSEP. ASLLSEP stands for averaging single extraction LLSEP.

3.1 The results of AAA-ICT

The condition of auto-reference and autocorrelation and adaptation interference cancellation is shown in Fig.3. In Fig.3, the top part shows the condition of cancellation between the best reference signal (B-EES) and E-EES. The middle part of Fig.3 shows SSLSEP. The bottom part shows ASSLSEP which is the averaging signal of SSLSEP. The numbers in the figure show the measurement results of the main waveforms' character. It is shown in the form of (latency, amplitude). The unit of latency is ms. The unit of amplitude is μV . The unit of scale division is shown in the right above corner. The scale division of axle X is ms/D (millisecond/degree). The scale division of axle Y is $\mu V/D$ (microvoltage/degree). The number 6 in the right below means it is the condition of the sixth stimulation.

We can find from Fig.3 and Fig.4 that the effect of single trial is obvious. In Fig.3 (the sixth single trial of twenty times), The waveform of upper limb SLSEP N20 is show obviously in the figure. What's more, by contrasting the result of ASSLSEP to traditional averaging result, there is little difference of waveforms, but the results of average single trial cancel parts of DC signal contrasting to the averaging (shown in the top and middle parts of Fig.4).

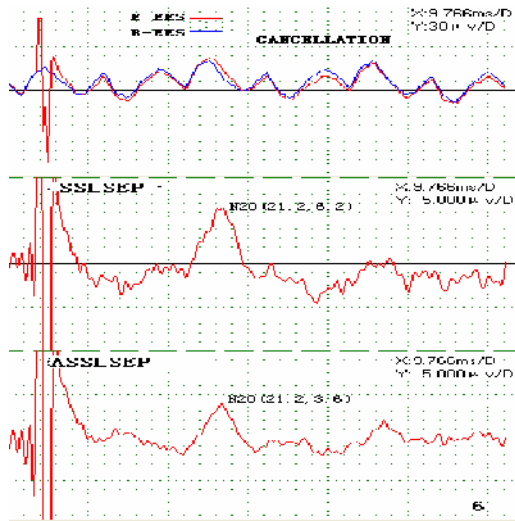


Fig. 3 The interference cancellation based on AAA-ICT

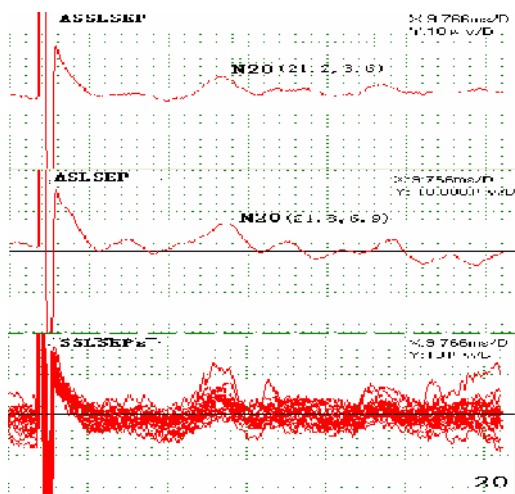
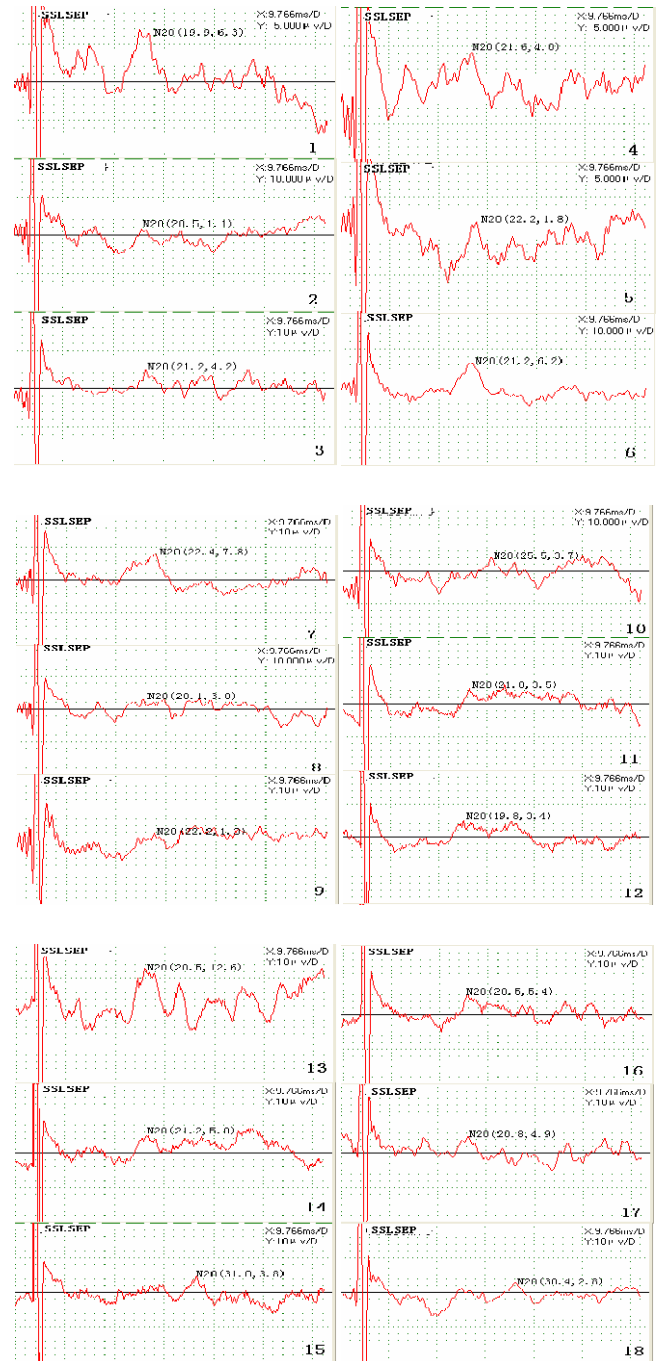


Fig. 4 ASSLSEP,ASLSEP and Overlapping of SSLSEPs

3.2 ASSLSEP, ASLSEP and twenty times of overlapping of SSLSEP

The condition of twenty times of SSLSEP, ASSLSEP and ASLSEP is shown in Fig.5. In the lower part, there is the condition of overlapping of SSLSEP. It indicates that each SSLSEP has a good repeatability. In the middle part, there is ASLSEP. ASSLSEP is shown in the superior part. That indicates both of the waveforms are very similar. The measurement result of the waveform of N20 is shown in the figure.

3.3 Twenty times of SSLSEP



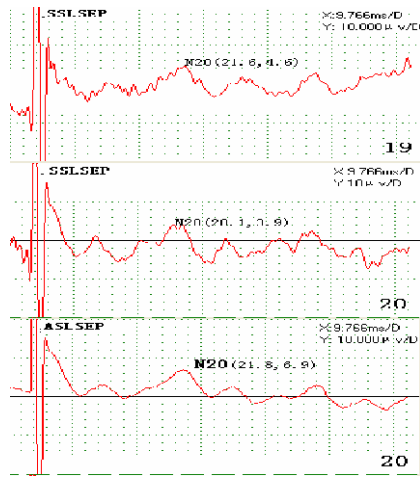


Fig. 5 Twenty SSLSEPs and their ASLSEP

3.4 The measurement results of twenty SSLSEPs respective characteristic wave

The measurement results of latency and amplitude of twenty times SSLSEP of N20 are shown in Table 1. The distribution histogram is shown in Fig.6. From Figure 6, we can find that the changes of latency are small while the changes of amplitude(opposite to the baseline) are large. If using the value RD(relative deviation) of zero dimension to replace the variation degree of ratio, it is defined to be:

$$RD = SD/Mean \tag{8}$$

In the Table 1, there are measurement data of latency and amplitude of N20 belonged to ASSLSEP and ASLSEP(which are shown in the middle and lower part of Fig.4). The latencies are the same. The amplitudes are some different. But they are both different from the arithmetic average value of N20.

Although the averaging of SEP includes the averaging results of background interference, it indeed contains the average value of evoked potential components which are the components owned by all generated by stimulation. This is

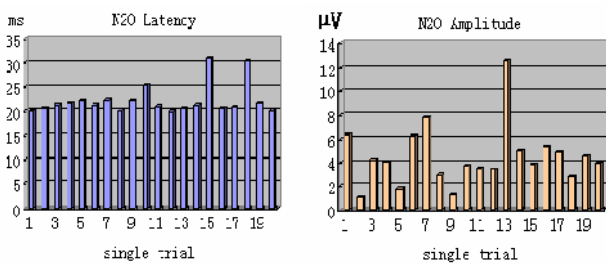


Fig. 6 The distributions of the latencies and the amplitudes of the N20 waveforms in 20 SSLSEPs of a subject.

the reasonable connotation. Frankly speaking, the averaging SEP(ASEP) extracted by traditional averaging technique can be only averaging SEP(ASEP) including the averaging results of all the background interference.

But from the results of averaging, we can find that the averaging single trial cancelled the DC component in B-EES and it has more affluent detailed components. That is to say, the single extraction and averaging single extraction do not cancel the differences of the latency and amplitude among each stimulation. The single trial of SEP has wider application prospect and study value than the traditional averaging.

Table 1 The measurement results of latency and amplitude of twenty times SSLSEP of N20

N20	1		2		3	
	La-tency	Ampli-tude	La-tency	Ampli-tude	Latency	Ampli-tude
	19.9	6.3	20.5	1.1	21.2	4.2
	4		5		6	
	La-tency	Ampli-tude	La-tency	Ampli-tude	Latency	Ampli-tude
	21.6	4.0	22.2	1.8	21.1	6.2
	7		8		9	
	La-tency	Ampli-tude	La-tency	Ampli-tude	Latency	Ampli-tude
	22.4	7.8	20.1	3.0	22.2	1.3
	10		11		12	
	La-tency	Ampli-tude	La-tency	Ampli-tude	Latency	Ampli-tude
	25.5	3.7	21.0	3.5	19.8	3.4
	13		14		15	
	La-tency	Ampli-tude	La-tency	Ampli-tude	Latency	Ampli-tude
	20.5	12.6	21.2	5.0	31.0	3.8
	16		17		18	
	La-tency	Ampli-tude	La-tency	Ampli-tude	Latency	Ampli-tude
	20.5	5.4	20.8	4.9	30.4	2.8
	19		20		Mean	
	La-tency	Ampli-tude	La-tency	Ampli-tude	Latency	Ampli-tude
21.6	4.6	20.1	3.9	22.2	4.5	
SD(±)		ASSLSEP		ASLSEP		
La-tency	Ampli-tude	La-tency	Ampli-tude	Latency	Ampli-tude	
3.2	2.5	21.2	3.6	21.8	6.9	

ACKNOWLEDGMENT

This article is supported by the Chinese National natural science foundation (grant No: 30670536).

REFERENCES

1. Pan YF. (2000) Evoked Potentials in Medical Practice. 2nd ed. People's Medical Publishing House, Beijing, 2000, pp 62-91.
2. Zhang MD, Chen XS. (1995) Evoked Potentials on Brains. Shanghai Scientific and Technological Education Publishing House, Shanghai, 1995, pp 143-182.
3. Hunan medical college. (1978) Physiology. People's Medical Publishing House, Beijing, 1978, pp 376-377.
4. Nie N, Yao DZ and Xie ZX. (2005) Biological Medical Digital Signal Processing Technology and Application. Science Press House, Beijing, 2005, pp 289-291.
5. Jorge GB, Gregory LB (2007). Somatosensory Evoked Potentials: Clinical Applications[J].Medicine. July 25,2007, 1-6.
6. Xie ZX, Chen LC, Zhang SQ, et al. (1992) Medical Signal's Digital Processing and Its Application. Scientific and Technical Literature Publishing House, Beijing, 1992, pp 78-80, pp 31-36.
7. Hong B, Pan YF. (2000) ICA in the Single-trial Estimation and Analysis of VEP. Chinese Journal of Biomedical Engineering, 2000, 19(3), pp 334-341 .
8. Li LP, Cheng JZ, Ma RS et al. (1998) Application of Time-frequency Filter of Wavelet to Single-trial ERP Extracting. Journal of Biomedical Engineering, 1998, 15(2), pp 116-119.
9. Zhang H, Zheng CX. (2003) Evoked Potential Extraction Based on Multi-channel Time-frequency Coherence. Acta Biophysica Sinica, 2003, 19(3), pp 303-307.
10. Rix R, Korth M. (1997) Response in the Human Electroretinogram Under Different Degrees of Wakefulness. Albrecht Von Graefes Arch Klin Exp Ophthalmol, 1977, 204(3), pp 215-221

Author: Wang Ying

Institute: Department of Biomedical engineering in Chongqing Medical University

Street: Yixueyuan Road

City: Chongqing

Country: China

Email: Wendy8657@163.com

Corresponding Author: Xie Zhengxiang

Institute: Department of Biomedical engineering in Chongqing Medical University

Street: Yixueyuan Road

City: Chongqing

Country: China

Email: bmezxxie@163.com

A Finite Element Study of The Response of Thoracolumbar Junction to Accidental Mine Blast Scenario

Q.H. Zhang¹, J.Z. Li², H.N. Serena Tan², E.C. Teo¹

¹ School of Mechanical & Aerospace Engineering, Nanyang Technological University, Singapore

² DMERI@DSO, Singapore

Abstract — A comprehensive, geometrically accurate, nonlinear FE model of thoracolumbar spine multisegment (T12-L5) was developed to simulate the response of thoracolumbar spine under the mine blast condition with two initial postures. The vertical accelerations along the Y-axis of the T12-L5 FE model were applied on the inferior surface of L5 based on the simulated sitting postures. For both postures, the L5 inferior surface was constrained to move only in vertical direction. The predicted responses of each motion segment during the first 100ms were computed and compared under the two conditions. The results showed that the motion segments oscillate during and after the sudden impact. The maximum compressive deformation of the discs and segmental rotations occurred at around 36ms which also corresponds to the ending of the impact force. After that, the discs expand in the opposite direction. During the expansion phase, the disc heights exceeded their original position. The predicted frequency of the vibration of the motion segments was around 15Hz, which implied that a number of oscillations occur in less than one second before dying out (with the larger amplitudes of these oscillations occurring during the first hundredths of a second). Compared against sitting posture, although the resultant magnitude of disc deformations and segmental rotations were higher due to the relative anterior position of the mass point for the napping posture, the basic trends of segmental motions and predicted injury location were similar. Under such a rapid high axial impact (up to nearly 30G within 30ms), a slight difference between the position of centre of body gravity will not produce any differences in response of the thoracolumbar spine.

Keywords — Finite element, Thoracolumbar spine, mine, vibration, posture.

I. INTRODUCTION

Mechanical loads imposed on the human spine during daily strenuous activities play a significant role in the onset of spinal disorders for soldiers [1, 2]. Under sudden transient impacts, such as pilot ejection, car collisions, stepping into war zone with mines, the individuals are especially susceptible to traumatic injuries due to impact loading, which releases energy rapidly over a short period of time. The thoracolumbar junction (TLJ) is a common site of traumatic injuries, with TLJ injuries contributing to 30–60%

of all spinal injuries [3]. Although burst fractures account for only approximately 15% of these injuries, the frequency of neurological deficit in patients with burst fractures can reach up to 50–60% [3-5]. An adequate comprehension of burst fracture mechanism is therefore useful for effective prevention, mitigation and treatment.

Despite the fact that it is of immense clinical significance to know the pathomechanism [6] of the spinal fractures and that burst fractures occur during impact rather than during static loading [7, 8], not much FE studies have been performed to quantitatively and systematically analyze the mechanism of thoracolumbar burst fractures. In current study, a detailed FE model of T12-L5 multi-segment would be developed to investigate the biomechanical response of the thoraco lumbar spine under high-speed impact loading conditions.

II. MATERIALS AND METHODS

An anatomically realistic three-dimensional (3D) FE model of T12-L5 multi-segment was created based on embalmed vertebral specimens from a 56-year-old male subject. Each vertebral body had a cancellous core enclosed by a 1.0-mm thick cortical wall. The posterior elements consisted of the pedicle, spinous process, transverse process and articulating processes. While the geometry of bony structures were obtained from the dry embalmed specimen, the associate ligaments and intervertebral discs were modeled based on the information obtained from literature [9-11]. The intervertebral disc was made up of the annulus and nucleus. The 0.5-mm thick bony endplates were modeled at the interfaces between the intervertebral disc and the vertebral bodies. The annulus was modeled as composite material with three concentric laminar layers of fibers embedded in a homogeneous matrix. Taking into account the effect of lordosis, the anterior and posterior heights of the disc were modeled based on literature [9, 10]. The vertebrae, endplate, annulus and nucleus were meshed using 8-node brick elements. The material properties of these components were simplified to be linear elastic, homogenous and isotropic, in which the nucleus had a Poisson's ratio of 0.499 to exhibit an incompressible behavior. The fibers and ligaments were

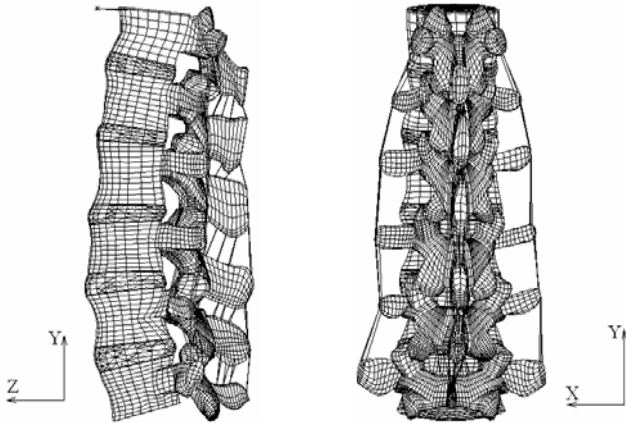


Fig. 1 Finite element mesh of T12-L5 spine model.

Table 1 Material properties used in the study

Materials	E (MPa)	ν	Density (kg/mm ³)
Cortical bone	12,000	0.30	1.70×10^{-6}
Cancellous bone	340	0.2	1.10×10^{-6}
Posterior elements	3,500	0.25	1.40×10^{-6}
Endplate	500	0.30	1.20×10^{-6}
Disc-annulus	20	0.45	1.05×10^{-6}
Disc-nucleus	5	0.499	1.02×10^{-6}
Annulus fiber	500	0.3	1.00×10^{-6}

modeled with tension-only cable elements. In addition, the hourglass coefficient of 0.1 was used to minimize hourglass energy for the discs and endplates. Facet articulations were simulated by frictionless sliding contact, with an average initial gap of 0.5mm between the two contacting surfaces at each facet joint. The final intact T12-L5 model consisted of 27,884 solid elements and 4,330 cable elements (Fig.1). The detailed material properties used in this study are listed in Table 1.

To simulate the response of thoraco-lumbar spine under high impact, such as the mine blast condition, two vertical (axial) acceleration profiles (Fig.2) obtained under sitting and napping postures provided by DMERI were used. The vertical accelerations along the Y-axis of the T12-L5 FE model were applied on the inferior surface of L5 based on the simulated sitting postures. In the whole process, the L5 inferior surface was constrained to move only in vertical direction. A 40kg concentrated mass element, connected with rigid rod, was attached to the T12 superior surface to simulate the upper body mass. For napping posture, the mass element was located 10mm anteriorly to simulate the shift of mass centre away from sitting posture. The predicted reactions of each motion segment during the first 100ms after impact were then collected and compared under the two conditions.

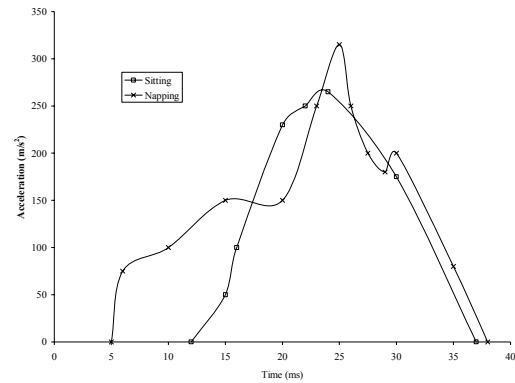


Fig. 2 Input acceleration on L5 for mine blast simulation.

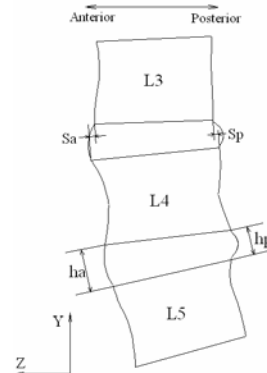


Fig. 3 Schematic illustration of the definition of disc height at mid-sagittal plane and shear displacement of disc superior surface with respect to inferior surface at mid-sagittal plane.

To analyze the behavior of the thoraco-lumbar spine during impact, the following variables were extracted: relative segmental rotational angles vs. time of each motion segment in sagittal plane, variation of disc height (Δh_a and Δh_p) at mid-sagittal plane, and shear displacement of superior surface with respect to inferior surface of each disc at mid-sagittal plane (ΔS_a and ΔS_p) (Fig.3). In which,

$$\Delta h_i = h_i(t) - h_i(0)$$

$$\Delta S_i = S_i(t) - S_i(0) \quad i=a,p;$$

III. RESULTS AND DISCUSSION

Fig.4-6 showed the predicted rotational history and disc deformation of each motion segment at mid-sagittal plane when the crew member was under normal sitting posture before impact. After subjected a sudden axial loading, all the discs were highly compressed (Fig.4) and the motion segments began to push the mass point representing the

upper body mass to move upward. At the same time, the whole structure of T12-L5 multi-segment rotated around the mass point due to its huge mass magnitude. Combined with the initial lordosis curve of the thoraco-lumbar spine structure, the shear deformation of disc (Fig.5) and relative rotations of each motion segment (Fig.6) with respected to its adjacent level were further generated. The complex geometric nonlinearity of the spine caused obvious difference of the deformations and rotations among motion segments. Relatively, the thoraco-lumbar junction (T12-L2) experienced largest anterior compression and relative rotation while the lower level (L3-L5) suffered greatest posterior compression. When compared with the normal range of motion of lumbar spine at sagittal plane (within 6 deg.) under 10Nm moment [13], it is obvious that T12-L2 were more possible to be injured. This result agreed with the previous observation that burst fractures are mainly localized in the thoraco-lumbar junctional region. Compared with the motion in sagittal plane, the displacement of disc at frontal plane and segmental rotation in frontal and transverse planes were small.

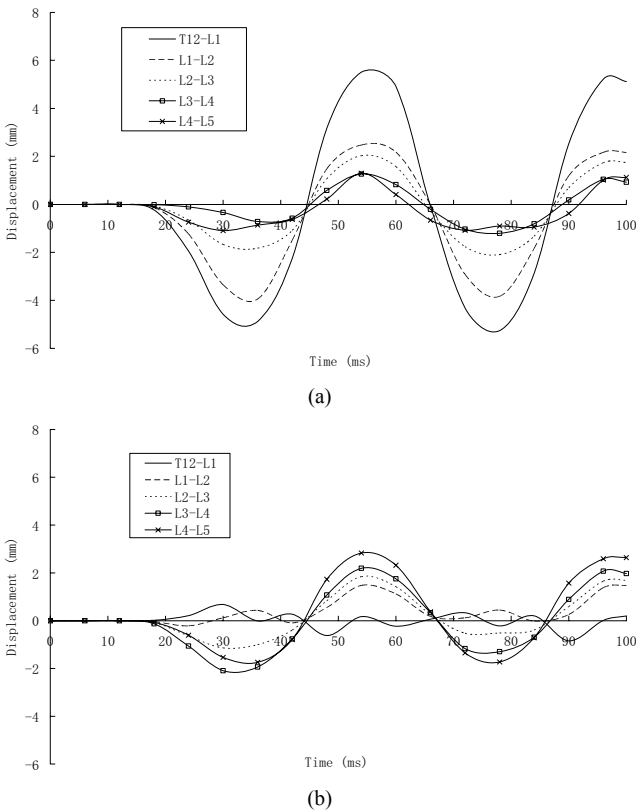


Fig. 4 Variation of disc height of each motion segment at mid-sagittal plane for sitting posture. (a) anterior region (Δh_a); (b) posterior region (Δh_p).

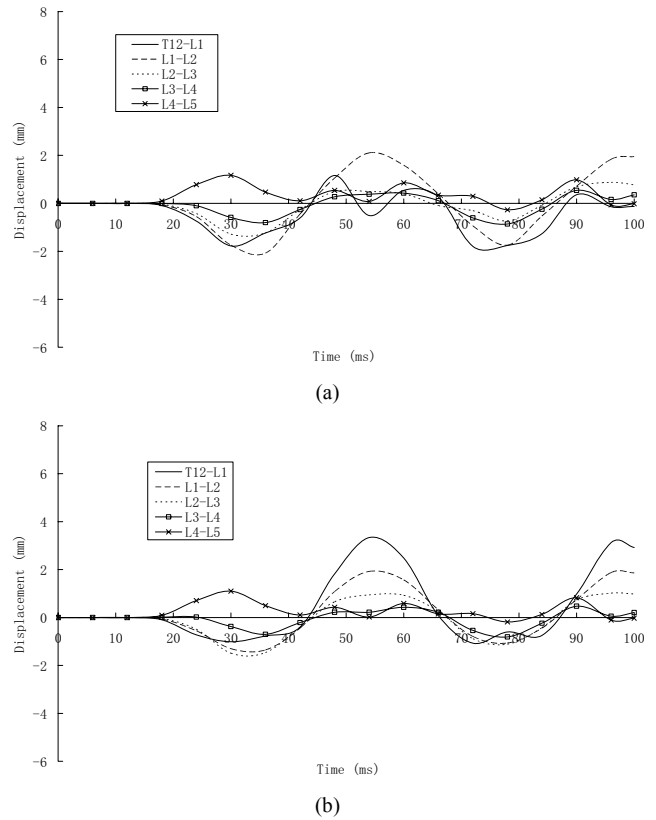


Fig. 5 Variation of disc superior surface shear displacement with respected to inferior surface of each disc at mid-sagittal plane for sitting posture. (a) anterior region (ΔS_a); (b) posterior region (ΔS_p).

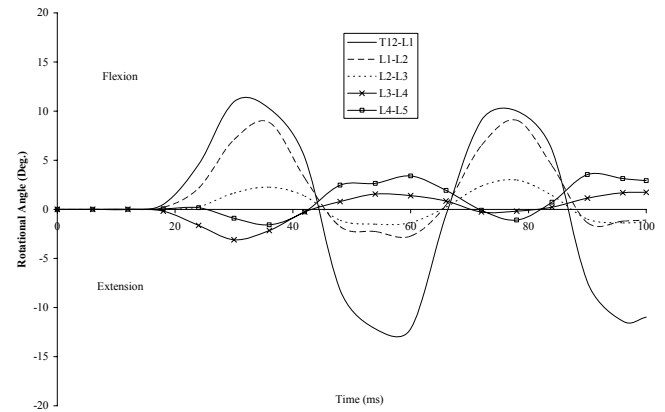


Fig. 6 Rotational history of each motion segment in sagittal plane for sitting posture.

From all the figures, it can be seen that the motion segments will vibrate after a sudden impact. The maximum compressive deformation of the discs and segmental rotations were almost all reached at around time 36ms, corre-

sponding to the ending of the impact force. After that, the discs expand in the opposite direction. During the expansion phase, the disc heights exceeded their original position. As shown in the figures, the frequency of the vibration of the motion segments was around 15Hz, which implied that a number of vibrations occur in less than one second before dying out (with the larger amplitudes of these vibrations occurring during the first hundredths of a second). In other words, a sudden impact will first cause the vertebrae to draw closer due to the compression and at the same time, the disc will bulge circumferentially. When the impact force disappeared, the vertebrae withdraw from one another even further than the normal distance (Fig.4) and at the same time, the margins of the disc recede inward. Therefore, the intervertebral disc acts as a shock absorber, damping the oscillations of the FSUs in spine, distribute loads applied to the spine, and also stabilize the spine by anchoring adjacent vertebral bodies to each other, while at the same time allow movement between vertebrae, thus giving the spine its flexibility.

The effect of initial posture of crew member on the response of the thoraco-lumbar spine after impact was not obvious. Although the resultant magnitude of disc deformations and segmental rotations were higher due to the relative anterior position of the mass point representing the upper body mass, the basic trends of segmental motions and predicted injury location were all same. Under such a rapid high axial impact (up to nearly 30G within 30ms), a slight difference between the position of centre of body gravity will not produce a better condition for the lumbar spine.

IV. CONCLUSIONS

The motion segments oscillate during and after the sudden impact. The intervertebral disc acts as a shock absorber thus giving the spine its flexibility. Burst fractures are

mainly localized in the thoracolumbar junctional (T12-L2) region. The effect of initial posture of crew member on the response of the thoracolumbar spine after impact was not obvious.

REFERENCES

1. Sharma M, Langrana NA, Rodriguez J. (1995) Role of ligaments and facets in lumbar spinal stability. *Spine* 20:887-900.
2. Shirazi-Adl A, Ahmed AM, Shrivastava SC. (1986) Mechanical response of a lumbar motion segment in axial torque alone and combined with compression. *Spine* 11:914-27.
3. Kifune M, Panjabi MM, Liu W, et al. (1997) Arand M, Vasavada A, Oxland T. Functional morphology of the spinal canal after endplate, wedge, and burst fractures. *J Spinal Disord* 10:457-66.
4. McEvoy RD, Bradford DS. (1985) The management of burst fractures of the thoracic and lumbar spine. Experience in 53 patients. *Spine* 10:631-7.
5. Trafton PG, Boyd Jr CA. (1984) Computed tomography of thoracic and lumbar spine injuries. *J Trauma* 24:506-15.
6. Shirado O, Kaneda K, Tadano S, et al. (1992) Influence of disc degeneration on mechanism of thoracolumbar burst fractures. *Spine* 17:286-292.
7. Tran NT, Watson NA, Tencer AF, et al. (1995) Mechanism of the burst fracture in the thoracolumbar spine. The effect of loading rate. *Spine* 20: 1984-1988.
8. Yingling VR, Callaghan JP, McGill SM. (1997) Dynamic loading affects the mechanical properties and failure site of porcine spines. *Clin Biomech* 12:301-305.
9. Brinckmann P, Grootenboer H. (1991). Change of disc height, radial disc bulge, and intradiscal pressure from discectomy: an in vitro investigation on human lumbar discs. *Spine* 16: 641-646.
10. Malmivaara A, Videman T, Kuosma E, et al. (1987) Facet joint orientation, facet and costovertebral joint osteoarthritis, disc degeneration, vertebral body osteophytosis, and Schmorl's nodes in the thoracolumbar junctional region of cadaveric spines. *Spine* 12: 458-63.
11. Chazal J, Tanguy A, Bourges M, et al. (1985) Biomechanical properties of spinal ligaments and a histological study of the supraspinal ligament in traction. *J Biomech* 18:167-176.
12. Schultz, A. B., Warwick, D. N., et al. (1979). Mechanical Properties of Human Lumbar Spine Motion Segments - Part I: Responses in Flexion, Extension, Lateral Bending, and Torsion. *J Biomech Eng* 101: 46-52.

Experimental modeling and biomechanical measurement of flatfoot deformity

Wenxin Niu^{1,3}, Yunfeng Yang², Yubo Fan³, Zuquan Ding¹, Guangrong Yu²

¹ School of Life Science & Technology, Tongji University, Shanghai, China

² Orthopaedic Department, Tongji Hospital, Tongji University, Shanghai, China

³ Bioengineering Department, Beihang University, Beijing, China

Abstract — Treatment of the flatfoot requires a quantitative understanding of the biomechanical factor on this common deformity. Seven unembalmed foot-ankle complex specimens were used in this study to model experimental flatfoot deformity by release of plantar fascia, spring ligament, long and short plantar ligaments. Digital speckle correlation method (DSCM) and strain gauges were applied to measure displacements and strains of specimens before and after ligaments resection. Acquired data were compared with each other and statistically analyzed. Results of this experiment showed different appearance of foot-arch according to release of different ligament or complex. Obvious flatfoot deformity appeared only after at least three of the four main ligaments were cut off. Under the condition that four ligaments were completely released, the arch height decreased, longitudinal arch prolonged, forefoot abducted, force in various tissues redistributed, and center of bearing shifted forwards. This method is suitable for constructing experimental model of flatfoot deformity. This study accumulated large amounts of data for further research.

Keywords — Flatfoot; Experimental model; Ligament resection; Foot-ankle biomechanics.

I. INTRODUCTION

Flatfoot is a common disease, whose main clinical manifestations are plantar medial rotation of talus, decrease in the medial arch height, supination and abduction of the forefoot, even joint and soft tissue lesions, resulting in lower extremity pain, weakness and walking inconvenience [1,2]. Many factors may lead to flatfoot, including insufficiency of posterior tibial tendon, inflammatory joint disease, trauma (Lisfranc joint injuries, fractures of the calcaneus), Charcot foot, Achilles tendon contracture, mid-foot instability, imbalance of foot neuromuscular and so on [2]. Although biomechanical research on flatfoot is in the ascendant, it is hard to construct a good experimental model for this disease, and the knowledge of biomechanical environment under flat foot condition is also insufficient [3]. In light of these problems, this study was to construct an experimental model of the flatfoot by releasing plantar ligaments on cadaver specimens, and compare mechanical parameters of displacement, strain of various foot bones between normal and flat foot in normal standing state.

II. METHODS

A. Experiment preparations

Seven unembalmed cadaver foot-ankle specimens (median age 41.4, standard deviation 15.8; 4 males and 3 females; 4 left and 3 right side) were collected. Radiograph was taken on them to exclude any osseous pathology of pre-existing disease or trauma. The skin and muscles above the ankle joint were detached while kept the ligaments around the ankle intact. Tibia residuals were levered by clinical instrument, fibulas residuals were amputated to 6cm below tibia ones and these fibulas sections were reserved for strain measurement. Tibia residuals were fixed to material test machine, with which loading was controlled by programs. The maximum loading, 700N, simulating normal body weight single-foot standing, was achieved through an increment of 100N, and within every increment loading was halted for 10 seconds, while all data were harvested by other equipments. Before the formal trial, specimens were preconditioned to 300N for five times with a rate of 2mm/min. Loading rate of formal trial was also 2mm/min. Test machine accurately recorded time, force and displacement during whole range. After experiment of intact specimen, plantar fascia, spring ligament, long and short plantar ligaments were cut off according to different sequences, and experimental operation above was repeated.

B. Displacement Measurement with DSCM

Custom-made black pins were inserted to corresponding 10 bones (tibia, fibula, calcaneal, navicular, media cuneiform, and five metatarsal bones) as markers. Standard marker was fixed to custom-made bedplate. Two series of CCD system positioned at inboard and front of the specimen with 90° angle, connected to image processing computers respectively, were used to catch trial images while static moment in every stages. Bones shot by inboard camera include tibia, calcaneal, navicular, media cuneiform, and the 1st metatarsal, as shot by foreside camera include others (Fig.1). With the application of DSCM programs, displacements in 2-D or 3-D can be calculated. Final analysis rejected fibulas, and results from tibias were used to compare with data given by test machine.

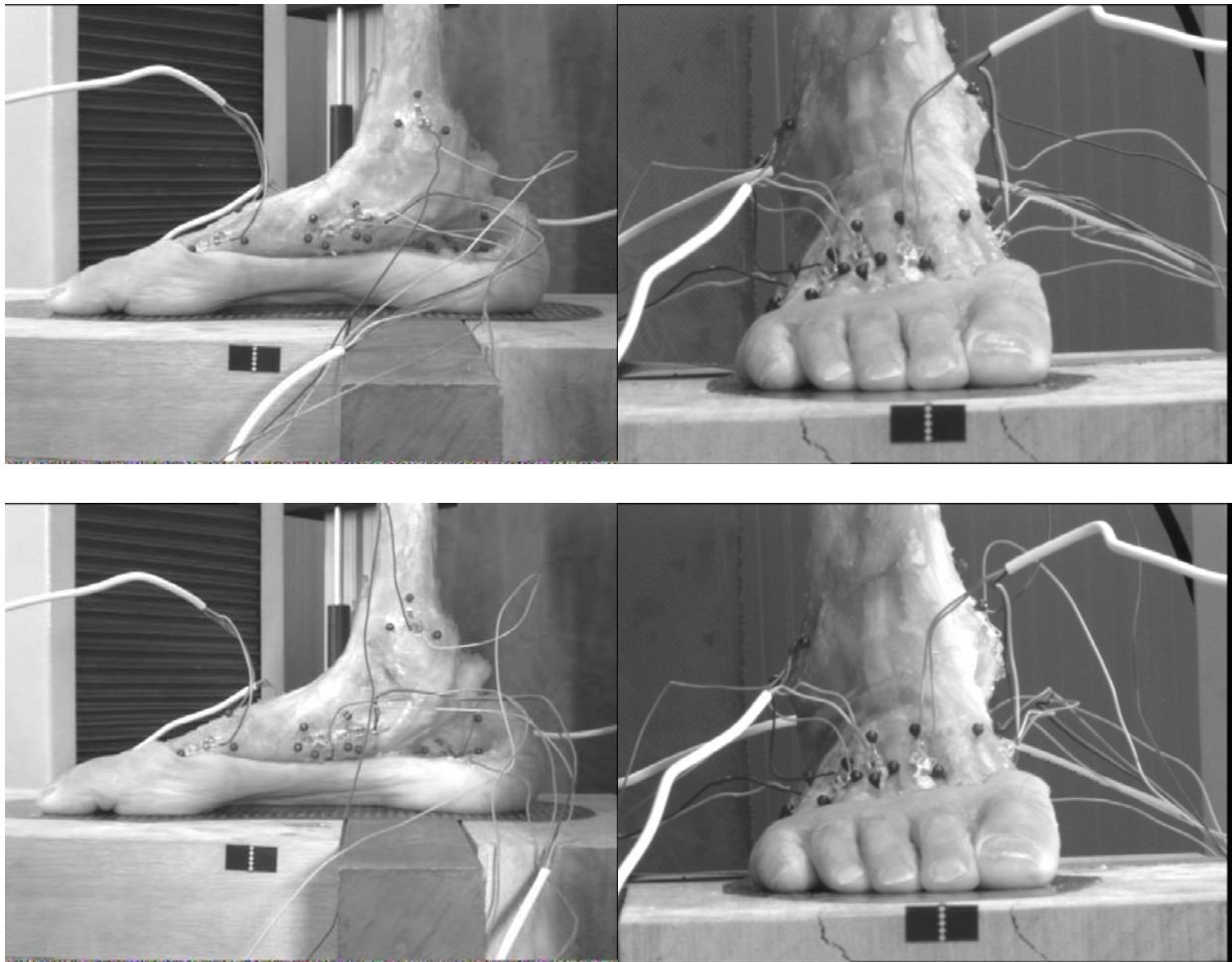


Fig. 1 Experimental images under 700N axial loading (Left-top: normal specimen in medial view; Right-top: normal specimen in fore-side view; Left-bottom: ligaments released specimen in medial view; Right-bottom: ligaments released specimen in fore-side view.)

C. Strain Measurement with Strain Gauge

Strain gauges used to measure bone surface strain were connected to static strain indicator (DH-3818) with 1/4 bridge converter and common compensating gauge. For every specimen, 10 gauges were pasted with 502-glye to the bones surface nearby DSCM markers. Before this operation, bones surface was trimmed, lipid was removed with acetone, and drying operation was carried out with anhydrous ethanol. Temperature compensating gauge was pasted to fibula section mentioned before.

D. Statistical analysis

All data were demonstrated quantitatively as mean \pm standard deviation ($\bar{x} \pm s$), and statistically analyzed in

SPSS13.0 software. Analysis of variance was employed in significance test of different groups, followed by S-N-K test with equal variances and Dunnett's test with unequal variances.

III. RESULTS

A. Displacement Measurement Results

For intact specimens, tibias displacement in vertical dimension is 4.66 ± 1.42 mm under 400N loading, and 5.55 ± 0.74 mm under 700N loading. For specimens off 4 main ligaments, this value is 9.00 ± 2.48 mm under 400N loading and 11.27 ± 1.77 mm under 700N lading. After ligaments resection, it could be visible that specimens took a typical of flatfoot deformity, arrangement of different bones

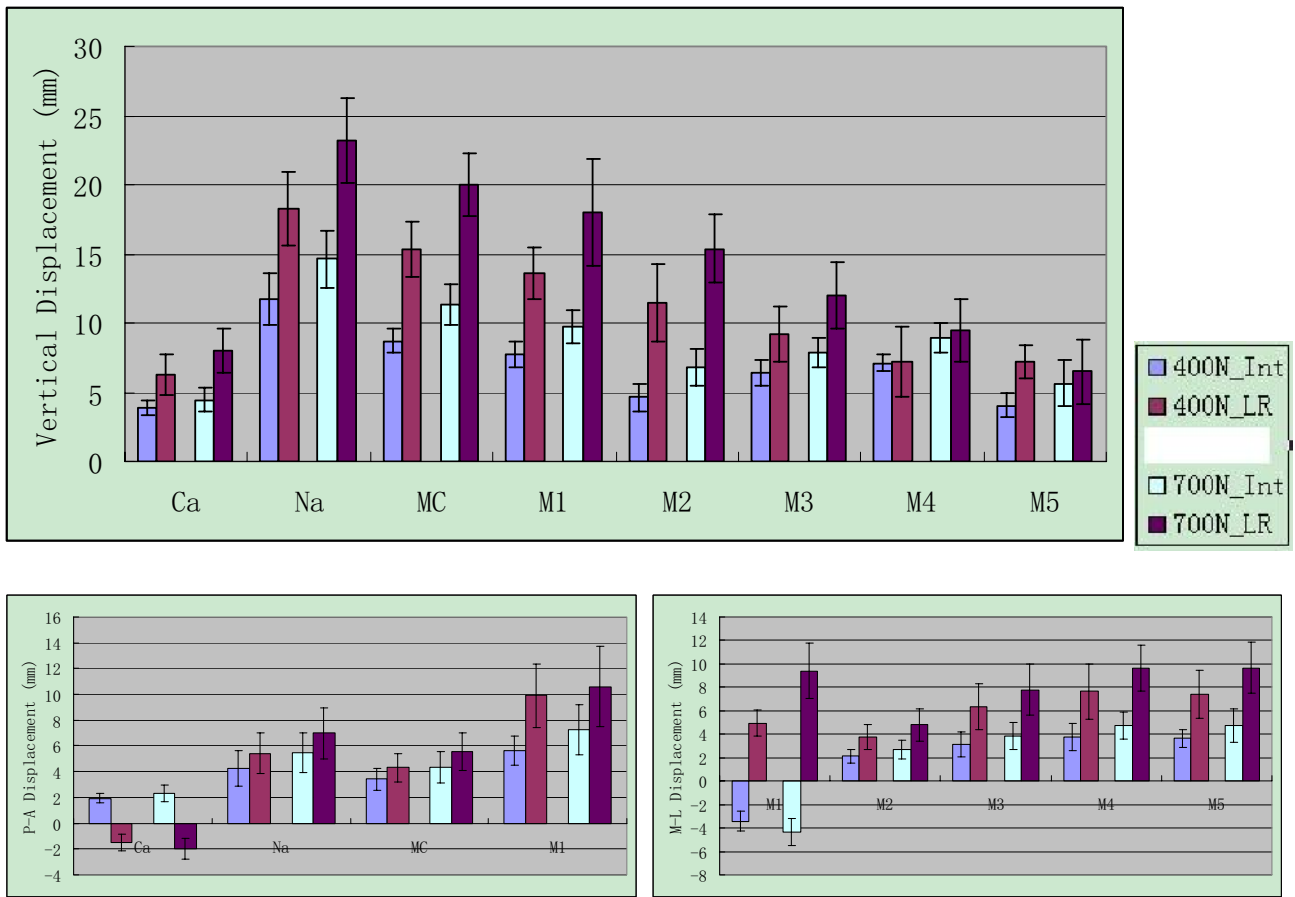


Fig. 2 Three-dimension Displacements of various bones (Int=Intact; LR=Ligaments release; Ca=Calcaneal; Na=Naviculare; MC=Medial Cuneiform; M1~M5: 1st~5th Metatarsal.)

in the structure changed, especially in the longitudinal arch, and abduction of the forefoot was obvious. Except that calcaneal bones in ligaments resection specimens retracted, all bones in media longitudinal arch had antedisplacements in different degrees under loading. Difference of these antedisplacements lead to an increasing prolongation of the medial longitudinal arch, which was about 3.7mm under 400N loading and 5.0mm under 700N loading for intact specimens, about 11.4mm under 400N loading and 12.6mm under 700N loading for ligaments resection specimens. Under intact state, the 1st metatarsal had an inward displacement with load increasing, while the other four metatarsals abducted, and the degree of abduction increased from the inside outwards. After ligaments resection, all metatarsals abducted, the most obvious change was in the 1st metatarsal. Measurement data of the displacements in all planes are shown as Figure 2. There is significant difference between the data before and after ligament resection with exception

of vertical displacements of M4 under both loading, M5 under 700N.

B. Strain measurement results

Measurement results of strain gauges increased with loading force increasing, regardless of tensile or compressive strain. Because of low strain rates under lower load, there was greater measurement error, and it is difficult to discover regularity, so only values of various bones under 700N load were shown in Fig.3. Because of strictly controlled experimental conditions, the distribution of these data is very ideal. All bones, except naviculare bone, displayed compressive strain at the measurement location. After ligaments resection, strain of naviculare, the 1st, 2nd, and 4th metatarsal increased significantly, and calcaneus bone had a decreased trend.

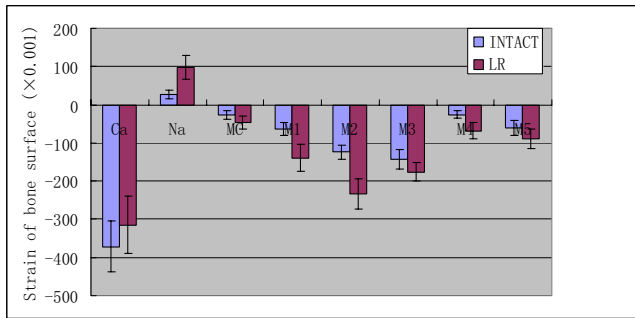


Fig. 3 Strains of different gauges

IV. DISCUSSION

A. The effect of ligaments injury on foot-arch structure

Connection and encasement of ligaments is important for maintaining the foot structure. Many researches have been developed on the change of foot-arch height after relaxation and complete release of ligaments. This study concerned plantar fascia, spring ligament, long and short plantar ligaments. Many researches on the importance of plantar fascia to the foot-arch are based on mathematical models [4-7]. These models were mainly based on the theory raised by Hicks [8], that stabilizing role of plantar fascia on foot-arch structure was considered a windlass mechanism, and plantar fascia is more like a bow string, which braced both ends of the longitudinal arch, preventing it from separation and collapse. More accurate finite element model also confirmed the effect of plantar fascia relaxation on structure [9-12]. Through passively dorsal flexing toes, tension of plantar fascia can be seen by naked eyes [13]. Through cadaver experiment Huang et al [14] considered that resection of plantar fascia decreased the height of foot-arch by 25%. In some experiments [15], resection of plantar fascia lead to decreasing of arch height, increasing of length, abduction of the forefoot, and medial rotation of talus. Murphy et al [16] used metal markers to label foot structure, monitored them with X-ray while axial loading, and found that complete release of plantar fascia, compared to partly release, would lead to collapse of media and lateral longitudinal arch by 62~100%. There is no supporting structure between the calcaneus and navicular, therefore, caput tali is supported by spring ligaments fibrocartilago complex and posterior tibial tendon at the below. Rupture of the spring ligaments fibrocartilago complex may lead to insufficiency of posterior tibial tendon, support losing and collapse of caput tali, occurrence of flatfoot disease finally [17-19]. Clinical reports have identified it [20,21]. Plantar ligaments rise from facies

plantaris and anterior tubercle of calcaneus, its deep fibers, the short plantar ligament, extend to cuboid bone crest at plantar surface, and tuberosity of cuboid bone, and superficial layers, the plantar long ligament, extend to the 4th and 5th metatarsals. Plantar ligaments are thick and tough to maintain lateral longitudinal arch. It is usually difficult to distinguish between them, and they are often described as an entirety [14]. From the view of position or functions, plantar ligaments can be seen important complement of plantar fascia [22].

Huang et al [14] studied the relationship between effects of skeletal structure and ligaments on maintaining foot arch structure, and considered that 63% contribution was offered by skeletal structure, and 37% was offered by spring ligament, long and short plantar ligaments, plantar fascia. In this study, for sequences inconsistency of ligaments resection, there was little statistical significance on the effects of single ligament or combinations of two or three ligaments, but it was still observed that the effect of plantar fascia is the most obvious. With the help of finite element analysis [10,11], this study considered that foot structure is a dynamic and stable system maintained by coordination of bones, muscles, ligaments, and so on. Contribution of multi-factors on maintaining the structure has coupling effect, is not a simple addition of many single factors. So it is incorrect to quantify contribution of single factor and multiple factors to the form of percentage. Injury of ligaments leads to a phenomenon of disorganization, decreasing of arch height, prolongation of arch length, and abduction of the forefoot. Disorganization will deteriorate the mechanical environment, make the center of bearing moving forward, and redistribute the force in the transverse arch. It is worth noting that, strains of metatarsals in complete ligaments release state were higher than that in intact state, but not higher than that in state that three of the four ligaments were released. It proved that complete ligaments resection severely damaged the structure, and metatarsals gradually lost their supporting role. For location and direction dependence of the strain gauge measurement, and lack of reference of related research, this study should be enhanced by improving the method and optimizing experimental design.

B. Experimental modeling of the flatfoot deformity

Flatfoot is series of diseases featured as lower or disappear of foot arch, including developmental and acquired flatfoot. Developmental flatfoot may be caused by maldevelopment of bones or joints, and systemic relaxation of the ligaments, such as Manfan's disease. Acquired flatfoot often associated with posterior tibial tendon insufficiency, over-stress of musculus triceps surae, relaxation of mid-foot, supination and abduction of the forefoot, eversion of hind-

foot, dislocation of talus, traumatic deformity, plantar fascia rupture, Charcot's foot, and neuromuscular imbalance diseases (such as polio, cerebral palsy, closed injury of brain, etc.) [23]. Causes of flatfoot are divergent. There is no uniform view on the development of this disease, and no quantitative indicator to define it in clinic. Clinical research focused on it with visible symptomatic deformity, when changes of mechanical environment have emerged, and simple surgery on soft tissue can not correct deformities or prevent disease recurrence.

Most researches on flatfoot were confined to analysis of clinical observation, and mathematical model is hard to construct for lack of knowledge. Cadaver experimental was used some studies [24-26]. But there was no recognized modeling method on experimental model of flatfoot deformity. A simple and practical method is through incision of joint capsules and release of ligaments on normal foot specimens [27]. Others constructed model by eliminating the force in the tibialis posterior muscle to simulate a complete tear of the tibialis posterior tendon and reducing by 50% the strength of the spring ligament, the short plantar ligament and portions of the long plantar ligament, and the plantar fascia [28]. However, no detailed measurement data based on the flatfoot model was described before, and it is hard to formulate different modeling method for deformity in different degrees and types. This study showed different biomechanical performance of foot-arch after different ligaments were released. Obvious deformity appeared only after three of four main ligaments were released. Though there is no statistical analysis on the state that less than four ligaments were released, more data and experience have been accumulated to further study in expanding samples.

V. CONCLUSION

Ligaments resection is an effective method to model flatfoot deformity in different types and degrees. The cause of flatfoot deformity is multifactorial, and various factors have coupling effect with each other. Quantitative research with advanced methods can offer advice for clinical operations.

REFERENCES

1. Friedman MA, Draganich LF, Toolan B, et al. (2000) The effects of adult acquired flatfoot deformity on tibiotalar joint contact characteristics. *Foot Ankle Int.* 22:241-246
2. McCormack AP, Ching RP, Sangeorzan BJ. (2001) Biomechanics of procedures used in adult flatfoot deformity. *Foot Ankle Clin.* 6:15-23.
3. Richie DH. (2007) Biomechanics and clinical analysis of the adult acquired flatfoot. *Clin Podiatr Med Surg.* 24: 617-644
4. Wangdo K, Arkady SV. (1995) Role of plantar fascia in the load bearing capacity of the human foot. *J Biomech.* 28:1025-1033.
5. Salathe EP, Aranglo GA. (2002) A biomechanical model of the foot: the role of muscles, tendons, and ligaments. *J Biomech Eng.* 124:281-287
6. Gefen A, Megido-Ravid M, Itzhak Y, et al. (2000) Biomechanical analysis of the three-dimensional foot structure during gait: a basic tool for clinical applications. *J Biomech Eng.* 122:630-639
7. Arangio GA, Chen C, Salathe EP. (1998) Effect of varying arch height with and without the plantar fascia on the mechanical properties of the foot. *Foot Ankle Int.* 19:705-709
8. Hicks JH. (1955) The foot as a support. *Acta Anat.* 25:34-45.
9. Gefen A. (2002) Stress analysis of the standing foot following surgical plantar fascia release.
10. Yang YF, Yu GR, Huang SP, et al. (2007) Effect of the plantar fasciotomy on the movement of the foot arch. The 1st International Conference on Bioinformatics and Biomedical Engineering. 486-489.
11. Yang YF, Yu GR, Niu WX, et al. (2007) Effect of the plantar ligaments injury on the longitudinal arch height of the human foot. *Life System Modeling and Simulation, International Conference, LSMS 2007, Lecture Notes in Computer Science.* 4689:111-119
12. Cheung JT, Zhang M, An KN. (2004) Effects of plantar fascia stiffness on the biomechanical responses of the ankle-foot complex. *Clin Biomech.* 19: 839-846
13. Viel E, Esnault M. (1989) The effect of increased tension in the plantar fascia: a biomechanical analysis. *Physiotherapy Practice.* 5:69-73
14. Huang CK, Kitaoka HB, An KN, et al. (1993) Biomechanical evaluation of longitudinal arch stability. *Foot Ankle.* 14:353-357.
15. Thordarson DB, Kumar PJ, Hedman TP, et al. (1997) Effect of partial versus complete plantar fasciotomy on the windlass mechanism. *Foot Ankle Int.* 18: 16-20.
16. Murphy GA, Pneumaticos SG, Kamaric E, et al. (1998) Biomechanical consequences of sequential plantar fascia release. *Foot Ankle Int.* 19:149-152.
17. Mann RA, Thompson FM. (1985) Rupture of the posterior tibial tendon causing flat foot. Surgical treatment. *J Bone Joint Surg Am.* 67:556-561
18. Gazdag AR, Cracchiolo A 3rd. (1997) Evaluation of injury of the spring ligament and clinical assessment of tendon transfer and ligament repair. *J Bone Joint Surg Am.* 79:675-681.
19. Deland JT. (2001) The adult acquired flatfoot and spring ligament complex: Pathology and implications for treatment. *Foot Ankle Clin.* 6: 129-135.
20. Davis WH, Sobel M, Dicarolo EF, et al. (1996) Gross, histological, and microvascular anatomy and biomechanical testing of the spring ligament complex. *Foot Ankle Int.* 17:95-102.
21. Choi K, Lee S, Otis JC, et al. (2003) Anatomical reconstruction of the spring ligament using peroneus longus tendon graft. *Foot Ankle Int.* 24: 430-436.
22. Crary JL, Hollis JM, Manoli A. (2003) The effect of plantar fascia release on strain in the spring and long plantar ligaments. *Foot Ankle Int.* 24:245-250.
23. McCormack AP, Ching RP, Sangeorzan BJ. (2001) Biomechanics of procedures used in adult flatfoot deformity. *Foot Ankle Clin.* 6:15-23.

24. Logel KJ, Parks BG, Schon LC. (2007) Calcaneocuboid distraction arthrodesis and first metatarsocuneiform arthrodesis for correction of acquired flatfoot deformity in a cadaver model. *Foot Ankle Int.* 28:435-440.
25. Vora AM, Tien TR, Parks BG, et al. (2006) Correction of moderate and severe acquired flexible flatfoot with medializing calcaneal osteotomy and flexor digitorum longus transfer. *J Bone Joint Surg Am.* 88A:1726-1734.
26. Havenhill TG, Toolan BC, Draganich LF. (2005) Effects of a UCBL orthosis and a calcaneal osteotomy on tibiotalar contact characteristics in a cadaver flatfoot model. *Foot Ankle Int.* 26:607-613.
27. Thordarson DB, Schmotzer H, Chon J, et al. (1995) Dynamic support of the human longitudinal arch. A biomechanical evaluation. *Clin Orthop Relat Res.* 316:165-172.
28. Arangio GA, Reinert KL, Salathe EP. (2004) A biomechanical model of the effect of subtalar arthrodesis on the adult flexible flat foot. *Clin Biomech.* 19:847-852

Numerical Simulation of A Bidirectional Cavopulmonary Anastomosis Connection with Antegrade Pulmonary Blood Flow

Qi Sun¹, Dawei Wan², Jinfen Liu¹, Yingzheng Liu², Ming Zhu¹, Haifa Hong¹, Qian Wang¹

¹ Department of Cardiothoracic Surgery, Shanghai Children's Medical Center, Shanghai Jiao Tong University Affiliated Xinhua Hospital, Shanghai, China

² School of Mechanical Engineering, Shanghai Jiao Tong University, Shanghai, China

Abstract — Whether the antegrade pulmonary blood flow (APBF) should be preserved or not at the time of bidirectional cavopulmonary anastomosis (BCPA) is controversial in the management of patients with single-ventricle physiology. In this study, we attempted to investigate the fluid dynamic features of this kind of connection using computational fluid dynamics (CFD) and tried to provide some useful information for better understanding of this issue. The patient-specific three-dimensional geometry of a BCPA with native pulmonary artery (PA) trunk was reconstructed according to the computer tomography (CT) scans. Transient simulations were performed at three predetermined levels of pulsatile APBF. Results showed that during one cardiac cycle, the flow ratio of left pulmonary artery (LPA)/right pulmonary artery (RPA) was 1.91 when the average APBF was 0.5L/min and the ratio increased to 2.06 and 2.46 respectively at the level of 1L/min and 1.5L/min. Moreover, mass flow rate of the RPA at the end of the systolic period approached nearer to zero at the average APBF level of 1.5L/min than at the levels of 0.5L/min and 1L/min. The amplitude of static pressures in LPA, RPA and superior vena cava (SVC) during one cardiac cycle was bigger as the amount of APBF increased. We concluded that in this patient-specific three-dimensional BCPA with APBF connection, as the amount of APBF increased, the flow ratio of LPA/RPA became larger and the mass flow rate of RPA at the end of the systolic period approached nearer to zero. Though the pulsatility of the static pressures in LPA, RPA and SVC became more prominent as the amount of APBF increased, the mean static pressures in them remained stable.

Keywords — Computational Fluid Dynamics, Numerical Simulation, Bidirectional Cavopulmonary Anastomosis, Antegrade Pulmonary Blood Flow.

I. INTRODUCTION

BCPA is a standard interim procedure in the staged strategies to the surgical palliative management of patients with single-ventricle physiology.[1-3] This kind of procedure allows stepwise adaptation of the ventricle geometry to the change of volume load in the interval between preliminary conditions and the completion of final Fontan procedure while providing controlled pulmonary blood flow. However the limited pulmonary blood flow may have ad-

verse effect on the potential growth of the pulmonary arteries. One method to increase the pulmonary blood flow in BCPA connection was to preserve the native pulsatile pulmonary forward flow from the ventricle to the stenosed or banded PA trunk, the other method is to establish a Blalock-Taussig shunt.[4,5]

Whether the preserved APBF is beneficial or not to the patients after BCPA or final Fontan procedure is still controversial. Some researchers [6,7] argued that the persistent APBF increased the systemic arterial oxygen saturation and stimulated pulmonary artery growth after BCPA. Moreover the presence of APBF also prevented development of intrapulmonary arteriovenous malformations late after BCPA. Conversely, other researchers [8,9] held the viewpoint that the maintenance of APBF led to higher volume load on the ventricle after BCPA as well as elevated systemic venous pressure thus in turn resulted in higher rate of superior vena cava syndrome and persistent pleural effusions. The influence of APBF on the outcomes after BCPA and Fontan procedure reported in various studies was not identical either.[5-7,9-11]

The objective of this study was to investigate the flow features in the configuration of a BCPA connection with APBF from the native PA trunk using CFD. We hope our results can provide some useful information for better understanding of this kind of connection.

II. MATERIAL AND METHODS

A. Clinical data and three-dimensional reconstruction of the geometry

The patient-specific geometry of this BCPA with APBF connection was reconstructed according to the CT images acquired by a GE LightSpeed 16 Multislice CT scanner (the General Electric Company, America) from a 5-year-old boy who suffered from functional single ventricle. The requirement for patient consent was waived by Shanghai Children's Medical Center.

There are about 200 slices of continuous cross-sectional CT images over the connection investigated, with image

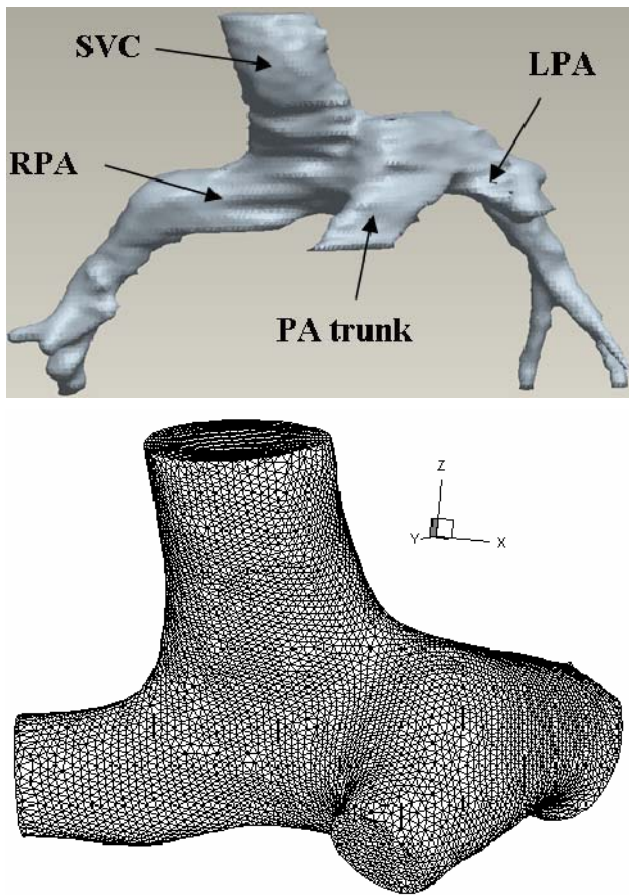


Fig. 1 Three-dimensional geometry of the bidirectional cavopulmonary anastomosis with native PA trunk connection (up) and unstructured grid of the central connection (down) (SVC: superior vena cava, LPA: left pulmonary artery, RPA: right pulmonary artery, PA trunk: pulmonary artery trunk)

matrix being 512×512 pixels. The thickness of each slice is 0.625mm and the distance between adjacent slices is 0.3mm. The reconstructed geometry and the unstructured grid of the central connection area were shown in Figure 1. It consists of SVC, LPA, RPA, PA trunk and the anastomotic site. The inlet and outlet vessels were transected vertical to the long axis of them near the anastomotic site. The SVC, LPA, and RPA were prolonged for later numerical simulation.

B. Boundary conditions and simulations

We assumed that the vessel walls were rigid, fixed and impermeable. The fluid was homogeneous, incompressible and Newtonian ($\rho=1060\text{kg/m}^3$, $\mu=3.5 \times 10^{-3} \text{ Pa}\cdot\text{s}$). We also assumed no-slip boundary conditions at the vessel walls. The

SVC, LPA and RPA were prolonged 30 times of their diameters to guarantee full development of the velocity profiles when the fluid entered and left the investigated configuration. The PA trunk was not prolonged in order to acquire a flat velocity profile at this inlet.[12] When the average APBF was 1.5L/min, the mean Reynolds number in PA trunk was 1200. The fluid in the connection was deemed laminar.

The assumed cardiac output was 2.5L/min. The flow rate of SVC was stable throughout the cardiac cycle and proportioned 40% of the cardiac output, which was 1L/min. In transient simulations, the duration of a cardiac cycle was assumed 0.5s. The systolic and diastolic period proportioned 50% of the cardiac cycle respectively. The waveform of time-dependent flow rate of the PA trunk was sinusoidal in the systolic period and remained zero in the diastolic period to simulate periodic pulsatile blood flow through the PA trunk. The average values of the APBF in one cardiac cycle met with 0.5L/min (group 1), 1L/min (group 2) and 1.5L/min (group 3) respectively. The flow rate of SVC and time-dependent flow rate of PA trunk were imposed on the CFD model as inflow boundary conditions.

The CFD simulations were performed in ANSYS-CFX 11.0[®]. At the beginning of our study, steady-state simulation was performed with equal outlet pressure 1330Pa and the mass flow rate through PA trunk 0 kg/s.

The results of the steady-state simulation were utilized as initial state for each group of transient simulation. Considering the accuracy of the calculation and time of CFD calculation simultaneously, we choose 312,000 cells to perform our transient simulations. Three cardiac cycles with a fixed time step of 0.001 second were simulated to guarantee that a pulsatile regime was reached. The cyclic convergence criterion adopted relied on the flow rate calculation in LPA and RPA and a relative percentage error less than 1% was accepted. Temporal discretization was carried out using a second-order backward Euler time integration scheme.

After the simulations, we recorded the mean pressure and mass flow rate at the cross section where we had cut and extended the vessels every 20 time steps in the third cardiac cycle. Additionally, values at the time of 0.125s and 0.25s were also recorded when APBF reached its peak value in the systolic period and was zero at the end of the systolic period. So there were altogether 28 series of data recorded for analysis in each group of simulation. When calculating the flow ratio of LPA/RPA in a cardiac cycle, the mass flow rate at the 28 time points were averaged.

III. RESULTS

A. Mass flow rate of LPA and RPA

The absolute values and changing tendency of time-dependent mass flow rate of LPA and RPA in the three groups were shown in Figure 2. As was shown in the figure, the mass flow rates of LPA and RPA ascended in the accelerating period of the APBF and reached their peak values together with APBF and then returned gradually to their original level at the end of the diastolic period in all the three groups. The pulsatility of the mass flow rate in both LPA and RPA became more prominent as APBF increased.

At any specific time point in the cardiac cycle, the mass flow rate of LPA increased as the amount of APBF became larger. Differently, the mass flow rate of RPA decreased at the end of the systolic period and during the diastolic period as the amount of APBF became larger.

The flow ratio of LPA/RPA during one cardiac cycle was 1.91 in group 1 and the ratio increased to 2.06 and 2.46 respectively in group 2 and group 3. Moreover, the mass flow rate of RPA at the end of the systolic period approached nearer to zero in group 3 than the other two groups.

B. Static pressures of LPA, RPA and SVC

The maximum, minimum, mean value and amplitude of static pressures of LPA, RPA and SVC in the three groups in the third cardiac cycle were shown in Table 1.

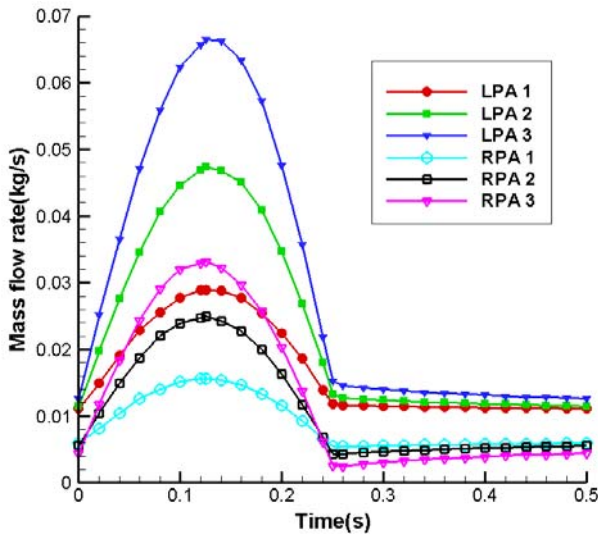


Fig. 2 Mass flow rates of LPA and RPA in the third cardiac cycle in the three groups (LPA: left pulmonary artery, RPA: right pulmonary artery)

Table 1 Static pressure of LPA, RPA and SVC in different groups

	Max(Pa)	Mean(Pa)	Min(Pa)	Amplitude(Pa)
LPA 1	1856.95	1378.75	803.85	1053.10
LPA 2	2337.30	1399.64	361.13	1976.17
LPA 3	2689.60	1438.98	-167.97	2857.57
RPA 1	1846.65	1383.63	835.64	1011.01
RPA 2	2314.37	1395.56	429.11	1885.26
RPA 3	2657.98	1409.31	-107.05	2765.03
SVC 1	1912.80	1409.13	805.28	1107.52
SVC 2	2416.62	1444.77	362.73	2053.89
SVC 3	2795.33	1477.32	-235.40	3030.73

Pressure amplitude of LPA, RPA and SVC became larger as the amount of APBF increased. On the contrary, the mean static pressure values of LPA, RPA and SVC remained stable.

IV. DISCUSSION

The debate on whether we should maintain APBF or eliminate the additional source of pulmonary blood supply during BCPA has been going on. Among the clinical studies concerning this issue, there are several reports which pointed out that appropriately controlled APBF achieved by banding the PA trunk will do benefit to the outcomes of the patients who had undergone BCPA.[4,13] But few numerical studies were designed to investigate the influence of different amount of APBF on the flow features in this kind of connection. In this study, we simulated the blood flow in a BCPA with APBF connection at different levels of pulsatile APBF through native PA trunk by means of CFD simulations and analyzed the time-dependent mass flow rates in the pulmonary arteries as well as the periodic variation of the static pressures in the LPA, RPA and SVC.

It is impossible to completely explain the clinical issues about this kind of connection and give definite suggestions to the surgeons only by this numerical study. However the results of it gave us some useful information to better understanding of the influence of APBF on the flow features in the connection. In this patient-specific three-dimensional BCPA with APBF connection, the flow ratio of LPA/RPA became larger as the amount of APBF increased. This result reminds us that increasing APBF may have the potential to exaggerate the unbalanced blood flow distribution to the lungs. The flow rate of RPA approached nearer to zero at the end of the systolic period and the beginning of the diastolic period as the APBF increased. We speculate that flow reversal may appear when the amount of APBF increases beyond a specific value. The unbalanced lung perfusion and flow reversal may have adverse effect on the development of the pulmonary artery tree. [14]

The pulsatility of the mass flow rate and static pressure in the pulmonary arteries became more prominent when the amount of APBF increased. Kurotobi S and colleagues [15] have reported the impact of pulsatility on pulmonary endothelial function. The maintenance of appropriate APBF was useful to protect the function of the endothelium. Unfortunately this study can not tell us directly which amount of APBF is the best choice to this patient. More clinical and numerical studies need to be done to answer this troublesome question.

Although the assumptions we have made about the inflow rates were reasonable according to clinical experience and pertinent literatures [12,16], the time-dependent inflow rate especially that entered through PA trunk was sure to be different from real conditions. The static pressures initially imposed on the CFD model at two outlets were not patient-specific either. This may attenuate the accuracy of the results, but the change of hemodynamic features caused by different levels of pulsatile inflow rate was useful to identify the influence of APBF on this kind of connection.

V. CONCLUSIONS

In this patient-specific three-dimensional BCPA with APBF connection, the flow ratio of LPA/RPA became larger as the amount of APBF increased. This result reminds us that increasing APBF may have the potential to exaggerate the unbalanced blood flow distribution to the lungs.

As the amount of APBF increased, the mass flow rate of RPA approached nearer to zero at the end of the systolic period and the beginning of the diastolic period.

The pulsatility of the mass flow rates in LPA and RPA as well as static pressures in LPA, RPA and SVC became more prominent as the amount of average APBF rate increased. However the mean pressures in them did not change a lot.

ACKNOWLEDGMENTS

This work was supported by the National Nature Science Foundation of China under grant number 30672087 and the Science and Technology Committee of Shanghai Municipality under grant number 064307056.

REFERENCES

1. Bridges ND, Jonas RA, Mayer JE et al. (1990) Bidirectional cavopulmonary anastomosis as interim palliation for high-risk Fontan candidates. Early results. *Circulation* 82(5 suppl):IV170-176
2. Tanoue Y, Sese A, Ueno Y et al. (2001) Bidirectional Glenn procedure improves the mechanical efficiency of a total cavopulmonary connection in high-risk Fontan candidates. *Circulation* 103:2176-2180
3. Tanoue Y, Sese A, Imoto Y et al. (2003) Ventricular mechanics in the bidirectional Glenn procedure and total cavopulmonary connection. *Ann Thorac Surg* 76:562-566
4. Yoshida M, Yamaguchi M, Yoshimura N et al. (2005) Appropriate additional pulmonary blood flow at the bidirectional Glenn procedure is useful for completion of total cavopulmonary connection. *Ann Thorac Surg* 80:976-981
5. McElhinney DB, Marianeschi SM, Reddy VM (1998) Additional pulmonary blood flow with the bidirectional Glenn anastomosis: does it make a difference? *Ann Thorac Surg* 66:668-672
6. Berdat PA, Belli E, Lacour-Gayet F et al. (2005) Additional pulmonary blood flow has no adverse effect on outcome after bidirectional cavopulmonary anastomosis. *Ann Thorac Surg* 79:29-36
7. Gray RG, Altmann K, Mosca RS et al. (2007) Persistent antegrade pulmonary blood flow post-Glenn does not alter early post-Fontan outcomes in single-ventricle patients. *Ann Thorac Surg* 84:888-893
8. Mainwaring RD, Lamberti JJ, Uzark K et al. (1995) Bidirectional Glenn. Is accessory pulmonary blood flow good or bad? *Circulation* 92(9 suppl):II294-297
9. Mainwaring RD, Lamberti JJ, Uzark K et al. (1999) Effect of accessory pulmonary bidirectional Glenn procedure. *Circulation* 100(19 suppl):II151-156
10. Migliazza L, Seddio F, Anecchino FP et al. (2004) The clinical impact of antegrade pulmonary blood flow on the bidirectional cavopulmonary shunt in infants. *Cardiol Young* 14 (Suppl 3):44-47
11. Berdat PA, Belli E, Lacour-Gayet F et al. (2004) Additional pulmonary blood flow has no adverse effect on outcome after TCPC. *Thorac Cardiovasc Surg* 52:280-286
12. Migliavacca F, de Leval MR, Dubini G et al. (1996) A computational pulsatile model of the bidirectional cavopulmonary anastomosis: the influence of pulmonary forward flow. *J Biomech Eng* 118:520-528
13. Caspi J, Pettitt TW, Ferguson TB Jr et al. (2003) Effects of controlled antegrade pulmonary blood flow on cardiac function after bidirectional cavopulmonary anastomosis. *Ann Thorac Surg* 76:1917-1921
14. de Zélicourt DA, Pekkan K, Parks J et al. (2006) Flow study of an extracardiac connection with persistent left superior vena cava. *J Thorac Cardiovasc Surg* 131:785-791
15. Kurotobi S, Sano T, Kogaki S et al. (2001) Bidirectional cavopulmonary shunt with right ventricular outflow patency: the impact of pulsatility on pulmonary endothelial function. *J Thorac Cardiovasc Surg* 121:1161-1168
16. de Leval MR, Dubini G, Migliavacca F et al. (1996) Use of computational fluid dynamics in the design of surgical procedures: application to the study of competitive flows in cavo-pulmonary connections. *J Thorac Cardiovasc Surg* 111:502-513

The address of the corresponding author:

Author: Jinfen Liu
 Institute: Shanghai Children's Medical Center
 Street: Dongfang Road
 City: Shanghai
 Country: China
 Email: liujinfen2002@yahoo.com

Numerical Study on the Changes of the Pressure Waveform in a Large Artery

F. He and X.Y. Li

College of Mechanical Engineering & Applied Electronics Technology,
Beijing University of Technology, Beijing, 100022, China

Abstract — To study the changes of the pressure waveform in a large artery, a fluid-wall interaction model was constructed and the finite element method was employed. The numerical results indicate that the pressure wave is reflected and the peak pressure gradually increases. The changes of the pressure waveform in a large artery were simulated successfully. The results are in agreement with physiological facts. The model can be used to investigate other mechanical properties of arteries in future.

Keywords — hemodynamics, fluid-wall interaction, pressure waveform

I. INTRODUCTION

Blood vessels are compliant, vessel walls are subjected to dynamic blood flow and withstand pulsatile blood pressure. On one hand, pulsatile pressure induces wall displacement, on the other hand, wall displacement affects blood flow. Therefore this is a fluid-wall interaction phenomenon. Recently, there have been some simulations of unsteady flow with fluid-wall interaction models[1-4]. Physiological and clinical relevant blood flow could be simulated by fluid-wall interaction models. In addition, it is well known that there are some changes in pressure waveform. That is, pulsatile blood pressure progresses in a wave and the pressure wave can be reflected, furthermore, the peak pressure increases gradually in large arteries with the distance away from the heart.

However in much research, there is no reflection in the pressure waveform and the peak pressure gradually decreases. The purpose of this study is to construct a fluid-wall interaction model to simulate reflected pressure waveform and increased peak pressure, and analyze stress and strain distributions of vessel wall in a large artery.

II. THE MODEL AND METHOD

A. The fluid model

The unsteady blood flow was assumed to be laminar, Newtonian and incompressible. For the fluid model, the Navier-Stokes equations were used as the governing equations.

$$\rho \left(\frac{\partial \mathbf{u}}{\partial t} + \left((\mathbf{u} - \mathbf{u}_m) \cdot \nabla \right) \mathbf{u} \right) = -\nabla p + \mu \nabla^2 \mathbf{u} \quad (1)$$

$$\nabla \cdot \mathbf{u} = 0 \quad (2)$$

Where $\mathbf{u} = \{u, v, w\}$, u, v, w are the radial, circumferential and axial velocities respectively, \mathbf{u}_m is the fluid mesh velocity, ρ the fluid density, μ the dynamic viscosity. Blood was modeled to have a density $\rho = 1050 \text{ kg/m}^3$ and a dynamic viscosity $\mu = 0.0035 \text{ Pa s}$.

A pressure profile (Fig.1) and a velocity profile (Fig.2) were prescribed at the inlet and outlet respectively. No-slip boundary conditions were imposed at the wall. The initial conditions in the whole field were assumed to zero.

The finite element method was employed. The parameters of healthy thoracic descending aorta of human being were selected for the calculation. The diameter in the fluid domain was 20mm. There were 19747 tetrahedral elements in the fluid domain.

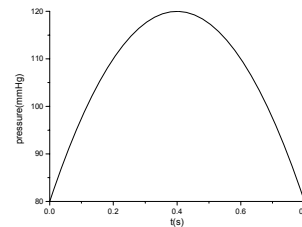


Fig. 1 The map of pressure at the inlet

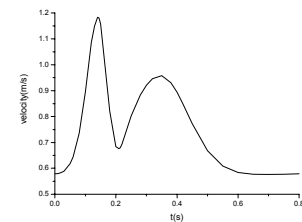


Fig. 2 The map of velocity at the outlet

B. The wall model

The vessel wall was assumed to be linear, elastic, isotropic and incompressible. Actually, the arterial wall behaves nonlinearly but a simple linear model was used because we only wanted to find a methodology of blood-wall interaction analysis, so we addressed it using a simple model. The methodology may be used for a more complex model in the future. Thus, for the wall model, the linear-elastic constitutive equations were used as the governing equations.

$$\sigma_{ji,j} = 0 \tag{3}$$

$$\epsilon_{ij} = \frac{1}{2}(d_{i,j} + d_{j,i}) \tag{4}$$

$$\epsilon_{ij} = \frac{1+\nu}{E}\sigma_{ij} - \frac{\nu}{E}\sigma_{kk}\delta_{ij} \tag{5}$$

Where, E is Young's modulus, ν is Poisson's ratio. The body force was neglected.

The length of the tube was 300mm, and the inner diameter was 20mm and the outer diameter was 24mm in the wall domain (a straight cylindrical tube). The Young's modulus was $1.08 \times 10^8 \text{Pa}$ and the Poisson's ratio was 0.499. The boundary conditions in the wall domain were that one end of the blood vessel was entirely fixed and the other end was free. There were 7200 hexahedral elements in the wall domain.

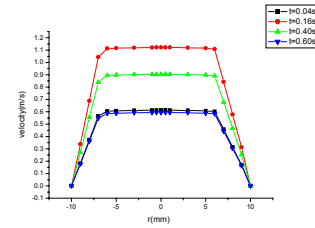
On the fluid-wall interface, the displacements, velocities and normal stresses of them should be compatible as follows:

a. $u_f = u_s$; b. $d_f = d_s$; c. $\sigma_f \cdot n_f = \sigma_s \cdot n_s$

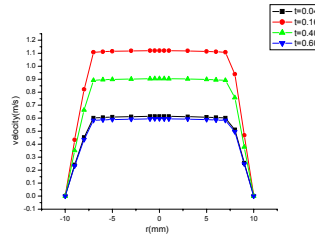
Where d , σ , n are displacement, stress tensor and boundary normal respectively, the subscript f , s denote fluid and solid.

III. RESULTS AND DISSCUSION

The results were obtained through numerical calculation. In order to obtain convergent and steady solutions, three cycles were calculated. The solutions are steady and extracted in the third cycle. L represents the distance away from the inlet in the following figures.



$L = 0.10m$



$L = 0.25m$

Fig. 3 The distributions of velocity at different sections

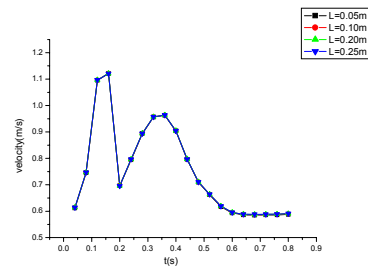


Fig. 4 The maximal velocity at different time

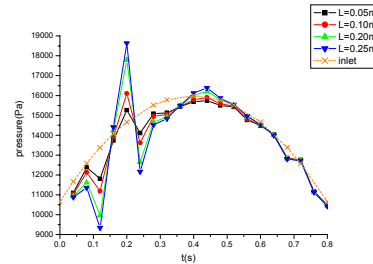
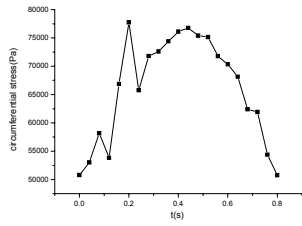
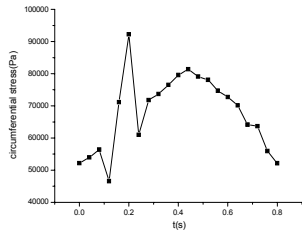


Fig. 5 The distributions of pressure at different time

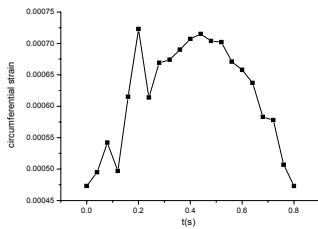


$L = 0.10m$

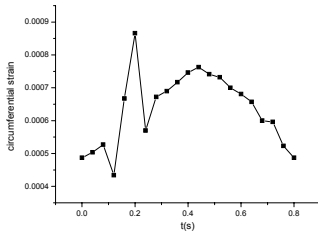


$L = 0.25m$

Fig. 6 The stresses of inner wall at different sections



$L = 0.10m$



$L = 0.25m$

Fig. 7 The strains of inner wall at different sections

The velocity distributions almost do not change in different sections and are blunt in the middle zone (Fig.3), which is in agreement with the Womersley's theory[5]. The maximal velocity at different time maintains the outlet velocity

profile (Fig.4). The peak pressure gradually increases from the inlet to outlet and there is obvious reflection in the pressure waveform (Fig.5). The wall stress and strain waveforms are the same as the fluid pressure waveform and the peak stress and strain also gradually increase (Figs.6 and 7).

From physiological facts, the peak pressure gradually increases away from the heart and there is reflection in the pressure waveform. The calculated results are in agreement with physiological facts, but the prescribed parabolic pressure profile at the inlet is a simplification so that the obtained results departure from the true conditions partly.

The wall stresses and strains change with the fluid pressure, that is, the wall stresses and strains are the concomitant of the fluid pressure. The reason is that the fluid pressure transfers to the wall via the fluid-wall interface and becomes a load acting on blood vessel walls. The wall stress and strain waveforms are accordant with the pressure waveform because the vessel wall is assumed to be linear-elastic.

Several simplifying assumptions were made in the current analysis, which ignored anisotropy, nonlinear-elastic properties of the arterial wall, and the non-Newtonian property of blood, etc. All these higher order effects can be considered in future. However the assumptions do not make essential changes of the whole flow distributions and wall stresses qualitatively. So the assumptions and the calculated results are acceptable.

IV. CONCLUSIONS

A numerical simulation was performed to investigate the changes of the pressure waveform in a large artery. According to numerical results, several conclusions can be drawn. Namely, a fluid-wall interaction model was set up successfully and the pressure wave was reflected and the peak pressure was increased in the model. The changes of the pressure waveform in a large artery can be simulated numerically. The wall stresses and strains change with the fluid pressure, that is, the wall stresses and strains are the concomitant of the fluid pressure. The significance of the paper is that the constructed fluid-wall interaction model has been proven effective and correct in simulating the change of the pressure waveform, and the model can be extended to investigate other mechanical properties of arteries.

ACKNOWLEDGMENT

We thank National Natural Science Foundation of China for financially supporting this research project (10372010).

REFERENCES

1. Zhao S.Z, Xu X.Y, Hughes A.D. et al (2000) Blood flow and vessel mechanics in a physiologically realistic model of a human carotid arterial bifurcation. *Journal of Biomechanics*. 33:975-984.
2. Tang D, Yang C, Walker H. et al (2002) Simulating cyclic artery compression using a 3D unsteady model with fluid-structure interactions. *Computers and Structures*. 80:1651-1665.
3. Moayeri M.S, Zendejbudi G.R. (2003) Effects of elastic property of the wall on flow characteristics through arterial stenoses. *Journal of Biomechanics*. 36:525-535.
4. Valencia A, Solis F. (2006) Blood flow dynamics and arterial wall interaction in a saccular aneurysm model of the basilar artery. *Computers and Structures*. 84, 1326-1337.
5. Fung Y.C. (1984) *Biodynamics: circulation*. New York: Springer.

The address of the corresponding author:

Author: Fan He
Institute: Beijing University of Technology
Street: No.100 PingLeYuan, Chaoyang District
City: Beijing
Country: China
Email: hf@emails.bjut.edu.cn

A Lumped Parameters Dynamic Model for Cerebral Circulation

Shengzhang Wang

Department of Mechanics and Engineering Science, Fudan University, Shanghai, P. R. China

Abstract — A lumped parameters dynamic model for cerebral blood circulation is constructed according to the hydrodynamic model, and the simulations prove the validity of this model. Given the values of the parameters and inputted the waveform of pressure, cerebral blood flow (CBF) can be computed by solving the governing equation of the model. The simulated results show that when artery blood pressure (ABP) drops 15mmHg, CBF drops rapidly at the same time, but in a short time it recovers to almost the same value as before ABP drops. When ABP rises to 15mmHg higher than the normal, the procedure, CBF recovers to the normal value in a short time, is simulated too. Both the dynamic behavior of cerebral blood circulation are simulated numerically by this model, and the results prove that the model can exhibit the cerebral auto-regulation mechanism and should be a good reference for the further research to the modeling the cerebral blood circulation. The knowledge how to fit the parameters of the model to the measured data sets and the influence of the parameters on the system is essential. These topics are discussed as an outlook for further research.

Keywords — Lumped Parameters, Dynamic Model, Cerebral Circulation

I. INTRODUCTION

About 30% of the blood of our body flows through the brain to guarantee a sufficient supply with oxygen. The supply with oxygen saturated blood to the brain is guaranteed by the two main arteries on both sides of the throat. This main arterial then divides up in to smaller and smaller blood vessels until they reach a diameter of only a few microns. These blood vessels are then called capillary. The main oxygen exchanges from the blood to the cells happen in this region.

The brain tissue itself is surrounded by a fluid called cerebrospinal fluid (CSF) to protect the soft tissue from shocks and movements of the head. It works as a kind of damping by using a fluid circulation through small vessels. Three processes can be distinguished in the system: production, circulation and absorption.

Studying the mechanics of cerebral circulation is very valuable to physicians for the diagnosis and therapy of the cerebrovascular diseases.

II. MODEL

A. Hydrodynamic model

As described in the previous section the system “brain” can be separated into a few compartments connected by resistances and capacitances to describe the overall hydrodynamic processes. In this work, we will use 6 compartments to describe the system:

A=arterial, C=capillary, V=venous,
S= sinus sagitalis, B=brain tissue, F=CSF.

The first 4 compartments (A, C, V, S) describe the blood circulation. The overall volume is constant due to the cranial bone. This assumption is also known as the doctrine of Monroe-Kellie. Putting together all the knowledge about the system we obtain our model (see Fig. 1). Since we are dealing with blood vessels, which can be treated as elastic materials, we will not only model the resistances between the compartments, but also the capacitances due to the elastic behavior of the blood vessels. A well satisfied medical approximation is the assumption of only modeling the arteries and veins as capacitances, the capillary compartment and the sinus sagitalis can be assumed as hard walled.

Since the production of CSF is working on capillary level, we have modeled the production as a resistance between C and F. The absorption process of CSF works in the same way between F and S. To put the model into equations, we can use two possible approaches: first using a hydrodynamic model, which is a “realistic” description, and second an electric circuit as an analogue to the hydrodynamic one, which is more “intuitive” for physicians [1].

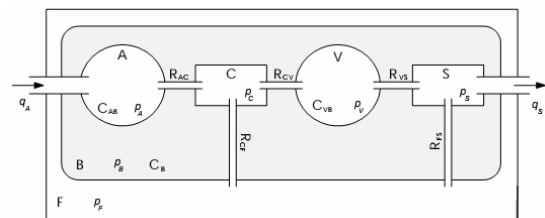


Fig. 1 Hydrodynamic model for cerebral circulation

B. Assumptions for the Hydrodynamic Model

For the hydrodynamic model we use the following basic assumption to simplify the model:

- The blood and CSF is a *fluid* so we can assume it as incompressible and therefore a constant density in the compartments ($\rho = \text{const} \Rightarrow d\rho/dt = 0$). Furthermore an *isotropic* medium is assumed.
- In contrast to the fluid, the brain tissue is a *compressible* medium, so $\rho \neq \text{const} \Rightarrow \rho(t) = f(p(t))$ for given volume and temperature ($V, T = \text{const}$). In our model we always assume the temperature to be constant.
- The membranes between the compartments i.e. the blood vessels are assumed to consist of an elastic media. Accordingly, the pressure difference $p_m = p_A - p_B$ determines the size of the volume: $V = f(p_A - p_B)$, i.e. for elastic media/membrane: $V = \kappa(p_A - p_B)$.
- As resistances we assume *capillary* between the compartments, since the flow is laminar and the flux is accordingly: $\text{Flux} = \Delta p/R$ (Hagen-Poiseuille-law).
- As mentioned before, the total volume is *constant* following the “Monroe-Kellie-Doctrine”:

$$\sum_i V_i = V_{\text{total}} \Rightarrow \sum_i \frac{dV_i}{dt} = 0$$

As the basic equation for determining the pressures and volumes in the model one can use the “conservation of mass” since all volumes/medias are isotropic:

$$\sum_i q_i = \frac{dm}{dt} = V \left. \frac{d\rho}{dt} \right|_{V=\text{const}} + \rho \left. \frac{dV}{dt} \right|_{\rho=\text{const}}$$

since $m(t) = V(t) \cdot \rho(t)$.

The sum of all fluxes into and out of the volume must be equal to the change of mass.

C. Electric Circuit as an Analogue

The electric circuit describes a system analog to the hydrodynamic model. All elements (resistances, capacitances, diodes) are known from circuit theory, as well as Kirchhoff-laws. To simulate the elastic behavior of the arteries/veins and the compressibility of the brain tissue, one uses capacitances. For simplicity of the calculation we assume that the pressures in the brain tissue (B) and in the cerebrospinal fluid (F) are equal. Using the basic equation of “conservation of charge”:

$$\sum I_{\text{in}} = \sum I_{\text{out}} \text{ or } \sum_i I_i = 0$$

at each point (A,C,V,S,B) in the circuit, one can write down the full set of equations. For most physicians this descrip-

tion is probably more intuitive, therefore many papers published on this subject are dealing with electric circuits. Some of the leading publications are [2] and [3]. Still one has to mention the publications on the hydrodynamic approach, since a lot of scientists are working with this one, see [4]. But most of these publications do not take into account the compressibility of the brain tissue, which will be shown later. Therefore it makes us confident that the model presented in this work (taking the compressibility etc. into account) is a good starting point for the further research.

D. Model transformation

Without going too much into details, we will list in the following the nonlinear elements which are necessary to simulate the hydrodynamic processes:

- The autoregulation mechanism, which ensures a constant blood flow through the arteries, acts as a feedback loop. The main variables to change are the resistance of the arteries R_{AC} and the capacitance C_{AB} . If the pressure between the arterial and capillary compartment drops, the resistance reduces to keep the flow constant and vice versa. In the Figure 2 one can see the cerebral blood flow (CBF) and the dependence of the resistance on the pressure difference $c_{pp} = p_A - p_C$. Further a time constant must be taken into account, since the arteries do not act instantaneous. The curve can be fitted by a third order polynomial as follows.

$$CBF = a_3 \cdot c_{pp}^3 + a_2 \cdot c_{pp}^2 + a_1 \cdot c_{pp} + a_0$$

$$a_3 = 0.000016, a_2 = -0.006219, a_1 = 0.789699, a_0 = 20.282461$$

- In the CSF circulation, only cerebrospinal fluid can be produced at the capillary level and absorbed in the sinus sagitalis, so that no reversal of the flux is possible. Therefore the resistances R_{CF} and R_{FS} must be modeled as diodes.
- The capacitance of the vein is ignored because it is very small.
- The model as Fig. 2 is transformed into the model as Fig. 4 in terms of the circuit theory.

The resistances R_{AS}' , R_{AB}' , R_{BS}' are defined as

$$R_{AS}' = \frac{R_0^2}{R_{CB}}, R_{AB}' = \frac{R_0^2}{R_{CS}}, R_{BS}' = \frac{R_0^2}{R_{AC}}$$

where

$$R_0^2 = R_{AC} R_{CB} + R_{AC} R_{CS} + R_{CB} R_{CS}$$

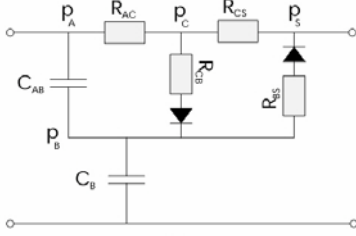


Fig. 2 Lumped parameters dynamic model

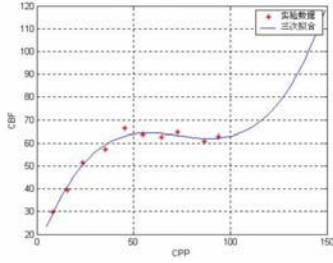


Fig. 3 CBF variables with respect to CPP

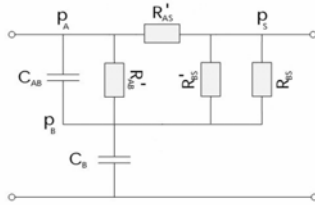


Fig. 4 Transformed model

E. Impedance Computation

- The total impedance in the circuit can be calculated by

$$Z = \frac{1}{\frac{R_{CB}}{R_0^2} + \frac{1}{j\omega C_{AB} + \frac{R_{CS}}{R_0^2} + \frac{1}{\frac{1}{R_{BS}} + \frac{R_{AC}}{R_0^2}}}}$$

where $j = \sqrt{-1}$ and ω is frequency. So the impedance depends on the frequency and wave number and can be formulated by

$$Z(k) = \frac{1}{\frac{R_{CB}}{R_0^2} + \frac{1}{jk\omega C_{AB} + \frac{R_{CS}}{R_0^2} + \frac{1}{\frac{1}{R_{BS}} + \frac{R_{AC}}{R_0^2}}}}$$

III. NUMERICAL SIMULATION

A. Parameters Value

By using the constructed model, it is possible to simulate the whole process of cerebral circulation. The values of the parameters in the simulations are chosen as Table 1[5]. The resistance R_{AC} is calculated by equation (2)

$$R_{AC} = \frac{CPP}{CBF} \tag{1}$$

where $CPP = P_A - P_B$. CPP is measured and CBF is calculated by equation (1).

Table 1 The value of parameters in the model

Parameter	Value	Unit
R_{AC}	40000	dyn-s/cm ⁵
R_{BS}	1.8×10^5	dyn-s/cm ⁵
R_{CB}	6×10^5	dyn-s/cm ⁵
R_{VS}	600	dyn-s/cm ⁵
C_B	2×10^{-6}	cm ⁵ /dyn
C_{AB}	1.5×10^{-7}	cm ⁵ /dyn

B. Flow Computation

The measured pressure is a group time series and is Fourier transformed into a set of pressure value in frequency domain,

$$P(k) = \sum_{n=0}^{N-1} p(n)e^{-jnk\omega}, k = 0, 1, \dots, N-1$$

Therefore, the flow value in frequency domain can be computed by

$$Q(k) = \frac{P(k)}{Z(k)}$$

By using the inverse Fourier Transform, the flow value in time domain can be computed by

$$q(n) = \frac{1}{N} \sum_{k=0}^{N-1} Q(k)e^{jnk\omega}, n = 0, 1, \dots, N-1$$

C. Dynamical Behavior

To validate the correct behavior of the model we will present two simulations and compare the results with clinical observation. The first simulation shows, how the cerebral blood flow and the resistance of the auto regulation reacts on a short time raise of the arterial blood pressure. In reality this can be simulated by dilating one of the arteries leading to the brain. This clinical test is a possibility for the

physicians to validate, whether the autoregulation of the patient is working or not, since this is one of the main regulation mechanisms in the brain.

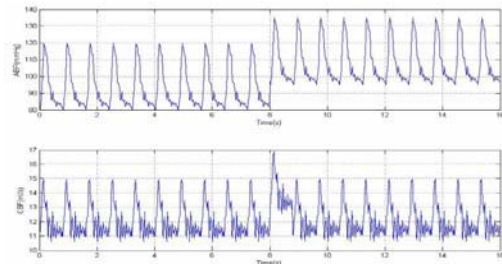


Fig. 5 Simulated results of flow for artery blood pressure drops. Upper: artery blood pressure drops rapidly; Lower: flow reacts

By lowering the arterial blood pressure the system tries to compensate the drop of the cerebral blood flow by lowering the resistance of the arteries.

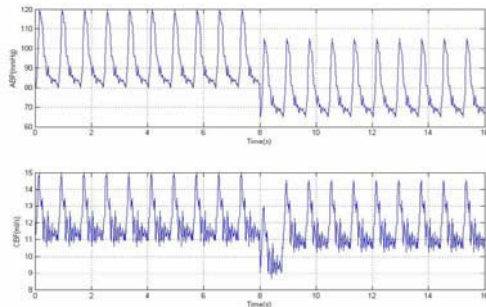


Fig. 6 Simulated results of flow for artery blood pressure raises. Upper: artery blood pressure raises rapidly; Lower: flow reacts

D. Parameters Dependence

As mentioned above, especially the influence of the parameters on the system is of great importance for the physicians, since the evaluation of the parameters using only the measured data sets, would make it possible to determine the state of health of the patients.

They are using a slightly different autoregulation mechanism: the resistance itself is not directly regulated, but the capacitance of the arteries and therefore indirectly the resistance. This regulation mechanism can also be used in our model. To get to a point, at which the system starts to oscillate by itself, one has to change the parameters of the system. Mainly the absorption of the CSF into the venous blood must be reduced and the compressibility of the brain tissue has to be changed slightly. With these changes the

system gets to an unstable fixed point. After having produced these two simulations, we are now confident to use the model for further research of the long time behavior of the system. This behavior is the most interesting one for physicians treating patients on cerebrovascular diseases.

IV. CONCLUSIONS

In this work we have presented a lumped parameters dynamic model for cerebral circulation. The goal was to obtain a better insight into the mechanism of cerebrovascular diseases. We have developed the model and go on to study the behavior of this dynamical system. It was shown, that two different approaches can be used to study the hydrodynamic processes in the brain: a purely hydrodynamic and an electric circuit as an analogue. The nonlinear elements between the compartments play a central role and make the system behave complex. Still one can reproduce typical clinical phenomena and a study of the parameter dependence is possible. In the future work, we want to couple the oxygen levels of the blood and the brain tissue to the presented model. This could give further insight into the processes in the brain. Another option would be study the problem of parameters identification by the clinical data, which would be more valuable for diagnosing the early stage cerebrovascular diseases

REFERENCES

1. Jung Andreas. (2002) A mathematical model of the hydrodynamical-processes in the brain – a rigorous approach. Proceedings of Workshop GK "Nonlinearity".
2. Ursino M. (1988) A mathematical study of human intracranial hydrodynamics part 1: The cerebrospinal fluid pulse pressure. Annual of Biomedical Engineering, 16:379-401.
3. Ursino M, Lodi. (1997) A simple mathematical model of the interaction between intracranial pressure and cerebral hemodynamics. Journal of Applied Physiology, 82:1256-1269.
4. Kadas ZM, Lakin WD, Yu J, et al. (1997) A mathematical model of the intracranial system including autoregulation. Neurool Res, 19:441-450.
5. Yao Wei. (1999) Hemodynamic parameters identification and clinic application of cerebral circulation model. Master Thesis, Fudan University, 6-12.

Author: Shengzhang Wang
 Institute: Dept. of Mechanics, Fudan University
 Street: 220 Handan Road
 City: Shanghai
 Country: P. R. China
 Email: szwang@fudan.edu.cn

The Motion Simulation of Human Lower Extremity Based on Dynamics

Jin Li, Qiuju Cheng, Hong Liang, Zhuowei Guo

Automation College, Harbin Engineering University, Harbin, China

Abstract — Based on the knowledge of Human Anatomy and the multi-body dynamics, a simplified model of the human lower extremity is firstly established using the ADAMS in this paper. In process of modeling for lower extremity, the lower extremity is simplified as thighbone and shankbone joined by knee joint for the patella is very small. There is another assumption that the femur and tibia are simulated as cylindrical rigid body for their shape, which is similar to cylinder. Then, the motion of flexion-extension and medial or lateral rotation of Human's thigh and lower leg's flexion-extension motion is simulated in this paper. In addition, the muscles which are related to the flexion-extension motion are added to the model in the form of point-point force. Lastly, several general movements of muscles-bones of human lower extremity are simulated for researching the principles of force and torque of every joint in process of movement using the kinematics and dynamics analysis function of ADAMS. The results of the simulation are analyzed as well in this paper.

Keywords — ADAMS, muscular model, lower extremity, point-point force, motion simulation

I. INTRODUCTION

The computer simulation of human movement is an effective means of studying the principles of the human motion, and it is emerged as an important technology with the combination of biomechanics and computer vision. And it has very broad and important applications [1]; also, it plays an important role in robotics, human-machine interaction, virtual reality and other related fields. The research of modeling and simulation of human body and the acquirement of relevant data is very important for the athletes training, the protection of casualties, the analysis of traffics and the design of sports rehabilitation equipment, etc. Also the modeling and simulation of the human is an important part of the virtual reality field [2]. So, based on the knowledge of Human Anatomy and the multi-body dynamics, the movement of human lower extremity is simulated in this paper.

II. THE ESTABLISHMENT OF BONE MODEL FOR HUMAN LOWER EXTREMITY AND MUSCULAR MODEL

A. The establishment of bone model for human body

The human lower extremity can be considered as the thigh, leg and foot during human movement, and it is con-

nected with hip, knee and ankle joints. In process of modeling for lower extremity, the lower extremity is simplified as thighbone and shankbone joined by knee joint for the patella is very small [3], and the joints play very important role. Using the more rigid methods, the hip is considered as rotated joint during researching the human motion, and the knee may be simulated as rotated joint for having a freedom degree. The pelvis is viewed as a relatively fixed during the movements of human lower extremity. In process of modeling for lower extremity, there is another assumption that the femur and tibia are simulated as cylindrical rigid body for their shapes are similar to cylinder. The parameters of these rigid bodies are in Table 1 [4].

The regression equation is $Y = B_0 + B_1M + B_2H$, after specifying the standard weight and height of the body ($M=65\text{kg}$, $H=1.7\text{m}$) in the regression equation, the value is shown in Table 2. The visualization of lower extremity model is shown in Fig. 1.

B. Muscular model

On study of muscle mechanical model, it is mostly studied that separating the muscle's two characteristics of length and velocity. Although the results of research could reflect the characteristics of the muscle, it has great lack in the

Table 1 The quality and the data of regression equation

arthromeres		B0	B1	B2
thigh	quality (m)	-0.093	0.152	-0.0004
	Ix	-3664.89	5.549	28.078
	Iy	65.27	7.165	-1.461
	Iz	-3705.38	4.284	28.621
leg	quality (m)	-0.834	0.061	-0.0002
	Ix	-299.164	2.93	2.09
	Iy	-17.776	0.792	-0.033
	Iz	-301.044	2.99	2.012

Table 2 The lower extremity rigid body model parameters

arthromeres	thigh	leg
the shape of rigid body	cylinder	cylinder
length	48(cm)	37(cm)
quality	9.1(kg)	2.8(kg)
Ix(kg-cm ²)	1469.1	246.6
Iy(kg-cm ²)	282.63	28.09
Iz(kg-cm ²)	1438.7	235.3

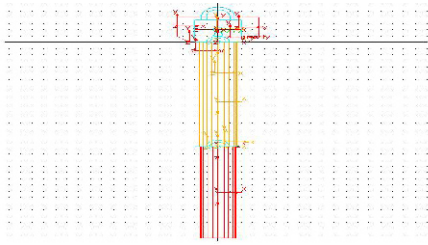


Fig. 1 Rigid model of the human lower extremity

actual application. Therefore, a muscular model that simple to use and could make up tension-length model and the tension-velocity model is inevitable trend in the future research. The muscular model which is put forward by Qi chaohui professor is adopted in this paper [5].

$$F = KS^2 + Ce^{-|v|} + F_0 \tag{1}$$

Where, F is muscle tension, along the long axis of the muscle and point to the centre of muscle; K is the coefficient of muscle's tension-length; S is the variety of the muscle's length; C is the coefficient of muscle's tension-velocity, and the value in the same movement is unchanged; v is the muscle contraction velocity along the long axis; F_0 is human's incentives at initial state of human movement, and this parameter depending on the motion effect which human is willing to achieve.

III. THE ESTABLISHMENT OF MUSCLES-BONES MODEL

A. The muscles-bones model for flexion-extension motion of the thigh

The data which is measured by Xu Qinglei, Ni Weiming and Wan Nianyu of the hip muscles around the beginning and ending points is adopted [6]. The beginning and ending points coordinates of the muscles that related to the flexion and extension motion is shown in Table 3.

There are many muscles related to the motion of the flexion and extension, in order to facilitate research, the muscles can be simplified under the premise of not affecting the effects of action and the muscle's role [5].The rectus femoris muscle and tensor muscle of broad fascial are treated as one muscle group according to the coordinates of them, as well as semitendinosus, semimembranosus and biceps muscle of thigh, so the two muscles' information is calculated from the five muscles can be behalf of the original five muscles. The simplified muscle information of attachment points and length is shown in Table 4. And the motion model is shown in Fig. 2.

Table 3 The relative position of the muscles that related to flexion and extension of the thigh

muscle	points that attached to pelvis (mm)			points that attached to thighbone (mm)		
	X	Y	Z	X	Y	Z
iliopsoas	26	22	5	-2	56	14
rectus femoris	40	37	29	40	-404	4
pubis muscle	41	-4	-36	-3	-125	42
tensor m. of road fascial	46	84	53	18	-404	38
gluteus	-88	66	-39	-8	-122	47
semimembranosus	-43	-28	-0.7	-27	-411	-31
semitendinosus	-51	-35	-14	-2.1	-427	-38
biceps	-51	-35	-14	-22	-427	37

Table 4 Simplified muscle information of points and length

muscle	the points that attached to pelvis(mm)			points that attached to thighbone(mm)			original length of muscles(mm)
	X	Y	Z	X	Y	Z	
muscle 1	26	22	5	-2	56	14	44.96
muscle 2	43	60.5	41	29	-404	21	465.14
muscle 3	41	-4	-36	-3	-125	42	150.54
muscle 4	-88	66	-39	-8	-122	47	221.68
muscle 5	-48.3	-32.67	-9.57	-17.0	-422	-10.7	390.26

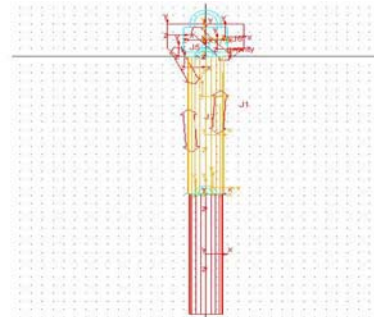


Fig. 2 The motion model of the thigh's flexion and extension

In the process of the flexion motion, the groups of No 1, No 2 and No3 play active role. In the process of motion, active muscles have initial state, and the force of the muscle is affected by the contraction velocity and the muscle's length, but the force of the passive muscles is changed by its length under the role of the active muscles. In the extension motion, the active muscles are No 4 and No 5, and the initial settings are consistent with the flexion motion. The initial states of these muscles are set by the muscular model which is referred upward.

B. The muscles-bones model for medial or lateral rotation motion of the thigh

The data of muscles which are related to this motion is deal with the same way as the flexion-extension motion. And the planform of this model is shown as Fig. 3.

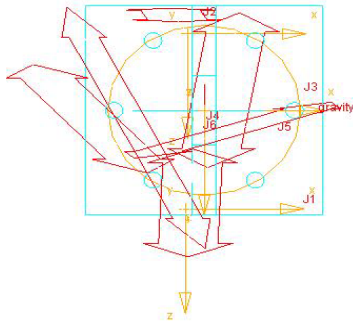


Fig. 3 Planform of motion model for thigh's medial or lateral rotation

C. Muscles-bones model for flexion-extension motion of leg

Adding the muscle groups which are related to this motion into visualization model of human lower extremity in the form of point-point force, the flexion-extension motion model of the leg is obtained. And it is shown in Fig. 4.

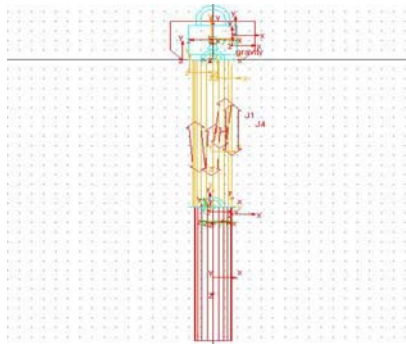


Fig. 4 The muscles-bones model for flexion-extension motion of the leg

IV. THE SIMULATION RESULTS

The flexion-extension motion can be simulated through setting the initial states of the muscle groups in the flexion-extension model of the thigh. And the force-time curve and velocity-time curve are shown as Fig. 5 and Fig. 6.

The Fig. 7 is consistent with the muscular model of Hill, the muscular model which is adopt in this paper is accorded with the physiology in the condition of some initial incentive.

In a motion cycle of the thigh, the angular acceleration of the muscle groups is shown in Fig. 8.

The flexion motion for the human thigh is a process which accelerate first and then decelerate, it also a accelerate process when the length of the muscles change from the maximum length to initial position [8]. In the flexion and extension process for human's thigh, a motion cycle is accomplished through the switching of the active and passive

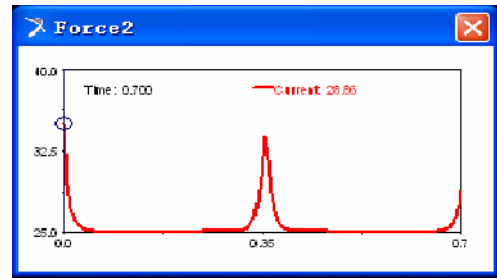


Fig. 5 The force-time curve for the thigh's muscle groups

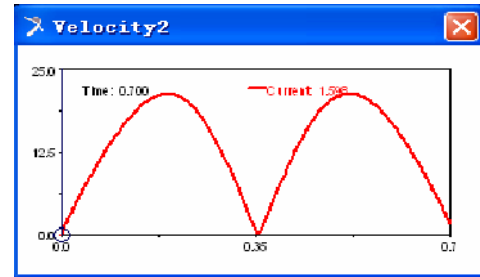


Fig. 6 The velocity-time curve for the thigh's muscle groups

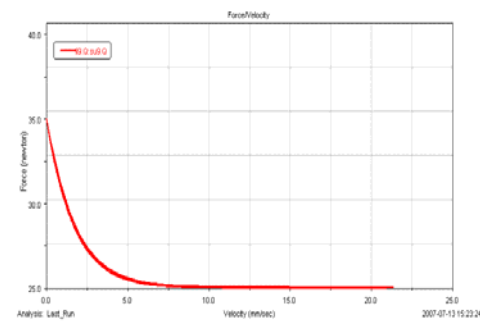


Fig. 7 The force-velocity curve for the thigh's muscle groups

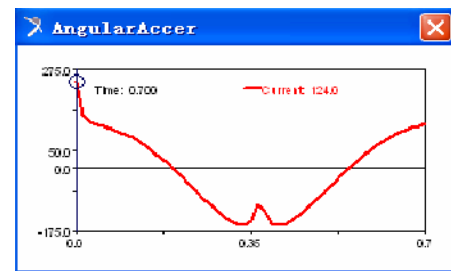


Fig. 8 Curve of angular acceleration for the thigh's muscle groups

muscle groups. The swing scope depends on the size of the initial size of the incentives to a large extent.

In order to find the relations between the force and the velocity, the curve of them is obtained through merger the

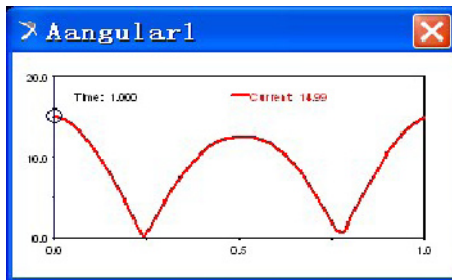


Fig. 9 The figure of the angular acceleration

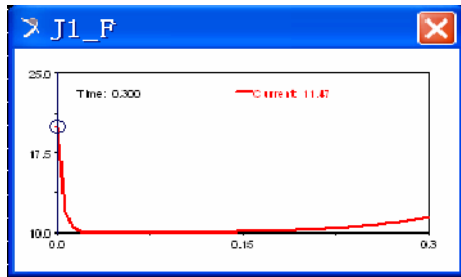


Fig. 10 The force curve of the active muscle J1

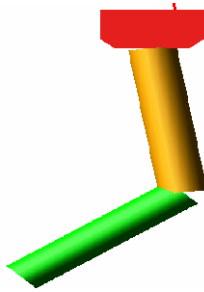


Fig. 11 Visualization figure of the leg's extension motion

Fig. 5 and Fig. 6 using ADAMS in this paper [7]. And it is shown in Fig. 7.

The simulation results for medial or lateral rotation motion of the thigh are shown as Fig. 9.

From the simulation figures above, they are obviously shown that the scope of the medial or lateral rotation motion is smaller than the flexion and extension motion, and the angular velocity is more stable too. Simulation time is set to one second, and medial or lateral rotation motion is completed within a cycle. Based on the anatomy, the angle of thigh's rotating motion is between 40° and 80° , and in the flexion and extension motion, the angle scope can be arrive at 106° , which is consistent to the simulation results in this paper. Simulate to the model for flexion-extension motion of the leg, and the force of the active and the passive muscle groups can be obtained, the force curve of the active muscle is shown in Fig. 10.

In the process of motion, the active muscles have some initial incentive, and the whole system's movement began with this incentive, then, this force decrease gradually, which can be seeing obviously from Fig. 10. The passive muscles's length is changed gradually under the circumstances of null initial force, then the force arrive the maximum which is affected by the length. The simulation Figure at 0.3 second is shown in Fig. 11.

V. CONCLUSIONS

The human body is a complex and multi-body system, in the field of humanoid bodies, researchers have been looking for a design that more reasonable and follow the performance of human movement. From the start of the dynamics and human anatomy, the human motion and muscles' related characteristics is researched using the kinematics and dynamics analysis function of ADAMS in this paper. The routine motions of human lower extremity are simulated; this offers a method for seeking a humanoid body design which is reasonable.

REFERENCES

1. Xu Li, Guo Qiao, Chen Haiying. Modeling Methods of Virtual Human Movement System [J]. Journal of System Simulation, 2004, 16(8), pp 1789-1793.
2. Luo Xiaomei, Yuan Qinghe. The Research of Human Upper Extremity Dynamic Modeling and Simulation Based on ADAMS [J]. The Technology of Electrical and Mechanical engineering, 2006, 35(10), pp 44-47
3. Luo Xiaomei. The Research of Human Body Dynamics Modeling and Simulation Based of ADAMS [D]. Guangzhou: Guangdong University of Technology, 2006, pp 1-30
4. Lei Jianhe. Research on Human Body Motion and Modeling Based on Multi-information Fusion [D]. Hefei: University of Science and Technology of China, 2006., pp 62-66
5. Sun Guangyan. Biomechanics Modeling of Human Hip Joint [D]. Dalian: Dalian University of Technology, 2006, pp 8-47
6. Xu Jinglei, Ni Weiming, Wan Nianyu. Establishment and Application of Three-dimensional Biomechanical Model of Hip Musculature [J]. Medical Journal of Trauma and Disability, 2003, 11(3), pp 13-14
7. Zheng Jianrong. The entry and improvement of virtual prototyping based on ADAMS [M]. Beijing: Machinery Industry Press, 2005
8. Gu Xiaosong. Human Anatomy[M]. Beijing: The Press of Science, 2004

Author: Li Jin
 Institute: Harbin Engineering University
 Street: 45, Nantong Street, Nangang District, 150001
 City: Harbin
 Country: China
 Email: lijn999@hotmail.com

Design of Active Artificial Knee Joint

Liang Song¹, Xitai Wang¹, Siyuan Gong², Zengguang Shi², Lingling Chen²

¹ National Research Center for Rehabilitation Technical Aids, Beijing, China

² Electrical Engineering and Automation School, Hebei University of Technology, Tianjin, China

Abstract — A passive above knee prosthesis being currently in use does not respond adequately to the needs of daily living activities of an amputee due to its limited functions. Therefore, this study deals with design of an active above knee prosthesis. The essential part of this prosthesis is the knee joint actuator based on active control of basic flexion and extension functions of the knee joint with the DC motor. The failure of a single sensor has catastrophic consequences on control. Small inertial measurement unit adhering to the sound leg and two electrodes on stump detect the sound leg gesture and stump SEMG. Using echo control scheme for gait control, which modified knee trajectory from sound leg attitude value and SEMG switch signal.

Keywords — Active knee joint, Inertial measurement unit, Biomechanics, Echocontrol

I. INTRODUCTION

In recent years, the number of amputation patient continues to rise due to disease, traffic accidents as well as work-related injuries and accidents in a variety of the working environment. At present, China has 82.96 million people with disabilities, including physical disabilities 24.12 million. According to the China Disabled Person's Federation (CDPF) statistical data the lower limb disabled person is about 2 million people. The most important issue of the lower limb amputations is artificial limb's assembly. Artificial leg's major function part is the knee joint and the false foot, and the main research of this study is the artificial limb knee joint, which may help the body to achieve the support of standing and the nimbleness and gracefulness while walking^[1]. Specifically, a good artificial limb knee joint can guarantee the stability in the support phase (a period from the heel to tip to the toe to lift-off) and the flexibility of the swing phase (a period from the toe to take-off to the heel to tip), so the amputee gait could close to natural gait. At the same time, the artificial limb knee joint is also the determining factor of the entire artificial limb's performance and life^[2]. Most traditional artificial limb knee joint uses the mechanical organization, which is passive. Its damping size cannot be adjusted or changed along with the gait, and the artificial limb is mainly driven through the residual limb to achieve walks. Therefore the artificial limb knee joint is stiff while flexion and exten-

sion in the gait oscillation cycle, and in support phase the stability is mainly through mechanical load-bearing self-locking institutions to achieve. Along with scientific and technological development, people started to study the using of the chip to control the movement of artificial limb knee joint, and have developed many kinds of chip-control hydraulic pressure/barometric pressure cylinder damping to control the artificial limb knee joint's flexion and the extension and the support phase stability^[3]. But is still relying on the remnant thigh to drive the artificial limb, the amputees has a large energy consumption and easy fatigue. And the adjustment of walking rate mainly depending on the adjustment of the barometric pressure/hydraulic pressure's damping according to the sensor feedback gathering information^[4]. For these issues, this paper plans to design a active control artificial limb to compensate the missing function of the body, so the patients could take care daily living of oneself and complete the work thus return to the society.

II. THE CONSTRUCTION OF ACTIVE ARTIFICIAL KNEE JOINT

The system of active artificial knee joint is composed of electromechanical system for driving knee joint movement, IMU for measuring nature lower limbs gesture, the measuring unit for stump leg's SEMG (Surface Electromyography Signal). The system structure is shown as Fig. 1.

Electromechanical system composed of DC servo motor, digital quadrature encoder, planetary gearhead, driver gear, IMU and wireless communication unit is used to receive the signal from IMU and SEMG measurement unit, then solve the main arithmetic to generate active artificial knee joint's expected trajectory, through motor rotation controlling the swing speed of crus and torque of knee joint to expected state. Electromechanical system is installed at position of knee joint to achieve the function of natural knee.

Gesture measurement unit is composed of inertial measurement unit, low power consumption single chip controller and wireless communication module. It locates

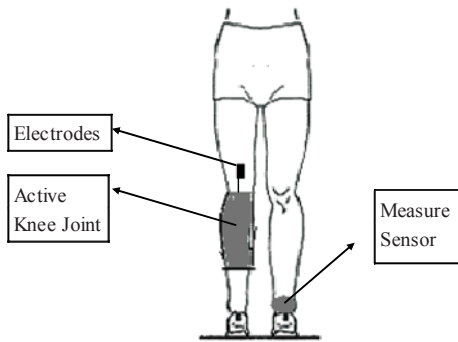


Fig. 1 The general structure of artificial knee joint system

at the unilateral sound leg, measures the health crus gesture and movement gesture in real time, then send the measuring data to the main controller.

The measuring unit of SEMG is used to measure the SEMG of vastus intermedius and semintendinosus, then transferred the SEMG voltage value to the main controller to judge the tendency weather the stump be going to move. Figure 2 shows the connection diagram of the above part.

III. SERVO SYSTEM

It is used TMS320F2812 DSP^[5] with maximum clock frequency 150Mhz in the core processor of controller. Chip

include two event management unit (EVA, EVB) designed for PWM outputs, quadrature encoder circuit (QEP), speed measurement, pulse width measurements. Communication interface include two Universal Asynchronous Serial Port (SCI), a universal synchronous serial (SPI). It can connect all the necessary peripheral devices and accurately manage power of the device with all the necessary analog feedback and control signals. At the same time , it also has a standard JTAG interface for download and debug procedures. Thus provides users with a complete and reliable programmable system solutions. After level conversion, MAX232 chip is using for RS232 serial communication function between DSP on-chip SCI module and computer. Wireless communication unit connected with main controller and gesture measuring unit are used for RF communications module whose core is CC2500. Host module works 50 times per second to send wake-up signal for starting gesture measuring unit and waiting for receiving feedback signal.

Electromechanical system is composed of motor, motor drive circuit and mechanical parts. It used RE40 DC motor made by Switzerland Corporation Maxon Motor. H-bridge driver chip TLE4203 containing integred free-wheeling diodes is chosen as the motor amplifier. Mechanical parts included a transmission gear unit which transform Motor rotation to the swing of the active knee prostheses. Current sensor chip LTS25-NP based on ASIC (Application Specific Integrated Circuit) made by Lem company is used in the system for measuring armature current. The electromechanical system adopts three closed loops controlling electric current, voltage and rotational speed.

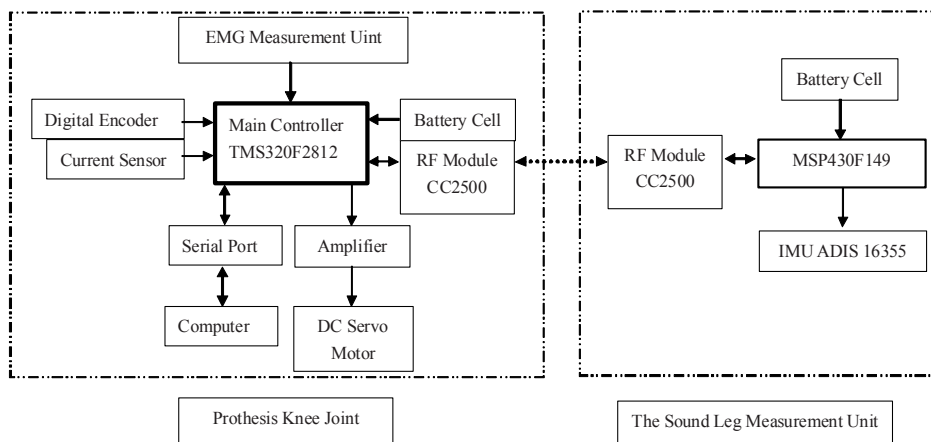


Fig. 2 Schematic block diagram of the whole system

Active prosthesis knee joint movement trace can be deduced from sound leg gesture signal using echo control method described by Grimes et al, in which a modified knee trajectory form the sound leg is played back on the contralateral side^[6,7].

IV. GESTURE MEASURING UNIT

In functional electrical stimulation (FES) and prosthetic systems, the failure of a single sensor has catastrophic consequences on control. This has motivated research on methods to base FES and hybrid assistance of locomotion on natural or artificial micromachined sensors, which have been applied broadly on daily activities quantification^[8].

Gesture measuring unit is composed of MSP430F149^[9], IMU for ADIS 16355 and RF Module CC2500. Depending on wake-on-radio functionality, activated by radio signal from prosthesis leg RF module, Collecting information from the side of the sound leg is 50 per second, then sent the data to the main controller TMS320F2812, after this detecting system to low power consumption sleep mode, until comes the next wakeup signal.

The TI ultralow-power microcontroller MSP430F149 which is optimized to achieve extended battery life in portable measurement application includes two synchronous SPI interface. The digitally controlled oscillator (DCO) allows wake-up from low-power modes to active mode in less than 6 μ s.

The ADIS16355 is a multi-axis motion sensor that cost-effectively combines gyroscopes and accelerometers to measure all six possible degrees of mechanical freedom (6DOF); linear motion in the X, Y, and Z axes and rotation around the X, Y, and Z axes.

The CC2500 is a highly integrated multichannel RF transceiver designed for low-power wireless applications in the 2.4 GHz Industrial Scientific Medical (ISM) band. In this system, the CC2500 can be used together with MSP430F149 microcontroller and a few extra low-cost passive components.

V. MEASURING SYSTEM FOR EMG

The echo control approach restricts the use of the prosthesis to unilateral amputees and also presents a problem for "odd" numbers of steps, in which an echoed step is undesirable. A more subtle, although perhaps more significant shortcoming of the echo-type approach is that suitable motion tracking requires a high output impedance of the prosthesis,

which forces the amputee to react to the limb rather than interact with it.

The surface electromyographic signals of lower limb were extracted to be switch signal, and translate into movement information^[10].

The SEMG measuring system includes two detection channels. Hardware of each channel composes a instrumentation amplifier INA2321, a low-pass filter, a operational amplifier OPA2335, a high-pass filter, a micro-power sampling analog-to-digital converter ADS8321.

VI. CONCLUSION AND SIGNIFICANCE

The IMU configuration can provide sufficient redundant information to control a novel active above knee prosthesis for dynamically adaptation of prosthesis knee joint attitude. Moreover, collection and enrichment of biomechanical data form the sensor can be obtained for motion analysis. RF transceiver gives a wireless route from IMU to the main controller. The real time data acquisition from the sound leg makes the controller able to mimic its movements. The DC motor actuator provides strong power to drive the prosthesis knee joint.

REFERENCES

1. Au, S. Bonato, P., Herr, H., "An EMG-Position Controlled System for an Active Ankle-Foot Prosthesis: An Initial Experimental Study," Proceedings of the IEEE Int Conf. on Rehabilitation Robotics, pp. 375-379, 2005.
2. Fite, K.B., Mitchell, J., Barth, E.J., and Goldfarb, M. A Unified Force Controller for a Proportional-Injector Direct-Injection Monopropellant-Powered Actuator, ASME Journal of Dynamic Systems, Measurement and Control, vol. 128, no. 1, pp. 159-164, 2006.
3. Flowers, W.C., "A Man-Interactive Simulator System for Above-Knee Prosthetics Studies, Department of Mechanical Engineering PhD Thesis, MIT, 1973.
4. Atakan Varol. Progress towards the intelligent control of a powered transfemoral prosthesis, Masters thesis, Vanderbilt University. 2007
5. Texas Instruments. TMS320F28x DSP Peripherals Reference Guide. 2003
6. Grimes, D. L. An Active Multi-Mode Above Knee Prosthesis Controller. Department of Mechanical Engineering PhD Thesis, MIT, 1979.
7. Grimes, D. L., Flowers, W. C., and Donath, M. Feasibility of an active control scheme for above knee prostheses. ASME Journal of Biomechanical Engineering, vol. 99, no. 4, pp. 215-221, 1977.
8. Huseyin G. Wu, Z. Ladin, The study of kinematic transients in locomotion using the integrated kinematic sensor, IEEE Rehab. Eng. 4 (3) (1996) 193-200.

9. MSP430x13x, MSP430x14x, MSP430x14x1 Mixed Signal Microcontroller (Rev. F), 03 Jun 2004
10. Lingling Chen, Peng Yang,, Fuzzy Support Vector Machine for EMG Pattern Recognition and Myoelectrical Prosthesis Control, 2007, Lecture Notes in Computer Science, numb 4492, pages 1291-1298.

Author: Liang Song
Institute: National Research Center for Rehabilitation
Technical Aids
Street: A6,Baijiazhuang Road
City: Beijing
Country: China
Email: clearpotato@sina.com

Importance of Anterior Mitral Basal Stay Chords for Left Ventricular Outflow Hemodynamics: A Computational Study

F. Xiong¹, J.H. Yeo¹, K.H. Lim¹, P. Zhang², Y.L. Chua³ and W.A. Goetz⁴

¹ School of Mechanical and Aerospace Engineering, Nanyang Technological University, Singapore

² School of Mechanical and Automatic Engineering, Shanghai Institute of Technology, Shanghai, China

³ Department of Cardiovascular Surgery, National Heart Center, Singapore

⁴ Department of Cardiovascular Surgery, German Heart Center Munich, Munich, Germany

Abstract— Anterior mitral basal stay chords are transferred to correct prolapse of the anterior mitral leaflet (AML) and it has been supposed to transect the stay chords to treat functional ischemic mitral regurgitation. This numerical study seeks to clarify the effect of stay-chord transection (SCT) on hemodynamic aspects of left ventricular outflow. Two three-dimensional left ventricular models including the left ventricular outflow tract and saddle-shaped mitral valve before and after SCT were constructed. After SCT, the anterior mitral leaflet was specified to be more concave and the aorto-mitral angle to be narrower than before SCT. Time-dependent turbulent flow in a flow range of 10–28 L/min during rapid ejection was simulated using commercial software FLUENT. Left ventricular outflow before SCT was streamlined along the AML throughout rapid ejection. After SCT this flow was redirected in the vicinity of the AML creating a zone of persistent low-momentum recirculation associated with additional energy loss. Consequently, the axial forward flow delivered into the aorta after SCT was diminished. High wall shear stress, concentrated at the fibrous trigones before SCT, was redistributed along the inter-trigonal distance after SCT. The stay chords, which maintain the natural profile of the AML, are essential to streamline left ventricular outflow, facilitate flow delivery into the aorta, minimize dissipation of potential energy, and create an optimum wall shear stress pattern that conforms to the fibrous trigones. Transection of stay chords compromises local hemodynamics, resulting in greater energy loss and unfavorable wall shear stress distribution. The study emphasizes the importance of preserving stay-chord function in mitral valve surgeries.

Keywords— Stay chords, mitral valve, hemodynamics, energy loss, numerical simulation

I. INTRODUCTION

The basal stay chords are the thickest and longest of the second-order chords that originate from anterolateral and posteromedial papillary muscles and insert into the ventricular surface of the anterior mitral valve leaflet (AML). The stay chords remain taut during the entire cardiac cycle tethering the lateral portion of the AML in place. Assuming they are not critical in mitral and ventricular function, the

stay chords are transferred to correct prolapse of the AML and it has even been suggested to transect the stay chords to abolish anterior leaflet tethering in ischemic mitral regurgitation [1-4]. It has been shown through in-vitro and in-vivo experimental studies that the stay chords are important in mediating the valvular-ventricular interaction and maintaining an optimal left ventricular (LV) systolic pump function [5-7]. To date, however, there is still only limited information about the role that the stay chords play in blood flow dynamics. Our previous studies in sheep models have revealed that stay-chord transection (SCT) has changed the geometrical profile of the AML and left ventricle, and accordingly remodeled the diastolic inflow and systolic outflow funnels [8,9]. We hypothesize that this geometrical change should have an adverse impact on LV flow dynamics. To elucidate the consequences of SCT in hemodynamic aspects of LV systolic outflow a numerical simulation was performed. Detailed local flow phenomena such as vortex formation, flow separation and recirculation, potential energy loss and turbulent wall shear stress were presented and analyzed.

II. MATERIALS AND METHODS

A. Model Construction and Boundary Conditions

Two three-dimensional LV models before and after SCT were constructed. The mitral annulus had a nonplanar saddle-shaped configuration. The posterior mitral leaflet with a billow shape was sealed against the AML at the free margins, simulating a fully-closed mitral valve position. In the model after SCT, the lateral portion of the AML became more concaved into the left atrium and the aorto-mitral angle was narrowed by about 5 deg than before SCT as revealed in our earlier findings [8,9]. The left ventricle was modeled as a cone-shape structure with a flat intraventricular septum. The aorta was assumed to be a circular conduit, and the sinus was simplified as three identical hemispheres to permit a general description of the aorta and the left heart structure. Figure 1 shows schematically the model configu-

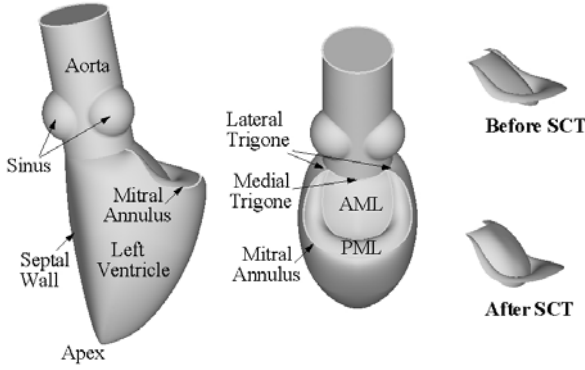


Fig. 1 Geometrical configuration of the numerical model and relevant terminology. AML, anterior mitral leaflet; PML, posterior mitral leaflet; SCT, stay-cord transection.

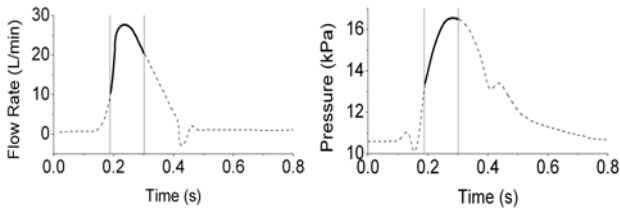


Fig. 2 Flow (Left) and pressure (Right) waveforms. The portion of each waveform applied in the study corresponding to the rapid ejection phase is indicated by the bold solid line.

ration with relevant terminology. The dimensions for constructing the model are obtained from the literature [10-12].

The blood was modeled as incompressible, homogeneous and Newtonian fluid with a dynamic viscosity of $0.004 \text{ kg m}^{-1} \text{ s}^{-1}$ and a density of 1060 kg m^{-3} . The model was in axial direction bounded by an LV (inflow) and an aortic (outflow) cross-sectional plane. The model was at the inflow boundary plane fed with a time-dependent flow with flow rate varying between $10\sim 28 \text{ L/min}$, and at the outflow boundary plane loaded with the static aortic pressure ranging between $13.2\sim 16.5 \text{ kPa}$ (Fig. 2) with the bold solid lines. The prescribed conditions correspond to the rapid ejection phase, which lasts about 0.13 s at a heart rate of 75 beats/min . The flow and the pressure waveforms used were adapted from Ganong [13]. The walls of the left ventricle and aorta were assumed to be rigid and stationary.

B. Modeling Approach

The effect of turbulence was simulated using the $k-\varepsilon$ turbulence model. Let \vec{U} , P , ρ and μ be the blood flow velocity, static pressure, blood density and dynamic viscosity, respectively. The unsteady, isothermal, incompressible

turbulent blood flow is governed by the Reynolds Averaged Navier-Stokes equations:

$$\rho \frac{\partial \vec{U}}{\partial t} + \rho \vec{U} \cdot \nabla \vec{U} = -\frac{1}{\rho} \nabla P + \mu \Delta \vec{U} - \rho \nabla \cdot R \quad (1)$$

$$\nabla \cdot \vec{U} = 0 \quad (2)$$

A control-volume-based code FLUENT (Fluent Inc., Lebanon, NH) was employed to solve the above equations. The solution was considered converged when the residuals about each velocity component, mass creation rate, and k and ε strictly dropped to 1×10^{-4} within each time step.

C. Calculation of Energy Loss and Wall Shear Stress

The energy loss at peak systole was calculated based on the Bernoulli equation and the continuity equation:

$$h_E = (P_i - P_o) + \left(\frac{1}{2} \rho K Q^2 \right), \quad K = \frac{A_o^2 - A_i^2}{A_o^2 \times A_i^2} \quad (3)$$

Here P_i and P_o are the static pressure at the inflow and outflow boundaries, respectively; A_i and A_o the corresponding surface area; K the area coefficient; and Q the volume flow rate. The energy loss coefficient used the form defined by Garcia et al. (14):

$$\xi_E = \frac{Q}{50 \times \sqrt{h_E} / 133.3} \quad (4)$$

In this equation, h_E is expressed in Pa, Q in mL/s, and ξ_E in cm^2 .

The wall shear stress vector is defined by $\vec{\tau}_w = (\tau_{rx}, \tau_{r\theta})$, where τ_{rx} , $\tau_{r\theta}$ are the wall shear stress components in axial and circumferential directions, respectively, based on cylindrical coordinates.

III. RESULTS

Figure 3 compares the predicted flow fields during rapid ejection in the median plane of the two models. At the onset of ejection, a potential flow of mainstream was directed along the LV outflow tract into the aorta (Fig. 3a). In the model before SCT, the velocity vectors close to the AML followed the wall contour of the AML and very uniform flow patterns were observed through the LV outflow tract as well as in the aorta. After SCT, the flow began to separate

along the curved surface of the AML, the velocity vectors near the wall exhibited irregular paths and the volume of the forward flow in the mainstream was diminished compared with the case before SCT.

As the systolic acceleration progressed, the overall flow patterns remained similar to those at the earlier stage (Fig. 3b). In the model after SCT, the flow separation in the vicinity of the AML was a persistent feature, and the irregular and skewed motion of the fluid near the aortic wall became increasingly more prominent.

By peak systole, the turbulent flow in the aorta reached the highest speed (Fig. 3c). In each model, immediately downstream of the sinus the flow was skewed against the aortic wall. The flow skewing was more pronounced in the model after SCT, accompanied also by flow separation along the aortic wall. The model after SCT was again characterized by a zone of slowly recirculating flow at the undersurface of the AML.

During deceleration, the slowly recirculating flow at the undersurface of the AML in the model after SCT became more expansive and the surrounding fluid was directed across the mainstream toward the septal wall (Fig. 3d). As a result, the amount of the forward flow delivered into the aorta appeared to be reduced compared with the case before SCT. There was still no sign of flow disturbance along the AML in the model before SCT.

The energy loss h_E and energy loss coefficient ξ_E between the inflow and outflow boundaries at peak systole were calculated. The pressure drop $P_i - P_o$ before SCT was about 2344.3 Pa, and after SCT this value increased to 2607.2 Pa. By subtracting the dynamic pressure component, the energy loss h_E before and after SCT yielded 2135.7 Pa and 2409.2 Pa, respectively. The resulting energy loss coefficient ξ_E decreased from 2.33 cm^2 to 2.20 cm^2 after SCT.

For each model, the base area of the mitral valve experienced the most significant variations in shear stress (Fig. 4). In the model before SCT, the highest shear stress with magnitude of 20.2 Pa appeared at the location of the fibrous trigone. In comparison, high shear stress in the model after SCT was redistributed evenly along the inter-trigonal distance of the mitral annulus. The maximum magnitude was elevated to 38.5 Pa and shifted away from the trigone to the inter-trigonal position.

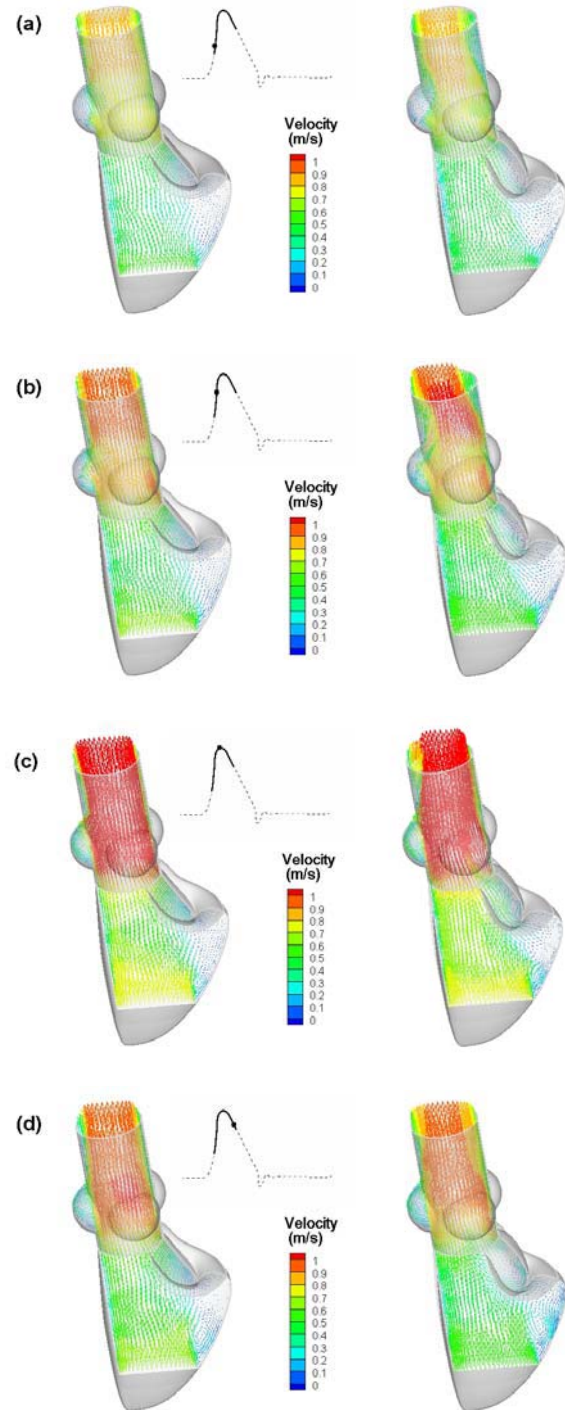


Fig. 3 Velocity vector plots at four time points of rapid ejection in the median plane before (left) and after (right) stay-chord transection. The vectors are colored by velocity magnitude.

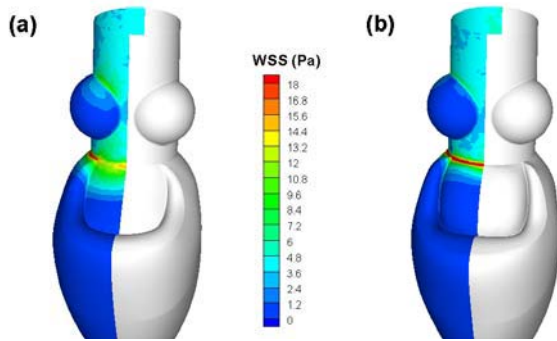


Fig. 4 Contour plots of wall shear stress magnitude at peak systole on the three-dimensional surface before (a) and after (b) stay-chord transection.

IV. DISCUSSION

Our numerical results show that SCT has profoundly altered the LV outflow hemodynamics. In the model with the stay chords preserved, the blood is guided fairly smoothly through the LV outflow tract into the aorta. The streamlined flow passage also ensures the maximum volume of axial forward flow in the aorta. After SCT, the blood flow is characterized by an expansive, low-momentum recirculation in the vicinity of the AML as well as pronounced flow skewing and separation along the aortic wall. These phenomena arise during systolic acceleration and prevail for the remainder of rapid ejection. The flow separation and low-momentum recirculation do not aid in flow delivery, but rather tend to induce additional energy loss. Indeed, the calculation shows that 12.8% more potential energy has been lost at peak systole after SCT. Whether this increase in the energy loss has a significant clinical consequence is not known. However, it may account, at least partially, for the decreased aortic forward flow after SCT observed by Obadia et al. [5]. Consistently, our numerical results show also that SCT results in reduced axial net forward flow in the aorta with disturbed near-wall flow patterns.

In addition to hampering flow delivery, flow separation and low-momentum recirculation results in redistribution of wall shear stress. Before SCT, the highest turbulent shear stress at peak systole appears at the specific sites which in anatomy correspond to the anterior and posterior fibrous trigones, and this may represent a teleological reason for nature's creation of these strong fibroelastic components. After SCT, high shear stress is relocated evenly along the distance of the mitral annulus connecting the trigones, and the maximum magnitude became nearly twofold greater than in the case before SCT.

These results have implications for surgical procedures in which stay chords are marginalized or transected. In mitral valve repair, the second-order chords have been transferred from the body to the free margin of the AML to correct prolapse caused by anterior chordal rupture or elongation [1,2]. Recently, transection of stay chords has been proposed as a treatment for ischemic mitral regurgitation to facilitate coaptation of the mitral leaflets by alleviating leaflet tethering [3,4]. In mitral valve replacement, surgeons prefer to sacrifice all the anterior leaflet chordae tendinae mainly for ease of technical execution. However, in view of the impaired flow patterns and wall shear stress distribution induced by SCT revealed in the present study, caution is urged with regard to any procedure that may change the natural anatomy of the stay chords.

V. CONCLUSIONS

The tethering of the stay chords on the AML creates a streamlined LV outflow funnel that facilitates flow delivery into the aorta with minimal dissipation of energy loss by limiting flow separation and instability. The stay chords also serve to ensure an optimum wall shear stress distribution that conforms to the fibrous trigones. Transection of stay chords compromises local hemodynamics, resulting in greater energy loss and unfavorable wall shear stress distribution. This study emphasizes the importance of preserving stay-chord function in mitral valve surgeries.

REFERENCES

1. Grossi EA, Galloway AC, LeBoutillier M III, et al. (1995) Anterior leaflet procedures during mitral valve repair do not adversely influence long-term outcome. *J Am Coll Cardiol* 25:134-136
2. Sousa UM, Grare P, Jebara V, et al. (1993) Transposition of chordae in mitral valve repair: mid-term results. *Circulation* 88(suppl II):II-35-II-38
3. Messas E, Guerrero JL, Handschumacher MD, et al. (2001) Chordal cutting: a new therapeutic approach for ischemic mitral regurgitation. *Circulation* 104:1958-1963
4. Messas E, Pouzet B, Touchot B, et al. (2003) Efficacy of chordal cutting to relieve chronic persistent ischemic mitral regurgitation. *Circulation* 108:111-115
5. Obadia JF, Casali C, Chassignolle JF, et al. (1997) Mitral subvalvular apparatus: different functions of primary and secondary chordae. *Circulation* 96:3124-3128
6. Nielsen SL, Timek TA, Green GR, et al. (2003) Influence of anterior mitral leaflet second-order chordae tendinae on left ventricular systolic function. *Circulation* 108:486-491
7. Rodriguez F, Langer F, Harrington KB, et al. (2004) Importance of mitral valve second-order chordae for left ventricular geometry, wall thickening mechanics, and global systolic function. *Circulation* 110(suppl II):II-115-II-122

8. Goetz WA, Lim HS, Pekar F, et al. (2003) Anterior mitral leaflet mobility is limited by the basal stay chords. *Circulation* 107;2969-2974
9. Goetz WA, Lim HS, Lansac E, et al. (2003) The aortomitral angle is suspended by the anterior mitral basal "stay" chords. *Thorac Cardiovasc Surg* 51(4):190-195
10. Babburi H, Oommen R, Brofferio A, et al. (2003) Functional anatomy of the normal mitral apparatus: a transthoracic, two-dimensional echocardiographic study. *J Heart Valve Dis* 12(2):180-185
11. Sakai T, Okita Y, Ueda Y, et al. (1999) Distance between mitral annulus and papillary muscles: anatomic study in normal human hearts. *J Thorac Cardiovasc Surg* 118:636-641
12. Thubrikar M (1990) *The Aortic Valve*. CRC Press, Inc., Boca Raton, Florida
13. Ganong WF (2003) *Review of Medical Physiology*. 21st edition, McGraw-Hill Medical, New York

Author: Yeo Joon Hock, PhD
Institute: School of Mechanical and Aerospace Engineering, Nanyang Technological University
Street: 50 Nanyang Avenue, Singapore 639798
City: Singapore
Country: Singapore
Email: mjhyeo@ntu.edu.sg

A Theoretical Model for Binary Adhesion of Cells in Flows

Ying Fang¹, Yonghua Lao¹, Quhuan Li², Cheng Zhu³, Jianhua Wu¹

¹ School of Bioscience and Bioengineering, South China University of Technology, Guangzhou, 510640, China

² School of Life Science, Sun Yat-Sen University, Guangzhou, 510275, China; ³ Coulter Department of Biomedical Engineering and Woodruff School of Mechanical Engineering, Georgia Institute of Technology, Atlanta, GA 30332

Abstract — the adhesion of flowing cells to the vascular surface in localized sites will occur in many physiological and pathological processes, such as inflammatory reaction, tumor metastasis, and thrombus formation. This transport dependent process depends not only on the specific interactions of adhesive molecules but also on the hemodynamics of blood flow. A theoretical model for binary adhesion of flowing cells is developed here for exploring the action and interplay of the factors, which may govern this process. Our numerical results show that, the hydrodynamic interaction of cells in flows may also be a dominating factor in the adhesion of flowing cells, especially in the case of too many cells having been tethered in surface. Similar to the increasing of the cellular on-rate, the more the upstream flowing cells, the larger the tethering rate of the flowing cells against flow direction. The spatial and temporal distributions of such adhesion are sensitive to both the cellular on-rate and the interaction of the crowding cells. This model may be also used in extracting the reaction kinetic information of flowing cells from flow chamber data.

Keywords — Cell adhesion, Hydrodynamic interaction of cells, Cellular on-rate, Flow chamber.

I. INTRODUCTION

The adhesion of flowing cells to the vascular surface in localized sites will occur in many physiological and pathological processes, such as inflammatory reaction, thrombus formation, and tumor metastasis. Such adhesions are transport-dependent processes, which depend not only on the specific interactions of adhesive molecules but also on the hemodynamics of blood flow [1,2].

The spatial and temporal distributions of such adhesion are related to the expression and regulation of adhesive receptors and ligands that mediate the specific interactions between the flowing cells and the endothelial cells lining the vessel wall, the reaction kinetics of the interacting molecules, and the hemodynamics of blood flow by which the cells are transported. In the past years, one had paid his main attention on the counter-intuitive shear threshold phenomenon in the cell adhesion. The possible molecular mechanism for this phenomenon is that, the fluid shear may increase not only the effective on-rates but also the lifetime of adhesive bonds [3,4,5].

In the case of higher cell density, the hydrodynamic interaction of cells will disturb their transport in flows, and, perhaps, may be not negligible for the adhesion of the flowing cells. For this reason, as a first step toward developing a framework for exploring the action and interplay of this factor, we describe here a minimal model and its numerical results. Another goal is to develop a theoretical method for evaluating the cellular on-rate from the spatial and temporal distributions of the adhesive cells measuring by the flow chamber experiment.

II. MODEL

The model only treats binary adhesion or irreversible association, i.e., the cell will be arrested once it forms the first bond with the surface and it will not dissociate. Let ψ be the number density (in μm^{-2}) of flowing cells sufficiently close to the surface such that interactions become possible, ψ_B be the tethered cell density after passing through time t , and K_{ad} be a rate constant for cell association, or a cellular on-rate (in s^{-1}). They are related by the kinetic equation:

$$\frac{\partial}{\partial t}\psi_B(x,t) = K_{ad}\psi \quad (1)$$

The motion of a cell near the flow chamber bottom is analyzed here by using the theory of Goldman et al. [6], which relate the forces and torques acting on a neutrally buoyant sphere near a wall translating and rotating slowly in parallel to the wall in a viscous simple shear flow. Consider a very thin “boundary layer” of flowing fluids immediately above the chamber floor, in which the cells are considered capable of tethering (but have not yet tethered) to the surface. Further above the boundary layer the cells are assumed to be too far away from the surface to bind. ψ will change as the cells are transported downstream because some are removed from the boundary layer by binding (efflux at the bottom) and others are added by sedimentation (influx at the top). Such changes are described by the following equation of the conservation of cells:

$$\frac{\partial \psi}{\partial t} - \frac{\partial}{\partial x} \left(D_s \phi \frac{\partial \psi}{\partial x} \right) + \frac{\partial}{\partial x} (u \sigma \psi) + K_{ad} \psi = w_c C(x,t) \quad (2)$$

for $t > 0$ and $x > 0$. Where, ϕ and σ describe, respectively, the effects of the hydrodynamic interaction of crowding cells for the diffusivity and the transportation of the cells, $\phi = 1 + 1.45\pi a^2(\psi + \psi_b)$, $\sigma = 1 - 6.5\pi a^2(\psi + \psi_b)$ [7,8]. D_s is the cell diffusive coefficient, $D_s = k_B T(6\pi\mu a)^{-1}$, t is the time, a is the cell radius, u is the fluid velocity components along the x directions, k_B , T , μ and w_c express the Boltzmann constant, the absolute temperature, the fluid viscosity and the z component of cell velocity in the z direction (vertically downward toward the surface), respectively. $C(x,t)$ is the concentration of the flowing cells on the upper surface of the boundary layer.

The cellular on-rate k_{ad} , the aggregate parameter that lumps the forward-rate of molecular interaction, k_f , with the densities of the receptors and ligands, m_r and m_l , on the respective cell membrane and vessel surface, the collision frequency f_c , contact time t_c , and contact area A_c , can be directly measured according to

$$k_{ad} = (n / T_0) / (mu T_0 / L_0) \quad (3)$$

where n is the number of adherent cells observed in an area during time T_0 , m is the number of cells appeared in the same area at the instant when a cell is observed to tether to the surface, u is the velocity of the flowing cells and L_0 is the length of the observation area in the direction of flow.

The governing Equations 1-2 must be imposed the appropriate initial and boundary conditions for predicting the adhesion pattern ψ_B . For simplicity, here, the initial and boundary condition are given as follows

$$\psi(0,t) = \psi_0, \quad \psi(\infty,t) = 0; \quad \psi(x,0) = 0 \quad (4)$$

The above problem is directly integrated numerically with the second-order Crank-Nicolson implicit finite difference scheme that was implemented as an Excel (Microsoft) macro and run on a PC. In numerical computation, we had nondimensionalized Eqs. 1, 2 and 4 with the density of the upstream flowing cells, ψ_0 , the characteristic length L (cm) and the time u/L (1/s). In modeling, it is assumed that the different numbers of cells suspended in the same volume (1 ml) were sent to the flow chamber with a channel width of 1 cm, a length of 4 cm, and a thickness of 110 μm . Further, for simplicity, C , the concentration of the flowing cells on the upper surface of the boundary layer, is neglected here for the consideration that, our main attention focus at the effect of the interaction of cells on the cell adhesion. And, generally, the cell diffusive effect can be ignored for enough small Peclet number Pe ($= uL/D_s$) in our problem. We had not dropped it in our modeling just for convenience in the numerical stabilization of the numerical computation.

III. RESULTS AND DISCUSSION

The above problem is modeled numerically for cell radius a (0.25-5 μm), different wall stress τ_w (0.25~4 dyne.cm^{-2}) and cell densities (0.2~1 million/ml) at $\mu = 0.01\text{dyne.m}^{-2}/\text{s}$, $T = 300\text{K}$. The dimensionless temporal and spatial distributions of the adhesive cells, ψ_B/ψ_0 , versus the dimensionless time and position, ut/L and x/L , for the fixed cell radius a (=5 μm), wall stress τ_w (3 dyn.cm^{-2}) and cellular on-rate K_{ad} (0.15/s), are plotted in Figures 1-2 with different upstream flowing cell densities $\psi_0 = 10, 50$ and 70 per a view field area A being 0.121 mm^2 .

Figure 1 shows that, in the early stage of adhesion of flowing cells, the effects of the upstream flowing cell density on the cell adhesion is very small and can be neglected, but, afterwards, the more the upstream flowing cells, the less the relative tethering cell density (the ratio of the tethering and the flowing cells near the wall in the same view field). This implies that, in the case being a larger number of the tethering cell in the upstream position, the cells flowing downstream will face with a larger obstruction, and it will weaken not only the transport but also the tethering of the flowing cells.

The variation of the spatial distributions of adhesive cells versus the upstream flowing cells is shown in Figure 2. As it is predicted, after passing some time, higher densities of the upstream flowing cells will decrease the level of the relative tethering cell density ψ_B/ψ_0 and lead its spatial distribution become steeper. The possible physical mechanism may lie in that, in the front position, more flowing cells will lead more cells to be tethered, the tethering cells then become the barrier in the pathway of flowing cells to downstream, and weakens the transport of flowing cells, then decrease the tethering rate of the cells in downstream.

The dimensionless temporal and spatial distributions of the adhesive cells, ψ_B/ψ_0 , is plotted in Figure 3-4 versus the dimensionless time and position, ut/L and x/L , for fixed cell

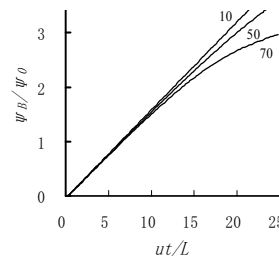


Fig.1 The dimensionless temporal distributions, ψ_B/ψ_0 , for different upstream flowing cell densities ψ_0 being 10, 50 and 70 A^{-1} at $x/L = 0.5$ and $A=0.121\text{mm}^2$.

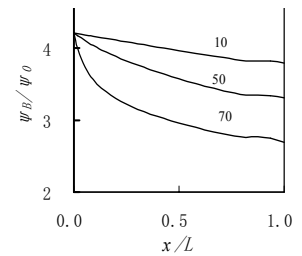


Fig.2 The dimensionless Spatial distributions, ψ_B/ψ_0 , for different upstream flowing-cell densities ψ_0 ($= 10, 50$ and $70A^{-1}$) at $ut/L = 20$ and $A=0.121\text{mm}^2$.

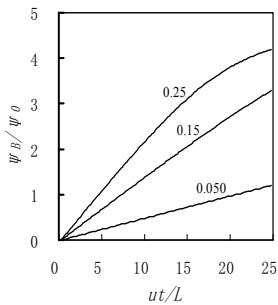


Fig.3 The dimensionless temporal distributions, ψ_B/ψ_0 , for different cellular on-rate K_{ad} (0.05, 0.15 and 0.25/s) at $x/L = 0.5$.

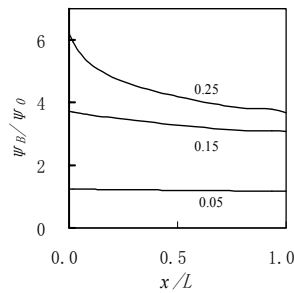


Fig.4 The dimensionless spatial distributions, ψ_B/ψ_0 , for different cellular on-rate K_{ad} (0.05, 0.15 and 0.25/s) at $ut/L = 20$.

radius $a(=5\mu\text{m})$, wall stress τ_w ($3\text{dyn}\cdot\text{cm}^{-2}$), upstream flowing cell density ψ_0 (50 per a view field) with different cellular on-rates K_{ad} (0.05, 0.15 and 0.25/s). As it should be, the larger the value of the cellular on-rates K_{ad} , the faster the tethering of the flowing cells, and the more the tethering cells, as Figure 3 shows. Figure 4 shows the increase of the cellular on-rates K_{ad} will increase the level of the relative tethering cell density ψ_B/ψ_0 and lead its spatial distribution become steeper too.

Lastly, it should be point out that, with fixed upstream flowing cell density ψ_0 and dimensionless cellular on-rates $K_{ad}L/u$, and cell radius a , the wall stress τ_w has no effect on the temporal and spatial distributions of the adhesive cells. This is because that, in our model, the effect of the wall stress on the adhesion of flowing cells just implies in the cellular on-rates K_{ad} , which is dependent on the wall stress.

IV. CONCLUSIONS

In the adhesion of flowing cells, except the parameters, such as the expression and regulation of adhesive receptors and ligands that mediate the specific interactions between the flowing cells and the endothelial cells lining the vessel wall, the reaction kinetics of the interacting molecules, and the hemodynamics of blood flow, the hydrodynamic interaction of cells may be another important factor too. The hydrodynamic interaction of cells will disturb their transport in flows, and, may be not negligible for the adhesion of the crowding flowing cells.

Past the early stage of adhesion of flowing cells, the hydrodynamic interaction of cells may become more and more important. As time past through, it become more remarkable

that the relative tethering cells density (the ratio of the tethering and the flowing cells near the wall) may decrease as the increasing of the upstream flowing cells. The crowding flowing cells will decrease the level of the relative tethering cell density and lead its spatial distribution become steeper, just as a larger cellular cell rate does.

Our results show that, the hydrodynamic interaction of cells in flows may also be a dominating factor to the adhesion of flowing cells to the surface, especially in the case of too many cells having been tethered in surface. The sensitivity of the spatial and temporal distributions of such adhesion to both the cellular on-rate and the large number of upstream flowing cells may provides a clue to develop a new technique for extracting the reaction kinetic information of flowing cells from flow chamber data, even though the sedimentation of flowing cells above the “boundary layer” is neglected for simplicity.

ACKNOWLEDGMENTS

This work is supported by NSFC grant 30570457, 10372118 and NIH grant 1R03TW007529-01.

REFERENCES

1. Doggett, T.A., G. Girdhar, A. Lawshe, D.W. Schmidtke, I.J. Laurenzi, S.L. Diamond, and T.G. Diacovo. (2002) Selectin-like kinetics and biomechanics promote rapid platelet adhesion in flow: the GPIb-vWF tether bond. *Biophys.J.* 83:194–205.
2. McEver, R.P. (2001). Adhesive interactions of leukocytes, platelets, and the vessel wall during hemostasis and inflammation. *Thromb. Haemost.* 86:746–756.
3. Evans, E., A. Leung, D. Hammer, and S. Simon. (2001). Chemically distinct transition states govern rapid dissociation of single L-selectin bonds under force. *Proc. Natl. Acad. Sci. USA.* 98:3784–3789.
4. Chang, K.-C., and D.A. Hammer. (1999). The forward rate of binding of surfacetethered reactants: effect of relative motion between two surfaces. *Biophys. J.* 76:1280–1292
5. Yago, T., Wu, J., Wey, C.D, Klopocki, A.K, Zhu, C., and McEver, R.P. (2004). Catch bonds govern adhesion through L-selectin at threshold shear. *J. Cell Biology* 166(6):913-923
6. Goldman, A. J., Cox, R. G. & Brenner, H. (1967) Slow viscous motion of a sphere parallel to a plane wall. II. Couette flow. *Chem. Eng. Sci.* 22:653-660.
7. Batchelor, G.K. (1976) Brownian diffusion of particles with hydrodynamic interaction. *J. Fluid Mech.* 74:1-29
8. Batchelor, G.K. (1977) The effect of Brownian motion on the bulk stress in a suspension of spherical particles. *J. Fluid Mech.* 84:97-117.

Corresponding Author: Jianhua Wu

Address: School of Bioscience and Bioengineering, South China University of Technology, Guangzhou 510006, CHINA

Email: jianhua59@yahoo.com.cn

A New Structure-Activity Relationship of Linear Cationic α -helical Antimicrobial Peptides

Li Liu¹, Ying Fang¹, Qingsheng Huang², Qiaoling Pan², Jianhua Wu¹

¹School of Bioscience and Bioengineering, South China University of Technology, Guangzhou, China

²School of Life Science, Sun Yat-Sen University, Guangzhou, China

Abstract — With the growing of pathogenic organisms' resistibility to conventional antibiotics, antimicrobial peptides (AMPs), which have been isolated and characterized from tissues and organisms ranging from prokaryotes to humans, are recognized as a possible source of pharmaceuticals for the treatment of antibiotic-resistant bacterial infections. Many efforts have been made to increase the potency and specificity of these peptides so that they are toxic to microbes and not to mammals. A new structure-activity relationship of AMPs is revealed by analyzing the data of the antimicrobial assays here. Our results show that, not as in the receptor-mediated process, there is a linear correlation between the flexibility and the antimicrobial activity. The smaller the flexibility of the AMPs, the stronger the antimicrobial activity of the AMPs. This new structure-activity relationship may be used not only to predict the antimicrobial activity of AMPs from their sequences, but also in structural prediction, drug design and other AMPs' researches.

Keywords — Structure-activity relationship, Antimicrobial peptide, Flexibility

I. INTRODUCTION

The emergence of bacterial resistance to common antibiotics poses a serious threat to human health and has stimulated interest in antimicrobial peptides (AMPs) as substitutable pharmaceuticals [1]. AMPs have been isolated and characterized from tissues and organisms representing virtually every kingdom and phylum, ranging from prokaryotes to humans, and they are variously active against a wide range of pathogens, including gram-positive and gram-negative bacteria, fungi, and protozoa [2-3].

Numerous studies have been carried out on the structure-activity relationship of AMPs in the last two decades, trying to make the mechanisms of action and resistance clear, and serve the drug design ultimately [4-13]. It is demonstrated that a Pro residue near the central position of those α -helical AMPs plays an important role in their bacterial cell selectivity, and the deletion of the hinge sequences decreases significantly the bactericidal rate [4-10].

So far, almost all works on the structure- activity relationship of AMPs are restricted in the conventional approaches, such as the deletion, addition and replacement of

one or more residues, and usually, are not only lack of both the validity and the pertinence, but also expensive and time-consuming. Thus, it often results in a halt of investigating, especially while a new antimicrobial peptide is found. As we know, the antimicrobial activity of an antimicrobial peptide is related to itself structural parameters, such as the conformation, charge, hydrophobicity, amphipathicity and polar angle [3]. Recently, it has been recognized that protein flexibility has an obvious effect on many biological phenomena, such as enzymatic reaction and control, protein folding, and *etc.* [14-15]. The AMPs' flexibility also may influence their antimicrobial activity [4, 7, 10]. Does there exist a dominant one among the structural parameters governing the antimicrobial activity? If so, what is the dominant structural parameter? As a challenge, is there a structure-activity relationship of AMPs mainly governed by its flexibility?

As it is well known, the linear cationic α -helical AMPs are the most abundant and widespread in nature, and been widely investigated. It is their relatively simple structures, such as being short (≤ 40 residues) and accessible to chemical synthesis [16-17], that win an advantage over study. For this reason, as a first step, we here only focus our attention at the linear cationic α -helical AMPs and attempt to reveal the relationship of their activity and their flexibility.

II. MATERIALS AND METHOD

Almost every antimicrobial peptide can inhibit the growth of *E. coli*. Thus, we use the minimum inhibition concentration (MIC) aimed at *E. coli* to assess antimicrobial activity of different antimicrobial peptides here. Obviously, the smaller of the MIC value, the stronger of the antimicrobial activity for an antimicrobial peptide. The data of sequences and MICs aimed at *E. coli* for three different AMPs groups, such as HP(2-20), IsCT and Nigrocin-2 as well as their analogues, come from Park S and other's published works [18-21], and are shown in Table 1. These three AMPs groups are the linear cationic α -helical, and their antimicrobial assays were described by Park S and others in detail [18-20]. One can see from Table 1 that, for any one of the three different AMPs group, each peptides has same length,

and their difference lies in one or more amino acids residues being replaced. In this situation, the amphipathic α -helical structures are still preserved, and it can be considered that there are not great discrepancy on holistic conformation and amphipathicity of each peptide in any group. These mean that the changes of conformation and amphipathicity may be not taken into account by numerical analysis, as we do here for simplicity.

The AMPs' flexibilities are predicted from amino acid sequence with the method of Bhaskaran and Ponnuswamy in this study [21]. The flexibilities of 20 amino acids had been given with their standard values, which are based on parameters derived from their three-dimensional structures, and are listed in Table 2 [22]. Here, the average flexibility of an antimicrobial peptide is regarded as the arithmetic mean of all components of the amino acids' flexibility array corresponding the amino acid sequence of the antimicrobial peptide.

ProtParam (<http://us.expasy.org/tools/protparam.html>) is used as a supplementary analysis tool of the protein chemico-physical characteristics.

Table 1 Values of sequences and MICs (μM) aimed at *E. coli* for three different AMPs and their analogues

Name	Sequences	Length	MICs
HP(2-20)	AKKVFKRLEKLFISKIQNDK	19	6.25
HPA1	AKKVFKRLEKLFISKIQNWK	19	3.12
HPA2	AKKVFKRLEKLFISKIWNNDK	19	3.12
HPA3	AKKVFKRLEKLFISKIWNWK	19	1.56
HPA4	AKKVFKRLEKSFISKIQNDK	19	6.25
HPA5	AKKVSKRLEKLFISKIQNDK	19	6.25
IsCT	ILGKIWEGIKSLF	13	4
[A6]-IsCT	ILGKIAEGIKSLF	13	64
[L6]-IsCT	ILGKILEGIKSLF	13	16
[K7]-IsCT	ILGKIWKGIKSLF	13	2
[L6,K11]-IsCT	ILGKILKGIKSLF	13	2
Nigrocin-2GRa	GLLSGILGAGKHIVCGLSGLC	21	25
Nigrocin-2GRb	GLFGKILGVGKKVLCGLSGMC	21	3
Nigrocin-2GRc	GLLSGILGAGKNIVCGLSGLC	21	50

Table 2 Average flexibility of 20 amino acids

Name	Value	Name	Value	Name	Value	Name	Value
A	0.360	E	0.500	M	0.300	Q	0.490
R	0.530	G	0.540	F	0.310	K	0.470
N	0.460	H	0.320	P	0.510	W	0.310
D	0.510	I	0.460	S	0.510	Y	0.420
C	0.350	L	0.370	T	0.440	V	0.390

III. RESULTS AND DISCUSSION

The chemico-physical characteristics of the peptides, such as the theoretical isoelectric point (pI) and GRAVY, are analyzed by ProtParam and shown in Table 3. GRAVY index represents the hydrophilicity of the peptides. The changes of charge and hydrophobicity will lead to the fluctuations of pI and GRAVY. Our statistical analyses show that, the variation of not only pI but also GRAVY has no regular and remarkable effects on the MIC values in every group.

The average flexibilities of the antimicrobial peptides, shown in Table 2, are calculated by using the values in Table 1. As it should be, there are no obvious variations between values of AMPs' average flexibility for each AMPs groups as shown in Table 3. The reason comes from that, the average flexibility values of 20 amino acids lie in a narrow domain ranging from 0.300 to 0.540. It is confirmed in Table 3 immediately. In other words, the MICs delegate their change trend to the small variations of AMPs' average flexibilities. In order to magnify the variations, we defined the relative change rate of average flexibility, RF_i , as

$$RF_i = 100 \times (F_i - F_0) / F_0$$

Where, F_0 and F_i are the average flexibilities of the AMPs template and its analogues, respectively. The AMPs template expresses HP(2-20), IsCT or Nigrocin-2GRa. The relationship of MICs and relative change rate of average flexibilities for the three different AMPs groups is plotted in Figure 1, which shows that, there exists a clear linear correlation between relative change rate of average flexibility and MICs, and the values of MICs increase with the relative

Table 3 Values of AMPs' average flexibility and results of the chemico-physical characteristics analysis

Name	Average Flexibility	pI	GRAVY
HP(2-20)	0.441579	10.3	-1
HPA1	0.431053	10.68	-0.863
HPA2	0.432105	10.3	-0.863
HPA3	0.421579	10.68	-0.726
HPA4	0.448947	10.3	-1.242
HPA5	0.452105	10.3	-1.189
IsCT	0.443846	8.59	0.777
[A6]-IsCT	0.447692	8.59	0.985
[L6]-IsCT	0.447692	8.59	1.138
[K7]-IsCT	0.441538	10.3	0.746
[L6,K11]-IsCT	0.443077	10.48	0.869
Nigrocin-2GRa	0.441429	8.07	1.329
Nigrocin-2GRb	0.437619	9.39	1.09
Nigrocin-2GRc	0.448095	8.06	1.314

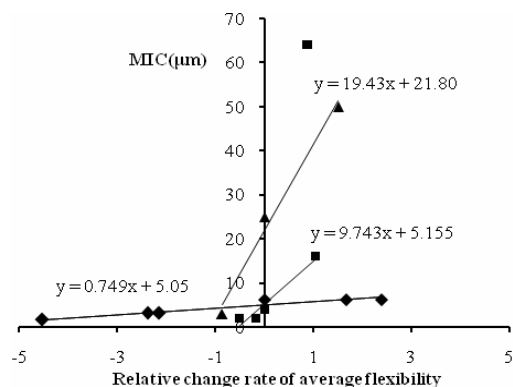


Fig.1 Correlation between MICs and relative change rate of average flexibility of group HP(2-20) (◆), group IsCT (■) and group Nigrocin-2 (▲). The solid lines are the trendlines of each group, and mathematical expressions are the formulas of trendlines

change rate of average flexibility, or say that, the antimicrobial activity decreases with the increase of AMPs' average flexibility.

Usually, one sees the structural parameters of an antimicrobial peptide to be the coordinate elements of antimicrobial activity determination, because they are interdependent, and modification of one parameter often leads to compensatory alterations in others. But our results display that the antimicrobial activity of the AMPs is not sensitive to the parameters except the average flexibility. This implies that, AMPs' flexibility outstrips other structure parameters, and the average flexibility may be a key score for the antimicrobial activity of AMPs. Perhaps, the AMPs' average flexibility can be regarded as a macroscopic measurement index, which has synthesized the effects of all structural parameters, of the corresponding antimicrobial activity.

On the other hand, as it had been indicated, in receptor-mediated or enzymatic reactions, high activity is corresponding to high flexibility [23-24]. There reveals a completely contradictory relationship with ours. One explanation should lie in the antimicrobial mechanism of AMPs. Although no any certain mechanism is capable of adequately describing the action of AMPs, there must have a process, which should be related to their structures, as AMPs meet the bacteria. The more reasonable process is that, firstly, AMPs interact target cells via electrostatic, hydrophobic or other affinities based on biochemical and biophysical correspondence; secondly, they make conformational phase transition in the framework of the target membrane; thirdly, accumulation to a threshold stoichiometry facilitating active peptide monomer or multimer nonspecific membrane disruption, or self-association ensuing pore or channel formation happen; fourthly, transient or prolonged membrane disruption are induced to yield permeabilization, depolarization, and related perturbations that may

cause direct and indirect dysfunction; finally, AMPs enter the membrane to access and inhibit intracellular targets [3].

Doubtlessly, AMPs' insertion is a pivotal step in whole process. To realize this process successfully, there are two necessary conditions as a guarantee. One is the appropriate contact area between AMPs and cell membrane; the second is the enough rigidity of AMPs. Both are related to flexibility.

The essence of the AMPs' flexibility is the fluctuation amplitude of atoms which are the component parts around their equilibrium positions due to thermal motion and positional disorder [25]. Hence, the peptide can be regarded as an indefinite density object with a moving boundary. For a larger value of an antimicrobial peptide's average flexibility, one may consider the peptide having a looser structure, which leads to the contact area between the peptide and the cell membrane being larger. The complete touch might lead the whole peptide to be willing to stay this status instead of changing conformation for insertion, or make it difficult to change conformation by conquering this great gravitation. Furthermore, it is natural that a thin and hard needle inserting a plane is much easier than a spreadable and limp thread. Maybe, a large flexibility means a large obstruction to insertion the membrane for a peptide. On the contrary, perhaps, a small flexibility representing a compact structure would be better.

Moreover, it is believed that all proteins endeavor to attain a balanced compromise between these features: the need for a compact, stable three-dimensional structure under the environmental conditions, and in contrast, an open, flexible structure to allow the conformational alterations related to activity, and AMPs are no exception [23]. Before the insertion into membrane, AMPs need to form certain stable structures (e.g. α -helical structure) to reach membranes. In addition, for the short peptides, such as the linear cationic α -helical AMPs, they are generally not well stable. Decreased flexibility has been demonstrated to be the main stabilizing principle in thermostable proteins [25]. In order to maintain the basic forms and indispensable conformations, AMPs might not need large flexibility. Thus, perhaps, it exists a possible antimicrobial mechanism for the AMPs, that the more small the flexibility of the peptides, the more stable the peptides, and then the more advantageous the realization of antimicrobial activity.

This relationship that the antimicrobial activity decreases with the increase of AMPs' average flexibility may be one side of a coin. As showed in many researches, a hinge structure which makes a peptide more flexible can increase antimicrobial activity markedly [4-5]. On the other hand, the formation of α -helical structure before interacting with membrane may not be beneficial. In short cecropin/melittin hybrid analogues with lysine and glutamine residues placed

so as to form lactam bonds in a helical conformation, the antimicrobial activity of such preformed helical peptides was considerably reduced [26]. It would indicate that antimicrobial activity is related to the inducibility of an α -helical conformation in a membrane-mimicking environment, rather than intrinsic helical stability. These studies had exhibited the positive effect of flexibility. Then, maybe, there is a threshold of flexibility in every group. When below it, the reaction is flexibility-limited. Otherwise, the reaction is stability-limited.

IV. CONCLUSIONS

A new structure-activity relationship of the linear cationic α -helical antimicrobial peptides is uncovered by analyzing the data of the antimicrobial assays in this study. Based on the relationship between the flexibility and MICs of the peptides, one may make the deletion, addition and replacement of residues being purposive. Correspondingly, this new structure-activity relationship may be used not only to predict the antimicrobial activity of AMPs from their sequences, but also in structural prediction, drug design and other AMPs' researches.

ACKNOWLEDGMENTS

This work is supported by NSFC grant 10772069.

REFERENCES

- Zasloff M. (2002) Antimicrobial peptides of multicellular organisms. *Nature* 415:389-395
- Brogden K A. (2005) Antimicrobial peptides: pore formers or metabolic inhibitors in bacteria? *Nat Rev Microbiol* 3:238-250
- Yeaman M R, Yount N Y. (2003) Mechanisms of antimicrobial peptide action and resistance. *Pharmacol Rev* 55:27-55
- Oh D, Shin S Y, Lee S et al (2000) Role of the hinge region and the tryptophan residue in the synthetic antimicrobial peptides, cecropin A(1-8)-Magainin 2(1-12) and its analogues on their antibiotic activities and structures. *Biochemistry* 39:11855-11864
- Lee D G, Hahn K S, Shin S Y. (2004) Structure and fungicidal activity of a synthetic antimicrobial peptide, P18, and its truncated peptides. *Biotechnology Letters* 26:337-341
- Lee D G, Park Y, Jin I et al (2004) Structure-antiviral activity relationships of Cecropin A-Magainin 2 hybrid peptide and its analogues. *J.Peptide Sci* 10:298-303
- Lee S, Kim Y K, Lim S S et al (2007) Solution structure and cell selectivity of Piscidin 1 and its analogues. *Biochemistry* 46:3653-3663
- Zhu W L, Lan H, Park Y et al (2006) Effects of Pro \rightarrow peptoid residue substitution on cell selectivity and mechanism of antibacterial action of Tritrpticin-amide antimicrobial peptide. *Biochemistry* 45:13007-13017
- Patrzykat A, Friedrich C L, Zhang L et al (2002) Sublethal concentrations of Pleurocidin-derived antimicrobial peptides inhibit macromolecular synthesis in *Escherichia coli*. *AAC* 46:605-614.
- Lim S S, Kim Y, Park Y et al (2005) The role of the central L- or D-Pro residue on structure and mode of action of a cell-selective α -helical IsCT-derived antimicrobial peptide. *Biochemical and Biophysical Research Communications* 334:1329-1335
- Chi S W, Kim J S, Kim D et al (2007) Solution structure and membrane interaction mode of an antimicrobial peptide gaegurin 4. *Biochemical and Biophysical Research Communications* 352:592-597
- Wang G, Li Y, Li X. (2005) Correlation of three-dimensional structures with the antibacterial activity of a group of peptides designed based on a Nontoxic bacterial membrane anchor. *JBC* 280:5803-5811
- Roch P, Yang Y, Toubiana M et al (2007) NMR structure of mussel mytilin, and antiviral-antibacterial activities of derived synthetic peptides. *Dev Comp Immunol* DOI 10.1016/j.dci.2007.05.006
- Carlson H A, Mccammon J A. (2000) Accommodating protein flexibility in computational drug design. *Molecular Pharmacology* 57:213-218
- Gohlke H, Kuhn L A, Case D A. (2004) Change in protein flexibility upon complex formation: analysis of Ras-Raf using molecular dynamics and a molecular framework approach. *Proteins* 56:322-337
- Tossi A, Sandri L, Giangaspero A. (2000) Amphipathic, α -helical antimicrobial peptides. *Biopolymers* 55:4-30
- Brogden K A. (2006) Antimicrobial peptides: pore formers or metabolic inhibitors in bacteria? *Nature* 3:238-250
- Park S, Kim M, Hossain M A et al (2007) Amphipathic α -helical peptide, HP(2-20), and its analogues derived from *Helicobacter pylori*: pore formation mechanism in various lipid compositions. *Biochim Biophys Acta* DOI 10.1016/j.bbamem.2007.09.020
- Lee K, Shin S Y, Kim K et al (2004) Antibiotic activity and structural analysis of the scorpion-derived antimicrobial peptide IsCT and its analogs. *Biochemical and Biophysical Research Communications* 323:712-719
- Conlon J M, Ghaferi N A, Abraham B et al (2006) Antimicrobial peptides from diverse families isolated from the skin of the Asian frog, *Rana graham*. *Peptides* 27:2111-2117
- Vihinen M, Torikkila E, Riikonen P. (1994) Accuracy of protein flexibility predictions. *Proteins* 19:141-149
- Bhaskaran R, Ponnuswamy P K. (1988) Positional flexibilities of amino acid residues in globular proteins. *Int J Peptide Prot Res* 32:241-255
- Collins T, Meuwis M A, Gerday C et al (2003) Activity, stability and flexibility in glycosidases adapted to extreme thermal environments. *J Mol Biol* 328:419-428
- Zacodszky P, Kardos J, Svingor A et al (1998) Adjustment of conformational flexibility is a key event in the thermal adaptation of proteins. *Biophysics* 95:7406-7411
- Parthasarathy S, Murthy M R N. (2000) Protein thermal stability: insights from atomic displacement parameters (B values). 13:9-13
- Houston ME, Kondejewski LH, Karunaratne DN et al (1998) Influence of preformed α -helix induction on the activity of cationic antimicrobial peptides. *J Pept Res* 2:81-88

Corresponding Author: Jianhua Wu

Address: School of Bioscience and Bioengineering, South China University of Technology, Guangzhou 510006, CHINA

Email: jianhua59@yahoo.com.cn Tel: 02

Numerical Simulations of Colliding Particle Distribution in Flow Chamber

Yonghua Lao¹, Jianguo Lin¹, Ying Fang¹, Quhuang Li², Cheng Zhu³, Jianhua Wu¹

¹ School of Bioscience and Bioengineering, South China University of Technology, Guangzhou, China, 510006;

² School of Life Science, Sun Yat-Sen University, Guangzhou, China, 510275; ³ Coulter Department of Biomedical Engineering and Woodruff School of Mechanical Engineering, Georgia Institute of Technology, Atlanta, GA 30332

Abstract — The adhesion of flowing cells to the vascular surface occurs in many physiological and pathological processes. The Parallel flow chamber (PFC) system is usually used to investigate this transport-dependent process. Understanding of the cells locomotion near the bottom, cells collision with the wall and the spatial distribution of the colliding particles in the chamber bottom should have useful in modeling of the cells adhesion and analyzing of the PFC biological experimental data. Here, with ADINA-F finite element analysis software, the collision events of small spherical particles pouring into inlet to PFC are numerically simulated for different wall shear stresses, 0.25, 0.5, 1, 2, 3 and 4dyn/cm². And, by tracing the trajectory of the particles from the inlet to the bottom of flow chamber, the spatial distribution of the colliding particles in the PFC was predicted. The results show that, the collision events between the particles pouring into flow chamber and the flow chamber bottom decrease as increasing shear stress, the collision fraction of the particles is less than 12.5% under different shear conditions, and the front bench positions of the colliding particles are dependent on the initial position being released from inlet. The aim of our numerical simulation lies in give one some enlighten in the design of the flow chamber and the data analysis of flow chamber experiments.

Keywords — flow chamber, numerical simulation, cell adhesion

I. INTRODUCTION

The adhesion of flowing cells to the vascular surface is related to many physiological and pathological processes, such as inflammatory reaction, thrombus formation, and tumor metastasis. This transport-dependent process depends not only on the specific interactions of adhesive molecules but also on the hemodynamics of blood [1,2].

As a key tool, the parallel-plate flow chamber (PFC) system was widely used to investigate the adhesion of cells in flows for many researchers, focusing at the governing mechanisms cells adhesion under flow [3, 4]. Now, various types of flow chambers were designed to study cells-substrates interaction. The PFC system allows to be investigated from a top-down view and under laminar flow that occurs in the post-capillary venules, the physiologically relevant site for most leukocyte emigration [5].

No matter what PFC experiment does, it is necessary that cells in the blood must move close to the blood vessel wall before their biological interaction come into being. In fact, just the flowing cells, enough near the blood vessel wall, have chance for them to be tethered on the vascular surface, by linking of the adhesive molecules expressing respectively in the flowing cells and the endothelium of blood vessel wall. Thus, it is a first step for investigating the occurrence of cell adhesion in flows that how the flowing cells are transported and interacted with blood vessel.

For the tiny seized cells, the vessel is so highly large as to be simulated, in spite of the different shape of PFC from the cylindrical blood vessel. In the flow of the PFC, cells locomotion principally goes with the flow streamlines, even the parallel-plate flow chamber have filled with innumerable cells. From the PFC's flow profile under conditions similar to blood flow in the vasculature, one can get a glance at how the flowing cells approach the chamber bottom, and the relevant knowledge to predict and analyze the location and adhesion process of cells in the vessel.

Here, by numerical simulation of flow field in PFC, the collision, location and spatial distribution of cells near the flow chamber bottom are modeled. The goal is to get more knowledge for elucidating the hydrodynamic mechanism in the adhesion of flowing cells, and to give one some enlighten in the design of the flow chamber and the data analysis of flow chamber experiments.

II. MATERIALS AND METHODS

A parallel-plate flow chamber (PFC) (2.2cm×0.5cm×0.0254cm) with inlet/outlet radius 0.1cm is built up to a finite element model (Fig.1). The flow in the PFC is assumed to be laminar with fluid density m (1.023g.cm⁻³) and viscosity μ (7×10⁻³g.cm⁻¹s⁻¹) at 20°C, and the cells are modeled as the spherical particles with radius a (6 μ m) and mass m_c (1.08m). The fluid filled with a lot of spherical particles will enter the PFC from its cylindrical inlet of 0.5cm length, which is so sufficient long that it could allow the fluid could flow into PFC after full development behind its entrance.

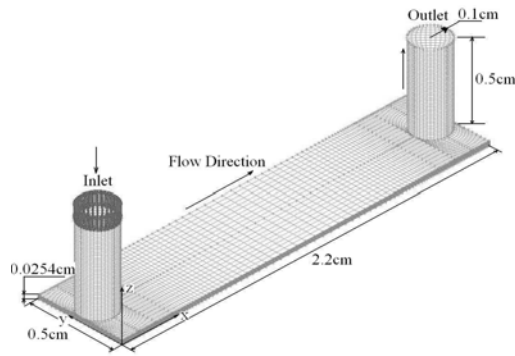


Fig.1 Model of the parallel-plate flow chamber configuration by ADINA-F

The ADINA-F analysis software is used to numerically simulate the flow in a PFC for different wall shear stresses ($0.25\text{--}4\text{dyn}\cdot\text{cm}^{-2}$). The boundary conditions, such as the inlet uniform velocity at the inlet, zero velocity at the wall, and the atmospheric pressure at the outlet, are imposed on the Navier-stokes equations. The inlet vertical velocities are, respectively, taken as 0.0611, 0.1222, 0.2445, 0.4890, 0.7334, and 0.9779cm/s for each simulation, with the restriction that Reynolds number Re does not exceed 1400 to ensure being in laminar flow conditions.

The particles' locomotion was numerically simulated by tracing the streamline of the fluid flow. The position of the colliding particles in the chamber bottom is obtained in the post-processing of ADINA software. A collision event is regarded as being happened, if a particle just reaches the chamber bottom, or the horizontal velocity of the particle is inclined to zero. The spatial concentration distribution of the cells at the bottom is predicted by tracing the position of the particles that reach at the chamber bottom.

III. RESULTS AND DISCUSSION

The spherical particles are leased into the PFC from its inlet, and traced their locomotion for different wall shear stress in the numerical simulation. The trumpet-shaped streamlines in the neighborhood region of PFC inlet at the PFC centro-symmetrical section is plotted in Figure 2, which shows that, near the inlet, in the centro-symmetrical section of the chamber, the suspended particles within the mixed liquid pouring into the flow chamber at shear stress $0.5\text{dyn}\cdot\text{cm}^{-2}$ will move almost along the trumpet-shape streamline, and only particles in neighborhood of the inlet axis could reach the chamber bottom, whereas other particles does not so.

Under different wall shear stresses condition (0.25, 0.5, 1, 2, 3 and 4 dyn/cm^2), the particles at 0.001cm intervals

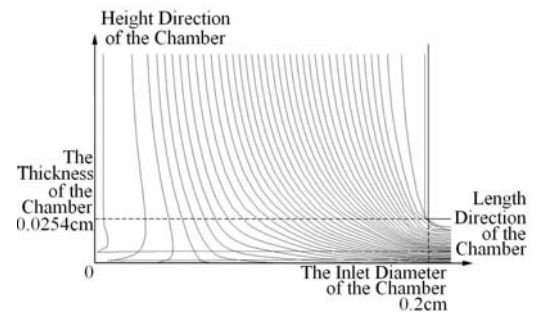


Fig.2 Trumpet-shaped streamlines in the neighborhood region of PFC inlet at the PFC Centro-Symmetrical Section

vertical from the inlet axis were leased from the inlet of PFC model. The time for the particles reach close to and stop to move at the chamber bottom was counted. The ratios of these particles, which will collide with the bottom, to all being poured to PFC, were evaluated as shown in Fig.3. One can see from Figure 3, that, the collision fraction of the total particles being able to reach enough the chamber bottom will decrease from 12% to 7.5% as the shear stress increases from $0.25\text{dyn}\cdot\text{cm}^{-2}$ to $4\text{dyn}\cdot\text{cm}^{-2}$. This may mean that there is no enough time to reach the chamber bottom for cells at larger velocity. It seems to be a paradox that the collision fractions are less than 12.5%, the reason may lies in that, the roughness of the cell surface and the diffusion of cells will have advantage of the collision events between the cells and the bottom.

On the chamber bottom, the front bench position of the colliding particles is shown in Figure 4 at shear stress 0.5dyn/cm^2 . For the front bench position of the colliding particles, more near the central axis, more away from the inlet, as it should be. It also can be seen from the Figure 4 that, the front edge positions of the colliding particles on the chamber bottom lie in a range approximately from 0.14 to 0.2cm away from the inlet edge of the chamber in the flow direction, and the front edge is parabola-type with top at the length axis of the bottom plane. It may be explained as that,

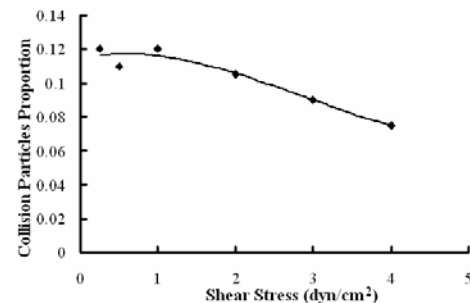


Fig.3 The collision fraction of the particles for different shear stress

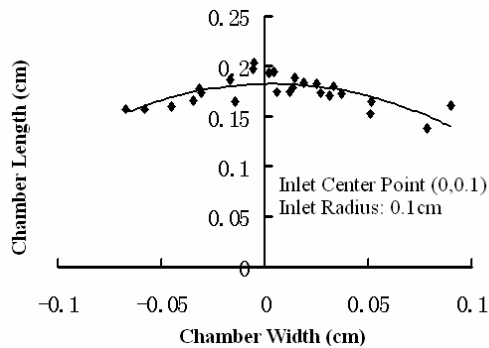


Fig.4 Collision Particles Positions in the Horizontal Plane of the Chamber Bottom Plate at Shear Stress 0.5 dyn/cm^2

the front edge is related to the initial velocity of the particles to be poured to the flow chamber from the inlet, in which, the flow can be approximately regard as an axisymmetrical parabola-type velocity distribution

The motion of a cell near the flow chamber bottom can be analyzed by using the theory of Goldman et al., which relate the forces and torques acting on a neutrally buoyant sphere near a wall translating and rotating slowly in parallel to the wall in a viscous simple shear flow [6]. Here, for simplicity, the cell sediment is regard as being no remarkable for small gravity effect, and the cells are mainly droved by fluid forces. In fact, the cell density (e.g., 1.086 g/cm^3 for leukocytes) is almost equal to the density of the fluid media (e.g., 1.023 g/cm^3 in our simulation), so the particles mainly move with along the streamline of fluid, and the particles sediment can be ignored.

IV. CONCLUSIONS

Just only the cells that could reach the chamber bottom can get the chance to tether, to roll, and to bind in the wall, or say, collision events is the first step. Understanding of the hydrodynamic mechanism for cells locomotion near the bottom, cells collision with the wall and the spatial distribution of the colliding particles in the chamber bottom, should be useful in modeling of the cells adhesion and analyzing of the PFC biological experimental data.

The collision events of the particles pouring into the PFC can be numerically simulated with ADINA-F finite element analysis software. Our results show that, the collision events between the particles pouring into flow chamber and the

flow chamber bottom will decrease as increasing shear stress, the collision fraction of particles is less than 12.5% under different shear conditions. For the front bench position of the colliding particles, more near the central axis of the inlet, more away from the inlet. The front edge positions of the particles on the chamber bottom lie in a range approximately from 0.14 to 0.2cm away from the inlet edge of the chamber in the flow direction, and the front edge is parabola-type with top at the length axis of the bottom plane.

Above results may be give one some enlighten in the design of the flow chamber and its corresponding biological experiments, as well as the data analysis of the cell adhesion in flows

ACKNOWLEDGMENTS

This work was supported by NSFC grant 30570457 and NIH grant 1R03TW007529-01.

REFERENCES

1. Doggett, T.A., G. Girdhar, A. Lawshe, D.W. Schmidtke, I.J. Laurenzi, S.L. Diamond, and T.G. Diacovo. (2002) Selectin-like kinetics and biomechanics promote rapid platelet adhesion in flow: the GPIb α -vWF tether bond. *Biophys.J.* 83:194–205.
2. McEver, R.P. (2001). Adhesive interactions of leukocytes, platelets, and the vessel wall during hemostasis and inflammation. *Thromb. Haemost.* 86:746–756.
3. Jones DA, Smith CW, McIntire LV (1996) Methods for in vitro analysis of leukocyte adhesion under flow conditions. in Weir's handbook of experimental immunology (Edited by Herzenberg L A, Weir D M, Blackwell C) Cambridge, Blackwell Science, Inc., Vol II: 69.1-69.10.
4. Yago, T., Wu, J., Wey, C.D, Klopocki, A.K, Zhu, C., and McEver, R.P. (2004). Catch bonds govern adhesion through L-selectin at threshold shear. *J. Cell Biology* 166(6):913-923
5. David C Brown, Richard S Larson (2001) Improvements to parallel plate flow chambers to reduce reagent and cellular requirements. *BMC Immunology*, 2001, pp2-9
6. Goldman, A. J., Cox, R. G. & Brenner, H. (1967) Slow viscous motion of a sphere parallel to a plane wall. II. Couette flow. *Chem. Eng. Sci.* 22:653-660.

Address of the corresponding author:

Author: Jianhua Wu
 Address: School of Bioscience and Bioengineering, South China University of Technology, Guangzhou 510006, CHINA
 Email: jianhua59@yahoo.com.cn

Analysing the effect of gas press's little wave in measuring result of velocity of ultra-sound

Xiaoning Wang^{1,2}, Mengsun Yu^{1,3}

1 Department of Medical Electronic Engineering, Faculty of Biomedical Engineering, Fourth Military Medical University, Xi'an, China 710032

2 Experimental Instrument Plant, the Academy of Military Medical Sciences, Beijing, China 100850

3 Institute of Aviation Medicine, Air Force, Beijing, China 100036

Abstract—As one of common measuring technology, ultrasonic measuring technology was used in many science and technology fields with. Such as: length and distance measuring, environmental surveillance, velocity of flow measuring, gas surveillance, and so on. Expanding with the application area, there are higher and higher demand about *Fund item : Imbursed item by supporting plan of the national important task (2006BAI03A00)

As known, air surveillance, for example: aerometry, is a very complex task involved of ultrasonics, aerodynamics, hydromechanics, electronics, material science, refrigeration science, computer application and other science subjects. Even in the condition of linear acoustics, it's very difficult to measure the velocity of sound in gas accurately. There are very close relationship with gas's press, temperature, humidity, velocity of flow, specific heat, chemical composition, and so on. That is the reason why in normal ultrasonic measuring method, the condition is always invariable, for example, invariable pressure, humidity, even temperature. The point is to simplify the measuring devices, optimize the compute function, and economize the spending on software and hardware if the result met our pre-design.

Pointing to gas press whether in perfect state or practice state, its value has been regarded as a constant or changed very slowly physical parameter, so its affection is neglected often. This disposal is fit for measuring in atmosphere reasonably. But involved in human's aerometry such as expiring gas survey, there are always some unable controlled influence factors in process of aerometry. It is one of worthy paying attention problem how extent these factors' influence will be severity to.

Measured in a smart environment, if surveyed gas comes under the fast changing outside force, the gas press will be changed synchronously. And this change will effect the result of ultrasonic measure. So in practical survey, if gas press is changed very quickly and its waving range can not be neglected, the difference would be there between theoretic compute and result of fact experiment. It must be taken into account when we need accurate measuring values under the fast changing environment. In this processing, the author discovered a special affection about the survey result arose by gas press changing.

Phase difference theory is that velocity of sound was gained by comparing the time of ultra sound sending and the time of sound receiving. In this paper, the changing of sound's velocity

is very little, so using this method is rather reasonable to computing it. Δt is the time of passing the length L. The writer designed a sample and hold electrical circuit in order to convert the value of Δt to linear value of voltage ΔVH . The value of ΔVH and velocity of sound C will change synchronously when the value of Δt changed. So changing of ΔVH will be expressed the time change Δt .

The author discovered the relationship between gas press and velocity of sound using ultrasonic sensors in the smart environment. By engineering method, a new point of view was brought forward that is "There is a differential coefficient relationship between the changing velocity of gas press and the velocity of sound, while the gas press is waved around the standard atmosphere", a first-order differential equation was proposed which described this phenomenon, and a tentative explanation was given. The function will be valuable to some extent in future working and studying. This function need to be proved its correctness through a lot of physical experiments.

Keywords—Ultrasonic, velocity of sound, gas press, differential coefficient arithmetic, method of phase difference

I. INTRODUCTION

As one of common measuring technology, ultrasonic measuring technology had many characteristics, for example: quickly responding, low cost and long longevity, and was used in many science and technology fields with. Such as: medically detection for human, ultrasonic detection for mistake, length and distance measuring, environmental surveillance, velocity of flow measuring, air surveillance, and so on. Expanding with the application area, there are higher and higher demand about ultrasonic measuring precision and veracity. So it is significant and worthwhile to some extent to research and explore its characteristics. Velocity of sound, which was made mention of in this paper, all pointed to the velocity of sound in gas under the condition of laboratory.

Ultrasonic^[2] is the wave of sound which the number of frequency is bigger than 20000Hz (Human being will not

hear this sound. They can only hear the sound which the number of frequency between 20~20000Hz). As known, air surveillance, for example: aerometry, is a very complex task involved of the subject of ultrasonics, aerodynamics, hydromechanics, electronics, material science, refrigeration science, computer application and other science subjects. Even in the condition of linear acoustics, it's very difficult to measure the velocity of sound in gas accurately. There are very close relationship with gas's press, temperature^[3], humidity, velocity of flow, specific heat, chemical composition, and so on.^[1]

There is a little by little developing course in proper sequence to learn and understand these factors.

Newton, a very famous physical scientist and mathematician of United Kingdom, brought forward one law of velocity of sound, 'velocity of sound should equal to the square root of the ratio of gas press to gas density.' Described as formula (1)

$$c = \sqrt{\frac{P}{\rho}} \quad (1)$$

Where:

c—velocity of sound

P—gas press

ρ —gas density

In 1759, another European scientist, Euler got a more clarity analyzing method based the Newton's theory., and computed the number of sound velocity. But this result was out of accord with experiment value of sound, and the difference between two number was big.

Laplace, a famous astronomer and mathematician of France, developed this formula. He considered that velocity of sound should equal to the square root of the ratio of gas press to gas density and multiply the r . Described as formula (2)

$$c = \sqrt{\frac{\gamma P}{\rho}} \quad (2)$$

Where:

r —ratio of molecular specific heat at constant volume and molecular specific heat at constant pressure

Based on formula (2), the difference between the theoretic value of sound and the experiment value of sound was small.

And there is perfect gas equation, or Clausius-Clapeyron gas equation^{[4][5][6]}. As formula (3)

$$\frac{P}{\rho} = \frac{RT}{M} \quad \text{或} \quad PV = \frac{nRT}{M} \quad (3)$$

Where:

n—gas quality

M—molecular weight

R—gas constant (R=8.314J/mol•K)

T—Kelvin degree

In normal engineering problem, there is only need the equation of perfect gas, which based the equation under the condition of absolutely isolated heat^[5]. As formula (4)

$$c = \sqrt{\frac{\gamma P}{\rho}} = \sqrt{\frac{\gamma RT}{M}} \quad (4)$$

In modern acoustics theory, if think about the effect of moisture in gas, the formula of velocity of sound can be expression by formula (5)^[1]

$$c = \sqrt{\frac{\gamma RT}{M} \left(1 + 0.3192 \frac{e}{P} \right)} \quad (5)$$

Where:

e—tensility of water vapor

With easy acquiring parameters, formula (5) have been certificated widely, accepted in engineering calculation frequently, and used in many precision survey occasion, such as: gas temperature measure, mean gas molecular weight measure, detecting velocity of sound and length and distance precision measure, and so on.

Pointing to gas press whether in perfect state or practice state, its value has been regarded as a constant or changed very slowly physical parameter in all formula as we known, so its affection is neglected often. This disposal is fit for measuring in atmosphere reasonably. But involved in a smart environment, if surveyed gas comes under the fast changing outside force, the gas press will be changed synchronously. And this change will effect the result of ultrasonic measure. So in practical survey, if gas press is changed very quickly and its waving range can not be neglected, the difference would be there between theoretic compute and result of fact experiment. It must be taken into account when we need accurate measuring values under the fast changing environment.

II. EXPERIMENTAL

A. Phase difference method of echo wave

In order to measure the changing of velocity of sound precisely, phase difference method of echo wave had been used in this experiment. This method could detect the little change more exactly than other measure methods. The experiment result had met the precision require, so this method was right to be used in this experiment.

Phase difference theory is that velocity of sound was gained by comparing the time of ultra sound sending and the time of sound echoing.

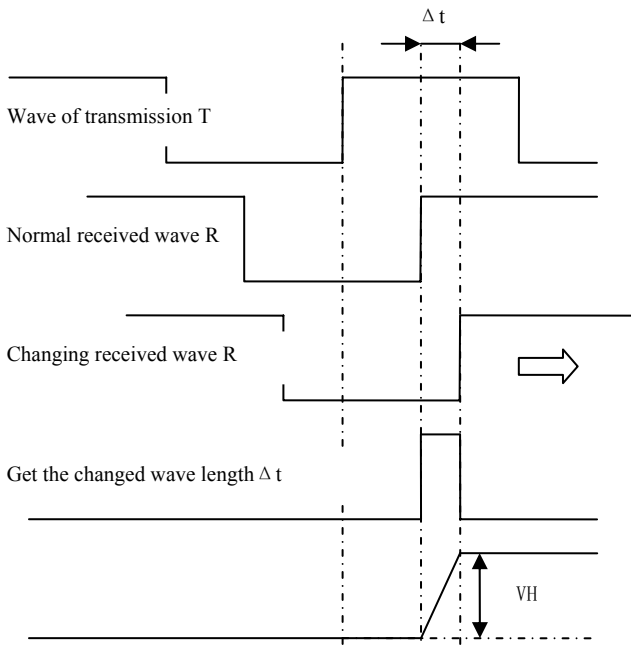


Fig.1 Phase difference chart

In this paper, the changing of sound's velocity is very little, so using this method is rather reasonable to computing it. Δt is the time of passing the length L. The writer designed a sample and hold electrical circuit in order to convert the value of Δt to linear value of voltage ΔVH . The value of ΔVH and velocity of sound C will change synchronously when the value of Δt changed. So changing of ΔVH will be expressed the time change Δt .

B. Experimental data processing

Recording every parameters of gas in the airproof box while experimenter is giving box a force from outside. The data can be gained, as figured on the Fig.2. Using formula (5), analyzing and processing the data, a conclusion can be founded. The gas press's little wave can affect the value of ΔVH and this is the main reason why ΔVH changed, while the value of temperature t is changed very little even not altering. So make differential on gas press P.^[7]

$$a \frac{dP}{ds} \tag{6}$$

Where:

a—constant, can be decided by environment

$\frac{dP}{ds}$ —differential coefficient of gas press P to recording time s

If a=1, get the Fig.2 Output of signal by differential coefficient function

Where:

First wave P, y-axis is value of gas press, units is Kilo-Pascal, x-axis is recording time, units is 8 millisecond.

Second wave VH, y-axis is value of voltage, units is Voltage, x-axis is recording time, units is 8 millisecond.

First wave $a \frac{dP}{ds}$, y-axis is none dimension parameter, x-axis is recording time, units is 8 millisecond.

While temperature's wave is very little (in fact, can not detect the change), gas press's wave is the main reason to effect the ΔVH . Although absolute value and relative value don't accord with the value of voltage VH completely, the both changing trend is coincident. So the point of view of reference [7] is right.

So there is new formula (7)^[7] about computing velocity of sound

$$c = \frac{L}{t} = \sqrt{\frac{\gamma RT}{M} \left(1 + 0.3192 \frac{e}{P} \right)} \frac{1}{1 + a \frac{dP}{ds}} \tag{7}$$

C. Analyzing result

Author believes there are two reasons probably which can explain this phenomenon.

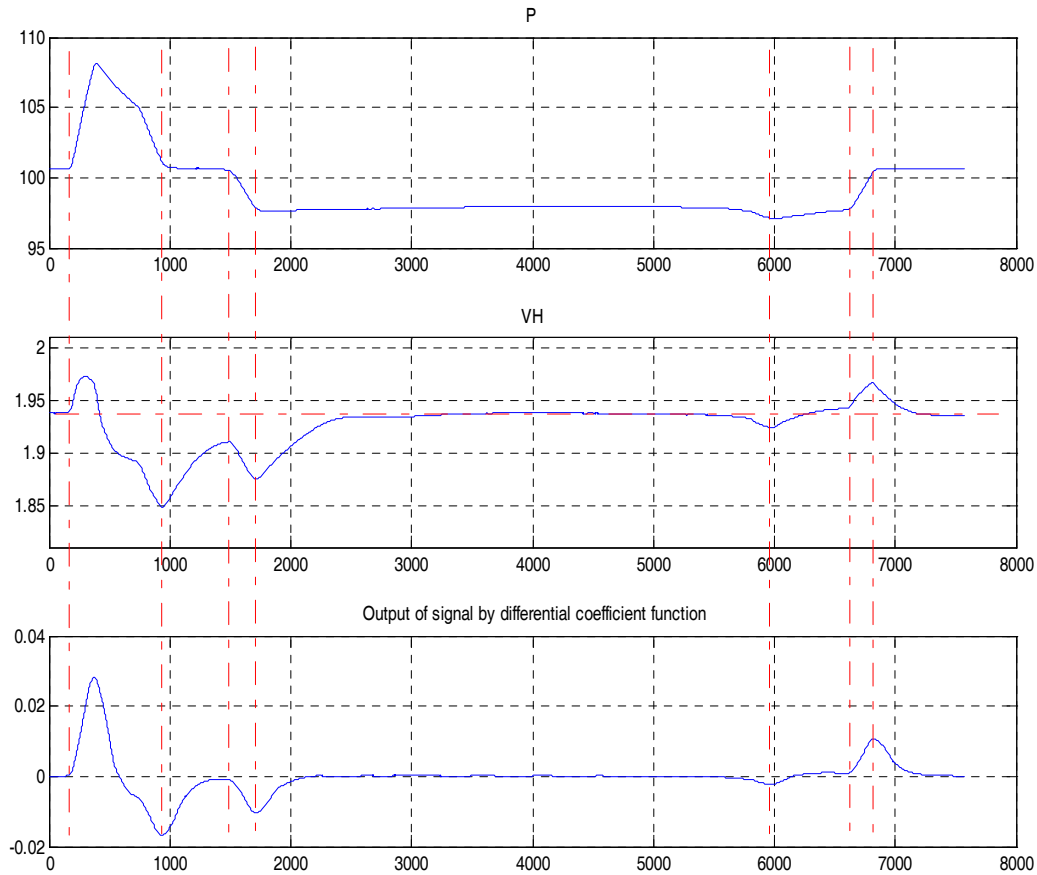


Fig.2 Output of signal by differential coefficient function

First possibility:

Changing of gas press is much quicker than changing of gas density. So, with unchanged other parameters, if gas press will not change also, velocity of sound will keep steadiness. When the value of gas press increase,

$\frac{\Delta P}{\Delta \rho} > \frac{P}{\rho}$, there will be a upwards fastigium wave of ve-

locity of sound. The other way round, when the value of gas

press decrease, $\frac{\Delta P}{\Delta \rho} < \frac{P}{\rho}$, there will be a downwards fas-

tigium wave of velocity of sound.

Second possibility:

With unchanged other parameters, in process of gas press's quickly change, gas in exam box will flow in some order, thereby velocity of sound changing. When value of gas press don't vary, the gas will stop flow. So velocity of sound comes back to the former state which before the gas press changed.

For those two possibilities, the author think the first one is more reasonable.

III. CONCLUSION

By engineering method, a new point of view was brought forward that is "In an airproof space, there is a differential coefficient relationship between the changing velocity of gas press and the velocity of sound, while the gas press is waved around the standard atmosphere."

Even in the condition of linear acoustics, it's very difficult to measure the velocity of sound in gas accurately. There are very close relationship with gas's press, temperature, humidity, velocity of flow, specific heat, chemical composition, and so on.^[1]

In the paper, the author discovered the relationship between gas press and velocity of sound using ultrasonic sensors in the smart environment and proposed a first-order differential equation which described this phenomenon.

Although this equation is not perfect, even has some mistakes in it, this research work has much positive significance for going deep into analyzing and studying the influence factors while ultrasonic transmission in gas.

REFERENCES

- [1] FENG R. Ultrasonics handbook[M]. Nanjing University Press 1999.
1. Timothy G. Leighton, What is ultrasound?[J] Progress in Biophysics and Molecular Biology 93 (2007) 3-83.
 2. Michael S. Strano, Temperature- and pressure-dependent transient analysis of single component permeation through nanoporous carbon membranes[J], Carbon, 40(2002) 1029-1041.
 3. Oveon Cramer. The variation of the specific heat ratio and the speed of sound in air with temperature, pressure, humidity and CO₂ concentration[J]. J Acoust Soc Amer. 1993, 93, 2510~2516
 4. J.W.Daly and D.R.F.Harriman[US], Hydrokinetics[M], Peoples Education Press, 1981
 5. WANG P, HAN ZH X, Encyclopedia of Fluid Mechanics[M], Bei Hang University Press, 1991
 6. Wang Xiaoning, Yu Mengsun, Discovering air press's appended effect in measuring result of velocity of sound with ultrasonic sensors[J], CHINESE JOURNAL OF SCIENTIFIC INSTRUMENT (No.4 2008), **in press**

Writer introduction:

WANG Xiaoning, male, born in may 1974. He received BSc from Tianjin University of China. He is currently an engineer in the Academy of Military Medical Sciences and working toward the PhD degree of Fourth Military Medical University. His research field is measurement and analyse technology, involved in projects of biomedical signal.

Tel: +86-10-66927048; E-mail: wxnamms@sina.com

Author: WANG Xiaoning
 Institute: The Academy of Military Medical Sciences
 Street: Taiping road
 City: Beijing
 Country: China
 Email: wxnamms@sina.com

A new respiratory training system for astronauts

Chunhua Hu, Hongwei Hao, Bozhi Ma, Yuan Yuan, Fangjun Liu, Luming Li

School of Aerospace, Tsinghua University, Beijing, China

Abstract — More and more astronauts and common people will be sent to space. When going to space from the earth or return to the earth from space in a spaceship, especially in emergency, men will suffer from hyper-gravity. Hyper-gravity can induce much sickness, and endanger the life of human. Respiratory training in advance can help astronauts to tolerate much higher gravity values. A new respiratory training system was developed for astronauts. The system can be well worked for astronauts now.

Keywords — Respiratory training, astronauts, hyper-gravity.

I. INTRODUCTION

Although only three countries, the United States, Russia and China, possess the means to launch humans into orbit, but people from more than 30 different countries have flown in space. There will be more and more astronauts or common people going into space. China is new to the space age. China has developed much launch capabilities and has placed taikonauts into orbit, and has plans to develop and build a space station of their own.

Increased gravitational forces, known as hyper-gravity, are generated when the body is subjected to linear or angular acceleration when going to space from the earth or return to the earth from space in a spaceship, especially when the spaceship must be force-landed for some emergency.[1] Through the study on rhesus macaque, the sustained +Gx simulating emergent recovering of space vehicle can result in significant injury of lungs.[2] So protective measure should be taken in this condition.

The human +Gx tolerance is limited by hard breath and chest pain. Scientists did many efforts to improve +Gx tolerances of astronauts. Almost all experiments for +Gx tolerances were examined on human centrifuge. In the experiment of Chinese scientists, heavy blocks were used to simulate hyper-gravity. The testers were trained how to breathe with the rhythm. The change of respiratory type, breath rate, electrocardiogram, heart rate, arterial oxygen saturation(SaO₂), subjective symptom and vision were real-time monitored during the +Gx tolerance examination. Compared with pre-training, the +Gx tolerance increased after training.[3]

A training system based network was built to help training astronauts to tolerate hyper-gravity.[4] It is usable, but not effective. Our goal was to develop and assess a procedure for rapid and non-invasive determination of the respiratory training to increase human +Gx tolerance.

II. SYSTEM DESCRIPTION

A. Mechanism system

When going to space from the earth or return to the earth from space in a spaceship, astronauts must be fixed in the seat in order to tolerate hyper-gravity. In the ground, the centrifuge is mostly used to produce hyper-gravity. But the centrifuge needs much time to prepare and needs many people to work together. Because the +Gx tolerance is mainly limited by hard breath and chest pain, if we use some mechanism to simulate the effect of hyper-gravity, astronauts can be trained how to breathe when in hyper-gravity process.

Normally, the height of astronaut is between 165cm and 175cm, and the weight is between 55kg and 70kg. The mechanism must be accord with the stature of astronaut in order to produce simulated hyper-gravity. Figure 1 is the picture of astronaut in the seat. So we design two profile parts to cover the chest and abdomen of the astronaut. The iron blocks with different weight are superposed to the profile part. With different weight, the astronaut can experience different effect of hyper-gravity, such as chest pain and



Fig. 1 Astronaut in the seat

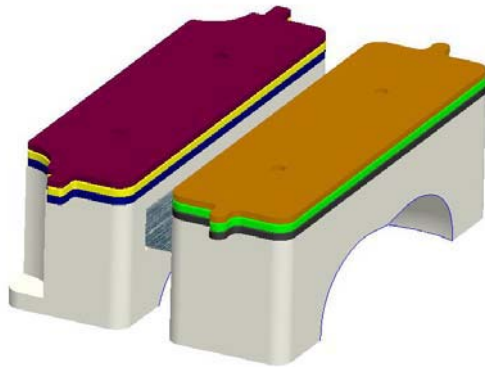


Fig. 2 The profile parts and the iron blocks

hard breath. The instructor can tell the astronaut how to breathe to tolerate uncomfortable feeling. With such training, the astronauts can do well when enduring hyper-gravity in centrifuge. Figure 2 is the profile parts and the iron blocks.

B. Hardware system

There are 8 channels of signals should be collected, which are two channels of electrocardiogram, two channels of electromyogram, two channels of breath, one channel of skin impedance and one channel of skin temperature. The physiology signal is very weak, so the amplifiers are needed to magnify the signal to 0~3Vpp.

Micro-controller C8051F040 was used to serve as CPU. It integrates CAN bus and A/D conversion circuits. AD8231 was selected as amplifier of ECG and EMG. It is a zero drift, digitally programmable instrumentation amplifier, so the gains can be adjusted by command from position machine.

There are two channels of breath signal. In order to avoid the coupling between them, two kinds of oscillation signal were used to excite the source signal. The frequency of one oscillation signal is 50kHz, another is 150kHz.

The resistance of skin is calculated through measuring voltage between two points of skin. The source current is DC, and the current value is 10uA.

Figure 3 shows the circuit block diagram.

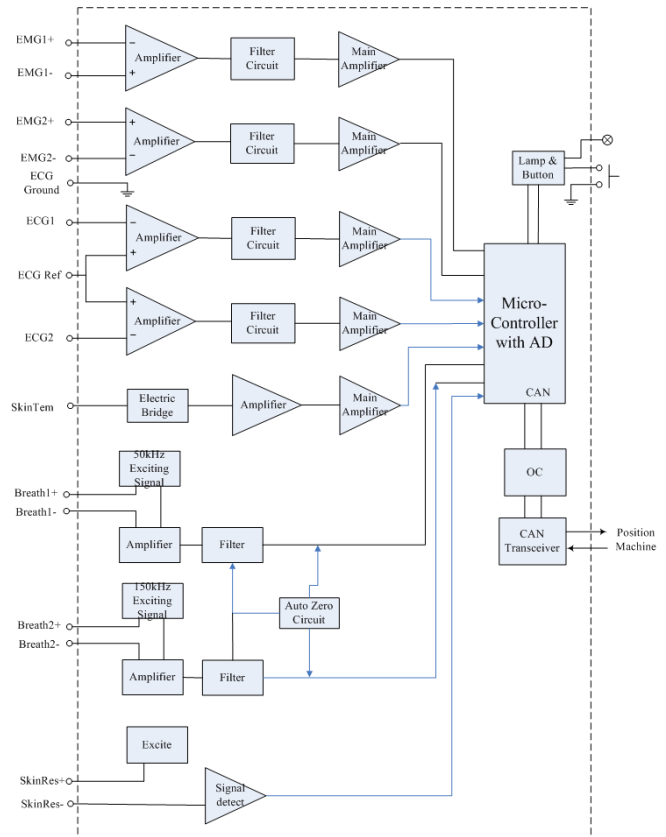


Fig. 3 The circuit block diagram

C. Software system

The software system includes physiology signal collection software and monitor software. The signal collection software is embedded in hardware, and the 8 channels of signal value are transferred to the monitor system via CAN bus. The CAN bus signal is converted to USB signal via a CAN-USB card.

The monitor software is divided to two parts, one is real-time monitoring module, and the other is analysis module. When needed, the instructor can record the data in experiment, and analyze them after experiment. Both software modules are deployed in one computer.

Figure 4 shows the interface of the monitor software.

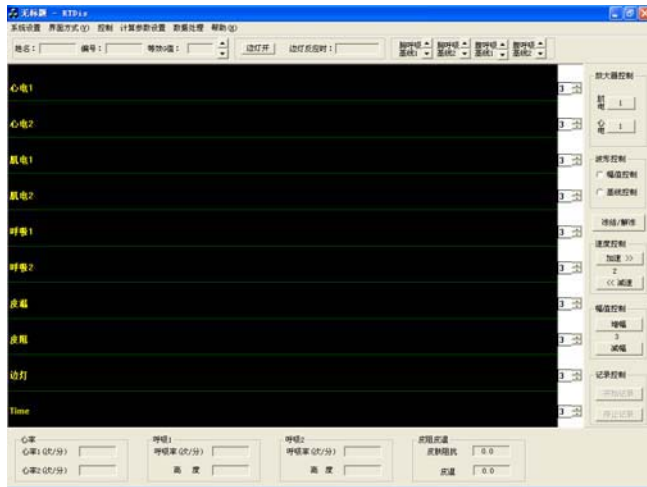


Fig. 4 The interface of the monitor software

III. CONCLUSIONS

The respiratory training system can be well worked now. For astronauts without training experience in centrifuge, the equipment can help him to learn respiratory methods for +Gx environment. The equipment needs little time and few people to operate. Only a few minutes were needed to finish one test, while in centrifuge, several days and many people were needed. The equipment is very safe. Strong motion and high voltage are not needed here. In the future, the experiments on astronauts will be done to compare the results on the centrifuge. And the comparison methods should be studied in order to confirm the relation between the weights of iron blocks and gravity values on centrifuge.

ACKNOWLEDGMENT

The authors thank Wu Bin, Gu Zhiming and Wu Ping for technical expertise. Wen Xiongwei and Jiang Yanping facilitated the successful execution of the project. The authors especially thank the subjects of this study, each of whom gave hundreds of hours of their time to this research endeavor.

REFERENCES

1. Rohdin, M., J. Petersson, P. Sundblad, et al. (2003) Effects of gravity on lung diffusing capacity and cardiac output in prone and supine humans. *Journal of Applied Physiology* 95: 3-10.
2. Niu Zhongying, Wu Bin, Zhang Jianzhong, et al. (2003) Effect of sustained +Gx on pathological changes of lung in rhesus macaque. *China Journal of Aerospace Medicine*, Vol. 14, No. 4:204-207.
3. Xue Yueying, You Guangxing, Wu Bin, et al. (2002) Study on Anti +Gx Respiratory Maneuver and Its Training Method. *Space Medicine & Medical Engineering*, Vol. 15, No. 6: 402-405.
4. Yang Jianqun, Ma Dianfu. (2003) Research on multi-channels of physiology signal collection and process based on network. *The Proceeding of 6th China conference of human-machine-environment system engineering*, pp. 104-114.

Address of the corresponding author:

Author: Chunhua Hu
 Institute: School of Aerospace, Tsinghua University
 Street: Room 803, Main Building, Tsinghua University
 City: Beijing
 Country: China
 Email: huchunhua@tsinghua.edu.cn

Computational Simulation for Osteoporosis at the Basic Multicellular Unit Level

H. Gong^{1,3}, Y.B. Fan² and M. Zhang¹

¹ Department of Health Technology and Informatics, The Hong Kong Polytechnic University, Hong Kong SAR, P.R.CHINA

² Department of Bioengineering, Beihang University, Beijing, P.R.CHINA

³ Department of Engineering Mechanics, Jilin University, Changchun, P.R.CHINA

Abstract — In this study, we built computational simulation models of osteoporosis for both cortical bone and trabecular bone at the basic multicellular unit (BMU) level according to bone functional adaptation and Frost's mechanostat theory. For cortical bone, cortical thickness was taken as controlling variable, and for trabecular bone, porosity was. The coupling relationship between mechanical factor and biological factor was fulfilled by osteoblastic formation threshold and BMU activation threshold. For cortical bone remodeling model, the analysis was performed on a representative rectangular slice of the cross section of cortical bone volume. The pQCT data of femur and tibia by Eser et al. [1] were used as an example of mechanical disuse to validate the model. For trabecular bone remodeling model, the analysis was done on a representative cross section of 100 mm² of trabecular bone in the lumbar spine of a postmenopausal woman. The clinical data by Recker et al. [2] were used for the comparison of our simulation outcomes with clinical data. Results: For the femur cortical model, the simulated steady state value of cortical thickness was 2.04mm and the clinical data was 2.17mm with relative difference of 5.99%. For the tibia cortical model, the simulated steady state value was 4.13mm and the clinical data was 3.94mm with relative difference of 4.82%. Trabecular bone: When disuse was maintained, a number of different magnitudes of changes in osteoblastic formation threshold and/or changes in BMU activation threshold could give results that were consistent with the bone loss patterns seen at menopause. The computational models for osteoporosis occurred at cortical and trabecular bone developed in this study can be further used to quantify and predict the effects of mechanical and biological factors on cortical thickness and trabecular architecture, and help us to better understand the relationship between bone morphology and mechanical and biological environment.

Keywords — Remodeling, Cortical bone, trabecular bone, Basic Multicellular Unit, Osteoporosis.

I. INTRODUCTION

A major component of human musculoskeletal system is bone, which supports our body weight, facilitates our body motion and plays critical roles in mineral homeostasis and production of various blood cells.

The skeleton is made up of cortical bone and trabecular bone. Cortical bone, also known as compact or lamellar bone, forms the thin outer shell in the long bones and the major

portion of the cortex of other bones. Trabecular bone is also known as spongy or cancellous bone. It is made of a network of intersecting plates and rods (trabeculae) within the cortex, and serves as the supportive infrastructure of the bone.

Throughout life, bone is constantly resorbed and new bone is formed by a process called bone remodeling, which is performed by groups of osteoblasts and osteoclasts organizing into Basic Multicellular Units (BMUs). About 5% of the bone mass is remodeled by about 2 million BMUs in the human skeleton at any time. The renewal rate for bone is about 4% per year for cortical bone and 20% per year for trabecular bone [3].

Osteoporosis is a systematic skeletal disease characterized by low bone mass and micro-architectural deterioration, with a consequent increase in bone fragility and susceptible to fracture. Skeletal disuse, whether due to micro-gravity caused by spaceflight, prolonged bed rest, paralysis, localized stress shielding following arthroplasty, or cast immobilization may lead to bone loss in humans, as well as laboratory animals [4, 5]. Aging, estrogen deficiency, and drug treatments are known as biological factors.

The observed adaptation of bone mass and architecture to the typical mechanical usage indicates that some mechanism exists monitoring the mechanical usage and controlling bone modeling and BMU-based remodeling activities.

In this study, we built computational simulation models of osteoporosis for both cortical bone and trabecular bone at the basic multicellular unit (BMU) level according to bone functional adaptation and Frost's mechanostat theory [6].

II. METHODS

The computational simulation models were built according to bone functional adaptation and Frost's mechanostat theory. For cortical bone, cortical thickness was taken as controlling variable, and for trabecular bone, porosity was. The coupling relationship between mechanical factor and biological factor was fulfilled by osteoblastic formation threshold and BMU activation threshold. In the models, mechanical factor was described by local mechanical stimulus, and biological factor was described by BMU activation frequency, resorption period, reversal period, refilling period, local resorption rate and local formation rate.

A. Cortical thickness changes

An imbalance between bone resorption and refilling leads to changes in cortical thickness. The rate of change in cortical volume was assumed to be a function of the bone resorption rate ($Q_r(t)$) and bone refilling rate ($Q_f(t)$) for each BMU, and the density of resorbing and refilling BMUs/area ($N_R(t)$ and $N_F(t)$, respectively)

$$\frac{d \frac{h(t) \cdot l}{h_0 \cdot l}}{dt} = Q_r(t)N_R(t) - Q_f(t)N_F(t) \quad (1)$$

where the resorption rate $Q_r(t)$ and the refilling rate $Q_f(t)$ were assumed to be linear in time: $Q_r(t) = \frac{A}{T_r}$ and

$$Q_f(t) = \frac{A}{T_f} \text{ with } A \text{ representing the area of bone resorbed}$$

by each BMU. $h(t)$ was the cortical thickness at time t , l was the length of the representative rectangular slice and h_0 was the initial cortical thickness.

Hence

$$\frac{dh(t)}{dt} = h_0(Q_r(t)N_R(t) - Q_f(t)N_F(t)) \quad (2)$$

B. Trabecular porosity changes

The imbalance between bone resorption and refilling would inevitably lead to changes in porosity. The rate of change in porosity $dP(t)/dt$ was assumed to be a function of bone resorption rate ($Q_r(t)$) and bone refilling rate ($Q_f(t)$) for each BMU, and the density of resorbing ($N_R(t)$) and refilling ($N_F(t)$) BMUs/area

$$\frac{dP(t)}{dt} = Q_r(t)N_R(t) - Q_f(t)N_F(t) \quad (3)$$

where the resorption rate $Q_r(t)$ was assumed to be constant, i.e. $Q_r(t) = Q_r \max$. For the refilling rate $Q_f(t)$, the osteoblastic formation threshold $akob(t)$ was introduced:

$$Q_f(t) = Q_f \max \times \left(1.0 / \left(1 + e^{\frac{kbob(kcob - \phi(t))}{akob(t)}} \right) \right) \quad (4)$$

$kbob$ and $kcob$ defined the slope and inflection point of the curve, respectively. $akob(t)$ was the osteoblastic formation threshold. $\phi(t)$ was defined as the mechanical stimulus.

$N_R(t)$ and $N_F(t)$ were calculated as:

$$N_R(t) = \int_{-T_r}^t f_a(t') dt' \quad (5)$$

$$N_F(t) = \int_{-(T_r+T_i+T_f)}^{t-(T_r+T_i)} f_a(t') dt' \quad (6)$$

$f_a(t)$ was the BMU activation frequency.

C. BMU activation frequency

The relationship between BMU activation frequency and mechanical load was assumed to be sigmoidal, similar to the response found in pharmacological application [7].

$$fa(t) = \frac{fa(\max)}{1 + e^{\frac{kbfa(\frac{\phi(t)}{akfa(t)} - kcfa)}}} \cdot S_A \quad (7)$$

where $fa(\max) = 0.299 \text{ BMUs/mm}^2/\text{day}$ for cortical bone and $0.5 \text{ BMUs/mm}^2/\text{day}$ for trabecular bone, $kbfa$ and $kcfa$ were coefficients defining the slope and inflection point of the curve, respectively. $akfa(t)$ was the BMU activation threshold. S_A was specific surface area [7]. Sensitivity analyses were done first for the coefficients in these functions to fit the curves within known experimental data ranges.

D. Examples of cortical bone osteoporosis

The pQCT data showing the relationship between the duration of paralysis and bone structure of spinal cord injured patients by Eser et al. [1] was used as an example of mechanical disuse. Eighty-nine motor complete spinal cord injured men (24 tetraplegics and 65 paraplegics) with a duration of paralysis of between 2 months and 50 years were included. The age range was 41.5 ± 14.2 for all subjects. The reference group comprised 21 healthy able-bodied men of the same age range.

The remodeling behaviors of cortical bone in the femur, as well as in the tibia were both simulated in this paper. The representative cross section of the femur cortical bone was located at 25% of total bone length from the distal end for the femur, and at 38% for the tibia as the locations of diaphyseal scans in Eser et al. [1]. For simplification, the cortical bone volume was assumed to be cylindrical and the endosteal surface and periosteal surface were assumed to be concentric circle.

E. Example of trabecular bone osteoporosis

For trabecular bone osteoporosis, the analysis was done on a representative cross section of 100 mm² of trabecular bone in the lumbar spine of a postmenopausal woman. The clinical data by Recker et al. [2] were used for the comparison of our simulation outcomes with clinical data. The sum-of-squares for error (SSE) was used to determine how well the model predicts the results of clinical studies [8]:

$$SSE = \sum (\Delta_m - \Delta_p)^2 \tag{8}$$

where Δ_m was the measured change in BMD by Recker et al. [2], and Δ_p was the predicted change in this paper. The SSE and trends of changes in BMD in the analysis were used to evaluate the models.

III. RESULTS

A. Simulation results of cortical bone osteoporosis

Figure 1 and Figure 2 shows the numerical outcomes of cortical osteoporosis of the femur and tibia models. The simulated cortical bone thicknesses for both models were both consistent with the clinical data [1], which can be seen from the following aspects:

- (1) The similarity of our numerical outcomes with clinical data can be seen directly from Fig. 1 and Fig. 2.
- (2) The times to reach steady state in the simulation were in agreement with the clinical investigation, i.e. approximately 5.1 years for femur cortical bone and 6.9 years for tibia cortical bone.
- (3) The simulated steady state values of cortical thickness

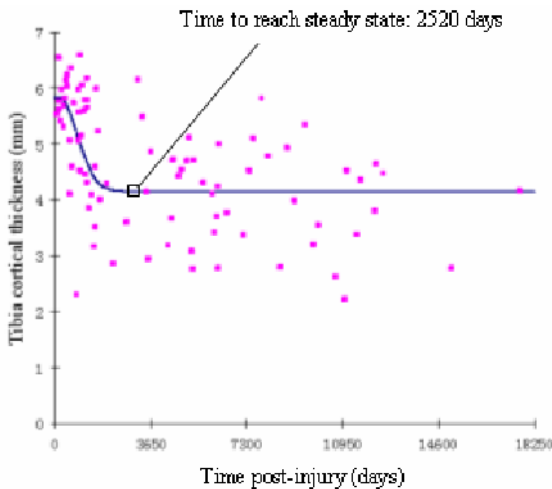


Fig. 1 Simulation result of cortical thickness of tibia model

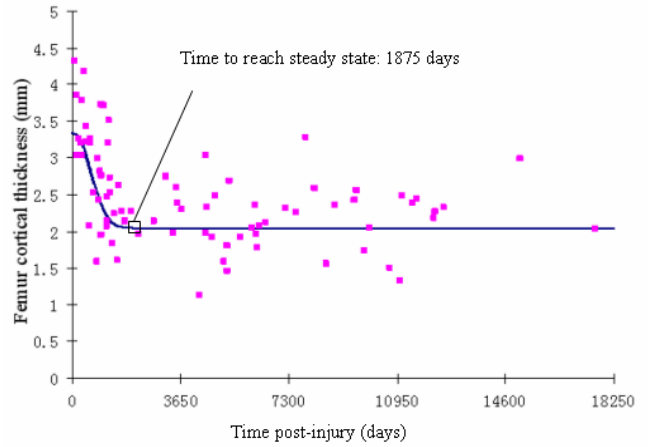


Fig. 2 Simulation result of cortical thickness of femur model

in both models were close to the clinical data. For the femur model, the simulated steady state value of cortical thickness was 2.04mm and the clinical data was 2.17mm with relative difference of 5.99%. For the tibia model, the simulated steady state value was 4.13mm and the clinical data was 3.94mm with relative difference of 4.82%.

B. Simulation results of trabecular bone osteoporosis

When disuse was maintained, this was the characteristic of mechanical loading condition for the ages around menopause, a number of different magnitudes of changes in osteoblastic formation threshold and/or changes in BMU activation threshold could give results that were consistent with the bone loss patterns seen at menopause. Figure 3 shows the simulation outcomes of trabecular bone osteoporosis in two cases. For both cases, disuse was maintained. And in

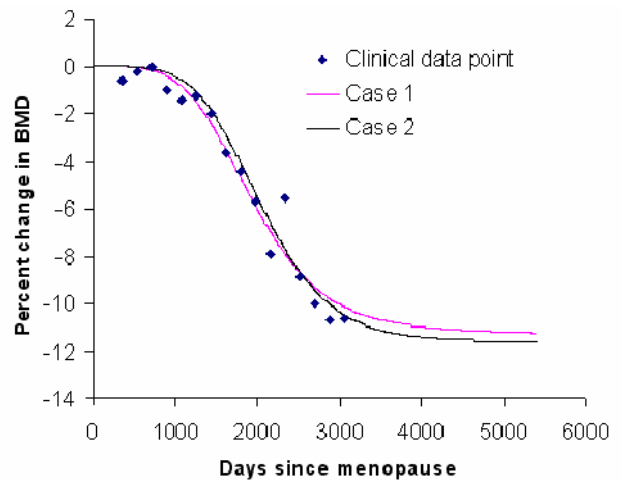


Fig. 3 Simulation results of trabecular BMD in two cases

case 1, BMU activation threshold was increase by 110% (maintained), osteoblastic formation threshold was increased by 100% (maintained), and disuse condition was 8%, SSE=9.73. In case 2, BMU activation threshold was increase by 70% (maintained), osteoblastic formation threshold was increased by 60% (transient), and disuse condition was 19%, SSE=9.86.

The BMD value decreased about 11% during menopausal transition.

IV. CONCLUSIONS

The computational models for osteoporosis occurred at cortical endosteal surface and trabecular bone developed in this study can be further used to quantify and predict the effects of mechanical factors and biological factors on cortical thickness and trabecular architecture, and help us to better understand the relationship between bone morphology and mechanical as well as biological environment, furthermore, they can also help us to gain more insight into the mechanism of osteoporosis and identify improved osteoporosis treatment and prevention.

ACKNOWLEDGMENT

This work is supported by The Hong Kong Polytechnic University Research Grants (Nos. 1-BB81 and G-U273) and grants from National Natural Science Foundation of China (10502021 and 10529202).

REFERENCES

1. Eser P, Frotzler A, Zehnder Y et al. (2004) Relationship between the duration of paralysis and bone structure: a pQCT study of spinal cord injured individuals. *Bone* 34: 869-880
2. Recker R, Lappe J, Davies K et al. (2000) Characterization of perimenopausal bone loss: a prospective study. *J Bone Miner Res* 15: 1965-1973
3. Ganong WF (2005) In Review of medical physiology [electronic resource] (Lange Medical Books/McGraw-Hill. New York)
4. LeBlanc A, Shackelford L, Schneider V (1998) Future human bone research in space. *Bone* 22: 113s-116s
5. Paga A, Jasty M, Bragdon C et al. (1991) Alterations in femoral and acetabular bone strains immediately following cementless total hip arthroplasty: an in vitro canine study. *J Orthop Res* 9: 738-748
6. Frost HM (2001) Seeking genetic causes of "osteoporosis": insights of the Utah paradigm of skeletal physiology. *Bone* 29: 407-412
7. Hazelwood SJ, Martin RB, Rashid MM et al. (2001) A mechanistic model for internal bone remodeling exhibits different dynamic responses in disuse and overload. *J Biomech* 34: 299-308
8. Hernandez CJ, Beaupre GS, Carter DR (2003) A theoretical analysis of the changes in basic multicellular unit activity at menopause. *Bone* 32: 357-363

The address of the corresponding author:

Author: Ming Zhang
 Institute: The Hong Kong Polytechnic University
 Street: Hung Hom, Kowloon
 City: Hong Kong SAR
 Country: P.R.CHINA
 Email: htmzhang@polyu.edu.hk

Synthesis, Characterization and Cell-uptake of Porphyrin-capped Gold Nanoparticle

Lü Feng, Liu Tianjun*, Wu Li

Institute of Biomedical Engineering, Chinese Academy of Medical Sciences & Peking Union Medical College,
The Tianjin Key Laboratory of Biomaterial Research, Tianjin 300192, PR China

Abstract—In order to improve the cell uptake effect of porphyrins and their derivatives, gold nanoparticle was chosen as carrier. We report our preliminary result on synthesis and characterization of thiol tailored porphyrin and porphyrin capped gold nanoparticle, their interaction with cell by TEM, UV-Visible spectra, fluorescent spectra and confocal microscopy. Our results show that porphyrins modified gold nanoparticles have low cytotoxicity and acceptable fluorescence emission, and reliable cell uptake ability. Gold nanoparticle is an ideal carrier to delivery the porphyrin molecule into cell which make porphyrin modified gold nanoparticles as a potential agent in PDT and molecular image.

Keywords—Iporphyrin, gold nanoparticle, cell uptake, photosensitizers, fluorescence probe

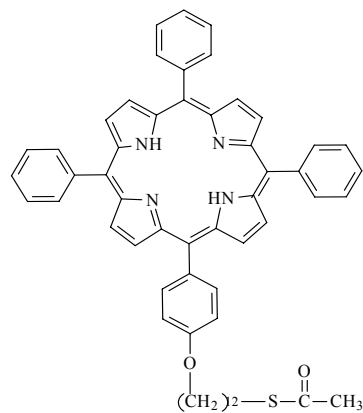
I. INTRODUCTION

Porphyrins and their derivatives have extension electronic conjugated structure, large visible to NIR absorption extinction molar constant, acceptable fluorescent quantum yields, and more important is their biocompatibility, so their application in biomedical fields are wide including photodynamic therapy (PDT) triplet sensitizer^[1-2], fluorescent imaging probe^[3-5], as well as oxygen carriers^[6]. Either as which mentioned above, all of require function into cell, so their cell-uptake mechanism as well as their cytotoxicity is predominant concern. Cell uptake ability for a component is dictated by their chemical properties, size, charge and hydrophilic-lipophilic character. Furthermore, the type of the carrier used for delivering to the target cell also strongly influences the intracellular accumulation and distribution. The cell-penetrating property of the component is a key factor. In order to improve the cell uptake effect of porphyrins and their derivatives, we chose gold nanoparticle (AuNP) as carrier and discuss the cell uptake of porphyrin modified gold nanoparticle.

II. MATERIALS AND METHODS

2.1 Materials

H₂AuCl₄ (99.99%) were purchased from Aldrich. Thiol-derivatized porphyrin (Schedule 1) was synthesized according to the literature^[7]. AuNP was prepared by the citrate reduction of chloroauric acid^[8] Porphyrin-capped gold nanoparticle were directly prepared by reduction of H₂AuCl₄ with NaBH₄ in toluene/water containing thiol-derivatized porphyrin^[7]. All solvents and chemicals were of reagent grade quality, obtained commercially and used without further purification unless otherwise noted.



Schedule 1 Thiol-Derivatized Porphyrin

2.2 Structure characterization and spectral measurements.

UV-visible spectra were obtained on a Shimadzu UV-3100PC spectrometer at 298 K. Fluorescence spectra were taken using a Shimadzu spectro fluorophotometer (RF-5000PC).

2.3 Biocompatibility Assay.

Liver cancer cells (10 000 cells) were cultivated in a 96 well plate at 37 °C in 5% CO₂. After 24 h, the medium was replaced with fresh medium containing gold nanoparticle solution, porphyrin or porphyrin-modified nanoparticles in 0.1% DMSO solution, cultivation again for 24 h. At the end of each exposure, the toxicity level of gold nanoparticles was assessed by MTT assay.

2.4 Cell uptake of porphyrin-capped gold nanoparticle by CLSM

The liver cancer cells were grown in EMEM medium containing 10% fetal bovine serum (FBS) at 37 °C in controlled 5% CO₂ atmosphere. Cells (10 000 cells) were cultivated in a 96 well plate at 37 °C in 5% CO₂. After 24 h, the medium was replaced with fresh medium containing 10 μM gold nanoparticles or 10 μM porphyrin-modified gold nanoparticle. At ~ 80% confluency, the cells were trypsinized with trypsin-EDTA solution (0.25% trypsin, 1 mM EDTA) for 5~10 min at 37°C to detach the cells, centrifuged at 1000 rpm for 3 min and resuspended in the medium. About 20 μl of cell suspension was dropped onto a cover glass slide and then imaged immediately with a leica confocal microscope.

III. RESULTS AND DISCUSSION

3.1 Preparations and Characterization.

Porphyrin-modified gold nanoparticle was synthesized. TEM showed that the mean diameter of porphyrin-capped gold nanoparticle was 12nm. The absorption spectra of por-

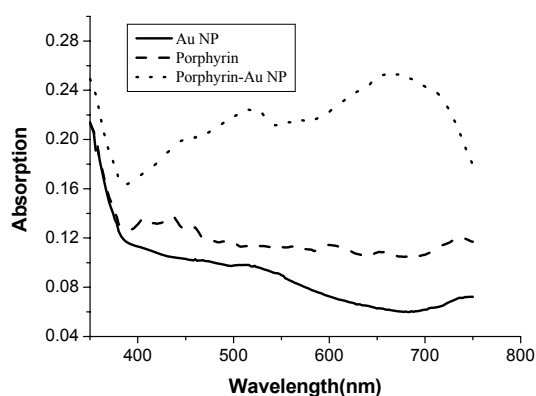


Fig.1 UV-visible spectra of Thiol-Derivatized Porphyrins (dotted line,) gold nanoparticle (solid line), porphyrin-AuNP (dashed line) in THF at r.t. $c = 1.0 \times 10^{-5} \text{ mol.dm}^{-3}$

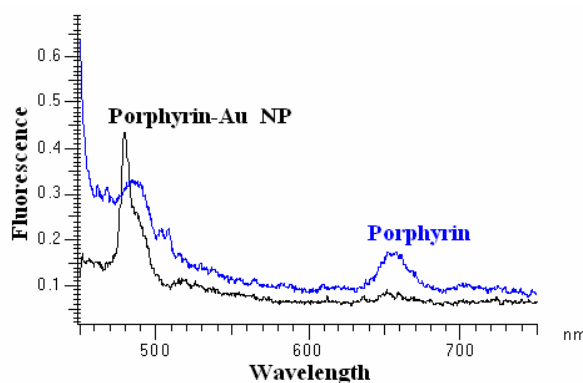


Fig.2 Fluorescence spectra of Thiol-Derivatized Porphyrins, porphyrin AuNP excited at 420nm in THF at r.t. $c = 1.0 \times 10^{-5} \text{ mol.dm}^{-3}$.

phyrin in tetrahydrofuran and the colloidal solution of Au are shown in Fig.1. Characteristic bands of the porphyrin are seen at 417 nm and at 500-650 nm. The gold nanoparticles also show characteristic surface plasmon band in the visible region, as can be seen at 520 nm. The absorption of porphyrin-capped gold nanoparticle is at 450nm, 520nm and 650nm; display both the characteristics of gold nanoparticle and porphyrin respectively

Fluorescent spectra of porphyrin and porphyrin-modified gold nanoparticle (Fig.2) were recorded in THF excited at soret band, 420nm, where the absorbance was adjusted to be identical. Both peak position (655 nm) and shape of the emission are similar for either of porphyrin ligand or porphyrin capped Au nanoparticle. But the fluorescent intensity is relatively weak for AuNP compared with the porphyrin ligand, this demonstrated moderate quenching of the steady-state fluorescence of porphyrin-modified by gold nanoparticle. Contrary to completely fluorescent quenching reported by some literature, here moderate fluorescent quenching is due to the long spacer 12-carbon alkyl chain retard the energy transfer efficiency. Fig.2 shows that the fluorescence of porphyrin at 490nm and 660nm is strong, while the fluorescence of porphyrin-capped gold nanoparticle only existed at 490nm. This may be due to quenching of the porphyrin excited states by gold through energy transfer mechanism^[7, 9].

3.2 Biocompatibility of porphyrin-capped gold nanoparticle

The cytotoxicity of gold nanoparticles *in vitro* was evaluated in terms of the effect of gold nanoparticles, porphyrin and porphyrin-capped gold nanoparticle on cell proliferation by MTT assay. The relative cell viability (%) related to control wells containing cell culture medium without gold nanoparticles was calculated by $[A]_{\text{test}}/[A]_{\text{control}} \times 100$. a

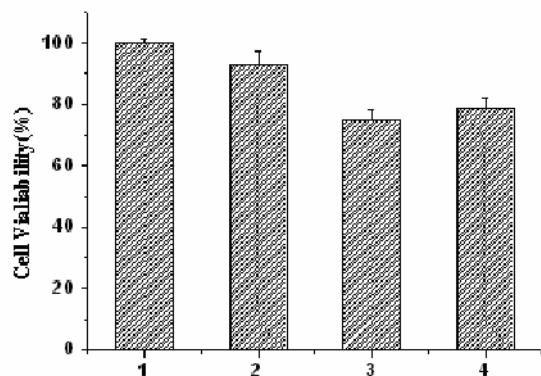


Fig.3 Cytotoxicity profiles of gold nanoparticle, porphyrin- and related Porphyrin AuNP (1 Control, 2 Gold nanoparticle, 3 PorphyrinAuNP, 4. Porphyrin)

marginal decrease in cell viability to 93%, 82%, 78% for treatment by AuNP, porphyrin and porphyrin capped nanoparticle respectively. This slight decrease in cell number accounted for that in presence of these adducts such as porphyrin etc cell depletion nutrients level in media decreased in the experimental condition. These results show that Au nanoparticles alone do not show detectable cytotoxicity over 72 h exposures. Porphyrin slight enhanced, while porphyrin-capped gold nanoparticle affected the metabolic activity show adducts effect, strongest, the viability value reached 80% as compared to untreated controls. Interestingly, this interaction is concentration dependent. Below this concentration of $1\text{mg}\cdot\text{ml}^{-1}$, less cellular toxicity was detected for porphyrin-AuNP. This result seem shown that gold nanoparticle as a vector or carrier could enhance the porphyrin cytotoxicity in some concentration range.

3.3 Cell uptake of porphyrin-capped gold nanoparticle

Cellular uptake of porphyrin and porphyrin-capped gold nanoparticle was detected using confocal fluorescence microscopy by incubating liver cancer cell with experimental sample for 3h (Fig. 4). The more the cell uptake was, the stronger the fluorescent intensity in cell. The cells incubated with porphyrin displayed a pattern of weak intracellular porphyrin fluorescence emission, indication of weak cell uptake. Whereas in the same experimental condition, such as concentration and temperature, employed with porphyrin-capped gold nanoparticle, the cells exhibited an intense and diffuse intracellular fluorescence. Additional, it can be seen some aggregation of Au nanoparticle. Fig. 4 clearly shows the advantage of porphyrin capped gold nanoparticle in cellular membrane permeability of photosensitizer or probe.

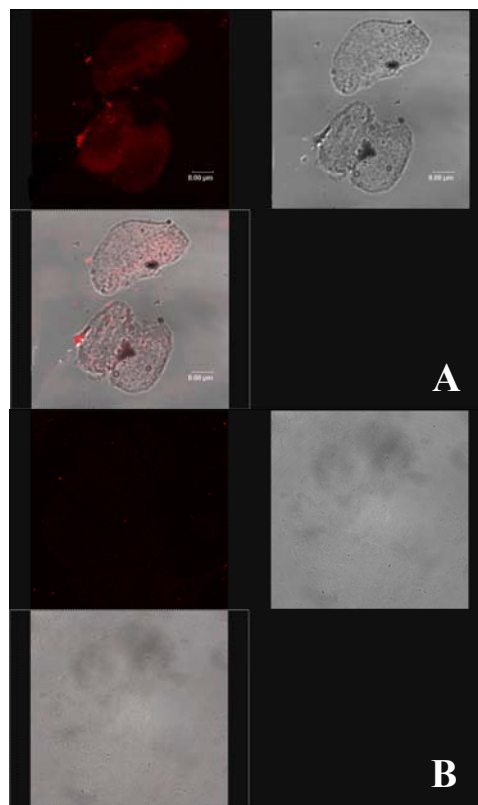


Fig.4 LCSM of cells incubated with porphyrin-AuNP (A), porphyrin (B)

Porphyrins and their derivatives application as either photo sensitizer or image probe, usually work in a monomeric form. Due to their giant chemical surface, big aromatic planar structure and its hydrophobicity, most of porphyrin-like photosensitizers or probes tend to aggregate in aqueous media [10]. This state is one of the critical factors, which can hinder the efficacy of cell uptake and limit its capacity to absorb light. Here we demonstrated that gold nanoparticle have better membrane permeability as the drug delivery carrier. In this paper, gold nanoparticle modified with porphyrin can improve the cell uptake of porphyrin molecule, which is important for porphyrin as photosensitizer or probe.

IV. CONCLUSION

Our preliminary results show that gold nanoparticle is obviously a better carrier for porphyrins and their derivatives. The porphyrins modified gold nanoparticles have enhanced cytotoxicity and acceptable fluorescence emission. Importantly, it can optimize the effect of cell uptake. Gold nanoparticle is an ideal carrier to delivery the porphy-

rin molecule into cell. Thus, we have successfully synthesized porphyrins modified gold nanoparticles, which could be considered as potential agents in PDT and molecule probe in image.

ACKNOWLEDGMENT

This work is supported by the National Basic Research Program of China (No.2006CB705703) and National Key Basic Research and Development Program of China (No.2006CB933202).

REFERENCES

1. Konan YN, Cerny R, Favet J, et al. (2003) Preparation and characterization of sterile sub-200 nm meso-tetra (4-hydroxylphenyl) porphyrin-loaded nanoparticles for photodynamic therapy. *European Journal of Pharmaceutics and Biopharmaceutics* 55(1) 115-124
2. Kramer G, Serpa C, Szurko A, et al. (2006) Spectroscopic properties and photodynamic effects of new lipophilic porphyrin derivatives: Efficacy, localization and cell death pathways. *Journal of Photochemistry and Photobiology B: Biology* 84 (1) 1-14
3. Ghoroghchian PP, Frail PR, Susumu K, et al. (2005) Broad Spectral Domain Fluorescence Wavelength Modulation of Visible and Near-Infrared Emissive Polymersomes, *J Am Chem Soc* 127(44)15388-15390
4. Rao JH, Dragulescu A, Yao H. (2007) Fluorescence imaging in vivo: recent advances. *Current Opinion in Biotechnology*, 18(1)17-25
5. Ghoroghchian PP, Frail PR, Susumu K, et al. (2005) Near-infrared-emissive polymersomes: Self-assembled soft matter for in vivo optical imaging. *PNAS* 102(8) 2922-2927
6. Komatsua T, Oguroa Y, Teramura Y, et al. (2004) Physicochemical characterization of cross-linked human serum albumin dimer and its synthetic heme hybrid as an oxygen carrier. *Biochimica et Biophysica Acta* 1675(1)21-31
7. Imahori H, Kashiwagi Y, Endo Y, et al. (2004) Structure and photo-physical properties of porphyrin-modified metal nanoclusters with different chain lengths. *Langmuir* 20(1) 73-81
8. Chithrani BD, Ghazani AA, Chan WC (2006) Determining the size and shape dependence of gold nanoparticle uptake into mammalian cells, *Nano letters* 6(4)662-668
9. Imahori H, Fujimoto A, Kang S, et al. (2006) Structure and photoelectrochemical properties of nanostructured SnO₂ electrodes deposited electrophoretically with the composite clusters of porphyrin-modified gold nanoparticle with a long spacer and fullerene, *Tetrahedron* 62 ,1955-1966
10. Stasio BD, Frochot C, Dumas D, et al. (2005) The 2-aminoglucosamide motif improves cellular uptake and photodynamic activity of tetraphenylporphyrin. *European Journal of Medicinal Chemistry* ,40(11) 1111-1122

Author: Lü Feng, LIU Tianjun, WU Li
 Institute: Institute of Biomedical Engineering, Chinese Academy of Medical Sciences & Peking Union Medical College
 Street: No.236 Baidi Road
 City: Tianjin
 Country: China

Corresponding author * Email: Liutianjun@hotmail.com

Preparation of nanoparticle of methoxy poly(ethylene glycol)/poly(ϵ -caprolactone)/ methoxy poly(ethylene glycol) triblock copolymer for drug delivery applications

N.V. Cuong, C.H. Chen, Y.T. Chen and M.F. Hsieh

Department of Biomedical Engineering , Chung Yuan Christian University 200, Chung Pei Rd., Chung Li, Taiwan 32023, R.O.C

Abstract — Triblock copolymers of monomethoxy poly(ethylene glycol) (mPEG, $M_w = 5000$) and poly(ϵ -caprolactone) (PCL) were prepared with different length of PCL compositions. Initially diblock copolymer of mPEG-PCL was synthesized by ring opening polymerization of mPEG with ϵ -caprolactone with SnOct as catalyst. The diblock copolymer was reacted with carboxylic acid terminated mPEG via coupling reaction. The amphiphilic block copolymers were based on hydrophobic (PCL) segments and two hydrophilic (PEG) segments. The structures of ring opening polymerization and triblock copolymer were characterized by ^1H NMR and FT-IR spectroscopy. These copolymers can self-assemble into nanoscopic micelles. The size and size population distribution of micelles were also determined by dynamic light scattering (DLS). The nanoparticle sizes are around 16-30 nm. The cytotoxicity of copolymeric nanoparticles was investigated against mouse fibroblast cells lines (L929).

Keywords — monomethoxy poly(ethylene glycol); poly(ϵ -caprolactone); triblock copolymers

I. INTRODUCTION

It is well-known that biodegradable nanoparticles such as micelles and vesicles play an important role in the biomedical engineering fields and are of attractive interest for medical and pharmaceutical applications. Poly(ϵ -caprolactone) (PCL) is a biodegradable thermoplastic polymer, an inexpensive polyester; low viscosity, and it is easy to process. It is hydrophobic segments and with short degradation time [1, 2]. The amphiphatic block copolymers can self-assemble to form polymeric micelles in an aqueous solution. The previous reaches claimed the sizes of polymeric micelles are approximately less than 100 nm, which give them an enhanced vascular permeability. The polymeric micelles (PEG-PLC) are composed of a hydrophilic (PEG) outer shell and a hydrophobic (PCL) inner shell. Poly(ethylene glycol) (PEG) is a hydrophilic and nontoxic segment, which allows PEG to be used in wide medical applications. PEG segments are also known to prevent plasma protein adhesion and increase the circulation time of nanoparticles following intravenous injection. Polymeric micelles with nanosize are known as an alternative delivery carrier for several

hydrophobic drugs such as anti-cancer agents [3, 4]. In this present study, we reported the preparation of triblock copolymer, which composed of two hydrophilic segments (PEG) and one hydrophobic segment (PCL). The structure of triblock copolymers were characterized by ^1H NMR, FT-IR and differential scanning calorimetry (DSC).The self-assembled polymeric micelles were also studied in an aqueous solution. In addition, the cytotoxicity effects against mouse fibroblast cells lines (L929) were investigated. In this study we aimed at understanding the micellar formation and in vitro cytotoxicity properties of such triblock copolymers for the potential drug delivery applications.

II. MATERIALS AND METHODS

A. Materials

Monomethoxy-PEG (mPEG, $M_w=5000$) was purchased from Scientific polymer products. Inc. ϵ -caprolactone, and stannous 2-ethyl hexanoate (stannous octoate, SnOct) were purchased from A Johnson Matthey Company. The mPEG was purified by re-crystallization on the dichloromethane/diethyl ether system, and ϵ -caprolactone was dried using CaH_2 and distilled under reduced pressure. N,N' -dicyclohexylcarbodiimide (DCC) and 4-dimethylamino pyridine (DMAP) were supplied by A Johnson Matthey Company. 1,4-dioxane, dichloromethane, ethanol, and diethyl ether, tetrahydrofuran and other chemicals were reagent grade and used without further purification.

B. Synthesis of PEG-PCL-PEG triblock copolymers

The synthesis procedures are demonstrated below. mPEG-PCL diblock copolymer, reported elsewhere [5] was synthesized by ring opening polymerization of ϵ -caprolactone in the presence of mPEG as a macro initiator with SnOct as catalyst at 130°C for 24 h. Carboxylic acid terminated mPEG-COOH was prepared according to the procedure which was published by Bae Y.H et al [6, 7]. methoxy poly(ethylene glycol)/poly(ϵ -caprolactone)/methoxy poly(ethylene glycol) copolymer (from here define as PEG-

PCL-PEG) were prepared by coupling reaction of carboxylic acid terminated mPEG-COOH with mPEG-PCL in presence of DCC and DMAP.

C. Characterizations of mPEG-PCL block copolymers

The formations of block copolymer were confirmed by ^1H NMR and FT-IR. The FT-IR spectras were measured by FT-IR spectrometer (Jasco, FT-IR 410) in the range from 4000 to 500 cm^{-1} . The powdery block copolymers were compressed into KBr discs for measurements. ^1H NMR spectra of the block copolymers were recorded by using a Bruker spectrometer operating at 500 MHz using CDCl_3 as solvents.

D. Determination of critical micelle concentration

The critical micelle concentration of copolymers was determined by UV-Vis spectroscopy using 1,2-diphenyl-1,3,5-hexatriene (DPH) as the fluorescent probe. Samples for UV-Vis measurement were prepared according to the literature [5,6,7] and the concentration of aqueous copolymers solution ranged from 0.001 wt% to 1 wt% and concentration of DPH was 4×10^{-6} M.

E. Preparation of micelles nanoparticles

PEG-PCL-PEG nanoparticles were prepared by nanoprecipitation method. Thirty milligrams (30.0 mg) triblock copolymers were dissolved in 2 mL THF. The solution was added dropwise into 2 mL distilled water under moderate stirring at 25 $^\circ\text{C}$. The resulting solutions were transferred to dialysis bag and dialyzed against 500 mL of double distilled water using cellulose dialysis membranes (molecular weight cut off 50,000 Da). The suspension obtained was passed through a syringe filter (pore size 0.2 μm) to remove aggregates. The final micellar concentrations were 2.5 mg/mL.

F. Particle size measurements

Dynamic light scattering: The micelle solution was diluted in various concentrations (2.5, 1.25, 0.5 and 0.1 mg/mL) then filtered before measurement. The mean diameter and size distribution micelles were determined by dynamic light scattering (DLS) using a 90Plus/BI-MAS Multi Angle Particle Sizing Option at fix angle of 90° , 659 nm and 25 $^\circ\text{C}$. Mean and standard deviation of particle sizes were calculated by assuming a lognormal distribution, and the measured intensity autocorrelation function of scattered light was corrected using Stokes-Einstein equation.

G. Cytotoxicity: MTT assay

The cytotoxicity of mouse fibroblast cells (L929) experiments was seeded in 48-well microplates at 10^3 cells at 37 $^\circ\text{C}$ under humidified atmosphere containing 5% CO_2 . Control was defined that cells were grown without adding polymeric micelles. PEG-PCL-PEG micelles solutions (0.01, 0.1, 0.25 and 0.5 mg/mL) was added into the wells and incubated for 2 days. After predetermined incubation periods, MTT solution was added to each well followed by 4 hours of incubation at 37 $^\circ\text{C}$. Subsequently, the medium was removed and violet crystals formed were solubilized with DMSO. After shaking slowly twice for 5 seconds, the absorbance of each well was determined using a Multiskan Spectrum spectrophotometer (Thermo Electron Corporation, Waltham, MA) at 570 nm. The cell viability was expressed as a percentage of the control.

III. RESULTS AND DISCUSSIONS

A. Synthesis of PEG-PCL-PEG triblock copolymers

The mPEG-PCL was prepared with different feeding molar ratio of mPEG/ ϵ -CL with the molecular weight of mPEG 5000. The triblock copolymers were prepared by coupling of PEG-PCL with the modified mPEG ($M_w=5000$) to delivery PEG-PCL-PEG with the same PEG segments and different PCL segments ($M_n=8000$ and 3600). They will be defined as PEG-PCL80-PEG and PEG-PCL36-PEG. The molecular weight (M_n) was calculated using ^1H NMR spectroscopy according to the previous literature [8] ($M_n=M_{n\text{PCL}} + M_{n\text{PEG}}$). The typical signals of ^1H NMR spectra of both PEG and PCL were detected when CDCl_3 was used as solvent, thus confirming the ring opening polymerization and coupling reaction were carried out. In the ^1H NMR spectra of triblock copolymers dissolved in CDCl_3 , the characteristic chemical shifts corresponding to both PCL (1.37, 1.62, 2.28, and 4.05 ppm) and MPEG (3.36 and 3.62 ppm) were observed.

Figure 1 shows the FT-IR spectra of unmodified PEG-PCL and PEG-PCL-PEG with two compositions. A strong carbonyl band appeared at 1724.0 cm^{-1} , 1729.8 cm^{-1} and 1733.5 cm^{-1} for PEG-PCL, PEG-PCL36-PEG and PEG-PCL80-PEG; respectively. The wavenumber of carbonyl groups increased slightly from PEG-PCL36-PEG to PEG-PCL80-PEG. These results could be attributed to the lower molecular weight of PCL segment of PEG-PCL36-PEG. The absorption bands at 11079-1110 cm^{-1} are determined to be the C-O-C stretching of PEG.

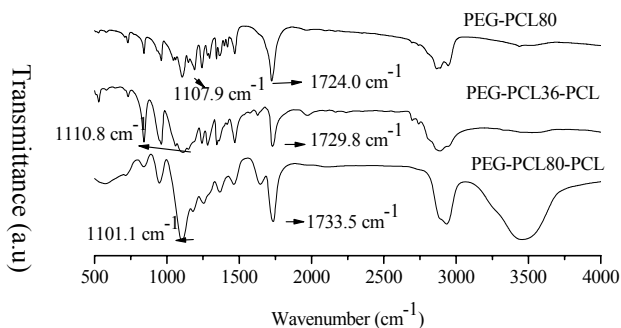


Fig. 1 The FT-IR spectra of PEG-PCL and triblock copolymers

Characterization of micelles nanoparticles

The amphiphilic triblock copolymers composing of hydrophobic block and hydrophilic block have been widely applied as carriers for drug delivery. The critical micelles concentration (CMC) of triblock copolymer were evaluated by using a fluorescence spectroscopic method based on DPH as the fluorescent probe as described above. As expected; the CMC of PEG-PCL80-PEG and PEG-PCL36-PEG were detected in a range of 0.79×10^{-3} - 1.26×10^{-3} and 5×10^{-3} - 5.6×10^{-3} respectively. The lower CMC value of PEG-PCL36-PEG micelles may be due to the short PCL segment, indicating that the hydrophilic length of PCL plays a relative role on the thermodynamic stability of micelles formation [3].

The size and size distribution of polymeric micelles was determined by dynamic light scattering. The results showed that the size of nanoparticle of triblock copolymers PEG-PCL80-PEG and PEG-PCL36-PEG were in a range of 23-25 nm and 16-20 nm; respectively. The results are summarized in Table 1.

To investigate the affect of micelles concentration to the particle size formation, several concentrations were prepared and measured. The initial triblock copolymer concentration was 2.5 mg/mL, and then was diluted to 0.1, 0.5 and 1.25 mg/mL for DLS measurements. Interestingly the results demonstrated that the micelles concentration effected slightly to the particle size of micelles (Table 1).

Table 1 Properties of micelles of triblock copolymers

Concentration (mg/mL)	PEG-PCL80-PEG		PEG-PCL36-PEG	
	Particle size (nm)	Polydispersity	Particle size (nm)	Polydispersity
0.1	23.6±0.9	0.256	16.2±5.4	0.219
0.5	25.2±0.7	0.233	19.8±0.6	0.221
1.25	24.8±0.8	0.249	17.7±0.3	0.246
2.5	24.2±0.3	0.231	17.9±0.2	0.237

B. Cytotoxicity: MTT assay of PEG-PCL80-PEG and PEG-PCL36-PEG

The cytotoxicity of micelles to L929 cells were evaluated using MTT assay method. Figure 2 demonstrates the cell viability after 48 h incubation with polymeric micelles of triblock copolymer PEG-PCL80-PEG and PEG-PCL36-PEG at several concentrations (0.01, 0.1, 0.25 and 0.5 mg/mL).

The results show that cells viability cultured with PEG-PCL36-PEG decreased to a round 75% with the increasing of micellar concentration. The high cell viability was observed when the cell was cultured with PEG-PCL80-PEG (higher than 92% for 0.1, 0.25 and 0.5 mg/mL). However PEG-PCL80-PEG micelle solution shows the higher cytotoxicity effect to the L929 fibroblast cells with a concentration of 0.01 mg/mL. It could be attributed to the unstable micellar particles (DLS measurements; data are not shown). The cells viability suggests that these triblock copolymers micelles have generally low cytotoxicity to the L929 fibroblast cells with higher molecular weight of PCL segments.

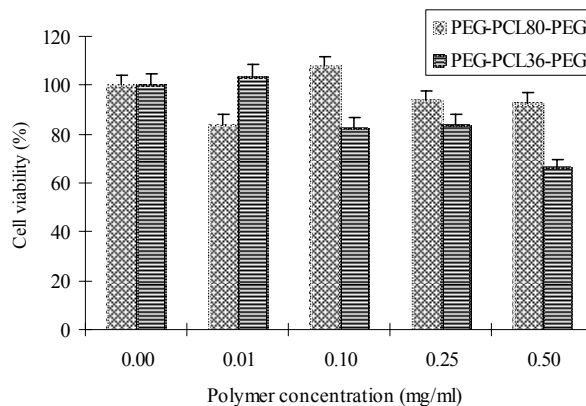


Fig. 2 The cytotoxicity of micellar solutions of triblock copolymers

IV. CONCLUSIONS

In this present work we have successfully prepared the biocompatibility triblock copolymers (EPG-PCL-PEG) with same PEG segments and different molecular weight of PCL segments. The self assemble of triblock copolymers were also investigated with particle size in a range of 16-30 nm. The cytotoxicity of triblock copolymer micelles were studied against L929 fibroblast cells. The results show a round 92% and 75% cell viability for PEG-PCL80-PEG and PEG-PCL36-PEG; respectively.

ACKNOWLEDGMENT

This work was supported by the National Science Council, Republic of China under grant number NSC95-2218-E-033-008 and the specific research fields in the Chung Yuan Christian University under grant number CYCU-95-BE

REFERENCES

- [1] Panyam J and Labhasetwa V. (2003) *Adv Drug Deliv Rev* 55, 329.
- [2] Lu C, Guo S, Liu L, Zhang Y, Li Z, Gu J. (2006) *J. Polym Sci Pol Phys*. 44, 3046.
- [3] Wang Y.C, Tang L.Y, Sun T.M, Li C.H, Xiong M.H and Wang J. (2008) *Biomacromolecules*. 9, 388.
- [4] Otsuka H, Nagasaki Y and Kataoka K. (2003) *Adv. Drug Delivery Rev.* 55, 403.
- [5] Hsieh M.F, Lin T.Y, Gau R.J, Chang H.T, Lo Y.L and Lai C.H. (2005) *J. Chin. Inst. Chem. Engrs.* 36, 1.
- [6] Bae Y.H, Huh K.M, Kim Y and Park K. (2000) *J. Control. Release.* 64, 3.
- [7] Hsieh M.F, Cuong N.V, Chen C.H, Chen Y.T and Ye Y.M. (2008) *J. Nanosci. Nanotechnol (accepted manuscript)*.
- [8] Choi C, Chae S.Y, Kim T.H, Jang M.K, Cho C.S, and Nah J.W. (2005) *Bull. Korean Chem. Soc.* 4, 26.

Biological responses of endothelial cells to aligned nanofibers of MWNT/PU by electrospinning

Z.Z. Han^{1*}, H. Kong^{1*}, J. Meng², C.Y. Wang³, S.S. Xie³, H.Y. Xu¹

¹ Department of Biomedical Engineering, Institute of Basic Medical Sciences, Chinese Academy of Medical Sciences & Peking Union Medical College, Beijing 100005, R.P. China

² Department of Pathophysiology, Institute of Basic Medical Sciences, Chinese Academy of Medical Sciences & Peking Union Medical College, Beijing 100005, R.P. China

³ Institutes of Physics, Chinese Academy of Sciences, Beijing 100080, R.P. China

* The two authors contributed equally in this work

Abstract — Nanofibrous scaffold of carbon nanotubes/polyurethane composite (MWNT/PU) with aligned topography was fabricated by electrospinning for endothelium cells growth. The diameter of the generated fiber was around 300nm-500nm. Experimental results indicated that the nanofibrous scaffold of MWNT/PU exhibited promotional influence on the cell proliferation. It was also observed that the scaffold possessed an advantage of supporting ECs migrating and aggregating along the axis of the aligned nanofibers, which is one of the important functions in the process of endothelium regeneration. It was also demonstrated that the endothelial cells growing on the scaffold expressed non-thrombogenic phenotype with low tissue factor released. These results indicated the favorable interactions between ECs and the nanofibrous scaffold of MWNT/PU, implying that the aligned nanofibrous scaffold has a promising potential for vascular engineering.

Keywords — carbon nanotubes, electrospun scaffold, endothelial cells

I. INTRODUCTION

Tissue-engineering scaffolds play important roles in cell growth and tissue formation. It has been widely accepted that the scaffolds should be analogous to native extracellular matrix (ECM) in terms of both chemical composition and physical structure^[1]. Many technologies have been developed to fabricate three-dimensional porous architectures to fill this role, among those the electrospinning process is a simple, feasible and economical means to produce scaffolds of ultra-fine fibers derived from a variety of polymers. Many evidences have indicated that nanofibrous scaffolds formed by electrospinning may represent promising structures for tissue engineering applications because the nanofibrous network is similar to the microstructure of natural ECM and can induce favorable interactions between cells and the scaffolds^[2-5]. Besides, nanofibrous architecture, chemical contribution of the scaffolds has also attracted

intense attention; a variety of biomaterials has been used to fabricate nanofibrous structures by electrospinning to study their suitability in tissue engineering application^[6-8].

In the field of vascular tissue engineering, the problem of thrombogenicity may finally cause the failure of the grafts^[9]. ECs are capable of synthesizing molecules in response to the surrounding blood, ECM and peripheral cells, regulating vascular tone, thrombosis, and fibrinolysis^[10]. Therefore, an ideal vascular tissue-engineering scaffold should have a confluent endothelial cell lining flow and possess desirable physiologic functions such as anticoagulation abilities.

In the current work we made the nanofibrous scaffold from the multiwalled carbon nanotubes/polyurethane composite (MWNT/PU) with aligned fibrous architecture and unique chemical component of carbon nanotubes by electrospinning technique. The influence of the scaffold upon the growth behaviors and anticoagulation function of the human primary endothelial cells was investigated. The current design was based on our previous investigations^[11] and the consideration that carbon nanotubes have electrically conductive property as well as excellent mechanical property, which are desirable features for tissue engineering scaffolds in which electrical signals are propagated and the scaffold could be reinforced.

II. EXPERIMENTAL DETAILS

MWNT/PU was prepared according to the procedure previously reported^[12]. The percentage of MWNT incorporated in PU was around 3% (w/w). The particulates of MWNT/PU and PU control were dissolved in acetdimethylamide respectively at the concentration of 10% respectively. The nanofibrous scaffolds of both MWNT/PU and PU were fabricated respectively by electrospinning technique under optimum conditions. As controls, smooth films of MWNT/PU and PU

were prepared by casting the solutions into glass molds. Substrate samples, either the casting films and nanofibrous scaffolds, were trimmed carefully to fit the size of wells in cell culture plate. Before seeding cell, all scaffolds were coated with collagen type I from calf skin (in 0.1 M acetic acid; Sigma), with concentration of $20\mu\text{g}/\text{cm}^2$, and sterilized under the UV light over 1 h. The character of aligned nanofibrous scaffold was observed through scanning electron microscopy (SEM, Hitachi S-5200).

Human umbilical vein endothelial cells (HUVEC) were isolated from fresh umbilical cords according to the reference [13]. The ECs were culture at 37°C in 5% CO_2 in M199 medium supplemented with endothelial cell growth factor (ECGF, Roche, USA), 15% fetal bovine serum (Hyclone, USA), 100units/ml penicillin and 100 units/ml streptomycin, 2mM L-glutamin, $50\mu\text{g}/\text{ml}$ heparin. During cell culture, the culture medium was changed every 3 d. After the ECs reached 80% confluence, they were trypsinized and passaged at 1:2-1:3.

In the test of cell viability, ECs were seeded at a density of 4,000 cells/well onto the scaffolds set in the 96-well culture plate in a humidified incubator with 5% CO_2 at 37. On days 1, 5, and 7 after cell seeding, unattached cells were washed out and the attached cells were quantified by MTS assay (CellTiter 96 AQueous One Solution Cell Proliferation Assay, Promega) with Bio-Rad Automated EIA Analyzer.

Immunohistochemistry staining was performed to observe and compare the difference of ECs morphology on different substrates as well as to visualize the organization of the cytoskeleton protein. In this test α -actin, β -tubulin, vinculin in ECs was marked with rhodamine and FITC respectively, viewed with laser scanning confocal microscopy (Confocal Vokogawa CSU10).

The release of tissue factor (TF) was measured by anti-human total tissue factor ELISA kit (BPB Biomedicals, USA).

All attachment and proliferation measurements were collected in triplicate and expressed as mean \pm standard deviation (SD). Single-factor analysis of variance (ANOVA) was employed to assess statistical significance of the results. Difference was considered statistically significant at $p < 0.05$.

III. RESULTS AND DISCUSSION

The morphology of electrospun aligned nanofibrous scaffold of both MWNT/PU and PU control were observed and characterized through scanning electron microscopy, shown in Figure 1. Most of the fibers in the scaffold were aligned with an average fiber diameter of 300 nm-500 nm.

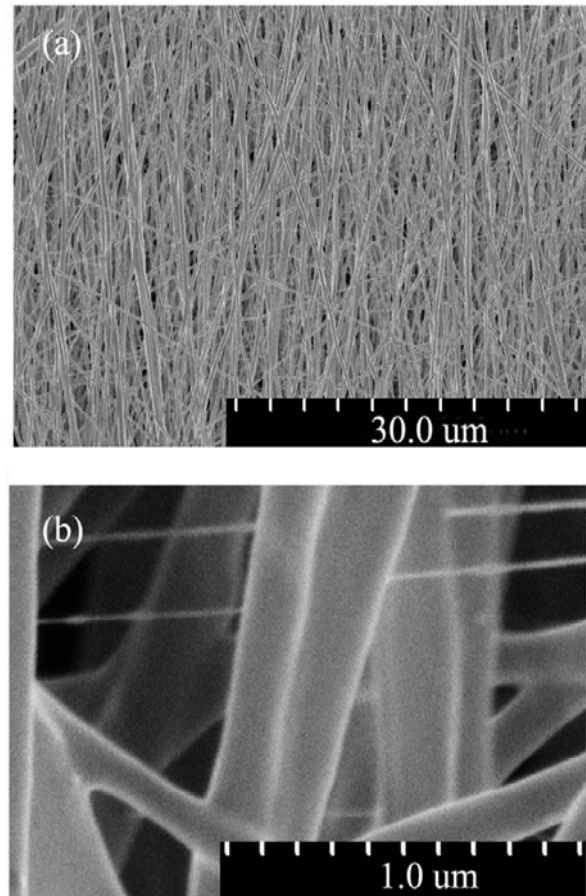


Fig. 1 SEM images of the aligned nanofibrous scaffold of MWNT/PU

Proliferation experimental results showed that the nanofibrous scaffold of MWNT/PU exhibited highest enhancement to the endothelial cell proliferation, followed by the nanofibrous scaffold of PU, compared with the smooth film of PU (Figure 2). It is suggested that nanofibrous structure and MWNT incorporated in the PU matrix enhanced the cells proliferation in a coordination way.

Figure 3 presented the morphology and cytoskeleton development of the ECs growing on the nanofibrous scaffold of MWNT/PU and smooth film of PU respectively. It could be seen that after cultured for 2 d, cells growing on the smooth film of PU exhibited a separate and flat appearance, to the contrast, majority of the cells on the nanofibrous scaffolds of MWNT/PU arranged in an orientation parallel to the direction of nanofibers in the scaffold, displaying the extending morphology as in natural tissues. Additionally, ECs both growing on the smooth film of PU and on the nanofibrous scaffold of MWNT/PU displayed clear skeleton fibers. The above observation implied that the aligned nano-

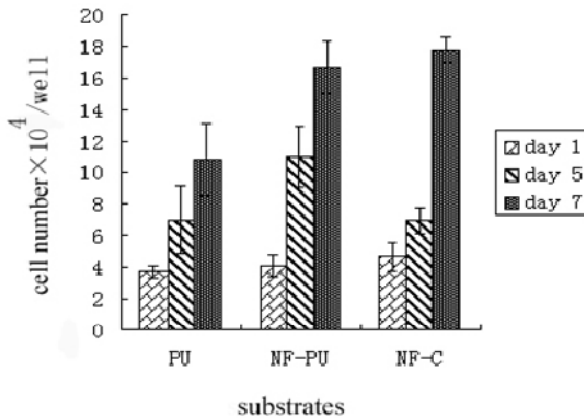


Fig. 2 The viability of the ECs growing on different substrates during 1 week.

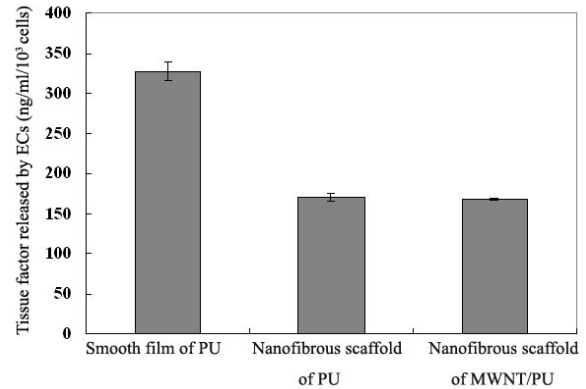


Fig. 4 TF release from ECs seeded on the substrates.

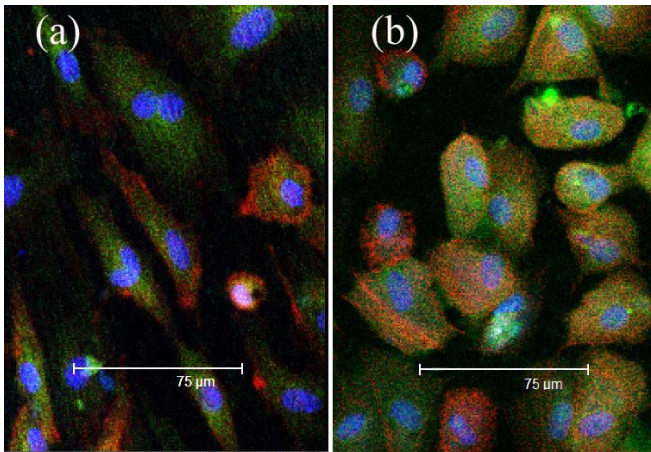


Fig. 3 Morphology of cytoskeleton of ECs after 2 days of growing on substrate: (a) cells growing on aligned nanofiber scaffold; (b) cells growing on PU film.

fibrous scaffold provided a friendly microenvironment and encouraged ECs growth.

Furthermore, the anticoagulation function of the ECs growing on the various substrates was examined; the data was given in Figure 4. It was shown that the ECs growing on nanofibrous scaffolds of MWNT/PU and PU released significantly lower amount of tissue factor than those growing on the smooth film of PU. Tissue factor is one kind of initiation molecule secreted by ECs to promote coagulation when the integrity of ECs was interrupted. On normal ECs, TF expression is low. Therefore, the above analysis data indicated the cells growing in the nanofibrous scaffolds of both MWNT/PU and PU exhibited more relevant phenotype than the cells on the smooth film of PU, suggesting that the aligned nanofibrous structure is one of most factors for the scaffolds for endothelial cells engineering.

IV. CONCLUSIONS

Hence, the scaffold with nanofibrous architecture and carbon nanotubes component provided friendly microenvironment for endothelial cells proliferation. The endothelial cells growing on the aligned nanofibrous scaffolds exhibited non-thrombogenic phenotype. The aligned nanofibrous scaffold of MWNT/PU showed the application potentials for cell amplification in large scale in vitro, tissue repair and regeneration, and surface modification for biomedical devices.

ACKNOWLEDGMENT

National Key Scientific Projects of China (2006CB933203), Natural Science Foundation of China (90606018) and National Center of Nanoscience and Technology, China

REFERENCES

1. S. L. Goodman, P. A. Sims and R. M. Albrecht, *Biomaterials* 17, 2087 (1996).
2. C. Xu, R. Inai, M. Kotaki and S. Ramakrishna, *Tissue Engineering* 10, 1160 (2004).
3. X. M. Mo, C. Y. Xu, M. Kotaki, S. Ramakrishna, *Biomaterials* 25, 1883 (2004).
4. T. Sun, S. Mai, D. Norton, J. W. Haycock, A. J. Ryan and S. Macnil, *Tissue Engineering* 11, 1023 (2005).
5. W. J. Li, R. Tuli, C. Okafor, A. Derfoul, K. G. Danielson, D. J. Hall and R. S. Tuan, *Biomaterials* 26, 599 (2005).
6. F. Yang, R. Murugan, S. Wang, S. Ramakrishna, *Biomaterials* 26, 2603 (2005).
7. Y. Ji, K. Ghosh, X. Z. Shu, B. Li, J. C. Sokolov, G. D. Prestwich, R. A. F. Clark and M. H. Rafailovich, *Biomaterials* 27, 3782 (2006).
8. H. Yoshimoto, Y. M. Shin, H. Terai, J. P. Vacanti, *Biomaterials* 24, 2077 (2003).

9. A. Ratcliffe, *Matrix Biol* 19, 353 (2000).
10. A. P. McGuigan and M. V. Sefton, *Biomaterials* 28, 2547 (2007).
11. J. Meng, L. Song, J. Meng, H. Kong, G. J. Zhu, C. Y. Wang, L. H. Xu, S. S. Xie and H. Y. Xu, *J. Biomed. Mater. Res. A* 72, 298 (2006).
12. J. Meng, H. Kong, H. Y. Xu, L. Song, C. Y. Wang, S. S. Xie, *J. Biomed. Mater. Res. A* 72, 208 (2005).
13. E. A. Jaffe, R. L. Nachman, C. G. Becher and C. R. Minick, *J. Clin. Invest.* 52, 2745 (1973).

Address of the corresponding author:

Author: H. Xu
Institute: Department of Biomedical Engineering Institute of Basic
Medical Sciences, Chinese Academy of Medical Sciences &
Peking Union Medical College
Street: Dong Dan San Tiao 5#, 100005
City: Beijing
Country: R.P China
Email: xuhy@pumc.edu.cn

Preparation, Characterization and Cellular Biological Impact of Water Soluble Multiwalled Carbon Nanotubes

J. Meng^{1*}, M. Yang^{1*}, L. Song², H. Kong¹, C.Y. Wang², R. Wang³, C. Wang³, S.S. Xie², H.Y. Xu¹

¹Institute of Basic Medical Sciences, Chinese Academy of Medical Sciences & Peking Union Medical College, Beijing 100005, China.

²Institute of Physics, Chinese Academy of Sciences, Beijing 100080, China.

³National Center of Nanoscience and Technology, Beijing 100080, China

* The two authors contributed equally in this work

Abstract — Biological effect and multiple application potentials of carbon nanotubes have been becoming important issues attracting intense research interests and concerns. In this work, water dispersible oxidized multiwalled carbon nanotubes (o-MWNTs) were prepared by an optimal combination of ultrasonication and concentrated acids oxidation; stable concentrations of 0.3mg/ml were obtained in deionized water of surfactant free. The o-MWNTs dispersing in water displayed a strong characteristic adsorption at 253nm in the spectra of UV/VIS/NIR. XPS analysis showed the presence of carboxylated groups on the o-MWNTs. SEM observation indicated that after the oxidation, the as received MWNTs were cut short; the average length was around 500nm-800nm, the maximum effective size obtained by DLS measurement was about 340nm. It was inferred that the oxidation degree was one major key factor to determine the stable dispersion concentration of o-MWNTs in water. The o-MWNTs dispersing in water entered into the cells and located in the cytoplasm. Cells proliferation and living cycle were affected by the o-MWNTs dispersing in the culture medium in a concentration dependant manner; the cells cultivated in the medium with high concentration of o-MWNTs underwent apoptosis to a point determined by flowcytometry and TEM respectively, while low concentration of o-MWNTs induced light suppression of cells proliferation examined with cell viability assay.

Keywords — Carbon nanotubes, characterization, biological effect, cell cycle, apoptosis

I. INTRODUCTION

Carbon nanotubes have attracted rapid increasing attention due to their potential applications in multiple biomedical fields, particularly as transporters for delivery of various bioactive molecules such as peptides, proteins, DNAs, RNAs, or drugs [1-4]. Regarding to developing novel effective biomedical reagents, carbon nanotubes technology for biomedical applications is still facing some challenges, for instance, dispersing carbon nanotubes in aqueous to form stable concentrated "solution" of surfactants free, making quantification of the concentration of carbon nanotubes in aqueous, and understanding the mechanisms of influences

of carbon nanotubes upon the biological systems at molecular, cellular, or tissue level as well.

There have been many reports on the functionalization of carbon nanotubes for their solubilization through oxidation and/or surface modification [5]. However, the crucial factors that determine the dispersing amount and stability of carbon nanotubes in water need further investigation.

As of biological impacts of carbon nanotubes, some groups have reported the internalization of single walled carbon nanotubes and multiwalled carbon nanotubes into various cell types with independence of functional groups and cell type. Some other researchers reported that carbon nanotubes exhibited obvious cytotoxicity to some kinds of cell types including human keratinocyte cells, murine alveolar macrophage cell etc [6-10].

In this work, We demonstrated that the oxidation degree was a major key factor of determining the stable dispersion concentration of o-MWNTs in aqueous. The o-MWNTs dispersing in water entered into the cells and were located in cytoplasm, which was suggested to result in an influence upon cells proliferation and living cycle in a concentration dependant manner. Cells cultivated in the medium with high concentration of MWNTs underwent apoptosis to a point, while low concentration of carbon nanotubes induced light suppression of cells proliferation.

II. MATERIALS AND METHODS

A. Preparation of oxidized MWNTs aqueous solution

Multiwalled carbon nanotubes (MWNTs) were purchased from Chengdu Organic Chemicals Co. Ltd., (Chengdu, China). In a typical oxidation reaction, 250mg of as received MWNTs were added to 70ml of a 3:1 mixture of 98% sulfuric acid and 70% nitric acid aqueous solution in the reaction vessel that was subjected to the sonication. The final obtained oxidized MWNTs (o-MWNTs) were dried completely and dispersed in DI water at the concentration of 0.3mg/ml to afford a stable aqueous solution of o-MWNTs.

B. Characterization of o-MWNTs in the aqueous solution

The o-MWNTs were characterized by X-ray photoelectric spectroscopy (XPS, VG ESCALAB MKII, UK), scan electron microscopy (SEM S-5200, Hitachi), and dynamic laser light scattering analysis. A concentration calibration curve of o-MWNTs aqueous solution was established by the optical absorption at 253nm (UV/VIS/NIR spectroscopy).

C. Cell morphology observation by optical microscopy

The o-MWNTs were dispersed in IMDM at 0.3mg/ml by sonication assistance to afford a stable culture medium with suspension of o-MWNTs (o-MWNTs/IMDM) which was diluted by IMDM according to the required concentration. 3T3 L1 fibroblasts Cells cultivated in control IMDM and in o-MWNTs/IMDM with different concentration were monitored routinely by a phase contrast inverted microscopy (Nikon TE2000-U).

D. Flow cytometry analysis

3T3 L1 fibroblasts of 1×10^5 were cultivated in 6-well cell culture plates (Iwaki) in IMDM at 37°C, 5% CO₂ for 2h to allow the cells to adhere to the plates, then IMDM in each well was replaced with o-MWNTs/IMDM of different concentration with 2.5ml per well respectively. After 2 days of culture, the cells were harvested in clean tubes followed by centrifugation at 1000rpm for 10min, and were resuspended and fixed in 70% cold ethanol at 4°C for at least 24h. The fixed cells were concentrated, washed and resuspended in normal saline (0.9% NaCl). The resulting suspensions were supplemented with 50μl of RNAase (25μg/ml) and propidium iodide (PI, 50μg/ml), and placed in water bath of 37°C for 30min prior to the flow cytometry measurement (Coulter Epics XL). The graphs displayed here represented the intensity of red fluorescence detected in a population of 10, 000 cells, and the data gave the percentage of sub G1 phase of 3T3 fibroblast.

E. MTS assay s

The CellTiter 96 AQ non-radioactive assay (MTS assay, Promega) was applied to evaluate the viability of 3T3 L1 fibroblasts cultivated in o-MWNTs/IMDM.

3T3 L1 fibroblasts of 4×10^3 were cultivated in 100μl diluted o-MWNTs/IMDM of 0.03mg/ml and 0.01mg/ml for 4 days at 37°C in a humidified, 5% CO₂ atmosphere. At each testing time, the culture medium in each well was replaced with 100μl of IMDM and 20μl MTS/PMS solution, the cells were incubated for 90min at 37°C in a humidified, 5% CO₂ atmosphere. All the reacted solutions were transferred into a

new 96-well cell plate and the absorbance of the final solutions was measured at 490nm. Triplicate samples were prepared for each time. The viable cell numbers were calculated by the calibration curve established.

III. RESULTS AND DISCUSSION

A. Characterizations of o-MWNTs dispersing in water

The o-MWNTs dispersible in DI water under ambient conditions with the concentration of 0.3mg/ml and no precipitations were observed after prolonged standing (weeks). Photographs of typical aqueous dispersions of o-MWNTs were shown in Figure 1; each solution was obtained from the original concentrated dispersion subjected to a different centrifugation force, including 5000g, 18000g and 50000g. The visual observation indicated that the concentration of o-MWNTs in water decreased with the centrifugation force increased, some of o-MWNTs were precipitated from the solution.

In order to figure out the major factor determining the precipitation order of o-MWNTs from the solution, we conducted 3 sets of experiments below:

(1) Dropping each supernatant on a silica substrate for SEM. The SEM images showed that the o-MWNTs staying in each supernatant had similar length distribution as well as the typical tube-like shape with diameter around 30nm was kept well, the length of o-MWNTs mostly ranged from 500nm to 800nm (Figure 2), which was much shorter than that of the as received MWNTs.

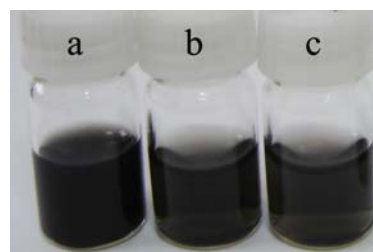


Fig. 1 Optical picture of the supernatants obtained from the original o-MWNTs aqueous solution experienced different centrifugation force, in which a: 2000g, b: 18000g, and c: 50000g.

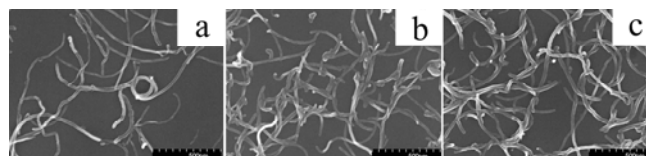


Fig. 2 SEM images of o-MWNTs filtrates obtained from the supernatants obtained from original solutions subjected to the different centrifugal force of a: 2000g, b: 18000g, and c: 50000g respectively

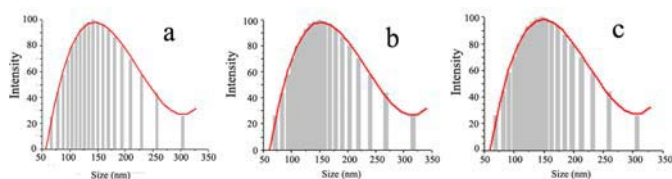


Fig. 3 Size distribution of o-MWNTs aqueous solution analyzed by DLS. The solutions were obtained from original solutions subjected to the different centrifugal force of a: 2000g, b: 50000g

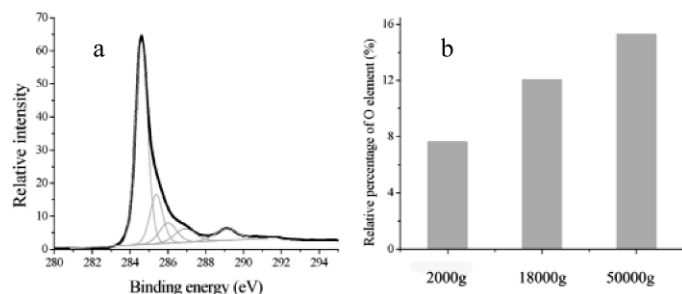


Fig. 4 XPS analysis of o-MWNTs filtered from the supernatants obtained from the original o-MWNTs solution subjected to different centrifugal forces of 2000g, 18000g, and 50000g respectively. a: The resolved spectra of C1s, b: oxygen percentage of o-MWNTs in the supernatants.

(2) The size distribution of o-MWNTs in the each supernatant was quite similar, the effective size was ranged from 70nm to 350nm; the average one was around 140nm (Figure 3). The results obtained from SEM and DLS suggested that the size of o-MWNTs deposited from the three supernatants was in similar pattern.

(3) Figure 4a presented the typical C_{1s} spectrum of o-MWNTs that provided the evidence of introducing oxygen-containing groups to the MWNTs. Figure 4b gave the oxygen percentage of o-MWNTs in each of the above supernatants, showing that o-MWNTs staying in the supernatant obtained from the solution subjected to higher centrifugation force had higher oxygen percentage correspondingly. Combining the above three sets of experiments (SEM observation, DLS measurement, and XPS analysis), it could be inferred that the oxidation degree was the major key factor that determined the amount of o-MWNTs staying in water and their stabilities.

B. Influence of o-MWNTs upon the cell growth

The cellular biological effects of o-MWNTs in IMDM on 3T3 L1 fibroblasts were investigated by optical and electron microscopy observation, flow cytometry analysis, as well as MTS assay respectively. MTS assay displayed a decreased enzymatic conversion in the fibroblast cells with >40% inhibition at the 3rd and 4th day of culture in the medium

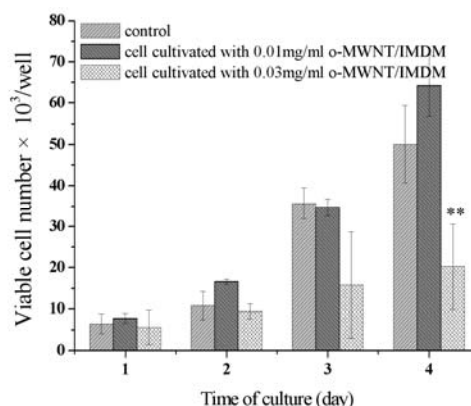


Fig. 5 MTS-conversion (cytotoxic assay) of 3T3 L1 fibroblasts cultivated in the o-MWNTs/IMDM of 0.03mg/ml (n=3, mean values with standard deviation, ** indicated $p < 0.01$.)

containing o-MWNTs at 0.03mg/ml, while no significant inhibition was observed when the cells was cultured in the medium containing o-MWNTs at 0.01mg/ml(Fig. 5).

In this current work, when fibroblast cells were cultivated in o-MWNTs/IMDM of 0.03mg/ml, it could be clearly seen from optical microscope that the cytoplasm of fibroblasts became black after 2 days of culture, leaving a much clearer nucleus region at the center, implying that o-MWNTs had entered into the cytoplasm and color it dark (Figure 6b). It was noted in the experiment that the area of cytoplasm became obvious dark after 2 days of co-incubation with o-MWNTs, which implied that o-MWNTs needed certain time to be taken up by the cells and accumulated in the cells. Additionally, cells seemed become slight swollen and the nucleus become a little bigger compared with the control cells, suggesting that the cells underwent some other changes besides proliferation suppression.

Figure 7 presented the percentage of sub-G₁ phase cells, which closely related to the progression of apoptosis, increased in a manner of o-MWNTs concentration-dependence. It was shown that a dramatic population (71.9%) of fibroblasts appeared at sub-G₁ phase after cultivated in o-MWNTs/IMDM of 0.3mg/ml for 2 days. When diluting the

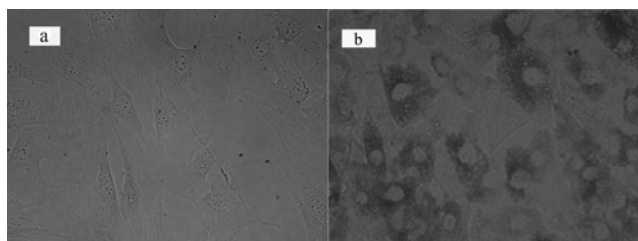


Fig. 6 Optical micrographs of 3T3 L1 fibroblast ($\times 200$) cultivated in the medium of IMDM (a) and o-MWNTs/IMDM (b).

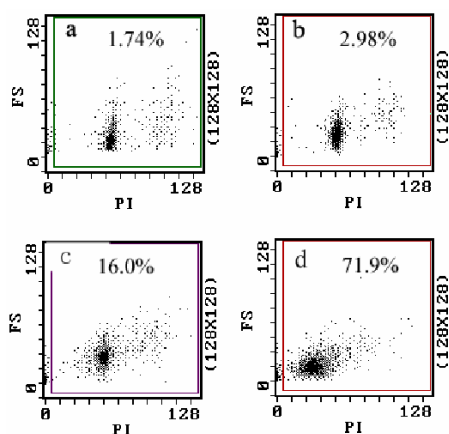


Fig. 7 PI uptake dot-plots displaying prevailing apoptotic cells determined by flow cytometric analysis. The cells were cultivated with the indicated concentration of o-MWNTs/IMDM for 2 days, in which (a) normal IMDM as control; (b) o-MWNTs/IMDM of 0.01mg/ml; (c) o-MWNTs/IMDM of 0.03mg/ml; (d) o-MWNTs/IMDM of 0.3mg/ml.

original o-MWNT/IMDM of 0.3mg/ml with IMDM to 0.03mg/ml and 0.01mg/ml respectively, the percentage of sub-G1 phase cells decreased correspondingly to 16% and 2.98%.

Combining the cellular experiments, it could be noticed that the biological effects of o-MWNTs on the cells exhibited an obvious concentration-dependent manner. Apoptosis might occur when the cells encountered high amounts of o-MWNTs, while proliferation suppression was a dominant phenomenon induced by low dose of o-MWNTs. In current study, it could be seen clearly that major of o-MWNTs entering into the cells were located in the cytoplasm; no appreciable o-MWNTs were located in the area of cell nuclei under optical microscopy observation. As it is known, there are plenty kinds of proteins in cytoplasm, they play very important roles in cells growth behaviors, such as differentiation, proliferation, migration, and apoptosis. Hence, we would suggest that when o-MWNTs accumulated to a certain amount in the cells, they cause the cell proliferation suppression and cell apoptosis through a possible way of interacting with some functional protein molecules in cytoplasm.

IV. CONCLUSION

In this work, we demonstrated that it was the oxidation degree that determine the dispersion concentration and stability of o-MWNTs in aqueous instead of the nanotubes' size. The o-MWNTs dispersing in the culture medium affected the cells proliferation and cell cycle in a concentration-dependent manner; the cells cultivated in the medium

with high concentration of o-MWNTs underwent apoptosis, while the major influence of low concentration of o-MWNTs was the suppression on cell proliferation.

ACKNOWLEDGMENT

The authors acknowledge financial support from Natural Science Foundation of China (grant nos.: 90306004), National Center of Nanoscience and Technology of China, National Key Scientific Projects of China (2006CB933203).

REFERENCES

1. Arnold MS, Guler MO, Hersam MC, Stupp SI. Encapsulation of carbon nanotubes by self-assembling peptide amphiphiles. *Langmuir*. 2005 May 10; 21(10): 4705-9.
2. Zorbas V, Ortiz-Acevedo A, Dalton AB, Yoshida MM, Dieckmann GR, Draper RK, Baughman RH, Jose-Yacamán M, Musselman IH. Preparation and characterization of individual peptide-wrapped single-walled carbon nanotubes. *J Am Chem Soc*. 2004 Jun 16;126(23):7222-7
3. Zheng M, Jagota A, Strano MS, Santos AP, Barone P, Chou SG, Diner BA, Dresselhaus MS, McLean RS, Onoa GB, Samsonidze GG, Semke ED, Usrey M, Walls DJ. Structure-based carbon nanotube sorting by sequence-dependent DNA assembly. *Science*. 2003 Nov 28;302(5650):1545-8
4. Liu Z, Winters M, Holodniy M, Dai H. siRNA delivery into human T cells and primary cells with carbon-nanotube transporters. *Angew Chem Int Ed Engl*. 2007;46(12):2023-7
5. Wang Y, Iqbal Z, Mitra S. Rapidly functionalized, water-dispersed carbon nanotubes at high concentration. *J Am Chem Soc*. 2006 Jan 11;128(1):95-9
6. Liopo AV, Stewart MP, Hudson J, Tour JM, Pappas TC. Biocompatibility of native and functionalized single-walled carbon nanotubes for neuronal interface. *J Nanosci Nanotechnol*. 2006 May;6(5):1365-74
7. Sayes CM, Liang F, Hudson JL, Mendez J, Guo W, Beach JM, Moore VC, Doyle CD, West JL, Billups WE, Ausman KD, Colvin VL. Functionalization density dependence of single-walled carbon nanotubes cytotoxicity in vitro. *Toxicol Lett*. 2006 Feb 20; 161(2):135-42.
8. Dumortier H, Lacotte S, Pastorin G, Marega R, Wu W, Bonifazi D, Briand JP, Prato M, Muller S, Bianco A. Functionalized carbon nanotubes are non-cytotoxic and preserve the functionality of primary immune cells. *Nano Lett*. 2006 Jul; 6(7):1522-8.
9. Shvedova AA, Castranova V, Kisin ER, Schwegler-Berry D, Murray AR, Gandelsman VZ, Maynard A, Baron P. *J Toxicol Environ Health A*. 2003 Oct 24;66(20):1909-26
10. Monteiro-Riviere NA, Nemanich RJ, Inman AO, Wang YY, Riviere JE. Multi-walled carbon nanotube interactions with human epidermal keratinocytes. *Toxicol Lett*. 2005 Mar 15; 155(3):377-84.

Address of the corresponding author:

Author: H. Xu
 Institute: Department of Biomedical Engineering Institute of Basic Medical Sciences, Chinese Academy of Medical Sciences & Peking Union Medical College
 Street: Dong Dan San Tiao 5#, 100005
 City: Beijing
 Country: R.P China
 Email: xuhy@pumc.edu.cn

Hapten-Modified Tumor Vaccines Enhance Lymphocytes' Cytotoxicity Against Human Breast Cancer Cells

W. Wang¹, Y. Hu¹, Z. Sun², J.H. Duan¹, S.C. Chen² and X.-D. Yang^{1,2}

¹ Institute of Basic Medical Sciences/Department of Physiology, Chinese Academy of Medical Sciences and Peking Union Medical College, Beijing, China

² Peking Union Medical College Hospital/Department of Oncology, Chinese Academy of Medical Sciences and Peking Union Medical College, Beijing, China

Abstract — Anti-tumor immunotherapy is an important form of adjuvant cancer treatment, with the potential to improve the prognosis[1-4]. It has been shown that tumor cell vaccines (TCVs) modified with the nano-sized hapten dinitrophenyl (DNP) are efficacious against malignant melanoma, both in animal studies and human trials[5, 6]. However, whether DNP-modified TCVs can also induce effective immune reactions against other types of malignancy has not been well evaluated. In this work, we investigated whether DNP-modified TCVs could enhance lymphocytes' cytotoxicity against two types of human cancer cells *in vitro*, including the breast cancer cell line MCF7 and the lung cancer cell line H23. The results showed that both the unmodified and the DNP-modified TCVs produced significantly higher tumor inhibition rates in MCF7 and H23 cells compared to the cases without TCVs. In the MCF7 study, the DNP-modified TCVs also resulted in a significantly higher tumor inhibition rate than the unmodified TCVs. Moreover, DNP was compared with another TCV modification agent, the New Castle Disease Virus of Ulster Strain (NDV Ulster)[2], and was found to have similar effects as the latter in enhancement of anti-tumor immune reaction. In addition, both the unmodified and the modified TCVs triggered significantly stronger inhibition of the tumor cells than the non-tumor cells, suggesting that the anti-tumor immune effects were relatively tumor-specific. These findings suggest that DNP-modification of TCVs may have prospective application in immunotherapies against multiple types of human cancer in addition to malignant melanoma.

Keywords — Tumor Vaccine, DNP, NDV Ulster, anti-tumor, immunotherapy

I. INTRODUCTION

The significance of immunotherapy as an adjuvant anticancer treatment has been well recognized[1, 3, 4]. While chemotherapy faces the issues of accumulative toxicity and drug resistance, anti-tumor immunotherapy usually has few adverse effects, good patient tolerance, and the potential to significantly improve the prognosis[2]. Some clinical trials of immunotherapy achieved promising results in treating malignancies such as melanoma, malignant glioma, or renal cell carcinoma, which tended to respond poorly to chemo-

therapies[5, 7-9]. Cancer cells often develop immune tolerance and immune escape mechanisms[10, 11]. A key issue of the anti-tumor immunotherapy field, therefore, is to develop new technologies that can further improve the treatment outcome. In order to mount an anti-cancer immune reaction, current immunotherapies employ TCVs made of inactivated cancer cells, dendritic cells (DC) that have been exposed to tumor antigens, or cytokines that modulate the immune function[12-14]. Among the TCV techniques, it has been shown that DNP-modified TCVs are efficacious against malignant melanoma, both in animal studies and human trials[5, 6]. However, whether DNP-modified TCVs could also induce effective immune reactions against other types of malignancy has not been evaluated so far. This is worth of investigation because the DNP modification method may have broader application range than just treating malignant melanoma alone.

In this work, we investigated whether DNP-modified TCVs could enhance lymphocytes' cytotoxicity against two types of human tumor cells *in vitro*, including breast cancer cell line MCF7 and lung cancer cell line H23. We also compared DNP with another agent frequently used in modifying TCV, the Ulster Strain of New Castle Disease virus (NDV Ulster)[2], in their effects for induction of anti-tumor immune responses.

II. MATERIAL AND METHODS

Tumor Cell Vaccine Preparation:

MCF7 or H23 cancer cells were inactivated by co-incubation with mitomycin C for 60 minutes, followed by thorough wash with PBS for 5 times. The cells could then be used as unmodified TCVs. For DNP modification of TCVs, the inactivated tumor cells were exposed to DNP according to the protocol of Berd et al[5], which involves a 30-minute incubation of tumor cells with DNP, followed by washing with saline. For NDV-modification of TCVs, 10⁷ inactivated tumor cells were exposed to NDV Ulster at 100 HU for 30 min, followed by thorough wash with saline.

Tumor Inhibition Assay:

Peripheral blood mononuclear cells (PBMCs) were isolated by Ficoll centrifugation from fresh blood of healthy human donors. PBMCs were then adjusted to 2×10^6 /ml and co-incubated in 96-well with TCVs (unmodified or modified), at a PMBC to TCV cell ratio of 10:1. After 3 days incubation, the PBMCs were collected and washed for subsequent experiments described below.

The tumor inhibition assay was performed in 96-well round-bottom plates. The target cells were added to the wells in culture medium and incubated overnight so that the cells became adherent. Effector cells were either nonactivated PBMCs, or cells that had been preactivated by TCVs as described above. Effector cells were mixed in the wells according to the designed effector to target cell ratios. The total volume per well was 200 μ L. The plate was then incubated in a CO₂ incubator at 37 C. The positive control and the background control each used 6 wells. The experimental wells were performed in 6 duplicates. After 3 days, the supernatants were removed, the plates were washed twice with PBS, then 100 μ L RPMI + 5% FCS and 20 μ L MTS solution (MTS Cell Titer Kit, Promega) were added per well and incubated for 90 minutes at 37 C per manufacture's instruction. The plates were then measured by using an ELISA plate reader with a 490nm filter. The background was taken from 6 wells containing only medium and MTS solution. The percent tumor growth inhibition was calculated according to the following equation:

$$\% \text{ Growth Inhibition Rate} = 1 - \frac{\text{Experimental well-Background}}{\text{Positive control-Background}}$$

III. RESULTS

The human breast cancer cell line MCF7 was first studied because it had been frequently used in immunotherapy research in the past[15]. To evaluate the effects of DNP-modification on TCVs' immune function, the *in vitro* experiments of anti-tumor immune studies were carried out in 3 groups. In the first group, the MCF7 was mixed with lymphocytes only (MCF7+T). In the second group, the MCF7 was mixed with lymphocytes that had been co-incubated with unmodified TCVs (MCF7+T+MCF7TCV). In the third group, the MCF7 cells were mixed with lymphocytes that had been co-incubated with DNP-modified TCVs (MCF7+T+DNP_MCF7TCV). Tumor inhibition rate was measured using standard MTS inhibition assay 3 days later.

The anti-tumor cytotoxicity by the lymphocytes was measured with tumor inhibition rate. While the MCF7+T group showed some baseline cytotoxicity against the tumor cells, the MCF7+T+MCF7TCV and the MCF7+T+DNP_MCF7TCV groups produced higher tumor inhibition rates than the MCF7+T group (Figure1a). Among these three groups, the MCF7+T+DNP_MCF7TCV group generated the highest tumor inhibition rate, suggesting that DNP-modified TCV initiated the strongest anti-MCF7 immune response by the lymphocytes.

A study parallel to the MCF7 study was also carried out with the human lung cancer cell line H23. There were also 3 experiment groups: H23+T, H23+T+H23TCV, and H23+T+DNP_H23TCV. Similar to the MCF7 study results, with the H23 cancer cells, both the H23+T+H23TCV and the H23+T+H23DNP_TCV groups produced higher tumor inhibition rates than the H23+T group (Figure1b). However, when comparing the H23+T+H23TCV and the H23+T+H23DNP_TCV groups, the effect of DNP modification was not as significant as in the MCF7 study.

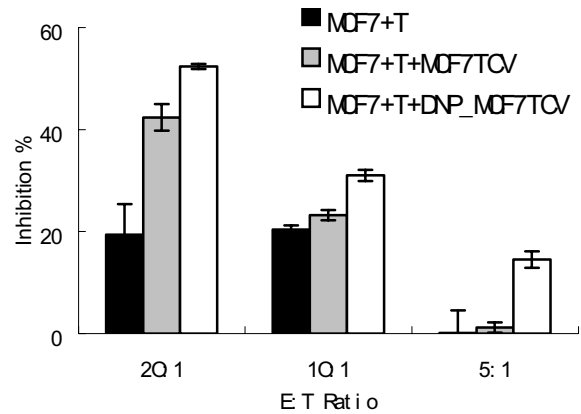


Fig. 1a Tumor inhibition study using the MCF7 as the target cells

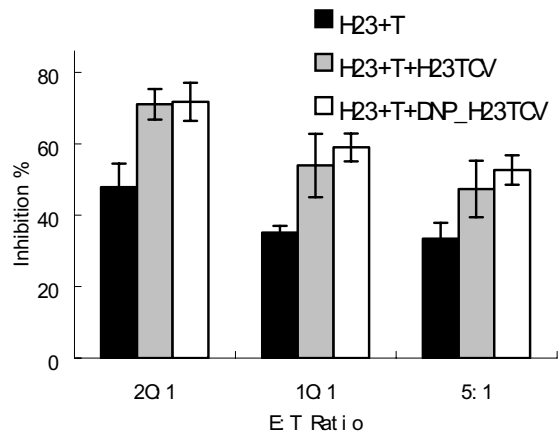


Fig. 1b Tumor inhibition study using H23 as the target cells

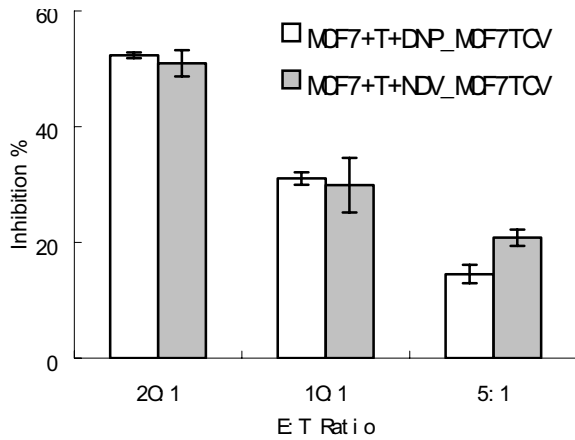


Fig. 2a Comparison of tumor inhibition by DNP- or NDV Ulster-modified TCVs, with MCF7 as the target cells

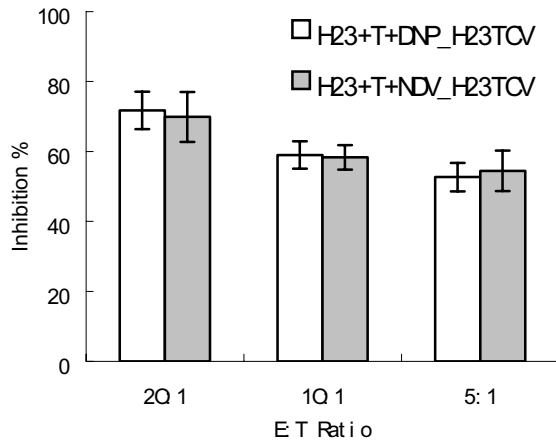


Fig. 2b Comparison of tumor inhibition by DNP- or NDV Ulster-modified TCVs, with H23 as the target cells

In addition to DNP, NDV Ulster was another widely used TCV modification agent, with multiple clinical trials published involving colon cancer, breast cancer, and glioblastoma. It is therefore interesting to compare DNP and NDV Ulster, regarding their effects in inducing anti-cancer immunity. Studies with NDV Ulster as the modification agent of TCV were thus conducted and directly compared with the DNP modification results. As shown in Figure 2a and b, NDV Ulster showed similar profile as the DNP in enhancing the anti-tumor immune reactions. The results suggested that, similar to NDV Ulster, DNP might also be applied to treat multiple types of human cancers.

While DNP-modified TCVs enhanced the anti-tumor immune reaction, it is important to investigate whether this immune reaction was relatively specific against the tumor cells that were targeted by the therapy. During the therapy,

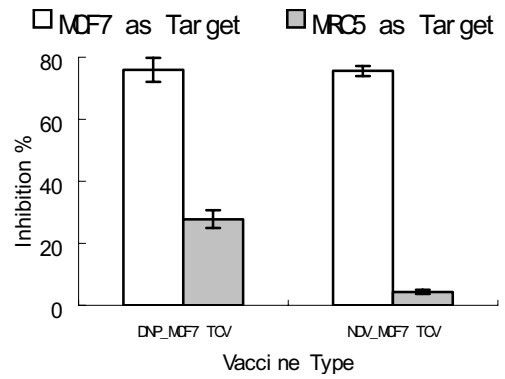


Fig. 3 Inhibition of MCF7 and MRC5 cells by unmodified or modified MCF7 TCVs

the non-tumor cells are preferably not inadequately attacked by the lymphocytes, in order to minimize autoimmune diseases. To address this issue, we designed another study wherein the TCVs and the DNP- or NDV-modified TCVs were still made from MCF7, but the target cells employed either MCF7 or a non-tumor human cell line MRC5. In order to fully expose the immune effect, a relatively high effector:target cell ratio of 40:1 was used in this experiment. As shown in Figure 3, the MCF7 TCVs, whether modified or not, produced significantly less inhibitions on the non-tumor cells MRC5. The results suggested that the immune reaction induced by MCF7TCVs were relatively specific against the tumor cells intended to treat (MCF7 in this case). This feature is favorable for minimizing autoimmune disease during anti-tumor immune therapy.

IV. DISCUSSION

The aim of this study was to investigate whether whether DNP-modified TCVs could enhance lymphocytes' cytotoxicity against several types of human tumor cells *in vitro*, in addition to malignant melanoma. We found that, with the human breast cancer cells MCF7 and lung cancer cells H23, both the unmodified TCVs and the DNP-modified TCVs produced higher tumor inhibition rates in MCF7 and H23 compared to the control. In the MCF7 study, the DNP-modified TCVs also resulted in a significantly higher tumor inhibition rate than the unmodified TCVs. Moreover, DNP was compared to another TCV modification agent NDV Ulster, and was found to have similar effects as the latter in enhancement of anti-tumor immune reaction. In addition, both the TCVs and the DNP- or NDV-modified TCVs produced significantly lower immune responses against the non-tumor cells MRC5, suggesting that the anti-tumor effects were relatively selective against the tumor cells.

Berd et al have found that DNP modification can be an effective way to induce anti-melanoma immune response[5]. However, whether DNP can serve as a general way to overcome immune tolerance and be used in treating other types of human malignancy, have not been well explored. In this study, we applied DNP immunotherapy to two more types of human cancer, the breast cancer MCF7 and the lung cancer H23, in an attempt to widen the method's applicable range. While DNP modified TCV showed significant improvement over the unmodified TCV in the MCF7 study, the advantage of DNP modification was not obvious in the H23 study. Nevertheless, in both MCF7 and H23 studies, DNP modification did not lower the anti-tumor immune reactions. These results suggest that the DNP modification of TCV probably will be beneficial when treating human tumors with immunotherapy. To further investigate whether the DNP modification method could be used to treat more types of human cancers, further research works are necessary.

In order to overcome the immune escape mechanisms of tumor, TCV can be modified either chemically such as with DNP, or biologically such as with NDV Ulster[2, 5]. NDV Ulster has been extensively studied in immunotherapy studies, involving multiple human tumors[2]. While both DNP and NDV are effective modification agents for TCVs, their immune effects have never been directly compared in the past. The results of this study show that both DNP and NDV Ulster can produce effects favorable for inducing stronger anti-tumor immune reactions, suggesting that DNP might possibly be applied to treat multiple cancers, in a similar way as NDV Ulster.

In summary, this study showed that the DNP-modification of TCVs enhanced the anti-tumor immune reaction *in vitro*. The results suggest that DNP-modification may have application in immunotherapy of multiple human cancers in addition to melanoma.

ACKNOWLEDGMENT

This work was supported by China Medical Board, National Key Scientific Projects of China (2006CB933204), and Natural Science Foundation of Beijing (Z0005190043511).

REFERENCES

- Rosenberg, S.A. (2001) Progress in human tumour immunology and immunotherapy. *Nature* 411: 380-384.
- Schirrmacher, V. (2005) Clinical trials of antitumor vaccination with an autologous tumor cell vaccine modified by virus infection: improvement of patient survival based on improved antitumor immune memory. *Cancer Immunol Immunother* 54: 587-598.
- Takayama, T., Sekine, T., Makuuchi, M., Yamasaki, S., Kosuge, T., Yamamoto, J., Shimada, K., Sakamoto, M., Hirohashi, S., Ohashi, Y., Kakizoe, T. (2000) Adoptive immunotherapy to lower postsurgical recurrence rates of hepatocellular carcinoma: a randomised trial. *Lancet* 356: 802-807.
- Vermorken, J.B., Claessen, A.M., van Tinteren, H., Gall, H.E., Ez-inga, R., Meijer, S., Scheper, R.J., Meijer, C.J., Bloemena, E., Ransom, J.H., Hanna, M.G., Jr., Pinedo, H.M. (1999) Active specific immunotherapy for stage II and stage III human colon cancer: a randomised trial. *Lancet* 353: 345-350.
- Berd, D., Sato, T., Maguire, H.C., Jr., Kairys, J., Mastrangelo, M.J. (2004) Immunopharmacologic analysis of an autologous, hapten-modified human melanoma vaccine. *J Clin Oncol* 22: 403-415.
- Sojka, D.K., Felnerova, D., Mokyr, M.B. (2002) Anti-metastatic activity of hapten-modified autologous tumor cell vaccine in an animal tumor model. *Cancer Immunol Immunother* 51: 200-208.
- Rosenberg, S.A., Yang, J.C., Topalian, S.L., Schwartzentruber, D.J., Weber, J.S., Parkinson, D.R., Seipp, C.A., Einhorn, J.H., White, D.E. (1994) Treatment of 283 consecutive patients with metastatic melanoma or renal cell cancer using high-dose bolus interleukin 2. *Jama* 271: 907-913.
- Rosenberg, S.A., Yang, J.C., White, D.E., Steinberg, S.M. (1998) Durability of complete responses in patients with metastatic cancer treated with high-dose interleukin-2: identification of the antigens mediating response. *Ann Surg* 228: 307-319.
- Yu, J.S., Liu, G., Ying, H., Yong, W.H., Black, K.L., Wheeler, C.J. (2004) Vaccination with tumor lysate-pulsed dendritic cells elicits antigen-specific, cytotoxic T-cells in patients with malignant glioma. *Cancer Res* 64: 4973-4979.
- Chatterjee, M., Draghici, S., Tainsky, M.A. (2006) Immunotheranostics: breaking tolerance in immunotherapy using tumor autoantigens identified on protein microarrays. *Curr Opin Drug Discov Devel* 9: 380-385.
- Muller, A.J., Scherle, P.A. (2006) Targeting the mechanisms of tumoral immune tolerance with small-molecule inhibitors. *Nat Rev Cancer* 6: 613-625.
- Banchereau, J., Schuler-Thurner, B., Palucka, A.K., Schuler, G. (2001) Dendritic cells as vectors for therapy. *Cell* 106: 271-274.
- Copier, J., Dalglish, A. (2006) Overview of tumor cell-based vaccines. *Int Rev Immunol* 25: 297-319.
- Yang, J.C., Childs, R. (2006) Immunotherapy for renal cell cancer. *J Clin Oncol* 24: 5576-5583.
- Haas, C., Lulei, M., Fournier, P., Arnold, A., Schirrmacher, V. (2006) A tumor vaccine containing anti-CD3 and anti-CD28 bispecific antibodies triggers strong and durable antitumor activity in human lymphocytes. *Int J Cancer* 118: 658-667.

Address of the corresponding author:

Author: Xian-Da Yang, MD, PhD
 Institute: Institute of Basic Medical Sciences, PUMC
 Street: 5 Dong Dan San Tiao
 City: Beijing
 Country: China
 Email: ayangmd@gmail.com

A New Heuristic Weighting Function for FDK-based reconstruction of Cone Beam Tomography

Han Zheng¹, Zikuan Chen², Yan Kang^{2,3}, Jiren Liu^{1,3}

¹ College of Information Science and Engineering of Northeastern University, Shenyang, China

² Sino-Dutch Biomedical and Information Engineering School of Northeastern University, Shenyang, China

³ Neusoft Group Ltd, Shenyang, China

Abstract—Cone beam computed tomography (CBCT) represents advanced technique of computer tomography. And FDK is a kind of efficient reconstruction algorithm of CBCT, which suffers density drop artifact in cone angle direction. A new weighting function is proposed to correct the density drop artifact of FDK reconstruction algorithm. The function corrects angle mismatch during the reconstruction plane away from the midplane. 3D Shepp-Logan phantom is used to evaluate the new heuristic weighting function. The result shows the new weighting function has obviously inhibitory effect to the density drop artifact, and it also has higher time resolution than other FDK reconstruction algorithm.

Keywords—Cone beam computed tomography (CBCT), FDK, Heuristic Weighting Function, reconstruction, density drop artifact.

I. INTRODUCTION

Cone beam computed tomography (CBCT) represents advanced technique of computer tomography, which is real three-dimensional (3D) imaging characterized by volume data acquisition and fully 3D reconstruction. The volume reconstruction of CBCT can be implemented by the efficient FDK [1] algorithm. As circular trajectory is widely used in real scan for its simply structure. But the circular trajectory is not consummate scan trajectory, not all the data of reconstruction region can be collected by the scan method. Since a cone dataset acquired from a circular scanning trajectory cannot completely fill the 3D radon domain. The data does not satisfy the Tuy-Smith condition [2] since a plane parallel to the trajectory may intersect the object but not the trajectory [3]. As the reconstruction plane away from the midplane, the data loss becomes severe. It manifesting a donut-like entity illustrates by Fig1.

The shadow zone around z-axis in the donut-like entity is a region where data are unavailable from the circular cone-beam projection scanning. The FDK-based reconstruction can be considered as a collection of tilted fan-beam reconstructions. Since FDK reconstruction algorithm fills the shadow zone by using zero padding, the reconstruction is essentially an approximate, which becomes server for

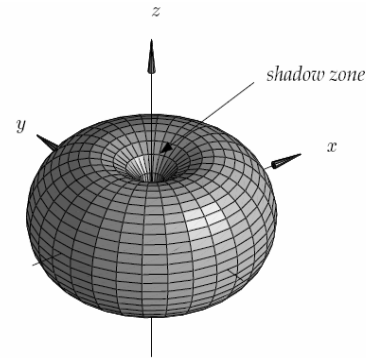


Fig.1 The donut-like entity by circular scan trajectory

regions away from the midplane. It suffers density drop along the rotation axis (the longitudinal z direction), which falls off rapidly with large z values. Lots of researchers make great efforts to diminish the density drop artifact, and some efficient algorithms are proposed such as P-FDK, T-FDK [3]. But all the algorithms need rebinning process and it hard to realization in practical situation.

S. Mori and M. Endo proposed a new weighting function for FDK [4]. The function has higher time resolution without density drop artifact amelioration. And Dong Yang and Ruola Ning ameliorate the parker function of half scan. Since the heuristic weighting function [5] can reduce the angle mismatch effect, the density drop artifact can be allayed in half scan reconstruction.

II. THEORY

A. High time resolution weighting function

The new weighting function S. Mori and M. Endo proposed is an angular smooth function. It uses all the scan data of circular scan, and weight all the data by projection angle. The weighting function is shown as equation (1)

$$w(\gamma, \beta) = \begin{cases} \sin^2\left(\frac{\pi}{4} \frac{\beta}{\pi/2 - \gamma}\right) \dots 0 \leq \beta \leq \pi - 2\gamma \\ \sin^2\left(\frac{\pi}{4} \frac{2\pi - \beta}{\pi/2 + \gamma}\right) \dots \pi - 2\gamma \leq \beta \leq 2\pi \end{cases} \quad (1)$$

As equation (1) shows, the weighting function is a variation of Parker function. It expands the projection angle from $\pi + fanangle$ to 2π . In S. Mori and M. Endo's results, the function has higher time resolution and useful for imaging of moving organs. As Parker function, the equation (1) is not appropriate in the big cone angle reconstruction. It suffers density drop along the rotation axis (the longitudinal z direction), which falls off rapidly with large z values.

B. Angle Inconsistency

Since the X-ray source of cone beam computed tomography (CBCT) is different form original CT, the cone angle can not be neglected. The angle inconsistency cased by cone angle is shown as Fig. 2.

As Fig. 2 shows, S is the X-Ray source on the circular trajectory scan plane. O is the midpoint of the detector, and T is a random point of the midplane. Since S, O and T are all on the midplane, the angle γ is same as the fanangle in the fan beam reconstruction. And the equation (1) is also fit this situation. But in cone beam reconstruction, not all the X-ray is on the midplane. The point O' and T' are two points, which is away form midplane. O' and T' is on a reconstructed plane parallel to the midplane, and $OT = O'T'$, so we can know angle γ is different to angle γ' . But in the S. Mori and M. Endo's function the weight is only accounts for projection angle β and an invariable parameter γ . It means the weight is not changed when projection angle is invariable. And the equation (1) is not precise in cone beam reconstruction.

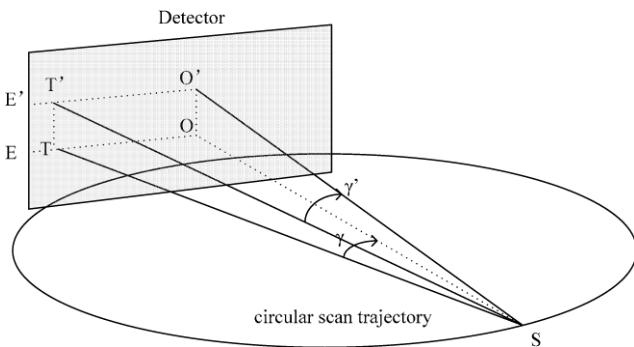


Fig. 2 Angle inconsistency cased by cone angle

C. The new heuristic weighting function

In Sections II-B we discuss the angle inconsistency phenomenon in the cone beam reconstruction. And if we use equation (1) in big cone angle reconstruction, equation (1) can introduce error or unsteadiness to the images for its imprecise character. So we need improve the equation (1) for cone beam reconstruction.

We notice that if we want reduce the cone angle inconsistency phenomenon; we should not only change the form of equation (1) but also introduce new parameters to the new function. Since the new weighting function should reduce the angle inconsistency phenomenon, we introduce two new parameters β' and γ' . β' is the projection angle for different reconstruction planes. γ' is the ray angles for different reconstruction planes. The new weighting function be expressed as

$$w(\gamma', \beta') = \begin{cases} \cos^2\left(\frac{\pi \times (\pi - 2\gamma' - \beta')}{2\pi - 4\gamma'}\right) \dots 0 \leq \beta' \leq \pi - 2\gamma' \\ \cos^2\left(\frac{\pi \times (\pi - 2\gamma' - \beta')}{4\gamma' + 2\pi}\right) \dots \pi - 2\gamma' \leq \beta' \leq 2\pi \end{cases} \quad (2)$$

Equation (2) is similar to equation (1) in form but different in inbeing. Both two parameters are changed during cone angle. The parameters can be calculate by

$$SO' = \sqrt{SO^2 + OO'^2} \quad (3)$$

$$\beta' = \frac{\beta}{\sqrt{1 + \frac{OO'^2}{SO^2}}} \quad (4)$$

$$\gamma' = a \tan\left(\frac{E'O'}{SO'}\right) \quad (5)$$

As Fig. 2 shows, SO' is the distance form reconstructed detector plane to the X-ray source. And γ' is the fanangle of reconstructed plane. β' is projection angle of reconstructed plane. Form equation (3) to (5) we can find the parameters of new weighting function are all heuristic associated with cone angle.

We reform the FDK reconstruction process by four steps. First pre-weighting by cone angle as original FDK

$$\tilde{p}^F(\beta, a, b) = \frac{R}{\sqrt{R^2 + a^2 + b^2}} p^F(\beta, a, b) \quad (6)$$

$p^F(\beta, a, b)$ represents the RAW data acquainted by detector. a and b represents detector excursion. R is the rotation radius. Second weighting by equation (2)

$$\tilde{p}^W(\beta, a, b) = w(\gamma', \beta') \tilde{p}^F(\beta, a, b) \quad (7)$$

The next step is filter by R_L kernel.

$$\tilde{p}^R(\beta, a, b) = \tilde{p}^W(\beta, a, b) * g^P(a) \quad (8)$$

$g^P(a)$ represents the R_L kernel. After convolution backprojection step is performed as original FDK-based reconstruction. It can be denoted by

$$f(x, y, z) = \int_0^{2\pi} \frac{R^2}{U(x, y, \beta)^2} \tilde{p}^R(\beta, a(x, y, \beta), b(x, y, z, \beta)) d\beta \quad (9)$$

Where $f(x, y, z)$ is the point to be reconstructed, and U is the distance between voxels and X-ray source.

We notice that, the new heuristic weighting function for FDK-based reconstruction doesn't need to change the process of the FDK reconstruction. It only introduced a weighting function into the original FDK reconstruction method.

III. SIMULATION RESULTS AND DISCUSSION

For comparison purposes, we performed simulation studies on full-scan FDK reconstruction algorithm, half-scan FDK reconstruction algorithm, and the new heuristic weighting function. We use a 1/2 weighting to cancel the projection redundancy associated with the full circular scanning. 3D Shepp-Logan phantom is used to evaluate the reconstruction algorithm. The scan parameters are shown in Table 1.

Table 1 Cone-beam imaging parameters used in simulation

Reconstruction parameters	Value
Rotation Radius (mm)	570
Distance source to detector (mm)	1040
Channels	672
Rows	256
Interval of Channels (mm)	1.513918
Interval of Rows (mm)	3.0
Projection number	180
Reconstruction size	512*512*512
Field of View (mm)	400

A. Noiseless data simulation

In this simulation we use computer simulation phantom data without noise. We preformed FDK full scan with weight 1/2, FDK half scan with Parker weighting function and the new heuristic weighting function FDK reconstruction algorithms. For comparing the restraint of density drop artifact, we only compare the sagittal slices images ($y=318$). The result is shown as Fig. 3.

Compared to the phantom images and other images, the FDK reconstruction using new heuristic weighting function has better images quality in big cone angle. And the density drop artifact is much infirm than other reconstruction algorithms. Profiles of scan lines in reconstruction images are presented for evaluating the attenuation coefficient drop in quantitative method. Profiles of Fig. 3 ($x=256$) is shown in Fig. 4.

Fig. 4 shows that four different reconstruction algorithms have the same reconstruction quality under small cone angle. When cone angle became larger the other three reconstruction algorithms suffer heavily density drop artifact, but the reconstruction algorithm using the new heuristic weighting function still have better reconstruction quality.



Fig. 3 Sagittal slices in 3D images, reconstructed images using the FDK algorithm(first row middle),the weighting function FDK(first row right) reconstructed images using the FDK half scan (second row left), the weighting function proposed in this paper (right). (Window Width=15,Window Level=88)

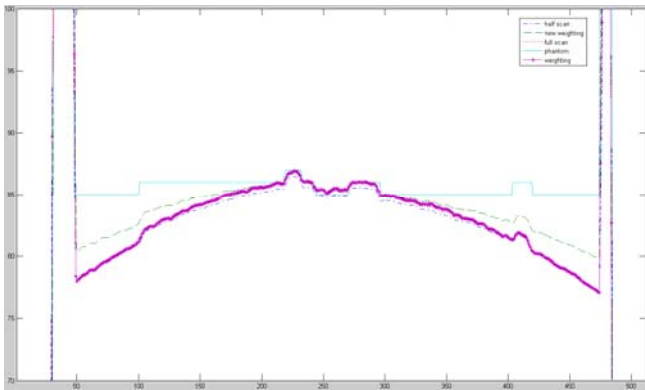


Fig. 4 Profile of FDK, half scan, weighting function and new heuristic weighting function reconstruction algorithms at x=256.

B. Noise data simulation

For validating the noisy sensitivity, we introduce 10% noise to the RAW data. We performed FDK full scan with weight 1/2, FDK half scan with Parker weighting function

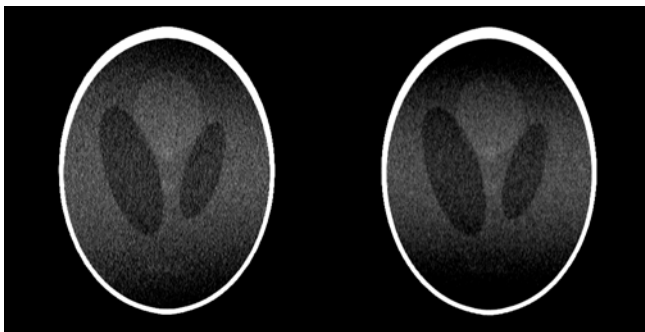


Fig. 5 Sagittal slices in 3D images using noise RAW data, reconstructed images using the new heuristic weighting function (left) the FDK algorithm (right). (Window Width=15, Window Level=88)

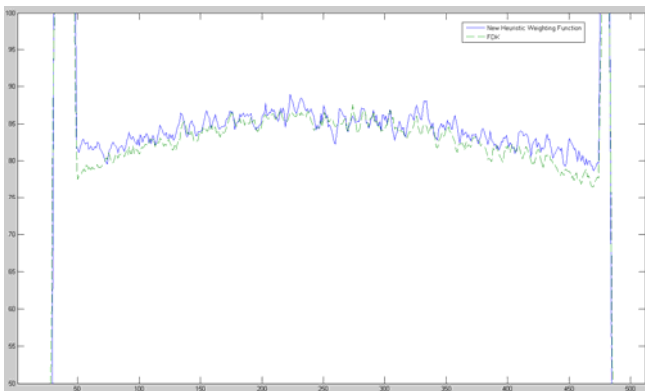


Fig. 6 Profile of FDK and new heuristic weighting function reconstruction algorithms with noise(x=256).

and the new heuristic weighting function FDK reconstruction algorithms. The result is shown as Fig. 5.

As Fig. 4 shows, the reconstruction using the weighting function has the same noisy sensitivity to other reconstruction algorithms. But it has better image quality in large cone angle. For comparison, the profiles of Fig. 5(x=256) is shown in Fig. 6

From Fig. 5 and Fig. 6, we can know, the inaccuracy of scanning plane geometry is reduced by weighting process. And the new heuristic weighting function has corrected the density drop artifact to a certain degree along the rotation axis in both noiseless and noisy condition.

IV. CONCLUSION

To our knowledge, the heuristic weighting function we proposed is a new method to correct the density drop artifact in FDK full scan reconstruction. Although there are other methods that can correct the density drop artifacts in FDK, such as P-FDK, T-FDK and FDK-SLANT, all of these methods need interpolations among different projection data. These algorithms require that all the projection data should be acquired before reconstruction, which is not preferred in practice. The heuristic weighting function proposed in this paper can overcome this shortcoming by introducing a weighting function into the original FDK reconstruction method. This method can correct the density drop artifact along the rotation axis. It has important value in CBCT clinical applications.

REFERENCES

1. L. A. Feldkamp, L. C. Davis, and J. W. Kress. (1984) Practical cone-beam reconstruction. *Journal of the Optical Society of America A*, A 1: 612–619.
2. Tuy, H. (1983). An inversion formula for cone-beam reconstruction. *SIAM Journal of Applied Mathematics* 43, 546–552.
3. H. Turbell. (2001) Cone-beam reconstruction using filtered back projection, Linköping Studies in Science and Technology, Thesis no 672.
4. S. Mori, M. Endo, T. Tsunoo, K. Murase, H. Fujiwara. (2004) Evaluation of Weighted FDK Algorithms Applied to Four-dimensional CT (4D-CT). *IEEE Nuclear Science Symposium Conference Record*, 5, 3243- 3245.
5. Dong Yang, Ruola Ning. (2006) FDK Half-Scan with a Heuristic Weighting Scheme on a Flat Panel Detector-Based Cone Beam CT (FDKHSCW). *International Journal of Biomedical Imaging*, 1-8

Author: Han Zheng
 Institute: College of Information Science and Engineering of
 Northeastern University
 Street: Wen Hua street
 City: Shenyang
 Country: China
 Email: zhenghan@neusoft.com

Elementary Design and Implementation of Liver Treatment Planning System

Hong-jian Gao¹, Shui-cai Wu¹, Yan-ping Bai¹ and Chun-lan Yang¹

¹College of Life Science & Bioengineering, Beijing University of Technology, Beijing, China

Abstract — [Objective] To implement a computer aided system for liver hyperthermia treatment planning. [Methods] VC++ 6.0 and MITK(Medical Imaging ToolKit) were chosen as the development platform for a good efficiency in both runtime and development phases. Based on these, the system framework was designed. By Amira and ANSYS, the system could be initially implemented. [Results] The designed system can be applied for liver hyperthermia treatment planning, and was expected to guide the process of clinical operation by further improvement. [Conclusion] The system can offer scientific and reliable evidences for hyperthermia treatment planning, and it can make hyperthermia treatment parameters quantificational and treatment process settled. All of these can reduce the dependent degree to clinical experience for doctors.

Keywords — Liver, Image processing, 3-D visualization, ITK, Hyperthermia

I. INTRODUCTION

The liver tumor has become one of the most dangerous diseases of humans, and about 250,000 persons die of that every year according to statistics evidence. The traditional treatment methods for liver cancers include surgical, radiotherapy and chemotherapy, but the curative effect is not very good. At present, hyperthermia treatment has become one of useful means to treat liver tumors, and it kills tumor cells by heating them by application of microwaves. At present, microwave coagulation therapy has been applied to clinical operations^[1-2]. The task of Hyperthermia treatment is to optimize parameters and styles to heat just the tumor region and as few of the surrounding healthy tissue as possible[3]. At present doctors can learn the position and size of the tumors by 2-D slices(CT,MRI) during the process of the treatment, so the subjective experience plays critical roles[4]. But the introduction of the computer-aided treatment planning system increases the reliability and exactness of the treatment, which is very important to improve treatment quality and lessen treatment trauma. The improvement of computer, medical imaging and engineering techniques makes computer-aided treatment practical.

Fig. 1 describes the framework of liver treatment planning system. Before the treatment, 2-D slices(CT,or MRI) must be obtained. Firstly, and the slices should be pre-processed(segmentation, registration, filtering, etc) by computer. At last, 3-D visualization of liver and tumors should

be accomplished. On the other hand, the temperature field database of different hyperthermia parameters should be built. Then the model of temperature field will be matched with 3-D visualization model, so hyperthermia parameters can be obtained. Thus the most suitable hyperthermia treatment planning scheme could be established. During the operation, the scheme is applied to undergo surgery. After the treatment, CT or MRI scanning should be accomplished any more to get the slices, and then slices should be loaded into the computer and be compared with the raw slices. Thus the treatment evaluation results can be obtained, which is useful for further improvement. In the whole system, image-processing, building the temperature field database, and getting the best suitable treatment planning scheme are the key parts.

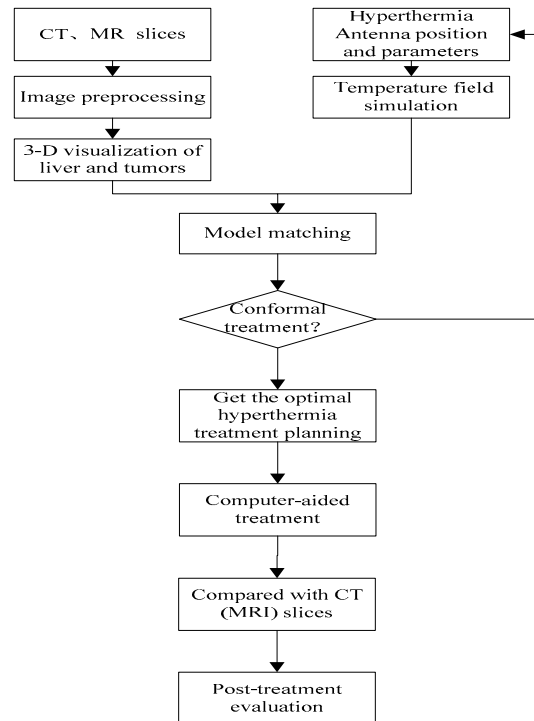


Fig. 1 The framework of computer-aided hepatic treatment planning system

II. ANALYSIS OF THE FUNCTION REQUIREMENT

The aim of the system of treatment planning and forecasting with computer for the microwave coagulation therapy of liver cancer is to help doctors get the most suitable hyperthermia parameters and set down the treatment planning. Based on these requirements, the system should implement the following functions:

Data input and output: The system may load all kinds of medical images, including BMP, JPEG, RAW, IM0, TIFF and DICOM, which is the general medical slice format in hospitals. Besides, the system can save and export segmentation data, mesh data, 3-D model data, and measure results.

Image pre-processing: The system should supply with image pre-processing function(data cropping, filtering, etc) to make doctors easy to analyze and observe.

Image segmentation: The system should offer a comprehensive segmentation toolbox, which can implement manual segmentation and automatic segmentation.

3-D visualization: 3-D results of liver and tumors can be obtained by surface rendering and volume rendering methods. Also 3-D mesh simplification function should be implemented to reduce data quantity and make the data convenient to be shown and saved.

Image measuring: The system should offer measuring tools to get 3-D physical parameters (short axis length, long axis length, etc) of liver and tumors.

Microwave coagulation treatment planning: The system should obtain the best suitable hyperthermia parameters, and offer scientific and reliable evidences for doctors.

Also, the system should be operated interactively and easy to be used for doctors. On the other hand, the system should be easy to extend and improve.

III. DESIGN OF THE SYSTEM

A. System framework

Due to large data quantity, VC++ was chosen as system develop platform. To make good use of the present algorithms and reduce the workload, the system was developed by MITK(Medical Imaging ToolKit) framework. MITK, based on VTK and ITK, is an integrated medical image processing and analyzing toolkit. Its main purpose is to provide a consistent framework to combine the function of medical image segmentation, registration and visualization. MITK use the data flow model to design the computational framework.

B. Function structure of the system

Analysis of work flow: The flow of liver hyperthermia treatment planning is as following: Firstly, CT or MRI slices were obtained to form 3-D volume data and then 3-D segmentation of ROI(region of interest) were accomplished. Secondly, 3-D visualization results could be obtained for measuring and analysis. At last, 3-D model and temperature field model matching would be accomplished to get the optimal hyperthermia parameters.

Module partition of the system: As is shown in Fig. 2, the system consists of three modules.

3-D visualization module: The main function of the module is to get 3-D visualization results by 2-D slices and export model data. The module is made up of two parts: one part is to use MITK framework under VC++ 6.0 platform, and the part implements image segmentation, image registration, image filtering, 3-D visualization, mesh simplification, and image measuring, etc. The other part is commercial 3-D visualization software Amira 3.1, which can be used to conduct initial experiments and compare the results.

Finite element simulation module: The main function of the module is to simulate the distributing of temperature field. By adjusting hyperthermia parameters, all kinds of temperature field models can be obtained, and then the database of temperature field can be built for model matching. The module is composed of two parts: one part is to simulate the temperature field under VC++ platform, and the other part is commercial finite element software ANSYS for contrast and validation. 3-D individuation finite element models(FEM) play critical roles in the liver hyperthermia treatment planning system.

Treatment planning and forecasting module: The main function of the module is to set down liver hyperthermia treatment planning scheme for clinical operation. The module consists of model matching system and the optimal treatment scheme forming system. The first system is used to match 3-D visualization model and FEM and make con-



Fig. 2 System main interface of module partition

formal estimation. The second system is to obtain hyperthermia parameters (time, power, time-sharing rate, etc) and the optimal treatment planning scheme. At last, the scheme can be export in the form of written “*.txt”format.

IV. CONCLUSIONS

The paper introduced the design framework of the system of treatment planning and forecasting with computer for the microwave coagulation therapy of liver cancer .Based on 3D visualization models of liver and cancers and FEM, doctors can set the suitable location of the microwave antenna, calefaction power and time for hyperthermia and choose optimal treatment scheme by the system. Therefore, the research is expected to be applied for hospitals and to lessen the treatment trauma to the patients in the future.

ACKNOWLEDGMENT

This work was supported by Beijing Nature Science Foundation (No: 3072004) and foundation of BJUT startup for doctors (52015998200702).

REFERENCES

1. J. B. Van De Kamer, et al. Thermal ablative therapy for malignant liver tumors. *Journal of Gastroenterology and Hepatology*. 2003, 18(6): 616-623
2. Liang Ping, Dong Baowei, and Yu Xiaoling. Experimental and Clinical Study on Thermal Distribution of US-guided Microwave Coagulated Therapy for Liver Cancer. *Chinese Journal of Ultrasound In Medicine*. 2002, 18(3):161-164
3. GAO Hong-jian, WU Shui-cai, REN Xin-ying, LI Ying. 3-D Reconstruction of liver slice images based on MITK Framework, The 1st International Conference on Bioinformatics and Biomedical Engineering (ICBBE2007). 2007.7:952~955
4. Wang ZG, Tang ZS. VR based computer assisted stereotatic neurosurgery system. *Chinese Journal of Computers*. 2000, 23(9):932~937

Deformation-Based Morphometric study on Blind men's brain structures

Chunlan Yang, Shuicai Wu, Yanping Bai, Hongjian Gao

College of life science & Bioengineering, Beijing University of Technology, Beijing, China

Abstract — Many studies have shown the functional relevance of cross-modal plasticity in blind men. However, few researches have focused on whether such functional plasticity is associated with macroscopic changes of structural anatomy in brain regions. Fortunately, deformation based morphometry (DBM) provides an important tool for the computational anatomy research. In this study we detected the changes of regional volume in brain structures between the blind men and normal controls with DBM method. Information of the difference is derived from the deformation field acquired during HAMMER non-rigid registration. The experimental results show that the regions expanded in the blind men's brain are located at Brodmann 19,31 while the contracted regions located at Brodmann 17,18. This research is very helpful to discover the relationship between structural anatomy and functional data of blind men at a macroscopic level from neuroimaging perspective.

Keywords — deformation based morphometry, blind men, non-rigid registration

I. INTRODUCTION

In recent years, many studies have demonstrated the plasticity of cross-modal in functional reorganization induced by vision deprivation [1]. For example, the primary visual cortex and the visual association areas of the congenital blind are activated by various tactile tasks [2, 3]. In addition, somatosensory representation of the fingers is topographically disordered in certain blind population [4]. However, few researches have focused on whether such functional plasticity is associated with macroscopic changes of structural anatomy in brain regions. This study just proceeded from this objective.

Fortunately, with the development of imaging technique, magnetic resonance imaging (MRI) is popular used in the anatomical studies of the brain. Accordingly, more and more approaches focusing on the shape and neuroanatomical structure emerged. Neuroimaging is such an emerging research field which dedicates to find the relationship between neuroanatomical structure and human diseases. The approaches are commonly used in comparing healthy and diseased subjects to detect the difference between them. The methods can be generally classified into those which are based on region of interest (ROI) and those based on voxels in the whole brain. The ROI method needs much more hu-

man effort and enough accurate prior knowledge to define the regions which may appear distinct difference. On the contrary, those voxel-based methods such as voxel-based morphometry (VBM) and deformation based morphometry (DBM) can detect any local difference on the whole brain. So the latter methods are more unbiased and objective.

Since voxel based morphometry [5-7] throws away the global scale differences into the spatial normalization, deformation based morphometry may be a good tool to analyze the shape difference between the subjects [8-10]. In this study, Jacobian determinant at each point is derived from the deformation field which maps each corresponding point from the template to the subject. Thus, local volume changes such as expansion or contraction will be detected by calculating the value of Jacobian determinant. This study used DBM method in order to detect the difference of brain structures between blind men and the normal controls.

II. MATERIALS AND METHODS

A. Subjects and Image acquisition

In this study, we have analyzed 11 blind men and 9 sighted control subjects. They are all Chinese and right-handed. The average age of the two groups are generally matched (the blind people are 18 to 50 years old and normal subjects are 20 to 45 years old). What's more, most of the blind people lost their sights since their infancy under 3 years old. They are all Braille readers. All the analyzed data are achieved by 1.5 T (Tesla) Philips MRI scanner with a T1-weighted RF-FAST sequence. Imaging parameters are as follows: TR 11ms, TE 4ms, flip angle 90°, matrix size 256×256, FOV 240mm×240mm, 125 slices, slice thickness 1.2mm.

B. Image processing and analysis

The images were analyzed using deformation-based morphometry. Different with voxel-based morphometry, deformation-based morphometry needs a relative high dimensional image registration. Since HAMMER aims to improve the anatomical correspondence decreasing the ambiguity in many intensity based registration often occurred [11], we take this registration method and applied the statistical

analysis on the deformation fields generated during the registration. The detailed operations are as following.

First, all the acquired images were transformed in Analyze format and radiology convention.

Second, we removed non-brain tissue from the MRI using Brain Surface Extractor method [12], which uses a combination of anisotropic diffusion filtering, Marr-Hidreth edge detection, and mathematical morphology. We did this work using BrainSuite software. Manual intervene was also applied to the non-brain part which can't be removed automatically. In addition, since the cerebellum may be important for our study, we also remain the cerebellum and just remove the brainstem.

Third, the brain tissues were classified into gray matter (GM), white matter (WM) and cerebrospinal fluid (CSF). Before the classification, we also did the intensity correction. After the bias field correction (BFC), the iterated conditional modes (ICM) algorithm was used to optimize the labeling of the brain based on a maximum a posterior model. The model encourages local similarity of voxels through the use of a Gibbs prior. So the result of the labeled regions is also smooth.

Forth, following the instructions of HAMMER framework, the ventricle CSF should be specially labeled. The accuracy of labeling is very crucial for the registration. However, for the images of the subjects whose ventricles are relative small, especially the narrow part, the ventricle CSF can't be labeled completely. In this case, we labeled the ventricle manually.

After the preprocessing, we then do the registration under HAMMER software (<https://www.rad.upenn.edu/sbia/rsoftware.html>). One of an important step is to choose an appropriate template which all the subject images will be registered to. According to the author of [11], since HAMMER registration is based on the features, the template should be an individual brain while not the average normalized images referred in some studies. The edges on the average template are often smooth and HAMMER needs clear edge type for the tissues. On the other hand, the template should be roughly located in the center of statistical distribution of all samples. We invited an experienced neurosurgeon to select a brain with a median size of ventricle and regular shape from the normal subjects as a template. Certainly, the normal control subjects used in the study referred in the above has excluded the template.

After affine transformation, the subject image was warped to the template using a multi-resolution strategy. Deformation field from each voxel of the template to the subject was also generated. The deformation field includes a lot of information such as the global position, orientation and size, also the shape. In principle, the Jacobian matrices of the deformations should be more reliable for indicating

local brain shape than just the absolute deformations. Absolute deformations represent positions of brain structures, rather than local shape. However, the shape variations are more important for us to study the differences between the two groups. Jacobian matrix not only contains information about the local stretching, but also shearing and rotation. Assuming that deformation filed has been achieved for each point (x,y,z) in the template to the point (U,V,W) in the subject, where

$$\begin{cases} U = x + dx \\ V = y + dy \\ W = z + dz \end{cases} \quad (1)$$

then the Jacobian matrix at the point (x,y,z) can be defined as follows,

$$J = \begin{bmatrix} \partial U / \partial x & \partial U / \partial y & \partial U / \partial z \\ \partial V / \partial x & \partial V / \partial y & \partial V / \partial z \\ \partial W / \partial x & \partial W / \partial y & \partial W / \partial z \end{bmatrix} \quad (2)$$

The determinant of the Jacobian matrix $\|J\|$ represents the relative volume. Assuming that the infinitesimal area A around the point (x,y,z) in the template is mapped to an area B around the point (U,V,W) in the subject. $\|J\|=B/A$ will quantify the local expansion or contraction resulting from this mapping [9].

C. Statistical analysis

In this study, we use $\|J\|$ as the information for the voxel wise statistical analysis. Since $\|J\|$ for each voxel in all the subjects stands for the local expansion or contraction relative to the template, group difference can be detected by voxel wise t-test. Before we perform the statistical analysis, the images of $\|J\|$ were smoothed with a Gaussian filter of full-width half-maximum equal to 12mm. Compared with the two groups, we can achieve a t-map, thus a t-score for each voxel in the template can be calculated. The t score which is positive means the expansion for blind men compared to NC and negative value means the contraction.

For each voxel V_i in the t-map,

$$t_i = \frac{\overline{J_i^{FES}} - \overline{J_i^{NC}}}{\sigma_i \cdot \sqrt{\frac{1}{N_{FES}} + \frac{1}{N_{NC}}}} \quad (3)$$

$$\sigma_i = \sqrt{\frac{(N_{FES} - 1)\sigma_{FES}^2 + (N_{NC} - 1)\sigma_{NC}^2}{N_{FES} + N_{NC} - 2}} \quad (4)$$

where $\overline{J_i^{FES}}$ is the mean of Jacobian determinant for Vi during the registration for all the blind men warped to the template, and $\overline{J_i^{NC}}$ is the mean of Jacobian determinant for Vi during the registration for all the NC warped to the template, N_{FES} and N_{NC} are the number of blind men and NC respectively. σ_{FES} and σ_{NC} are the standard deviations of J_i^{FES} and J_i^{NC} respectively.

III. RESULTS

Only the clusters that exceeded a threshold of $P < 0.001$ after correction by Monte Carlo simulation are reported. Compared with the normal controls, the regions expanded in the blind men's brain located at Brodmann 19,31 where are left occipital lobe, cuneus, superior occipital gyrus, limbic lobe, cingulate gyrus. While the contracted regions located at Brodmann 17,18 where are left occipital lobe and lingual gyrus.

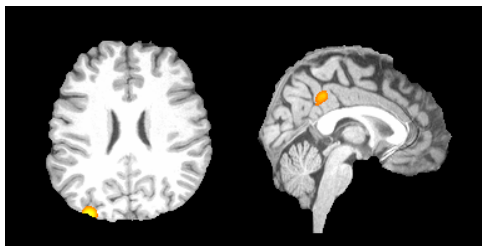


Fig. 1 Expanded brain regions in blind men



Fig. 2 Contracted brain regions in blind men

IV. CONCLUSIONS AND DISCUSSIONS

From the experimental results, we can see that DBM method can detect the local volume changes in the whole brain effectively.

We conclude that early visual deprivation can lead to changes in the structural anatomy which is consistent with the cortical cross-modal reorganization found by functional

imaging. Long term living in an environment without visual input can not only induce large changes in visual cortex but also other areas. This may help to discover the relationship between structural anatomy and functional data at a macroscopic level from neuroimaging perspective. More works focusing on blind men are significant and welcome in the future.

ACKNOWLEDGMENT

The authors thank Professor Tianzi Jiang of Institute of Automation, Chinese Academy Sciences for his support and instruction. This work was supported by the foundation of BJUT startup for doctors (52015998200702) and partially supported by the Natural Science Foundation of China, Grant No. 30425004.

REFERENCES

1. N Sadato, A Pascual-Leone, J Grafman, et al. Neural networks for Braille reading by the blind. *Brain*, 1998, 121:1213-1229.
2. C Buchel, C Price, R S J Frackowiak, et al. Different activation patterns in the visual cortex of late and congenitally blind subjects. *Brain*, 1998, 121: 409-419.
3. L G Cohen, P Celnik, A Pascual-Leone, et al. Functional relevance of cross-modal plasticity in blind humans. *Nature*, 1997, 389: 180-183.
4. A Sterr, M Müller, T Elbert, et al. Changed perceptions in Braille readers. *Nature*, 1998, 391: 134-135.
5. J.Ashburner, Computational neuroanatomy, PhD Thesis, University of London, England, 2001.
6. J.Ashburner and K.J.Friston, Voxel-based morphometry----the methods, *Neuroimage*, 11(6),805-21,2000.
7. J.Ashburner and K.J.Friston, Why voxel-based morphometry should be used, *Neuroimage*, 14:1238-43, 2001.
8. C.Gaser, H.P.Volz, S.Kiebel, S.Riehemann, and H.Sauer, Detecting structural changes in whole brain based on nonlinear deformations---Application to schizophrenia research, *NeuroImage*, 10: 107-113, 1999.
9. C.Davatzikos, M.Vaillant, S.Resnick, J. L.Prince, S.I.Letovsky, and R.N.Bryan, A computerized method for morphological analysis of the corpus callosum, *J.Compt.Assisted Tomogr*, 20: 88-97,1996.
10. M.K.Chung, K.J.Worsley, T.Paus, C.Charif, D.L.Collins, J.N.Giedd et al., A unified statistical approach to deformation-based morphometry, *NeuroImage*, 14 (3): 595-606, 2001.
11. D.Shen and C.Davatzikos, HAMMER: hierarchical attribute matching mechanism for elastic registration, *IEEE Trans. Med. Imaging*, 21:1421-1439, 2002.
12. D.W.Shattuck and R.M.Leahy, Graph Based Analysis and Correction of Cortical Volume Topology, *IEEE Transactions on Medical Imaging*, 20(11):1167-1177, 2001.

Author: Chunlan Yang
 Institute: Beijing University of Technology
 Street: No.100 Pingleyuan
 City: Beijing
 Country: China
 Email: clyang@bjut.edu.cn

Automated detection of exudates on color fundus image using region merging by k -NN graph

Wei Lin¹, Hongzhi Liu², Mantao Xu³ and Jiwu Zhang³

¹ Department of Biomedical Engineering, Shanghai JiaoTong University, Shanghai, China

² Department of Computer Science and Engineering, Fudan University, Shanghai, China

³ Global R&D Center, Carestream Company, No.27, New Jinqiao Road, Shanghai, China.

Abstract — Diabetic retinopathy is a serious disease diabetic eye disease as a leading cause of blindness. In this paper, we propose an automated algorithm of detecting exudates in diabetic retinopathy image. The algorithm merges regions using k nearest neighbor graph, and identifies exudates according to color information and pixel locations. The algorithm is quite fast but achieves an average specificity of 95.42% with the average sensitivity of 91.08% in detection of the exudates in a test case with 8 diabetic retinopathy images. This method can be implemented as a prototype for automatic exudates detection in a clinical environment.

Keywords — Diabetic retinopathy, retinal images, region merging, k nearest neighbor graph, exudates.

I. INTRODUCTION

Diabetes is a very serious disease that disables the body's ability to use insulin. It leads to many severe organ damages, for example, diabetic retinopathy (DR). DR is one of the leading causes of blindness and vision defects in adults. The progression of DR can be inhibited if the disease is diagnosed and appropriate treatments are taken as early as possible. Diabetic retinopathy is often asymptomatic in the early stage, and therefore many diabetic patients do not have their eyes examined until the loss of visions. However, the diseases are becoming very serious in this stage, of which the retinal damages are too late for treatments. Therefore, it is of great importance for diabetic patients to have regular ophthalmologic examinations as early as possible. This will help the early identification of DR, which is able to reduce the occurrence of blindness significantly. Conventionally, identification of diabetic retinopathy is mainly done by ophthalmologists' manual examinations. However, it is very time consuming as well as needs more effort and expertise from ophthalmologists. The high prevalence of diabetes makes it impractical for every diabetic patient to have regular eye examination due to the lackness of trained experts to identify the styles and degrees of DR on fundus photographs. Thus, it is of valuable merit to develop a reliable automatically computerized method to detect and as-

sess the lesions on fundus images, which can assist the ophthalmologic professionals to improve diabetes diagnosis.

This work focuses on the automated detection of exudates on fundus photographs. Exudates on fundus photographs usually appear as yellow-white patches with different shapes. They can be divided into two kinds according to their marginality: hard exudates and soft exudates, with clear and unclear borders respectively. Exudates are primary signs of nonproliferative Diabetic Retinopathy (NPDR), which is a presentation of initial stage of DR. Therefore the automatic detection of exudates will contribute to screening for sight threatening diabetic retinopathy.

A considerable interest has arisen in automatic identification of hard exudates in fundus photographs based on gray level [1-2], contrast [3-6] or color [7-8]. Remarkably, Sánchez et al [9] observed that the colors of optic disk and hard exudates are in very similar appearance in fundus photograph. To make their algorithm more robust to variation of brightness, contrast and colors, they apply the color information of optic disk to detect hard exudates as well as an edge detector to localize their sharp edges.

The results obtained by most of the previous approaches often miss interest regions close to the edges of hard exudates. More importantly, the shapes and sharpness of hard exudates are very important signs in classifications of DR. In this paper, we investigate an automated exudates detection algorithm, by which the segmentation of exudates is significantly improved. The retinal image is first segmented by a fast agglomerative clustering method using a k -Nearest Neighbor graph. And then the exudates regions are identified by removing the false positive regions included optical disk (OD). The main merit of this contribution hinges on its algorithmic robustness and efficiency, by which many exudates can be detected quickly even if they are in variation of appearance.

II. METHODOLOGY

The method attempts to detect exudates by clustering. Therefore, exudates detection is carried out in the following stages:

- Pre-processing: enhancing and detection of optic disk;
- Segmentation of retinal images by a fast agglomerative clustering method using a k -Nearest Neighbor graph;
- Identification of yellowish regions by the statistics of color information;
- Removement of the false positive regions included optic disks by the information of colors and locations of OD centers;
- Post-processing of positive regions.

A. Enhancing

The original images are enhanced at the first so that the contrast of exudates gets higher. The method applied for enhancing is from the reference[9]. First, transform the original RGB image into NTSC color space. Then perform an operation of the channels (N_1, N_2, N_3) of the NTSC color space:

$$N'_1 = 1.5N_1 - N_2 - N_3 \quad (1)$$

And then convert the image obtained (N'_1, N_2, N_3) into the RGB color space again to get a new image. In that way, both contrasting attributes of lesions and the overall color saturation in the image are improved. The OD and the exudates appear with very similar color, and are independent of their locations.

B. Detection of OD

For detection of OD, we have to identify the retinal vessels first. Blood vessels are extracted by the method of combination of Gaussian filter matching and iterative threshold tracking.

The extracted result of blood vessels is used as the input of a so-called fuzzy convergence algorithm[10] to detect the optical disk center by determining the origination of the blood vessels network.

C. Segmentation of retinal images

In our method, regions are merged together to form a segmentation of the image according to their "homogeneity". The process can start with pixels or little regions. Merging have to be repeated for several times until reaching some stopping condition. The process mentioned above is quite time-consuming. For making the process faster, we start with little regions, and introduce the k nearest neighbor graph for searching regions that should be merged.

To obtain little regions used at the beginning of merging process, we use a simple algorithm in our paper. First we do a sorting on pixels by their intensity. Then build a stack and predefine a threshold, namely color deviation σ . The algorithm starts with the smallest pixel, and set it as the seed of a new region. Then search the region's 8-neighbors, if the difference between the region and the neighbor's intensity is smaller than σ , label this neighbor pixel included in the current region, push it into the stack, and update the mean intensity of the current region. After all the region's neighbors have been compared, pop a new pixel from the stack and repeat this process. If the stack is empty, search the next smallest pixel which is not assigned to any existing regions and create a new region. After all the pixels are assigned to certain regions, the algorithm is terminated. Because the each pixel is searched once, so the complexity of the algorithm is $O(N)$. And we can control the result by modifying σ .

Before creating the k -NN graph, an edge image E is drawn using the method proposed in [9]. Kirsch's mask (3) are rotated in different directions and applied to the brightness image respectively. The highest respond is recorded to obtain a raw edge. The raw edge image is thresholded to obtain the final edge image E .

$$\begin{pmatrix} 5 & 5 & 5 \\ -3 & 0 & -3 \\ -3 & -3 & -3 \end{pmatrix} \quad (2)$$

The edge response $Edge(i, j)$ between pixels p_i and p_j is defined on the edge image E as below:

$$Edge(i, j) = \max_{k \in line(i, j)} (E_k) \quad (3)$$

where $line(i, j)$ is the line connecting p_i and p_j (3) actually selects the maximum value on $line(i, j)$ in E as edge response.

To merge regions according to their natural property, we propose a new homogeneity definition between regions. Take a brightness image for example. For pixel p_i and p_j in image I , we define their similarity as:

$$\omega_{ij} = \begin{cases} e^{-\frac{\|I_i - I_j\|^2}{\sigma_1^2} - \frac{Edge^2(i, j)}{\sigma_2^2}} & \|X_i - X_j\| \leq r \\ 0 & \|X_i - X_j\| \geq r \end{cases} \quad (4)$$

where X_i and I_i denote the coordinate and intensity of p_i respectively, $Edge(i, j)$ is obtained from the formula (3), which denotes the probability of an edge existing in the region among p_i and p_j . σ_1 and σ_2 are parameters to modify the effect of intensity and edge information in ω_{ij} . A radius parameter r is also set. If two pixels are too far away, or their distance is more than r , ω_{ij} is directly set to be 0. Here we only use intensity and edge information, and control the effective neighbors' range of p_i by modifying the spatial distance. If we want to use other information, we only need to define a function in the form like Edge information and make ω_{ij} multiply with the defined item.

Let $d_i = \sum_j \omega_{ij}$ be the total similarity from p_i to all other pixels. The similarity between region A and B is defined as:

$$W(A, B) = \frac{\sum_{i \in A, j \in B} \omega_{ij}}{\sqrt{\left(\sum_{i \in A} d_i\right) \left(\sum_{i \in B} d_i\right)}} \quad (5)$$

The region similarity is defined as the sum of the pixel similarity between every pair of pixels from region A and B respectively. To avoid the preference of merging big regions, we divide the sum of similarity by the normalized item, square root of the product of $\sum_{i \in A} d_i$ and $\sum_{i \in B} d_i$.

$\sum_{i \in A} d_i$ and $\sum_{i \in B} d_i$ can be regarded as the volume of region A and B . Different from other definition, in our definition disjoint regions may have high similarity value. This can improve the detail parts in segmentation result, especially the small disjoint part of the segmentation. According to the above formulation, the most similar pair of regions is the ones which have the highest value of (5).

We choose the k -nearest neighbor graph as the data structure of partitions. k -NN graph is a weighted directed graph $G=(V, E, W)$. V is the set of nodes representing regions and E is the set of edges representing pointers from a region to its neighbor regions. Every node has exactly k edges to its k nearest regions. All the regions' similarities are computed and assigned to the corresponding edges as weights. The search for the most similar pair of regions is repeated for several times per iteration and every search requires $O(k)$ region similarity computation. And the traditional data structure is a undirected graph, which needs $O(N)$ region similarity computation every search. Therefore, we reduce

the time complexity from $O(N)$ to $O(k)$ by using the k -NN graph. In the detection of retinal exudates, k is set to be 8, which gets a relatively good result. At the beginning of the merging process, each node in the graph represents a little region.

We use the double linked algorithm of k -NN graph to perform the merging process. For each node R_a , we build two lists: a k -NN list containing the pointers to its k nearest neighbors and another list containing the back pointers which point to the regions taking R_a as one of their k nearest neighbors.

In each merging iteration, the algorithm first finds the most similar pair of nodes. This process takes constant time while the merging and updating process is more time consuming. After that, the node R_a and R_b are merged to one node named R_{ab} . Recomputing the the k -nearest neighbors of R_{ab} may bring high time complexity, So we direct select k nearest regions from the $2k$ neighbors of nodes R_a and R_b . Actually the number of neighbors for the cluster R_{ab} may be smaller than k . At last the node R_a is replaced by R_{ab} and the node R_b is deleted. Then we compute both the edges from R_{ab} and the edges pointed to R_{ab} . At the same time, insertion sort is applied and no more than k nearest neighbors are kept. With the back pointer link, this procedure requires $O(\tau + \tau/k \cdot \log_2(\|\Delta_k(R)\|))$ [11], here τ is the number of updates required in each iteration. The sorted original k NN graph is stored in a heap, so we also need to update the heap at the end of each iteration.

There are several ways to set a stop condition, such as predefining a number of regions, and setting a threshold of similarity. In this paper, we set a threshold of similarity. If all of the region similarity(5) are smaller than this threshold, the merging process is terminated automatically.

D. Identification of exudates

We use the location of OD which is obtained in the step B to extract the potential regions of exudates. We compute average color value of pixels around the OD center, and

extract the regions of which colors are similar with this value. The extracted regions usually contain the OD region, so we have to utilize the location of OD center again to eliminate OD. The diameter of OD is quite stable. For example, in the 605*700 image, the OD region is about 100*160. Therefore, we eliminate all of the regions in the window of 100*160 centered at OD center.

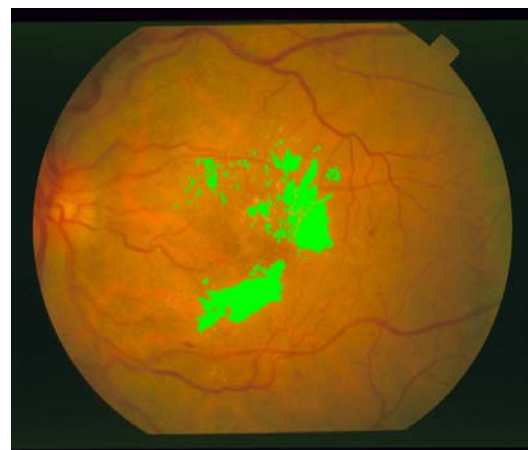
At last, we perform a morphological operation to fill up the gaps in the exudates regions. Fig. 1 shows the result.



(a)



(b)



(c)

Fig. 1 (a) original retinal image with exudates, (b) image after enhancement, (c) detection of exudates of (a).

III. RESULTS

We have evaluated the algorithm on STARE database of eighty-one 605x700 digital fundus images and eight of them have exudates. And the results obtained by the algorithm have been compared with the results marked by an ophthalmologist on these images.

The algorithm has detected all of 8 images with exudates. Every image needs approximate 2 minutes to completing the entire algorithm. For evaluation of the detection performance of the system, the numbers of true and false positive pixels have to be determined for each image with exudates. The sensitivity and speciality can be estimated in a comparison to the ground truths of those exudates which is marked by an ophthalmologist. Table 1 list the sensitivity and speciality of all the images.

Though the quality of the images is not very good, the proposed algorithm attained a good performance. The average sensitivity is 91.08% and the highest sensitivity obtained of the images reaches 100%. Because we mainly focus on the edges, shapes and details of exudates, we obtain high speciality by adjusting parameters. The average speciality is 95.42%, and the highest speciality is 99.70%. We think it is a good result. Generally, sensitivity rises with the reducing of speciality. If we need higher sensitivity, we can reduce the speciality by adjusting the parameters properly.

Table 1 Sensitivity and speciality of images with exudates

Image No.	Sensitivity	Speciality
001	98.29%	90.64%
002	91.57%	98.80%
003	78.72%	99.70%
009	98.89%	93.29%
017	83.13%	99.58%
049	89.26%	98.39%
050	88.75%	95.82%
139	100%	87.14%

IV. CONCLUSION

In this paper, we propose an automated algorithm of detecting exudates in diabetic retinopathy image. The algorithm merges regions using k nearest neighbor graph, and identifies exudates according to color information and pixel locations. The algorithm is quite fast but achieves an average specificity of 95.42% with the average sensitivity of 91.08% in detection of the exudates in a test case with 8 diabetic retinopathy images. Our results suggest that this

method can be implemented as a prototype for automatic exudates detection in a clinical environment.

Future work will look for some database containing more images with exudates, and address the issue of improving the sensitivity by improving the results of other tasks, as texture recognition, and trying to find small and faint exudates

V. REFERENCES

1. N. P. Ward, S. Tomlinson, and C. J. Taylor. (1989) Image analysis of fundus photographs - The detection and measurement of exudates associated with diabetic retinopathy. *Ophthalmol* 96:80-89.
2. R. Philips, J. Forrester, and P. Sharp. (1993) Automated detection and quantification of retinal exudates. *Graefe's Arch. Clin. Ophthalmol*, 231:90-94.
3. K. Akita and H. Kuga. (1982) A computer method of understanding ocular fundus images. *Pattern Recogn.* 21:431-443.
4. T. Walter, J.-C. Klein, P. Massin et al (2002) A contribution of image processing to the diagnosis of diabetic retinopathy - Detection of exudates in color fundus images of the human retina. *IEEE. Trans. Med. Imag.* 21:1236-1243.
5. H. Li and O. Chutatape. (2000) Fundus image features extraction. *Proc. 22nd Annual Int. Conf. of the IEEE Engin. Med. Biol. Soc.*, Chicago, USA, 2003, pp. 3071-3073.
6. H. Li and O. Chutatape. (2003) A model-base approach for automated feature extraction in fundus images. *Proc. 9th. Int. Conf. of the IEEE Comp. Vision, ICCV, Nice, France, 2003*, pp. 50-53.
7. K. G. Goh, W. Hsu, M. L. Lee et al. (2000) ADRIS: an automatic diabetic retinal image screening system. *Medical Data Mining and Knowledge Discovery*. Ed. K. J. Cios, NJ: Springer-Verlag., pp. 181-210.
8. H. Wang, W. Hsu, K. G. Goh et al. (2000) An effective approach to detect lesions in color retinal images. *IEEE Conference on Computer Vision and Pattern Recognition, 2000*, vol. 2, pp. 181- 186.
9. C. I. Sánchez, R. Hornero, M. I. López et al. (2004) Retinal image analysis to detect and quantify lesions associated with diabetic retinopathy. *Proceedings of the 26th Annual International Conference of the IEEE EMBS, San Francisco, USA, 2004*, pp. 1624-1627.
10. A. Hoover, M. Goldbaum. (2003) Locating the optic nerve in a retinal image using the fuzzy convergence of the blood vessels. *IEEE Trans. On Med. Imag.* 22:951-958.
11. P. Franti, O. Virmajoki and V. Hautamaki. (2006) Fast agglomerative clustering using a k-Nearest Neighbor graph. *IEEE Trans. Pattern Anal. Machine Intell.* 28:1875-1881.

An Investigation of Interpolation Methods in Rebinning Circular Cone-beam data into Parallel-fan-beam Data

Feng Han¹, Nianming Zuo², Jiwu Zhang^{1,2}, Xiaochuan Pan³

¹Department of Biomedical Engineering, Shanghai Jiao Tong University, No.800, Dongchuan Road, Shanghai, China

²Global R&D Center, Carestream Company, No.27, New Jinqiao Road, Shanghai, China

³Department of Radiology and the College, The University of Chicago, 5841 S. Maryland Avenue, Chicago, IL 60637

Abstract— The Tent-FDK algorithm is one of common approaches to reconstruct images from parallel-fan-beam data, which is obtained by rebinning the cone-beam data acquired with a circular trajectory. Such data rebinning is for saving computational cost as well as the improved quality of image presentation. The rebinning step is in common achieved by using interpolation methods. Different interpolation methods lead to different numerical presentations and noisy textures in the reconstructed images. This presentation systematically evaluates three interpolation methods in rebinning cone-beam data into parallel-fan-beam data in the framework of the Tent-FDK algorithm in Cone-beam CT.

Keywords— Tent-FDK algorithm, Rebin Projection Data, Interpolation, MTF

I. INTRODUCTION

The original FDK algorithm^[1], which is based on a circular trajectory and reconstructs images efficiently and satisfactorily in the small cone angle case, has been extensively employed in medical and industrial imaging applications. However, it suffers the attenuation coefficient drop in the rotation axis direction in the large cone angle case. The Tent-FDK algorithm^[2], proposed by M.Grass in 2000, is a modified FDK approach for image reconstruction. The cone-beam data acquired with a circular trajectory should be rebinned into parallel-fan-beam data in the framework of the Tent-FDK algorithm, which is computationally more efficient than FDK's original approach and yields an improved image quality.

Such data rebinning is usually achieved by using interpolation methods. And the performance of rebinning data may highly depend upon the chosen interpolation methods. For instances, different interpolation methods lead to different numerical presentations and noisy textures in the reconstructed images. Therefore, it is important to evaluate the impact of different interpolation methods on cone-beam image reconstruction. In this work, we investigated the performance of three interpolation methods in rebinning circular cone-beam data to parallel-fan-beam data in the framework of the Tent-FDK algorithm.

II. INTERPOLATION METHODS

We acquired the cone-beam projection data with a circular trajectory shown in Figure 1. The cone-beam projection data $P(\beta, m, n)$ are rebinned to the parallel-fan-beam projection data $Pv(\theta, t, s)$ shown in Figure 2. Where β is the projection angle defined in the scanning plane, γ is the fan-angle and κ is the cone angle, m, n denote the axes of the virtual detector1. And θ is the projection angle of the rebinned data, t, s denote the axes of the virtual detector2. As showed in Figure 3, the relationships^[3] are as follows:

$$\beta = \theta - \arcsin \frac{t}{R} \quad (1)$$

$$m = tR / \sqrt{R^2 - t^2} \quad (2)$$

$$n = sR^2 / (R^2 - t^2) \quad (3)$$

Where R is the distance from source to the origin.

$$Pv(\theta, t, s) = P(\theta - \arcsin \frac{t}{R}, tR / \sqrt{R^2 - t^2}, sR^2 / (R^2 - t^2)) \quad (4)$$

Since the parameters are discrete, interpolation methods are in common adopted in this rebinning step.

The first interpolation method (referred to as the M1 method) rebinned data on the target parallel-fan-beam ray between the two adjacent parallelized existing rays. These two rays were chosen according to their corresponding two adjacent cone-beam projections. A linear combination scheme was used to fill in CT values for the empty ray between the adjacent parallelized existing rays. This is shown in Figure 4.

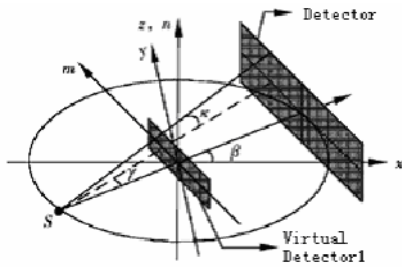


Fig. 1 The geometry of cone-beam scanning^[3]

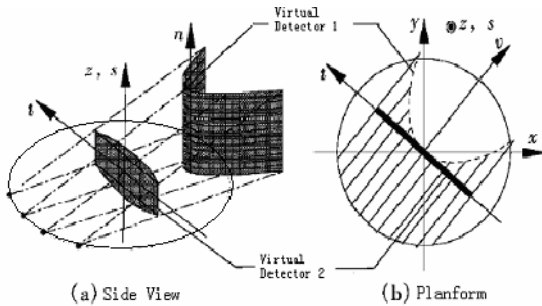


Fig. 2 The geometry after rebinning data^[3]

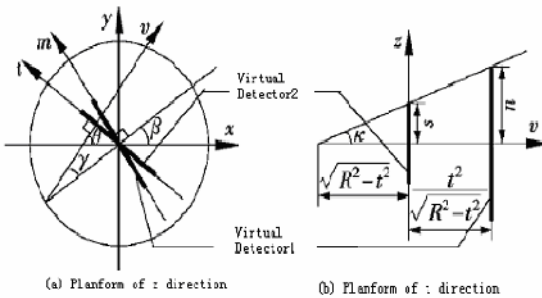


Fig. 3 Relationship between two coordinates^[3]

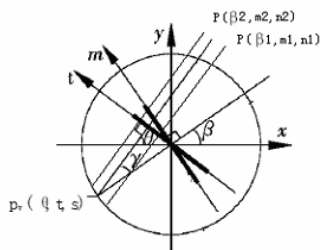


Fig. 4 Planform of z direction in M1

The second method (referred to as the M2 method) selected a target projection ray under a virtual cone beam. For filling CT values for the pre-selected ray, two additional existing rays were needed to be determined from two

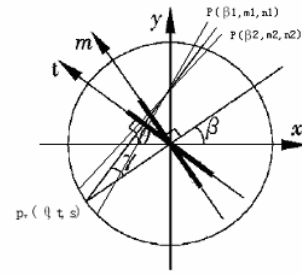


Fig. 5 Planform of z direction in M2

adjacent views but they should belong to the same detector coordinate system. A linear combination scheme was then used to interpolate data from the two rays to the pre-selected ray. This is shown in Figure 5.

The third method (referred to as the M3 method) first extracted the intersection point of a target ray and the virtual detector plane across the rotation center. The normal direction of the virtual detector can be viewed as a virtual cone-beam view containing this pre-selected ray. To interpolate the pre-selected ray, the two existing rays, of which each was through the intersection point, should be selected from the two adjacent cone-beams respectively. The data in the pre-selected ray was filled according to the same interpolation scheme as in M1 and M2. This is shown in Figure 6.

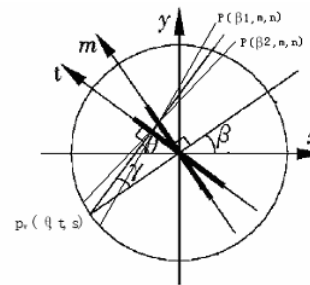


Fig. 6 Planform of z direction in M3

III. RESULT

We generated circular cone-beam projection data from 3D Shepp-Logan phantom. For each circular trajectory $n=900$ projection views were simulated using the distances $S = 570$ mm (source to origin) and $D = 1005$ mm (source to detector) for the system geometry. Line integrals for 256 by 256 detector elements were calculated. A cone-angle of 30 degree and a fan-angle of 30 degree were chosen for the focus-centered detector. The mathematical phantoms were completely in the cone-beam of x-rays. The projection data

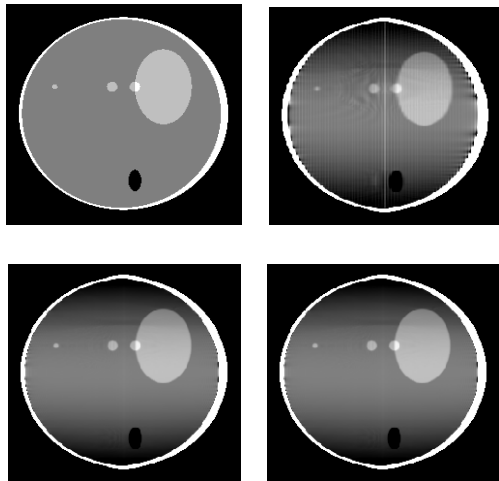


Fig. 7 Reconstructed image at $X=0\text{mm}$ ($n=900$, gray scale[1.0,1.04]). In the first line, the left one is phantom and M1 is used in the right one. In the second line, M2 is used in the left one and M3 is used in the right one

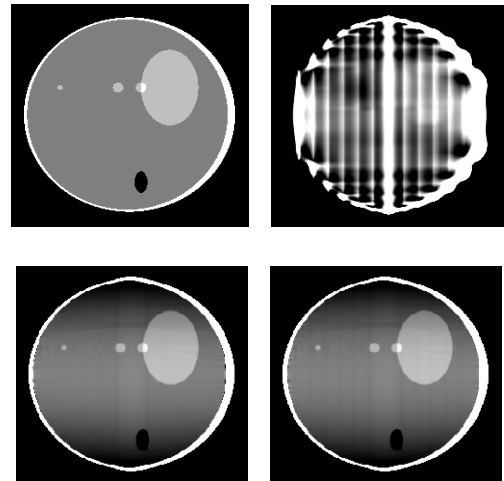


Fig. 9 Reconstructed image at $X=0\text{mm}$ ($n=180$, gray scale[1.0,1.04]). In the first line, the left one is phantom and M1 is used in the right one. In the second line, M2 is used in the left one and M3 is used in the right one

were obtained by analytical forward projection using mathematical phantoms.

The above interpolation methods were applied to rebin the cone-beam data into parallel-fan-beam respectively. Here we presented the reconstruction results from the rebinned projection data by the Tent-FDK algorithm. We also evaluated the performance of the underlying interpolation methods by adopting different number of projection views in exposure.

According to our experiments, it turns out that the M1 method may incur severe artifacts when the number of projection views decrease. However, according to our visual observation and assessments, the M2 method and the M3 method outperform the M1 method get the similar results and also incur a few artifacts if the number of projection views is small. And under the same number of projection

views, M2 and M3 got the much better result than M1.

Modulation transfer function (MTF) analysis:

The relative reconstruction MTF was calculated as the magnitude of Fourier Transform of the impulse response MTF associated with specific reconstruction algorithm and acquisition parameters.

A single point was used as a delta function and was reconstructed with 360 projection views by implementing the Tent-FDK algorithm with the three interpolation methods respectively.

A one-dimensional Fourier Transform through the row of pixels with the impulse response on the reconstruction plane ($X=0\text{mm}$ and $Z=0\text{mm}$) was performed to compute the relative reconstruction MTF. It showed that M2 and M3 led to the same result and better than M1.

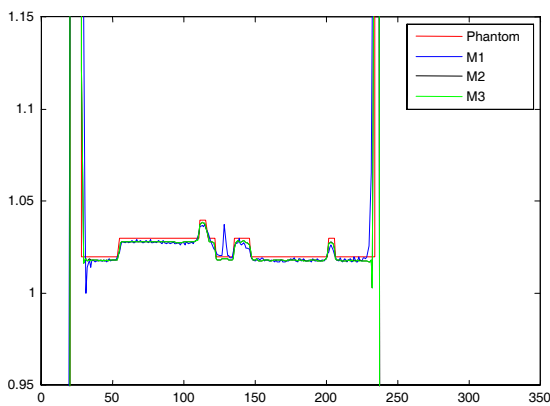


Fig. 8 Respective line profile comparison of $X=0\text{mm}$ and $Z=-25\text{mm}$

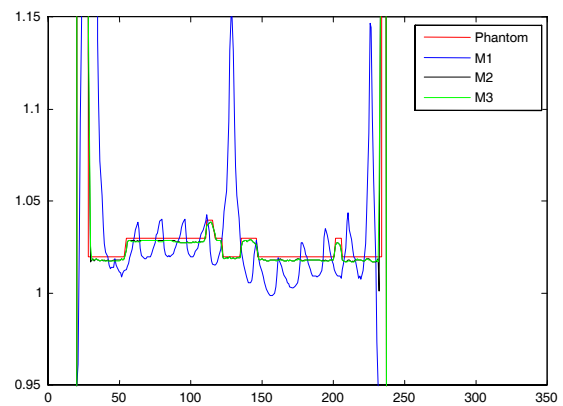


Fig. 10 Respective line profile comparison of $X=0\text{mm}$ and $Z=-25\text{mm}$

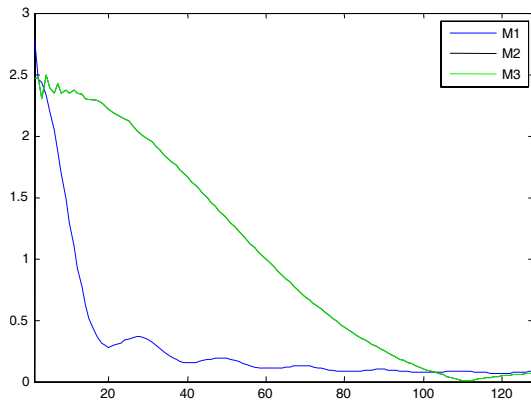


Fig. 11 Respective MTF result comparison

IV. CONCLUSION

Three interpolation methods have been reviewed in rebinning the circular cone-beam data to the parallel-fan-beam data in the framework of the Tent-FDK algorithm. Even if the rebinning data is interpolated according to very different geometric presentation, the three methods utilize the same linear combination scheme. However, the experimental results demonstrate that they achieved

significantly different rebinning performance. Thus, the interpolation method in rebinning data must be carefully chosen for the Tent-FDK algorithm. The contribution of this presentation can be viewed as a pilot study on evaluating the interpolation methods in Cone-beam CT reconstruction.

REFERENCE

1. Feldkamp L A, Davis L C, Kress J W. (1984) Practical cone-beam algorithm. [J]. *J.Opt.Soc.Am.A*/Vol.1: 612-619
2. M Grass, Th Kohler and R Proksa. (2000) 3D cone-beam CT reconstruction for circular trajectories. *Phys. Med. Biol.* 45: 329-347
3. 王蔚林, 姜晓彤, 罗立民, 舒华忠. (2004) 利用投影数据重排进行锥形束体积重建的改进算法. *东南大学学报 (自然科学版)* 第34卷 第3期

Author: Feng Han
 Institute: Shanghai Jiao Tong University
 Street: 800# Dongchuan Road, Minhang District
 City: Shanghai
 Country: China
 Email: feng.han@carestreamhealth.com

A Novel Fast Marching Segmentation Algorithm for Pulmonary Nodules in Chest Radiographs

Qiyong Guo¹, Mantao Xu² and Jiwu Zhang²

¹ Department of Computer Science and Engineering, Fudan University, Shanghai, China.

² Global R&D Center, Carestream Health Company, Shanghai, China.

Abstract — Segmenting nodule region in chest radiographs is a particularly challenging problem due to the complexity and variability of human anatomy. In this work, in order to solve the boundary leakage problem in conventional fast marching method, we present a novel fast marching segmentation algorithm for pulmonary nodule in chest radiographs. The proposed algorithm begins by training a nodule model via support vector machine classification algorithm as a prior knowledge. Then it calculates the decision value on each pixel in chest image to constrain front marching in fast marching evaluation process. The performance of our method is evaluated on 50 nodule images set and compared with conventional fast marching method and Watershed method respectively. The preliminary results show that our proposed algorithm is superior to the above two methods distinctly and can raise the robustness and precision of nodule segmentation due to the benefit of nodule prior knowledge.

Keywords — Fast Marching, Support Vector Machine(SVM), Nodule Segmentation.

I. INTRODUCTION

Chest radiography serves as a common diagnostic tool for detection of early stage lung cancers, which often appear as solitary pulmonary nodules. However, detection of solitary pulmonary nodules in chest radiography image is very challenging due to the appearance of superimposed anatomical structures in Chest X-ray image [1]. This clinical importance of chest radiographs and their associated difficulties in diagnostic interpretation are the main motivation for development of computer aided detection (CAD) algorithms to assist radiologist in reading chest images.

Computer aided detection of solitary pulmonary nodules is faced with many difficulties due to the existence of complicated anatomical structures in chest radiographs. Automatic classification of the regions of interest (ROI) as nodules needs to extract a class of powerful region-based features. The performance of region-based feature extraction hinges on a successful nodule segmentation algorithm of suspicious regions [2].

Several nodule segmentation technologies have been proposed to solve this tractable problem, e.g. region growing [3], mean shift clustering [4], watershed [5], and fast

marching method [6]. Such technologies will fail to process one chest radiograph with lower contrast structure and unclear boundaries. To make those problems tractable, this paper presents a novel nodule segmentation algorithm by incorporating the support vector machine classification (SVM) into fast marching segmentation method.

Our method falls in knowledge-based segmentation category [7], the common goal of which is to integrate available a prior knowledge with sophisticated image segmentation techniques. We introduce a nodule model learned by support SVM algorithm as prior knowledge to constrain front marching. Our method mainly includes three steps: construction of a SVM training set, training of SVM classifier, and fast marching algorithm by using SVM classifier. The experimental results demonstrate that our proposed method outperforms watershed algorithm and conventional fast marching algorithm.

The rest of this paper is organized as follows: the related work is shown in Section 2. In Section 3, our algorithm framework is described in detail. Section 4 presents some experimental results. Finally, Section 5 ends with a brief discussion.

II. RELATED WORK

A. Fast marching method

In 1996, Sethian [8] proposed a fast marching method (FM method) for monotonically advancing fronts, which is a numerical scheme for computing solutions to the non-linear Eikonal equation and related Hamilton-Jacobi equations. FM method is a consistent, accurate and highly efficient algorithm based on fully utilizing entropy-satisfying upwind schemes and fast sorting techniques. The computational complexity of FM algorithm is $O(n \log n)$, where n is the total number of points in the domain. The detail of FM method can be found in [9, 10].

This technique has a wide range of applications, classifying problems in fluid mechanics, combustion, and manufacturing of computer chips, computer animation, image processing, structure of snowflakes, and the shape of soap bubbles.

B. SVM classification

A non-linear SVM classification is first introduced in 1992 [11] and widely used for data classification due to its good performance in this research area. A SVM is a hyper-plane that separates a set of positive examples from a set of negative examples with maximum margin. We can obtain an optimal classifier by maximizing this margin.

Given train data set $X = \{x_i, i = 1, 2, \dots, n\}$ with labels set $Y = \{y_i, i = 1, 2, \dots, n\}$, where $y_i \in \{-1, 1\}$. This model can be described to solve the following quadratic optimization problem:

$$\begin{aligned} \min_{\alpha} \quad & f(\alpha) = \frac{1}{2} \alpha^T Q \alpha - e^T \alpha \\ \text{subject to} \quad & 0 \leq \alpha_i \leq C, i = 1, 2, \dots, l, \\ & y^T \alpha = 0, \end{aligned} \quad (1)$$

where e is the vector of all ones, C is the upper bound of all variables, Q is an l by l symmetric matrix with $Q_{ij} = y_i y_j K(x_i, x_j)$, and $K(x_i, x_j)$ is the kernel function.

The SVM classification method has been used in many regions due to its excellent performance in term of accuracy and computational complexity. Many of the application in the literature involve handwritten digital recognition [12], object recognition [13], text categorization [14], classification validation of cancer tissue samples [15], and classification of multiple tumor types [16].

III. ALGORITHM FRAMEWORK

In chest radiographs, most of solitary nodules appear as subtle abnormalities with unclear boundaries, variation of densities and sometimes are overlapped by ribs or vessels. Thus it is a challenging problem to segment such nodules. To make those problems tractable, we present a novel nodule segmentation algorithm by incorporating SVM classification into the fast marching segmentation algorithm.

A. Construction of a SVM training set

The first and most important step is the training nodule model. Currently, we only have a fairly small database of 400 chest image with solitary pulmonary nodules of varying size nodule marked by a radiologist to represent nodule case.

Above all, we extract about 20 pixel points inside and outside nodule boundary from each chest radiograph in above dataset, which are labeled different class tags (The pixels inside nodules are labeled as +1 whereas the pixels outside the nodules are labeled as -1). Then a set of local chest image features (i.e., shape, intensity and texture of

g_3	g_2	g_1
g_4	g_c	g_0
g_5	g_6	g_7

Fig. 1 8-neighbor patch of pixel g_c in chest image.

nodules) is extracted over each pixel, which can be treated as nodule prior knowledge. In our work, we only exploit neighborhood intensities and gradient feature to obtain the corresponding feature $G_c = (g_c, g_0, g_1, \dots, g_7, M_c)$ for the pixel g_c (shown in Fig.1), where M_c is the length of gradient of g_c . Then we can obtain training data set.

B. Training of SVM classifier

We conduct the training of a SVM classifier based on the training set obtained in the previous step. In this work, we use Lasvm method, which is a fast SVM algorithm based on active learning [17]. We train a SVM classifier of our nodule training set.

Then we use this SVM classifier to calculate decision value of each pixel in suspicious region in chest radiograph, which reflects the confidence level on how a pixel belongs to nodule region. In order words, the decision values distribution illustrates the confidence level of pixel neighbors belong to nodule. The smaller the expectation of decision values distribution is, the lower the confidence level is.

C. Fast marching algorithm via decision values

The conventional fast marching algorithm only takes into account the velocity term, which is calculated by incorporating the local image features (e.g., gradients). The velocity term vanishes or becomes very small when the advancing front approaches the suspicious nodule boundary. However, this criterion does not work if the practical nodule boundaries are unclear and their margins are poor-defined. Those weak nodule boundaries incur the so-called boundary leakage problem, in which the advancing front goes beyond and far away from the practical nodule boundary. To remedy this problem, we incorporate the prior knowledge of weak boundaries into velocity functions.

The velocity function of our algorithm is designed according to the local image gradient and intensity as well as the decision values of the SVM classification. We define the

velocity function of points (i, j) in 8 directions is formulated as follows,

$$V_{i,j,k} = \alpha_{i,j} * \frac{g_{i,j}^a}{(|G_{i,j,k}| + eps)^b}, k = 1, 2, \dots, 8 \quad (2)$$

where $\alpha_{i,j}$ factor of velocity is, $V_{i,j,k}$ is velocity of point (i, j) in direction k , $g_{i,j}$ is the intensity at point (i, j) , $G_{i,j,k}$ is the projection of gradient at point (i, j) in direction k , eps is infinitesimal, and a, b are parameters.

In Eq.2, $\alpha_{i,j}$ plays an important role in evolvement process, which is decided by the decision value of point (i, j) . The decision value reflects the confidence level on how a pixel belongs to nodule. In other words, the smaller the decision value is, the smaller the velocity at pixel p_0 is, and vice versa. We recur to decision values of (i, j) neighborhood pixels to define $\alpha_{i,j}$ as,

$$\alpha_{i,j} = \begin{cases} 1.5 & m_{i,j} > 0.4 \\ 1 & m_{i,j} > 0.1 \\ 0.5 & m_{i,j} < 0.0 \\ 0.1 & m_{i,j} < -0.4 \end{cases} \quad (3)$$

where $m_{i,j}$ is the average of the three least decision values in (i, j) neighborhood.

At each iteration step of our method, find active pixel p_0 with the shortest arrival time, extract some points in the 5×7 rectangular neighborhood of p_0 along the tangent direction of active curve, and calculate the velocity based on the Eq.2. When the degrees of confidences of all active points' neighborhoods are very low, we treat that the current front reaches the nodule boundary and stop our evolutionary process.

Our algorithm framework can be briefly described as follows:

- **Construction of a SVM training set.** Choose pixel points in chest radiography dataset, label them +1 or -1, and extract features (intensity, gradient feature) of every point to construct one training set.
- **Training of SVM classifier.** Use Lasvm to train the above training set, obtain one nodule SVM classifier, and calculate decision value of each pixel in suspicious region.
- **Fast marching algorithm via decision values.** Calculate velocity value of each candidate pixel according to Eq.2 and constrain front marching.

IV. EXPERIMENTAL RESULTS

Our proposed algorithm is evaluated over a nodule image library with 50 chest radiographs. As a comparison, the conventional fast marching algorithm and watershed segmentation algorithm are tested respectively over the same image library. The average recall value is 92% and the average precision value is 87%. The proposed outperforms the watershed segmentation algorithm over 90% of test cases whereas it outperforms the conventional FM algorithm over 70% of test cases and performs as good as the conventional FM algorithm over 15% of test cases. For the nodule cases with weak boundaries, our algorithm is significantly superior to the other two methods.

Fig.2 demonstrates the results of applying our method to three chest images. The first column shows original chest radiographs and the second describes the ground truth of nodule marked by the radiologist. Column (c) and (d) show the results of the FM method and our method respectively. In the top example, the true positive rate is 0.976099 and precision is 0.9572 under our method, however, FM method reveals true positive rate with 0.89675 and precision with 0.8790. For the second line example, we obtain true positive rate with 0.939463 and precision with 0.8225 under our method, and FM method shows true positive rate with 0.920046 and precision with 0.8055.

V. CONCLUSIONS

We have developed a novel fast marching approach for pulmonary nodule in chest radiographs, which combines the prior knowledge of pulmonary nodule boundary into the nodule segmentation algorithm via the SVM classifier. The proposed segmentation algorithm implements a robust and adaptive velocity function of advancing front in particular for the suspicious pulmonary nodules with weak boundaries. The experimental results demonstrate that the proposed algorithm significantly outperforms the watershed segmentation algorithm and conventional fast marching algorithm.

ACKNOWLEDGMENT

This work was partially supported by NSFC under contract 60473104, the National Basic Research Program under the Grant 2005CB321701.

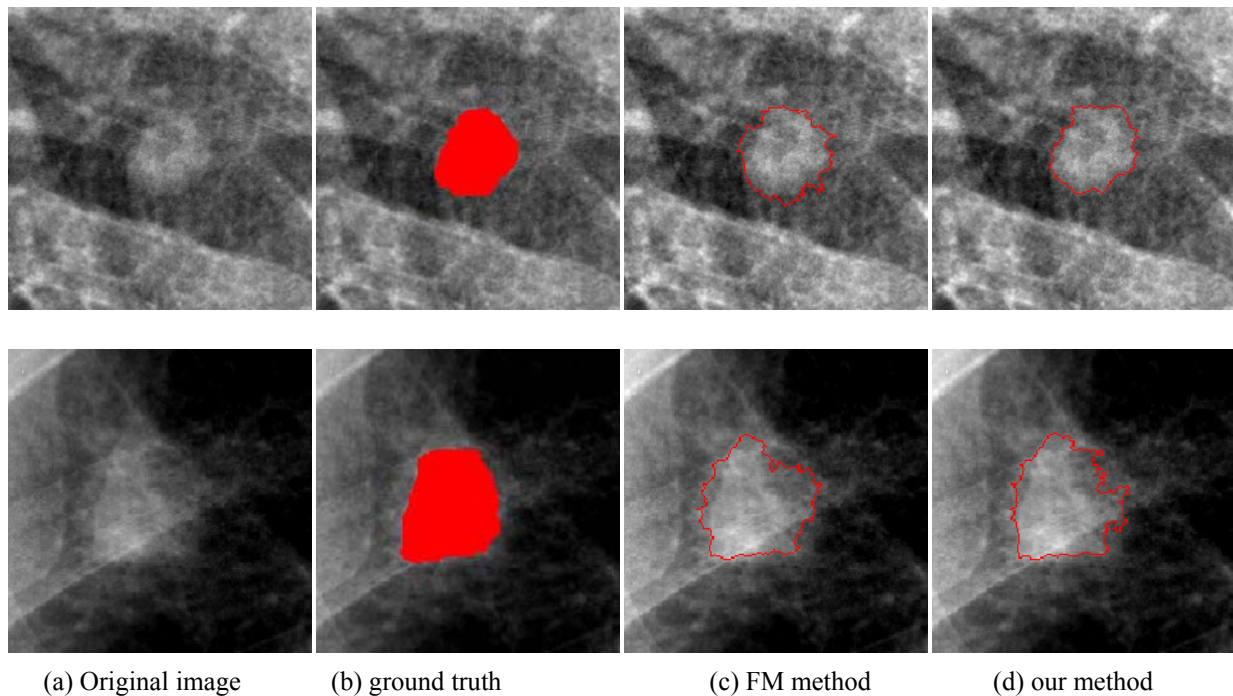


Fig. 2 The first column shows original chest radiographs and the second describes the ground truth of nodule checked by the radiologist. Column (c) and (d) show the results of the FM method and our method respectively.

REFERENCES

1. L. Quekel, A. Kessels, R. Goei, and J. V. Engelshoven, "Miss rate of lung cancer on the chest radiograph in clinical practice," *Chest*, vol. 115, no. 3, pp. 720-724, 1999.
2. G. Coppini, S. Diciotti, M. Falchini, N. Villari, G. Valli, Neural networks for computer-aided diagnosis: detection of lung nodules in chest radiograms. *IEEE Transactions on Information Technology in Biomedicine*, Vol.7, pp 344-357, 2003.
3. S. Matsumoto, H. L. Kundel, Pulmonary Nodule Detection In CT Images With Quantized Convergence Index Filter, *Medical Image Analysis*, Vol. 10, pp 343-352, 2006.
4. D. Comaniciu, P. Meer, Mean Shift: A Robust Approach Toward Feature Space Analysis, *IEEE Transactions On Pattern Analysis And Machine Intelligence*, Vol. 24, pp 1-18, 2002.
5. H. Yoshida, X. Xu, K. Doi, and M. Giger, Computer-aided diagnosis scheme for detecting pulmonary nodules using wavelet transforms, *Proc. SPIE*, vol. 2434, pp. 621-626, 1995.
6. J. A. Sethian, *Level Set methods and fast marching methods: evolving interfaces in computational geometry, fluid mechanics, computer vision, and materials science*, Cambridge University Press, 1999.
7. R. Boscolo *et al*, Medical image segmentation with knowledge-guided robust active contours. *RadioGraphics*, Vol.22, pp 437-228, 2002.
8. J. A. Sethian. A fast marching level set method for monotonically advancing fronts. *Proceedings of the National Academy of Science of USA*, Vol.93, pp 1591-1595, 1996.
9. J. A. Sethian. *Level set methods and fast marching methods*. Cambridge University Press, 1999.
10. Web resource: <http://math.berkeley.edu/~sethian/>
11. B.E. Boser *et al*. A Training Algorithm for Optimal Margin Classifiers. *Proceedings of the Fifth Annual Workshop on Computational Learning Theory* 5 pp 144-152, 1992.
12. C. Cortes and V. Vapnik. Support vector networks. *Machine Learning*, Vol.20, pp 273-297, 1995
13. V. Blanz, B. Schölkopf, H. Bülthoff, C. Burges, V. Vapnik, and T.Vetter. Comparison of view-based object recognition algorithms using realistic 3D models. *Proceedings of the International Conference on Artificial Neural Networks*, Vol.1112, pp 251-256, 1996.
14. T. Joachims. Text categorization with support vector machines. *Proceedings of European Conference on Machine Learning (ECML)*, 1998
15. T. Furey, N. Cristianini, N. Duffy, D. Bednarski, M. Schummer, and D. Haussler. Support vector machine classification and validation of cancer tissue samples using microarray expression data. *Bioinformatics*, Vol.16, pp 906-914, 2000.
16. C. H. Yeang *et.al*. Molecular classification of multiple tumor types. *Bioinformatics*, Vol.17, pp 316-322, 2001.
17. A. Bordes, S. Ertekin, J. Weston, and L. Bottou. Fast Kernel Classifiers with online and active learning. *Journal of Machine Learning Research*. Vol.6, pp 1579-1619, 2005.

Approximate algorithms for $2N+1$ sources cone-beam CT along saddle trajectories

Yang Lu, Jun Zhao

Department of Biomedical Engineering, Shanghai Jiao Tong University, Shanghai, China

Abstract — This paper presents approximate reconstruction methods for cone-beam CT with saddle scanning loci. The $2N+1$ x-ray sources and their corresponding $2N+1$ detectors are symmetrically placed around the circle with radius much larger than the object. They are moving along the $2N+1$ saddle trajectories respectively and the projection data are collected by corresponding detectors. Two approximate algorithms are proposed. One is the full-scan algorithm which consists of three steps: a) cone-beam data to fan-beam data conversion via a cosine correction; b) one-dimensional convolution with S-L kernel or R-L kernel along the u-axis in a local coordinate on the detector; c) three-dimensional backprojection of the filtered data. The other is super-short-scan algorithm which consists of four steps: a) cone-beam data to fan-beam data conversion via a cosine correction; b) derivative of the fan-beam data; c) Hilbert transform along the u-axis in a local coordinate on the detector; d) multiply the filtered data with a weighting function and then backproject it to the reconstructed image. The weighting function is decided by the number of x-ray sources and the starting and ending angle of each source. Although these two algorithms both have a Feldkamp-type reconstruction procedure, the super-short-scan algorithm requires less restriction of the data sufficiency condition and it can be used for region of interest imaging.

Keywords — Computed tomography, approximate algorithm, saddle trajectory, $2N+1$ sources

I. INTRODUCTION

Since the improvement of detector techniques, the concept of helical cone beam CT has been worldwide accepted and studied. Different exact or approximate algorithms are proposed by researchers. Scanning along helical trajectory is mainly concerned on so called long-object problem. However, it may cause mechanical difficulties when the object is small. In some cases, we need to monitor a motion object to get adequate information. To solve these problems, a new trajectory called saddle is proposed recently [1, 2]. The saddle trajectory has the following features: firstly, it is always single-connected, continuous, closed and bounded [2]; secondly, the convex hull of the saddle satisfies Tuy's condition, thus exact reconstruction could be achieved if the cone beam projec-

tions are non-truncated. Many researchers have paid their attention to it and develop some algorithms [2-4]. Based on our previously work on triple-source helical cone beam CT [5], we consider deriving approximate algorithms for saddle trajectories. Although the algorithms are not theoretically exact, they work much faster than exact algorithms and are suitable for practical applications.

II. THEORIES

A. The saddle trajectories

The saddle trajectory was first introduced by Zeng *et al* [1]. By the definition of Pack *et al* [2], it is the curve at the intersection of two surfaces. In polar-angle parameterization, the saddle can be described as:

$$\vec{a}_i(\lambda) = [R \cos \lambda, R \sin \lambda, H \cos(2\lambda + \lambda_i)]$$

$$\lambda_i = \frac{2\pi}{2N+1} i, i = 0, \dots, 2N, N \in \mathbb{N}, \quad (1)$$

where R is the distance between the X-ray source and the rotation axis, H is the amplitude of the saddle. i is the number corresponding to the X-ray source. λ is the rotation angle of the X-ray source and λ_i is the starting angle of each source. The sources are symmetrically spaced at one circle and each with a virtual flat detector on the opposite side of the corresponding source (refer to Figure 1).

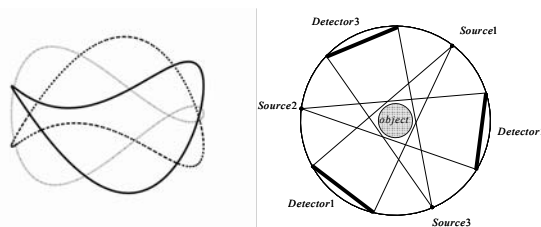


Fig. 1 Left: The saddle trajectories
Right: The positions of the X-ray sources and detectors when $N=1$

B. The full-scan algorithm

Feldkamp-type algorithm [6] is the most widely used approximate algorithm for cone beam CT. It has an efficient data flow structure and needs no extra requirements for the detectors and the scanning trajectories. All these merits are very important to practical applications. Even recently, many researchers are working on it and get satisfying results [7, 8]. Our first algorithm is derived from the general Feldkamp algorithm by Wang *et al* [9]. It can be described as follows:

$$f(\vec{x}) = \sum_{i=1}^{2N+1} F_i(\vec{x}, \lambda_i, \lambda_{i+1}), \quad (2)$$

$$F(\vec{x}, \lambda_s, \lambda_e) = \frac{1}{2} \int_{\lambda_s}^{\lambda_e} \frac{R^2}{(R-s)^2} \int_{-\infty}^{\infty} g(\lambda, u, v) \cdot h\left(\frac{Rt}{R-s} - u\right) \frac{R}{\sqrt{R^2 + u^2 + v^2}} dud\lambda, \quad (3)$$

where λ_s and λ_e are the starting and ending points of each segment, s and t are the rotated coordinate system defined as:

$$\begin{pmatrix} s \\ t \end{pmatrix} = \begin{bmatrix} \cos \lambda & \sin \lambda \\ -\sin \lambda & \cos \lambda \end{bmatrix} \begin{bmatrix} x \\ y \end{bmatrix}, \quad (4)$$

where h is the convolution kernel.

C. The super-short-scan algorithm

The super-short-scan algorithm is first proposed by Noo *et al* [10] as a way to solve the region of interest imaging problem in the fan beam CT. Yu *et al* [11] extend their formula to the three-dimensional case. Our second algorithm is derived from the formulae by Yu *et al* [11]. It can be described as:

$$f(\vec{x}) = \sum_{i=1}^{2N+1} F_i(\vec{x}, \lambda_i, \lambda_{i+d}), \quad (5)$$

$$F_i(\vec{x}, \lambda_s, \lambda_e) = \frac{1}{2\pi} \int_{\lambda_s}^{\lambda_e} d\lambda \left[\frac{\sqrt{R^2 + (\tilde{u})^2}}{R \|\vec{x} - \vec{a}_i(\lambda)\|} \times w(\lambda, \tilde{u}) g_F(\lambda, \tilde{u}, \tilde{v}) \right]_{\tilde{u}=\tilde{u}^*(\lambda, \vec{x}), \tilde{v}=\tilde{v}^*(\lambda, \vec{x})}, \quad (6)$$

$$g_F(\lambda, \tilde{u}, \tilde{v}) = \int_{-u_m}^{u_m} \frac{du h_H(\tilde{u} - u) \frac{R}{\sqrt{R^2 + u^2}}}{\partial \lambda \left[\frac{\sqrt{R^2 + u^2}}{\sqrt{R^2 + u^2 + v^2}} g(\lambda, u, v) \right]} \quad (7)$$

where $\tilde{u}^*(\lambda, \vec{x})$ and $\tilde{v}^*(\lambda, \vec{x})$ are the coordinates of \vec{x} projected on the detector, h_H is the Hilbert transform kernel, d is the spanning angular of each arc, $w(\lambda, \tilde{u})$ is the weight function defined as:

$$w(\lambda, \tilde{u}) = \frac{\eta(\lambda)}{\eta(\lambda) + \eta(\lambda + \pi - 2 \tan^{-1}(\tilde{u} / R))}, \quad (8)$$

where

$$\eta(\lambda) = \begin{cases} \cos^2 \frac{\pi(\lambda - \lambda_s - \delta)}{2\delta} & \text{if } \lambda_s < \lambda < \lambda_s + \delta \\ 1 & \text{if } \lambda_s + \delta < \lambda < \lambda_e - \delta \\ \cos^2 \frac{\pi(\lambda - \lambda_e + \delta)}{2\delta} & \text{if } \lambda_e - \delta < \lambda < \lambda_e \\ 0 & \text{others} \end{cases} \quad (9)$$

D. Computational structure of the proposed algorithms

Both of the approximate algorithms have Feldkamp-type structures, which result in a very computational efficiency of the reconstruction. The flowchart is shown in Figure 2. The conventional Feldkamp-type algorithm consists of three steps: cosine correction, one-dimensional convolution and three-dimensional backprojection. Derivation is an extra and important step in the super-short-scan algorithm.

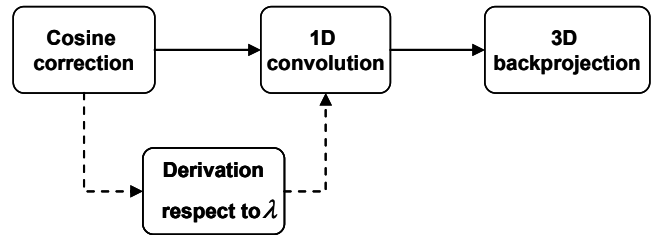


Fig. 2 The flowchart for the numerical implementation of the proposed Feldkamp-type algorithms.

III. NUMERICAL STUDIES

In the simulation, the virtual detectors are placed perpendicular to the line that intersects the z-axis orthogonally and connects the corresponding source and the detector center, and are parallel to the z-axis at the distance 20cm from the corresponding x-ray sources. Each detector consists of 250×250 elements with size of $0.5\text{mm} \times 0.5\text{mm}$. The scanning radius and the amplitude of each saddle are 20cm and 3cm, respectively. There are 600 projections per turn for each source.

Both Sheep-Logan phantom and the clock phantom are used in the simulation for the purpose of testing our algorithms in static and dynamic cases. The phantoms are located at the center of the global coordinate system within a spherical support of radius 6cm. The reconstruction grid is 257×257 .

Figure 3 and Figure 4 show the reconstructed images. Images in Figure 3 are reconstructed by full-scan algorithm with $N = 0, 1, 2, 3$, respectively. The clock phantom is rotated with the angular velocity of 20 degrees/s and the rotation speed of each X-ray source is 1s per turn. The results show that the motion artifacts are significantly reduced when N increases, and the scanning time is only one-third or one-fifth of the conventional method. The top right and the bottom left images in 4Figure are recon-

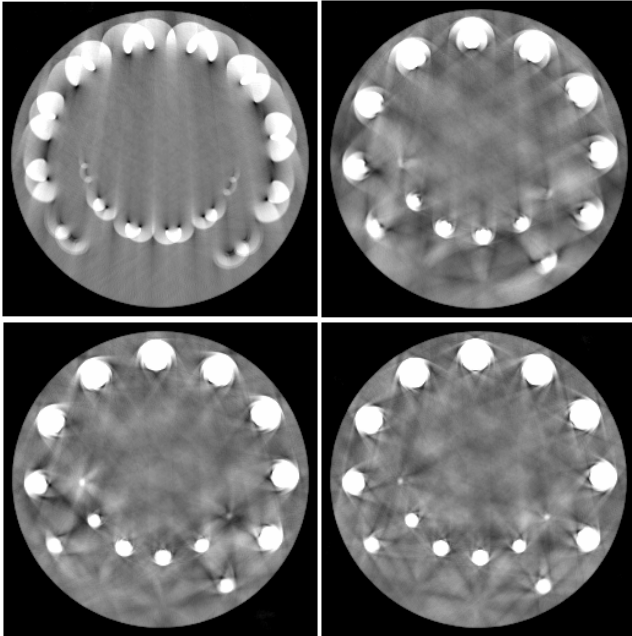


Fig. 3 Images reconstructed by full-scan algorithm. Top left: $N = 0$; top right $N = 1$; bottom left: $N = 2$; bottom right: $N = 3$. The gray-scale was compressed to the range $[0.5, 1.5]$

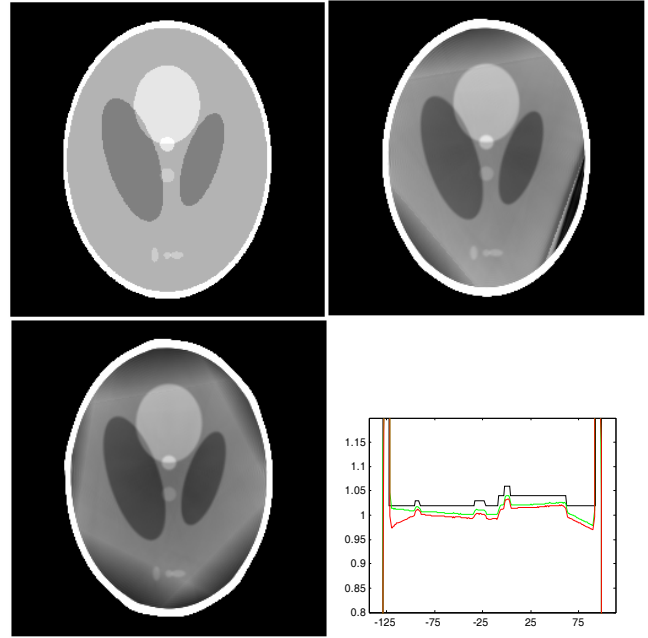


Fig. 4 Images reconstructed by super-short-scan algorithm. Top left: standard Sheep-Logan phantom at slice $z = -1.5\text{cm}$; Top right: $N = 1$; bottom left: $N = 2$; bottom right: density profiles along line $x = 0$ for the phantom (black), $N = 1$ (green), $N = 2$ (red). The gray-scale was compressed to the range $[0.95, 1.05]$

structed by super-short-scan algorithm with $N = 1, 2$, respectively. The top left image is the standard Shepp-Logan phantom at slice $z = -1.5\text{cm}$. The spanning angular is 80° when $N = 1$ and 55° when $N = 2$. The results show that images reconstructed by super-short scan algorithm preserve good qualities while the dose cost is reduced to 66.7% and 76.4%. Noted that the area and the volume we interested in are decided by the starting and ending angles of each source. So, for a specific area or volume, these parameters should be pre-calculated.

IV. CONCLUSION

In this paper, we propose two approximate algorithms for $2N+1$ sources cone-beam CT along saddle trajectories. One is derived from traditional Feldkamp-type algorithms, and can be used for a full-scan reconstruction. The other is derived from Noo's super-short-scan algorithm for fan-beam projections, which is specifically excellent for region of interest imaging. Both of them can improve temporal resolution, reduce the motion artifacts and obtain better image quality. They may have significance for practical applications such as cardiac imaging.

ACKNOWLEDGMENTS

This work was supported in part by National Natural Science Foundation of China (30770589) and (30570511).

REFERENCES

1. G. L. Zeng, G. T. Gullberg, and S. A. Foresti, "Eigen Analysis of Cone-Beam Scanning Geometries," *Three-Dimensional Image Reconstruction in Radiation and Nuclear Medicine. COPYRIGHT*, pp. 75-86, 1996.
2. J. D. Pack, F. Noo, and H. Kudo, "Investigation of saddle trajectories for cardiac CT imaging in cone-beam geometry," *Physics in Medicine and Biology*, vol. 49, pp. 2317, 2004.
3. H. Yu, S. Zhao, Y. Ye, and G. Wang, "Exact BPF and FBP algorithms for nonstandard saddle curves," *Medical Physics*, vol. 32, pp. 3305, 2005.
4. H. Yang, M. Li, K. Koizumi, and H. Kudo, "Exact cone beam reconstruction for a saddle trajectory," *Physics in Medicine and Biology*, vol. 51, pp. 1157, 2006.
5. J. Zhao, M. Jiang, T. Zhuang, and G. Wang, "An exact reconstruction algorithm for triple-source helical cone-beam CT," *Journal of X-Ray Science and Technology*, vol. 14, pp. 191, 2006.
6. L. A. Feldkamp, L. C. Davis, and J. W. Kress, "Practical cone-beam algorithm," *J. Opt. Soc. Am. A*, vol. 1, pp. 612-619, 1984.
7. X. Tang, J. Hsieh, R. A. Nilsen, S. Dutta, D. Samsonov, and A. Hagiwara, "A three-dimensional-weighted cone beam filtered backprojection (CB-FBP) algorithm for image reconstruction in volumetric CT - Helical scanning," *Physics in Medicine and Biology*, vol. 51, pp. 855, 2006.
8. M. Yan and C. Zhang, "Tilted plane Feldkamp type reconstruction algorithm for spiral cone beam CT," *Medical Physics*, vol. 32, pp. 3455, 2005.
9. G. Wang, T.-H. Lin, P.-C. Cheng, and D. M. Shinozaki, "General cone-beam reconstruction algorithm," *IEEE Transactions on Medical Imaging*, vol. 12, pp. 486, 1993.
10. F. Noo, M. Defrise, R. Clackdoyle, and H. Kudo, "Image reconstruction from fan-beam projections on less than a short scan," *Physics in Medicine and Biology*, vol. 47, pp. 2525, 2002.
11. H. Yu and G. Wang, "Feldkamp-type VOI reconstruction from super-short-scan cone-beam data," *Medical Physics*, vol. 31, pp. 1357, 2004.

Address of the corresponding author:

Dr. Jun Zhao
 Department of Biomedical Engineering,
 Shanghai Jiao Tong University
 800 Dong Chuan Road
 Shanghai
 China
 junzhao@sjtu.edu.cn

Using Fast Marching in Automatic Segmentation of Retinal Blood Vessels

Chao Liu¹, Huihai Lu² and Jiwu Zhang^{1,2}

¹ School of Biomedical Engineering, College of Life Science & Biotechnology, Shanghai Jiao Tong University, Shanghai, China

² Global R&D Center, Carestream Health Company, Shanghai, China

Abstract— The appearance of blood vessels in retinal images plays an important role in diagnosis of many eye diseases and system diseases. This presentation investigates a novel algorithm for automatic segmentation of blood vessels in retinal images by using vessel enhancement techniques and Fast Marching (FM) method. The algorithm includes the following major steps: Morlet wavelet transform, curvature estimation, matched filtering, and Fast Marching. The wavelet transform and the curvature-based method are first applied to detect the skeleton of vessels, which serve as the initial seeds of the Fast Marching algorithm. The matched filter is then used to enhance the vessels in order to extract the features used by the Fast Marching's velocity function. Finally, the Fast Marching algorithm is applied to obtain final segmentation of retinal blood vessels.

This algorithm provides effective segmentation results of retinal vessels, which can be analyzed in later processing stages leading to a complete diagnosis system.

Keywords— retinal image, blood vessel segmentation, matched filter, curvature, Fast Marching

I. INTRODUCTION

Retinal images have been commonly used to diagnose retinopathies and other vasculature-related diseases, such as diabetes and hypertension, because these diseases often lead to measurable abnormalities of blood vessels in color, diameter, tortuosity and length. To facilitate computer-aided diagnosis, an accurate segmentation of vessels is needed as the essential input of further diagnosis. This is particularly important for remote and rural areas since physicians may be less experienced. Furthermore blood vessels can be used as landmarks for localizing other anatomical structures in retina.

Previous blood vessel segmentation methods can be grouped into two major categories: thresholding based, such as edge detection and tracing based. In the thresholding methods the pixels are labeled as vessels or non-vessels by an enhancement-detection process. The vessels are enhanced by convolving mask operators with the retinal image, and are detected by thresholding the enhanced image. The Gaussian-shaped templates are the most widely used masks.

The gray-level profile of the cross section of a blood vessel can be approximated by a Gaussian-shaped curve [1]. So twelve Gaussian-shaped matched filters are designed to detect piecewise linear segments of blood vessels. Each of the twelve filters is convolved with the retinal image and only the maximum of all filter responses is preserved. The Otsu's automatic thresholding algorithm is applied to the enhanced image to obtain the final results. Gabor filter [2], Kalman filter [3], Sobel operator [4], and morphological operator [5] are also developed in other works.

The tracing algorithms start with initial seed points, and search for the next segment of blood vessels based on the information of current segment. An effective piecewise multi-threshold tracing algorithm is proposed by Hoover *et al.* [6]. Several thresholds are applied to the probed segment and a set of criteria is tested to stop the probing process and to decide whether the probed area is blood vessel or not. The criteria take into consideration both the local feature of blood vessels and the global feature of vessel net.

In this paper we propose a novel algorithm for automatic segmentation of blood vessels in retinal images by using vessel enhancement techniques and the Fast Marching (FM) method. First, the initial vessel segmentation is obtained by using the Morlet wavelet transform and Otsu thresholding algorithm. Vessel centerlines are then extracted with the mask of initial vessel segmentation. Thirdly, Gaussian-shaped matched filters are applied to the original image to enhance vessel presentation. The features of the enhanced image are used in the Fast Marching velocity function. Finally the Fast Marching algorithm is applied to obtain the segmentation results. Initial seed points of Fast Marching algorithm are the vessel centerlines extracted before.

II. MATERIALS AND METHODS

A. Materials

The most commonly used fundus image databases in vessel segmentation are DRIVE and STARE databases. A retinal image from DRIVE database is presented in Fig. 1. The green channel is used as input to the proposed algorithm since the red and blue images are noisier and have a



Fig. 1 A fundus image

lower contrast. The round area in the middle of the retinal image is called FOV (Field of View). The FOV is expanded to remove the strong contrast between the fundus and the black background.

B. Vessel centerline extraction

The vessel centerline extraction involves three steps: enhancement with Morlet wavelet filter, thresholding and curvature measurement.

The 2-D Morlet wavelet is defined as [7]:

$$\psi_M(\mathbf{x}) = \exp(j\mathbf{k}_0 \cdot \mathbf{x}) \exp\left(-\frac{1}{2} |A\mathbf{x}|^2\right) \quad (1)$$

where $j = \sqrt{-1}$ and $A = \text{diag}[\varepsilon^{-1/2}, 1]$, $\varepsilon \geq 1$ defines the anisotropy of the filter. The continuous wavelet transform is defined as:

$$T_\psi(\mathbf{b}, \theta, a) = C_\psi^{-1/2} \frac{1}{a} \int \psi^*(a^{-1}r_{-\theta}(\mathbf{x} - \mathbf{b})) f(\mathbf{x}) d^2\mathbf{x} \quad (2)$$

where C_ψ , ψ , a , \mathbf{b} , and θ denote the normalizing constant, mother wavelet, the scale, the displacement vector and the rotation angle. The Morlet wavelet filter is rotated from 0 to 165 degrees at step of 15 degree. Then apply the twelve filters to the retinal image. Only the maximum of filter responses over all orientations is taken. Then an automatic thresholding algorithm is applied to the enhanced image to obtain the initial segmentation. Fig. 2 illustrates the binary image after thresholding.

Thirdly, vessel centerlines are then extracted using curvature estimation method with the mask of initial vessel segmentation. This is done in a similar way to the trench or ridge extraction when the retinal image is presented in a 3-D space. The vessel centerlines represent local maximum of curvature and therefore the curvature estimation method

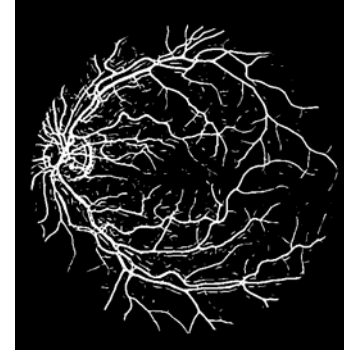


Fig. 2 Initial segmentation after Morlet filtering and thresholding



Fig. 3 Extracted blood vessel centerlines

could be used to locate the centerlines [8]. In this paper method described in [8] is used with two minor modifications. First the curvature estimation is applied within the mask of initial segmentation rather than the whole retinal image. Secondly the threshold t in [8] is set to zero. The vessel centerlines extracted after this method is shown in Fig. 3.

C. Matched filter enhancement

Chaudhuri *et al.* [1] presented that the cross section profile of a blood vessel could be approximated by a Gaussian-shaped curve. So a Gaussian-shaped zero-sum filter is rotated fifteen degrees each time to form a set of twelve filters which is designed to detect piecewise linear segments of blood vessels along all orientations. The matched filter is represented as:

$$K_i(x, y) = -\exp(-u^2 / 2\sigma^2) \nabla \bar{p}_i \in N \quad (3)$$

The filter size is $N = \{(u, v) \mid |u| \leq 3\sigma, |v| \leq L/2\}$. L is chosen to be 9 and σ is 1.5. The twelve Gaussian filters are convolved with the padded green channel image respec-

tively, by which only the maximum response is chosen as the output of the matched filter, called matched filter response (MFR) image. The blood vessels are effectively enhanced in the MFR image, the feature of which is used in the velocity function of Fast Marching algorithm.

D. Fast Marching method

Fast Marching method is a special case of Level Set which is proposed by Sethian and Osher. The function of Fast Marching is

$$|\nabla T| F = 1 \quad (4)$$

where F is speed with which an interface propagates, and T is arriving time of the interface passing through a point. F is always positive so that the interface expands from the initial seed points. The seed points for Fast Marching are the vessel centerlines extracted in Section II-B. When the propagation stops, the interface represents the segmentation results of blood vessels.

The velocity function F is designed in association with two features, the grey value and the gradient of the MFR image. Inside the vessels the gradient should be small and the grey level should be high, so that the interface can move quickly in areas of low gradient and high gray level. The speed F is

$$F = \frac{k^\alpha}{|\nabla I|} \quad (5)$$

where $|\nabla I|$ is projection of gradient in speed direction and α is parameter.

$$k = \begin{cases} 1 & \text{for } I(x,y) \geq 100 \\ \frac{I(x,y)}{100} & \text{others} \end{cases} \quad (6)$$

so that $0 \leq k \leq 1$. The MFR image is normalized with a mean contrast equal to 70, in order to eliminate the influence of environmental light.

The interface propagation in Fast Marching stops in two conditions: either a threshold of T is reached or the maximum number of iteration is reached.

The Fast Marching method is described as follows:

1. The vessel centerlines are labeled as *alive*, and the non-alive neighbors of *alive* are labeled as *close*. Label all other pixels as *far*.
2. Calculate the speed of *close*, and then calculate their arriving time.

3. Choose a point A with the smallest T from *close*, and label it as *trial*.
4. If the neighbor of A is in *far*, add it to *close* and calculate its F and T . Else if the neighbor of A is in *close*, renew its T .
5. Label A as *alive*.
6. If the stop criteria are met, stop. Else, return to 3.

III. EXPERIMENTS AND RESULTS

The method proposed in this paper is tested on twenty retinal images from DRIVE database, including normal and abnormal cases. One of the segmentation results is illustrated in Fig. 4. The results are compared with hand labeled segmentations to estimate algorithm performance. Any hand labeled pixel which is also labeled as vessel by the algorithm is a true positive. Any pixel which is hand labeled as non-vessel but is labeled as vessel by the algorithm is a false positive. The true positive rate is the ratio of true positives to sum of pixels which are hand labeled as vessel. The false positive rate is the ratio of false positives to sum of pixels which are hand labeled as non-vessel.

The performance of Fast Marching depends on the velocity function and stop criteria. For parameter α in velocity function (5) we choose 21. For each image, Fast Marching algorithm stops until either the arriving time $T > 4500$ or the number of iteration steps is greater than 30000.

The average true positive rate over all test images is 80.5%, and the average false positive rate is 6.1%. The true positive rate varies from 90.0% to 73.1%. The average true positive rate for abnormal cases is relatively lower. Compared with hand labeled segmentations, our algorithm is quite effective for large and middle sized vessels and some small vessels. Some small vessels are mis-detected due to low contrast in the images. False detections usually occur at the border of the optic disc, exudates and other abnormalities where present strong contrast.

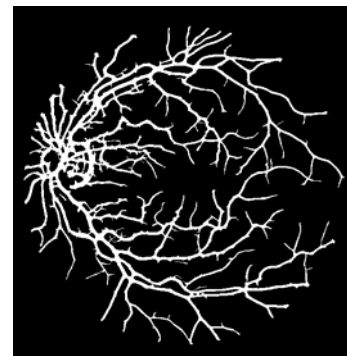


Fig. 4 Segmentation result of Fig. 1 using our algorithm

IV. DISCUSSIONS AND CONCLUSIONS

This paper presents a novel vessel segmentation algorithm based on vessel enhancement techniques and Fast Marching method. It consists of three main steps: vessel centerline extraction, matched filter enhancement and Fast Marching. The combination of Morlet wavelet transform and curvature measurement is very effective in vessel centerline detection, since both the local shape feature and curvature feature of vessels have been taken into consideration. The vessels are oriented piecewise linear segments and the centerlines present regional maximum of curvature. Then the Gaussian-shaped matched filters enhance the blood vessels effectively. Since the average gray level of the MFR image is regulated and both the features of gray-level and gradient of MFR image are used in velocity function, Fast Marching method could segment blood vessels effectively. The experimental results demonstrated that our method could be used for computer-aided diagnosis of fundus images in future research.

REFERENCES

1. Chaudhuri S, Chatterjee S, Katz N, Nelson M and Goldbaum M (1989) Detection of Blood Vessels in Retinal Images Using Two-Dimensional Matched Filters. *IEEE Trans. Med. Imag.* 8(3):263-269.
2. Li Q, You J, Zhang L and Bhattacharya P (2006) Automated Retinal Vessel Segmentation Using Gabor Filters and Scale Multiplication, *IPCV 2006*, pp 22-28
3. Chutatape O, Zheng Liu, and Krishnan S M (1998) Retinal blood vessel detection and tracking by matched Gaussian and Kalman filters, *Proc. 20th Annual Int. Conference of IEEE Eng. in Med. and Biol. Soci.*, vol. 20, No. 6, 1998, pp 3144-3149
4. Wang Y and Lee S C (2006) A fast method for automated detection of blood vessels in retinal images, *Conference Record Thirty-First Asilomar Conference on Sign., Syst. & Comp.*, 2006, pp: 1700-1704
5. Zana F and Klein J (2001) Segmentation of vessel-like patterns using mathematical morphology and curvature evaluation. *IEEE Trans. Image Processing*, 10(7):1010-1019.
6. Hoover A, Kouznetsova V and Goldbaum M (2000) Locating blood vessels in retinal images by piecewise threshold probing of a matched filter response. *IEEE Trans. Med Imag.*, 19(3):203-210.
7. Soares J V B, Leandro J J G, Cessari R M Jr., Jelinek H F and Cree M J (2006) Retinal Vessel Segmentation Using the 2-D Morlet Wavelet and Supervised Classification. *IEEE Trans Med Imag.*, 25:1214-1222.
8. Garg S, Sivaswamy J and Chandra S (2007) Unsupervised curvature-based retinal vessel segmentation, *ISBI, 2007* pp: 344-347.

The address of the corresponding author:

Author: Chao Liu
 Institute: School of Biomedical Engineering, College of Life Science & Biotechnology, Shanghai Jiao Tong University
 Street: B0708091 No. 800 Dongchuan Road
 City: Shanghai
 Country: China
 Email: chaoliutj@sjtu.edu.cn

A Robust Fiber Tracking Method in Diffusion Tensor Imaging

Lifeng Song^{1,2}, Zikuan Chen¹ and Wei Xing²

¹Northeastern University, Sino-Dutch Biomedical & Information Engineering, Shenyang, China.

²Northeastern University, Department of Mathematics, Shenyang, China.

Abstract — Diffusion tensor imaging (DTI) can be used to study the evolving pathology in the central nervous system by tracking the nerve fibers. To explore a technique for overcoming the obstacles associated discretized nerve fiber images and to find the most likely directions of nerve fibers, we presented a new robust fiber tracking method in diffusion tensor imaging. The robustness lies in that it includes three situations and the joint utilization of the preference direction determined by tensor analysis, the fractional anisotropy values, and the previous propagation directions. Based on fiber tracing with a DTI dataset, we demonstrated the water diffusing patterns and fiber bundle tracks in a brain. This technique is expected to find use in the understanding of brain structure and the image-guided brain surgery.

Keywords — Fiber tracking, Diffusion Tensor Imaging (DTI), fractional anisotropy, preference direction, previous propagation directions.

I. INTRODUCTION

Diffusion tensor imaging(DTI) is a magnetic resonance (MR) acquisition technique which has gained acceptance in medical imaging in recent years. It enables recovery of the structure of white matter within the human brain in vivo which is of great interest for neuroscience[1]. Water in white matter diffuses more along brain fibers than perpendicular to it[2]. In case of this anisotropic diffusion in white matter, diffusion is usually characterized by a tensor coefficient—Diffusion tensor(D). Diffusion tensor is represented by a 3*3 symmetric matrix with six independent elements:

$$D = \begin{bmatrix} D_{xx} & D_{xy} & D_{zx} \\ D_{yx} & D_{yy} & D_{yz} \\ D_{zx} & D_{zy} & D_{zz} \end{bmatrix}$$

Diagonalizing D, we can get three eigenvalues λ_1, λ_2 and λ_3 , and their corresponding eigenvectors $\varepsilon_1, \varepsilon_2$ and ε_3 [3]. The task of fiber tracking lies in generating the water diffusion paths in brain through the use of diffusion tensor imaging (DTI) in magnetic resonance imaging (MRI) modality. The basic assumption of the fiber tracking technique includes two folds: 1) water paths manifest as a fiber bun-

dle, and 2) the fiber orientation corresponds to the major eigenvector of the diffusion tensor. In conventional DTI-based fiber tracking methods, the procedure consisting of finding the direction of fiber by calculating the tensor matrix, which corresponds to the main eigenvector of the diffusion tensor. However, there is no preference among the eigenvectors defined in isotropical regions or in regions with planar anisotropy. Namely, in regions with low anisotropy, the main diffusion direction is meaningless[4]. For overcoming these obstacles and finding the most likely directions of nerve fibers in low anisotropical regions, we presented a new robust fiber tracking method in diffusion tensor imaging. The method includes three situations and the joint utilization of the preference direction determined by tensor analysis, the FA values, and the previous propagation directions[4-8]. The 3D Cyrus Beck algorithm is used to calculate the propagation points on the grid for next step[9].

II. METHODOLOGY

A. Diffusion tensor and Fractional Anisotropy

The data of DT-MRI were obtained from a healthy human brain. Diffusion weighted MRI was performed along six independent axes, as indexed by {xx,yy,zz,xy,yz,xz}.. So we can get the b_i (the sensitivity gradients), S_0 (no diffusion weighted) and S_i (the measured signal) in six directions. Using the equation (1), the ADC_i (the apparent diffusion coefficient in each direction) can be calculated[8].

$$ADC_i = -\frac{1}{b} \ln \frac{S_i}{S_0} \quad (1)$$

with the b matrix given by

$$b = \begin{bmatrix} b_{x1}^2 & b_{y1}^2 & b_{z1}^2 & 2b_{x1}b_{y1} & 2b_{y1}b_{z1} & 2b_{z1}b_{x1} \\ b_{x2}^2 & b_{y2}^2 & b_{z2}^2 & 2b_{x2}b_{y2} & 2b_{y2}b_{z2} & 2b_{z2}b_{x2} \\ b_{x3}^2 & b_{y3}^2 & b_{z3}^2 & 2b_{x3}b_{y3} & 2b_{y3}b_{z3} & 2b_{z3}b_{x3} \\ b_{x4}^2 & b_{y4}^2 & b_{z4}^2 & 2b_{x4}b_{y4} & 2b_{y4}b_{z4} & 2b_{z4}b_{x4} \\ b_{x5}^2 & b_{y5}^2 & b_{z5}^2 & 2b_{x5}b_{y5} & 2b_{y5}b_{z5} & 2b_{z5}b_{x5} \\ b_{x6}^2 & b_{y6}^2 & b_{z6}^2 & 2b_{x6}b_{y6} & 2b_{y6}b_{z6} & 2b_{z6}b_{x6} \end{bmatrix} \quad (2)$$

The tensor D can be calculated from these ADC values and the b matrix by using the equation (3):

$$b \begin{bmatrix} D_{xx} \\ D_{yy} \\ D_{zz} \\ D_{xy} \\ D_{yz} \\ D_{zx} \end{bmatrix} = \begin{bmatrix} ADC_1 \\ ADC_2 \\ ADC_3 \\ ADC_4 \\ ADC_5 \\ ADC_6 \end{bmatrix} \quad (3)$$

We can get three eigenvalues(λ_1 , λ_2 and λ_3) and three eigenvectors(ε_1 , ε_2 and ε_3) of the D matrix. FA is used most frequently for anisotropy measure. The FA value of a given voxel can be obtained by equation (4).

$$FA = \sqrt{\frac{1}{2} \sqrt{\frac{(\lambda_1 - \lambda_2)^2 + (\lambda_2 - \lambda_3)^2 + (\lambda_3 - \lambda_1)^2}{\lambda_1^2 + \lambda_2^2 + \lambda_3^2}}} \quad (4)$$

The FA value is a measure of the directionality of the water diffusion within a given voxel, with the range from 0 to 1. A fully anisotropic tissue has a factor FA=1, and an isotropic tissue has a factor FA=0 [5].

B. Principal Concept of Robust Fiber Tracking Method

Basically, a nerve fiber tracking method is based on DTI by eigenvectors and eigenvalues analysis. The direction of the fiber is assumed to be given by the eigenvector associated with the largest eigenvalue. Firstly, we get a coarse fiber direction by utilizing a simple method. Because of the low curvature of the fiber, it can be seen as a transcendent direction to direct fiber tracking. Secondly, according to the value of FA, we classify three situations for fiber direction determination. A large FA value indicates high anisotropy. We use the main eigenvector direction of the point as the fiber direction. For low anisotropic regions, we jointly use two bigger eigenvectors and their eigenvalues, FA and the previous propagation direction to determine the fiber tracking. The local direction and the previous propagation direction are weighted by a function of the fractional anisotropy. When the anisotropy is too low to tell the fiber direction, the previous propagation direction is used for the current point.. The fiber direction is expressed by

$$v_k = \begin{cases} e_1 & FA(i, j, k) \geq 0.7 \\ (1 - FA(i, j, k))v_{k-1} + FA(i, j, k) \left(\frac{\lambda_1}{\lambda_1 + \lambda_2} e_1 + \frac{\lambda_2}{\lambda_1 + \lambda_2} e_2 \right) & 0.4 \leq FA(i, j, k) < 0.7 \\ v_{k-1} & 0.2 \leq FA(i, j, k) < 0.4 \end{cases} \quad (5)$$

Where the unit vector v_k is the fiber direction at the current point, and the unit vector v_{k-1} is the previous propagation direction. $FA(i, j, k)$ is the FA value of the current voxel. $\lambda_1, \lambda_2, e_1, e_2$ are the larger eigenvalues and eigenvectors of the current voxel. Two thresholds with respect to the FA value for the subsection function are set empirically.

When fiber tracking is applied in brain tissue, it should stop following fibers in regions of low anisotropy. Another criterion to stop tracking fibers is to define a maximum allowable angle C between two steps, it can avoid sharp turns in fiber tracking[4]. Where C is defined as:

$$C = |v_k \bullet v_{k-1}| \quad (6)$$

In this paper, FA of 0.2 was used as a stopping criterion to keep tracked fibers in the white matter. The curvature threshold C was set to 0.7 (approximately 45°).

The procedure of fiber tracking of is described as follows:

Step 1: Define the a region of interest (see Fig. 3 a)

Step 2: Calculate the tensor matrix D, eigenvalues and eigenvectors of the D matrix, and the FA value of each voxel in ROI.

Step 3: Select the seed point in ROI. In this paper, we select the center point of voxel whose FA value is larger 0.7 as the seed point.

Step 4: Starting from a user-selected seed point in a region of interest (ROI), implement the procedure of positive tracking.

Step 5: Implement the procedure of negative tracking.

Step 6: Loop Step 3 to Step 5 in the ROI.

The procedure of positive tracking of a seed point is described as follows:

Step 1: Starting from a selected seed point in a region of interest (ROI), a line in the direction of positive major eigenvector is followed until the boundary of the current voxel is encountered.

Step 2: Using the 3D Cyrus Beck algorithm to calculate the propagation points on the grid.

Step 3: Using the ListInterpolation to get the eigenvalues, eigenvectors and the FA value of the propagation.

Step 4: If the FA value of the propagation is larger 0.2, go to step 5, else end.

Step 5: Calculate the direction vector of propagation by the tracking function(5).

Step 6: Calculate the maximum allowable angle C by Eq.(6). If the C is larger 0.7, then go to step 7, else end.

Step 7: The direction vector of propagation is followed until the boundary of the current voxel is encountered.

Step 8: Loop step 2 to step 7 in the ROI.

Step 9: Link all propagations, we can get a fiber in ROI.

The procedure of negative tracking is similar to the positive tracking. Only the negative eigenvectors and the negative vector of propagation replace the positive.

III. RESULTS

A. Image data and preprocessing

We used a collection of the DT-MRI data that were obtained from a healthy human brain whose size is 128x128x30. Fig. 1 shows a few slices of the DTI dataset. The ADC_i and the b matrix can be calculated by using the equation (1),(2). The ADC_i (in form of images) and the b matrix are as follows

$$b^{-1} = \begin{bmatrix} -0.333333 & +0.666667 & +0.666667 & +0.444444 & +0.444444 & -0.888889 \\ +0.666667 & -0.333333 & +0.666667 & +0.444444 & -0.888889 & +0.444444 \\ +0.666667 & +0.666667 & -0.333333 & -0.888889 & +0.444444 & +0.444444 \\ -0.166667 & -0.166667 & -0.666667 & +0.555556 & +0.222222 & +0.222222 \\ -0.166667 & -0.666667 & -0.166667 & +0.222222 & +0.555556 & +0.222222 \\ +0.666667 & +0.166667 & +0.166667 & -0.222222 & -0.222222 & -0.555556 \end{bmatrix}$$

Using the equation (3), we can get the diffusion tensor matrix D, whose size is 30*128*128*3*3. Namely, there is a symmetrical 3x3 matrix in each voxel. We compute the eigenvectors, eigenvalues and fractional anisotropy value of each voxel. Fig.2 shows a slice of the FA value. As shown in Fig.2, in regions with high anisotropy the intensity of the color is very bright, while in the less important iso-

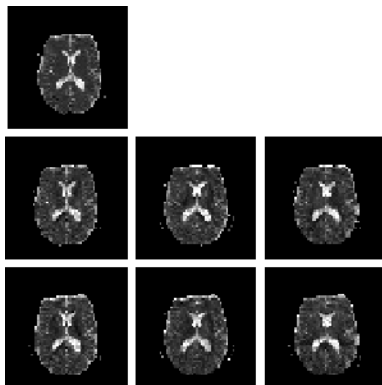


Fig. 1 ADC0—ADC6 in the 16th layer

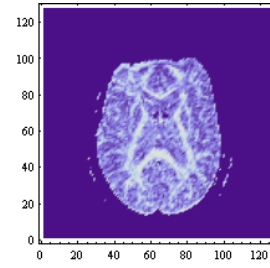


Fig. 2 The FA value in the 16th layer

tropic regions the color with appear dark. Fig.3 show a slice of the in-plane components of the main vector in ROI. The arrows represent the in-plant components of the vector.

B. Reconstruction Images

We have implemented the whole process of fiber tracking in the region of interest (in Fig. 3 a) by Mathematica programming. Fig. 4 shows the tracking result in ROI in different view. We do not compare and contrast our results with other methods due to the different data.

The images show that the reconstructed fibers can describe the bundle of fibers more precisely.

IV. DISCUSSION

The fiber tracking method presented in this paper detinvolves the preference direction determination by tensor analysis, the FA values, and the previous propagation directions, all these factors are considered jointly to overcome the problem caused by partial volume effect and abrupt changes in directionality.

Weistein et al presented the tensorline technique for finding the most likely direction of propagation of the fiber. The propagation vector(v_{prop}) is a combination of three vectors, e_1 (local main eigenvector), v_{in} and v_{out} , as expressed by:

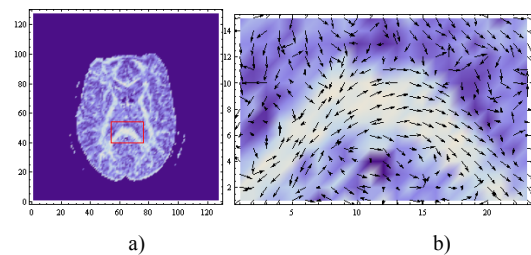


Fig. 3 a) The region of interest that we choosed. b) the in-plane components of the main vector in ROI in the 16th layer

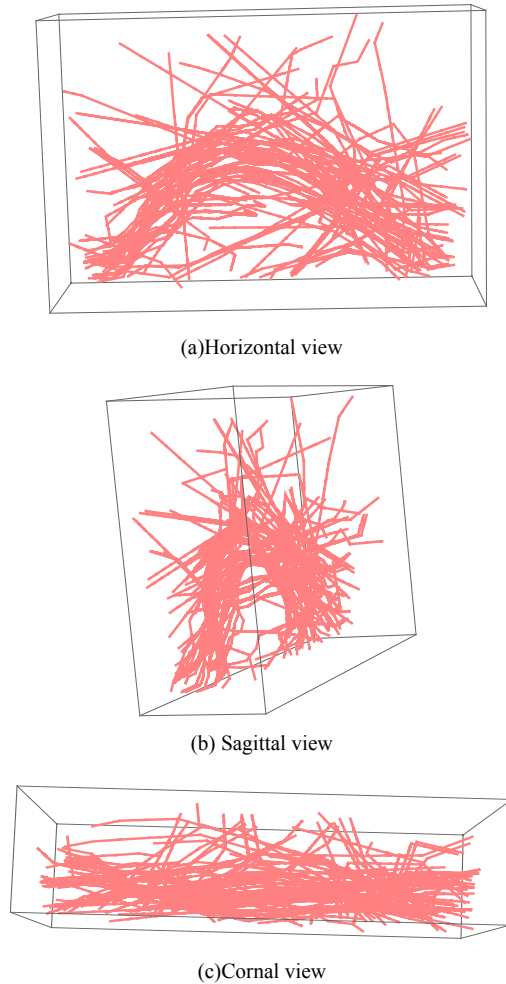


Fig. 4 One of the reconstruction images of fibers in the brain white matter in different view.

$$v_{prop} = Cl \times e_1 + (1 - Cl) \times ((1 - \omega_{punct})v_{in} + \omega_{punct}v_{out})$$

Where ω_{punct} is a user controlled parameter, Cl is the linear anisotropy indices, v_{in} is the direction of the previous propagation direction and v_{out} is the incoming direction transformed by the tensor matrix D [6-7]. The fiber direction is calculated by the formulat in Eq. (5).

Using a simple method get a transcendent direction to reduce the calculation quantity during calculating the propagation points on the grid for next step by the 3D Cyrus Beck algorithm.

In regions with high anisotropy, the main eigenvector can be regarded as the fiber direction. But in regions with low anisotropy, the main diffusion direction is meaningless.

Hence we must use different formulas to describe the fiber direction according to different diffusion shape.

V. CONCLUSION

Diffusion tensor image (DTI) is an important technique for the in-vivo investigation of brain white-matter connectivity. In this paper, we presented a new robust fiber tracking method in diffusion tensor imaging. The method include three situations and the joint utilization of the preference direction determined by tensor analysis, the FA values, and the previous propagation directions. This method can reduce the error between the tracking direction and the real fiber direction. The results show the improvement on fiber tracking by generating more smooth fiber bundles with less errors.

ACKNOWLEDGMENT

The authors thank Chunying Zhang, Jia Liu for helpful discussions on fiber tracking of diffusion tensor imaging and Han van Triest for Mathematica programming guidance.

REFERENCES

1. Dorit Merhof,Markuu Sonntag, Frank Enders, Hybrid Visualization for White Matter Tracts using Triangle Strips and Point Sprites. IEEE Transactions on visualization and computer graphics, vol.12, NO.5, September/October 2006
2. P.J. Basser, J. Mattiello, and D. LeBihan, MR diffusion tensor spectroscopy and imaging. Biophys J, vol. 66, no. 1, pp. 259-267, 1994.
3. 李德军,包尚联,马林,基于PC Matlab 平台的扩散张量参数的计算.Chin J Med Imaging Technol, vol.20, no. 7,2004
4. 陈穗芬,刘哲星,江贵平,陈武凡,基于扩散形状的DTI纤维跟踪算法研究.中国医学物理学杂志, vol.24, no. 3, May, 2007.
5. Xin Zhao, Mingshi Wang, Wei Gao, Haiying Liu, White Matter Fiber Tracking Method by Vector Interpolation with Diffusion Tensor Imaging Data in Human Brain. Proceedings of the 2005 IEEE Engineering in Medicine and Biology 27th Annual Conference, September 1-4, 2005
6. 赵欣,基于扩散张量的脑白质内神经纤维的重建算法.中国学术期刊电子杂志社, 2006, pp 39-48.
7. Weinstein D, Kindlmann G, Lundberg E. Tensorlines: advection-diffusion basee propagation through diffusion tensor fields. IEEE Visualization Proceedings, San Francisco, 1999, pp 249-253.
8. Lazar M, Weinstein D M, Tsuruda J S, et al. White matter tractography using diffusion tensor deflection. Human Brain Mapping, 2003, vol. 18, no. 4, pp 306-321
9. David F. Rogers 著,石教英,彭群生等译,计算机图形学的算法基础(原书第2版).机械工业出版社 2002, pp 177-181

Detection of blood vessels in retinal images using improved iterative threshold probing of a matched filter response

Yongli Wang¹, Huihai Lu², Mantao Xu² and Jiwu Zhang²

¹ Department of Biomedical Engineering, Shanghai Jiao Tong University, Shanghai, China

² Global R&D Center, Carestream Company, No. 27, New Jinqiao Road, Shanghai, China

Abstract — In this paper, an automated method is proposed to segment blood vessels in retinal images. An input retinal image is first filtered by Gaussian filters, outputting a so-called matched filter response (MFR) image. Feature points are then extracted from the MFR image and used as starting points for improved iterative adaptive local threshold probing.

Keywords — Retinal images, blood vessels segmentation, matched filter, local threshold, threshold probing.

I. INTRODUCTION

There is a lot of physiology information contained in retinal images. Many diseases, including diabetes, hypertension, and arteriosclerosis, which are relevant to cardiovascular, can be detected earlier in retinal blood vessels. Veins and arteries have many observable features, including diameter, color curvature, and opacity (reflectivity), which can serve as diagnostic indicators. As in normal retinal image, the ratio between diameter of arteries and vein is about 2:3, and when a patient appears abnormal, such as hypertension, the ratio changing to about 1:1, vascular reflectivity become smaller, along with the vascular also change the direction of straight. With clear retinal blood vessels, eye care specialist could do better treatment evaluation.

Previous method to segment retinal blood vessels generally fall into three categories: window-based [1] [3] [4], estimate a match at each pixel for a given model against the pixel's surrounding window. Classifier-based, a low-level algorithm is first used to produce a segmentation of spatially connected regions, and then the regions are classified as blood vessel or not blood vessel [4]. Tracking-based, utilize a profile model to incrementally step along and segment a vessel [6].

In this paper, we propose an automated method for segmenting blood vessels in retinal images. This algorithm contains three parts. First preprocess on raw retinal images. Second convolve the matched (Gaussian) filter with pre-processed image. Third Feature points are then extracted from the MFR image and used as starting points for iterative adaptive local threshold probing.

II. ALGORITHM

A. Pre-processing

The preprocessing algorithm can be divided into three components.

First, for the convenient of image process, getting the region of interesting in retinal images.

Second, getting green band of retinal images. In order to simply enhance the contrast of retinal fundus image, some information is commonly discarded before processing; green band displays the best vessels/background contrast, and the greatest contrast between the optic disk and the retinal tissue [2].

Third, illumination equalization [7]. The illumination in a retinal image is uneven. The imbalance is primarily due to an optical aberration, which is the result of an improper focusing of light through an optical system. The result is that the brightness of the image generally decreases radially outward from near the center of the image. So illumination equalization is necessary.

B. Matched (Gaussian) Filter for Blood Vessel

Based on the observation that cross-section intensity profiles of blood vessels are Gaussian shaped [2], a few representative samples of blood vessel gray-level profiles along directions perpendicular to their length are plotted in Fig.1. A pre-processed retinal image is filtered by a set of Gaussian filters with different orientations, outputting a so-called matched filter response (MFR) image. A set of 12 such kernels is applied to a fundus image and at each pixel only the maximum of their responses is retained.

Gaussian curve used in this paper:

We truncate the trail at $u = \pm 3\delta$. A neighborhood N is defined such that

$$N = \{(u, v) \mid |u| \leq 3\delta, |v| \leq L/2\} \quad (1)$$

The corresponding weights in the kernel are given by

$$k_i(x, y) = -\exp(-u^2 / 2\delta^2), \forall \bar{p}_i \in N \quad (2)$$

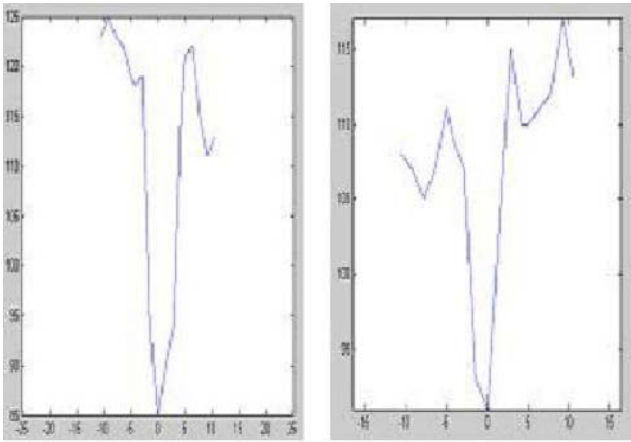


Fig. 1 The gray-level profiles of cross section of several blood vessels in the image of Fig. The X-coordinate is the distance in pixels from center of blood vessel, and the Y-coordinate is gray level intensity

C. Improved Iterative Threshold Probing

Feature points are then extracted from the MFR image and used as starting points for iterative adaptive local threshold probing. This part includes two steps.

First, extract seeds from MFR image [2]. Threshold the MFR image [5], skeleton and get VCL (vessel central lines) of MFR image, then make an empty queue, EndPntsQueue, and initialize it according to the following:

- Erase all branchpoints in the VCL image. (Branchpoints may be discovered as any pixels for which a traverse of the eight bordering pixels in clockwise order yields more than two foreground-to-background transitions.)
- Discard segments which are less than a pre-defined threshold, MinLength.
- Find endpoints and put them into EndPntsQueue. (Endpoints may be discovered as any pixels for which a traverse of the eight bordering pixels in clockwise order yields only one foreground-to-background transition.)

Second, start from seeds for iterative adaptive local threshold probing, and get the result image. During the threshold probing, we set a series of criteria to test the probing area, and ultimately decide whether the area being probed is blood vessel or not. Probe pixels in EndPntsQueue conduct the following tests.

- a. Get first pixel in EndPntsQueue P, $T = \text{gray-level-of-P}$.
- b. If $T > T\text{-level}$, region grow.
 - i) If pixel P has been labeled as vessel, find P's 3*3 neighbors {
If there is pixel hasn't been labeled as vessel {Go to step b.ii}
Else {Find in P's 5*5 neighbor

If there are pixels haven't been labeled as vessels { find the biggest gray pixel P', then replace P with pixel P'. Go to step b.ii }
Else make region S has no pixel, go back to step a) }

- ii) All pixels connected to P with gray level not lower than T & haven't been labeled as vessel are putted into region S.
- c. Test region S.
 - i) If the size of region is zero, go back to step a.
 - ii) If pixel P has been labeled as vessel, during T varies from T1 to T2 (where $T1 - T2 = 20 * \text{Dec}$), the size of region grow not more than 20 pixels, go to step e.
 - iii) If the size of region is smaller than Smax {Save this region in a temporary vector temp1.}
Else {If temporary vector temp1 is not empty {Replace the region S with vector temp1. Go to step e.} }
 - iv) If pixel P has been labeled as vessel {
If the branches in the region is smaller than 5 { Save this region in a temporary vector temp2.}
Else {Replace the region S with vector temp2. Go to step e.} }
 - v) If pixel P hasn't been labeled as vessel {
If the ratio (total-pixels-in-piece/branches-in-piece) $\geq T\text{-tree}$ { Save this region in a temporary vector temp3.}
Else {Replace the region S with vector temp3. Go to step e.} }
 - d. If all tests are ok, $T = T - \text{Dec}$ (const) and go back to the step 2.b.
 - e. If any test failed { If pixel P has been labeled as vessel {If S (size of region S) < S-fixed (const) or S touches previously vessel-classified region {
Label region S as vessels.
Add endpoints of S into EndPntsQueue.}
Else if S (size of region S) > Smin or S touches previously vessel-classified region {
Label region S as vessels.
Add endpoints of S into EndPntsQueue.} } }
 - f. Go back to step a till EndPntsQueue is empty.

III. RESULTS AND DISCUSSIONS

There are six parameters for our algorithm: S-max; S-min; T-tree; T-level; S-fixed and Dec. In this paper we used the parameter as followed: S-max = 5000, S-min = 50, T-tree = 100, T-level = the lowest gray level of MFR image, S-fixed = 1000, Dec = (the highest gray level of MFR images - the lowest gray level of MFR image)/1000.

We test our methods on 20 images, which include both normal and abnormal retinal fundus images [8]. One of the results is below.

The method proposed in my paper is more effective in detecting small vessels for it has special probing tests on small vessels. The results prove that it has obviously improvement on detecting small vessels.

Performance was established as follows. Any pixel which was hand labeled as vessel, and also be thought as vessel during this algorithm was counted as a true positive.

Any pixel which was hand labeled as not vessel but be thought as vessel during this algorithm was counted as a false positive. The true positive rate is established by dividing the number of true positives by the total count of pixels hand labeled as vessel. The false positive rate is established by dividing the number of false positives by the total count of pixels hand labeled as not vessel. The method described in this paper segments roughly 80% of the vessels in a retinal fundus image, and the false position rate is only 5%.



Fig. 2 A raw retinal images

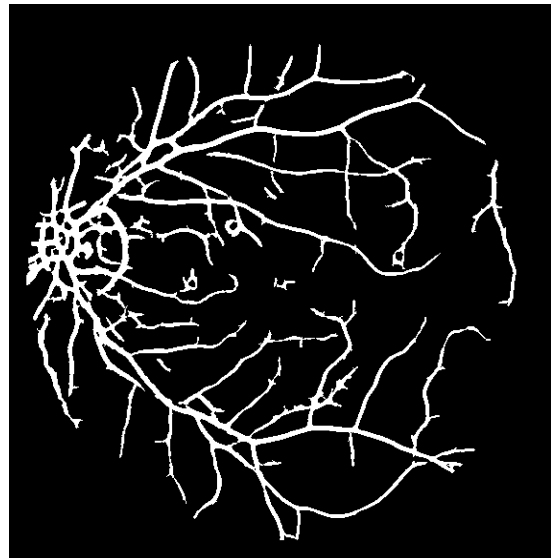


Fig. 4 A result from improved iterative threshold probing

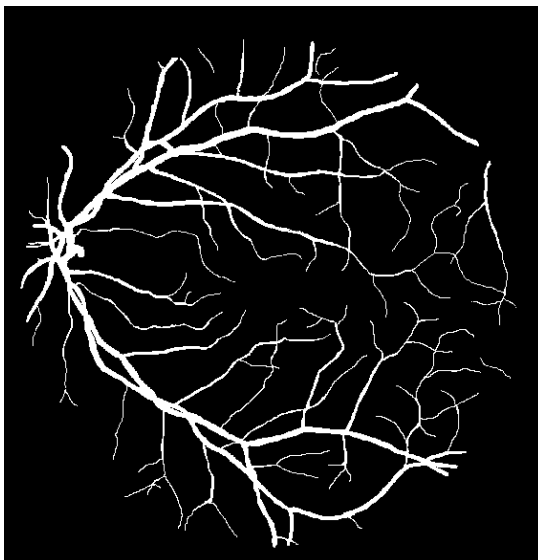


Fig. 3 A hand-labeled ground truth vessels segmentation of Fig.2

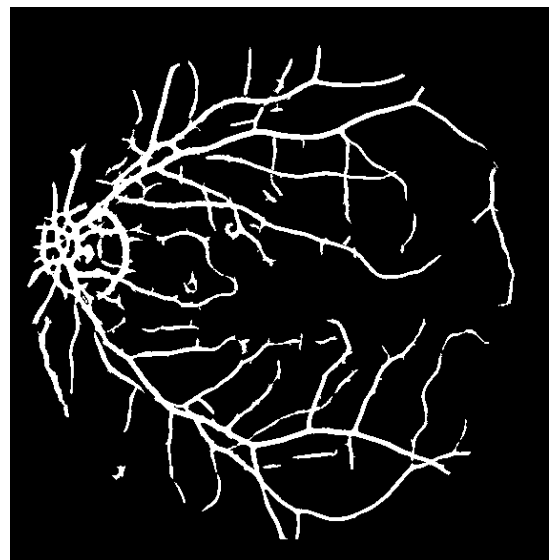


Fig. 5 A result from threshold probing for comparison

IV. CONCLUSION

In this paper, we use improved iterative adaptive local threshold probing, which is better than global threshold and morphology, for this probing method is more stable. Also the method proposed in my paper is more effective in detecting small vessels for it has special probing tests on small vessels. The results prove that it has obviously improvement on detecting small vessels. The seeds we need for probing are easier to be detected. Because of low vessels/background contrast and different gray level of vein and arteries, local threshold is more feasible. Experimental results show that the method is suitable to detect both large and small blood vessels.

REFERENCES

1. S. Chaudhuri, S. Chatterjee, N. Katz, M. Nelson, and M. Goldbaum, "Detection of blood vessels in retinal images using two-dimensional matched filters," *IEEE Trans. Med. Imag.*, vol. 8, pp. 263–269, Sept. 1989
2. A. Hoover, V. Kouznetsova, and M. Goldbaum, "Locating blood vessels in retinal images by piece-wise threshold probing of a matched filter response," *IEEE Trans. on Medical Imaging*, vol. 19, no. 3, pp. 203–210, 2000
3. Qin Li, Jane You, Lei Zhang, Prabir Bhattacharya: "Automated Retinal Vessel Segmentation Using Gabor Filters and Scale Multiplication." *IPCV 2006*: 22-28
4. Soares J.V.B., Leandro J.J.G, Cesar Jr, R.M., Jelinek H.F. and Cree M.J., "Retinal Vessel Segmentation Using the 2-D Morlet Wavelet and Supervised Classification", *IEEE Trans. Med. IM.*, 25, pp. 1214-1222, 2006
5. Xue Dong Yang, Vipin Gnpta, "An improved Threshold Selection Method for Image Segmentation." *Electrical and Computer Engineering. 1993. Canadian Conference on*. Vol.1, pp.531-534. Sep. 1993
6. Y. Tolia and S. Panas, "A fuzzy vessel tracking algorithm for retinal images based on fuzzy clustering," *IEEE Trans. Med. Imag.*, vol. 17, pp. 263–273, Apr. 1998
7. A. Hoover and M. Goldbaum, "Locating the optic nerve in a retinal image using the fuzzy convergence of the blood vessels," *IEEE Trans. on Medical Imaging*, vol. 22, no. 8, pp.951-958. Aug. 2003
8. University Medical Center Utrecht, Image Sciences Institute, Research section, Digital Retinal Image for Vessel Extraction (DRIVE) database, [Online]. Available: <http://www.isi.uu.nl/Research/Databases/DRIVE>

An Auto-Reference, Auto-Correlation and Adaptive Interference Cancellation Theories and Techniques (AAA-ICT) Used to the Single Trial of Slow Cortical Auditory Evoked Potentials

Zhengxiang Xie, Hong Li, Zhifang Wang, Ying Wang, Yuhong Liu

The Department of Biomedical Engineering in Chongqing Medical University, Chongqing, China

Abstract — An auto-reference, auto-correlative and adaptive interference cancellation theories and techniques (AAA-ICT) used in the single trial of Slow cortical auditory Evoked Potentials (SCAEP, including the P1-N1-P2) was proposed on the basis of analyzing the defects of traditional averaging theory for extracting evoked potential, knowing of the characteristic of spontaneous electroencephalo-signal (S-EES) and the special environment of extracting evoked potential (EP). The segment of reference signal, which has the best correlation with evoked electroencephalo-signal (E-EES), was obtained according to the method of calculating the sliding correlation point by point between E-EES and reference signal, and then, the cancellation factor between E-EES and the most correlative reference signal segment was derived by the least square method (LSM), at last, single trial of FVEP was acquired by interference cancellation.

Keywords — Slow cortical auditory EPs, Single trial, Auto-reference, auto-correlation, adaptive interference cancellation, Multi-media sound technique

I. INTRODUCTION

The traditional extraction method of Evoked Potential (EP) is the averaging technique^[1]. The defects of this technique are: (1) It is hard to judge the change of latency and/or amplitude of EP between stimuli; (2) Background electroencephalo-signal (B-EES) is not the pure random signal (the EES used in clinical diagnosis includes Δ wave (Frequency: 0.5~3Hz), Θ wave (Frequency: 4~7Hz), A wave (Frequency: 8~13Hz), B wave (Frequency: 14~31Hz)), whose mean is zero; (3) Averaging lose the higher frequency component which is related with the stimuli^[2-4]. There is much attempt about the single trial of EP^[5-14].

The spectrum analysis of the slow cortical auditory Evoked Potentials (SCAEP) shows that the main frequency of SCAEP overlaps with the B-EES seriously. So, it is hard to achieve the single trial of SCAEP using the normal filtering methods (including Kalman filtering, wavelet filtering etc.).

Based on the defects of the traditional averaging and the research of single trial home and aboard, according to the characteristic of the EES and the special environment of extracting the reference signal of S-EES from the same

electrode where the E-EES extracted, we present the Auto-reference and Autocorrelation and Adaptation Interference Cancellation Theories and Techniques (AAA-ICT)^[4], to realize the single trial of SCAEP.

II. BACKGROUND

The original of single trial is the clinic practice and the theoretical analysis. The clinic practice shows EP is not the signal whose latency and amplitude is unchanged.

2.1 Defects of SCAEP using averaging method

2.1.1 Basic assumption of averaging method

(1) Background signals, including the B-EES, 50Hz power frequency signal and other interference, are not white noise (Mean=0);

(2) SCAEP is the signal whose latency and amplitude is unchanged;

(3) SCAEP signal is always plused to background signal.

Only that all of these assumption are definite, we can extract the SCAEP based on following theory:

$$\begin{aligned} \text{SCAEP}(t) &= \sum \text{EES}_i(t) / N = \sum (\text{SCAEP}_i(t) + \text{BG}_i(t)) / N \\ &= \text{SCAEP}(t), i=0, 1, 2, \dots, N-1, N \rightarrow \infty \end{aligned} \quad (1)$$

SCAEP(t) means the characteristic unchanged SCAEP signal between stimuli. $\text{EES}_i(t)$, $\text{SCAEP}_i(t)$ and $\text{BG}_i(t)$ means the portion of i^{th} stimulus attributable to evoked EES including SCAEP(t), SCAEP signal and all background interference, respectively.

If the mean of B-EES is not 0, the E-EES between stimuli is changing^[18], then

$$\begin{aligned} \text{SCAEP}(t) &= \sum \text{EES}_i(t) / N = \sum (\text{SCAEP}_i(t) + \text{BG}_i(t)) / N \\ &= \text{ASCAEP}(t) + \text{P-ASCAEP}(t), i=0, 1, 2, \dots, N-1, N \rightarrow \infty \end{aligned} \quad (2)$$

ASCAEP(t) is the averaged SCAEP(t), P-ASCAEP(t) (pseudo- ASCAEP(t)) is the result of averaged background signals, we call artificial ASCAEP.

2.1.2 Defects of the basis suppose for averaging

(1) B-EES is not white noise: ① B-EES have special waves in clinical diagnosis, which are random because of the sampling rate; ② The mean of B-EES is not 0, it will be averaged

in SCAEP; ③B-EES includes the DC component^[17], the DC also will be include in SCAEP.

(2) SCAEP's characteristics (such as Latency and amplitude) are changing with the stimuli^[4, 15].

2.1.3 Defects of the averaging SCAEP

(1) Averaging SCAEP is the averaging of EP produced by every stimulus, it smoothes the variance of the latency and the amplitude of the EP^[4, 15].

(2) The averaging SCAEP smoothes the higher frequency related with the stimulus.

(3) Averaging SCAEP includes the DC component of B-EES and the averaging result, especially, the DC component can not be removed by the averaging technique, only can be eliminated by AAA-ICT.

2.1.4 Rationality meaning of averaging SCAEP

Although the averaging smoothes the latency and amplitude variance in each EP^[4, 15], certainly it includes the mean of each EP's common component. This is the reasonable meaning of averaging. Correctly, SCAEP extracting using traditional averaging technique not only have the averaged SCAEP, also include all averaged background signal.

2.2 Auditory stimulator based on the Multi-media sound technique

For the single trial of Auditory Evoked Potentials, the Multi-media sound technique was used to design an auditory evoked potentials stimulator. This stimulator is controlled by a personal computer. The stimulator can control the stimulating frequency, latency and volume of the sound stimuli. It is designed based on the Microsoft Windows operation system.

III. AAA-ICT

3.1 Basic hypothesis of AAA-ICT

(1)B-EES is chaotic signal, with the characteristic of infinite loop but incomplete repeated, but in a certain precision bound, B-EES has approximately repeating characteristic^[16]. So, there is a segment of signal in B-EES, which has the best correlation with E-EES, this segment can mostly cancel the B-EES included in the E-EES, and only left the evoked component SCAEP related with the stimulus.

(2) SCAEP plus with the B-EES.

(3)No apriority suppose of the SCAEP's characteristic.

3.2 Special environment of the extracting of EP

The points of the special environment of the extracting of EP have: the stimulus (evoked) signal can be controlled and be produced discontinuously, but the EES produces continu-

ously. The EES with no stimulus called spontaneous EES(S-EES), and after stimulus called evoked EES(E-EES). EES can be obtained with the special electrode on the scalp, and the S-EES and E-EES can be obtained in succession, it makes sure that we obtain a sufficient reference signal with the same electrode. Thus, the reference signal obtained with the same electrode called auto-reference signal. To obtain the auto-reference signal which is in the absolute same test environment with the E-EES is the key point of the AAA-ICT.

3.3 Basic theory of AAA-ICT

3.3.1 Basic idea of A AA-ICT

The basic theory of AAA-ICT is shown in the Fig1. In Fig1, the dash line of the reference signal REF(q) means using the same electrode as the E-EES X(n). The AAA-ICT used in the single trial of EP has three main processes: (1) beginning with the REF(q) (q=0), calculate the sliding correlation point by point between X(N) and REF(q), then choose and output the segment of the REF_m(n) which has the best correlation with the X(n); (2) By the least square method(LSM), the cancellation factor W is self-adaptively chose by the X(n) and the REF_m(n), and output W* REF_m(n); (3) Complete the cancellation of the X(n) and W* REF_m(n), and the EP(n) is acquired. For general meaning of this technique, special evoked EES sign is not invited here.

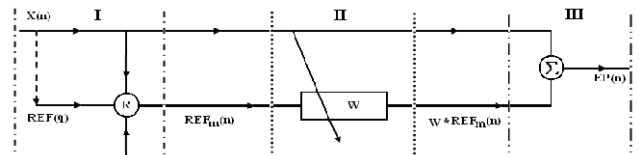


Fig. 1 The scheme of AAA-ICT

3.3.2 AAA-ICT basic operation

(1)Auto-reference: the reference signal from an electrode is called auto-reference signal;

(2)Auto-correlation: produce the signal segment of the REF_m(n) which has the best correlation with the X(n) in the reference signal REF(q)^[4].

Suppose the length of REF (q) is Q, the length of X(n) is N, and Q>>N, showing as the Fig2. Beginning with the REF(q) (q=0), choose the same length REF_i(q) with X(n) and calculate the sliding correlation point by point between

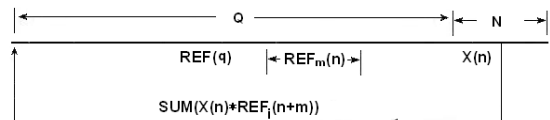


Fig. 2 The scheme for finding maximal correlation sequence REF_m(n)

$X(N)$ and $REF_i(q)$, then obtain a correlation coefficient serial $R(p)$, $i=p=0,1,2,\dots,P-1$,

$$P = 1 + Q - N \quad (3)$$

The correlation coefficient serial is

$$R(p) = \sum [X(n) * REF_i(n)], \quad i=0,1,2,\dots,P-1 \quad (4)$$

The max correlation coefficient is

$$R(m) = Max [R(p)] \quad (5)$$

In the formula above, m is the beginning point of $REF(q)$ serial which has the max correlation coefficient with $X(n)$, this serial is marked as $REF_m(n)$. $REF_m(n)$ has the best correlation with $X(n)$. The sliding correlation between two signals which are obtained from the same electrode is called (sliding) auto-correlation.

(3) Adaptive: by the least square method (LSM), calculate the cancellation factor W of $REF_m(n)$ and $X(n)$.

$REF_m(n)$ can ensure the best statistic comparability with $X(n)$, but cannot ensure the least square (least energy error). For canceling B-EES most, the LMS is used to calculate the cancellation factor W . Suppose

$$EP(n) = X(n) - W \times REF_m(n), \quad n=0,1,2,\dots,N-1 \quad (6)$$

then the error energy is

$$\sum EP^2(n) = \sum [X(n) - W \times REF_m(n)]^2, \quad n=0,1,2,\dots,N-1 \quad (7)$$

based on the LMS, calculate the first step derivative about W of formula (7), and let it equal to 0,

$$\frac{d[\sum EP^2(n)]}{dw} = \frac{d[\sum [X(n) - W \times REF_m(n)]^2]}{dw} = 0, \quad n=0,1,2,\dots,N-1 \quad (8)$$

then we can acquire the condition of the least energy error

$$W = \frac{\sum [X(n) \times REF_m(n)]}{\sum REF_m^2(n)}, \quad n=0,1,2,\dots,N-1 \quad (9)$$

(4) Interference cancellation: introducing the cancellation factor calculated in formula (9) into the formula (6), can cancel the interference signal including B-EES mostly, then acquire the evoked signal $EP(n)$.

IV. OBJECT AND METHOD

This research is agreed by the ethic committee in Chongqing medical University, and choose 20 young volunteer aged between 20~30 and 20 old volunteer aged between 60~70 to take the experiments. The software, which is used to acquire the single trial of SCAEP by AAA-ICT, is designed by self. In this research, the intensity of sound stimu-

lus is 30dB, the duration is 32ms, and the stimulating frequency is 1Hz. The Ag/AgCl electrodes like dish are invited in collection signals, whose diameters are 10mm. The position of the electrodes is: the active electrodes on the Cz, the passive electrodes on each earlap, the floating GND electrodes on the center of forehead juxtaposition. The places where electrodes are placed is got rid of lipid by absolute alcohol first. The electrodes are smeared with the electricity guided cream, this can pledge the resistance between electrode and skin is below 5KΩ. The examination is taken in the shielding room. The volunteer is sitting, relax, close eyes for 5minutes. Then start to sample the E-EES. The sampling rate is 512 Hz, the duration of B-EES is 120s and E-EES is 1s. The filtering band width is 0.1Hz to 75Hz, the gain is 20,000 fold.

V. RESULTS

5.1 Application of AAA-ICT

The interference cancellation based on AAA-ICT as the Fig3. In Fig3, the up is the best reference EES(B-EES), the below is the single trial of SCAEP(S-SCAEP). The main characteristics of PI-N1-P2 are the latency and amplitude, the unit of latency is millisecond (MS) and the amplitude is microvoltage (μV) as shown in Fig3. The horizon is the latency, and the vertical is the amplitude.

5.2 20 overlapping S-SCAEP, A-S-SCAEP and A-SCAEP

In Fig4, the overlapping of S-SCAEP shows that the single trial SCAEP have the repeating characteristic, but it also shows the latency and amplitude of S-SCAEP are changing obviously with the stimuli. The results in Fig3 and Fig.4 are form the young health individual.

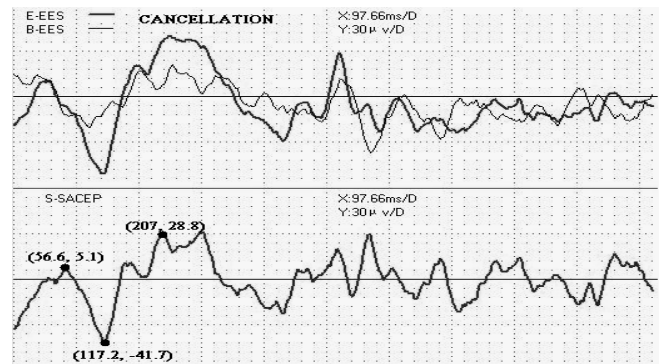


Fig. 3 the interference cancellation based on AAA-ICT

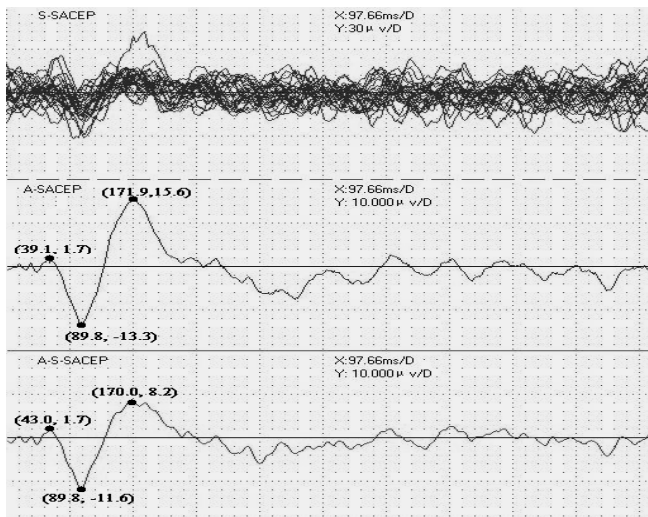


Fig. 4 Overlapping of S-SCAEP, A-SCAEP and A-S-SCAEP

5.3 Mean and SD of the latency and amplitude

According to the theories mentioned above, we constructed the hardware system, designed the software system, and successfully, stably extracted the single trial of slow cortical auditory evoked potentials (including the P1-N1-P2) from 20 healthy young individuals and 20 old individuals with the sampling frequency of 512Hz and 512 sampling points, whose ages are ranged from 20 to 30 years old and from 65 to 75 years old. For example, the mean and SD of the latency of P1, N1, P2 in 20 measurements of a young individual are 45.5094 ± 11.1 , 94.8927 ± 16.7833 and 165.4677 ± 26.7583 , respectively.

5.3.1 Young Health individuals

The mean and SD of the latency of P1, N1, P2 of 20 young individual are 46.5820 ± 15.918 , 94.6289 ± 20.6055 and 163.0859 ± 14.6484 , then mean and SD of the amplitude of P1, N1, P2 are 2.0325 ± 3.8269 , -5.8289 ± 4.7913 and 7.2754 ± 9.5947 , respectively.

5.3.2 Old individuals

The mean and SD of the latency of P1, N1, P2 of 20 old individual are 44.2425 ± 20.2106 , 103.1087 ± 31.6569 and 204.8340 ± 43.2129 , then mean and SD of the amplitude of P1, N1, P2 are 1.7037 ± 3.91156 , -4.0536 ± -4.0029 and 4.5726 ± 3.3620 , respectively.

5.3.3 Conclusion of the signal trial

The mean and SD of latency and amplitude show: (1)The amplitude varies much faster with the stimuli than latency; (2)The latency of P1 is the most stably; (3)The latency of P2 of old individuals is much longer than young individuals.

VI. CONCLUSION

The system established on the basis of our idea and theories about the Auto-Reference, Auto-Correlative and Adaptive Interference Cancellation has worked very well for singly extracting slow cortical auditory evoked potentials (including the P1-N1-P2). It is demonstrated that the idea, theories and techniques are more correct and better. The novelty of the key idea about the auto-reference signal is very distinct.

ACKNOWLEDGMENT

I would like to express my heartfelt gratitude to the support by the National Natural Science Foundation of China. My deepest gratitude goes to Professor Xie zhengxiang. I am greatly indebted to the teachers and my fellow classmates at the Department of Biomedical Engineering in Chongqing Medical University. I also owe my sincere gratitude to my friends and the volunteer who give me their help.

REFERENCES

1. Pan YF. Evoked Potentials in Medical Practice. 2nd ed. People's Medical Publishing House, Beijing: 2000: 341-342
2. Schmidt RF and Thews G. Human Physiology. Berlin. Germany: Springer-Verlag, 1983: 151-157.
3. Hunan medical college. Physiology. People's Medical Publishing House, Beijing: 1978: 376-377
4. Nie N, Yao DZ and Xie ZX. Biological Medical Digital Signal Processing Technology and Application. Science Publishing House, Beijing: 2005: 289-291
5. Zouridakis G, Iyer D, Diaz J, Patidar U. Estimation of individual evoked potential components using iterative independent component analysis. *Phys Med Biol*. 2007;52(17):5353-68
6. Zhang H, Zheng CX. Evoked Potential Extraction Based on Multi-channel Time-frequency Coherence. *Acta Biophysica Sinica*, 2003; 19(3): 303-7
7. Zouridakis G, Jansen BH, Boutros NN. A fuzzy clustering approach to EP estimation. *IEEE Trans Biomed Eng*. 1997;44(8):673-80.
8. Zenker F, Barajas JJ. Auditory P300 development from an active, passive and single-tone paradigms. *Int J Psychophysiol*. 1999;33(2):99-111
9. Lam BS, Hu Y, Lu WW, et al. Multi-adaptive Filtering Technique for Surface Somatosensory Evoked Potentials Processing. *Med Eng Phys*, 2005; 27(3): 257-66
10. Thakor NV. Adaptive Filtering of Evoked Potentials. *IEEE Trans Biomed Eng*, 1987; 34(11): 6-12
11. Vaz CA, Thakor NV. Adaptive Fourier Estimation of Time-varying Evoked Potentials. *IEEE Trans Biomed Eng*, 1989; 36(4): 448-55
12. Westerkamp JJ, Williams R. Adaptive Estimation of Single Response Evoked Potentials. *Biol Psychol*, 1995; 40(1-2): 161-8
13. Parsa V, Parker PA. Multireference Adaptive Noise Cancellation Applied to Somatosensory Evoked Potentials. *IEEE Trans Biomed Eng*, 1994; 41(8): 792-800

14. Li LP, Cheng JZ, Ma RS et al. Application of Time-frequency Filter of Wavelet to Single-trial ERP Extracting. *Journal of Biomedical Engineering*, 1998; 15(2): 116-9
15. Truccolo WA, Ding M, Knuth KH, et al. Trial-to-trial Variability of Cortical Evoked Responses: Implications for the Analysis of Functional Connectivity. *Clin Neurophysiol*, 2002; 113(2): 206-26
16. Xie ZX, Chen LC, Zhang SQ, et al. *Medical Signal's Digital Processing and Its Application*. Scientific and Technical Documents Publishing House, Beijing: 1992: 78-80, 31-36

Address of the corresponding author:

Author: Xie zhengxiang
Institute: The Department of Biomedical Engineering in Chongqing Medical University
Street: Yixueyuan Road No.1
City: Chongqing
Country: China
Email: bmezxxie@163.com

Study on the Algorithm of Surface Reconstruction of Defective Bone Based on Delaunay Triangulation

Fei You^{1,2}, Qingxi Hu¹, Qi Lu¹ and Yuan Yao¹

¹ Rapid Manufacturing Engineering Center, Shanghai University, Shanghai, China

² School of Mechanical Engineering, Jiangsu Teachers University of Technology, Changzhou, China

Abstract — 3D model reconstruction of defective bone is of great practical value in the application for medical diagnosis of bone, plastic, prosthesis surgery planning and so on. Based on Delaunay triangulation, an algorithm of surface reconstruction is proposed to reconstruct surface of defective bone in this paper. In the algorithm, data of CT 2D-images are input to build the space point dataset. The bounding box theory is applied to search k-nearest neighbors of p_i , and its normal vector is computed. K-nearest neighbor points of p_i are projected on the tangent plane, and its Delaunay 2D-neighbors are chosen from those projected points. Delaunay 3D-neighbors of p_i are gotten by mapping Delaunay 2D-neighbors. Delaunay 3D-neighbors are searched and matched to construct triangular mesh of surface. Then, the topology of Delaunay 3D-neighbors is reconstructed to identify the feature of hole. Subsequently, a weighted undirected connected graph is generated. EMST of this graph is generated by using Prim algorithm. After searching EMST based on the depth-first principle, the normal vector is adjusted to orient the same direction of surface. Lastly, according to the constructed topological relation, 3D geometric model of defective bone is reconstructed. The validity and reliability of algorithm are verified by computing a typical example, and its time and space complexity is lower.

Keywords — defective bone, surface reconstruction, Delaunay triangulation, k-nearest neighbor, local deformable spherical map

I. INTRODUCTION

The surface reconstruction technology was widely applied to medical analysis, reverse engineering, visualization, etc. Especially, 3D reconstruction of medical image is one of the research focuses in recent years. In this field, the surface reconstruction technology of defective bone is one important research. This technology is of great practical value in the application for medical diagnosis of bone, plastic, prosthesis surgery planning [1,2,3]. According to whether the reconstructed surface includes sampling points, algorithms can be divided into two categories. One is the interpolation algorithm as Delaunay tetrahedralization algorithm proposed by Marco Attene et al [4], Delaunay neighbors algorithm proposed by M. Gopi and Dongri Shan et al [5,6], deformable spherical map algorithm proposed by George K. Knopf et al

[7], and SOMF and RBF neural network algorithm proposed by Shengling Geng et al [8]. Another is the approximation algorithm as MC algorithm proposed by Hoppe et al [9], tangent plane approximation algorithm proposed by Xuemei Huang et al [10], local tangent planes algorithm proposed by Yupeng Li et al [11], improved MC algorithm proposed by Bangshu Xiong et al [12]. These are well applied to many fields. However, some limitation is still in these algorithms' application, as follows:

1. Sometimes the point set must respect conditions like uniform density if the algorithm is to reconstruct the surface correctly.
2. Many algorithms can only reconstruct surface without holes.
3. Many algorithms are limited in usage because they require excessively high computation times.

II. THE PROPOSED ALGORITHM

In this paper, an algorithm of surface reconstruction is proposed based on Delaunay triangulation. In the algorithm, data of CT 2D-images are input to generate the space point set P . The bounding box theory is applied to search k-nearest neighbors, and its normal vector is computed. Subsequently, Delaunay 3D-neighbors are computed to construct the triangular mesh of surface. The topology of Delaunay 3D-neighbor is readjusted to identify the feature of holes on the surface. Then, the normal vector is adjusted to orient the same direction of surface. Lastly, according to the constructed topological relation, 3D geometric model of defective bone is reconstructed.

A. Acquisition of space point set

Space point data of bone is obtained from 2D-image sequence that is gotten by using CT layered scan. The scan layer spacing S is from 0.5 to 5mm. If CT 2D-image sequence is arranged in the 3D coordinate W , coordinate value z of every pixel point on the last picture is zero, and z of every pixel point on the i th picture is $i \times S$. According to many experiment results, the gray threshold of CT image of

bone, δ , is from 90 to 228. If the gray value of one pixel point meets $\delta_i \in \delta$, coordinate value x and y of this pixel point in the scanning coordinate W' are computed. Then, they are transformed from W' to W , and one point, (x, y, z) , on the surface of bone is gotten by incorporating z of this point. After computing every pixel point of all pictures, the dataset of space points of bone can be generated.

B. Searching of k-nearest neighbors

K-nearest neighbors of p_i are one point set consisted of k points, for which the distances between p_i and them are shortest in P . The point in k -nearest neighbors is termed nearest neighbor point of p_i [13]. The steps for searching k -nearest neighbors are as follows:

Step 1: Range those unorganized points of P according to the coordinate value in order of z, x, y .

Step 2: Search the point in the cubical bounding box, which edges are parallel to coordinate axes, and its edge length is e and p_i is its centre.

Step 3: If the number of point in the box is less than k , then let $e=2e$ and repeat *Step 2*. Otherwise, label k -nearest points of p_i .

Step 4: Repeat *Step 2* and *Step 3* for all points of P .

C. Computation of vertex normal vector

The normal vector is computed by using k -nearest neighbor information. The normal vector \vec{n}_{pi} is the vector that minimizes the variance of the dot product between itself and the vectors from p_i to its k -nearest neighbors. If k -nearest neighbors are q_1 to q_k , the vectors from p_i to its k -nearest neighbors are $\vec{V}_j = q_j - p_i (1 \leq j \leq k)$. We want to find \vec{n}_{pi} such that it minimizes

$$\min \left(\frac{\sum_{j=1}^k (D_j - \frac{\sum_{j=1}^k D_j}{k})^2}{k} \right) = \min \left(\sum_{j=1}^k \left(\left(\vec{V}_j - \frac{\sum_{j=1}^k \vec{V}_j}{k} \right) \cdot \vec{n}_{pi} \right)^2 \right) \quad (1)$$

where $D_j = \vec{n}_{pi} \cdot \vec{V}_j \quad (2)$

The vectors \vec{V}_j can be viewed as the coordinates of the k -nearest neighbors with p_i as the origin, and the centroid of k -nearest neighbors is

$$C = \frac{\sum_{j=1}^k \vec{V}_j}{k} \quad (3)$$

Thus, the above equation can be rewritten as,

$$\min \left(\sum_{j=1}^k \left(\left(\vec{V}_j - C \right) \cdot \vec{n}_{pi} \right)^2 \right) \quad (4)$$

If A is a $k \times 3$ matrix where $\vec{V}_j - C (j=1,2,\dots,k)$ defines the row vectors, then the above expression reduces to

$$\min \left(\| A \vec{n}_{pi} \|_2 \right) \quad (5)$$

This minimization can be posed as the standard singular value decomposition. The eigenvector, which corresponds to the smallest eigenvalue of A , is the normal vector [5].

D. Computation of Delaunay nearest neighbor

The plane including p_i , which normal vector is \vec{n}_{pi} , is defined as the tangent plane Tp_i of p_i . The k -nearest neighbor point is projected to Tp_i to get the projected point set denoted as Set_Pro . The plane rectangular coordinate system, $X'O'Y'$, is set to Tp_i with p_i as its origin, line through p_i and the closest projected point (denoted as N_Pro) as X -axis. Delaunay 2D-neighbors of p_i are chosen from Set_Pro . Delaunay 2D-neighbor point is mapped to space to get Delaunay 3D-neighbor point set of p_i (showed as Fig.1). For Delaunay triangulation set (DTs) of one point set (PS) on the plane, two fundamental theorems are as follows [6]:

Theorem 1: If $p_1 \in PS, p_2 \in PS, p_3 \in PS$, where p_2 is the nearest point of p_1 , and the field angle formed by p_3 opposite in direction from edge p_1p_2 is the biggest, then $\Delta p_1p_2p_3$ is a triangle of DTs.

Theorem 2: If $p_1 \in PS, p_2 \in PS, p_3 \in PS, p_4 \in PS$ and $\Delta p_1p_2p_3$ is a triangle of DTs, where p_4 locates in the outside of p_1p_2 , and the field angle formed by p_4 opposite in direction from p_1p_2 is the biggest, then $\Delta p_1p_2p_4$ is a triangle of DTs.

Based on the proposed theorem, the searching algorithm of Delaunay 2D-neighbors of p_i is as follows:

Step 1: Let $p_1 = N_Pro$. Search p_2 from Set_Pro such that the field angle formed by p_2 opposite in direction from p_1p_1 is the biggest, and label $\Delta p_1p_1p_2$ and p_2 .

Step 2: Search p_3 from Set_Pro such that the field angle formed by p_3 opposite in direction from p_1p_2 is the biggest, where p_3 locates in the outside of p_1p_2 . Label $\Delta p_1p_2p_3$ and p_3 .

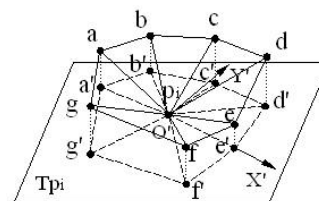


Fig.1 mapping relation from 2D-neighbor to 3D-neighbor of Delaunay

Step 3: If $p_3 \neq p_1$ then let $p_1 = p_2$, $p_2 = p_3$, and go to Step 2. Otherwise, end the algorithm.

E. Triangulation of point set

The most important task of surface reconstruction is to reconstruct triangular mesh which is equivalent to the original surface. Vertices p_{i-1} , p_i , and p_{i+1} form a triangular face if and only if $\{p_i, p_{i+1}\}$, $\{p_{i+1}, p_{i-1}\}$ and $\{p_{i-1}, p_i\}$ are consecutive Delaunay neighbors in ordered Delaunay neighbor lists of p_{i-1} , p_i , and p_{i+1} respectively. Matching Delaunay 3D-neighbor set of every point, the topology of triangular mesh of surface is easily reconstructed.

F. Topology reconstruction of holes' feature

1. Algorithm of local deformable spherical map

In the spherical SOFM lattice showed as Fig. 2, the nodes are arranged on a tessellated unit sphere, where each node represents a cluster unit. The self-organizing architecture arranges the weights, $W_{i,j,k}$, such that they reflect the inputs $X^n = [x_1^n, x_2^n, x_3^n] (n=1,2,\dots,N)$. X^i is connected to every node in the lattice by $W_{i,j,k}$. A unit located at (i, j, k) on the deformable sphere surface has an associated Region-of-Influence (ROI) defined by $NE_{i,j,k}$, which represents the time varying neighborhood radius. The steps of the algorithm are as follows [7]:

Step 1: Initialize the weights to small random values. Set the learning parameter μ and the number of cycles N_c .

Step 2: For each selected point, compute the error $D_{i,j,k}^n$

$$D_{i,j,k}^n = \sum_{m=1}^3 (x_m^n - w_{m,i,j,k})^2 \tag{6}$$

Step 3: The node with the lowest error value is selected as the winner. Update the weights to the winning node and all other nodes that are valid neighbors in the ROI.

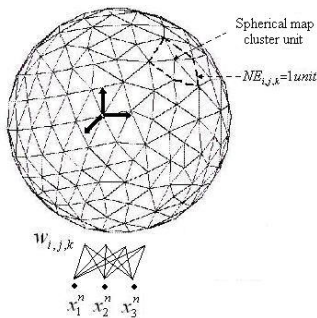


Fig.2 the basic structure of spherical self-organizing feature map

$$w_{i,j,k} (new) = w_{i,j,k} (old) + \alpha [X^n - w_{i,j,k} (old)] \tag{7}$$

where

$$\alpha = 0.001 + 0.2 \left[1.0 - \frac{NE_{i,j,k}}{3.0} \right] \tag{8}$$

Step 4: $NE_{i,j,k}$ is reduced based on the number of cycles. N_{ci} is the remaining number of training.

$$\text{IF } N_{ci} \leq \left(\frac{N_c}{3.0} \right) \text{ THEN } NE_{i,j,k} = 3units, \tag{9}$$

$$\text{IF } \left(\frac{N_c}{3.0} \right) \leq N_{ci} \leq \left(\frac{2N_c}{3.0} \right) \text{ THEN } NE_{i,j,k} = 1unit, \tag{10}$$

$$\text{IF } N_{ci} > \left(\frac{2N_c}{3.0} \right) \text{ THEN } NE_{i,j,k} = 0. \tag{11}$$

Step 5: At the end of each training cycle, Search the list for valid and invalid neighbors in the ROI. Replace any invalid neighboring node with one identified as valid.

Step 6: Repeat the process from Step 1 to Step 5 until N_{ci} is equal to N_c , and that is end.

2. Computation of ROI

The ROI is restricted to those lattice nodes that lie within the current span of $NE_{i,j,k}$. Only the nodes that are deemed linked to the winning node within $NE_{i,j,k}$ (showed as Fig. 3) will undergo an iterative weight change [7].

The ROI for every node is updated at the end of each training cycle while maintaining its total number of linked neighbors. The basic step is as follows:

Step 1: Select a central node and find its immediate connected neighbors.

Step 2: Use a distance measure to determine whether the current neighboring nodes are valid. Replace the invalid node with a new valid node. Label all valid neighbors.

Step 3: Select one of the labeled nodes and identify valid neighbors. Perform the same labeling process for all nodes connected to the central node selected in Step 1.

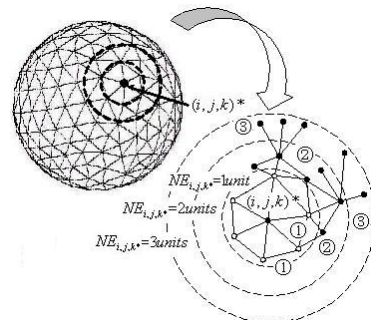


Fig.3 reassignment of neighbors within ROI of the winning node

Step 4: Repeat *Step 3* for all nodes identified as valid, and continue the evaluation process until the connected nodes extend to the boundary of $NE_{i,j,k}$.

G. Uniformization of normal vector

The vertex normal vector computed in 2.3th segment can be in two opposite direction. To uniform their normal vector, one normal vector direction can be adjusted to meet $\vec{n}_{pi} \bullet \vec{n}_{pj} \approx 1$. The steps are as follows:

Step 1: Connect every two points of neighbors with an edge, and assign $1 - |\vec{n}_{pj} \bullet \vec{n}_{pk}|$ to the edge. Construct the weighted undirected graph G with p_i as the root node.

Step 2: Generate EMST of G by using Prim algorithm. Search EMST based on the depth-first principle and adjust \vec{n}_{pi} . If $\vec{n}_{pj} \bullet \vec{n}_{pk} < 0$, then let $\vec{n}_{pj} = -\vec{n}_{pk}$.

Step 3: Compute the normal vector average of three vertices, \vec{n}_{ijk} and adjust the normal vector of triangle, \vec{N}_Δ . If $\vec{n}_{ijk} \bullet \vec{N}_\Delta < 0$ then reverse \vec{N}_Δ .

H. Geometric model reconstruction of surface

After reconstructing the topological relation, the information of edges and triangles containing the vertex is saved in the data structure of every point; the information of start-point and end-point of edge and two edge-shared triangles is saved in the data structure of every edge; and the information of three vertices, three edges, and three other triangles relative to vertices is saved in the data structure of every triangle. In this way, the reconstruction of geometric model can be done according to the topological structure of the constructed triangular mesh, such that the reconstructed smooth surface approximates the original surface.

III. IMPLEMENTATION AND CONCLUSION OF ALGORITHM

The algorithm of surface reconstruction described in this paper has been implemented with the typical example. The point cloud of local data of one defective skull is showed as Fig. 4. This space point set is consisted of 125668 points. The reconstructed surface model included 41889 triangles is showed as Fig. 5 by using the proposed algorithm, and the computation time is 297 seconds. From this it can be seen that the validity and reliability of algorithm are verified, and its time and space complexity is lower.

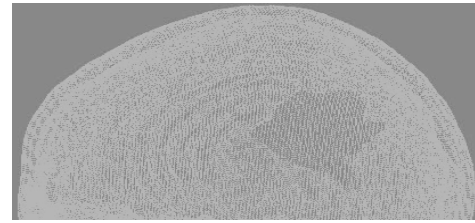


Fig.4 the point cloud of local data of one defective skull

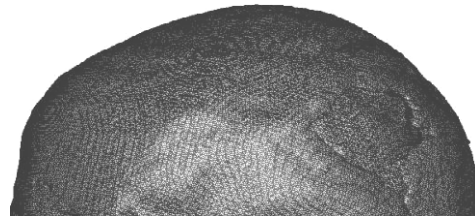


Fig.5 Local surface model of one defective skull

In this paper, the algorithm of surface reconstruction of defective bone based on Delaunay triangulation is proposed. A new algorithm for searching k-nearest neighbors and Delaunay 2D-neighbors are applied to accelerate the surface construction. These algorithms are very high effective to process massive data of the unorganized point set. The algorithm of local deformable spherical map described in this paper is better to solve the problem of the feature identification of holes in the surface reconstruction, and the precise surface of defective bone is generated. Moreover, the reconstructed surface will provide a more precise digital model for the repair of defective bone and 3D model construction of the bio-scaffold.

ACKNOWLEDGMENT

The authors express deep gratitude to National Natural Science Foundation of China (No. 50775134) for the financial support of this research project.

REFERENCES

1. Xujia Qin (2001) Study on the techniques for 3D reconstruction and visualization of medical images. Dalian university of technology, Dalian
2. Taifa Zhang (2006) The study of 3D surface reconstruction algorithm based on CT medical images. Xi'an university of technology, Xi'an
3. Xiuxia Liang (2006) Study on some problem of visualization of medical image data. Shandong university, Jinan
4. Marco Attene, Michela Spagnuolo. (2000) Automatic surface reconstruction from point sets in space. EUROGRAPHICS'2000, 19(3): 491-500

5. M. Gopi, S. Krishnan, C.T. Silva. (2000) Surface reconstruction based on lower dimensional localized Delaunay triangulation. EUROGRAPHICS'2000, 19(3):467-479
6. Dongri Shan, Yinglin Ke. (2003) Surface reconstruction from scattered 3D points based on 2D Delaunay neighbors. CHINA MECHANICAL ENGINEERING, 14(9):756-759
7. G.K. Knopf, A.P. Sangol. (2006) Freeform surface reconstruction from scattered points using a deformable spherical map. International Journal of Image and Graphics, 6(3):341-356
8. Shengling Geng, Baosheng Kang. (2007) Freeform surface reconstruction by SOMF and RBF neural network. Computer Engineering and Design, 28(12):2925-2927
9. Hoppe H, DeRose T, Duchamp T, et al (1992) Surface reconstruction Unorganized Points, SIGGRAPH'92 Proc. vol.2, Chicago, USA, 1992, pp 71-78
10. Xuemei Huang, Jiehong Chen, Pingjiang Wang. (1997) On the approximation of 3-D random data with a tangent plan. J. Huazhong Univ. of Sci. & Tech., 25(4):16-17
11. Yupeng Li, Lirong Luo. (2004) The method of accurate shape reverse based on 3D local tangent planes. Journal of Yanshan University, 28(3):214-217
12. Bangshu Xiong, Mingyi He, Huajing Yu. (2005) Fast reconstruction of surface based on spatial connectivity. JOURNAL OF SYSTEM SIMULATION, 17(1):75-78
13. Rurong Zhou, Liyan Zhang et al. (2001) Algorithmic research on surface reconstruction from dense scattered point. Journal of Software, 12(2):249-255

Author: Fei You

Institute: Rapid Manufacturing Engineering Center, Shanghai University

Street: 99 Shangda Road

City: Shanghai

Country: China

Email: yfreeman@shu.edu.cn

An Anisotropic Diffusion Model for Medical Image Smoothing by Using the Lattice Boltzmann Method

Yu Chen¹, Zhuangzhi Yan¹ and YueHong Qian²

¹ School of Communication and Information Engineering, Shanghai University, Shanghai 200072, China

² Institute of Applied Mathematics and Mechanics, Shanghai University, Shanghai 200072, China

Abstract — The anisotropic diffusion equation model proposed by the Perona and Malik is sometimes unstable. In this paper, we introduce an anisotropic diffusion model based on the Lattice Boltzmann method, and apply it to the fast anisotropic smoothing for medical images. Furthermore, we show that the LBM-based model is stable if the relaxation parameter is equal to or larger than one but smaller than two. To quantitatively evaluate and validate the model in medical image smoothing, we compared the model with Perona and Malik's method by calculating the signal to noise ratio. The experimental results show that our method outperforms over Perona and Malik's method in image denoising.

Keywords — Lattice Boltzmann method, Anisotropic equation, Image smoothing, Evolution equation

I. INTRODUCTION

Image denoising is a fundamental problem in the field of image processing and computer vision. Numerous image denoising algorithms exist in the computer vision and image processing literature. One of the most widely used models is the algorithm based on the anisotropic diffusion model proposed by Perona and Malik in 1990. Their goal is to smooth a region and keep its boundary sharp. The entire operation is a combination of forward and backward diffusion processes. However, the backward diffusion is an ill-posed process with the solution highly sensitive to tiny perturbations of the initial data [1]. This is mainly due to the unstable backward diffusion at the edges [2]. Furthermore, even when the initial data is smooth, the anisotropic diffusion equation may not have a solution.

The lattice Boltzmann method (LBM) is a newly developed numerical technique for solving partial differential equations [3]. One of the most important advantages of LBM is that it has parallel feature of implementation, because all nodes of LBM can be updated simultaneously. In this paper, we introduce an anisotropic diffusion model based on the lattice Boltzmann method, and apply it to the fast anisotropic smoothing for medical image. Numerical simulation shows that the LBM-based anisotropic diffusion model is accurate. For quantitatively evaluating our model in medical image smoothing, we compared the model with Perona and Malik's method by calculating the Signal to

Noise Ratio. The experimental results indicate that our method can smooth the noisy medical images very efficiently, and have a higher Signal to Noise Ratio than Perona and Malik's method.

II. LATTICE BOLTZMANN METHOD

LBM originated from lattice gas cellular automata (LGA) initially proposed by Frisch, et al. in their seminal paper [4]. They have shown that the Navier-Stokes equations can be derived in a suitable macroscopic limit from some simplified kind of "billiard game" representing streaming and collision of fluid particles. Suppose that particles are distributed over the nodes of a two-dimensional square lattice with diagonal links, and they propagate and collide on the nodes, as shown in Fig.1. A commonly used LGA model can be described as follows.

Let $n_i(\vec{r}, t)$ denote the particle state in direction i , at node \vec{r} and time step t , \vec{C}_i be the unit vector in direction i , and Ω_i be a collision operator of $n_i(\vec{r}, t)$. Assume that

$$n_i(\vec{r} + \Delta h \cdot \vec{C}_i, t + \Delta t) = n_i(\vec{r}, t) + \Omega_i(\vec{r}, t), \quad (1)$$

where Δt and Δh stand for the time and spatial intervals, respectively. The choice of \vec{C}_i is

$$\vec{C}_i = \begin{cases} (0,0), & i=0 \\ (\cos\theta, \sin\theta), & \theta=(i-1)\pi/2, \quad i=1,3,5,7 \\ \sqrt{2}(\cos\theta, \sin\theta), & \theta=(i-5)\pi/2+\pi/4, \quad i=2,4,6,8 \end{cases} \quad (2)$$

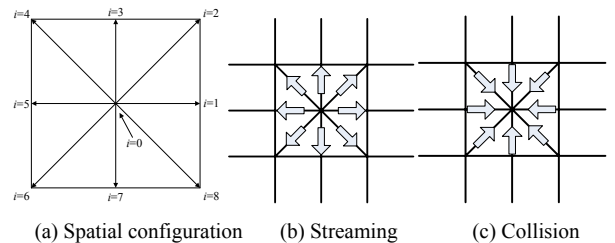


Fig.1 Spatial configuration of LBM, and streaming and collision of particles in the nodes.

Let $\rho(\bar{r}, t)$ be the total density at node \bar{r} and is defined as

$$\rho(\bar{r}, t) = \sum_i f_i(\bar{r}, t) \quad (3)$$

where f_i is the distribution function of n_i .

The original LGA models have two drawbacks: non-Galilean invariance and statistical noise. To overcome the original LGA shortcomings, let us substitute the collision operator with the Bhatnagar-Gross-Krook (GBK) approximation proposed in [5]:

$$f_i(\bar{r} + \Delta h \cdot \bar{C}_i, t + \Delta t) = f_i(\bar{r}, t) + \frac{1}{\zeta} [f_i^{(0)}(\bar{r}, t) - f_i(\bar{r}, t)], \quad (4)$$

where ζ is the relaxation time and $f_i^{(0)}(\bar{r}, t)$ an equilibrium function. It is showed that, for a given PDE, that there is a proper equilibrium function $f_i^{(0)}(\bar{r}, t)$ such that the PDE can be approximated by evolving (4). A proper equilibrium function can be given as [6]:

$$f_i^{(0)}(\bar{r}, t) = \beta_i \rho(\bar{r}, t), \quad (5)$$

where, according to the definition in [14], the value of β_i is defined as:

$$\beta_i = \begin{cases} 1 - \frac{5M}{9}, & i = 0 \\ \frac{M}{9}, & i = 1, 3, 5, 7, \dots \\ \frac{M}{36}, & i = 2, 4, 6, 8, \dots \end{cases}, \text{ and } M \in [0, 1]. \quad (6)$$

The main interest is that evolution of the new model consisting of Equations (3)-(6) permits solution to a certain partial differential equation.

III. ANISOTROPIC DIFFUSION MODEL BASED ON LBM

Anisotropic diffusion equation plays an important role in the application of partial differential equation for image processing. However, the reports about LBM for resolving the anisotropic diffusion equation are very rare. In this section, we will propose a diffusion model based on LBM.

For eliminating the staggered invariants in LBM models [7], Qian suggested that the particles should move out of the lattice nodes with certain probabilities, our derivation shows that this model will lead to a nonlinear global equation if the probability is not a constant. So in our study we introduced a medium between the nodes of the lattice, and suppose that the particles can pass through the medium with a probability of

$g_i(\bar{r})$, or can bounce back with a probability of $(1 - g_i(\bar{r}))$ as shown in Fig.2. The LBM evolution equation is modified as:

$$f_i(\bar{r} + \Delta h \bar{C}_i, t + \Delta t) = g_i(\bar{r}) \left\{ f_i(\bar{r}, t) + \frac{1}{\zeta} [f_i^{(0)}(\bar{r}, t) - f_i(\bar{r}, t)] \right\} + [1 - g_i(\bar{r})] \left\{ f_i(\bar{r} + \Delta h \bar{C}_i, t) + \frac{1}{\zeta} [f_i^{(0)}(\bar{r} + \Delta h \bar{C}_i, t) - f_i(\bar{r} + \Delta h \bar{C}_i, t)] \right\} \quad (7)$$

Using the Chapman-Enskog expansion, we have:

$$f_i = f_i^{(0)} + \varepsilon \cdot f_i^{(1)} + \varepsilon^2 \cdot f_i^{(2)} + \varepsilon^3 \cdot f_i^{(3)} + \dots, \quad (8)$$

$$\partial_x = \varepsilon \partial_\alpha, \quad (9)$$

$$\partial_y = \varepsilon \partial_\beta, \quad (10)$$

$$\partial_t = \varepsilon \partial_{t_1} + \varepsilon^2 \partial_{t_2}, \quad (11)$$

where $f_i^{(0)}(\bar{r}, t)$ and $(\varepsilon^n \cdot f_i^{(n)})$ are the equilibrium function and the n -th order perturbed term with a small ε , respectively.

Expanding equation (7) in a Taylor series about \bar{r} and t , and considering $O(\varepsilon^1)$ of both sides of equation (7), we have:

$$\frac{\partial}{\partial t_1} \rho = - \sum_i g_i(\bar{r}) v(\bar{C}_i \cdot \nabla_{\alpha\beta}) f_i^{(0)}, \quad (12)$$

$$f_i^{(1)} = \frac{\zeta}{9} \Delta t v \sum_i g_i(\bar{r}) (\bar{C}_i \cdot \nabla_{\alpha\beta}) f_i^{(0)} - g_i(\bar{r}) \zeta \Delta t v (\bar{C}_i \cdot \nabla_{\alpha\beta}) f_i^{(0)} \quad (13)$$

Considering $O(\varepsilon^2)$ of both sides of equation (7), we have:

$$\frac{\partial}{\partial t_2} \rho = \frac{1}{2} v^2 \Delta t \sum_i g_i(\bar{r}) (\bar{C}_i \cdot \nabla_{\alpha\beta})^2 f_i^{(0)} - \frac{1}{\Delta t \zeta} \sum_i g_i(\bar{r}) f_i^{(2)}. \quad (14)$$

If we set $\zeta=1$, according to equations (8)-(14), we have:

$$\frac{\partial}{\partial t} \rho = \frac{M \Delta h^2}{18 \Delta t} \sum_i g_i(\bar{r}) (\bar{C}_i \cdot \nabla)^2 \rho - \frac{M \Delta h}{9 \Delta t} \sum_i g_i(\bar{r}) (\bar{C}_i \cdot \nabla) \rho - \frac{\varepsilon^2}{\Delta t \zeta} \sum_i g_i(\bar{r}) f_i^{(2)} \quad (15)$$

Equation (15) is very similar to the anisotropic equation

$$\frac{\partial \rho}{\partial t} = \text{div} [c(\nabla \rho) \nabla \rho], \quad (16)$$

if we expand the right side of the anisotropic equation. The difference between equation (15) and (16) is that, equation (15) only has forward diffusion processes. This means the LBM-based anisotropic model is more stable.

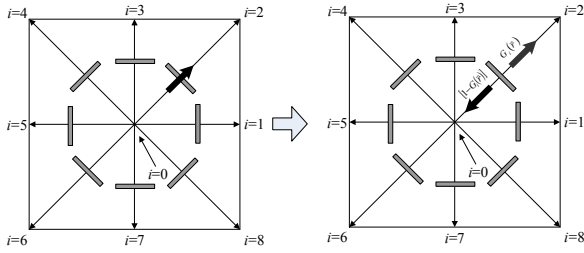


Fig.2 The spatial configuration of the LBM

According to equation (15), we can see that the diffusion coefficient is determined by parameter M , space interval Δh and time interval Δt . Commonly, in image processing, space interval Δh is always set as 1. Time interval Δt will determine the accuracy of the computation. A smaller Δt will produce a more accurate computation result. This means time interval Δt must be adjustable. However, the adjustment of Δt will change the value of the diffusion coefficient in equation (15). In our study, we set the proportion of parameter M to time interval Δt as a constant. If we denote $\frac{M\Delta h}{9\Delta t}$ by k , the parameter M can be set as $\Delta t = \frac{M\Delta h}{9K}$.

IV. EXPERIMENT AND DISCUSSION

A. Experimental results

In the experiment, we use the LBM-based model to implement medical image smoothing. Fig.3 shows the experiment results. In Fig.3, the first column of each row is the original image, the second column is generated by adding Gaussian noise (the noise variance is 100) to the original image. The third and fourth column of each row is the experimental result processed by the Perona and Malik’s method and the LBM-based anisotropic model, respectively. Fig.3 shows that the results of our method are very similar to those of Perona and Malik’s method. This means our method is effective.

Moreover, with only forward diffusion processes, our method can eliminate the “staircasing effect” which is a drawback of Perona and Malik’s method. As Fig.4 shown, (a) is the experimental result by Perona and Malik’s method, and (b) the LBM-based anisotropic diffusion model. (c) and (d) are the details of the region indentified by the white frame in (a) and (b) respectively. According to Fig.4(c) and Fig.4 (d), we can see that the Perona and Malik’s method

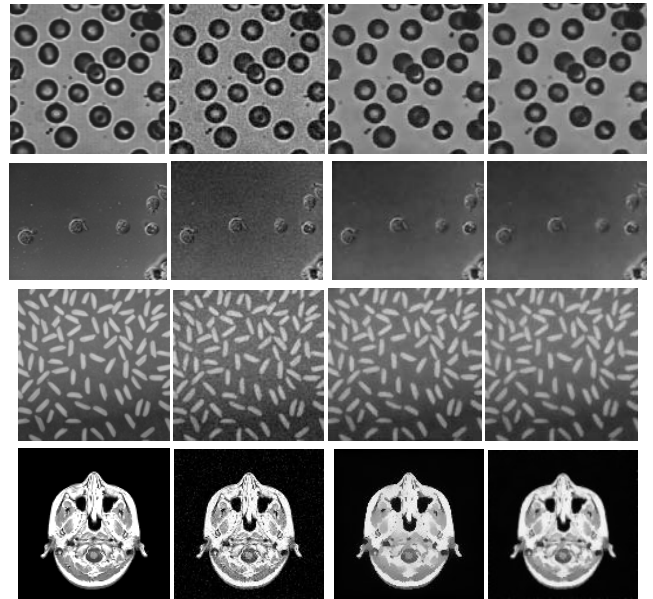


Fig.3 experiment results

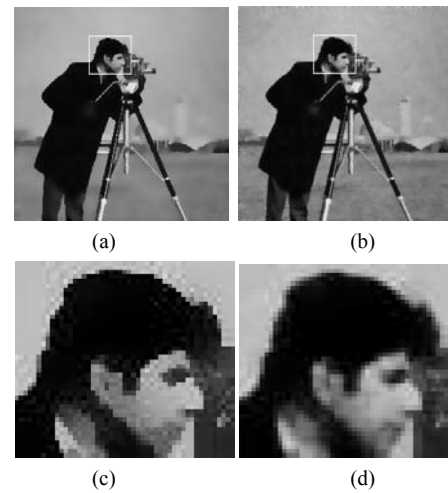


Fig.4 Local details of the experiment results

caused obvious staircasing effect in the region of eyes, nose, and mouth, while our method can overcome this drawback.

B. Numerical simulation

To demonstrate the accuracy of the LBM-based approach, we use the equation (17) as the test pattern and compare the resolutions by using the proposed approach and the analytical method, respectively.

$$\partial_t \rho = \nabla^2 \rho \tag{17}$$

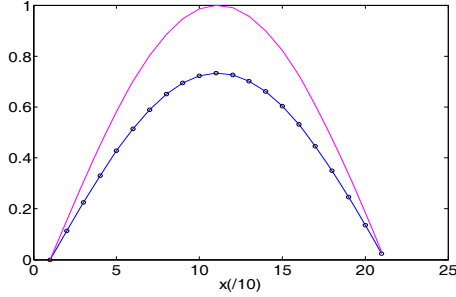


Fig.5. Resolve equation (17) by LBM.(Simulation results: $y=101$)

Boundary condition:

$$\rho(x, y, 0) = \sin\left(\frac{\pi x}{\ell_x}\right) \sin\left(\frac{\pi y}{\ell_y}\right), \rho(0, y, t) = \rho(x, 0, t) = 0,$$

$$\rho(\ell_x, y, t) = \rho(x, \ell_y, t) = 0, \rho(0, \ell_y, t) = \rho(\ell_x, 0, t) = 0$$

Let $g_i(\bar{r}) \equiv 1$, $k=1$, $\zeta=1$, $\Delta h=1$, $\Delta t=0.1$, $t=160$ and $\ell_x = \ell_y = 202$. Fig.5 shows the curve of $\rho(\bar{r}, t) = 0$ at $\bar{r} = \begin{pmatrix} x \\ 101 \end{pmatrix}$. In Fig.5, the label circle represents the numerical solution by the LBM, the red real line is the initial value and the blue real line represents the analytical solution. We can see that the numerical solution is in good agreement with the analytical solution. This shows that the proposed LBM-based anisotropic model is accurate.

C. Evaluation

To evaluation the experiments, we use the Signal to Noise Ratio (SNR) to compare the experiment results of Perona-Malik’s method and our method. At first, we use the Lena image as the original image I . By adding Gaussian noise with different variance to the original image we obtained a set of test images. Using Perona-Malik’s method and our method to denoising these test images and calculating the SNR of the results, we can obtain two curves as Fig.5 shown. Where the SNR is defined as:

$$PSNR = -10 \log \left(\frac{\sum_{\bar{r}} (\rho(\bar{r}, t) - I(\bar{r}))^2}{255^2} \right) \quad (18)$$

In Fig.6, the blue circles denote the variance of the SNR of our method and the red circles the Perona-Malik’s method. Fig.6 shows that the results of our method always have a higher SNR than Perona-Malik’s method.

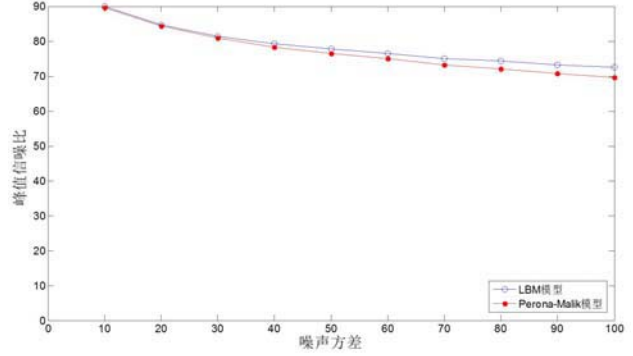


Fig.6 The variant of SNR with noise variance

V. CONCLUSIONS

To overcome the numerical instability problem which exists in the Perona-Malik’s model, we proposed in this paper a LBM-based anisotropic diffusion model. Using this model, we implement the image smoothing to medical images. Numerical simulation shows that the LBM-based anisotropic diffusion model is accurate and efficient. For quantitatively evaluating our model in medical image smoothing, we compared the model with Perona and Malik’s method by calculating the Signal to Noise Ratio. The experimental results shows that our method can smooth the noise medical image very well, and have a higher Signal to Noise Ratio than Perona and Malik’s method.

ACKNOWLEDGEMENTS

ZZY would like to thank the support from the Shanghai Leading Academic Discipline Project No. T0102. YHQ would like to thank the support from the NSF of China No. 10625210, the Shanghai Science and Technology Commission Nos05ZR1449, 07PJ14040. and the Shanghai Education Commission NoB.10-0401-07-001.

REFERENCES

1. Kichenassamy S. (1997) The Perona-Malik paradox, SIAM J. Appl. Math., 57: 1328-1342
2. Gilboa G, Sochen N, and Zeevi Y Y. (2002) Forward-and-backward diffusion processes for adaptive image enhancement and denoising, IEEE Trans. Image Process., 11: 689-703
3. Ginzburg I and d’Humières D. (2007) Lattice Boltzmann and analytical modeling of flow processes in anisotropic and heterogeneous stratified aquifers, Adv. Water Resour., 30:2202-2234
4. Frisch U, Hasslacher B, and Pomeau Y. (1986) Lattice-Gas automata for the Navier-Stokes equation, Phys. Rev. Lett., 56:1505-1508

5. Qian Y H, d'Humieres D and Lallemand P. (1992) Lattice BGK Model for Navier-Stokes Equation, Europhysical Letters, Europhys., 17:479-484
6. He X Y, Luo L S, and Dembo M. (1996) Some progress in lattice Boltzmann method, Part I. Nonuniform Mesh Grids, J. Comput. Phys., 129:357-363
7. Qian Y H. (1997) Fractional propagation and the elimination of staggered invariants in lattice-BGK models, International Journal of Modern Physics C, 8:753-761

Authors: Yu Chen, Zhuangzhi Yan
Institution: School of Communication and Information Engineering,
Shanghai University
Street: Yanchang Road
City: Shanghai
Country: China
Email: {tzc, zzyan}@shu.edu.cn

YueHong Qian
Institution: Institute of Applied Mathematics and Mechanics,
Shanghai University
Street: Yanchang Road
City: Shanghai
Country: China
Email: qian@shu.edu.cn

Lung region segmentation based on multi-resolution Active Shape Model

Chunyan Wang¹, Shengwen Guo¹, Jianbo Wu², Qiong Liu¹, Xiaoming Wu¹

¹Department of Biomedical Engineering, South China University of Technology, Guangzhou, China

²Computing Center in South Campus, South China University of Technology, Guangzhou, China

Abstract — Objective: Segmentation of lung region in chest radiographs is a key point in lung disease diagnosis. Because the complexity of anatomical structures and the overlap of organ and tissues' intensity ranges in chest radiographs, it has set a higher demand for the lung region segmentation than the sharp-edged medical image, and the performance of low-level segmentation methods that use local intensity criteria only are not so satisfactory in chest radiographs. In this article, we presented a new segmentation method in chest radiographs. **Methodology:** We investigated Active Shape Model (ASM) segmentation in chest radiograph. However, the original ASM suffers from the loss of accuracy and low speed in real time applications. In this paper, automatic point insertion, semi-automatic adjustment of initial placement and multi-resolution framework were introduced to improve the performance of original ASM. **Results:** 80 chest radiographs have been used to test our algorithm, and the result showed that 68 images were segmented effectively. Experiments also showed that the multi-resolution search took less CPU time required by the original method because the new method converges after less iteration. **Conclusions:** The improved Active Shape Model provides a fast, effective, semiautomatic and model-based method for lung region segmentation in chest radiographs. Besides chest radiographs, multi-ASM can also be used in other medical images, such as CT, MRI, ultrasound images and so on.

Keywords — chest radiographs, multi-ASM, lung region segmentation, initial placement, Point Distribution Model

I. INTRODUCCION

Segmentation of lung region in chest radiographs is a prerequisite in much disease diagnosis. Accurate manual delineation of the structures of interest by a human expert is time-consuming and also subject to large intra- and inter-observer variability. Hence, fast and reliable segmentation methods that yield accurate and consistent results on a wide range of images are needed to make quantitative analysis of large series of images feasible in routine clinical practice. A typical problem with projective radiographs is the lack of contrast between overlapping objects, which induces ambiguity about the true location of the object boundaries in the image. Low-level segmentation methods that use local intensity criteria only, such as threshold, region growing or edge detection, are therefore insufficient for accurate object delineation in this kind of images and more powerful model

based strategies are required that rely on a priori information about the shape of the object to guide the segmentation process in low contrast areas.

Active Shape Model is a model-based method put forward by T.F.Cootes [1], which does permit local shape control by presenting the contour as a polygon with a fixed number of labeled points. An ASM consists of a shape model controlling, a set of landmark points, together with a statistical model of the grey-levels expected around each landmark. Both the shape model and the grey-level models are trained on sets of labeled example images.

Our work has aimed at improving both the speed and the accuracy of the ASM method. In this paper, we describe a multi-resolution approach to modeling the gray-levels around each landmark, and a coarse-to-fine strategy for image search [2]. Besides this, we insert some points automatically during constructing Point Distribution Models (PDM) and adjust the initial placement semiautomatically, which can improve the performance of original ASM.

II. METHODOLOGY

A. Original ASM

Cootes et al [3] described how to build flexible shape models called Point Contribution Models (PDM). These are generated from examples of shapes, where each shape is represented by a set of labeled landmark points. The modes can be used to generate new shapes using the equation.

$$x = \bar{x} + \phi b \quad (1)$$

Where $x = (x_1, y_1, \dots, x_n, y_n)^T$

(x_k, y_k) is the k^{th} model point

\bar{x} represents the mean shape

ϕ is a $2n \times t$ matrix of t unit column vectors

$b = (b_1 \dots b_t)^T$ is a set of shape parameters

The column of ϕ are orthogonal and span the space of shape variations observed in the training set. If the shape parameters b is chosen inside suitable limits (derived from

the training set) then the shapes generated by (1) will be similar to those in the training set.

In addition the local gray-level environment about each landmark point can be modeled. Statistical information is gathered about the mean and covariances of the values of the pixel in the vicinity of each landmark, typically on profiles normal to the object boundary at that point. This data can be used to assess how well the gray-level in a particular area of an image match those expected around a given model landmark point.

Given a rough starting approximation an Active Shape Model can be iteratively fitted to an image [2]. By choosing a set of shape parameters b for a Point Distribution Model, we defined the shape of a model object in an object centered co-ordinate frame. We can create an instance X , of the model in the image frame by defining the position, orientation and scale:

$$X = M(s, \theta)[x] + X_c \quad (2)$$

Where $X_c = (X_c, Y_c \dots X_c, Y_c)^T$

$M(s, \theta)[\cdot]$ Performs a rotation by θ and a scaling by s .

(X_c, Y_c) is the position of the centre of the model in the image frame.

An iterative approach to improve the fit of the instance, X , to an image proceeds as follows:

1. Examine a region of the image around each point to calculate the displacement of the point required to move it to a better location.
2. From these displacements calculate adjustments to the pose and the shape parameters.
3. Update the model parameters: by enforcing limits on the shape parameters, global shape constraints can be applied ensuring the shape of the model instance remains similar to those in the training set.

The procedure is repeated until no significant changes result. Because the models deform to better fit the data, but only in ways which are consistent with the shape found in the training set they are called 'Active Shape Models'.

To find a better location for each model point (step (1) above), we sample a profile perpendicular to the boundary at the point, and run the gray-level model along it to find the best match. The suggested movement is then toward the point on the sampled profile which gave the best match to the model. We denote the set of such adjustment as a vector

$$dX = (dX_0, dY_0, \dots, dX_{n-1}, dY_{n-1})^T \quad (3)$$

Given such a set of suggested changes we can use a least squares approach to find the best change in pose

$(dX_c, dY_c, ds, d\theta)$ and changes to the shape parameters (db) to move the points from their current locations in the image frame, X , to be as close as possible to the suggest new locations $X + dX$. We can then update the pose and shape parameters, apply limits to the shape parameters to ensure only 'legal' shapes are generated and repeat.

B. Improvements of original ASM

Although the original ASM has been applied to many areas successfully [4], the accuracy and speed of the algorithm are not very satisfactory. We propose a new scheme with the following kinds of improvements upon the original ASM.

- Multi-resolution Framework

ASM includes shape model and gray-level appearance model. These appearance models are constructed for multiple resolutions. The number of resolutions is denoted manually. The finest resolution uses the original image and a step size of one pixel when sampling the profiles. The next resolution is the image observed at scale and a step size of two pixels. Subsequent levels are constructed by doubling the image scale and the step size.

The doubling of the step size means that landmarks are displaced over larger distances at coarser resolutions. The result is that the fitting at coarse resolution allows the model to find a good approximate location based on global images structures, while the later stages at fine resolutions allow for refinement of the segmentation result.

- Adjusting initial placement

An improper initial placement may cause the model matching to be caught in nearby local minima. We solved this problem to a certain extent by changing the model's initial position, size semiautomatically before iterating.

First, the initial shape model is divided into two parts: left lung and right lung, so we can adjust the initial placement of left and right lung separately, and reduce the influence of different distance between the two parts of lung in different people. Then, we annotate the size of lung region manually, according to the scaling relation of the lung's size in the shape model and the testing image, the initial placement can be adjust automatically, which will make model matching procedure start in a more appreciate initial placement and converge in few iterations.

Besides these, we insert some points automatically during two landmark points, which can reduce workload and avoid edge blur.

III. RESULTS

50 chest radiographs made training images, and other 80 chest radiographs were used to test the performance of segmentation. All these chest radiographs were obtained with direct digital radiograph system from General Hospital of Guangzhou Military Area Command.

A. Shape model

We labeled 40 points in each training image (20 in left lung and 20 in right lung), then insert 3 points between the adjacent 2 points. The total number of the points is 162, (81 in left lung and 20 in right lung). Notice that between the demarcation of the left lung and right lung, we didn't insert any points.

Then, the shapes can be aligned by translating, rotating and scaling so as to minimize the sum of squared distance between the landmark points. The mean model shape is given in Fig.1.

After that, we trained sets of grey-level models for each landmark, one at each pyramid level. The grey-level models were 11 pixels long (5 pixels long at each side).

Fig.2a shows the initial placement before iterating in a training image, which was obtained by choosing a set of pose parameters and setting all the shape parameters to zero (corresponding to the mean model shape). The adjusting initial placement is given in Fig.2 (b).

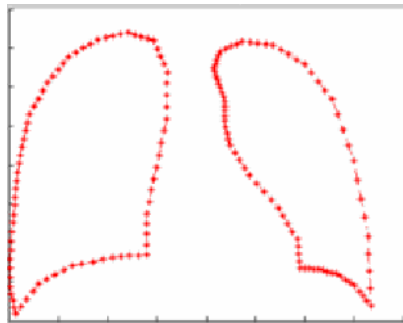


Fig. 1 Mean Shape

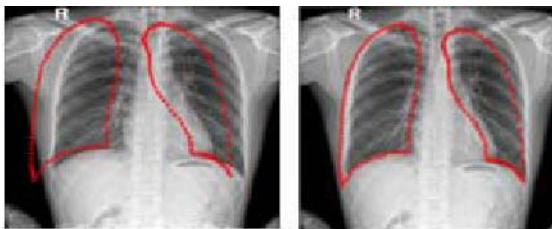


Fig. 2(a) Initial placement (b) Adjusting initial placement

B. Iteration result

Fig.3 (a-d) shows the model instance after 2-5 iterations. After 5 iterations (Fig.3 (d)) the model appears to give a good fit to the data.

From the experiments, we also conclude that the more iterative times it processed, the more accurate the segmentation result is, but the more time is consumed. The detail is showed in Fig.4

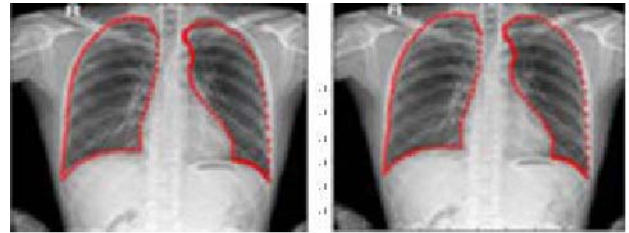
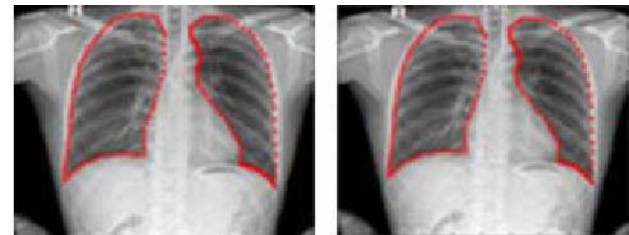


Fig.3(a) After 2 iterations (b) After 3 iterations



(c) After 4 iterations (d) After 5 iterations.

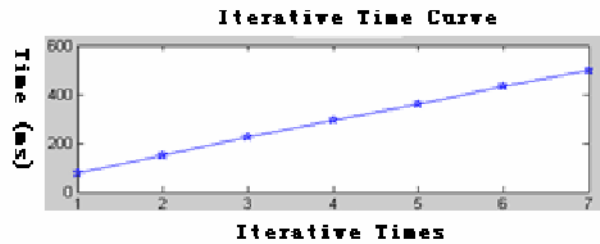
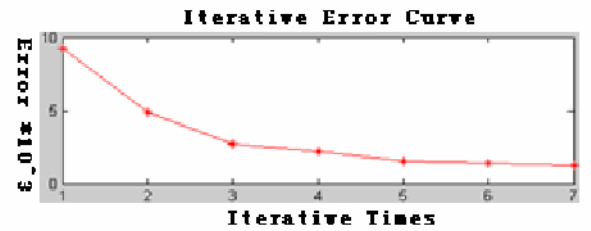


Fig. 4 Experiments also show that using original ASM should take 8 iterations to converge while the improved ASM needs only 5 iterative times. That means our algorithm reduces the CPU time required by the origin ASM.

IV. DISCUSSIONS

80 chest radiographs have been used to test our algorithm, and result showed that 68 images were segmented effectively. Analyzing the rest 12 images, we found they have some common characteristics: the boundary of their lung region exceeds the extent of shape model, or the lung region is blurred by some disease. Besides these, the disabled segmentation may be caused by the reasons below:

- The initial placement

As analyzed above, the initial placement is a very important factor in ASM algorithm, if the initial model shape is far away from the target, the grayscale of the searching path may be influenced by the illumination, contrast, noise and other chest tissues, which will cause the searching stage aim a wrong target.

We solved this problem to a certain extent by changing the model's initial position, size semiautomatically before iterating, which can make model matching procedure start in a more appreciate initial placement.

- The Registration of different chest radiographs

Because all the chest radiographs we took in these experiments were not registered, different patient body positions and different chest structures could influence the initial shape model and appearance model, which will lead an improper initial shape model and a wrong target during iterating.

- The training set

In statistical and learning algorithm, the overlay of data and data stream is always the key point. It is a pity that the given data can't cover the real data distribution in different applications, so the inaccuracy is unavoidable. There is a same problem in ASM, if the testing set is more similar with training set, the ASM segmentation result will be much better and vice versa. If choosing plentiful typical images to make up training set, the performance of segmentation will be improved.

- The chest histology

Because the complexity of chest, the lung region often overlap with rib, and will be covered by cardioid and vein, which cause the loss of signal data and influence the performance of the algorithm

V. CONCLUSIONS

We conclude by stating that Active Shape Model provides a fast, effective, semiautomatic and model-based method for lung region segmentation in chest radiographs. The new method introduced in this paper significantly improves the original method through the use of multi-resolution search. Our accomplishment in lung region segmentation is the basis of computer assisted diagnosis (CAD), with which the radiologist can use computer output as a "second opinion" and make the final decision more accurate. Besides chest radiographs, the improved ASM can also be used in other medical images, such as CT, MRI, ultrasound images and so on. And we also believe that this approach holds considerable promise as a practical and generic technique for automated image interpretation.

ACKNOWLEDGMENT

General Hospital of Guangzhou Military Area Command is gratefully acknowledgement for allowing the use of their chest radiograph data and clinical knowledge. The authors would also like to thank the other members of the image laboratory in SCUT for their help and advice.

REFERENCE

1. T.F. Cootes, A. Hill, C.F. Taylor, J. Haslam.(1994) The use of active shape models for locating structures in medical images. *Image and Vision Computing* 12 (6) :355-365.
2. T.F.Cootes,C.J.Taylor,A.lanitis.(1994) Active Shape Model:Evaluation of a Multi-Resolution Method for Improving Image Search.*Proc. British Machine Vision Conference* 1(1):327-336
3. T.F. Cootes, C.J. Taylor, D.H. Cooper, J. Graham. (1995) Active shape models – their training and application. *Computer Vision and Image Understanding* 61: 38-59.
4. B.V. Ginneken, A.F. Frangi, J.J. Staal, B.M. Romeny, M.A. Viergever. (2002) Active shape model segmentation with optimal features.*IEEE Transactions on Medical Imaging* 21 (8) :924-933.

Correspond author: Chunyan Wang

Author: Chunyan Wang
 Institute: Department of Biomedical Engineering
 Street: South China University of technology (the south campus)
 City: Guangzhou
 Country: China
 Email:silence8525@126.com

A Fast Doppler Ultrasound Simulator Based on RF Beamlines

Minghui Zhen and Dong C. Liu

Computer Science College, Sichuan University, Chengdu, Sichuan, China

Abstract— To better understand the information contained in the Doppler signal and verify algorithms to be used in modern ultrasound scanners, numerical simulations governed by the scanner's data paths are necessary as a realistic tool for further research and development. Besides the simulation of the whole data flow of Doppler signals starting from the beamforming, baseband processing to the collection of Doppler I and Q signals for spectral Doppler and color flow mapping (CFM) process, we propose a fast way to reconstruct the Doppler waveform theoretically and verify it in two circumstances. First, there exist a cluster of random scatterers around the focal point moving at a constant velocity toward the transducer array in the ideal circumstance. Second, we consider that a cluster of random scatterers around the focal point moving at different velocities toward the transducer array in the realistic environment. Finally, the Doppler signals and power spectrum can be displayed.

Keywords— Doppler ultrasound, PRF, CFM, RF Beamline, Doppler power spectrum,

I. INTRODUCTION

Doppler ultrasound is a powerful tool for non-invasive measurements of blood flow velocities. There are existing Doppler ultrasound simulation models in the literature; however, most of them have the following limitations: produce signals only from laminar flow, consider the random nature of the Doppler signal but do not relate to the physical process that generate the Doppler signals, follow point scattering models of the Doppler ultrasound physics but only assume steady flow. Our proposed model is highly correlated to the physical processes that a modern Doppler ultrasound scanner is doing, and this model offers theoretical formulation of Doppler in-phase and quadrature (i.e., Doppler I and Q) components based on time domain focusing beamlines interrogated from a moving cloud of random scatterers with arbitrary flow patterns.

In Section 2, the formulation of the Doppler signals is given in the ideal circumstance that there exist a cluster of random scatterers around the focal point moving at a constant velocity toward the transducer array, followed by a brief description of the mean frequency computation. Section 3 gives a list of modular design as the software implementation. The result of computer simulation and discussions are given in Section 4.

II. FORMULATION OF THE DOPPLER SIGNALS

The Doppler principle states that if a receiver moves at a velocity v_z in the direction of the source which emits sound waves at a frequency f_0 then the frequency detected by the source is not equal to f_0 and the difference frequency f_d of the echo is given by

$$f_d = \frac{2v_z}{c} f_0 \quad (1)$$

where c is the wave propagation velocity. In our simulation we have assumed that there exists a cluster of random scatterers around the focal point (x^0, z^0) moving at a constant velocity v_z toward the transducer array. The time-domain formulation of the l -th A-line can be written as

$$A_l(t) = \sum_{j=1}^N \left\{ \varepsilon_j \sum_{k=1}^M \eta_k \sum_{i=N_s}^{N_e} \gamma_i P \left(i - \frac{R_{i,k}^l}{c} - \frac{R_{j,k}^l}{c} - \tau_i - \tau_j \right) e^{-\alpha R_{i,k}^l} e^{-\alpha R_{j,k}^l} + N_j(t) \right\} \quad (2)$$

where

$$R_{i,k}^l = \sqrt{(x_i - x_k^l)^2 + (z_k^l)^2}$$

$$x_k^l = x_k^0, \quad z_k^l = z_k^0 - l v_z T_p$$

and T_p denotes the inverse of the pulse repetition frequency PRF. The time window is moving with different A-lines and its width is the same as the pulse length.

To obtain the Doppler signal one has to use a demodulation process to extract the Doppler information contained as frequency shifts in the returning echo. Suppose the signal $P(t)$ in Eqn (2) can be described by

$$P(t) = p(t) \sin(\omega_0 t) \quad (3)$$

where $\omega_0 = 2\pi f_0$ is the ultrasonic angular frequency. Ignoring diffraction effects, the Doppler shifted echo $A_l(t)$ received from a moving target will have a general form

$$A_l(t) = AP \left(t - \frac{2z_0}{c} + l \frac{2v_z T_p}{c} \right) \cos \left[(\omega_0 + \omega_d) \left(t - \frac{2z_0}{c} + l \frac{2v_z T_p}{c} \right) + \phi_d \right] \quad (4)$$

where ω_d denotes the Doppler shift frequency and A describes the echo amplitude and ϕ_d its phase relative to the transmitted wave at $t = 0$. The Doppler I and Q components D_I^I and D_I^Q can be extracted from Eqn (4) by a coherent demodulation which involves first multiplying them by $\sin(\omega_0 t)$ and $\cos(\omega_0 t)$ respectively, and then removing the high frequency terms in the region of $2\omega_0$ by performing a convolution with the impulse response ω_{ow} of a low-pass filter,

$$D_I^I = \frac{A}{2} P(t - \tau_0 + l\beta T_p) \quad (5)$$

$$\cos[w_d t + w_0(1 + \beta)(-\tau_0 + l\beta T_p)]$$

$$D_I^Q = \frac{A}{2} P(t - \tau_0 + l\beta T_p) \quad (6)$$

$$\sin[w_d t + w_0(1 + \beta)(-\tau_0 + l\beta T_p)]$$

where $\tau_0 = 2z_0 / c$ and $\beta = 2v_z / c$.

The reconstructed Doppler waveform \bar{r}_I and \bar{r}_Q can be obtained from an adequate sampling of Eqns (5) and (6). The index of the sampling position for D_I^I and D_I^Q is computed by

$$x_l = 1 + l \frac{f_s v_z T_p}{c} \quad (7)$$

where f_s is the sampling frequency. If x_l is not an integer the amplitude of I (and Q) signal can be computed from interpolation. To remove the large signals scattered or reflected from stationary and slow moving objects such as the vessel wall one may use a high-pass filter to r_I and r_Q [3]. We, then, obtain \bar{r}_I and \bar{r}_Q as the Doppler I and Q signals. The Doppler power spectrum $P(\omega)$ is therefore computed by

$$P(\omega) = R_I^2(\omega) + R_Q^2(\omega) \quad (8)$$

where $R_I(\omega)$ and $R_Q(\omega)$ are the Fourier transform of $r_I(t)$ and $r_Q(t)$ and respectively.

If the cross-section of the vessel is uniformly illuminated, the mean frequency $\bar{\omega}$ can be represented by

$$\bar{\omega} = \frac{\int_{-\infty}^{\infty} \omega P(\omega) d\omega}{\int_{-\infty}^{\infty} P(\omega) d\omega} \quad (9)$$

and the mean velocity \bar{v} is related to

$$\bar{v} = \frac{c\bar{\omega}}{2\omega_0} \quad (10)$$

by using the basic Doppler equation. According to the Wiener-Khinchine's theorem, the autocorrelation function of a signal (e.g. $r(t) = r_I(t) + jr_Q(t)$) is the Fourier transform of its power spectrum, Eqn (9) can be expressed by the autocorrelation of $r(t)$ and its first derivation [2]. From some manipulations one can show that

$$\bar{\omega} = \frac{1}{T_p} \tan^{-1} \frac{\text{Im}(R(T_p))}{\text{Re}(R(T_p))} \quad (11)$$

where $R(T_p)$ is the autocorrelation of $r(t)$ with the averaging interval W_τ

$$R(T_p; \tau, t) = \int_{t-\tau}^{t+\tau} r^*(r^l - T_p, t) r(\tau', t) d\tau' \quad (12)$$

or in a digital form,

$$R(T_p; nT_p, m\Delta) = \sum_{k=n}^{n+N_a-1} r^*(r^l - T_p, m\Delta) r[kT_p, m\Delta] \quad (13)$$

where N_a is the temporal averaging number and Δ is the sampling interval in t (could be treated like a spatial variable contrast to τ in Eqn (12) of the time variable). Also, from [1], the variance (flow disturbance) σ^2 can be written as

$$\sigma^2 = \frac{1}{T_p} \left\{ 1 - \frac{|R(T_p)|}{R(0)} \right\}$$

where $R(0)$ is simplified by

$$R(0) = \sum_{k=n}^{n+N_a-1} (r_I^2[nT_p, m\Delta] + r_Q^2[nT_p, m\Delta])$$

III. VELOCITY ESTIMATORS BASED ON PHASE SHIFTS

By using Eqs (10) and (11) we can compute the mean velocity due to the Doppler Effect in a constant velocity field. In this section we will consider velocity estimations of a parabolic flow by using the same technique (phase-shift measurements of successive echoes) as that in section 2.

We now assume that there exists a moving cloud of random scatterers with a parabolic velocity profile inside a

vessel of D mm diameter. The interested region of the Doppler effect is along the focal line with the diameter h mm. The direction of the flow is given by θ degree with respect to the beam propagation. After dividing the vessel by N_c streams, the RF signal of the s -th stream for the l -th echo can be computed first by

$$A_i^s(t) = \sum_{j=1}^N \left\{ \varepsilon_j \sum_{k=1}^M n_k \sum_{i=N_s}^{N_c} \gamma_i P \left(i - \frac{R_{i,k}^l}{c} - \frac{R_{j,k}^l}{c} - \tau_i - \tau_j \right) \right. \\ \left. e^{-\alpha R_{i,k}^l} e^{-\alpha R_{j,k}^l} + N_j(t) \right\} \quad (16)$$

where

$$R_{i,k}^l = \sqrt{(x_i - x_k^l)^2 + (z_k^l)^2} \\ x_k^l = x_k^s - l v_x^s T_p$$

are the coordinates of the shifted scatterers with respect to (x_k^s, z_k^s) according to the x and z component of the given velocity v^s respectively. Each signal will then be sampled in the z direction and the index of the sampling point is

$$x_i^s = 1 + l \frac{f_s v_z^s T_p}{c} \quad (17)$$

To obtain the Doppler signal one has to use a demodulation process to extract the Doppler information contained as frequency shifts in the returning echo. We can suppose the signal $P(t)$ in Eqn (16) is the same form in Eqn (3) [4]. Ignoring diffraction effects, the Doppler shifted echo A_i^s received from a moving target will have a general form

$$A_i^s = AP \left(t - \frac{2z_k^s}{c} + l \frac{2v_z^s T_p}{c} \right) \\ \cos \left[(w_0 + w_d) \left(t - \frac{2z_k^s}{c} + l \frac{2v_z^s T_p}{c} \right) + \phi_d \right] \quad (18)$$

The time-domain formulation of the l -th A-line can, therefore, be written as

$$A_l(t) = \sum_{s=1}^{N_c} A_i^s \quad (19)$$

The Doppler I and Q components $D_{l,s}^I$ and $D_{l,s}^Q$ can be extract from Eqn (19) by a coherent demodulation which involves first multiplying them by $\sin(\omega_0 t)$ and $\cos(\omega_0 t)$ respectively, and then removing the high frequency terms in

the region of $2\omega_0$ by performing a convolution with the impulse w_{low} of a low-pass filter,

$$D_{l,s}^I = e^{-(t-\tau_0+l\beta T_p)^2 * pw^2} \cos(w_0 * t) \\ \cos[w_d t + w_0 * (1 + \beta) * (-\tau_0 + l\beta T_p)] \quad (20)$$

$$D_{l,s}^Q = e^{-(t-\tau_0+l\beta T_p)^2 * pw^2} \cos(w_0 * t) \\ \sin[w_d t + w_0 * (1 + \beta) * (-\tau_0 + l\beta T_p)] \quad (21)$$

where $\tau_0 = 2z_k^s / c$ and $\beta = 2v_z^s / c$.

The signals in the consecutive streams could have an overlap according to the geometry of the system. The starting and ending indices of the overlapped region between the $(i-1)$ and i -th stream are

$$s_i = 1 + n \text{int} \left(\frac{(i-1)\Delta z}{c T_p} \right) \quad (22)$$

$$e_i = 1 + n \text{int} \left(\frac{h \cot \theta + (i-2)\Delta z}{c T_p} \right) \quad (23)$$

respectively where $\Delta z = D \sec \theta / N_c$ denotes the width of the stream. It is clear that there is no overlap if $s_i > e_i$ in Equations (19) and (20).

The Doppler I and Q signal for each stream and its mean velocity can be computed as those of in section 2.

IV. PROCESS DESIGN

Fig. 1 shows the functional block diagram of our Doppler computer simulation process. With selected ultrasound system parameters and values of Doppler flow related variables we can generate a sequence of RF beamlines with Doppler frequencies embedded in the signals. The RF signals are then demodulated and filtered to remove the probe carry frequency to obtain quadrature signals followed by the range gate accumulation. After that, the Doppler I and Q signals will be filtered by a highpass filter [5] to remove the clutter (or the wall) signals.

The wall filtered Doppler signals now go to the FFT spectrum module where we apply windowed FFTs to a section of Doppler signals with certain overlap to increase the signal to noise ratio. Finally, the Doppler spectrum is displayed and the Doppler waveform, e.g., the minimum, the mean and the maximum frequency curves can be obtained.

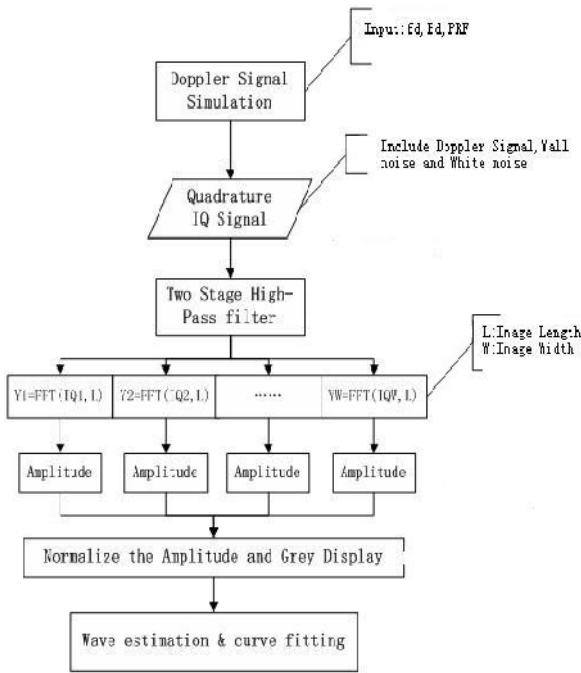


Fig.1 Functional block diagram of the Doppler computer simulation

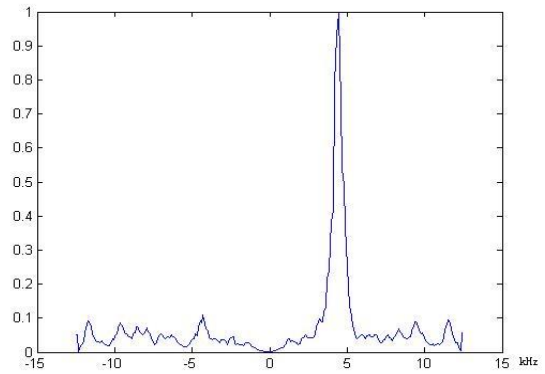
V. RESULT

In the simulation of the Doppler signal reconstruction, we use the following system related parameters: sample frequency of $F_s=40$ MHz, Doppler PRF of 25 kHz, a 3.5 MHz probe with a bandwidth of $B_d=0.01PRF$. Also, we have modeled the wall signals with varied carry frequencies and bandwidths to simulate realistic environment where the signal scattered form blood is corrupted by signals scattered from muscular tissue, such as vessel walls (wall noise), typically with 40 to 100 dB stronger than that the blood signal. Moreover, there is white noise in our simulation.

Fig. 2 shows our simulation results where the gray scale image is the Doppler spectrum with 128 columns. It's clear that, from our simulation, the proposed RF-beamline based Doppler signal generator can be used as a tool to generate Doppler spectrum and use it as a platform to analyze Doppler related algorithms.



(a)



(b)

Fig.2a The Doppler spectrum with 128 columns; 2b the FFT from the 108-th column

REFERENCES

1. C. Kasai, K. Namekawa, A. Koyano and R. Omoto, (1985) "Real-time two-dimensional blood flow imaging using an autocorrelation technique", IEEE Trans. Son. Ultrasonic. Vol.SU-32, pp.458-463.
2. Kerr, A. T., and Hunt, J.W., (1992) A method for computer simulation of ultrasound Doppler color flow images. I. theory and numerical method, Ultrasound Med. Biol. 18, 861-872
3. Mo L. Y. L. and Cobbold R. S. C.(1986) "Speckle" in C.W Doppler ultrasound spectra: a simulation study. IEEE Trans. Ultrasonic Ferroelec. Freq. Control UFFC-33, 747-753.

4. van Leerwen, G.H., Hoeks, A.P.G, and Reneman, R. S.,(1986), Simulation of real-time frequency estimators for pulsed Doppler systems, *Ultrasonic Imaging* 8, 252-271.
5. L.R. Rabiner, C.A. McGonegal and D. Paul,(1979) "FIR windowed filter design program – WINDOW", in *Programs for Digital Signal Processing*, edited by the Digital Signal Processing Committee, IEEE ASSP, John Wiley & Sons, inc. NY.

Author: Minghui Zhen and Dong C. Liu
Institute: School of Computer Science, Sichuan University
Street: The First Ring Road
City: Chengdu
Country: China
Email: zhenminghui06@163.com

Volumetric Non-rigid Registration via Thin-plate Spline Model

F. Babapour^{1*}, A. Abbaspour¹, R. Zoroofi², S.H. Akhlaghpour³

¹Engineering Faculty, Science and Research Campus, Islamic Azad University, P. O. Box 14515-775, Tehran, Iran

²Control and Intelligent Processing Center of Excellence, Elec. and Comp. Eng. Department, University of Tehran, Tehran 14399, Iran

³Department of Radiology, Faculty of Medicine, Tehran University of Medical Sciences, Tehran, Iran

Abstract — Registration and warping are essential steps in volumetric data fusion. Medical images are of major parts in diagnosing and treatment and actually are considered a total evaluation of work. In recent years medicines have been using diagnosing devices contain computers as a complementary in detecting harms, evaluating the amount of harm deciding the way of treatment. By quick developing in construction of three dimensional medical imaging devices, high resolution modalities could be used to produce lots of images. This issue is crucial specially in case of medical imaging like Ultrasound, CT and MRI which helps medicines in diagnosing, treatment and investigations.

In radiation therapy these information includes surface texture, extracting specified object area in image, and detecting of tumor which can increase the power of medical doctor diagnosing power and usage of image processing techniques will become important in these area. Finding the exact location of target with enough magnification is one of the primary needs in effective radiation therapy.

Results show that a Thin Plate Spline is a sufficient model for a volumetric non-rigid registration. The technique is evaluated by mapping of a sphere to a cube and then on a medical object. Experimental result declares that the employed technique is robust in the presence of the noise, changing the number of control points and works effectively in different object resolutions.

Keyword — Registration, Warping, Thin-plate Spline.

I. INTRODUCTION

In combination of medical images, the selection of registration approach based on precision and percent of noise acceptance of the mapping model is of important stages, which in this study is a practical approach in developing and evaluating of Thin Plate Spline in registration of medical images.

Choosing the control points is also of major parts. Control points can be extracted from transverse, coronal and sagittal slices. Totally to choose control points we use features of objects because they are unique points. After extracting control points in two volumes it is necessary to specify the type of registration based on robust, speed and precision. After analyzing we finally chose Thin Plate Spline model. But since we didn't have a total evaluation, in this study we evaluate the thin plate Spline method.

Simple understanding, strength and precision in three dimensional volumetric images respect to two dimensional slices led us use volumetric Thin Plate Spline method. This study is prepared for analyzing the sensitivity of mapping functions of Thin Plate Spline respect to the number of control points, total number of points (which defines the resolution of the imagine system) and analyzing the effect of noise.

One of the most complicated examples which are concerned in registration is mapping of unit sphere to cubic. For this aim we used two unit spheres with different points. Each sphere with 15 points was bringing to a cubic as control points. Control points in cubic are constructed by 8 vertexes, 6 cross sectional points of two diameter and (0, 0, 0) point.

In this part a total evaluation was obtained by introduced approach. First a sphere and a cubic were considered with the same points. Then relative error was calculated first by choosing some points as control points then problem solving of thin plate Spline equations and finally exerting function of map on medical object. Gaussian noise with zero average and different Variances were added to three dimensional objects coordinate (all points). And after exerting mapping, relative error was obtained for 10 step repetitions that results as well as errors are shown in plots.

In this research, by assuming that corresponding control points in original and transformed volumes are given, the mapping function is estimated for the registration process. The introduced approach is based on a previous work and we have employed the technique for non-rigid registration of volumetric objects. In this regard, first we explain the mathematic model of a Thin Plate Spline that is utilized to perform volumetric registration next we explain the procedures for corresponding implementation.

II. MATERIALS AND METHODS

Registration with control points is the main goal of this study. The original image (initial volume) is considered as reference and the warped image is considered as float image. First we suppose that $p_1 = (x_1, y_1, z_1)$, $p_2 = (x_2, y_2, z_2)$, ... $p_n = (x_n, y_n, z_n)$ are n control

points of the coordinate of reference volume. Then values obtained by $r_{ij} = |p_i - p_j|$ to create matrix K which introduces the distance between i, j [7].

$$P = \begin{bmatrix} 1 & x_1 & y_1 & z_1 \\ 1 & x_2 & y_2 & z_2 \\ \vdots & \vdots & \vdots & \vdots \\ 1 & x_n & y_n & z_n \end{bmatrix}, \quad n \times 4; \quad (1)$$

$$K = \begin{bmatrix} 0 & r_{12} & r_{13} & \cdots & r_{1n} \\ r_{21} & 0 & r_{23} & \cdots & r_{2n} \\ \vdots & \vdots & \vdots & \cdots & \vdots \\ r_{n1} & r_{n2} & r_{n3} & \cdots & 0 \end{bmatrix}, \quad n \times n; \quad (2)$$

$$L = \begin{bmatrix} K & P \\ P^T & Z \end{bmatrix}, \quad (n+4) \times (n+4); \quad (3)$$

T is transpose operator and Z is 4*4 zeros matrix.

In this study $Q_1 = (u_1, v_1, w_1)$, $Q_2 = (u_2, v_2, w_2)$, ... $Q_n = (u_n, v_n, w_n)$ are n control corresponding points in warped volume. Then matrix V&Y are:

$$V = \begin{bmatrix} u_1 & u_2 & \cdots & u_n \\ v_1 & v_2 & \cdots & v_n \\ w_1 & w_2 & \cdots & w_n \end{bmatrix}, \quad 3 \times n; \quad (4)$$

$$Y = (V | 0 \ 0 \ 0 \ 0)^T, \quad 3 \times (n+4); \quad (5)$$

In next step coefficients of, $W = (w_1, w_2, \dots, w_n)$, $\alpha_1, \alpha_u, \alpha_v$ and α_w were calculated.

$$L^{-1}Y = (W | \alpha_1 \ \alpha_u \ \alpha_v \ \alpha_w)^T, \quad (6)$$

Last step is using above coefficients in following registration equation:

$$f(u', v', w') = \alpha_1 + \alpha_u u + \alpha_v v + \alpha_w w + \sum_{i=0}^n w_i |P_i - (u, v, w)|. \quad (7)$$

So each voxel (u_i, v_i, w_i) of floating volume converted to new coordinate (u'_i, v'_i, w'_i) . Then following formula was applied to compute error:

$$err = \sum_{i=1}^n \|P_i - Q_i\| \quad (8)$$

P_i & Q_i are corresponding points in reference and floating volumes respectively.

III. RESULTS

In this step first a sphere mapped to a cube in low and high resolution. For this preparation we used two spheres with number of control points $n = 1024$ & 4096 . Each sphere with 15 landmarks converts to a cube. Landmarks on cube are 8 vertices, 6 cross sectional points of diagonal incidents in cube and $(0, 0, 0)$. Results are shown in figures 1 and 2.

We selected a medical object for clinical evaluation. This object was segmented with doctor of CT slices and 3D volume obtained with this slices (original volume). One warped volume was created by original volume (warped volume). Gaussian noise (zero mean and different vari-

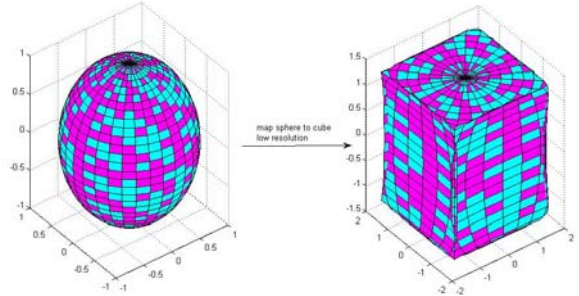


Fig.1 mapped sphere to cube with $n = 1024$.

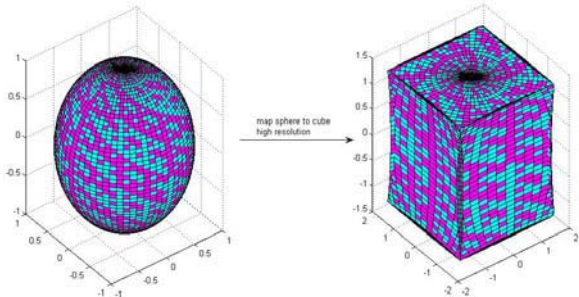


Fig.2 mapped sphere to cube with $n = 4096$.

ances) was added to warped volume in different variances and relative error for 10 iterative was calculated. Results are shown in following figure.

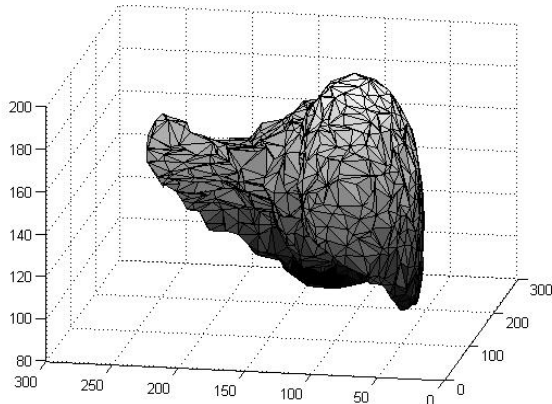


Fig.3 liver with n=997.

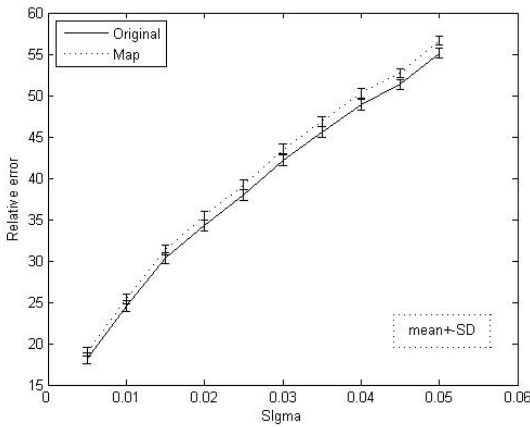


Fig.4 Relative error before and after mapping with noise for n=417.

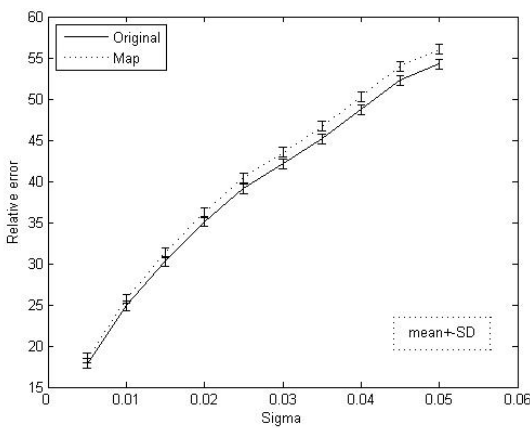


Fig.5 Relative error before and after mapping with noise for n=997.

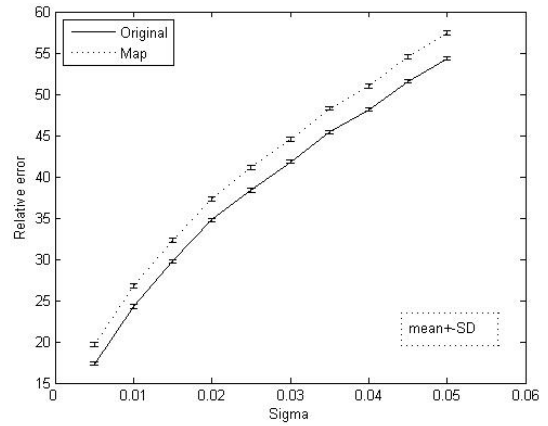


Fig.6 Relative error before and after mapping with noise for n=1825.

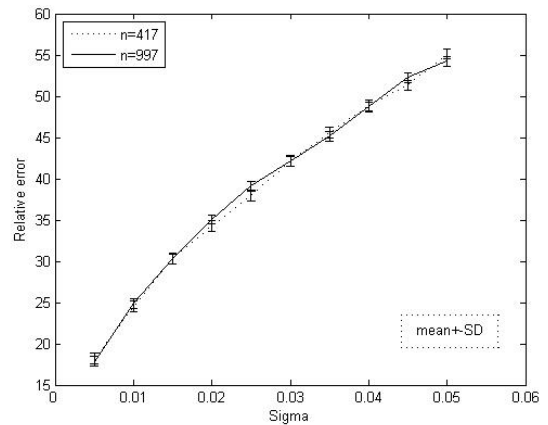


Fig.7 relative error between n=417&n=997.

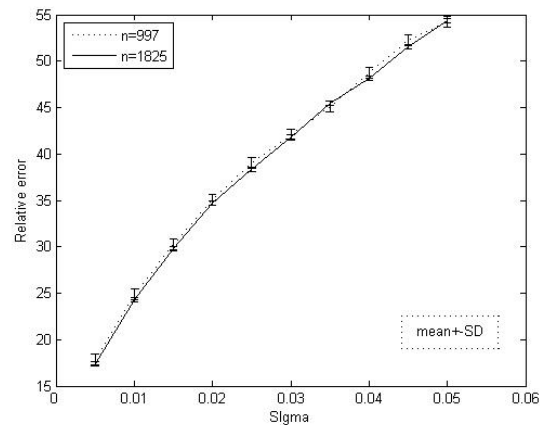


Fig.8 relative error between n=997&n=1825.

IV. DISCUSSION

In results section first we showed mapping a sphere to a cube with two different total control points (resolution) and then affectability of Thin Plate Spline model in different variances was investigated on number of total control points (volumetric resolution), number of control points (landmarks) and Gaussian noise (with zero mean and different variances).

The error reduction percent with 15 control points in variance distance of (0.05-0.005) between total control points 417&997points was less 3% and for total control points 997&1825 points was less 2.8%. And also regarding to figures 4-6 we can show that in high resolution, n=1825 error will decrease considerably. Note that this issue is not important in low resolution. On the other hand the steps of each data were repeated several times that had the same results which shows analytical feature of this mapping. One of the advantages of this method is that the number of control points is not necessarily a lot.

V. CONCLUSION

In this paper the major aim is to explain the mathematical model and to implement volumetric image registration with Thin Plate Spline model and then to evaluate model in non-rigid volumetric model which contain evaluation of capability of this model in elastic registration and formability of volumetric images. For this purpose the sensitivity of map functions of thin plates was calculated respect to the number of control points, the number of total points and map. After inspecting the results, we found out that Thin Plate Spline model is a quick, accurate model in registering volumetric non rigid images.

Results show that a Thin Plate Spline is a sufficient model for a volumetric non-rigid registration. The technique is evaluated by mapping of a sphere to a cube and mapping 3d medical object. Experimental result declares that the employed technique is robust in the presence of the noise, changing the number of control points and works effectively in different object resolutions.

We recommend that in future investigations registration of 3d medical images by Thin Spline model, which is an

applied method in medical image registration [7-10], would be better to apply on non rigid images like liver, prostate and etc [1-6].

Liver registration, among different phases, before and after injecting porter substance have been applying for better diagnose and effective treatment procedure, to achieve this goal we have to use the best mapping model. This investigation suggests an effective method in liver registration.

REFERENCES

1. CHEDID, A.; MENDENHALL, C.L.; GARTSIDE, P.; ET AL. Prognostic factors in alcoholic liver disease. VA Cooperative Study Group. *American Journal of Gastroenterology* 86(2):210-216, 1991.
2. Marsano LS, Mendez C, Hill D, Barve S, McClain CJ, Diagnosis and treatment of alcoholic liver disease and its complications, *Alcohol Research Health*. 2003; Vol. 27, No. 3, pp.247-56.
3. Bosch FC, Munoz N. Hepatocellular carcinoma in the world: epidemiologic questions. In Tabor E, et al., eds. *Etiology, Pathology, and Treatment of Hepatocellular Cancer in North America*. Woodlands, TX: Portfolio Publishing; 1991:35.
4. Seong-Jae Lim, Yong-Yeon Jeong, Yo-Sung Ho: Segmentation of the Liver Using the Deformable Contour Method on CT Images", pp. 570-581 *Pacific Rim Conference on Multimedia 2005: Jeju Island, Korea*
5. CHEN E.-L, CHUNG P.-C, CHEN C.-L, TSAI H.-M, CHANG C.-I, "An automatic diagnostic system for CT liver image classification" *IEEE TRANSACTIONS ON BIOMEDICAL ENGINEERING*, VOL. 45, NO. 6, JUNE 1998.
6. Masutani Y, Uozumi K, Akahane K, Ohtomo K, "Liver CT image processing: A short introduction of the technical elements", *European Journal of Radiology*, Volume 58, Issue 2, pp. 246-251, 2006.
7. Fei B, Kemper C, Wilson DL. A comparative study of warping and rigid body registration for the prostate and pelvic MR volumes. *Comput Med Imaging Graph*. 2003 Jul-Aug;27(4):267-81.
8. Rohr K, Stiehl HS, Sprengel R, Buzug TM, Weese J, Kuhn MH. Landmark-based elastic registration using approximating thin-plate splines. *IEEE Trans Med Imag* 2001;20(6):526-34.
9. Goshtasby A. Registration of images with geometric distortions. *IEEE Trans Geosci Remote Sensing* 1988; 26(1):60-4.
10. Bookstein FL. Thin-plate splines and the atlas problem for biomedical images. *Lecture Notes in Comp Sci* 1991; 511:326-42.

Author: FARSHID BABAPOUR MOFRAD

Institute: Engineering Faculty, Science and Research Campus, Islamic Azad University

Street: POONAK

City: TEHRAN

Country: IRAN

Email: Farshid.mofrad@yahoo.com

Interactive Display Methods for Ultrasound Strain Imaging

Fei Luo and Dong C. Liu

School of Computer Science College, Sichuan University, Chengdu, Sichuan, China

Abstract — Recently, ultrasound strain imaging is an adequate supplement for commonly used diagnostic procedures to detect tumors, which have a higher mechanical hardness than the surrounding tissue with the specific elastic properties. The strain image is acquired while the organ is slightly compressed by the ultrasound probe. Then the detected strain values can be displayed as a gray scale image where the dark areas correspond to the hard tissue and the light areas indicate the soft tissue. Because a sequence of strain images always represents a compression or decompression cycle in the exam, the calculated strain values at the transition frames, in general, are not reliable and result in errors shown as artifacts in display. These artifacts will significantly distract the ability to interpret the strain information in real-time or display in cine loop. The purpose of this paper is to present display techniques which are particularly useful for detecting the noisy strain frames during the transition between the compression and decompression process. Moreover, we applied a local motion detector to compensate the probe motion during the exam so that we can enhance the signal to noise ratio in display based on the right spatial registration. This paper also presents an interactive graphics tool where a motion displacement curve is synchronized with the strain imaging frame by frame. One can use this tool as feedback to ensure reliable data acquisition. Furthermore, one can select a right section of compression and decompression cycle and use this section for display.

Keywords — Strain image, display techniques, segmentation methods, color transparency, motion compensation

I. INTRODUCTION

Strain images [1] are created by comparing echo data obtained before and after a slight compression of the tissue. The results of the comparison are displayed as an 8-bit gray scale image on which the dark areas correspond to the hard tissue and the light areas indicate the soft tissue. Because a sequence of strain images always represents a compression or decompression cycle in the exam, the calculated strain values at the transition frames, in general, are not reliable and result in errors shown as artifacts in display.

In this paper, we first present display methods to make strain imaging more easily perceived and with no flash artifact in section II. These methods include persistence for reducing strain noise and a re-mapping technique that maintains constant brightness within the entire image for

removing the flash artifact. A contrast enhanced algorithm is also needed to enhance the detected hard tissues.

In section III we propose segmentation methods to ignore bad strain image frames before one can use the color transparency to display both the original B-mode tissue image and the color coded strain image. This segmentation method used a quality factor derived from the mean and difference of strain images to modify the color coding of unreliable strain images. Moreover, we also propose a technique to estimate the probe motion and use it to determine the motion displacement displayed as a graphics tool synchronizing the operator's compression or decompression process during the scan. As we know the soft tissue is prone to be deformable and inconsistent with the probe motion along the beam direction; while the hard structure, like hard tumor or tissue edges, is coherent to the probe motion. Then we propose a method based on ultrasound statistics (e.g., a ratio of local variance to the local mean is useful to extract edges from log compressed ultrasound image) to extract structure tissue and use them for motion registration. By using the motion detection algorithm, we can calculate the probe velocity from each frame and display its axial component where the positive value means the velocity along the compression and the negative one represents the decompression. By integrating the velocity curve we can obtain the displacement curve where it shows a nice compression and decompression cycle. With this cycle, one can apply the calculated tissue strain using adaptive persistence to display a peak hold value. This result will show the highest signal to noise ratio for the hard tissue.

The proposed display algorithms have been verified and validated by almost 80 clinical test data sets. They are them breast images with benign or malignant tissues. These *in vivo* images were recorded from Siemens Elegra and their corresponding strain images were estimated and verified in our lab. By comparing the strain image and its color transparency display, one can more easily extract the hard tissue in color and also ignore the noise shown as the background color.

II. ALGORITHM DEVELOPMENT OF STRAIN IMAGING IN GREY SCALE DISPLAY

The quality of strain image depends on many factors, for example, the size of search window in speckle matching, the signal to noise ratio of the image, the force applied to the body during the scan, the uniformity of the compression and decompression, and other scan techniques like the orientation of the probe to the body. Therefore, the straightforward display always results in abrupt change in image brightness and also in noisy images during the transition between compression and decompression scanning.

In this Section, we proposed a display technique for using a persistence average to reduce the strain noise:

$$I_{k+1}^{(p)} = pI_k^{(p)} + (1-p)I_{k+1} \quad (1)$$

followed by a re-mapping method,

$$I' = \beta(I - \mu) + H \quad (2)$$

where p is a constant between 0 and 1 for persistence averaging, β controls the contrast (e. g. $\beta=1.2$ means a 20% increase in contrast), μ defines the global mean of the image, and H is a constant to adjust the display brightness. Because this is a linear processing, it shouldn't bring any artifacts in contrast. Also, the implementation should be very simple: compute the mean and then a LUT of 256 bins followed by a re-mapping of the whole image.

The purpose of applying the mapping is to maintain a constant brightness of the strain images for removing the possible flash artifact. Because the hard tissue is displayed in low intensity, one may need to enhance this part by using an S-shape curve, for example, the sigmoid function, [2]

$$S(x) = \frac{255}{1 + e^{-\frac{x-128}{a}}} \quad (3)$$

where the parameter a in $S(x)$ determines different levels of enhancement (i.e. for smaller a we have better contrast in the dark regions but it also enhance the noise). In Eqn (3) use the "break point" at $x=128$ we then set the brightness H of Eqn (2) as 128 to get enhancement more consistently.

III. ALGORITHM DEVELOPMENT OF STRAIN IMAGING IN COLOR DISPLAY

Because strain imaging is just seen as a parametric imaging without spatial information, i.e., there is no clue to correlate the tissue anatomy to the brightness of the strain image, we present a color transparency technique[3] to

overlay the color-coded strain image on the original tissue image so that one can locate the strain values to their corresponding tissue structures.

The basic color transparency method can be seen as an interpolation between the tissue image I_b and the color-coded strain image I_s ,

$$I(R, G, B) = \alpha I_b + (1 - \alpha) Cmap[F(I_s)] \quad (4)$$

where α is a transmission coefficient between 0 and 1. In Eqn(4), the strain image I_s is processed by a function F to reduce noise during data acquisition. The function F responds to segmentation methods to ignore bad strain image frames before using the color transparency. In this section we will describe the function F later.

For a sequence of display, the colorization of the image pixel always enhances the noise and deteriorates the display performance. At the turning point from the compression to the decompression or vice versa, there will be no significant stress to the body that results in "noisy" estimation in strain calculation. Moreover, if the operator does not apply a uniform compression/decompression, for example, a twist during the process, the strain computation may also introduce errors. Therefore, we need a systematic way to detect these "bad" image frames and then remap these frames shown as tissue image only, e.g., force them to background color.

We first propose a method based on the quality of acquired image frames to detect "noise" image frames. For each frame, we compute its global mean where a low value may correspond to either large areas of hard tissues or just a frame without much pressure, e.g., at the turning point between the compression and the decompression. Also, we compute the mean D_i of the absolute difference of each pixel from two successive strain images. A big number of this difference always corresponds to a bad frame because we assume the strain change from two successive frames should be continuous. Moreover, the strain image used to calculate the difference is that after the histogram equalization which means the image has been normalized and enhanced.

We now show how to determine these weighting coefficients where we have two piecewise linear curves: Eqn (5) for global mean and Eqn (6) for difference,

$$u_1 = \begin{cases} c_1 & , x \leq p_1 \\ \frac{c_2 - c_1}{p_1 - p_2} (x - p_1) + c_1 & , p_1 < x \leq p_2 \\ c_2 & , p_2 < x \leq p_3 \\ \frac{c_3 - c_2}{p_4 - p_3} (x - p_2) + c_2 & , p_3 < x \leq p_4 \\ c_3 & , p_4 < x \end{cases} \text{ and}$$

$$u_2 = \begin{cases} u_1 + c_4 & , x \leq P_1 \\ u_1 + c_5 & , P_1 < x \leq P_2 \\ u_1 + c_6 & , P_2 < x \leq P_4 \\ u_1 + c_7 & , P_4 < x \end{cases} \quad (5)$$

$$d_1 = \begin{cases} 50 & , y \leq 2 \\ (y - 2) \frac{58 - 50}{2.5 - 2} + 50 & , 2 < y \leq 2.5 \\ (y - 2) \frac{2}{2.5} + 50 & , 2.5 < y \end{cases} \text{ then}$$

$$d_1 = \begin{cases} d_1 + 10 & , 65 < z < 70 \\ d_1 + 15 & , 70 \leq z \end{cases} \text{ and } d_2 = d_1 + 10 \quad (6)$$

where x is the mean of a sequence of global means and C_i, P_j ($i=1,2,\dots,7$ and $j=1,2,3,4$) are parameters. From a set of test data and their global means, we can define the coefficients u_1 and u_2 and use them to group the mean value to several categories. In each category, the estimated mean maps to a weighting coefficient γ_1 from an increasing piecewise linear curve. Similarly, we set proper parameters to define Eqn (6), where y is the ratio of z , the mean of sequence of D_i to x to get d_1 and d_2 from difference values. Then use d_1 and d_2 to determine another weighting coefficient γ_2 from a decreasing piecewise linear curve because a bigger difference means larger error and the weighting coefficient should be lower. By combining these two parameters, we obtain a new weighting parameter γ ,

$$\gamma = 0.7 \text{MIN}(\gamma_1, \gamma_2) + 0.3 \text{MAX}(\gamma_1, \gamma_2) \quad (7)$$

called it the quality ratio and use it to suppress the noisy frame.

The second detection method is based on the estimation of the local motion vectors and computes their global mean in axial direction. This value will indicate how fast the operator applies the probe in axial direction during the exam. A small value should correspond to a static frame that always gives unreliable strain values.

Because the hard structure is not easy to deform during the compression and decompress cycles, we try to extract hard structure tissue, like edges, from log compressed

ultrasound image with a method based on ultrasound statistics [4] (e.g., a ratio of local variance to the local mean is used to extract edges) to get edge image, Fig.1. Then we use the edges image to an image registration based motion estimation method, e.g. the sum-absolute-difference method, to calculate the local tissue motion. We assume the internal edges motion can be ignored compared with the external probe motion. The mean of all detected local motion along the compression direction will be used to approximate the external probe motion. This value coupled with the quality ratio of Eqn (7) will be used as a segmentation tool to modify the strain image for reducing the noise. For example, if the motion is within 15% of the maximum velocity of a sequence of images, the current strain image will be seen as a noise image and enforce it with background color.

Besides using the motion estimation to identify the noise image, we apply it for adaptive persistence to compensate the motion in strain display. On each local area of the original tissue image, e.g., an 8*8 window, we compute the motion vector from the frame k to $k+1$ and accumulate all of the motion vectors starting from a reference frame. This motion information will be used to compensate the motion in strain display. On each strain image frame, every pixel could be shifted back referred to the starting reference frame so that each pixel should be at its right position without the effect of the motion.

This procedure will make the temporal process more accurate, for example, we apply the peak hold persistence, i.e., taking the maximum value between the current compensated pixel and the pixel on the previous frame. This peak hold persistence method will significantly increase the signal to noise ratio of the strain image display because it extracts all the strong signals, i.e., the hard tissue in our case, and also reduces the noise pixels with the help of right registration.

By using the motion detection methods to find out the global motion of each frame, we can display the motion

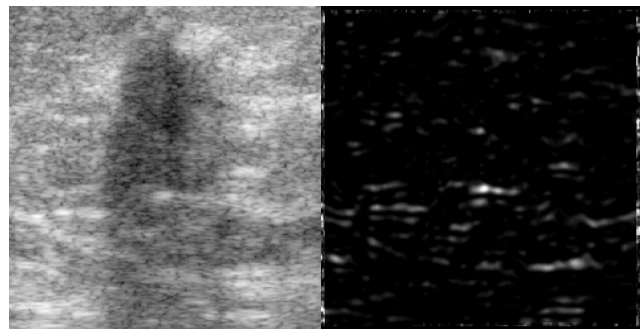


Fig. 1 The right one is the enhanced edge image of the left image

vector as a function of the image frame. Moreover we can display not only the velocity component but motion displacement by integrating the velocity component frame by frame. This curve will trace the motion pattern in the spatial domain.

IV. RESULTS AND CONCLUSIONS

In this paper, we present one of clinical case as an example to verify our algorithms. For a sequence of images, Fig.2 displays the mean of the difference (the solid line), and the global mean of each strain image (the dotted line). It seems that the region with high difference values always corresponds to that with low mean values and they show lots of noise in original strain images.

Fig.3 shows the processed images where the left top is the original tissue image and the right top is the strain image after the remapping processing of Eqn (2), followed by the left bottom of the histogram equalized strain image, and finally the color transparency image of the right bottom. It's clear that, by comparing the strain image and its color transparency display, one can more easily extract the hard tissue in color and also ignore the noise shown as the background color.

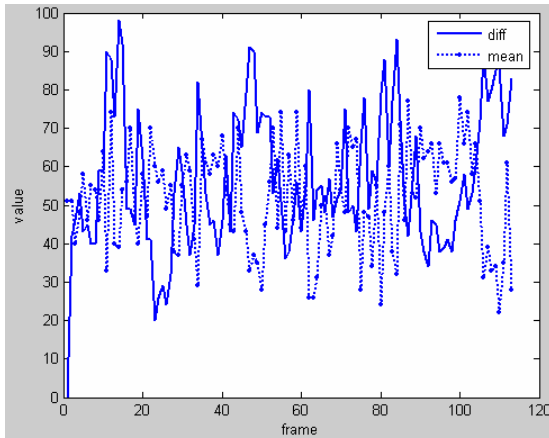
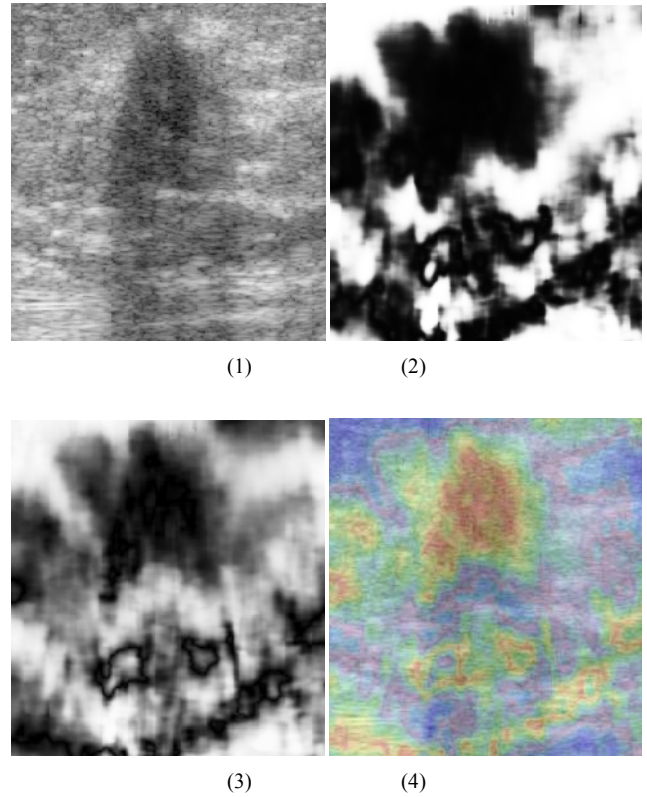


Fig.2 The mean difference (solid) and the mean (dotted) of each frame

Fig.3 (1) the original tissue image (2) the strain image with remapping (3) the histogram equalized strain image (4) the color transparency image

By using the motion detection algorithm, we can calculate the velocity from each frame and display its axial component in left panel of Fig.4 where the positive value means the velocity along the compression and the negative one represents the decompression. It seems that the first 25 frames are almost static and this situation can be verified from Fig.2 where the first 25 frames show higher differences and lower mean intensities. By integrating the velocity curve of Fig.4 we can obtain the displacement curve shown as the right panel of Fig.4 which shows a nice compression and decompression cycle between frames 35 to 77.

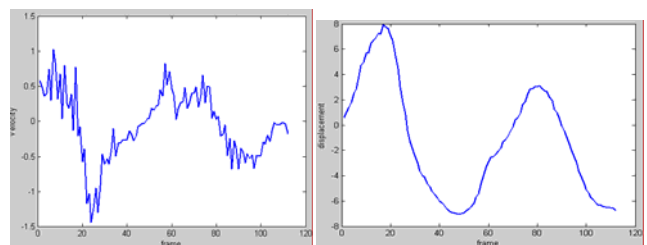


Fig.4 (1) The axial velocity (2) The displacement curve

Fig.5 is the result of applying the motion velocity in the adaptive persistence to display a peak hold value. This result shows the highest signal to noise ratio for the hard tissue. Moreover, for a cine sequence, we show the motion displacement as a graphics curve synchronizing with the probe motion during the exam, Fig.6 where a flat part of the displacement curve always indicates a very slow motion occurred during that period. This graphics tool could be used as an interactive feedback so that the operator may use it to make sure an appropriate compression/decompression procedure has been obtained.

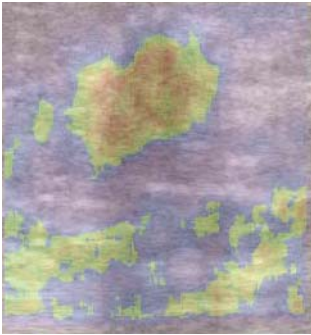


Fig.5 Color transparency picture of a peak hold strain image

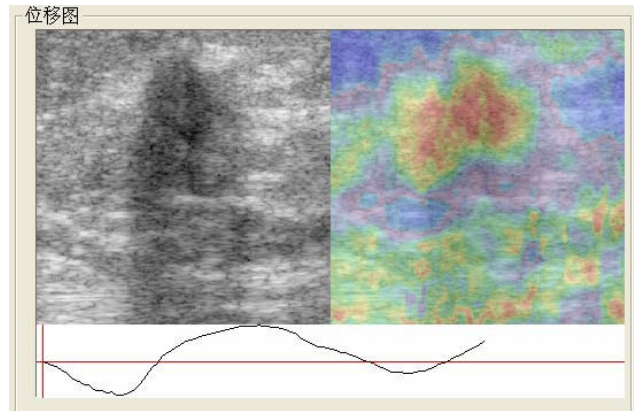


Fig.6 A graphics tool to show synchronized probe motion and strain images

REFERENCES

- [1] Pesavento A, Lorenz A, et.al, (2000) Frame-to-frame statistics of real-time strain images, IEEE Ultrasonics Symposium, vol. 2, pp.1809-1812 .
- [2] Tanaka G, Suetake N et.al., (2007) Image enhancement based on multiple parametric sigmoid functions, Intelligent Signal Processing and Communication Systems., ISPACS 2007, pp.108-111.
- [3] Flinn GS Jr.,(1975) Gray scale color coding of abdominal B-scan ultrasonograms, Journal of Clinical Ultrasound, vol. 3, pp. 179-185.
- [4] Lin C H, Lin M, et.al., (2007)Ultrasound motion estimation using a hierarchical feature weighting algorithm, Computerized Medical Imaging and Graphics, vol. 31, pp.178-190.

Author: Fei.Luo, Dong C. Liu
 Institute: School of Computer Science, Sichuan University
 Street: The First Ring Road
 City: Chengdu
 Country: China
 Email: feifei0723@gmail.com

Adaptive Spatial Processing for Autocorrelation-based Ultrasound Color Flow Imaging

Qiang Wang and Dong C. Liu

School of Computer Science College, Sichuan University, Chengdu, Sichuan, China

Abstract—The Doppler ultrasound technique is now commonly used in noninvasive blood flow examination. A standard 1D narrowband phase-shift technique has been used to estimate the Doppler frequency shift by averaging a number of successive received echoes through the autocorrelation method. This method was regarded as an optimal algorithm in view of the estimation fidelity and its simplicity for real time implementation; however, it suffers the aliasing for velocities exceeding the Nyquist limit. To handle velocity ambiguity and offer better robustness under heavy noise conditions, we have published a spatial-temporal averaging method as a modified autocorrelation technique (MA). This method can be seen as a special case of more general 2D autocorrelation methods. This paper, then, presents an adaptive spatial averaging process for the MA method so that we can enhance the velocity detectability and also maintain the high resolution of velocity differentiation.

Keywords— Doppler color flow mapping, aliasing, autocorrelation, cross-correlation, spatial averaging

I. INTRODUCTION

Color flow mapping (CFM) is an important noninvasive technique for measuring blood velocity shown as pseudocolor display overlaid on the tissue image. A standard 1D narrowband phase-shift technique offers a simple way to estimate the flow velocity [1], called TA in this paper, but it suffers the aliasing for velocities exceeding the Nyquist limit. Other methods based on phase and time delay, for example, cross-correlation methods lead to no velocity ambiguity but need to locate the precise delay through interpolation [2]. To remove the fluctuation of the Doppler amplitudes, a spatial-temporal averaging method as a modified autocorrelation technique (MA) was proposed [3] which may need a sufficiently large window size for spatial averaging.

Applying the spatial averaging with a window size larger than the coherence interval in the spatial domain will deteriorate the color flow imaging performance in terms of loss of velocity resolution. Recently, [4] presented a way to choose the right size for the spatial averaging window and in this paper, we improve [4] by proposing an adaptive way, called AA, to fine tune two parameters, the variance computed from the MA method with an initial spatial window size, and a local correlation value, called LCV,

obtained from Doppler signals of two consecutive spatial samples. The correlation value can be estimated from the standard minimum of sum-absolute-difference (SAD) within a pre-defined searching window.

It's clear that a larger minimal SAD means less correlation from which more velocity variety could have occurred within the selected range gate. In this case, a shorter coherence interval is observed and our algorithm will apply a small size of spatial window for averaging to preserve better velocity resolution. The variance computed from the MA method may relate to the case of heavy noise environment which we could use a big size of spatial window for averaging to increase the signal-to-noise ratio (SNR) and for anti-aliasing purpose.

Section II describes Doppler signal formulation for CFM imaging where we have derived equations for MA (the fixed size of spatial averaging window) and algorithm design of AA (with varied size of spatial window). Computer simulation and results are discussed in Section III, followed by Conclusion, Section IV.

II. DOPPLER SIGNAL FORMULATION AND ALGORITHM DEVELOPMENT

The synthetic time domain Doppler signal has been generated by calculating the inverse Fourier transform of a spectrum with Gaussian shape where information about the frequency of blood signal, the bandwidth, pulse repetition frequency, the ensemble size of Doppler signals (i.e., the number of echoes used to generate each velocity estimate) and the system noise have been included [5].

Using the well-established autocorrelation method, the Doppler shift frequency f_d at depth n is given by

$$f_d = \frac{1}{2\pi T} \arg(R(n)) \quad (1)$$

where T is the pulse repetition period and the autocorrelation function $R(n)$ can be estimated by

$$R(n) = \frac{1}{2K+1} \frac{1}{M-1} \sum_{k=-K}^K \sum_{m=0}^{M-2} S^*(n+k, m) S(n+k, m+1) \quad (2)$$

with averaging performed in both space (i.e., the axial direction in k) and time (i.e., the temporal direction corresponding to pulse transmissions in m). The variance is then

$$\sigma^2(n) = \frac{2}{T^2} \left(1 - \frac{|R(n)|}{P(n)} \right) \quad (3)$$

where

$$P(n) = \frac{1}{2K+1} \frac{1}{M} \sum_{k=-K}^K \sum_{m=0}^{M-1} I^2(n+k, m) + Q^2(n+k, m) \quad (4)$$

is the Doppler power.

Algorithm development in this paper involves the adaptive way to determine the window size of the spatial averaging which depends on two parameters, the variance and the correlation value. Simulation results show that computed variance is a good estimator for SNR of the signal. The local correlation value, called LCV can be approximated by the sum-absolute-difference (SAD) method whose value is related to the velocity resolution. Mathematically, the SAD is defined by

$$SAD(w) = \sum_i |S_1(i) - S_2(i+w)| \quad (5)$$

where w denotes the shift of the second signal S_2 with respect to the reference signal S_1 . A small SAD means a stronger correlation.

The proposed algorithm is as follows: Compute variance from the MA method with an initial spatial window size which it will be used to judge whether the current sample in the scanning line is under high noisy environment. If the current sample is under low noise, a small spatial averaging window size will be used. Repeat this procedure until the end of the scanning line. If the current sample is under high noise, then calculate the minimum SAD around the current sample to get the final size of the averaging window.

III. COMPUTER SIMULATION AND RESULTS

In computer simulation, three different methods are used to get the values of variance and velocity. The first is the traditional autocorrelation method, TA which works only in time domain. The second is modified autocorrelation method, with a sufficiently large window size, MA (use 5 in this paper). The third is the proposed adaptive spatial averaging method AA.

Figs. 1 and 2 show the signal variance and estimated flow velocity from three methods of TA, MA and AA under a high SNR (SNR= 20dB) environment. For the high SNR

the velocity calculation from those methods doesn't change too much and the computed variance is always small too (generally smaller than 0.05). In this case, TA and AA use the spatial window size of 1. For MA with a big spatial window, however, the performance is the worst.

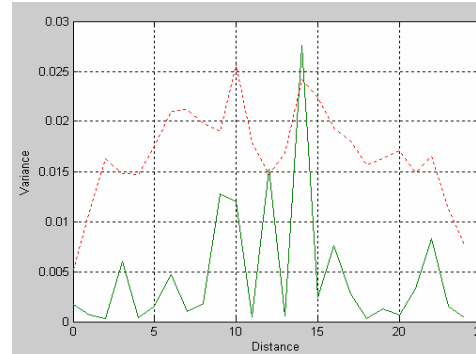


Fig. 1 Variances calculated by TA, MA, AA. The curves of TA and AA are the same; since both use the same window size (window size is 1). MA (dotted line) with a large window size shows the worst result.

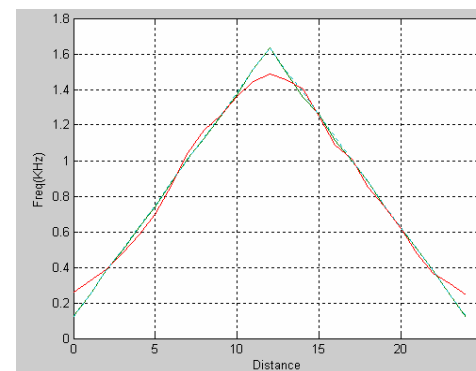


Fig. 2 Velocities calculated by TA, MA, AA. The curves of TA and AA are the same; MA (with a peak at the center) with a large window size shows the worst result.

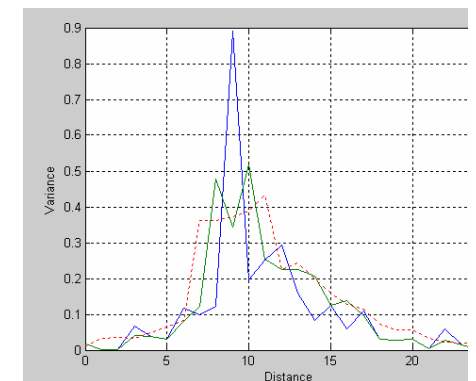


Fig. 3 Variances calculated by TA, MA, AA under high noise. TA (a peak at the center) performs worst. MA (dotted line) and AA reduce the variance.

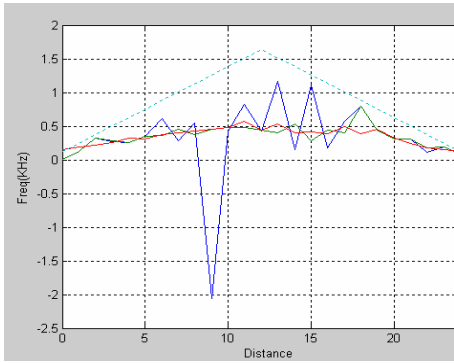


Fig. 4 Velocities calculated from TA, MA AA with same parameters as in Fig. 4. TA suffers the aliasing (a negative velocity). MA and AA (dotted line) avoid aliasing. The green line AA performs better than the red MA compared with the true velocity of triangular curve.

Signals used in Figs.3 and 4 are with high noise where we set SNR to be -5 dB. The added high noise results in velocity aliasing, for example, the very big variance around the center of TA curve in Fig.3 and the corresponding negative velocity shown in Fig. 4. Both MA and AA can avoid the aliasing with more spatial averaging. Moreover, AA performs better than MA with varied sizes of spatial window.

We have mentioned that the spatial window size is a function of variance and correlation value. The effect of variance has been discussed, and now, the effect of correlation value will be discussed. Correlation value is obtained from Doppler signals of two consecutive spatial samples. The correlation value can be estimated from the minimum SAD within a pre-defined searching window.

In our simulations, the selection of the spatial window size depends on noise value which again, is a function of the estimated variance. The variance range in section (0.0~0.05, 0.05~0.1, 0.1~0.4, 0.4~1) corresponds to the window size of 1, 3, 5 and 7, respectively. When the window size is determined by the variance as 1 or 3, current sample is considered as a low noise one, so it is unnecessary to calculate its minimum SAD. And when the window size is determined by the variance as 5 or 7, this sample is treated as a high noise sample, and it is necessary to calculate its minimum SAD to judge whether the noises of its surrounding sample are low or not.

When a sample in the scanning line is judged under high noisy environment, it has to be handled with spatial averaging. Under this condition it should not only be compared with noise of the current sample but also with the surrounding samples. If the noise level of surrounding samples is also large, we may not need to use too large a window size; otherwise, the noise of the current sample could be increased. This situation could be verified from

Figs. 5 and 6 where we add more noise around the peak shown in Fig. 3.

Minimum SAD represents the correlation differences among samples within a selected range gate. Larger minimum SAD value means greater differences. In the case of a sample with large noise and also larger minimum SAD with its surrounding samples, it is possible to have neighborhood under a low noisy level. Only under such condition, we can apply a large window size for spatial averaging.

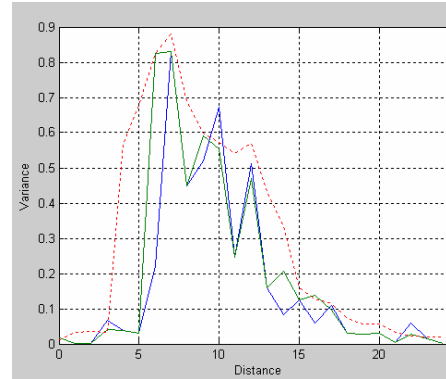


Fig. 5 Variances calculated by TA, MA, AA by adding more noises around the peak in Fig. 3. The variance from MA method (dotted line) has been greatly increased by added noises.

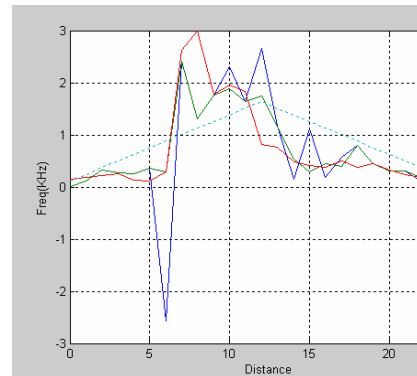


Fig. 6 Velocities calculated from TA, MA AA with same parameters as in Fig. 5. TA suffers the aliasing with negative velocities. The green line AA performs better than the red MA compared with the true velocity of triangular curve

According to the simulation results, the minimum SAD values can be divided into three sections (>15, 10~15, 0~10). These three sections are named C, D, E, respectively. Under the assumption of large noise for the current sample, if the minimum SAD belongs to section C, it means the noises of its surrounding samples are low. At this time, using a large window size can help reduce the noise of

current sample and avoid aliasing. A large window size of 5 or 7 is chosen for spatial averaging. If the minimum SAD belongs to section E, it means the noises of its surrounding samples are high. At this time, using a large window size will increase the noise of current sample, so the signal can be averaged only in the time domain, i.e., setting the window size of 1. If the minimum SAD belongs to section D, a medium size of 3 is chosen for the window size.

IV. CONCLUSION

This paper proposes an adaptive spatial averaging method, AA, based on previous published modified autocorrelation method (MA). Both AA and MA can improve SNR of ultrasound Doppler signals with heavy noises, compared with the standard autocorrelation method, TA which always suffers aliasing artifact under noisy environment.

In this paper we focus on the characteristics of noisy signals and local correlation values within a selected range gate. By looking at conditions such as noise of current flow sample (one flow sample corresponds to a set of Doppler signals with a specified ensemble size) and its surrounding samples, the correlation between two flow samples in spatial domain, we propose our AA method to determine the most appropriate window size for spatial averaging. Such method can reduce noises, especially when noises are high, and also increase the velocity resolution by using a small size of spatial window in the case of high SNR environment.

Our future work will be the integration of the proposed AA method to a digital ultrasound scanner made in our lab. Experiments using a flow phantom to test our method are under investigation in our lab.

ACKNOWLEDGEMENT

I greatly appreciate the help from my classmate Xu Yong.

REFERENCES

1. Kasai C, Namekawa K et.al. (1985) Real-time two-dimensional blood flow imaging using an autocorrelation technique, *IEEE Trans. Sonics Ultrason*, vol. SU-32, pp. 458-464
2. Bonnefous O and Pesque (1986) Time domain formulation of pulse-Doppler ultrasound and blood velocity estimation by crosscorrelation, *Ultrason. Imagzng*, vol. 8, pp. 73-85
3. Liu DC, Kim J et.al (1991) Modified autocorrelation method compared with maximum entropy method and Rf cross-correlation method as mean frequency estimator for Doppler ultrasound", *Proc. IEEE Ultrasonics Symposium*, pp.1285-1290
4. Xu Y, Liu DC (2007) Autocorrelation technique of Doppler color flow image in spatial domain, *CBME 2007 (in Chinese)* pp.782-785
5. Bjarum S, Torp H et.al (2002) Clutter filter design for ultrasound color flow imaging, *IEEE Trans. UFFC*, vol. 49, pp.204-216

Author: Qiang Wang and Dong C. Liu
 Institute: School of Computer Science, Sichuan University
 Street: The First Ring Road
 City: Chengdu
 Country: China
 Email: heremysow@163.com

Rationalized Gain Compensation for Ultrasound Imaging

Mingwang Tang and Dong C. Liu

School of Computer Science, Sichuan University, Chengdu, China

Abstract — Most of the automatic time gain compensation used in ultrasound scanners introduces artifacts and weakens the edges due to over-gains especially in the anechoic regions. One more procedure has been added in this paper to the algorithm developed by Pye et al. by computing both the axial (along the scan line) and lateral gains to find out the anechoic regions. Then, a further process has been applied to the anechoic regions to reduce the artifacts. The extended algorithm has been tested using ultrasound phantom and *in vivo* images. The detection of anechoic regions is determined by two constraints with information from different size of processing windows along axial and lateral direction, respectively. One constraint detects the dark areas along the axial direction and the second one detects the lateral direction in order to remove the case of uniform area. By controlling the constraint parameters we can define different level of anechoic regions. Test results have shown that the extended algorithm has better contrast in different tissue types than the original one in images with anechoic regions.

Keywords — ultrasound imaging, time gain control, rationalized gain compensation, image uniformity, anechoic

I. INTRODUCTION

In ultrasound imaging, the pulse signals are attenuated strongly by the tissues examined [1]. When the transducer received the pulse-echo signals, they would span a large dynamic range. This makes the signals unsuitable for direct display on the video screen before a further signal gain compensation applied. The first stage of compensation is applied on the radio-frequency (RF) amplifier in the receiver. The RF amplifier varies the voltage gain with time so that echoes from deep structures compensated more than the superficial ones in order to reduce the dynamic range [2]. This process is known as “time gain compensation” (TGC) or “depth gain control”, also see Pye et al. [3].

The shortcoming of the manual TGC has been addressed by [3], such as the inflexible gain control function which is irrespective to the non-uniformity of the tissues. In addition, accurate adjustment of the TGC has always been a major source of difficulty to operators. Therefore, an adaptive time gain compensated scan is very desirable.

There are many designs of automatic time gain compensation (AGC) but most of them introduce artifacts, especially, in the region of large fluid spaces, such as liquor

amnia, the bladder or gallbladder. The purpose of our rationalized gain compensation (RGC) system is, besides the two issues just mentioned, to extend the adaptive TGC algorithm developed by Pye et al. with concentration on images with large anechoic regions. We reduce the artifacts (noise) from over-gains in those anechoic areas and raise the intensities around the edges in images with large fluid spaces. Section II describes Pye et.al.’s original method and its limitation, followed by our proposed algorithms. Computer simulation and results are discussed in Section III and then Conclusions, Section IV.

II. METHODS AND ALGORITHMS

The RGC system can be used to process gray-scale image either before scan conversion or after scan conversion. In addition, the RGC system can be treated as a stand alone TGC system and it also adapts to the system with initial TGC setting.

A. Algorithm review of Pye et al.

In echo domain, Pye et al.[3] determined the gain function from two components: one component is derived using echo information locally in the axial direction, the other component is derived using echo information averaged over a large part of image:

$$G(x,y) = \begin{cases} G^{(g)}(y) & \text{if } G^{(l)}(x,y) \geq G^{(g)}(y) \\ \beta G^{(l)}(x,y) + (1-\beta)G^{(g)}(y) & \text{otherwise} \end{cases} \quad (1)$$

where y is the depth measured from the transducer along a scan line, $G(x,y)$ is the gain applied at depth y of the x^{th} scan line, $G^{(l)}(x,y)$ is the local gain function at the depth y from the x^{th} scan line with a window length of few millimeters, and $G^{(g)}(y)$ is a gain function at depth y averaged over several centimeters.

Note that, in Eqn (1), the gain function $G^{(l)}(x,y) \geq G^{(g)}(y)$ means the local signal level is less than the average (i.e., needs more gains relative to close points at same depth), which could corresponds to vessels or other anechoic regions. Otherwise, $G^{(l)}(x,y) < G^{(g)}(y)$, the local signal level is larger than the average. Such signals are the ones that could be in saturation.

Mathematically, $G^{(l)}(x,y)$, the local gain along the axial direction at the point (x,y) or (i,j) with $1 \leq i \leq M$ and $1 \leq j \leq N$, is defined by

$$G^{(l)}(i, j) = \frac{\bar{h}_i^{(y)}}{h_{i,j}^{(y)}}, \quad (2)$$

where

$$h_{i,j}^{(y)} = \frac{1}{W_y} \sum_{k=j-\frac{W_y}{2}}^{j+\frac{W_y}{2}} I_{i,k}$$

is the intensity $I_{i,k}$ averaging in the axial direction with a window length of W_y , and

$$\bar{h}_i^{(y)} = \frac{1}{N} \sum_{l=1}^N h_{i,l}^{(y)}$$

is the mid-gray level along the axial direction. Similarly, the global gain $G^{(g)}(y)$ will be

$$G^{(g)}(j) = \frac{\bar{H}}{H_j} \quad (3)$$

where

$$H_j = \frac{1}{W_g} \sum_{k=j-\frac{W_g}{2}}^{j+\frac{W_g}{2}} L_k$$

is the average in the axial direction based on the lateral intensities of

$$L_j = \sum_{i=1}^M I_{i,j}$$

and

$$\bar{H} = \frac{1}{N} \sum_{j=1}^N H_j$$

is the mid-gray level along the axial direction. Eqn (1) and its mathematical formulations of Eqns (2) and (3) are the basic processing formulas of the adaptive time-gain compensation algorithm developed by Pye et al. [3]. The clinical trials of this algorithm (with $\beta=0.5$ in Eqn (1)) are described by [4], who report that 80% of the images produced by this algorithm in abdominal and obstetric scanning were significantly better than manually set TGC images of the same tissue sections.

B. New algorithms

Pye et al.'s algorithm may need improvements in two issues: (1) raise the intensities around the edges in images with large areas of anechoic regions, (2) reduce the artifacts (noise) in the region of large fluid spaces. Because Eqns (2) and (3) always give a uniform intensity in image by compensating more in the dark areas which could weaken the edges especially in the case of having large areas of anechoic regions. Moreover, the low attenuation of these anechoic structures (e.g. liquor amnia, the bladder or gallbladder) confuses the system and produces incorrect compensation which introduces artifacts (i.e., apply more gains than necessary).

To raise the intensities around the edges we can use the maximum value of the original pixel and the updated value of Eqn (1) especially in the case of already having initial TGC in the system. Note that this simple adjustment can be extended to work with manual TGC system in the following steps, also see Fig. 1:

1. Set an initial TGC in the system.
2. Use the image (envelope data before the scan conversion) from the initial TGC as the input to the proposed automatic TGC algorithm and update the image pixels.
3. If user defines a new TGC curve, the new parameters (gain or loss as the function of the depth) will go to the RGC system and then compute the new gain (where it is only depth dependent).
4. The output of the RGC will be the output from Item 2 with a modification of user defined gain curve.

To reduce the noise from the over-gain in the anechoic regions we need to detect where the large anechoic region is by using one more formula in the lateral direction.

$$h_{i,j}^{(x)} = \frac{1}{W_x} \sum_{k=i-\frac{W_x}{2}}^{i+\frac{W_x}{2}} I_{k,j} \quad (4)$$

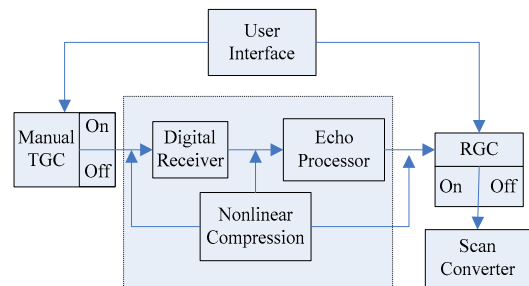


Fig. 1 Functional blocks of RGC system

and its mid-gray level

$$\overline{h}_j^{(x)} = \frac{1}{M} \sum_{l=1}^M h_{i,j}^{(x)}$$

The large anechoic regions could be detected by using the following constraints from Eqns (2) and (4),

$$\begin{aligned} h_{i,j}^{(y)} &< \varepsilon \overline{h}_i^{(y)} \\ h_{i,j}^{(x)} &< \eta \overline{h}_j^{(x)} \end{aligned} \quad (5)$$

where $0 \leq \varepsilon, \eta \leq 1$ are two constants. The first equation of (5) detects the dark areas along the axial direction and the second one detect the lateral direction in order to removes the case of uniform area. A smaller ε or η defines strong (but a smaller area) anechoic regions. If the current pixel is under the constraint of Equations (5), it will be updated by

$$I'_{i,j} = \gamma I_{i,j} \quad (6)$$

where $0 \leq \gamma \leq 1$. All the updated pixels in Eqn (6) will be smoothed through a simple low-pass filter, e.g., a 3×3 box filter.

At last, we adopt a linear stretch transformation function Eqn (7) to adjust the brightness and contrast of the image.

$$I_{new} = \alpha(I_{old} - m) + M \quad (7)$$

where $0 \leq \alpha \leq 1$, I_{new} is the new pixel value, I_{old} is old pixel value, m is the mean value of old image, M is new mean value of the desired image.

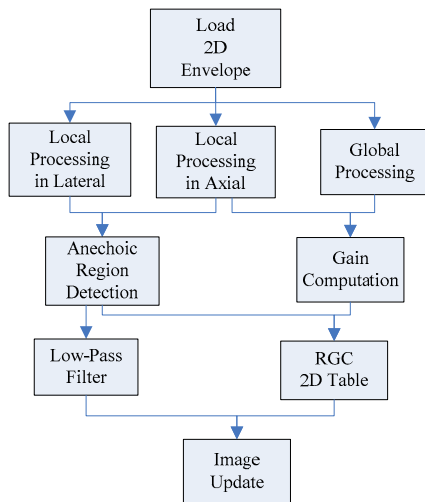


Fig. 2 Flow chart of the computation of the rationalized gain control

Consequently, the proposed RGC algorithm is summarized as follows, see Fig. 2:

1. Load the 2D envelope data which have already been compensated by initial TGC or system gains such that useful information has not been lost.
2. Compute the local gain in the axial direction of Eqn (2), the global gain of Eqn (3) and the local gain intensities in the lateral direction of Eqn (4).
3. Compute the gain function defined by the maximum of original one and the value of $G(x,y)$ in Eqn (1).
4. Modify the gain function obtained from Item 3 for detected anechoic points by using Eqns (5) and (6).
5. Update the image data (i.e., the 2D envelope data) and taking a 2D low-pass filter to those anechoic points.
6. Apply a linear stretch function of Eqn (7) to the result of Item 5.

III. COMPUTER SIMULATIONS AND RESULTS

In this section we will test the RGC algorithm in phantom and some *in vivo* images. We first apply the original AGC algorithm (i.e., the algorithm developed by Pye et al. [3]) to the test phantom. Fig. 3.1, the original phantom, Fig. 3.2–4 show the results from the local gain only, Eqn (2), the global gain only, Eqn (3) and the mix of the local and global gains, Eqn (1) with $\beta=0.5$. There are little differences for this phantom image. However, we can see the local gain works badly around bottom of the phantom due to loss of contrast. Global only and the mix of the local and global gains give similar performance.

However, as Pye et al. [3] discussed, the global only is not recommended because the penetration in image is not good and also the signal level could be either too low or in saturation. Therefore, our modification will be based on the mix of the local and global gains, Eqn (1) with $\beta=0.5$. In the following tests we will use a local window of 1 cm in axial direction, Eqn (2), a local window of 1 cm in lateral, Eqn (4), and a window of 3 cm in axial and whole scanning in lateral for global computation, Eqn (3).

Fig. 4.1 shows the image with manual TGC in saturation around the edges so that reverberation artifacts could be seen on image. If we applied the original AGC to it, the edges are not clear due to the over-smoothed image, Fig. 4.2. The proposed RGC, Fig. 4.3, shows more clear structure in the deep depth and preserve edges in shallow depth. The constraint condition of Eqn (5) for detecting the large anechoic regions has been validated in Fig. 4.3 where we use $\varepsilon=0.6$ and $\eta=0.8$. It is clear that the RGC has better contrast in different tissue types than the original algorithm.

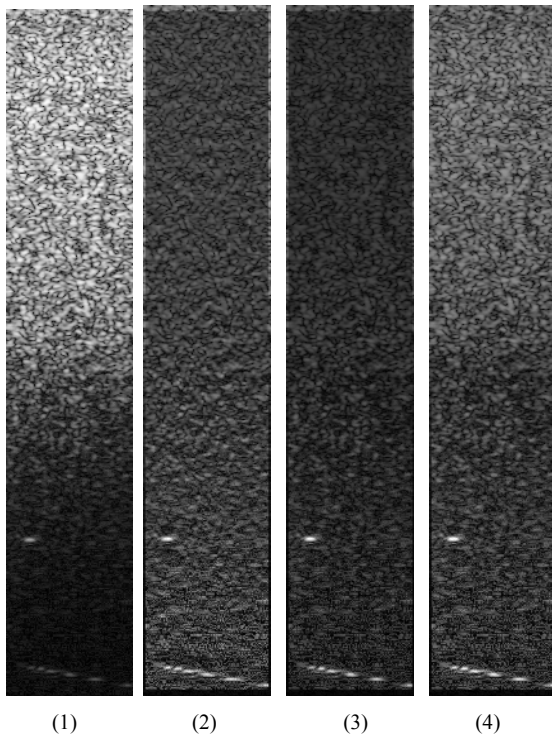


Fig. 3 Ultrasound phantom images: (1) original image (2) local gain only (3) global gain only (4) a mix of local and global gains

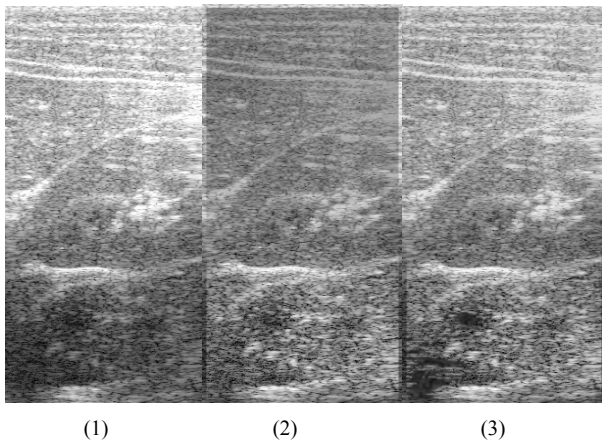


Fig. 4 Ultrasound *in vivo* images: (1) original image (2) output of AGC system (3) output of RGC system

IV. CONCLUSIONS

In this paper we first implemented the adaptive time gain compensation algorithm presented by Pye et al. [3]. We, therefore, extended their algorithm by adding one more procedure from the local intensities change in the lateral direction. The effects of our improvements will provide more control to detect the large anechoic regions in image which will help to reduce the artifacts (noise) from over-gains in those areas and preserve a better edge detectability.

Besides as a stand alone AGC, the current RGC algorithm can work with the existing manual TGC system in two ways: initial time gain compensation displayed to user in the beginning; or automatically TGC with enhancements/droops in the areas determined from user.

The current RGC algorithm could be seen as a preprocessing for statistics based speckle reduction due to its ability to provide a uniform image and also for image enhancements because of more clear tissue structure could be obtained.

The future work of the RGC system will concentrate on optimization of system parameters to get more desirable images.

REFERENCES

1. Checkovich P (1998), Time-gain control sharpens ultrasound, Analog Devices, Design news vol.15, pp103-104
2. Blackwell R (1993), Ultrasound Equipment, in Abdominal and General Ultrasound, vol. 1, edited by D. Cosgrove, H. Meire and K. Dewbury, Longman Group, UK
3. Pye S.D, Wild S.R, McDicken W.N (1992), Adaptive time gain compensation for ultrasonic imaging, Ultrasound in Med.& Biol., vol. 18, pp.205-212
4. Pye S.D, Wild S.R, McDicken W.N (1998), Clinical trial of a new adaptive TGC system for ultrasound imaging, Brit. J. Radiology, 61, pp. 523-526

Author: Mingwang Tang and Dong C. Liu
 Institute: School of Computer Science, Sichuan University
 Street: The First Ring Road
 City: Chengdu
 Country: China
 Email: tmw507@126.com

Interactive Frequency Compounding to Medical Ultrasound Images

Xiaoming Zhou and Dong C. Liu

School of Computer Science, Sichuan University, Chengdu, Sichuan, China

Abstract — Frequency compounding applies similar ideas of incoherent averaging of signals with different speckle characteristics by changing the spectrum of the acoustic pulses in transmission, reception, or both. Previous works in the literature showed that simple frequency compounding (e.g., by changing the acoustic center frequency of the transmitted pulse) with a fixed bandwidth system may degrade image quality due to the loss of axial resolution. Therefore, a new model of frequency compounding proposed in this paper is needed which can offer flexible ways to control the number of sub-bands, the level of overlaps, the weighting applied to each sub-band, the transition bandwidth, stopband suppression, and steepness of the transition band. These parameters can be adjusted from the user interactively to maximize the improvement in SNR by speckle reduction with a predefined axial resolution loss.

Keywords — Speckle noise, Frequency compounding, Gaussian interpolation, spectrum, SNR.

I. INTRODUCTION

Speckle reduction is one of important research areas in medical ultrasound field for improving contrast resolution [1]. The signal-to-noise ratio of a B-mode image can be improved by a frequency diversity process [2]. The correlation between narrowband images decrease with increasing center frequency separation. A corresponding increase in SNR is also observed. The filters separation in terms of their center frequencies is determined by the number of sub-band filters. Few sub-band filters deal with filter separation.

Because the big frequency separation width is important than the big filter separation, so we must use more sub-band filters with narrow bandwidth to deal with the spectrum. The frequency filters should be chosen to evenly partition and completely span the received-pulse spectrum.

Several research areas may get help through a flexible frequency diversity process: (1) image enhancement by locating the frequency independent parts from each sub-band signal, (2) attenuation estimation in broadband system as suggested by [3] by using a split-spectrum processing for reducing the errors which come from the frequency downshifting of the received-echo spectrum

This paper provides mathematical formulations for computing a set of multi-band Gaussian filters as a frequency diversity process in an interactive way. This technique in-

cludes the following steps from a functional view point: (1) estimate the standard deviation of the received-echo spectrum by a Gaussian fit where the spectrum could be obtained from experiments in speckle regions or approximated by the transmission spectrum with appropriate frequency shift;

(2) the original wideband echo signal will be filtered by M narrow-bandpass Gaussian filters. These filters together cover the total useful frequency range of the received-echo spectrum, and the center frequencies of these filters are evenly distributed. To modify the balance between the independence of the adjacent bands and the ability of the sub-band signals to cover the useful frequency range, we can define a ratio, r , the height of the cross point of two adjacent bands. A small value of r means more independent of two adjacent bands but a larger gap left in the frequency domain;

(3) apply weighting coefficients W_i to each sub-band signals to enhance frequency independent features. The parameters M , r and W_i are given by user interactively, i.e., user can look at imaging in real time during the adjustment.

In this paper we present a simple moving peak based Gaussian interpolation to the normalized received spectrum, followed by a theoretical formulation to derive M split spectra, also called Gaussian shaped decorrelation curves. This theoretical work makes the real time implementation feasible.

II. GAUSSIAN INTERPOLATION OF THE RECEIVED-ECHO SPECTRUM

The purpose of a Gaussian interpolation of the spectrum is to obtain its standard deviation for estimating the sub-band filters in the next Section. The spectrum could be obtained from the approximation by the transmit spectrum with the frequency shift. As we know the original spectrum has higher harmonics, so we must do interpolation. In general, we know the spectrum may not be Gaussian. But we could have the Gaussian spectrum to estimating the sub-band filters. Therefore, Gaussian interpolation of the received-echo spectrum is needed. The Gaussian filter is for estimating the standard deviation of the spectrum from which we can obtain the standard deviation of the sub-band filter. For minimizing the interpolation error, we must have a simple algorithm based on the peak moving and the width changes of the Gaussian function.

Algorithm 1: Gaussian interpolation to the normalized function $g(x)$

1. Define $x_0^{(j)} = \tilde{x}_0$, the peak position of $g(x)$

2. Set the initial η_i .

2.1 Find ω_r and ω_l such that $g(x_0^{(j)} + \omega_r) = g(x_0^{(j)} - \omega_r) = \eta_i$. Compute $f(x, x_0^{(j)}, \sigma_k)$, $\sigma_{\min} \leq \sigma_k \leq \sigma_{\max}$ where $\sigma_{\min} = \frac{\min(\omega_r, \omega_l)}{\sqrt{-2 \ln \eta_i}}$ and $\sigma_{\max} = \frac{\max(\omega_r, \omega_l)}{\sqrt{-2 \ln \eta_i}}$

2.2 Find $\sigma_j \equiv \sigma_{k^*}$, such that Error [$g(x)$, $f(x, x_0^{(j)}, \sigma_{k^*})$] is the minimum $\forall \sigma_k$.

2.3 Repeat steps (2.1) and (2.2) by changing $x_0^{(j)}$ in the range of $\tilde{x}_0 - \Delta x_0 \leq x_0^{(j)} \leq \tilde{x}_0 + \Delta x_0$. We will obtain a sequence of σ_j 's corresponding to a local best fit to $g(x)$ for a given $x_0^{(j)}$. Find $\sigma_i \equiv \sigma_{j^*}$, such that Error [$g(x)$, $f(x, x_0^{(j)}, \sigma_{j^*})$] is the minimum $\forall \sigma_j$.

3. Repeat step 2 by changing η_i in the range of -3dB down to. We will obtain a sequence of σ_j 's. Find $\sigma^* \equiv \sigma_{i^*}$ such that Error [$g(x)$, $f(x, x_0^{(j)}, \sigma_{k^*})$] is the minimum for all σ_i and $x_0^{(j)}$. The interpolated Gaussian func-

tion is then $f(x) = e^{-\frac{(x-x_0^*)^2}{2\sigma_*^2}}$

By changing the two parameters, standard deviation and the peak position in Algorithm 1, we can obtain a best fit.

III. COMPUTATION OF THE SUB-BAND GAUAAIN FILTERS

In this Section we will compute M split spectrums with a given ratio $r^{(0)}$ of the cross point of the first two adjacent bands under the assumption that each equidistant split spectrum has the same standard deviation. The M split spectrum should cover the total useful frequency range of the received pulse spectrum.

The derivation of the split-spectrum is equal to resolve the following system equation:

$$a_k e^{-\frac{(x-x_k)^2}{2\sigma_1^2}} = a_{k+1} e^{-\frac{(x-x_{k+1})^2}{2\sigma_1^2}} \quad (1)$$

$$a_k e^{-\frac{(x-x_k)^2}{2\sigma_1^2}} = e^{-\frac{x^2}{2\sigma^2}} = r$$

with the auxiliary conditions

$$\frac{a_{k+1}}{a_k} = e^{-\frac{1}{2\sigma^2}(x_{k+1}^2 - x_k^2)} = e^{-\frac{1}{2\sigma^2}(2k+1)\Delta x^2}$$

$$a_k r^{(k)} = a_k e^{-\frac{(x-x_k)^2}{2\sigma_1^2}} \quad (2)$$

The variables a_k and r^k define the height and the ratio at the cross point of the k -th sub-band function. The ratio r in Eqn (1) is a given number which is related to how wide of the original spectrum to be covered by M split spectrums. The variables σ and σ_1 denote the standard deviations of the interpolated Gaussian and the split spectrum.

From Eqn (1) and the first auxiliary condition we obtain

$$x - x_k = \frac{\Delta x}{2} [1 + (2k+1) \frac{\sigma_1^2}{\sigma^2}]$$

where $\Delta x = x_{k+1} - x_k$. According the second auxiliary condition, we also obtain

$$\ln r^{(k)} = -\frac{\Delta x^2}{8\sigma_1^2} [1 + (2k+1) \frac{\sigma_1^2}{\sigma^2}]^2 \quad (3)$$

Because $r^{(k+1)} < r^{(k)}$ implies $r^{(k)}$ is a decreasing function of k so the ratios of the cross points for each k will be decreased.

$$\frac{x_k^2}{2\sigma^2}$$

From Eqn (2) and $a_k = e^{-\frac{x_k^2}{2\sigma^2}}$ we obtain

$$k\Delta x + \sigma_1 \sqrt{2\left(-\frac{k^2 \Delta x^2}{2\sigma^2} - \ln r\right)} = \sqrt{-2\sigma^2 \ln r} \quad (4)$$

According to the Eqns (3) and (4) we obtain:

$$\ln r^{(0)} = -\frac{\Delta x^2}{8\sigma_1^2} \left(1 + \frac{\sigma_1^2}{\sigma^2}\right)^2$$

$$k\Delta x + \sigma_1 \sqrt{2\left(-\frac{k^2 \Delta x^2}{2\sigma^2} - \ln r\right)} \leq \sqrt{-2\sigma^2 \ln r}$$

So we also obtain:

$$2k\sqrt{-2\ln r^{(0)}} \frac{\sigma_1 \sigma^2}{\sigma^2 + \sigma_1^2} + \sigma_1 \sqrt{8k^2 \ln r^{(0)} \left(\frac{\sigma_1 \sigma}{\sigma^2 + \sigma_1^2}\right)^2 - 2\ln r} \leq \sigma \sqrt{-2\ln r} \quad (5)$$

From Eqn (5) we have:

$$k^2 \leq \frac{\ln r}{\ln r^{(0)}} \left(\frac{\sigma^2 + \sigma_1^2}{2\sigma\sigma_1}\right)^2$$

which reduces to the representation of σ_1 by

$$\sigma_1 = \sigma \left[k \sqrt{\frac{\ln r^{(0)}}{\ln r}} \pm \sqrt{k^2 \frac{\ln r^{(0)}}{\ln r} - 1} \right] \quad (6)$$

Obviously, when we select the negative sign, σ_1 is less than σ . We know the input parameters are $M=2k+1$, the number of sub-bands, $r, r^{(0)}$. If we only consider the odd number of sub-band filters in this paper, we should obtain result from even number.

Algorithm 2: Computations of the split spectrums

1. From Eqn (6), if $k^2 \leq \ln r / \ln r^{(0)}$ we obtain

$$\sigma_1^{(0)} = \sigma \left[k \sqrt{\frac{\ln r^{(0)}}{\ln r}} - \sqrt{k^2 \frac{\ln r^{(0)}}{\ln r} - 1} \right],$$

$$\sigma_1^{(1)} = \sigma_1^{(0)} - \xi, \dots, \sigma_1^{(n)} = \sigma_1^{(n-1)} - n\xi,$$

where ξ denotes the iteration step.

$$\Delta x = 2\sqrt{-2\ln r^{(0)}} \frac{\sigma_1 \sigma^2}{\sigma^2 + \sigma_1^2}$$

define $\sigma_1 = \sigma_1^{(i)}$ and then

According to the above deduction, we can know the split spectrum is obtained as

$$y_i(x) = a_i e^{-\frac{(x-i\Delta x)^2}{2\sigma_1^2}}, \quad 0 \leq i \leq k,$$

where a_i could be computed from the interpolated Gaussian.

IV. COMPUTER SIMULATION AND RESULTS

In this section, we will transform the RF signal into the spectrum, and then do Gaussian interpolation of the spectrum, Fig.1 shows the results of five sub-band Gaussian filters which fully span a given spectrum with a bandwidth of 1.58MHz. The input parameters are $N=5, r^{(0)}=-6$ dB, and $w_i=1$.

Ideally, we should determine the sub-band filters from the received-echo spectrum. We will use a transmit spectrum to deal with five sub-band filters and see the ability of these five narrow band filters to cover all the information of the received spectrum.

In Fig2, we applied Algorithm 1 to get a Gaussian fit of the original spectrum with the calculated bandwidth of 1.58MHz.

To see the ability of these five sub-band filters to cover a complete span of the received spectrum we use a RF spectrum from one of the test sets. It is clear that, the five sub-band filters together can span the full useful range of the received spectrum, Fig. 3.

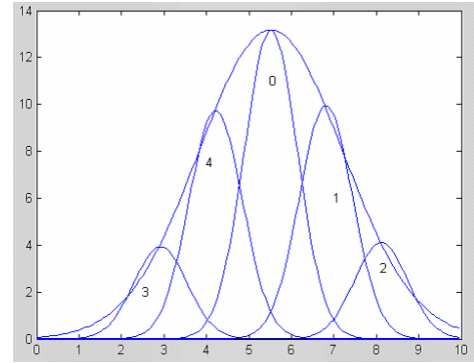


Fig. 1 The spectrum covered by 5 sub-bands

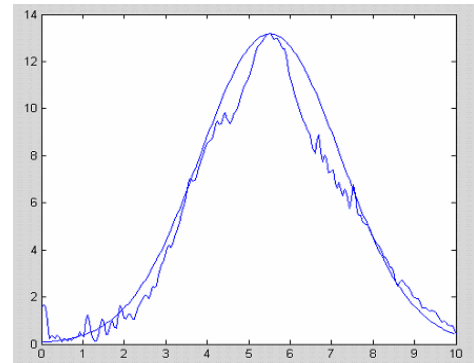


Fig. 2 The Gaussian fit of the original spectrum

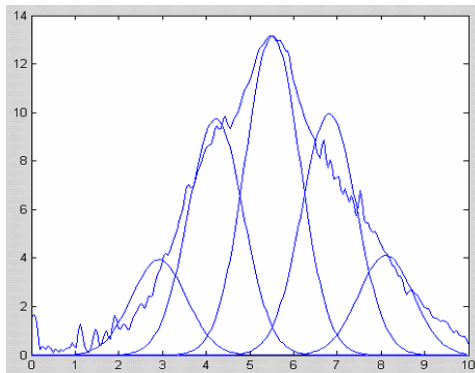


Fig. 3 A real spectrum covered by 5 sub-bands

We also tested our algorithms in phantom images. Fig. 4a shows the original image and the compounding results of the sub-band filters is shown in Fig. 4b and 4c with -6 and -12 dB overlap from the first two adjacent filters, respectively. We found that, from Fig. 4, the -12dB overlap filtering gives more soothing in the speckle areas but suffers more loss in detail resolution. Therefore, our frequency compounding algorithm can be seen as a tool to adjust the level of speckle reduction and the control of the loss in the axial resolution.

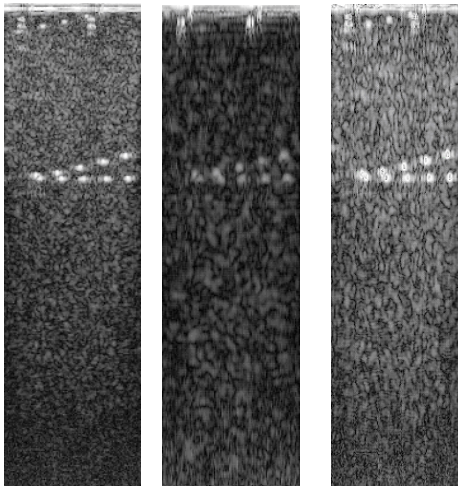


Fig. 4a The original phantom image, 4b: the compounding image with -6 dB overlap; 4c: the compounding image with -12 dB overlap

V. CONCLUSIONS

Simulation results showed that to keep the lateral resolution of the compounded image constant with changing band overlap, the sub-bandwidths have to be non-equal. Based on identified decorrelation curves, the SNR improvement for frequency compounding can be predicted. The application of extreme frequency compounding with more than three bands and no band overlap degrades the image resolution noticeably.

However, specialized applications such as the support of tissue characterization will benefit from the improvement in SNR and the enhancement from weighted frequency components proposed in our algorithm. These issues have been verified from our *in vivo* testing.

Therefore, we can see that frequency compounding can really reduce speckle noise and provide dramatic increases in the speckle pattern signal-to-noise ratios. By changing the three parameters: number of filters, the frequency overlap of the two adjacent bands and the weightings applied to each sub-band signal through interface directly, we can not only reduce speckles but enhance some frequency independent features.

REFERENCES

1. Bamber JC (1993) Speckle deduction, Advanced in ultrasound techniques and instrumentation, edited by P.N.T Wells, Churchill Livingstone, Inc.
2. Galloway RL, B.A. McDermott BA et.al, (1988), A frequency diversity process for speckle reduction in real-time ultrasonic images, IEEE Trans. Ultra Ferroelec Freq. Control, vol.35, no.1, pp.45-49.
3. He P (1989) Acoustic attenuation estimation for soft tissue from ultrasound echo envelope peaks, IEEE Trans. Ultra. Ferroelec. Freq. Control, vol.36, no.2, pp.197-203

Author: Xiaoming Zhou and Dong C. Liu
 Institute: School of Computer Science, Sichuan University
 Street: The First Ring Road
 City: Chengdu
 Country: China
 Email: softzhou621@163.com

Study on a novel tumor cell recognition system based on orthogonal image moments

Haiping Ren¹, Aizhen Liu², Ziliang Ping³ and Dongting Bai¹

¹ National Institute for the Control of Pharmaceutical and Biological Products, Beijing, China

² Beijing Tongren Hospital, Beijing, China

³ Inner Mongolia Normal University, Inner Mongolia

Abstract — Auto tumor cell recognition is always a research focus. Auto cancer cell recognition is always a research focus. Various types of features have been utilized to recognize cell image patterns in a number of applications. A novel image feature has been chosen for tumor cell recognition. The method is studied and a system is developed.

Keywords — moment, tumor, cell, recognition

I. INTRODUCTION

Cytological examination is indispensable for clinical diagnosis, therapy and research. It is extensively used for diagnosis of haemal system diseases, contagious diseases and tumors by samples of blood, cerebrospinal fluid and pleural effusion. However, the examination is nearly completely done by experienced experts, which is time consuming and hard sledding, thus not suitable for disease screening. Automatic, fast and accurate cell image recognition is needed to be realized urgently. Auto tumor cell recognition is always a research focus. Auto cancer cell recognition is always a research focus. Various types of features have been utilized to recognize cell image patterns in a number of applications. Moment is a highly concentrated image feature that has the invariant properties of moment function in multi-distortion of an image such as translation, scaling, rotation, and changing intensity. Therefore, it has been extensively employed as the invariant global features of an image in pattern recognition, image classification, target identification, and scene analysis [1-6]. A novel image moment feature has been chosen for tumor cell recognition. The method is studied and a system is developed.

II. METHODOLOGY

A. Image features

We had suggested to choose triangular function as radial function and proposed a new moment named Radial-Harmonic-Fourier moments (RHFMs) [7]. Compared with other orthogonal moment, RHFMs have a superior performance near the origin and better description ability for small images in terms of image reconstruction errors and noise

sensitivity. Former study shows that radial harmonic Fourier moments (RHFMs) are multi-distortion invariant. They are not only highly concentrated image features but also have a good property of anti-distortion and anti-noise. The definition of RHFMs is as following:

Function set $P_{nm}(r, \theta)$ defined in a polar coordinate system (r, θ) contains radial function $T_n(r)$ and Fourier factor in angle direction $\exp(jm\theta)$:

$$P_{nm}(r, \theta) = T_n(r) \exp(jm\theta) \quad (1)$$

here

$$T_n(r) = \begin{cases} \frac{1}{\sqrt{r}} & \text{if } n = 0 \\ \sqrt{\frac{2}{r}} \sin[(n+1)\pi r] & \text{if } n = \text{odd} \\ \sqrt{\frac{2}{r}} \cos(n\pi r) & \text{if } n = \text{even} \end{cases} \quad (2)$$

The set of $P_{nm}(r, \theta)$ is also orthogonal over the range $0 \leq r \leq 1$:

$$\int_0^{2\pi} \int_0^1 P_{nm}(r, \theta) P_{kl}(r, \theta) r dr d\theta = \delta_{nmkl} \quad (3)$$

where δ_{nmkl} is the Kronecker symbol and $r=1$ is the maximum size of the objects that can be encountered in a particular application. The image $f(r, \theta)$ can be decomposed with the set of $P_{nm}(r, \theta)$ as:

$$f(r, \theta) = \sum_{n=0}^{\infty} \sum_{m=-\infty}^{+\infty} \Phi_{nm} T_n(r) \exp(jm\theta) \quad (4)$$

here

$$\Phi_{nm} = \int_0^{2\pi} \int_0^1 f(r, \theta) T_n(r) \exp(-jm\theta) r dr d\theta \quad (5)$$

Φ_{nm} is defined as RHFMs.

B. Normalization and invariance

RHFMs are not invariant themselves, but they can be normalized into invariant for shifting, scaling, rotation and intensity distortion of an image [7]. Firstly, using the first-order geometrical moments to determine the center of the image and to be the origin of the coordinate system. All the moments calculated in this coordinate system are shift invariant. Secondly, since the angle function is a Fourier factor, a rotation of the image by an angle φ will result in a phase factor $e^{jm\varphi}$ for all order of Φ_{nm}^i . The modulus of RHFMs, $|\Phi_{nm}^i|$, are rotational invariant. Finally, Lower order Fourier-Mellin transfer $\frac{M_{10}^i}{M_{00}^i}$ [8] is computed for every distorted image in the training set. Using formula (6) and (7) to calculate k_i and g_i for each image with the ratio $\frac{M_{10}^i}{M_{00}^i}$ being a constant and slightly smaller than the minimum $\frac{M_{10}^i}{M_{00}^i}$ of all the images in the training set to ensure that the normalized images remain inside the unit circle.

$$k_i = \left(\frac{M_{10}^i}{M_{00}^i} \right) / \left(\frac{M_{10}}{M_{00}} \right) \quad (6)$$

$$g_i = \left[\left(\frac{M_{10}^i}{M_{00}^i} \right) / \left(\frac{M_{10}^i}{M_{00}^i} \right) \right]^2 \cdot \frac{M_{00}^i}{M_{00}} \quad (7)$$

Φ_{nm}^i is then calculated by formula (8) and (9) for all images of the training set, which is scaling and intensity distortion invariant.

$$\phi_{nm}^i = \int_0^{2\pi} \int_0^{k_i} g_i f(r/k_i, \theta) T_n(r/k_i) e^{-jm\theta} r dr d\theta \quad (8)$$

$$\Phi_{nm}^i = \phi_{nm}^i / g_i k_i^2 \quad (9)$$

Here, Φ_{nm}^i is the invariant moment of the image i .

C. pattern recognition experiment

Cell images were segmented from phlegm, urine, hydrothorax and ascites samples by manual work. The tumor cells include normal cells and cancer cells. 100 cell images were chosen to be the training set with intensities ranging from 0 to 255 in 64×64 pixel matrices after normalization. The reference set was obtained through rotating each reference object by 15, 30 and 45 degree and scaling it by 1.5 and 2 times, so as to determine the in-class variance of the RHFMs. The reference set includes 250 images. The testing set images were the rotated- (60 and 150 deg), scaled- (0.4

and 3 times), and intensity- (0.5 and 3 times) changed versions of the training images, without or with zero-mean additive noises $\sigma = 400$ and $\sigma = 2500$.

We used 25 RHFMs with $m, n=0,1,2,3,4$ to describe the images, and then obtained a 25-dimensional feature space $(x_1, x_2, \dots, x_{25})^T$. Testing objects were classified in the feature space using the weighted minimum-mean-distance rule. The weighted distance was calculated as:

$$d_i(M, N) = \left\{ \sum_{n,m=0}^{M,N} \frac{[|\Phi_{nm}| - (\Phi_{nm})_i]^2}{(\sigma_{nm})_i^2} \right\}^{1/2} \quad (9)$$

where $|\Phi_{nm}|$ is the modulus of the RHFMs of the testing object, $(\Phi_{nm})_i$ is the RHFMs of the reference object of class i and $(\sigma_{nm})_i^2$ is the in-class variance of the $(\Phi_{nm})_i$. M and N are the maximum circular harmonic order and highest degree of the radial polynomials respectively.

D. Result

For all 450 phlegm sample cell testing images, 5 are misclassified. False positive rate is 1.1%, False negative rate is 0. For all 450 urine sample cell testing images, 2 are misclassified. False positive rate is 0.4%, False negative rate is 0. For all 450 hydrothorax and ascites sample cell testing images, 5 are misclassified. False positive rate is 0%, False negative rate is 1.1%.

III. CONCLUSIONS

Image recognition experiments showed that the recognition system is good. But only use one kind of feature for recognition is not enough. Use both morphological features and RHFMs will be better and more accurate. And our work is focused on 2D images. Further study must be done on 3D images for further clinical use.

ACKNOWLEDGMENT

The research project is supported by the National Nature Science Foundation and the Inner Mongolia Nature Science Foundation.

REFERENCES

1. Hu M K. (1962) Pattern recognition by moment invariants. IRE Trans Inf Theory IT-8: 179-187.
2. Teague M R. (1980) Image analysis via the general theory of moments. J Opt Soc Am 70:920-930.

3. Sheng Y, Shen L.(1994) Orthogonal Fourier—Mellin moments for invariant pattern recognition. *J Opt Soc Am A* 11(6): 1748-1757.
4. Born M, Wolf E. (1980) *Principle of Optics*, Sixth edition, Pergamon Press 767-772.
5. Ping Z L, Wu Rigen, Sheng Y L. (2002) Image Description with Chebyshev-Fourier moments. *J Opt Soc Am A* 19(9):1748-1754.
6. Ren Haiping, Ping Ziliang, Bo Wurigen, et. Al (2004) Image Description with Jacobi-Fourier Moments. *ACTA OPTICA SINICA* 24(1):5-10.
7. Ren Haiping, Ping Ziliang, Bo Wurigen, et. al. (2003) Multi-distortion invariant image recognition with Radial-Harmonic-Fourier Moments. *J Opt Soc Am A* 120(4): 631-637.
8. Sheng Y L, Shen L X. (1994) Orthogonal Fourier-Mellin moments for invariant pattern recognition. *J Opt Soc Am A* 11:1748-1757.

Deformable Mesh based Motion Tracking for Ultrasound Strain Imaging

Zhiqiang Jiang and Dong C. Liu

Ultrasound Medical Imaging Lab, Sichuan University, Chengdu, China

Abstract — In this paper, we propose a method to estimate tissue motion from ultrasound images. The original image sequence is processed before the motion tracking in order to reduce decorrelation noise and enhance the images. The first image of the sequence will be used to generate “structure energy”, which represents the quality of locations for motion tracking. A mesh will be laid on the images uniformly at first, then the mesh nodes will be adjusted according to the “structure energy”. Every four tracking nodes are used to form one mesh node by interpolation in order to reduce errors. Motion tracking is performed on the processed image sequence using basic sum-absolute-difference (SAD) algorithm in order to ensure the efficiency. Mesh nodes’ positions are then obtained from every four tracking nodes to generate deformable tracking mesh. The motion result is used to calculate strain of the tissue. In displaying the ultrasound elastography, we suppress the strain errors according to the globe motion and strain level. *In vivo* B-Mode image sequences are used to verify the quality and efficiency of the method.

Keywords — ultrasound image, motion tracking, deformable mesh, strain imaging, elastography

I. INTRODUCTION

Before the advent of diagnostic imaging using elastography, palpation was one of the main methods of estimating the stiffness of the tissue. However, it is comparatively subjective and not very accurate. Elastography is based on the measurements of local tissue deformation, which provides doctors with a more powerful and reliable diagnostic tool, and can offer the valuable information of tissue stiffness while the traditional B-Mode image can not. Elastography was first introduced by Ophir J.[1] in 1991. Several methods have been invented to generate strain images in the literature, including cross-correlation functions (CCF), phase angle tracking CCF, finite element analysis of the deformable field where RF data, envelop data, or image data sources are used. In recent years, some commercial ultrasound systems are being developed to be applied clinically. In order to make the algorithm efficient, we estimate the tissue structure deformation though motion tracking with deformable mesh.

Our deformable mesh is formed by mesh nodes, and mesh nodes are calculated from every four neighboring tracking nodes. The classical SAD (sum-absolute-difference)

method is used to calculate tracking nodes’ locations in image sequence. The initial tracking nodes’ locations will affect the result, we use “structure energy” to promote its performance while keep the excellence of efficiency.

In vivo breast B-Mode image sequence is used to test our algorithm. After motion tracking, we suppress the strain errors and display the result using pseudo color overlap on the B-Mode image.

II. METHOD

A. Preprocessing

The quality of the original B-Mode sequence is affected by several factors which makes it not proper for motion tracking. The main defects are discussed as follow:

1. Random electronic noises: The image information is received from data processing hardware; it induces random electronic noises.

2. Speckle decorrelation: Under large strain, scatterers in tissue may move out of the imaging plane, causing changes in speckle formation.

3. Gray value sudden change: The freehand ultrasound operation may induce big changes between successive frames.

Because of those defects of original B-Mode image sequence, we need a preprocessing. We use persistence and histogram average mapping method.

We consider three successive images I_{n-1} , I_n , I_{n+1} the n -th frame output image after persistence is defined by:

$$I'_n = I_{n-1} / 4 + I_n / 2 + I_{n+1} / 4 \quad (1)$$

This process makes the output image more stable and reduces electronic noises.

Then we use the first output frame I'_n to generate a histogram average mapping table, and use this mapping table to enhance the image sequence after persistence.

$$I''_n = \text{map}(I'_n) \quad (2)$$

We blur the image slightly to reduce the electronic noises and other random noises. Then we perform bilinear interpolation on the pixels to increase the sensitivity of motion tracking to half a pixel. The image becomes four times bigger.

B. Structure energy

As we mentioned above, some locations are better than others to place tracking nodes. Structure energy represents the tissue structures, and locations with higher structure energy represent the locations more proper for motion tracking compared with those with lower structure energy.

In order to get structure energy of the first B-Mode image frame, we perform the following two steps:

1. Bandpass filtering,
2. Speckle histogram matching,

1. Bandpass Filtering

Fai Yeung mentioned the feature adaptive tracking idea in his paper [2], 1998. As we know, in frequency domain of the image, high frequency data represent details while low frequency data represent main background and main gray value. Random electronic noises are high frequency data and they carry little meaningful informations or induce noises we don't want. Main background of B-mode image is low frequency data, and they carry no useful information. We can use bandpass filter to filter both of them in frequency domain or use corresponding spacial filter.

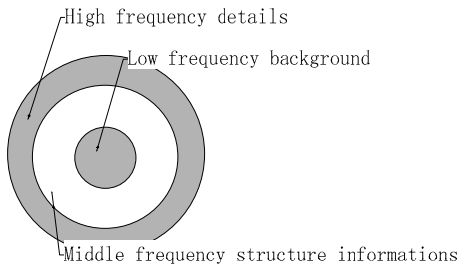


Fig. 1 Bandpass filter to preserve useful information

$$I_0'' = \text{BandPass}(I_0') \tag{3}$$

where I_0'' is the first frame of preprocessed B-Mode image and I_0' is the result after filtering.

2. Speckle Histogram matching

Liu [3] introduced histogram-based speckle reduction method in 1998. Histogram statistical information of the B-Mode image can be used to determine the region similarity of fully developed speckle using a running window. Although middle frequency structure information is kept, some fully developed speckles are kept as well. In the next step, we try to suppress them using techniques similar to [3].



Fig. 2 The histogram of a typical 15x15 speckle region in a discrete form

In pre-compressed B-Mode images, the histogram of fully developed speckle obeys Rayleigh distribution. We let the experienced ultrasound doctor select a small (15 pixels width, 15 pixels height) region of typical fully developed speckle region, and calculate its histogram statistic information. The gray value range of a B-Mode image varies from 0 to 255, and we divided it into 32 levels for histogram representation. The histogram of a typical fully developed speckle derived in Fig. 2 in a discrete form.

A corresponding window (15 pixels width, 15 pixels height) is used on the first image frame to calculate its histogram information at each pixel position of the image. Then we use the histogram information to match the model histogram and calculate the difference between it and the mode, using the equation:

$$Differ_p = \sum_{i=1}^{32} power(e, -(H_{pi} - H_{mi})^2 * C) \tag{4}$$

The p represents the specific position in the image, the variable i varies from 1 to 32 because gray values are divided into 32 levels, H_{pi} represents the level i histogram information at position p , C is a constant which is used to adjust the result range.

In order to reduce errors, the histogram information at the specific position in the image needs to be shifted according to the model histogram before matching calculation. We search the peak position of both specific histogram and the model histogram, then shift one of them to ensure they are at the same gray level.

Smaller $Differ_p$ means the region is more likely to be fully developed speckle. We make the $Differ_p$ vary from 0 to 1 and use this value to multiply the result after bandpass processing to suppress the influence of fully developed speckle.

$$Se_p = Differ_p * I_{0p}''' \tag{5}$$

The symbol Se_p represents the structure energy of the first B-Mode frame image. The structure energy of first frame image and original first frame B-Mode image are shown below:

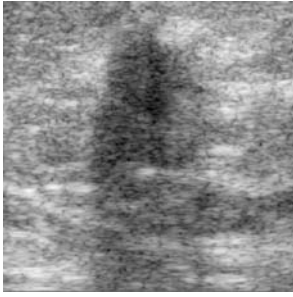


Fig. 3 B-Mode image



Fig. 4 Structure energy of Fig. 3

of the quadrangle can decrease the single tracking node's error further. The deformable Mesh tracking of a set of *in vivo* breast B-Mode image sequence is shown below:

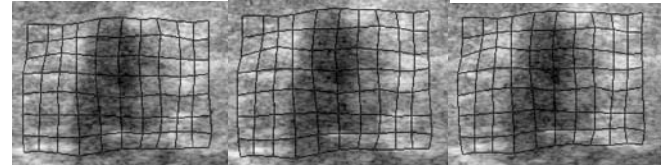


Fig. 8 Frame 0

Fig. 9 Frame 10

Fig. 10 Frame 20

C. Deformable motion tracking mesh

We use the deformable mesh to track the motion, the mesh is formed of mesh nodes and each mesh node's location is calculated from four tracking nodes. Tracking nodes are located uniformly on the first frame image of B-Mode image sequence and will be adjusted according to the structure energy later.

After the tracking node is placed uniformly on the image, we find the nearby location which has the largest structure energy of the region and adjust tracking nodes on more suitable locations in the region as the figures shown:

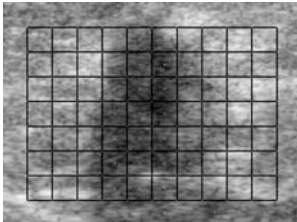


Fig. 5 Uniform mesh

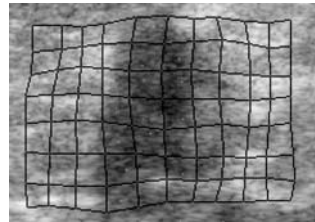


Fig. 6 Adjusted mesh

Each tracking node uses SAD to track the local motion in the successive frames. Basarab [4] mentioned the idea of bilinear transformation in motion tracking in his paper. Every four tracking nodes form a quadrangle; we use the gravity center of the quadrangle as the corresponding mesh node's position.

Although the initial tracking nodes' positions are adjusted in order to reduce errors, the using of gravity center

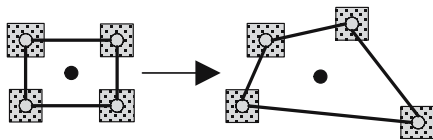


Fig. 7 Position of the mesh node

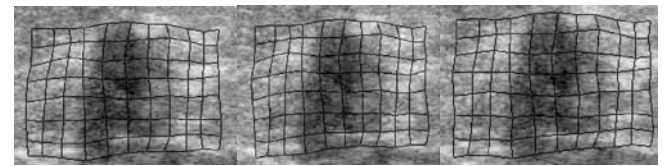


Fig. 11 Frame 30

Fig. 12 Frame 80

Fig. 13 Frame 100

We get the motion vectors from the mesh, the motion field of the 10th and 30th frames are shown in Figs. 14,15.

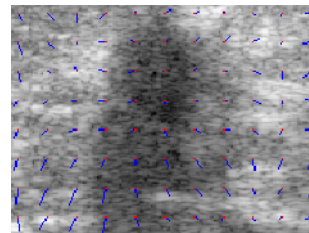


Fig. 14 The 10th frame

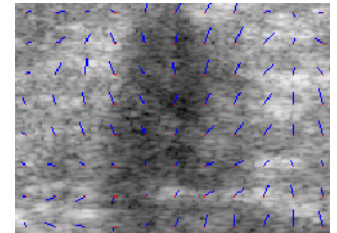


Fig. 15 The 30th frame

The red point is the location of the mesh node at the first frame; blue line is drawn from the red point to the current corresponding mesh node's position in the current frame.

D. Elastography

We use the motion tracking results to construct the strain image of the ROI using the equation below:

$$Y = \sigma / \delta, \tag{6}$$

where Y represents the Young's modulus, σ represents the stress and δ means strain. The actual stress is unknown, we assume that at a specific time the stress of horizontal plane is uniform and we use the inverse of the strain δ to present the value of tissue stiffness. When the motion of local region is small, the δ is small as well, which means the tissue

of local region is stiff. When δ is big, it means the tissue is comparatively softer. Using Eqn (6), we can calculate the stiffness information at the mesh nodes' positions. Since we don't know σ , we use a constant instead. Except the points at mesh nodes' position, we bilinear interpolate the others.

Because the small strain change will results in small strain as well (for example, if there is no stress changes in a period of time, the tissue will almost not move and δ is very small), it will induce errors. Chaturvedi [5] introduced the idea of global companding using global motion in his paper. In order to suppress these errors, we calculate the global motion first, and suppress the errors using global motion and the stress level using a compound power-law function shown below:

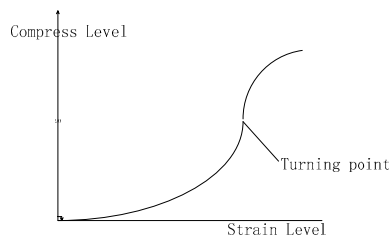


Fig. 16 A power-law function for strain enhancement

The function is combined by two parts, the part before turning point has the parameter larger than one and the other part's parameter is smaller than one. The larger strain level is, the greater compress level is. The turning point can be shifted and power law parameter can be adjusted to change the display result.



Fig. 17 Strain image at frame 13 Fig. 18 Strain image at frame 18



Fig. 19 Strain image at frame 8 Fig. 20 Strain image at frame 10

Then we did persistence processing to the strain result and blurring the strain result in order to make it more natural in the ROI. Finally, we designed a green to red color map (red for hard region) to mapping the compressed stress value to pseudo color and overlap it on the original B-Mode image in the ROI. The result is shown below:

The *in vivo* image sequence is the breast B-Mode image with malignant tumor. Though our method, we can see clearly that there is a hard inclusion inside the patient's breast tissue. Moreover, the hard tissue has been displayed with colors from green to red synchronized with the probe motion during the real time scan.

III. CONCLUSIONS

Our method is based on a deformable mesh and uses image data instead of RF data. The motion tracking result is used to generate elastography. From our work, we confirm the feasibility of image data source based elastography. We made the program on VC platform; the whole process can be done in real time, see Fig. 21 of the PC-based user interface. This interactive tool offers a flexible environment for algorithm development, testing and parameters optimization efficiently and effectively.

From performance viewpoint, our deformable mesh based motion tracking method is not very accurate compared with the RF based algorithms because our image-based methods don't use any phase information. Moreover, we may apply finite element analysis methods to calculate the tissue stiffness after the tracking result is obtained. These two issues are under investigation in our lab.

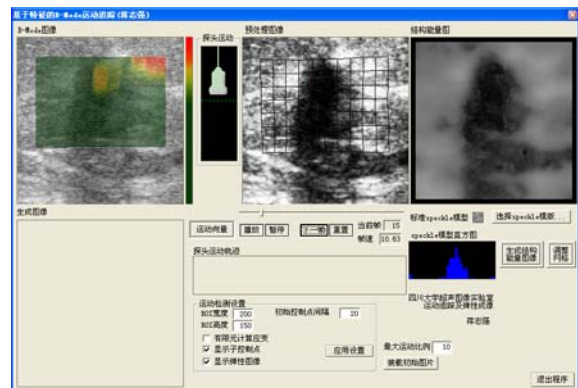


Fig. 21 The user interface panel of our algorithm development platform

REFERENCES

1. Ophir J, Cespedes I, Ponnekanti H et al.(1991) Elastography: A Quantitative Method for Imaging the Elasticity of Biological tissues, *Ultrasound Imag*
2. Yeung F, Levinson SF, Fu D et al. (1998) Feature-Adaptive Motion Tracking of Ultrasound Image Sequences Using A Deformable Mesh, *IEEE Trans. Medi. Imag.* , vol. 13, no. 6
3. Liu DC, Czenszak S, Kim J (1998) Adaptive speckle reduction with color transparency display, *Proc. of IEEE Ultrasonic Symposium*, pp.1611-1614,.
4. Basarab A, Aoudi W, Liebgott H et al. (2007) Parametric Deformable Block Matching For Ultrasound Imaging, *ICIP2007*
5. Chaturvedi P, Insana M, Hall T (1998) 2-D Companding for Noise Reduction in Strain Imaging, *IEEE Trans. Ultrason.* , vol. 45, no. 1

Author: Zhiqiang Jiang and Dong C. Liu
Institute: School of Computer Science, Sichuan University
Street: The First Ring Road
City: Chengdu
Country: China
Email: zhiqiangjiang@126.com

Development of a noninvasive glucose measurement system based on orthogonal twin polarized lights and its primary experimental investigation

Hong Wang^{1,2}, Baoming Wu¹

¹ Research Institute of Surgery & Daping Hospital of the Third Military Medical University, Chongqing, 40042, China

² College of Bioengineering, Chongqing Institute of Technology, Chongqing, 400050, China

Abstract— In this paper, a highly sensitive optical polarimetric sensing system has been demonstrated using method of Orthogonal Twin Polarized Light (OTPL), which converts micro-angle rotated by optical active substance such as glucose to energy difference of OTPL. By detecting the small polarization rotation of polarized laser light passing through a glucose-containing fluid, this sensing system is suitable for noninvasive glucose monitoring for diabetes patients. A resolution glucose level of 40 mg/dl has been obtained, with a 0.9777 correlation coefficient between the glucose concentration and the measured values. The advantages of this system are that it can make use of visible light, reducing influence of phase significantly, easily available and it can be easily miniaturized.

Keywords— Glucose monitoring, optical polarimetric sensing, Orthogonal Twin Polarized Light

I. INTRODUCTION

Recently there have been extensive studies on developing noninvasive blood glucose monitoring for diabetes patients because of the inconvenience and danger of the conventional invasive methods. By shining light through human interstitial fluids at translucent dermal positions such as finger tips, ear lobes, or through ocular aqueous humor in the eyes, information about the glucose levels can be obtained optically by infrared spectroscopy [1], Raman spectroscopy [2], or optical polarization changes [3], [4], [5]. These methods do not break human tissues and, therefore, are noninvasive. Near infrared (NIR) is the most generally used in research of noninvasive glucose measurement. But this technique has several limitations. The absorption coefficient of glucose in the NIR band is low and is much smaller than that of water by virtue of the large disparity in their respective concentrations. In their NIR the weak glucose spectral bands only overlap with the stronger bands of water, but also of hemoglobin, proteins and fats. As regards the scattering coefficient, the effect of a solute (like glucose) on the refractive index of a medium is non-specific, and hence it is common to other soluble analytes.

Indeed, investigation of the polarization changes induced by glucose is an ancient technique for noninvasive glucose measurement in human. Because a glucose solution rotates

a polarized light beam's polarization proportional to its concentration, various polarimetric glucose sensors have been developed, such as using Faraday rotators to directly modulate the beam's polarization state [3] or using a Zeeman laser in optical heterodyne detection [4]. The advantages of this technique are that it can make use of visible light, reducing influence of phase significantly, easily available and it can be easily miniaturized. Heterodyne method is most used in investigation of the polarization changes [5]. The disadvantages of this method are that it is sensitive to phase change, large drift, and frequently calibration [6].

Despite considerable progress, however, until now truly noninvasive glucose monitor in blood is not a reality.

Our goal is to obtain an original method which allows us to measure the blood glucose level by a noninvasive optical method, without blood test or use lancets; therefore without extraction. In this stage we proposed a polarimetric glucose sensor based Orthogonal Twin Polarized Light (OTPL), which converts micro-angle rotated by optical active substance such as glucose to energy difference of OTPL as well as the preliminary results of a noninvasive method for glucose level measurement. OTPL takes advantages of simplicity of directly detection method and highly sensitivity of heterodyne method and overcomes its phase sensitivity.

II. MATERIALS AND METHODS

A. Overview of the Experimental System

The block diagram of the system designed and implemented during this research is illustrated in Fig. 1. A diode laser emitting 3 mW of power at a wavelength of 650 nm (red) is used as the light source. The laser beam is then linearly polarized (X-direction) by the Glan-Thompson polarizer present in the optical train. This polarizer is oriented in the direction of the laser's preferred polarization state in order to maximize the transmitted power. Rotation of the polarization vector is then provided by the Faraday rotator which is driven by a dc voltage supply at 0–200 mA. The linearly polarized beam was modulated by a photo modulator, which is driven by Positive, and Negative Alternation Square Wave Signals (PNASWS) generated by

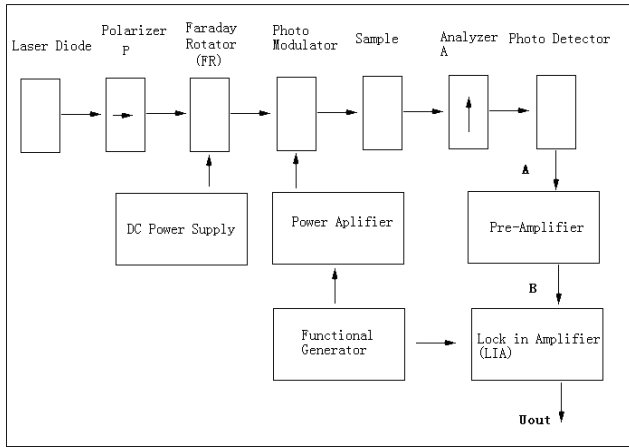


Fig. 1. OTPL system block diagram

functional generator and amplified by a power amplifier. Thus the angle of the polarization plane of output light from the photo modulator was $\pm\theta$ ($X \pm \theta$ directions) to the polarization plane of polarizer (Fig. 2.). When θ equaled 45° , the light became OTPL. This modulated signal then propagates through a sample cell constructed of optical-grade glass with a path length of 20 cm. Following the sample cell is another Glan–Thompson polarizer known as the analyzer. Cross-polarization of the system is achieved by orienting the analyzer 90 degree with respect to the initial polarizer—bisection line of two polarized lights. This configuration of the analyzer transforms the modulation of the polarization vector into intensity modulation according to Malus’ law. Projection of the components of two polarized lights on the polarization plane of analyzer is obtained by a photo-diode light detector who terminates the optical train. This detector outputs a voltage proportional to the detected light intensity which is used as the input into the pre-amplifier in front of Lock-In Amplifier (LIA).

B. Modeling of the Detected Signal

This technique is based on the phenomenon that occurs when polarized light passes a solution containing optically active solutes (such as glucose): the light, in fact, rotates its polarization plane by a certain angle, which is related to the concentration of the optically active solutes.

When sample is not placed on beam path, a volts d.c. is got by photo detector because of the equation of the two components ($E \sin \theta$, if E is electrical field vector of light) of two polarized lights on the polarization plane of analyzer—the difference of the two signals equals zero. On the other hand, when sample is placed on beam path, the two directions of polarization plane will change—one component

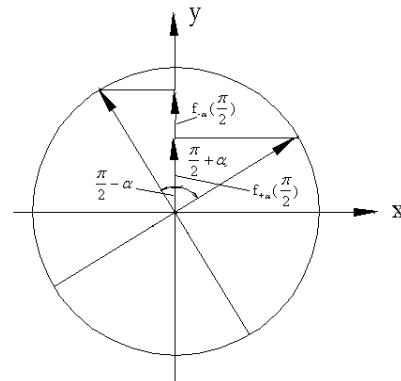


Fig. 2. Diagram of vectors difference of OTPL passed through analyzer

vector induces by one polarized light increases, $E \sin(\theta + \alpha)$, and that of another one decreases, $E \sin(\theta - \alpha)$.

According to Malus’ law, those two intensity components are:

$$f_{+\alpha}(\theta) = E^2 \sin^2(\theta + \alpha)$$

$$\text{and } f_{-\alpha}(\theta) = E^2 \sin^2(\theta - \alpha).$$

Their difference is

$$\Delta f(\theta) = E^2 \sin^2(\theta + \alpha) - E^2 \sin^2(\theta - \alpha) \quad (1)$$

θ is limited in $[0, \frac{\pi}{2}]$, so, $\Delta f(\theta)$ gets maximum value

$$\text{when } \theta = \frac{\pi}{4}$$

$$\Delta f_{\max}(\theta = \frac{\pi}{4}) = E^2 \sin 2\alpha \quad (2)$$

In blood glucose level, $\Delta f_{\max} = 1.4 \times 10^{-4} E^2$, this difference can be detected by cross-correlation principle. Because of $\theta = \frac{\pi}{4}$, the two components are perpendicular each other, it is called Orthogonal Twin Polarized Light (OTPL).

So signals detected by photo detector are superposition of square wave and volts d.c. Separated volts d.c. and amplified by preamplifier. A lock-in amplifier (LIA) (module ND-207) is used to measure the relative amplitude of the signal present at the modulation frequency (PNASWS). LIA has highly strong capacity of inhibiting noise because of cross-correlation principle. The LIA allows precise measurement of the signal of interest at 4.88 kHz while rejecting low-frequency (50 Hz and multiples) and high-frequency

electromagnetic noise. It locks and processes signals from frequency and phase of reference signal, and out put volts d.c. which is proportional to glucose signal detected.

The measurement system is calibrated and compensated by Faraday Rotator (FR) next to polarizer. When linearly polarized light is passed through a FR in the presence of a magnetic field, the linear polarization vector of the light rotates an amount which is proportional to the magnetic field.

$$\Phi = VHL \quad (3)$$

Where, V is Verdet constant of magnetic optical material, L is the length, and H is magnetic field intensity.

Our particular rotator, made by ourselves, allowed $0 \pm 2^\circ$ rotation at 650nm and consisted of a 30mm polished and antireflection coated glass rod enclosed by an electromagnetic coil. The current through the coil was linearly proportional to the magnetic field across of rotation of the linearly polarized light passing through the glass rod. When sample was not placed in the path of beam in the measurement system, LIA would output a volts d.c. **Uout** because polarizer and analyzer are not absolutely perpendicular each other. The system has been calibrated after we adjusted the current to I_0 on the coil of Faraday Rotator to minimize Uout of LIA.

When sample is placed in the path of beam in the measurement system, LIA outputs a volts d.c. **Uout** because of glucose (illustrated by a schematic diagram in Fig. 2.). We adjusted the current to I_1 on the coil of FR to minimize Uout of LIA again. Then the difference of currents $\Delta I_R = (I_1 - I_0)$ on the coil of FR was proportional to the angle rotated by optically active solutes. If optical length is L, glucose

concentration is calculated by $C = k \frac{\Delta I_R}{L}$

C. Experimental Protocol

Implementation of the OTPL system uses a 20cm test cell.

The laser diode(650nm) is a polarized 3mW uniphase model.

The two fixed polarizers are calcite Glan laser prism polarizers with extinction ratios of 5×10^4 .

The photo detector is a silicon photodiode(GD3252Y) operated in the zero voltage mode. At 650nm the diode has a responsivity of 0.5A/W.

The photo modulator (ZY605) whose half wave voltage was 360V employed LiNbO₃ crystal.

The power amplifier made by ourselves was a high voltage amplifier applied Pa85 chip of APEX. It output Positive

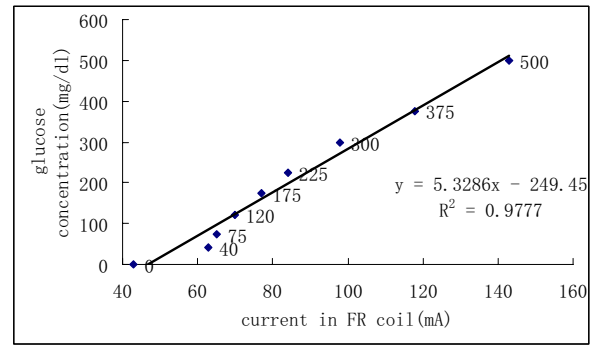


Fig. 3. Glucose concentration vs. current in FR coil

and Negative Alternation Square Wave Signals (PNASWS)($\pm 180V$) to drive the photo modulator.

The Faraday Rotator uses a 30mm optical core(diamagnetic Faraday rotator glass) with a diameter of 5mm wrapped with a coil having an unknown number of turns. The inductance of the coil was measured to be 16mH.

A stock 500mg/dL solution of glucose is prepared and allowed to equilibrate for 24 hours at room temperature. The stock solution is diluted into the desired concentration series and allows equilibrating another three hours before use.

The test cylinder which is fixed in place to maintain same position during filling and flushing. After alignment of the optical system, with the cylinder fills with de-ionized water, the system is calibrated when the current on the coil of Faraday Rotator is adjusted to 43mA to minimize Uout of LIA to 1.57uV. At this status, A is assumed to be at right angles to P. Three rinses of de-ionized water are used and the output voltage and DC current are read after the third filling. The water is repeated for each of the series of measurements. All measurements are made with water and solutions at 20°C. Data is plotted and analyzed using Microsoft Excel.

III. RESULTS

After calibration of the system, the introduction of glucose concentrations ranging from 40mg/dl to 500 mg/dl resulted in the currents in FR coil depicted in Fig. 3. The currents observed ranged from 43mA at a concentration of 40mg/dl to 143mA at 500mg/dl. A resolution glucose level of 40 mg/dl has been obtained, with a 0.9777 correlation coefficient between the glucose concentration and the measured values.

IV. DISCUSSION AND CONCLUSION

We have demonstrated a new technique of optical glucose sensing and shown using our OTPL measurement system, that it is possible to noninvasively measure the glucose concentration and preliminary results. Overall using OTPL improves system sensitivity and stability. At present results suggest that with additional refinement, this system could become a robust, noninvasive glucose sensor.

REFERENCES

1. Andrea Tura, Alberto Maran, Giovanni Pacini, Non-invasive glucose monitoring: Assessment of technologies and devices according to quantitative criteria. *Diabetes Research and Clinical Practice* 2006
2. Michael J. Vilaboy, Aysegul Ergin, Alain Tchouassi, Richard *Greed*, Gordon A. Thomas, Optical Measurement of Glucose Concentrations using Raman Spectroscopy. 0-7803-7767-2/03/\$17.00 02003 IEEE
3. Brent D. Cameron, Gerard L. C'ote, Noninvasive Glucose Sensing Utilizing a Digital Closed-Loop Polarimetric Approach. 0018-9294/97\$10.00 1997 IEEE
4. C. Chou, W.C. Kuo, T.S. Hsieh, H.K. Teng, Optical activity measurement by use of a balanced detector optical heterodyne interferometer. *Opt. Commun.* 230(2004) 259.
5. Chien-ming Wu , Ying-Chieh Tsai, Angular displacement-enhanced heterodyne polarimeter for the measurement of optically active media. doi:10.1016/j.snb.2006.02.023
6. J.S.Baba, G.L. Cote, S. Theru, An investigation of Rabbit corneal birefringence for the purpose of improving noninvasive polarimetric in-vivo glucose detection, Proceeding of the Second Joint EMBS/BMES Conference, Houston, TX, USA, October 23-26, 2002

Correspondence Author: Wu Baoming
 Institute: Research Institute of Surgery & Daping Hospital of the
 Third Military Medical University
 Street: 10 , changjiangzhi road
 City: Chongqing
 Country: China
 Email: bmwu@vip.163.com

Effect of Interface Characteristics of Substrates on Performance of Biosensors Based on Supported Mimetic Biomembranes

Shengping Liu^{1,2}, Yongbo Wu², Yunlong Wei¹

¹College of Bioengineering, Chongqing Institute of Technology, Chongqing, 400050,

China²Department of Machine Intelligent and System Engineering, Akita Prefectural University, Honjo, 015-0055, Japan

Abstract — A novel method for the interface processing of substrates of Supported Mimetic Biomembranes (SMBs) was proposed and applied. The surface characteristics of substrates processed were investigated for improving the performance of SMBs. For obtaining the surface with variant roughness, some electrodes were prepared by embedded stainless steel probes coated Teflon film into resin. The electrodes were lapped with a polisher. The surface roughness and Three-Dimension microscopical morphologies of substrates polished were measured and visualized. The dependence of surface roughness of substrates and the electrochemical characterization of SMBs was examined and analyzed by Cyclic Voltammetry (CV). The experimental results show that the lapped surface with small roughness benefits the SMBs forming. This research could ameliorate the stability and promote the application of SMBs for biosensors development.

Keywords — Biomembranes, interface, micro-morphology, surface roughness, biosensors

I. INTRODUCTION

More and more biosensors have been applied in medical clinic for diseases detection and diagnosis [1, 2]. The early and quick detection of diseases is beneficial to the therapy and recover of patients. For satisfied with the demands of point-of-care and clinical real-time monitoring, many researchers have concentrated on the investigation and development of all kinds of novel biosensors for diseases detection and diagnosis. Supported Mimetic Biomembranes (SMBs) reconstituted *in vitro* were widely used as model system of biomembranes and biosensors development due to the favorable biocompatibility and facile enzymes immobility [3, 4]. SMBs can form on variety of different substrates, involving gold, silver, polymers, solid silica, quartz, glass and stainless steel and so on. By embedded diverse modifiers, SMBs can quickly and sensitively detect the counterparts in solutions. SMBs modified are an ideal material for the different novel biosensor development. But, the life-time of SMBs prepared by conventional methods is short. Also, the electrochemical property is poor. These drawbacks restrict greatly the application of SMBs in practical fields. In the past, most of researchers focused on the ingredients of forming solution for improving properties of

SMBs [5, 6]. There have few researches considered the surface characteristics of substrates of SMBs which may affect the properties of SMBs. Kalani J. Seu et al studied the effect of the surface treatment of glass substrates on diffusion and domain formation in supported lipid bilayer [7]. In our previous works, the influence of surface roughness on the electrochemical property of bare electrodes and membranes was preliminarily investigated [8]. The present investigation concentrated on the surface characteristics of substrates which possibly ameliorate the performance of SMBs. Herein, stainless steel wires were selected as the substrate of SMBs due to the well electron transport capacity and facilitated processing. Various surfaces of substrate with different roughness were prepared by lapped with a polisher. Topically, for gaining the surface of substrate with variant roughness, the stainless steel substrates embedded in resin were polished by applied a variety of treatment conditions. Before SMBs formed, the substrates were treated using a variety of different chemical methods, including surface clean and activation. These chemical treatment methods will benefit SMBs to form on the surface of substrates. The electrochemical properties of surface of substrate and SMBs were studied by Cyclic Voltammetry.

II. MATERIALS AND METHODS

A. Materials and instrumentations

Stainless Steel wire coated Teflon film with diameter 1mm was used for electrode fabrications. Chemicals for biomembrane forming are Lecithin, n-decane, n-decane and Cholesterol purchased from Wako Pure Chemical Industries, Ltd., Japan. Valinomycin was adopted as modifier embedded into SMBs. Other reagents include KCl, Acetone, Dehydrated alcohol, Distilled Water and so on. All reagents were used without further purification.

A polisher consisted of RotoForce-4 and RotoPol-25 (Marumoto Struers K.K.) was utilized for surface lapping. An electrochemical instrument (Type CHI600C, CH Instruments, Inc., USA) was used for the electrochemical property analysis of electrodes before and after biomembranes formed. Three-Dimension Laser Microscope (Type

VK-8710, KEYENCE Co. Ltd., Japan) was employed for the measurement of surface roughness and the view of Three-Dimension microscopical morphologies of substrates polished.

B. Preparation of SMBs

The procedures of SMBs fabrication include three main steps, namely electrodes fabricating, substrates preprocessing and membranes forming. In the present work, four electrodes treated under different lapping conditions were investigated. Stainless steel wires coated Teflon film were embedded in resin by a heating embed machine. The heating time is 9 minutes at 180°C. The cooling time is 6 minutes. Thus, an electrode containing two probes was fabricated. By this way, the surface of substrates can be finished conveniently with the polisher (RotoForce 4 and RotoPol 25). The schematic of electrode lapping is shown as Fig. 1.

Different electrodes were lapped under various polishing conditions to produce a series of particular surface with variant roughness. The polishing conditions of four electrodes are summarized in Table 1.

During lapping, diamond abrasives with different grain sizes of 3-9 μm were used in order to obtain the surface of electrode with different values of roughness. Subsequently,

the surface roughness of probes lapped was measured and the Three-Dimension microscopical morphologies were viewed with the Three-Dimension Laser Microscope. Herein, surface roughness parameter was characterized with the arithmetical mean deviation of the profile, which is expressed with Ra.

Appropriate mixtures of Lecithin and Cholesterol were dissolved in n-decane for the forming solution preparation. Valinomycin, which can chelate K^+ , was added into the forming solution for potassic ion in solution detecting. Before biomembrane forming, the electrodes lapped were pretreated by immersing in 0.4M H_2SO_4 , simultaneously scanned by Cyclic Voltammetry until CV curve become stability. The range of scan potential is -0.5~0.5V. The scan rate is 0.1V/s. Followed, the electrodes were extensive rinsed with distilled water and cleaned in dehydrated alcohol with ultrasonic apparatus. After air drying, the surface of each probe embedded in the electrode was dipped a drop of SMBs forming solution. After 10 minutes, the electrode was moved into 0.1M KCl buffer solutions for membrane self-assembly. Around 30 minutes later, the biomembrane will self-assembly form on the surface of the probe. At that time, the electrochemical property of SMBs could be measured and analyzed with CHI 600C instruments.

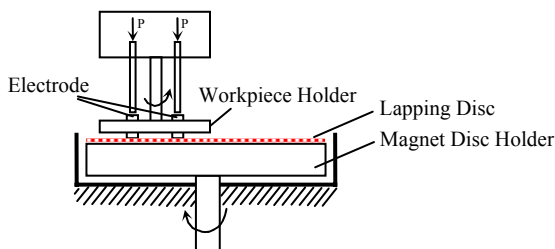


Fig. 1 Schematics of electrode lapping setup

Table 1 Lapping conditions of electrodes

Sample No.	Rotate Speed (Rev)*	Applied Force (N)	Lapping Time (Min)	Lapping Disc	Abrasive
Sample 1	400	30	1	Crude	9 μm Diamond
Sample 2	400	30	5	9 μm	9 μm Diamond
Sample 3	400	30	1	Crude	9 μm Diamond
	400	30	10	3 μm	3 μm Diamond
Sample 4	400	30	1	Crude	9 μm Diamond
	400	50	10	3 μm	3 μm Diamond

Note: *Rotate Speed is the Rotate Speed of RotoPol-25, which can be arbitrarily adjusted. RotoForce-4 runs reversely at a constant speed 150 Rev.

III. RESULTS AND DISCUSSION

Fig. 2 shows the surface roughness and Three-Dimension microscopical morphologies of four samples lapped, respectively. All samples were lapped at the same rotate speed 400 Rev. Followed the first polish under the same conditions as Table 1, sample 3 and 4 were lapped once more with 3 μm lapping disc by applied different force, respectively. From Fig. 2, it can be seen that the sample used finer abrasive or applied larger force has the smooth surface with small Ra.

A system of three electrodes was utilized for the electrochemical analysis of SMBs formed on the substrate lapped. The electrode fabricated hereinbefore was acted as the work electrode. Pt wire was used as the counter electrode. The Ag/AgCl reference electrode was used for all measurements. The measuring parameters of CV were set as following: scan potential is -0.5~0.5V; scan rate is 0.1V/s; quiet time is 5s. Ten reciprocal sweeps were recorded for each sample at different duration, respectively. The average value of ten sweeping CV curves was adopted for the final analysis. All measurements were carried out in 0.1M KCl solution. The CV curves of four probes before and after membranes formed are plotted in Fig. 3.

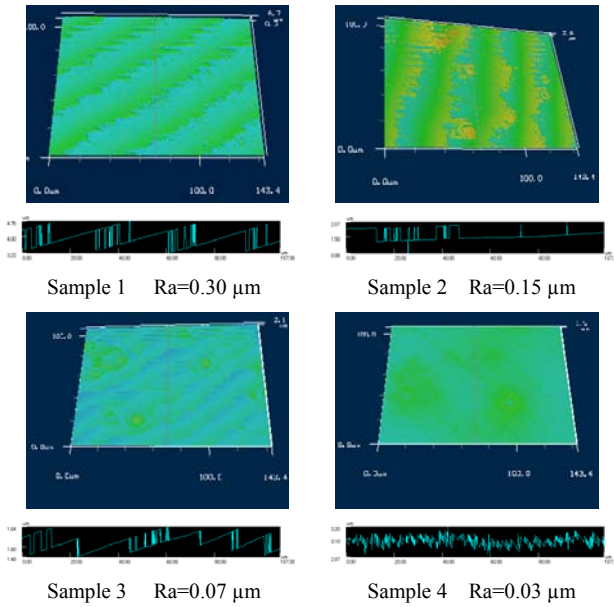
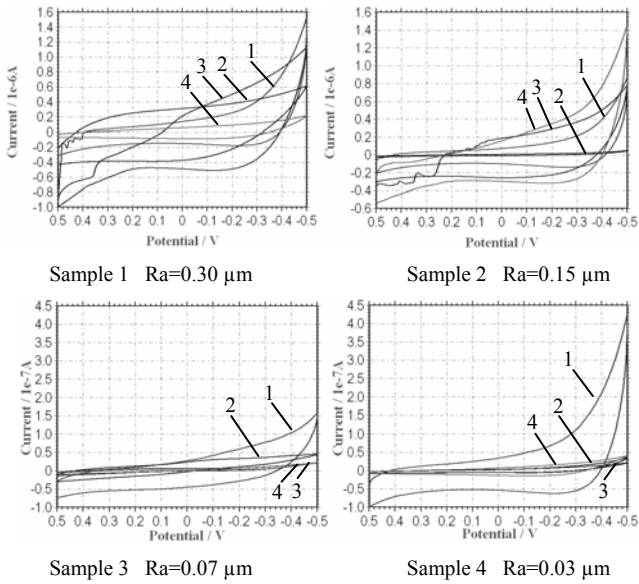


Fig. 2 Three-Dimension microscopical morphologies of substrates



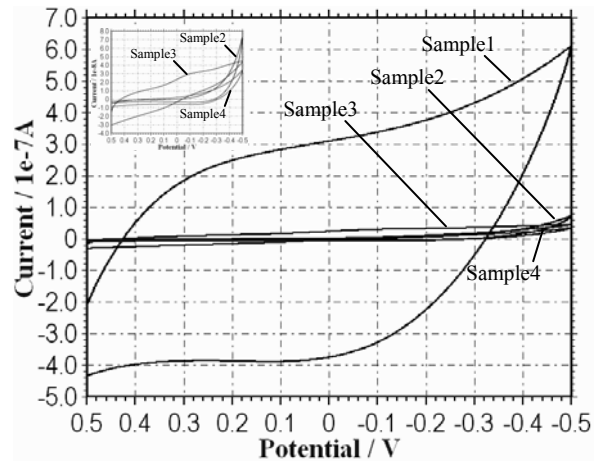
1 denotes the CV curve of bare probe in 0.1MKCl
 2 denotes the CV curve of probe with SMBs in 0.1M KCl just formed
 3 denotes the CV curve of probe with SMBs in 0.1M KCl after 2 hours
 4 denotes the CV curve of probe with SMBs in 0.1M KCl after 12 hours

Fig. 3 CV curves of the probe with and without SMBs

Due to the well electricity insulativity of SMBs, the equivalent impedance of the probe will increase after membranes formed. As a result, the CV current of probe with SMBs will decrease. From Fig.3, the CV current of the bare

probe is much larger than that of the probe SMBs fabricated. So, we can say that SMBs have formed on the surface of sample probes processed by the novel fabrication method. That is to say the novel fabrication method by lapped style suits for the SMBs forming. Sample 1, which has the largest surface roughness in four samples, has the strongest CV current after SMBs fabricated. Also the CV current changed greatly within 12 hours. With increasing of smoothness of substrate surface of probes, the variation of CV current reduces gradually within 12 hours. It could be related to the membrane stability. Smooth surface of substrate is in favor of the arrangement of molecules of biomembrane in order so as to form a compact and uniform configuration. SMBs formed on the smooth interface come into being a stronger binding force between molecules and interface of substrate comparing with that formed on the rough interface. Thus, SMBs formed the smoother surface is more stable than that formed rough surface. So SMBs formed on the smooth substrates just have a little variation of CV current at the same duration.

The CV curves of four sample electrodes formed SMBs in 0.1 M KCl solution were obtained with CHI600C electrochemical instrument as shown in Fig. 4. From this figure, with the surface roughness Ra of substrate lessening, the CV current of probes formed SMBs decreases. Namely, the CV current of SMBs formed on smooth surface is smaller than that formed on roughness surface. The results are the cause of the configuration of SMBs formed on the probe. As mentioned above, SMBs have a high impedance characteristic. SMBs formed on the probe will increase the equivalent impedance of probe. The more compact and uniform SMBs formed on the surface of probe, the larger the equivalent impedance of the probe is. Therefore, during CV meas-



Insert plot is the enlarged CV curves of Sample2, 3 and 4

Fig. 4 CV curves of electrodes formed SMB in 0.1 M KCl solution

uring, the CV current will be smaller. Thus, it can deduce that SMBs formed on the smooth surface are much compact and uniform than that on the rough surface.

IV. CONCLUSIONS

A preliminary investigation with regards to the influence of surface characteristics of substrates on supported mimetic biomembranes was performed. A new method, namely lapping method, for supported mimetic biomembranes preparation was proposed. Experimental results indicate that supported mimetic biomembranes can form on the surface of substrate prepared by the novel method. The connection between surface roughness of substrates and the electrochemical characterization of supported mimetic biomembranes was investigated by Cyclic Voltammetry. Based on the electrochemical characteristics (CV curves) of supported mimetic biomembranes, the smaller surface roughness of substrates could be beneficial to membrane forming compactly and uniformly on the end face of substrates. It will improve the stability of supported mimetic biomembranes. Ultimately, it will accelerate the application of supported mimetic biomembranes for novel biosensors development, which could apply to the clinical detection and diagnosis of diseases. Theoretically, there should have an optimum scope of surface roughness of the substrate which helps to supported mimetic biomembranes forming. Concerning this point, it is worthy of investigation in details in the next step.

ACKNOWLEDGMENT

This work is partially supported by the National Natural Science Foundation of China (Granted No. 503751655 and 50175067) and Natural Science Foundation of Chongqing (Granted No. 8665 and 8124).

REFERENCES

1. Bansil D Malhotra and Asha Chaubey, (2003) Biosensors for clinical diagnostics industry, *Sensors and Actuators B: Chemical* Volume 91, Issues 1-3: 117-127
2. Silvana Andreescu and Omowunmi A. Sadik, (2004) Trends and challenges in biochemical sensors for clinical and environmental monitoring, *Pure Appl. Chem.*, Vol. 76, No. 4: 861-878
3. H. Ti Tien, Samuel H. Wurster, Angelica L. Ottova., (1997) Electrochemistry of supported bilayer lipid membranes: background and techniques for biosensor development, *Bioelectrochemistry and Bioenergetics*, 42: 77-94
4. H. Ti Tien and Angelica L. Ottova, (1999) From self-assembled bilayer lipid membranes (BLMs) to supported BLMs on the metal and gel substrates to practical application, *Colloids and Surfaces, A Physicochemical and Engineering Aspects*, 149: 217-233.
5. Thomas Starke-Peterkovic, Nigel Turner, Mark F. Vitha, et al., (2006) Cholesterol Effect on the Dipole Potential of Lipid Membranes, *Biophysical Journal*, Volume 90: 4060-4070
6. Frank Giess, Marcel G. Friedrich, Joachim Heberle, et al., (2004) The Protein-Tethered Lipid Bilayer: A Novel Mimic of the Biological Membrane, *Biophysical Journal*, Volume 87: 3213-3220
7. Kalani J. Seu, Anjan P. Pandey, Farzin Haque, et al., (2007) Effect of Surface Treatment on Diffusion and Domain Formation in Supported Lipid Bilayers, *Biophys J BioFAST*, as doi:10.1529/biophysj.106.099721
8. Shengping Liu, Yongbo Wu, Surface processing and characterization of metal substrate for the development of supported BLMs-based biosensors, *Proceedings of Workshop of the Japan Society for Precision Engineering (Tohoku Branch)*, pp 51-52, 2007. 12.1

A Novel Taste Sensor Based on Ion Channels Incorporated in Nano-lipid Bilayer Membranes

Qingjun Liu^{1,*}, Jinjiang Yu², Zongbin Liu², Wei Zhang¹, Ping Wang¹ and Mo Yang²

¹ Biosensor National Special Laboratory, Department of Biomedical Engineering, Zhejiang University, Hangzhou, P. R. China

² Department of Health Technology and Informatics, The Hong Kong Polytechnic University, Kowloon, Hong Kong

Abstract — Biological studies have elucidated the gustatory detection of taste receptor cells often take place on ion channels or receptors in cells membranes. In this study, we build a novel electronic tongue based on ion channels of channel-active peptides gramicidin incorporated in lipid bilayer membranes with highly ordered nanopores. By impedance analysis, this novel biomimetic sensing systems can separate tastants by their functional characters to ion channels. This nano-lipid platform is useful to study special ion channels or receptors with potential detecting for special kind of taste.

Keywords — Taste sensor, Electronic tongue, Ion channel, Nanopores, Lipid bilayer Membranes

I. INTRODUCTION

Traditional taste sensors with global selectivity are composed of different lipid/polymer membranes for transforming information of taste substances into electric signals [1]. The different output of the response electric potential patterns for chemical substances show different taste qualities, such as saltiness and sourness. The technique has been successfully used in analysis of food and drugs, even environment monitors.

It has become clear that the lipid bilayer membranes can sense those basic taste qualities. However, lots of biological studies have elucidated that the gustatory detection of taste receptor cells often take place on ion channels or receptors of cells membranes, but never on lipid membrane itself [2]. And, with the development of the biology and nano-techniques, impedance analysis and single ion channel recordings have realized on nanopores suspended lipid bilayers [3].

In this study, we will build electronic tongue based on ion channels of gramicidin incorporated in lipid bilayer supported by highly ordered nanopores for taste sensors.

II. EXPERIMENTAL

A. Fabrication of the nanoporous

Nanoporous anodic aluminum oxide, also known as alumina, is of particular interest because of its established fabrication process as well as its suitable to lipid bilayer membranes for ion channels incorporated in it [3].

Nanoporous anodic aluminum oxide is prepared by a two step anodization. The first anodization process has been taken in 0.25 M oxalic acid. Then, the aluminum was etched in a mixture of 4% (w/w) chromic acid and 8% (w/w) phosphoric acid. The second anodization step was repeated in 0.25M oxalic acid for about 4 hours again. Finally, the nanoporous was observed by scanning electron microscope (SEM) and atomic force microscope (AFM).

B. Incorporated Ion channels in lipid bilayer

The significant developments in nanoporous membrane sensor platforms, seems them to be the leading candidates for creating viable chip formats for functional transmembrane protein (ie. ion channels) measurements.

Lipid bilayer was formed on the surface of nanopores functionalized by 1 mM of DPPTTE (1,2-Dipalmitoyl-sn-glycero-3-phosphothioethanol), which renders the surface hydrophobic. Then, the surface surrounding was primed with DPhPC (1,2-diphytanoyl-sn-glycero-3-phosphocholin) in pentane. And, 10 μ L of DPhPC in n-decane were painted over the DPPTTE-functionalized surface. Finally, the channel-active peptides gramicidin D (in 0.1 M Na₂SO₄) was inserted to the lipid bilayer to form the ion channel.

C. Impedance detection of tastants

Studies have show that taste sensing based on impedance measurement had different information from potentiometric measurements, and hence will be effective for the detection of nonelectrolyte taste substances [1].

In our study, AC impedance was performed using the impedance analyzer HP 4192A. The absolute values of the impedance $|Z|$ (Ω) between voltage and current were recorded within a frequency range of 101-105 Hz. Impedance data were recorded with LabView. Subsequently, we monitored impedance response after four basic tastants (0.3 mol/l NaCl for salty; 0.1 mol/l glutamate and 0.01 mol/l HCl for sour; 0.5 mol/l sucrose for sweet; 0.01 mol/l CaCl₂ and 0.03 mol/l MgSO₄ for bitter), applied to the lipid layer with ion channels.

III. RESULTS AND DISCUSSION

A. Alumina nanoporous

SEM was the primary tool used to determine the presence of the nanoporous structure, as well as the pore diameter and membrane thickness. Surface topography and uniformity of nanoporous alumina membranes were determined using tapping mode AFM.

Fig. 1 and Fig. 2 shows alumina nanopores were successfully fabricated by two-step anodization in our lab, observed by SEM and AFM. This two-step anodization process is capable of fabricating highly ordered nanopores array in the range of 50-120 nm depending on the anodization voltage. The first anodization time mainly affects the pore arrangement, and the second anodization time only influences the pore length.

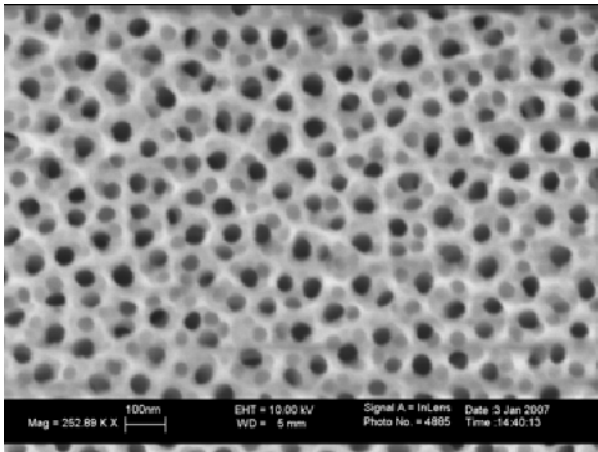


Fig. 1 Scanning electron microscope image of nanoporous.

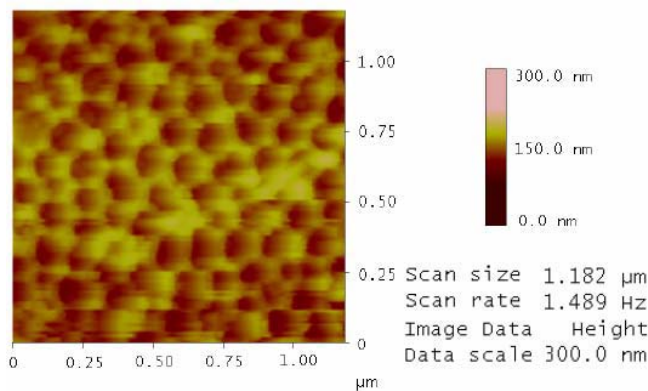


Fig. 2 Atomic force microscope image of nanoporous.

B. Impedance of ion channels in lipid bilayer

Impedance spectroscopy was a non-invasive technique that enables separating the dielectric properties of biological substances by choosing appropriate frequency domains. The impedance property of alumina has been demonstrated [3]. The impedance difference with and without lipid bilayer on the surface of nanopores is very significant, which prove the impedance change can be very sensitive to ion channels formed in it.

Fig. 3 shows the impedance spectrum of the nanopores with lipid layer. Insertion of gramicidin took place quite rapidly, resulting in a decrease in resistance from 10^5 to $10^4 \Omega \cdot cm^2$ during the measurement in 40 min. The stability of the membrane can keep intact and almost all pores covered in 70 hours. This incorporation of channels active peptides into the supported membrane demonstrated here suggested it's a good model of ion channel based biosensors.

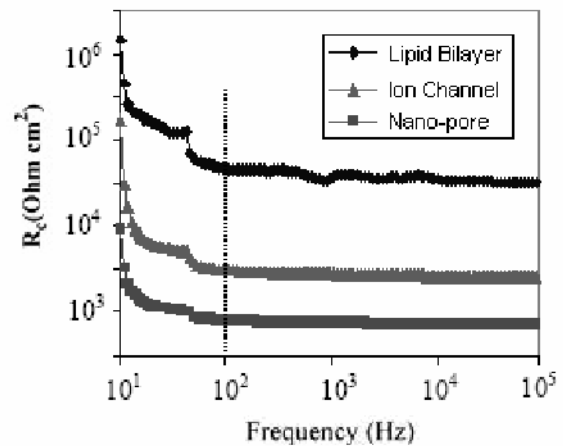


Fig. 3 Impedance characterization of nanopores, lipid bilayer and ion channels. Broken line at 100 Hz is the selected frequency for next taste measurement.

C. Tastants detection

There are different cellular transduction mechanisms corresponding to different taste. Salty, sour, and some bitter tastes are elicited by ions. These stimuli function via permeation through or modulation of ion channels. However, transduction mechanisms for sugars are believed to involve membrane receptors, G-protein and second messengers. Both ion channels and receptors are all membrane proteins. Gramicidin has been used as a sensory element for bilayer lipid membranes sensors by measuring selective ion transport through its open pore, when they were incorporated in supported lipid membranes for the sensor development.

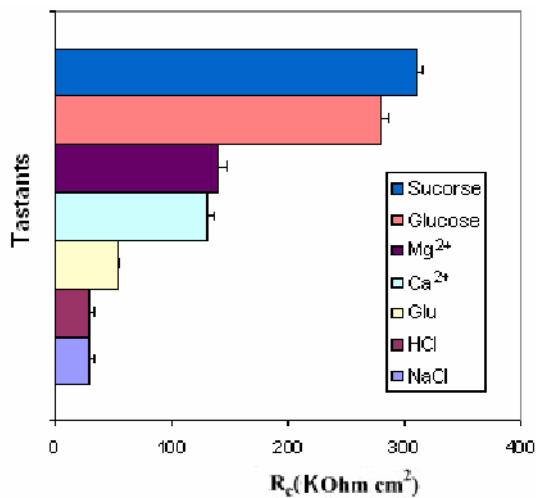


Fig. 4 Impedance characterization of different tastes at 100Hz (n=6).

Our results as Fig. 4 shows a significant decrease of impedance at 100 Hz for salty (NaCl) and sour (glumate and HCl). The ions transport through ion channels plays a significant role. However, the impedance decreased for bitter (CaCl₂ and MgSO₄) only about 30% to salty or sour. And, the impedance of sweet (sucrose) changed very little. Maybe, the reason is the ion selectivity of lipid membrane containing gramicidin for transport of monovalent cation [4] (i.e. Na⁺ for salt and H⁺ for sour) greater than for divalent cation (i.e. Ca²⁺ and Mg²⁺ for bitter), and very little for organically molecules (for sweet). Gramicidin is the often used channel forming ion pore with its low cost, structural stability, and ion selectivity. The ion selectivity of the bilayer lipid membranes containing gramicidin D for transport of mono-valent ions is greatest for ammonium ion relative to sodium and lithium.

Existing taste sensors can detect some physics-chemical taste properties of the taste substance, but they can not simulate the taste sense of the real biological system [5]. In mammals, the detection of the chemical substances is performed in the biological membranes of taste and olfaction cells. Those studies have mainly been investigated from the lipid bilayer membranes themselves, and have not much given attention to the protein receptors or ion channels [6]. Therefore, the development of this ion channel sensor is based on a very different concept from that of conventional taste sensors, which using lipid/polymer membranes. Discrimination and recognition of the taste itself and its quantitative expression can be made by this more bio-mimic sensor system.

In the next step, we will study special ion channels or receptors with potential detection for special kinds of taste.

For example, a bitter receptor of TAS2R10 recombinant protein (a new discovered bitter receptor on taste receptor cells [7]) will be used compose a bitter biosensor applied to detect bitter. This will be very useful for food and pharmaceuticals industries.

IV. CONCLUSIONS

Based on channels active peptide of gramicidin incorporated in lipid bilayer supported by nanopores, this novel biomimetic taste sensing systems can separate taste by their functional characters similar to biology detection mechanism to ion channels on taste receptor cells.

ACKNOWLEDGMENT

This work has been funded by the National Natural Science Foundation of China (Grant Nos. 60725102, 30700167) and the China Postdoctoral Science Foundation (Grant Nos. 20070420235).

REFERENCES

1. Toko K (2000) Taste sensor. *Sens Actuators B* 64:205–215 DOI 10.1016/S0925-4005(99)00508-0
2. Gilbertson T A, Damak S, Margolskee R F (2000) The molecular physiology of taste transduction. *Curr Opin Neurobiol* 10:519–527 DOI 10.1016/S0959-4388(00)00118-5
3. Romer W, Steinem C (2004) Impedance analysis and single-channel recordings on nano-black lipid membranes based on porous alumina. *Biophys. J.* 86:955–965 DOI 0006-3495/04/02/955/11
4. Steinem C, Janshoff A, Galla H J et al (1997) Impedance analysis of the ion transport through gramicidin channels incorporated in solid supported lipid bilayers. *Bioelectrochem. Bioenerg.* 42:213–220 DOI: 10.1016/S0302-4598(96)05113-6
5. Wang P, Liu Q, Xu Y et al (2007) Olfactory and taste cell sensor and its applications in biomedicine. *Sens. Actuator A-Phys.* 139:131–138 DOI:10.1016/j.sna.2007.05.018
6. Yoshimoto M, Nishikanbara M, Nomoto M et al (2005) Dynamical behavior of lipid bilayer membranes for taste substances under random membrane-potential fluctuations *Biophys. Chem.* 118:1–6 DOI:10.1016/j.bpc.2005.06.008
7. Adler E, Hoon M, Mueller K et al (2000) A novel family of mammalian taste receptors. *Cell.* 100:693–702 DOI :10.1016/S0092-8674(00)80705-9

The address of the corresponding author:

Author: Qingjun Liu
 Institute: Biosensor National Special Laboratory, Department of Biomedical Engineering, Zhejiang University
 Street: Zheda Road 38
 City: Hangzhou
 Country: P. R. China
 Email: lqjmail@sina.com

Micro-Electrode Cell-Based Biosensor Using Electrochemical Impedance Spectroscopy for Cancer Research

Qingjun Liu^{1,*}, Jinjiang Yu², Hui Yu¹, Lidan Xiao¹, Ping Wang¹ and Mo Yang²

¹ Biosensor National Special Laboratory, Department of Biomedical Engineering, Zhejiang University, Hangzhou, P. R. China

² Department of Health Technology and Informatics, The Hong Kong Polytechnic University, Kowloon, Hong Kong

Abstract — In this study, cell biosensor chip with micro-electrode arrays was used to monitor the culture behaviour of mammalian cancer cells and evaluate the chemosensitivity of anti-cancer drugs using electrochemical impedance spectroscopy. The electrode arrays were fabricated by semiconductor technology with diameter from 50 μm to 10 μm of each electrode. The human oesophageal cancer cell lines (KYSE 30) were cultured on the surface of the electrode with the help of fibronectin. Morphology changes of cells adhesion, spreading, and proliferation can be detected by impedimetric analysis in a real time and non-invasive way. Anti-cancer drug of cisplatin was added to cells for potential drug screening applications. The experimental results show that drug's chemosensitivity effects can be detected by this cell based biosensor.

Keywords — Cell-based biosensor, Micro-electrode arrays, Cancer, Impedance spectroscopy, Chemosensitivity, Anti-cancer drugs

I. INTRODUCTION

In recent years, cancer is rapidly becoming the number one killer in many countries. And, chemotherapy (anticancer drugs) is still one of most important treatment methods in clinic. In pre-clinical testing studies, there is a great demand to develop more rapid and simple techniques for studying cancerous cells, especially for understanding their interactions with drugs and toxins. Conventional methods currently used in cancer cell biology mainly include fluorescent imaging, radioactive detection, and even animal experiments. These techniques often need extensive experimental process and stringent laboratory conditions, besides instrumentation and cost. In addition, they are not able to provide continuous monitoring of a sample and in consequence the information achieved may not reflect the real changes of cell activities at a specific time to a specific agent. In this context, there is a need to develop minimally invasive, reliable, inexpensive, and easy to use instrumentation for studying real-time biological events *in vitro*.

In the last decades, cell-based biosensors are the most studied novel techniques for cell monitoring methods due to their simplicity, sensitivity, and low cost. Using whole cells as the bio-recognition elements, those sensors can detect agents functionally with physiological changes to cells. One

of kind of them is sensors using electrochemical impedance spectroscopy, which first reported as electric cell-substrate impedance sensing (ECIS) technique for cell proliferation, morphology, and motility monitoring. The basic idea of the measurement is that when mammalian cells attach and spread on the surface of a planar gold-film electrode the behave essentially like insulating particles that hinder unrestricted current flow from the electrode into the bulk electrolyte and thereby increase the overall electrode impedance. Now, the ECIS as well as other now commercially available systems have been developed and applied as one of the most interesting label-free technology for studying cell adhesion on a surface and give real-time and kinetic information of cell behaviors. Recently, those impedance biosensors have been used for assessment of cytotoxicity [1] and pharmacological apoptosis [2], and even drug effect ions related with special disease [3].

In this study, the cancer cell lines will be cultured on the surface of the micro-electrodes coated with Fibronectin, the connecting protein for tumor cells metastasis and adhesion in extracellular matrix, to monitor cells adhesion, proliferation, and morphology by impedance detecting. Then, some well-known anti-cancer drugs (for example Cisplatin) were added to prove if this sensor system is a useful *in vitro* method to chemosensitivity evaluation.

II. EXPERIMENTAL

A. Fabrication of the electrode arrays

This chip is fabricated using semiconductor technology. The 4-in. silicon wafers (thickness of 450nm), was thermoxidized with SiO_2 for better contact with metal in later process. It needs sputtering with Cr thin film (100nm) as bond between metal and substrate, onto which the 300 nm Au was deposited, for Au is a highly conducting and durable biocompatible material. The electrodes were fabricated using wet etching technique and the passivated layer of $\text{SiO}_2/\text{Si}_3\text{N}_4/\text{SiO}_2$ was deposited above the metal layer by PECVD. Finally the circular hole of each electrodes and the bonding pad were etched out with RIE technique. The diameter of circular hole of each electrode is 30 μm . A micro-

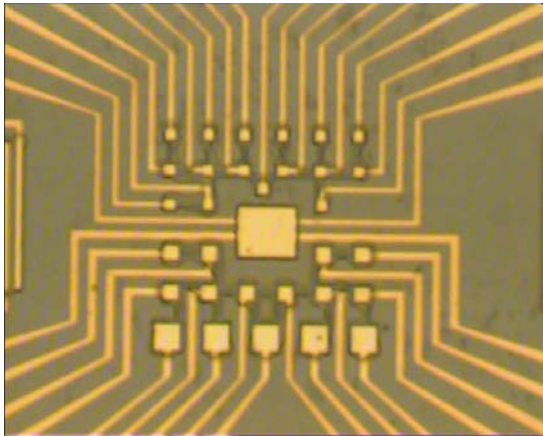


Fig. 1 Photo of the micro-electrode arrays.

graph of the fabricated electrode array substrate is shown in Fig. 1 with an electrode array pattern. The electrode diameter is from $50\ \mu\text{m}$ to $10\ \mu\text{m}$. The dimensions of the electrode pads were $1\text{cm} \times 1\text{cm}$.

B. Device and cell culture

A $5 \times 5 \times 1\ \text{cm}^3$ micro-chamber was formed by PDMS (polydimethylsiloxane) on the chip to culture cells. The cell line employed in our project is the human oesophageal cancer cell lines (KYSE 30) obtained from American Type of Culture Collection. They were maintained routinely in minimum essential medium (JRH BioSciences) supplemented with 5% fetal bovine serum (Hyclone) together with penicillin and streptomycin (Invitrogen). They were cultured on a 35 mm diameter tissue culture dish (Nunc GmbH & Co. KG, Germany) in a humidified incubator at $37\ ^\circ\text{C}$ with 5% CO_2 / 95% air. About 20 ml of 1 to 2 million cells per ml suspension was plated onto sensor coated with Fibronectin ($10\ \text{mg/mL}$), the connecting protein for tumor cells metastasis and adhesion in extracellular matrix, prior to cell seeding.

C. Impedance detecting

The impedance detecting setup was shown in Fig. 2. During experiments, sensor chip with cultured cells was inserted into a chip cartridge, with 40 independent electromechanical relays. Each relay has a normally closed, normally open, and common terminal. For the array of electrodes, each sensing electrode had a solderable pad at the edge of the chip. Wires connected to common terminals were soldered to these pads. Then, the cartridge was put into incubator with wires contacted to detecting machine. Culture medium and solution containing anti-cancer drugs was injected alternatively by a peristaltic pump into the micro-chamber

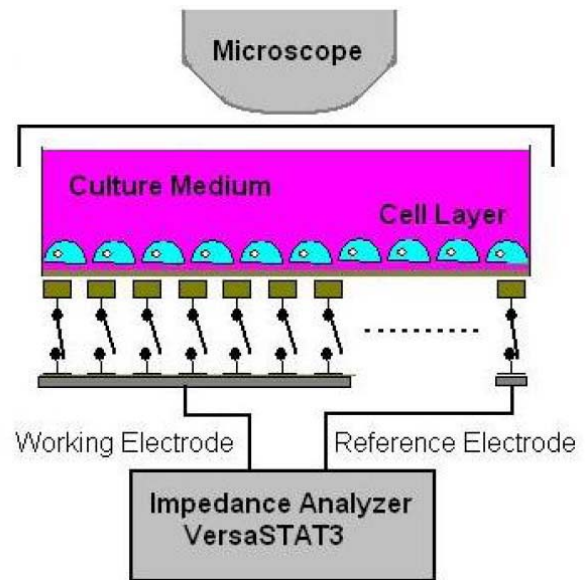


Fig. 2 Cell impedance detecting system.

through a degasser and a selection valve. All the measurements were performed at $37 \pm 0.2\ ^\circ\text{C}$.

Impedance spectra was performed using the impedance analyzer VersaSTAT3 (Princeton Applied Research, USA) controlled by a personal computer. The impedance $|Z|$ (f) between voltage and current were recorded within a frequency range of 1 Hz to 1 MHz. A pure sinusoidal AC voltage of 10 mV amplitude (peak-to-peak) was applied and 100 data points per frequency decade chosen to be equidistant on the logarithmic scale were recorded, which need about 7 min. Then, impedance of the electrodes in the cell culture medium was measured at a fixed frequency (10 kHz) every minute during the impedance sweep interval to obtain real time recording.

D. Pharmacology

To validate the applicability of this cancer cell chips in pharmacological bioassays, well-established anti-cancer drugs, such as of cisplatin (Sigma-Aldrich Co. USA), were added for potential chemosensitivity screening applications. Various concentrations ($0.1\ \mu\text{M}$, $1\ \mu\text{M}$, $10\ \mu\text{M}$) of the above pharmacological agents were prepared in normal culture solution. A drug-cycle protocol was employed. Basal parameters were recorded after cells cultured on the chips, followed by completely replacing the culture medium with one that contained one of drugs in a certain concentration. Recordings were made in the presence of drugs for about 4 hours (15000 s). The cell recovery was achieved by gently washing with normal culture medium five times at 1-minute intervals.

III. RESULTS

A. Cellular adhesion on electrodes

Fibronectin is a major extracellular matrix component of cancer-associated biological stroma. Because interactions mediated by fibronectin are implicated to modulate cancer cell's invasion to normal cells and tissues through matrix. Impedance analysis is very good at studying cell adhesion on a surface, and give real-time and kinetic information of cell behaviors. Here, we examined the cell adhesion on microelectrodes modified by fibronectin.

Fig. 3 shows the KYSE 30 cells cultured on electrode surface after 24 h.

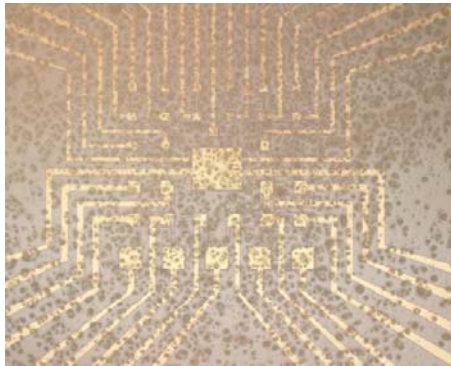


Fig. 3 KYSE 30 cells cultured on electrode surface after 24 h.

B. Impedance detection

In Fig. 4, a equivalent circuit represented the impedance spectrum of our system [3]. The resistor R_s is mainly due to the conductivity of the bulk solution and the wire connection. The Z_{CPE} represents the dielectric properties of the electrode/electrolyte and surface morphological information. R and C are the resistance and the capacitance of the layer of the absorbed proteins. R_c and C_c are elements related to the cell layer. Values of R_s , Z_{CPE} , R and C remain constant in the equivalent circuit while values of R_c and C_c components vary with cells changes.

Fig. 4 also shows the impedance spectrum of biosensor before and after KYSE 30 cell lines cultured on the electrode. The difference in the total impedance indicating that impedance reading at 100 Hz to 100 KHz passes a maximum value. So we selected 10 KHz as the fixed frequency to obtain real time process of cells adhesion. We find after cells seeded on the electrode, the impedance begin to increase (Fig. 5). After about 5 min cells begin attached on the electrode, the impedance increased greatly.

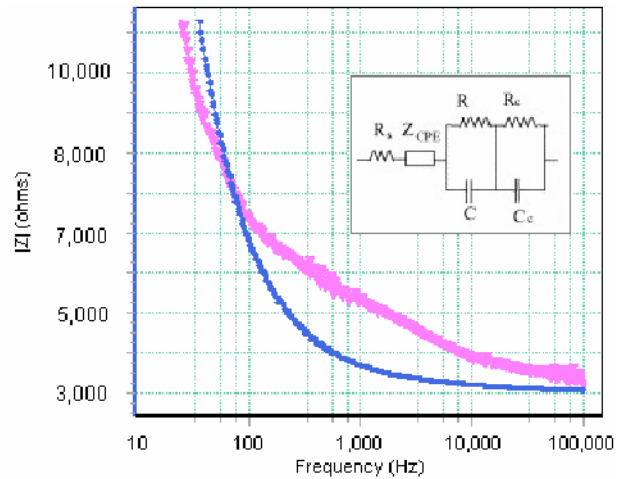


Fig. 4 One channel impedance detection of the micro-electrode array, before (blue line) and after (red line) KYSE 30 cell seeded. The equivalent circuit represented the impedance spectrum of the system.

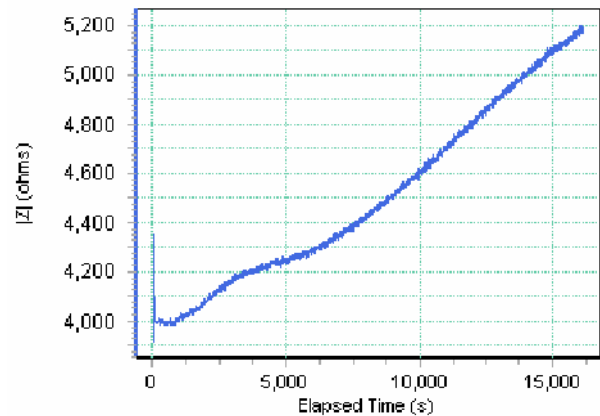


Fig. 5 The real time impedance detection after cells seeded on the electrode. With cells adhesion, spreading and proliferation, the signal increased greatly.

C. Drug's chemosensitivity analysis

Cisplatin is one of the older chemotherapy drugs. It is an active medicine against many cancers. Cisplatin cross-links DNA in several different ways, and then interfering cell division by mitosis. The damaged DNA elicits DNA repair mechanisms, which in turn activate apoptosis when repair proves impossible. All of these pharmacological changes contacted with cell's morphology changes. In our study, when added Cisplatin to cells, the impedance decreased greatly (Fig. 6).

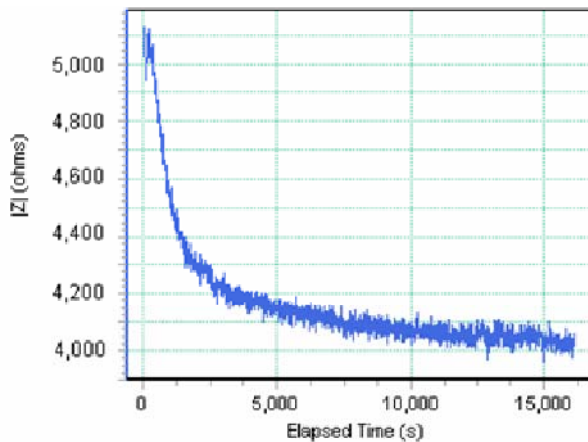


Fig. 6 Impedance detection of the Cisplatinum.

Many investigators have used lots of methods for assessing the extent of cell killing to anticancer drugs and radiation, based on early functional changes (such as dye uptake), or on growth inhibition, rather than on clonogenic survival. These can lead to incorrect assessments of overall cell kill. However, our study established a novel functional analysis method. Maybe, based on a microchip technology successfully used in drug screening, this test may well mean a break through for clinical tumor therapy, as it provides a very innovative way to monitor tumor cell responses to chemotherapeutics.

IV. DISCUSSION

In the case of cancer research, cell adhesion into extracellular matrix is the precondition to tumor metastasis, and then tumor clone is formed with unbounded cell proliferation. Currently used adhesion assay is an *in vitro* method used to determine the rate or strength of adhesion of different cell types to extracellular matrix proteins by labeled with the fluorescent dyes. And, cellular morphology is one of most important parameters in cancer biology at all times. Especially, most of anticancer agents currently employed that target the cytoskeleton, do so through interactions with the microfilaments now. The cytoskeleton consists of a complex network of filamentous proteins which are involved in regulation of cell morphology and adhesion. Moreover, the concept that tumor cells exposed to anticancer drugs usually die from apoptosis has become a widely held tenet of modern cancer treatment.

Through above analysis, we can find that cellular adhesion, proliferation, and morphology (such as caused by cytoskeleton or apoptosis) can be monitored with impedance sensors. Thus, this sensing technology could be used

for multiple purposes in cancer cell biology and therapeutics. Maybe, they could complement conventional cell-culture methods for studying biological processes involved in cell proliferation or as screening devices for drug testing. Although some groups have reported cancer cells, such as human ovarian cancer cells and human hepatocarcinoma cell lines, cultured on the surface of quartz crystal or indium tin oxide electrodes for cell's adhesion and cytotoxicity detection by impedance analysis, those cells just used as a kind of cell source, and their tumorous biological characters never thoroughly investigated.

V. CONCLUSIONS

Cell chip with micro-electrode arrays was used to monitor the culture behaviour of mammalian cancer cells and evaluate the chemosensitivity of anti-cancer drug using electrochemical impedance spectroscopy. Morphology changes of cells adhesion, spreading, and proliferation can be detected by impedimetric analysis. Anti-cancer drug added to cells for potential drug screening applications. The experimental result shows that this well-known drug has chemosensitivity effects detected by micro-electrodes.

ACKNOWLEDGMENT

This work has been funded by the National Natural Science Foundation of China (Grant Nos. 60725102, 30700167) and the China Postdoctoral Science Foundation (Grant Nos. 20070420235).

REFERENCES

1. Ceriotti L, Ponti J, Colpo P et al (2007) Assessment of cytotoxicity by impedance spectroscopy. *Biosen. Bioelectron.* 22:3057–3063 DOI:10.1016/j.bios.2007.01.004
2. Arndt S, Seebach J, Psathaki K et al (2004) Bioelectrical impedance assay to monitor changes in cell shape during apoptosis. *Biosen. Bioelectron.* 19:583–594 DOI:10.1016/S0956-5663(03)00269-0
3. Yang M, Lim C C, Liao R et al (2007) A novel microfluidic impedance assay for monitoring endothelin-induced cardiomyocyte hypertrophy. *Biosen. Bioelectron.* 22:1688–1693 DOI:10.1016/j.bios.2006.07.032

The address of the corresponding author:

Author: Qingjun Liu
 Institute: Biosensor National Special Laboratory, Department of Biomedical Engineering, Zhejiang University
 Street: Zheda Road 38
 City: Hangzhou
 Country: P. R. China
 Email: lqjmail@sina.com

Piezoelectric Biosensor Based on Olfactory Receptor Expressed in a Heterologous Cell System for Drug Discovery

Chunsheng Wu¹, Haimin Tan², Hui Yu¹, Luhang Zhao², Ping Wang^{1*}

¹Biosensor National Special Laboratory, Key Laboratory of Biomedical Engineering of Ministry of Education, Department of Biomedical Engineering, Zhejiang University, Hangzhou 310027, China

²Department of Biochemistry and Molecular Biology, Medical College of Zhejiang University, Hangzhou 310058, China

*Correspondence should be addressed to Wang Ping (email: cnpwang@zju.edu.cn)

Abstract — Nowadays, there is an urgent need to find novel tools and approaches to improve the overall efficiency of drug discovery. In the present study, we developed a quartz crystal microbalance (QCM)-based biosensor in which olfactory receptor expressed in a heterologous cell system was used as sensitive elements. An olfactory receptor protein of *C. elegans*, ODR-10, which was serve as a model of G-protein-coupled receptors (GPCRs), was expressed on the plasma membrane of human embryonic kidney (HEK)-293 cells. For targeting the ODR-10 on the surface of cell membrane, the rho-tag import sequence was inserted into the N-terminus of the ODR-10. The membrane expression of ODR-10 was shown by the enhanced green fluorescent protein (EGFP) which sequences was inserted into the C-terminus of the ODR-10. After that, the membrane fraction of HEK-293 cells containing ODR-10 was extracted and then coated on the electrode surface of QCM. The interactions between odorant molecules and olfactory receptors were monitored by QCM. The results indicate that ODR-10 was functionally expressed on the plasma membrane of HEK-293 cells and it can respond to diacetyl with high specificity, which is a natural ligand for ODR-10. All the results suggest one conclusion: this novel QCM-olfactory receptor hybrid biosensor can be used to detect the interactions between GPCRs and their ligands, and suggest it could be a potential tool for drug discovery and even for drug evaluation.

Keywords — Quartz crystal microbalance, G-protein-coupled receptors, Olfactory receptor, Drug discovery, Biosensor

I. INTRODUCTION

The process of drug discovery is a long, complex and multi-stage process. The successful odds of this process is very low due to the lack of powerful tools and approaches for drug screen and evaluation. Nowadays, there is an urgent need to find new tools and approaches to improve the overall efficiency of drug discovery and development. GPCRs, which are characterized by their seven transmembrane spanning domains, form the largest single family of integral membrane receptors. GPCRs mediate a diverse array of biological functions including hormones, neuro-

transmitters, peptides, odorants and light[1]. As a result, GPCRs have become the single most important drug targets for medical therapy. Olfactory receptors (ORs) belong to the large family of GPCRs[2], which can mediate the interactions of odorous compounds with olfactory receptor neurons. It has been implied that the olfactory system can recognize and discriminate a large number of structurally diverse odorous molecules at minute concentrations. It displays both an unmatched chemical space and a high sensitivity mainly due to their various ORs. It is thus tempting to use ORs as sensitive elements to develop novel hybrid biosensors for odorant recognition and finally for drug discovery.

Various secondary sensors including QCM have been used to develop biosensors[3]. The basic principle of QCM is that the tiny mass change on the crystal surface will result in the resonant frequency change of the crystal[4]. According to this principle, QCM can be used to detect the mass change of the coated material on the crystal surface. Because of simplicity, low cost, high sensitivity, rapid response and real time dynamic detection, QCM is widely used for detecting the interactions between biological molecules.

In this study, a novel QCM-based biosensor incorporated with heterologous expressed olfactory receptor was fabricated, and then the sensitivity and specificity were examined as an olfactory biosensor. An olfactory receptor protein of *C. elegans*, ODR-10[5], was used as a model of GPCRs to serve as sensitive elements. ODR-10 was expressed on the plasma membrane of HEK-293 cells. After confirming the cell surface expression of ODR-10, the crude membrane containing ODR-10 was extracted and then coated on the electrode surface of QCM. The interactions between odorant molecules and olfactory receptors were monitored by QCM.

II. MATERIALS AND METHODS

2.1 Plasmid constructions

The *odr-10* full-length sequence was amplified by PCR from *pBluescript SK⁻/odr-10*. The forward and reverse primers were 5'-GAGTTGGAATTCATGTCGGGA GAATTGTGG-3' and 5'-CAGTAAGGATCCCGCGTCG GAACCTTGAGACAAATT-3', respectively. The *rho-tag* import sequence was 5'-GTCGCACTCGAGATGAAC GGGACCGAGGGCCCAAACCTTCTACGTGCCTTCTC CAACAAGACGGGCGTGTTGGAATTCGCTGGA-3', which was synthesized by Takara (Japan). The *rho-tag* gene sequence can be found in NCBI. The *rho-tag* sequence was inserted into the *pEGFP-N1* mammalian expression vector using sites XhoI and EcoRI of the multiple cloning sites (MCS). Then the *odr-10* gene sequence was subclone into the MCS sites between EcoRI and BamHI of *pEGFP-N1/rho-tag*. The *pEGFP-N1/rho-tag/odr-10* clone was sequenced.

2.2 Cell lines and transfection

HEK-293 cells were cultured at 37°C in Dulbecco's Modified Eagle's Medium (GIBCO) containing 10% fetal bovine serum (FBS), penicillin (100 U/ml) and streptomycin (100µg/ml), in 5% CO₂ incubator. One day before transfection, HEK-293 cells were seeded on 6-well plates. Lipofectamine (GIBCO) was used as the DNA carrier. When being 80% confluent, HEK-293 cells were transfected with 4µg of plasmid DNA (*pEGFP-N1/rho-tag/odr-10* or control plasmid *pEGFP-N1*) for each well. The cells were incubated with the mixture for 6 hr at 37°C. The transfected cells were used for further experiments 24 hr after transfection.

2.3 Fluorescence microscopy

For fluorescence microscopy, HEK-293 cells were grown on 6-well plates and transfected as described above. To visualize the surface expression of ODR-10::EGFP fusion proteins, cells were observed on a Olympus IX 70 fluorescence microscopy (Japan) with excitation at 488nm.

2.4 Extract of membrane fraction and coating methods

The transfected HEK-293 cells were washed with phosphate buffered saline (PBS, pH 7.4) and harvested from 6-well plates. Then these cells were sonicated with a probe-type sonicator for 5 min and centrifuged at 16,000 g for 40 min. Supernatant is a cytosol fraction and pellet is a membrane fraction. The QCM was purchased from HRBio Co. (Beijing, China), which was AT-cut crystals with an

initial frequency of 5 MHz. A 1 µl aliquot of the membrane fraction containing ODR-10 was evenly spread on the gold electrode of the QCM, and then completely dried at room temperature. Membrane fraction of HEK-293 cells without ODR-10 was used as control.

2.5 Measurement

The frequency of the QCM was measured before and after the coating of the membrane fraction of the cells. When the resonant frequency reached a steady baseline, odorants were applied to the surface of the QCM. Odorants were prepared as 0.1 M stock solutions in dimethyl sulfoxide (DMSO) and diluted to a concentration of 0.1 mM with sterilized water for further experiments. Saturated vapor of the odorants solution was injected into the detection chamber. After injection, the detection chamber was washed with fresh air without odorants. The minimum interval between the injections was 10 min to rule out the influence of remainder odorant and allow QCM to return to a steady state.

III. RESULTS AND DISCUSSION

3.1 Construction of *pEGFP-N1/rho-tag/odr-10* expression plasmid

The mammalian expression vector *pEGFP-N1* was chosen to construct the *odr-10* expression vector for its encoding a red-shifted variant of wild-type GFP which has been optimized for brighter fluorescence and higher expression in mammalian cells. To make sure *odr-10* cloned into the MCS of *pEGFP-N1* will be expressed as fusion proteins to N-terminus of EGFP, the stop codons of *odr-10* were removed by PCR. So EGFP can be used to visualize and confirm the surface expression of *odr-10* in HEK-293 cells [6]. For targeting the ODR-10 on the surface of cell membrane, the *rho-tag* import sequence was inserted into the N-terminus of the *odr-10*. Fig.1 shows the schematic of constructed vector. Fig.2 shows the Gel electrophoresis of constructed vector digested with restricted enzymes. Combining with the results of sequencing of constructed vector, it is suggested that *pEGFP-N1/rho-tag/odr-10* expression plasmid was successfully constructed.

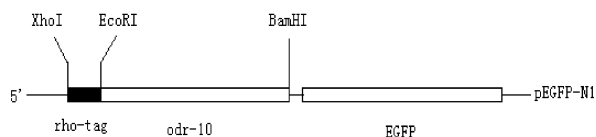


Fig.1 Schematic diagram of the constructed *pEGFP-N1/rho-tag/odr-10* plasmid. The *rho-tag* import sequence was inserted into the N-terminus of the *odr-10*. The C-terminus of *odr-10* was immediately followed by EGFP.

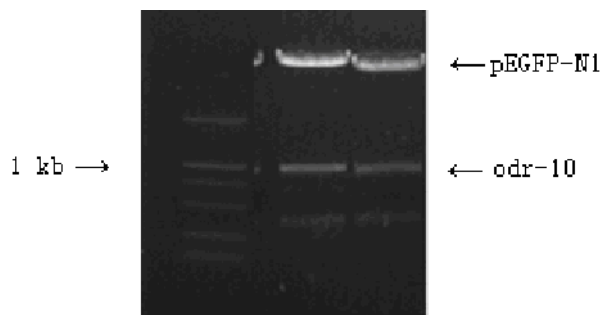


Fig.2 Gel electrophoresis of *pEGFP-N1/rho-tag/odr-10* digested by restricted enzymes. Lane 1: DNA size marker; Lane 2: *pEGFP-N1/rho-tag/odr-10* digested by EcoRI and BamHI; Lane 3: *pEGFP-N1/rho-tag/odr-10* digested by XhoI and BamHI.

3.2 Expression of ODR-10::EGFP fusion gene on the surface of HEK-293 cells

To use ODR-10 as sensitive elements of biosensors, it is necessary to express the protein in a heterologous cell system. In this study, HEK-293 cells were used as a heterologous cell system and ODR-10 was used as a model of GPCRs. To evaluate ODR-10 expression and determine whether ODR-10 could reach the surfaces of transiently transfected HEK-293 cells, we use fluorescence microscopy to observe the fluorescence on live cells (Fig.3). ODR-10 and EGFP were expressed as fusion protein and EGFP can serve as a reporter of ODR-10. The distribution of EGFP

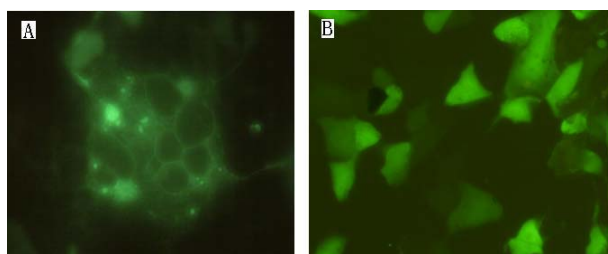


Fig.3 The expression of (A) ODR-10::EGFP fusion proteins and (B) EGFP in HEK-293 cells 24 hr after transfection. The fusion proteins were mainly distributed on the surface of HEK-293 cells. The EGFP was distributed evenly in the HEK-293 cells. Excitation and emission wavelengths were 488 and 507 nm, respectively.

can reflect the expression and subcellular location of ODR-10. From the pictures of transfected HEK-293 cells taken under the fluorescence microscopy, it is obviously that the ODR-10::EGFP fusion gene were mainly expressed on the surface of HEK-293 cells. But the control cells which were transfected with *pEGFP-N1* did not show this character, which fluorescence could be seen evenly distributed on live cells.

3.3 Response of QCM coated with membrane fraction of cells expressing olfactory receptor

QCM coated with membrane fraction containing ODR-10 could respond to diacetyl, which is a natural ligand for the ODR-10[5] (Fig.4). QCM coated with membrane fraction without ODR-10 also showed a response to diacetyl, but it was much smaller than that of ODR-10. The reason may be the non-specific interactions between the odorant molecules and the membrane fraction of cells. When other odorants such as acetic acid, hexanal and decyl alcohol were tested, the response of QCM were also much smaller than diacetyl. These results indicate that ODR-10 as a fusion protein with EGFP was functionally expressed on the plasma membrane of HEK-293 cells. Its response to diacetyl showed high specificity. By this means, other kinds of GPCRs can be used as sensitive elements in a QCM biosensor. Due to the importance of GPCRs in drug discovery, this kind of biosensors has great potential to be used as novel tools for drug discovery and even for drug evaluation.

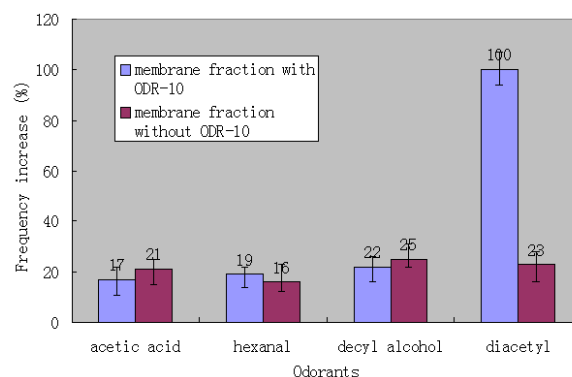


Fig.4 Responses of QCM coated with membrane fraction of cells with and without ODR-10 to different odorants. Compared with other odorants, diacetyl, which is a natural ligand for the ODR-10, interacts most strongly with ODR-10. The responses of control may be the non-specific interactions between the odorant molecules and the membrane fraction of cells.

The responses of QCM to various odorants were normalized their frequency increase to that of diacetyl.

IV. CONCLUSION

An olfactory receptor protein of *C. elegans*, ODR-10, was functionally expressed on the plasma membrane of HEK-293 cells. It can respond to diacetyl with high specificity. EGFP was successfully used to traffic the subcellular distribution of ODR-10. A QCM-based biosensor was fabricated in which ODR-10 expressed in HEK-293 cells was used as sensitive elements. All the results suggest one conclusion: this novel QCM-olfactory receptor hybrid biosensor can be used to detect the interactions between GPCRs and their ligands, and suggest it could be a potential tool for drug discovery and even for drug evaluation. This is the first step of fabricating an olfactory receptor-based biosensor for drug discovery. In the following work, we plan to develop a QCM array coated with various GPCRs to make this kind of hybrid biosensor suit for high-throughput drug screen and evaluation.

ACKNOWLEDGMENT

We take this opportunity to express our sincere appreciation to Cornelia I. Bargmann (Laboratory of Neural Circuits and Behavior, Howard Hughes Medical Institute, The Rockefeller University, NY, USA) for the odr-10 gene. This work was supported by the National Natural Science Foundation of China (Grant No. 60725102), the Zhejiang Province Natural Science Foundation of China (Grant No. R205502).

REFERENCES

1. Ferguson S S, Caron M G. (1998) G protein-coupled receptor adaptation mechanisms. *seminars in Cell & Developmental Biology* 9: 119-127
2. Dryer L, Berghard A. (1999) Odorant receptors: a plethora of G-protein-coupled receptors. *Trends. Pharmacol. Sci.* 20: 413-417
3. Wu C S, Wang L J, Zhou J, Zhao L H, Wang P. (2007) The progress of olfactory transduction and biomimetic olfactory-based biosensors. *Chinese Science Bulletin* 52: 1886-1896
4. Bunde R L, Jarvi E J, Rosentret J J. (1998) Piezoelectric quartz crystal biosensors. *Talanta* 46:1223-1236
5. Sengupta P, Chou J H, Bargmann C I. (1996) Odr-10 encodes a seven transmembrane domain olfactory receptor required for responses to the odorant diacetyl. *Cell* 84: 875-887
6. Kallal L, Benovic J L. (2000) Using green fluorescent proteins to study G-protein-coupled receptor localization and trafficking. *Tips* 21: 175-180

Use macro [author address] to enter the address of the corresponding author:

Author: Wang Ping
 Institute: Biosensor National Special Laboratory, Key Laboratory of Biomedical Engineering of Ministry of Education, Department of Biomedical Engineering, Zhejiang University
 Street: 38, Zheda Road
 City: Hangzhou
 Country: China
 Email: cnpwang@zju.edu.cn

A Flexible Thin-film Microelectrode for Optic-Nerve Visual Prosthesis

Xiaohong Sui^{1*}, Yinghui Li¹, Yijing Xie¹, Ting Liang¹, Wei Chen², Yiliang Lu¹, Gang Li³, Kai Wang⁴, Qiushi Ren¹

¹Institute for Laser Medicine and Bio-photonics, Department of Biomedical Engineering
Shanghai Jiao Tong University, Shanghai 200240, China

²Department of Anatomy, Histology & Embryology, Shanghai Medical College of Fudan University, China

³Nanotechnology Laboratory, Shanghai Institute of Microsystem and Information Technology
Chinese Academy of Sciences, Shanghai, China

⁴The Department of Ophthalmology, People's Hospital, Peking University, China

Abstract — A novel 16-channel flexible thin-film microelectrode was fabricated for optic-nerve visual prosthesis by MEMS (Micro Electromechanical System) technology. It was encapsulated by medical-grade silicone adhesive and suitable for chronic stabilization *in-vivo*. Testing results *in-vitro* showed that average impedance of each channel was 100k Ω at 1kHz and that the microelectrode had good biocompatibility with the optic-nerve glial cells. Proper surgery was adopted to implant the microelectrode in the optic-nerve dura.

Keywords — Visual Prosthesis, MEMS, Microelectrode, Biocompatibility

PACC: 0710C, 8770, 0670D

I. INTRODUCTION

The advancements in fabrication technology have led to the development of many different microelectrodes that can be inserted into the cortex, implanted subretinally, epiretinally and around the optic nerve for helping blind people restore some functional vision^[1-2]. As the physical interface with biological tissue, the microelectrode has direct effect on the stimulation selectivity and sensitivity for visual prosthesis. Determination of microelectrode material and configuration is considered primarily from biocompatibility, fabrication complexity, insertion trauma and channel uniformity, etc.

Psycho-physiological experiments with a pixelized vision have shown that a minimum of 625 pixels are necessary to restore a functional visual sensation for epiretinal visual prosthesis^[3]. As far as the optic-nerve stimulation is concerned, silicone-based cuff microelectrode and inserted metal microwires have been used. Four stimulation-sites cuff microelectrode enwraps the optic nerve and is attached to the surface of the dura^[4-5]. This approach means higher stimulation current threshold, and wrapping around the optic nerve will probably induce the function degeneration. Meanwhile, metal microwires are inserted through the dura to optic-nerve bundles. Although the inserted metal microwires can

effectively lower the stimulation current thresholds, they similarly have direct physical insertion trauma on the optic nerve. Consequently, the visual implant should provide the maximum level of flexibility to be able to support most of the stimulation strategies, and adheres to the optic nerve closely to lower the stimulation thresholds without more heat trauma.

In this study, we designed a novel flexible 10 μ m-thick microelectrode with 16 stimulation sites for optic-nerve vision rehabilitation. The fabrication process of the microelectrode by MEMS technology was detailed. Analyses of the electrical and biological characteristics showed that the microelectrode had good uniformity and biocompatibility with the optic-nerve glial cells.

II. METHODS

A. Design and Fabrication of the Multi-channel Flexible Microelectrode

A novel multi-channel flexible microelectrode for visual prosthesis was designed and manufactured. Configuration and biocompatibility was considered to select photosensitive polyimide Durimide 7510 (Arch chemicals, Norwalk, CT, USA) as the film material. A simple and low-cost process can be divided into six steps to fabricate the flexible microelectrode as follows:

- a) The silicon wafer was dipped in the 5% hydrofluoric acid for 5 minutes to remove the oxide on the surface, and then cleaned out according to RCA criteria.
- b) The silicon wafer was dried under 200°C. Then 1 μ m aluminum was evaporated on the surface and served as a sacrificial layer in the later release step.
- c) The lower photosensitive polyimide was spin-coated onto the silicon wafer and exposed. Then the 5 μ m polyimide film was obtained after heated in the nitrogen atmosphere at 350°C.
- d) The technique of sputtering and lift-off was applied to form the Ti/Pt (100Å/1500 Å) thin film for stimulation sites, connecting line, and the bonding pads.
- e) According to step a) to c), the upper 5 μ m polyimide was obtained to insulate the connecting lines with windows opened to expose the site of electrode and the welding points. Meanwhile, the 5 μ m-deep recess was formed to define the configuration of the microelectrode.

* corresponding author: email: suixhong@sjtu.edu.cn

- f) The aluminum layer is etched by electrochemical method, and the microelectrode was then released using the recess.

The fabricated thin film polyimide microelectrode must be encapsulated for further experiment, and the discrete steps are detailed in the following.

First, Enameled Φ -50 μ m metal wires were utilized as the lead cables to correspondingly electrically connect each bonding pad with an 18-pin connector. Second, the bonding pads were insulated and reinforced by epoxy resin, and then connecting fine wires were twisted into a bundle. Finally, based on a well designed mould, the medical degree silicone adhesive was used to seal the bonding pad area and the wire bundle to improve the biocompatibility.

B. Test of Electrical Characteristic

Impedance evaluation has become a common method to non-invasively determine the electrical continuity and condition of chronically implanted microelectrodes *in-vivo*. Since electrophysiological saline solution is the primary constituent of body fluids, it is generally assumed as the impedance-testing environment *in-vitro*.

When a metal electrode is immersed in the electrolyte, an electrochemical interface is formed between the two phases^[6]. At the instant, the metal and electrolyte are electroneutral. Immediately the transient electron-transfer oxidation and reduction reactions occur near the interface, and then an electric field is established with the net current is zero^[7-8]. Water dipoles orient themselves as a dielectric layer at the metal surface in the electric field. Besides, some chemical anions or cations are specifically adsorped to the surface of the solid electrode. Consequently, a double-layer capacitor is formed at the metal/electrolyte interface with a redox equilibrium potential called half-cell voltage E_{hc} .

When the amount of net electrons on the metal electrode is small during stimulation or recording, a charge-transfer resistor is

modeled in parallel with the double-layer capacitor without interfering with the electrical equilibrium at the interphase.

In addition to these two elements, spreading resistor is included due to the electrolyte. Generally, the three elements determine the impedance characteristics of the metal electrode.

The metal electrode/electrolyte interface mechanism is illustrated in Figure 1 together with the equivalent circuit model.

The impedance of an electrode-electrolyte interface depends on the species of metal, the type of electrolyte it contacts, the surface area, and the temperature. The impedance decreases with increasing area and surface roughness. It also decreases with increasing frequency due to C_d and increasing overpotential (difference between the applied voltage and the half-cell voltage) due to R_d reduction.

Considering these different factors, the applied potential for impedance evaluation is restricted to be less than 50mV peak experimentally.

Figure 2 shows diagram of the test chamber consisting of a culture dish containing 0.9% saline solution and a polymethyl methacrylate cover. The tested microelectrode was held by a clamp and immersed in the solution as the working electrode. A flat platinum counter electrode and an Ag/AgCl reference electrode enter the chamber through hermetic seals. The testing current/voltage signal was input between counter and working electrodes, and the reference electrode was used to define a reference potential of impedance measurement system.

Prior to impedance testing, the microelectrode was placed in a holder that allowed the electrode to be immersed in the electrolyte for 1h to allow stabilization of the ionic double layer. The impedance characteristics were monitored for time periods arranging from 1 to 8 hours. The impedance characteristics of the microelectrode after encapsulation were analyzed by Agilent E4980A Precision LCR Meter at room temperature.

Impedance measurements were obtained for input voltage levels of 50 mV at different frequencies. Impedance of resistance of the interface is in the kilohm range and the saline resistance is approximately 60 ohm-cm, so the resistance due to the saline bridge was assumed to be negligible^[9].

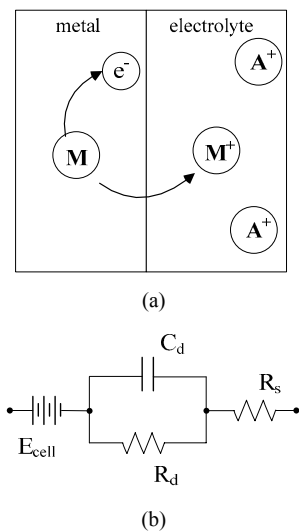


Fig.1. The metal/electrolyte interface: (a) physical illustration; (b) equivalent circuit

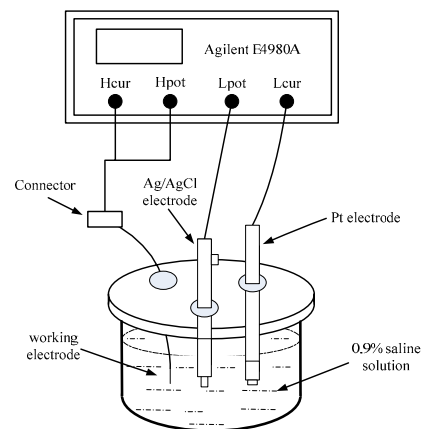


Fig.2. Three-electrode impedance test diagram

C. *In-vitro* Biocompatibility Evaluation

Optic nerve bundles are difficult to regenerate after injury, and biocompatibility is of important concern when designing an implanted microelectrode.

The optic-nerve is mainly composed of astrocyte and oligodendrocyte glial cells. As a result, optic-nerve glial cells are considered to evaluate the flexible microelectrode biocompatibility.

In order to determine the effect of microcurrent on the optic-nerve glial cells, an electric stimulator producing microcurrent was included with one channel in the flexible microelectrode and the tungsten wire as the return circuit shown in Fig.3.

Before the biocompatibility experiment between microelectrode and glial cells, the reference electrode tungsten wire was tested to show the effect on the culture solution. Two sterilized culture bottles were selected with the addition of uniform 15% fetal bovine serum. These bottles were considered as the counter group and tungsten group, respectively. The experiment results were recorded after 15days.

The biocompatibility experiment setting corresponding to Figure 3 was composed of three aspects: culturing the glial cells, examining the biocompatibility between polyimide material and glial cells, and investigating the glial cells proliferation and apoptosis under the pulse-signal stimulation.

Optic nerve of 2mm long was obtained from the neonatal three-day SD rats. Small pieces of optic nerves were obtained and cultured in a standard cell culture environment(37°C, humidified, 5% CO₂/95% air). After 35 days, the subcultured optic-nerve glial cells were divided into 2 groups. Group 1 as the counter group with polyimide flexible microelectrode in the chamber without microcurrent, and the influence of the microelectrode to the culture medium as well as the glial cell adhesion onto the microelectrode was observed consecutively for 13 days. Group 2 is considered as the microcurrent stimulation group with the measured pulse-signal diagram shown in Figure 4, where the pulse amplitude of ±2.5V and frequency of 100Hz was tested by oscillograph across the stimulation channel of the microelectrode and the tungsten reference electrode. The glial cells was evaluated with the microcurrent pulses applied to the microelectrode for 5 days twice a day, once 10 minutes, and the glial cell proliferation and

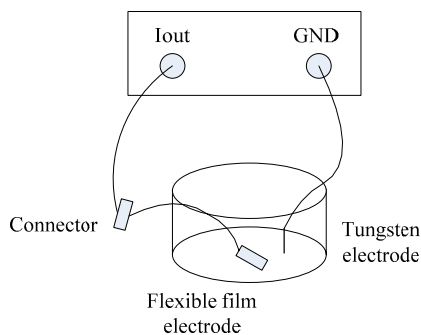


Fig.3. System Diagram of Biocompatibility including pulse-signal stimulator, flexible microelectrode, electrical connector and tungsten electrode

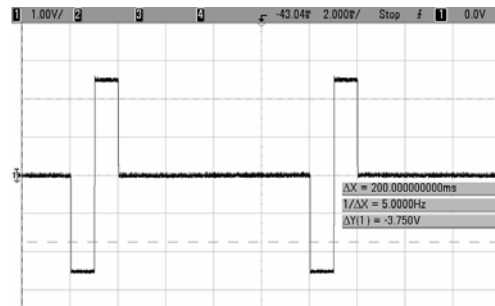


Fig.4. Stimulation pulse-signal waveform with the frequency of 100Hz and voltage amplitude of ±2.5V

apoptosis were compared by means of statistical cell number and cell morphology.

D. *In-vivo* Animal Surgery

Proper animal surgery was adopted to expose the optic nerve and aided the flexible microelectrode to closely contact the optic nerve. Rabbits were anesthetized with intravenous injection of 3% pentobarbital sodium (30mg/kg). After the skin of external canthus was dissected, conjunctiva and sub-Tenon space was opened at the limbus under surgical microscope. Lateral rectus muscle can be found easily and then snipped. Microsurgical forceps were used to expose the optic nerve near the eyeball to open a narrow cut at the optic nerve and to separate the pia and dura. The encapsulated flexible microelectrode was sewed on the sclera at the back eye through the silicon adhesive. And then the narrow part was inserted into the cut and sandwiched in the dura with the exposed stimulating sites faced the pia. The sketch map of Figure 5 details the stabilization approach and location at the optic nerve.

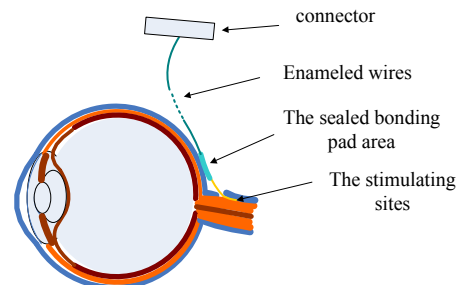


Fig.5. Location illustration of the stabilized microelectrode for optic-nerve stimulation

III. RESULTS AND DISCUSSION

A. *Fabrication and Encapsulation of Microelectrode*

The microelectrode was used for *in-vivo* application and stabilized in saline solution environment. Flexibility is a key factor for the microelectrode to closely contact the optic-nerve. Considering the compatibility with the MEMS fabrication process

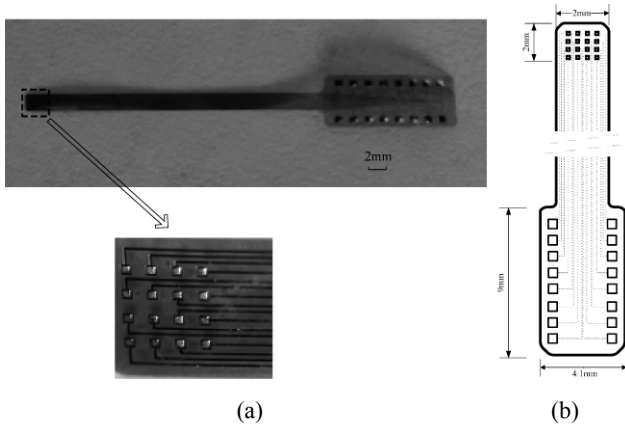


Fig.6. The flexible microelectrode before encapsulation: (a) the top view; (b) dimension illustration: the microelectrode consists of 16 stimulation sites in a 4×4 layout occupying 2 mm×2 mm, and the stimulation site is 0.1×0.1 mm. the square bonding pad is 0.3mm in one side, and the welding sites area is 4.1 mm×9 mm.

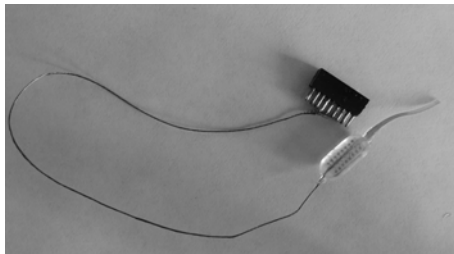


Fig.7. The 16-channel encapsulated flexible microelectrode: the silicon adhesive encapsulated part is 11mm long, 5mm wide and 2 mm thick.

technology, photosensitive Durimide 7510 is selected as the microelectrode substrate and platinum as the stimulation site material. In addition to biocompatible microelectrode material, medical-grade silicon adhesive SDG-A (M) was used as the encapsulation material to improve the biocompatibility.

The MEMS microelectrode and its layout design are displayed in Figure 6, and the picture of the encapsulated one with thin wires connected to the connector is showed in Figure 7.

The encapsulated size of the flexible microelectrode can be adjusted according to varied application fields.

B. Impedance Characteristics of Microelectrode

The average complex impedance spectrum was showed in Fig.8. In the figure, each data point represents an average of the 16 channel of the electrode under the same frequency. The average impedance of the probes of the array measured at 1 kHz was 100kΩ, indicating the probes are of more or less consistent electrical property.

Large impedance means severe tissue trauma with determined current amplitude. Since the stimulation current amplitude is on the order of tens to hundreds of μA, impedance of each channel must remain in the range of tens to hundreds of kΩ. From this

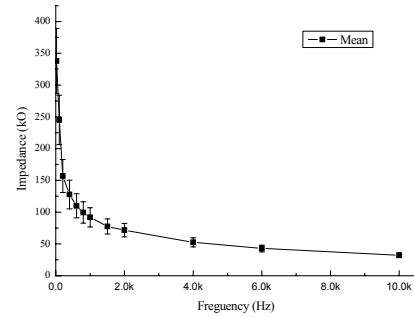


Fig.8. Average complex impedance values recorded from each channel of the microelectrode

view of point, the flexible microelectrode was satisfied for long-term optic-nerve stimulation. To enhance the stimulation effectiveness, some measures can be adopted to further reduce the channel impedance without site area increasing such as porous and three-dimension configuration of the stimulation sites.

C. In-vitro Biocompatibility Evaluation

After the reference electrode tungsten filament was immersed into the culture medium and maintained for 15 days, the medium’s color and PH had no significant changes, no deposition on the tungsten wire, shown in fig.9. This means that the tungsten has a good biocompatibility with the culture solution. The glial cells were cultured from the optic nerve tissue as shown in fig.10.

To testify the biocompatibility, the flexible microelectrode were stabilized in the culture solution to show the interaction between the polyimide and glial cells for successive 13 days without



Fig.9. The tungsten filament in medium in 15 days.



Fig.10. Cells moved from the edge of the optic nerve tissue (×100)

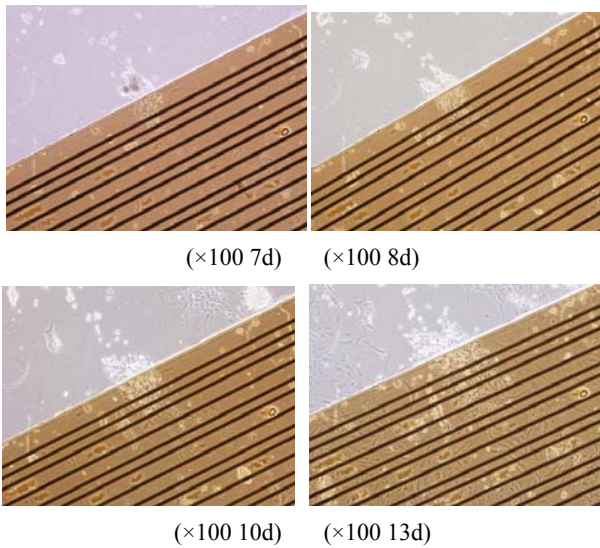


Fig.11. Glial cells were migrated and grew on the no-current electrode surface and continued to proliferation

microcurrent. After succeeding five days, the glial cells gradually moved forward and grow on the surface of the electrode. Pictures in fig.11 described the cell growth at the same position of the microelectrode, which showed that glial cells proliferation and apoptosis were not affected by the flexible microelectrode without microcurrent within 13 days.

Since the microcurrent was applied to the microelectrode for optic-nerve tissue stimulation, biocompatibility between microelectrode and glial cells with microcurrent was verified. Test results were shown in Fig.12. The experiment and counter group represented the system of microelectrode and glial cells with and without microcurrent, respectively.

This gives a hint that the flexible microelectrode has good biocompatibility with the optic-nerve glial cells, but the microcurrent with different amplitudes and duration time can greatly influence the stimulation efficiency.

D. In-vivo Animal Surgery

By means of the feasible surgery scheme in Section II, the encapsulated flexible microelectrode can be completely stabilized in the optic-nerve dura sheath of rabbit. Figure 13 revealed the picture of stabilized microelectrode in the surgical procedure. Figure 14 showed the experimental eye picture after two-week implantation. The rabbit is still healthy alive.

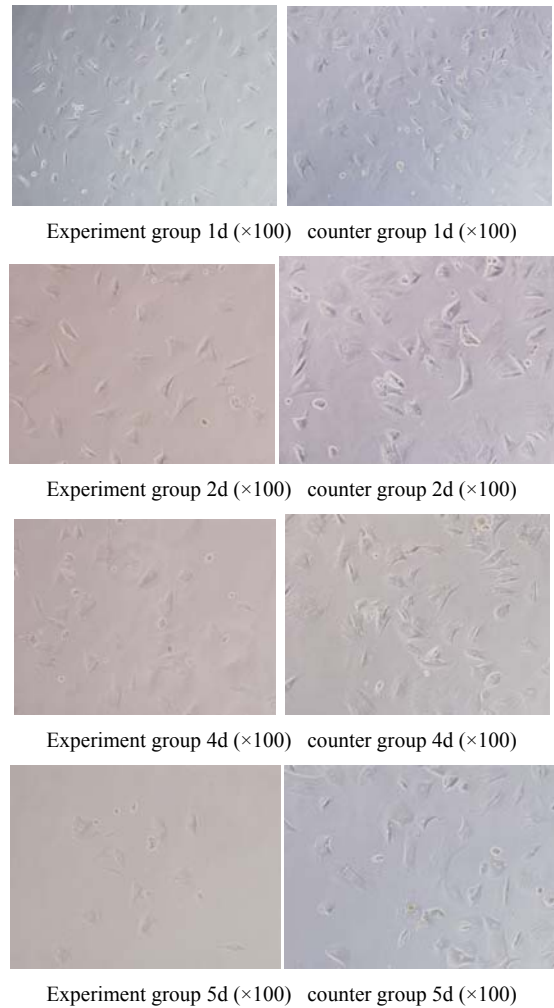


Fig.12. The comparison between the no-current electrode (control group) and current stimulation group (experiment group). Counter group (Right) showed that the number of glial cells and state were changed little for 3 days. Experiment group (Left) showed the number was reduced.

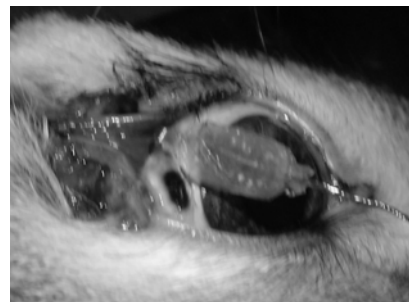


Fig.13. Encapsulated flexible microelectrode stabilization for optic-nerve stimulation.

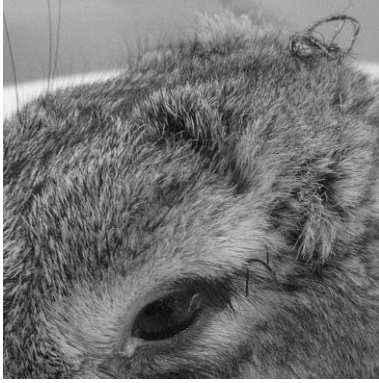


Fig.14. Eye picture of the rabbit after the implantation

IV. CONCLUSIONS

A 16-channel thin-film flexible polyimide microelectrode was fabricated by MEMS process technology, square biocompatible platinum was used as the stimulation site, and the material selected for thin-film microelectrode was biocompatible.

To realize the *in-vivo* stimulation, the flexible microelectrode must be electrically connected to connector. Consequently, the bonding pads were connected to corresponding connector pins by means of insulated wires. Medical-grade silicon adhesives aided to encapsulate the bonding pads to improve the mechanical characteristics and biocompatibility. Geometric size of the silicon adhesive encapsulated part is confined to be sutured to the sclera.

Although biocompatible material was selected to fabricate the encapsulated microelectrode, the process technology may affect the biocompatibility of the microelectrode with the optic-nerve tissue. As a result, *in-vitro* biocompatibility of the microelectrode was tested before *in-vivo* application. Testing results show that the microelectrode embodied good biocompatibility without stimulation micro current, and large-amplitude stimulation current will restrain the glial cells from normal growth. Parameters of stimulation current with proper amplitude, frequency and duration time will be decided to enhance the stimulation effectiveness of optic nerve.

Planar flexible microelectrodes had been used in epiretinal^[10-11], subretinal/suprachoroidal^[12], and cortical visual prosthesis^[13-14]. Cuff microelectrode was used for optic-nerve stimulation and the number of channels was limited. Appropriate animal surgery was utilized for optic-nerve exposure and microelectrode stabilization. As a result, the multichannel thin-film flexible microelectrode could be used for chronic optic-nerve visual prosthesis.

The *in-vivo* animal experiment is conducted forward to accomplish the optic-nerve visual prosthesis by means of multichannel thin-film flexible polyimide-based microelectrode.

ACKNOWLEDGMENT

This research is supported by the National Basic Research Program of China (973 Program, 2005CB724302), National Science Fund for Distinguished Young Scholars from The National Natural Science Foundation of China (60588101), by the 111 Project from the Ministry of Education of China (B08020), the National Natural Science Foundation for the Youth (30700217) and Shanghai Commission of Science and Technology (05DZ22318, 05DZ22325, 04DZ05114, 064119540).

REFERENCES

- [1] Ming-Shaung Ju, et al, "Design and Fabrication of Multi-microelectrode Array for Neural Prosthesis," *Journal of Medical and Biological Engineering*, vol 22(1), pp. 33-40, April 2002.
- [2] MEBrel'en, F Duret, B G'erard, J Delbeke and C Veraart, "Creating a meaningful visual perception in blind volunteers by optic nerve stimulation," *Institute of Physics Publishing Journal of Neural Engineering*, vol. 2, pp.22-28, February 2005.
- [3] Maysam Ghovanloo and Khalil Najafi, "A Modular 32-Site Wireless Neural Stimulation Microsystem," *IEEE Journal of Solid-State Circuits*, Vol. 39, pp. 2457-2466, December 2004.
- [4] M. O. Jean Delbeke, Claude Veraart, "Position, size and luminosity of phosphenes generated by direct optic nerve stimulation," *Vision Research*, vol. 43, pp. 1091-1102, 2003.
- [5] C. R. Claude Veraart, J. Thomas Mortimer, Jean Delbeke, Delphine Pins, and A. V. Ge´rardine Michaux, Simone Parrini, Marie-Chantal Wanet-Defalque, "Visual sensations produced by optic nerve stimulation using an implanted self-sizing spiral cuff electrode," *Brain Research*, vol. 813, pp. 181-186, 1998.
- [6] M. B. Daniel R. Merrill, John G.R. Jefferys, "Electrical stimulation of excitable tissue: design of efficacious and safe protocols," *Journal of Neuroscience Methods*, vol. 141, pp. 171-198, 2004.
- [7] D. A. Borkholder, "Cell Based Biosensors Using Microelectrodes," November, 1998.
- [8] K. Yoshida, A. Inmann, and M. K. Haugland, "Messurement of Complex Impedance Spectra of Implanted Electrodes," *Phil. Trans. Roy. Soc. London*, vol. A247, pp. 529-551, April 1955.
- [9] T. Turkle-Huslig, S.J. Carter, L.Howard and G.W. Gross, "Stabilty of Impedance Characteristics at the Microelectrode-Saline Inteface," *Biological Research Instrumentation. Texas*, vol. A247, pp. 529-551, April 1989.
- [10] C. B. KOURY, "Epiretinal Prosthesis Shows Promise for Blind Patients," *Retina Today*, 2006.12.
- [11] M. S. Humayun, J. D. Weiland, G. Y. Fujii, R. Greenberg, R. Williamson, J. Little, B. Mech, V. Cimarusti, G. Van Boemel, G. Dagnelie, and E. De Juan Jr, "Visual perception in a blind subject with a chronic microelectronic retinal prosthesis," *Vision Research*, vol. 43, pp. 2573-2581, 2003.
- [12] Nakauchi K et al. Transretinal electrical stimulation by an intrascleralmultichannel electrode array in rabbit eyes. *Graefes Arch Clin Exp Ophthalmol*, 243:169 - 174, 2005.
- [13] P. Troyk, M. Bak, J. Berg, D. Bradley, S. Cogan, R. Erickson, C. Kufta, D. McCreery, E. Schmidt, and V. Towle, "A Model for Intracortical Visual Prosthesis Research," *Artificial Organs*, vol. 27, pp. 1005-1015, 2003.
- [14] Patrick J. Rousche, et al, "Flexible Polyimide-Based Intracortical Electrode Arrays with Bioactive Capability," *IEEE Transactions on Biomedical Engineering*, vol. 48(3), pp. 361-371, March 2001

Study of enzyme biosensor for monitoring carbamate pesticides in seawater

Shu-ping Zhang^{1,2*}, Lian-gang Shan³, Yi Zheng¹, Lli-yi Shi^{2*}

¹ University of Shanghai for Science and Technology, Shanghai, China

² Shanghai University, Shanghai, China

³ Jiangsu Food Science College, Jiangsu, China

*CORRESPONDING AUTHOR: ZHANG_LUCY9999@YAHOO.COM.CN

Abstract—The paper describes a controllable layer-by-layer (LBL) self-assembly modification technique of multi-walled carbon nanotubes (MWNTs) and poly(diallyldimethylammonium chloride) (PDDA) towards glass carbon electrode (GCE). Acetylcholinesterase (AChE) was immobilized directly to the modified GCE by LBL self-assembly method with the activity value of 0.01U. The biosensor showed good sensitivity and stability towards the monitoring of carbofuran pesticides in seawater with the detection limit of 10^{-11} g·L⁻¹ and recovery of 99.8±5.7% to 10^{-8} g·L⁻¹

Keywords—carbamate pesticides, acetylcholinesterase, carbon nanotubes, modified electrode, layer-by-layer self-assembly, enzyme immobilization

I. INTRODUCTION

In the last decade, carbamate pesticides have come into wide spread use due to their lower environmental persistence. However, a great part of them are very toxic to non-target organisms, including fishes and aquatic invertebrates [1-2]. Furthermore, some of them appear to be much more persistent than previously believed. So, their extensive use has resulted in a high contamination risk to aquatic environment and a potential hazard to human health. Therefore, development of methods for the rapid and inexpensive analysis of carbamate pesticides, especially in field and on-line applications, is desirable. Biosensors seem to be suitable for this purpose [3-6].

Many methods are available for pesticide detection: chromatographic methods such as high performance liquid chromatography (HPLC) and gas chromatography (GC) are used as reference methods but they have some drawbacks. Moreover, the analysis usually has to be performed in a specialized laboratory by skilled personnel and is not suitable for in situ application. These issues turn out to be a major problem when rapid and sensitive measurements are needed in order to take the necessary corrective actions in a timely fashion [7,8].

Accordingly, a lot of efforts have been devoted to develop relatively inexpensive methods for the industrial processes and environmental monitoring. As a comparison,

enzyme inhibition technique provided a promising way to detect carbamate pesticides which was both rapid and simple [9,10]. With this method a mass of samples could be detected quickly. but how to prove the sensitivity and immobilize the Acetylcholinesterase (AChE) directly is the key technique.

II. EXPERIMENTAL

2.1 Reagents and instruments

Acetylcholinesterase (AChE, 317 U/mg) and acetylthiocholine chloride (ATCh) were purchased from sigma; 5, 5-dithio-bis (2-nitrobenzoic acid) (DTNB) was purchased from Junchuang bio-technique Co. Ltd. (Shanghai, China); poly (diallyldimethylammonium chloride) polymer (PDDA, M_w : 100,000-200,000) was obtained from Sigma-Aldrich. MWNTs, with >95% purity, were obtained from Shenzhen Nanotech Port Co. Ltd. (China). Seawater (pH 8.0, salinity 34) is collected from Qingdao. All other reagents were of analytical reagent grade and used without further purification.

Cyclic voltammetric and amperometric measurements were performed using an electrochemical analyzer CHI800 (Chenhua Instruments, Shanghai, China) connected to a personal computer. A three-electrode configuration was employed, consisting of a glassy-carbon electrode (GCE) serving as a working electrode, whereas a saturated calomel electrode as a reference electrode and a platinum wire as an auxiliary electrode.

2.2 Preparation of PDDA/MWNTs multilayer modified electrode and direct immobilization of AChE

MWNTs (0.10g) were first shortened and functionalized by refluxing process in 150 mL concentrated HNO₃ for 24 hours. After extensive washing in double-distilled water, the MWNTs were dried in vacuum, then the MWNTs were dispersed in double-distilled water with the aid of ultrasonic agitation for 30minutes to obtain a uniform and stable black dispersion of 0.1 mg·mL⁻¹ MWNTs.

Electro-deposition of MWNTs on Surface-clean GCE was carried under the magnetic stirring for 2 hours with the deposition potential of 1.7 V. Then the modified electrode was dipped into borate buffer solution (pH 9.18) for 15 minutes so that the functional groups were negatively charged. Afterwards the self-assembled bilayer membranes of PDDA/MWNTs were fabricated by alternate immersion of GCE in 1% PDDA solution (the ionic strength was adjusted to $0.8 \text{ mol}\cdot\text{L}^{-1}$ with NaCl [11]) and $1 \text{ mg}\cdot\text{mL}^{-1}$ MWNTs dispersion of pH 9.18 borate buffer solution for 15 minutes either, this sequence was repeated until the desired PDDA/MWNTs bilayer number was obtained. Then The self-assembled bilayer membranes of PDDA/AChE were fabricated by alternate immersion of GCE in 1% PDDA solution and AChE solution for 15 minutes either, a PDDA membrane was fabricated at last in order to avoid the fall-off of AChE.

The establishment of enzyme activity is according to the Ellman method using the reaction between TCh and DTNB, the reaction was terminated by carrying the enzymatic electrode out of the ATChCl solution during determination of activity of immobilized AChE.

2.3 Detection of carbofuran in seawater

As for enzymatic electrode with certain AChE activity in PBS, different current value would be obtained in different corresponding amount of added ATChCl using amperometric *i-t* method. A max current (I_0) value will be obtained when the amount of ATChCl become excessive to the AChE, while smaller current value (I_1) will be obtained when the AChE is inhibited by carbofuran, so the concentration can be determined intensively and easily according to the inhabitation rate.

III. RESULTS AND DISCUSSIONS

3.1 Surface morphology of MWNTs and multilayer

Obviously, the MWNTs oxidized and functionalized by concentrated nitric acid are more homogeneous, uniform and pure. Meanwhile, Fig.1c showed homogeneous and uniform multilayer has been obtained, it can be attributed to the treated and good dispersion of MWNTs and the Layer-by-Layer assembly process with PDDA.

3.2 Electrochemical behavior of TCh on modified GCE

TCh can be electrochemically oxidized on the surface of GCE under a certain potential, the oxidation process can be described as:

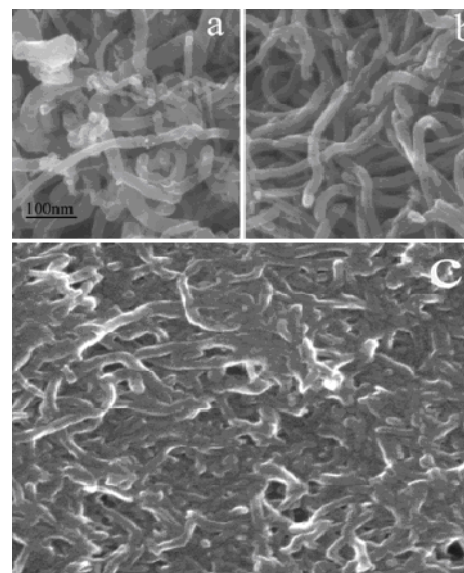
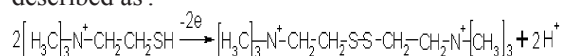


Fig.1. Scanning electron micrographs of raw MWNTs (a), oxidized MWNTs (b), and {PDDA/MWNTs}₅ assembled on a silicon slide (c).

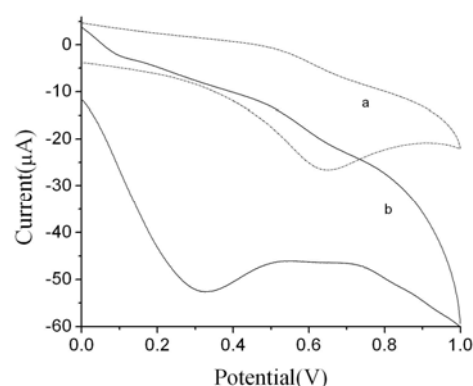


Fig.2. Cyclic voltammograms of $5 \times 10^{-3} \text{ mol}\cdot\text{L}^{-1}$ TCh with freshly polished bare GCE (a) and {PDDA/MWNTs}₅/GCE (b). Supporting electrolyte: phosphate buffer solution ($0.10 \text{ mol}\cdot\text{L}^{-1}$, pH 7.40); scan rate: $100 \text{ mV}\cdot\text{s}^{-1}$.

In our study, the voltammetric characteristics of thiocholine on GCE and {PDDA/MWNTs}₅/GCE were investigated by cyclic voltammetry in the potential range of 0-1.0 V at a sweep rate of $100 \text{ mV}\cdot\text{s}^{-1}$ in phosphate buffer. Typical cyclic voltammograms are shown in Fig.2. In $5 \times 10^{-3} \text{ mol}\cdot\text{L}^{-1}$ TCh solution, anodic oxidation peaks were observed both on bare GCE (curve a) and on {PDDA/MWNTs}₅/GCE (curve b). Noted that the anodic peak current of thiocholine on the {PDDA/MWNTs}₅/GCE ($I_{\text{pa}} = -54 \mu\text{A}$) is enhanced about two times compared of that at bare GCE ($I_{\text{pa}} = -27 \mu\text{A}$) and Meanwhile, the overvoltage of thiocholine at the {PDDA/MWNTs}₅/GCE ($E_{\text{pa}} = 0.35 \text{ V}$) is about a half less than that of bare GCE ($E_{\text{pa}} = 0.65 \text{ V}$).

The observed low oxidation overvoltage and high anodic oxidation peak of thiocholine at the {PDDA/MWNTs}₅/GCE may attribute to the electrocatalytic activity of MWNTs because of their edge-plane-like sites at the tube ends^[12-14].

3.3 Determination of AChE activity

The establishment of calculation formula of enzyme activity is according to the formula of A value obtained from reaction between TCh and DTNB to concentration of TCh^[15], that is, $A=0.133c$. The formula is listed as follows when the reaction time is 5 minute: $U=0.075A$, Hereinto, A means the A value at 412nm at 5minute.

3.4 Detection of carbofuran in seawater

As for the 0.01U activity of immobilized AChE, a good linearity between current value and the amount of ATChCl added to seawater once 10 μ L was obtained when the amounts of ATChCl was less than 80 μ L. Then it is proved that the current value (I) obtained when 80 μ L ATChCl was added to seawater decreased linearly with the activity decreasing of immobilized AchE. And a formula for calculation of inhibition rate of AChE is botained as follows: $\text{Inhibition \%} = [(I_0 - I) / I_0] \times 100\%$, Hereinto, I_0 was $9.93 \times 10^{-6}A$ as for 0.01U activity of immobilized AChE.

Inhibition rate was determined after the 5 minutes' immersion in different pesticide solutions of enzymatic electrode with 4 PDDA/AChE bilayers. Then the curves between inhibition rates and the current values were achieved.

The recovery rate of carbofuran was obtained by the determination of standard sample of 0.01ppm.

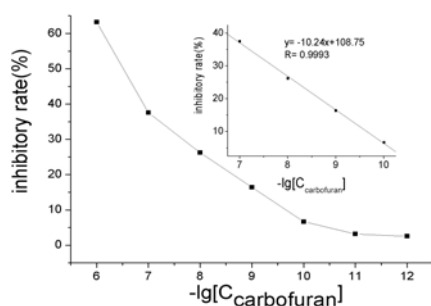


Fig.3 Relationship between enzyme inhibition rate and $-\lg[\text{carbofuran}]$.
Insert: Linearity of enzyme inhibition rate and $-\lg[\text{carbofuran}]$ between the concentration range of 10^{-10} - 10^{-7} $\text{g}\cdot\text{L}^{-1}$

As for pesticides carbofuran, inhibition rate was detected by immerse the enzymatic electrode into solutions with

various concentrations. Fig.3 shows a good linearity between inhibition rates and $-\lg[\text{carbofuran}]$ with a detection limit of 10^{-11} $\text{g}\cdot\text{L}^{-1}$.

An average recovery of $99.8 \pm 5.7\%$ was also obtained from ten times detection of 10^{-8} $\text{g}\cdot\text{L}^{-1}$ carbofuran samples in seawater, which indicated that the enzymatic electrode has a good stability and property in detection of pesticides in seawater

IV. CONCLUSIONS

The {PDDA/MWNTs}₅/ED/AChE/GCE electrode shows excellent electro-catalytical activity towards the carbofuran pesticides in seawater, which is due to the good conductivity and high surface area of the MWNTs, coupled with the advantages of LBL assembly method. Also the modified GCE also showed an excellent detection limit, wide linear range, good precision and operational stability. Because of their promising analytical characteristics, a fast development must be made in biosensor detection of pesticides in seawater. The biosensor is of great prospect at automatically and field monitoring of carbamate pesticides in seawater samples.

REFERENCES

1. La Rosa, C., Pariente, F., Hernandez, L., Lorenzo, E., 1995. Anal. Chim. Acta 308:129-136.
2. Colletier, J.P., Chaize, B., Winterhalter, M., Fournier, D., 2002. BMC Biotechnol. 2: 9-17.
3. Liu, G., Lin, Y., (2006). Anal. Chem. 78:835-843.
4. Marty, J.L., Garcia, D., Rouillon, R., (1995). Trends Anal. Chem. 14: 329-333.
5. Navas D'az, A., Ramos Peinado, M.C., (1997). Sens. Actuators B 38/39:426-431.
6. Singh, A., Flounders, A., Volponi, J., Ashley, C., Wally, K., Shoeniger, J., (1999). Biosens. Bioelectron. 14:703-713.
7. Luque de Castro, M.D., Herrera, M.C., (2003). Biosens. Bioelectron. 18:279-294.
8. Ristori, C., Del Carlo, C., Martini, M., Barbaro, A., Ancarani, A., (1996). Anal. Chim. Acta 325:151-160.
9. Schulze, H., Vorlov'a, S., Villatte, F., Bachmann, T.T., Schmid, R.D., (2003). Biosens. Bioelectron. 18:201-209.
10. Mulchandani, A., Chen, W., Mulchandani, P., Wang, J., (2001). Biosens. Bioelectron. 16: 225-230.
11. Sotiropoulou, S., Chaniotakis, N.A., (2005). Anal. Chim. Acta 530:199-204.
12. Tsai, H., Doong, R., (2005). Biosens. Bioelectron. 20:1796-1804.
13. Jin, S., Xu, Z., Chen, J., Liang, X., Wu, Y., Qian, X., (2004). Anal. Chim. Acta 523:117-123.
14. Yao, S., Meyer, A., Henze, G., (1991). Fresen. J. Anal. Chem. 339:207-211.
15. Liu, Y. Lin. Electrochem. Commun. J, 8(2006)251

Spectral analysis of heart rate variability applied in the exercise of professional shooting athletes

J.J. Zhuang¹, X.L. Huang¹, X.B. Ning¹, M. Zou^{2,3} and B. Sun³

¹ Institute for Biomedical Electronic Engineering, Department of Electronic Science and Engineering, Nanjing University, Nanjing, China

² Department of Investigation, Nanjing Forest Police College, Nanjing, China

³ Department of Sports, Nanjing Institute of Physical Education, Nanjing, China

Abstract— The aim of the study is to quantify the alteration in the autonomic nervous system (ANS) function of professional shooting athletes before, during and after the match and examine whether some indices reflecting the activity of the ANS are related to their sports capacity and performance. Seven male professional shooters with various sports capacity participated in the study. Heart rate variability (HRV) signals of each subject under three situations (rest, match and post-match) were collected by a one-channel recorder. Then a method of fast Fourier transform was used to calculate the power spectra of different frequency bands for all the data. The average heart rate (HR_{Ave}), and three frequency-domain parameters: normalized low frequency component (LFnorm), normalized high frequency component (HFnorm) and the ratio of low frequency component to high frequency (LF/HF) were evaluated. The results show that at rest, HR_{Ave} is 66 ± 7 beats/min, LFnorm is 47.46 ± 8.38 nu, HFnorm is 46.96 ± 10.26 nu and LF/HF is 1.33 ± 0.58 ; and during the match, HR_{Ave} is 82 ± 12 beats/min, LFnorm is 73.74 ± 13.55 nu, HFnorm is 24.55 ± 13.97 nu and LF/HF is 5.73 ± 4.59 . The differences of all the measures between rest and match are statistically significant (t test, $P < 0.05$). After the match, all the parameters go back toward their normal values. Therefore our preliminary findings suggest that during the match, the activation of sympathetic nerve of ANS in shooters is increased, whereas the activation of parasympathetic branch is withdrawn, and a sympathovagal balance is shifted to sympathetic predominance. Furthermore, it seems that all the three frequency-domain indicators in the high-level athletes with a good performance during the match have a wider varying range than those in the lower-level shooters. HRV spectral analysis may be a new approach to monitoring the process of shooting exercise. HRV frequency-domain indicators may have potential value in the assessment of training quality.

Keywords— shooting, sympathetic nerve, parasympathetic nerve, frequency-domain, psychological stressor.

I. INTRODUCTION

Shooting is a sports item demanding athletes to keep long-term psychological stability and mental concentration during the game.

Clinical studies show that psychological, mental or emotional fluctuations are closely associated with the autonomic

nervous system (ANS). Many changes in physiological variables may occur with chronic exposure to psychological stressors [1]. The accurate monitoring of these variables during exercise will be an effective method of enhancing the training quality [2]. Among so many physiological indicators in relation to ANS, heart rate (HR) is usually to be taken as a major measure for its simplicity and easy availability, and other indicators including skin resistor, respiration and blood pressure are hard to be applied in routine practice. Studies suggest that alterations in autonomic balance that accompany strenuous exercise can be examined non-invasively by assessing heart rate variability (HRV) [3-5]. Other than investigations focused on the evaluating modifications of cardiovascular system regulated by the ANS and overtraining or fatigue induced by exercise or a training period for endurance athletes using HRV analysis [6-12], the aim of our study is to quantify the alterations in the ANS function associated with psychological and emotional fluctuations of the professional shooting athletes before, during and after the match and further attempt to examine whether some spectral indices reflecting the activity of the ANS are related to the sports capacity and performance of the shooters.

II. METHODS AND MATERIALS

A. Subjects

Seven male professional shooters of free air pistol with various sports capacity were recruited in the study, among which three were from Jiangsu provincial shooting team, the other four were from its next-level municipal shooting teams for an intensified winter training. All the subjects are physically healthy, without heart diseases and diabetes. Their age is 21.3 ± 6.8 (mean \pm SD) years old, ranging from 17 to 36 years, and professional career year is from 3 to 18. A written and informed consent was obtained from each subject in accordance with the regulations of local sports ethic committee prior to the study.

B. Data acquisition

A one-channel recorder (ANS-100, designed by Institute for Biomedical Electronic Engineering, Nanjing University, China) and Holter electrodes (3M, Korea) were used to collect ECG signal from the subjects. The sampling frequency is 1 KHz and the resolution of A/D converter is 12 bit. Data acquisition under three states (rest, match and post-match) was carried out in Nanjing Fangshan provincial shooting range.

At rest: The subjects were asked to remain in a supine position and their ECG signals were collected using one of the limb leads one hour after lunch (1:00-2:00 p. m) in a quiet, dimly lighted room for over 30 minutes.

During match: The signal from each subject was recorded in the shooting gallery for about two hours using the monitoring Lead V₅ when they carried out a simulated shooting game. The reason that we selected Lead V₅ was to eliminate the motion and muscle artefacts induced by firing action, and meanwhile to diminish the influence of fixing the leads onto the body surface of the athletes on their technical execution. The shooting exercise was totally performed according to the requirements of a real shooting match, which would put extra psychological pressure on the athletes and bring about more psychological activities.

After match: The subjects were asked to sit in a chair and continue to be acquired for over 30 mins.

C. Methods

In the subsequent analysis, the R-wave peaks were accurately detected and RR time series were automatically extracted from their original ECG signals with artefacts filtered. Then a method of fast Fourier transform (FFT) was used to calculate the power spectra of different frequency components for all the HRV records. Normally, four main spectral components are distinguished in a spectrum: ultra low frequency (ULF: 0-0.003Hz), very low frequency (VLF: 0.003-0.04Hz), low frequency (LF: 0.04-0.15Hz), and high frequency (HF: 0.15-0.40Hz) components. The distribution of the power and the central frequency of LF and HF are not fixed but may vary in relation to changes in autonomic modulations of heart period. HF power is almost entirely mediated by the parasympathetic activity to the sinus node directly associated with respiratory activity, whereas LF power reflects the mixed modulation of sympathetic and parasympathetic activities or solely sympathetic activity. Sympathetic and parasympathetic activities are also evaluated by LF/HF ratio. Changes in the ratio LF/HF are taken as an indication of changes in sympathetic activity, although this ratio may also be an index of sympathovagal balance. The physiological explanation of the VLF compo-

nent is much less defined. Thus, VLF assessed from short-term recordings is a dubious measure. ULF is usually calculated when a long-term recording is analyzed. The measurement of ULF, VLF, LF, and HF power components is usually made in absolute values of power (milliseconds squared). LF and HF may also be measured in normalized units (usually called LFnorm and HFnorm, respectively), which represents the relative value of each power component in proportion to the total power minus the VLF component. The LFnorm and HFnorm emphasize the controlled and balanced behavior of the two branches of the ANS. Moreover, the normalization tends to minimize the effect of the changes in total power (TP) on the values of LF and HF components [13]. The output parameters in our software mainly include TP, ULF, VLF, LF, HF, LFnorm, HFnorm, LF/HF, maximum heart rate (HR_{Max}), minimum heart rate (HR_{Min}), and the average heart rate (HR_{Ave}) in each 3-min period.

In addition to HR_{Ave} in each 3-min time interval, only three frequency-domain parameters: LFnorm, HFnorm and LF/HF were evaluated in the following study.

III. RESULTS

After the calculation and statistical analysis, we have found that at a resting state, HR_{Ave} is 66±7 beats/min, LFnorm is 47.46±8.38 nu, HFnorm is 46.96±10.26 nu and LF/HF is 1.33±0.58; during the match, HR_{Ave} is 82±12 beats/min, LFnorm is 73.74±13.55 nu, HFnorm is 24.55±13.97 nu and LF/HF is 5.73±4.59. The differences of all the measures between two states are statistically significant (two tailed *t* test, *P*<0.05). After the match, all of the parameters gradually go back toward their normal values (HR_{Ave}: 72±9 beats/min, LFnorm: 56.72±11.23 nu, HFnorm: 38.41±9.76 nu and LF/HF: 3.25±2.18).

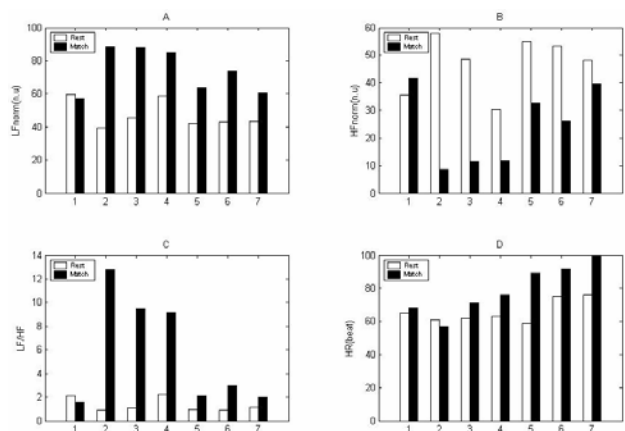


Fig. 1 change of LFnorm, HFnorm, LF/HF and HR_{Ave} from rest to match for all the subjects

IV. CONCLUSIONS

Our preliminary findings suggest that during the match, under a variety of external and internal psychological stressors, the activation of sympathetic nerve of the ANS in shooters is increased, whereas the activation of parasympathetic branch is withdrawn, and a sympathovagal balance is shifted to sympathetic predominance. Furthermore, as seen in Fig. 1., all the three frequency-domain indicators in subject No. 2, who is an elite athlete and got a good score in the match, have a wider varying range, and parameters from subject No. 7, who is a younger shooter from the next-level team, change within a smaller range, while those in subject No. 1, who is a senior athlete with a bad performance even vary conversely.

HRV spectral analysis may be a new approach to scientifically monitoring the process of shooting exercise. Frequency-domain indicators of HRV may have practical value in the assessment of training quality, evaluation of psychological stress and even psychological material selection for talented young shooters.

ACKNOWLEDGMENT

We appreciated here the assistance from Jing Lin Yin, the head coach of Jiangsu provincial shooting team. The project was partially supported by the National Natural Science Foundation of China (Grant No. 60501003 and Grant No. 60701002).

REFERENCES

- Wei S Q, Wang D P, Zhang S L et al. (2005) Study on heart rate variability affected by psychological stress. *J Prac Med* 22:807–809
- Foster C, Florhaug J A, Franklin J et al. (2001) A new approach to monitoring exercise training. *J Strength Cond Res* 15:109–115
- Hedelin R, Wiklund U, Bjerle P et al. (2000) Cardiac autonomous imbalance in an overtrained athlete. *Med Sci Sports Exerc* 32:1531–1533
- Middleton N, Vito G D (2005) Cardiovascular autonomic control in endurance-trained and sedentary young women. *Clin Physiol Funct Imaging* 25:83–89
- Sztajzel J, Atchou G, Adamec R et al. (2006) Effects of extreme endurance running on cardiac autonomic nervous modulation in healthy trained subjects. *Am J Cardiol* 97:276–278
- Hedelin R, Kentta G, Wiklund U et al. (2000) Short-term overtraining: effects on performance, circulatory responses, and heart rate variability. *Med Sci Sports Exerc* 32:1480–1484
- Mourot L, Bouhaddi M, Perrey S et al. (2004) Quantitative poincaré plot analysis of heart rate variability: effect of endurance training. *Eur J Appl Physiol* 91:79–87
- Pichot V, Roche F, Gaspoz J M et al. (2000) Relation between heart rate variability and training load in middle-distance runners. *Med Sci Sports Exerc* 32:1729–1736
- Schipke J D, Pelzer M (2001) Effect of immersion, submersion, and scuba diving on heart rate variability. *Br J Sports Med* 35:174–180
- Winsley R J, Armsrong N, Bywater K et al. (2003) Reliability of heart rate variability measures at rest and during light exercise in children. *Br J Sports Med* 37:550–552
- Winsley R J, Battersby G L, Cockle H C (2005) Heart rate variability assessment of overreaching in active and sedentary females. *Int J Sports Med* 26:768–773
- Earnest C P, Jurca R, Church T S et al. (2004) Relation between physical exertion and heart rate variability characteristics in professional cyclists during the tour of Spain. *Br J Sports Med* 38:568–575
- Task Force of the European Society of Cardiology the North American Society of Pacing Electrophysiology (1996) Heart rate variability: standards of measurement, physiological interpretation, and clinical use. *Circulation* 93:1043–1065

Author: Ning Xin Bao
 Institute Institute for Biomedical Electronic Engineering,
 Department of Electronic Science and Engineering,
 Nanjing University
 Street 22 Han Kou Road
 City Nanjing
 Country China
 Email xbning@nju.edu.cn

Using EMG to Evaluate Muscular Fatigue Induced during Video Display Terminal Keyboard Use Task

Haijun Niu, Ran Li, Guanglei Liu, Fang Pu, Deyu Li, Yubo Fan*

Department of Bioengineering, Beihang University, Beijing, P. R. China. 100083

Abstract — Work-related muscular fatigue is a common problem among office computer users. The purpose of this study was to examine shoulder and arm muscular fatigue induced during visual display terminal (VDT) keyboard use tasks. Electromyography signals were recorded from the right side upper trapezius, deltoid and extensors of the wrist/fingers during VDT task and during isometric contractions task respectively. Mean Power Frequency (MPF) and Root Mean Square value (RMS) were computed and used to evaluate the changes of EMG signal of all measured muscles. The results showed that MPF decrease and RMS increase with time during every isometric contraction experimental blocks for all measured muscles. However, RMS and MPF did not showed obvious trend with time throughout VDT experimental task and throughout isometric contraction experimental task, it means that MPF and RMS obtained during isometric contraction are not sensitive parameters of muscle fatigue. These results are helpful for finding effective objective assessment method that can identify office VDT workers who are at risk to develop chronic neck, shoulder and arm complaints.

Keywords — Visual Display Terminal (VDT); Muscular Fatigue; Electromyography (EMG); MPF; RMS

I. INTRODUCTION

In recent year, computers have widely been used in many offices as well as in home. According to the statistic by technology report, about 130 million computers were in use in China in 2007. So the number of the computer users is huge. Visual display terminals (VDT) are standard equipment for many office computer operators in the industrialized society, and their use can made psychological and physiological effects. In general, the physiological burden borne by VDT operators is different from that by traditional office operators and workshop workers. Some reports indicated that VDT operators experienced more musculoskeletal discomforts than other office workers [1-2], and the chance of the VDT operators suffer from muscular and skeletal illness is more than traditional office workers [3].

The cervical-shoulder-wrist syndrome is the fastest growing VDT illness in China. Although the mechanism underlying these computer-related cervical-shoulder-wrist disorders was controversial, it was generally assumed to be related to awkward constrained working posture, poor

workstation design, high workload, and job demands. VDT keyboard and mouse, overuse of the muscles, tendons, or nerves have also been found to contribute to shoulder, neck, back, and wrist-hand discomfort or pain [2-4]. However, office work-related shoulder and arm muscular fatigues are direct well-defined symptom of cervical-shoulder-wrist syndrome.

Fatigue in a muscle takes place as a result of an activity of this muscle and is reflected by certain changes in its electromyography (EMG) signal in either the time or frequency domains [5-6]. So EMG has been used extensively to record and describe changes in muscle function during fatigue. Most studies show that there is a shift of the power spectrum toward lower frequencies and an increase in the Root Mean Square (RMS) amplitude of the EMG signal when muscular fatigue [7]. However, some studies has found it is difficult to evaluate local fatigue using EMG during VDT task because interference and distortion. Up to now, only a few researches were done to analyze muscular fatigue of prolonged keyboard activities by continuous EMG recording.

This study use surface EMG to quantify the muscle activities during consecutive keyboard use with a common computer VDT task, and apply MPF and RMS parameters to evaluate the occurrence and the possible mechanisms of shoulder and arm muscular fatigue induced by prolonged VDT keyboard use.

II. EXPERIMENT AND METHOD

A. Subjects

Seven healthy male students, with a mean age of 22 years, were recruited from BME department in Beihang University as subjects. All subjects were right-handed users, free of wrist/forearm and shoulder pain, and familiar with computer Chinese word input.

B. Instrumentation

Figure 1 is a schematic view of the VDT experimental setup used in this study. This setup consists of two computers, an MP150 system (BIOPAC Systems Inc. US) and

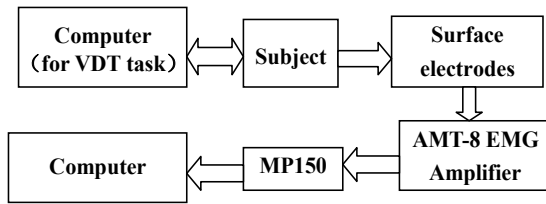


Fig 1: Schematic diagram of the experimental setup.

one 8-channel EMG signal amplifier (AMT-8, CA). One-off Al/AgCl surface electrodes (3M, USA) with 1cm diameter were used in the study.

C. Procedure

A word input task was designed. The subjects were required to input words use keyboard in a common rate. The VDT task consisted of four blocks, each corresponding to a 30-min period. Between every block, one minute isometric contractions task was carried. The subjects was required to hold a 2.5-kg dumbbell kept his right arm straight and elevated at 90° of abduction in the sagittal plane for 1 min. The EMG signals were recorded in VDT task and in isometric contractions task.

The EMG signals were recorded through the bipolar arrangement with an inter-distance of 1-2 cm. Surface electrodes were placed on the skin to record the muscle activities of the right side upper trapezius, deltoid and extensors of the wrist/fingers, and paralleled the direction of muscle fibers. The reference electrode was attached behind the subject's right ear. In large muscles such as trapezius muscle or deltoid muscle, surface EMG is able to measure the muscle contractions of the specific muscle. However, for extensors of the wrist/fingers, where muscles are small and closely packed, the EMG will pick up the signals of all muscles near the electrodes and it is impossible to determine exactly which muscle is providing the signal [2]. The Al/AgCl electrodes were wired to an EMG wire amplifier system with 2000 times gain. And then the signal was wired to the MP150 system. After converted from analog-to-digital (A/D), the raw EMG data at a sampling rate of 1k Hz for every channel were saved by Acknowledge software, and then the data were processed using Matlab 7.0.

The signal processing method was chosen based on the published guidelines [7]. Each 1-min recording was divided into 60 segments. The first and last segments were excluded. For each segment, the mean value for 1000 samples was calculated and added to the 1000 data points to form 1024 data points. The EMG signal was filter by a band pass (fourth-order Butterworth) filter in the range of 5–500 Hz. And then, FFT was performed to calculate power spec-

trums. The average value of the power spectrums of 58 segments were used to calculate MPF and MF. The RMS values of 58 segments also were averaged for one measurement. The mean values of MPF and RMS in the first test procedure were used as reference values for normalization.

III. RESULT

Figure 2 shows the value of MPF of trapezius measured from one subject during every isometric contractions task block and every VDT task block, respectively. Figure 3 shows the value of RMS of trapezius gotten from same subject during every isometric contractions task block and every VDT task block, respectively. The horizontal coordinates denote different experimental blocks. From the figure, we can see that the MPF shifts down during every isometric contractions task block. However, this trend does not appear during VDT task blocks. In contrast with MPF, the RMS shows an ascending trend during every isometric contractions task experiment block, especially during four and five block.

Figure 4 shows the mean value of normalized MPF and RMS measured from all subjects during VDT task as a function of four blocks. The horizontal coordinates denote different experimental blocks. However, from the trend of the MPF, we cannot judge the degree of the muscle fatigue. The result of a one-way analysis of variance (ANOVA) performed on the MPF showed there is not significant main effect of time. For RMS, for deltoid and extensors, there is a little increase as time goes by, but ANOVA analysis showed no significant main effect.

Figure 5 shows the mean value of normalized MPF and RMS measured under the same isometric contraction as a function of five blocks. The horizontal coordinates 1 to 5 denote the measurements for the first, second, third, fourth and fifth 1-min isometric contraction experimental blocks. For the upper trapezius, the MPF tended to decrease with time, but no significant main effect of time was detected. For the deltoid and the extensors of the wrist/fingers, the MPF did not showed an obviously change. For all studied muscles, the RMS showed no obvious change.

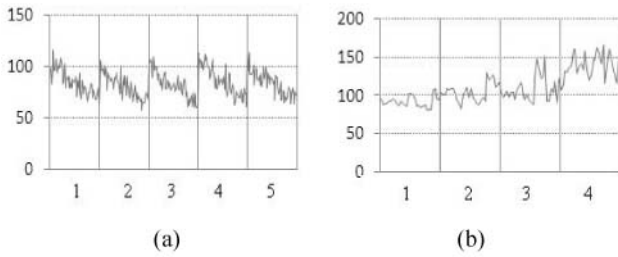


Fig.2 (a) MPF of trapezius during five isometric contractions task blocks. (b) MPF of trapezius during four VDT task block.

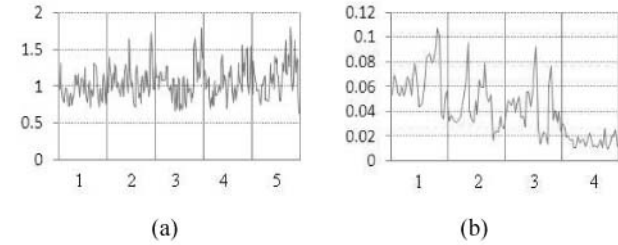


Fig.3 (a) RMS of trapezius during isometric contractions task five isometric contractions task blocks. (b) RMS of trapezius during four VDT task blocks.

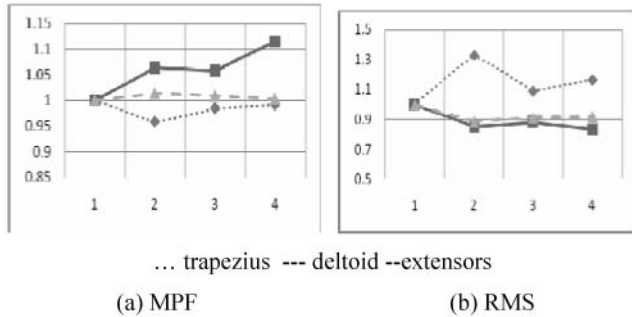


Fig.4 the mean value of Normalized MPF and RMS of all subjects measured during VDT task as a function of four blocks. 1, 2, 3, and 4 denote VDT experimental blocks

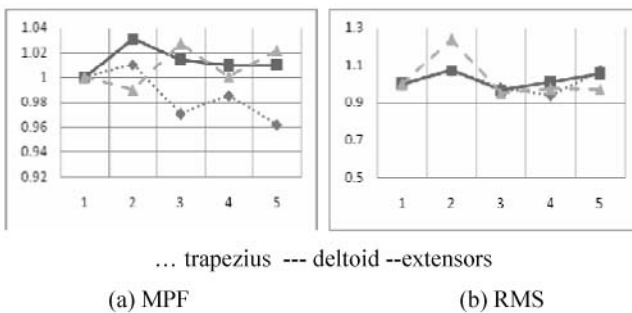


Fig.5 the mean value of Normalized MPF and RMS of all subjects measured under the same isometric contraction as a function of five blocks. 1, 2, 3, 4 and 5 denote isometric contraction experimental blocks.

IV. CONCLUSIONS

The shoulder and arm muscles are common sites of chronic and work-related disorders in VDT tasks. The purpose of this study was to investigate whether it is possible to objectively evaluate the shoulder and arm muscular fatigue induced during prolonged VDT keyboard use task by two EMG parameters: MPF and RMS.

In general, in the time domain, RMS of the EMG signal is considered the most reliable parameter. An increase of the RMS with advancing fatigue has been reported in many cases [11-12]. This phenomenon was also shown in every isometric contractions task block in our experiment, such as Figure 3(b). One research showed that the RMS of trapezius EMG tended to be higher during the experimental task than during no task loading and hypothesize the electrical activity of the trapezius muscle might increase with the accumulation of localized muscular fatigue [8]. However, for all studied muscles, the RMS did not show obvious increase trend with time throughout VDT experimental task and throughout isometric contraction experimental task in our experiment.

In frequency domain, the surface EMG power spectrum represents a summary of all the spectrum contributions of active motor unit action potentials that are recorded at the EMG sensor, and shifts in the power spectrum are often taken as indicators of muscle fatigue. MPF is one of the most commonly used single indexes of the power spectral alterations [9-10]. This study did not showed any apparent trend for downward shifts of MPF with time at VDT experimental task. No matter for extensors of the wrist/fingers, deltoid or for trapezius muscle, did not showed any EMG signs of fatigue during VDT task. Some other studies about VDT muscle fatigue also showed that the change of MPF is very small. However, during isometric contraction experimental task, only for upper trapezius, the MPF showed a little decrease with time, but no significant main effect of time was detected. This means that the MPF measured during isometric contraction is not a sensitive measure of muscle fatigue.

However, the experimental task of VDT keyboard usage is only a part of real computer tasks, and the results are not general. In the future study, mouse and key operation need to be included to simulate the real VDT computer tasks. In additional, more really effective EMG parameters need to be explored to describe the muscle fatigue induced by the low intensity, long time VDT task. This result is helpful for finding effective objective assessment method that can identify workers who are at risk to develop chronic neck, shoulder and arm complaints.

ACKNOWLEDGMENT

This study supported by National Natural Science Foundation of China. (Grant No: 10772018 and 10672014).

REFERENCES

1. U.Bergqvist, E.Wolgast, B.Nilsson, M.Voss, (1995) The influence of VDT work on musculoskeletal disorders, *Ergonomics* 38 (4) 754–762.
2. Baker NA, Jacobs K, Trombly C. (1999) The effect of Video Display Terminal (VDT) mouse use on muscle contractions in the neck and forearm. *Work*, 12(2): pp109-116
3. Armstrong TJ, Buckle P, Fine LJ, Hagberg M, Jonsson B, Kilbom A, Kuorinka IA, Silverstein BA, Sjøgaard G, Viikari-Juntura ER. (1993) A conceptual model for work-related neck and upper-limb musculoskeletal disorders, *Scand J Work Environ Health*. 19(2): pp73-84
4. Elizabeth AS, Kate M., Stewart T. F. M (1987) VDT Health and Safety: Issues and Solutions, Ergosyst Associates
5. Edwards RH. (1981) Human muscle function and fatigue. Human muscle fatigue: physiological mechanisms. Pitman Medical, London. Ciba found symp. pp1–18
6. Baratta RV, Solomonow M, Zhou BH, Zhu M. (1998) Methods to reduce the variability of EMG power spectrum estimates. *J Electromyogr Kinesiol*. 8(5): pp279-85,
7. Lindstrom, LH., Magnusson, RI. (1977) Interpretation of myoelectric power spectra: a model and its applications. *IEEE Transactions of Biomedical Engineering*. 65, pp 653–61
8. Atsuo M, Atsushi U, Syuichiro M, Yosuke T. (2003) Evaluation of Shoulder Muscular Fatigue Induced During VDT Tasks. *International Journal of human-computer Interaction*. 15(3), pp407–417.
9. Szeto GP, Straker LM, O'Sullivan PB. (2005) EMG median frequency changes in the neck–shoulder stabilizers of symptomatic office workers when challenged by different physical stressors. *J Electromyogr Kinesiol*. 15(6): pp544-55.
10. Hägg GM. (1992) Interpretation of EMG spectral alterations and alteration indexes at sustained contraction, *J Appl Physiol*. Oct; 73(4): pp1211-7.
11. Krogh-Lund, C, Jorgensen, K. (1993) Myoelectric fatigue manifestations revisited: power spectrum, conduction velocity, and amplitude of human elbow flexor muscles during isolated and repetitive endurance contractions at 30% maximal voluntary contraction, *European Journal of Applied Physiology* 66(2): pp 161-73.
12. Ohashi, J. (1993) Changes in relations between surface electromyogram and fatigue level by repeating fatiguing static contractions, *Annals of Physiological Anthropology* 12(5) pp 285-96.

Author: FAN Yubo
 Institute: Department of Bioengineering, Beihang University
 Street: Xueyuan Road 37#
 City: Beijing
 Country: P. R. China.
 Email: yubofan@buaa.edu.cn

The ERP Signal Analysis of Visual Influences on Auditory Intensity Perception

R. Cai, Z. Li, Y. Li, Y. Qiu, Y. Zhu, S. Tong

Department of Biomedical Engineering, Shanghai Jiao Tong University, Shanghai, China

Abstract — Pervious studies have reported the supramodal interactions in different sensory modalities. The aim of this paper is to investigate the influences of visual spatial sensory on the auditory intensity perception by event-related potentials (ERP) analysis. The subjects were requested to judge the sound level accompanied with phase-locked visual stimulus. Behavior results demonstrated more auditory judgment error when the subjects were stimulated with the resized visual patterns. The ERP waveforms elicited at C3 and T3 indicated significant amplitude enhancement in the components at 175–200ms and 200–220ms after the second stimuli onset. Both ERP and behavior results confirmed the existence of the Supramodal interaction between visual spatial sensory and the auditory intensity perception, i.e. that visual spatial sensory could suppress the perception of auditory intensity.

Keywords — ERP signal, supramodal interaction, illusion, visual spatial sensory, auditory intensity perception

I. INTRODUCTION

Literatures have suggested that one sensory perception be enhanced or degraded by another sensory modality in either spatial or temporal domain [1, 2, and 3]. The McGurk effect well proved that visual information influenced the auditory information detection [1]. In McGurk's experiments, the lip movement for 'ga' in synchronization with the speech of 'ba' resulted in an auditory perception of 'da'. On the contrary, Sekuler reported that auditory information could also change the visual perception of motion [2], i.e. auditory stimuli also can alter the visual temporal resolution [3]. Moreover, recent work [3] reported that auditory stimuli affect the temporal perception of the visual stimuli, e.g. when a single flash was followed by two auditory beeps, the subjects will percept two flashes instead of one, which suggests that sound alter visual perception in time domain. In addition, electrophysiological data also proved that sound did alter the visual evoked potentials (VEP) in human (Ladan Shams, 2001. Meylan, R.V., 2006), which supported the conclusion that auditory stimuli could result in a visual illusion. Based on these findings in supramodal interactions, there was a more general hypothesis that the sensitive perception in one sensory modality could enhance or degrade the less-sensitive perception in another modality of sensory [4]. Nonetheless,

the influence of visual stimulus on the auditory intensity perception has not been reported. The aim of this paper is to test the existence of the supramodal interaction between visual spatial sensory and auditory intensity.

II. METHODS

A. Experiments

Totally, 5 female and 7 male volunteers participated in this experiment with writing informed consents. All subjects were right handed. Each subject reported normal hearing, normal or corrected to normal vision, and no history of neurological and psychological problems. Subjects were paid for their participation after the experiments.

All experiments were completed within an acoustic and electric shielding room (Union Brother, Guangzhou, China). Subjects were seated 1.20m in front of the CRT screen. During the experiments, the subjects were requested to look at the screen with fixation in the center, as well listening to the auditory stimuli from the earphones. In each experiment, eight 40-trial blocks of stimuli were presented. Within each trial, the subject was presented with two similar visual stimuli, i.e. a circle (diameter=5 or 7 cm, filled color: black) in synchronization with a monotone auditory stimuli ($f=3.5$ kHz, SPL=90dB) by earphones. The duration of stimulus was 68ms or 80ms and inter stimulus interval (ISI) of visual stimuli was 230ms or 300ms. Totally we present two modes of stimuli: (a) the diameters for both circles in a trial were the same, i.e. $d_1=d_2=5$ cm; (b) the second circle was larger than the first one, i.e. $d_2=7$ cm, $d_1=5$ cm. The experimental procedures were illustrated in Fig.1. In order to investigate the robustness of the influence of visual stimuli on auditory intensity perception, the duration and ISI of visual stimuli were varying in the ranges of 68ms~300ms. Therefore, totally, we randomly presented 8 different stimuli in each block with a probability of 20%.

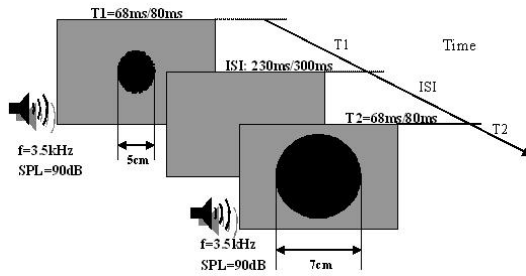


Fig. 1 Experiments protocols. The auditory stimulus was 3.5 kHz stereo sinusoidal tone (90dB). The duration T1 or T2 was 68ms or 80ms. ISI was 230ms or 300ms. Visual stimulus were circles (diameter=5cm) and its resized copies (diameter=7cm). Visual stimuli were presented in synchronization with the auditory stimuli.

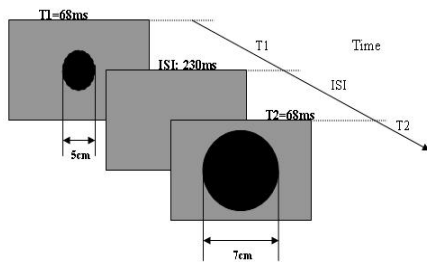


Fig. 2 the resized visual stimulus without auditory stimulus (V)

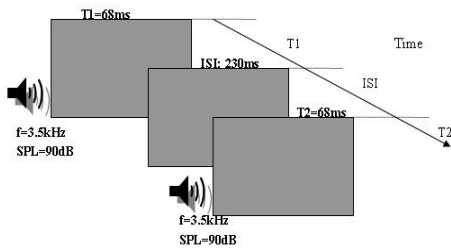


Fig. 3 the auditory stimulus with the same SPL (A)

Meanwhile, we recorded the electroencephalogram (EEG) activities throughout the experiments. We focused on recording ERP data to examine whether visual stimulus can influence auditory perception on the intensive. This group experiment contains 4 conditions: VA: the resized visual stimulus with the same SPL in auditory stimulus, which has been shown in Fig. 1, V: the resized visual stimulus without auditory stimulus as shown in Fig. 2, A: the auditory stimulus with the same SPL as shown in Fig. 3, AA: the auditory stimulus with different SPL. Stimulus duration was 68 ms and ISI on a given trial was 230 ms. Subjects were required to judge in the condition with auditory stimuli (VA, A, AA).

B. Signal Processing

Following the conventional experimental paradigm, we recorded the behavioral responses simultaneously. Under the auditory stimuli with the same SPL (VA), the subjects were requested to decide whether the subsequent two auditory stimuli have different SPL or not. EEG signals were recorded at 12 loci (Fp1, Fp2, F3, F4, C3, C4, O1, O2, T3, T4, T5, and T6) with Ag-AgCl electrodes complying with international 10-20 system with reference to linked earlobes. Before processing the trials with eye movements, blinks had been discarded. The EEG data were filtered into [0.5Hz, 60Hz] through a sixth order Butterworth band-passed filter before extracting the grand averaged ERP signals. Trials with blinks and eye movements were manually rejected off-line and an artifact criterion of $\pm 60\mu\text{V}$ was used at all scalp loci to remove the trials with excessive EMG or other noise transients. EEG epochs were sorted and averaged by stimulus type to compute the ERP. The ERP signals were averaged over all subjects from 200ms before first stimulus onset and 800 ms post second stimulus onset. Finally, the differential ERP waveforms of [VA-(V+A)] and [AA-A] are calculated respectively and the significance of the waveform change is checked by t-test. In order to exam the robustness of the influence of visual stimuli on auditory perception, we further investigated the supramodal interactions under visual stimuli with different duration and ISI.

III. RESULTS

A. Behavior results

Subjects identified auditory stimuli with more error when the auditory stimuli combined the resized visual stimuli than when they were presented with auditory stimuli with non-resized visual stimuli. In the condition of auditory stimuli with the same intension, this group of behavior results confirms that subjects identified the auditory stimuli with different intension, when they were presented resized visual stimuli. The mean of error discrimination percent for each condition have been shown in Fig.2. There is a significant difference ($p < 0.001$) for each pair condition with discrimination error percents increasing as the resized visual stimuli presented. The behavior results also showed significantly higher error rate (71%) of auditory intensity discrimination when the visual stimulus images were larger. While the stimuli with different durations (68ms and 80ms) and ISI (230ms and 300ms) did not significantly affect the behavior results ($p < 0.001$).

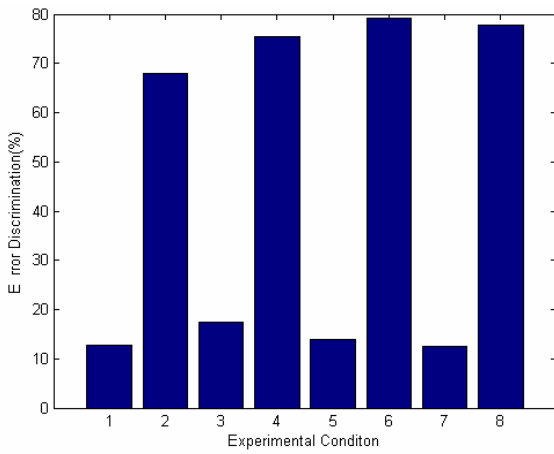


Fig. 4 Behavior results. Seven subjects' error discrimination data are shown for eight experiment conditions. In condition 1 and 2, the stimuli duration and ISI are 68ms and 230ms. In condition 3 and 4, the stimuli duration and ISI are 68ms and 300ms. In condition 5 and 6, the stimuli duration and ISI are 80ms and 230ms. In condition 7 and 8, the stimuli duration and ISI are 80ms and 300ms. The odd and own conditions correspond to the non-resized and resized visual stimuli, respectively.

B. ERP results

The ERP waveforms of [VA-(V+A)] and [AA-A] elicited at C3 and T3 indicated significant amplitude negative difference (ND) with respect to zero. The waveform of [VA-(V+A)] and [AA-A] enhancement in the components at

175~200ms (ND190) and 200~220ms (ND210) post the second stimuli onset ($p < 0.01$). Fig. 3 shows the waveforms of C3 with ND190 and ND210. In order to prove the significant difference among the two conditions, t-test for each time sample has been used. The amplitude difference of wave between [VA-(V+A)] and (AA-A) compared with zero was significantly different ($p < 0.01$) for ≥ 15 consecutive time samples. The waveform analysis identified that over the 175~200ms and 200~220ms post the second stimuli onset there are significant different amplitude from zero ($p < 0.01$). The time interval of different waveform are longer than 15 consecutive time samples (15ms) which can be considered as a stable interaction[5].

IV. DISCUSSION

The behavior results suggest that subjects reported error auditory intensity perception on an average of 71% in the condition with the resized visual stimuli. This result supports our hypothesis that visual stimulus influences on the auditory intensity perception. To study the physiologic basis of auditory illusion, illusion evoke waveforms were obtained by [VA-(V+A)] and real evoke waveforms were calculated by [AA-A]. The negative different components of [VA-(V+A)] and [AA-A] was localized to C3 and T3 at 175~200ms (ND190) and 200~220ms (ND210) post the second stimuli onset. Two major components were found both in the illusion evoke waveforms and real evoke waveforms demonstrates that visual stimuli can evoke the same components as evoked

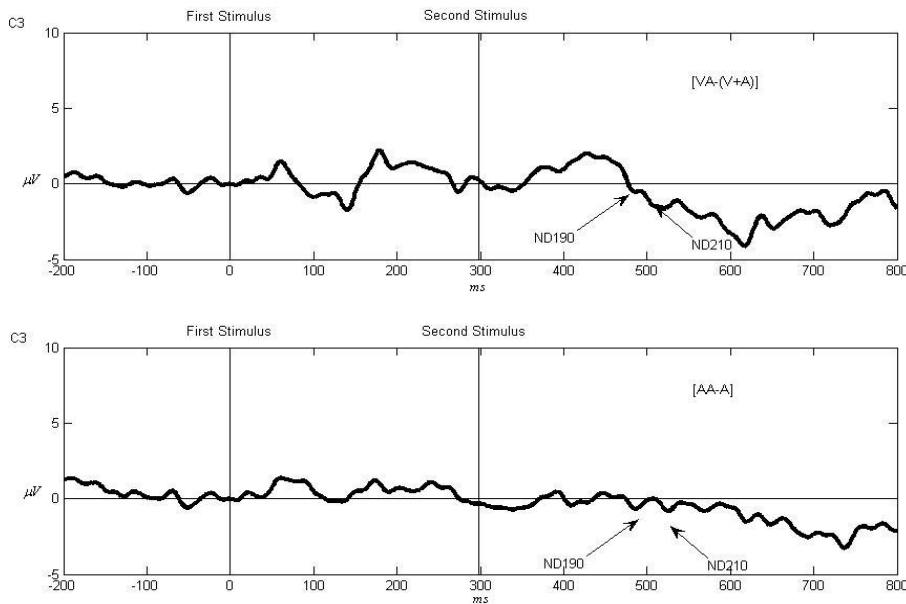


Fig.5 the ERP waveform elicited from C3

by auditory stimuli with different intensity at the early ERP components (250ms). Such findings are consistent with the earlier literatures suggesting that multisensory integration can occur early in visual processing [5]. Also the recent study [6] demonstrated that the ERP waveforms ND110 localized in auditory cortex during visual illusory. Both the illusory and real visual stimuli ERP waveforms were reported [7] to display a different component at ~200 ms, which was interpreted as a common physiologic basis for the illusory and real percepts. Our new results extend this result by demonstrating that visual stimuli can evoke the same negative different components at auditory cortex as that the auditory stimuli evoked.

V. CONCLUSIONS

Our results indicated that the resized visual stimuli can elicit the same ERP components under the VA condition as that of under AA condition. Both ERP and behavior results confirmed the evidence that visual spatial sensory can change the perception of auditory intensity, i.e. supramodal interaction between visual spatial sensory and the auditory intensity perception does exist. Besides, behavior results suggested that this interaction isn't affected by the duration and ISI of visual and auditory stimuli.

In this paper, we provide physiologic and behavior evidence for the supramodal interactions of visual stimulus on auditory intensity perception. Such a finding extends the traditional view that the interaction between visual and auditory system exist in either temporal or spatial domain.

REFERENCES

1. McGurk H, MacDonald J (1976) Hearing lips and seeing voices. *Nature* 264: 746-748
2. Sekuler R, Sekuler AB, Lau R (1997) Sound alters visual motion perception. *Nature* 385:308
3. Ladan S, Yukiyasu K, Shinsuke S (2000). What you see is what you hear. *Nature*, 408:783
4. Gregg H. Recanzone (2003) Auditory influences on visual temporal rate perception, *J Neurophysiology* 89: 1078-1093
5. Ladan S, Yukiyasu K (2001). Sound alters visual evoked potentials in humans. *NeuroReport*, 12: 3849-3852
6. Jyoti M, Antigona M, Terrence S et al (2007) Early cortical processes Underlie a Sound-Induced Illusory Flash *J. Neurosci.*, 27(15): 4120-4131
7. Watkins S, Ladan S, S Tanaka et al (2007), Sound alters activity in human V1 in association with illusory visual perception. *NeuroImage* 31: 1247-1256
8. Giard M.H., Peronnet F. (1999) Auditory-visual Integration during multimodal object recognition in humans: a behavioral and electrophysiological study. *Journal of Cognitive Neuroscience* 11: 473-490
9. Meylan RV, Murray M.M (2007) Auditory-visual multisensory interactions attenuate subsequent visual responses in humans, *NeuroImage* 35: 244-254
10. David B, Jennifer G (2006). Seeing sounds: visual and auditory interactions in the brain. *Current Opinion in Neurobiology* 16: 415-419

Author: Renyan Cai, Zhengjun Li, Yaqing Li, Yihong Qiu, Yisheng Zhu, Shanbao Tong

Institute: Department of Biomedical Engineering, Shanghai JiaoTong University

Street: No.800 Dongchuan Road

City: Shanghai

Country: China

Email: renyan_c@yahoo.com.cn

Dipole Analysis of Eye Movement Artifacts from the EEG

Weidong Zhou

College of Information Science and Engineering, Shandong University, Jinan, China

Abstract — Independent Component Analysis (ICA) is an efficient technique for blind source separation. With dipole model, the sources can be localized and modeled as dipoles whose parameters may be computed based on the observed scalp EEG. In this study, We evaluated the use of Independent component analysis combining EEG dipole model to automatically recognize eye movement artifacts from EEG without the reference to EOG. We separated the EEG data into independent components using the ICA method, and determined the source localization of these independent components with a single dipole model. EEGs from 12 patients were analyzed. The experimental results indicate that ICA with dipole model is very efficient at recognizing the eye movement artifacts. The proposed method by combing Independent Component Analysis with Dipole Model is a generally applicable and effective method for recognizing ocular artifacts from EEG recordings, although slow waves and ocular artifacts share similar frequency distributions.

Keywords — Intracarotid Amobarbital Procedure (IAP), Independent component analysis (ICA), Dipole Model, Artifact, EEG

I. INTRODUCTION

Eye movements and blink artifacts can cause pervasive problems in EEG analysis and research. Epochs contaminated by ocular artifacts can be manually excised, but at the cost of intensive human labor and substantial data loss. The electric potentials created during saccades and blinks can be orders of magnitude larger than the electroencephalogram (EEG) and can propagate across much of the scalp, masking and distorting brain signals.

The Intracarotid Amobarbital Procedure (IAP) used for the lateralization of language function and for assessing the potential for memory loss when considering surgical removal of epileptic brain tissue usually results in an abrupt appearance of large amplitude slow waves in the scalp EEG, mostly ipsilateral to injection, but with some spread to the contralateral side. It is often difficult to assess the presence of slow waves caused by the amobarbital because there are very frequent eye blinks and eye movements. The difficulty originates from the fact that slow waves and eye movement artifacts both predominate in the frontal regions, and eye movements are frequent and vigorous as the patient is constantly stimulated visually by showing various objects and asking the patient to perform motor tasks.

Independent component analysis (ICA), which is based on high statistics, emerged as a novel technique for blind source separation. ICA is able to decompose the signals into several statistical independent components according to statistical independency. It is known that most biomedical signals and artifacts are mutually independent in the sense of physiology and physics. In this study, we separated the EEG data recorded during the IAP into independent components using the ICA method.

One disadvantage of ICA analysis is that it is difficult to automate. An operator has to examine the components obtained by ICA analysis and decide which are the components representing the artifact that must be removed. Automated methods are preferable and significant for practical use.

Localizing electrical activity within the brain based on multichannel electroencephalograms (EEG) has been important in both basic and clinical neuroscience. With dipole model active neurons within small regions of the brain are often modeled as current dipoles whose parameters may be computationally determined based on the observed EEG data from the scalp. This has been an inverse problem of the EEG. In our study, each independent component is projected to the scalp, and is fitted with a single dipole model.

The aim of this study was to test an automated method for recognizing ocular contamination from EEG signals using Independent component analysis and dipole model without needing EOG as reference, and to obtain good quality EEG for further evaluation.

II. MATERIALS AND METHODS

A. EEG data collection

The EEGs from 12 patients were included in this study. Patients were selected consecutively, starting in April, 2003. The IAP was performed as part of the presurgical evaluation of patients with medically refractory epilepsy. EEG data were digitally recorded at a rate of 200 samples/s with a 12-bit resolution using the Harmonie system at the Montreal Neurological Hospital. Electrodes were placed according to the 10-20 system, at the following 16 locations: Fp1, F3, C3, P3, O1, F7, T3, T5, Fp2, F4, C4, P4, O2, F8, T4, T6 with a reference at Cz. EEGs were examined and analyzed after having been reformatted to a bipolar “double banana” antero-posterior montage.

The EEG was recorded during at least two minutes prior to injection and for at least 10 minutes after the injection. We examined sections taken in the two or three minutes following injection, a time at which the slow waves are the most prominent. We selected sections in each patient at which there were clear slow waves as well as clear eye movement artifacts.

B. Independent component analysis

ICA is performed by optimizing an objective function that approximates measures of independence between components. The ICA model of linear instantaneous mixture can be formulated as, $\mathbf{x}=\mathbf{A}\mathbf{s}$, where $\mathbf{s}=[\mathbf{s}_1,\dots,\mathbf{s}_m]^T$ is a vector of independent sources. These independent sources are mixed through a linear system (a mixing matrix) \mathbf{A} . The signals that can be measured are the mixed signals and we call them $\mathbf{x}=[\mathbf{x}_1,\dots,\mathbf{x}_n]^T$. In this situation, the source \mathbf{s} and the mixing system \mathbf{A} are unknown. We only measure the mixed signals \mathbf{x} . Blind source separation may be undertaken by adaptively adjusting the weight matrix \mathbf{W} (called the separating matrix) of a neural network using a particular learning algorithm and eventually make the network's output, $\mathbf{u}=\mathbf{W}\mathbf{x}$, composed of sources $[\mathbf{u}_1,\dots,\mathbf{u}_m]^T$ as independent as possible. \mathbf{u} is the estimation of \mathbf{s} with independent components and \mathbf{W} is the estimation of \mathbf{A}^{-1} .

For EEG analysis, the rows of the input matrix, \mathbf{x} , are EEG signals recorded at different electrodes and the columns are measurements recorded at different time points. The rows of the output data matrix, $\mathbf{u}=\mathbf{W}\mathbf{x}$, are the time courses of the ICA components or sources. The inverse, \mathbf{W}^{-1} , is referred as the mixing matrix, gives the spatial distribution of the respective components at each scalp electrode. EEGs free of ocular artifact were derived by reconstructing the EEG with selected non-artifactual ICA components: $\mathbf{x}_0=\mathbf{W}^{-1}\mathbf{u}_0$, where \mathbf{u}_0 is formed by replacing the ocular artifactual components of \mathbf{u} with zero vectors.

In this study, the ICA was performed by using the joint approximate diagonalization of eigenmatrices (JADE) algorithm, which achieves good statistical performance. JADE is an efficient batch algorithm, and has been successfully applied to the processing of real data sets, such as telephony and radar signals as well as biomedical signals. The advantage of JADE is that it works without parameter tuning. The weakest point of the current implementation is that the number of sources is limited to 40 or 50 depending on the available memory of the computer.

C. Dipole source localization of ICs

Localizing electrical activity within the brain based on multichannel electroencephalograms (EEG) has been im-

portant in both basic and clinical neuroscience. With dipole model active neurons within small regions of the brain are often modeled as current dipoles whose parameters may be computationally determined based on the observed EEG data from the scalp (Sun 1997). This has been an inverse problem of the EEG. In our study, each independent component is projected to the scalp, and is fitted with a single dipole model. The EEG signal was reconstructed by automatically excluding those components localized within the eye area.

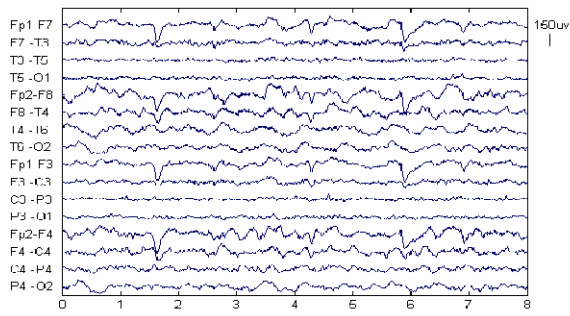
III. RESULTS

Experiments were carried out with the EEG data collected during IAP. Fig.1 shows the recognition of eye blinks and movements in EEG during IAP of Patient A. Time scale is in seconds. Fig. 1(a) is a 8-sec page of EEG recording during IAP. The separated components by ICA are shown in Fig.1 (b). Component 3 and 6 are automatically chosen as eye artifacts since their dipole location is within the eye area. The dipole location of Component 6 is given in Fig. 1(c). Fig. 1(d) gives the measured EEG during IAP with eye artifacts removed. Fig.2 is another example for recognition and removal of eye movement artifacts of Patient B.

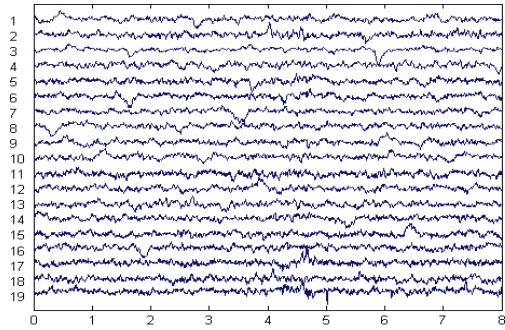
The EEGs from the other eight patients are not illustrated here, but they showed results very similar to those illustrated, with excellent recognition and removal of eye movement artifacts.

IV. CONCLUSION

The method of ICA to separate useful signal and artifacts was examined in this study. The reason that ICA is able to separate ocular artifacts from EEG slow waves during IAP is because ocular time courses are generally temporally independent from the EEG, and the eye movement potentials are distributed differently from sources of cerebral activity. Compared with other artifact removal methods, ICA has several advantages. The ICA algorithm is computationally efficient. It can simultaneously separate the EEG and artifacts into independent components without relying on the availability of reference artifacts. This avoids the problem of mutual contamination between EEG and EOG channels. In most cases, the ICA components representing the eye movements are very distinct. The corrected EEG can easily be derived by combination of the components without artifact. Not only can ICA avoid the problems inherent to filters, regression, and PCA, but it can also separate the artifacts contained in the multi-channel data without the need for extra EOG electrodes.



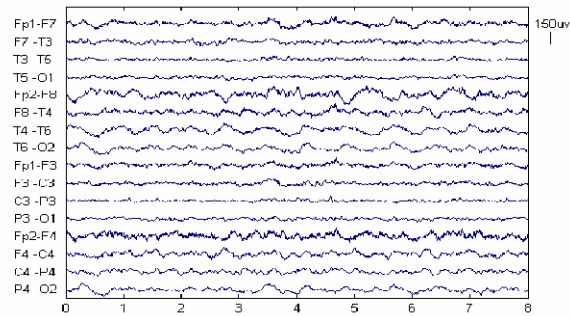
(a)



(b)

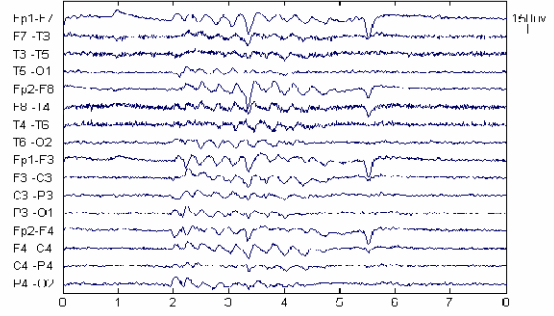


(c)

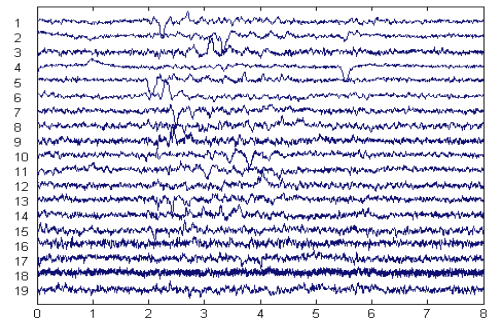


(d)

Fig. 1. Recognition of eye blinks and movements in EEG (Patient A). Time scale in seconds. (a) 8-sec page of EEG recording during IAP. (b) Separated components by ICA. Component 3 and 6 are chosen as eye artifacts. (c) The dipole location of IC6. (d) The measured EEG with eye artifacts removed.



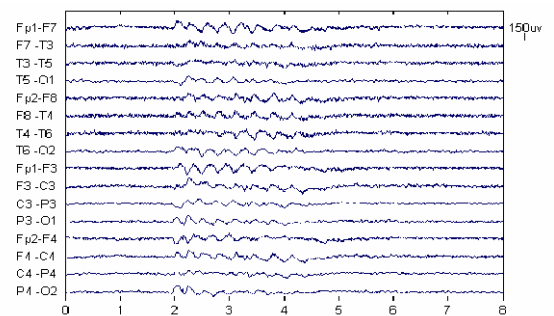
(a)



(b)



(c)



(d)

Fig. 2. Recognition of eye blinks and movements in EEG (Patient B). Time scale in seconds. (a) 8-sec page of EEG recording during IAP. (b) Separated components by ICA. Component 2 and 4, are chosen as eye artifacts. (c) The dipole location of IC2. (d) The measured EEG with eye artifacts removed.

This paper presents a novel, automated method for recognizing ocular contamination from EEG signals using Independent Component Analysis (ICA) and dipole model without need of EOG reference. This method appears to be a generally applicable and effective method for finding ocular artifacts from EEG recordings, although slow waves and ocular artifacts share similar frequency distributions. The principles of this method may be extended to certain other sources of artifacts as well.

ACKNOWLEDGEMENTS

We thank Prof. Jean Gotman for evaluating the experimental results and the help of this work, and Dr. F. Dubeau, Dr. A. Yankovsky and E Kobayashi for helping in the selection of EEG data at Montreal Neurological Hospital. This study was supported by the Natural Science Foundation of Shandong Province (No. Y2007G31) and in part by the Canadian Institutes of Health Research (grant MOP 10189).

REFERENCES

1. Jung TP, Makeig S, Humphries C et al.(2000) Removing electroencephalographic artifacts by blind source separation. *Psychophysiology* 37:163-178
2. Jung TP, Humphries C, Lee TW et al.(1998a) Extended ICA removes artifacts from electroencephalographic data. *Adv Neural Info Processing Systems* 10: 894-900
3. Jung TP, Humphries C, Lee TW et al.(1998b) Removing electroencephalographic artifacts: comparison between ICA and PCA. *Neural Networks for Signal Processing* 8: 63-72
4. Bell AJ and Sejnowski TJ (1995) An information maximization approach to blind separation and blind deconvolution. *Neural Computation* 7:1129-1159
5. Hyvarinen A and Oja E (2000) Independent component analysis: Algorithms and applications. *Neural Networks* 13: 411-430
6. Kobayashi K, James CJ, Nakahori T et al. (1999) Isolation of epileptiform discharges from unaveraged EEG by independent component analysis. *Clin. Neurophysiol.*110: 1755-1763
7. Iriarte J, Urrestarazu E, Valencia M et al. (2003) Independent Component Analysis as a tool to eliminate artifacts in EEG: a quantitative study. *Journal of clinical neurophysiology* 20: 249-257
8. Joyce CA, Gorodnitsky IF, Kutas M (2004) Automatic removal of eye movement and blink artifacts from EEG data using blind component separation. *Psychophysiology* 41: 313-325
9. Cardoso JF and Souloumiac A (1999a) Blind beamforming for non-gaussian signals. *IEEE Proceedings F* 140: 362-370
10. Cardoso JF (1999b) High-Order Contrasts for Independent Component Analysis. *Neural Computation* 11:157-192
11. Sun M (1997) An efficient algorithm for computing multishell spherical volume conductor models in EEG dipole source localization. *IEEE Trans. Biomed. Eng.*44: 1243-1252
12. Jung TP, Makeig S, Westerfield M et al. (2000) Removal of eye activity artifacts from visual event-related potentials in normal and clinical subjects. *Clin. Neurophysiol.*111: 1745-1758
13. Makeig S, Jung TP, Bell AJ et al. (1997) Blind separation of event-related brain responses into independent components. *Proc. Natl. Acad. Sci.* 94: 10979-10984

The address of the corresponding author:

Author: Weidong Zhou
 Institute: College of Information Science and Engineering,
 Street: 27 Shanda Road
 City: Jinan
 Country: China
 Email: wdzhou@sdu.edu.cn

BLDA Approach for Classifying P300 Potential

Anhu Huang, Weidong Zhou

College of Information Science and Engineering, Shandong University, Jinan, China

Abstract—Brain-computer interface (BCI) provides the brain with a new communication and control channel for conveying messages and commands to the outside world. BCIs require effective on-line processing of EEG or P300 which appeared just 300ms after the event happened. In this paper, we use a method of Bayesian linear discriminant analysis (BLDA) to classify P300 signals from the data set of BCI Competition III. P300 are obtained when subjects were facing a screen on which flashed objects were displayed. Before training a classification parameter for the BLDA, several preprocessing operations were applied to the data including filtering, trial extraction et al. With the BLDA algorithm, the classification accuracy in our experiment could be up to above 80%, depends on the averaged times of trials and SNR of the data. In summary, it is suitable to use LDA in the P300-based BCI system, and LDA will be a promising method to extract feature for BCI designs.

Keywords—Brain-computer interface (BCI), P300, Linear discriminant analysis (LDA)

I. INTRODUCTION

Brain-computer interface(BCI) is a device which enables people to control other mechanism-electronic device directly with their brain signal[1]. By linking the brain activity to a computer, the interface enables a person to communicate with others or control devices directly, without even using nerves and muscles. BCI device could help patients who suffer from severe motor impairments with an alternative form of communication, where the interaction between brain and device is realized in real time. BCI system will be helpful for the rehabilitant. There are kinds of BCIs based on the different brain signals. The brain waves which could be used in BCIs include EEG, EcoG et al. EEG is a noninvasive signal compared with ECoG which is a invasive signal. EEG is a more complicated signal which is nonlinear and nonstationary, and it is difficult to do pattern classification with spontaneous EEG signals.

People have designed some BCIs based on the user's response to specific sensory events or Event Related Potential. Event Related Potential is a special evoked potential which is particular for the need of subject's participated. The generated time of ERP is accurately locked with the event. A typical Event Related Potential is P300 which appeared just 300ms after the event happened. P300 is a

nonlinear and nonstationary signal which is complicated with noise. It is usually difficult to extract information through a single trial P300.

In 1988, Farwell and Donchin first introduced P300 potential into BCI. The P300 speller paradigm used to produce the P300 dataset of BCI Competition III is basically the same as that of Donchin et al., 2000[1][2]. In their experiments, a user focused on one out of 36 different characters, and the objective of BCI is to predict the correct character in each of the provided character selection epochs accurately and instantly.

There are many machine learning and pattern classification arithmetic about how to detect P300 potentials. Methods such as independent component analysis(ICA), Support Vector Machine (SVM), Boosting, Neural Network (NN), Fisher Linear Discriminant analysis (FLDA), and Kernel Fisher Discriminant (KFD) were studied[3][4][5]. In classification of P300 waves, there has been a trend to use SVM classifiers. It is shown that the FLD classifiers outperform the SVM classifiers. FLD classifier seems to be a very good candidate for real-time applications[3]. In this paper, we use a method of Bayesian linear discriminant analysis (BLDA) to classify P300 signals from the data set of BCI Competition III.

II. SIGNALS AND ARITHMETIC

A. P300 signals

For P300 signal collection, a P300 speller based on the protocol introduced by Farwell and Donchin[1][2] presented a subject with a 6 x 6 character matrix on a screen. For the spelling of a single character, each of the 12 rows and columns of the matrix was then intensified according to a random sequence. The subject was asked to focus its attention on the character he wanted to spell and then a P300 evoked potentials appeared in the EEG in response to the intensification of a row or column containing the desired character. In order to make the spelling procedure more reliable, this sequence of intensifications is repeated 15 times for each character to spell.

The data were collected with bandpass filtered from 0.1-60Hz and digitized at 240Hz from two subjects in five sessions each. Each session consisted of a number of runs. In each run, the subject focused attention on a series of

characters. For each character epoch in the run, user display was as follows: the matrix was displayed for a 2.5 s period, and during this time each character had the same intensity. Subsequently, each row and column in the matrix was randomly intensified for 100ms resulting in 12 different stimuli (6 rows and 6 columns). After intensification of a row/column, the matrix was blank for 75ms. All EEG signals of a 64-channel have been continuously collected[6].

B. BLDA

LDA is usually used in the pattern recognition for classification [3]. The aim of Fisher linear discriminant analysis (FLDA) is to compute a discriminant vector that separates two or more classes as well as possible. For two-class case. We are given a set of input vectors $x_i \in R^n, i \in \{1 \dots N\}$, and corresponding class-labels $y_i \in \{-1, 1\}$. The direct aim of FLDA arithmetic is to get product vector $w^T x$ is the output of FLDA where the input vector is x .

BLDA can be seen as an extension of FLDA. In contrast to FLDA, regularization is used to prevent overfitting to high dimensional and possibly noisy datasets in BLDA. Through a Bayesian analysis, the degree of regularization can be estimated automatically and quickly from training data without the need for time consuming cross-validation.

It is known that FLDA is a special case of least squares regression as a starting point for the description of BLDA. Least squares regression is equivalent to FLDA if regression targets are set to N/N_1 for examples from class 1 and to $-N/N_2$ for examples from class -1 (where N is the total number of training examples, N_1 the number of examples from class 1, and N_2 the number of examples from class -1). Considered the connection between regression and FLDA, the aim of BLDA is to do regression in a Bayesian framework and set target values as mentioned above[7].

III. DATA PROCESSING

The BCI Competition III provides four datasets, two for subject A and two for subject B. Of the two datasets for the same subject, one dataset is for training and the other is for testing. The dataset represents a complete record of P300 evoked potentials recorded with BCI2000 using a paradigm described by Donchin et al., 2000, and originally by Farwell and Donchin, 1988. The details of the datasets will be described as follow. All the data is stored in single precision. For each file, the recorded 64 channel EEG signal is organized in one big matrix. There are five matrixes in the training data which are Signal, Flashing, StimulusCode, and TargetChar, while the test data set does not contain StimulusType and TargetChar. There are 85 characters in one

training data, and 100 characters in one test. The goal of the competition is to use the labeled training data to predict the character in the test set. As the competition was over, the connotative characters in the test data have been published. We will output the predict character and the target characters as the result, and compute the prediction accuracy in the end.

Before training a classification function, we will apply several pre processing operations to the data. Eye blinks, eye movement or muscle activity can cause large amplitude outliers in the EEG, so we use the windsorizing to reduce the outliers. We also do same other pre operation to the data, like scaling and electrode selection, we test the effect of the pre operation. Single trials of duration about 208ms were extracted from the data. For the interval of every trials was only 175ms, the start of the duration and the duration time should be carefully selected.

To resolve these low-amplitude potentials against the background of ongoing EEG and other biological signals and ambient noise, signal averaging is usually required. We will compare different time averaging in the data processing.

Training data sets contained 170 target trails and 850 non-target trials. Bayesian linear discriminant analysis (BLDA) was used to learn classifiers. After the classifiers had been trained, they were applied to the test data.

IV. RESULT

According to the request of the BCI Competition III, the system was first trained by training data, and then, we use BLDA classifier to predict the character from the test data. Both the actual character and predicted character will be displayed as a result, and we also compute a percent of correct prediction.

The P300 signal drifted around 300ms after the stimulus. In our experiment, we extract 208ms to 517ms after the stimulus as one trial. The output of BLDA was summed over trials and the characters which number of rows and columns corresponding to the maximum of the summed output values in the group was then selected. The percent of correct prediction using BLDA is shown in Table 1. It is show that the correction ratio is improved obviously as the increasing of the number of averaged trials.

Table 1 Percent of correct prediction using BLDA

Number of average trials	5	10	15
Subject A	34%	58%	81%
Subject B	45%	66%	74%

V. CONCLUSIONS

Before training a classification parameter for the Bayesian linear discriminant analysis (BLDA), several preprocessing operations were applied to the data including filtering, single trial extraction, electrode selection et al. And then we use BLDA to compute a discriminant vector. With the BLDA algorithm, the average classification accuracy in our experiment could be up to above 80%. The classification accuracy depends on the number of averaged trials and the configuration of electrodes, and the SNR of the data.

In the classification of the P300 signals, the averaged time of intensifications of row/column will affect the classification accuracy obviously. More averaged time will improve the prediction correction, but the transfer bit will be slow.

BCI based on the P300 only required a small amount of training to achieve good classification accuracy. It is suitable to use BLDA in the P300-based BCI system, and BLDA will be a promising method to extract feature for P300 signals recognition and BCI designs. Further work will include the improvement of BLDA to yield higher classification accuracy using fewer trials.

ACKNOWLEDGMENT

This study was supported by the Natural Science Foundation of Shandong Province (No. Y2007G31).

REFERENCES

1. Farwell LA, Donchin E (1988) Talking off the top of your head: toward a mental prosthesis utilizing event-related brain potentials. *Electroencephalography and Clinical Neurophysiology*. 70:510-23
2. Donchin E, Spencer KM, Wijensinghe R (2000) The mental prosthesis: Assessing the speed of a P300-based brain-computer interface. *IEEE Trans. Rehab. Eng.* 8:174-179
3. Mirghasemi H, Fazel-Rezai R, Shamsollahi, MB (2006) Analysis of P300 classifiers in brain computer interface speller. *Proceedings of 28th Annual International Conference of the IEEE Engineering in Medicine and Biology Society* 1-15:4073-4076
4. Hoffmann U, Garcia GN, Vesin JM et al. (2005) A Boosting Approach to P300 Detection with Application to Brain-Computer Interfaces. *Proceedings of the IEEE EMBS Conference on Neural Engineering*, Arlington, VA, 2005, pp97 - 100
5. Wang Y, Zhang Z, Li Y, et al (2004) BCI Competition 2003–Data Set IV: An Algorithm Based on CSSD and FDA for Classifying Single-Trial EEG, *IEEE Trans Biomed Eng* 51: 1081-1086
6. BCI 2004 Competition data at http://ida.first.fraunhofer.de/projects/bci/competition_iii/
7. Hoffmann U, Vesin J, Diserens K, et al. (2007) An efficient P300-based brain-computer interface for disabled subjects. Submitted to *Journal of Neuroscience Methods*.
8. Kennedy PR, and Adams KD (2003) A decision tree for brain-computer interface devices. *IEEE Trans Rehab Eng*, 11(2):148
9. Wolpaw JR, Birbaumer N, Heetdlerks WJ, et al. (2000) Brain-computer interface technology: A review of the first international meeting. *IEEE Trans Rehab Eng.* 8(2): 164
10. Vaughan TM, Wolpaw JR, et al. (2006) The third international meeting on brain-computer interface technology: Making a difference. *IEEE Trans Rehab Eng.* 14(2): 126
11. Bian ZQ, Zhang XG (2000) *Pattern Recognition*. Tsinghua University Press, Beijing, China

The address of the corresponding author:

Author: Weidong Zhou
 Institute: College of Information Science and Engineering,
 Street: 27 Shanda Road
 City: Jinan
 Country: China
 Email: wdzhou@sdu.edu.cn

A GPRS-based Wrist Type Pulse Wave and Body Temperature Monitor for Children Healthcare

Yanhui Chen¹, Junnan Han², Kai Wu³, Xiaoming Wu⁴, Jing Zhou⁵

^{1,2}Postgraduate student of Department of Biomedical Engineering, South China University of Technology, Guangzhou, China

³Professor of Department of Biomedical Engineering, South China University of Technology, Guangzhou, China

⁴Professor of Department of Biomedical Engineering, South China University of Technology, Guangzhou, China

⁵Lectruer of Department of Biomedical Engineering, South China University of Technology, Guangzhou, China

Abstract—A GPRS-based wrist type pulse wave and body temperature monitor for children healthcare is presented in the article. The device, which detect the pulse wave signal and temperature signal of children and send the data to the server as well as the cell phone of their parents, enable the parents to find out their children's conditions in real time. The device has the advantages of high stability, wearable, low power consumption, high anti-jamming ability and seldom region limit because of GPRS.

Keywords—GPRS, Pulse Wave, Body Temperature, Wearable Detection, Children Healthcare

I. INTRODCUTION

Medical monitor device, integrated with the technology in the area of electronic, computer, material and information, plays an important role in the medical service system. With the help of the medical monitor, the doctor can get the up-date information about the concerning object. In the modern society, the physical condition and security of children has attracted more and more attention. The children, who are merely conscious about the conditions of themselves, are easily susceptible to the unexpected events, such as accidents and some kind of sickness. In order to supply a good guarantee for the children's daily life, a monitor designed to the children is needed. In other hand, the monitoring for the children requires wearable and wireless ability, so the wireless communication is the core part of the whole device. This study is aiming at designing a children monitoring device with good stability, wearable, low power consumption, low cost and high anti-jamming ability, which enable the parents acquaint themselves with the real-time condition of their children.

II. CONFIGURATION OF THE SYSTEM

The GPRS-based wrist type pulse wave and body temperature monitor is consisted of three main parts: wireless detection module, GSM communication module and server,

cell phone and relevant net devices. The wireless detection module mainly includes physical signal detection module and wireless communication module based on GPRS. Due to the wrist type, it is convenient for users to operate and take with them comfortably. The solid-state pressure-impedance sensor and DS18B20 are respectively used to acquire the signals of pulse wave and body temperature. After the processing of the MCU, the data are sent to the central server and cell phone of parents at a set time via GPRS. The warning signal is sent out immediately when the abnormal signals are detected. The data will receive further analysis in the central server and consequently a detailed report is available and then is sent to their parents' cell phone. Parents also can log in to the central server through internet and find out their children's historical record and up-date condition. The system is showed as Fig. 1.

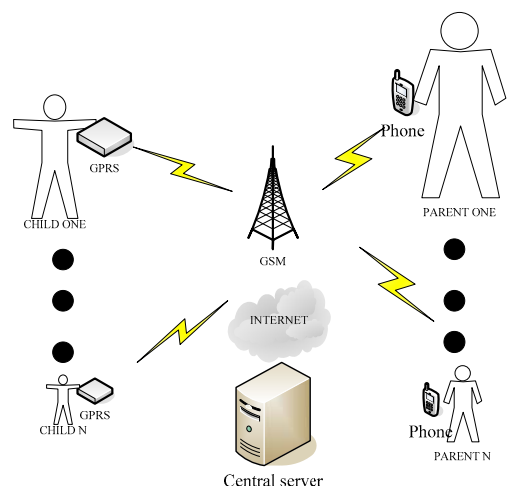


Fig.1 System framework

III. PULSE WAVE DETECTION CIRCUIT

A. Aim of the pulse wave detection

Pulse wave, one of the familiar physical phenomena, is the reflection of the condition of heart and blood vessel. The physical and pathological information, acquiring from pulse wave and served as the bases of clinic diagnosing and treatment, has attracted the attention of Chinese and western medical field^[1]. To a large extent, the shape (wave shape), intensity (swing), speed (wave velocity), rhythm (periods) and relevant information of pulse wave reflect characteristics of blood flow in the cardiovascular system. These characteristics of pulse wave can be easily detected from surface artery, such as the carotid and the radial artery^[2]. Regarding the convenience of children use, we are going to set the wrist type detection module above the radial artery.

B. Configuration of pulse wave detection system

The wireless pulse wave sensor consists of two main modules: signal detection module and wireless communication module. Due to the characteristics of bioelectrical signals, such as high impedance, weak intensity and low frequency as well as in a serious background noise, the analog circuit used in the physical information detection domain should characterize the high impedance and high CMRR. In order to adapt to the different range of input and output of physical signals, the enough gain should be guaranteed; in order to get high accuracy of signal output, the circuit not only filters different interferences but also has proper frequency range. The circuit is consisted of preamp circuit, band pass circuit, notch circuit, main amplify circuit and wireless communication circuit, the system showed as Fig. 2

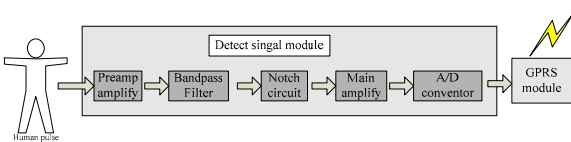


Fig. 2 Pulse wave detection system

C. Pulse wave detection system

The signal detection circuit is composed of preamp, band pass circuit, notch circuit and main amp circuit. The preamp circuit consists of three amplifiers and can supply the gain of 20 with seldom maladjustment and excursion. Due to that the frequency range of pulse wave is almost between 1 to 20 Hz, the four-order Butterworth filter is introduced in order

to filter the interferential signal come from other frequency range. Notch circuit is used to filter the 50Hz signals in order to protect the weak physical signals. After preprocessing, the signal will be amplified for the second time. Then, the signal will be converted into digital signal and sent to the wireless communication module eventually.

IV. BODY TEMPERATURE DETECTION CIRCUIT

A. Aim of the temperature detection

Body temperature, one of the most important characteristics of life, is necessary for metabolism and life activities. If the heat that produced from metabolism can not be emanated in time, it will lead to the turbulence of body temperature, even worse more than 40°C and then cause headache, vertigo, low blood pressure, high energy consumption, unconsciousness and crocking up of body temperature regulation function. In the other hand, when the produced heat is less than that of dissipating heat, the body temperature can not hold on and will lead to decreasing of metabolism^[3]. Body temperature served as an important index in the diagnoses of children diseases. Many diseases result from the change of children body temperature. In the reason that children hardly have the ability to tell themselves' conditions clearly, it will have a serious impact on the treatment of diseases if the parents can not find out the abnormal change of their children's body temperature in time.

According to the conditions discussed above, we have designed the wireless wrist type body temperature detection module. The module has the following advantages: ① Simple structure, small volume and wearable detection; ② High accuracy: 0.1°C; ③ Wireless communication; ④ Ability of warning: The system can set the different threshold for each child. The system will send the warning signal to the relevant staff once the abnormal data are detected.

B. Configuration of module

The module consists of DS18B20, MCU 89C51 and GPRS, showed as Fig. 3.

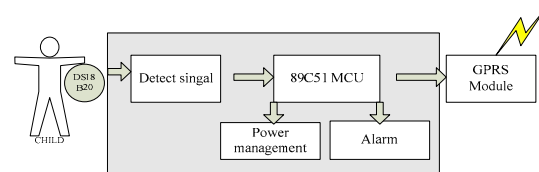


Fig. 3 Configuration of module

C. Body temperature detection

DS18B20, one kind of one wire digital temperature sensor that produced by DALLAS, is adopted in our module. The sensor has the advantages of small volume, temperature range between -55 to $+125^{\circ}\text{C}$, 9 to 12 bit A/D conversion precision and up to 0.0625°C resolution. The data acquired by DS18B20 will be changed from 16 bit in binary format to BCD code in decimal format and then displayed in dynamic scan way. In order to adapt to body temperature use, only three bits of valid number are reserved and the accuracy of system is up to 0.1°C .

V. GPRS MODULE AND CENTRAL SERVER

The data, processed by MCU, are sent out wirelessly under the GPRS protocol via the GPRS module [4]. The data that sent to the parents' cell phone are comparatively simple and can only include the value information of physical parameter. In the meanwhile, the data that sent to the central server will receive further modification and then a report about children's physical conditions is available. Parents can log in to the central server website to find out their children's condition at any time. Central server also would send the children's information to their parents at set time. Besides, parents can inquire about their children's position via GPS. When children get lost or in other accidents, GPS can enable their parents reach them as soon as possible. As the GPRS net has been integrated with GSM net of China Mobile, theoretically, the application of GPRS is no regional restrictions.

A. Data exchange

The wireless monitoring module sends the data that stored in the buffer to the parents' cell phone. Parents can also send SMS to the monitoring module to order the module to send the physical parameters and GPS information back to their cell phone in the SMS format. In this way, parents can get their children's heart rate value in recent ten seconds, average body temperature and position information (latitude and longitude).

B. Warnings

When detected physical parameters is out of normal range, such as heart rate and body temperature, the abnormal data and GPS information will be immediately sent to the central server and cell phone terminal and children can receive proper treatment as soon as possible.

C. Monitoring

When the system in the monitoring mode, the detection module will exchange data with central server every ten seconds, including children's heart rate value in recent ten seconds, average body temperature and position information (latitude and longitude). These data will be preserved in the database and the GPS information will be transformed to block information. The cell phone terminal can download the date from central server (historical records) or recent ten seconds information in real time.

VI. RESULTS

The new children monitor has a good performance in portability, low power consumption though the stability of wireless data communication is still to be enhanced. The acquired data are sent to the service station or the cell phone in the prearrange pattern. The warning function has a satisfied response performance when irregular signals occur. To some degree, the wireless data communication via GPRS has anti-jamming ability and Parents can get the pulse rate and body temperature of their children with mobile phone whenever they want.

VII. CONCLUSIONS AND SIGNIFICANCE

From the results above, we can easily tell that the wrist type monitor has reached our prearranged goals. The new monitor fully makes use of GPRS network so the cost of the device has been decreased significantly. With the help of the novel monitor faced to children, the present condition of children healthcare will have been improved increasingly. In addition, children are accessible to the proper help when they are suffered from some kind of accidents or sickness. As more and more attention will give to the fitness and security of children, the product would have a brilliant future definitely.

ACKNOWLEDGMENT

This work is supported by Guangdong Province Science and Technology Plan (2007B031302003 and 2007B010400055). We are grateful to Guangdong Province Science and Technology Department.

REFERENCE

1. Tai Yao, Bowei Wu. Physiology (6th Edition). Beijing: People's Medical Publishing House, 2003.12.
2. Guoquan Mie, Zuxiang Fang. Measurement and analysis of human pulse wave. Shanghai Journal of Biomedical Engineering.2006,Vol. 27,No.2:74-76
3. Hongfu Wang, Xuexing Li, Zhenhai Sun. Body temperature monitoring system. Chinese Medical Equipment Journal,2005, Vol.26,No.7:18-19
4. Meixia Wang, Zhangyong Li. Research on a GPRS based telemonitoring system for ECG. Chinese Journal of Medical Physics, Nov., 2006 Vol.23.N

Design of Physiological Parameter Acquisition and Communication Module Based on CC2430

Qi Zhao¹, Kai Wu¹, Jianbo Wu², Xiaoming Wu¹

¹Department of Biomedical Engineering, South China University of Technology, Guangzhou, China

²Computing Center in South Campus, South China University of Technology, Guangzhou, China

Abstract — To achieve the strict requirements for data acquisition and communication of modern medical monitoring, a design approach for physiological parameter acquisition and communication module based on ZigBee technology is presented. This approach used the chip of CC2430, which was integrated of AD converter, 8-bit strengthened MCU and wireless RF unit. It realized the functions of data acquisition, wave filtering and wireless transmission. It can also communicate with peripheral devices via serial ports and then instruct traditional medical care which cable connections are absolutely necessary. The system presented in this paper can enable patients to be tested in a more comfortable state, improving the quality of medical care. The module has a simple structure, low power consumption. It is suitable for developing family-oriented portable medical equipments.

Keywords — ZigBee, data acquisition, wireless transmission

I. INTRODUCTION

Modern medical monitoring system is composed of three parts: subject, communication system and medical staffs. The main function is to implement physiological monitoring under certain medical treatment service, send data promptly to hospital centre via communication medium if needed (e.g. heart rate is abnormal), and get doctor's advice after the doctor carries out the first step diagnose [1].

Since the faint electric signal of human body and its rich information, the correctness of signal acquisition and processing directly affects the quality of patient's monitoring during the measurement. Therefore high accurate acquisition appears especially important. A design approach for physiological parameter acquisition and communication module based on ZigBee technology is presented. The approach is to make use of wireless transmission, transfer information between medical sensors and monitoring equipment, cut down cable links, enable patients being tested in a more comfortable state and remit the pain of rushing around between family and hospital.

In this paper, system overview and design methods are presented in Part II, results are discussed in Part III. And we conclude the approach at the end of the paper and look

forward to the advancing prospect of wireless medical monitoring technology.

II. METHODS

A. System overview

A Pulse-SPO₂ medical monitoring system (as shown in Fig. 1), which is based on ZigBee, is introduced in this paper. Through the initializations of monitoring nodes for pulse and SPO₂, doctors, with the help of a PC and a wireless network, are able to know a patient's real-time condition and to make prompt treatment if needed. Besides, doctors can also collect long-time physiological data of a patient by the use of wireless sensing network. These data play an important role in scientific research in the hospital and the monitoring nodes which are initialized on the patients will bring little inconvenience to daily life. The monitoring equipment and ZigBee sensor nodes compose a mini monitoring network. A controller is installed on the sensor nodes and data will be collected through the control on the sensor which is used to detect the physiological data. Data will be sent to the equipment through wireless communication first and then to a connected PC or other network equipments. After that, professional medical staffs will conduct a statistic calculation over those data and provide necessary medical treatment. Medical sensor nodes are characterized as flexibility and extensibility due to their ability to change the setting according to different need. Meanwhile, a connecting to Internet can make such a network become as large as a community, a hospital, a municipi-

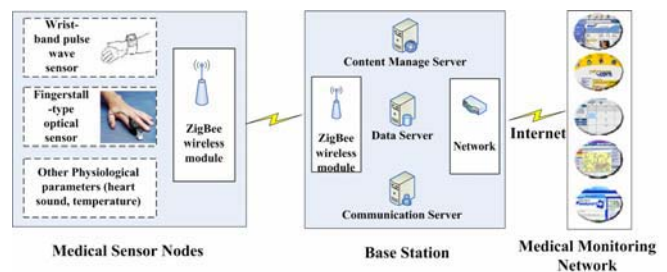


Fig. 1 Pulse-SPO₂ medical monitoring system

pal or a national network which supervises the medical treatment [2].

The wireless medical monitoring system is composed as follows:

- Wearable sensors transfer the physiology signals to CC2430;
- CC2430 is divided into three parts: (1) AD converter, to convert the analog signals into the digital signals, which includes sampling rate, sampling channels, etc; (2) eight-bit micro-control processing unit, to complete signal filtering, signal enhanced and data compressions, etc; (3) ZigBee wireless transmitter unit, to transmit digital signals to a remote part in the wireless way, which is used for real-time observation of a doctor or nurse.
- ZigBee base station: it can receive the detecting data of 6 patients at the same time; 2 ZigBee modules, sharing the data taking-over mission, are embedded in the base; furthermore it can execute corresponding procedure to display the real-time life characteristic in the form of digitals and direct graph (heart rate, ECG, pulse etc.)
- Power module will be responsible for entire circuit which supplies electricity.

B. Principles and methods

Medical sensor’s function is to collect physiology signals, or carry out dynamic monitoring on some medical equipment condition during curing process, transfer data to monitoring base via the wireless way. Medical sensor nodes and MCU modules are shown in Fig. 2.

Principles of medical sensor nodes and MCU modules: At the very beginning, the control unit will send an order, telling sensors to start monitoring some physiological parameters. And then the order will be sent to the physiological signal data collecting unit through a wireless data communication unit so as to collect data about human physiological signal, such as pulse and SPO₂. After the gain adjustment, the collected data will be sent to the data processing unit which is embedded in the control-display unit.

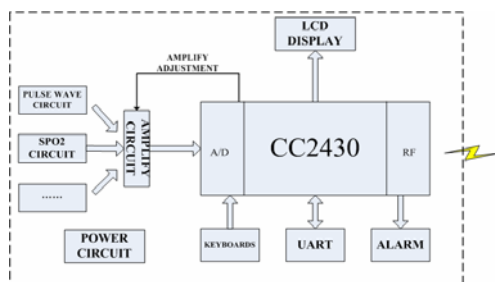


Fig. 2 Medical sensor nodes and MCU modules

Data processing unit will, on one hand, process and display the collected data, and on the other, send the final data to a PC through a wireless data transmission unit. Data will be stored in the PC for search and replay.

The module circuit includes the following modules:

- Physiological signal data acquisition module

In the current system, the medical sensor module performs the function of pulse and SPO₂ parameter detecting. Wrist-band pulse wave sensor is applied to detect pulse wave and fingerstall-type optical sensor is introduced to measure SPO₂.

1. Wrist-band pulse wave sensor detecting module

The characteristics of pulse wave are very easy to detect through the human arteries, such as carotid, brachial artery and radial artery [3]. Among them, as the radial artery drawing near the body peripheral blood vessels, it will get rich information and a convenient way for detection. Pulse can be felt when putting fingers on the finesse skin, so it is the best detecting site for collecting pulse wave.

Bioelectricity signals have characteristics of high impedance, weak signals and low frequency. It is located in a serious background noise. Based on these particularities, analog circuit used in physiological information should be measured with high input impedance and high common-mode rejection ratio; to adapt to different physiological signal amplitude and output range, there should be large enough gain; in order to obtain the maximum signal detection fidelity, it is necessary to filter all kinds of interference through the circuits, but also fit the right frequency band. Therefore, in this paper the design of the pulse wave signal amplification uses semiconductor piezoresistive sensors and pulse wave signal amplification circuit in accordance with the improved ECG signal amplification circuit. Detecting circuits consist of preamplifier circuit, band-pass filter circuit, wave trap, second amplifier circuit. Analog signals are converted to digital signal by AD converter.

2. Fingerstall-type optical sensor detecting module

SPO₂ is an important index that reflects the blood circulatory system and the respiratory circulatory system, which is indispensable for the clinical diagnosis, prevention, identification and treatment of the disease. SPO₂ measurement system adapts a highly sensitive noninvasive optical detection method, that is, double-optical wavelength measurement; sensor is used fingerstall type, measurement sites are human fingertip or earlobe [4].

Module process is as follows: first timing control circuit sends two timing sequences, drive red and infrared emitted diodes to light alternately. Through fingertip, the sensor will receive signals. After the signal separation, amplification, filtering, signals will be sent to AD channels, MCU will

calculate SPO_2 values, and transmit data through ZigBee wireless module.

In the design of the system, wireless sensor nodes reserve rich interface for extension. If other physiological parameters are needed, such as ECG, temperature, only need to access corresponding sensors to the reservations. So that new wireless sensor nodes will be created. And it can be added directly to the wireless networks after developing corresponding embedded control and processing software.

- Wireless data communication module

Medical monitoring equipments have high demand for electromagnetic radiation in the hospital. The electromagnetic waves radiated from devices cannot interfere with the normal work of other equipment, but also devices themselves should have certain anti-jamming capabilities, preventing electromagnetic radiation interference from other equipment. Therefore, wireless communication devices used in the hospital or family must consider the factors in the design [5].

In this system, 802.15.4/ZigBee standards are used. ZigBee is a new short-range, low-data-rate wireless communication technology. It is mainly used for short distance wireless connection, applicable to the field of health care. The design uses the chip of CC2430, it is consistent with the requirements of IEEE 802.15.4 standards to ensure that the effectiveness of short-distance communication and reliability. With the exploitation of this chip, wireless communication equipment support data transfer rates up to 250 kbit/s. It can rapidly form a multipoint-to-multipoint network. CC2430 provides hardware support for the data frame format of IEEE 802.15.4. MAC layer frame format is: head frame + data frame + check frame. PHY layer frame format is: synchronous frame + PHY head frame + MAC frame. The length of frame sequence can be changed via the register. A 16-bit CRC check is used to improve the reliability of data transmissions. Data frame, which is transmitted or received, is sent to the 128-byte RAM buffer zone, implementing corresponding frame packaging and unpacking operations.

- Data processing module

The current system adopts the ZigBee module CC2430, which is produced by Wuxianlong Company in Chengdu. CC2430 is produced by Chipcon with the latest SmartRF 03 and 0.18 μ m CMOS techniques. It is packaged with the size of 7 mm \times 7 mm QLP48. A RF transceiver is included as well as an enhanced 128KB programmable flash memory and an 8KB RAM. There are also an ADC, several Timers,



Fig. 3 ZigBee wireless module

an AES128 Coprocessor, a Watchdog Timer, a 32 KHz Crystal Oscillator Sleep Timer, a Power On Reset, a Brown Out Detection and 21 programmable I/O pins [6]. A few external components can enable the working of such a system. It is characterized as a low voltage (2.0 V~3.6 V), a low power consumption (27 mA when receiving data and 25mA when sending), a high degree of sensitivity (-97 dBm) and a maximal transmission rate (250 kb/s). Fig. 3 shows the framework of wireless data communication system.

- Power module

In order to make it cost less and easily to carry, Li-ion battery is used in the module and a DC/DC converter which is of high efficiency and low power consumption is used to supply +3.3V power for the module circuit. Because the electric current consumption of CC2430 chip is less than 27mA in the receiving mode, or 25mA in the transferring mode, and the time for CC2430 to switch from Sleep Mode to Active Mode is short, the battery life can be extended. Meanwhile, Power module is responsible for the entire power supply circuit and will alarm if the battery power is less than 2.4 V (minimum effective operating voltage). Moreover, the setting of software can also reduce the power consumption of the system, with the Sleep Mode most frequently used. MCU is able to periodically awake MCU through Watchdog or an external affair and after executing the corresponding code, it goes back to the Sleep Mode. Crystal Oscillator stops vibrating in the Sleep Mode so as to reduce the consumption and there are only several amperes of electric current running through MCU. The working frequency of MCU is closely related to power consumption. The higher the frequency, the larger the power consumption.

- Software module

The wireless module design includes the hardware and the software of CC2430. To write a software program, it is necessary to make clear the transmission route and process of data in modules. As shown in the following figure.



Fig. 4 Transmission route

When transferring data, the data enter into the CC2430 DATA memory area via UART. High 128 byte in the DATA memory area are able to satisfy memory capacity request, therefore data are stored in this area. For improving data transmission speed, using DMA, data in memory area are transmitted to Radio buffer TXFIFO, which follows the rule of “First-In First-Out”. After the data enter into the Radio, through the process of hardware, data are sent via antenna. Radio receives wireless signal from antenna. Through the process of hardware, signals are changed to data and deposited in RXFIFO. Then data are sent to low 128 byte in the DATA memory area using DMA and put out via UART.

In software realization, adopting modularization design, functions are divided into main function module and sub function modules, which include the signal transformation, wave filtering, compression, wave analysis, keyboard intermit procedure, battery quantity inspected procedure and data sending procedure etc.

III. RESULTS AND DISCUSSIONS

Through the testing, the module can implement multiple physiological signals acquisition and wireless transmission and complete the analysis of multiple physiological parameters. It also can achieve signal processing, including digital filtering, transform and identification, pathological features positioning and assistant diagnosis. Users can reset sampling parameters (sampling channels) through keyboards. The design of system software includes MCU and computer communication. MCU mainly completes digital filtering, data compression and data transmission. Computer achieves parameter settings, serial port data reception, commands sending, waveforms or numerical values displaying and information storage.

IV. CONCLUSIONS

The module has a simple structure, low power consumption. It is suitable for developing family-oriented portable medical equipments. The module uses the ZigBee technology, changes the traditional cable data acquisition to the wireless data transmission, so that the mobility of the data acquisition and communication system is greatly improved. Consequently, it makes possibly that a large number of chronic diseases, cardiovascular diseases’ observation and monitoring can be carried out at home, and doctors can monitor users regularly. We believe, in the near future, with the help of wireless monitoring, long-distance consultations will be realized and the problem of “high expense” in the medical health reform will be fundamentally solved.

ACKNOWLEDGMENT

The above work is supported by the Technology Project of Guangdong Province (2007B031302003 and 2007B010400055), China.

REFERENCES

1. Xie Hongtao, Zhang Yonghong, Zhang Jupeng, Bai Jing et al. (2001) Development of a Portable Home ECG and Blood Pressure Monitoring Device Based on 80C196KC Micro-controller. Beijing Biomedical Engineering. Vol.20, No.4
2. Kai Wu, Xiaoming Wu (2007) A wireless mobile monitoring system for home healthcare and community medical services. 6–8 July 2007 Page(s):1190–1193 DOI 10.1109/ICBBE.2007.307
3. Cheng Yongmei, Xia Yaqin, Shang Lan (2006) A Human Blood Pulse Signal Detecting System. Beijing Biomedical Engineering. Vol.25, No.5
4. Ke Zili, Yao Guoxing, Lin Lizhong (2004) Introduction of Blood Oxygen Saturation Measurement. China Medical Devices Information. Vol.10, No.2
5. Luo Huiqian, Ren Yi, Shi Daosheng(2007) Research on the wireless medical monitoring system based on ZigBee technology. China Water Transport. Vol.5, No.4
6. Gan Surong, Zou Tao, Weng Zhe (2007) Design of ZigBee wireless communication based on CC2430. Science & Technology Information. No.22

Author: Xiaoming Wu
 Institute: Department of Biomedical Engineering
 Street: South China University of Technology Higher Education
 Mega Center, Panyu District, 510006
 City: Guangzhou
 Country: China
 Email: bmxmwus@scut.edu.cn

Improved System of Artificial Heart Valve Detector Based on Windows XP

Cheng Lu¹, Xiaogang Hu², Xi Zhang¹, Jianyu Wang, Shuo Wang³

¹ School of Traffic and Transportation, Beijing Jiaotong University, Beijing, China

² School of Electrical Engineering, Beijing Jiaotong University, Beijing, China

³ National Institute for the Control of Pharmaceutical & Biological Products, Beijing, China

Abstract—The essay confined itself to discuss the improvement of the data acquisition, disposal, count, analysis, database of building in relation to the control system of AHVD and make use of exploitation language, including Visual Basic 6.0, Access2000, in order to upgrade operating system for WindowsXP. In course of debugging, very good testing result has been achieved.

Keywords—artificial heart valve detector(AHVD), data acquisition, control process

I. INTRODUCTION

Biomechanical Research Center of Tsinghua University developed the AHVD that simulates the cycle of human physiological process. It can be used to measure the parameters of an artificial heart valve [1][2]. In a dynamic environment, the parameters of heart valve pulsing flow will be acquired, processed, calculated and analyzed by PCI-bus multifunction acquisition card. In this paper, on the basis of basic constructive principle of detector, we design and put into effect the artificial heart valve pulsing flow detection system based on WindowsXP environment. Visual Basic 6.0, Access2000 was used for the Software development language. The updated system has better ability to deal with data and the environmental adaptability and stability.

II. THE HARDWARE OF CONTROL SYSTEM

A. System components

Instrument Control System includes the two pressure sensors, a flowmeter probe, preamplifier, video boards, A / D acquisition card and PC. As shown in Fig.1:

In both ends of the aorta, two pressure sensors are placed, so as to detect the aortic pressure and ventricular pressure respectively. At the exit, a probe flowmeter is laid to measure the aortic flow. In a simulated heart throb of the circumstances, the three-way signal from the preamp passing through the video board are collected by A / D sampling card, and analyzed and calculated by computer. Meanwhile, the computer could also be used to control the linear motor drive waveform to generate different pulsatile flow.

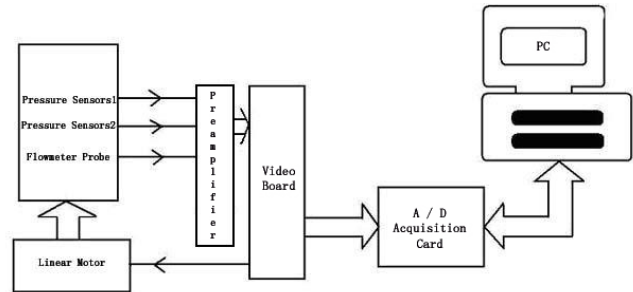


Fig.1 Block diagram of system

B. Hardware environment

Computer configuration:

The system uses a Pentium (R) 4 CPU 1.8GHz-compatible personal computers, memory 256 M, 40G hard drive, as well as independent graphics RADEON 9200SE.

A / D acquisition card:

PCI-9112 multifunction acquisition card is chosen as the Systems A / D sampling card, which is a 12-bit A / D resolution, up to 110 KS / s sampling frequency, conversion time is 8 μ s, 32-bit PCI bus support multifunction acquisition card. It can make 16 channels single-ended or 8 channels differential analog input, 2 channels over 12 switched analog output, 16-channels TTL digital input and output, and 1 channel 16 GM counter / timers, I / O 37-pin connector D-sub slot[3].

Internal settings of A / D card: internal timer trigger for the 2 MHz clock source is chosen in the system [4]. The system Include three single-ended analog inputs: aortic pressure, ventricular pressure, aortic flow; an analog output for the linear motor driven, connected to the acquisition card AI0, AI1, AI2, AO1 pin respectively. The PCL-9112 multifunction card can have more than one choice of input / output voltage range. According to the signal characteristics and the extent of pre-amplification, we choose Unipolar input of the aortic pressure and ventricular pressure 0 to +5 V, bipolar input of flow -2.5 ~ +2.5 V, motor output amplitude between 0 ~ + 10V (AO1) and the other termination +5 V, the final output of bipolar + / -5 V. Main use PC literacy

A / D card register the adoption of dynamic link library to achieve the A / D card operation and control.

Video board:

Optional terminal board system is Advantech PCLD-880 screw terminal board. It has two 20-pin plug-in rows and a 37-pin D-sub connector common terminal plate, screw connection with reliable row modules, and comes with two 1-meter-long cables ACL-10120 [5].

The Connections are aortic pressure input, ventricular pressure input, aortic flow input, aortic flow simulation, ventricular pressure simulation, aortic pressure simulation, corresponding board A3, A5, A7, A17, A18, A19 pin, and motor drive output and +5 V output, corresponding board B2, B17 pin.

III. THE SOFTWARE OF CONTROL SYSTEM DESIGN

For the software environment, all the functions of the system are run under Microsoft Windows XP Professional. Visual Basic 6.0 and Microsoft Access 2000 are utilized as software support. The report forms is designed by using Crystal Report through the operation of ADO database.

A. Design analysis

System Framework:

The control system is applicable to the single-database operations, so Access desktop database management system could be used as the underlying database platform. Through ODBC visit, we are able to make use of ADO object as database access method. Such kind of visit has a better scalability[6]. Interface adopts Visual Basic development, stand-alone operation. Database platform and procedures can run in the WindowsXP operating system.

Structural design of system software:

System consists of four components: Form, module, class module, data environmental design.

The form includes 17 parts and all parts cooperates each other to achieve functions of system. Through VB Object-oriented programming and related category called modules, the functions of initial calibration of pressure sensors and flowmeter probe, signal acquisition and waveform display; amendment of linear motor drive waveform; parameter calculation and data storage; report generation and print output capabilities would be completed by each of the main forms. Most of form controls are provided by the VB environment.

The major modules include three parts: multifunction data acquisition cards Win32 DLL Driver (PCIS-DASK),

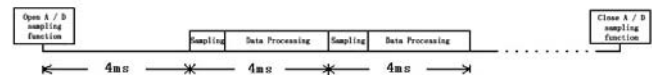


Fig.2 The course of hardware timing

the definition of overall variables and the form realizing systemic function often achieves some of subroutine calls. These subroutines primarily are responsible for A / D card data acquisition and control, mapping coordinates, curve drawing, signal processing analysis to support a code precisely handling the target, so it is easy to modify and maintain these objects.

Class modules create a self-defined category for controlling the acquisition mode of A / D data[7].

The three-way systems use single-ended analog inputs, including 2 ways Unipolar input and 1 way bipolar input in combination with the feature of A / D sampling card (PCI-9112), therefore the trigger approach of PCI-9112 is chosen as the internal timer trigger. PCI-9112 has three independent 16-bit subtraction counter / timers (COUNT 0, COUNT 1, COUNT 2). COUNT 2 internal clock is 2 MHZ. It and COUNT1 in series form a cycle counter, and its output of A / D triggering end. Let A / D sampling period is 4 ms, its hardware-timed the process as shown in Fig.2:

Because of the constant of timer $4 \times 2000 = 8000$, so the initial value of counter is 8000, which decreases by 1 for each trigger pulse. If the figure on the counter drops to 0, the counter (16 bit) value returns to $2^{16} = 65536$. We use the method of counter to monitor cycle counter. When a counter value is more than 8,000, it means that the time defined is over. Then the card starts to trigger sampling, on the other hand, counters set up once again its initial value at 8000 and continue to work Each datum collected has 16 bit, including low 4 bit AI channel address, high 12 bit A / D converter data [8] [9]. Therefore, the method for acquisition of data is as follows: after the data collected in the memory and get along with FFF0 and then divided by 16.

System Features:

(1)Initialization includes complete information of artificial heart valve and calibration of the pressure and flowmeter probe. Artificial valve testing information filled out is the beginning of the whole process, it includes: valve number, category, type, installation diameter, the type of experimental liquid, temperature, specific gravity, the name of test assistant, date of test, as well as units of submission. The information is stored in the valveInfo information table of the ValveInfo database and embodied in the printed report forms. The next step of operation could proceed only when all experimental information is completed.

Because this is a kind of detection system, at beginning of experiments all pressure and flowmeter probe should be calibrated, in order to determine the zero and slope of pressure and flow signal.

After the calibration of the sensor, the accuracy of data collection and reliability of follow-up testing process could be guaranteed.

(2)Signal acquisition includes 2 way pressure signals and 1 way flow signal. The system automatically startup the A / D sampling card and calculates the corresponding standard value by sampling. Pressure sensors install A / D card input range from 0 to +5 V, the conversion formula (1):

Pressure signal sampling = (measurement results of the quantitative value $\div 4096$) $\times 5$ (1)

A / D card 12 resolution $2^{12} = 4096$, A / D card maximum input is 5 V.

Flowmeter probe set A / D card input range from -2.5 to +2.5 V, the conversion formula (2): Traffic signal sampling = [(results of the quantitative measurement value -2048) $\div 2048$] $\times 2.5$ (2)

Bipolar Input $2^{12} \div 2 = 2048$, A / D card input range is 2.5 V for the largest amplitude.

The above data are stored in PreFlow information table of ValveInfo database for calculation, processing and preparation for analysis.

(3)Waveform display includes ventricular and aortic pressure waveform signal, traffic signal waveform, and waveform display of controlling pulsating flow produced by linear motor drive.

(4) Method of analysis: ventricular pressure, aortic pressure and flow of the three analog data from PreFlow table of valveInfo database are called, and the corresponding formula is used to get the mean arterial pressure, differential pressure valve, the percentage of fore flow, output, regurgitant fractions, to the flow of reflux percentage of the average flow, RMS flow, effective valvular orifices and simulated cardiac output, 12 artificial valve parameters.

Calculated parameter data stores valveInfo information table in the ValveInfo database. The solution in the print statements can be embodied.

(5)Output includes control of linear motor and printing of the report.

By changing the linear motor drive control waveform to produce different pulsating flow, in order to simulate the conditions of human blood inside the body environment.

B. Database Design

In the Microsoft Access 2000 database management, VB access the database using ADO through ODBC to create a database structure, query and update records in the database table, such as database operations.

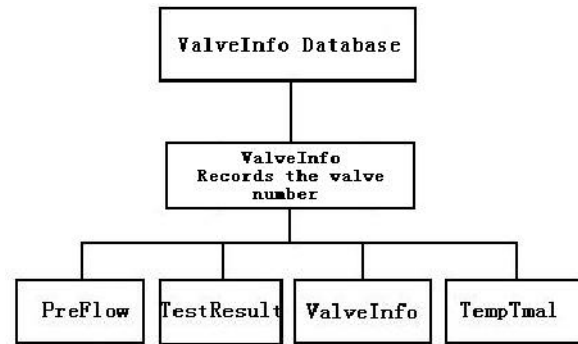


Fig.3 Block diagram of ValveInfo database

The whole system has ValveInfo and DriveCurve two databases.

ValveInfo database storage is the valve and valve parameter information from the four components of information table and gets across ValveIndex to connect an information table, as shown in Fig.3:

PreFlow information table includes the records of the valve number, time, ventricular pressure, atrial pressure, aortic flow.

TestResult information table includes the records of the valve number, test code number, simulated cardiac output, mean arterial pressure, differential pressure valve, the flow before the percentage of the risk, return flows, the percentage return, the average flow, flow RMS, the effective area.

ValveInfo information table is includes the records of the valve number, the valve factory, valve type selection, types of valves, valve diameter, the testing date, testing, inspection units, the proportion of valve type selection, valve type, experimental liquid, valve models.

TempTmal information, provisional data storage table, can be transferred directly from table data to other data window to show. DriveCurve database storage is the information of motor drive waveform from a DriveCurve information table composition, including waveform code, the creation date, time, Remarks, 10 CurvePoint records the location of the point. After database has been designed, firstly, an empty Access database is established and then ODBC connections are set up, intitle a name pointing at the mdb file, and then ERStudio will introduce table structure, and generate database.

C. Report Design

Crystal Report is used to design report forms [10].

Items in printed report forms include the cover and the overall detection information, PG, percentage of reflux effective area, the cardiac output corresponding to the valve parameters.

Statements show to be standardized formula, so report design needs to use formula field VB syntax creating self-defined formats. Code as follows:

```
formula = CStr({temp. Data}, "##0.0") + "±" +
CStr({temp. Deviation values}, "0.0")
```

After the layout of report forms in accomplished, the data source for citation should be added. The database information table used in the report forms should be chosen, updated dynamically. Finally, we can view the report forms and its effectiveness. Dynamic Database Connection updated code:

```
Report.DiscardSavedData
Rport.Database.SetDataSource
frmRport.datWhichValve.Recordset, 3, 1
```

D. Examples

Measurement of artificial valve, the first step of measurement is to input valve information, to set drive curves, and to calibrate the sensor completely. Then the systems begin to work and detect the relevant parameters of biological valve. Then, the test report will be printed.

IV. ANALYSIS OF THE RESULTS

(1)The original design takes the advantage of DMA (direct memory access) capabilities in acquisition card, which can provide the efficient use of CPU, so as to achieve both data access and analysis management in parallel. But then the PCI-9112 board set up only in the same analog input mode, which are imported for unipolar or bipolar input can use DMA function. This restriction and pressure in the system is only unipolar signal input, and aortic flow is bipolar input. Therefore, the design does not work.

Finally it was decided to switch to the internal timer trigger way, under such condition sampling and data analysis processing are carried out in sequence, although this method is slower than using DMA function, but there is no limit for physiological signal and acquisition speed is sufficient. It also overcomes the sampling errors and sampling failure problems often happened before improvement..

(2)The original design takes the advantage of DAO (Data Access Object) Operating database, but because the restrictions of DAO version, there is an issue of compatibility under different Windows operating systems. So we switch to use ADO object via ODBC visit and the scalability is very good.

Addition of Data Environment, as a container, which could be used to place various well-designed reports Using its drag-and-drop function, designers can move the report

from Data Environment to the designated forms. On the one hand, this gives easy-to-use visual environment, and it also provides uniformity of programming interface.

As the use of the WindowsXP operating system, it resolves the compatibility issues of operating system occurred before upgrade, there is no longer dead operation usually happened and failure to access to.

(3)After the on-line debugger, the parameters, such as return flow and reflux percentage, are quite different from previous standard parameters.

After checking formula, analytical procedures, calibration board, no problems are found ultimately. Subsequently by comparison of standard parameters, it is obvious that the value from formula for calculating the flow sampling is not the cumulative value of a cardiac cycle back flow sample, but a cardiac cycle flow sampling prior to the end of 20 cumulative value of the sample. Therefore, the main reason making variance is the ignorance of small flow fluctuations during the closure of artificial valve.

After revision of the scope of sampling cumulative value in the formula, the value measured is basically consistent with the standard parameters. These improvements increase the reliability and repeatability of parameters, Greater difference between the test results and data fluctuation phenomena no longer happens.

(4)System uses graphics RADEON 9200SE, off-the PC-CPU and memory space, the occupancy rate of the CPU released and the system's data processing capabilities improved for further improvement of control systems.

(5)Systemic use of Crystal report, it realizes the printing of detection report of, including the current pages show and pages of print storage, preview function for printing. On the printed page, it contains not only the records of all system parameters, as well as some of the waveform parameters, it also contains the relevant information to ensure the integrity of the information.

After upgrade of the system, Crystal statements are used as development tools, which can be derived complex interactive charts, together with other controls in the WebForm use, and can be dynamically statements derived a variety of formats (such as: pdf, doc, xls, html), as well as reserve escalated again after a lot of space.

V. SUMMARY

The control system of artificial heart valve pulsing flow detector makes use of WindowsXP platform with VB6.0 programming and Access2000 database. Experimental operation of the test system shows that it has strong compatibility, easy operation and maintenance, testing stability and good reproducibility. All these features lay a solid technical

foundation of hardware and software for further in-depth study and constantly improvement of the system.

REFERENCES

1. XI Baoshu (1986) Artificial heart valve detection technology information. Biomechanical Research Center of Tsinghua University, Beijing
2. WANG Jianyu, TANG Jinlong (2004) Artificial valve hemodynamics in experimental research. Chinese Journal of Traditional Chinese and Western Medicine. 15 (5) : 1544-1545
3. ADLink, PCI-9112 Datasheet at www.adlink.com
4. ADLink, PCI-9112 User's Guide at www.adlink.com
5. Advantech, PCLD-880 Datasheet at www.advantech.com
6. JIANG Tiehai (2003) ADO database access controls on the various skills. Micro-Computer Information. 19(1): 65-66
7. CHEN Xuedong, CHANG Dan (2005) Visual Basic 6.0 Programming Guide. Tsinghua University Press, Beijing
8. ADLink, PCIS-DASK User's Guide at www.adlink.com
9. ADLink, PCIS-DASK Function Reference Manual at www.adlink.com
10. CR Advanced, Crystal Reports User's Guide at www.china.businessobjects.com

Author: LU Cheng
 Institute: School of Traffic and Transportation, Beijing Jiaotong University
 City: Beijing
 Country: China
 Email: laguna33@sohu.com

Wireless monitoring system via ZigBee in ICUs

Shaojie Lin, Qiong Liu, Xiaoming Wu, Shanglin Li and Zhicong Zhao

South China University of Technology, Guangzhou, China, 510006

Abstract — In modern ICU (Intensive Care Unit), many operations on patients are hampered by the attached monitoring and treatment equipments, which obstructs nursing staff and hinders the patients from moving freely. Fortunately, wireless transfusion controlling and monitoring network not only aids physicians and nurses in providing convenient treatments and comforts to the patient but also regulates the model of therapy based on the physiologic parameters. The paper presents a wireless monitoring system via ZigBee, including sensor and radio frequency miniature modules, wireless BSNs, wireless transfusion devices, base stations, and centre server. An experiment that the patients were monitored (including ECG-II, pulse wave, SpO₂ and respiration) and transfused continuously in 24 hours, demonstrates that the system is characterized as wireless, miniature, highly reliable, anti-jamming, low power consuming and intelligent. The advantages of the approaches utilized in our work - ZigBee wireless communication technology - break the traditional monitoring and transfusion pattern in ICU thus the quality and efficiency of medical treatment are improved.

Keywords — ZigBee, ICU, Monitoring, Network

I. INTRODUCTION

ICU (Intensive Care Unit) is an essential section where intensive patients are monitored and transfused. The most concern of staff is whether or not the current status critical to patients' lives. APACHEIII is the most popular and authoritative illness intensiveness evaluation system [1]. The system evaluates the patient's condition according to current physiologic parameters, age, and medical record. The patient's condition is determined by several significant parameters, such as heart rate, blood pressure, respiration rate, body temperature, and blood routine.

In modern ICU, many operations on patients are hampered by the attached monitoring and treatment equipments, which obstructs nursing staff and hinders the patients from moving freely. However, rapidly developed wireless technologies are expected to solve these problems. We have constructed miniature and low-cost BSN (body sensors network) using ZigBee - a simple, low power consumption and low-delay wireless technology [2] - to reduce the number of cables, which aids physicians and nurses in providing convenient treatments and comforts to the patient. In addition, the monitoring system obtains the physiologic param-

eters from the patient via the BSNs and regulates the model of therapy based on a closed-loop controlling mechanism of transfusion. The staff can easily and more effectively control the process, and implement integrative therapy more safely.

II. MATERIALS AND METHODS

The system is consisted of wireless BSNs, wireless transfusion devices, bedside base station, and centre server, as shown in Fig. 1.

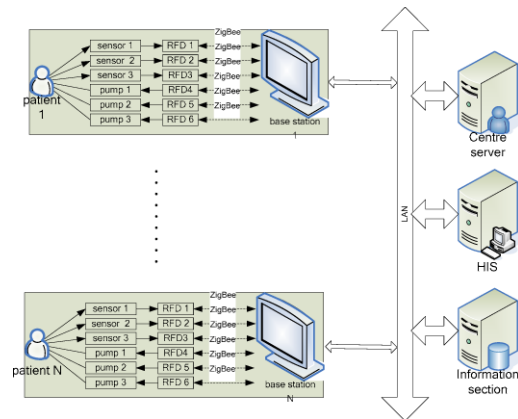


Fig. 1 The frame of system

A. Miniature sensor modules

As the feelers of the BSN, the miniature ECG (electrocardiogram), SpO₂ (oxygen saturation), pulse wave, impedance pneumograph and temperature modules are assigned to detect many fundamental physiologic parameters. Since the signals collected from the sensing units are weak and immersed by noises, they are amplified, denoised and isolated by the preprocessing modules. And then, these analog signals are converted into digital data with 12-bit resolution by the analog/digital conversion in CC2430—main RF chip, made by Chipcon Corporation. Timer 1 controls the sam-

pling rate (250 samples per second). The RF (radio frequency) transceiver of CC2430 sends the data above to the coordinator (COORD) of the BSN.

B. WSN based on ZigBee

ZigBee is a short distance wireless communication technology under united standard. Its PHY layer and MAC layer protocol is constituted by IEEE 802.15.4 while its network layer is established by ZigBee alliance. Most important of all, application layer can be developed according to users' demand [3]. Working at free ISM (Industrial, Scientific and Medical) band 2.4 GHz, the network is divided into 16 channels. The available communication distance is from 30 to 70 meters. The transmitting speed is 250 kilo bits per second, but the power of emission is only 3.6dBm at most. All above parameters of the network can accommodate the condition of ICU.

An attractive option is CC2430 which is an excellent micro control unit embedded 8051 core. It integrates micro controller, radio frequency, and analog/digital conversion together in the chip. We chose ZigBee™-subset/IEEE 802.15.4™ Multi-platform Protocol Stack, exploited by Mississippi State University, in the microchip stack.

The network structure in ICU is relatively steady since data are only transmitted between the RFDs (Restrict Function Devices, connected to the sensors and transfusion devices) and the COORDs. Thus the star topology, which has great efficiency as well as easy establishment, is the best choice. In the network, the IEEE address of every node is distributed uniquely and the short address of the destination endpoint is specific, therefore, the system uses static PAN IDs and direct message mode to prevent from network conflict. Further more, in consider of the flexibility of the network, `aplRejoinNetwork()` function is used to enhance its reliability and maintenance.

At first, the management entity of coordinator scans available channel [4]. If it successes, and then chooses a PAN ID to form a new network. After that, every RFD resets the MAC layer, scans channel, chooses PAN ID, and requests linking. Getting the response of COORD, they join the network successfully. Now all the sensors and transfusion devices start to run. Moreover, we establish a long address to short address map mechanism; hence all the data transmitting uses the 16 bits but not 64 bits in the network to improve its efficiency and performance.

Theoretically speaking, the transmitting speed of ZigBee is 250 kilo bits per second. Actually, if it transmits 1 byte data it should adds about 50 bytes excess frame information. Even working on non-ACK mode, it spends at least 5 milliseconds in sending and receiving. Fortunately, FIFO (first in first out) buffer technology can solve above headache.

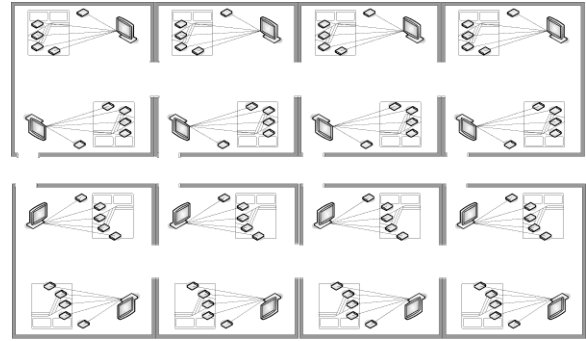


Fig. 2 The multi-networks in ICU

Every RFD buffers the sampling data until it is commanded to send them to COORD. At the same time, COORD sends command to every RFD every four interrupts (16 milliseconds). Due to the tradeoff between real-time data and efficient network, buffer technology accelerates the effective speed.

Specially, there are several relative self-existent networks in relative limit space (see Fig.2). Consequently, the coordination is significant among several networks. Although ZigBee has 16 channels, every channel is fully loaded. This means that there are only 16 BSNs at most in ICU. Additionally, assigning static PAN IDs and different channels is necessary, which ensures each network is in possession of a unique PAN ID and channel, and avoids network conflict with each other.

To guarantee data integrity, FCS (frame check sequence) is used in MAC layer. FCS is a 16 bits sequence which has strong ability of verifying data. It can detect below errors: less than 3 errors in any position, all the odd number of errors, less than 16 bits continuous errors, and most of mass of paroxysmal errors. Checking out the integrality of the data, FCS can execute advanced physical error control. On the one hand, the sender calculates the sequence number according to all bits of one frame. On the other hand, the receiver also calculates the sequence number according the same frame based on the same algorithm and compares the sequence number from the sender with that from the receiver.

Involving in wireless transfusion, the safety of network is vital. To keep from baleful incursion, the system is armed with network safety services based on the link layer key and network layer key. Setting the property of PIB (PAN Information Base) can provide the network with safety services. Meanwhile, COORD verifies the RFD to prevent illegal access. Thus, the system could furnish the patients with secure transfusion control.

C. Bedside base station

The bedside base station assembles more than ten wireless sensors and transfusion devices so the treatment based on close-loop control is available by integrating the therapy and its response [5]. It is responsible for not only monitoring and alarming but also controlling several transfusion devices wirelessly. Further more, it grades the state of the patient in terms of other biochemistry parameters and information. The bedside base station provides an integrative management of monitor and transfusion data with patients and connects to the centre server.

D. Centre server

Located in the ICU workroom, the centre server connects several bedside base stations together so that nurses can monitor the condition of all patients simultaneously. Also, it manages patients' information and integrates into the HIS (hospital information system) [6].

III. RESULTS

To evaluate the system, the centre server supervises 10 bedside base stations and each bedside base station monitors one patient who carries 5 to 8 wireless pumps. Four physiologic parameters of each patient, including ECG-II, pulse wave, respiration and SpO₂, are collected by every BSN.

In the experiment, the patients were monitored and transfused continuously in 24 hours, which demonstrates that the effect of close-loop transfusion could fulfill the physicians' requirement thus the reliability of the system is accessible.

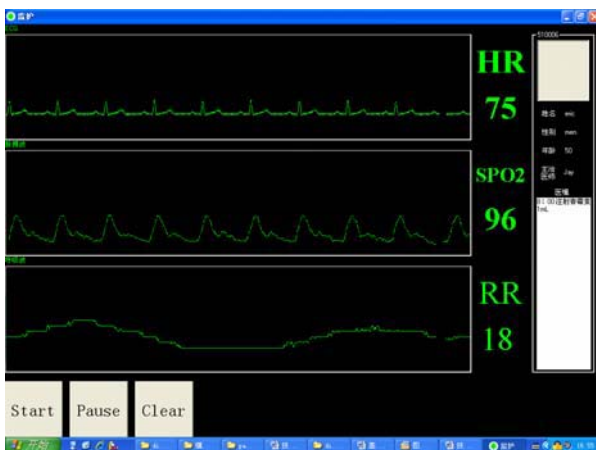


Fig. 3 The platform of bedside base station

Moreover, the BSNs were merely interfered by the therapy devices in ICU and consequently the wireless networks have good anti-jamming performance.

IV. DISCUSSION

Our study turns out that the high reliability, anti-jamming, and low power consuming of this system is evident. The wireless network, which connects the body sensors, bedside base station and transfusion pump together, makes it preferable for staff to implement the operation along with easy-wearing sensors for patients. The system, characterized by wireless, miniature, and intelligent, is a united network that fulfills the clinical requirements and would have a considerable importance in the ICU.

V. CONCLUSIONS

The advantages of the approaches utilized in our work - ZigBee wireless communication technology - break the traditional monitoring and transfusion pattern in ICU thus the quality and efficiency of medical treatment are improved. Our accomplishments are paving the way under the public sanitation calls for wireless monitoring and transfusion controlling. The further work is to make it into a practical component in modern ICUs.

ACKNOWLEDGMENT

This work is supported by Guangdong Province Science and Technology Plan (2007B031302003, 2007B010400055 and 2004B10401012). We are grateful to Guangdong Province Science and Technology Department.

REFERENCES

1. Knaus WA, Wagner DP, Draper EA, et al. (1991) The APACHE III prognostic system: Risk prediction of hospital mortality for critically ill hospitalized adults. *Chest* 100:1619-1639
2. Lei Qu, Shengde Liu, Xiangbin Hu. (2007) Technology and application of ZigBee. Beijing University of Aeronautics & Astronautics, Beijing
3. Ting Jiang, Chenglin Zhao. (2006) Technology and application of ZigBee. Beijing University of Post and Telecommunication, Beijing
4. Yongzheng Li, Fei Gao, Xiaoming Wu. (2008) A wearable multi-parameter WPAN based on ZigBee. *Control & Automation*

5. Dudde, R. Thomas Vering Piechotta, G. Hintsche, R. (2005) Computer aided continuous drug infusion-setup and test of a mobile closed loop system for the continuous automated infusion of insulin. The IEEE Transactions on Information Technology in Biomedicine. 2005, pp 395-402.
6. Kai Wu, Xiaoming Wu. (2006) The Design and Implementation of Multiple Physiological Parameter Remote Virtual Measurement Instrument. Control & Automation 1-1:145

Corresponding Author:

Author: Xiaoming Wu
Institute: Department of Biomedical Engineering
Street: South China University of Technology (The South Campus)
City: Guangzhou
Country: China
Email: bmxmwus@scut.edu.cn

Largest Lyapunov index of EHRV for analyzing status of cardiovascular system

Xia Li, Tianliang Kang, Jinghua Liu, Xin Tian

Capital medical university, School of Biomedical engineering
(xlee313@yahoo.com.cn)

Abstract — This paper mainly studied exercise heart rate variability (EHRV) which was extracted by exercise electrogram (EECG) recorded during step exercise test. Largest Lyapunov index (LLI) was calculated from EHRV to analysis two groups of hypertensives and controls. The whole exercise duration was divided to three stages, namely pre exercise stage (PES), exercise stage (ES) and after exercise stage (AES). And LLI was calculated in three durations respectively. All the indexes were analyzed with statistics, LLI of AES was found to be significantly different between hypertensives and controls, and as an effective parameter, it could be used to reflect the status of cardiovascular system.

Keywords — Exercise heart rate variability, Largest Lyapunov index, hypertensive

I. INTRODUCTION

Cardiovascular diseases are increasing all around the world and impair people's health seriously. Assessment on function status of cardiovascular system in early age is very important for prevention. Studies discovered that R-R interval contained abundant information of cardiovascular. In clinic, exercise test is one of the most common methods to detect coronary heart disease and myocardial ischemia, which could be used to assess cardiac function and degree of myocardial ischemia by change of characteristic parameters extracted from exercise ECG.

Heart rate variability (HRV) analysis is an important non-invasive method to study many kinds of cardiovascular diseases^[1,2]. Most of HRV data are from MIT-BIH standard ECG database, which were generally processed and analyzed in time domain and frequency domain.

HRV data includes short HRV and long HRV which is distinguished by the length of recording time. Short exercise HRV was analyzed in this paper.

Non-linear methods were well developed during last four decade years, which bring a new prospect to signal processing. Studies discovered cardiovascular system behaved with non-linear characters^[3]. Different non-linear parameters were extracted to obtain effective information covered in cardiovascular system^[4,5], such as complexity, approximate entropy, Lyapunov exponent, poincare plot, dimension, etc.

This paper mainly studied Exercise ECG (EECG) which was recorded by physiological multi-parameter monitor

developed by Tsinghua university. Lyapunov index was extracted from EHRV and analyzed to study status of cardiovascular system in hypersensitive group and control group.

II. METHODOLOGY AND DATA PROCESSING

Step exercise was adopted to obtain exercise ECG of test subject. Duration of the whole test is about 11 minutes, including 5 minutes of rest stage before exercise, 1 minute of exercise stage, and 5 minutes of rest stage after exercise. Exercise HRV (EHVR) was extracted by preprocessing ECG recorded with wavelet transform. Here Daubechies wavelet *db5* was adopted to decompose $RR(t)$ into 5 levels. Then the approximate component $c(t)$ was reconstructed as exercise heart rate respondent (EHRR) signal including VLF component of $RR(t)$, while the detail component $d(t)$ was reconstructed as exercise heart rate variability (EHRV) signal which includes LF and HF components of $RR(t)$.

Lyapunov index measures regular degree of a system from dynamics^[6,7]. It represents the average exponent rate of convergence or divergence between neighbor tracks in phase space. One n-dimension dynamics system corresponds to n Lyapunov indexes, and among them the largest one is called largest lyapunov index. If largest lyapunov index is above zero, the system is judged to be in chaos status.

There are some inevitable disadvantages in conventional algorithm to calculate Largest Lyapunov exponent, including: it depends on the length of data; it sensitively lies on inset dimension and time delay; it takes too much time for calculation. In 1993, to improve the conventional algorithm based on orbit idea and track method, Rosenstein and etc^[8] presented small data method to calculate Largest Lyapunov exponent. This method has several advantages such as fast operation, easily implementation, and shows strong robust to insert dimension, time delay and size of data. In this paper, this method was adopted to calculate the LLI of EHRV.

We chose two groups of test subjects, namely 42 elder hypertensives as group A and 87 young healthy people as group B. The LLI of three stages of exercise test was calculated respectively. Results are shown in table 1 as follows.

Table 1 LLI of EHRV

	λ_1 of EHRV in PES	λ_1 of EHRV in ES	λ_1 of EHRV in AES
Control group	0.165+0.0165	0.118+0.0127	0.1495+0.0241
Hypertensive group	0.172+0.037	0.116+0.0157	0.171+0.0340
P	0.486424	0.466292	0.000368

III. CONCLUSION

Results showed the LLIs from three stages of EHRV were all above zero, and this validated the non-linear dynamics really exist in cardiovascular system.

LLI of EHRV in PES and ES were not significantly different, while LLI of EHRV in AES had significant difference between hypersentive group and control group. This indicated more valuable information could be contained in physiological signals after exercise. That is, exercise could induce subject’s modulation of cardiovascular system to stress status, so LLI could reflect the physiological modulated capability of a test subject. The LLI of AES could be used to classify hypertensives and healthy people, as well as to reflect status of cardiovascular system. Further work is necessary to do for studying how LLI reflects real status of cardiovascular system.

ACKNOWLEDGEMENT

This work was supported by Beijing municipal education commission. The data was supplied by Baijing Laboratory, department of biomedical engineering, Tsinghua University.

REFERENCES

1. Mercedes R. Carnethon, Ronald J. Prineas, MD, et al (2006), The Association Among Autonomic Nervous System Function, Incident Diabetes, and Intervention Arm in the Diabetes Prevention Program, *Diabetes Care*. 29(4): 914-919
2. Rollin McCraty, William A. Tiller, and Mike Atkinson (1996), Cardiac Coherence: A New, Noninvasive Measure of Autonomic Nervous System Order, *Alternative Therapies in Health and Medicine*. 2(1): 52-65
3. G Krstacic and A Krstacic et al (2002), Non-linear Analysis of Heart Rate Variability in Patients with Coronary Heart Disease, *Computer in Cardiology*, 29:673-675
4. Laitio TT, Huikuri HV, Kentala ES, et al (2000), Correlation properties and complexity of perioperative RR-interval dynamics in coronary artery bypass surgery patients, *Anesthesiology*, 93(1):69-80
5. Krstacic G, Krstacic A, Smalcelj A, et al (2007), The "Chaos Theory" and nonlinear dynamics in heart rate variability analysis: does it work in short-time series in patients with coronary heart disease?, *Ann Noninvasive Electrocardiol*, 12(2):130-6
6. GuillenP ,Vallverdu M ,Jugo D,et al (2000).Non-linear dynamics in heart rate variability of normal subjects and chagasic patients. *IEEE*. 4 : 2414-2415
7. Signorini M.G, Cerutf S (1994). Lyapunov exponents calculated from heart rate variability time series .*IEEE*. 1 : 119-120
8. M.T.Rosenstein, J.J.Collins and C.J.De luca (1993). A practical method for calculating largest Lyapunov exponents from small data sets, *Physica D*, 65: 117-134

Author: Li Xia
 Institute: Capital Medical University
 Street: No.10 xitoutiao,You’anmen wai
 City: Beijing
 Country: China

Wavelet transform for on-off switching BCI device

C.S. Li and H. Wang

Northeastern University, Shenyang, China

Abstract — This paper introduces a new kind of EEG-based Brain-Computer Interface Device (NEU BCI-II) that permits a person to switch on and off electrical appliance based on wavelet decomposition. The device was developed due to the increases of the alpha component amplitude of EEG spectrum when people close their eyes. The device detects the EEG difference between opening eyes and closing, which makes the electrical appliance be on or off. The system adopts wavelet decomposition to separate the different alpha activity conditions. In NEU BCI-II Device, LabVIEW software and embedded MATLAB scripts are used to analyze EEG signal online. Compared with other spectrum method, wavelet method shows its merits in suppressing noise and improving reliability.

Keywords — Electroencephalograph(EEG), Brain-Computer Interface(BCI), Wavelet Transform, Eye Closure.

I. INTRODUCTION

It is well-known that alpha activity in the EEG is dominant in normal individuals during an eyes-closed resting condition, and is suppressed with visual stimulation. This was first reported in the 1930s when several researchers exposed participants to light and noted decreases in occipital alpha activity [1]. Some other studies also showed that the decrease of alpha activity was most pronounced in posterior regions when individuals opened their eyes [2]. Although the underlying mechanisms remain unclear [3], alpha desynchronization to visual input is generally considered to reflect increased functional innervation of the visual system, which activates the entire cortex. Recently the differences between eyes-closed and eyes-open under resting condition have been reported [4].

The research of brain-computer interfaces (BCIs), which aim to provide their users communication and control capabilities that do not depend on the brain's normal output channels of peripheral nerves and muscles, arouses more and more interests of late years[5, 6]. Present-day BCIs determine the intent of the user from a variety of different electrophysiological signals. These signals include visual evoked potential (VEP), slow cortical potentials (SCP), P300 potentials, and mu or beta rhythms. Alpha rhythm has also been used to control environmental control system (ECS), and which shows useful to people with spinal cord injury [7]. One disadvantage is that using alpha activity as input signal depends on the voluntary movement of closing

and opening eyes. In fact this disadvantage also occurs in VEP BCI, which needs eye-ball movements. Since alpha rhythm is more prominent than mu and beta rhythms, there is less training process. It is believed that alpha activity occurs in a large percentage of the population during eye closure [8].

Wavelet decomposition is a multilevel bases wavelet transform. The decomposition process can be iterated, with successive approximations being decomposed in turn, so that one signal is broken down into many lower resolution components. This builds wavelet decomposition tree. Different basis will result in different classification performance. Due to the non-stationary property of EEG signals, traditional analysis methods are not very suitable for this work, such as fast Fourier transform (FFT). This device is based on the result that the energy in alpha rhythm frequency range (8-13Hz) will increase when eyes closed. The corresponding coefficients of wavelet decomposition were selected as feature to represent energy.

II. METHODS

A. System structure

Like other BCI devices [9], the NEU BCI-II device includes following four parts: analog signal acquisition, digitizing, feature extraction and transformation algorithm. It is shown in Fig. 1.

The analog signal acquisition part includes three amplifiers and a low-pass filter. The gains of amplifiers are 20dB, 46dB, 20dB, hence the sum is 86dB. The cut-off frequency of low-pass filter is 30Hz. The National Instrument USB-6008 is used as digitizer, and its sample rate is set at 200Hz. The digitizer buffer is read every half a second, and then

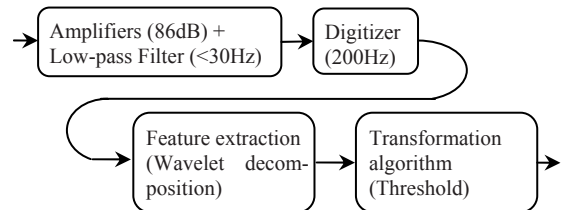


Fig. 1 System structure

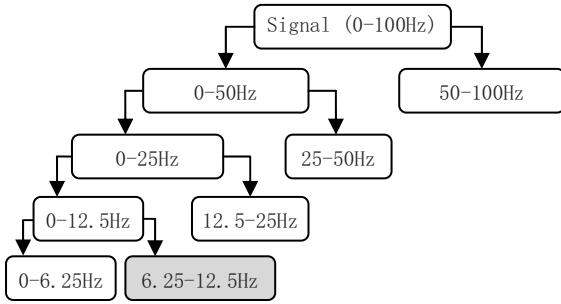


Fig. 2 Coefficients corresponding to frequency

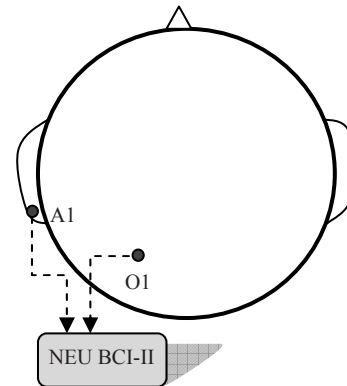


Fig. 3 Electrodes configuration

100 points are acquired. The feature extraction and transformation algorithm are implemented in LabVIEW framework. The MATLAB scripts node is also used in LabVIEW, and wavelet decomposition functions are called. By calculating corresponding coefficients, we obtain the energy of alpha rhythm.

The alpha rhythm frequency is between 8 and 13 Hz normally, and the sample rate is 200Hz. So we choose Daubechies wavelet to do 4-level decomposition. The corresponding frequencies are shown in Fig. 2.

In NEU BCI-II device, the 6.25-12.5Hz coefficients are used. And the energy is calculated by the following formula:

$$E_j = 1/N \sum_k d_j^2(k)$$

Where E_j is the energy of decomposition level j, k is the index of coefficients in level j.

B. EEG signal detection

Two silver/silver chloride electrodes configured in differential mode are pressed against the scalp (O1, international 10-20) and left earlobe, which is shown by Fig. 3. The earlobe electrode works as a reference point. The signal is acquired and analyzed, and then saved for offline analysis.

Firstly, participants will take a training period lasting 30 seconds. In this period the participants are asked to keep their eyes open 15 seconds and close 15 seconds under operator’s instruction. These training signals are used to generate the threshold for following automatic analysis. There are two thresholds (thr1 and thr2), thr1 is calculated from 6.25-12.5Hz range, and thr2 is calculated from 25-50Hz range. If thr1 was exceeded, and thr2 was not exceeded in respective spectrum range, the device switches its status, i.e., on to off or off to on. If thr2 is exceeded by corresponding energy, the device turns into deaf mode. In

the following 2 seconds the device will not react to any input.

When device turns into deaf mode, the user interface of device will light a red LED to prompt participants. When device switches its status, it pronounces a short voice to prompt participants.

Two healthy people took part in this experiment, the on-line results were registered, and the original EEG data was saved for later offline analysis.

III. RESULTS

In order to evaluate the performance of the device, we choose false positive and false negative as criterion. False positive refers to unintentional activation during opening eyes. False negative refers to activation during closing eyes uninterrupted.

The difference of energy in corresponding range of frequency is described in Fig. 4. It shows that the energy in alpha rhythm (from 0.13 to 0.54) increases obviously, while 25-50Hz takes less change.

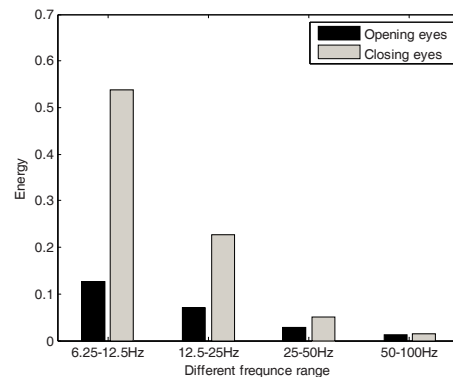


Fig. 4 Variance of energy in opening eyes and closing eyes

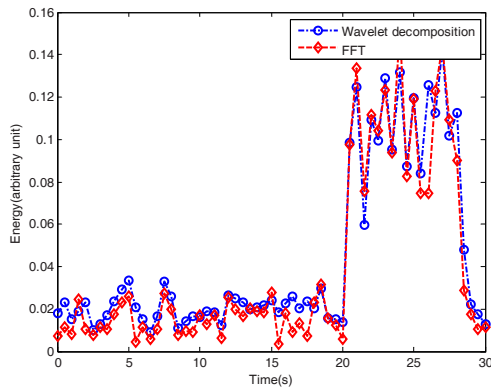


Fig. 5 Wavelet decomposition analysis comparing with FFT method

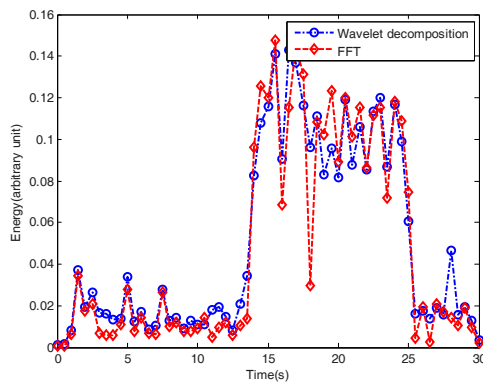


Fig. 6 Wavelet decomposition analysis comparing with FFT method

The results obtained by Wavelet decomposition and FFT are compared in Fig. 5. It shows that FFT result is close to wavelet result in the variance of energy and onset of alpha activity.

But there are some exceptions, such as Fig. 6 shows large variation of energy obtained by FFT method when eyes closed, which causes more false negatives registered in offline analysis by FFT method.

Some studies [10] have analyzed onset of alpha activity by using peak detection and FFT methods. Our method provides a more flexible real-time solution to analyze onset of alpha activity.

IV. CONCLUSIONS

The NEU BCI-II is introduced by using wavelet decomposition method. We also compare it with spectrum analysis method, and obtain lower false negative counts. It is neces-

sary to advance its classification method instead of using thresholds. Some novel classification methods, such as neural network, can be used to get more prominent results. At present, each participant needs a training period, 30s now and sometimes longer, to determine the thresholds, which also needs to be optimized. There exists some non-linear method to classify different alpha activity status without training. When this device is used by severe disabled people, this feature will be more necessary. By using 25-50Hz range as additional information, the device suppresses lots of interference.

ACKNOWLEDGMENT

This work was supported by National Science Foundation of China (50435040).

REFERENCES

- Berger H. (1933) Uber das Elektroencephalogramm des Menschen. Arch F Psychiat 98:231-254
- Chapman RM, Armington JC, Bragdon HR. (1962) A quantitative survey of kappa and alpha EEG activity. Electroencephalogr Clin Neurophysiol 14:858-868
- Fisch BJ. (1999) Fisch and Spehlmann's EEG primer : basic principles of digital and analog EEG. Elsevier, Amsterdam
- Barry RJ, Clarke AR, Johnstone SJ et al. (2007) EEG differences between eyes-closed and eyes-open resting conditions. Clin Neurophysiol 118:2765-2773
- Wolpaw JR, Birbaumer N, McFarland DJ et al. (2002) Brain-computer interfaces for communication and control. Clin Neurophysiol 113:767-791
- Wolpaw JR, Birbaumer N, Heetderks WJ et al. (2000) Brain-computer interface technology: a review of the first international meeting. IEEE Trans Rehabil Eng 8:164-173
- Geddes LA, Baker LE. (1989) Principles of Applied Biomedical Instrumentation 3rd edn. Wiley, New York
- Craig A, Tran Y, Craig D et al. (2005) Improving correct switching rates in a 'hands-free' environmental control system. J Neural Eng 2:L9-L13
- Schalk G, McFarland DJ, Hinterberger T et al. (2004) BCI2000: a general-purpose brain-computer interface (BCI) system. IEEE Trans Biomed Eng 51:1034-1043
- Kirkup L, Searle A, Craig A et al. (1998) Three methods compared for detecting the onset of alpha wave synchronization following eye closure. Physiol Meas 19:213-224

Author: Hong Wang
 Institute: Northeastern University
 Street: No. 3-11, Wenhua Road, Heping District
 City: Shenyang
 Country: China
 Email: hgwang@mail.neu.edu.cn

Optimization of the Coil to Focalize the Electrical Field Induced by Magnetic Stimulation in the Human Brain

Lina Pu, Tao Yin, Hao An, Song Li, Zhipeng Liu*

Institute of Biomedical Engineering Chinese Academy of Medical Sciences
Peking Union Medical College, Tianjin, China

Abstract — The design of the magnetic stimulating coil is one of the key technique in the magnetic stimulating system, it is the hotspot in the research of magnetic stimulation. A coefficient to evaluate the focus of the electrical field intensity induced by magnetic stimulation is firstly presented in this study, which was used as an index of focus, Matlab was used as the tool to simulate the distribution of induced electrical field, result is obtained that the four-leaf rose shape coil is the best compared with other five different shapes of coil. As a result of optimizing other parameters of the coil, the smaller radius of the coil is the better choice and the angle between four-leaf rose coil of 102° degree is better than other value. Furthermore, when the four-leaf coil with angle of 112° degree assembled with a coil of 89°, the more focused electrical field is obtained. The coefficient proposed in this study may be a guideline to the optimization of the coil's parameters.

Keywords — magnetic stimulating coil, focus, induced electrical field, comparing coefficient

I. INTRODUCTION

More and more researcher focused on the study of function and disease of nerve as the morbidity of spirituality disease mounted up continually. Magnetic field can excite nerve was found by d'Arsonval in a process of observing the magnetic flash phenomenal in 1896. The magnetic stimulation was used on human brain and achieved to stimulate the nerve centre by Baker in 1985^[1]. rTMS can be used to alleviate depression^[2], falling sickness and neural regeneration, so it has been a hotspot in the therapy of neuropathic disease. The magnetic stimulator system was composed of a capacitance, static switches and a coil. An instant strong current passed the coil while the coil was placed over the prefrontal cortex to stimulate the related point^[3,4]. As

shown in the Figure 1^[5], $\nabla \times E = \partial B / \partial t$ was got from Faraday's law. It means that electromagnetic field will be induced around the coil which was passed a strong current. Then the nerve activity will be excited or restrained because electrophysiology activity in the cortex was changed by the induced electrical field.

The stimulator used in nerve stimulation was required to be more advanced, specially the design of the stimulating

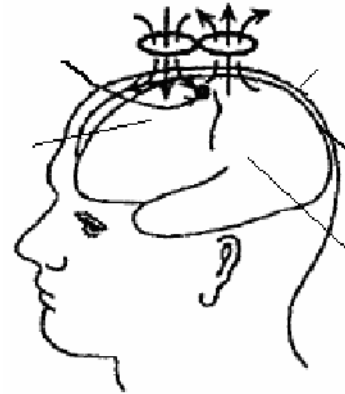


Fig.1 The simple model of hominine head

coil corresponding with the key technique in a stimulator system. When the magnetic stimulation was carried, the electrical field intensity is required to exceed the threshold stimulus intensity of nerve tissue, however the electrical field intensity in the non-stimulating field is required to be small enough to avoid excite the needless nerve tissue. The objective in this research is to improve the focus of the stimulating coil. Development of focus was made on some coil array^[6] and restrained coil^[7], therefore the coils were limited by complicated technical manipulation. Further more, the electrical field intensity attenuate and radiate when it penetrates the tissue, hence, the penetrability is required to be enhanced in the deep tissue. In this paper, a coefficient was presented to discuss the coil's focus and optimize the coil's shape and angle.

II. BUILDING MATHEMATIC MODEL AND IMITATION METHOD

A mathematiccal model [8-11] was built on the semi-infinite space here. As shown in Figure 2, following

Faraday's law: $\nabla \times E = \partial B / \partial t$, if the magnetical induction B in a medium was changing with time, an electrical field intensity E was induced. B and E can be determined in terms of a magnetical vector potential A and a scalar potential ϕ by

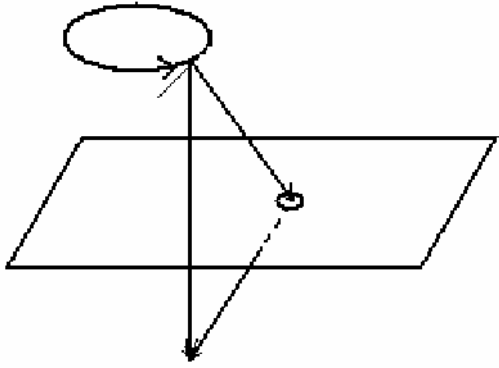


Fig.2 The vectorgraph of the semi-infinite space

$$B = \nabla \times A \tag{1}$$

$$E = -\frac{\partial A}{\partial t} - \nabla \phi = E_1 + E_2 \tag{2}$$

Here, we denote $E_1 = -\frac{\partial A}{\partial t}$, $E_2 = -\nabla \phi$.

To the arbitrary point P(x,y,z), r is the vector of current element, dl is the direction of the current element, current I passes the closed coil, the vector potential A has the following form for line sources along the closed path of the current:

$$A = \frac{\mu_0 I}{4\pi} \oint_L \frac{1}{r} dl \Rightarrow E_1 = -\frac{\partial A}{\partial t} = \frac{\partial I}{\partial t} \frac{\mu_0}{4\pi} \oint_L \frac{1}{r} dl \tag{3}$$

Here, $dl = dl_x \cdot i + dl_y \cdot j + dl_z \cdot k$, and

$$r = r_x \cdot i + r_y \cdot j + r_z \cdot k$$

Similarly, when the coil has an angle with the semi-infinite space, the scalar potential ϕ can be expressed in terms of the surface charge density q as following:

$$\phi = \frac{1}{4\pi\kappa\epsilon_0} \int \frac{q}{|r-r'|} dS \Rightarrow E_2 = -\nabla\phi = -\frac{1}{2\pi} \int \frac{(r-r')q}{|r-r'|^3} dS' \tag{4}$$

In the above formulas, μ_0 is free space permeability, ϵ_0 is the permittivity of free space, dS' is an area element in the air-tissue surface, r' is a vector to a position on the air-tissue surface. For a semi-infinite surface boundary, there is the following charge distribution: $q = -2\kappa\epsilon_0 \mathbf{n} \cdot \mathbf{E}_1$.

The component E_1 can be calculated from the mathematic model above. As shown in Figure 3, when the coil had a angle with the semi-infinite space, the single loop can be got and put in formula (4) to calculated E_2 . As an example of the positive half coil of the 8-figure, the

coordinate expression of arbitrary point Q on the coil that paralleled the semi-infinite space can be expressed as:

$$\begin{cases} x_0 = R(1 + \cos \alpha) ; \\ y_0 = R \sin \alpha ; \\ z_0 = 0 ; \end{cases} \tag{5}$$

When the coil has an angle of φ with the semi-infinite space, the coordinate expression of arbitrary point Q' can be expressed as follows:

$$\begin{cases} x_0 = R(1 + \cos \alpha) \cos \varphi ; \\ y_0 = R \sin \alpha ; \\ z_0 = R(1 + \cos \alpha) \sin \varphi ; \end{cases} \tag{6}$$

In this study, the calculation of the induced electrical field was very complex. The simulation tool of Matlab was used to calculate the electrical field induced by the stimulating coil.

The LCR discharge loop of the stimulator system satisfy

the equation $L \frac{d^2 q}{dt^2} + R \frac{dq}{dt} + \frac{q}{C} = 0$, the damp coefficient in this surge loop has the following form

$$\lambda = \frac{R}{2} \sqrt{\frac{C}{L}} \tag{7}$$

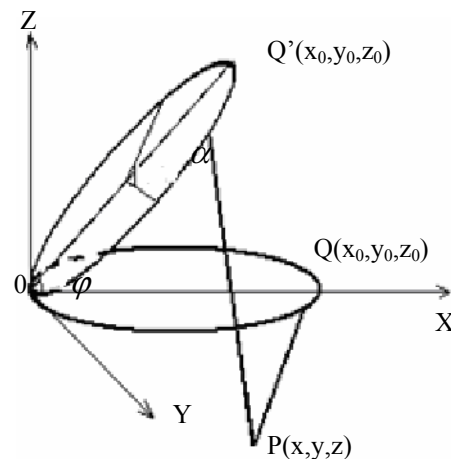


Fig. 3 The map of the coil not paralleled with the semi-infinite space.

Considering a great rate of discharge was needed, the damp coefficient should satisfy $\lambda \leq 1$, So

$$i = CU\omega_2 e^{-\omega_1 t} \left[\left(\frac{\omega_1}{\omega_2} \right)^2 + 1 \right] \sin(\omega_2 t) \quad (8)$$

In the equation (8), $\omega_2 = \sqrt{\frac{1}{LC} - \frac{R^2}{4L}}$.

Using the mathematic model above and the LCR circuit parameters in our laboratory (resistance R was 0.0786Ω, inductance L was 10.21μH, capacitance C was 2200μF, charge voltage U was 400V. The damp coefficient can be calculated to be $\lambda=0.5769$ from the equation (7). The dis-

charge and the rate of discharge (di/dt) were shown in Figure 4, and it was obvious that the maximum of the rate was $3.9178 \times 10^7 \text{A/s}$. In this study, the focus six types of coils shown in Figure 5 were simulated, and assumption was made that the circle of the coils were homology and the maximum of di/dt was 3.9178×10^7 .

III. COILS

The target position should locate the cerebral cortex according to the average thickness of scurf is 0.5-0.7 cm and skull is 0.5 cm, and the stimulating objective plane was supposed to have a distance of 1.3 cm under the coil's plane.

A. Attenuation and coefficient

The induced electric field (E) of y direction when the radii of coil (as shown in Figure 5(I)) was 2 cm and the stimulating depth was 1.3 cm. As shown in Figure 6, the maximum of E (E_{\max}) was under the point of the twain coil's intersection, and the negative peak value (E_{\min}) was under the point of x axis and the coil's intersection. E_{\max} was changed as shown in Figure 7(a) when the radii of the coil was changed from 0.5 cm to 4 cm. In Fig. 7(b), when the stimulating depth was changed from 0.5cm to 4cm. It was obvious that E_{\max} was changed when the depth and the radii of the coil was different. E_{\max} would be increased when the radii was increased in the case of the depth was immovably about 1.3 cm. E_{\max} will be decreased when the radii was changeless and the stimulating depth was increased.

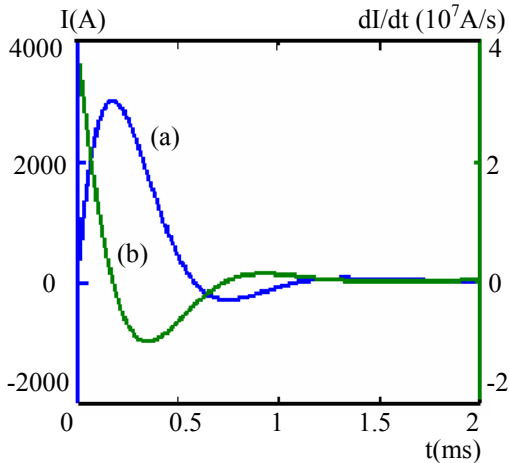


Fig. 4 In the state of underdamping, (a) the graph of the discharge current. (b) the graph of the rate of change of the discharge current.

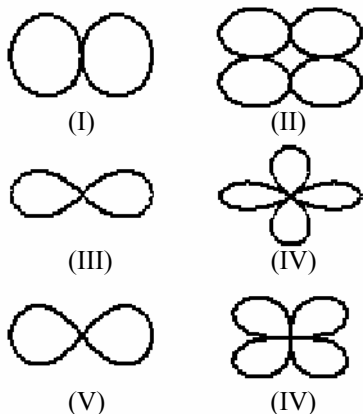


Fig. 5 The figure of six kind of coils, (I) two-Round, (II) four-Round, (III) two-leaf rose line, (IV) four-leaf Rose line, (V) two-Bernoulli line, (VI) four-Bernoulli line.

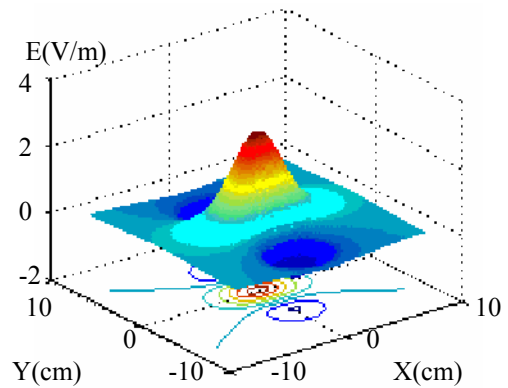


Fig. 6 The induced electric field of y direction when the radii of coil was 2cm and the depth of the stimulation.

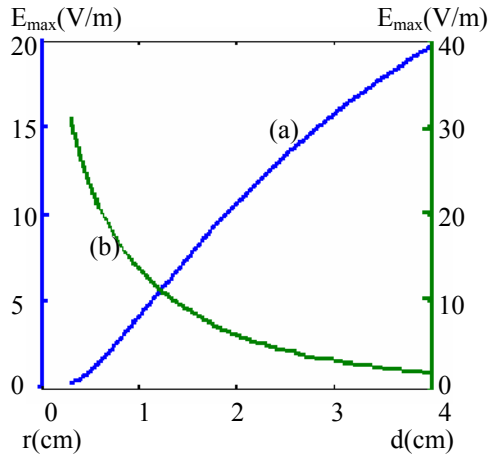


Fig. 7 The max. of the induced electric field as in Fig. 6 in different term,(a)when the radii of the coil was changed from 0.5cm to 4cm,(b)when the depth of the stimulation was changed from 0.5cm to 4cm.

E in the target position is required to reach stated stimulation intensity when it passed through scurf to target position. An idea of attenuation is presented here to study the E_{max} 's attenuation of different coil. The definition was as follows:

$$\eta = \frac{E_s - E_0}{E_s} \tag{9}$$

Here, E_s was the induced electric field of y direction in the scurf 0.2 cm away from the point of twain coil's interaction, E_0 was the maximal induced electric field of y direction in the target position. Attenuation has a direct ratio with the difference of E_s and E_0 and has an inverse ratio with E_s . Therefore, rational coil's parameters help to reduce attenuation will be beneficial to attain perfect stimulation intensity at the depth of target position.

As shown in Figure 7(a), the bigger coil obtained a

smaller attenuation and a stronger E_{max} , and the half-breadth (B_h) is larger. Here, B_h was the breadth between E_{max} and the half of E_{max} . The stimulation area would be increased with B_h , hence, the smaller B_h the worse focus. Here, B_{h1} was denoted as the half-breadth of x direction and B_{h2} of y direction, then the product of B_{h1} and B_{h2} was taken as the stimulation area. In addition, some unwanted stimulation are produced in the non-target area because of the negative peak value. The best parameters of the coil are required to get appropriate attenuation, B_h and the contrast of E_{max} and E_{min} (E_{max}/E_{min}), therefore the comparing coefficient ξ was defined as follows:

$$\xi = \frac{\eta B_{h1} B_{h2} |E_{min}|}{\alpha^2 E_{max}} \tag{10}$$

In the equation (10), ξ had a direct ratio with the attenuation and stimulating area, and a inverse ratio with $E_{max} / |E_{min}|$. The smaller attenuation and the smaller stimulating area, the better focus of the coil may be obtained. Here, E_{min} was defined to be the induced electrical field under the point of the twain-coil's intersection. $E_{max} / |E_{min}|$ was represented the variety gradient when the induced electrical field in the range of diameter. The greater $E_{max} / |E_{min}|$, the quicker E changed and the smaller the functionary area to get the better focus. As a result the smaller comparing coefficient is corresponding to the better focus.

B. Comparing the shape of the coils

Using the mathematic model and the equations (9) and (10), the coils' (as shown in Fig. 5) E of y direction along x axis and y axis was shown in Figure 8.

The parameters of the six coils, such as E_{max} , B_h , attenuation and comparing coefficient were showed in the Table 1.

Table 1 The parameters of different kinds of coils

parameters \ Coil's shape	2-round coil	2-rose coil	2-Bernoulli line	4-rose coil	4-round coil	4-Bernoulli line
η	0.7158	0.7372	0.7158	0.7372	0.4188	0.7158
E_{max}	10.6410	6.1930	7.5243	8.7592	13.0548	10.6410
E_{min}	-4.0425	-2.6969	-3.2397	-2.1746	-4.1450	-2.8868
B_{h1}	1.50	1.60	1.65	1.15	1.65	1.25
B_{h2}	2.35	1.90	2.00	3.20	4.15	3.30
$\xi = \frac{\eta B_{h1} B_{h2} E_{min} }{\alpha^2 E_{max}}$	0.9586	0.9759	1.0171	0.6736	0.9364	0.8010

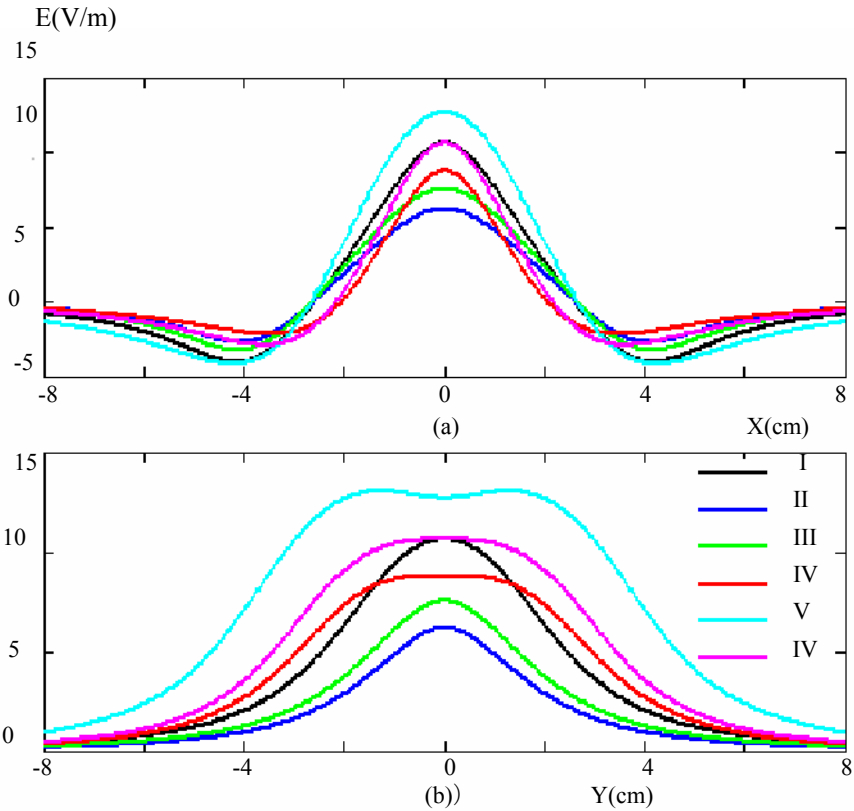


Fig. 8 The profile distributing map of the introduced electric field of different coils, and they were all of y direction along different axis:(a)along the X axis,(b)along the Y axis.

The comparing coefficient of 4-rose coil (shown in 5(IV)) was the least, whose equation was Shown as follows:

$$r = 2R\sin(2\theta) \quad \theta \in (0, 2\pi)$$

The 4-rose coil is obtained the best focus, it will be discussed in detail.

C. Comparing the coil's(4-rose shape) radius

As shown in Figure 7(a), E, which was induced at the depth of 1.3 cm, was increased with the radius. As shown in Figure 7(b), E induced by the coil with radius of 2 cm was decreased when the stimulating depth increased, and the velocity of the attenuation in the superficial tissue was quicker than the deeper tissue, so it was known that the stimulating depth, E was effected by the radius, and E at stimulating depth had a relationship with the radius of the coil.

From the mathematic model and the equations (9) and (10), the curve of the comparing coefficient of the 4-rose coils with different radius was shown in Figure 9, here, the

stimulating depth was 1.3cm. It was obvious that the comparing coefficient of the 4-rose coils was increased with the radius, and the velocity of the augment was larger when the radii smaller than 4 cm.

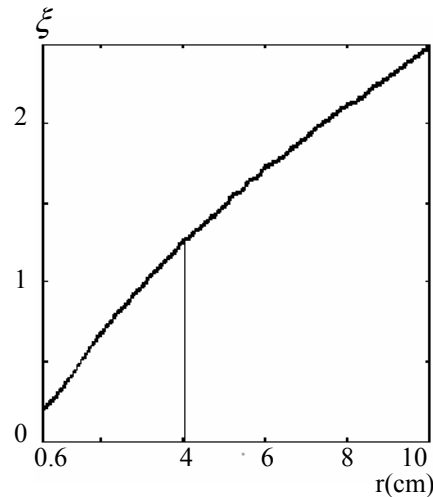


Fig. 9 The curve of the comparing coefficient of the four-leaf coils with different radii

D. Comparing the angle of the coil

The 4-rose coils, which has a angle of θ , was shown in Figure 10. The coil had an angle of $(\pi - \theta)/2$ with the semi-infinite. It was found that the angle is required to be larger than 75 degree, or the coil would be piled up and couldn't get a symmetry distributing. The logarithmic curve chart of the comparing coefficient of different assembled coils was shown in Figure 11(a). Hence, the coil with 102 degree has the lest comparing coefficient.

Furthermore, the coils with different angles could be assembled to be a coil array. As shown in Figure 11(b), it was the logarithmic curve of the comparing coefficient of the coil array that was assembled the coil with 112 degree and the coil with an arbitrary angle. It was found that the best focus was obtained from the coil with 112 degree assembled with the coil with 89 degree. The profile distributing of the induced electrical field of y direction along x-axis by three different assembled coils was shown in Figure 12. Here, coil I was with 89 degree, coil II was 112 degree, III was the coil array. The parameters such as E_{max} , E_{min} , B_h were listed in Table 2.

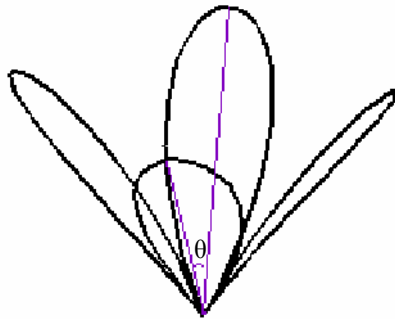


Fig. 10 The sketch map of the four-leaf coil with a stated angle

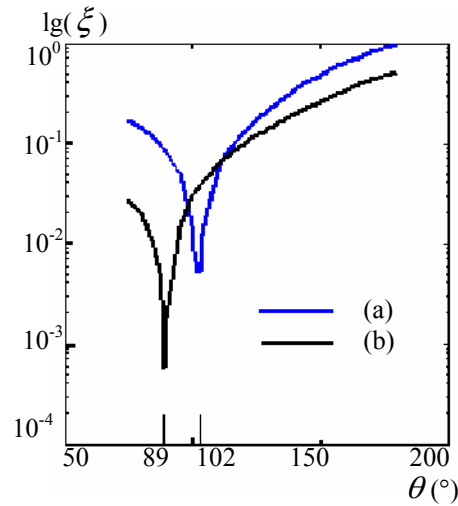


Fig. 11 The logarithmic curve chart of the comparing coefficient of different assembled coils:(a) the angle of the coil was changed from 0 degree to 180 degrees, (b) the coil with 112 degrees combined with the coil with a arbitrary angle.

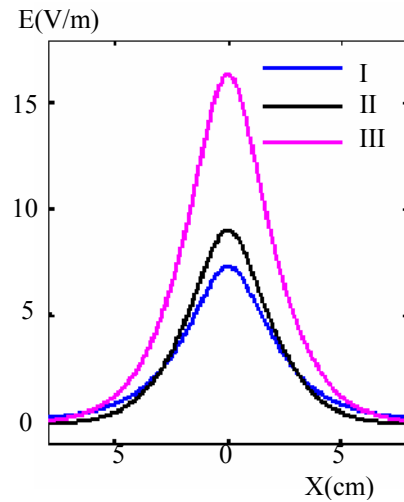


Fig. 12 The profile distributing map of the introduced electric field of y direction along X axis by three different assembled coils.

Table 2 The parameters of different assembled coils

coils \ Data	E_{max}	E_{min}	B_{h1}	B_{h2}	η	ξ
I	7.3237	0.1478	0.0216	0.0291	0.6795	0.0862
II	9.0272	-0.1456	0.0198	0.0317	0.6775	0.0686
III	16.3508	0.0022	0.0206	0.0306	0.6784	5.75×10^{-4}

IV. CONCLUSION AND DISCUSSION

(1) Considering figure-8 coil and the data in Table 1, we can find that the comparing coefficient of the 4-rose coil is least, and the focus of the 4-rose coil is best.

(2) In Figure 9, the better focus of the 4-rose coils is obtained with the smaller radius when the stimulating depth is 1.3 cm.

(3) In Figure 11(a), the comparing coefficient of 0.0051 is the least, and the best focus is obtained when the 4-rose coil with angle of 102 degree. In Figure 11(b), it was obvious that the least comparing coefficient was 5.75×10^{-4} , which was smaller than the comparing coefficient of the coil with 102 degree, which the coil with 112 degree assembled with the coil with 89 degree. It was obvious in Table 2 that it was mostly minished the induced electrical field at the coil's edge when the coils with different angle were assembled, and the diversification grads of the induced electrical field was increased. Uniting 4-rose coils with different angle, so assembling a few troop coils with different angles to be a coil array, the parameters may be optimized by the method presented in this paper.

In this paper, the comparing coefficient was presented and used to compare the different coil to optimize the parameters such as coil's shape, radii, and the composing angle to improve the focus of the stimulating coil. The optimal parameters improved the focus of the coil was presented given the stimulating depth was static in the process of stimulating. This method also may be used to optimize the coils' parameters given the arbitrary stimulating positions. In the future study, the method would be validated by experiments. Undoubtedly, this study will improve the effective application of the rTMS technology.

REFERENCES

1. George MS, Wasserman EN. Rapid-rate transcranial magnetic stimulation I (rTMS) and ECT. *Convulsive Ther*, 1994, 10:251–3.
2. Martin JL, Barbanoj MJ, Schlaepfer TE, et al. Repetitive transcranial magnetic stimulation for the treatment of depression. *Br J Psychiatry*, 2003, 182:480–491.
3. Hoppner, Schulz M, Irmisch G. Antidepressant efficacy of two different rTMS procedures: high frequency over left versus low frequency over right prefrontal cortex compared with stimulation. *Eur Arch Psychiatry Clin Neurosci*, 2003, 253:103–109.
4. Eschweiler GW, Wegerer C, Schlotter W, et al. Left prefrontal activation predicts therapeutic effects of repetitive transcranial magnetic stimulation (rTMS) in major depression. *Psychiatry Res*, 2000, 99:161–72.
5. WANG Xiu-xin, HU Wei-ping, YANG Yong-xu et al. Computation of Depth Induced Electric Field Distribution in the Magnetic Stimulation. *Chinese Journal of Medical Physics*, 2005, 22 (5): 660–662, 634.
6. GRO Ming-Xia, WANG Xue-Min, WANG Ming-Shi. Design of the coil array and calculation of the field distribution of transcranial brain multichannel magnetic stimulation. *Journal of Tianjin Medical University*, 2001, 7(1):38-40.
7. Liu ZP, Yin T, Guan XG, A project of magnetic coils newly designed to restrain the negative value of the intensity of magnetic induced electric field. *Sheng Wu Yi Xue Gong Cheng Xue Za Zhi*, 2003, 20 (1):45–48.
8. Yin T, Liu ZP. Mathematic model and computational imitation in the research of the electric field intensity's distribution induced by magnetic stimulation used in human brain. *Chinese Journal of Biomedical Engineering*, 2004, 23 (6):529–536.
9. Ren CY, Tarjan PP, Popovic DB. A novel electric design for electromagnetic stimulation -the slinky coil. *IEEE Transactions on Biomedical Engineering*, 1995, 42 (9):918–925.
10. Frank Padberg, Flavia di Michele, Peter Zwanzger, et al. Plasma Concentrations of Neuroactive Steroids before and after Repetitive Transcranial Magnetic Stimulation (rTMS) in Major Depression. *Neuropsychopharmacology*, 2002, 27 (5):874–878.
11. Jennifer L. Couturier. Efficacy of rapid-rate repetitive transcranial magnetic stimulation in the treatment of depression: a systematic review and meta-analysis. *Rev Psychiatry Neurosci*, 2005, 30 (2): 83-90.

A miniature telemetric system base on chip nRF24E1for recording EEG activity in freely moving rat

Zhanping Wang, Chong Luo, Chunpeng Zhang, Yang Xia

University of Electronic Science and Technology of China, Chengdu, P.R.China, 610054

Abstract — In this paper, we designed a telemetric system to record the electroencephalogram (EEG) from adult freely moving rats. The system has two units: Transmit-end and Receive-end. The Transmit-end is consists of three parts: the preamplifier, which is used instrument amplifier AD620; the LPF (low-pass filter) and the 50 Hz frequency notch filter, which is used the precision amplifier LM324; the transmitter, which is used nRF24E1 chip embedded 8051 core and 8 input ADC transmit the modulated signal at 2.4GHz. The Receive-end is consists of two parts: the receiver, which is used nRF24E1 chip also (nRF24E1 embed RF transmitter and receiver); the interface of Receive-end and PC, which is used MAX3232 (RS-232 chip). The Transmit-end fettered on the back of the rat has light weight (10g including battery) and small size (20mm×50mm).The system can measure the EEG signal of the rat in freely moving over a wireless transmission distance of up to 8 m and also can provide a new platform for behavioral and neurophysiological experiments.

Keywords — telemetric system, Wireless, nRF24E1, EEG, rat

I. INTRODUCTION

Telemetric recordings of the EEG in freely moving animals is currently an important issue in neurosciences. With the development of Electrophysiological researches, we need to keep the animal's freely movement in some specifically researches like learning and memory, but the most of cable recording system that have cable connecting the EEG electrode on the animal's head restricts animal's locomotion, exploratory behaviors and even have a influence to its various physiological parameters. Telemetric recording system offers the advantage to monitor physiological parameters in freely moving animals without any restrictions in their explorative behavior.

Recently, many companies develop their telemetric systems, but most of them are embedded equipment that are placed into the body of experimental animals through surgery, so the user may has to spend more time on the surgery and require more experimental animals. In a word, it's difficulty to use them to carry out mass experiments.

In this paper, we present a inexpensive, portable and reusable telemetric system to record the electroencephalo-

gram (EEG) from adult freely moving rats under various experimental conditions. The design uses the cheap chips to structure a system that has light weight, small size and long transmitting distance. We can put the device (including battery) on or off the body of any experimental animals quickly, and then the mass animals' experiments can be fulfilling easily.

II. SYSTEM OVERVIEW

The system contains 3 parts: EEG amplifier, RF communication part and interface of PC. The RF communication part includes transmitter and receiver. To obtain the EEG signals, firstly, the EEG amplifier is used to collect the EEG signal from the adult freely moving rat accurately, and then the singles are sent to the RF transmitter after the A/D conversion and modulator. When the RF receiver gets the data, it will send them to PC thought the interface. Finally, the PC will store and process the data by our software. The schematic illustration of the system configuration is shown in Fig.1.

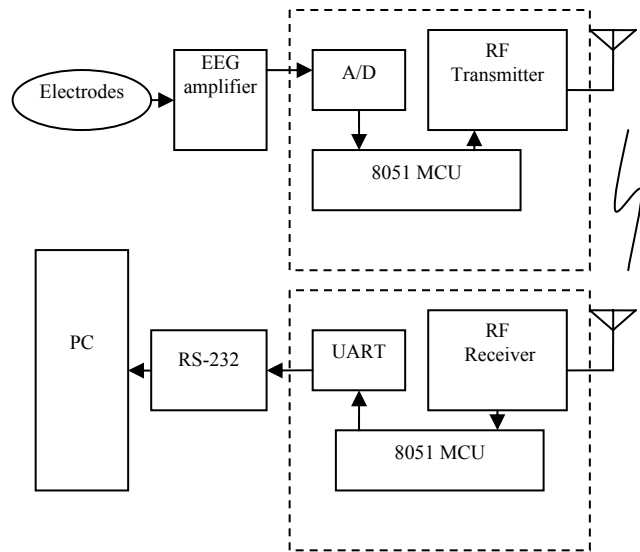


Fig. 1 The schematic representation of the system

III. SYSTEM DESIGN

The system hardware contains 2 parts: Transmit-end (carried by Rats) and Receive-end. The Transmit-end device is designed on a two-layer PCB with 20mm×50mm and 3.7g weight, and the Receive-end is about 40mm×70mm.

A. Transmit -end device

The EEG signal frequency we concern is arranged from 0.5Hz to 40Hz. The EEG amplifier is consisted of 2 units: AD620 for preamplifier and LM324 for filter (including 0.5Hz high-pass filter and 60Hz low-pass filter), the total gain of the EEG amplifiers is designed about 60dB. The configuration of the EEG amplifier is shown in Fig.2.

When the gain of AD620 is 10, its common mode rejection ratio can reach about 100dB, and the difference mode input impedance is 100GΩ, so it is very effective to restrain the common mode interference of the signal from the Electrodes.

We use the LM324 to design the LPF (low-pass filter) to meet the requirements of the system. The 50Hz interference must be concerned, and then we need the 50 Hz frequency notch filter. But the Q value of the 50 Hz frequency notch filter does not high enough, so the LPF uses 60Hz cut-off frequency but not 40Hz to gain an accurately 40Hz low-pass filtering. All the high-pass filter and low-pass filter use 2-order Butterworth Filter to keep the linear in the transmission bands.

We chose nRF24E1 to transmit the EEG signal. In order to ensure the enough wireless signal transmission distance and low bit error rate, we must have a matching network for

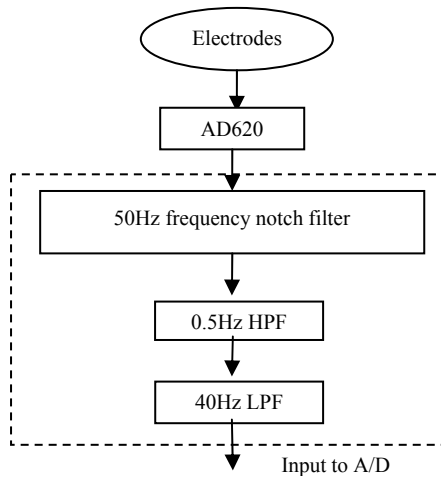


Fig.2 The configuration of the EEG amplifier

the antenna to reduce the signal attenuation and reflection. The result of the optimization by ADS software is shown in Fig.3. It shows that positive gain (S12 and S21) increased significantly at 2.4 - 2.5 GHz and the reflection (S11 and S22) has a great reduce.

We use an antenna which length is 20%-30% longer than the theoretical length in order to gain the best effect by tune the prototype. The purpose bending the trace is only to keep the enough length of the antenna and small dimension of the PCB. The distance between the open end of the antenna and the edge of ground plane should be as large as possible, and the shortest distance should be 10 mm at least or more. Cutting the length will depress the gain of the antenna. The

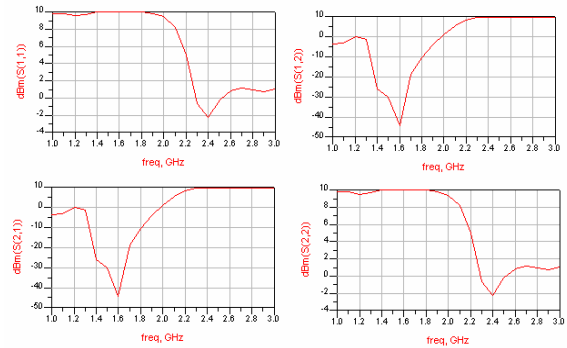


Fig.3 (a) before the optimization

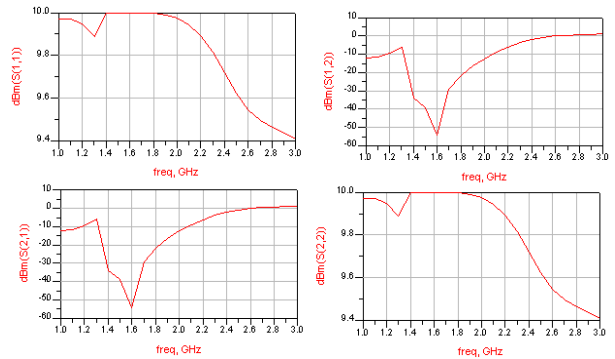


Fig.3 (b) after the optimization

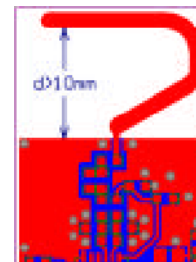


Fig.4 The design of the antenna

design of antenna is shown in Fig.4.

B. Receive-end device

The Receive-end has no special requirements about the weight, dimension and low power consumption, and so on. So we use the USB to supply power. This part contains nRF24E1 and MAX3232 (RS-232 chip). The nRF24E1 receives the data modulated on the RF electromagnetic wave and send it to PC to process thought MAX3232. We use the all-purpose RF communication antenna to receive the data. The photo of the Receive-end is shown in Fig.5.

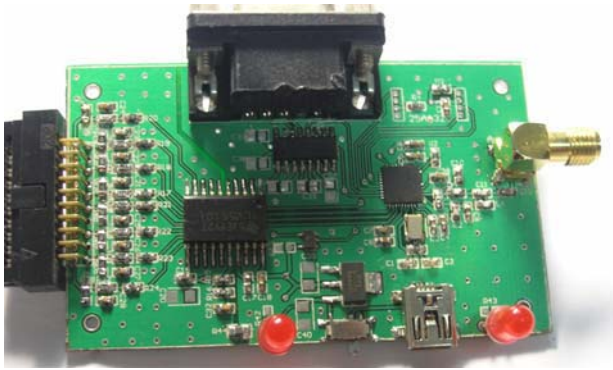


Fig.5 The photo of the Receive-end

C. Design of Software

We use the timer interrupt to keep the sampling rate 250Hz, and then use 8051 control the data transmit. We also design a communication protocol to reduce the error rate in the process of wireless transmission. We set up an interactive mode of response, no matter receiver receive correct or erroneous data, and it will give a signal back to the Transmit-end device to make sure the transmitter know what work it should do in the next. But if it receives erroneous data more than 3 times, it will discard the wrong data, and a notice information will deliver back to the Transmit-end to transmit the next data to ensure the real-time sampling. Another mechanism is used that when a transmit channel is appropriated, the system will change other channel to make sure system can work normally.

All of this design is make sure the system can work perfectly; the system has a long transmit distance (10m) and a very low bit error rate.

D. Other Design

We use a Lithium battery which weighs 5.6g, 350mAH and can support 10 hours of work time to supply power. The

Transmit -end device is fixed through vest in rats' back, and we can change the battery and get the vest off after experiment.

IV. EXPERIMENTAL RESULTS

We use this system to measure the Rats' EEG in different states: resting state, sleep and epilepsy. The results are shown in Fig.6. By comparing with the data of the cable recording system, it is shown that this system can provide precise and sensitive EEG signal under different condition animals.

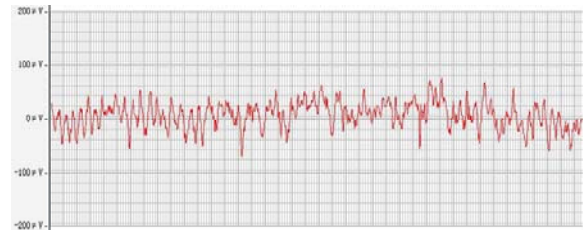


Fig.6 (a) EEG of resting state.

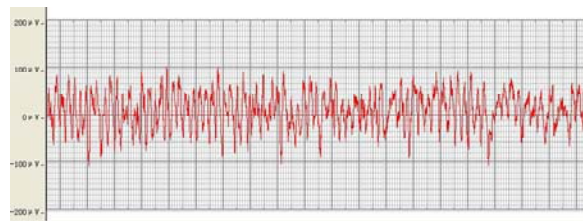


Fig.6(b) EEG of sleep.

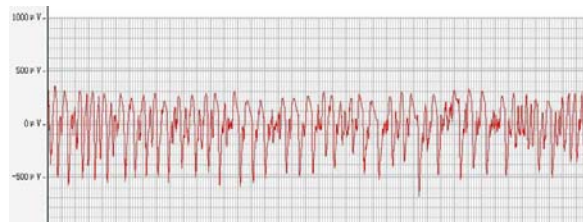


Fig.6(c) EEG of epilepsy

V. CONCLUSION

This design can measure the EEG signal of Rat's with it's freely moving in a long distance at very low error data rate. Based on this design, we will develop a multi-channel system and use it to actualize more complex experiments.

ACKNOWLEDGMENT

This work was supported by grant from the National Science Fund 3057047 and 973 Project 2003CB716106

REFERENCES

1. XU Lusheng, LI Feng, DING Deyun. The development of EEG radio telemetry and analysis system [J]. Chinese Journal of Medical Instrumentation, 1996, 20 (4) :1942~1951.
2. Metting AC, PeperVRA, Grim bergen CA. A wireless infrared link for a 162 channel EEG telemetry system [J]. IEEE TransBiomed Eng, 1994, 2 (5) : 9062~9071.
3. Marco Weiergräber, Margit Henrya, Jqrgen Hescheler, Neil Smyth, Toni Schneider. Electrographic and deep intracerebral EEG recording in mice using a telemetry system. Brain Research Protocols 14 (2005) 154~164.
4. Chung-Chiun Liu, Edward O'Connor, and Kingman P. Strohl. A Multichannel Wireless Telemetric Microsystem for Small Animal Studies. IEEE SENSORS JOURNAL. 2006.
5. J. Morizio, P. Irazoqui, V. Go, and J. Parmentier. Wireless headstage for neural prosthetics. In Proc. 2nd Int. IEEE EMBS Conf. Neural Engineering, Arlington, VA, Mar. 2005.
6. Nordic VLS I ASA nRF24E1 Data sheet [EB]. <http://www.nordicsemi.no>. 2004.6.
7. Using the analog device s active filter design tool[EB]. <http://www.analog.com>. 2004. 6.

address of the corresponding author:

Author: Xia Yang
 Institute: University of Electronic Science and Technology of China
 Street: No.4, Section 2, North Jianshe Road
 City: Chengdu
 Country: China
 Email: xiayang@uestc.edu.cn

Spatial Sensitivity of NIRS Tissue Oxygenation Measurement using a Simplified Instrument

R. Liu¹, X. Liu¹, F. Scopesi², G. Serra², J.W. Sun¹, P. Rolfe^{1,3,4}

¹Harbin Institute of Technology, Harbin, China

²Gaslini Institute, Genova University, Genova, Italy

³OBH Ltd., Maidstone, Kent, England

⁴Advanced Research Institute, Waseda University, Tokyo, Japan

Abstract— Near infra red spectroscopy (NIRS) is of interest for chemical and structural analysis in cells, tissues and organs. We describe simplified instrumentation aimed at clinical applications. This is a four-wavelength system (735nm, 760nm, 810nm and 850nm) for tissue oxygenation measurement, using light-emitting diodes (LED) as light sources and a sensitive photodiode (OPT101) detector. *In vitro* testing was done using ink solutions of varying concentrations and the NIRS instrument results were compared with those from a spectrophotometer. Changes in chromophore concentration were calculated using the modified Lambert-Beer Law together with the application of Diffusion Theory. The *in vitro* results showed good correlation between the new instrument and the laboratory standard at all four wavelengths. We examined the *in vivo* performance in the diffuse reflectance mode on the adult forearm. In arterial occlusion experiments we saw the expected changes in the values of HHb and HbO₂. We investigated the spatial sensitivity of the instrument by varying the source-detector spacing from 20mm to 35mm also with arterial occlusion. There were progressive changes in HHb concentration, with return to baseline after occlusion. For spacings of 20mm and 22mm the HHb changes were much smaller than those seen at spacings of 25mm, 29mm, 30mm and 35mm. This is because at the smaller spacings a more superficial layer of skin is interrogated and this has a lower blood volume than the deeper sections seen for higher spacings. The simplified instrument has performance that is adequate for diffuse reflectance measurements and could be useful in some clinical applications.

Keywords— NIRS, Tissue Blood Oxygen content, diffuse reflectance.

I. INTRODUCTION

Near Infra-Red Spectroscopy, NIRS, is a promising non-invasive physiological measurement technology, and is of great interest for chemical and structural analysis in cells, tissues and organs [1] [2]. Although apparently feasible, NIRS instruments have not entered routine clinical use, partly because of physiological/clinical factors and also due to the cost and complexity of the instrumentation. We have been particularly concerned with the development of the

method for monitoring cerebral phenomena in ill newborn babies and the fetus, but there are also many important applications in adults including measurement in the brain, muscle, breast, kidney and skin.

Approaches to achieve absolute quantitation involve the determination of absorption and scattering parameters of the target sample. Such methods require theoretical models of photon propagation upon which to base a measurement and analysis strategy. This includes Transport theory and Diffusion theory. The laboratory use of femto/pico second Ti-Sapphire lasers and streak camera detectors have their place in research, but simpler, lower cost instruments are needed for routine clinical use.

The deeper penetration of tissues by NIR wavelengths as compared with the visible part of the spectrum has been utilised in neonatal applications, but for some applications useful information may be gathered from reflectance measurements that interrogate just superficial layers [3]. Furthermore, semi-quantitative analysis can be achieved with simple instrumentation by monitoring change from baseline within one subject. In order to control such diffuse reflectance measurements it is essential to use source-detector spacing and geometry appropriate for the tissue structure under study, for example cutaneous vasculature. The ultimate aim of our work is to design a low-cost and simple NIRS-based tissue oxygenation measurement system for clinical use. The objectives of the present study were to assess the *in vitro* and *in vivo* performance of a simplified NIRS instrument, with regard to spatial sensitivity when used in the diffuse reflectance mode.

II. METHODS & MATERIALS

A. Use of Modified Lambert-Beer Law

In the near-infrared region, the major chromophores of interest in tissue are HbO₂, HHb, and oxidised cytochrome aa₃. The Beer-Lambert law is the starting point of the analysis, given by:

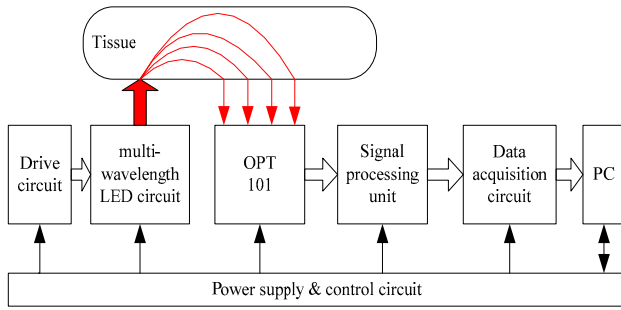


Fig. 1. This shows a schematic of the simplified NIRS instrument. The source-detector configuration is chosen according to the application.

$$I = I_o e^{-\epsilon CL}$$

where I_o is the intensity of the incident interrogating electromagnetic energy, I is the intensity of the emerging energy, C is the concentration of an absorbing specie in μmolar , ϵ is the molar extinction coefficient of the absorber and L is the physical (geometrical) path length. As the tissue is a strong scattering media, this law does not accurately describe the propagation of light through tissue and in order to correct the multiple scattering effects in the tissue we use the modified Beer-Lambert law [4]:

$$OD = \log \frac{I_o}{I} = (DPF \times r \times \epsilon \times C) + G$$

where OD is the optical density, DPF is the pathlength factor, which accounts for increases in the photon pathlength caused by tissue scattering, r is the distance between light source and detector, and G is a factor which accounts for the measurement geometry. A change in the chromophore concentration causes the detected intensity to change. When the concentration changes, the extinction coefficient ϵ and distance r usually remain constant and we assume that DPF and G remain constant. Thus, for a particular wavelength at the same position, the change in OD can be rewritten as:

$$\Delta OD = \log \frac{I_{t_1}^\lambda}{I_{t_2}^\lambda} = DPF \times r \times (\epsilon_{HbO_2}^\lambda \times \Delta C_{HbO_2} + \epsilon_{HHb}^\lambda \times \Delta C_{HHb})$$

where, $I_{t_1}^\lambda$ and $I_{t_2}^\lambda$ are the measured intensities before and after the concentration change, ΔC_{HbO_2} and ΔC_{HHb} are the concentration change in HbO_2 and HHb . In this analysis we do not consider other chromophores. By measuring the change in OD for multi-wavelengths and multi-positions, and using the known extinction coefficients of

HbO_2 ($\epsilon_{HbO_2}^\lambda$) and HHb (ϵ_{HHb}^λ) at those wavelengths, we can calculate the concentration changes of HbO_2 and HHb [5].

B. Design of Instrumentation

We constructed a multi-wavelength NIRS measurement system, using four light-emitting diodes (LED) as light sources having wavelengths of 735nm, 760nm, 810nm and 850nm (see Fig. 1). These wavelengths cover the absorption bands of HbO_2 , HHb and $cyt\ a_{a_3}$. The LEDs were switched on sequentially using a pulse train so that the detected signals at each wavelength could be separated.

As a detector we used a photodiode (OPT101) having high sensitivity and low quiescent current. The OPT101 is integrated with a trans-impedance amplifier to convert the light intensity into an output voltage signal, and this helps to eliminate problems such as leakage current errors, noise pick-up and gain peaking due to stray capacitance. The output signal is sent to the signal-processing unit and acquired by the data acquisition circuit, which can achieve multi-channel synchronised data collection.

The source and detector may be arranged to meet the requirements of specific applications. Thus, both transmission and backscatter situations can be accommodated. In order to carry out measurements by diffuse reflectance the radiation sources and the detector were positioned side-by-side on the surface of a test sample or tissue. The spacing between the light source and detector can be adjusted from 20 mm to 35 mm allowing penetration depth to be adjusted.

III. RESULTS

Firstly, the sensitivity and linearity of the instrument were assessed by comparing the determinations by the instrument of the attenuation of ink solutions with those obtained from a spectrophotometer (UV-2550). Aqueous ink solutions have been used by others to simulate the absorption of blood or melanin in tissue [6]. To vary the absorption coefficient of the solution and observe its influence, the concentration of ink was adjusted to 5%, 10%, 20%, 40%, 60%, 80% and 100%. The comparisons were made at the four wavelengths used in the instrument. The results obtained at 850 nm are shown in Fig. 2. It can be seen that the *in vitro* determinations of attenuation by ink solutions compared well with spectrophotometer measurements. Similar results were found for all four wavelengths.

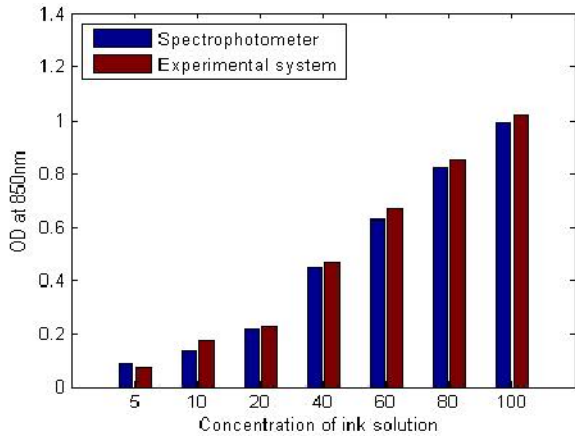


Fig. 2. OD measurements of varying concentrations of ink solutions. The instrument results at 850 nm are compared with a spectrophotometer.

A. Limb Arterial Occlusion

Preliminary *in vivo* studies were done in adult forearms using arterial occlusion to initiate blood oxygenation changes. For our forearm occlusion experiments, the source-detector assembly was fixed to the volar surface of the forearm. A pneumatic cuff was applied to the upper arm and after 15 seconds it was inflated to a pressure of 240 mm Hg for approximately 30 seconds, then the cuff was deflated. The change in the concentration of HHb and HbO₂ was calculated and an example of the results is shown in Fig. 3.

In order to examine *in vivo* spatial sensitivity we varied the spacing between the light sources and the detector from around 20mm to 35mm, whilst making measurements from the adult forearm. Blood oxygenation changes of the limb were induced again by performing arterial occlusion using

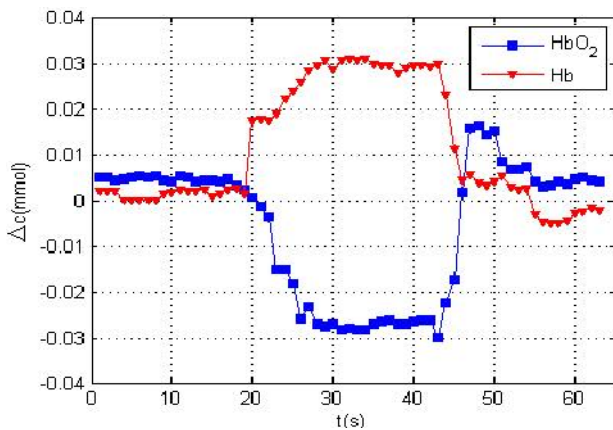


Fig. 3. This shows changes in blood oxygenation in an adult forearm after arterial occlusion followed by release of the occluding pressure.

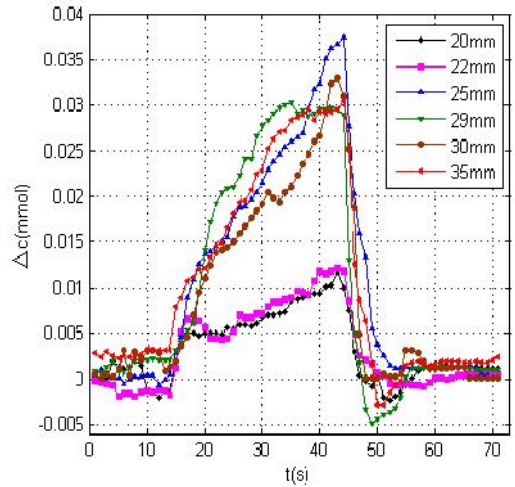


Fig. 4 Change in concentration of HHb for different source-detector spacing in the adult forearm during arterial occlusion.

an upper arm cuff. Indications of tissue oxygenation were derived from the NIRS measurements and these were derived for each source-detector spacing from 20mm to 35 mm. The Change in concentration of HHb for different spacings is shown in fig.4. It is also possible to derive estimates of blood volume change from total haemoglobin.

In Fig. 4 we can see that the time course for spacings of 20mm and 22mm are similar. Also the time course for spacings of 25mm, 29mm, 30mm, and 35 mm are similar.

IV. DISCUSSION

We are developing simplified NIRS instrumentation that is ultimately aimed at clinical applications, and the purpose of the study reported here was determine the *in vitro* and *in vivo* performance of a basic instrument design. Earlier instruments described in the literature have used a variety of approaches for either semi-quantitative or fully quantitative measurements [1]. The latter require either time-of-flight determinations, using femto/pico sec lasers and fast detectors, or intensity modulation and with phase-shift measurement. Both of these are complex and expensive. Although NIRS instruments are available commercially they have not found widespread clinical use. This may be due to their high cost or to the lack of clear evidence of the usefulness of the method. We wished to explore the potential of simplified instrumentation to see if cost might be an important

In the study described here we have used LEDs as light sources instead of semiconductor laser diodes. The latter have the advantage of producing a considerably narrower spectral output and also they can be used at higher power output, which is necessary when interrogating deeper tissue

segments. Nevertheless we were interested to determine whether or not the LED-based system had sufficient performance for physiological studies. Sensitivity is influenced by the overall system design, including the characteristics of the detector and the methods used for signal processing.

The results of the instrument's determination of ink solution OD compared with data from a laboratory spectrophotometer show acceptable performance in terms of linearity. Nevertheless this study did not explore the limit of detection of the instrument and this will need to be done. The lowest value of absorbance used here was with an ink concentration of around 5 and this appeared to correspond to an absorbance of approximately 0.4 OD.

The *in vivo* assessment of the instrument was carried out using the sources and detector in the diffuse reflectance mode. This involved placing them in a co-planar position. The initial arterial occlusion studies gave results that are in line with the known physiological phenomena. Following cessation of arterial inflow HbO₂ will decrease as oxygen is consumed and there should be a concomitant rise of HHb; our results demonstrated these changes. Thus the instrument can clearly be used for this kind of study as well as for the investigation of peripheral circulatory phenomena in general.

Diffuse reflectance techniques are being used for the study of tissue optical properties, for example for the detection of skin cancer, as well as for the measurement of cardiovascular phenomena. Our study was designed to investigate the influence in diffuse reflectance mode of source-detector spacing on penetration depth into the adult forearm, with arterial occlusion used to create a physiological effect. The result shown in Fig. 4 indicates that for source-detector distance of ≥ 25 mm large and progressive blood oxygen changes following arterial occlusion can be clearly seen. However, with spacing of ≤ 22 mm there is an initial abrupt change of HHb followed by a small progressive change, following the fall in oxygenation. It is reasonable to classify the responses seen into two groups of source-detector spacing, one being equal to or less than 22 mm the other being greater than 22 mm.

The difference in magnitude of the changes in HHb seen at the two spacings could be explained on the basis of the different tissue segments being interrogated. For the smaller spacing we could consider that a superficial layer, or slab, of tissue is seen and this will contain the cutaneous capillary structure. At the larger source-detector spacing the instrument will respond to changes in both the superficial layer as well as a deeper layer., the latter containing a substantial degree of vascularisation.

V. CONCLUSIONS

We have described a simplified NIRS instrument using four LEDs as sources and a sensitive photodiode detector. The instrument was assessed with both *in vitro* and *in vivo* experiments. The linearity of the instrument was found to be good, when compared with a laboratory spectrophotometer for measuring the absorbance of varying concentrations of ink. Studies performed in adult forearms using a diffuse reflectance configuration during arterial occlusion demonstrated the ability of the instrument to follow physiological changes in tissue oxygenation. Segmentation of depth response in tissue was found when using a range of source-detector spacings from 20mm to 35mm.

Further development of the simplified instrument is required to refine its sensitivity and to construct sensors that will be suitable for convenient attachment to subjects during clinical applications. Further methods of analysis will be required in order to process the data obtained from such clinical sensor assemblies.

ACKNOWLEDGMENT

We are grateful to Harbin Institute of Technology for the provision of facilities to conduct the experimental work. Support was also provided by the Gaslini Institute, Genova, and we wish to express our gratitude for this.

REFERENCES

1. Rolfe P, "In Vivo Near Infrared Spectroscopy", *Annu. Rev. Biomed. Eng.* vol. 2, pp. 315-354, April 28, 2000.
2. Rea P A, Crowe J, Wickramasinghe Y and Rolfe P Non-invasive optical methods for the study of cerebral metabolism in the human newborn: a technique for the future? *Journal of Med Eng and Tech*, 9 (4): 160-166, 1985.
3. Nishidate I, Y Aizu and H Mishina Estimation of Absorbing Components in a Local Layer Embedded in the Turbid Media on the Basis of Visible to Near- Infrared (VIS-NIR) Reflectance Spectra. *Opt Rev* Vol 10(5):427-435, 2003.
4. Delpy, D.T., et al., Estimation of optical pathlength through tissue from direct time of flight measurement. *Phys. Med. Biol*, 1988. 33(12): pp. 1433-1442.
5. Frank. PB. Refractive Index of some mammalian Tissues using a Fiber optic cladding Method [J]. *Appl Opt*, 1989, 28:2297-2304
6. Pogue, B.W. and M.S. Patterson, Review of tissue simulating phantoms for optical spectroscopy, imaging and dosimetry. *Journal of Biomedical Optics*, 2006. 11(4): 0411021-04110216

Adaptive Liver Segmentation from Multi-slice CT Scans

J. Liu, Q. Hu, Z. Chen and P. Heng

Shenzhen Institute of Advanced Technology, Shenzhen, China

Abstract — In this paper, an adaptive method was proposed to segment the liver from computed tomography (CT) images. Four sets of CT images were segmented by a binary classification method, support vector machine (SVM), after supervised thresholding and K means clustering. A leave-one-out method was applied to compare with the adaptive method. The result shows that the adaptive method can more accurately identify the class of the pixel with evidently lower false negative volume fraction than that of the leave-one-out method.

Keywords — Adaptive method, Segmentation, Texture analysis, Thresholding, Support Vector Machine

I. INTRODUCTION

The imaging techniques of multi-slice computed tomography (CT) featuring high spatial resolution and fast scan speed provide a great clinical diagnostic tool for examining liver pathologies such as cirrhosis, liver cancer and fulminant hepatic failure. In order to extract the anatomical and pathological information of the liver, the large amount of data yielded from CT scanners requires a post image processing which is both laborious and time-consuming by manual process and visual inspection. Digital image processing and machine learning techniques may provide semi-automatic and automatic methods of liver segmentation for automatic detection of liver cancer or other hepatic diseases as well as the measurement of the liver volume for living donor liver transplantation or 3D volume rendering for computer aided surgical planning prior to hepatic resection. In literature, live-wire segmentation approaches, gray level based liver segmentation, model fitting, probabilistic atlases and level set approaches are the most commonly used techniques for liver segmentation. However, automatic liver segmentation remains unsolved and open for further investigation. Indeed the liver shape model based methods can not meet the need for describing complex liver shape while other methods suffer from the incorrect separation of the liver from neighboring organs such as muscles, spleen and stomach, due to the overlap in gray level ranges and the inter-subject variation in position and shape across the soft tissues in the abdomens. Recent studies of liver segmentation using texture analysis have shown that extraction of the texture features from CT images is a promising method for solving this challenging segmentation task by assuming

homogeneity and consistency of the texture information across multiple slices of a single organ. Among the normal texture analysis methods including Haralick co-occurrence matrices, fractal dimension, Gabor filtering and Markov random fields, the agreement of demonstrating Haralick co-occurrence matrices as the most significant texture characteristics in differentiating the liver tissue in CT scans is achieved across different independent studies in literature using texture analysis in liver segmentation. Compared to the gray level based method (first-order properties of an image), Haralick co-occurrence method gives second-order properties of images to describe the homogeneous anatomical structure of the liver allowing tissue separation between the liver and its neighboring organs at the areas where gray level ranges overlap [1]. After texture feature extraction, common image segmentation techniques, such as clustering techniques, mathematical morphology operation, and region growing, or machine learning methods, such as neural networks, SVM, and fuzzy rules are applied to separate the organs in CT images. Though unsupervised techniques can offer faster segmentation than the supervised techniques, the accuracy of these methods is still poor as the parameters and settings of these methods may vary between different patients and CT scanners. However, this problem can not be avoided in the case of supervised methods since training process is performed on the data sets that could be collected in different conditions from the target data for segmentation. We therefore proposed an adaptive framework for liver segmentation, which adaptively selects CT slices for training within the target data set. The adaptive method includes the following steps: 1) supervised thresholding and automatic liver segmentation using k-means clustering on four sets of abdominal CT images; 2) manual selection of three slices that were properly segmented by a radiologist in step 1); 3) calculation of the texture features in each slice of the CT images chosen from 2); 4) the SVM method (due to its simplicity and accuracy in data classification) was chosen to classify the images using the selected slices for data training. The segmentation result was compared to leave-one-out method in which we used slices from three different data sets for model training instead of using slices in the target data set for training purpose.

II. METHOD

A. Supervised thresholding and K means clustering

Four sets of abdominal CT images were obtained from Shang Dong University. The data consists of multiple, serial, axial computed tomography images derived from helical, 64 multi-slice CT using SIEMENS Sensation Cardiac 64. The data was stored in DICOM format of size 512 by 512 and have 12-bit gray level resolution.

In order to test if texture feature may help in segmenting the liver region from the other tissues that cannot be simply acquired by thresholding based on gray level, we thus cut off the pixels outside a gray level range by setting the outer pixel value to zero.

The gray level range, R_g , was selected from the four sets of data with ground truth (GT), which was manually segmented by an experienced radiologist. For a set of the normal abdominal CT data, anatomically, the gray level range of the liver should vary within a narrow range. This anatomical range is dependant upon individuals being scanned. After choosing the pre-defined window and level range of the DICOM data, the histogram of each image and GT was calculated. Since the gray level of the level in CT image is relatively high, the image with maximum mean gray level was considered as the image with the maximum liver region. Mean and standard deviation of the histogram of this slice was computed as the gray level range of this data set for the thresholding operation. In our case, four gray level ranges are [23, 236], [-5, 218], [16, 229] and [7, 223], respectively.

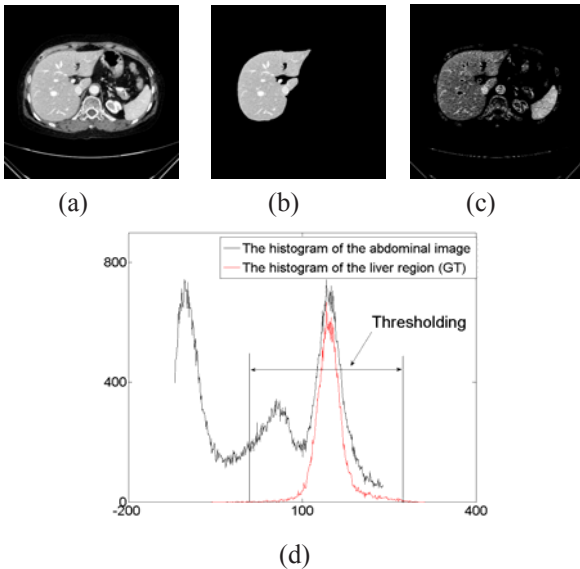


Fig. 1 (a) Original CT slice (b) Ground truth (c) Image after supervised thresholding (d) The histogram of the image in (a). The x-axis is the gray level and y-axis is the pixels in one gray level.

Fig.1 shows how we chose the threshold for the supervised thresholding.

Considering the affect of perturbations of even more serious intensity inhomogeneity and noise, the gray level range relaxed by multiplying the standard deviation by 2.5. The resultant slices were than normalized into 8-bit images by setting the lowest gray value to 0 and highest to 255.

The adjoining tissues or muscles in the liver have mainly higher or lower gray value than that of the liver [2]. We selected three centroid for the K means clustering. With help of the radiologist, three slices from each data set were chosen as the fine initial liver region for the later experiment.

B. Texture feature extraction

By analyzing and quantifying the texture patterns within a small neighborhood of size N by N around a pixel of interest, texture extraction may provide a way to extract the liver region from the surrounding tissues within overlapping gray level range [1].

According to the method applied in [1], we chose a 9 by 9 window for extracting the pixel-level texture. For computational efficiency purposes, only the pixel-pairs at the angle of 0° and the displacement at one pixel were used to calculate the gray level co-occurrence matrix (GLCM).

Once GLCM was obtained, nine Haralick texture descriptors, including entropy, energy, contrast, sum average, variance, correlation, maximum probability, inverse different moment, and cluster tendency, were calculated as:

$$Entropy: - \sum_i \sum_j P_{ij} \log P_{ij} \quad (1)$$

$$Energy: \sum_i \sum_j P_{ij}^2 \quad (2)$$

$$Contrast: \sum_i \sum_j (i-j)^2 P_{ij} \quad (3)$$

$$Sum Average: \frac{1}{2} \sum_i \sum_j (iP_{ij} + jP_{ij}) \quad (4)$$

$$Variance: \frac{1}{2} \sum_i \sum_j ((i-\mu_r)^2 P_{ij} + (j-\mu_c)^2 P_{ij}) \quad (5)$$

$$Correlation: \sum_i \sum_j \frac{(i-\mu_r)(j-\mu_c)P_{ij}}{\sqrt{\sigma_r^2 \times \sigma_c^2}} \quad (6)$$

Maximum Probability (MP):

$$\underset{i,j}{\text{Max}} P_{ij} \quad (7)$$

Inverse Difference Moment (IDM):

$$\sum_i^N \sum_j^N \frac{P_{ij}}{1+|i-j|^2} \quad (8)$$

Cluster Tendency:

$$\sum_i^N \sum_j^N (i-\mu_r + j-\mu_c)^2 P_{ij} \quad (9)$$

where μ_r , μ_c , σ_r^2 , and σ_c^2 are the means and variance of row and column defined in [3].

C. Adaptive method for classification

After obtaining the texture features, we then applied the proposed adaptive method to classify the data.

From each data set, the radiologist will randomly select three slices which were segmented by K means clustering in step A.

The SVM was then exploited to classify the data, due to its simplicity and accuracy in data classification. The two-class (liver and non-liver) training was based on the results from the K means segmentation. Open source software, LIBSVM, was employed to this task. The radial basis function (RBF) was selected for the training process, as it can handle the case when the relation between class labels and attributes are nonlinear [4].

At the testing procedure, we used the trained parameters which were calculated during the training process by LIBSVM to test the whole data set.

By this means, the testing results are based on the trained parameters from the same data set, which may avoid the texture variation between different subjects or CT scanners. Four data sets were classified by the adaptive method described above.

D. Leave-one-out method for classification

In order to compare the adaptive method proposed above with a non-adaptive method, leave-one-out method was applied.

Instead of using the trained parameters from the target data set itself for the testing process, the training images were selected from the other three data sets. For example, three images were chosen by the radiologist from three different data sets respectively for the training phase. Then the result was employed to classify the rest data set.

Four data sets were classified by the leave-one-out method described above.

E. Region grow and result evaluation

Finally, three dimensional (3D) region grow algorithm was applied to the resultant volumes to separate the liver region from other tissues.

False negative volume fraction (FNVF) and false positive volume fraction (FPVF) were calculated to evaluate the segmentation, which are the fractions between the false negative volume and GT volume for FNVF and false positive volume and GT volume for FPVF, respectively [5].

III. RESULT

Table 1 gives the overall result of this study. The FNVF obtained from adaptive method is lower than that of leave-one-out method indicating a more accurate segmentation result. However, in two cases, the FPVF of the adaptive method is higher than the leave-one-out method. This can be explained by the fact that the leave-one-out method can only classify a little amount of the liver causing a low value of FPVF.

As shown in Fig. 2, the adaptive method evidently performs better than the leave-one-out method. In Fig. 2. (b), the holes in the segmented CT images are mainly caused by the high intensity of the hepatic blood vessels in contrast-enhanced CT images.

In Fig. 3, a 3D reconstructed liver was obtained from one set of the segmented images by MeVisLab, free software, developed by MeVis Research in Bremen, Germany.

Table 1 Overall result

Subject	Adaptive Method		Leave-One-Out Method	
	FNVF	FPVF	FNVF	FPVF
1	10.71%	0.035%	51.32%	0.0013%
2	13.10%	0.19%	30.06%	0.15%
3	11.07%	0.21%	24.81%	0.59%
4	12.05%	0.18%	39.36%	0.25%

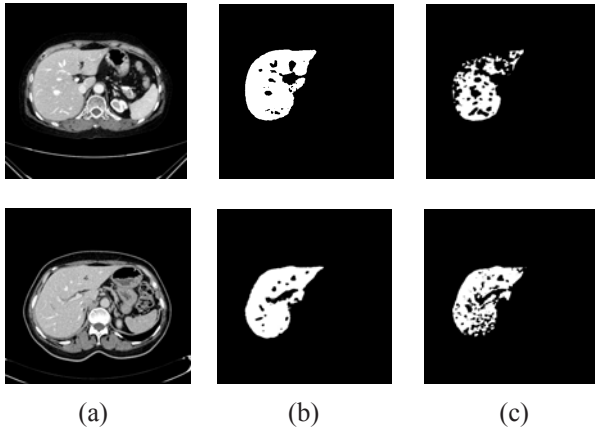


Fig. 2 Comparison between adaptive method and leave-one-out method. (a)Original CT slices (b) result from adaptive method (c) result from leave-one-out method.



Fig. 3 A 3D reconstructed liver from the segmented images.

IV. DISCUSSION AND CONCLUSIONS

As addressed in the introduction section, problem of the liver segmentation is still open. Texture analysis may, however, provide a series of features that can help in separating the liver from other neighbor organs with overlapping gray level range, when supervised classification method is exploited for image segmentation. However, due to the inter-subject variation and different conditions (humidity in the air, different CT scanners, and etc.) when obtaining the CT images, the training result from prior data sets may not satisfy the segmentation task, we therefore propose an adaptive segmentation framework for CT image classification. The encouraging result shows that the proposed method is very promising, though this study is still at a preliminary stage. The result is in accordance with our hypothesis that the supervised classification performs better when using the target data set for the training procedure.

The FNVF is much higher than FPVF in our study and, interestingly, we observed that the values of FNVF in 4 cases (adaptive method) are quite close. This can be explained by the 9x9 window we applied to calculate the GLCM. A small amount of the edge of the liver might thus be missed. A compensate method should be considered in the future work. Another limitation if our study goes to the thresholding operation. The gray level ranges were decided by the histogram of the GT which is not normally available before segmentation. However, in our study, the main aim is to test if the texture feature can be used to extract the liver from the surrounding organs with similar gray levels when applying the adaptive method. We also noticed that the gray level ranges of the four sets are similar. A general range may be defined based on the ground truth of a much larger data set. Hence, we think that the use of GT for choosing the thresholds is acceptable in this pilot study of the adaptive method.

In conclusion, this adaptive method provides a semi-automatic framework for liver segmentation using texture analysis. Classification model trained from the slices adaptively selected from the target data set ensure more accurate segmentation than leave-one-out method.

REFERENCES

1. M. Pham, R. Susomboon, T. Disney, et al. (2007) A Comparison of Texture Models for Automatic Liver Segmentation. SPIE Medical Imaging Conference, San Diego, CA, February 2007, pages 65124E
2. Seong_Jae L, Yong-Yeon J and Yo-Sung H. (2006) Automatic liver segmentation for volume measurement in CT Images. *J. Vis. Commun. Image R.* 17: 860-875
3. Robert M. Haralick (1979) Statistical and Structural Approaches to Texture. *Proceedings of the IEEE*, VOL. 67, NO.5: 786-804
4. Chih-Wei H, Chih-Chung C and Chih-Jen L (2008) A Practical Guide to Support Vector Classification. at <http://www.csie.ntu.edu.tw/~cjlin>
5. Hu QM, Qian GY, Teisler M, Huang S. (2008) Automatic and Adaptive brain morphometry of magnetic resonance scans. *RadioGraphics* 2008; 27(3)

Address of the corresponding author:

Author: Jia Liu
 Institute: Shenzhen institute of advanced technology
 Street: Nanhai Da Dao 1019
 City: Shenzhen
 Country: P. R. China
 Email: jia.liu@siat.ac.cn

Investigation of multifunctional cell physiological analysis instrument based on integrated chip

Hua Cai, Shi Zhu, Hui Yu, Lidan Xiao, Zhaoying Hu, Wei Zhang, Ping Wang *

Biosensor National Special Laboratory, Key Laboratory of Biomedical Engineering of Education Ministry,
Department of Biomedical Engineering, Zhejiang University, Hangzhou, 310027, China

Abstract — This paper describes a novel multifunctional cell physiological analysis instrument based on integrated chip. And we introduces a novel cell sensors chip which integrated MEA, ECIS and light addressable potentiometer sensors (LAPS) which is designed for the purpose of detecting the cell physiological parameters. The instrument has been integrated with a multi-channel high precision open circuit potential measurement system for micro electrode array as well as a potentiostat in ECIS. And an analog lock-in amplifier is also presented to measure the response of LAPS. In addition, in order to achieve multiple analysis, we first tested every parameters of the chip, then we raise different cells on the surface of the chip. The result shows that such biosensors have numerous applications including pharmaceutical screening, cellular physiological analysis, toxin detecting, peripheral nerve regeneration and environment monitoring..

Keywords — Multifunctional Instrument; Cell Physiological Analysis; Integrated Chip; Microphysiometer; MEA; ECIS.

I. INTRODUCTION

Cells provide and express an array of naturally evolved receptor, ion-channels, and enzymes that may be the targets of biological or biologically active analytes. When stimulated, the living cells response and take actions: induce electronic activity, excrete something or absorb something. Cell-based biosensors (CBBs) that treat cells as biological sensing elements have the capability to respond to analytes in a physiologically relevant manner.

However, the reported CBBs only can detect single parameter independently. For example, Microphysiometer [1] normally only be able to used for detecting cell metabolism, while micro electrode array sensor(MEAs) [2]only for cell action potential, and electric cell-substrate impedance sensor (ECIS)[3] only for attachment and spreading of mammalian cells.

Recently, with the development of cell electrophysiology and micro-fabrication techniques, miniature and integrated biosensors are now able to give a strong tool for the moni-

toring micro environment and electrophysiology of living cells.

This paper introduces a novel multifunctional cell physiological analysis instrument with integrated chip. The sensor chip is integrated MEA, ECIS and light addressable potentiometer sensors (LAPS), which is designed by us for the purpose of detecting the cell physiological parameters.

II. INSTRUMENT

A. Integrated Chip Design[4]

The surface photograph of a novel integrating multifunctional cell sensor chip combined with LAPS, MEAs and ECIS is shown in Fig.1. This chip can be separated into three functional areas, so the fabrication process is also divided into three parts. All fabrication steps of this silicon chip are close to CMOS (Complementary Metal-Oxide-Silicon) processing techniques.

The 4-in. silicon wafers (thickness of 450nm), was thermo-oxidized with SiO₂ for better contact with metal in later process. For MEA parts, firstly, it needs sputtering with Cr thin film as bond between metal and substrate, onto which the 300 nm Au was deposited and electrodes were fabricated using wet etching technique, typically the minimal line width is 30μm, and the passivated layer of SiO₂/Si₃N₄/SiO₂ (each layer of 500nm) was deposited above the metal layer by PECVD. Then the circular hole of each electrode (diameters of 30, 50μm respectively) and the bonding pads were etched out with RIE technique. The electrode has a sheet resistance of 40 ohm/square. Au is a highly conducting and durable biocompatible material that adheres well to the substrate and allows observations to be made from either side of the tissue being studied.

Secondly, for IDA part, the effective area of the IDA sensor is 8.4 mm². The width of the electrodes and the distance between were both 50 μm. The length was 7mm for the 12 pairs of fingers of IDA. The fabricating process of MEAs and IDA are similar and this offers great convenience for integration. Since these electrodes and pads are thin gold films sputtered on silicon substrates, the electrodes

* corresponding author. Tel.: +86 571 87952832; Fax.: +86 571 87951676; Email: cnpwang@zju.edu.cn

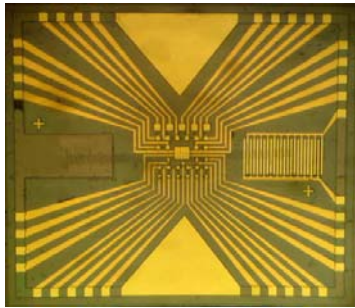


Fig.1 The photograph of integrated sensor devices.

should be galvanized with platinum to better reduce electrode impedance, which is still under experiment.

Thirdly, for LAPS part, besides of above mentioned fabricating process, a 50 μm Si₃N₄ or SiO₂ membrane was deposited on the silicon substrate by PECVD. A 1-μm-thick aluminum membrane was sputtered on the backside of the wafer to create an ohmic contact.

Finally, a micro-chamber was formed by polydimethylsiloxane on the integrated chip to culture cells.

B. Hardware Design

The instrument has been integrated with a multi-channel high precision open circuit potential measurement system (Fig.2a) for micro electrode array as well as a potentiostat (Fig.2b) in ECIS. And an analog lock-in amplifier is also presented to measure the response of LAPS, Fig.2c. With the embedded firmware, the instrument can perform the entire analysis automatically, thus provide a perfect solution for fully automatic on-line analysis.

The basic structure of analog lock-in amplifier is depicted in Fig.3. It mainly includes the signal generator, and signal demodulator. And the detected signal is transferred to computer by MCU (Micro Controller Unit).

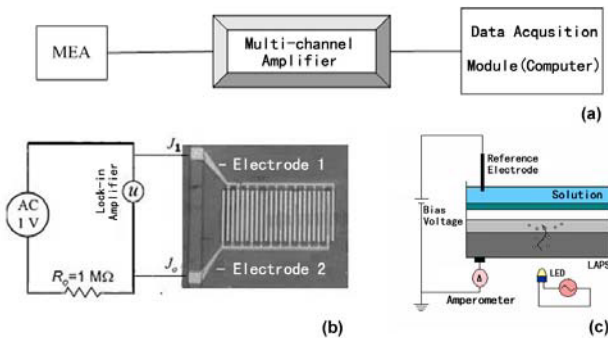


Fig. 2 The hardware system for micro electrode arrays (a), ECIS (b), and LAPS (c).

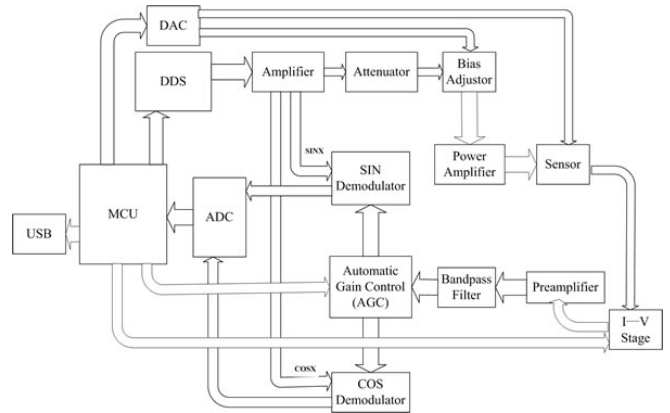


Fig. 3 The basic structure of analog lock-in amplifier

C. System

Fig.4 shows the schematic drawing of the system. The whole instrument includes the integrated chip, corresponding hardware described in section IIB, fluidic and thermal regulation systems.

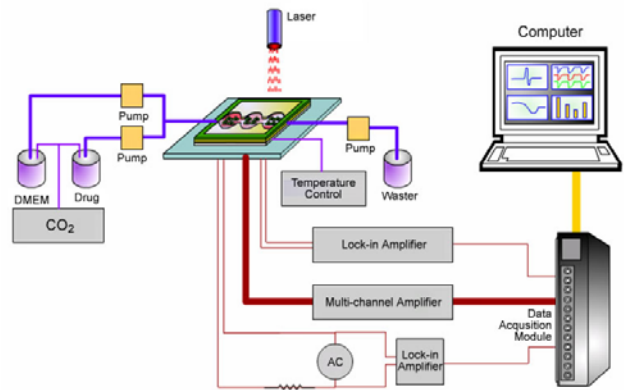


Fig. 4 The schematic drawing of the instrument system

III. RESULTS AND DISCUSSION

A. Cell Culture

Cardiac myocytes were gained from baby rat born in 1-3 days. The tissue was cut into small pieces and incubated in 0.25% trypsin solution for 30 min. Cells were plated on the chip with a density of 5×10⁵ cells/ml, and maintained for 3-5 days on the chip at 37°C under the standard conditions of humidified air with 5% CO₂ and fed with fresh DMEM.

After cardiac myocytes were inoculated on chip for 2 days, the measurement was done. The chip was first ob-

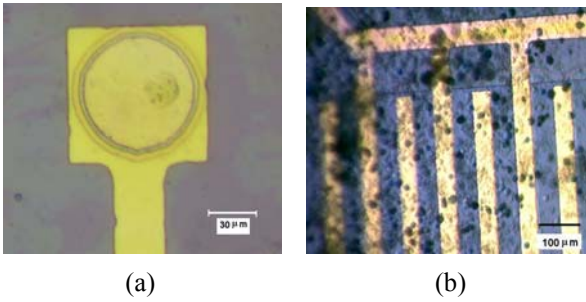


Fig. 5 Cultured cardiac myocytes on the integrated chip with MEA (a) and IDA (b).

served by microscope to insure most of the exposed electrodes were effectively coupled with cells before long-term monitoring. Fig.5 shows the photograph of cultured cardiac myocytes on the integrated chip. It is obvious that the morphology is normal and cells on the chip surface appear well.

B. MEA Noise

In order to avoid the power frequency disturbance, when detecting the Noise of the chip, the instrument and the chip are placed into Faraday Box. Fig.6 is the detected signal. The noise becomes more steady when the electrode size of MEA is bigger.

But when analyzing the amplitude of noise, we find that the noise amplitude of 50μm electrode is 20-30μV, and the noise amplitude of 70μm and 120μm electrodes are 20μV. Such noise amplitude with integrated chip is enough for

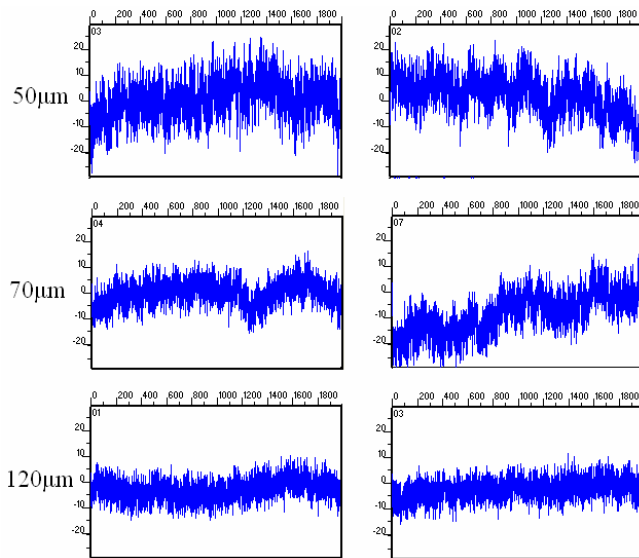


Fig. 6 MEA Noise with different electrode size.

extracellular amplitude detection.

C. Electrochemistry impedance spectrum measurement

IDA sensor was evaluated by Electrochemistry impedance spectrum measurement both in 200ul 10mM $[Fe(CN)_6]^{3-/4-}$ (1:1) solution, with signal amplitude of 5mV, scan frequency of 1-100kHz. Fig.7 shows the detected impedance spectrum. The amplitude decrease to hundreds ohm at the frequency of 10kHz. The results are consistent with the model fitting curve.

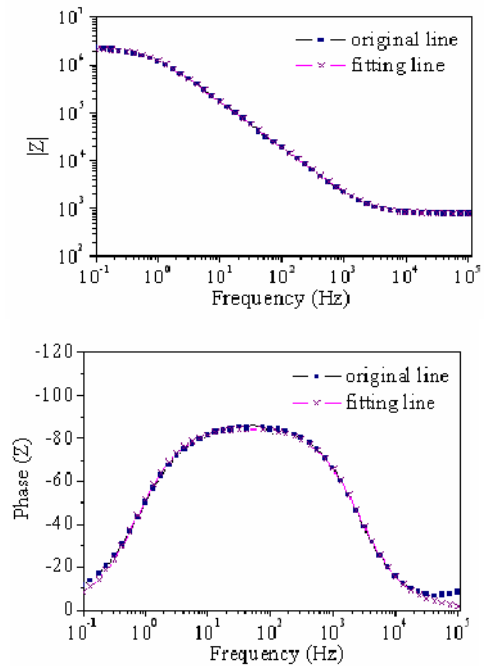


Fig.7 Electrochemistry impedance spectrum of IDA sensor that both in $[Fe(CN)_6]^{3-/4-}$ solution. The solid line is the model fitting curve.

D. Ion concentration measurement

Four species of solution with pH of 6, 7, 8, 9 were used as the measured solution, and the LAPS response curve was detected. The normalized photocurrent response curve was shown in Fig.8a. From the figure we can see that the transition part of the LAPS curve had a good linearity. Fig.8b shows the relationship between the four curves' bias voltage and the corresponding pH where the normalized photocurrent was 0.5. It is obvious that the voltage had a linear relationship with the pH, the linearity is 0.9978. So it can be calculated that the sensitivity (slope) is 50.65mV/pH. Because the total linear range of the I-V curve is about 600mV, wherever the solution pH was changed by 1 pH, the

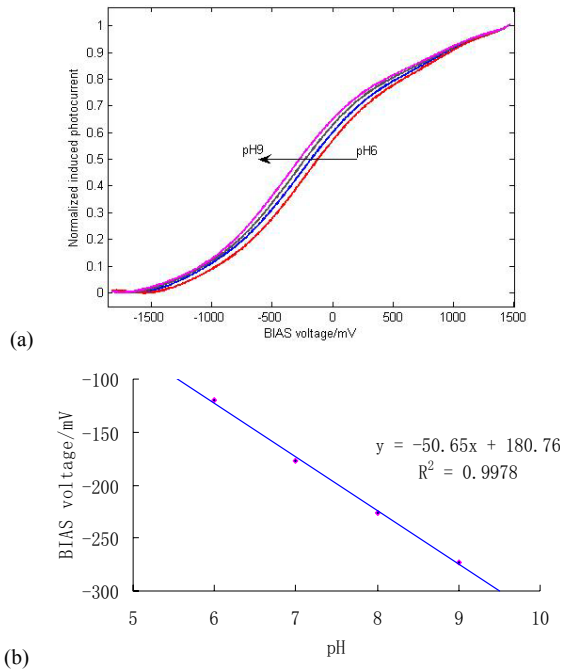


Fig.8 (a) Normalized IV curve of solution with different pH.
(b) Relationship between pH and bias voltage.

corresponding bias voltage would be changed by 50.65 mV, so the measuring range of this system was about 12 pH.

IV. CONCLUSION

In this paper, a novel multifunctional cell physiological analysis instrument based on integrated chip was reported.

This instrument was applied for recording extracellular pH changes due to extracellular acidification was adapted, detecting changes in cellular adhesion and morphology, and the extracellular action potentials. These three sensor functions are to be incorporated into a multi parametric instrument.

Such biosensors have numerous applications including pharmaceutical screening, cellular physiological analysis, toxin detecting, peripheral nerve regeneration and environment monitoring.

ACKNOWLEDGMENT

This work was supported by the National Natural Science Foundation of China (Grant No. 30570492), the key project from National Natural Science Foundation of China (Grant No. 30627002), the Natural Science Foundation of Zhejiang Province of China (Grant No. R205505).

REFERENCES

1. D.G.Hafeman, J.W.Parce, H.W.McConnell. Light addressable potentiometric sensor for biochemical system. *Science*, vol.240, pp.1182-1185,1988.
2. Borkholder, D. A., 1998. Cell based biosensors using microelectrodes. *Electrical engineering*. USA, Stanford university. Ph.D Thesis.
3. R.Ehret, W.Baumann, M.Brischwein. Monitoring of cellular behaviour impedance measurements on by interdigitated electrode structures. *Biosensors Bioelectron*, vol.12, pp. 29-41,1997.
4. XU Ying, YU Hui, CAI Hua, et al. Integrated Cell-based Biosensor for Extracellular Electrophysiological Monitoring.IEEE International Conference on Information Acquisition, Jul.7th, Korea, 2007.

AMS Based Spectrum Subtraction Algorithm with Confidence Interval Test

Xin Ma, Weidong Zhou

College of Information Science and Engineering, Shandong University, Jinan, China

Abstract — Amplitude Modulation spectrogram (AMS) can reflect the orthogonality between the “periodotopical” organization and the tonotopical organization in neurons, and can be used as a reliable discrimination between speech and noise. This paper presents a novel approach of robust speech recognition by using AMS and Spectrum Subtraction with Confidence Interval Test. By dynamic using Confidence Interval Test, the error of estimated SNR was decreased. Experiment results show the proposed method yield good performance for attenuating the effect of noises and can improve the robustness of ASR.

Keywords — Confidence Interval, AMS, Speech recognition

I. INTRODUCTION

Noise robustness research is an important aspect in speech recognition. Automatic recognition of speech (ASR) has good performance in clean environment, but When the speech -to-noise ratio (SNR) decreases, or fluctuation of noise increases, the performance of ASR will degrade[1]. Different algorithms for improving the Noise robustness of ASR are known from the literature, and they can be mainly summarized as noise-robust speech feature extraction, acoustic model adaptation[2], noise compensation[3], Parallel model[4]. Noise compensation method such as spectral subtraction is usually realized by directly eliminating the noise. But as the noise is not stable even for the stationary noise, when fluctuation of noise increases, or the SNR changes, spectral subtraction can lost its effect for the improvement of ASR.

SNR estimation is often used as an auxiliary method of noise compensation. Many different algorithms for SNR estimation can be used in improving ASR. But most of them depend on the effects of voice activity detection (VAD). For example, typically SNR estimation is realized by updating a measure of the background noise in speech pauses, while noise suppression for automatic speech recognition requires a fast and reliable estimate of the local noise level or SNR. Neurophysiological finding suggests the “periodotopical” organization of the neurons with respect to different best modulation frequencies are almost orthogonal to the tonotopical organization of neurons with respect to center frequencies[5], Motivated by this, amplitude modulation spectrogram (AMS) pattern has been designed as a novel

approach of classification, and the AMS pattern can contribute a reliable discrimination not only between voiced speech and noise but also between unvoiced speech and noise. It is suitable for SNR estimation of continuous speech.

The modulation spectrogram (MSG) has been proposed by Kingsbury et al.(1998) as a robust visual representation of speech which is supposed to change only very little when noise or reverberation changes. modulation spectrogram method are introduced to improve the robustness of ASR by Hermansky[6]. Tchorz and Kollmeier[7] introduced a method for broad band and sub-band SNR that is based on amplitude modulation spectrograms for 32ms long time segments and apply it in isolated-digit recognition experiments. The accuracy of SNR estimator by Tchorz depends on the input SNR. Underestimation and overestimation will appear when input SNR is low and high respectively. This will constrain this method in robust speech recognition especially in large vocabulary case.

This paper extends the method cited above by applying confidence interval to test the result of AMS SNR estimation, which have been shown to increase the robustness of ASR for noisy speech signals in digit recognition, and gives experiment results for noisy speech recognition in large vocabulary case.

II. FEATURE EXTRACTION AND CONFIDENCE INTERVAL TEST

A. Feature Extraction

The time signal has to be processed and converted into a spectro-temporal representation. The process of Feature Extraction can be illustrated as Figure 1:

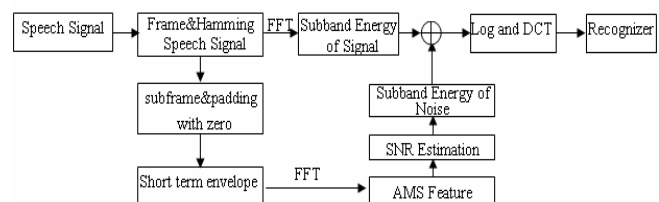


Fig. 1 Feature Extraction

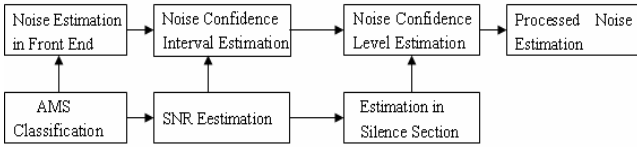


Fig. 2 Processing of Noise Estimation γ_k

B. Confidence Interval Test

We can use the internal of sentence to acquire the noisy statistics, and calculate the expectation and variance of noise as cited above, overestimation and underestimation might make the discreteness of noise energy become larger, although the error from it cannot be accumulate, but it can result the error accumulation in Viterbi decoder of ASR. The whole processing of noise estimation are illustrated as Figure 2.

The mean μ and variance δ^2 of subband energy of short time speech are calculated for estimating the statistics of whole sentence. According to the Tchebycheff's inequality, the probability of one value in one random sequence exceed the scope of $[\mu - \delta, \mu + \delta]$ is little, so we can think if the value X meet follows condition, the result of SNR estimation is correct.

$$|X - \mu| \leq \delta \quad (1)$$

For facility using the AMS based SNR estimation in ASR, we design a type of features weighted by triangle filters which suitable for recognizer. Confidence interval test is used in this paper to improve the reliability of the estimation of SNR. In the training process, a large of statistics are made to get the confidence interval information of the SNRs. In the recognizing process, the confidence interval is used to decide reliability of the used SNRs. By dynamic using confidence interval test with AMS and spectrum subtraction, the error of estimated SNR is decreased. Experiment results show the proposed method yield good performance for attenuating the effect of noises and can improve the robustness of ASR.

III. RECOGNITION EXPERIMENTS

The recognition experiments were carried out using the continuous speech data of Chinese 863 database. Different noises were artificially added to the speech to form the noisy speech. Before mixing speech and noise, target values for the speech-to-noise ratio (SNR) were calculated in dB for twenty-six sub-bands derived from the ratio of RMS

values of speech and noise respectively. The noisy speech is 16kHz sampling rate and 16bit Quantization. The first processing stage is a pre-emphasis of the input signal with a first-order high pass filter. The next steps for forming the AMS feature are almost same as the AMS model made by Tchorz apart from a few modifications.

We use 32ms frame as long frame with 16ms overlapping, then the 32ms frame was further subdivided into overlapping subframe of 4.0 ms duration (64 samples) with a progression of 0.25 ms (four samples). Every subframe is multiplied by Hamming window, padded with zeros to obtain a frame of 128 samples, and transformed with an FFT into a complex spectrum with a spectral resolution of 125 Hz. The 64 values are transformed into 26 energy coefficients according MEL scale[2], with characteristic frequency ranging from 100 to 7300Hz. Then every coefficient along time axis with the same characteristic frequency from one section is used to calculate the modulation frequency and transformed to a Bark scale. Finally, from every 32ms long frame, one pattern of 26x15 can be gotten .

These pattern can be used as inputs of a neural network for classification in training and test stage. For training of the neural network, mixtures of speech and noise are generated artificially to control the SNR. The clear signal and noise signal are also divided by 32ms with 16ms overlapping. After FFT is made, the FFT results in 26 frequency channels are filtered with triangle filters, and the SNRs of the 26 channels are recorded before the mixtures of speech and noise. The 26 channels SNRs value can be used as Neural Network Classification input in training stage.

After the SNRs γ_k were estimated by AMS Neural Network Classification, we can get energy of subband signal $|\hat{S}_K|^2$ by using Spectral Subtraction as

$$|\hat{S}_K|^2 = |Y_k|^2 / (1 + \frac{1}{\gamma_k}) \quad (2)$$

and get the energy of noise subband $|\hat{N}_k|$ by

$$|\hat{S}_K|^2 / \gamma_k = |\hat{N}_k|^2 \quad (3)$$

We use 32 frame's noise energy value to calculate the expectation and variance of noise as

$$\mu_k = \frac{1}{32} \sum_{j=1}^{20} N_k(j) \quad (4)$$

$$\delta_k = \sqrt{\frac{\sum_{j=1}^{20} (N_k(j) - \mu_k)^2}{32}} \quad (5)$$

Before the starting of speech or in the interval of speech, the noise energy can be directly used for calculating μ_k and δ_k . Then the recursive calculation was made to get the renewed values as follows:

$$\mu_k(i) = [\mu_k(i-1) \times (i-1) + N_k(i)] / i \quad (6)$$

$$\delta_k(i) = \sqrt{\frac{\delta_k^2(i-1) + (N_k(i) - \mu_k)^2}{i}} \quad (7)$$

Finally we can use formula (1) conduct the Confidence Interval validation. The process is as follows:

If $N_k - \mu > \delta$ the energy of noise is $\mu + \delta$

ELSE IF $N_k < \mu - \delta$ the energy of noise is $\mu - \delta$

ELSE the energy of noise is result of AMS.

IV. EXPERIMENTS RESULTS AND ANALYSES

Two types of noises were used in the test data, one is Babble, which is nonstationary noise, another is Gaussian, which is generally thought as stationary noise. Baseline system has not any noise processing. AMS+ISS stands for using AMS and Spectral Subtraction for processing noise, AMS+CIT stands for AMS and Confidence Interval test for processing noise.

From the Table 1, we find that the recognition accuracy will degrade under noisy environment when the SNR is less than 10dB. Noise attenuating processing can improve the performance of ASR evidently. For Gaussian noise, the difference between the AMS with Spectral Subtraction and AMS with confidence interval test is not distinct, but for

Table 1 The syllable recognition Accuracy rates of BASELINE, AMS+ISS, AMS+CIT

SNR (dB)	Babble			Gaussian		
	Baseline	AMS+ISS	AMS+CIT	Baseline	AMS+ISS	AMS+CIT
-10	N/A	N/A	10.95	N/A	N/A	N/A
-5	-3.07	N/A	18.24	N/A	10.07	25.23
0	0.07	45.32	62.04	0.49	51.02	64.56
10	35.55	60.68	68.13	20.42	58.73	68.05
20	70.37	71.26	75.06	51.08	73.85	76.39
30	75.08	71.17	77.21	72.14	70.47	74.04

Babble noise, the AMS with confidence interval test is superior to the AMS with Spectral Subtraction.

V. CONCLUSIONS

This paper presents one method for noisy speech recognition, this method can effectively apply the AMS SNR estimation for ASR system in some extent, it can avoid the impact of the overestimation and underestimation for ASR system. It can be used as an supplement to AMS estimation in noisy speech recognition.

Confidence interval test is used in this paper to improve the reliability of the estimation of SNR. In the training process, a large of statistics are made to get the confidence interval information of the SNRs. In the recognizing process, the confidence interval are used to decide reliability of the used SNRs. Experiment results show the proposed method yields good performance for attenuating the noises and can improve the robustness of ASR. Further study will test the proposed approach with more types of application cases for robust speech processing.

ACKNOWLEDGMENT

This study was supported by the Natural Science Foundation of Shandong Province (No. Y2007G31)

REFERENCES

- Xin M, Zhou WD (2006) Robust speech feature extraction based on dynamic minimum subband spectral subtraction. Lecture Notes in Control and Information Sciences 345: 1056-1061
- Flores JAN, Young SJ (1994) Continuous speech recognition in noise using spectral subtraction and HMM adaptation. ICASSP 1:409-412
- Raj B, Seltzer M, and Stern R (2000) Reconstruction of damaged spectrographic features for robust speech recognition. Proceedings of the International Conference on Spoken Language Processing 1: 375-360
- Gales, MJF, Young SJ (1996) Robust continuous speech recognition using parallel model combination. IEEE Transactions on Speech and Audio Processing 4, 352-359.
- Langner G, Sams M, Heil P, et al. (1997) Frequency and periodicity are represented in orthogonal maps in the human auditory cortex: Evidence from magnetoencephalography. J. Comp. Physiol.181: 665-676
- Hermansky H (1997) The Modulation Spectrum in Automatic Recognition of Speech. IEEE Workshop on Automatic Speech Recognition and Understanding 140-147
- Tchorz J, Kollmeier B (2003) SNR Estimation Based on Amplitude Modulation Analysis With Applications to Noise Suppression. IEEE Transactions on Speech and Audio Processing 11: 184 - 192

System of magnetic coupled PPM transcutaneous wireless communication

Weiming Wang¹, Bozhi Ma¹, Hongwei Hao¹, Luming Li¹

¹Tsinghua Space Center, Tsinghua University, Beijing, China

Abstract — There are still some problems in telemetry technique for implantable medical systems now, such as relatively high power consumption, complex circuits or large bulk. In order to solve above problems, an effective pulse position modulation (PPM) method is adopted in this paper, that make possible the design of simultaneously lower power consumption, good communication distance and good displacement tolerance while keeping circuitry simple, particularly in the implantable device. PPM is frequently used in lower power consumption or high reliability systems. We use 2-PPM in this paper, all the coding and decoding processes of PPM are completed with microchip. The approach of transmitting signal is via two magnetic coupling coils, air-cored coil of $\Phi 50\text{mm}$ for programmers and ferrite-cored coil of $\Phi 3.8\text{mm}$ for implantable device. A magnetic coupled PPM transcutaneous wireless communication resolution is presented in this paper. Full-bridge topology with push-pull driving is adopted as amplifier in programmer. Compared with the common-used class-E amplifier, the full-bridge one is simple and reliable. In this paper, over two inches bidirectional communication distance between implantable device in the body, with titanium container, and programmer outside the body is realized, at the same time, the communication system is with good displacement tolerance and coil displacement mismatch question is well solved. The average power consumption is about 33uA under typical condition for implantable communication device in the PPM system, it is lowered greatly compared with our amplitude shift-keying (ASK) system, ASK's average power consumption is about 10.3mA at the same test condition.

Keywords — Implantable, transcutaneous wireless communication, PPM, low power consumption, coupled coils.

I. INTRODUCTION

The tendency of implantable medical device wire communication technique is higher data transfer speed, lower power consumption, smaller bulk, higher reliability, better communication distance and displacement tolerance.

Modulation and demodulation method is very important for communication system performance. ASK is widely used for easy realized in implantable medical device [1], but it is of high power consumption and slow data transfer speed. With the development of wireless communication technique, pulse modulation method such as PPM for its low consumption and high reliability has been tried in implantable medical systems [2], but PPM is hard to realize for receiver need synchronization.

The continuing interest in implantable medical device has popularized the use of inductive links as primary means for wireless communication. Air-cored coils are usually used as antenna [3] and the designed communication distance is about 40 mm. Cored coils tried also [4], but no great improvement was made. In this paper, Cored coil has been used again in implantable device aiming for better performance and small bulk.

The formula (1) is given in article [5], where d_1 and d_2 is diameter of programmer coil and implantable device coil respectively. This formula is verified by many following studies when short column air-coiled used. In this paper, we get result beyond the formula.

$$d_1^2 = d_2^2 + 4D^2 \quad (1)$$

Several typical forms of coil misalignment were given in article [6]. For PPM system in this paper, coil misalignment question is well solved because transmitting power and efficiency is improved further.

II. MATERIALS AND METHODS

A. PPM frame format and waveform design

In this paper, 2-PPM is used for data modulation. When data is '0', the pulse position remains where it is, and pulse interval is still pulse period; when data is '1', an offset occurs. The formula of 2-PPM modulation is given by $s(t)$:

$$s(t) = \sum_{k=-\infty}^{\infty} p(t - kT_f - b_k\delta_p) \quad (2)$$

Where $b_k \in \{0,1\}$ is data, δ_p is pulse offset, T_f is pulse period, $P(t)$ is basic pulse signal, $\sum_{k=-\infty}^{\infty} p(t - kT_f)$ is pulse series.

Shown in Fig 1 is PPM waveform and in Fig 2 is frame format in this paper.

We design carrier frequency is about 160kHz. For high data transfer speed, PPM need higher carrier frequency, but the carrier frequency is limited by encapsulation material titanium.

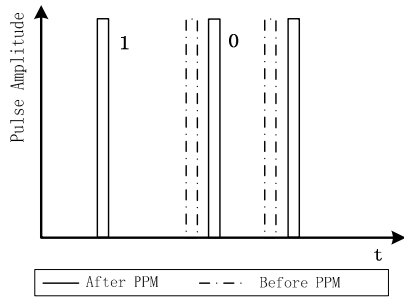


Fig. 1 Waveform of 2-PPM

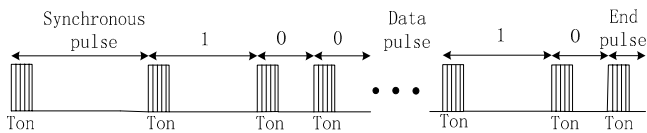


Fig. 2 Sketch of designed PPM data protocol

PPM signal is of high average-power-efficiency because of its narrow pulse and method of modulation. In this paper, the pulse duration T_{on} is set less than $3\mu S$.

Different pulse waveforms of PPM are designed in this paper according to implantable medical device application need. The waveform of programmer antenna transmitting is equal amplitude carrier, which makes implantable device receiving circuit simple, and the waveform of implantable device transmitting is damped carrier, which makes implantable device transmitting circuit simple, and can decrease power consumption farther compared with equal amplitude carrier. Experimental waveforms are shown in Fig 5 .

B. PPM system design

The sketch of the programmer is shown in Fig 3 . RS232 is used in communication between programmer and PDA. The programmer mainly consists of transmitting circuit in real line frame and receiving circuit in broken line frame.

Microprocessor, resonant capacitor and antenna coil is common-used by transmitting and receiving circuit for decreasing bulk and avoiding disturbance from two antennae. The microprocessor is mainly used for coding when programmer transmitting and decoding when programmer receiving. Resonant capacitor and antenna coil works in series-resonance mode when transmitting or receiving data.

Programmer amplifier uses full-bridge topology with push-pull driving instead of class-E, no mismatching between the switching frequency of the driving device and the resonant frequency of the load network occurs when using class-E, which will cause excessive power loss in the active

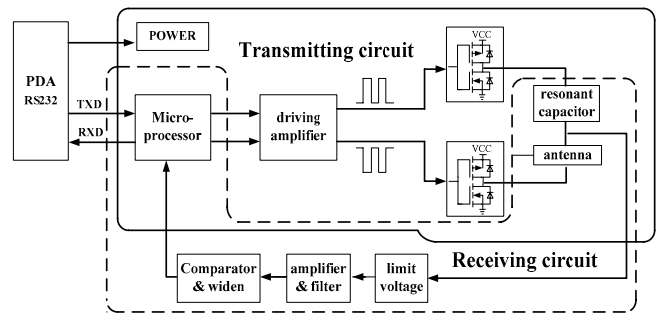


Fig. 3 Design of the programmer

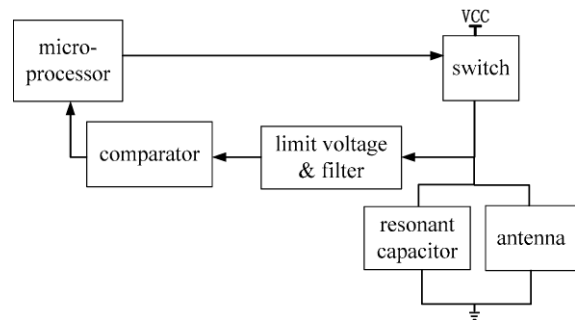


Fig. 4 Design of implanted communication circuit

device and may destroy the active device. Programmer amplifier working in LC series-resonance mode in PPM system in this paper, so the efficiency is higher than typical class-E amplifier working in LCR series-resonance mode, Programmer is powered by PDA battery.

The sketch of the implantable communication circuit is shown in Fig 4 . The implantable communication circuit mainly consists of PPM transmitting circuit and receiving circuit. Microprocessor, resonant capacitor and antenna is common-used by transmitting and receiving circuit for decreasing bulk and avoiding disturbance from two antenna. The antenna is ferrite-cored coil. The microprocessor is mainly used for coding when implantable communication circuit transmitting and decoding when implantable communication circuit receiving. Resonant capacitor and antenna coil works in parallel-resonance mode for circuit simple when transmitting data. Receiving circuit is simple and mainly consists of comparator and filter because of receiving equal amplitude PPM waveform.

C. About magnetic coupling

Magnetic coupling of programmer antenna coil and implantable antenna coil is one of the most important parts in the system design, and it has great influence on the distance

and displacement tolerance of communication. No wide-ranging treatment of such coil design has been published, perhaps because the specification imposed are so diverse that entirely different designs result.

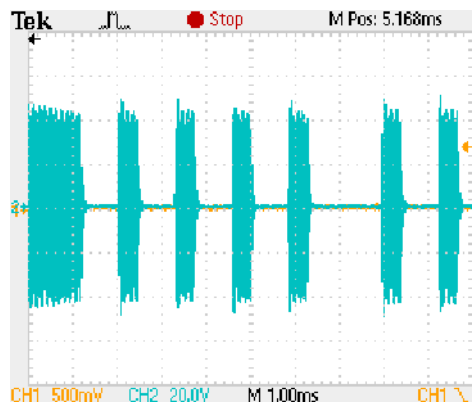
The programmer and implantable communication device antenna coils circle number ratio, coil shape and resonance frequency is considered on the whole in this paper. PPM carrier frequency of programmer and implantable communication device is nearly same, which bring great improvement of coupling coefficient.

III. RESULTS AND DISCUSSION

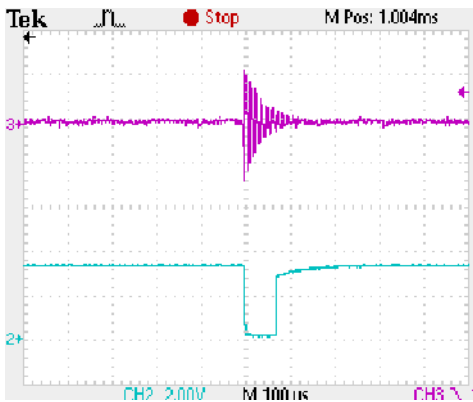
A. PPM test waveforms

Fig 5 shows the waveform of PPM on programmer antenna.

The Waveform of programmer antenna transmitting is equal amplitude carrier with about 166 kHz, which makes implantable device receiving circuit simple. The waveform



(a) Waveform of antenna transmitting



(b) Waveform of antenna receiver& demodulated signal

Fig. 5 Waveform of PPM on programmer antenna

of programmer antenna received is damped carrier with about 166 kHz, which makes implantable device transmitting circuit simple, and can decrease power consumption farther compared with equal amplitude carrier.

B. Communication distance and displacement tolerance

The test parameters, communication distance and displacement tolerance test results are shown in Tab. 1 and Fig. 6. Over two inches wireless bidirectional communication distance between devices implanted in the body, with titanium container, and controller outside the body is realized, and the wireless communication system is with good displacement tolerance.

Table 1 Test parameters

Parameters	Programmer Coil 1	Programmer Coil 2	Implantable device coil
Antenna diameter(mm)	Φ50	Φ70	Φ3.8
Antenna High (mm)	4.5	3.5	3
Coil	Air coil	Air coil	Ferrite coil
Antenna inductance(μH)	33	33	560
Carrier frequency (kHz)	160	160	160

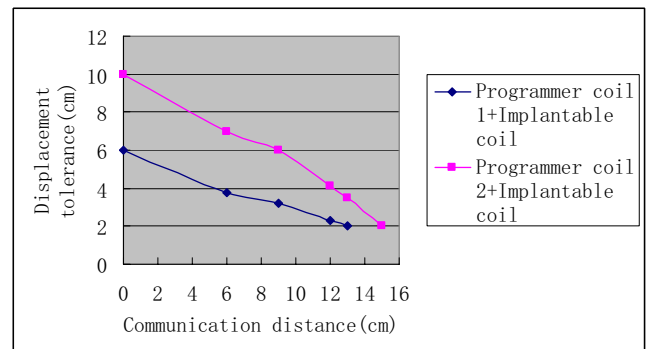


Fig. 6 Communication distance and displacement tolerance test

C. Designed PPM programmer

The implantable neuro-stimulator, includes implantable communication circuit, weighs 34 g, with a size less than 47mm×49mm×10mm.

Fig. 7 shows PDA and the programmer. The bulk of PPM programmer is decreased greatly compared with our ASK programmer, And PPM system is powered by PDA battery.



(a) PDA and designed PPM system (b) PDA and ASK system

Fig. 7 PDA and programmer

D. Implantable device power consumption

The average power consumption is about 33uA under typical condition for communication device implanted in the body in this PPM system, it is lowered greatly compared with our ASK modulation system, ASK's average power consumption is about 10.3mA at the same test condition.

IV. CONCLUSIONS

We have presented a transcutaneous wireless bi-directional communication system resolution. In this system, 2-PPM is successfully used for data modulation. All the coding and decoding process of PPM is completed with microchip. Magnetic coupling coils are used for signal transmission in this system, Coil time-shared common-used makes communication circuit bulk decreased. Full-bridge topology with push-pull driving is adopted for amplifier instead of the common-used class-E amplifier in programmer.

Experiments show the whole system is with lower power consumption, good communication distance and good displacement tolerance, at the same time, circuitry simple and small bulk. Coil misalignment question is well solved at about 40mm communication distance.

ACKNOWLEDGMENT

This study is supported by the National High Technology Research and Development Program ("863" Program) of China and National Key Technology R&D Program of China.

REFERENCES

1. Hong Yu, Rizwan et al. (2006) A low power ASK clock and data recovery circuit for wireless implantable electronics, IEEE Custom Intergrated Circuit Conference (CICC),2006, pp 249-252
2. Wu Dongqing, Wang Baohua et al. (1998) A Multichannel implantable electronic system with TDM, Proc. Vol.4, IEEE engineering in medicine and biology society, 1998, pp 1921-1923.
3. Troyk PR, Schwan MA. (1992) Class E drive for transcutaneous power and data link for implanted electronic device. Med. & Biol. Eng. & Comput. 30:69-75
4. Cao Nini(2002),Data communication between external programmer and implantable medical device. Master dissertation of Xi'an Jiaotong University.
5. Ko, W. H., Liang, S. P. and Fung, C. D. F. (1997) Design of radio-frequency powered coils for implant instruments. Med. & Biol. Eng. & Comput.,15:634-640
6. Mani Soma, Douglas C et al. (1987) Radio-frequency coils in implantable devices: misalignment analysis and design procedure. Proc. Vol.4, IEEE transactions on biomedical. Engineering, 1987, pp 276-282

Author: Li Luming
 Institute: Tsinghua Space Center, Tsinghua University
 Street: Rm.803, Central Main Building, Tsinghua University, Beijing 100084
 City: Beijing
 Country: China
 Email: lilm@tsinghua.edu.cn

SPME-GC analysis of alkanes and aromatic hydrocarbons in human breath to screen lung cancer

Hao Yu¹, Ping Wang²

¹ Biomedical Engineering Department, School of Electronics and Information Engineering, Shenzhen Polytechnic, Shenzhen, China

² Biosensor National Special Laboratory, Department of Biomedical Engineering, Zhejiang University, Hangzhou, China

Abstract — in the article, a new method using Solid Phase Microextraction and Gas Chromatography (SPME-GC) was applied to analyze alkanes and aromatic hydrocarbons in human breath to screen lung cancer. This method was thoroughly evaluated. And total thirty breath samples, half from lung cancer patients and the other half from healthy persons, have been measured by this method. It got significant differences between lung cancer patients and health persons, demonstrating that the method is new and feasible to apply in lung cancer breath screening.

Keywords — Solid Phase Microextraction, Gas Chromatography, alkanes and aromatic hydrocarbons, lung cancer, screen

I. AIM OF STUDY

Since 1999, researchers have reported some VOCs in human breath as markers of lung cancer, most of them were alkanes and aromatic hydrocarbons from 10^{-12} ppt to 10^{-9} ppb^[1-3]. Alkanes and aromatic hydrocarbons in human breath are much lower than major compounds, thus pre-concentration became a very important step before analyzing those VOCs. However, traditional pre-concentration methods had disadvantages, such as require complex devices, cost long time to prepare and need multi-components sorbent for especial VOCs^[4-7].

Solid phase microextraction (SPME) was invented by Pawliszyn in late 1989 as a new pre-concentration technology^[8,9], in which a fused-silica fiber coated with a stationary phase was used. SPME was greatly developed and widely adopted, for it more solventless, rapid, economical, non-labor intensive, and integrated than traditional sampling method^[10-12]. Hundreds of papers have been published, but at present SPME isn't applied in detecting alkanes and aromatic hydrocarbons in human breath. In this experiment, the applicability of SPME to pre-concentrate alkanes and aromatic hydrocarbons in human exhaled air with gas-chromatography (GC) to screen lung cancer has been studied.

II. EXPERIMENTS

Preparation of calibration gas: Reagents of Benzene, Styrene, Propyl benzene, Decane, and n-Undecane (all in HPLC grade) were all purchased from Acros Organics through local J&K Chemical LTD, prepared for calibration gases. Gas sampling bulbs (2.5L) with screw cap and silicon septum, were supplied by local BFC tech Co. Different levels of saturated vapor of VOCs were separately taken from headspaces of corresponding solutions at 25°C by Hamilton Series 1700, injected into the bulb filled with purified nitrogen gas, to prepare calibration gas.

Collection of human breath: 5L Tedlar[®] sampling bags supplied by Alltech Associate, Inc., were used to transport breath gas to laboratory for analysis. The bags will not be the source of contamination. Every time before collecting human breath, the bags were cleaned by acetone then thoroughly rinsed by deionized water for several times, and the bags were filled with purified nitrogen and dried at 80°C for 12 hours to completely eliminate rest acetone.

Pre-concentration conditions: A manual SPME holder with Polydimethylsiloxane film (PDMS 100µm, Supelco 57300-U) was adopted for extracting hydrocarbons. SPME extract alkanes and aromatic VOCs in calibration gases and VOCs in same controlled extracting conditions. The conditions were optimized at 25°C and 100% relative humidity for extracting 20 minutes^[13-15]. After extracted, the analysis were detached from the SPME fiber in the injection port at 320°C, non-split operation, 60 ml min⁻¹ split vent flow.

Instrumentation conditions: Analyzing VOCs was performed by Shimadzu GC17A gas chromatograph (GC), which equipped with flame ionization detector (FID). DB-1 fused-silica capillary column (0.25µm film, 0.25mm ID x 30m) was purchased from Sigma-Aldrich, Inc. The oven temperature we programmed 10mins at 40°C, then 5°C min⁻¹ to 150°C for 10mins. Injector and detector temperature were 280°C and 320°C respectively. The GC column flow was nominally 1 ml min⁻¹

III. RESULTS AND DISCUSSION

The experiments were separated into two parts. First, thoroughly evaluated this method, and then applied this method in thirty breath samples.

A. Method evaluation

The characteristics of SPME-GC method were thoroughly evaluated by calibration gases. The relationship between SPME-GC peak area response and every VOC concentrations were established, in order to analyze the feasibility of this method.

Repeatability: Static extractions in same determinate conditions were performed for five times on every Benzene, Styrene, Propyl benzene, Decane, and n-Undecane standard gases separately in same concentration in same conditions. The relative standard deviations (%RSD, n=5) of the static extraction method were detailed in Table 1.

Linearity: The relationship between SPME-GC peak area responses and VOC concentrations was also investigated by studying the linearity of this method. Four level concentrations from 10^{-7} g/ml to 10^{-9} g/ml of every VOC were measured, and the measurement of every VOC in every concentration was performed for three times to get the average result. Table 1 also indicated the linear parameters and correlation coefficients for line regression.

Limit of detection: The sensitivity of SPME restricts the detection limit. We defined signal-to-noise ratios equal to 3 as the detection limit and signal-to-noise ratios equal to 10 as quantification limits of VOCs. The results were also showed in Table 1.

As results, relative standard deviations (% R.S.D., n=5) of the static extraction method were less than 9.8 %; Correlation coefficients for linear regression were relatively high and ranged from 0.9845 to 0.9966; the lowest detection limit was achieved in 1.2×10^{-2} ng/ml, and the lowest quanti-

fication limit was achieved in 0.04ng/mL. It indicates that this SPME-GC method is feasible for analysis alkanes and aromatic hydrocarbons in human breath.

B. Human breath analysis

This method was applied in analyzing 30 human breath, 15 of which were from lung cancer patients and the other 15 of which were from controlled healthy persons.

Breath sampling: In human breath, two-thirds of breath is from lung alveolar, and other one-third is the dead space air, including from mouth, nose, pharynx, trachea, and bronchi^[16]. To ensure collect more information breath, the subjects were required to smoke-free for one month and equilibrium with environment for more than 24hours, then wear a nose clip, exhaled several deep breath to the Tedlar[®] sample bags. Environmental air has been bumped into another Tedlar[®] sample bag.

Breath Analysis: 30 subjects including 15 lung cancer patients numbered from 1a to 15a, and 15 health subjects numbered from 1b to 15b. The breath samples have been analyzed, and counteracted the environmental effects. These breath samples were all quantitatively analyzed. The results from lung cancer patients and health subjects were showed in Table 2.

In thirty human breath samples, it was found total 13 breath samples contained the alkanes and aromatic hydrocarbons, in which 11 breath samples were from lung cancer patients and the other two breath samples from controlled healthy persons. So the VOCs were detected in 73.3 % lung cancer breath, significantly higher than in control breath (13.3 %). Although all the lung cancer patients were smoke-free for one month, we still considered they had smoked. There were no obvious evidences demonstrated any relationship between smoked one month ago and the VOCs in lung cancer patients' breath.

Table 1. The relationship between SPME-GC response peak area with analyte concentrations. Every Point is an average of five measurements. In linearity, $y = p1 * x + p2$ (y is Peak Area, x is analyte concentration in ng/ml)

Analyte Name	Repeatability		Linearity		Detection Limit	
	Precision n=5 (%RSD)	p1	p2	Correlation Coefficient	Detection Limit, S/N=3 (ng/ml)	Quantification Limit, S/N=10 (ng/ml)
Benzene	8.2	1.201×10^3	6.359×10^3	0.9935	2.5×10^{-1}	0.84
Styrene	3.7	2.380×10^2	6.563×10^2	0.9966	1.26	4.2
Propyl benzene	5.1	4.437×10^3	-5.704×10^3	0.9845	6.7×10^{-2}	0.23
Decane	9.8	2.327×10^4	1.216×10^2	0.9924	1.2×10^{-2}	0.04
n-Undecane	5.9	3.542×10^3	1.965×10^3	0.9882	2.7×10^{-2}	0.08

Table 2. The VOCs concentrations detected in thirty subjects' breath, all units in ng/ml. 1a to 15a from lung cancer patients, and 1b to 15b from control human.

Subject Number	Benzene	Styrene	Propyl benzene	Decane	u-Undecane
1a		18.14		1.15	1.03
2a		10.18	2.50		
4a	38.1				
7a					0.21
8a			3.21		8.51
9a	1.02		1.61	0.10	
11a		18.39		0.34	0.23
12a					0.17
13a	7.91		0.77		
14a		1.53		0.89	0.10
15a	2.35			0.32	0.24
8b				0.049	
9b					0.15

IV. CONCLUSION

The work proposed SPME-GC method to detecting alkanes and aromatic hydrocarbons for screening lung cancer. Significant differences results have been got between lung cancer patient breath and healthy person breath. It was shown that we have established a new and feasible SPME-GC method to analysis alkanes and aromatic hydrocarbons in human breath for screening lung cancer conveniently and non-invasively. Furthermore, if some types of SPME stationary phase can be adopted for testing other VOCs in human breath, this method can be adopted to screen other diseases conveniently and non-invasively by breath detection techniques.

REFERENCES

- [1] Phillips M, Gleeson K, Hughes JM, Greenberg J, Cataneo RN, Baker L, McVay WP. (1999) Volatile organic compounds in breath as markers of lung cancer: a cross-sectional study. *Lancet* 353:1930-1933
- [2] A. Manolis. (1983) The diagnostic potential of breath analysis. *Clin. Chem.* 29: 5-15.
- [3] Krotozynski B.K., Gabriel G., O'Neill H.J. (1977) Characterization of human expired air a promising investigative and diagnostic technique *Chromatogr. Sci.*, 15:239-244.
- [4] Ebeler SE, Clifford AJ, Shibamoto T. (1997) Quantitative analysis by gas chromatography of volatile carbonyl compounds in expired air from mice and human. *J Chromatogr B Biomed Sci Appl* 702: 211-215
- [5] Groves, W.A., Zellers, E.T., Frye, G.C. (1998) Analyzing organic vapors in exhaled breath using a surface acoustic wave sensor array with preconcentration: selection and characterization of the preconcentrator adsorbent. *Anal. Chim. Acta* 371:131-143.
- [6] Gordin, A., Amirav, (2000) A. new method and device for vapor and gas sampling. *J. Chromatogr. A.* 903(1-2):155-72.
- [7] Van Gossum, A., Shariff, R., Lemoyne, M., Kurian, R., Jeejeebhoy, K.N. (1988) Increased Lipid Peroxidation after Lipid Infusion as Measured by Breath Pentane Output. *Am. J. Clin. Nutr.*, 48:1394-1399.
- [8] R. Berlardi, J. Pawliszyn, (1989) The Application of Chemically Modified Fused Silica Fibers in the Extraction of Organics from Water Matrix Samples and Their Rapid Transfer to Capillary Columns. *Water Pollut. Res. J. Can.* 24: 179-191.
- [9] C.L. Arthur, J. Pawliszyn. (1990) Solid phase microextraction with thermal desorption using fused silica optical fibers. *Anal. Chem.* 62: 2145-2148.
- [10] A. Balinova. (1996) Strategies for chromatographic analysis of pesticide residues in water. *J. Chromatogr. A* 754:125-135.
- [11] H.G.J. Mol, H.G.M. Janssen, C.A. Cramers, J.J. Vreuls, U.A.T. Brinkman. (1995) Trace level analysis of micropollutants in aqueous samples using gas chromatography with online sample enrichment and large volume injection. *J. Chromatogr. A* 703:277-307.
- [12] J.R. Dean, G. Wade, I.J. Barnabas. (1996) Determination of triazine herbicides in environmental samples: Review *J. Chromatogr. A* 733:295-335.
- [13] PROSEN, Helena, ZUPANČIČ-KRALJ, Lucija. (1999) Solid-phase microextraction. *TrAC, Trends anal. Chem.* 18: 272-282.
- [14] C. L. Arthur, L.M. Killam, K. D. Bucholz and J. Pawliszyn. (1992) Automation and Optimization of Solid-Phase Microextraction. *Anal. Chem.*, 64:1960-1966.
- [15] P. A. Martos, J. Pawliszyn. (1997) Calibration of Solid Phase Microextraction for Air Analyses Based on Physical Chemical Properties of the Coating. *Anal. Chem.* 69:206-215.
- [16] Periago JF, Prado C, Ibarra I, Tortosa J. (1993) Application of thermal desorption to the biological monitoring of organic compounds in exhaled breath. *J Chromatogr A.* 657: 147-153.

Author: Yu Hao
 Institute: Shenzhen Polytechnic
 City: Shenzhen
 Country: China
 Email: vinyyu@hotmail.com

Application of Independent Component Analysis on Artifacts Removal in the Time-Frequency Analysis of Transient Evoked Otoacoustic Emissions

Ying Zhao, Liang Dong, Qiushi Ren, Xinyu Chai

Department of Biomedical Engineering, Shanghai Jiao Tong University, Shanghai, 200240 China

Abstract — TEOAEs (Transient evoked otoacoustic emissions) analysis has become a clinical evaluation of peripheral auditory system as a basic and safe and objective means. Currently, one of the most effective OAEs analysis methods is time-frequency analysis method. In order to study the time-frequency distribution of TEOAEs, we established an improved TEOAEs simulation model which was based on the existing international generic TEOAEs simulation and the latency of TEOAEs in the latest research.. To the new model, we compared the results which had been got by Linear class, Cohen's class, Affine class, Rearrangement class time-frequency distribution, and come to the conclusion that the cone-shaped kernel distribution (CKD) is the best description for TEOAEs. Meanwhile, in view of the problem that the TEOAEs artifacts affect the CKD, we proposed the application of ICA (independent component analysis) to remove the artifacts so as to improve the SNR (signal to noise ratio) and verified its reliability in disposing the TEOAEs contaminated by the artifacts. Ultimately we have established a two-step analysis method called FastICA-CKD. The new method was used to investigate into the real TEOAEs which were recorded in linear recording mode under different stimulus intensities. After that, it also has been discussed that was the difference among the TEOAEs which were recorded in linear recording mode before and after FastICA and the TEOAEs which were recorded in derived nonlinear recording (DNLR) mode under different stimulus intensities. Their correlation and the integrity of these useful components of TEOAEs in the CKD have been compared.

Keywords — TEOAEs, time-frequency analysis, CKD, ICA, FastICA-CKD.

I. INTRODUCTION

Otoacoustic Emissions (OAEs) are the phenomenon that peripheral auditory system can generate sound wave actively except receiving sound passively. OAEs are low-level sound signals produced by the inner ear of normal-hearing people, which pass through the ossicular chain and eardrum to the external auditory meatus [1]. Due to the close relationship between the phenomena with the physiological process of sound wave in the cochlea, it becomes the objective standards for estimating the function of peripheral auditory system.

Transient evoked OAEs (TEOAEs) are one of OAEs, which occur after shortly clicks or tone-burst stimuli[1,2]. Nowadays, TEOAEs have been widely used in testing the capability of hearing, diagnosing the cochlea disorders of hearing losing patients, monitoring the ototoxicity induced by medicine and identifying the hearing impairment cause by some special matters.

Because OAEs represent the actively mechanical movement in cochlea, analyzing TEOAEs in Time-Frequency domain is important to study and demonstrate the generant mechanism of TEOAEs and the relationships among OAEs response, cochlear mechanical movement and physiological characters. However, due to traditional Fourier transformation has the shortcoming that this technique only defines the whole frequency distribution and cannot show any frequency varieties, it is not an appropriate analysis method to process the TEOAEs' signals. Therefore, some investigators suggest that joint time-frequency representation (TFR) is a more useful method to present the signal in time and frequency domains at the same time. Furthermore, Linear class, Cohen's class, Affine class, Rearrangement class time-frequency distribution are used in analyzing all kinds of physiological signals [6-11]. Therefore, using these methods in the non-stationary signals such as TEOAEs becomes a advisable choice.

According to the former researches, time-frequency analysis is one of the most effective methods for OAEs and achieves obvious results. Nevertheless artifacts become another factor which always affects the results of different analysis. The purpose of this study presented here is to remove the artifacts using independent component analysis (ICA) method in processing TEOAEs signal. The rest of the paper is organized as follows: Section II provides a detailed description of the trial and processing method. In section III, the results are presented in detail. Finally, the conclusion and discussion are given in section IV.

II. MATERIALS AND METHODS

Meanwhile, in the view of the problem that the TEOAEs artifacts affect the CKD, the independent component analysis (ICA) method is proposed to remove the artifacts so

as to improve the signal to noise ratio (SNR) and verified its reliability in disposing the TEOAEs contaminated by the artifacts.

A. Materials

Four volunteers (3 male and 1 female) participated in the trial. All of them are fully informed the procedures and purpose of the experiment before the formal trial. And they were with normal hearing and had no ear disease history.

The recording device was Otodynamic ILO88 system (Otodynamics Ltd, UK), and the probe was chose as the for-adult type. During the process of measuring TEOAEs, clicks were about 65~88 dB SPL. Linear mode and based on Derived Nonlinear recording mode were selected for testing. In order to reduce the artifacts in the response, a time window which was between 25 ms and 20 ms was chose to process the finial data.

B. Methods

Based on the synthesized five-gammatone click-evoked emission signal model, an improved TEOAEs simulation model is proposed, which used the existing international generic TEOAEs simulation and the latency of TEOAEs in the latest research [3-5].

In the new model, after the comparison between Linear class, Cohen’s class, Affine class and Rearrangement class time-frequency distribution, it can be seen that the

cone-shaped kernel distribution (CKD) is the best description for TEOAEs.

Cone-Shaped Kernels Distribution (CKD) was introduced by Zhao et al [6] and also called Zhao-Atlas-Marks distribution. CKD is a bilinear distribution which not only keeps the characters of finite time support but can improve spectral peaks and reduce cross-terms. The kernel distribution of CKD is:

$$\psi(t, \tau) = \begin{cases} g(\tau) & |\tau| \geq \alpha|t| \\ 0 & \text{otherwise} \end{cases} \quad (1)$$

Where α is the parameter used to adjust the cone slopes with the range of $2 \leq \alpha \leq \infty$. In order to control the bandwidth of low pass filter, finite and smooth function is selected as the cone function $g(\tau)$. Then the CKD is presented that:

$$CKD_x(t, v) = \int_{-\infty}^{+\infty} \left[g(\tau) \int_{-|t|/2}^{+|t|/2} x(s+\tau/2)x^*(s-\tau/2)ds \right] e^{-j2\pi vt} d\tau \quad (2)$$

FastICA algorithms is one of the common used ICA algorithms [12,13]. It is a computationally highly efficient method for performing the estimation of ICA. It uses a fixed-point iteration scheme that has been found in independent experiments to be 10-100 times faster than conventional gradient descent methods for ICA. Another advantage of the FastICA algorithm is that it can be used to perform projection pursuit as well, thus providing a general-purpose data analysis method that can be used both in an exploratory fashion and for estimation of independent components (or sources).

C. Procedures

The formal trial of TEOAEs was processed in the room shielded sound. Subject sat in the soft chair to keep silence. The basic sampling parameters were: the sample rate was 25 kHz, 12 bit A/D transformer was used, sampling time was 20ms and the length of sampling was 512 points. The band-pass filter was 600~6000Hz. The low frequency cut-off was used to restrain the reflected artifact of emissive sound wave, environment and the noise in the body. On the contrary, the high frequency cut-off was used to avoid mix overlap in FFT and restrain the noise of devices. For the sake of ensuring the correct collection of OAEs signal, the OAEs signal for one ear of one person was constituted by repetitions of multiple 20ms periods. Usually, it needed about 260 periods to get the OAEs signal. According to the former research, it reduced to 160 periods to get OAEs signal using ICA algorithms. There were four stimular groups per period to achieve linear and non-linear mode.

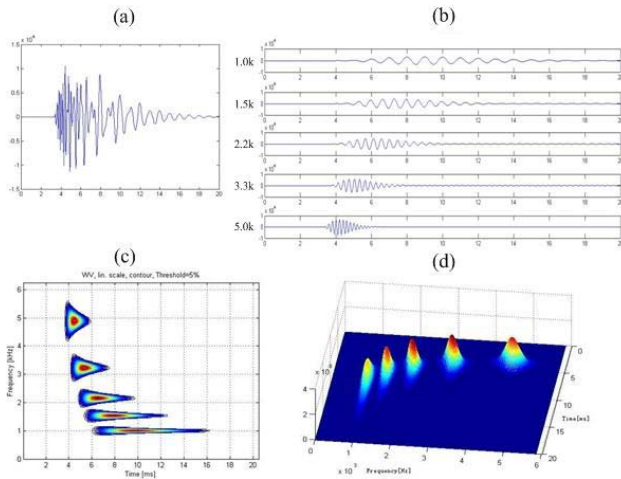


Fig. 1 Improved simulated click-evoked OAEs (CEOAEs) signal model in 68 dB SPL: (a) The simulated CEOAEs signal synthesized five-gammatone click-evoked emission signal model with latency; (b) five gammatones with central frequencies at 1.0, 1.5, 2.2, 3.3 and 5.0 kHz and corresponding latencies: 9.0, 7.5, 6.3, 5.3 and 4.4 ms ;(c) the time-frequency contour map of the improved CEOAE signal; (d) ideal time-frequency distribution of the improved CEOAE signal.

III. RESULTS

A. Materials

According to the definition of artifacts, a simulation artifact has been simulated and added into the new emulational TEOAEs signal in terms of different iterative coefficients. Ultimately a two-step analysis method called FastICA-CKD has been established.

Fig. 2 and Fig. 3 showed a testing result of one person's right ear during 10 stimulating intensities. When the linear recording mode was used, there would occur stimulating artifact during the beginning 0~6 ms. As the processing result of FastICA-CKD distribution showed, the component which was lower 1 kHz and among 2.5 ms and 5.0ms was easy to be gotten rid of. At the same time, the frequency segments occurred in the other time weren't affected by this distribution and preserved commendably. It indicated that the FastICA-CKD distribution can eliminate the effect of the CKD distribution of TEOAEs caused by artifact components, exhibit the full TEOAEs signals in time-frequency domain and offer the real time-frequency distribution for clinical study of OAEs.

The new method has been used in the real TEOAEs which were recorded in linear recording mode under different stimulus intensities. After that, the difference among the TEOAEs which were recorded in linear recording mode before and after FastICA and the TEOAEs which were recorded in derived nonlinear recording (DNLR) mode under different stimulus intensities has been compared. At the same time, their correlation and the integrity of these useful components of TEOAEs in the CKD has been shown in Fig. 4.

In the linear-stimulation mode, FastICA-CKD can eliminate the interfere of artifact which is the low frequency components occurred in 2.5-5.0 ms, preserve the useful components of TEOAEs after 6 ms perfectly and show the TEOAEs signal in the time-frequency space integrally. It not only improved the accuracy of time-frequency analysis, but also reflected the characters and information of the cochlea veritably.

In the nonlinear-simulation mode, DNLR-CKD can also eliminate the interfere of artifact which is the low frequency components occurred in 2.5-5.0 ms. However, it lost most main components of TEOAEs under low stimulative intensity (< 81dB SPL) and affected the distributing of CKD. Although the status can be improved by increasing the intensity, it is still lower than the status after FastICA in the linear-stimulation mode.

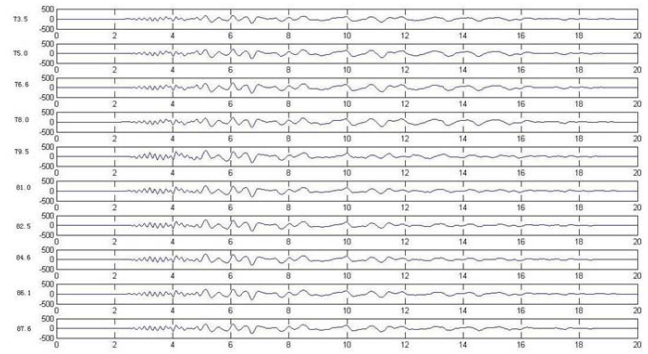


Fig. 2 The waveform of TEOAEs which was processing by ICA

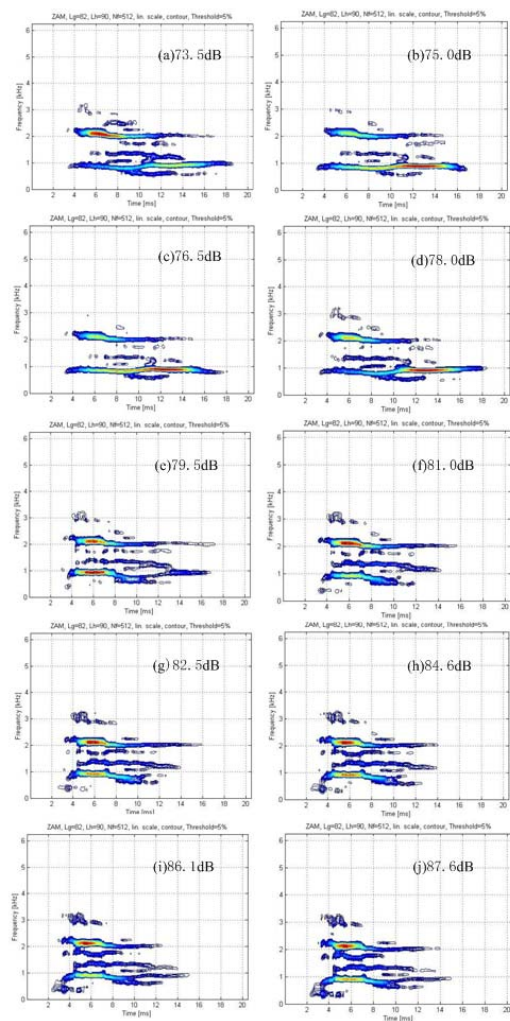


Fig. 3 The result of FastICA-CKD distribution which was 10 stimulating intensities sampling from one ear of one person..

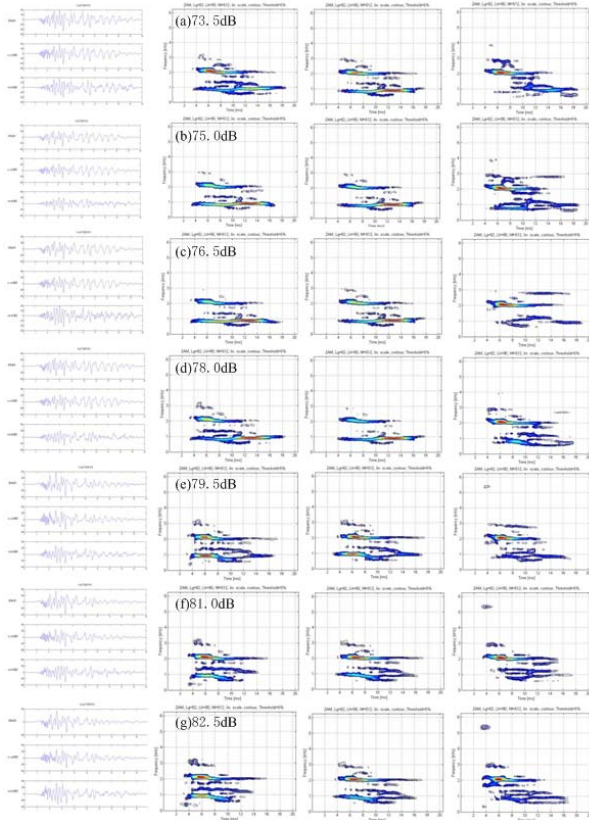


Fig. 4 Compared maps of original TEOAEs signal, after FastICA processing, after DNLN processing waves and CKD distributions among seven stimulating intensity: the waveforms from top to down are original, after FastICA processing and after DNLN processing waves; the CKD distributions from left to right are original TEOAEs, TEOAEs which was after FastICA processing and TEOAEs which was after DNLN processing.

After compared the results between DNLN-CKD after 6 ms and the original signal, it was found that some time-frequency aberrance occurred which caused that different asynchronous frequency components have varied phasic shift and noises under different stimulative intensity. So the DNLN-CKD method can't show the TEOAEs signal in the time-frequency analysis and reflected the characters and information of the cochlea veritably.

IV. DISSICUSION AND CONCLUSION

In order to investigate the method of removal the artifacts effect in time-frequency distribution of TEOAEs, we established an improved TEOAEs simulation model which was based on the existing international generic TEOAEs simulation and the latency of TEOAEs in the latest research. Based on the new model, we compared the results which had been got by different time-frequency distributions, and come

to the conclusion that the cone-shaped kernel distribution (CKD) is the best description for TEOAEs. Meanwhile, due to the problem that the TEOAEs artifacts affect the CKD, we proposed the application of ICA to remove the artifacts. After that, we have established a two-step analysis method called FastICA-CKD. The new method has been used to investigate the real TEOAEs which were recorded in linear recording mode under different stimulus intensities. Then, the two methods of FastICA-CKD and DNLN-CKD have been used in processing TEOAEs signals. After the comparison the two methods' correlation and the integrity of these useful components of TEOAEs in the CKD, we get the conclusion that FastICA-CKD can eliminate interfere of artifact, preserve the useful components of TEOAEs after 6 ms perfectly and show the TEOAEs signal in the time-frequency space integrally. It not only improved the accuracy of time-frequency analysis, but also reflected the characters and information of the cochlea veritably.

ACKNOWLEDGMENT

This research is supported by The National Natural Science Foundation of China (60671059); National High Technology Research and Development Program of China (863 Program, 2006AA04Z356); This research is supported by the National Basic Research Program of China (973 Program, 2005CB724302).

REFERENCES

1. Kemp D. T. (1978) Stimulated acoustic emissions from within the human auditory system. *J. Acoust. Soc. Am.* 64, 1386-1391.
2. Whitehead M. L., Stager B. B., and Lonsbury-Martin B. L. (1994) Measurement of otoacoustic emissions for hearing assessment. *IEEE Engineering in Medical and Biology*, April-May 1994, 210 - 226.
3. Wit H.P., van Dijk P. and Avan P. (1994) Wavelet analysis of real and synthesized click evoked otoacoustic emissions(Kemp-echoes). *Hear. Res.* 73,141-147.
4. Gabriella T., Ferdinando G., Paolo R. (1997) Time-frequency distributions of click-evoked otoacoustic emissions. *Hearing Research*, 106: 112-122.
5. Gabriella T., Ferdinando G., Paolo R. (1996) Latency distribution of click-evoked otoacoustic emissions. 18th Annual International Conference of the IEEE Engineering in Medicine and Biology society, Amsterdam, 5.8.1: Acoustic Phenomena.
6. Zhao Y, Altas LE et al. (1990) The use of cone-shaped kernels for generalized time-frequency representations of nonstationary signals. *IEEE Trans. On ASSP.* 37(6): 1084-1091.
7. Nawab,S.N. and Quatieri,T.F. (1988) Short-time Fourier transform, in *Advanced Topics in Signal Processing*, Lim, J.S. and Oppenheim, A.V., Eds, Prentice-Hall, Englewood Cliffs.
8. Grossman, A. and Morlet, J. (1984) Decomposition of Hardy functions into square integrable wavelets of constant shape, *SIAM J. Math.* 15,723-736.
9. Cohen,J. (1989) Time-frequency distribution-review, *Proc. IEEE*, 77:941-981.

10. O. Rioul, P. Flandrin. (1992) Time-Scale Energy Distributions: A General Class Extending Wavelet Transforms. *IEEE Trans. SP*, 40 (7): 1746 - 1757.
11. P. Flandrin, et al. (1996) *Appl. Comp. Harm. Anal.* 3(1): 10 - 39.
12. Hyvarinen A, Oja E. (1997) A fast fixed-point algorithm for independent component analysis. *Neural Computation*. 9(7): 1483.
13. Hyvarinen (1999) A. Fast and robust fixed – point algorithms for independent component analysis. *IEEE Trans. On Neural Networks*, 10(3): 626-634.

Author: Xinyu Chai
Institute: Department of Biomedical Engineering, Shanghai Jiao Tong University
Street: Dongchuan Road 800
City: Shanghai
Country: China
Email: xychai@sjtu.edu.cn

Based on the FPIA of high-throughput gene and protein detection analysis system

Ni Yuan¹, Ju Zhang², Lihong Yang¹, Yanhai Guo², Zhili Chen¹, Guoshao Chen¹

1. Xi'an University of Technology, Xi'an, China
2. Fourth Military Medical University, Xi'an, China

Abstract — A fluorescence polarization immunoassay (FPIA) technology of gene and protein the fluorescence polarization detection analysis systems, including overall design, optical systems and testing the basic structure principle, the test system hardware configuration, process control testing, test data processing, display, clinical results show fluorescence polarization automatic detection system design advanced, reliable operation, high accuracy detection and clinical testing to meet requirements.

Keyword — FPIA; gene and protein ; detection analysis systems; Optical System

I. INTRODUCTION

Certain substances certain wavelengths of light radiation, in the relatively short period of time launched a wavelength longer than laser light, such as fluorescent light on. This substance called fluorescent material.

The fluorescent material of a single plane polarized light irradiation, it can absorb solar energy to leapfrog into the excited state in the return to the ground state, energy and the release of a single plane fluorescence polarization. Fluorescence polarization and fluorescence polarization of the material by the excited molecules inversely proportional to the speed of rotation. Fluorescence polarization degrees are defined as follows:

$$P = (IVV - IVH) / (IVV + IVH) \quad (1)$$

The subscript before and after the two letters were fired and said the incident light polarization direction, and V (vertical) vertical, H (horizontal) level.

Because of the small molecular weight substances in solution in a lively rotating movement, launched its small degree of polarization of light. Molecular weight of the material, because rotational movement inhibited when it subject to certain of the direction of vibration excitation light after another out according to a certain wavelength of the direction of vibration of light polarization strong. Fluorescent labeling of the material in a particular material on the molecular fluorescence signs of small molecular weight substances because, it launched the degree of polarization of light on small, on the other hand, when the fluorescent signs material and the material of macromolecules, molecular weight great, fluorescence polarization large degree^[1].

Fluorescence Polarization (FP) detection technology is a fluorescent detection technology, when fluorescent signs substances measured by biochemical reactions and materials (such as biological macromolecules) combined with polarized light to stimulate tested substances, can be measured on strong polarization of the emitted light. In the optical path difference with the appropriate location polarizer and analyzer can measure the polarization of the measured fluorescence intensity, greatly improving the methods of sensitivity, specificity. In the analysis of the combination of elements, FP law is a unique approach, because the method does not need separation of the free and tracer, and all of the solution, can achieve real balance, which is fast, simple and accurate characteristics.^[2]

Available on the market fluorescence detector, although different wavelengths can detect the fluorescence intensity values, the primary function of the pathogenic microorganisms for genetic testing. But fluorescence detector there is the inadequacy of: detection by the fluorescence intensity of the fluorescence background interference so prone to false positive results, leading to inaccurate results; function can only be used for genetic testing, not an analysis of the gene structure, we can not meet clinical pathogenic microorganisms commonly used in the analysis of protein detection, thus limiting its clinical testing in the application.

FP test results only because of its two vertical vibration and the polarization of the ratio of the difference can be effectively excluded background light interference factors, the test high accuracy. It can be used to analyze a lot of the interaction between biological molecules, including DNA-protein and protein - protein antigen - antibody binding, particularly in the determination of trace concentrations of protein and drug treatment has been demonstrated their superiority. The technology and enzyme-linked immunosorbent assay and radioimmunoassay method of comparison, is simple, rapid, and without plate washer, automation, non-polluting, non-merits of the destruction of the environment, and longer-term preservation of reagents^[3].

II. SYSTEM DESIGN

Detection and analysis of high-throughput gene SCM system by fluorescence polarization control of the measuring system and host computer and management software.

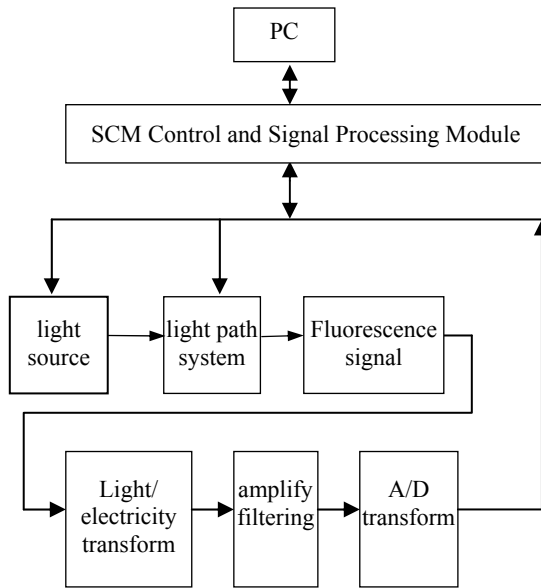


Fig. 1 diagram of the overall measurement system

Fluorescence polarization measurement system mainly by optical detection module, control module, the signal acquisition and processing module communication module components. Fluorescence polarization measurement system signal processing diagram as shown in Figure 1, by the photoelectric conversion device from the analog signal amplification, filtering, processing, analog-digital conversion to enter through the MCU, the MCU on the acquisition after the signal preprocessing, will be digital signal through its serial communications transmission to a computer, computer software and through the upper received real-time digital signal acquisition, real-time analysis and processed, the data storage and processing, such as printing statements. A detection system can be 384 samples.

III. OPTICAL PATH SCHEMATIC

Optical Measurement System principles as shown in Figure 2: reflection condenser light source (Halogen Tungsten Lamp) a convergence in the optical aperture holes, from collimating mirror collimator parallel after injection, the excitation filters and polarizer after a single color polarized light, monochromatic polarized reflectance spectroscopy will be arrived at the tested sample, the sample fluorescence excitation material issued by the fluorescent signal after spectroscopy, firing and filter analyzer, the lens focused on optoelectronic tubes of coke in front of the aperture, by the photomultiplier tube receiver. So far, the samples have been measured by fluorescence polarization of the corresponding signal.

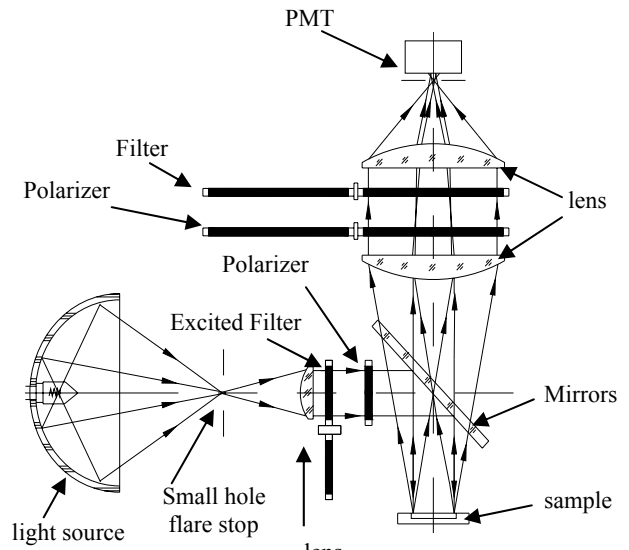


Fig. 2 Optical detection system schematics

Optical detection system excitation and emission filters filter generally have several films, by the Electrical and Mechanical control system options can be certain requirements with the use of detection. There were two partial seizure polarizer components, electrical and mechanical control system options, respectively to detect light intensity and the direction parallel to the direction of polarization vertical strong^{[4][5][6]}.

IV. CONTROL SYSTEM HARDWARE DESIGN

Fluorescence polarization measurement system under the crew used MCS-51 with 32 K 27256 EPROM expansion of storage space; choose 12 of the A / D converter AD574 to meet the measurement accuracy. Selection MAX232 chip on the circuit and computer communications through RS232 communication interface.

Measurement System Campaign module using stepper motor control. First of all stepper motor driven disc samples, in order to achieve 384 measurement hole location; detection method followed under the (corresponding to the different excitation and emission wavelengths) different, stepper motor driven by selective excitation filter and The filter should be fired, horizontal and vertical Polaroid Polaroid choice stepper motor is used to control. Stepping stepper motor control action by the MCU to achieve.

V. SOFTWARE DESIGN

A. Under the design software

Under the completion of major software components of the motor control, the election-channel acquisition and data collection, these controls are in the PC carried out under the instructions. Given the C language has good readability and portability [6], the next crew procedures using SCM C51 language preparation, use integrated development environment KeiluVision2 SCM C language as a development platform.

B. Based on VB on the design of computer program

PC procedures used VB language, as an object-oriented visual programming tools, easy to learn, flexible, convenient and easy-to-scale features. It provides a serial port MSComm control procedures to provide for the use of serial Communications. Shielding the control of the communication process in the bottom of operation, application programmers, and only set up to monitor MSComm control attributes and events can be completed on the serial port initialization and data input and output; and a VB powerful database access capabilities, it can support Access, SQL Server, such as dBase and FoxPro database. These features make the VB fluorescence polarization measurement system software prepared more easily.

Fluorescence polarization measurement system software requires the use of simple, easy to operate. When the operator completed test methods and test holes settings, and require a system to automatically detect. This requires that PC users can be set up according to generate the corresponding command sets, and the crew issued in a timely manner. Set a record procedures used command sets recList storage system running through the revolving records were removed

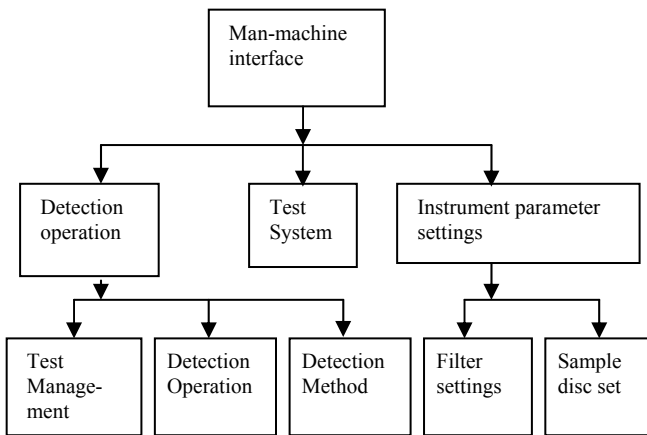


Fig. 3 software chart

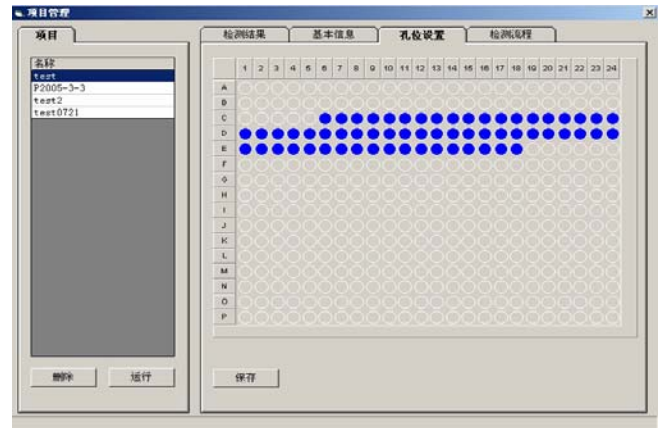


Fig. 4 Software interface map

on the instructions for automatic detection. Specific flow chart shown in Figure 3. Part of the user interface design in Figure 4

VI. CONCLUDING REMARKS

We will be the first time use FP technology in a variety of pathogenic microorganisms identification, classification and detection of drug resistance mutations areas, the establishment of technology-based FP types of human papillomavirus, herpes simplex virus type, CTS, the URA, NG, MP, CP, hepatitis B virus, Helicobacter pylori, Mycobacterium tuberculosis and other pathogenic microorganisms resistance-associated mutations hot spot analysis system. Clinical test results show that the analytical method is simple and accurate characteristics apply to clinical samples for rapid high-throughput screening; FP technology, develop human papillomavirus type, CTS, URA, NG, MP, CP, hepatitis B virus, Helicobacter pylori, Mycobacterium tuberculosis fluorescence polarization detection kit, including human papillomavirus type, CTS, the URA, NG, MP, CP fluorescence polarization detection kit has been Drugs biological products through national test sampling identified^{[7][8]}.

Using high-throughput analysis of gene protein detection system in the Fourth Military Medical University Xijing Hospital has selected 100 cases confirmed by clinical pathology pointed condyloma, cervical cancer specimens, with various types of specific primer amplification methods determine the type, HPV6B which were detected in 18 cases of infection, HPV11 infection in 27 cases, HPV16 infection in 23 cases, HPV18 infection eight cases, of which there have been six B/11, 16/18 mixed infection specimens were nine cases and 7 cases, the remaining eight cases, 4 Other cases of infection and four cases of HPV-negative infection.

The results measured by fluorescence polarization with the same results. The results show that fluorescence polarization detection automatic detection system running stable, reliable process control, detection of high precision^{[9][10]}.

REFERENCES

1. 许金钩, 王尊本. (2006) 荧光分析法[M]. 科学出版社,[2].
2. Zhang Ju, Zhongcan Chen, Yane Gao. (2006) A novel fluorescence polarization based assay for 14 human papillomavirus genotypes in clinical samples. *J Virol Meth*, [1] 134, 223-229
3. 朱广华, 郑洪, (2004) 荧光偏振免疫分析技术的进展; 分析化学, [1], 1, 102-016
4. 吴敏, 丁建华, 王传晶, (2005) 偏振荧光光谱在肝病诊断中的应用研究[J]. *激光技术*, [1], Vol 29, No 6, P579-58.
5. 李晨, 石岩, 倪旭翔等. (2005) 生物芯片荧光检测光学系统综述[J]. *光学仪器*. [1], Vol 27, No 3, P89-94.
6. 王忠东, 关晓晶, 王玉田. (2005) 一种以AOTF为核心的农药荧光检测系统[J]. *光电工程*, [1], Vol.32, No.1, P81-84
7. ZHANG Ju YAN Xiaojun, SUN Jianzhong et al. (2003) A high throughput assay for human papillomavirus genotypes with fluorescence polarization. *Chin Med J*, [1], 116(8):1137-1140.
8. GAO Yan-E, ZHANG Ju. (2005) Application of TDI-FP for Analysis of A647G Variation in HPV 16 E7 Gene from Cervical Cancer Patients, [1], 32(12):1199-1203
9. GAO Yan-e, ZHANG Ju, SONG Tian-bao, et al. (2002) Cloning of HPV16 E2 gene from a cervical cancer biopsy. *Reproduction & Contraception*, [1], 13(3):146-151.
10. 陈中灿; 张菊; 高艳娥等. (2004) 荧光偏振方法快速检测HPV16 E7第29位密码子点突变[J]. *第四军医大学学报*, [1], P1403-1406

Author: Ni Yuan
 Institute: Xi'an University of Technology
 Street: Jinhua North Road On the 4th
 City: Xi'an
 Country: China
 Email: ny930@xatu.edu.cn

Thresholding-based Wavelet Packet Methods for Doppler Ultrasound Signal Denoising

Jiangfeng Yu, Dong C. Liu

School of Computer Science, Sichuan University, Chengdu, China

Abstract — Doppler ultrasound is widely used to diagnose vascular diseases because of its noninvasive advantages. Denoising of Doppler signals is necessary as a pre-processing for a high quality Doppler ultrasound system. Recently, there has been much work on denoising methods based on noise statistics and the spectrum distribution. Wavelet packet decomposing methods not only process low frequency components well, but also perform multi-level decomposition on high frequency contents, which is quite applicable in Doppler ultrasound signals because they have comparatively high frequency components dependent on flow velocity.

This paper presents a threshold-based wavelet packet denoising method, which preserves useful high frequency components and offers higher signal-to-noise ratio (SNR) compared with straightforward wavelet-based denoising methods. We then propose several algorithms to improve the selection of the threshold, and these methods are adaptive in the sense of coefficients obtained from different decomposed levels using the characteristics of the wavelet transform. In computer simulations, we have tested our algorithms and show improved SNR of simulated Doppler I/Q signals and better visualization of displayed Doppler spectrum.

Keywords — Doppler signal, wavelet packet analysis, threshold shrinkage denoising

I. INTRODUCTION

Doppler ultrasound technology has been widely used in the clinic to diagnose vascular diseases, but the noise in Doppler systems deteriorates the quality of detected spectrum and velocity waveforms. Recently, there has been much work on denoising methods based on noise statistics and the spectrum distribution. Methods based on Fourier transform have less success because the frequency band of the signal is always overlapped with that of the noise. Methods based on wavelet transform, however, have comparatively satisfying results because the wavelet analysis offer better time-frequency analysis compared with Fourier analysis. Currently, the most extensively used wavelet-based denoising methods, for example, the wavelet shrinkage denoising, can be seen as optimized approximation under least mean square error (MSE).

The wavelet decomposing method is suitable for signals with useful low frequency components, but may result in problems for signals with meaningful high frequency contents because it may treat them as noise and denoise them. In this paper we present a threshold-based wavelet packet denoising method where two threshold functions have been proposed to account for the pros and cons of the standard hard and soft thresholding functions.

Section II describes the mathematical modeling of the ultrasound Doppler signals used in computer simulation. Wavelet packet analysis and thresholding has been introduced in Section III where we present our improved thresholding functions. Simulation results and analysis are discussed in Section IV.

II. MATHEMATIC MODELING OF THE DOPPLER SIGNALS

The detection of blood flow with ultrasound depends on the Doppler principle which determines that, when ultrasound is reflected from a moving structure, the frequency of the reflected waves is different from that of the incident waves. Besides the flow, other tissues such as vascular wall and cardiac muscle also reflect ultrasound wave. But the signal reflected by vascular wall and cardiac muscle are much stronger than that of flow. It is necessary to remove them, or called clutter, to extract useful flow signals.

To investigate the performance of our denoising method, it's necessary to have computer simulations of Doppler signals with varying mean blood frequencies plus clutter components, see Bjarum et.al [1]. Both the clutter and blood signal power spectra have a Gaussian shape as

$$S_k(f) = r_k e^{-\left(\frac{f_k - f_d}{B_d}\right)^2} \quad (1)$$

where r_k is random noise with uniform distribution. For a blood signal, $f_d = f_b$ of Eqn (1) is the blood signal center frequency and $B_d = B_b$ (assume $B_b = 0.1 f_b$) is blood signal root-mean-square (RMS) bandwidth. Similarly, the clutter signal has the same form as Eqn (1) with $f_d = f_c$, a small value for low frequency (i.e., low velocity) and $B_d = B_c$, the clutter signal RMS bandwidth (e.g., $B_c = 0.01$ pulse repetition frequency, PRF).

The synthetic time domain signal is generated by calculating the inverse Fourier transform of Eqn (1) consisting of MN samples of signal where M is the number of Doppler samples along the temporal direction and N defines the number of iterations required for statistics. Mathematically,

$$\begin{aligned} I(t) &= \text{Real} [\text{FFT}^{-1}(S_k; t)] \\ Q(t) &= \text{Imag} [\text{FFT}^{-1}(S_k; t)] \end{aligned} \quad (2)$$

Repeat Eqn (2) for clutter signal (I_c, Q_c) and add to blood signal (I_b, Q_b) and white noise of $R(t)$, we have the synthetic Doppler signal (I_d, Q_d) as

$$\begin{aligned} I_d &= I_c + \alpha I_b + \beta R(t) \\ Q_d &= Q_c + \alpha Q_b + \beta R(t) \end{aligned} \quad (3)$$

where

$\alpha = 10^{\frac{\gamma_1}{20}}$ is for signal to clutter ratio (i.e., γ_1 is a negative SCR) and $\beta = \alpha 10^{\frac{\gamma_2}{20}}$ is for noise to signal ratio (i.e., γ_2 is a negative NSR).

III. WAVELET PACKET ANALYSIS AND THRESHOLDING

3.1 Wavelet decomposition and reconstruction

Wavelet analysis is a time-frequency analysis [2] which has a fixed window size and variable shape. In low-frequency part it can get a higher frequency resolution and lower time resolution; and in high-frequency part it can get a higher time resolution and lower frequency resolution. But in practical application, we may want to improve high-frequency band resolution in high-frequency part. Wavelet packet analysis has overcome the shortcomings of low frequency resolution in high-frequency part of the wavelet analysis. It can do the orthogonal decomposition [3] in the whole range of frequency bands, specially can do more sophisticated classification in high frequency band, so it has a stronger adaptability in characterization of signal characteristics.

In this paper we use the orthogonal wavelet packet decomposition [4] and define the following notations: $\phi(x)$ is an orthogonal scaling function and $\psi(x)$ is the corresponding wavelet function, $\{V_k\}$ is a multi-resolution space, also called scale space generated by $\phi(x)$. $\{W_k\}$ is a wavelet space generated by $\psi(x)$, W_{k-1} is an orthogonal fill space differences between V_k and V_{k-1} so $L^2(R)$ can be decomposed as:

$$L^2(R) = \dots \circ + W_{-1} \circ + W_0 \circ + W_1 \circ + \dots \quad (4)$$

And

$$\{2^{k/2} \phi(2^k t - l) : l \in Z\}$$

is a group of orthonormal bases of W_k [5].

Wavelet packet transform could be seen as an improvement from wavelet transform. Define a sequence of functions as follows:

$$\begin{cases} \phi_{2n}(x) = 2^{j/2} \sum_k h_k \phi_n(2^{j/2} x - k) \\ \phi_{2n+1}(x) = 2^{j/2} \sum_k g_k \phi_n(2^{j/2} x - k) \end{cases} \quad (5)$$

where $j, k \in Z$ (Z is an integer set) and j is a scale parameter, k is time or location parameter, $n \in N$ (N is a non-negative integer set), h_k is a low-pass filter coefficient, g_k a high-pass filter coefficient. Moreover, $\{h_k\}$ and $\{g_k\}$ are a group of conjugate mirror filters \square

$$\sum_{n \in Z} h_{n-2k} h_{n-2l} = \delta_{k,l} \sum_{n \in Z} h_n = \sqrt{2} \quad g_k = (-1)^k h_{1-k} \quad (6)$$

Then we have two-scale equations of wavelet packet transform:

$$\begin{cases} \phi_{2n}(x) = \sqrt{2} \sum_k h_k \phi_n(2x - k) \\ \phi_{2n+1}(x) = \sqrt{2} \sum_k g_k \phi_n(2x - k) \end{cases} \quad (7)$$

The fast discrete wavelet packet transform can be implemented using Mallat decomposition algorithm:

$$\begin{cases} C_{2m}^{j+1}(k) = \sum_n h_{n-2k} C_m^j(n) \\ C_{2m+1}^{j+1}(k) = \sum_n g_{n-2k} C_m^j(n) \end{cases} \quad (8)$$

The signal can be expanded by the following orthogonal wavelet packet bases function:

$$f(t) = \sum_{lnk,j} C_n^j(k) 2^{k/2} \phi_n(2^{k/2} t - j) \quad (9)$$

where

$$C_n^j(k) = 2^{k/2} \int_R f(t) \phi_n(2^{k/2} t - j) dt \quad (10)$$

The reconstruction formulation of a discrete signal is then

$$C_m^j(k) = \sum_n \bar{h}_{k-2n} C_{2m}^{j+1}(n) + \sum_n \bar{g}_{k-2n} C_{2m+1}^{j+1}(n) \quad (11)$$

\bar{h}_{k-2n} and \bar{g}_{k-2n} can be obtained by reversing order of h_{k-2n} and g_{k-2n} .

Wavelet packet decomposition has an essential effect that it can decompose the signal to different frequency bands in different levels. We can also get the beginning and the ending of a frequency band if we have sufficient decomposed levels. Therefore, we can separate the clutter noise and white noise from the original signal.

3.2 The improvements of thresholding function

The key step of denoising is estimating the wavelet coefficients. Donoho [6,7] proposed a very concise method by setting the threshold

$$\lambda = \sigma \sqrt{2 * \log_2 N} \quad (12)$$

where N is the length of signal and σ is the standard deviation. There are two kinds of thresholding functions, hard thresholding and soft thresholding functions. The hard thresholding function is defined as:

$$\hat{W}_{j,k} = \begin{cases} W_{j,k}, & |W_{j,k}| \geq \lambda \\ 0, & |W_{j,k}| < \lambda \end{cases} \quad (13)$$

and the soft thresholding function is defined as:

$$\hat{W}_{j,k} = \begin{cases} \text{sign}(W_{j,k})(|W_{j,k}| - \lambda), & |W_{j,k}| \geq \lambda \\ 0, & |W_{j,k}| < \lambda \end{cases} \quad (14)$$

While these two methods are widely used in practice, they are simple and effective, but the methods have many potential shortcomings. For example, the estimated value of Eqn (13) is discontinuous at λ in the hard thresholding function, so it will have oscillation when the signal is reconstructed. Despite the soft thresholding function can get better overall continuity, for big wavelet coefficients, the estimated values of Eqn (14) have more bias compared with the original wavelet coefficients $W_{j,k}$. Therefore, the accuracy of the signal reconstruction can't be guaranteed.

In this paper, we propose two algorithms to improve the thresholding functions, taking into account the advantages and disadvantages of the hard and soft thresholding functions. Define the threshold function of Method 1:

$$\hat{W}_{j,k} = \begin{cases} \text{sign}(W_{j,k})(W_{j,k} - \alpha\lambda_j + \frac{2\alpha\lambda_j}{1+e^{-\frac{W_{j,k}}{\lambda_j}}}), & |W_{j,k}| \geq \lambda_j \\ 0, & |W_{j,k}| < \lambda_j \end{cases} \quad (15)$$

where $0 \leq \alpha \leq 1$. When $\alpha=0$, Eqn (15) becomes hard threshold and it will be the soft thresholding when $\alpha=1$. The parameter α can adjust the bias between the original signal and the denoised signal.

Define threshold function of Method 2:

$$\hat{W}_{j,k} = \begin{cases} \text{sign}(W_{j,k})(W_{j,k} - \lambda_j + \frac{\lambda_j}{2\alpha+1}), & |W_{j,k}| \geq \lambda_j \\ \frac{(W_{j,k})^{2\alpha+1}}{(2\alpha+1)\lambda_j^{2\alpha}}, & |W_{j,k}| < \lambda_j \end{cases} \quad (16)$$

where $0 \leq \alpha < +\infty$. In Eqn (16), the parameter α can adjust the power of the function. When $\alpha=0$, Eqn (16) is equivalent to the original signal for less than λ , and it becomes the hard thresholding for larger than λ . When α approaches $+\infty$ Eqn (16) trends to the soft thresholding. This improvement makes that a smooth transition zone exists between the original signal and the noisy signal, so it may get better continuity of the signal.

IV. SIMULATIVE EXPERIMENTS AND ANALYZE RESULTS

The major steps of the thresholding-based wavelet packet methods are [8]:

- (1) Decompose the noisy signal using sym4 (the Symlets wavelet) in four levels with orthogonal wavelet packet, and then get a full decomposition tree.
- (2) Calculate the Shannon entropy (used as a cost function) of each node. Compare the entropy of the parent node and the sum of entropy of the two children nodes. If the sum of entropy is larger than that of parent's entropy, take the parent's entropy, so as to get a group of the best bases of wavelet packet decomposition.
- (3) Threshold the best bases of wavelet packet decomposition by using the four threshold functions mentioned in this paper.
- (4) Reconstruct the wavelet packet decomposition coefficients, and get denoised signal.

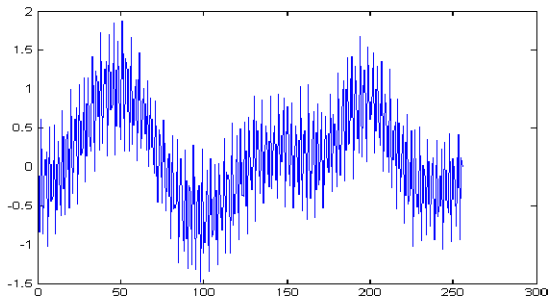


Fig.1 The simulated Doppler signal with strong clutter components

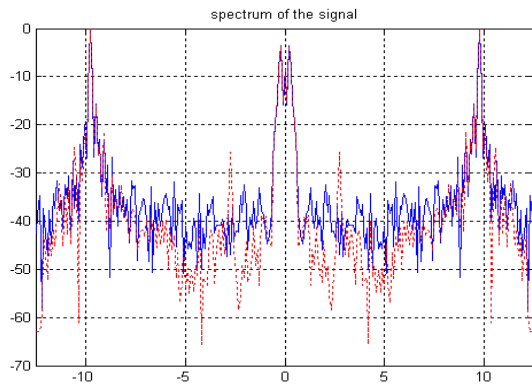


Fig.2 Solid line: the spectrum of the original signal; dotted line: the spectrum of denoised signal by using the soft threshold function

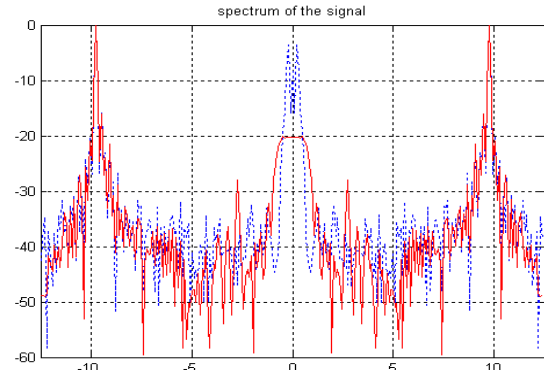


Fig. 3 Dotted line: the spectrum of the original signal; solid line: the spectrum of denoised signal by using the proposed Method 1

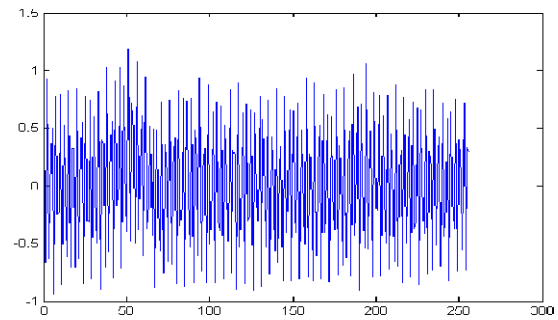


Fig.4 The denoised signal by using the proposed Method 1

To verify our proposed algorithms, we have generated simulated ultrasound Doppler signals using Eqns (1) to (3). Considering a set of Doppler signal with a PRF of 25 kHz, set the following parameters: the blood flow signal is at 0.38 PRF, the clutter signal is at 0.02 PRF, the signal to noise ratio is 19 dB and the signal to clutter ratio is -0.9 dB. →It is clear that the clutter components of this signal has the same level of amplitude as the blood flow signal but with much lower carry frequency, i.e., much lower velocity, see Fig. 1 for the estimated Doppler signal.

Fig. 2 shows the spectrum of the original signal of Fig. 1 in solid line where the peak content of the clutter signal is close to DC with amplitude similar to that in flow signal. The dotted line in Fig. 2 shows the spectrum of the denoised signal by using the soft threshold function. We have applied the hard threshold function to the original signal and obtained similar results as that from the soft threshold function.

We have used our proposed Method 1 as the threshold function and set large threshold in low frequency and small threshold in high frequency adaptively for denoising. As shown in Fig. 3 the proposed method can significantly re-

duce the clutter signal and have better SNR, also see Fig. 4 where we can obtain a clean Doppler signal with blood flow contents. It also show that the local processing has better effect than the overall processing, because it might not denoise the white noisy signal completely if we use small overall threshold, and the clutter signal could be still there if we use large overall threshold. Similarly, we have used the proposed Method 2 and obtain similar results as shown in Figs. 3 and 4.

REFERENCES

1. Bjarum S, Torp H et.al (2002) Clutter filter design for ultrasound color flow imaging, IEEE Trans. UFFC, vol. 49, pp.204-216
2. J Cui (1995) Conspectus of wavelet analysis, Xi'an Jiao tong University Press (in Chinese)
3. I Daubechies (1998) Orthonormal bases of compactly supported wavelets, Commun. Pure Appl., 41, pp. 909 -996.
4. Z Cheng (2006) Wavelet analysis and applications, Xi'an Jiao tong University Press, pp.177-179
5. S. Mallat (1989) A theory for multiresolution signal decomposition: the wavelet representation. IEEE Trans Pattern Anal and Machine Intell, 11(7), pp. 647-693

6. Donoho D, Johnstone (1994) Ideal spatial adaptation by wavelet shrinkage, *Biometrika*, 81(3), pp. 425- 455.
7. Donoho D (1995) De-noising by soft-thresholding, *IEEE Trans on Information Theory*, 41 (3) pp. 613-627.
8. Wang D, Peng J (2006) Wavelet analysis and its application in signal processing, Publishing house of electronics industry, pp.162-170

Author: Jiang Feng Yu and Dong C. Liu
Institute: School of Computer Science, Sichuan University
Street: The First Ring Road
City: Chengdu
Country: China
Email: jiangfy2002@163.com

Physiological Monitoring in the Ventilated Neonate: A Rationale

P. Rolfe^{1,3,4}, F. Scopesi², J.W. Sun¹, G. Serra²

¹Harbin Institute of Technology, Harbin, China

²Gaslini Institute, Genova University, Genova, Italy

³OBH Ltd., Maidstone, Kent, England. E-mail: PeterRolfe@aol.com

⁴Advanced Research Institute, Waseda University, Tokyo, Japan

Abstract—This paper concerns physiological monitoring of newborn babies needing mechanical ventilation for respiratory distress. Technologies for monitoring and ventilation continue to evolve and choices must be made based on technical and clinical performance as well as on safety and cost. We describe a preliminary approach for the rationalisation of technology selection, with emphasis on sensors and instruments used for measurement. The most important variables to be measured are blood gases and pH, blood pressure and heart rate, compliance, airways resistance, work of breathing, and the ventilator control variables based on flow and pressure. We then describe the use of a decision tree approach to technology selection, with the aim of providing a tool for use in different clinical settings.

Keywords— Neonatal monitoring, blood gas and pH, mechanical ventilation, sensors, decision trees.

I. INTRODUCTION

Methods and apparatus for the care of the fetus and the small, sick, pre-term baby have evolved steadily since the middle of the last century [1][2][3][4]. The creation of technological solutions to problems of measurement, for example through micro-sensors and advanced signal conditioning and processing, have supported basic physiological research but have not always been carried through to clinical success. Although there were early attempts to assess the possible clinical benefits of the technologies [5], formal clinical trials were not carried out before they were used clinically. One clear example of this was the introduction in the 1960's of electronic fetal monitoring (EFM) based on analysis of patterns of fetal heart rate and uterine contractions. More recently, however, the introduction of pulse oximetry for intra-partum fetal use has been scrutinised through trials [6], with the conclusion that it does not assist in reducing Caesarean section rates.

Within neonatal care the management of babies with respiratory distress syndrome (RDS) remains the central focus. In particular the control of arterial oxygen levels within safe limits, avoiding both hyperoxaemia and hypoxaemia, is still of paramount importance, demanding the time of doctors and nurses, for example to adjust inspired oxygen concen-

tration, F_iO_2 , or some parameter of mechanical ventilation, such as pressure or minute ventilation. There is a myriad of measurement sensors and instruments, for example for cardiorespiratory monitoring, blood gas and pH assessment, and lung function measurements. Of course arterial oxygen and carbon dioxide levels must first be determined. This can be done with invasive procedures for blood sampling to enable measurement of P_aO_2 , P_aCO_2 , pH and acid-base balance. In addition, there are non-invasive techniques for transcutaneous O_2 and CO_2 , end tidal CO_2 , or arterial O_2 saturation with pulse oximetry. Undoubtedly therapeutic technologies such as continuous positive airway pressure (CPAP), surfactant replacement therapy, and the many modes of mechanical ventilation, are a critical part of this. In addition, however, there is little doubt that there are important needs for reliable and convenient physiological data provision to guide the application and optimisation of such therapies.

We are aiming to rationalise the measurement strategy in order to assist in the optimisation of mechanical ventilation of the ill newborn having RDS. This involves both physiological measurements in the baby as well as measurements related to the ventilator itself.

II. MEASUREMENT SENSORS & INSTRUMENTS

It is important to identify the measurement requirements and the systems available. Sensors and instruments are needed both for physiological surveillance of the subject and for providing clear indications of the performance of the ventilatory technology.

A. Monitoring the baby

The ventilated baby requires basic cardio-respiratory monitoring for heart rate and respiratory efforts, as well as possibly for apnoea detection during weaning from the ventilator. These tasks are straightforward, using electrocardiograph (ECG) electrodes with transthoracic impedance measurement to derive an indication of depth of breathing.

Table 1. This shows the measured variables considered.

Baby	Pulmonary Mechanics	Ventilator
<i>Invasive</i>		
P_aO_2	Compliance	Pressure
S_aO_2	Airways R	Flow
pH	Work	Volume
P_aCO_2	$P-V$	Frequency
BP	$P-F$	Insp/Exp
P_{oes}		
<i>Non-invasive</i>		
P_aO_2		
S_aO_2		
P_aCO_2		
$P_{ET}CO_2$		
BP		
HR		
Resp		
T		

Tidal volume and respiratory rate during ventilation are controlled and monitored by the ventilator itself but there is still some value to have additional means with which to detect spontaneous breathing efforts made by the baby especially prior to the initiation of mechanical ventilation.

Direct monitoring of arterial blood pressure, using a strain-gauge pressure sensor attached to an indwelling arterial catheter, is possible if a decision is taken to insert an umbilical artery (u.art) catheter. The decision as to whether or not a u.art catheter is inserted is critical since it influences the overall strategy of monitoring with respect to the choice between invasive and non-invasive methods. Non-invasive measurement of arterial blood pressure based on the oscillometric principle with a limb-encircling cuff is possible and acceptable accuracy can be achieved [7]. Use of the Finometer® has also recently been found to provide accurate measurement of systolic, mean and diastolic pressures on a beat-by-beat basis [8].

The thermal balance of the ill newborn baby is a very important part of clinical management [9] and ensuring that the infant is maintained in a thermoneutral environment may minimise oxygen requirements and thereby help in respiratory therapy. Measurement of central temperature (rectal, oesophageal) with thermistor or thermocouple sensors can be carried out, although this is generally not done and instead reliance is placed on the use of an abdominal mounted skin surface sensor that is part of the incubator or warmer servocontrol system. Regular measurement of the

baby's body weight is also important and this can be done using scales incorporated into the incubator/warmer.

We have included in the process of rationalisation consideration of the measurement of critical physiological variables [10]. Blood gas and pH assessment with either invasive or non-invasive sensors has been evaluated. The use of umbilical artery (u.art) catheterisation was examined, particularly in relation to risks. Catheter tip sensors for PO_2 , PCO_2 and pH were considered. The most common approach for neonatal use has been that of an electrochemical cell comprising of a Pt or Ag working micro-electrode, held at around $-600mV$ with respect to a Ag/AgCl reference electrode, with surrounding electrolyte contained within a polymeric membrane. For O_2 measurement the membrane controls diffusion of O_2 molecules from the surrounding blood to the cathode surface where the applied potential electrochemically reduces the O_2 giving electrons which form a current. The magnitude of the current under diffusion controlled conditions is proportional to the blood PO_2 . Although many attempts have been made over the years to develop intra-arterial sensors for routine clinical use in the newborn [11], currently the use of such devices is not widespread. Part of the problem for this lies in the fact that generally the sensors have lacked sufficient reliability for clinical use due to problems of protein adsorption to the polymer catheter and membrane surfaces [12]. An approach has been to use phospholipid-derived materials that have been found to exhibit significantly improved haemocompatibility [13] and it has been shown that these materials can significantly reduce the adsorption of proteins to the surfaces of arterial catheter sensors [14].

Fibre optic sensors for O_2 , CO_2 and pH can now offer prospects for clinical use [15][16]. The clinical evaluation of this multiparameter sensor (MPIAS) [16] in 27 babies who were undergoing intensive care showed overall bias (mean difference: MPIAS-ABG) and precision (standard deviation of differences) values of: -0.002 and 0.022 , respectively, for pH ; $+0.26$ and 0.52 for P_aCO_2 (kPa); and -0.19 and 0.99 for P_aO_2 (kPa).

We have considered the options for non-invasive blood gas monitoring. Pulse oximetry is regarded as a possible alternative to transcutaneous sensors for $P_{tc}O_2$ monitoring whilst transcutaneous sensors for $P_{tc}CO_2$ monitoring or capnometry for end-tidal CO_2 monitoring were evaluated in relation to ventilator control and avoidance of possible adverse influences on cerebral perfusion/oxygenation by hypocarbia.

There has been considerable interest in near infra-red spectroscopy (NIRS) to interrogate the brain and monitor changes in blood volume and blood oxygenation [17]. The method can allow indications of changes in cerebral HbO_2 , HHb and Hb_{tot} to be seen on a continuous basis and it may

also provide a spatial image of such changes. Despite the interest for neonatal cerebral monitoring the method has not yet been used widely in the clinical setting, although there clearly are prospects to evaluate its potential for providing data to assist in the application of mechanical ventilation. In particular it may provide data with which to assess cerebral perfusion and oxygen delivery.

B. Ventilatory Measurement

We have considered all of the possible modes of ventilation that may be applied to the newborn. These particularly include those that achieve synchronisation of the ventilator with the spontaneous breathing efforts of the baby. However, regardless of the mode of ventilation there are needs to monitor the key respiratory system parameters, including total or pulmonary compliance, C_p , airways resistance, R_a , and work of breathing. This requires measurement of tidal flow and volume, airway pressure and intra-pleural pressure. For on-line calculation of pulmonary mechanical parameters and work of breathing ideally measurement of oesophageal pressure, P_{oes} , with an oesophageal balloon or water filled gastric tube is necessary, although this is invasive..

C. Decision analysis

Following assessment of all sensing and measuring instruments we have begun the development of decision tools that ultimately could be used in a variety of circumstances. The establishment of a rationale for selecting sensors and instruments may be derived from the key variables shown in Table 1. The AI methodologies are then applied to a clinician's decision-making processes.

It is not straightforward to determine the overall root attribute node for the defined task of 'selecting optimal monitoring for the ventilated newborn'. A clinical department may well have its own policies and protocols in terms of clinical care, but the matter of monitoring is likely to be dealt with in a less formalised way. We have made some assumptions regarding the provision of monitoring equipment and these constitute the boundary conditions.

III. RESULTS

The critical boundary conditions for the selection of monitoring equipment for the ventilated newborn are:

1. the provision of a laboratory blood gas analyser;
2. cardio-respiratory monitoring
3. a ventilator with in-built measurement of pressure, flow, O_2 concentration.

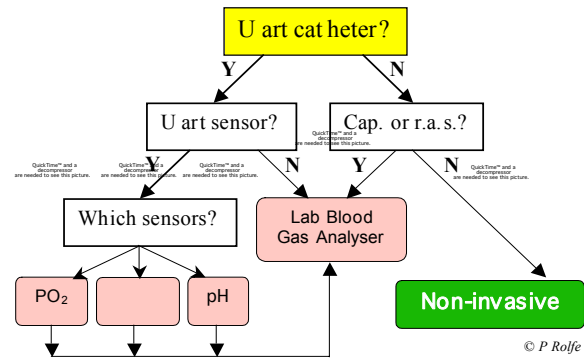


Figure 1 This is the Decision Tree for selection of blood gas and pH measurement. See text for explanation.

The subsequent decisions regarding blood gas, pH, blood pressure, and pulmonary mechanics parameters measurement are then based on consideration of the availability and performance of the various sensors and instruments for measurement of the range of relevant variables, as shown in Table 1.

An example of a decision tree created from the tabulated key variables is shown in Fig. 1. For assessment of respiratory system parameters we found that some modern mechanical ventilators (e.g. The Draeger Babylog 8000) measure and display the primary control parameters directly; these include airway pressure, tidal/minute flow/volume, "leak", F_iO_2 , Insp-Exp times or respiratory rate. In some cases ventilators also derive estimates of total compliance. However, we find that the calculation of pulmonary compliance, functional residual capacity and work of breathing are not easily derived from most ventilators. Oesophageal pressure needs to be measured and this requires insertion of a saline filled tube.

Umbilical artery catheterisation carries risks and benefits. Improvements to the catheter sensors by reducing protein adsorption and thrombus formation could lead to more reliable sensor performance. Capillary sampling and *in vitro* analysis is useful but it is still moderately invasive and may miss transients.

Fig. 1 indicates non-invasive monitoring under the condition that U. art. catheter is NOT used AND Capillary sampling AND radial artery stab are not used. In fact this is misleading since non-invasive monitoring can be used in addition to Cap. and r.a.s.

The decision tree for non-invasive monitoring needs further refinement to take into account current research on pulse oximetry and NIRS. Transcutaneous O_2 monitoring has declined in popularity and pulse oximetry, although convenient, can lack precision in detection of hyperoxaemia, so care is required. Transcutaneous CO_2 monitoring is useful but still requires care in interpretation of data.

IV. DISCUSSION

The task of monitoring the ventilated newborn is an important part of clinical care. The potential technological solutions are many and various and it is by no means straightforward to determine the optimum selection. For our work we have set some boundary conditions regarding the basic provision of certain instruments. However, we have not yet included a constraint regarding economic factors and these can be very significant indeed. For example, it is not merely the question of whether or not funds are available for the purchase of a certain instrument, but whether there is also an adequate budget for on-going technical support.

Decision trees have been developed for selection of blood gas/pH sensors, including the decisions relating to the use of invasive and non-invasive devices. The decision as to whether or not a u.art catheter is inserted is critical since it influences the overall strategy of monitoring with respect to the choice between invasive and non-invasive methods. The principle of 'minimal handling' is well accepted when caring for the ill newborn baby and this may be interpreted as 'minimal invasiveness'. Although umbilical artery catheterisation has been used widely for more than four decades to ease blood sampling, fluid infusion and blood pressure monitoring, the risks (infection, vascular perforation, thrombus) are also well recognised so it is a balance between risks and benefits.

Pulse oximetry has now largely replaced transcutaneous PO_2 monitoring for oxygen monitoring even though there are limitations of the former in reliably detecting hyperoxaemia. A recent study has concluded that the safety limits for pulse oximeters are higher and narrower in neonates (95%–97%) than in adults, and that clinical guidelines for neonates may require modification [18].

The work described to date has not fully considered the decisions relating to the assessment of pulmonary mechanics. Clearly this is an essential part of the whole exercise of delivering effective and safe mechanical ventilation. We have made an initial assumption regarding the type of ventilator being used, in that it will incorporate sensors for pressure and flow measurement as well as for O_2 and CO_2 . Such an advanced ventilator also has the facility for calculating total compliance and of displaying P-V and P-F loops. The addition of oesophageal pressure measurement would allow calculation of work of breathing but this is not usually performed as a clinical routine but can be useful for research.

V. CONCLUSIONS

Decision trees have been developed to rationalise monitoring of the ventilated newborn. Critical decision points

relate, firstly, to the option of inserting umbilical artery catheters and, secondly, to the method used for lung function assessment. Any measurement and monitoring protocol will depend on resources, both technological and human, but also upon appraisal of efficacy of the technologies.

ACKNOWLEDGMENT

We acknowledge with thanks the support of Harbin Institute of Technology, Harbin, China and the Gaslini Institute, Genova, Italy, for providing support of our work described here.

REFERENCES

1. Macrae DJ. Monitoring the heart of the foetus and the newborn. *Lancet*. 1959 Sep 5;2:266-9
2. Brady JP, James LS. Heart rate changes in the fetus and newborn infant during labor, delivery, and the immediate neonatal period. *Am J Obstet Gynecol*. 1962 Jul 1;84:1-12
3. P Rolfe, Monitoring in newborn intensive care, *Biomed Eng.*, 1975, 10: 339-404, 413.
4. P. Rolfe Sensors for Fetal and Neonatal Monitoring. In: *Sensors in Medicine and Health Care: Sensors Applications*, Vol. 3., Öberg, P. Å., Togawa, T., Spelman, F. A. (eds.), Wiley-VCH, Weinheim, 2004, 187-242
5. Paul RH, Hon EH. Clinical fetal monitoring. V. Effect on perinatal outcome. *Am J Obstet Gynecol*. 1974 Feb 15;118(4):529-33
6. East CE, Chan FY, Colditz PB, Begg LM. Fetal pulse oximetry for fetal assessment in labour. *Cochrane Database Syst Rev*. 2007 Apr 18;(2):CD004075.
7. Stebor AD. Basic principles of noninvasive blood pressure measurement in infants. *Adv Neonatal Care*. 2005 Oct;5(5):252-61
8. Yiallourou SR, Walker AM, Horne RS. Validation of a new noninvasive method to measure blood pressure and assess baroreflex sensitivity in preterm infants during sleep. *Sleep*. 2006 Aug 1;29(8):1083-8.
9. Singhaus CJ, Touch SM, Greenspan JS, Wolfson MR, Shaffer TH: *Biomed Instrum Technol*. 40(2):150-63, 2006.
10. Rolfe P, Scopesi F, Serra G. Biomedical instruments for fetal and neonatal surveillance. *Journal of Physics: Conference Series*. 2006 48: 1131–1136. doi:10.1088/1742-6596/48/1/210.
11. Goddard PJ, Keith I, Marcovitch H, Robertson NRC, Rolfe P, Scopes JW: *Arch. Dis. Child.*, 49: 853-860, 1974.
12. Rolfe P: In: *Medical Electronics Monographs* No 18-22, Hill D W, Watson B W, eds., Peter Peregrinus Ltd, Stevenage, 1976.
13. Ishihara K, Tsuji T, Kurosaki T, Nakabayashi N: *J Biomed. Mater. Res.*, 28, 225-32, 1994.
14. Zhang S, Rolfe P, Tanaka S, Ishihara K: *Biosensors & Bioelectr.*, 11, 1019-29, 1996.
15. K. Rais-Bahrami, O. Rivera, G. T. Mikesell, B. L. Short: *Perinatol*. Vol. 22 No. 5, pp 367-9, 2002.
16. Morgan C, Newell SJ, Ducker DA, Hodgkinson J, White DK, Morley CJ, Church JM: *Arch Dis Child Fetal Neonatal Ed* 80: F93–8, 1999.
17. P. Rolfe: *Ann Rev Biomed Eng*. Vol 2 pp 315-54, 2000.
18. S-Y PK Shiao and C-N Ou. Validation of oxygen saturation monitoring in neonates. *Am J Crit Care*. 2007 March; 16(2): 168–178.

Research on Multi-Parameter Physiological Monitor Based on CAN Bus

Le Yang, Peng Yang, Aiying Tian, Xin Guo

College of Electrical Engineering and Automation, Hebei University of Technology, Tianjin, China

Abstract — The design of multi-parameter physiological monitor based on CAN bus is presented. This article describes the design of the hardware and software in the monitor. The monitor with CAN bus receives the physiological parameters which are detected by Cygnal MCU and display the parameters through GUI in ARM/Linux system. This method implements the long transmission of the data and the plug and play of data collection and display.

Keywords — physiological parameter, monitor, CAN, Linux, ARM

I. INTRODUCTION

Recently, people are concerned about their health more and more, health surveillance has become an important subject. Multi-parameter physiological monitor could detect the patients' physiological parameters real-timely and continuously.

There are some insufficiencies in research on multi-parameter physiological monitor in china. Most monitors adopt holistic encapsulation technology. It is that the collection and display of physiological parameter are encapsulated together. This encapsulation does not avail the long transmission of the data and is deficient in the mobility of plug and play. The design of this monitor is aimed to realize the tele-monitoring and appease the patients' need. This article describes a design of monitor based on CAN bus. It solves the problem of the long transmission of the data and the plug and play of each module.

II. DEVELOPMENT PLATFORM

The monitor consists of the collection and display of physiological parameter which are independent. The whole system of collection includes several gather modules. Every module collects different physiological parameters. For example, the ECG, RESP, NIBP, SPO2, pulse, temperature and so on. Acquisition circuit amplifies the signals which enter the MCU through A/D conversion. The MCU can calculate the parameters and transmit them via CAN bus. The display modules receive the parameters and display them through GUI. The display module converts the parameters data into waved data and implements the dynamic display of data.

A. Hardware system

The primary component of collection is C8051F005 MCU which is manufactured by Cygnal.

The whole CAN bus system is made up of the MCP2510 which is a stand-alone CAN controller with SPI Interface and the TJA1050 which is the interface between the CAN protocol controller and the physical bus.

MCP2510 is a Full CAN protocol controller implementing CAN specification V2.0 A/B. It supports CAN 1.2, CAN 2.0A, CAN 2.0B Passive, and CAN 2.0B Active versions of the protocol, and is capable of transmitting and receiving standard and extended messages. It is also capable of both acceptance filtering and message management. It includes three transmit buffers and two receive buffers that reduce the amount of microcontroller (MCU) management required.

The MCU communication is implemented via an industry standard Serial Peripheral Interface (SPI) with data rates up to 5 Mb/s.

The TJA1050 is the interface between the CAN protocol controller and the physical bus. It is primarily intended for high-speed automotive applications using baud rates from 60k baud up to 1M baud. It provides differential transmit capability to the bus and differential receiver capability to the CAN protocol controller.

The display components adopt the embedded MCU S3C2410 based on ARM9 processor and LCD.

B. Data collection

The physiological signals are collected by 6 biosensors and enter the C8051F005 through A/D conversion. The MCU filters the signals and calculates different physiological parameter in different algorithms.

In the calculations, the ECG measure via the cable which includes 5 electrodes, and the ECG gain is optional. The respiratory impedance shares the electrodes with ECG. The thoracic impedance method is adopted to calculate the respiratory rate. The measure of SPO2 and pulse is based on the Lambert-Beer principle, using the relative intensities at two wavelengths in the red and infrared ranges. The body temperature is measured by thermal resistor, the resolution is 0.1. The noninvasive blood pressure is measured through oscillometric method.

C. Data transmission

The physiological parameters is transmitted by CAN bus in C8051F005 MCU, and the S3C2410 receives the data via CAN bus interface also.

The CAN is a serial communications protocol which efficiently supports distributed real-time control with a very high level of security.

Its domain of application ranges from high speed networks to low cost multiplex wiring. In automotive electronics, engine control units, sensors, anti-skid-systems, etc. are connected using CAN with bit rates up to 1M bit/s. The intention of this specification is to achieve compatibility between any two CAN implementations. Compatibility, however, has different aspects regarding e.g. electrical features and the interpretation of data to be transferred. To achieve design transparency and implementation flexibility CAN has been subdivided into different layers.

The whole CAN bus system is made up of the MCP2510 which is a stand-alone CAN controller with SPI Interface and the TJA1050. When using the MCP2510, it is essential to initial it. Differently with other CAN controllers, the MCU communication is implemented via SPI.

Commands and data are sent to the device via the SI pin, with data being clocked in on the rising edge of SCK. Data is driven out by the MCP2510, on the SO line, on the falling edge of SCK. The CS pin must be held low while any operation is performed.

The Write Instruction is started by lowering the CS pin. The write instruction is then sent to the MCP2510 followed by the address and at least one byte of data. It is possible to write to sequential registers by continuing to clock in data bytes, as long as CS is held low. Data will actually be written to the register on the rising edge of the SCK line for the D0 bit. If the CS line is brought high before eight bits are loaded, the write will be aborted for that data byte, previous bytes in the command will have been written. Refer to the timing diagram in Fig.1-a for more detailed illustration of the byte write sequence.

The Read Instruction is started by lowering the CS pin. The read instruction is then sent to the MCP2510 followed by the 8-bit address. After the read instruction and address are sent, the data stored in the register at the selected address will be shifted out on the SO pin. The internal address pointer is automatically incremented to the next address after each byte of data is shifted out. Therefore it is possible to read the next consecutive register address by continuing to provide clock pulses. Any number of consecutive register locations can be read sequentially using this method. The read operation is terminated by raising the CS pin. (Fig.1-b)

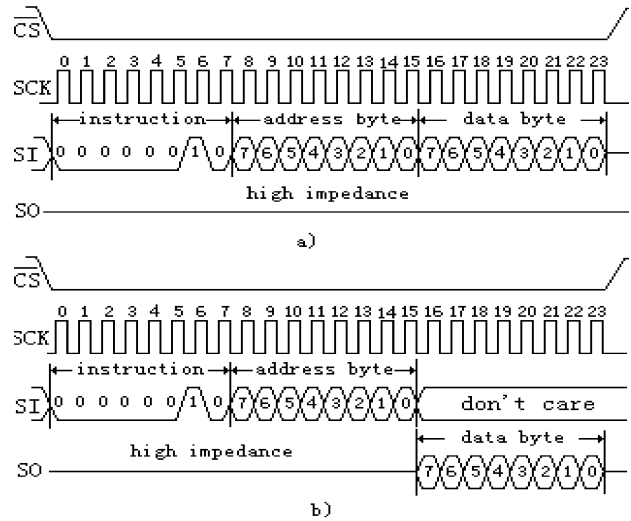


Fig. 1 SPI read and write instruction

D. Data storage

Because of the data storage and display modules are implemented via S3C2410 in which there is not enough memory to store the large numbers of data, the SD card is adopted to resolve this problem.

The SD Memory Card system defines two alternative communication protocols: SD and SPI. Applications can choose either one of modes. Mode selection is transparent to the host. The card automatically detects the mode of the reset command and will expect all further communication to be in the same communication mode. Therefore, applications which uses only one communication mode do not have to be aware of the other.

Single and multiple blocks read commands are supported in SPI mode. However, in order to comply with the SPI industry standard, only two (unidirectional) signals are used. Upon reception of a valid read command the card will respond with a response token followed by a data token of the length defined in a previous SET_BLOCKLEN (CMD16) command. A multiple block read operation is terminated, similar to the SD protocol, with the STOP command.

Single and multiple blocks write operations are supported in SPI mode. Upon reception of a valid write command, the card will respond with a response token and will wait for a data block to be sent from the host. CRC suffix, block length and start address restrictions are identical to the read operation.

After a data block has been received, the card will respond with a data-response token. If the data block has been received without errors, it will be programmed. As long as the card is busy programming, a continuous stream of busy tokens will be sent to the host.

E. Data display

The display module converts the parameters data into waved data and implements the dynamic display of data. Because the ARM embeded the Linux system and the QT designer in the Linux has advantage in GUI, we use the QT designer to develop the interface to display the physiological parameters.

The signals and slots mechanism is a central feature of Qt and probably the part that differs most from the features provided by other frameworks. When a signal is emitted, the slots connected to it are usually executed immediately, just like a normal function call. When this happens, the signals and slots mechanism is totally independent of any GUI event loop. So we can easily divide the display system into several parts which contains communication module, data storage module, data format conversion module and data display module.

When we need to refurbish the data, we call the draw function that is defined a slot function. When the timer emits a signal that the time is up, the draw function will be called. So the data in the display interface could be refurbished, and display in dynamic state. The GUI is Fig.2

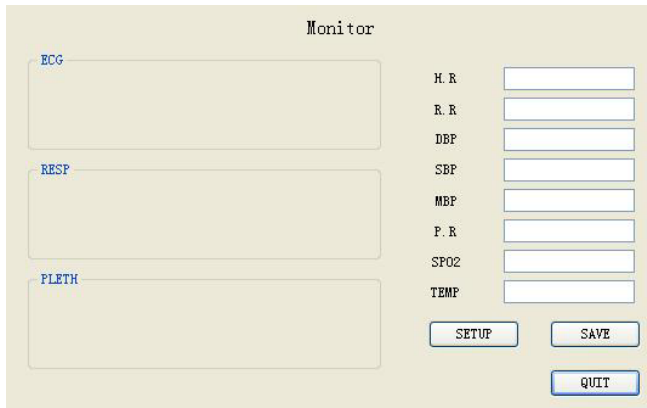


Fig. 2 man-machine interface

III. CONCLUSIONS

We actualize the physiological parameter monitoring based on ARM embedded Linux system. The monitor has advantage in multi-parameter, easy customization and extension. Through the experiment, it is proved that the veracity of parameter transmit based on CAN bus is very high and the display module can easily plug and play. Therefore, this control method and communication module has more reliability and mobility. As a field equipment bus, the CAN is more reliable and higher performance to price ratio than other bus.

To sum up, because of the superior performance of ARM-Linux system and the reliability and real-time performance of the data transmitted on CAN bus, the CAN bus combined with ARM-Linux is appropriate to industry and it has wide applied foreground in process control, motor manufacture, agricultural equipment, iatrical equipment and so on.

ACKNOWLEDGMENT

The authors would like to thank the professors of National Research Center for Rehabilitation Technical Aids. They give us much help.

REFERENCES

1. Shaomiao Chen (2000) Principle measure and operation method of multi-parameter monitor. Medical Equipment, 2000,Vol.13 No.5, P.3-5
2. Lian Huang, Cunxi Xie, Tie Zhang (2007) Multiple Physiological Parameter Monitoring Embedded System Based on ARM. Microcomputer Information, 2007,7-2:116-118
3. Yantang Wang, Yibin Li, Rui Song (2007) Design and implementation of CAN device driver under embedded ARM Linux operating system. Computer Engineering and Applications, 2007,43(15),79-82

Author: Le Yang
 Institute: College of Electrical Engineering and Automation, Hebei University of Technology
 Street: guangrong road 8#
 City: Tianjin
 Country: China
 Email: cole1984@163.com

The Study of C0 Complexity on Epileptic Absence Seizure

Yi Zhou¹, Lingli Xie², Gaohang Yu², Fang Liu¹, Yi Zhao², Yu Huang²

¹ Department of Biomedical Engineering, Zhongshan School of Medicine, Sun Yat-sen University, Guangzhou, China 510080

² Department of Mathematics, Sun Yat-sen University, Guangzhou, China 510275

Abstract — Absence seizure is one of the most common types of epileptic seizure; it is characterized by a short duration, an abrupt start and termination with high frequency and complex dynamic transition. Complexity can reflect the regulation level of dynamical system. This paper employ C0 complexity, which can well describe and quantify non-linear and nonstable biomedical signals, to calculate and analyze dynamic changes of complexity for EEG signals during the process of epileptic absence seizure. Meanwhile, it also study the dynamical changes of complexity for both original EEG signals and filtered EEG signals as well as the different influence of improved C0 complexity algorithm on the outcome.

Keywords — Epileptic absence seizure, EEG (electroencephalography), C0 Complexity

I. INTRODUCTION

Epilepsies are dynamical diseases of brain systems since they are manifestation of the property of neuronal networks to display multistable dynamics. It is characterized by sudden, recurrent and transient cerebral dysfunction which is caused by cerebral neuron discharge due to excessive excitation.

Some researchers [1] recognized that at least two states of the epileptic brain are possible: the interictal state characterized by a normal, apparently random, steady-state electroencephalography (EEG) ongoing activity, and the ictal state, which is characterized by paroxysmal occurrence of synchronous oscillations and is generally called a seizure in neurology. The transition between these two states can either occur: 1) as a continuous sequence of phases, like in some cases of mesial temporal lobe epilepsy (MTLE); or 2) as a sudden leap, like in most cases of absence seizures. Such a transition can occur either due to the influence of external or endogenous factors or due to a random perturbation [2]. In first type of ictal transition, the seizure may be anticipated in its early, preclinical phases. In the second case, where a sharp critical transition takes place, according to a random route toward seizures, it may be unpredictable.

EEG signals reflects the electronic activities in the brain, during ictal event EEG signal change dramatically and display complicated dynamic transition. The ability to predict an impending seizure well ahead of its clinical or electro-

encephalographic onset provides an opportunity for new diagnostic and therapeutic applications that can revolutionize the medical and surgical management of epilepsy [3]. So, some research groups try to predict epileptic seizure. By employing analytical techniques develop for the analysis of complex nonlinear systems, they demonstrate and quantify specific spatiotemporal dynamical changes in the EEG that begin several minutes before and end several minutes after a seizure [4-6].

Although the existence of the preictal transition period has recently been confirmed and further defined by other investigators [7-8], the characterization of this spatiotemporal transition is still far from complete. At the same time, much of their work is focused on the first type of epilepsy which we have mentioned before and has an obvious preictal period. Absence seizures are one of the most common types of seizure. It is characterized by short duration (5 to 20 s in most cases), an abrupt start and termination, an impairment of consciousness, and a high frequency throughout the day [9]. Some models [10] show that a random process governs the occurrence of paroxysmal activity.

We reconstruct phase space with filtered EEG digital data of absence seizures. By calculating largest Lyapunov exponents from small data sets and using improved method of calculating short-term maximum Lyapunov exponents (STLmax) and approximate derivative of STLmax etc, we attempt to reveal and quantify the spatiotemporal dynamic transition of absence epilepsy from preictal to ictal stage. This transition is to some degree similar to the first type epilepsy [11]. However, EEG signals are nonstable, earlier study on the spatiotemporal dynamic transition of EEG signals from epileptic absence seizure patients are limited. Considering that the sensitivity of different patients toward different characteristic value varies, we attempt to construct a comprehensive index system in order to use many characteristic values to describe this transition.

Regulation of the system can be reflected by complexity as an aspect of dynamic systems. Different systems display diverse behavior with divergent regulation degrees, so do a system with different inner parameters. Complexity can identify the systems by describing their regulations. It is employed to investigate characters of output signals from systems [12] without proving the existence of chaos, there-

fore, it does not require dynamical knowledge which can be obtained from reconstruct attracters.

The dynamic transition of cerebral activities during epileptic seizure is significantly different from it is during the interval: it is low dimensional and significantly non-linear during the seizure, while high dimensional and of little nonlinearity during the interval [13]. According to our former study, Lyapunov index is relatively smaller during epileptic seizure while it is larger during the interval stage.

Comparing with Lyapunov index and related dimension, algorithm of complexity require relatively small data sets. Hundreds to thousands of data sets can meet the requirement of a relatively robust estimation. In some cases, data obtained hardly meet the requirements of Lyapunov index and related dimension since it is very difficult to collect enough data in remarkably instable life system without changing of basic conditions. On the other hand, complexity algorithm can efficiently resist noise. Hence complexity is considered as a suitable method for biomedical signal analysis.

II. METHOD AND EXPERIMENT

A. Research Method

Complexity is a general concept with different definitions which are employed from different angles to evaluate regulation degree of Signals [14-17]. Those definitions mainly stem from two research areas, Information Theory and Symbolic dynamics. Those methods to demonstrate system complexity include Lempel-Ziv Complexity, approximate entropy, C0 Complexity and so on. Not only algorithmic complexity such as LZ Complexity [18], C1 Complexity and C2 Complexity [19] but also constant from the angle of dynamics such as approximate entropy [20] can be employed to reflect system complexity of time series.

F. J. Gu and J. H. Xu provide the concept of C0 Complexity [21]. C0 Complexity which is aimed to divide original signal into two divergent components, irregular component and regular component are defined as the ratio of irregular component to the original signal. More robust estimation of biomedical signals which are characterized as intense nonlinear and instability can be gotten rapidly by C0 Complexity. And this process apparently avoids over coarse graining such as binaryzation to the original signals. The algorithm is listed as follows:

First step: Construct Fast Fourier Transforms (FFT) for original time series $s(t)$ and get amplitude spectrum $x(k)=FFT(s(t))$.

Second step: calculate average value of amplitude spectrum \bar{x} , set the part which is larger than average value as

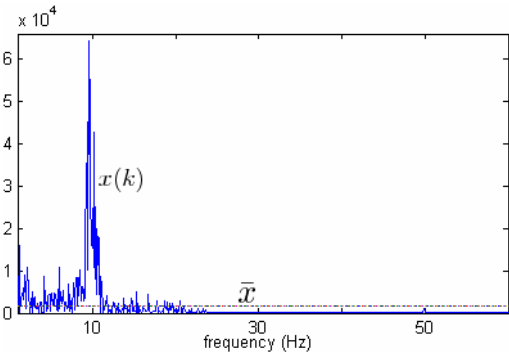


Fig. 1 Amplitude spectrum from FFT of EEG time series

regular component of the series and the part which is equal to or less than average value as irregular component. We only need the contribution of regular component.

$$x'(k) = \begin{cases} x(k), & \text{if } |x(k)| > \bar{x} \\ 0, & \text{if } |x(k)| \leq \bar{x} \end{cases} \quad (1)$$

Third step: Construct Inverse Fast Fourier Transforms (IFFT) $s' = IFFT^{-1}(x'(k))$ for amplitude spectrum of regular component and get $s'(t)$. Consider $s'(t)$ as regular time series.

Fourth step: Define C0 Complexity as the ratio of area of $|s(t)-s'(t)|$ to the area of $s(t)$.

$$C0 = \frac{\sum_{t=1}^N |s(t) - s'(t)|}{\sum_{t=1}^N |s(t)|} \quad (2)$$

Afterwards, some improvements of C0 complexity algorithm focusing on the separation are proposed by J. Z. Cai. They replace amplitude spectrum with power spectrum, calculate average value of power spectrum and use the value

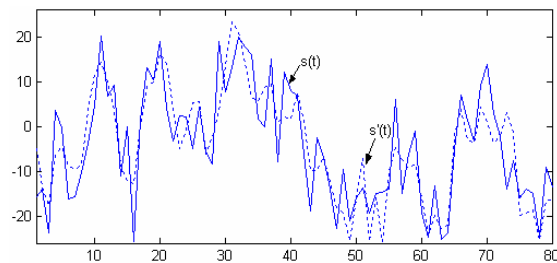


Fig. 2 Two curves of EEG time series through computing by algorithm of C0 Complexity

as a criteria to separate regular component and irregular component [22]. Namely the modification is focused on the second step of the original algorithm as show below:

$$x'(k) = \begin{cases} x(k), & \text{if } |x(k)|^2 > \overline{|x|}^2 \\ 0, & \text{if } |x(k)|^2 \leq \overline{|x|}^2 \end{cases} \quad (3)$$

B. Experiment and result

Our experimental scalped EEG data were obtained by using video electroencephalograph of 16 electrodes. We employed recordings obtained from electrodes placed on the scalped. Continuous EEG signals were typically analyzed for 70s including one time of epileptic seizure (39 seconds preictally, 18 seconds ictally and 13 seconds postictally). The data is sampled with a frequency of 200 Hz and the total data quantities are 14000 points of each electrode.

Fig. 3(a) shows EEG data sets of one epileptic seizure from one electrode, Fig. 3(b) shows a segment of the data sets, Fig. 3(c) shows a segment of EEG signals filtered following clinical criteria [23] (filter out signal components with frequencies lower than 0.30 Hz by lowpass filter, signal components with frequencies higher than 35 Hz by highpass filter and power line interference with the frequency of 50 Hz).

1. Employ C0 Complexity to analyze EEG data

Firstly, we determine the quantity of time series which will be used in calculating C0 Complexity. The quantity of time series used to calculate complexity varies from hundreds to thousands. Due to the character of instability of

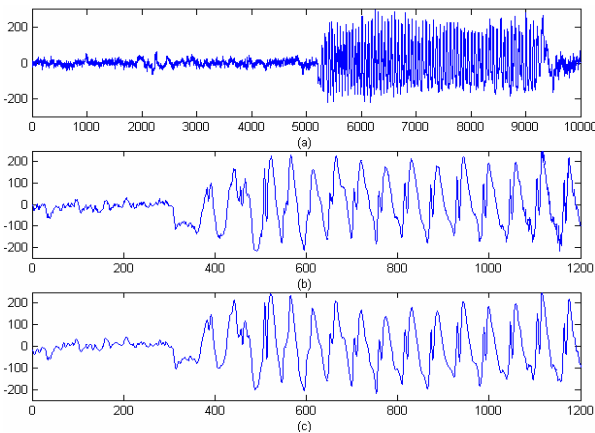


Fig. 3 EEG signal segment from Fp2 electrode: (a) EEG signals including one seizure; (b) Original EEG signals (contain interference signals); (c) EEG signals filtered according to clinical criteria

EEG signal, we choose smaller amount of EEG data to calculate complexity in order to reflect the dynamical change of EEG signal along time. In this research we choose first 70 seconds (14000 points) continuous EEG data extracted from electrode Fp2 to analyze this time series. Fig. 4 demonstrate that if we choose 1000 points to calculate complexity, the curve(Fig. 4(c)) of C0 Complexity can not precisely reflect dynamical change of complexity during ictal event; While if we choose 200 points, larger fluctuations appear in the curve(Fig. 4(a)) of C0 Complexity and computing speed is slow. In this experiment, we choose 600 points as quantity to compute a value of complexity.

Secondly, we choose appropriate step length of slipping window. In this research we calculate complexity by using 600 points each time. In order to demonstrate clearly dy-

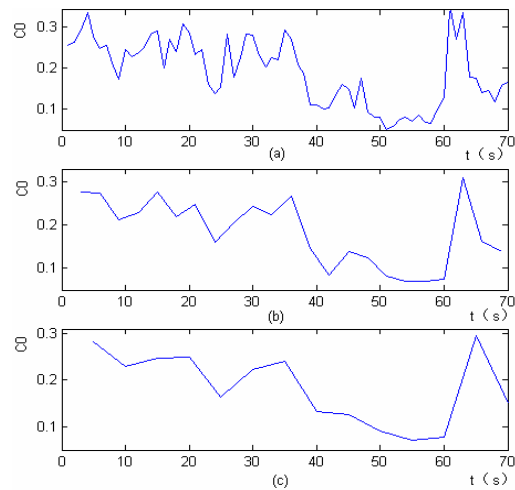


Fig. 4 C0 Complexity curves of original EEG data from Fp2: (a) data quantity: 200; (b) data quantity: 600; (C) data quantity: 1000.

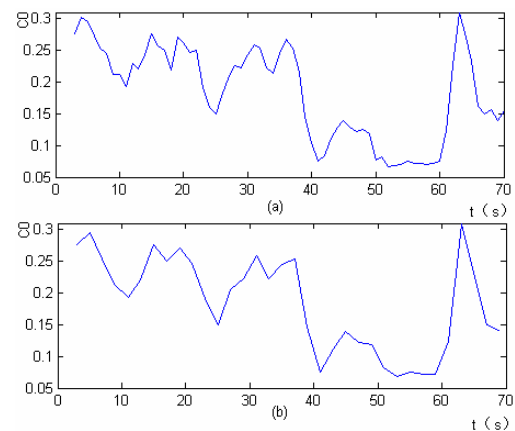


Fig. 5 C0 Complexity of original EEG data from Fp2: (a) quantity: 600 step: 200 (b) quantity: 600 step: 400

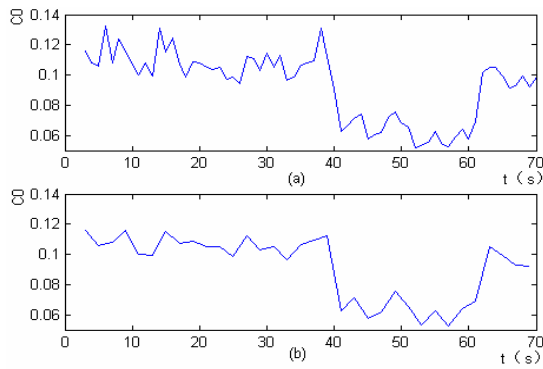


Fig. 6 C0 Complexity of filtered EEG data from Fp2: (a) quantity: 600 step: 200 (b) quantity: 600 step: 400

namical change of EEG signal along time, we slip 200 points forwards to calculating a new complexity value. Hence 400 points will overlap when next complexity value is calculated.

Finally, we study dynamical change of C0 Complexity of filtered EEG data. We calculate C0 Complexity of filtered EEG data from Fp2 and get the curve of dynamical change in order to observe the influence of filtering to complexity. Contrasting to Fig. 5, Fig. 6 show us that the pattern of complexity curve only changes slightly but with the total amplitude decreasing, especially the amplitude of complexity in interictal stage. However, the complexity of filtered data in ictal period is almost the same as that of original data.

2. Study the change of complexity when a external high frequency disturb suddenly

Fig. 4 to 6 demonstrate dynamical change of C0 Complexity of normal EEG signal during epileptic absence seizure. However, how could dynamical change be while sudden and abrupt external noises characterized as high frequency are added? We calculate C0 Complexity of original EEG data from T3 electrode. Fig. 7 (a) shows that high frequency disturbance begins in 45 second. Fig. 7 (b) demonstrates that complexity of EEG data decrease to some degree in 39 second when epileptic absence seizure happens; however, complexity intensely increases during ictal period due to high frequency disturbance, even exceeds the value during interictal stage. In Fig. 7 (c), EEG signals are filtered by clinical criteria. However, since high frequency disturbance can not be removed entirely and efficiently, complexity of EEG signals during ictal period almost keeps the same with that during interictal period. Also, the effects of noise to C0 Complexity decrease to some degree if filtered EEG signals are used.

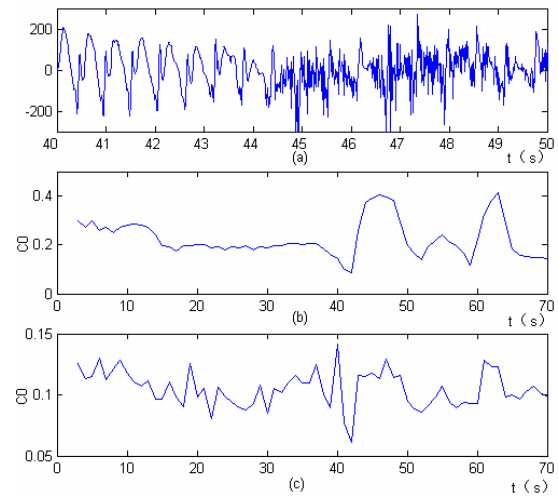


Fig. 7 EEG data and C0 Complexity from T3 electrode: (a) high frequency disturbance during absence seizure; (b) C0 Complexity of original EEG data; (c) C0 Complexity of filtered EEG data

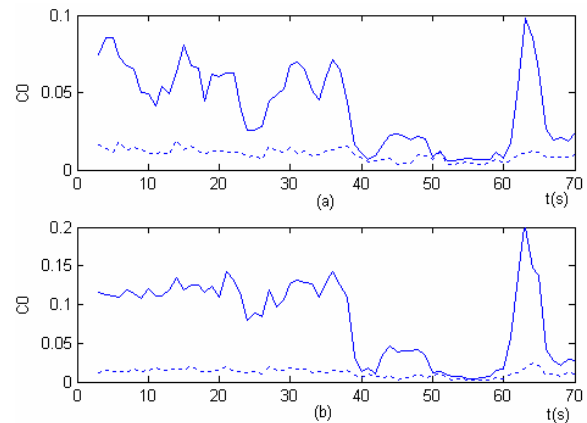


Fig. 8 Analyze C0 Complexity by using improved algorithm: (a) curve of C0 Complexity from Fp2 (b) curve of C0 Complexity from F4

3. Employ improved algorithm of C0 Complexity to analyze EEG signal

As it is mentioned before, some improvements of C0 complexity algorithm focusing on the separation are proposed by J. Z. Cai. They replace amplitude spectrum with power spectrum, calculate average value of power spectrum and use the value as a criterion to separate regular component and irregular component. We calculate C0 Complexity of EEG signals from Fp2 and F4 electrodes by using improved C0 Complexity algorithm. Solid line in Fig. 8 represents C0 Complexity of original EEG signal while dotted line represents those values coming from filtered EEG signal. Fig. 8 demonstrates the exterior pattern of curves from

improved algorithm is similar with that from original algorithm, but the value of C0 Complexity calculated by improved algorithm is smaller than those calculated by original algorithm. The advantages of using improved C0 Complexity are not remarkable according to the curve of improved C0 Complexity in this experiment.

III. CONCLUSIONS

In this research, we can find the amplitude of C0 Complexity during preictal period is totally larger than that in ictal period. This conclusion can efficiently prove some hypotheses proposed by former researchers. It can be observed in our study that C0 complexity tend to lower progressively during preictal period, then C0 complexity of EEG signals from electrodes would increase in value before decline; during postictal period, the complexity would increase again and even exceed preictal values sometime.

Apparently, interference signals can have either positive or negative influences during our computation and analysis. Since the various sensitivity of preictal and ictal period varies, the interference signals makes the value of complexity partially larger, consequently the value difference of complexity between interval and ictal period is further extended, which makes the results easier to observe. Complexity values for filtered EEG signals decrease in a total, with greater reductions for interval EEG signals and less reductions for ictal EEG signals. But interference signals have little influence on the shape of the complexity curve. Therefore, this complexity algorithm is able to resist certain noises. However, a remarkable influence on complexity value may occur when irregular and sudden interference signals, especially signals with frequency components within the frequency range of normal EEG signals, exist during the process of EEG signal monitoring.

Complexity algorithm is employed to investigate characters of output signals from systems without proving the existence of chaos; therefore, it does not require dynamical knowledge which can be obtained from reconstruct attractors. Meanwhile, we can get conclusion from former study that this algorithm require less data sets and can obtain stable results even if the amount of data sets varies. However, external interference, especially irregular ones we have mentioned which happen in a sudden, may have significant influences on the complexity of T3 electrode. In our earlier study [11,24], we can work out stable maximum Lyapunov components based on phase space reconstruction even the interference exists. Therefore, although phase space reconstruction of EEG signals is a challenging and tedious work, the application of this method in analyzing nonstable non-linear time series is significant too.

Through our study above, we can see C0 Complexity can be considered as a good algorithm for study unstable data of life system. This algorithm requires less data set and can provide relatively robust results to reasonably describe dynamical change of complexity during epileptic absence seizure. Especially, this algorithm has capability of resisting regular external disturbance. Hence, we prove that C0 Complexity is suitable to be considered as a criterion in our later studies of epileptic seizure prediction and added in comprehensive evaluate index system.

ACKNOWLEDGMENT

This work was supported by the National Natural Science Foundation of China (10671213, 10771222) and research data is provided by the Department of Neurology, the First Affiliated Hospital of Sun Yat-sen University.

REFERENCES

1. Lopes da Silva, Wouter Blanes, Stilian N. Kalitzin, et al. Dynamical Diseases of Brain Systems: Different Routes to Epileptic Seizures[J]. *IEEE Transactions on Biomedical Engineering*, 2003,50: 540-548.
2. M. Steriade, D. Contreras, Spike-wave complexes and fast components of cortically generated seizures. I. Role of neocortex and thalamus, [J]. *J. Neurophysiol.*, vol. 80, no. 3, pp. 1439-1455, 1998.
3. Witte H, Iasemidis LD, Litt B. Towards epileptic seizure prediction and control: a survey of methods and models. *IEEE Trans Biomed Eng, Spec Issue Seizure Prediction*, Ed 2003;50:537-9
4. L.D. Iasemidis, D.S. Shiao, P.M. Pardalos, et al. Long-term prospective on-line real-time seizure prediction[J]. *Clinical Neurophysiology* 116 (2005) 532-544.
5. Witte H, Iasemidis LD, Litt B. Towards epileptic seizure prediction and control: a survey of methods and models. *IEEE Trans Biomed Eng, Spec Issue Seizure Prediction*, Ed 2003;50:537-9.
6. Alessandro M, Vachtsevanos G, Esteller R, et al. A multi-feature and multi-channel univariate selection process for seizure prediction [J]. *Clin Neurophysiol* 2005, 116:506-16.
7. Elger CE, Lehnertz K. Seizure prediction by non-linear time series analysis of brain electrical activity [J]. *Eur J Neurosci* 1998;10:786-9.
8. Le Van Quyen M, Martinerie J, Navarro V, et al. Characterizing neurodynamic changes before seizures [J]. *J Clin Neurophysiol*, 2001, 18(3):191.
9. Pierre Loiseau. Epileptic syndromes in infancy, childhood and adolescence, chapter Childhood absence epilepsy, pages 135-150. John Libbey & Company Ltd., 2nd edition, 1992.
10. P. Suffczynski, S. N. Kalitzin, F. H. Lopes da Silva, Dynamics of non-convulsive epileptic phenomena modeled by a bistable neuronal network [J]. *Neuroscience* 126 (2004) 467-484.
11. Yi Zhou, Yi Zhao, Wei Sun, et al. Quantification of Spatiotemporal Dynamic Transition of Absence Seizures. *Proceedings of the 4th International Conference on Impulsive and Hybrid Dynamical Systems*, (2007.7)2628-2633. (Supplementary volume to DCDIS Series A: Mathematical Analysis, ISSN 1201-3390).
12. Rapp PE. Chaos in the neurosciences: cautionary tales from the frontier, *Biologist*. 1993, 40(2):89-94.

13. ZHOU Yi, ZHAO Yi, CHEN Ziyi, et al. The Application of Chaotic Theory during the Study of Epilepsy. Chinese Journal of Nervous and Mental Diseases[J]. 2007, 33(6): 382-383.
14. Gu F, Meng X, Shen E et al. Can we measure consciousness with EEG complexities? [J]. International Journal of Bifurcation and Chaos, 2003, 13(3):733-742.
15. Wackerbauer R, Witt A, Atmanspacher H, et al. A comparative classification of complexity measures, Chaos, Solitons and Fractals, 1994, 4:133-173.
16. Rapp PE, Schmah TI. Complexity measures in molecular psychiatry Molecular Psychiatry, 1996, 1:408-416.
17. Rapp PE, Schmah TI. Dynamical analysis in clinical practice[A]. In Lehnertz K, Amhold J, Grassberger P and Elger CE (eds), Chaosin-Brains[C]. Singapore: WorldScientific, 2000, 52-62
18. Kasper F, Schuster HG. Easily calculable measure for the complexity of spatiotemporal patterns [J], Physical Review A, 1987, 36(2):842-848.
19. JH.Xu, ZR.Liu, R.Liu, et al. Information transmission in human cerebral cortex [J], Physica 1997, D106:363-374.
20. Pincus S.M. Approximate Entropy as a Measure of System Complexity. Proc.Natl.Acad.Sci.USA. 1991; 88(3): 2297 -2301.
21. Chen Fang, Gu Fanji, Xu Jinghua, et al. ACTA BIOPHYSICA SINICA, A new measurement of complexity for studying EEG mutual information, 1998, (3):508-512
22. SHEN En_hua, CAI Zhi_jie, GU Fan_ji. Mathematical Foundation of C0 Complexity. Applied Mathematics and Mechanic, 2005,(9): 1083-1090.
23. Becker HC, Mickle WA, Heath RG. A variable frequency, variable selectivity filter for electroencephalography [J]. Electroencephalogr Clin Neurophysiol Suppl. 1958 Nov; 10(4):731-5.
24. ZHOU Yi, ZHAO Yi, XIE Lingli et al. Computation and Analysis of parameters in phase space reconstruction of epileptic EEG signal [J]. Acta Scientiarum Natralium Universitatis Sunyatseni.2007, 46(3):5-9.

Author: Yi Zhou

Institute: Department of Biomedical Engineering, Zhongshan School of Medicine, Sun Yat-sen University

Street: No.74 Zhongshan Er Road,

City: Guangzhou, Guangdong Province

Country: China

Email: zhouyi@mail.sysu.edu.cn

Research of Virtual Nerve Induce Electrical Signal Auto-check Technology

Min Wu^{1,2}, Zhi-hui Wei¹, Li-ming Tang², Yu-bao Sun¹, Tie-bing Liu²

¹ Nanjing University of SCI & TECH /Department of Computer Science and Engineering , Nanjing, China

² Nanjing General Hospital of Nanjing Region/Department of Medical Engineering, Nanjing, China

Abstract — AIM: Epilepsy neurons in the brain caused by abnormal discharge or part of the overall dysfunction of the brain characterized by chronic diseases, simulated biological visual perception system, according to the sparse neuronal response characteristics of the high-risk population for epilepsy nervous system electrophysiological screening, early detection and intervention of the relevant population, reduce the extent of involvement of epilepsy and maiming, death rate. **Methods:** Selecting the suitable decomposition of matching pursuit algorithm, with new atomic less to rebuild normal EEG and specific types of diseases EEG, the convenience of the various diseases of the nervous system - the characteristics of EEG identification and extraction. **Results:** Treatment 16-Standard EEG, isolated from epilepsy wave characteristics, and to identify characteristics of wave to be in the diagnosis of epilepsy, epilepsy basis of this characteristic wave reflected strikes into the 16-standard electrode, the relevant sources of electricity bit software localization of epileptic foci preliminary. **Conclusion:** Sparse representation model can obtain EEG signals that an effective method of EEG signals through the effective component machine identification, summed up the series features wave patterns for clinical diagnostic information, which reduces the workload of epilepsy signal recognition, enhanced the efficiency and accuracy of identifying and realizing the scale of epilepsy screening.

Keywords — Induced signal, Sparse Representation, Matching Pursuit, Epilepsy Characteristic Wave, Compact Flash (CF) Interface, Personal Digital Assistant (PDA)

I. INTRODUCTION

Nervous system signals induced by the test is the basis of modern medicine and clinical application of research and clinical diagnosis and treatment activities of the foundation work. Signal induced by the test can be obtained human potential physiological information in the handling of such information^[1], analysis on the basis of the disease and can be found not only observe the occurrence of disease, development and the outcome of the process, so symptomatic timely Treatment to the best therapeutic effect, and better with the lifting of the pain, but also found that the human body can be summarized a number of objective mechanisms, and reveal the mysteries of life movement. Induced signal test system usually includes inducing signal in signal acquisition and induced two parts, induced a partial signal

can be required to produce the signal induced, or through the electrodes and various transducer role in the human body so that human-induced nerve signals generated; evoked EEG electrode or acquisition will be part of the sensor input signal and display the necessary conditioning, storage, or to the digital signal and digital signal further processing.

Compared to the huge volume of evoked EEG testing system, and in many applications where its small size and portable performance in the high requirements, such as operating theatres, animal experiments and operation of certain diseases, such as large-scale screening . To meet the physiological basis of research, disease screening, such as clinics and practical application requests, we have designed a PDA-based mobile computing platforms, such as CF interface technology and the nerve-induced signal test systems. Its analog signal analysis and processing of visual perception system, according to the sparse response neurons characteristic of the natural image made that the effective way to reduce conventional EEG signals a huge amount of data, the establishment of a more rapid, simple and suitable for the analysis model, Sparse (the sparse representation) model, a number of images can be regarded as the linear combination of function, and only a small function of the larger non-zero coefficient.

II. STRUCTURE AND COMPOSITION OF VIRTUAL NERVE INDUCE ELECTRICAL TEST SYSTEM

The virtual nerve induce electrical test system provided with such structure of virtual instrument., with two-induced signal output channels and 16-physiological signal input channels can be output repetition frequency of 0.01 Hz ~ 100Hz, the duty cycle of 5% ~ 95% , the range of 0 V ~ ± 5V and adjustable for various function or arbitrary definition of induced electrical signal to the 50kps real-time sampling rate of input signal acquisition induced potentials, and the input signal can be analog, digital signal processing, to meet research needs.

Based on the CF interface of the PDA and other mobile computing devices we design CF + card worked in the IO model, and prepared to run on Windows CE operating system platforms, such as the mobile device drivers and data

acquisition, processing, complete evoked EEG and induced potentials in the formation of the collection. System hardware design is simple, perfect software design platform. Practice shows that PDA-based mobile computing devices such as CF interface technology and induced potential testing system for excellence and induced signal in real-time acquisition, processing signals induced potential ability to meet the most evoked potential physiological research needs.

The nerve-induced signal test system based mobile computing devices such as PDA and CF interface technology includes CF interface, controller of the DDS signal generator, induced signal conditioning and power amplification of the signal preconditioning,^[2] physiological signals conditioning of the analog-digital conversion and digital signal processing, also power management, in Figure 1. The middle four parts realized by one FPGA (Altera Corporation Cyclone series EP1C6F256), which reduces the complexity of PCB design and improves circuit reliability, but also decreases the circuit board area, cuts power consumption down so can meet the requirements of portable devices.

CF interface and controller system major complete the information exchange from mainframe data,^[3] identifying the mainframe host systems and collaborative completed initialization steps in the application process to accept orders and host data, and then controlling occurrence and conditioning of the induced signal, evoked EEG signal acquisition and processing, while collect the data which sent to the mainframe by a timely manner (using interrupt or host search). DDS signal generator system will mainly make the completion of the induced signal waveform into simulation of the data signals, and change induced signals in the frequency, amplitude and duty cycle, and other parameters in accordance with the instructions from mainframe. Induced signal conditioning and power amplification will

major be a filter for the output signal of DDS signal generator, filtering high-frequency component to make signal smooth, and at last export signal with a certain large power. Physiological signals conditioning major make input physiological signal buffering and amplification, with anti-aliasing filter filtering high frequency components to reduce the analog-digital conversion of the digital signal after the pseudo-low-frequency noise, and in accordance with mainframe 's instructions, adjust its gain to the input signal amplitude for ADC requirements. Analog-digital conversion and digital signal processing based in part on the mainframe install in a certain sampling rate physiological signal analog signal acquisition, and process digital signal under the control of the mainframe by hardware, distill a real physiological signal from great background noise, or make the signal for various transform (FFT, Wavelet Transform, for example), which can review nerve induce signals from the other perspective (time domain and frequency domain or other space). Power management will make voltage from 3.3 V or 5.0 V by CF interface to the needs of converter system, and when necessary, closing some of the power supply circuit to reduce power consumption, extend the PDA and other mobile computing devices battery life.

III. ESTABLISHMENT OF EEG ANALYSIS MODEL BASED ON SPARSE REPRESENTATION

Seeking "Sparse Representation" for objective things has been a research objective of the experts in the fields of computer vision, mathematics, data compression, and so on. Sparse (the sparse representation) model, a number of images can be regarded as the linear combination of function, and only a small function of the larger non-zero coefficient. The basis functions here is as atom-function, while a collection of basis functions as a dictionary. When the dictionary is over maturity, the decomposition for the signal is not the only. Seeking "Sparse Representation" is a combination of search needs. To solve the optimization problem known polynomial algorithm does not exist. Based on the sparse redundant dictionary that itself is an NP-hard problem, needing for a sub-optimal approximation method. In the past few years, the methods of seeking "Sparse Representation" mainly included greed method and convex relaxation method.^[4] Typical greedy algorithm involves matching pursuit and orthogonal matching pursuit. Typical convex typical relaxation methods are basis pursuit algorithm and FOCUSS (focal under-determined system solver) algorithm. This research used matching pursuit algorithm, in-depth theoretical study showed that when the question decomposition of the original signal sparse enough, here is the numerical algorithm to track its most sparsely representation.

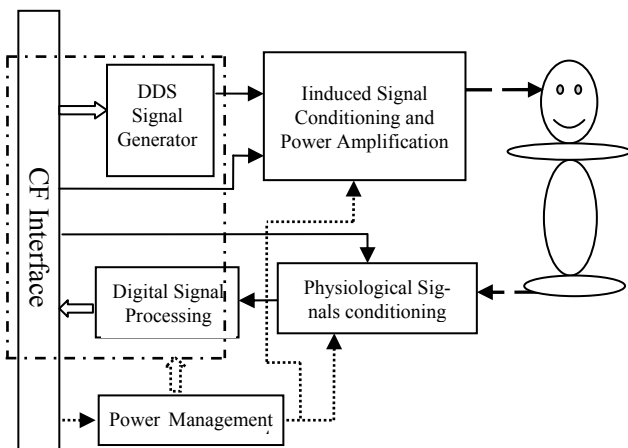


Fig. 1 Structure of Virtual Nerve Induce Electrical Test System

So there are two levels problem need to solve, namely, one is how to get the signal decomposition dictionary, and the other is how to get images of sparse representation.

Design of a dictionary function

There are usually three kinds of approach to get decomposition signal dictionary. At first, existing frameworks such orthogonal basis combination as wavelet, wavelet packet and Contourlet. Secondly, transformation of parameters generated dictionary through the design parameters of a function. Thirdly, seeking dictionary through learning algorithm. Based on image structure, EEG signal can be expressed as a linear combination of atomic signal. Sparse representation means denoting a signal with the lowest possible number of atoms, which can reflect the main features of the signal, The main features of these atoms can be used for classification and identification signals. At present, from the point of view of sparse representation of EEG signals, the study used mainly in two directions: study and source separation method.^[5]

Numerical method for sparse representation of image

Mallat and Zhang used Matching pursuit(MP) of the wavelet signal to the gradual decomposition, their ideology is directly from the decomposition of the starting signal, choosing the atoms with the largest correlation coefficient, through a gradual iterative to decompose signal. Form each of its iteration, we have taken an appropriate "atomic" from comprehensive library and through multiple iteration, when meeting the convergence conditions, it can be signal sparse expression. Matching pursuit algorithm use of greedy techniques to reduce the computational complexity. It is a recursive algorithm of iteration, As choosing the most relevant atom from the dictionary step by step, as the approach of signal makes more optimization.^[6]

Algorithm specific steps are as follows:

a. Initialization, $R^0 f = f$, $i = 0$, $\alpha_\gamma = \langle f, \phi_\gamma \rangle$

' $R^0 f$ ' means initial residual signal, ' f ' means the original signal, ' i ' means initial iteration times, ' α_γ ' means inner product of atoms.

b. Actively search of inner product, $\gamma_i = \arg \max_{\gamma \in \Gamma} |\alpha_\gamma|$

c. Residual signal updated, $R^{i+1} f = R^i f - \alpha_{\gamma_i} \phi_{\gamma_i}$

d. Coefficient of inner product updated, $\alpha_\gamma = \langle R^{i+1} f, \phi_\gamma \rangle$

e. Stop rules: If residual signal energy to be less than the value, $\|R^i f\|^2 \leq \xi_{stop}$, then stops iteration. Otherwise,

$i = i + 1$, go to Step b, searching for the matching atoms with the residual signal in the dictionary.

IV. EXPERIMENT & RESULTS

Comprehensive analysis results of various Epilepsy sparse EEG, generally, it was believed that epilepsy is characterized by paroxysmal EEG with high amplitude activity. The waveform and frequency are vary, some forms have special diagnostic significance.^[7] Typical EEG waveform of epilepsy is as Figure 2:

EEG epilepsy sparse decomposition of the matching process is based on tracking MSVis2ual C++ 7.0 and Mat-Lab7. Platform 01 or MS Embedded Visual C++ 4.0 development platform for the design, running on Windows2000 / XP or Pocket PC 2003 / Mobile Windows XP environment. On the one hand, through the USB bus EEG detection module implementation of control and detection module from the EEG read data, thus completing the epileptic EEG data collection. On the other hand through the man-machine interface, with sparse decomposition matching pursuit algorithm, rebuild EEG signal with new less atoms, the signal or image becomes more concise. Thereby completing the analysis of epilepsy EEG, realize the scale of epilepsy screening.

Application of Virtual induced signal test system, we can gather and record of epilepsy EEG easily, and with the decomposition analysis based on sparse data collected

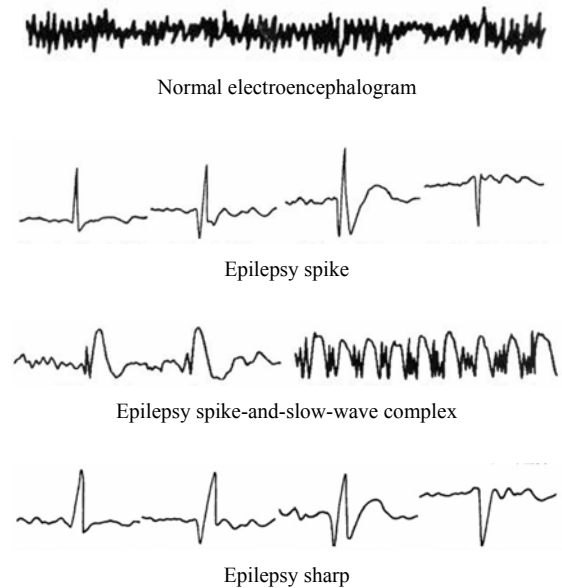


Fig. 2 Comparison of waves between normal and epilepsy electroencephalograms

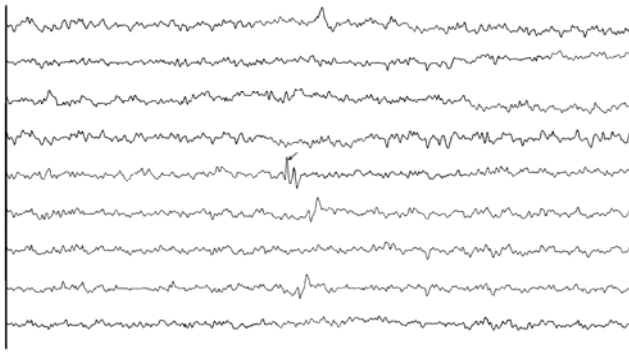


Fig. 3 Epilepsy EEG after Sparse representation analysis ("↑" shows the spikes)

model for processing. After matching pursuit algorithm processing, we can get nine independent path clear signal from the original 16-EEG data, in which, there are one road signal strength and can be investigated obvious and easily differentiate between sharp nail-like spikes from both waveform intensity and characteristics, eight other signals are basically does not contain sharp nail-like spikes, as shown in Figure 3.

V. CONCLUSION

With sparseness decompose theory, the encephalon electrical signal induced and collected system based on the mobile compute technology platform is developed, which realize the check of the nervous system disease; the check data is disposed with the sparseness figure analysis technology, the variable component of encephalon electrical signal is progressed effective machine recognition on the aspects of the recognition, validity, etc. the result is referenced clin-

ical diagnosis, thus the workload of the epilepsy signal recognize is reduced, the recognize efficiency and validity is improved, thus the check of the epilepsy is realized.

REFERENCES

1. Joseph R. Smitha, Karl Sillayc, Peter Winklerd. Orbitofrontal Epilepsy: Elec- troclinical Analysis of Surgical Cases and Literature Review. *Stereotactic Functional Neurosurgery*, 2004. (82):20-25
2. Wang editor-in-chief of New Delhi, Professor Qin editor-in-chief. *Nervous System Clinical Electrophysiology (EEG study) / (neurology Vol2)*. Beijing: People's Military Medical Press, 2004:1-5, 35-38, 62-69, 116-120,295-297
3. Zhang Ming Dao, when Bernadette. *Evoked potentials of the brain. The first edition*. Shanghai: Shanghai Science and Technology Education Press. 1997
4. Tie-Bing Liu, Tang Liming, Wu Min, Chang Kang. CF interface technology based on the evoked potential testing system. *Beijing Biomedical Engineering*. 2006, 25 (5):524-527
5. Tang Liming, Chang Kang, Tie-Bing Liu, and others. DDS technology based on neural stimulation threshold Development. *Beijing Biomedical Engineering*. 2003, 26(3):191-194, 197
6. Tang Liming, Chang Kang, Tie-Bing Liu, and others. Human biological signal frequency and duty cycle measurement circuit design and application. *Space medicine and medical engineering*. 2002, 15 (6):433-436
7. Li-ming Tang, Ben-kang Chang, Tie-Bing Liu, et al. Induced bioelectrical signal in human nervous system and its significance to the research of neuron-threshold. *Chinese Journal of Clinical Rehabilitation*. 2003, 7 (28): 382-383

Author: Min Wu^{1,2} Zhi-hui Wei¹ Li-ming Tang² Yu-bao Sun¹
Tie-bing Liu²
Institute: Research of Virtual Nerve Induce Electrical Signal Auto-check Technology
Street: East Zhongshan road 305
City: Nanjing City, Jiangsu Prov.
Country: China
Email: njzywm@163.com

Development of Implantable Neuro-Stimulator Used for Brain and Nerve Stimulation

L.M. Li, H.W. Hao, B.Z. Ma, X.W. Wen, F.J. Liu, C.H. Hu

School of Aerospace, Tsinghua University, Beijing, China

Abstract — The aim of this paper is to develop a programmable and implantable neuro-stimulator for animal research and clinical application. The neuro-stimulator includes implantable pulse generator, extension (if necessary) and lead implanted in the body, and controller, PDA and magnet used outside the body for telemetry/programming. It provides electrical pulse stimulation to the target nerve or brain nucleus, with adjustable pulse parameters of pulse width, frequency, amplitude, on time and off time. The ultra-low power consumption circuit based micro-processor was developed, and welded with primary lithium battery, then were sealed by titanium case and feedthroughs hermetically using laser welding. The implantable pulse generator has the weight of about 34 g, the size less than 47*52*11 mm, and two kinds of circuit can be installed in it, i.e. current pulse control for nerve stimulation and voltage pulse control for brain stimulation. The pulse parameters of amplitude, pulse width, frequency and electrode configuration can be programmed by controller and PDA, e.g. pulse amplitude is 0-10V in 0.05V or 0.1V steps for voltage pulse control, 0-3.5mA in 0.1mA steps for current voltage pulse control. The neuro-stimulator has been validated the safety and function during long-term implantation by animal experiments of vagus nerve stimulation (VNS) using 20 rabbits and deep brain stimulation (DBS) using 1 rabbit, and DBS experiments for PD treatment using rhesus monkey is in process. The developed neuro-stimulator can be used in clinical application of DBS, VNS and other brain/nerve stimulation, and also an instrument platform for animal experiment research of implantable neuro-stimulation to study therapy mechanism and optimized stimulation parameters.

Keywords — Implantable neuro-stimulator, DBS, VNS, Animal experiment.

I. INTRODUCTION

Implantable neuro-stimulation (INS) therapy has been applied to clinic widely, involving more than 20 neuro-disorder diseases such as deep brain stimulation (DBS) for Parkinson's disease (PD) and tremor, vagus nerve stimulation (VNS) for refractory epilepsy and depression, and spinal cord stimulation (SCS) for pain^[1-4]. Currently, implantable neuro-stimulator is supplied by several companies in USA mainly, including Medtronic, Cyberonics, Advanced Neuromodulation Systems (division of St. Jude Medical), and Advanced Bionics (division of Boston Scientific). As we know, neuro-stimulator is similar to pacemaker

in structure and function, the main parts are implantable pulse generator (IPG), lead and extension (if necessary), and the main functions are voltage or current pulse generation, telemetry/programming and manufacture using bio-compatible materials.

Also, INS therapy has been used more and more widely in China, but some limits are still very important. Firstly, it's too expensive since the price of an implantable device (including IPG and lead) is usually as high as 100-200 thousand CNY. Secondly, the pulse parameters of some products have too large error, especially pulse amplitude.

Driven by the strong demands from clinical application and fundamental research, we have developed INS systems which has been tested and used in animal experiments.

II. SYSTEM DESIGN

A. System description

As shown in Fig.1, the INS system includes implantable parts (IPG, lead and electrode) and telemetry/programming parts outside the body (controller, PDA and magnet). The IPG is implanted under the skin in breast, the electrode is fixed to the target of brain nucleus or nerve, and the electrical pulse generated by IPG was transmitted to electrode through extension (if necessary) and lead under the skin. The physician operates the PDA to get the IPG information and program the pulse parameters, and communication between PDA and IPG is realized with the controller as a bridge. The magnet can switch the IPG output on and off.

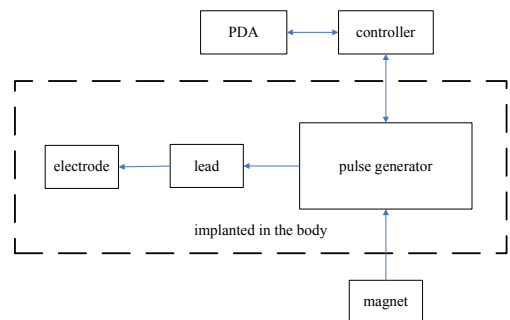


Fig. 1 Diagram of the neuro-stimulator

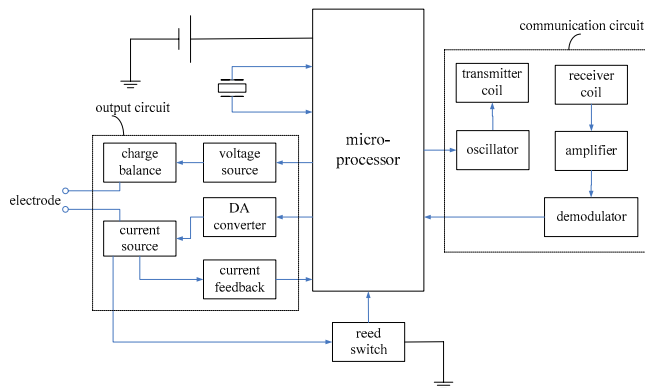


Fig. 2 Circuit design of the implantable pulse generator

B. IPG circuit

IPG circuit is composed of battery, logic control unit, output circuit, RF communication circuit and magnet control circuit, as shown in Fig.2.

1) Lithium carbon monofluoride (Li/CF_x) battery is used, which is a kind of medium rate primary battery suitable for neuro-stimulator with the outstanding advantages of high power density, flat discharge curve, very small self discharge and excellent safety in long-term implantation. [5]

2) Logic control unit is designed base on high integration and low power micro-processor of MSP430, which can work in several low power modes, with FLASH, RAM, timer, UART, DA converter integrated.

3) Output circuit in Fig.2 shows the design of constant current pulse output circuit, which includes DA converter integrated in MCU, programmable voltage source (DC-DC converter), current source and current feedback, and charge balance circuit to ensure the net DC current is zero. For multi-electrodes (more than two electrodes) design, analog switches are needed before charge balance circuit.

4) Communication circuit is designed for bi-directional percutaneous RF data exchange with the communication distance more than 1 inch. Our design is based on magnetic coupled coils, in which the former design uses 2ASK (amplitude shift keying), and the new design uses PPM (pulse position modulation) with the advantages of much lower power consumption and longer communication distance.

5) Magnet control circuit is based on a reed switch, which responds the magnet control outside the body.

C. Controller circuit

Controller circuit is composed of signal transmitter, signal receiver and power source, as shown in Fig.3.

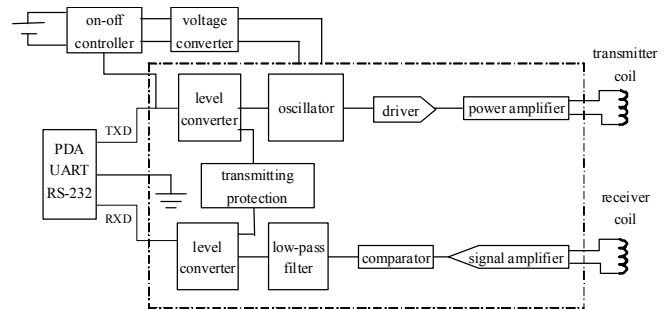


Fig. 3 Circuit design of the implantable pulse generator

1) Signal transmitter receives the RS-232 signal from PDA, converts the signal level, controls the oscillator on and off to realize 2ASK modulation, then drives the coil to transmit the signal.

2) Signal receiver gets signal from coil, amplifies, filters and demodulates the signal, then converts level and enters PDA.

3) Power source converts battery voltage to the voltages needed by transmitter and receiver, automatically turns on when communication data appears, and automatically turns off after specified idle time.

III. IPG PROTOTYPE

The battery and circuit are sealed in titanium case and welded by pulse laser welding, the stimulation pulse is introduced from circuit to header using feedthroughs.

Two kinds of circuit can be installed in the IPG, i.e. current pulse control for nerve stimulation and voltage pulse control for brain stimulation. The pulse parameters for brain stimulation are shown in Table 1. For nerve stimulation, the

Table 1 Parameters of implantable brain stimulator

Parameters	Available values
Pulse amplitude	0 - 10V: 0-6.35V (in 0.05V steps), 6.35-10V (in 0.1 V steps)
Pulse frequency	2 - 250 Hz (62 values)
Pulse width	60 - 450 μ s (in 30 μ s steps)
On time	0.1s - 24h: 0.1s - 1s (in 0.1s steps), 1 - 60 s (in 1 s steps), 1 - 30 min (in 1 min steps), 0.5 - 24 h (in 0.5 h steps)
Off time	same as On time
Day cycle on time	0.5 - 24h (in 0.5h steps)
Day cycle off time	Same as Day cycle on time
Soft start/stop	1, 2, 4 or 8 seconds
Electrode polarity	Case: Positive or Off 1, 2, 3, 4 electrode: Positive, Negative or Off

pulse amplitude is 0-3.5mA (in 0.1mA steps), and other parameters of pulse frequency, pulse width, On time, Off time and soft start/stop are similar. All the parameters can be programmed by controller and PDA.

As the results, IPG has the weight of about 34g, and the size less than 47*52*11 mm. For typical stimulation parameters and battery discharge of 2Ah, the stimulator can work over 10 years for VNS and about 4-5 years for DBS.

IV. ANIMAL EXPERIMENTS

Twenty animal experimental cases using rabbits have been finished for VNS. The nerve stimulator is shown in Fig.4, and the surgery procedure was similar to operation on patients, as shown in Fig.5.

The stimulator was programmed using controller and PDA (as shown in Fig.6) and the electrical stimulation was started 1 week after surgery. The stimulation pulse was

measured using Neuroscan EEG system (including Sys-Amp2 EEG amplifier and Scan 4.3 software) as shown in Fig.7. The rabbits had been kept in health after implantation, and no obvious side effects were observed during long term stimulation and telemetry/programming more than 6 months.

One animal experimental case using rabbit has been finished for DBS. The lead implantation to subthalamic nucleus (STN) using stereotactic surgery is shown in Fig.8, also IPG and extension is shown in Fig.9. One monkey has been established PD model successfully, and the implantation surgery is being prepared.

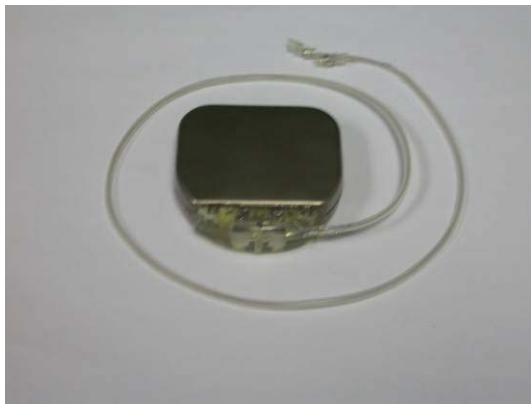


Fig. 4 IPG, lead and electrodes of nerve stimulator



Fig. 6 Controller and PDA

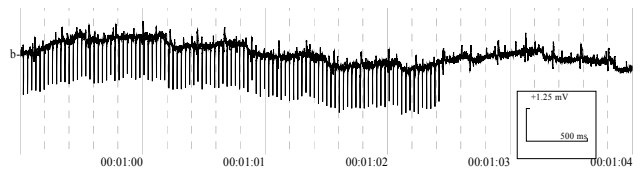


Fig. 7 Signal of VNS measured on the skin



Fig. 5 Surgical implantation of stimulator used in VNS



Fig. 8 Surgical implantation of lead used in DBS



Fig. 9 Surgical implantation of IPG and extension used in DBS

V. CONCLUSIONS

We have developed the implantable neuro-stimulator system including IPG, lead, controller and PDA. The whole prototype has been used in rabbits, realizing deep brain stimulation and vagus nerve stimulation, and showing that the function and safety in long term implantation.

The neuro-stimulator system can be used in animal experiments for basic research, studying therapy mechanism and optimized stimulation parameters. Further it can be used in clinical neuro-stimulation therapy, to provide a relatively cheap and easy used choose option for patients.

ACKNOWLEDGMENT

This study has been supported by National High Technology R&D Program of China (863 program) (Grant No.2006AA02Z4E9) and National Key Technology R&D Program of China (Grant No.2006BAI03A18).

The authors thank Prof. G.M. Luan, Dr. Y.E. Lv of Beijing Sanbo Fuxing Neurosurgical Hospital and Prof. J.G. Zhang, Dr. Y. Ma of Beijing Tiantan Hospital for animal surgery.

REFERENCES

1. Rushton D (1997) Functional electrical stimulation. *Physiol Meas* 18: 241-275.
2. Horch K, Dhillon G (2004) *Neuroprosthetics: Theory and Practice*. World Scientific, Singapore.
3. The Deep-Brain Stimulation for Parkinson's Disease Study Group (2001) Deep-brain stimulation of the subthalamic nucleus or the pars interna of the globus pallidus in Parkinson's disease. *N Engl J Med* 345: 956-963.
4. DeGiorgio C, Schachter S, Handforth A, et al (2000) Prospective long-term study of vagus nerve stimulation for the treatment of refractory seizures. *Epilepsia* 41: 1195-1200.
5. Greatbatch Inc. at <http://greatbatch.com/Medical/>

Author: Luming Li
 Institute: School of Aerospace, Tsinghua University
 Street: Rm.803, Central Main Building, Tsinghua University
 City: Beijing
 Country: China
 Email: lilm@tsinghua.edu.cn

3D Vessel Tree Reconstruction from Rotational C-arm Projections by Multi-view Stereo Reconstruction

Wei Zhang^{1,2}, Zikuan Chen¹ and Xuefeng Zhang²

¹Northeastern University, Sino-Dutch Biomedical and Information Engineering, Shenyang, 110004, China

²Northeastern University, Department of Mathematics, Shenyang, 110004, China.

Abstract— In biplane angiography, a three-dimensional (3D) vessel tree can be reconstructed from two-view stereo reconstruction. During an intervention procedure, the rotational C-arm scanning produces a sequence of cone-beam projections (angiograms) that can be used for vessel tracking and vessel tree reconstruction. Since any two projection images can be considered as a two-view pair as captured by a biplane system, a 3D vessel tree can be reconstructed by searching the corresponding points in two projection images followed by two-view stereo reconstruction. The geometry of the 3D tree can be measured in the calibrated Euclidean space. During C-arm angiographic imaging, the contrast bolus flowing through blood vessels may sustain a bolus/blood equilibrium state in the scan field of view, which can be considered as quasi-static or stationary state, the C-arm images can be used for vessel tree reconstruction. In this paper, we propose a vessel tree reconstruction method from C-arm images: 1) add epipolar constraint on the search for corresponding points (feature points); 2) apply depth-first search strategy for tree construction from node points and point correspondence; 3) find fundamental and projection matrices for projective reconstruction; 4) reconstruct the 3D tree in Euclidean space with a cube phantom calibration; 5) perform 3D tree measurements (tree segment lengths). Computer simulations and tree phantom experiments under a rotational C-arm system are reported, which justify the method in this paper.

Keywords—Rotational C-arm system, Stereo reconstruction, Point correspondence, Projection reconstruction, Euclidean reconstruction

I. INTRODUCTION

In biplane angiography, a 3D vessel tree can be reconstructed from two-view simultaneous projections by stereo vision reconstruction. The rotational C-arm scanning produces a sequence of cone-beam projections as distinguished by view angles. During C-arm angiographic imaging, the contrast bolus flowing through blood vessels may sustain a bolus/blood equilibrium state in the scan field of view, which can be considered as quasi-static or stationary state, the C-arm images can be used for vessel tree reconstruction. By rearranging the cone-beam projections into numerous two-view pairs or multi-view subgroups, we can reconstruction the 3D tree-like object by searching the corresponding points in two projection

images followed by two-view stereo reconstruction. Thus the rotational C-arm projections can be used as a biplane system for vessel tree reconstruction.

Two perspective images of a single rigid object/scene are related by the so-called epipolar geometry—the intrinsic projective geometry between two views, which can be described by a 3×3 matrix of rank 2, called fundamental matrix. It is independent of scene structure, and only depends on the cameras' internal parameters and relative pose. The fundamental matrix can be computed from correspondences of imaged scene points alone, without requiring knowledge of the cameras' internal parameters or relative pose. It contains all geometric information that is necessary for establishing correspondences between two images, from which three-dimensional structure of the perceived scene can be inferred. The importance of the fundamental matrix has been stressed in the last few years and it is now believed that it will have a significant role in future applications of computer vision. Applications using the fundamental matrix include 3D-structure recovery, motion segmentation, camera self-calibration, match and tracing.^[1-4] Therefore, an accurate and robust estimation of the fundamental matrix is crucial in computer vision.

In this paper, we first add topology constraint in epipolar constraint on feature points' correspondence and realize the control points' auto matching^[5]. Then we imply the algorithm in [6] to achieve the Euclidean reconstruction. The idea underlying the algorithm in [6] is based on the well-known fact that a projective structure can be reconstructed from two views given that the epipolar geometry is known^[3,7]. If the positions of a set of points are known in 3-D Euclidean space, then the projective distortion matrix can be computed to bring the projective structure to a Euclidean one, which eventually allows us to recover the camera projection matrix and Euclidean reconstruction. The two-step Euclidean reconstruction is described as follows:

Step 1: Estimate the fundamental matrix by weighted translation algorithm^[8] using all available information;

Step 2: Recover Euclidean reconstruction from projective reconstruction with a cube phantom calibration.

II. EPIPOLAR GEOMETRY AND POINT CORRESPONDENCE

A. Epipolar geometry and the epipolar constraint

The epipolar geometry of two different perspective views of the same 3D scene is described in Fig. 1, where C_1 and C_2 are two ray sources of the two cameras, I_1 and I_2 are the two image planes obtained by the two cameras, M is arbitrary point in 3D space, m_1 and m_2 are the two projection points of M in two image planes, line C_1C_2 is called base line, M , C_1 and C_2 are coplanar, plane MC_1C_2 is called epipolar plane, the intersect lines L_1 and L_2 of the epipolar plane and the two imaged planes are called epipolar lines. Since m_1 (m_2) belongs to the epipolar plane MC_1C_2 and the image plane I_1 (I_2), m_1 (m_2) must lie on L_1 (L_2), i.e., the correspondence point of m_1 (m_2) lies on the epipolar line L_2 (L_1). This implies that, given a point in one image, one can search the corresponding point in the other along a line and not in a 2D region, thus reducing the correspondence point search significantly.

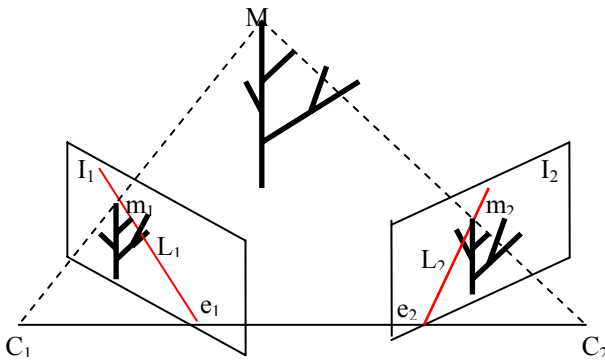


Fig. 1 Epipolar geometry

B. Matching feature points using topology constraint and epipolar constraint

Before reconstructing the structure of the vessel tree, we should first match the feature points such as vessel branches and endpoints in two images and then apply stereo reconstruction algorithm to reconstruct the feature points in the scene. In this paper, we add topology constraint in epipolar constraint on feature points' correspondence and realize the feature points' auto matching.

Matching the feature points using topology constraint is shown in Fig. 2, where the parent nodes P_1 and P_2 are the correspondence pairs. As shown in Fig. 2 (a), if P_1 and P_2 all have only single children nodes C_1 and C_2 , then C_1 and C_2 must be the correspondence pairs. As shown in Fig. 2 (b) and Fig. 2 (c), if C_1 and C_2 all have two children nodes C_{11} , C_{12} and C_{21} , C_{22} , there are two possible cases and should be matched by the epipolar constraint. As shown in Fig. 2 (c), if

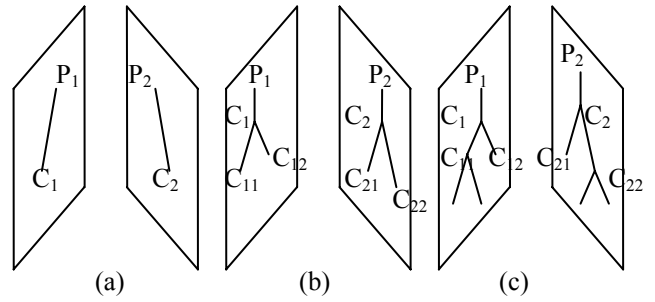


Fig. 2 Matching feature points by topology constraint

the numbers of the children nodes of C_{11} and C_{12} are different, and then we can determine C_{11} , C_{22} and C_{12} , C_{21} are the correspondence pairs by topology constraint.

The algorithm is described as follows:

- Step 1: Auto recognize the root nodes N_0 and N'_0 of the tree-like objects in the two images, record the conjugate points (N_0, N'_0) and denote N_0 , N'_0 as the parent nodes P_1 and P_2 , respectively;
- Step 2: Find the children nodes of P_1 and P_2 , if P_1 and P_2 don't have children nodes then go to step 9;
- Step 3: If the number of the children nodes of P_1 and P_2 is not equal or bigger than 2, then report error in topology structure and go to step 9;
- Step 4: If P_1 and P_2 have only one children node C_1 and C_2 respectively, then record conjugate points (C_1, C_2) and go to step 8;
- Step 5: If P_1 and P_2 all have two children nodes C_{11}, C_{12} and C_{21}, C_{22} respectively, then find the children nodes of C_{11}, C_{12}, C_{21} and C_{22} ;
- Step 6: If the numbers of the children nodes of C_{11} and C_{12} are not equal, then match C_{11}, C_{12}, C_{21} and C_{22} according to the topology constraint, record the conjugate points and go to step 8;
- Step 7: Using the obtained conjugate points to improve the projection matrices and match C_{11}, C_{12}, C_{21} and C_{22} using epipolar constraint, note the new conjugate points;
- Step 8: Denote the new conjugate points as parent nodes P_1 and P_2 , go to step 2;
- Step 9: End.

III. TWO-STEP EUCLIDEAN RECONSTRUCTION

A. Weighted translation algorithm

The weighted translation algorithm introduces the weight of every tied-point into the estimation of the fundamental matrix. Provided that $m = [x \ y \ 1]^T$ and $m' = [x' \ y' \ 1]^T$ denote the homogenous coordinates of the tie-point $m \leftrightarrow m'$, then $m'^T F m = 0$. Since there exist noise and mismatch problem, the value of $m'^T F m$ is often not 0. Therefore we define the residual error

$$r_i = |m'^T F m|$$

and the epipolar distance

$$d_i = \left[\frac{1}{\sqrt{(Fm_i)_1^2 + (Fm_i)_2^2}} + \frac{1}{\sqrt{(F^T m'_i)_1^2 + (F^T m'_i)_2^2}} \right] |m_i'^T F m_i|$$

where $(Fm)_j$ ($j=1,2$) is the j -th component of the vector Fm . Define

$$r_{x_i} = \frac{1}{|m_i'^T F m_i| / |(Fm_i)_1|} \quad \text{and} \quad r_{y_i} = \frac{1}{|m_i'^T F m_i| / |(Fm_i)_2|}.$$

In order to ensure the stability of the algorithm, we choose 10^5 as threshold and

$$r_{x_i} = \begin{cases} r_{x_i}, & r_{x_i} < 10^5, \\ 10^5, & \text{otherwise.} \end{cases}$$

Define the weight as follows (N is the total number of the matched points):

$$w_{x_i} = \frac{r_{x_i}}{\sum_{i=1}^N r_{x_i}} - \frac{1}{N} \quad w_{y_i} = \frac{r_{y_i}}{\sum_{i=1}^N r_{y_i}} - \frac{1}{N}$$

$$w'_{x_i} = \frac{r'_{x_i}}{\sum_{i=1}^N r'_{x_i}} - \frac{1}{N} \quad w'_{y_i} = \frac{r'_{y_i}}{\sum_{i=1}^N r'_{y_i}} - \frac{1}{N}$$

With these definitions, we can estimate the fundamental matrix by the weighted translation algorithm as described as follows:

Step1: Estimate the fundamental matrix by the 8-point algorithm^[9];

Step 2: Compute the weight $w_{x_i}, w_{y_i}, w'_{x_i}$ and w'_{y_i} ;

Step 3: Translate the original center point to (C_{mx}, C_{my}) and (C'_{mx}, C'_{my}) , where (C_{mx}, C_{my}) and (C'_{mx}, C'_{my}) are the central points of the new-ly

$$\text{obtained points } m_{new} = \begin{bmatrix} 1+w_{x_i} & 0 & 0 \\ 0 & 1+w_{y_i} & 0 \\ 0 & 0 & 1 \end{bmatrix} m_i \quad \text{and}$$

$$m'_{new} = \begin{bmatrix} 1+w'_{x_i} & 0 & 0 \\ 0 & 1+w'_{y_i} & 0 \\ 0 & 0 & 1 \end{bmatrix} m'_i;$$

Step 4: Compute the translation matrices T and T' , then normalize the points as: $\tilde{x} = T x$, $\tilde{x}' = T' x'$, where

$$T = T_s T_t = \begin{bmatrix} \frac{1}{C_{mx}} & 0 & 0 \\ 0 & \frac{1}{C_{my}} & 0 \\ 0 & 0 & 1 \end{bmatrix} \begin{bmatrix} 1 & 0 & -C_{mx} \\ 0 & 1 & -C_{my} \\ 0 & 0 & 1 \end{bmatrix}$$

$$T' = T'_s T'_t = \begin{bmatrix} \frac{1}{C'_{mx}} & 0 & 0 \\ 0 & \frac{1}{C'_{my}} & 0 \\ 0 & 0 & 1 \end{bmatrix} \begin{bmatrix} 1 & 0 & -C'_{mx} \\ 0 & 1 & -C'_{my} \\ 0 & 0 & 1 \end{bmatrix};$$

Step 5: Estimate the fundamental matrix using the newly obtained points \tilde{x} and \tilde{x}' by the 8-point algorithm;

Step 6: $F = T'^T \tilde{F} T$.

B. Projective reconstruction

Once we have computed the fundamental matrix between two images, we are able to compute a projective reconstruction of the scene. Let F be the fundamental matrix for the two cameras. There are an infinite number of projective bases which all satisfy the epipolar geometry. One possibility is to factor F as a product of a skew matrix $[e_r]_{\times}$ (e_r is the epipole in the right image) and a matrix M , i.e., $F = [e_r]_{\times} M$.

Here $[e_r]_{\times}$ is the skew matrix such that $[e_r]_{\times} = e_r \times x$ (and \times denotes the cross product)^[10]. A canonical representation can then be used: $P_l = [I \ 0]$ and $P_r = [M \ e_r]$.

The factorization of F into $[e_r]_{\times} M$ is generally not unique, because if M is a solution, then $M + e_r v^T$ is also a solution for any vector v . One way to do the factorization is as follows^[10]. Since $F^T e_r = 0$, the epipole in the second image is given by the eigenvector of matrix FF^T that has the smallest eigenvalue. Using the relation $\|v\|^2 I_3 = vv^T - [v]_{\times}^2$ for all vectors v , we have

$$F = \frac{1}{\|e_r\|^2} (e_r e_r^T - [e_r]_{\times}^2) F = \frac{1}{\|e_r\|^2} e_r e_r^T F + [e_r]_{\times} \left(-\frac{[e_r]_{\times} F}{\|e_r\|^2} \right)$$

The first term on the right hand is equal to 0 because $F^T e_r = 0$. We can thus define the M matrix as

$$M = -\frac{[e_r]_{\times} F}{\|e_r\|^2}$$

This decomposition is used in [11].

Now that the camera projection matrices of the stereo with respect to a projective basis are available, we can reconstruct 3-D structures with respect to that projective basis from point matches. This reconstruction can be done for all matches, but for calibration purposes, we only need to reconstruct those points corresponding to the calibration objects. Given a pair of points in correspondence:

$$m = [u \ v \ 1]^T \text{ and } m' = [u' \ v' \ 1]^T .$$

Let $\tilde{x} = [x \ y \ z \ t]^T$ be the corresponding 3-D point in space with respect to the projective basis. Following the pinhole model, we have

$$s[u \ v \ 1]^T = P[x \ y \ z \ t]^T \tag{1}$$

$$s'[u' \ v' \ 1]^T = P'[x \ y \ z \ t]^T \tag{2}$$

where s and s' are two arbitrary scalars. Denote p_i be the vector corresponding to the i -th row of P , and p'_i be the vector corresponding to the i -th row of P' . The two scalars can then be computed as

$$s = p_3^T \tilde{x} \quad s' = p_3'^T \tilde{x}$$

Eliminating s and s' from Equation (1) and Equation (2) yields the following equation:

$$A\tilde{x} = 0 \tag{3}$$

where A is a 4×4 matrix given by

$$A = [p_1 - up_3 \quad p_2 - vp_3 \quad p'_1 - u'p'_3 \quad p'_2 - v'p'_3]^T .$$

As the projective coordinates \tilde{x} are defined up to a scale factor, we can impose $\|\tilde{x}\| = 1$, and then the solution to Equation (3) is well known to be the eigenvector of matrix $A^T A$ that has the smallest eigenvalue.

C. Euclidean reconstruction

Now we have reconstructed a set of 3-D points $\tilde{x}_i = [x_i \ y_i \ z_i \ t_i]^T$ ($i = 1, 2, \dots, n$) with respect to a projective basis. For each of these points, we know precisely its 3-D coordinates in a Euclidean reference frame, because it belongs to the calibration object. Let the set of 3-D Euclidean be $\tilde{X}_i = [X_i \ Y_i \ Z_i \ 1]^T$ ($i = 1, 2, \dots, n$). The projective points \tilde{x}_i are related to the Euclidean points \tilde{X}_i by a collineation (a 4×4 matrix), which we would like to call the projective distortion matrix D , i.e.,

$$\lambda_i [x_i \ y_i \ z_i \ t_i]^T = D [X_i \ Y_i \ Z_i \ 1]^T$$

or

$$\lambda_i \tilde{x}_i = D \tilde{X}_i \tag{4}$$

where

$$D = \begin{bmatrix} D_{11} & D_{12} & D_{13} & D_{14} \\ D_{21} & D_{22} & D_{23} & D_{24} \\ D_{31} & D_{32} & D_{33} & D_{34} \\ D_{41} & D_{42} & D_{43} & D_{44} \end{bmatrix}$$

and λ_i is an arbitrary scalar, because D is only defined up to a scale factor. From Equation (4), the two vectors \tilde{x}_i and $D\tilde{X}_i$ are related by a scalar. Let $v = D\tilde{X}_i = [v_1, v_2, v_3, v_4]^T$, then we have the following three independent equations:

$$\begin{aligned} x_i v_4 - t_i v_1 &= 0 \\ y_i v_4 - t_i v_2 &= 0 \\ z_i v_4 - t_i v_3 &= 0 \end{aligned} \quad (5)$$

Let $x = [D_{11}, D_{12}, \dots, D_{44}]^T$ be the vector of the 16 parameters of the distortion matrix to be computed. It is easy to show that Equation (5) is equivalent to the following equation:

$$B_i x = 0 \quad (6)$$

where

$$B_i = \begin{bmatrix} -t_i \tilde{X}_i & 0 & 0 & x_i \tilde{X}_i \\ 0 & -t_i \tilde{X}_i & 0 & y_i \tilde{X}_i \\ 0 & 0 & -t_i \tilde{X}_i & z_i \tilde{X}_i \end{bmatrix}$$

Given n correspondences $(\tilde{X}_i, \tilde{x}_i)$, we have n equations of the type of Equation (6). The problem is then to estimate x by minimizing the following error function:

$$F = \sum_{i=1}^n (B_i x)^2 = x^T \left(\sum_{i=1}^n B_i^T B_i \right) x \quad (7)$$

Let $B = \sum_{i=1}^n B_i^T B_i$, which is a symmetric matrix. As D is only defined up to a scale factor, we can normalize x with $\|x\| = 1$. It is well known that the solution to Equation (7) is the eigenvector of B corresponding to the smallest eigenvalue of B .

Let the Euclidean camera projection matrices be M and M' . Following the pinhole model, we have

$$\begin{aligned} s[u \ v \ 1]^T &= M[X \ Y \ Z \ 1]^T \\ s'[u' \ v' \ 1]^T &= M'[X \ Y \ Z \ 1]^T \end{aligned}$$

Compare the above equations with Equation (1) and Equation (2), we have at once the Euclidean camera projection matrices given by

$$\begin{aligned} M &= PD \\ M' &= P'D \end{aligned}$$

Now we can reconstruct \tilde{X} in Euclidean space using the Euclidean camera projection matrices M and M' .

IV. SIMULATION AND EXPERIMENT

A. Simulation

In simulation experiment, the distance of the ray source and the detector plane is 80 cm, the rotation radius is 50 cm, the real size of the detector plane is $40 \times 40 \text{ cm}^2$, the size of the projection image is 128×128 in pixels. Figs. 3 (a) and (b) are the two projection images of the simulation tree in two different views; Fig. 4 is the reconstructed simulate tree; Figs. 5 (a) and (b) are the reprojection images of the reconstructed tree of the same views in Figs. 3; Table 1 collects the calculated values of the fundamental matrix F , the two projection matrices P_1 and P_2 in projective space, the projective distortion matrix D and the two projection matrices M_1 and M_2 in Euclidean space.

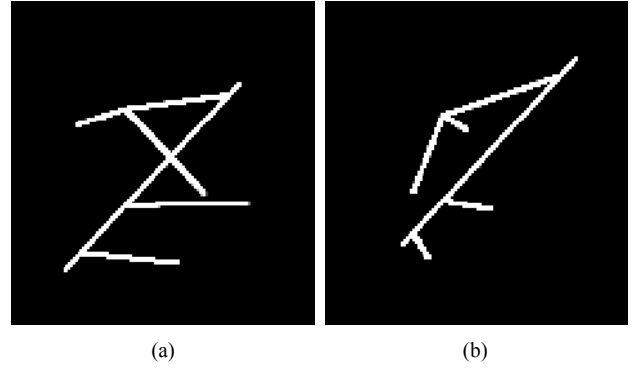


Fig. 3 Two projection images of the simulate tree in two different views

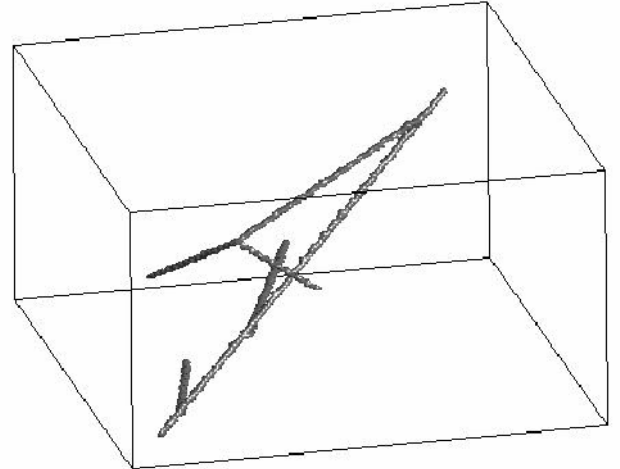


Fig. 4 Reconstructed simulate tree model

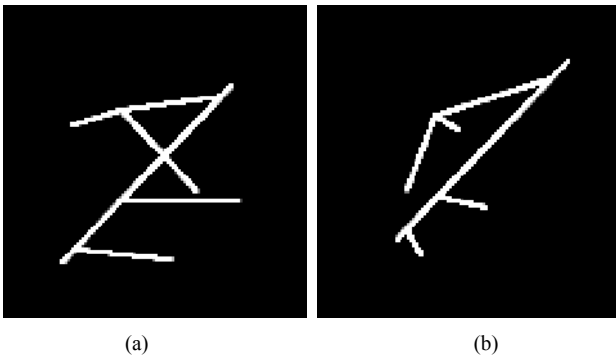


Fig. 5 Reprojection images of the reconstructed tree of the same views in Figure 3

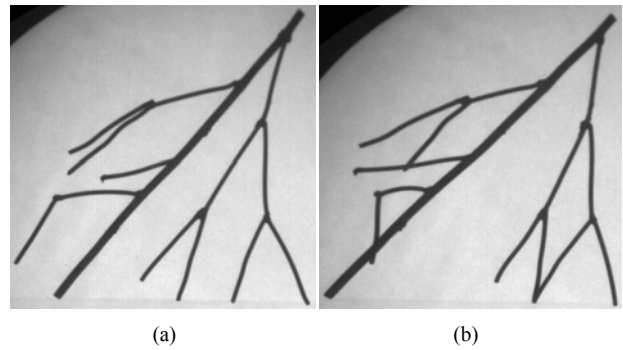


Fig. 6 Projection images of the wire tree in two different views

Table 1 Values of F, P₁, P₂, D, M₁ and M₂ in simulation

$F = \begin{bmatrix} -0.0000 & -0.0001 & 0.0055 \\ -0.0001 & 0.0000 & -0.0170 \\ 0.0055 & 0.0267 & -0.6822 \end{bmatrix}$
$P_1 = \begin{bmatrix} 1 & 0 & 0 & 0 \\ 0 & 1 & 0 & 0 \\ 0 & 0 & 1 & 0 \end{bmatrix}$
$P_2 = \begin{bmatrix} 0.0011 & 0.0052 & -0.13176 & 0.9812 \\ -0.0054 & -0.0262 & 0.6693 & 0.1931 \\ -0.0001 & 0.0000 & -0.0177 & 0.0030 \end{bmatrix}$
$D = \begin{bmatrix} 0.0136 & -0.0557 & 0.0000 & -0.7018 \\ 0.0138 & 0.0000 & 0.0551 & -0.7073 \\ 0.0002 & 0.0000 & 0.0000 & -0.0109 \\ 0.0015 & 0.0005 & -0.0002 & 0.0230 \end{bmatrix}$
$M_1 = \begin{bmatrix} 0.0136 & -0.0557 & 0.0000 & -0.7018 \\ 0.0138 & 0.0000 & 0.0551 & -0.7073 \\ 0.0002 & 0.0000 & 0.0000 & -0.0109 \end{bmatrix}$
$M_2 = \begin{bmatrix} 0.0016 & 0.0004 & 0.0000 & 0.0196 \\ 0.0000 & 0.0004 & -0.0015 & 0.0195 \\ 0.0000 & 0.0000 & 0.0000 & 0.0003 \end{bmatrix}$

B. Tree phantom experiment

For tree phantom experiment on rotational C-arm angiography system, we have made a calibration cube with cubic length 6cm and a wire tree. Fig. 6 (a) and (b) are the two projection images of the wire tree obtained from the C-arm angiography system at different scan angles; Figs. 7

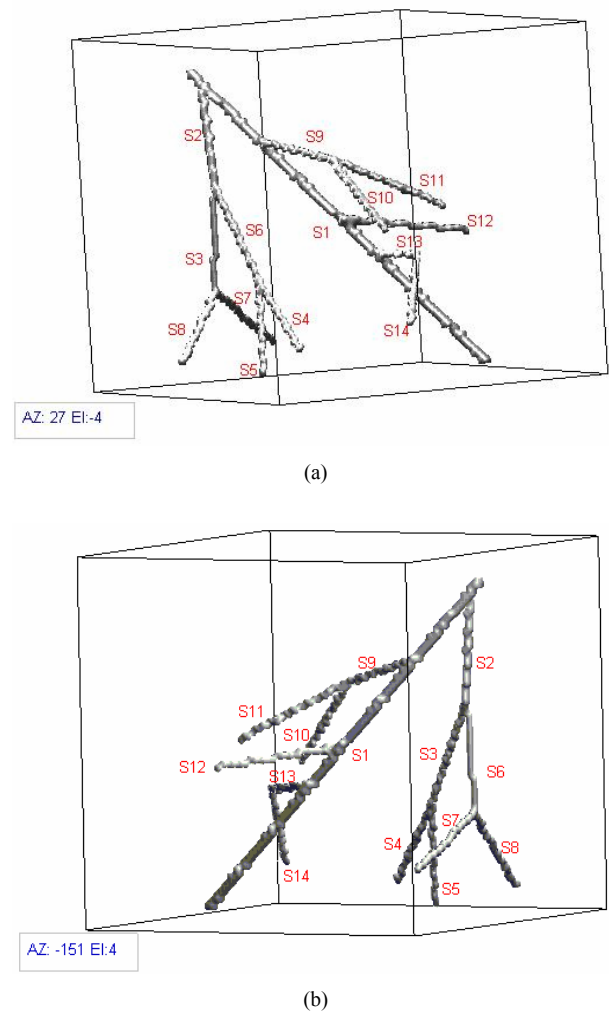


Fig. 7 Reconstructed wire tree shown in two different views

(a) and (b) are the reconstructed wire tree shown in two different views; Table 2 collects the calculated values of the fundamental matrix F, the two projection matrices P₁ and P₂

in projective space, the projective distortion matrix D and the two projection matrices M_1 and M_2 in Euclidean space of the wire tree model experiment; Table 3 provides the comparisons of the truth (by physical measurement) and calculation (by stereo-reconstruction) of the wire tree.

Table 2 Values of F , P_1 , P_2 , D , M_1 and M_2 in tree phantom experiment

$$F = \begin{bmatrix} -0.0000 & 0.0000 & -0.0000 \\ 0.0000 & -0.0000 & -0.0007 \\ -0.0000 & 0.0006 & 0.0204 \end{bmatrix}$$

$$P_1 = \begin{bmatrix} 1 & 0 & 0 & 0 \\ 0 & 1 & 0 & 0 \\ 0 & 0 & 1 & 0 \end{bmatrix}$$

$$P_2 = \begin{bmatrix} -0.0000 & 0.0000 & 0.0001 & -1.0000 \\ -0.0000 & 0.0006 & 0.0204 & 0.0064 \\ -0.0000 & 0.0000 & 0.0007 & 0.0000 \end{bmatrix}$$

$$D = \begin{bmatrix} -0.0275 & -0.0908 & 0.0018 & 0.7900 \\ 0.0072 & -0.0065 & -0.0946 & 0.5982 \\ 0.0000 & -0.0000 & 0.0000 & 0.0016 \\ -0.0000 & 0.0001 & 0.0000 & -0.0005 \end{bmatrix}$$

$$M_1 = \begin{bmatrix} -0.0275 & -0.0908 & 0.0018 & 0.7900 \\ 0.0072 & -0.0065 & -0.0946 & 0.5982 \\ 0.0000 & -0.0000 & 0.0000 & 0.0016 \end{bmatrix}$$

$$M_2 = \begin{bmatrix} 0.0187 & -0.0547 & -0.0006 & 0.5135 \\ 0.0059 & 0.0002 & -0.0600 & 0.3722 \\ 0.0000 & -0.0000 & 0.0000 & 0.0010 \end{bmatrix} \times 10^{-3}$$

Table 3 Comparisons of the truth and calculation of the wire tree phantom (units: cm)

	Real size	Reconstructed size	Error
S_1	11.25	11.2521	0.0021
S_2	2.65	2.6877	0.0377
S_3	3.20	3.1626	0.0374
S_4	2.73	2.7399	0.0099
S_5	2.75	2.7267	0.0233
S_6	2.75	2.7708	0.0208
S_7	3.15	3.1552	0.0052
S_8	3.15	3.1657	0.0157
S_9	2.55	2.5377	0.0123
S_{10}	3.10	3.1069	0.0069
S_{11}	3.30	3.3429	0.0429
S_{12}	3.00	2.9940	0.0060
S_{13}	2.75	2.7777	0.0277
S_{14}	2.80	2.7770	0.0230

V. CONCLUSION

In this paper, we address the problem of the reconstruction of the tree-like objects from C-arm angiography system by two-view stereo reconstruction. We first add topology constraint in epipolar constraint on feature points' correspondence and realize the control points' auto matching. Then we estimate precisely the epipolar geometry which is valid for a wide range in space from all available matches, thereby conduct a projective reconstruction. Finally, using the priori knowledge of the calibration cube, we are able to achieve Euclidean reconstruction. Simulation and the tree phantom experiment on rotational C-arm angiography system justify the method in this paper. The rotational C-arm scanning produces a sequence of cone-beam projections as distinguished by view angles. Any two projection images can be considered as a two-view pair. But some feature points are identifiable in some projection images while indistinguishable in other projection images (due to projection superimposition), which makes the reconstruction results different when choose different image pairs. Moreover, the angle between the two images has great impact on the numeral stability of the reconstruction result. These problems deserve further investigations.

ACKNOWLEDGMENT

This work was in part supported by Chinese National Science Foundation (Funding Project number: 30770591).

REFERENCES

1. Faugeras, O. Three-Dimensional Computer Vision: A Geometric Viewpoint, Cambridge, MA: MIT Press, 1993.
2. Deriche, R., Zhang, Z., Luong, Q.T., et al. Robust recovery of the epipolar geometry for an uncalibrated stereo rig. In: Eklundh, O.J., ed. Proceedings of the 3rd European Conference on Computer Vision. Vols. 800-801 of the Lecture in Computer Science. Stockholm: Springer-Verlag, 1994. 567-576.
3. Faugeras, O. What can be seen in three dimensions with an uncalibrated stereo rig? In: Sandini, G., ed. Proceedings of the 2nd European Conference on Computer Vision. Vol.558 of Lecture Notes in Computer Science. Santa Margherita Ligure: Springer-Verlag, 1992. 563-578.
4. Quan, Long, Kanade, Takeo. Affine structure from line corresponding with uncalibrated affine cameras. IEEE Transactions on Pattern Analysis and Machine Intelligence, 1997,19(8):834-845.
5. 黄家祥, 郁道银, 孙正, 谢洪波, 陈晓冬, 冠脉树三维重建中血管段的匹配. 光电子·激光, 2003, 14(10):113-117
6. Zhengyou Zhang, Olivier Faugeras, Rachid Deriche. An effective technique for calibrating a binocular stereo through projective reconstruction using both a calibration object and the environment. VIDERER1:1, pp58-68,1977.

7. Richard Hartley, Rajiv Gupta, & Tom Chang. Stereo from uncalibrated cameras. In Proceedings of the International Conference on Computer Vision and Pattern Recognition, pages 761–764, Urbana Champaign, IL, June 1992. IEEE.
8. 陈泽志,吴成柯.一种高精度估计的基础矩阵的线性算法[J]. 软件学报, 2002, 13(4): 840-845
9. LONGUET-HIGGINSH C. A computer algorithm for reconstructing a scene form two projections[J]. Nature, 1981(10), 293: 133-135.
10. Q.-T. Luong & T. Vi'eville. Canonic representations for the geometries of multiple projective views. In J-O. Eklundh, editor, Proceedings of the 3rd European Conference on Computer Vision, volume 1 of Lecture Notes in Computer Science, pages 589–599, Stockholm, Sweden, May 1994. Springer-Verlag.
11. Paul Beardsley, Andrew Zisserman, & David Murray. Navigation using affine structure from motion. In J-O. Eklundh, editor, Proceedings of the 3rd European Conference on Computer Vision, volume 2 of Lecture Notes in Computer Science, pages 85–96, Stockholm, Sweden, May 1994. Springer-Verlag.

Implementation of Convolution/Superposition Model of Photon Dose Calculation

Jiandong Li^{1,2}, Tie Zhang²

¹ School of Information Science & Engineering, Northeastern University, Shenyang, China

² Radiotherapy Product Department, Neusoft Medical System Co., Ltd., Shenyang, China

Abstract — The implementation, accuracy and performance of a collapsed cone convolution/superposition dose calculation algorithms is presented. The primary fluence or TERMA (total energy released per unit mass) is calculated using a polyenergetic spectrum which is modified with depth to account for water effective depth hardening and with off axis position to account for softening of the beam. An Inverse square law correction for kernel tilting is applied at the dose deposition site. The algorithm uses energy deposited kernels generated by use of EGSnrc Monte Carlo Code. In addition, this work also reports on some of the initial test that was conducted during the commissioning of a commercially available 3D treatment planning system. And the algorithm was verified by using AAPM phantom data with open, unwedged, and tilting fields for both symmetric and asymmetric collimator settings with variant energy (4MV, 18MV). Also measured data from variant linac and practical clinical data are used for verifying applicability and feasibility of the algorithm. Results presented in this paper show good agreement between measured data and calculated results in homogeneous and homogeneous media for different fields, and demonstrate the correct behaviour of collapsed cone convolution/superposition dose calculation algorithms.

Keywords — TPS, photon beam, dose calculation, convolution/superposition, EGSnrc

I. INTRODUCTION

Radiotherapy using high x-ray is an important modality on clinic. The goal of accurate dose calculation is delivering a prescribed dose to a target volume while minimizing radiation damage to the surrounding healthy tissue. Three dimensional dose calculations for radiation therapy using convolution/superposition algorithms have been investigated by many researchers [1, 2], and been applied to many commercial treatment planning systems [3, 4].

In this paper, implementation, accuracy and performance of a collapsed cone convolution/superposition dose calculation algorithms is presented. The basic theory of the model was discussed. Calculated and measured dose in homogeneous and inhomogeneous media were compared for wedged and unwedged fields. Results using AAPM test package and practical data show agreement of 2% or 3mm in most case. These tests demonstrate the correct behaviour of the collapsed cone implementation of the algorithm.

II. MATERIALS AND METHODS

The dose equation for monoenergetic irradiation of a homogeneous phantom with a parallel beam is given by [5, 6]:

$$D(\vec{r}) = \int_V T(\vec{r}') A(\vec{r} - \vec{r}') d^3\vec{r}' \quad (1)$$

Where $T(\vec{r}')$ is TERMA describing total energy released per mass of primary photon in the volume element $d^3\vec{r}'$ and $A(\vec{r} - \vec{r}')$ is energy deposit kernel generated in water. The kernels are generated by use of EGSnrc Monte Carlo code. The geometry of the basic theory of convolution is given in Figure 1.

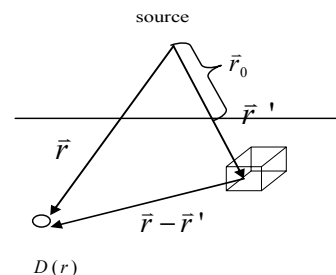


Fig. 1 The geometry of the basic theory of convolution

The dose equation (1) is exactly valid for an arbitrary distribution of the fluence to monoenergetic photons incident in a parallel beam on an infinite medium (a highly idealized situation).

For polyenergetic beam sources in inhomogeneous media which is true clinic condition, the dose is calculated through [6, 7]:

$$D(\vec{r}) = e^{\mu_d} \int_0^{E_{\max}} \int_V T_E(\vec{r}') dE \frac{\rho(\vec{r}')}{\rho_0} c^2(\vec{r}, \vec{r}') \bar{A}(c(\vec{r}, r') \bullet (\vec{r} - \vec{r}')) d^3\vec{r}' \quad (2)$$

Where energy spectrum includes all energy range from 0 to E_{\max} , $T_E(\vec{r}')$ is differential in energy of photon. For each monoenergetic, and $T_E(\vec{r}')$ is given by

$$T_E(\vec{r}) = \left(\frac{\vec{r}_0}{\vec{r}}\right)^2 \left(\frac{\mu}{\rho}\right)_E E\Phi_{0E} \exp\left(-\left(\frac{\mu}{\rho}\right)_E \int_0^{\vec{r}} \rho(\vec{r}') d\vec{r}'\right) \quad (3)$$

Where E is the energy of photons, $(\mu/\rho)_E$ is the mass attenuation coefficient of the primary photons of energy E in water, Φ_{0E} is the energy fluence, differential in energy, of primary photons at \vec{r}' . $\int_0^{\vec{r}} \rho(\vec{r}') d\vec{r}'$ is calculated by performing a ray trace method [8]. \vec{r}_0 is the distance between photon beam source and surface along \vec{r}' path (see Figure 1).

In equation (2), $e^{\mu_{cd}}$ is hardening correction factor. $(\vec{r}_0/\vec{r})^2$ is inverse square law correction for kernel tilting

In equation (2), $\bar{A}(\vec{r} - \vec{r}')$ is the polyenergetic dose-spread kernel, averaged over the local spectrum of the beam and weighted with TERMA at reference \vec{r}_{ref} (usually central axis at surface of phantom). The photon spectrum is represented by a set of relative photon fluence values. We generated energy deposited kernels by use of EGSnrc Monte Carlo Code. EGSnrc Monte Carlo Code, developed by Mackie *et al* [9], is an improved version of EGS4. The kernels are stored in files. Spectra used in the algorithms are from published spectra by Mohan *et al* [10]. Specifically, for reducing running time of the algorithm, we used fewer spectrums than Mohan's. The relative spectral weights are variables that can be modified by the physicist to fit calculations to measured dose distributions. The photon spectrum is assumed to soften with its transverse distance from the central axis of the beam. The off-axis softening parameter can be modified by the user in fitting the measured dose distributions. The factor $c(\vec{r}, \vec{r}')$ is the spatially dependent scaling factor which calculates the mean density along the line from interaction site to the dose deposition site.

III. RESULTS

AAPM Task Group 23(TG-23) has developed a test package for verification of the accuracy of treatment planning systems for clinical photon external beam therapy [11]. The package includes measured fundamental beam data for 4MV and 18MV x rays, and test cases with measured dose values at selected points, which serve as the reference for determination of calculated dose accuracy. In this paper, we used the TG-23 package to evaluate the accuracy of the algorithms. Comparisons were made between computed and

measured dose values for each of the test cases. The accuracy criterion of dose calculation is determined with standard error:

$$STD = \sqrt{\sum_i^N (x_i - x'_i)^2 / (N - 1)} \quad (4)$$

Where N is the number of test points. x_i is calculated value and x'_i is measured value.

Table 1 and 2 enumerate test cases, test results, respectively. Table 3 is a summary of test results. In Table 1, No.1-6 and No 11-16 are open field; No.7 and 17 are wedge field; No.8 and 18 are off-central plane; No.9 and 21 are irregular field; No.10 is oblique case; No.19 is lung inhomogeneous; No.20 is bone inhomogeneous.

Table 1 Dosimetric test cases proposed by TG-23

No.	Energy(MV)	Field(cm)	SSD(cm)	Depth(cm)	Off axis(cm)
1	4	5×5	80	1,3,5,10,15, 20,25,35	0,±1,±5
2	4	10×10	80	1,3,5,10,15, 20,25	0,±3,±9
3	4	25×25	80	1,3,5,10,15, 20,25,35	0,-9,-19
4	4	5×25	80	1,3,5,10,20, 25,35	0,±1,±5
5	4	25×5	80	1,3,5,10,15, 20,25,35	0,-9,-19
6	4	10×10	70	1,5,9,13,17, 21,25,33	0,±2.5,±7
7	4	9×9	80	1,3,5,10,15, 20,25,35	±2.5
8	4	10×10	80	1,3,5,10,15, 20,25,35	0,±3,±8
9	4	16×16	80	1,3,5,10,15, 20,25,35	0,-6
10	4	10×10	80	1,3,5,10,15, 20	0,±3
11	18	5×5	100	3,5,10,15,2 0,25,35	0,±1,±5

12	18	10×10	100	3,5,10,15,2 0,25,35	0,±3,±9	7	0.786	8	1.298	8	0.841	8	0.271	16
13	18	25×25	100	3,5,10,15,2 0,25,35	0,±9,-19	8	1.213	8	0.496	16	1.123	16	0.235	16
14	18	5×25	100	3,5,10,15,2 0,25,35	0,±1,±5	9	0.894	8	0.534	8	—	—	—	—
15	18	25×5	100	3,5,10,15,2 0,25,35	0,±9,-19	10	0.741	6	1.249	12	—	—	—	—
16	18	10×10	85	3,5,10,15,2 0,25,35	0,±2.5,±7	11	0.765	7	0.754	14	0.667	14	0.126	14
17	18	9×9	100	3,5,10,15,2 0,25,35	±2.5	12	0.829	7	0.879	14	0.674	14	-0.155	14
18	18	10×10	100	3,5,10,15,2 0,25,35	0,±3,±8	13	0.835	7	0.614	14	1.057	7	0.201	7
19	18	16×16	100	11,11.5,12, 15,20,25,35	0,±2,±5	14	0.755	7	0.804	14	0.347	14	0.106	14
20	18	16×16	100	7.5,8,10,15, 20,25,35	0,±4	15	0.815	7	0.664	14	0.897	7	0.124	7
21	18	16×16	100	3.01,5.01,1 0.01,15.01, 20.01,25	0,-6	16	0.743	7	0.445	14	0.456	14	-0.256	14
						17	0.837	7	0.926	7	1.046	7	0.175	14
						18	1.108	7	1.136	14	0.459	14	0.163	14
						19	0.695	7	0.925	28	—	—	-0.169	14
						20	0.921	7	0.864	14	—	—	0.109	14
						21	1.452	6	0.755	6	—	—	—	—

Table 2 Dosimetric test results

No.	Central Axis		In beam		Out beam		Rad. width(cm)	
	Error (%)	Point	Error (%)	Point	Error (%)	Point	Error (%)	Point
1	0.297	8	0.520	16	0.118	16	0.101	16
2	0.227	7	0.664	14	0.384	14	0.058	14
3	0.793	8	1.455	8	0.693	8	0.179	8
4	0.591	7	1.033	14	0.699	14	-0.294	14
5	0.565	8	1.293	8	1.829	8	0.107	8
6	0.356	8	0.763	16	0.379	16	0.264	16

Table 3 Summary of dosimetric test results

No.	Description	Cen-axis	In beam	Out beam	Rad. width
1	open field	0.835	1.455	1.057	0.201
2	4MV 25×5	0.591	1.293	1.829	-0.294
	18MV 25×5	0.815	0.804	0.897	0.124
3	4MV, Irreg. field	0.894	0.534		

	18MV, irregular field	1.452	0.755		
4	4 MV, oblique	0.741	1.249		
5	18MV, bone and lung	0.921	0.925	-0.1693	
6	18MV, off-cen plane	1.213	1.136	1.123	0.235
7	wedge field	0.837			0.271
8	Variant SSD	0.743	0.763	0.456	0.264

Dose calculations using variant spectra in homogeneous water phantom for both Varian accelerator and Primus accelerator were performed. Percent depth dose(PDD) curves and transverse profiles were measured using water phantom for the fields of $3 \times 3 \text{cm}^2$, $10 \times 10 \text{cm}^2$, $15 \times 15 \text{cm}^2$, $20 \times 20 \text{cm}^2$, and $40 \times 40 \text{cm}^2$.

Figure 2-6 display the calculated and measured depth dose curves and transverse profiles of 6 MV beams. Figure 2-4 are the Varian 600C accelerator. Figure 5-6 are the Primus accelerator.

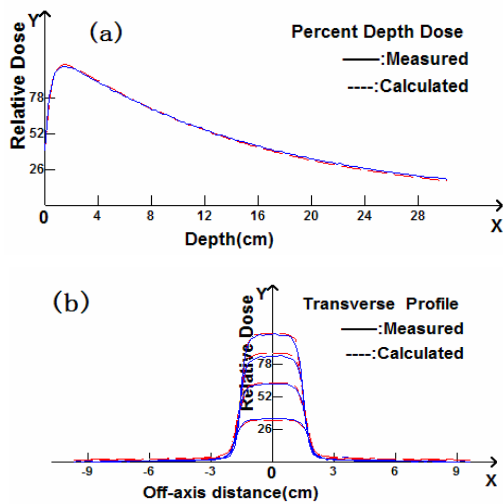


Fig. 2 $3 \times 3 \text{cm}^2$ (a) Percent depth dose curves. (b) Transverse profiles, from the top down, depth are 1.4, 5.0, 10.0 and 20.0cm, respectively.

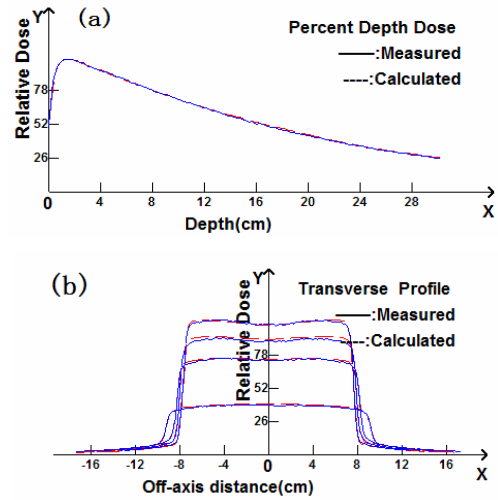


Fig. 3 $15 \times 15 \text{cm}^2$ (a) Percent depth dose curves. (b) Transverse profiles, from the top down, depth are 1.4, 5.0, 9.18 and 21.98cm, respectively.

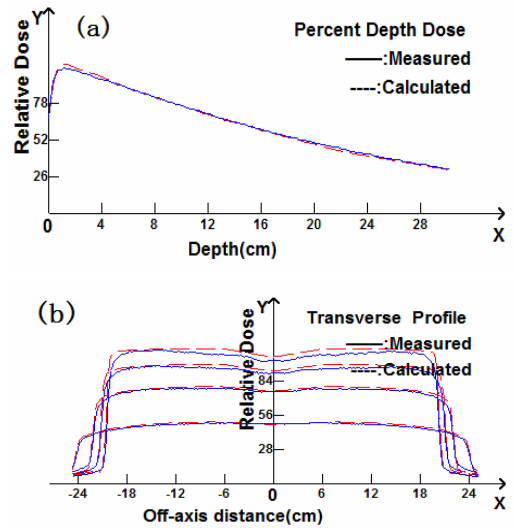


Fig. 4 $40 \times 40 \text{cm}^2$ (a) Percent depth dose curves. (b) Transverse profiles, from the top down, depth are 1.4, 5.0, 10.0 and 20.0cm, respectively.

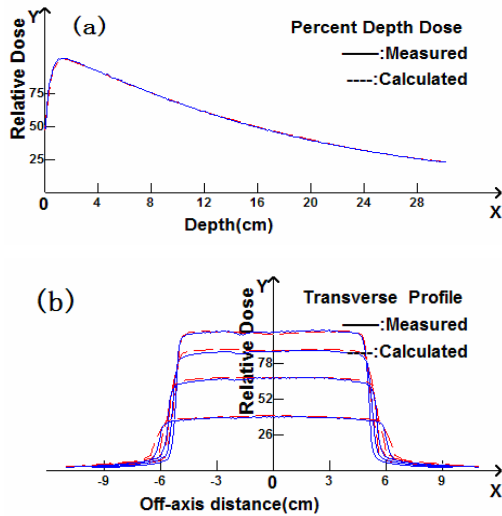


Fig. 5 $10 \times 10 \text{cm}^2$ (a) Percent depth dose curves. (b) Transverse profiles, from the top down, depth are 1.5, 5.0, 10.0 and 20.0cm, respectively.

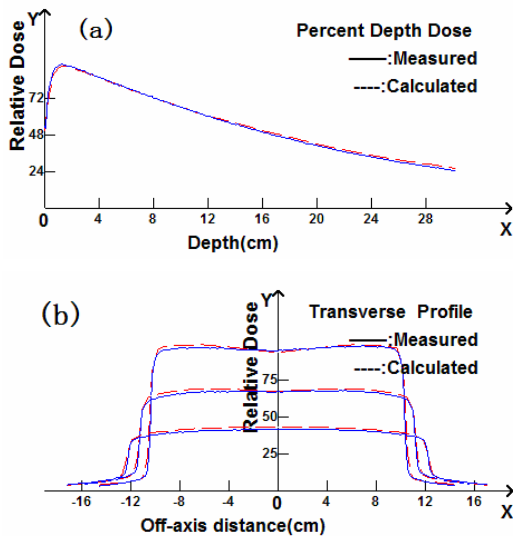


Fig. 6 $20 \times 20 \text{cm}^2$ (a) Percent depth dose curves. (b) Transverse profiles, from the top down, depth are 1.5, 5.0, 10.0 and 20.0cm, respectively.

I. CONCLUSIONS

Results presented in this paper show good agreement between measured dose and calculated dose for different fields. However, spectra are dependent on different linac. For a given linac, an independent adjustment is needed, which will add difficulties to users and vendor. It is the future work how to tune automatically spectra according to measured data.

REFERENCES

1. Mackie T R, Scrimger J W, Battista J J (1985), A convolution method of calculating dose for 15-MV x rays. *Med. Phys.* 12(2):188-196
2. Papanikolaou N, Mackie T R, Carol M E et al. (1993) Investigation of the convolution method for polyenergetic spectra. *Med. Phys.* 20(5):1327-1336
3. Miften M, Wiesmeyer M, Monthofer S et al. (2000) Implementation of FFT convolution and multigrid superposition models in the FOCUS RTP system. *Phys. Med. Biol.* 45(4):817-833
4. Lydon J M (1998) Photon dose calculations in homogeneous media for a treatment planning system using a collapsed cone superposition convolution algorithm. *Phys. Med. Biol.* 43(6):1813-1822
5. Aspradakis M M, Redpath A T (1997) A Technique for the fast calculation of three-dimensional photon dose distributions using the superposition model. *Phys. Med. Biol.* 42(8):1475-1489
6. Ahnesjö A, Aspradakis M M (1999) Dose calculations for external photon beams in radiotherapy. *Phys. Med. Biol.* 44(11):R99-R155
7. Hoban P W (1995) Accounting for the variation in collision kerma-to-terma ratio in polyenergetic photon beam convolution. *Med. Phys.* 22(12): 2035-2044
8. Siddon R L (1985) Fast calculation of the exact radiological path for a three-dimensional CT array. *Med. Phys.* 12(2):252-25
9. Mackie T R, Bielajew A F, Rogers D W et al. (1988) Generation of photon energy deposition kernels using the EGS Monte Carlo code. *Phys. Med. Biol.* 33(1):1-20
10. Mohan R, Chui C (1985) Energy and angular distributions of photons from medical linear accelerators. *Med. Phys.* 12(5):592-597
11. Radiation treatment planning dosimetry verification: A test package prepared by task group 23 of the American Association of Physicists in Medicine at <http://www.aapm.org>

Author: Li Jiandong
 Institute: School of Information Science & Engineering
 Street: No.11, Lane 3, WenHua Road
 City: Shenyang
 Country: China
 Email: Jiandong.Jackson.Li@gmail.com

Author: Zhang Tie
 Institute: School of Information Science & Engineering
 Street: No.11, Lane 3, WenHua Road
 City: Shenyang
 Country: China
 Email: ztmath@163.com

Quality assurance of helical tomotherapy intensity modulated radiation therapy

Shouping Xu¹, Xiaowu Deng², Xiangkun Dai¹, Lianyuan Wang¹, Yunlai Wang¹, Chuanbin Xie¹,
Ruigang Ge¹, Hanshun Gong¹

¹ Department of Radiation Oncology, PLA General Hospital, Beijing 100853, China

² Department of Radiation Oncology, Cancer Center of Sun Yat-sen University, Guangzhou 510060, China

Abstract — Helical tomotherapy, like helical CT, has the fan beam continuously rotating around the patient as the couch is transporting the patient longitudinally through the ring gantry. The approach requires synchrony of gantry rotation, couch translation, accelerator pulsing and the opening and closing of the leaves of the binary multileaf collimator used to modulate the radiation beam. In the course of clinically implementing helical tomotherapy intensity modulated radiation therapy, we have developed a quality assurance (QA) system for patient treated with intensity modulated radiation therapy (IMRT) of helical tomotherapy. We describe the procedure developed in the Radiation Oncology Department of PLA General Hospital, and present the verification results of 84 patients. This procedure is composed of two kinds of measurements that are the absolute dose at the reference point of target volume with an ionization chamber of small sensitive volume, the relative dose distribution in a transverse plane with film. Here the method and results of IMRT are summarized and the QA system is set out along with the experimental details of its implementation. The systematic error is discussed during the phantom setup.

Keywords — Helical tomotherapy, IMRT, dose verification, quality assurance.

I. INTRODUCTION

Currently conformal fields are delivered for most IMRT treatment with multileaf collimator of conventional linear accelerator (Linac). Helical tomotherapy is the delivery of IMRT with a continuously rotating CT-like ring gantry simultaneously with the translation of the patient through the bore of the gantry. The Tomotherapy Hi-ArtTM unit has been designed for image-guided intensity-modulated radiotherapy (IMRT) [1,2]. The system is ideal for conformal avoidance of the delivery of dose to sensitive normal tissue. The IMRT is delivered with a binary collimator, which is composed of sixty four 6.5 mm wide leaves opening and closing independently. The primary collimator or jaws can be set at different widths, ranging from 0.5 cm to 5 cm, to form a variety of desirable treatment field lengths. The motorized treatment couch is synchronized with the gantry and the collimator to move at the correct speed, based on the planned pitch ratio, to perform a helical IMRT. The dose

calculation algorithm is convolution/superposition (C/S) based. This requires that the energy fluence magnitude and spectrum be quantified. This is common for many commercially available radiotherapy systems. Helical tomotherapy constantly superimposes a rectangular beam that is up to 40 cm wide in the transverse direction and up to 5 cm wide in the longitudinal direction. The beam superimposition is along the longitudinal direction of the patient [4,5]. (This is the direction of couch travel.) This mandates that the dose calculation be extremely accurate in this direction as small errors in the longitudinal dose profile quickly add to significant amounts. So it is necessary that Tomotherapy planning system can accurately calculate the dose, more important that helical tomotherapy IMRT QA system need to be achieved for the patient before delivery. According to the technical complexity of tomotherapy, clinical physicist should not only simulate the patient setup, but also verify the dose of tomotherapy patient planning [5,6].

II. MATERIALS AND METHODS

One ion chamber and one film type were used for all measurements. The Standard Imaging A1SL ion chamber and multiple channels TomoElectronmeter were used (Middleton, WI, USA). The collector lengths and collecting volumes were 4.0 mm long and 0.056 cm³ wide. Kodak EDR2 film was used (Rochester, NY, USA). The Vidar Pro Advantage film digitizer (Herndon, VA, USA) digitized the films. Separate calibration exposures were used to convert the optical density values to dose values.

A. The optimization of Tomotherapy IMRT planning

First, the patient images were collected from the Philips CT-Sim machine, then were sent to the Pinnacle AcQSim or CMS FocalSim workstation to contour the target and normal tissue structures. Secondly, Patient CT data and structure sets were transferred to the planning station using DICOM protocol. The red moveable laser in the planning was adjusted to align with the three marks on the patient surface so that the reference coordinate was set in the

planning. Similar to the objective function setting of the conventional IMRT planning, the choice of some new delivery parameters particular to helical tomotherapy, field width, pitch and modulation factor(MF), start to calculate the planning process^[1,7]. The planning process is based on a superposition/convolution dose calculation engine^[8] and an iterative least square optimization process^[9]. If the plan is then accepted by physician, it can be saved to the Cluster server. After verification, it would be delivered at that time.

B. Dose verification

Dose verification mainly includes two kinds of measurement that are the absolute dose and the relative dose. Of course, the absolute and relative dose refer to the point of target volume with an ionization chamber of small sensitive volume^[10] and the relative dose distribution in a transverse plane, respectively. The doses and isodose curves measured by the chamber and the film were consistent with those predicted by the planning.

1. The Virtual Water phantom

A series of measurements was recorded in a specially fabricated cylindrically symmetric Virtual Water phantom (Med-Cal,USA). The phantom is 30 cm in diameter and 18 cm long. The phantom is divided into two halves such that film may be placed between them. Additionally, a row of ion chamber holes was drilled in the phantom along a radial line perpendicular to the film plane. This allows for subsequent verification of film measurement by rotating the phantom 90°. The holes are separated 1 cm away from each other, starting 5 mm from the center of the phantom. Virtual

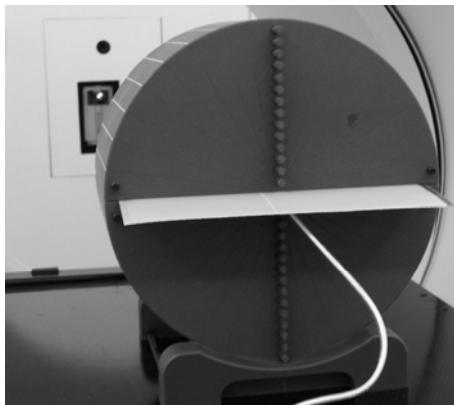


Fig. 1 This is a picture of the cylindrical Virtual Water phantom used to measure the Helical tomotherapy IMRT planning. The rectangular sheet extending between the two halves shows the EDR2 film in place. An ion chamber is shown 5mm below the film.

Water sticks are inserted into holes that do not hold ion chambers. This phantom is illustrated in Fig. 1. This phantom was placed on a specially designed base. This allowed sufficient support with minimum attenuating material. Therefore, the center of the phantom had almost the same radiological path at all gantry angles.

2. Delivery Quality Assurance (DQA) planning

After setting up on the CT-Sim couch, the phantom will be scanned according to the same condition as patient's set-up, such as slice thickness and KV value. Then the images of the phantom were sent to the tomotherapy planning system, and used for the verification images. In order to verify the accuracy of the dose, it was very important that there should be the same thickness of CT slices between the patient and phantoms images in the DQA planning. First, the dependent curve of the HU value vs physical density was selected. Following the removal of the CT-Sim couch, Tomotherapy fiber couch should be added. Secondly, the position of the phantom was selected to make sure that the measuring point should be kept in the area of the low dose gradient as soon as possible. Finally, after adjusting the movable laser to the phantom, the dose distribution would be calculated. Of course, currently the fraction dose of the phantom planning should be kept the same as the dose of the patient delivery per fraction.

3. The measuring process

The DQA planning is loaded from the Cluster server. The set-up of the phantom is illustrated in Fig.1. EDR2 film was placed between the phantom halves. The chamber was placed at the most central ion chamber position, 0.5 cm below the isocenter. The set-up offsets of the phantom can be determined on a daily basis by registering the verification CT acquired at the time of the planning CT. So the set-up of the cylindrical phantom was guided for verifying the position. Eventually, the beam was delivered to the phantom.

4. Data processing

Following the verification of 84 tomotherapy IMRT patients planning, the systematic offset of the phantom set-up would be gotten. According to the measuring data, the dose error of the chamber reference point was required to calculate out. The relative dose distribution in a transverse plane with EDR2 film was used, and compared with the planning dose plane. If the dose error was within the preset tolerance ($\pm 5\%$) and the relative dose distribution was satisfied, we

would not perform any other measurement. Otherwise, we would try to find the possible reason of the measurement. If possible, the absolute doses at more points were measured till to get the well-approving results.

III. RESULTS

The set-up error of the phantom was able to be kept within 1mm in the longitudinal and transverse direction. But there was about 2mm offset along the vertical direction of couch from the virtual isocenter to beam isocenter with the registering results of 84 patients plan. Fig. 2 shows the absolute dose distribution of 84 tomotherapy IMRT patients planning. The error between the measured absolute dose and predicted dose in the measured points was less than $\pm 3\%$. The average offset value of Tomotherapy IMRT plan for 84 patients was -0.12% . And the standard error was 1.2%.

Indeed, the relative isodose measurement is also one of the important elements in the IMRT treatment. After analyzing the film intensity qualitatively, the relative isodose distribution was well consistent with that calculated by Tomotherapy planning system. Fig. 3 (a, b) and Fig. 4(a, b) illustrate the comparison of the EDR2 film measurement and calculated dose distribution on the axial plane.

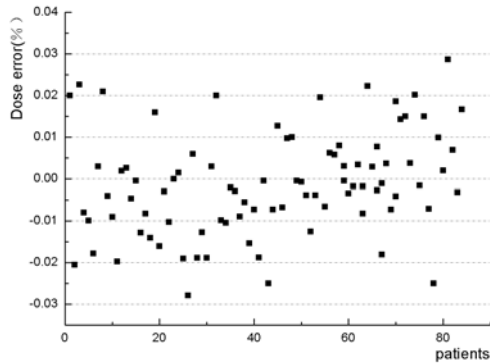
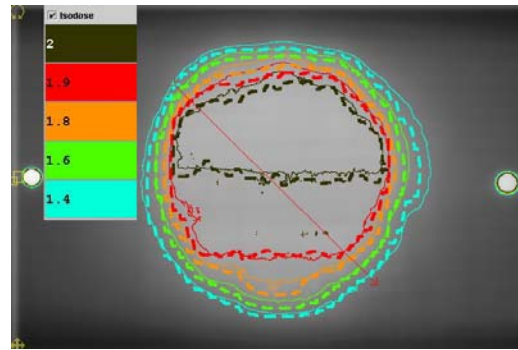
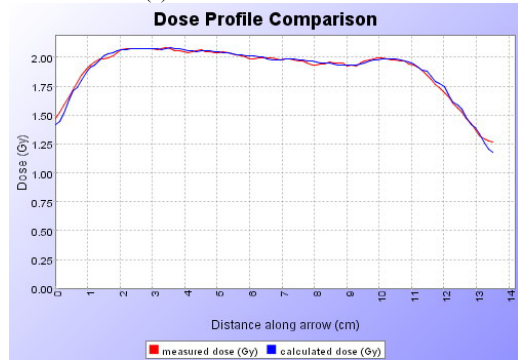


Fig. 2 This shows the absolute doses about the verification of 84 patients.

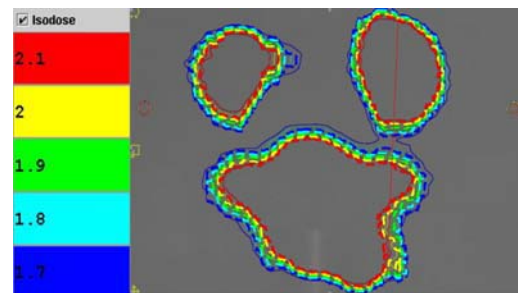


(a). Film isodose distribution

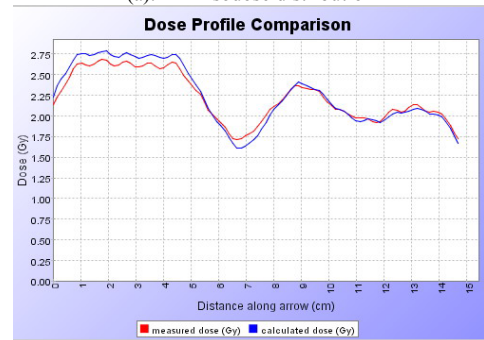


(b). The dose profile comparison of the arbitrary surface

Fig. 3 This shows the comparison of the EDR2 film and calculated dose distribution with one target.



(a). Film isodose distribution



(b). The dose profile comparison of the arbitrary surface

Fig. 4 This shows the comparison of the EDR2 film and calculated dose distribution with multiple targets.

IV. DISCUSSION

Helical tomotherapy combines a novel technique to deliver intensity modulated radiation therapy (IMRT) with the ability to acquire megavoltage computed tomograms (MVCTs) for patient/target localization prior to treatment. The technique of treatment planning and delivery is different from the IMRT treatment of conventional Linac. Due to the dynamic characteristic of Tomotherapy machine, quality assurance of tomotherapy IMRT was indispensable. From the registration data of the phantom in the vertical direction of the couch, we could get the 2mm offset. The reason was that there was the gravity of the couch and the phantom when the couch holding out. So the systematic error should be considered during the phantom setup.

Currently, we could achieve the absolute and relative dose verification of tomotherapy IMRT using the cylindrical phantom. This kind of method was clearly different from most IMRT verification of conventional Linac which was done only at gantry 0°. However, we should know that the film measurement have a little impact on the external environment, such as the film developer. During the quality assurance of 84 patients, there were 7 patients planning not to get the good result for the film processing problem. So the more experiences need to be gained later.

In general, now we have changed the preset tolerance of the absolute dose from $\pm 5\%$ to $\pm 3\%$. The procedures for quality assurance of Tomotherapy IMRT are feasible in our experience. We have developed Helical Tomotherapy IMRT QA system, and will continue to improve it.

REFERENCES

1. Mackie TR, Holmes T, Swerdloff S, et al. (1993). Tomotherapy: A new concept for the delivery of conformal radiotherapy. *Med Phys*, **20**:1709–1719.
2. Mackie TR, Balog J, Ruchala K, et al. (1999). Tomotherapy. *Semin Radiat Oncol*, **9**: 108–117.
3. Yang JN, Mackie TR, Reckwerdt P, et al. (1997). An investigation of tomotherapy beam delivery. *Med. Phys.* **24**:425–436.
4. Balog J, (1998) Tomotherapy dosimetry and the tomotherapy workbench, University of Wisconsin, Madison, thesis, Chap. 8.
5. Ezzell GA, Galvin JM, Low D, et al. (2003). Guidance document on delivery, treatment planning, and clinical implementation of IMRT: report of the IMRT subcommittee of the AAPM radiation therapy committee. *Med Phys*, **30**:2089-2115.
6. Dong L, Antolak J, Salehpour M, et al. (2003). Patient-specific point dose measurement for IMRT monitor unit verification. *Int J Radiat Oncol Biol Phys*, **56**:867-877.
7. Olivera GH, Shepard DM, Ruchala K, et al. (1999). Tomotherapy Modern Technology of Radiation Oncology.
8. Mackie TR, Olivera GH, Reckwerdt PJ et al. (2000) Convolution/superposition photon dose calculation. In: Shui AS and Mollenberg DE (eds) General practice of radiation oncology physics in the 21st century. Published for AAPM by Medical Physics Publishing, Madison WI, 39-56.
9. Shepard DM, Olivera GH, Reckwerdt PJ et al. (2000). Iterative approaches to dose optimisation in tomotherapy. *Phys. Med. Biol.* **45**: 69-90.
10. J.R. Dai, Y.M. Hu, H.Zh. Zhang et al. (2004) Plan-specific dosimetric verification for patient treated with intensity modulated radiation therapy. *Chinese Journal of Radiation Oncology*, **13**:229-233.

Author: XU Shouping
 Institute: Radiation Oncology Department of PLA General Hospital
 Street: Fuxing Road, No. 28
 City: Beijing
 Country: China
 Email: xshp228@163.com

Electron spectrum reconstruction as nonlinear programming model using micro-adjusting algorithm

Gui Li¹, Aidong Wu^{1,2}, Hui Lin³, Yican Wu¹

¹ Institute of Plasma Physics, Chinese Academy of Sciences, P.O. Box 1126, Hefei, 230031, China

² Departments of Radiotherapy, Anhui Provincial Hospital, Hefei 230001, China

³ Colleges of Science, HeFei University of Technology 230009, China

Abstract — In accurate radiotherapy, the electron spectra should be considered to improve the accuracy of dose calculation, because the electron beams that reach the surface traveling through the collimation system of the accelerator are not monoenergetic. For determining the energy spectra of Clinical electron beams effectively, the nonlinear programming model and a new inversion algorithm "micro-adjusting algorithm" were studied, by using the measured percent depth dose (PDD). The key issue was how to reconstruct the energy spectra from an ill-posed integral equation linking with the measured PDD, energy spectra and monoenergetic PDD. The monoenergetic PDD was calculated by bipartition model. And the nonlinear programming model with micro-adjusting algorithm was developed to solve this ill-posed integral equation. Testing samples for a Varian Clinac 1800 medical accelerator that considered and ignored the photon contamination were both used to test this method. The reconstructed results showed even if including 5% photon contamination the reconstructed energy spectra still agreed well with the original spectra – error of reconstructed PDD was less than 0.05%, while the one that subtracted photon contamination was less than 0.006%. It could be concluded that the method of the nonlinear programming model with the micro-adjusting algorithm was feasible to reconstruct electron energy spectra.

Keywords — radiotherapy, electron spectrum, measured percent depth dose, nonlinear programming model, micro-adjusting algorithm

I. INTRODUCTION

The energy spectra of electron are necessary for accurate dose calculation, both in Monte Carlo method and analytical method. It is sure that the most accurate method is the Monte Carlo simulation by modeling the source [1]. Nevertheless, the Monte Carlo is only a simulation method with little flexibility that need construct a complex model to fit a special accelerator. An accurate way to experimentally determine the spectrum is with a Compton scatter spectrometer [2], yet prohibitively expensive. The reconstruction of a spectrum from a set of dose measurements in water is a better way to determine the electron energy spectra comparing with the methods of direct measurement and modeling the source.

The useful algorithms to assess the dose contribution of treatment head bremsstrahlung to electron beam dose distributions in practice have been investigated by Faddegon and Bleves [3] and Deng et al [4]. By use of their method, therefore, we can reconstruct the energy spectra in considering and ignoring the photon contamination. The influence of the initial angular spread of incident electrons on the reconstructed spectra was reported by A. Chvetsov et al [5]. And hence, we limit our topic to the spectra reconstruction only on mono-directional and normally incident electrons in water. In this paper, we present an effective method to determine the electron spectra by constructing nonlinear programming model and its corresponding micro-adjusting algorithm, in which this algorithm is based on the perturbation idea from quantum mechanism. And the testing results would find its feasibility and effectivity.

II. NONLINEAR PROGRAMMING MODEL AND MICRO-ADJUSTING ALGORITHM

A. Modeling and its Algorithm

Supposed that the electron beams have the energy spectrum curve $\Phi(E)$ before penetrating into a water phantom, and under the normally incident condition the dose distribution generated by monoenergetic electrons with energy is $D(E, z)$ in water. If incident beams are normally enter into the water phantom, the dose distribution $D(z)$ at depth z of electron beam reads

$$D(z) = \int D(E, z) \Phi(E) dE \quad (1)$$

When discretized, it is

$$D(z_j) \approx \sum_i D(E_i, z_j) \Phi(E_i) \Delta E = K \Phi \quad (2)$$

where $K = [D(E_i, z_j) \Delta E]_{M \times N}$.

If having solution, due to Eq.(2) the solution of electron spectra should read,

$$\Phi(E_i) \approx (KK^T)^{-1} K^T D(z_j) \tag{3}$$

In fact, Eq.(1) is the Fredholm integral, an ill-posed equation [6, 7], so Eq.(3) is also an unstable solution. The reason is mainly because of the errors from discretization, one from monoenergetic curve $D(E,z)$ and another from dose distribution $D(z)$. If we got their discretization errors, the exact solution of energy spectra would be got. However, we cannot obtain them in practice. There is an effective idea from quantum mechanism that inspires us to find their eigenvalues respectively of these two matrixes. And hence, we bring two parameters α and β respectively to K and $D(z_j)$ as a sort of eigenvalues to replace the matrix of their discretization errors; if micro-adjusting α and β suitable, the solution of the energy spectra is stable.

$$\Phi(E_i) = [(K + \alpha I)(K + \alpha I)^T]^{-1} \cdot (K + \alpha I)^T [D(z_j) + \beta I] \tag{4}$$

In it, the matrix I is the unit matrix. To find the range of α and β , two strategies are introduced. Firstly, it is obtained the better approximate solution of the energy spectra before micro-adjusting α and β . The method is to find the better discrete approach of the coordinate z ,

$$z_j = z_0 + (j - 1)\delta \tag{5}$$

Here, δ is the step, and z_0 is initial site of the coordinate. With this, a better approximate solution of the energy spectra by Eq.(3) will be got. Though the solution of Eq.(3) with Eq.(5) is still unstable, but it can help reduce the range of the α and β to find the stable solution. The second strategy is to make the dose normalization for $D(z)$, and have the maximum relative dose of $D(E,z)$ about 2 unit. By these two strategies, the range of α and β can restrict each range in $[-1, 1]$ and $[-2, 2]$ respectively. Also the micro-adjusting step of them should no less than the discrete accuracy. As micro-adjusting α and β is relative to the discrete coordination of depth z , we call this algorithm as "micro-adjusting depth algorithm".

The reconstructed error is assessed by the error between the measured PDD as $D(z)$ reconstructed PDD as D' , and the following equation is a general mathematical mean method to calculate the relative error Er :

$$Er = \frac{1}{z_m} \int_0^{z_m} \left| \frac{D' - D(z)}{D(z)} \right| dz \tag{6}$$

In summary, the above discussion can be attributed to solve this nonlinear programming model: subject to non-

negative energy spectra etc, and by micro-adjusting α and β , to find the minimum object of error Er . Namely,

$$\text{Min } Er = \frac{1}{z_m} \int_0^{z_m} \left| \frac{D' - D(z)}{D(z)} \right| dz$$

Subject to:

$$\Phi(E_i) \geq 0$$

$$\Phi(E_i) \approx (KK^T)^{-1} K^T D(z_j)$$

$$z_j = z_0 + (j - 1)\delta$$

$$0 \leq z_0 \leq z_m, 0 < \delta \leq (z_m - z_0) / N$$

$$\Phi(E_i) = [(K + \alpha I)(K + \alpha I)^T]^{-1} (K + \alpha I)^T [D(z_j) + \beta I]$$

$$K = [D(E_i, z_j) \Delta E]_{M \times N}$$

$$\alpha \in [-1, 1], \beta \in [-2, 2]$$

$i=1,2,3,\dots,M; j=1,2,3,\dots,N$.

The detail of the micro-adjusting algorithm can be described as five steps in the following:

- ① Initialization: set the initial search value of the coordinate $z_0, z_0^{(1)} = 0$ (initial step $a=1$), and the step $\delta, \delta^{(1)} = b$ (e.g. $b=1$); introduce the shrinkage factor $\gamma \in [0, 1]$, the search order n , and the termination rule ϵ .
- ② In $0 \leq z_0 \leq z_m$ and $0 < \delta \leq (z_m - z_0) / N$, z_0 and step δ are respectively searched by the steps a and b due to equation $z_j = z_0 + (j - 1)\delta$; get a set of energy spectra $\Phi(E_i) \approx (KK^T)^{-1} K^T D(z_j)$, to distinguish if this discrimination function is true or not: $\Phi(E_i) \geq 0$

If true, select the solution of $\Phi(E_i)$ as $\Phi^{(0)}$ owing to $\text{Min}(Er) = Er^{(0)}$, then turn to the step ③; if failing, go to the step ④.

- ③ Micro-adjust the depth z_j with z_0 and δ to increase the precision of $\Phi^{(0)}$. Here, z_0 and δ are ranged in $z_0 \in (-\gamma^n a, \gamma^n a)$ and $\delta \in (-\gamma^n b, \gamma^n b)$, and the corresponding step is $\gamma^{n+1} a$ and $\gamma^{n+1} b$ respectively, ($n=1,2,3,\dots$). With these, we will get a set of $\Phi(E_j)$, then distinguish if the following rule is true or not:

$$Er^{(n-1)} > Er^{(n)} \quad (n=1, 2, 3, \dots)$$

If true, $n=n+1$, keep searching the solution with the lower error Er ; If failing, turn to the step ④.

- ④ Termination rule: to distinguish this rule is true or not, $Er^{(n)} \leq \epsilon$
 If true, return a set of solution of the spectra $\Phi^{(n)}$, z_0 and δ , and turn the next step; else, shrink a and b as γa and γb respectively, then turn to the step ②.
- ⑤ Discretize the measured PDD $D(z)$ and the monoenergetic curve $D(E,z)$ by $z_j = z_0 + (j-1)\delta$, and micro-adjust α and β with certain step (e.g. 10^{-3} , equal to the discrete accuracy) in the range of $[-1,1]$ and $[-2,2]$ respectively to find the optimum solution of energy spectra in the object of the minimum error Er .

B. Calculated Results and Discussion

To test the above-mentioned method, the monoenergetic curves $D(E,z)$ (Fig.1) is obtained by bipartition model to calculate an infinitely broad beam electron dose [7, 8]. The grid spacing is 2.0 MeV, from 4 to 22MeV.

The measured PDD in water ($20 \times 20 \text{cm}^2$ field) is from a Monte Carlo simulation (EGSnrc) [9] for a nominal energy of 20 MeV of a Varian Clinac 1800 medical accelerator. Here, considering the electron lateral equilibrium [10], the field size as $20 \times 20 \text{cm}^2$ is used to simulate the infinite broad beam electrons; It is sound that the range of 20MeV electron is about 10cm in water (shown in Fig.3), and the electrons in lateral equilibrium will hardly affect the center percent depth dose curve. The exact original spectra (Fig.2) is inputted into the Monte Carlo simulation and its results is as the measured PDD (Fig.3); the photon contamination

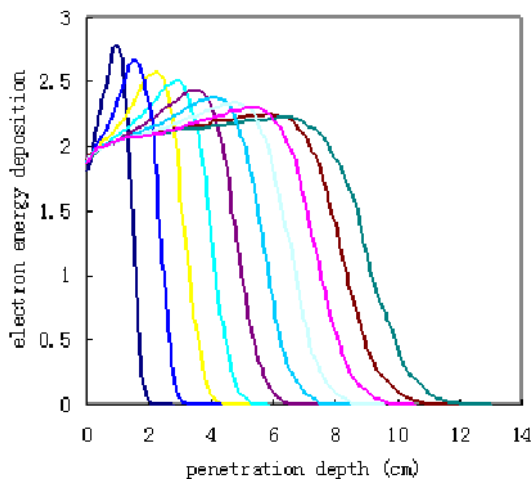


Fig. 1 Energy deposition of broad beam electrons with 4, 6, 8, 10, 12, 14, 16, 18, 20 and 22 MeV in water [6, 7]

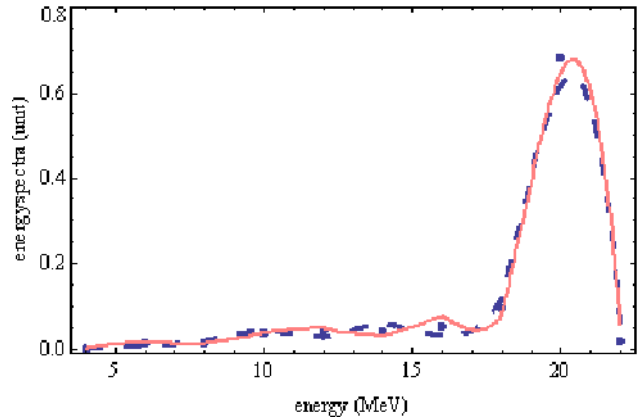


Fig. 2 The calculated spectra by the nonlinear programming model with the micro-adjusting algorithm, the dotted line (•••) is the original spectra, the dashed line(—■—) is the reconstructed spectra including about 5% photon contamination, and the straight line is the reconstructed spectra by subtracting the photon contamination. As there are ten points for each calculated energy spectra, the interpolation technique is used to reconstruct the continued curve.

(head-generated photon dose and phantom-generated photon dose) are also obtained (about 5%), and can be subtracted by Deng et al's method. Both the measured PDD and monoenergetic curve have a statistical uncertainty less than 0.5%. Before calculation, the measured PDD is made normalization and interpolation as continued curve.

Table1 shows the reconstructed parameters by using micro-adjusting algorithm, where it calculated two situations of the testing sample with and without 5% photon contamination. The calculated results are shown in Fig.2 and Fig.3. In Fig.2, we find that the reconstructed energy spectra agreed well with the original one, when having the photon contamination subtracted. Otherwise, the reconstructed energy spectra have a small deviation to the original, when including about 5% photon contamination. Fig.3 shows the reconstructed PDD met well with the measured PDD, even if including 5% photon contamination.

There are no general rule to set the steps to search z_0 and δ . But we find that when given the step about 0.2 or less will be enough, and here we set them as 0.125 and 0.1 for A and B in table1 respectively. The less step will find the more accurate z_0 and δ , but it will consume much time. For α and β , the search step is 10^{-3} (discrete accuracy). We find that no

Table 1 Reconstructed parameters

Factors	z_0	δ	α	β	Er
Sample					
A: No photon contamination	0.4	0.7	-0.015	-0.007	0.000061
B: 5% photon contamination	1.1	0.7	-0.045	-0.021	0.000475

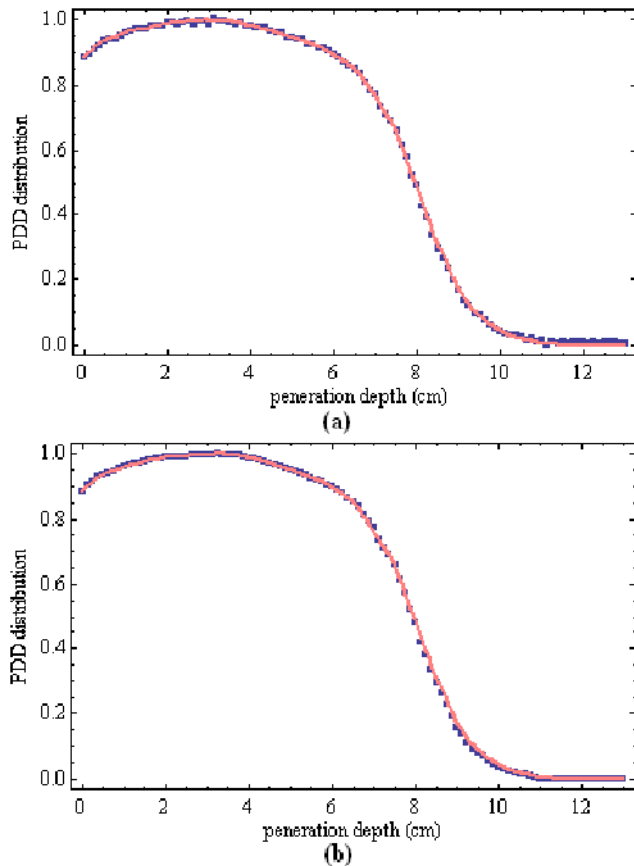


Fig. 3 Comparison of reconstructed PDD curves (straight line) with the measured PDD (dot line), Figure 3(a) shows the reconstructed PDD including about 5% photon contamination, while Figure 3(b) is subtracted this photon contamination.

need the search range as its original. Both the range of α and β as $[-0.1, 0.1]$ are enough to obtain the higher accurate solution of energy spectra. With these, the total calculated time is 88.1s and 225.8s respectively for A and B in Table 1 (Win XP, P-4 CPU: 2.0 GHz, and RAM: 256 Mb).

III. CONCLUSIONS

According to the above calculated results and discussion, it can be concluded that the non-linear programming with micro-adjusting algorithm could reconstruct the electron spectra accurately and effectively. And even if including 5% photon contamination the reconstructed energy spectra still agreed well with the original spectra. So the 5% photon contamination could be ignored by use of this method to reconstruct the electron energy spectra. The calculated time was a little long, but it was not the main considering factor for the energy spectra reconstruction.

We should admit that our method will not work if failing to find the approximate electron energy spectra in the first step in coordinate discretization -- because the larger error exists due to discretization, photon contamination, and measurement. In this situation, the help is to solve the model as accurate as possible, and have the error as small as possible. Also, the point number of the energy spectra is not large enough. So more point number of the energy spectra will be needed. As increasing the point of the energy spectra, it will need more monogenetic curves, and may lead no solution to the coordinate discretization in our algorithm at the first step. Because more discrete error will create in a large matrix (larger than 10×10), and will fail to obtain the nonnegative energy spectra. So the following investigation should make this improvement. A possible solution is based on the "blocking idea" from inversion theory. Namely, it is separated the energy spectra as several partitions that each partition covers the whole range of the spectra, then reconstructed the energy spectra for each partition, and finally made combination based on normalization.

ACKNOWLEDGMENT

The authors sincerely thank for all members from FDS Team. This work is supported by "The National Key Fundamental Research Project (973 Project 2006CB708307)" and "The Natural Science Foundation of Anhui Province (070413081)".

REFERENCES

1. Rogers D, Faddegon B, Ding G, Ma C-M, We J and Mackie T 1995 BEAM: a Monte Carlo code to simulate radiotherapy treatment units *Med. Phys.* 22 503-24
2. Landry D J and Anderson D W 1991 Measurement of accelerator bremsstrahlung spectra with a high efficiency, *Med. Phys.* 18 527-32
3. B. A. Faddegon and I. Blevis 2000 Electron spectra derived from depth dose distribution *Med. Phys.* 27, 514-526
4. J. Deng, S. B. Jiang, T. Pawlicki, J. Li, and C. M. Ma 2001 Derivation of electron and photon energy spectra from electron beam central axis depth dose curves *Phys. Med. Biol.* 46, 1429-1449
5. A. Chvetsov and G. A. Sandison 2003 Angular correction in reconstruction of electron spectra from depth dose distributions *Med. Phys.* 30, 2155- 2158
6. A. Chvetsov and G. A. Sandison 2002 Reconstruction of electron spectra using singular component decomposition *Med. Phys.* 29, 578-591
7. Zhengming and D. Jette 1999 On the possibility of determining an effective energy spectrum of clinical electron beams from percentage depth dose PDD data of broad beams, *Phys. Med. Biol.* 40, N177-N182
8. Luo Z and Brahme 1992 A High energy electron transport *Phys. Rev.* B46 15 739-52
9. <http://www.irs.inms.nrc.ca/EGSnrc/EGSnrc.html>
10. Jikun Wei, George A. Sandison and Alexei V. Chvetsov 2006 Reconstruction of electron spectra from depth doses with adaptive regularization *Med. Phys.* 33(2), 354-359

Effect of EMP on Superoxide Dismutase and Malondialdehyde in K562 cells

Xue-Jun Xie, Gui-Ying Zeng, Yao Guo, Guo-Zheng Guo, Li-Hua Zeng, Dong-Qing Ren

Department of Radiation Medicine, Faculty of Preventive Medicine, Fourth Military Medical University, Xi'an 710032, China
Tel: 086-(029)84774876 Ext.17, Fax: +86-29-84774873, E-mail: xuejunx@fmmu.edu.cn

Abstract — AIM To observe effect of EMP on the kinetic equilibrium of produce and elimination of free radicals. **METHODS** Human erythroleukemia K562 cells were exposed or shamly exposed to EMP before the activity of SOD and the contents of MDA were measured using NBT and TBA methods respectively. **RESULTS** The activity of SOD decreased 12h after $200\text{kV}\cdot\text{m}^{-1}$ EMP exposure, the contents of MDA increased 24h after $200\text{kV}\cdot\text{m}^{-1}$ EMP exposure. The contents of MDA increased and the activity of SOD decreased at 12h and 24h after $400\text{kV}\cdot\text{m}^{-1}$ EMP exposure. **CONCLUSION** Excessive free radicals produced from impact of EMP on the kinetic equilibrium of produce and elimination of free radicals maybe a way through which EMP exposure inducing cell damage.

Keywords — electromagnetic pulse (EMP), Free radical, Superoxide Dismutase (SOD), Malondialdehyde (MDA), K562

I. INTRODUCTION

One possible mechanism for bio-effects of EMF is that EMF interfere with chemical reactions involving free radical production[1]. It is well established that free radicals have pleiotropic effects which may vary from cytotoxic to mitogenic responses depending on the dose intensity, the duration of exposure, and the type of cell or tissue[2]. In this study, we observed the effect of EMP on the kinetic equilibrium of produce and elimination of free radicals by determining the level of Malondialdehyde (MDA) together with SOD activities in human erythroleukemia K562 cells exposed or shamly exposed to EMP, so as to explore the relation between EMP and free radical.

II. MATERIALS AND METHODS

A. Cell culture

Human chronic myeloid (K562) leukaemia cells were maintained in exponential growth in RPMI 1640 bicarbonate medium (pH 7.2) supplemented with 10% (v/v) heat-inactivated foetal calf serum (FCS), 2 mM glutamine and 0.1mg/mL of both penicillin and streptomycin and kept at 37°C in a humidified atmosphere of 5% CO₂ in air.

B. EMP exposure

The EMP pulses were generated by a spark gap pulse generator and transmitted into a GTEM cell. In the GTEM cell, there are different electric field intensities at different distances (it is 400kV/m at 10cm and 200kV/m at 95cm) from the source end of GTEM cell. For EMP exposures, cells were exposed to EMP for 200 pulses with 2s interval. Three exposure conditions were used: sham exposure as control group, 200 kV/m EMP and 400kV/m EMP exposures. During the sham exposure, all EMP exposure conditions were maintained except trigger pulses were never generated to cause discharge across the spark gap.

C. Malondialdehyde and superoxide dismutase determination

MDA content was measured using the thiobarbituric acid (TBA) method. Superoxide dismutase (SOD) activity was measured through the inhibition of nitroblue tetrazolium (NBT) reduction by O₂- generated by the xanthine/xanthine oxidase system.

D. Statistical analysis

All values were expressed as mean±SE. Statistical significance between two groups of parametric data was evaluated by ANOVA. All statistical analyses were performed with the SPSS statistical package (SPSS10.0 for Windows; SPSS, Inc, Chicago, IL). P value of <0.05 was considered significant.

III. RESULTS

Our experiments showed that, the activity of SOD in K562 cells decreased at 12h after exposure to 200kV EMP, and the difference was significant statistically at 24h after exposure to 200kV EMP ($p<0.01$). When K562 cells were exposed to 400kV EMP, the decrease of SOD activity were observed as early as 12h after exposure and persisted till 24h post exposure($p<0.05$), (Tab.1).

The MDA content as an index of lipid peroxidation was significantly higher at 12h after exposure to 200kV EMP than in control group ($p<0.05$). At 24h post 200kV EMP

Table 1. Changes of catalytic activity of SOD in K562 cells after exposure to EMP

 $(n=6, \bar{X} \pm s, \text{nu/ml})$

Group	Time after EMP exposure (h)		
	0h	12h	24h
control	27.75±1.9	28.78±1.7	25.36±1.4
200kV/m	27.75±1.9	21.44±3.3	18.26±2.5 ^a
400kV/m	27.75±1.9	17.56±2.9 ^a	21.80±1.6 ^a

^a $P < 0.05$ vs control

Table 2. Changes of MDA contents in K562 cells after exposure to EMP

 $(n=6, \bar{X} \pm s, \text{nmol/ml})$

Group	Time after EMP exposure (h)		
	0h	12h	24h
Control	0.48±0.08	0.43±0.07	0.51±0.12
200kV/m	0.48±0.08	0.86±0.11 ^a	0.64±0.15
400kV/m	0.48±0.08	0.82±0.09 ^a	0.75±0.06 ^a

^a $P < 0.05$ vs control

exposure, MDA contents was still higher compared with control group but with no statistical significant. MDA contents was significantly higher at 12h and 24h after K562 cells exposed to 400kV EMP than in control group ($p < 0.05$) (Tab 2).

IV. DISCUSSION

Free radicals are atomic or molecular species with unpaired electrons on an otherwise open shell configuration. These unpaired electrons are usually highly reactive, so free radicals are likely to take part in chemical reactions and play an important role in a number of biological processes, some of which are necessary for life, such as the intracellular killing of bacteria by neutrophil granulocytes. Free radicals have also been implicated in certain cell signaling processes [3]. It has been demonstrated that low levels of reactive oxygen species trigger intracellular signals that involve the transcription of genes and lead to responses including proliferation [4].

However, because of their reactivity, these same free radicals can participate in unwanted side reactions resulting in cell damage. For example, hydroxyl radicals, one of the most important oxygen-centered free radicals derived from molecular oxygen under reducing conditions, can interact with DNA and form primarily 8-OHdG adducts, resulting in single strand breaks [5]. Adducts or strand breaks are recognized and usually removed quite efficiently by specific repair mechanisms. Nevertheless, DNA damage could become a site of mutation and a key step to carcinogenesis if the damage were extensive enough to overcome the repair capacity of the cell [6,7]. Some of the symptoms of aging

such as atherosclerosis are also attributed to free-radical induced oxidation of many of the chemicals making up the body.

Reactive oxygen species (ROS) have been tentatively proposed to mediate the effects of EMF[8]. Lipid peroxidation induced by free oxygen radicals is one of the most important causes of cellular damage. Lipid peroxidation occurs in response to elevated levels of ROS with the liberation of reactive aldehydes, such as MDA. The human body has a complex antioxidant defense system that includes the antioxidant enzymes SOD, catalase, and glutathione peroxidase. SOD is an oxygen radical scavenger which converts superoxide anion radicals present in the upper stream of reactive oxygen metabolism cascade, protects cells against damage[9]. A decrease in the antioxidant capacity of tissues may be the consequence of increased oxidative processes.

In this study, we found that at 12h after exposure to 200kV/m EMP, MDA(an oxidative stress marker) levels were higher in K562 cells than in control group($P < 0.05$); at 24h after 200kV/m EMP exposure, SOD activities decreased significantly compared to control group($p < 0.01$). When K562 cells were exposed to the EMP with higher electric field intensity (400kV/m), MDA levels increased significantly compared to control group($p < 0.05$), while the SOD activities decreased significantly than the control group($p < 0.05$), at 12h and 24h post exposure.

V. CONCLUSIONS

In conclusion, this study suggests that exposure to either 200kV/m or 400kV/m EMP may cause increased production of free radical in K562 cells, and the stronger effect was observed with higher electric field intensities (400 kV/m). After EMP exposure, the production of free radical increased and the antioxidant capacity were inhibited, leading to the imbalance of the kinetic equilibrium of produce and elimination of free radicals, which may alter the levels of intracellular free radicals and mediate the effects of EMP.

ACKNOWLEDGMENT

This study was supported by the National Hi-Tech Research and Development Program (863) of China (2006AA02Z4C3) and Natural Science Foundation of China (No.60601026).

REFERENCE

1. Lacy-Hulbert A, Metcalfe JC, Hesketh R. Biological responses to electromagnetic fields. *FASEB J.* 1998 12 (6): 395–420.
2. Davies KJ. The broad spectrum of responses to oxidants in proliferating cells: a new paradigm for oxidative stress. *IUBMB Life.* 1999, 48 (1) 41–47.
3. Pacher, P., Beckman, J. S., Liaudet, L. Nitric Oxide and Peroxynitrite: in Health and disease. *Physiological Reviews* 2007, volume 87(1), 315-424.
4. Torres M., Mitogen-activated protein kinase pathways in redox signaling. *Front Biosci.* 2003 Jan 1;8:d369-91. Review.
5. Marnett LJ. Oxyradicals and DNA damage. *Carcinogenesis.* 2000 Mar; 21(3): 361-70.
6. Epe B. Role of endogenous oxidative DNA damage in carcinogenesis: what can we learn from repair-deficient mice? *Biol Chem.* 2002 Mar-Apr;383(3-4):467-75
7. Jackson AL, Loeb LA. The contribution of endogenous sources of DNA damage to the multiple mutations in cancer. *Mutat Res.* 2001 Jun 2;477(1-2):7-21. Review.
8. Wolf FI, Torsello A, Tedesco B, Fasanella S, Boninsegna A, D'Ascenzo M, Grassi C, Azzena GB, Cittadini A. 50-Hz extremely low frequency electromagnetic fields enhance cell proliferation and DNA damage: Possible involvement of a redox mechanism *Biochim Biophys Acta.* 2005 Mar 22;1743(1-2):120-9
9. Rhodes CJ. *Toxicology of the Human Environment - the critical role of free radicals*, Taylor and Francis, London (2000).

Hsps expression in three human glioma cell lines after radio-frequency field exposure

G.R. Ding¹, X.W. Wang¹, K.C. Li¹, J. Miyakoshi² and G.Z. Guo¹

¹ Department of Radiation Medicine, School of public health, Fourth Military Medical University, Xi'an 710032, China;

² Department of Radiological Technology, School of Health Sciences, Faculty of Medicine, Hirosaki University, 66-1 Hon-cho, Hirosaki, 036-8564, Japan

Abstract — AIM To investigate and compare the effect of radio-frequency field exposure on stress response genes (Hsps) expression in three human glioma cell lines. METHODS Glioma cells were from MO54, A172 and T98 three human glioma cell lines. Exponentially growing cells were exposed to sham conditions or 1950 MHz continuous-wave for 1h. PC randomly determined which of the two waveguides was exposed. Specific absorption rates (SARs) were 1 and 10 W/kg. After treatment, the expression level of Hsp27 and p-Hs27 as well as Hsp70, was determined by Western blotting. RESULTS The Hsp27 expression level of A172, MO54 and T98 cells exposed to RF fields (SAR: 1 W/kg, 10 W/kg) for 1h showed no difference compared with sham-exposed cells. Phosphorylated Hsp27 level of A172, MO54 and T98 cells exposed to RF fields (SAR: 1 W/kg) for 1 h showed no differences compared with sham-exposed cells. However, exposure to an RF field at 10 W/kg for 1h slightly decreased the level of phosphorylated Hsp27 in MO54 cells other in A172 and T98 cells. For the expression of Hsp70 in A172, MO54 and T98 cells after exposure to RF fields (SAR: 1 W/kg and 10 W/kg) for 1 h, no obvious changes in Hsp70 expression were observed in RF-exposed cells compared with sham-exposed cells. CONCLUSIONS Our results suggest 1950 MHz RF field has little or no apparent effect on HSP70 and HSP27 expression in MO54, A172 and T98 cells, it may only slightly inhibit the phosphorylation of Hsp27 at Serine 78 in MO54 cells.

Keywords — Radio-frequency field, Hsp70, Hsp27, protein expression, glioma cells.

I. INTRODUCTION

In recent years, with the rapid introduction of mobile telecommunication devices, the possible health effects due to exposure to radio-frequency (RF) fields from mobile phones have become a public concern^[1-3], which has led to an increase in epidemiological and experimental investigations. In mammalian cells, heat shock proteins (Hsps) function as chaperones and are essential for a correct folding, assembly, and intracellular translocation of proteins expressed during normal growth conditions. Induction of Hsp synthesis can result in stress tolerance and cytoprotection against stress-induced molecular damage^[4]. In this study, we investigated whether exposure to an RF field could act

as an environmental insult to invoke a stress response in human glioma cells using Hsp 27 and Hsp70 as stress markers.

II. MATERIAL AND METHODS

Exponentially growing cells were cultured in 35 mm dishes (3×10^5 cells/dish) and then moved to dish holders in two waveguides (one for sham, the other for exposure). Cells were exposed to sham conditions or 1950 MHz continuous-wave for 1h. PC randomly determined which of the two waveguides was exposed. Specific absorption rates (SARs) were 1 and 10 W/kg. According to the records of exposure apparatus, none of the exposure conditions produced a rise in temperature greater than 0.1°C . Cells were treated at 43°C for 3 h, as a positive control for the induction of Hsp expression. After treatment, the expression level of Hsp27 and p-Hs27 as well as Hsp70, was determined by Western blotting. The antibodies used in this experiment were as follows: anti-Hsp27 goat polyclonal antibody (C-20 Santa Cruz Biotechnology), anti-Hsp70 mouse monoclonal antibody (StressGen Biotechnologies Corp), anti-phospho-Hsp27 (78Ser) rabbit polyclonal antibody (Stressgene), anti- β -actin mouse monoclonal antibody (Sigma), anti-goat IgG horseradish peroxidase (Santa Cruz Biotechnology), anti-mouse IgG horseradish peroxidase (Amersham-Pharmacia Biotech), and anti-rabbit IgG horseradish peroxidase (Amersham-Pharmacia Biotech). The blot was visualized with an ECL kit (Amersham-Pharmacia Biotech). Densitometric analysis was performed using ATTO Image Analysis Soft-ware.

III. RESULTS

A. Effects of RF field exposure on expression of Hsp27 and p-Hsp27.

The Hsp27 expression level of A172, MO54 and T98 cells exposed to RF fields (SAR: 1 W/kg, 10 W/kg) for 1h showed no difference compared with sham-exposed cells. Heat treatment (43°C , 3 h) did not change the expression

IV. DISCUSSION

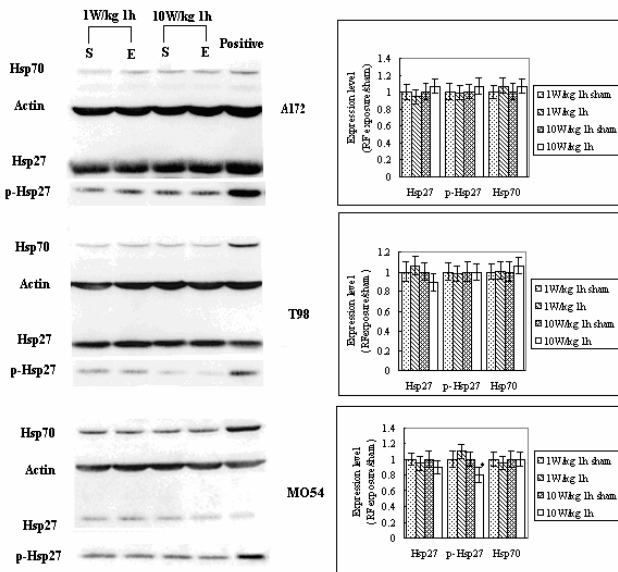


Fig.1 Representative western blots and expression ratio (RF exposure/sham) of Hsp27, p-Hsp27 and Hsp70 in response to RF field exposure in A172, MO54 and T98 cells. Exponentially growing cells were exposed to RF field for 1 h at SARs of 1 W/kg and 10W/kg, and the lysates were prepared immediately after exposure. Western blot analysis was performed as described in the Materials and Methods. The experiment was performed at least twice. *p <0.05, compared with sham.

levels of Hsp27. Phosphorylated Hsp27 level of A172, MO54 and T98 cells exposed to RF fields (SAR: 1 W/kg) for 1 h showed no differences compared with sham-exposed cells. However, exposure to an RF field at 10 W/kg for 1h slightly decreased the level of phosphorylated Hsp27 in MO54 cells other in A172 and T98 cells (Fig. 1). In positive control, heat treatment (43°C, 3 h) obviously increased the level of phosphorylated Hsp27 in three cell lines (Fig. 1).

B. Effects of RF field exposure on Hsp70 expression.

The expression of Hsp70 in A172, MO54 and T98 cells after exposure to RF fields (SAR: 1 W/kg and 10 W/kg) for 1 h and the ratio of exposure to sham conditions is shown in Fig.1. No obvious changes in Hsp70 expression were observed in RF-exposed cells compared with sham-exposed cells. Heat treatment (43°C, 3 h) obviously increased the level of Hsp70 in three cell lines.

Mobile phones emit RF fields into the heads of their users. This has resulted in significant concern that there may be a health issue as a result of this exposure. It is generally accepted that the SAR of RF energy from mobile phone in the human head is not sufficient to cause significant bulk heating of tissue. Activation of Hsps is a normal defense response to a cellular stress^[5]. Induction of heat shock responses by low SAR (non-thermal) RF field exposure is still inconclusive. Kwee et al^[6] have reported that the expression of Hsp70 but not Hsp27 was induced when exposed transformed human epithelial amnion cells to a GSM signal of 960 MHz at a SAR of 0.0021W/kg for 20 min. it has also been reported that RF/ microwave radiation (27/2450 MHz, CW signal) at much higher SARs (25 and 100 W/kg) for 2 h failed to induce the heat shock response in HeLa and CHO cells^[7], which is consistent with our results that exposure to a 1950 MHz RF field for 1h had no effects on Hsp70 and Hsp 27 expression in A172, T98 and MO54 cells when the SAR was less than 10 W/kg (Fig.1). It has been suggested that phosphorylation is important for Hsp27 function^[8, 9], and that phosphorylation could be induced without inducing the synthesis of the heat shock proteins^[10]. We found that the level of phosphorylated Hsp27 in MO54 cells exposed to RF field (SAR: 1 W/kg) for 1h showed no differences compared with sham-exposed cells (Fig. 1). However, exposure to an RF field at 10 W/kg for 1h decreased the level of phosphorylated Hsp27 significantly (Fig. 1) in MO54 cells other than A172 and T98 cells. This suggested that RF field exposure (SAR: 10 W/kg) inhibited the constitutive phosphorylation of Hsp 27 in MO54 cells. Our results suggest 1950 MHz RF field has little or no apparent effect on HSP70 and HSP27 expression in MO54, A172 and T98 cells, it may only slightly inhibit the phosphorylation of Hsp27 at Serine 78 in MO54 cells.

REFERENCES

1. Munshi A, Jalali R (2002) Cellular phones and their hazards: the current evidence. *Natl Med J India* 15: 275-27.
2. Repacholi, M H (2001) Health risks from the use of mobile phones. *Toxicol Lett.* 120: 323-331
3. Blettner M, Berg G (2000) Are mobile phones harmful? *Acta Oncol* 39: 927-930
4. Parsell D A, Lindquist S (1994) Heat shock proteins and stress tolerance. Cold spring Harbor Laboratory Press, Cold Spring Harbor
5. Nollen E A and Morimoto R I (2002). Chaperoning signaling pathways: molecular chaperones as stress-sensing 'heat shock' proteins. *J Cell Sci* 115: 2809-2816

6. Kwee S, Raskmark P, Velizarov S (2001) Changes in cellular proteins due to environmental non-ionizing radiation. I. Heat-shock proteins. *Electro-and Magnetobiology* 20: 1061-1072
7. Cleary S F, Cao G, Liu L M et al (1997) Stress proteins are not induced in mammalian cells exposed to radiofrequency or microwave radiation. *Bioelectromagnetics* 18: 499-505
8. Lavoie J N, Lambert H, Hickey E et al (1995) Modulation of cellular thermoresistance and actin filament stability accompanies phosphorylation-induced changes in the oligomeric structure of heat shock protein 27. *Mol Cell Biol* 15: 505-516
9. Huot J, Houle F, Spitz D R et al (1996) HSP27 phosphorylation-mediated resistance against actin fragmentation and cell death induced by oxidative stress. *Cancer Res* 56: 273-279
10. Arrigo A P (1990) Tumor necrosis factor induces the rapid phosphorylation of the mammalian heat shock protein hsp28. *Mol Cell Biol* 10: 1276-1280, Erratum in: *Mol Cell Biol* 10: 3857

Author: G.R. Ding
Institute: Department of Radiation Medicine, School of public health,
Fourth Military Medical University
Street: Chang le west road 17
City: Xi'an
Country: China
Email: dingzhao@fmmu.edu.cn

Effects of Electromagnetic Pulses on the Rat Testis

Lihua Zeng¹, Chang-xu Zou², Jie Zhang¹, Xiao-Wu Wang¹, Dong-Qin Ren¹, Yu-Rong Li¹,
Guo-zhen Guo¹

¹Department of Radiation Medicine, Fourth Military Medical University, Xi'an, China,

²Department of Neuroanatomy, Fourth Military Medical University, Xi'an, China

Abstract — **AIM:** The present paper investigated the effects of electromagnetic pulses (EMP) on the male procreative system to establish personnel protection guidelines for the new type of electromagnetic radiation. **MATERIALS AND RESULTS:** Rats were used in this study, and EMP irradiation parameter: 100Kv/m field intensity, 3×10^6 and 4×10^6 pulses respectively. SD male rats were sacrificed at 6h, 12h, 24h and 48h after 4×10^6 pulses irradiation, and the testis were prepared for transmission electron microscopy (TEM). The contents of follicle-stimulating hormone (FSH), luteinizing hormone (LH) and testosterone (T) in the serum were examined using radioimmunoassay after different times exposed to EMP. The activity of total superoxide dismutase (T-SOD) and manganese superoxide dismutase (MnSOD) were determined according to xanthine oxygenation method. Meanwhile the density of maleic dialdehyde (MDA) was determined by thibaburic acid method. By semi-quantitative reverse transcription-polymerase chain reaction (RT-PCR), MnSOD and copper/zinc SOD (CuZnSOD) mRNA in the rat testis have been observed at different time after irradiation. The protein of NF κ Bp65 and I κ B α in rat testis was assayed by western blotting. Under TEM, the rat testis was damaged at different time after irradiation, the damage was more serious at 24h than the other times and it wasn't recovered until 48h after irradiation; After 3×10^6 or 4×10^6 pulses, FSH in the serum didn't change obviously, LH and T in the serum of the radiation groups were changed fluctuatedly compared with that of parallel control respectively; the activity of T-SOD and MnSOD in rat testis decreased at 24h and the contents of MDA increased at 6h after irradiation, MnSOD mRNA expression decreased in rat testis at 24h after exposure, and CuZnSOD mRNA expression didn't change; the protein of NF κ Bp65 and I κ B α in rat testis didn't change obviously after irradiation. **CONCLUSION:** The morphology was damaged and the function and metabolism of procreative system were altered on the rats after irradiation. EMP induced indiscriminate hormone secretion and excessive free radicals and over expression of some genes in the male procreative tissue played some roles directly or indirectly for the bioeffects.

Keywords — electromagnetic pulse (EMP); SD rat; testis; superoxide dismutase (SOD).

I. INTRODUCTION

Along with the development of electromagnetic wave technology, the denomination and intension of spatial electromagnetic radiation are increasing quickly. Nowadays, electromagnetic radiation has generally resided in our daily life and work environment. As a new environmental pollution, it is paid close attention recently. Electromagnetic pulse (EMP) is a special kind of electromagnetic irradiation which is produced as short high-voltage pulses with an extremely fast rise and a spectral bandwidth from 0 Hz to 1.5GHz. The unusual properties of EMP have raised concerns about their bioeffects and possible health hazards to humans. Doubts about the validity of these concerns, however, have been discussed by some investigators^[1,2].

More and more attention have been drawn gradually to the effect of electromagnetic irradiation on the procreative ability of male and female^[3]. In present, only a few studies of EMP bioeffects have been carried out, and also most of them were focused on behavioral and physiological effects of laboratory animals. The genetic effect of EMP was less reported. In addition, a number of studies have suggested that cell DNA may be a target for various types of electromagnetic radiations^[4,5]. It has been confirmed from experimental results of our department that, EMP can influence nervous system, immune system, endocrine system, endocrine system and genital system of animals. But it's disadvantage to living body still needs to be approved.

The present paper discusses the effects and mechanisms of EMP at some extends and EMP on the male procreative system to establish personnel protection guidelines for these new types of electromagnetic radiation. In this experiment, rats were used as the experiment subject, to observe the effects of EMP irradiation on the rat testis including the morphology, the endocrine, the contents and the gene expression and protein level which correlated with free radicals enzymes after EMP irradiation.

II. MATERIALS AND METHODS

Animals and Electromagnetic Pulse Exposure

Eight-weeks-old male SD rats (weight between 200-220g) were used. There were 25 rats to be divided randomly into five groups (control, 6h group, 12h group, 24h group, 48h group). 2 rats of each group were used for the ultra-structural observation, and 6 rats of each group were used for other experiment in this study.

The rats were hold in a constraining box made from plexiglass, and then exposed to EMP of 100kV·m⁻¹ field intensity, 3×10⁶ and 4×10⁶ pulses respectively at K polarization orientation.

Ultrastructure observation

The rats were anesthetized with sodium pentobarbital (45mg·kg⁻¹.ip) and fixed in 4°C 500 mL 2% Paraformaldehyde-2.5% Glutaraldehyde fixative (0.2mol·L⁻¹, pH7.4 PBS) at the 6h, 12h, 24h, 48h after 4×10⁶ pulses exposure, then the samples of rats testis were observed under transmission electron microscope.

Contents of FSH, LH and T assay

At 6h, 12h, 24h, 48h after 3×10⁶ and 4×10⁶ pulses EMP irradiation, the serum samples from the rat were harvested to examine the contents of FSH, LH and T using radioimmunoassay (Diagnostic Product Company, DPC, China).

Activity of SOD and the density of MDA analysis

SD male rats were sacrificed at 6h, 12h, 24h and 48h after 4×10⁶ pulses EMP irradiation, and the testises were prepared to measure the activity of T-SOD and MnSOD and the density of MDA. The activity of total superoxide dismutase (T-SOD) and manganese superoxide dismutase (MnSOD) were determined according to xanthine oxygenation method (Nanjing Jiancheng Lot.China). Meanwhile the density of maleic dialdehyde (MDA) was determined by thibabaturic acid method (Nanjing Jiancheng Lot.China).

Reverse transcription-polymerase chain reaction (RT-PCR)

At 6h, 12h, 24h, 48h after 4×10⁶ pulses EMP irradiation, the samples of rat testis were extracted and used to RT-PCR that performed as previously described^[6]. The cycling parameters for MnSOD and CuZnSOD gene expressions were as follows: cDNA synthesise and dena-

turation: 50°C 30min, 94°C 2min for 1 cycle; ②PCR reaction: 94°C 30s, 61°C 30s, 72 °C 1.5min for 28 cycles; ③final extension: 72°C 6min for 1 cycle, the total is 30 cycles. The rat MnSOD primers pairs (4) were sense: 5, -GCGACCTACGTGAACAATC TGAACG-3 and antisense: 5, -TCAATC CCCAGCAGTGGAAATAA GG-3, defining a fragment of 383 base pairs(bp). The rat CuZnSOD primers pairs^[7] were sense: 5, -AAGGC CGTGCGTGCTGAA- 3, and antisense 5, -CCTCATT TCCACCT TTGCCC-3, defining a fragment of 391 bp. Glyceraldehyde-3-phosphate dehydrogenase^[8] was used as an internal control. Each mRNA expression was semi-quantitatively analyzed using an image analyzer (National Instruments IMAQ Vision Builder6, USA). The relative expression intensity of each factor was calculated from the ratio of each transcript to GAPDH.

Western blotting analysis

At 6h, 12h, 24h, 48h after 4×10⁶ pulses EMP irradiation, the samples of rat testis were extracted and used to western blotting analysis. The samples were harvested and lyzed with 100 μL of western lysis buffer (50 mM Tris [pH 7.5], 1% NP-40, 0.25% SDC, 150 mM NaCl, 1 mM EGTA). The cell lysates were sonicated for 5 min and then centrifuged at 10 000g for 30 min. The supernatant was assayed to determine protein concentration and 20 μg per lane was applied to SDSpolyacrylamide electrophoresis (10%). The protein was then transferred to a nitrocellulose filter (Hybond-ECL; GE Healthcare Biosciences, Piscataway, NJ, USA) and the resultant filter was blocked with 5% non-fat milk in PBS. For detection of NFκBp65, IκBα and β-actin protein, the filters were probed with monoclonal anti- NFκBp65 antibody and mouse monoclonal anti- IκBα antibody (1:250, Santa Cruz Biotechnology, Santa Cruz, CA, USA) and polyclonal β-actin antibody (1:500, Santa Cruz Biotechnology, Santa Cruz, CA, USA), and incubated overnight at 4°C. Then HP-linked secondary antibodies against anti-mouse IgG (1:1000, GE Healthcare Biosciences) were incubated for 1 h at room temperature. Detection was carried out with a chemiluminescence-based method using the ECL Plus western blotting detection system (GE Healthcare Biosciences).

III. RESULTS

Testis ultrastructure

The control testis of SD rats showed no any abnormal change (Fig1A). These were some degree injures in the

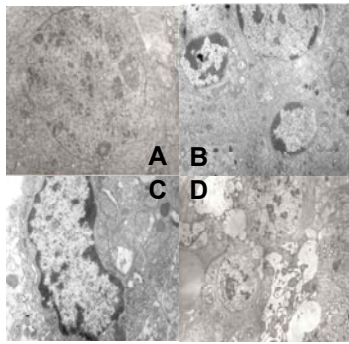


Fig1 The Ultrastructure of rat testis (A,B,C,D).A:Control, normal spermatogonium cells; B,C: At 24h after irradiation, chromatin gathered in the border of the spermatogonium cells and the interstitial cells;D: At 24h after irradiation, endoplasmic reticulum (ER) was dilated and vacuolated in sustentacular cells and interstitial cells

testis at different time after radiation, the testis damage at 24h was serious than that at the other times after radiation. At 24h after exposure, the chromatin was gathered in the border (Fig.1B,C) and the endoplasmic reticulum (ER) was dilated and vacuolated (Fig1D) in interstitial cell, spermatogonium cell of rat testis. The changes in sustentacular cell showed more serious than the other cells.

Changes of FSH,LH and T of serum

After 3×10^6 and 4×10^6 pulses radiation, FSH in the serum didn't change obviously (Table 1), LH and T in the serum of the radiation groups were changed fluctuatedly. After 4×10^6 pulses EMP irradiation, LH in the radiation group decreased distinctly at 12h ($P=0.006$) and rised at the 8d ($P=0.049$) than that of parallel control respectively(Table 2), T in the radiation group rised distinctly at 6h than that of parallel control ($P=0.008$); T in the radiation group decreased distinctly at 24h ($P=0.001$) and rised at the 7d ($P=0.050$) after 3×10^6 pulses radiation than that of parallel control respectively(Table 3).

Changes of SOD activity and the density of MDA in the rat testis

The activity of T-SOD and MnSOD in rat testis decreased significantly at 24h compared with the control, and the contents of MDA increased significantly at 6h compared with the control after 4×10^6 pulses radiation(Table 4).

Expression of T-SOD and Mn-SOD mRNA

The results of RT-PCR showed that MnSOD mRNA expression decreased than that of control at 24h after irradiation, but, CuZnSOD mRNA expression didn't change after radiation (Fig.2).

Table1 Effects of EMP irradiation on rat serum FSH

($N=6, mIU/ml, \bar{X} \pm s$)

Exposure pulses	Time after irradiation	Control	Irradiation	P
3×10^6 pulses	6h	2.088±0.444	2.193±0.418	0.730
	12h	2.200±0.444	2.052±0.433	0.608
	24h	1.660±0.344	2.002±0.917	0.457
	48h	1.962±0.694	2.044±0.462	0.831
	7d	1.962±0.964	2.046±0.774	0.861
4×10^6 pulses	6h	1.750±0.489	1.542±0.303	0.456
	12h	1.883±0.338	1.700±0.355	0.484
	24h	1.660±0.313	1.545±0.812	0.828
	8d	1.660±0.240	1.512±0.109	0.245

P value : vs parallel Control

Table2 Effects of EMP irradiation on rat serum LH

($N=6, \bar{X} \pm s, mIU/ml$)

Exposure pulses	Time after irradiation	Control	Irradiation	P
3×10^6 pulses	6h	6.126±2.265	6.450±1.948	0.827
	12h	7.248±3.032	5.872±2.927	0.486
	24h	6.810±1.475	6.978±3.687	0.927
	48h	7.142±2.284	5.252±2.799	0.276
	7d	6.976±1.821	4.886±2.687	0.096
4×10^6 pulses	6h	5.398±2.211	5.790±2.819	0.834
	12h	6.398±1.593	2.820±1.412 ^b	0.006
	24h	3.702±1.664	2.888±1.351	0.393
	48h	7.142±2.284	4.128±1.302	0.052
8d	2.703±0.719	4.498±1.353 ^a	0.049	

Table3 Effects of EMP irradiation on rat serum T

($N=6, \bar{X} \pm s, \mu g/dl$)

Exposure pulses	Time after irradiation	Control	Irradiation	P
3×10^6 pulses	6h	146.534±129.924	172.488±202.527	0.821
	12h	218.192±162.155	325.183±170.131	0.368
	24h	472.180±170.887	120.965±61.641 ^b	0.001
	48h	282.086±312.136	134.052±89.951	0.338
	7d	139.687±98.332	585.072±297.244 ^a	0.050
4×10^6 pulses	6h	83.560±11.567	242.876±84.68 ^b	0.008
	12h	123.493±123.793	140.086±77.312	0.812
	24h	171.840±115.204	220.535±111.296	0.522
	48h	175.480±125.241	156.590±33.111	0.783
8d	118.383±52.556	95.828±74.779	0.676	

P value : vs parallel Control

Table4 Changes of T-SOD and MnSOD activity in rat testis after EMP exposure

($n=6, \bar{X} \pm s$)

Group	T-SOD activity (U/mg·prot)	MnSOD activity (U/mg·prot)	MDA density (nmol/mg·prot)
Control	298.01±37.63	99.34±12.54	8.52±1.26
6h	273.37±29.92	91.12± 9.97	10.12±1.30 ^a
12h	294.94±29.49	98.31± 9.83	7.32±0.74
24h	255.67±17.66 ^a	85.22± 5.89 ^a	9.04±1.33
48h	308.78±47.87	102.93±15.96	8.46±0.31
1w	297.47±33.25	99.16±11.08	6.76±1.35

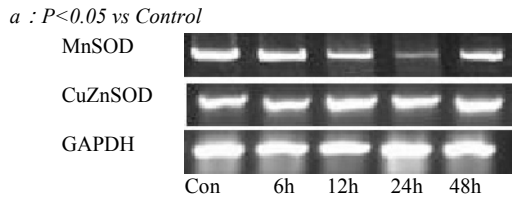


Fig2 The gene expression of MnSOD and CuZnSOD analyzed by RT-PCR

Changes of NF κ Bp65 and I κ B α protein in rat testis

The protein of NF κ Bp65 and I κ B α in rat testis didn't change obviously after 4×10^6 pulses radiation (Fig3) and also the protein of nuclear NF κ Bp65 and I κ B α protein in rat testis didn't change obviously after EMP irradiation (Fig4).

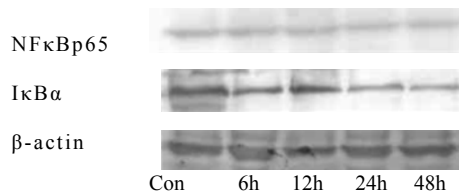


Fig3 Expression of NF κ Bp65 and I κ B α protein of the rat testis

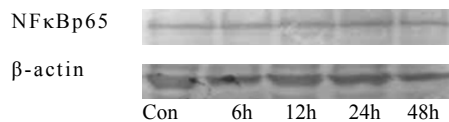


Fig4 Expression of nuclear NF κ Bp65 protein of the rat testis .

IV. DISCUSSION

The authors demonstrate here that the morphology was damaged and the function and metabolism of procreative system were altered at some extends on the male rats after exposed to EMP irradiation. Depend on this experiment, EMP induced indiscriminate hormone secretion and excessive free radicals and over expression of some genes in the male procreative tissue played some roles directly or indirectly for the bioeffects.

The results showed that the MnSOD gene expression was decreased and the ultrastructure of rat testis were damaged after exposed to electromagnetics. These changes may induce the other effects, and the change of MnSOD expression might reflect a defensive mechanism of rat body against oxidative stress. If these changes wouldn't regain in time, it may cause the worse effects. Thus, EMR could

induce some changes in the testis of rats so as to alter the procreative function.

SOD, a primary antioxidant enzyme, scavenges reactive free radicals by catalyzing the dismutation of superoxide anion (O $_2^-$) into molecular oxygen and peroxide^[9]. In mammals, three isozymes of SOD have been identified: mitochondrial manganese SOD (MnSOD), cytosolic copper/zinc SOD (CuZnSOD), and a high molecular weight extracellular SOD^[10]. Because harmful superoxide radicals are produced in the mitochondria and cause mitochondrial DNA damage^[11], mitochondrial-mediated free radical generation is a key event in apoptosis^[12]. MnSOD is localized in the mitochondria, and it can scavenge free radicals by catalyzing the dismutation of superoxide anion into molecular oxygen and hydrogen peroxide^[13]. In this study, MnSOD mRNA expression decreased at 24h, CuZnSOD mRNA expression didn't change after radiation, the ratio of MnSOD/CuZnSOD decreased at the 24h after radiation. Therefore, it is suggested that the change of MnSOD is might reflect a defensive mechanism of rat body against oxidative stress.

Cellular metabolism produces highly reactive free radicals such as superoxide anion (O $_2^-$), hydrogen peroxide(H $_2$ O $_2$), and hydroxyl radical(OH \cdot) in mammals. These reactive free radicals have wide-ranging effects on cells and tissues, including the degradation of hyaluronic acid and collagen in the extracellular matrix, the peroxidation of cell membrane lipids, and denaturing of enzymes, protein, and nucleic acids^[14]. As a defensive mechanism, some antioxidant enzymes, including SOD, catalase, glutathione peroxidase, and xanthine oxidase, are involved in the elimination of free radicals^[15]. If there were no balance of these systems in the body, the cells of the body would change from the morphology and function. There were some degree injures in the testis at different time after radiation, the testis damage at 24h after radiation was the most serious time than it at the other times after radiation.

The testis is a cell renewal system and sensitive to radiation and some damage. The metabolism of testis is very quickly and the mild damage would be recovered about 2 months later. But it didn't recovery at 48h after irradiation. The morphology and metabolism was damaged to cause the disordered function of testis, then the hormone secretion lost the normal function, and LH and T which can keep the male procreative ability changed fluctuantly.

Uckun,F.M.^[16] and Holian,O^[17] et al found electromagnetic fields stimulates the activity of Protein kinase C(PKC) and Protein Tyrosine K(PTK). As we know PKC and PTK are important in the regulating the activity of NF κ B^[18], and also NF κ B is important in the course of apoptosis^[19]. But with western blotting ,NF κ Bp65 and I κ B protein didn't change in the rat testis after irradiation,maybe the irradiation

tion parameter couldn't affect expression level of NF κ Bp65 and I κ B protein or through another pathway to affect the testis function.

Roy-S^[20], Gonet-B^[21], Jin Y^[22], Lai-H^[4] reported that EMR could induce free radicals to lead to a series of chain reaction inducing other effects. EMR can impact on the enzymes, membrane receptor and gene expression to have it rising or decreasing. Thus many researchers considered that cell communication system might be one of targets for various types of electromagnetic radiation. EMR, as a information, may be activate the enzyme system chain reaction of controlling metabolism, messenger and cell growth to impact on the various genes expression.

Further investigations are necessary to elucidate the roles of these antioxidant enzymes or free radicals caused by EMP exposure to affect the procreative system.

CONCLUSION

The morphology was damaged and the function and metabolism of procreative system were altered were decreased on the rats after exposed to EMP. Depend on this experiment, EMP induced indiscriminate hormone secretion and excessive free radicals and over expression of some genes in the male procreative tissue played some roles directly or indirectly for the bioeffects. The data from the current study show some effects on the male procreative system of EMP, but the mechanisms of the bioeffects need to be confirmed in the future.

ACKNOWLEDGMENT

This study was supported by National Natural Science Foundation of China (No:60601026) and Natural Science Foundation of Shaanxi(No: 2007C₂67).

REFERENCES

- Adair RK. Ultrashort microwave signals: A didactic discussion. *Aviation, Space, and Environmental Medicine*. 1995; 66: 792-794
- Merritt JH, Kiel JL, Hurt WD. Considerations for human exposure standards for fast-rise time high-peak-power electromagnetic pulses. *Aviation, Space, and Environmental Medicine*. 1995; 66: 586-7589
- Cobb BL, Jauchem JR, Mason PA, Dooley MP, Miller SA, Ziriach JM, Murphy MR. Neural and behavioral teratological evaluation of rats exposed to ultra-wideband electromagnetic fields. *Bioelectromagnetics*. 2000 Oct; 21(7): 524-37
- Lai-H, Singh NP. Melatonin and a spin-trap compound block radio-frequency electromagnetic radiation-induced DNA strand breaks in rat brain cells. *Bioelectromagnetics*. 1997; 18(6): 446-454
- Blank M, Goodman R (1997): Do electromagnetic fields interact directly with DNA? *Bioelectromagnetics* 1997; 18:111-115.
- Assem M, Teyssier J-R, Benderitter M, et al. Pattern of Superoxide dismutase enzymatic activity and RNA change in rat heart ventricles after myocardial infarction. *Am J Pathol* 1997; 119:493-501
- Su S-B, Motoo Y, Xie M-J, et al. Expression of pancreatitis-associated protein (PAP) in spontaneous chronic pancreatitis in the WBN/Kob rat: effect of herbal medicine Saiko-keishi-to (TJ-10). *Pancreas* 1999; 19:239-47
- Fort P, Marty L, Piechaczyk M, et al. Various rat adult tissues express only one major mRNA species from the glyceraldehyde-3-phosphate-dehydrogenase multigenic family.
- McCord JM, Fridovich I. Superoxide dismutase, an enzymic function for erythrocyte hemocuprin. *J Biol Chem* 1969; 244:6049-55
- Marklund SL. Human copper-containing superoxide dismutase of high molecular weight. *Proc Natl Acad Sci U S A* 1982; 79:7634-8
- Shigenaga MK, Hagen TM, Ames BN. Oxidative damage and mitochondrial decay in aging. *Proc Natl Acad Sci U S A* 1994; 91:10771-8
- Kinoshita KK, Oberley TD, Lom S, et al. Overexpression of superoxide dismutase protects against mitochondria-initiated poly (ADP-ribose) polymerase-mediated cell death. *FASEB J* 1999; 13:1601-10
- Fridovich I. The biology of oxygen radicals. *Science* 1978; 201:875-80
- Czako L, Takacs, Varga IS, et al. Oxidative stress in distant organs and the effects of allopurinol during experimental acute pancreatitis. *Int J Pancreatol* 2000; 27:209-16
- Roy-S, Noda-Y, Eckert-V et al. The phorbol 12-myristate 13-acetate (PMA) induced oxidative burst in rat peritoneal neutrophils is increased by a 0.1 mT (60 Hz) magnetic field. *FEBS-Lett*. 1995 Dec 4; 376(3): 164-166
- Uckun, F.M., Kurosaki, T., Jin J., Jun, X., Morgan, A., Takata, M., Bollen, J., and Luben, R. (1995) Exposure of B-lineage Lymphoid cells to low energy electromagnetic fields stimulates Lyn kinase. *J. Biol. Chem.* 270: 27666-27670
- Holian, O., Astumian, R.D., Lee, R.C., Reyes, H.M., Attar, B.M., and Walter, R.J. (1996) Protein kinase C activity is altered in HL60 cells exposed to 60 Hz AC electric fields. *Bioelectromagnetics* 17:504-509
- Baldwin, A.S. Jr. (1996) The NF κ B and I κ B proteins: New discoveries and insights. *Annu. Rev. Immunol.* 14:649-683
- Imbert, V., Rupec, R.A., Livolsi, A., Pahl, H.L., Traenckner E.B-M., Mueller-Dieckmann C., Farahifar, D., Rossi, B., Auberger, P., Baeuerle, P.A., and Peyron, J-F (1996) Tyrosine phosphorylation of I κ B α activates NF κ B without proteolytic degradation of I κ B α . *Cell*. 86:787-79
- Gonet-B. Effect of a magnetic field on ascorbate system in mice. *Physiol-Chem-Phys-Med-NMR*. 1991; 23(4): 239-245
- Jin Y, Wang H, Cheng Y et al. Effects of static magnetic fields on free radical metabolism of human body. *Wei Sheng Yan Jiu* 1998 Mar; 27(2): 97-9
- Lam M, Dubyak G, Chen LI, et al. Evidence that BCL-2 represses apoptosis by regulating endoplasmic reticulum-associated Ca²⁺ fluxes. *Proc Natl Acad Sci U S A*. 1994 Jul 5; 91(14): 6569-65

Author address

ZENG Lihua, Department of Radiation Medicine, Fourth Military Medical University, ChangLe west road 17, Xi'an, China, lzwei1998@gmail.com

corresponding author: GUO Guozhen, Department of Radiation Medicine, Fourth Military Medical University, ChangLe west road 17, Xi'an, China, guozhen@fmmu.edu.cn

Effect of EMP on lipid peroxidation of human gastric cancer cells MKN28

Yongbin Chen, Guozhen Guo

Department of Radiation Medicine, Faculty of Preventive Medicine,
Fourth Military Medical University, Xi'an, 710032, China
Phone/Fax: (029)84774873, E-mail: tling@fmmu.edu.cn; chen Yongbin2003@hotmail.com

Abstract — AIM To discuss the effect of EMP on lipid peroxidation of human gastric cancer cells MKN28. **METHODS** MKN28 cells were divided into 5 groups (control group, 50, 100, 200, 400kV·m⁻¹ groups), 16 wells for each group. 12 hours after the cell-planting, each group were exposed by 0, 50, 100, 200, 400kV·m⁻¹, respectively. 0, 6, 12, 24, 48h after EMP irradiation, the wells of each group were separated and detected by chemiluminescence analysator. The result was recorded in forms of value of first peak and 5s integral area. The data obtained from the experiment were analyzed by ANOVA. **RESULTS** compared with control group, the chemoluminescence intensity (value of first peak and 5s integral area) of 50, 100kV·m⁻¹ irradiation groups (0, 6, 24h after irradiation) and 200, 400kV·m⁻¹ irradiation groups (0, 6, 12, 24, 48h after irradiation) decreased significantly ($p < 0.01$). **CONCLUSION** Certain EMP irradiation can significantly decrease the level of lipid peroxidation of human gastric cancer cells MKN28.

Keywords — EMP; chemiluminescent; gastric cancer cell; MKN28 cell; oxygen free radical

I. INTRODUCTION

With the development of electromagnetic waves technique, the sorts and intensity of spatial electromagnetic radiation increases rapidly. So far, as a new sort of environmental pollution, electromagnetic radiation widely exists in our everyday life and work environment and has been paid close attention to^{[1],[2]}. Electromagnetic pulse (EMP), as instantaneous electromagnetic waves, can not only interfere and destroy electronic telecommunication equipment terribly, but also bring about some lesion to living body^[3]. Therefore, the study of its biological effect has been paid wide attention to. Some data indicates that simulative EMP can affect mammal's nervous system, immune system, Endocrine system, cardiovascular system and genital system. Chen's experiment^[4] indicated that certain intensity's irradiation of EMP on human umbilical vein (ECV-304 cell) can increase the level of lipid peroxidation and free radical. Few articles about EMP's effect on tumor lipid peroxidation have been reported.

With the quick development of photon detection technique, people found that all the organism, from cell to human being, can give off a kind of extremely weak spectro-

flow, named super weak luminescence or bioluminescence^{[5],[6]}. Biologic chemoluminescence means that chemical reaction makes reaction products to their excited states, and if they have the ability to give off fluorescence, they can give off photon, or they can rely on energy transfer mechanism and transfer the excitation energy to adaptor molecule which can give off photon in the end. Bioluminescence usually means a kind of chemoluminescence phenomenon which is joined by enzymes^{[7],[8]}. Bioluminescence has close relation with oxidative metabolism, deintoxication, cell division, cell death, photosynthesis, carcinogenesis and growing adjusting process. And on some level, bioluminescence has relation with free radical's chain oxidation reaction.

In our study, human gastric carcinoma cell MKN28 was used. Using biochemiluminescence detection method, we observed the effect of EMP on lipid peroxidation of human gastric cancer cell MKN28.

II. MATERIALS AND METHODS

2.1 Cells and grouping Human gastric cancer cells MKN28 were provided by Department of pathology, Fourth Military Medical University. The cells were cultivated by RPMI 1640 (10% FCS) and planted into cell culture wells (100·L, 1.5×10⁵·mL⁻¹, 37°C, 5% CO₂). The cells were divided into 5 groups (control group, 50, 100, 200, 400kV·m⁻¹ groups), 16 wells for each group.

2.2 Dealing with the cells 12 hours after the cell-planting, each group were exposed to 0, 50, 100, 200, 400kV·m⁻¹ EMP, respectively.

2.3 Main equipments and reagents EMP emulator (manufactured by Mian Yang Ninth Academy, Southeast University and Fourth Military Medical University); IFFM-D flow injection chemiluminescence analysator (manufactured by Rui-Mai electron technology limited company, Xi'an); luminal (Sigma), RPMI 1640 (Sigma), FCS (Sigma), H₂O₂.

2.4 Radiation parameter Electric field intensities were 50, 100, 200, 400kV·m⁻¹; interval time was 3s; pulse number of time was 200.

2.5 Experiment methods 0, 6, 12, 24, 48h after EMP irradiation, the wells of each group were separated and detected by IFFM-D flow injection chemiluminescence analyser. Firstly, we inject 50 μ L 5×10^{-6} mol \cdot L $^{-1}$ luminol to a well. Secondly, we inject 50 μ L 0.0078% H₂O₂ to the same well and then, the result was recorded in forms of value of first peak and 5s integral area. All the samples were detected with the same method.

2.6 Statistical method ANOVA.

III. RESULTS

The effect of EMP on MKN28 cells' lipid peroxidation can be indicated by the result of chemoluminescence intensity (value of first peak and 5s integral area).

3.1 The comparison of value of first peak (Table 1.):

After EMP's irradiation, compared with control group: ①0, 6, 24h after irradiation: 50, 100, 200, 400kV \cdot m $^{-1}$ groups decreased significantly ($p < 0.01$); ②12h after irradiation:

Table 1. MKN-28 cells' chemoluminescence intensity after EMP irradiation (value of first peak) ($\bar{x} \pm s, n=16$)

Intensity	Time point after irradiation				
	0h	6h	12h	24h	48h
0 kV \cdot m $^{-1}$	2595 \pm 1293	5341 \pm 1457	1231 \pm 432	580 \pm 196	991 \pm 460
50 kV \cdot m $^{-1}$	1467 \pm 583 ^a	3119 \pm 1379 ^a	1275 \pm 498	389 \pm 143 ^a	760 \pm 370
100 kV \cdot m $^{-1}$	1186 \pm 378 ^a	3357 \pm 837 ^a	982 \pm 314	245 \pm 105 ^a	532 \pm 160 ^a
200 kV \cdot m $^{-1}$	967 \pm 255 ^a	2296 \pm 751 ^a	701 \pm 246 ^a	212 \pm 55 ^a	455 \pm 359 ^a
400 kV \cdot m $^{-1}$	688 \pm 299 ^a	2203 \pm 465 ^a	569 \pm 193 ^a	309 \pm 167 ^a	349 \pm 199 ^a

^a $p < 0.01$, vs. control group

Table 2. MKN-28 cells' chemoluminescence intensity after EMP irradiation (5s integral area) ($\bar{x} \pm s, n=16$)

Intensity	Time point after irradiation				
	0h	6h	12h	24h	48h
0 kV \cdot m $^{-1}$	273855 \pm 153960	561663 \pm 160144	121174 \pm 42422	57462 \pm 19827	99331 \pm 47286
50 kV \cdot m $^{-1}$	156811 \pm 68336 ^a	318129 \pm 144729 ^a	126506 \pm 51373	38280 \pm 14225 ^a	76620 \pm 37252
100 kV \cdot m $^{-1}$	125432 \pm 41913 ^a	343857 \pm 94974 ^a	98400 \pm 32290	22979 \pm 10235 ^a	54044 \pm 15674 ^a
200 kV \cdot m $^{-1}$	102239 \pm 27069 ^a	230125 \pm 75731 ^a	67249 \pm 24114 ^a	20760 \pm 5261 ^a	44313 \pm 30005 ^a
400 kV \cdot m $^{-1}$	72392 \pm 33167 ^a	216016 \pm 46806 ^a	57763 \pm 16376 ^a	29821 \pm 16265 ^a	35391 \pm 19822 ^a

^a $p < 0.01$, vs. control group

tion: 200, 400kV·m⁻¹ groups decreased significantly ($p<0.01$); ③48h after irradiation: 100, 200, 400kV·m⁻¹ groups decreased significantly ($p<0.01$).

3.2 The comparison of 5s integral area (Table 2.):

After EMP's irradiation, compared with control group: ①0, 6, 24h after irradiation: 50, 100, 200, 400kV·m⁻¹ groups decreased significantly ($p<0.01$); ②12h after irradiation: 200, 400kV·m⁻¹ groups decreased significantly ($p<0.01$); ③48h after irradiation: 100, 200, 400kV·m⁻¹ groups decreased significantly ($p<0.01$).

IV. DISCUSS

Under physiological condition, body can continually generate and erase endogenous oxygen free radical, which is a kind of dynamic balance situation. When body is stimulated by outside stimulus, oxygen free radical can occur in few microseconds, which can change the systems of erasing oxygen free radical, including some kinds of enzymatic system and un-enzymatic system. Oxygen free radical can attack the unsaturated fatty acid in cellular membrane, which can increase the content of lipid peroxidation material to injure the tissue and cells. So, biomolecules' injury has very close relation with the generation of oxygen free radical. Chemoluminescence detection method has so many features such as easy-operating, high-sensibility. Therefore, it's a kind of reliable method to study and research the level of lipid peroxidation and the content of oxygen free radical.

In this study, MKN28 cells was exposed to EMP (200 pulses, 50, 100, 200, 400kV·m⁻¹). After EMP's irradiation, at certain time points, using biochemiluminescence detection method, we detected the chemoluminescence intensity of MKN28 cells, so that we could identify the effect of

EMP on lipid peroxidation of human gastric cancer cells MKN28.

In this study, we found that: compared with control group, the chemoluminescence intensity (value of first peak and 5s integral area) of 50, 100kV·m⁻¹ irradiation groups (0, 6, 24h after irradiation) and 200, 400kV·m⁻¹ irradiation groups (0, 6, 12, 24, 48h after irradiation) decreased significantly ($p<0.01$). The reason for this probably is that the EMP in our study stimulated MKN28 cells to occur excitatory effect, which could sharply increase the ability of erasing oxygen free radical.

Our study indicated that certain EMP irradiation can significantly decrease the level of lipid peroxidation of human gastric cancer cells MKN28.

REFERENCE

1. Repacholi MH. Low-level exposure to radiofrequency electromagnetic fields: health effects and research needs. *Bioelectromagnetics*. 1998;19(1):1-19.
2. Knave B. Electromagnetic fields and health outcomes. *Ann Acad Med Singapore*. 2001 Sep;30(5):489-93.
3. Naarala J, Höytö A, Markkanen A. Cellular effects of electromagnetic fields. *Altern Lab Anim*. 2004 Oct;32(4):355-60.
4. Chen Yongbin, Zhao Tao, Zhang Jie. Influence of THP on the effect of EMP on ECV-304 cells' chemoluminescence intensity. *J. Electromagnetic radiobiology (internal)*. 2004, 5(2): 185-189.
5. Roda A, Pasini P, Mirasoli M, Michelini E, Guardigli M. Biotechnological applications of bioluminescence and chemiluminescence. *Trends Biotechnol*. 2004 Jun;22(6):295-303.
6. Hesselink JW, van Dam GM. Bioluminescence: the potential of a molecular non-invasive biooptical imaging technique and improvement of animal research. *Tijdschr Diergeneeskd*. 2007 Apr 1;132(7):244-50.
7. Chen Che. *Cytochemoluminescence and disease*. Overseas medical science, surgery fascicle. 2001, (8)4:195-196
8. Zhu Yonbfei, Wang Yongshun, Yuan Jinwei, etc. Using chemoluminescence method to detect NO released by cultured cells. *Journal of China hygiene inspection*. 2000, (10)3: 277-279

Effects of electromagnetic pulse on the vimentin of mice testes

Xiao-Wu Wang¹, Chang-Hong Shi², Gui-Rong Ding¹, Tao Zhao¹, Li-Hua Zeng¹, Jie¹ Zhang, Xue-Jun Xie¹, Guo-Zhen Guo¹

¹Department of Radiation Medicine, Faculty of Preventive Medicine, Fourth Military Medical University, Xi'an, China

²Lab animal center, Fourth Military Medical University, Xi'an, China

Abstract — AIM To investigate the changes of the mice testes and the tight junction (Tj) relative molecular and to identify the molecular mechanisms of the mice blood- testis-barrier (BTB) permeability increasing after the mice were exposed to electromagnetic pulse (EMP). METHODS Observe the changes vimentin of the mice testes by laser scanning confocal technique. RESULTS After the 200kVm⁻¹ EMP (the accumulative pulse times was 200) exposure, the vimentin in sustentacular cells of testis became irregularly shortened and derangement, and the intensity of immuno- fluorescence also showed uniformity compared with control. CONCLUSION The increasing of mice BTB permeability perhaps caused by the changing of vimentin.

Keywords — electromagnetic pulse(EMP), vimentin, testicle, mice

I. INTRODUCTION

The BTB (Blood-testicle barrier) which formed by Sertoli cells of testicle tissue, not only relates to TJ(Tight Junction)-associated protein, but also relates to cytoskeleton of Sertoli cells. Vimentin is a kind of skeleton protein in sertoli cells which has a intimate relationship with TJ of BTB, its quantity and tendency have direct effects on BTB permeability.

This study was designed to observe the vimentin changes of the mice testes by laser scanning confocal technique (LSCM) after the mice were exposed to electromagnetic pulse (EMP), then to identify which role the vimentin playing in the EMP effects on BTB.

II. MATERIAL AND METHODS

Laboratory animal:

Male BALB/c mice (12±1g), 15-day-old (provided by Laboratory Animal Center, Fourth Military Medical University).

Irradiation condition:

EMP at 200kV/m for 200 pulses, mice were randomly divided into control and exposure groups, the control group was undertaken fake irradiance, while the exposure groups were put in EMP Generator radiation field

Culture and identification of mice primary sertoli cell:

Primary Sertoli cells were isolated from 15-day-old Sprague-Dawley rats as previously described[1,2]. Freshly isolated sertoli cells were cultured at high cell density (0.5×10^6 cells/cm²) on matrigel-coated 12-well dishes in serum-free ham F12 nutrient mixture and dulbecco modified eagle medium (DMEM) as described. Cells were then incubated at 35-38°C in a humidified atmosphere of 95% air: 5% CO₂ (v/v). Cultures were terminated at specified time points for identification of mice testes[3]. Then undertook vimentin and cellular nucleus double-standard dyeing, and observed by laser scanning confocal microscope. After HE dyeing the morphological characteristic of sertoli cells was observed by microscope.

III. RESULTS

Identification of mice primary sertoli cells

(1) The morphological characteristic of sertoli cells: 48h after cultured, sertoli cells became accrescent and paved on culture flask as membraniform, cellular nucleus appeared round or ellipse shape, located centre or dissymmetry slightly, nucleole observed clearly, and could see more granulo-mass or vacuole in cytoplasm, ephyma had grown in number and interlaced intensively (fig.1, fig.2).

(2) Feulgen dyeing: Feulgen dyed 8-day-culture sertoli cells, its cytoplasm wasn't colored, nucleoli was colored lightly, intranuclear had colored grana as satellite nucleosome around nucleoli (fig.3).

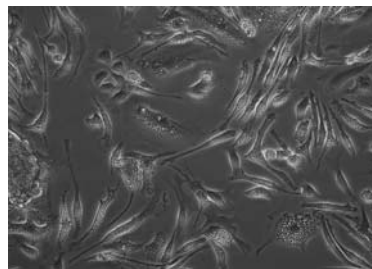


Fig.1 observation of 7-day-culture Sertoli cells by inverted phase contrast microsc (×200)

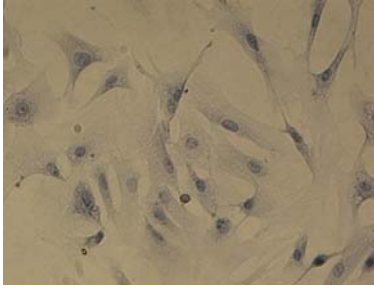


Fig.2 observation of 7-day-culture Sertoli cells by HE dyeing ($\times 200$)

(3)The expression of Fas-L: Fas-L were high level expression on the sertoli cells^[5], while fibroblast and sperm cells can't express, so Fas-L maybe used as marker for identification sertoli cells (fig.4) .

The effects on vimentin of sertoli cells by EMP irradiation: Experimental results showed that the primary sertoli cells of control group could express vimentin well, which presented radiate extension from cytoplasm which around nucleus to ambient cell membrane, the length, shape and coloration of colored vimentin micro-filament were uniformity(fig.5). After exposed to EMP at 200kV/m for 200 pulses, the length and coloration of sertoli cells' vimentin had some extent changes at different time point, and showed some derangement: 1h after EMP exposure, part of vimentin microfilament changed short, length and coloration became ununiformity(fig.6); 2h after EMP exposure, more proportional vimentin microfilament changed short and coloration became weaken(fig.7); 6h after EMP exposure, the length of vimentin microfilament had some extent increase, the length and color get close to control group(fig.8).

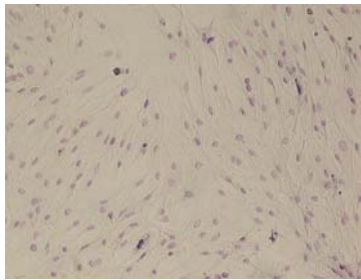


Fig.3 observation of 7-day-culture Sertoli cells by Feulgen dyeing ($\times 100$)

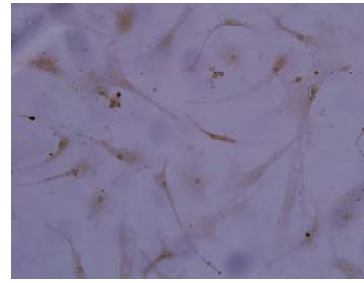


Fig.4 observation of 7-day-culture Sertoli cells by Fas-L immunohistochemistry dyeing ($\times 200$)

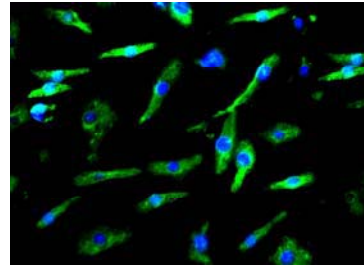


Fig.5 the expression of vimentin of control mice Sertoli cell ($\times 200$)

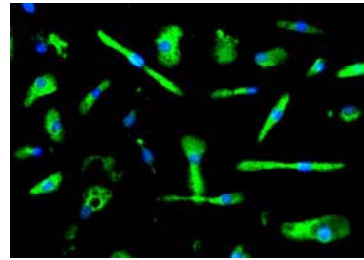


Fig.6 1 hour after EMP exposure, the expression of vimentin of Sertoli cell ($\times 200$)

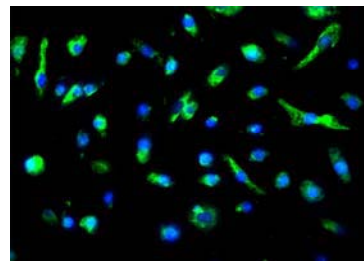


Fig.7 2 hour after EMP exposure, the expression of vimentin of Sertoli cell ($\times 200$)

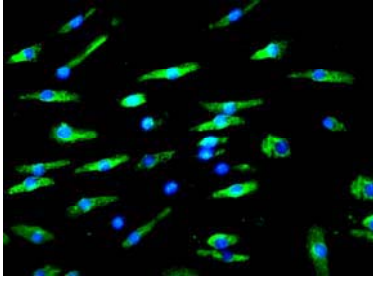


Fig.8 6 hour after EMP exposure, the expression of vimentin of Sertoli cell ($\times 200$)

IV. CONCLUSIONS

Sertoli cells is the main stroma-cell of testicle. Its basilar part links convoluted seminiferous tubules basal membrane, and another end outpocket to convoluted seminiferous tubules lumina. One sertoli cell connect with 5~6 circum-sertoli cells ephyma, and spermatogenic cell are packaged in sertoli cells cytoplasm. Different development stage of spermatogenic cell can be observed, the amount reaches 40~50 for every sertoli cell. Sertoli cells play a definitive role in male procreates function. It provides microenvironment for spermatogenic cell's differentiation and mature, it secretes many kinds of materials that can effect on its surrounding and itself [4].

Vimentin construct sertoli cells' cytokelet and plays an important role in spermateliosis process. Vimentin and cytokeratin are two kinds of interzonal fiber proteins, which reside in epithelium tissue and interstitium-derived cells respectively[5]. It is reported that normal mature sertoli cells have only express vimentin[6]. During the development of rat testicle, vimentin is the only interzonal fiber protein in Sertoli cells., though Sertoli cells express cytokeratin for some time, it will disappear at 15 days after birth^[9]. Vimentin spread around nucleus. It is not only relative with cell morphology, sperm secretion and so on exterior and interior cellular movement, but also with cell signal transduction and cell apoptosis. The changes of vimentin expression and tendency can lead to sertoli cells morphology changes, accordingly, may cause changes of TJ between sertoli cells, then result in permeability of BTB take place changes finally [7]. So, observation of changes about vimentin's quantity and tendency after expose to EMP that can provide theory base for mechanism of BTB permeability increasing after exposed to electromagnetic pulse (EMP).

In this study it had taken place some extent changes for the tendency of mice testicle sertoli cells' vimentin after exposed to EMP at 200kV/m for 200 pulses at different time point. Compared with control group, tendency of vimentin

appears some extent disorder at 1h, 2h, 6h after expose to EMP respectively, and between different exposure group no apparent different are observed. It main due to electromagnetic field can generate corresponding biological effect through create non-caloric effect on organism. A fairly slender stimulate of electromagnetic field energy can lead to organism target organ's strong responds. This kind of nonlinear appearance is similar to immunologic responses. This kind of strong respond may be the specific mechanism belonged to organism target organ's definite structure and system. It released when exposed to suitable stimulation conditions from external environment, this stimulation has only played a trigger or torch role, and it is the slender electromagnetic field in this paper.

So this experimental results showed, some extent intensity of electromagnetic radiation effects on expression of sertoli cells vimentin, which maybe one of reasons about electromagnetic radiation lead to permeability changes of BTB. The relationship between vimentin and TJ-associated protein after expose to EMP, and their regulation mechanism which EMP result in, expect to further investigation.

ACKNOWLEDGMENT

This study was supported by Natural Science Foundation of Shaanxi (No: 2007C267) and by National Natural Science Foundation of China (No: 60601026)

REFERENCES

1. Cheng CY, Mather JP, Byer AL, Bardin CW. (1986) Identification of hormonally responsive proteins in primary Sertoli cell culture medium by anion-exchange high performance liquid chromatography. *Endocrinology*.118:480-488.
2. Grima J, Zhu LJ, Cheng CY. (1997) Testin is tightly associated with testicular cell membrane upon its secretion by Sertoli cells whose steady-state mRNA level in the testis correlates with the turnover and integrity of inter-testicular cell junctions. *J Biol Chem*.272:6499-6509.
3. Galdieri M, Ziparo E, Palombi F, Russo MA, Stefanini M. Pure (1981) Sertoli cell cultures: a new model for the study of somatic-germ cell interactions. *J Androl*.5:249-259.
4. Lui WY, Lee WM, Cheng CY. (2001) Transforming growth factor perturbs the inter-Sertoli tight junction permeability barrier in vitro possibly mediated its effects on occludin, zonula occludens-1, and claudin-11. *Endocrinology*.142:1865-1877.
5. Jiang Y, Jahagirdar BN, Reinhardt RL, et al. (2002) Pluripotency of mesenchymal stem cells derived from adult marrow. *Nature*. 418 (6893):41

6. Snael J, Shoeman R, Hoeji M, et al. (1999) Cleavage of vimentin by different retroviral proteases [J]. Archives of Biochemistry and Biophysics.377 (2):241-245
7. Franke WW, Grund C, Schmid E. (1979) Intermediate- size filaments present in Sertoli cells are of the vimentin type. Eur J cell Biol.19:26

Author: Guo Guo-zhen
Institute: Department of Radiation Medicine, Faculty of Preventive
Medicine, Fourth Military Medical University
Street: 169 Changle west Lu St
City: Xi'an
Country: China
Email: guozhen@fmmu.edu.cn

Study on behavior of male rat 3 months after electromagnetic pulse irradiation

Yu-Hong Qi^{1,2}, Dong-Qing Ren¹, Xiao-Ming Su¹, Li Zhang¹, Kai-Dong Liu¹, Guo-Zhen Guo¹

¹Department of Radiation Medicine, Fourth Military Medical University, Xi'an, China,

²Department of Radiotherapy, Tangdu Hospital; Fourth Military Medical University, Xi'an, China

¹Abstract — AIM: The present paper investigated the effect on open-field behavior of male rat 3 months after electromagnetic pulse irradiation. **MATERIALS AND RESULTS:** Mature male rats were randomly divided into control group, 100P irradiation group and 1000P irradiation group. Rats in the EMP irradiation group were exposed to EMP. The field intensity was 100KV/m with 100 pulses and 100KV/m with 1000 pulses. The changes of behavior were observed with open-field test in rats 3 months after electromagnetic pulse irradiation. Accumulative Distance (AD), Accumulative Time (AT), AD of Walking, AT of Walking, AD of Resting, AT of Resting were recorded. Analysis of open-field test indicated that the activity of the EMP irradiation group has a significant decrease compared with control group ($P < 0.05$). And it was also indicated that there are no significantly difference between 100P irradiation group and 1000P irradiation group. **CONCLUSION:** It is inferred that Electromagnetic pulse irradiation can cause some disorders of behavior of rats, which may induce a significant decrease in the activity in rats 3 months after EMP irradiation.

Keywords—electromagnetic pulse (EMP); SD rat; behavior; Open-field.

I. INTRODUCTION

With the development of electromagnetic waves technique, the sorts and intensity of spatial electromagnetic irradiation increases rapidly. So far, as a new sort of environmental pollution, electromagnetic irradiation widely exists in our everyday life and work environment which may have potential damaging effects on living organisms. Electromagnetic pulse(EMP) is a special kind of electromagnetic irradiation which is produced as short high-voltage pulses with an extremely fast rise, providing for the spectral bandwidth from 0 Hz to 1.5GHz. The unusual properties of EMP have raised concerns about its bio-effects and possible health hazards to personnel. EMP can not only interfere and destroy electronic telecommunication equipment terribly, but also bring about some lesion to living body. Therefore, the study of its biological effect has been paid wide attention to. Some data indicates that simulative EMP can affect mammal's nervous system, immune system, endocrine system, cardiovascular system and genital system. However, there is still little information on its impaired

effects to human body on account of many reasons. Thus, there are extremely important military significance and pragmatic value to study on the bio-effects on EMP, especially its effects on behavior in mammal. In this assay, we observed the changes of the activity of rats 3 months after EMP irradiation in open-field test to explore the effects of EMP exposure on the function of the behavior of the rats.

II. MATERIALS AND METHODS

A. Animals and Electromagnetic Pulse Exposure

All animal experiments were performed in accordance with our institutional guidelines after obtaining the permission of the Laboratory Animal Committee. The experiments in the present study were designed to minimize the number of animals used and their suffering.

30 seven- to eight-week-old Sprague-Dewley rats (provided by Animal Center, Fourth Military Medical University) weighing 210~250g were kept at standardized room conditions. They were randomly divided into 3 groups including control group (n=10), 100P EMP irradiation group (n=10) and 1000P EMP irradiation group (n=10) after one week's feeding for accommodation.

The irradiated animals were placed in plastic irradiation capsules and exposed to EMP kept for 1 hour in liber body posture. The field intensity was 100KV/m with 100 pulses (100Pgroup) and 100KV/m with 1000 pulses(1000Pgroup). The animals in control group were placed in the same condition without EMP exposure.

B. Behavioral testing

The open-field test [^{1,2}] was performed as a measure of locomotor's activity, exploratory behavior, and habituation to novelty. The open-field apparatus consisted of a wooden square box measuring 100x100 cm with surrounded by 50-cm high black colored walls. It was illuminated by 1 shadowless lamp (100 W) positioned at a height of 100 cm above the center of the field. The floor of the box was marked into 32 segments by three concentric rings and four lines radiated from the center. At 3 months after EMP irradiation, each rat was tested individually and only once, testing order of individuals was randomized over the control

¹ corresponding author: Guo Guo-Zhen

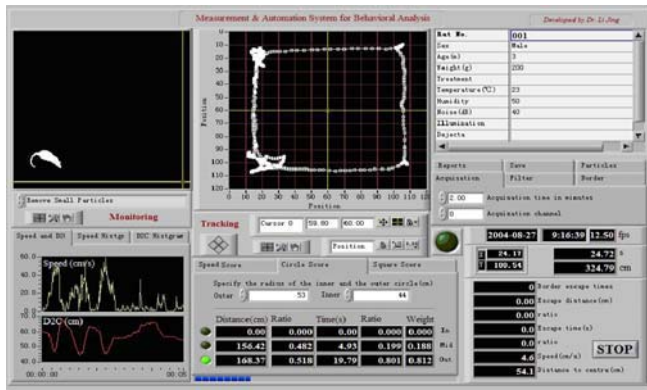


Fig. 1. Measurement and Automation System for rat behavioral analysis in Open-field test

group and the 2 irradiation groups. To begin the test, each rat was gently placed on the center of the field and its behavior was recorded for 5min (Accumulative Time) (AT) using circuit television system with a video camera suspended approximately 1.8m directly above the open field. This arrangement made certain that the experimenter was completely hidden from the rat's view during the test. The open field test was performed in a separated room with no interference of noise and maintained at an ambient temperature. Because defecation occurred during test, following completion of the test, the floor was wiped clean before reuse of the next test. All behavioral testing was performed between 09:00 and 12:00 am. In the current study the following parameters were recorded: (1) Accumulative Distance traveled (AD), (2) Accumulative Distance of Leaving the Border (AD_{LB}), (3) Accumulative Distance in the User Defined Area (AD_{UDA}), (4) AD outside the Outer Circle (AD_{OC}), (5) AD Between the Two Circles (AD_{BTC}), (6) AD inside the inner circle(AD_{IC}), (7) AD of Walking, (8) AT of Walking (AT_{WALK}), (9) AD of Resting (AD_{REST}) and (10) AT of Resting (AT_{REST}). The locomotor's activity was counted immediately using video camera. Dates were recorded and automated analysis by software as Figure 1.

C. Statistical analysis

The results of open-field test were processed using one-way and two-way ANOVA using SPSS 13.0 software and presented as ($\bar{x} \pm s$). Differences were considered statistically significant at P<0.05.

III. RESULTS

A. Behavioral measures

The spontaneous activity, exploratory behavior, and habituation to novelty were examined in rats from all 3 groups. Both of the irradiation group rats had significant reduction in Accumulative Distance (AD), Accumulative Distance of Leaving the Border (AD_{LB}), Accumulative Distance in the User Defined Area (AD_{UDA}), AD outside the Outer Circle (AD_{OC}), AD Between the Two Circles (AD_{BTC}), AD inside the inner circle(AD_{IC}), AD of Walking compared with control group rats, but there is no significant difference in AT of Walking (AT_{WALK}), AD of Resting (AD_{REST}) and AT of Resting (AT_{REST}) in both of the irradiation group rats compared with control group rats. All the parameters did not differ between 100P irradiation group and 1000P irradiation group rats, indicated that the two EMP irradiation-exposed groups seemed to show no significant difference in the activity of Open-Field Test. (Table 1).

Compared with control group, It was easily observed that the activity of rats 3 months after EMP irradiation in open-field test has a significant decrease (P<0.05),but there are no significantly difference between 100P irradiation group and 1000P irradiation group.

Analysis of open-field test indicated that the activity of the EMP irradiation group has a significant decrease compared with control group (P<0.05). And it was also indicated that there are no significant difference between 100P irradiation group and 1000P irradiation group.

Table1 Changes of the activity of rats 3 months after EMP irradiation in open-field test (N=10, $\bar{X} \pm s$)

	Control	100P	1000P
AD (cm)	2139.07±808.33	1302.15±412.76*	1422.76±426.61*
AD _{LB} (cm)	243.83±170.39	127.03±154.85*	114.62±114.07*
AD _{UDA} (cm)	2139.07±808.33	1302.15±412.76*	1422.78±426.21*
AD _{OC} (cm)	1309.71±577.21	798.27±262.88*	760.92±272.71*
AD _{BTC} (cm)	519.65±256.05	334.97±130.16*	452.31±147.50*
AD _{IC} (cm)	309.70±210.09	168.91±198.05*	209.54±201.31*
AD _{WALK} (cm)	1806.86±793.12	939.95±386.01*	1069.82±418.12*
AD _{REST} (cm)	332.21±28.45	362.20±58.53	352.95±44.13
AT _{WALK} (cm)	88.52±38.30	64.64±24.74	70.25±28.68
AT _{REST} (cm)	211.52±38.29	235.40±24.72	229.79±28.67

*P<0.05 vs parallel Control

It is inferred that Electromagnetic pulse irradiation can cause some disorders of behavior of rats, which may induced a significant decrease in the activity in rats 3 months after EMP irradiation.

IV. DISCUSSION

In the recent studies of the biological effect of electromagnetic waves, there are a few researches about interaction between transient electromagnetic field^[3] i.e. pulsed electromagnetic field and organism. Controversy and contradiction still surround the question of whether electromagnetic pulse cause any detectable biological effects, other than those attributable to heating at higher frequencies (microwave or RF range at 10^8 to 10^{11} Hz, e.g. radiation from mobile phones), or to induced electric currents at extremely low frequencies (ELF range at 1–1000 Hz, e.g. surrounding power lines). Several reports have adduced evidence for such effects – both harmful and beneficial – but the vast majority has found no effect whatsoever^[4]. EMP is a super broad spectra system, which means it contains from co current to multi-gigahertz^[5]. The biological effects of transient electromagnetic pulse to organism have many characters as follows. First, when its average power density is near zero, the biological effects of EMP are only concerned with pulse amplitude and width. Second, its effects to organism especially to cells are a nonlinear, transient and instable process, so there are extremely significant effects on EMP to organism^[6].

Open reports about the effects of EMP on the behavior are not yet seen all over the world on account of classifies military information. Up to now, there is a little information on effects of high power pulse microwave to behavior. We have not gotten documents about influence of EMP on behavior in mammal several months after irradiation, but one literature reported that different power density could make different results after rats were exposed to 2450 MHz microwave. Because of different experiments condition, we have not gotten a confirmative conclusion and compared with each result.

The irradiation source we used is one of the transient EMP, whose influence on the body is more obvious than continuous wave. In our experiment we observed that com-

pared with control group, the activity of rats 3 months after EMP irradiation in open-field test has a significant decrease ($P < 0.05$), but there are no significant difference between 100P irradiation group and 1000P irradiation group, which indicated irradiation reduced the activity of the rats. It showed that Electromagnetic pulse irradiation can cause some disorders of behavior of rats, which may induce a significant decrease in the activity in rats 3 months after EMP irradiation.

With regard to organism, EMP is an apparent wound agent and it could produce chronic damage to organism. On the basis of the changes of behavior in rats we observed, we think that functional changes were concerned with morphologic changes tightly, so EMP may injury nervous system which leads to decrease organism stress reaction ability to stimulation. Thus, when the powerful stimulation affects organism, EMP exposure has depressed function of nervous system and produce behavioral functional changes. The exact mechanism of the EMP-induced changes in the activity of irradiation rats is not known, which is yet to further study.

ACKNOWLEDGMENT

This study was supported by National Natural Science Foundation of China .

REFERENCES

1. Li Jing, Guo Guo-Zhen, Guo Yao, Wang Jin. Machine vision based measurement and automation system for rat behaviors. Theory and practice of Chinese medicine 2005, 15 (7): 1015 – 1017.
2. Hallam KT., Horgan JE., McGrath C., Norman TR. An investigation of the effect tacrine and physostigmine on spatial working memory deficits in the olfactory bullectomised rat. Behav Brain Res. 2004,153(2), 481-486.
3. Merritt J H, Kiel J L, Hurt W D. Aviat Space Environ Med, 1995, 66(6): 586-586.
4. Reyhan Gul Guven, K. G., Adam Dawe, John Worthington, Christopher Harvell, Amy Popple, Tim Smith, Brette Smith and David I. de Pomerai, 2006.Effects of radio-frequency fields on bacterial cell membranes and nematode temperature-sensitive mutants .Enzyme and Microbial Technology. 39(4), 788-795
5. Meilan ZHAO, Xiaozhe CAO, Dewen WANG, et al. Bulletin of The Academy of Military Medical Sciences, 2001, 25(3): 195-197.
6. Changqing WANG, Xili ZHU. Electron J, 1994, 22(6): 83-87.

Research of Environmental Control systems for Disabled people

Chunjing Tao, Xiaoyu Zhang and Xitai Wang

National Research Center for Rehabilitation Technical Aids, Beijing, China

Abstract — Environmental control system for disabled people has been growing rapidly over the past few years. Environmental control systems not only give disabled persons greater independence, but also provide a way to participate in their life activities and the same time increase the quality of their life. In this paper, we combine different control technologies together to design an environmental control system which is easy to use, cost effective, and can be used by many kinds of disabled people.

Keywords — Environmental control system, different control technologies, disabled people.

I. INTRODUCTION

The area of environmental control for people with a severe disability – such as high level spinal injuries and cerebral palsy has been growing rapidly over the past few years. This is kind of control not only includes the systems designed but also the products from the rapidly expanding environment control. Environmental control systems can provide disabled person with ability to control appliances and devices in hospital, home environment or community-based rehabilitation. The benefits of environmental control systems are consistently reported in the studies. Greater independence is the most common benefit identified. Environmental control systems increase the independence of the disabled persons; provide a way to participate in their life activities and the same time improve the quality of relationship with their relatives. At present, the majority of environmental control systems are expensive and not enough adaptable for persons with different types of disabilities, which results in the decrease of the system functionality and usability. Disabled people often have some difficulties while using environment controls or they are unable to use it at all, so the control technologies used in the system and the use interface should be specialized for the disabled person.

II. REVIEWS OF THE ENVIRONMENTAL CONTROL SYSTEM

A. Considerations for designing an environmental control system

Environmental control systems include house environment control (lighting, heating, shutters, motorized door and windows), entertainment equipments (TV, VCR, DVD and Audio systems) and security control (alarm for detection of intruders and safety alarms). Environmental control systems can be used to control telephones, sprinklers, curtains, electric beds and virtually any other device in a home that is electrically operated.

When an environmental control system is designed, many issues must be considered. What is the easiest way for the user to control the environmental control system is the first issue we should think about when we design an environmental control system. The second issue is what functions are the most important for disabled people in environmental control systems and whether they can control them or not. When using environmental control system, many systems must be operated from a fixed location, many systems require line of sight for effective operation and many systems can be operated from a person's wheelchair or person's bed. All those are vital consideration. In order to choose the best system for meeting the need of disabled people, it is important that their own unique environment, level of needs and amount of support available are taken into consideration. What appliances and functions the user wants to control in the environment that will need to be considered. If the user has other electronic devices that may have some potential for integration such as wheelchair and computer and if the system has multiple access options to allow for the needs of different users should be considered simultaneous. The third issue is safety considerations. Security and safety issues should be considered for the door opener, window opener and emergency call systems. When the environmental control system is designed, the reliability must be ensured. The fourth issue is setup and support considerations. The technological support by the director who has knowledge of the control system is critical for the user to seek assistance if needed.

B. The control methods of environmental control system

The environmental control system mainly utilizes the remained ability of the disabled person to produce at least a switch action. The remained ability includes shaking head, gathering brows, blinking, gnashing tooth, blowing and inhaling, voice, mouth stick, looking etc, especial to the high position paraplegia patient. There are many different methods for operating an environmental control system. They include switch-direct, switch-scanning, keypad, voice, control from a computer, control from a communication device, control from an integrated wheelchair controller etc.

When the disable person mobility is limited, especially when they are in bed, some environmental control systems do not meet this needs, different control way is adopted according to the status of the patient.

C. The control technologies of environmental control system

The technologies of control in environmental control systems are usually based on infra red, X-10 type systems and Radio Frequency (RF). Infra red enables control of appliances such as television, air conditioners, video, DVD, late model stereo and many other electrical appliances. Infra red has the advantages of portability and low installation costs. It also allows graduated control function, such as volume control, rather than just on-off. The limitation of infra red is that the controlling device must broadly be pointing at the appliance to be controlled.

X-10 technology is based on the X-10 Power Line Carrier (PLC) which can control signals to be transmitted anywhere in the house. X-10 has been a standard for sending commands over existing electrical wiring. Individual appliances are plugged into X-10 receivers and can be set to a unique address. The appliance is activated X-10 controllers. These controllers can be computer interfaces, control panels, telephones and remote controls.

RF transmission is also a method of controlling components of an environmental control system. RF transmission does not require line of sight between devices but signal strength and interference is a problem in some settings. Infra red, X-10 type systems and RF control technologies of control in the environmental control systems can be combined to increase the range of control.

D. User interfaces

The user interface includes touch screens, voice synthesis/recognition and traditional graphical user interfaces through keyboard, mouse, menus, buttons, etc. Many principles of user interface of the system are based on scanning

Windows control elements on a dialog-based menu. The user interface can be implemented in several levels dialog structure with pushbuttons. Each menu level can be enlarged without destroying the current structure. Although this kind of user interface using only one input key is slow, but it is the simplest way of implementation and no specific hardware is needed.

III. ENVIRONMENTAL CONTROL SYSTEM DESIGN

In this paper, we combine the different technologies into an environmental control system and design a much simpler environmental control system.

The environmental control system is consisted with input switch, controller and user interface. The input switch enables the disable person to access the menu and operate the controller. Three input methods is provided in this environmental control system, including pneumatic switches operated by sip-and-puff, big key switches operated by hand or arm and touching panel. The sip-and-puff operated system mainly is adapted to the patient with high level spinal injuries (Figure 1, just a sketch map). The big key is adapted to the disable patient whose limbs and trunk can be moved little. The big key can be made into different shape and different color aim to different generation (Figure 2, just a sketch map). The touching panel suits to the disable person whose hand and finger can move flexibly. Through the touch by the finger on the panel, the operation is carried out. In many cases speech is the most convenient and easy-to-learn alternative. We will take the voice control into account in the future research.

The controller is activated via a simple scanning menu format. In our environmental control system, technologies of X-10 and infra red are adopted simultaneously. For the appliances, such as electric bed, computer, electric curtains, electric doors, fan, heater, lamps, lights, radio, security system,



Fig. 1 Sip and puff switch

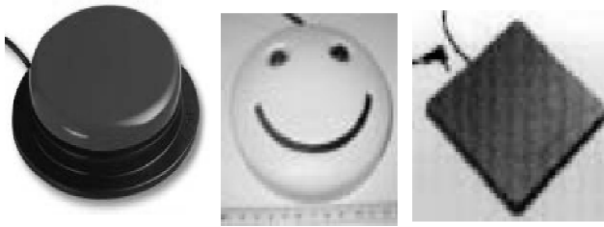


Fig. 2 Big keypad switch

sprinkler system, the X-10 technology is adopted to control them on-off. For the appliances, such as stereo system, air conditioner, television, video, the infra red technology is adopted to control them on-off.

Three or four levels dialog structure is implemented in the user interface. The 1st level is used to select one of all available controlled units including house environment unit, entertainment equipments unit and security control unit; the 2nd level is used to select one of all available equipments from the controlled units; the 3rd level is used to select one of all available commands (e. g. open, close, switch on, off, etc) from the selected controlled equipments. The more function or number level can be added into the user interface for further need of the disable person. The process is like (e.g. house environment unit -> Door -> open). The principle algorithm of the user interface which is just an example is shown in Figure 3. Each menu level can be enlarged according to the need of the disable person.

The main function of the user interface is to scan Windows menus with control options. When the user presses the switch the operative information is being sent to controller which is depending on the selected option command.

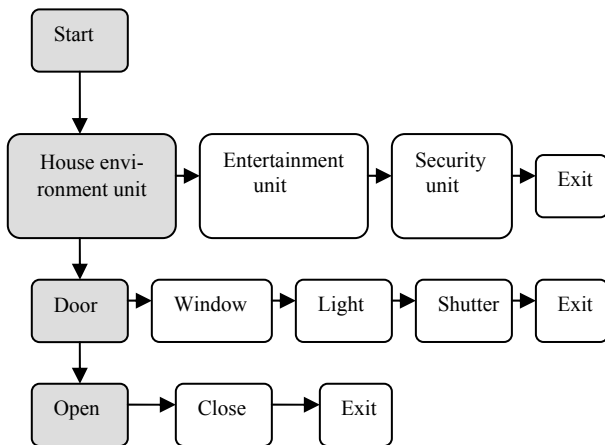


Fig. 3 The principle algorithm of the user interface

When the environmental control system is working, the disabled person requires obtaining the feedback information that their commands have been enacted. This feedback information can be provided by the lights on the display panel or the audio feedback. A PC is used for the user interface implementation.

The environmental control system is set on the disable patient’s bed or on the wheelchairs along with the other equipment.

The environmental control system as described above will be tested with many users before it is used in practice. Many of the users should be physically disabled person—some patients can’t walk and the other patients have difficulties to move their limbs. Each user should be trained to work with this interface before the test.

IV. DISCUSSION

Environmental control system can enhance the ability of disabled or elderly people allowing independence to be maintained. The benefit of environmental control systems is the provision of control for disabled people and the greater independence obtained by disabled people.

The environmental control system enables the disable patient to control many kinds of domestic appliances and other functions by remote control. Its potential application is far wider it could be used within any home by anybody. A great number of benefits would stem from the implementation of such systems: greater safety, autonomy and self-esteem, and consequently, better relationships with their relatives. The environmental control system is a multimedia integrated system that allows the elderly and other disable people to command and control domestic and working environments with a high living quality.

With the development of the society, the range of environmental control systems is expanding rapidly. Offering control over a comprehensive range of devices from a variety of locations and training requirements and compatibility of environmental control systems with other equipment should be taken into account for the future needs. Strong individual differences and preferences are evident and should be taken into account too.

REFERENCES

1. P. Serafinavičius, V. Lauruška, Home Environment Control System for the Disabled: User Interface Testing, ISSN 1392-1215 ELEKTRONIKA IR ELEKTROTECHNIKA. 2004. Nr. 4(53), T 115 Medicinos Technologija.
2. T. Russomano, F. Falcan, J. Gurgel, L. Piccoli, et al. Development of a lower body negative pressure box with an environmental control system for Physiological studies. Proceedings of the 2005 IEEE, Engineering in Medicine and Biology 27th Annual Conference, Shanghai, China, September 1-4, 2005
3. Fausal Karmali, Mark Polak, Aleksandar Kostov, et al. .Enviromental control by a Brain-Computer Interface, Proceedings of the 22nd Annual EMBS international conference, July 23-28, 2000, Chicago IL.
4. Brent David Marsden, Frank Breau, R. John Ellwood, et al. Light-Guided Environmental Control Device, 0-7803-8285-4/04/\$20.00, 2004 IEEE.
5. April Hiscox, Brooke Hallowell, John D. Enderle, Tap-Tap Environmental Controls Unit, 0-7803-6341-8/00/\$10.00, 2000 IEEE.
6. Zhenduo Han, Hua Jiang, Peter Scucces, PowerScan: a Single-Switch Environmental Controls System for Persons with Disabilities. 0-7803-6341-8/00/\$10.00, 2000 IEEE.

Author: Tao Chunjing

Institute: Ph.D., National Research Center for Rehabilitation Technical Aids, Beijing, China.

Street: No.1 Ronghuazhong Road, BDA

City: Beijing

Country: China

Email: taochj@gmail.com

The reference research of exercise therapy of residual limb in post-operative of lower limb amputation

Xiaoyu Zhang¹, Qidong Liu¹, Chunjing Tao¹ and Huiru Gu¹

¹ National Research Center for Rehabilitation Technical Aids, Beijing, China

Abstract — it is urged to apply various rehabilitation these non-ideal stumps, and to create better conditions for fitting prosthetics to benefit. Physical therapy can intenerate joint circumference tissue which is contracture malformed, cooperate to pull the contracture joint passively.

The isometric and isotonic constrictions are both conventional muscle physiologic constriction and have deficiency on measuring force and exercising. The isokinetic exercise has the advantage of isometric and isotonic exercise, i.e. it exerts maximum power (isometric) in the whole action range (isotonic). It costs less time than isotonic exercise, and can execute in different speeds without changing or moving appliances, even better than traditional muscle constriction exercise in force measure.

Our task, the system will be adopted to integrate and blaze new trails, research new system with digit control and feedback of hip joint and knee joint exercise system. Using this appliance in the department of bone surgery in hospital, limb injured and disabled rehabilitation center will relieve the difficulty of some amputee get no rehabilitation exercise in time after amputation at present.

Keywords — reference, therapy, residual limb, post-operative, amputation.

I. INTRODUCTION

With the increase of the amputee recently, there are over 900,000 amputees who need to fit the prosthesis, in which the lower limb amputees are most 80% in China.

The loss of an extremity or part of it represents a remarkable interference with the physical effectiveness of the individual concerned. Some patients, especially those with additional medical problems, will be unable to produce the extra energy required to independent ambulate, no matter how intensively they are trained.

Successful rehabilitation of the lower limb amputee depends on good co-operation between all members of the clinic team. All measures of rehabilitation should start at the earliest possible date. Exercise therapy is basic part of physical therapy. At first, the patient should be instructed how to take care of the residual limb. The physiotherapist (PT) must provide adequate exercise for muscle training, retention of range movement and prevention of joint contractures. It is particularly important that the patient displays

enthusiasm for the proposed rehabilitation program and the will to work hard. Even the most skilled and energetic PT will be unable successfully to train an amputee to achieve independent gait using prosthesis if the patient is uncooperative.

Post-operative of amputation physical therapy such as bed exercises for below-knee amputee: active exercises to maintain strength and mobility of remaining. It is most important to emphasize knee extension until the patient has good quadriceps power. Another exercise is in prone lying position. Stump and strengthen muscle maintain full joint mobility. Bed exercises for above-knee amputee: static exercises for the extensors, active and resisted, exercises for the hip abductors and adductors with emphasis on the adductors. The hip extension should be continually encouraged throughout the rehabilitation program and so on. Stump exercise and exercises to improve general strength and mobility should be continued.

The rehabilitation of post-operative is very important, but most of amputees in China have not been in progress the rehabilitation or not guided under the special PT.

II. DESCRIPTION

A. The concept of non-ideal stump

Compared with ideal stump, non-ideal stumps poorly meet with the conditions of perfection, carry difficulties with fitting prosthetics, some non-ideal stumps produce unsatisfied compensation, such as stump abnormality, joint contracture and other stump complication, some infection fitting the prosthetics, even can not fit the prosthetics. It is urged to apply various rehabilitation these non-ideal stumps, and to create better conditions for fitting prosthetics to benefit. At the same time, they can become better ones.

AK amputee, function damaging characteristics of this level are: save iliopsoas and gluted function, damage the function of iliotibial tract, popliteus rectus femoris, Sartorius and adductor, as a result of lose limb weigh, fall under the balance of coax muscle, may contracture on hip flexure, abduction, lateral spin. the higher level is, the bigger infection is, the gluteus maximus is driving muscle, extend the hip and the knee is unbend when the prosthetics touchdown.

It is very important to set up all right gait and with stand the coax flexure contracture.

BK amputee, knee joint flexure is one of the most common malformations. It influences the fitting and alignment of prosthetics socket, especially dynamic alignment when BK amputee flexure knee $>15^\circ$, prosthetics function will be influenced.

It is very useful to improve the joint activity, rectification malformation joint activity and joint malformation to exert the prosthetics functions. Common contracture in different level after amputation and relevant treatments are shown in Table 1 below.

Table 1 Common contracture in different level after amputation and relevant treatments

Amputation level	Joint	Familiar contracture	Correct exercise	Buildup muscle power exercise
AK	Hip	Flexure, Abduction, Lateral, Spin	Unbend, Adduction	Unbend, Adduction
BK	Knee	Flexure	Unbend	Unbend

B. The rehabilitation routes to improve non-ideal stump

The kinesitherapy is one of basic parts of physical therapy. Physical therapy can intertate joint circumference tissue which is contracture malformed and cooperate to pull the contracture joint passively.

The main aim of stump kinesitherapy is to rectify contracture malformed joints, to maintain joint function, to increase joint activity and muscle power, and to prevent muscle power from decreasing, to help recovery of muscle power, to improve stump condition of fitting prosthetics, to educe compensation function of prosthetics and to amend the gaits.

1. To improve activity and rectify contracture malformation of joints, priority must be given to initiative and passive kinesitherapy, combined with continuous traction when needed.

2. To build up muscle power, resistant muscle constriction is frequently applied with exercise appliances. If stamp muscle power is very poor, initiative muscle power exercise must be carried out as well as electric muscle power exercise appliance for passive exercise. The prosthetics is assembled when muscle power rises to grade

3. External fixation rectification: may use it prop open knee joint on flexion side to rectify the malformation when other operation approach don't work.

C. Comparison of isometric, isotonic and isokinetic exercises

1. Isometric exercise is a muscle contractive exercise when fixation or overload between two ends (origin and stop spot), i.e. when joint is not active under the peak load. The muscle reaches maximum constriction and keeps for several seconds each constriction. The muscle length will not be changed and can only bring about tensile force. 1 RM (1 repetition maximum): maximum power exerted on the muscle constriction maintaining for 5 seconds.

The isometric exercise is the some with muscle power tone exercise, when the joint is not active. The excellence of isometric exercise including: it takes little time, it enhances muscle power faster, it do not need special appliances and sites, the muscle will not ache after exercise and strength is easy to retain. The shortage may be hypertension, but power increasing is not obvious as isotonic and isokinetic exercise.

2. The isotonic exercise is a functional training. The tension will not change when the muscle is extended or shortened. Carrying out exercise by joint resists against resistance in move scope, the standard load is the repeatable maximum (RM). 1RM means highest weight one can bear while he does his best.

The excellence of isotonic exercise is that the power of muscle develops in the whole range of the action, and the power enhances as with the weight grows. At the same time, the feeble muscle group involve can be exercised. The shortage is that muscle ache and injury is easily of happened when unsuitable weight chosen. The isotonic exercise takes more time and energy than isometric exercise. It is easily getting tired, and needs longer time for recovery after exercise.

The isometric and isotonic constrictions are both conventional muscle physiologic constriction and have deficiency on measuring force and exercising.

3. The isokinetic exercise, also called adjustable impedance or constant speed movement. The speed is invariable the resistance of appliance succeed direct ratio with the power offered by exerciser, so that the muscle got the maximum load in action course all along. All these must be carried out with specialized isokinetic exercise appliance. James Perrinee proposed the theory of isokinetic exercise in 1967. Isokinetic exercise appliance has benefited rehabilitation workers so much. The theory has also fully developed in recent 40 years.

The isokinetic exercise has the advantage of isometric and isotonic exercise, i.e. it exerts maximum power (isometric) in the whole action range (isotonic). The muscle can accept maximum resistance in all directions. It costs less time than isotonic exercise, and can execute in different speeds without changing or moving appliances, even better than traditional muscle constriction exercise in force meas-

ure. In addition, this device also proceeds centrifugal constriction training, passiveness exercise, angle and force exercise.

D. To carry through proper rehabilitation with different amputation levels, some amputation site kinesiatrics in China are introduced below:

AK kinesiatrics

1. Exercise of muscle power strengthening:

As the uninjured side lower limb early resistance training, the stump limb must be doing isometric exercise. Stump limb gym should be carried out until initiative exercise is available. Patient can even walk with walking device, or raise leg to anti-resisting force muscle exercise.

2. Exercise of joint range of motion:

To avoid hip malformation, the patient must do hip joint exercise in all directions as early as he can after amputation. Stretching the contracture hip joint, enlarge activity range of adduction and extension.

3. Other muscle exercise methods for hip:

Gluteus maximus exercise can do centripetal isokinetic exercise and so on.

Adductor exercise can do constant speed isokinetic exercise at lateral position.

Hip intortor can do exercise of anti-man-made resistance.

Abdominal muscle can do isokinetic exercise steady at standing position.

BK kinesiatrics

1. BK amputee should keep knee at straightening position to prevent flexure malformation, and mainly exercise the stump function of quadriceps femoris and knee joint.

2. Stump limb exercise strengthens the flexor and extensor of knee, especially the extensor, so that the amputee can walk powerfully after fitting the prosthetics. The exercise of knee extensor anti-resistance: exercise of limb stump function is. a set of flexor and extensor isometric exercise under professional rehabilitation supervising when muscle power recovers, it carry out resistance exercise with tensioner, sandbag and quadriceps femoris exercise device to strengthen the muscle power.

3. BK knee ROM exercise can depend on appliances, such as tackle traction, hammer traction, training device of quadriceps femoris at chair sitting position, stall bar and parallel bar, as well as isometric muscle exercise and joint exercise of initiative extension and flexion. Patient of long-course can do passive joint exercise such as CPM.

E. Choose of power exercise appliances

Some power exercise devices in present China are shown as below:

1. Single platform machine, a power exercise device can offer to a muscle or a group of muscles.

2. Compound platform machine, a power exercise device can offer to two muscles or two groups of muscles.

3. Multi platform machine, a power exercise device can offer many muscles or groups of muscles.

4. Adjustable weight block device may add or subtract blocks at will, designed to reserve exercise process and to be capable of adjusting training intensity.

5. Tensile tendon device can help patient to posture at will and move all over the body when do all kinds of action.

6. Computerized or pneumatic devices, which are modern and high-tech in devices, are also designed to reserve exercise process. When you want to start a set of exercise which fits yourself, a single touch on the button or adjust the display on the screen. At slow speed, you can reach perfect effect of power exercise by keeping training intensity.

Most body builders of the lower limb stump exercise nowadays are built up for common person at first. The lower limb amputees in China have to face with devices very simple in composition and function which can not regulate intensity and range. On the other hand, they are so easy to injure stumps and joints. It is very difficult to perfect the effects of exercise. It is necessary to develop the function of lower limb stump exercise system.

F. Primary design for Topic

Our task, Lower Limb Residual Function Exercise System, national science and technology support plan, for solving exercise problems of lower limb stump function. This system will be adopted to integrate and blaze new trails, research new system with digit control and feedback of hip joint and knee joint exercise system. This system can select exercise pattern with thinking about the factors of weight and strength of amputee, position of amputation, stump condition and can adjust exercise reference with rehabilitation situation of amputee. This system has extensor drive fountain.

Through our study from clinic practice, it is not likely to sign a desk device to integrate exercise both BK & AK at the same time, and the frame is complex and not practicability. Our design is in clued two desks, one is sit mode exercise for BK with isokinetic exercise and isotonic exercise, the other is hip isometric and isokinetic exercise for AK.

BK exercise devices

1. Mechanism framework design is sit mode, initiative exercise mode is drive by DC motor and passiveness is controlled by damper.

2. Magnetism powder damper, need to confirm parameter of damper and DC motor.

3. Control quantum of the control system:

- Mode choice: touch screen or key-press fluid crystal screen;
- Magnetism powder clutch resistance moment M ;
- Motor rotate speed V : choose of 3 archives;
- Angle (calf) α : ray yard tray or sensor;
- $M=F(\alpha)$: through test and determine;
- Time T : prescription.

AK exercise devices

1. Mechanism frame work designed as stand mode;

2. The hip does extend, flexure, adduction and abduction with isotomic and isometric exercise;

3. To design exercise module of temporary prosthetics socket.

Exercise modes

1. Initiative exercise mode (entire patient initiative);
2. Passiveness exercise mode (entire motor driven);
3. Assist act exercise mode (motor driven+ patient initiative);
4. Biofeedback mode (using biology signal to assess patient, making rotation speed meet with physiology demand of patient)

Main design parameters

1. 2 freedom degrees;
3. The carrying capacity of flexion and extend organization $> 10\text{kg}$;
3. The maximum frequency of lower limbs' flexion and extend capacity is $10/\text{minute}$;
4. The organization can imitate flexion, extend, adduction and abduction sports of normal man's lower limbs;
5. The organization has both initiative and passive characters;
6. Good and scientific interaction between human and machine, automatic assessment of rehabilitation and real time display of rehabilitation.

G. Research of exercise parameters

It is urged for us to develop appliance exercise on lower limb amputation patients special with various situations. Uncorrected training not only do benefit patients, but also

bring about some risks (such as sports injury, malfunction of organs or failure, inducing cardiovascular diseases). When the lower limb amputee go along kinesitherapy, the P·T must accompany patients with one-to-one system cure, and constitute individuation exercise scheme with the aged, stump in stance and body circs of the amputee, include integer, phase follow-of ones, under the P·T's supervision, the lower limb amputee can use this appliance to accomplish the great mass of the exercises. At the same time, the P T can supervise more amputee to train.

III. CONCLUSION

Using this appliance in the department of bone surgery in hospital, limb injured and disabled rehabilitation center will relieve the difficulty of some amputee get no rehabilitation exercise in time after amputation at present. Mostly including:

1. Research on rules of exercise referring to time (recovery course): Recording the degree of flexion and extend of knee/hip during the training to definite the degree of flexion and extend of knee/hip of the amputee when fitting the prosthetics.

2. To definite the main parameters of influence factors in lower limb course: Recording various relative data and information of the users each time. Such as comparison on function of flexors before and after exercise, function of extensors before and after treatment, ratios of flexor and extensor's relatively apex moment before and after treatment (H/Q).

3. To amend and perfect the function parameters of the sample appliance on these grounds.

REFERENCES

1. Cui Shou-chang. Current amputation concept and the amputation rehabilitation, Chinese Journal of Clinical Rehabilitation, December 2002, Vol.6, No.24..
2. Yang Dong-yun. Rehabilitation after amputation, Chinese Journal of Clinical Rehabilitation, December 2002, Vol.6, No.24

Author: Zhang Xiao-yu

Institute: Professor, engineer-in-chief of National Research Center for Rehabilitation Technical

Street: No.1 Ronghuazhong Road, BDA

City: Beijing

Country: China

Email: zxy1949519@hotmail.com

Analysis of Emotional Expression of Finger Braille

Y. Matsuda¹, I. Sakuma², Y. Jimbo³, E. Kobayashi², T. Arafune⁴ and T. Isomura¹

¹ Department of Robotics and Mechatronics, Kanagawa Institute of Technology, Atsugi, Japan

² Graduate School of Engineering, The University of Tokyo, Tokyo, Japan

³ Graduate School of Frontier Sciences, The University of Tokyo, Kashiwa, Japan

⁴ National Institute of Advanced Industrial Science and Technology, Tsukuba, Japan

Abstract— Finger Braille is one of tactual communication media of deafblind people. In two-handed Finger Braille, index finger, middle finger and ring finger of both hands are likened to keys of a Braille typewriter. A sender dots Braille code on the fingers of a receiver like whether he/she does the type of the Braille typewriter. Then the receiver recognizes the Braille code. In one-handed Finger Braille, the sender dots the left column of Braille code on the DIP joints of three fingers of the receiver, and then the sender dots the right column of Braille code on the PIP joints of them. Deafblind people who are skilled in Finger Braille can catch up with speech conversation and express various emotions. Because there are small non-disabled people who are skilled in Finger Braille, deafblind people communicate only with interpreters. Objective of this study is development of a Finger Braille supporting device which assists not only verbal communication but also non-verbal (emotional) communication between deafblind people and non-disabled people who are not skilled in Finger Braille. In this paper, an experiment of emotional expression of Finger Braille was carried out. And we analyzed features of emotional expression of Finger Braille and discussed algorithm of emotion recognition. The features of emotional expression were: (1) the durations of code of Joy were particularly shorter than other emotions; (2) the durations of code of Sadness were particularly longer than other emotions; (3) the finger loads of Anger were particularly bigger than other emotions. To develop emotion recognition system, we discussed algorithm of emotion recognition using the accelerometers worn by tester. According to the results of discriminant analysis, it was considered that emotion recognition using the discriminant functions and the average of posterior probabilities in a sentence was possible.

Keywords— deafblind, Finger Braille, emotional expression, prosody, emotion recognition

I. INTRODUCTION

Recent surveys (The Deafblind Association of Japan, 2006) estimate that there are 16,354 deafblind people in Japan. Deafblind people use many different communication media according to the age of onset and what resources are available to them. “Yubi-Tenji” or Finger Braille is one of tactual communication media of deafblind people (see Fig.1). In two-handed Finger Braille, index finger, middle

finger and ring finger of both hands are likened to keys of Braille typewriter. A sender dots Braille code on fingers of a receiver like whether he/she does the type of Braille typewriter. Then the receiver recognizes the Braille code. In one-handed Finger Braille, the sender dots the left column of Braille code on the DIP joints of three fingers of the receiver, and then the sender dots the right column of Braille code on the PIP joints of them. Deafblind people who are skilled in Finger Braille can catch up with speech conversation and express various emotions, because of prosody of Finger Braille. Because there are small non-disabled people who are skilled in Finger Braille, deafblind people communicate only with the interpreter.

Objective of this study is development of a Finger Braille supporting device between deafblind people and non-disabled people who are not skilled in Finger Braille. Fig. 2 shows the concept of the Finger Braille supporting device. The features are: (1) the supporting device recognizes non-disabled people’s speech and teaches method of dotting of Finger Braille for non-disabled people (the Teaching System [1][2]); (2) the supporting device also recognizes dotting of Finger Braille by deafblind people and synthesizes speech for non-disabled people (the Recognition System [3][4]); (3) the supporting device is operated by non-disabled people and all sensors are worn by non-disabled people; (4) the supporting device intends to assist not only verbal communication but also non-verbal (emotional) communication. But the features of emotional expression of Finger Braille are not clear yet.

In this paper, an experiment of emotional expression of Finger Braille was carried out. And we analyzed features of emotional expression of Finger Braille and discussed algorithm of emotion recognition.

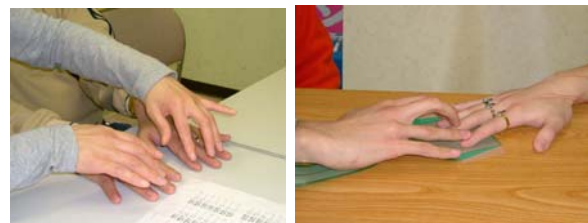


Fig. 1 Two-handed Finger Braille and one-handed Finger Braille

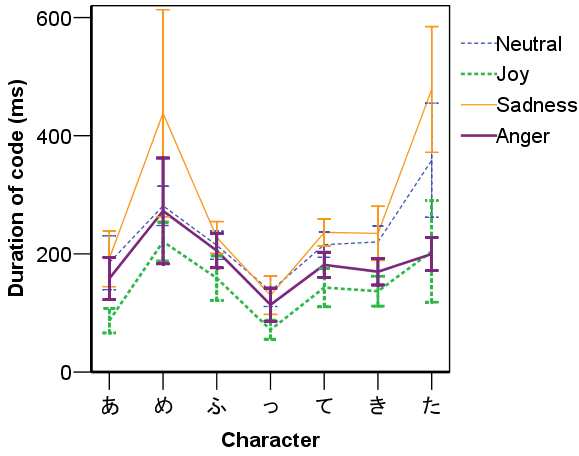


Fig. 4 Mean of duration of code as a function of emotions (Rain)

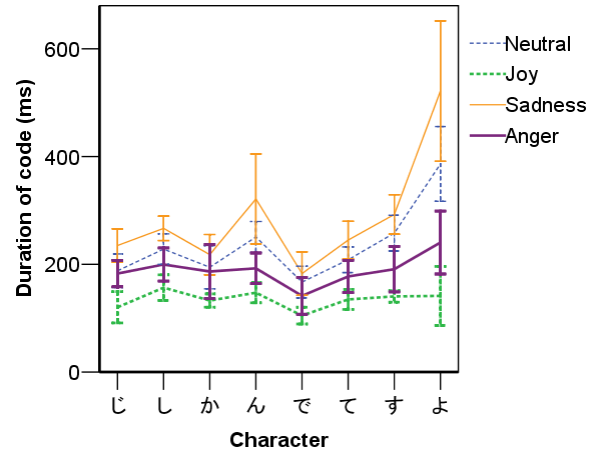


Fig. 7 Mean of duration of code as a function of emotions (Time)

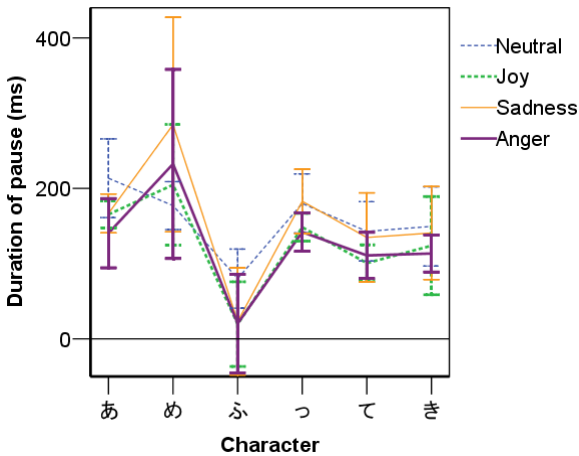


Fig. 5 Mean of duration of pause as a function of emotions (Rain)

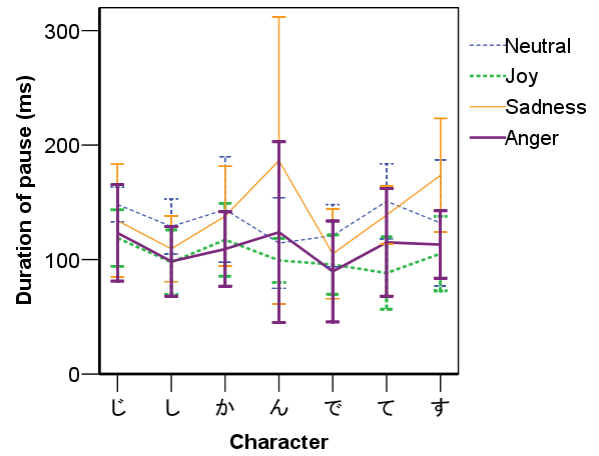


Fig. 8 Mean of duration of pause as a function of emotions (Time)

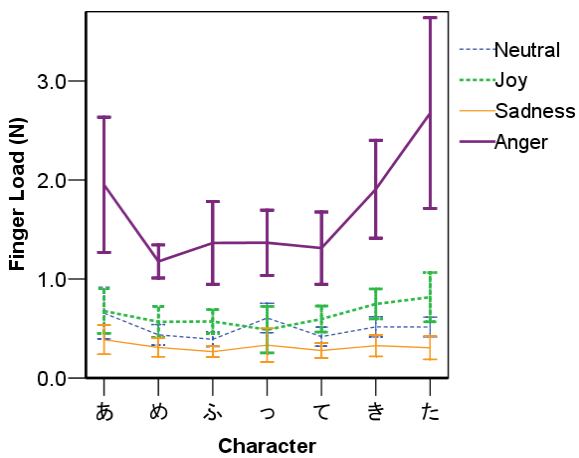


Fig. 6 Mean of finger load as a function of emotions (Rain)

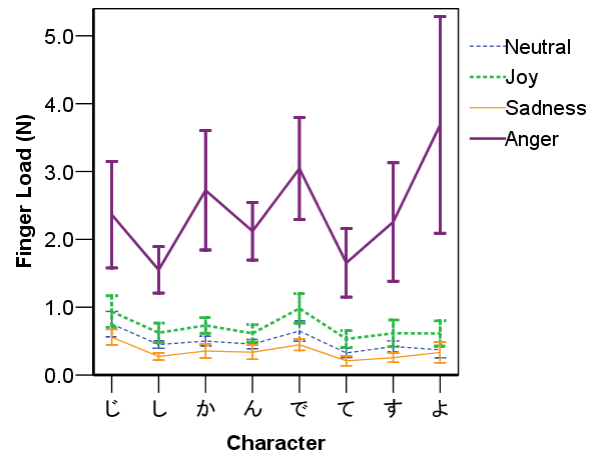


Fig. 9 Mean of finger load as a function of emotions (Time)

IV. DISCUSSION

The Finger Braille supporting device intends to assist emotional communication, teaching of emotional expression for non-disabled people and emotion recognition of Finger Braille dotted by deafblind people. To develop emotion recognition system, we discussed algorithm of emotion recognition using the accelerometers worn by tester. We noted the acceleration data of one-handed Finger Braille by subject A and calculated the duration of dotting (summation of duration of code and following pause) and the amplitude of shock acceleration by dotting. The result of ANOVA were: (1) the durations of dotting of Joy were particularly shorter than other emotions; (2) the durations of dotting of Sadness were particularly longer than other emotions; (3) the amplitudes of acceleration of Anger were particularly bigger than other emotions.

Next, discriminant analysis of emotions was carried out. Discriminant variables were the duration of dotting and the amplitude of shock acceleration by dotting. As the result of discriminant analysis, posterior probabilities for each emotion of all dotting were calculated. Each dotting was classified as the emotion of the maximum posterior probability. Fig. 10 shows territorial map of emotions. Discriminant ratio of all dotting was 63.6%.

As the algorithm of emotion recognition, we note average of posterior probabilities for each emotion in a sentence and classified by the average of posterior probabilities (see Fig. 11). As the result of classification, discriminant ratio of sentence was 95.0% (Neutral 90%, Joy 100%, Sadness 100%, Anger 90%). Thus it was considered that emotion recognition using the discriminant functions and the average of posterior probabilities in a sentence was possible.

V. CONCLUSIONS

In this paper, we analyzed features of emotional expression of Finger Braille and discussed algorithm of emotion recognition. As future plan, applying these results, we will develop the teaching method of emotional expression for non-disabled people and the emotion recognition system.

ACKNOWLEDGMENT

We greatly thank Ms. Satoko Mishina and Ms. Megumi Fukuma (interpreters of Finger Braille) for their support.

This study was supported by the Ministry of Education, Culture, Sports, Science and Technology of Japan under a Grant-in Aid for Scientific Research (No. 16700430).

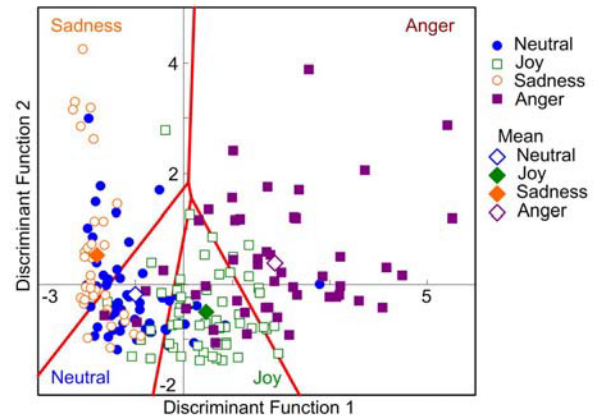


Fig. 10 Territorial map of emotions (dotting on PIP joints)

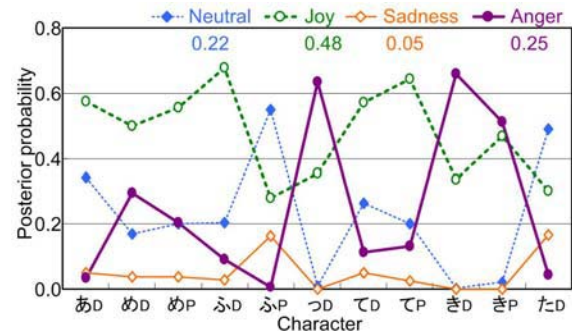


Fig. 11 Example of posterior probabilities of sentence (Rain with Joy)

REFERENCES

1. Matsuda Y et al. (2005) Finger Braille Teaching System for Non-disabled People who Communicate with Deafblind People, IFMBE Proc. vol. 8, 6th Asian-Pacific Conference on Med. & Biolog. Eng., Tsukuba, Japan, 2005, PA-2-36
2. Matsuda Y et al. (2007) Finger Braille Teaching System for People who Communicate with Deafblind People, Proc. of the 2007 IEEE International Conference on Mechatronics and Automation, Harbin, China, 2007, pp.3202-3207
3. Matsuda Y et al. (2006) Finger Braille Recognition System for Non-disabled People who Communicate with Deafblind People, IFMBE Proc. vol. 14, World Congress on Med. Phys. & Biomed. Eng. 2006, Seoul, Korea, 2006, pp.2812-2815
4. Matsuda Y et al. (2007) Analysis of Shock Accelerations by Dotting of One-handed Finger Braille, Proc. of the Third Asian Pacific Conference on Biomechanics, Tokyo, Japan, 2007, p S88

Address of the corresponding author:

Author: Yasuhiro Matsuda
 Institute: Kanagawa Institute of Technology
 Street: 1030 Shimoogino
 City: Atsugi-shi, Kanagawa
 Country: Japan
 Email: yasuhiro@rm.kanagawa-it.ac.jp

A Research on EMG Signal and Plantar Pressure Information for AK Prosthetic Control

Tengyu Zhang¹, Peng Yang¹, Qidong Liu², Lingling Chen¹ and Jie Liu¹

¹School of Electrical Engineering and Automation, Hebei University of technology, Tianjin, China

²National Research Center for Rehabilitation Technical Aids, Beijing, China

Abstract — With the development of prosthetics, the performance of AK (above-knee) prosthesis is highly required by the above-knee amputees. In the practical applications, there are many problems with the traditional AK prosthesis, the foremost one of which is that it has no variable speed and natural gait. In order to solve these problems, a method which based on EMG signal and plantar pressure information for gait analyzing and recognizing is proposed. With this method, the gait cycle could be effectively divided into four phases and the speed levels could be distinguished accurately. At the same time, the real-time and accuracy was greatly improved comparing with the control effect based on a single source. To control the AK prosthesis with this method can allow the AK amputees a more stable and natural gait when walking at variable speeds.

Keywords — EMG signal, plantar pressure, AK prosthesis, speed, gait

I. INTRODUCTION

With the development of science, computer and information technology has made substantial progress. The Research on AK prosthesis has gradually become the focus of the rehabilitation engineering. Though there was several hundred years of history on the AK prosthetic research both in domestic and foreign, many problems still existed in the traditional AK prosthesis, the foremost one of which was that it had no variable speed and natural gait. ^[1]

For the AK prosthesis, the damper can be adjusted by controlling the valve in the cylinder, so as to change the speed of knee flexion and extension. ^[2] In order to ensure the security, valve should be closed when the prosthesis bore the weight. So the current walking speed and the start time of each phase in a gait cycle must be obtained to control when and how much the valve should open, so as to control the prosthesis better. ^[3]

As the signal sources for controlling the AK prosthesis, plantar pressure information can intuitively reflect the current state of the body, while EMG signal is spontaneous and voluntary. So a method which based on both these two information for gait recognizing is proposed. To control the AK prosthesis with this method can allow the AK amputees a more stable and natural gait when walking at variable speeds.

II. MATERIALS AND METHODS

A. Experiment for signal collection

The experiment for signal collection mainly included two parts, which were plantar pressure measurement and EMG signals collection.

For plantar pressure measurement, many kinds of sensors could be used. By taking into account that the sensor would be installed in the shoes, it should have a small thickness and area. So in the experiment, FlexiForce force sensors were selected for force measurement. The thickness of the sensor was only 0.208mm, and the diameter of the force area was 9.53mm, as well as the linear error was less than $\pm 5\%$, it would be able to meet the requirement of experiment. A variety of factors, such as body weight, foot size and sensitive area of the force sensor, should be considered to choose the range of sensor. By considering the specific conditions, the range of sensor was chose as 25lbs.

Toe and heel are the focus when studying the information of plantar pressure, while the signals from them are most important for dividing the gait cycle and the gait phase. Extensive testing proved that people's walking gait could be accurately reflected only based on the force information from these two points (Figure 1).

So in the experiment, two force sensors were respectively installed on the toe and the heel, and the signals from them were used to judge whether these points touched the ground. When the force signal existed, the correlative point contacted with the ground, and this state was defined as "1"; instead, it would be left with the ground, and the state was defined as "0".



Fig.1 force sensor location

By taking into account that the small friction between the sole and the force sensor would reduce the veracity, a critical force should be set in the actual measurement, and the state would be defined as “0” only if the current force was not more than the critical force.

EMG (electromyography) signals are spontaneous and voluntary with reflecting the activity of each muscle when people walk [4]. As different muscles stretching in different motion modes, resulting in the corresponding EMG also have different characteristics in different modes. Therefore, EMG signals can be used as ideal control signals of the intelligent AK prosthesis.

In the experiment, EMG signal was collected by the MyoScan-Pro EMG sensor, which was made by the Thought Technology Company. After amplified and rectified, the EMG sensor automatically converted the SEMG signal to a root mean square (RMS) signal. When measuring the planter pressure, the EMG signals from eight femoral muscles were collected synchronously, which were Rectus femoris, Vastus lateralis, Biceps femoris, Semintendinosus, Semimembranosus, Tibialis anterior, Gastrocnemius and Soleus. All these muscles ware selected from the same side of the body and the sampling frequency was 2048Hz. Subject walked on a motor driven treadmill in order to keep even speed and the experiment was carried with natural gait at different walking speeds.

As the RMS signal had little noise, it could be used only with simple process, such as normalization. After this process, the differences of the EMG amplitude from different subjects would be minished.

B. Gait analysis based on plantar pressure

In the research of AK prosthesis, accurate gait analysis which contained gait cycle calculation and gait phases division is crucial.

Gait cycle is the time between two adjacent heel-strike and it is the inverse proportion of the swing speed. Therefore, to one subject, when the gait cycle was longer, the walking speed was slower; instead, when the gait cycle was shorter, the walking speed was faster. So the gait cycle could be calculated and the walking speed could be classified into several levels according to it.

Gait is performed by continuous body motions, generated by a sequential process of repeated motion patterns. To the unilateral lower limb, a gait cycle could be divided into the stance phase and the swing phase. In stance phase, the foot contacted with the ground and supported the weight; in swing phase, the foot left with the ground and swung forward. [5] The stance phase could also be divided into there phases which were foot falling, foot flat and foot ascending. Foot falling period included initial contact and loading re-

sponse, which started when heel struck and ended when all foot contacted with the ground. Foot flat was the period after foot falling which defined the heel off as the end. Foot ascending period in which the foot accelerated and left with the ground was started when heel off and ended when toe off. [6] So, according these four states (heel strike, foot flat, heel off, toe off), a single stride could be divided into four phases, which were foot falling stance, foot flat stance, foot ascending stance and swing.

C. Gait phase recognition based on EMG signal

In order to extract available feature for gait phases recognition, detailed EMG analysis was necessary. By taking into account the similarity among profiles within functional groups, the number of basic functions could be reduced. Through the analysis of the eight leg muscles, four muscles (Rectus femoris, Semimembranosus, Soleus and Gastrocnemius) were applied to classification. In a gait cycle, the pre-processed EMG signals from four muscles were showed in Figure 2.

For a single muscle, the EMC amplitude was obviously different in different phases as seen in Figure 2. For different muscles, their active phases were also different. So the integral of the absolute value (MAV) and the ΔMAV was used to identify the different phases in a gait cycle.

$$MAV = \frac{1}{N} \sum_{i=1}^N |x_i| \quad i = (1, 2, \dots, N-1, N) \quad (1)$$

$$\Delta MAV_i = MAV_{i+1} - MAV_i \quad i = (1, 2, \dots, N-1) \quad (2)$$

N: the Sample number; xi: amplitude of the EMG signal.

It was clearly that the EMG signal from a single muscle could not identify the four phases clearly. In order to ensure the recognition rate with least muscles, EMG signals from two muscles were selected, and their features were combined for gait phase recognition (Figure 3).

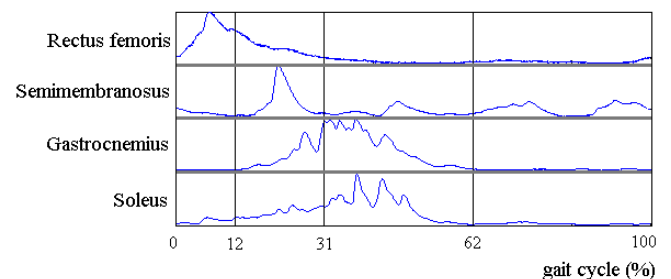


Fig.2 four EMG signals in a gait cycle

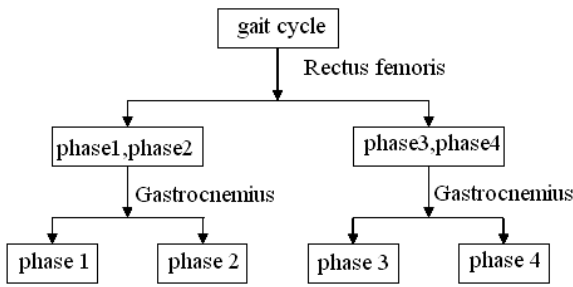


Fig.3 the period for gait phase recognition

III. RESULTS

Figure 4 showed the plantar pressure signals from one subject at different walking speeds.

Seen from Figure 4, it was easily known that gait cycle is obviously different at different speeds. Accordingly, the walking speed was classified into five levels, which respectively were very slow, slow, medium, fast and very fast.

In order to divide the gait phases, the contact states between foot and ground in a gait cycle were showed in Figure 5. Among them, f1 represented the state at the heel and f2 represented the state at the toe.

With the method mentioned in part II, a stride could be divided into four phases and each proportion in a gait cycle was respectively about 12%, 19%, 31%, 38% as seen in Figure 5.

Because of the facility and practicability, BP neural network was used as the classifier in the gait phase recognition.

In the collected signals, 15 groups of EMG signals were put into the network as the samples; the other five results of

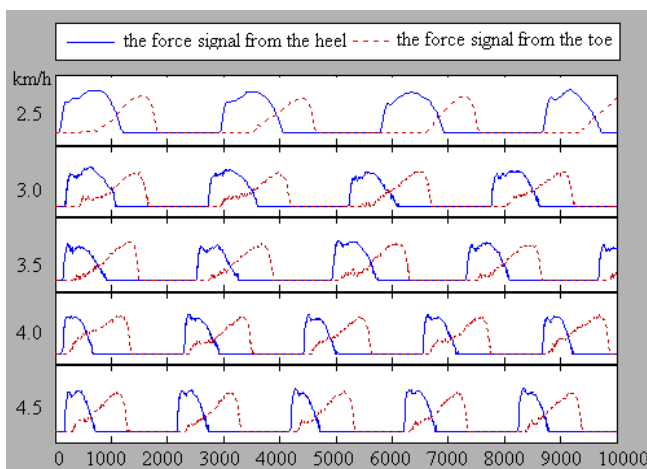


Fig.4 plantar pressure signals at different walking speeds

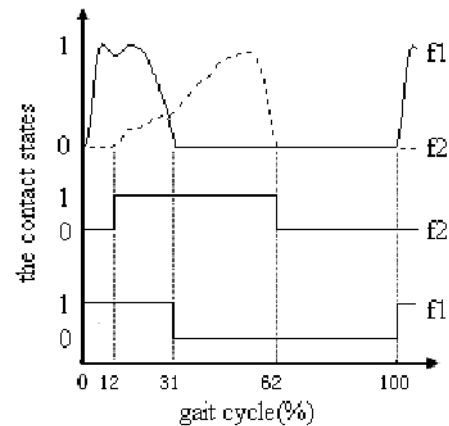


Fig.5 the contact states between foot and ground

Table 1 the recognition rate in each phase

	foot falling stance	foot flat stance	foot ascending stance	swing
Sample number	23	35	62	80
Correct number	19	29	54	73
recognition rate	82.6%	82.9%	87.1%	91.3%

experiments showed that, with this method, the gait cycle could be effectively divided into four phases and the recognition rate could be more than 80%(Table 1).

IV. DISCUSSION

The principle of the prosthesis illuminated that walking speed could be controlled with adjusting the valve. The best open sizes of the valve at different speeds were selected with extensive trials. By contrasting the open sizes of valve and the walking speeds, different control parameters were set at different speeds. With this method, the speed of AK prosthesis could fleetly follow the sound leg. As five speed levels had been classified, five open sizes of valve could be accordingly chosen. Figure 6 showed the relationship between the walking speed and the location of the valve opening.

Besides, in order to ensure the security, valve should be closed in the stance phase when the prosthesis bore the weight and opened in the swing phase. By analyzing the four phases mention above, the phase in which valve open or not was known. The period during which prosthesis bore the weight was the foot flat stance phase and the early foot ascending stance phase. So the valve should be lentamente closed at the foot falling stance phase; then at the middle of the foot ascending stance phase, it should be lentamente

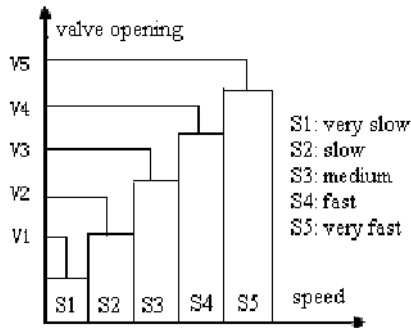


Fig.6 the relationship between speed and valve opening

opened; at the start of swing phase, the valve should have been opened to the needed size.

The plantar pressure information was used to classify the speed levels, so as to control the open size of the valve. At the same time, the EMG signals were used to forecast and identify the gait phase, in order to choose how much the valve opened. Controlling the AK prosthesis with this method, a natural gait would be easily achieved.

V. CONCLUSIONS

In summary, application of this method could not only identify the movement states on line, but also classify the speed into various levels, as well as achieve exact and real-time control effect. With the method, the expected goal had been achieved.

Combining the EMG signal and plantar pressure information and using them to control the AK prosthetic can provide reliable guarantee for good motion controlling. Besides, with the method, the motion could be controlled by the AK prosthesis according to the amputee's consciousness, fulfilling the amputee's desire to walk as well as a normal person. It is obvious that this method is of great significance in the AK prosthetic control.

By taking into account that the experiment is only a pilot study, more plentiful experiments are needed in the future study.

ACKNOWLEDGMENT

This work was supported by the National Natural Science Foundation of China (60575009), and National Science and Technology Support Program of China (2006BAI22B07). Thanks for the assistance.

REFERENCES

1. Genglin Zhang, Baoshi Jin, Yuguang Zhang.(2004)Current situation of artificial lower limbs of human body. Chinese Journal of Clinical Rehabilitation, May 15th
2. Tan Guanzheng, Xiao Hongfeng , Wang Yuechao.(2002)Optimal Fuzzy PID Controller with Incomplete Derivation and Its Simulation Research on Application of Intelligent Artificial Legs.Control Theory and Applications,19(3), pp462-466
3. Hugh Herr, Ari Wilkenfeld.(2003)User-adaptive control of a magnetorheological prosthetic knee. Industrial Robot: An International Journal. Volume 30, Number 1, pp42-55
4. Xin Guo, Peng Yang, Ying Li, Weili Yan (2004)The SEMG Analysis For the Lower Limb Prosthesis Using Wavelet Transformation. Proceedings of the 26th Annual International Conference of the IEEE EMBS, San Francisco, CA, USA, 2004, pp341-344
5. Ju-Won Lee and Gun-Ki Lee.(2005)Gait Angle Prediction for Lower Limb Orthotics and Prostheses Using an EMG Signal and Neural Networks, International Journal of Control, Automation and Systems, vol. 3, no. 2, pp152-158
6. Xinhe Xu, Hualong Xie, Binrui Wang et al (2006)Gait Perception and Coordinated Control of a Novel Biped Robot with Heterogeneous Legs, Proceedings of the 2006 IEEE/RSJ International Conference on Intelligent Robots and Systems, Beijing, China, 2006.pp356-361

Author: Tengyu Zhang
 Institute: School of Electrical Engineering and Automation
 Street: Mailbox452, Hebei University of technology (East Campus)
 City: Tianjin
 Country: China
 Email: zhangtengyu1985@163.com

Pixelized Images Recognition in Simulated Prosthetic Vision

Ying Zhao, Yukun Tian, Huwei Liu, Qiushi Ren, Xinyu Chai

Department of Biomedical Engineering, Shanghai Jiao Tong University, Shanghai, 200240 China

Abstract — A study and results about pixelized images recognition in simulated prosthetic vision were presented. Twenty object and five scene images were chosen from the databases which were almost familiar by everyone. Two kinds of image processing methods (binarization directly and edge extraction from low resolution images), two common shapes of pixel (square and circular) and six pixels numbers(8x8, 16x16, 24x24, 32x32, 48x48 and 64x64) were used to form pixelized images and presented on head-mounted display (HMD) one by one. According to the trials, the mean recognition accuracy increased with the increase of pixel array number. The threshold of objects recognition was within the interval of 16x16 to 24x24. For simple scenes, it was between 32x32 and 48x48. The images with the threshold resolution, binarization method and circular pixel shape have shown the best results for recognition.

Keywords — pixelized image, low resolution, simulated prosthetic vision, processing strategies, recognition.

I. INTRODUCTION

According to the statistic, China is the largest country in the world blind about 5 million, it accounts for 18% of the whole blind population. In addition, approximately 6 million people were low vision at the risk of becoming blind. Alarmingly, these numbers could be four times by the year 2020 without holding back the trends of annual increase 450,000 blind people. The enormous population has led many researchers to investigate state-of-art approaches to restore partial sight in blind and low vision patients. With the aim to replace the damaged optic tissues, several clinical trials of visual prosthesis prototypes have been built. These devices used the artificial signals created by electrical stimulations instead of visual neural signals to stimulate three different locations: retina, optic nerve or visual cortex in the visual pathway and elicit spots of light called phosphenes in the visual space [1-5].

Due to the limitation of electrode numbers, only low-resolution pixelized information can be transformed into electrical stimulations. Based on the trails from human, some investigators have studied simulated prosthetic vision with normal eyesight subjects [6-11]. Yet, most previous studies of pixelized image focused on the recognition rate of some special image patterns by choosing one or two simple objects. At the same time, these researches did not answer what kinds of image mode could optimize the recognition

rate on low resolution based on image processing technologies. Besides, only a few simple objects are not enough in developing visual prostheses while recognition of daily scenes is also significant for helping the blind in their daily life. The purpose of this study reported here is to investigate the primary factors in common object and scenes images recognition and optimize the recognition rate on low resolution using image processing technologies.

Based on the purpose and results of the other research, this paper presents a study and results about pixelized images recognition in simulated prosthetic vision. The rest of the paper is organized as follows: Section II provides a detailed description of the trial setting and procedures. In section III, the results are presented in detail. Finally, the conclusion and discussion are given in section IV.

II. MATERIALS AND METHODS

A. Materials

Images: As the basic material, twenty-five familiar images which are related with common life include 20 objects and 5 scenes were chosen with 288x288 pixels, as showed in Fig. 1.



Fig. 1 The original object and scene images: the upper four rows are objects; the last row is the simple scenes

Subjects: Thirty volunteers with normal or corrected-to-normal vision from Shanghai Jiao Tong University participated in this study as the subjects, 17 of them are male, and 13 are female. All the subjects were native Chinese and aged in the range of 21 to 26.

Trial setting: A head-mounted display (HMD) and computer with an experimental software package developed by us which is written in C++ language were used in the trials. The computer controlled the HMD to display the images which were acquired and preprocessed by a Digital Signal Processing (DSP) system which was designed and developed by us. The purpose of using HMD is to reduce the other irrelevant interference for vision such as ambient light or unstable visual angle. In order to obtain optimal result of recognition, the visual angle was 4.5° .

B. Methods

According to the former researches, there are a lot of factors such as the complexity of shape and texture of objects, pixel number, familiarity, processing strategies, gray scale, contrast, pixel size and shape, background noise, visual angle, etc., which could affect the recognition of objects and scenes in daily life. In this study, we focus on the impact of processing strategies, pixel shape and pixel numbers for recognition.

Pixel numbers: Because of the need of the trials, these images captured from the DSP system were resized into 288×288 pixels, 8 bit gray-scaled. Then, the 288×288 pixelized images were farther reduced into 64×64 , 48×48 , 32×32 , 24×24 , 16×16 and 8×8 step by step. The six pixel arrays were used as the one of three parameters for the trials.

Processing strategies: After resizing the original images to the determinative resolution, two methods of image processing means, binarization and edge extraction from low resolution images, were used to implement pixelized images. It was the second parameters. In the trials, the adaptive threshold selection for binarization was used, which is an important arithmetic for image segmentation. This method can separate the object and background in uncomplicated images and maintain the main features of objects. Another method which was used in the trials was edge extraction. As we all know, the image edge holds a lot of information such as location, shape, size and texture etc. Furthermore, Sobel operators are widely used in visual prosthesis image processing research [12]. In our research, four orientation kernels such as 0° , 45° , 90° and 135° were adopted to generate clear edge.

Pixel shapes: Additionally, the third parameter was the pixel shape. Two common shapes (square and circular) of pixel were selected and used as the simulate phosphenes.

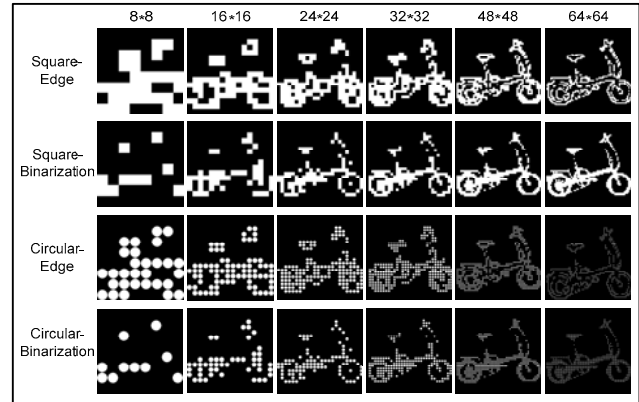


Fig. 2 Sample images used in experiment (bicycle). Each column corresponded to a given number of pixels (from 8×8 to 64×64) and each row corresponded to a given processing method and shape of pixel. The images were pixelized by white binary matrix pixels with 4.5° visual angle.

Two image processing methods and two kinds of pixel shapes were adopted in different image arrays respectively (8×8 , 16×16 , 24×24 , 32×32 , 48×48 , 64×64). Recognition accuracy of these objects and scenes with different pixel number and processing methods were tested by a simulated prosthetic vision system in normal eyesight individuals. The pixelized images of objects or scenes with different resolution were presented on HMD one by one. Fig. 2 showed an example of the pixelized image which was processed according to the need of trials.

C. Procedures

The experiments were performed in a quiet and dark room to obstruct the ambient light. There were two stage experiments. The first stage was called training program. It was carried out to make the subjects familiar with the whole experimental process, pixelized images and the interface of software. Moreover, the images which were used in training program were not contained in the formal testing database.

In the formal test, two processing strategies, two pixel shapes and six resolutions were assembled together to form the pixelized images. The object and scene images were selected randomly from the testing database.

The images were rendered on the screen of the computer and the HMD which wore by the subjects synchronously in term of 8×8 , 16×16 , 24×24 , 32×32 , 48×48 and 64×64 .

Whether the training program or formal test, the subjects were requested to tell object or scene's name when it was legible. On the contrary, subject should tell the administrator "no" when the object or scene was illegible. For simple scenes, as long as the main objects in them could be

described, it was correct. The acceptable answers and resolution for this image were shown at the bottom of the computer screen and HMD. However, because it was too tiny to identify on the screen of HMD, subjects can't see the answers. Subjects were asked to identify the rendered images as soon as possible, and moderately guess was permitted. Right after the participant's recognition, the administrator recorded the result immediately according to the participant's judgment by pressing the key "R" or "W", where "R" meant correct and "W" meant illegibility. The experiment software package recorded the recognition accuracy of each image.

III. RESULTS

After the trials with whole subjects, the statistical analysis of the results was received. In these statistical results, if the standard deviation of individual recognition accuracy was more than twice of the mean standard deviation, the data of individual would be considered to be unreliable and deleted from the overall data.

A. Objects:

As showed in Fig. 3, the trend of object recognition was improved with the increase of the pixel number. Although, the recognition accuracy is close to zero in 8x8 pixels array, the recognition with the combination of two processing methods and two pixel shapes reached almost near 100% when the resolution was up to 64x64.

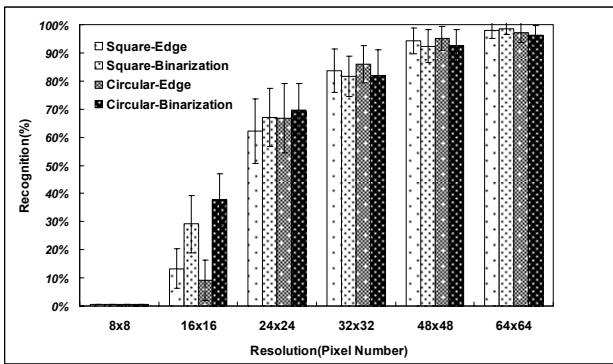


Fig. 3 Recognition of object images in four pixelized forms with different pixels array number

For the 16x16 pixels array, the recognition accuracy with binarization strategy shows noticeable increase more than the recognition accuracy with edge strategy. However, when the processing method was edge, the square pixel shape achieved better recognition than the shape of circular.

With the increase of resolution from 24x24 up to 64x64, the impact produced by the shape of pixels is not obvious relatively. The Circular-Binarization image was still the most easily identifiable

B. Scenes:

Accordingly, the trend of scenes recognition was rose when the pixel numbers increased from 8x8 to 64x64 just as the same as objects'. Fig. 4 showed the result of scene images recognition.

It is clear that the recognition with resolution from 8x8 to 24x24 was close zero from Fig. 4. When the resolution was up to 32x32, the recognition got remarkable increase. It suggest, for the scenes recognition, without sufficient priori information, it is very hard to identify the scenes while the resolution is lower than 32x32 pixels arrays.

At 32x32 pixels arrays, there is a great diversity of recognition accuracy for four methods: from Square-Binarization, Square-Edge and Circular- Binarization to Circular-Edge. For 48x48, the diversity of recognition accuracy of different image modes become negligible, meanwhile, the mean recognition accuracy of these four modes has an obvious growth (near 60%). For 64x64 the mean recognition accuracy reach near 80%, and the image of 'circular-edge' is easier to recognize.

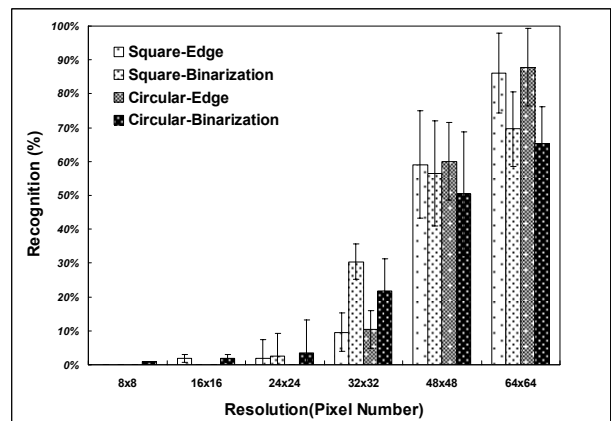


Fig. 4 Recognition of scene images in four pixelized forms with different pixels array number

IV. DISSICUSION AND CONCLUSION

Although vision prosthesis offers hope to the people whose visual system is damaged by disease or trauma facing the ultimate result blind, the limitations including manufacturing technology of stimulating electrodes, microelectronics and biocompatibility restrict the possibility that it can replace the complexity of the visual system up to now. Due to the limitation of the existing techniques it will be difficult to increase pixel number for the actual visual prosthesis. For the other factors like increasing grayscale level, which are useful method to increase recognition accuracy, its mechanism is not very clear.

As some former researches showed, there are a lot of factors which might have significant effects on the performance of the trials in simulation prosthetic vision.

Firstly, some psychological factors such as aprosexia may be one factor affected the final result of recognition if it occurred in the process of test. It might cause by long testing time. In order to avoid this factor, if subject felt aprosexia or tired, she or he can tell the administrator to have a break during the test.

Secondly, there was an interesting instance that some subjects can not recognize the pixelized images correctly which most subjects could identify. It may suggest that different acquired knowledge, experiences and spatial imagination ability of varied person make such phenomenon. For the sake of reducing such effect to the minimum, it is necessary to adopt the pre-testing or called training program before the formal trials.

Thirdly, under low resolutions, some objects which have the similar profile such as comb and banana, the recognition of them is lower than the other images which haven't similar profile. It is shown that if one object's profile could be identified more than two objects at low resolution, the profile information can not use as the only identified feature. It needs to introduce additional feature information and combine with the profile to realize the object identify. Some investigator used some other feature extraction methods to improve the recognition. Some groups [10, 13, and 14] had already showed their research for many of the basic local information of image.

As we mentioned before, the simple scenes were selected for this trials. Based on our research, the recognition of objects and simple scenes were achieved by relatively simple processing method. However, for some complex scenes, these methods cannot be used to extract the most useful information to instruct the recognition. Therefore, some methods which have been used in mechanism vision may be used in deal with the complex scenes recognition.

At the end of this paper, our research shows that the threshold of objects recognition is within the interval of 16x16 to 24x24. For simple scenes, it was between 32x32 and 48x48. Near the threshold of recognition on low resolution, there is great impact on recognition accuracy with different image mode. The images with the threshold resolution, binarization method and circular pixel shape have shown the best results for recognition. We hope these works are useful for design and development of visual prosthesis to provide functional vision for the blind in the near future.

ACKNOWLEDGMENT

The authors thank the volunteer subjects. This research is supported by the National Basic Research Program of China (973 Program, 2005CB724302), The National Natural Science Foundation of China (60671059); National High Technology Research and Development Program of China (863 Program, 2006AA04Z356); National Science Fund for Distinguished Young Scholars from The National Natural Science Foundation of China (60588101), by the 111 Project from the Ministry of Education of China (B08020), and Shanghai Commission of Science and Technology (05DZ22318, 05DZ22325, 04DZ05114, 064119540).

REFERENCES

- Humayun M. S., Weiland J. D., Fujii G.Y., Greenberg R., Williamson R., Little J., Mech B et al. (2003) Visual perception in a blind subject with a chronic microelectronic retinal prosthesis. *Vision Res.*, vol. 43, no. 24, pp. 2573–2581.
- Dobelle.W. H. (2000) Artificial Vision for the Blind by Connecting a Television Camera to the Visual Cortex. *Amer. Soc. Artificial Internal Organs*, vol. 46, pp. 3–9.
- Delbeke J., Oozeer M., and Veraart C.. (2003) Position, size and luminosity of phosphenes generated by direct optic nerve stimulation. *Vision Res.*, vol. 43, no. 9, pp. 1091–102.
- Veraart C., Raftopoulos C., Mortimer J. T., Delbeke J., and Pins D. (1998) Visual sensations produced by optic nerve stimulation using an implanted self-sizing spiral cuff electrode. *Brain Res.*, vol. 813, pp. 181–186.
- Rizzo J. F., Jensen R. J., Loewenstein J., and Wyatt J. (2003) Unexpectedly small percepts evoked by epi-retinal electrical stimulation in blind humans. *Invest. Ophthalmol. Vis. Sci.*, vol. 44, no. 5, pp. 4207–4207.
- Cha K, Horch KW. (1992). Normann RA. Simulation of a phosphenebased visual field: visual acuity in a pixelized vision system. *Ann Biomed Eng* 20, 439–449.
- Cha K et al. (1992). Mobility performance with a pixelized vision system. *Vision Res* 32, 1367–72.
- Hayes J. S. et al. (2003). Visually guided performance of simple tasks using simulated prosthetic vision. *Artif. Organs* 27, 1016–1028.
- Dagnelie, G. et al. (2007). Real and Virtual mobility performance in simulated prosthetic vision. *Journeal of Neural Engineering* 4, S92–S101.
- Boyle, J. R. et al.(2001). Challenges in Digital Imaging for Artificial Human Vision. *Proceedings of SPIE* 4299.
- Thompson R, et al.(2003). Facial recognition using simulated prosthetic pixelized vision. *Investigative Ophthalmology& Vision Science*, 44 (11), 5035-5042.

12. Snaith Martin et al. (1998). A low-cost system using spare vision for navigation in the urban environment. *Image Vision and Computing* 16, 225-238
13. Privitera C M, Stark L W. (2000). Algorithms for defining visual region of interest: comparison with eye fixations. *IEEE Transactions on Pattern Analysis and Machine Intelligence* 22 (9), 970-981.
14. Itti L, Koch C. (2000). A saliency based search mechanism for overt and covert shifts of visual attention. *Vision Research* 40 (10212), 1489-1506.

Author: Xinyu Chai
Institute: Department of Biomedical Engineering, Shanghai Jiao Tong University
Street: Dongchuan Road 800
City: Shanghai
Country: China
Email: xychai@sjtu.edu.cn

Artificial Horse for Rehabilitation

C.Y. Li¹, H.T. Gao¹, Y.B. Ma², C. Liu¹ and H. Wang¹

¹ Northeastern university, Shenyang, China

² LiaoNing Food & Drug Administration, Shenyang, China

Abstract — This essay gives a presentation about artificial horse for rehabilitation which is called rehabilitation horse. It is chiefly used for preventing and alleviating the cervical vertebra disease; it is also applied for burning extra fat of hip and belly. In other words, it can be effective for losing weight and shaping women's figure. We observed the law of horse movement and then proposed the kinematic sketch of mechanism of the rehabilitation horse. We also constructed out the three-dimension model with Pro/E. The model is adopted two-floor structures which are mostly made up of the crank-rocker, four-bar linkage mechanism and a slide. The crank-rocker mechanism is to simulate horse's main movement. And others are to simulate horse' muscle movement. It's essential to do simulations before product finished. We also did experiments to check whether it had effects on human body or mot. The electrodes were located on the 5th section of cervical vertebra to obtain EMG signal. Some electrodes were put on belly to get EMG signal, although this signal was a little fainter than the previous. The series of experiments obviously indicated that rehabilitation horse worked on human body effectively and efficiently. According to some medicinal principles, it is easy for us to draw a conclusion that the horse has a positive influence on the recovery rate of human body. We hope that our product will provide an interesting way to our healthy life and make us healthy more easily.

Keywords — Rehabilitation Horse, Cervical Vertebra Disease, Shaping Figure, Crank-rocker Mechanism, The Law of Horse Movement.

I. INTRODUCTION

A lot of people have the symptom with pains on the waist and back with the computer popularizing and the work pressure increasing. The symptom can turn to cervical vertebra disease gradually. It's reported that the number of the patients has exceeded 0.1 billion [1]. Moreover surveys show that the cervical vertebra disease which usually happens on the old people is tending to the younger year by year [2]. Though there are many ways for its treatment, the green and interesting method lacks. Medical researches indicate that riding a horse can prevent and alleviate the cervical vertebra disease.

People, especially the female pay more attentions to their figure as life quality improving. Women ask higher request

to their stature. So the number of those losing weight is going up dramatically. But there is lack of effective and enjoyable means. And burning extra fat of hip and belly is more difficult to realize. Riding a horse can make it easily [3]. It's reported that above 90% young ladies of beauty competition in the western countries choose riding a horse as their body building means. At the same time, riding a horse can apply for shaping waist, modeling the curve of thigh and beautifying posture and so on. Besides, it also has an efficacy of massage to the viscera organ. In a word, riding a horse has a lot of benefits.

But the high expenses of riding a horse makes many people terrify and horses are looked after difficultly. Furthermore it's inconvenient to ride a horse in a city. So a type of mechanical horse which simulates the law of horse is waiting for to come true. We hope that the rehabilitation horse can inject the new blood into people's green and sunshine life.

II. DRESIGNING CONTENT

A. The kinematic sketch of mechanisms

In order to find out the movement character of the horse, we have done lots of researches at first. We found that the law of horse movement could be divided into three conditions (walking slowly, walking quickly and running quickly). But it's not meaningful to research walking. We concentrated on running mainly. If described the horse running motion, it likes "draw the rounds" consecutively. The feeling of riding a horse is up and down as horse running.

It is clear that the leading mechanism is the crank-rocker mechanism which simulates horse's main movement. It can get better feelings when the whole mechanism goes back. The more important is that it is very similar to the law of horse movement. Secondary mechanisms which simulates horse' back muscle moving consist of the four-bar linkage and a slide mechanism. Riding a horse could achieve lots of effects partly depending on its muscle movement to bring about man's muscle group moving. It is also used for making up a displacement.



Fig. 1 The kinematic sketch of mechanism of rehabilitation horse

B. Designing processing

Lots of individual factors were considered in the design course. We constructed out the three-dimension model with three-dimensional software Pro/E basing on the kinematic sketch of mechanism. In this process we adopted two-floor structures boldly. The lower floor includes the crank-rocker and four-bar linkage mechanism. There is only a slide mechanism on the upper floor which a saddle can be installed. This model is fitted for our demands easily. At the same time, it's necessary to consider control method. One motor was introduced in terms of making control method more easily and economical. But one coin had two sides. The dimensional designing became more difficult because of one rod dimension relating to more bars'. We imaged each bar after the whole scheme was decided. Then the bars were assembled together so we could do simulations to test if the model satisfied our choosing parameters. To compare with real horse movement, we detected the curve of speed

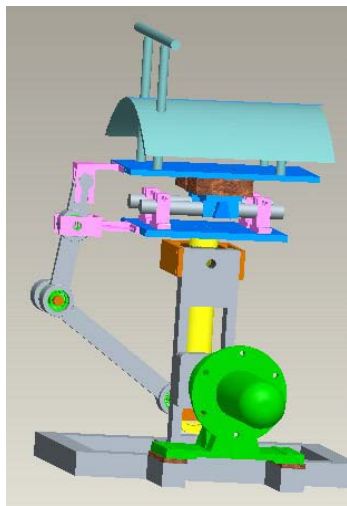


Fig. 2 Three-dimensional model

and acceleration of the model. We also adjusted motor's speed to find out better curve. Of course, it was essential to continually improve the model's dimension and size at the same time. The model was put in Adams to analyze its load conditions after the model was completed.

III. CONCLUSION

We have produced one product in a factory according to the three-dimensional model. But it is not enough. We must do experiments to check whether it has effects on human body or not. Medical researches show that the cervical vertebra disease mainly happens on the 4th, 5th, 6th sections of cervical vertebra [4]. We mainly put electrodes on the 5th sections of cervical vertebra to obtain EMG signal on the ground of experimental condition limiting. We used the TDS3012B OSCILLOGRAPH to collect data. We could get many groups of signal in one period of rehabilitation horse moving. But we could not put every group of signal in this essay .It is typical to exhibit one. Horizontal axis is time and vertical-axis is amplitude.

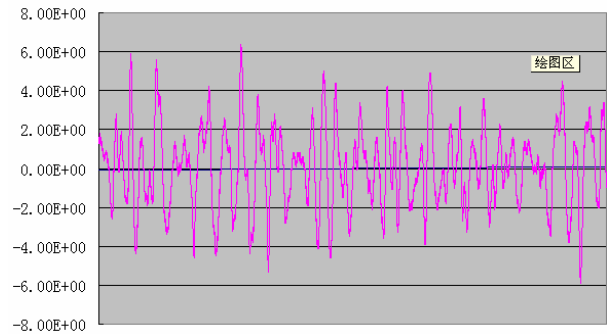


Fig. 3 Signal obtained from back

Some electrodes were also put on belly to get EMG signal. But this signal is fainter then the previous. One typical group of signal is following.

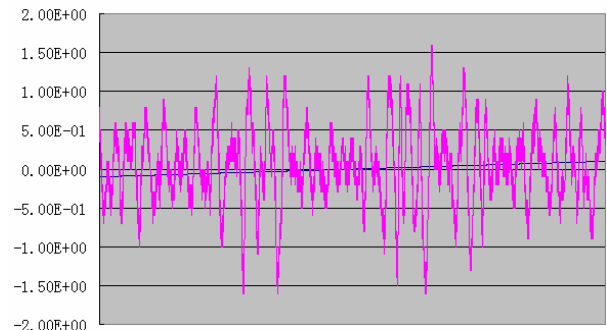


Fig. 4 Signal obtained from belly

Series of experiments shows that the horse could stimulate some muscle and some parts of cervical vertebra to exercise. It obviously indicated that rehabilitation horse worked on human body effectively and efficiently. According to some medicinal principles, it is easy for us to draw a conclusion that the horse has a positive influence on the recovery rate of human body.

It is no denying that we should explore by ourselves because there are not similar things to consult. Moreover various parameters of horse movement are lacking. However we create it.

ACKNOWLEDGMENT

This work was supported by National Science Foundation of China (50435040).

REFERENCES

1. Excising for Cervical Vertebra Disease Everyday at <http://www.39.net>
2. A Pressing Mission to Prevent Cervical Vertebra Disease at <http://www.sina.com.cn>
3. CHI LP (2007) Riding Horse for Excising and Shaping Figure .Popular Medicine 8:41
4. The Result So Surprisingly Consistent, Cervical Vertebra Disease happens on 4th, 5th, and 6th at <http://www.sina.com.cn>

Author: Hong Wang
Institute: Northeastern University
Street: No. 3-11, Wenhua Road, Heping District
City: Shenyang
Country: China
Email: hgwang@mail.neu.edu.cn

Effect of Shank Curve of High-heeled Shoe on the Plantar Pressure Distribution

Y. Cong, Y. Luximon and M. Zhang

Department of Health Technology and Informatics, The Hong Kong Polytechnic University, Hong Kong, China

Abstract — The purpose of this study is to investigate the effect of shank curve of high-heeled shoe on the plantar pressure distribution. In this preliminary study, plantar pressures were measured in four healthy women, during walking in high-heeled shoes (3 inches height) with 3 different shank curves described by the depth of last. The foot was divided into 3 regions (forefoot, midfoot, rearfoot). For each region, the parameters, namely pressure-time integrals (PTI), peak contact area (PA), and peak pressure (PP) were calculated from two stable steps of each walking trial. The PTI in forefoot region decreased as the depth of last increased, while it increased in midfoot and rearfoot regions. The higher depth of last generated the less peak pressure in the forefoot region in midstance phase. However, in rearfoot, the peak pressure did not significantly change ($p=0.869$). Because of extra arch support with increasing depth of last, the PTI, the PP and the PA in midfoot region all increased significantly ($p<0.05$).

Keywords — high-heeled shoes, shank curve, plantar pressure

I. INTRODUCTION

There is a strong possibility that numerous lower-extremity problems are associated with high-heeled shoes. Long-term wearers of high-heeled shoes are vulnerable to suffer from foot problems, such as hallux valgus, metatarsalgia and calluses, due to the abnormal high load in hallux and central forefoot region as heel height increases [1-3]. However, over midfoot region, the arch height may increase with increasing heel height, which will lead to the decrease in pressure and contact area [4-6]. Midfoot region might be considered to be important in redistributing the abnormal plantar loads in high-heeled shoes. So far, little research has focused on the effect of different shank curve designs for high-heeled shoes on the distribution of plantar pressure. Most designers pay more attention on the fashion of shoes but less consider the comfort issue. Results from this study will be useful in providing the evidence to redistribute the mechanical stresses in high-heeled shoes and some practical suggestions for wearers how to choose high-heeled shoes to prevent the related foot problems.

II. MATERIALS AND METHODS

Four female subjects were recruited for this investigation. Selection was made on the basis that individuals could fit comfortably into the selected high-heeled shoes and had clinical normal feet. The “clinical normal feet” means no report about particularly high or low arch, limb-length discrepancy, hallux valgus, tailor’s bunion, hammer digits, or plantar callosities. Additionally, those who have potentially impair walking, ankle, knee, hip and back problems, systemic diseases and neurological defects impairing gait will be also excluded from the study. The subjects in this study did not wear the high-heeled shoes very often, however, they have the experience of wearing high-heeled shoes, and their gait performed naturally. This requirement was set to make sure their feet are normal and minimize variation in motor control that could result from different levels of habituation. The average age of the subjects was 25 years (range 23-27 years), average body mass was 53 kg (range 48-55 kg), and average height was 160 cm (range 158-162 cm).

The shoes used in this study were 3-inches heel height. To keep the similar construction of the shoes such as foot contact points, heel height, toe box and pump style, insoles with different shapes were designed to simulate different shank curves. Shank curve is described by the depth of last (the distance from the waist of the last to the line jointing the heel breast and the ball tread). Three different shank curves were selected (5mm, 8mm and 11mm respectively). The insole material has hardness of about 60° (shore A). Plantar pressure distribution was measured used Tekscan in-shoe pressure measurement system (Tekscan Co., Boston, USA). To avoid slipping between the inside and the shoe, the inserts were adjusted to appropriate position and then attached inside the shoe.

The insoles with different shank curves were randomly assigned to the subjects. On each occasion, the subjects were first asked to walk along a 10m lab walkway as naturally as possible for a few minutes prior to data recording to familiarize the shoes and the different shank curves. After a short rest, the subjects were asked to walk at a constant comfortable cadence. Data was recorded at a frequency of 100Hz for 10s in their middle of the test walk. Repeated measure was conducted for each occasion until three successful trials completed. To prevent fatigue, each subject

took a 5-min rest in between. A total of 36 trials (4 subjects \times 3 shank curves \times 3 trials) were obtained for data analysis.

The foot was divided into 3 regions (forefoot 37% of foot length, midfoot 30% of foot length and rearfoot 33% of foot length). For each region, the parameters, namely pressure-time integrals (PTI), peak contact area (PA), and peak pressure (PP) were calculated from two stable steps of each walking trial.

III. RESULTS

In the whole stance phase, PTI was calculated to provide an understanding of the load distribution applied over time. The results (Fig. 1) show that the PTI in forefoot region decreased as the depth of last increased, while it increased in midfoot and rearfoot regions. Similar to PTI, the higher depth of last generated the less peak pressure in the forefoot region in midstance phase (Fig. 2). The peak pressure in midfoot region increased significantly ($p < 0.05$) because of

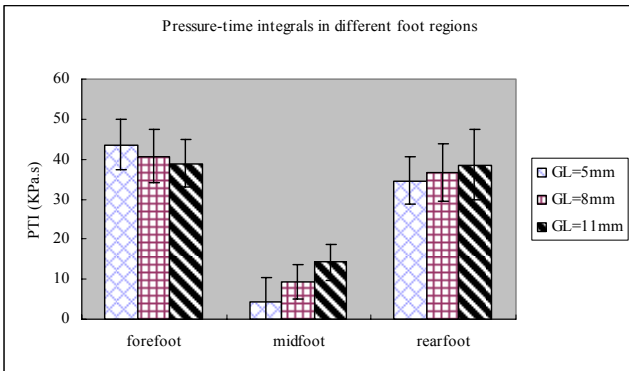


Fig. 1 Pressure-time integrals in different foot regions under different shank curves

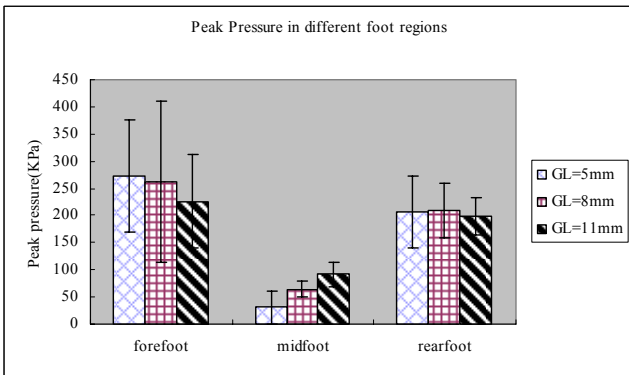


Fig. 2 Peak pressure in different foot regions under different shank curves during the midstance phase

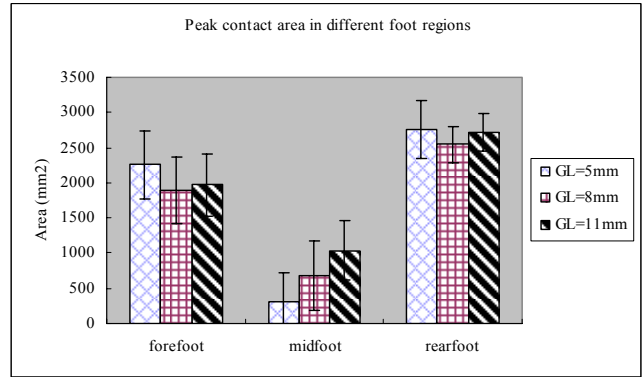


Fig. 3 Peak contact area in different foot regions under different shank curves

extra arch support with increasing depth of last. However, the peak pressure in rearfoot did not significantly change when the shank curve changed ($p=0.869$). As it is shown in Fig. 3, the peak contact area in midfoot region increased significantly ($p < 0.05$) with the depth of last, due to the extra arch support.

IV. DISCUSSION

It has been suggested that as heel height increases, the pressure and the contact area in midfoot decrease [7-10], because excessive dorsiflexion of the hallux led the medial longitudinal arch to rise [11, 12]. Shank curve design is very important in high-heeled shoes in terms of plantar load distribution. Ill-fitting shank curve design might cause flat foot due to insufficient arch support and injury of muscle or tendons because of the excessive support. At the first stage, the study attempted to investigate possible relationships between different shank curve designs and the distribution of plantar pressure. The results from this study demonstrated that different shank curve designs might contribute to the change of plantar pressure pattern. Increasing depth of last increased the contact area, peak pressure and PTI in midfoot region, while in forefoot region, the peak pressure during midstance phase and the PTI of the whole stance phase decreased. It might be explained by the fact that the extra arch support as an extension of the heel seat prevents foot sliding forward, and results in higher percentage of the weight being carried by the midfoot and heel seat. Previous studies have proved that arch support can effectively reduce the forefoot pressure [8], which might be benefited to reducing the risk of forefoot problems.

V. CONCLUSION

In high-heeled shoes, midfoot region can be considered to be an important foot region to redistribute the foot plantar pressure. Moderate shank curve might reduce the pressure in forefoot region, and make the plantar pressure distribution more even. It might benefit to reduce the risk of suffering from various foot problems.

ACKNOWLEDGEMENTS

This work was supported by the research Grant Council of Hong Kong (No. POLYU 5317/05E) and The Hong Kong Polytechnic University research studentship.

REFERENCES

1. Mandato MG, Nester E (1999) The effects of increasing heel height on forefoot peak pressure. *J Am Podiatr Med Assoc* 89(2):75-80
2. Al-Abdulwahab SS, Al-Dosry RD (2000) Hallux valgus and preferred shoe types among young healthy Saudi Arabian females. *Ann Saudi Med* 20:319-321
3. Kernozek TW, Elfessi A, Sterriker S (2003) Clinical and biomechanical risk factors of patients diagnosed with hallux valgus. *J Am Podiatr Med Assoc* 93(2):97-103
4. Schwartz RP, Heath AL (1959) Preliminary finding from a roentgenographic study of the influence of heel height and empirical shank curvature on osteo-articular relationship of the normal female foot. *J Bone Joint Surg Am* 41: 1065-1076
5. McCrory JL, Young MJ, Boulton AJM, Cavanagh PR (1997) Arch index as a predictor of arch height. *Foot* 7(2): 79-81
6. Morag E, Cavanagh PR (1999) Structural and functional predictors of regional peak pressures under the foot during walking. *J Biomech* 32(4): 359-370
7. Nyska M, McCabe C, Linge K, Klenerman L (1996) Plantar foot pressure during treadmill walking with high-heel and low-heel shoes. *Foot Ankle Int* 17(11): 662-666
8. Lee YH, Hong WH (2005) Effect of shoe inserts and heel height on foot pressure, impact force, and perceived comfort during walking. *Appl Ergon* 36:355-362
9. Hong WH, Lee YH, Chen HC et al. (2005) Influence of heel height and shoe insert on comfort perception and biomechanical performance of young female adults during walking. *Foot Ankle Int* 26(12): 1042-1048
10. Speksnijder CM, vd Munckhof RJ, Moonen SA et al. (2005) The higher the heel the higher the forefoot-pressure in ten healthy women. *Foot* 15:17-21
11. Shimizu M, Andrew PD (1999) Effect of heel height on the foot in unilateral standing. *J Phys Ther Sci* 11:95-100
12. Aquino A, Payne C (1999) Function of plantar fascia. *Foot* 9:73-78

Author: Prof Ming Zhang
 Institute: The Hong Kong Polytechnic University
 Street: Hung Hom, Kowloon
 City: Hong Kong
 Country: China
 Email: htmzhang@inet.polyu.edu.hk

Effects of Qinglongyi Polysaccharide on complex biochemistry function with the core of Band 3 on Erythrocyte

Chenfeng Ji, Yubin Ji, Xiang Zou, Feng Xiao

Postdoctoral Programme, Institute of Meteria Medica, Center of Research and Development on Life Sciences and Environment Sciences of Harbin University of Commerce, Harbin 150076, China
jyb@hrbcu.edu.cn; jichenfeng@hrbcu.edu.cn

Abstract — Objective: To explore the effects of Qing long yi polysaccharide on biochemical functions of band 3 core complex in S₁₈₀ mouse erythrocyte membrane.

Methods: We use SDS-PAGE method and G-250 dye to study the effect of qing long yi polysaccharide on band 3 content of S₁₈₀ mouse erythrocyte, use LSCM to measure the concentration of H⁺ in erythrocyte of S₁₈₀ mice, use fluorescence spectrophotometry to determine membrane fluorescence polarization and microviscosity, use spectrophotometer to measure sialic acid content on erythrocyte membrane, ATPase test kits to determine the activities of Na⁺,K⁺-ATPase and Ca²⁺,Mg²⁺-ATPase, use FCM to measure membrane potential.

Results: It showed medium(50mg/kg) and high-dosage (100mg/kg) of Qing long yi polysaccharide increased band 3 content. The result showed medium- dosage (50mg/kg) of Qing long yi polysaccharide signally increased band 3 function on Cl⁻ transportation, decreased the concentration of H⁺, decreased the concentration of Ca²⁺, increased membrane fluidity, increased sialic acid content, enhanced the activities of Na⁺,K⁺-ATPase and Ca²⁺,Mg²⁺-ATPase, heightened membrane potential.

Conclusion: Qing long yi polysaccharide can improve biochemical functions of band 3 core complex in S₁₈₀ mouse erythrocyte membrane, Which enhance the immunity function of erythrocytes, it may be one of the most important anti-tumor mechanisms.

I INTRODUCTION

Qing long yi is a traditional chinese medicine, which has extensive pharmacological effects, and its anti-tumour effect has been extensive identified. Our early experiment show Qing long yi polysaccharide can inhibit tumor cell growth of S₁₈₀ and H₂₂ mouse, on the basis of that, We investigate its mechanism of antitumour effect from erythrocyte membrane biology foundation. We explored the effects of Qing long yi polysaccharide on biochemical functions of band 3 core complex in S₁₈₀ mouse erythrocyte membrane.

II MATERIALS

2.1 Model and Cell Line

KM mouse(20±2.0)g, purchased from Harbin Medical University; sarcoma S₁₈₀, which has been maintained by the Institute of Cancer Studies of Heilongjiang Cancer Hospital. To form a mouse model with tumor, Cell line solution with a concentration of 2×10⁷个/mL was inoculated 0.2 mL a mice.

2.2 Groups and Dose

Mice are divided into 6 groups, including: normal control; negative control (saline group); positive control (5-FU); groups to be treated with low (25mg/kg), medium(50mg/kg), and high-dosage (100mg/kg) of Qing long yi polysaccharide.

2.3 Materials and Reagents

Qing long yi polysaccharide; SPQ; Fluo-3/AM; BCECF-AM; Rhodamine 123; protein content test kit; sialic acid test kit; ATPase test kit

III METHODS

3.1 The effect of Qing long yi polysaccharide on Cl⁻ Concentration in erythrocyte

SPQ with a final concentration of 2.5 mmol/L was added to the solution containing erythrocytes and buffer to react on Cl⁻. Then the solution was incubated under a condition of 37°C, 2h and observed on fluorescence spectrophotometer. Fluorescence was detected in absorption spectrum of 350nm and fluorescence spectrum of 460nm.

3.2 The effect of Qing long yi polysaccharide on H^+ Concentration in erythrocyte

BCECF-AM with a final concentration of 10 μ M was added to the solution containing erythrocytes and buffer to react on Cl^- . Then the solution was incubated under a condition of 37°C, 2h and observed on fluorescence spectrophotometer. Fluorescence was detected in absorption spectrum of 488nm and fluorescence spectrum of 535nm.

3.3 The effect of Qing long yi polysaccharide on Ca^{2+} Concentration in erythrocyte

Fluo-3/AM with a final concentration of 4 μ g/mL was added to the solution containing erythrocytes and buffer to react on Cl^- . Then the solution was incubated under a condition of 37°C, 2h and observed on fluorescence spectrophotometer. Fluorescence was detected in absorption spectrum of 488nm and fluorescence spectrum of 535nm.

3.4 The effect of Qing long yi polysaccharide on the fluidity of membrane lipids

2 mL of DPH solution was added to the standard tube, while the same amount of isotonic PBS buffer solution was added to the blank tube. Solution in the two tubes was mixed and incubated for 30 min at 25°C. Fluorescence spectrophotometer was used to measure the intensity P of fluorescence polarized light both when it was parallel to and when it was perpendicular to the direction of vibration of the excitation polarized light, excitation wavelength: 362 nm, emission wavelength: 432 nm.

3.5 The effect of Qing long yi polysaccharide on the content of sialic acid on the erythrocyte membrane

Erythrocytes were hemolysed in Tris-HCl (10 mmol/L, pH 7.4), and the protein in cell membrane was separated by centrifuge (12000 \times g 15 min, 4°C). During the hemolysis. The content of protein in the membrane was quantified by CBB_{G250}. The content of SA was determined on spectrophotometer depending on a purple compound formed by oxidated SA and 5-Methylresorcinol.

3.6 The effect of Qing long yi polysaccharide on the activities of Na^+, K^+ -ATPase and Ca^{2+}, Mg^{2+} -ATPase on the erythrocyte membrane

The sample was examined using the relevant test kit following procedures given in literature. Enzyme activity is expressed in number of moles of inorganic phosphorus produced by a milligram of protein per hour. The unit is μ mol Pi/(mg.pr.h).

3.7 The effect of Qing long yi polysaccharide on the membrane potential of erythrocytes

100 μ l of the blood solution was drawn and PBS was added to bring the volume to 2 ml to yield the needed erythrocyte suspension. 2 ml of PBS was added to the suspension, which was centrifuged for 6 min at 2,500 rpm, after which the supernatant was discarded. 0.5 ml of Rhodamine 123 with a final concentration of 10 μ g/ml was added to the residue, and the sample was incubated for 30 min at 37°C. Flow cytometer was used, excitation wavelength: 488nm, radiation wavelength: 530nm.

IV RESULTS

4.1 The effect of Qing long yi polysaccharide on Cl^- Concentration in erythrocyte

Tab.1 Effects of Qinglongyi polysaccharide on Cl^- Concentration compared with control: * $p < 0.05$, ** $p < 0.01$

Group	Flu-intensity
Normal	6.10 \pm 0.21
Control	1.59 \pm 1.09
5-FU	5.68 \pm 1.02**
Low	4.98 \pm 0.31**
Mid	4.57 \pm 0.98**
High	2.82 \pm 0.39

4.2 The effect of Qing long yi polysaccharide on H^+ Concentration in erythrocyte

Tab.2 Effects of Qinglongyi polysaccharide on $[H^+]$ of RBC of mice with tumor S₁₈₀

Group	ROI
Normal	10.67 \pm 2.10**
Control	85.39 \pm 6.12
5-FU	60.21 \pm 7.31
Low	49.13 \pm 6.21 **
Mid	47.87 \pm 5.19**
High	29.82 \pm 2.38 **

4.3 The effect of Qing long yi polysaccharide on Ca^{2+} Concentration in erythrocyte

Tab.3 Effects of Qinglongyi polysaccharide on $[Ca^{2+}]$ of RBC of mice with tumor S₁₈₀

Group	ROI
Normal	30.59±6.32**
Control	116.19±2.36
5-FU	98.62±5.69
Low	95.87±5.26*
Mid	56.97±3.62**
High	67.58±3.25 **

4.4 The effect of Qing long yi polysaccharide on the fluidity of membrane lipids

Tab.4 Effects of Qinglongyi on membrane fluidity of mice with RBC S₁₈₀

Group	P	η	LFU
Normal	0.13±0.01	0.78±0.10	21.67±2.14
Control	0.18±0.01	1.2574±0.10	10.36±1.38
5-FU	0.15±0.01**	0.97±0.11**	16.01±2.86**
Low	0.17±0.01*	1.13±0.11*	12.31±1.57*
Mid	0.16±0.00**	1.04±0.14**	14.46±1.596**
High	0.16±0.00**	1.03±0.14**	14.70±0.29**

4.5 The effect of Qing long yi polysaccharide on the content of sialic acid on the erythrocyte membrane

Tab.5 Effects of Qinglongyi polysaccharide on the content of SA from erythrocyte membrane

Group	SA(mmol/L)
Normal	1.086±0.097**
Control	0.667±0.014
5-FU	0.753±0.051
Low	0.828±0.038*
Mid	0.957±0.092**
High	0.892±0.049*

4.6 The effect of Qing long yi polysaccharide on the activities of Na^+,K^+ -ATPase and Ca^{2+},Mg^{2+} -ATPase on the erythrocyte membrane

Tab.6 Effects of Qinglongyi on RBC membrane Na^+,K^+ -ATPase and Ca^{2+},Mg^{2+} -ATPase activity of S₁₈₀ mice

Group	Na^+,K^+ -ATPase	Ca^{2+},Mg^{2+} -ATPase
Normal	0.31±0.031	0.29±0.01
Control	0.16±0.00	0.15±0.00
5-FU	0.20±0.01*	0.22±0.02**
Low	0.18±0.01*	0.18±0.03*
Mid	0.21±0.01*	0.21±0.01**
High	0.22±0.03*	0.22±0.01**

4.7 The effect of Qing long yi polysaccharide on the membrane potential of erythrocytes

Tab.7 Effects of Qinglongyi polysaccharide on the potential of erythrocyte membrane

Group	Flu-intensity(%)
Normal	99.1%±4.2%
Control	36.3%±3.0%
5-FU	68.7%±2.9%**
Low	50.5%±4.8%*
Mid	78.0%±5.1%**
High	87.3%±4.6%**

V DISCUSSION

Band 3 is the most prolific protein on erythrocyte membrane, which account for 25% - 30% membrane protein content, also it is the most important structural and functional protein. Band 3 is the most important anion exchange protein on erythrocyte membrane, which includes tdb3 and cdb3, and the anion exchange function is performed by tdb3. It showed Qing long yi polysaccharide signally increased band 3 function on CI transportation.

Cdb3 interacts with many skeleton proteins, mainly like ankyrin and protein 4.1. The interaction between cdb3and

ankyrin is dependent on pH. It showed qing long yi polysaccharide decreased the concentration of H^+ , pH trended to normal, which helps the combination between cdb3 and ankyrin. Protein 4.1 has a special structure domain controlled by $[Ca^{2+}]$, its structure would change if $[Ca^{2+}]$ increased, which caused the affinity with cdb3 weaken. we use LSCM to measure the concentration of Ca^{2+} in erythrocyte of S_{180} mice. It showed all three dosage of qing long yi polysaccharide decreased the concentration of Ca^{2+} , which controlled the structure change of Protein 4.1 and promoted the combination between cdb3 and protein 4.1, so the cell skeleton structure maintained stabilization.

The change of membrane protein can cause the digression of membrane fluidity, in pathology, the digression of membrane fluidity is related with the decreased content of band 3. The result showed all three dosage of qing long yi polysaccharide increased membrane fluidity, which is in accordance with band 3 content increase. Erythrocyte membrane liquidity depend mainly on the ratio of cholesterol and phospholipids, we use assay kit to measure the content of cholesterol and phospholipids in erythrocyte of S_{180} mice. The result showed all three dosage of qing long yi polysaccharide decreased cholesterol content, increased phospholipids content, so the ratio of cholesterol and phospholipids decended, and the membrane fluidity improved.

Negative charge on erythrocyte mainly come from pantothenic acid or Neu5Ac on glycoprotein or sugar ester, the changes of charge density and character are due to the

change of Neu5Ac enzyme content, ATP activity and sodium pump function caused by membrane structure change, so it caused cell membrane potential. It showed qing long yi polysaccharide could increase sialic acid content, enhance the activities of Na^+,K^+ -ATPase and Ca^{2+},Mg^{2+} -ATPase, heighten membrane potential.

REFERENCES

- [1] Han,B.G., Nunomura,W, Takakuwa,Y, Mohandas,N.&Jap,B.K. Protein 4.1 R core domain structure and insights into regulation of cytoskeletal organization. *Nat. Struct. Biol.* 2000,7,871-875.
- [2] Nunomura, W. Takakuwa, Y, Parra, M., Conboy, J.G. & Mohandas, N. Ca^{2+} -dependent and Ca^{2+} - independent calmodulin binding sites in erythrocyte protein 4.1. Implications for regulation of protein 4.1 interactions with transmembrane proteins. *J. Biol. Chem.* 2000,275, 6360-6367
- [3] Weber Roy E, Wolfgang Voelter, Angela Fago, *et.al.* Modulation of red cell glycolysis : interactions between vertebrate hemoglobins and cytoplasmic domains of band 3 red cell membrane proteins[J]. *Am J Physiol Regulatory Integrative Comp Physiol*, 2004,287,454-464
- [4] Yuxun Zhang, Lois R Manning, Jill Falcone. Human Erythrocyte Membrane Band 3 Protein Influences Hemoglobin Cooperativity[J]. *The journal of biological chemistry*, 2003, 278(41): 39565-39571
- [5] Chang,S.H.&Low,P.S. Identification of a critical ankyrin-binding loop on the cytoplasmic domain of erythrocyte membrane band 3 by crystal structure analysis and site-directed mutagenesis. *J. Biol. Chem.* 2003,278, 6879-6884

Studies on Effect of Saponins of Asparagus on Tumor Cell Apoptosis and its Mechanisms of Action

Yu-Bin Ji, Lei Yu, Lang Lang, Chen-Feng Ji

Postdoctoral Programme, Institute of Materia Medica, Center of Research and Development on Life Sciences and Environment Sciences of Harbin University of Commerce, Harbin 150076, China
jyb@hrbcu.edu.cn

Abstract — Objective To investigate the pro-apoptosis effect of saponins of asparagus on human gastric adenoma cells SGC-7901 and its mechanism. Methods: SGC-7901 was treated with different concentrations of saponins of asparagus. MTT assay was used to evaluate the influence of saponins of asparagus on cell proliferation. Flow cytometry was used to test reactive oxygen species (ROS) levels, intracellular mitochondrial transmembrane potential ($\Delta\psi_m$), and hypodiploid apoptosis peak in both SGC-7901. Results: saponins of asparagus obviously inhibited proliferation of SGC-7901 cells. When treated with 0, 15, 30, 60, 120, 240 $\mu\text{g}/\text{mL}$ of saponins of asparagus for 24 h, intracellular ROS levels of SGC-7901 were (1.6 \pm 0.5)%, (2.0 \pm 0.3)%, (5.5 \pm 0.4)%, (25.8 \pm 1.4)%, (83.7 \pm 1.2)% and (97.4 \pm 4.2)%, respectively; and $\Delta\psi_m$ were (98.6 \pm 4.3)%, (98.4 \pm 4.8)%, (95.7 \pm 5.4)%, (92.6 \pm 4.0)%, (74.0 \pm 5.6)% and (63.7 \pm 4.0)%, respectively; when treated with 0, 60, 120, 240 $\mu\text{g}/\text{mL}$ of saponins of asparagus for 48 h, cell apoptotic rates of SGC-7901 were (4.3 \pm 1.6)%, (9.1 \pm 3.8)%, (20.1 \pm 4.2)% and (55.4 \pm 4.9)%, respectively. Conclusions: saponins of asparagus generates ROS in both SGC-7901, which causes mitochondrial membrane permeabilization and $\Delta\psi_m$ decrease, therefore, leads to apoptosis.

Keyword — broccoli; saponins of asparagus; apoptosis; reactive oxygen species; mitochondrial transmembrane potential

I. INTRODUCTION

Cancer is a disease serious detrimental to people's health. According to statistics from the World Health Organization, about 5 million people die of cancer each year[1]. The search for components with anti-tumor activity having low toxicity and high effectiveness has become one of the hotspots in research for the prevention and treatment of cancer in China and abroad[2]. Studies have shown that saponins of asparagus produced through the hydrolysis of glucosinolates from broccoli, have high biological activity and are the main components with anti-tumor activity. It has also been found that saponins of asparagus can induce apoptosis in certain human cell lines. However, the mechanism involved in the apoptosis induced by saponins of asparagus is not yet clear, and it seems that the signal transduction mechanism is different for apoptosis induced by saponins of asparagus in different cell lines[3]. In this study, the effect

of saponins of asparagus from broccoli in inducing apoptosis in SGC-7901 and the possible mechanism involved were studied.

II. MATERIAL AND METHOD

2.1 Material

Saponins of asparagus (extracted from broccoli), provided by the Postdoctoral Programme, the Institute of Materia Medica, Harbin University of Commerce; RPMI-1640, trypsin, DMSO, MTT, PI, and RNase, all purchased from Sigma; DCFH-DA and rhodamine 123, purchased from Biyuntian Company. All other reagents are analytically pure and produced in China. Water used in the experiment was Mili-Q ultrapure water prepared by us.

human gastric adenoma cells SGC-7901 was incubated in RPMI-1640 culture medium containing 10% fetal bovine serum at 37°C and 5% CO₂. Culture transfer was performed every 2-3 d. Cells were taken for the experiment in the phase of logarithmic growth.

2.2 Methods

2.2.1 The effect of saponins of asparagus on the proliferation of SGC-7901 tested with MTT assay

The tumor cell line was incubated for 24 h on a 96-well culture plate at 37°C and 5% CO₂, after which 100 μL of drug was added to each well to reach final concentrations of 1, 50, 100, and 150 $\mu\text{g}/\text{mL}$, respectively. For the control group, 100 μL of culture medium was added to each well. After the treatment, the cells were incubated in the incubator for 72 h more. After the culture medium and the drug were discarded, 100 μL of 0.5 mg/mL MTT solution was added, and the cells were incubated for an additional 4 h. The supernatant was then sucked off, after which 100 μL of DMSO was added to each well. The culture plate was gently agitated to make purple formazan dissolve completely. After about 2 min, a microplate reader was used to measure the absorbance (A) of the solution at a wavelength of 570 nm. The value of the absorbance was used to calculate the

survival rate of the cells, which in turn was used to calculate the inhibition rate^[4-6].

2.2.2 Effect of saponins of asparagus on intracellular reactive oxygen species (ROS) of SGC-7901 measured using flow cytometry

DCFH-DA is a compound which in itself emits no fluorescence, but it can permeate cell membrane and be oxidated into DCF (dichlorofluorescein) by ROS. DCF emits rather intense fluorescence, and the intensity of the fluorescence reflects the total yield of cellular ROS. In this experiment, 2×10^5 cells in the phase of logarithmic growth were inoculated on a 6-well culture plate, which was incubated at 37°C and 5% CO₂ for 24 h, after which saponins of asparagus of different concentrations (with final concentrations of 0, 15, 30, 60, 120, and 240 µg/mL, respectively) was added. 24 h later, the cells were digested with trypsin, rinsed twice with PBS, and filtered with 300-mesh nylon net, after which the intensity of cellular fluorescence was measured using FCM. 30 min before the measurement was taken, DCFH-DA with a final concentration of 5 µmol/L was added to the samples, which were then incubated at 37°C. The excitation wavelength was set to 488 nm, and the emission wavelength, 525 nm^[7].

2.2.3 Effect of saponins of asparagus on the intracellular membrane potential of SGC-7901 ($\Delta\psi_m$) measured using flow cytometry

Rhodamine 123 is a specific fluorescent stain for marking membrane potential. It is membrane-permeable, with the fluorescent signals mainly concentrated in mitochondria. Changes in the intensity of its fluorescence reflect changes in $\Delta\psi_m$. In this experiment, 2×10^5 cells in the phase of logarithmic growth were inoculated on a 6-well culture plate, which was incubated at 37°C and 5% CO₂ for 24 h, after which saponins of asparagus of different concentrations (with final concentrations of 0, 15, 30, 60, 120, and 240 µg/mL, respectively) was added. 24 h later, the cells were digested with trypsin, rinsed twice with PBS, and filtered with 300-mesh nylon net, after which the intensity of cellular fluorescence was measured using FCM. 30 min before the measurement was taken, rhodamine with a final concentration of 5 µg/L was added to the samples, which were then incubated at 37°C. The excitation wavelength was set to 488 nm, and the emission wavelength, 525 nm^[8].

2.2.4 The induction of apoptosis in SGC-7901 by saponins of asparagus as tested using flow cytometry

When cells undergo apoptosis, DNA can be fragmented or even lost, so that DNA content would be less than in normal diploids. The FCM test was conducted in what is called the sub-G₁ phase prior to G₁ phase. 2×10^5 cells in the phase of logarithmic growth were inoculated on a 6-well

culture plate, which was incubated at 37°C and 5% CO₂ for 24 h, after which saponins of asparagus of different concentrations (with final concentrations of 0, 15, 30, 60, 120, and 240 µg/mL, respectively) was added. 48 h later, the cells were digested with trypsin, rinsed twice with PBS, fixed with 70% ethanol, and left at 4°C for the night. The samples were stained with 50 µg/mL PI and incubated away from light for 30 min at 37°C, and then filtered with 300-mesh nylon net before they were mounted on the flow cytometer to be tested. 10^4 cells were tested, under an excitation wavelength of 488 nm and an emission wavelength of 630 nm^[9]

III. RESULTS

3.1 The effect saponins of asparagus on the proliferation of SGC-7901

Saponins of asparagus from broccoli obviously has a cytotoxic effect on SGC-7901, and IC₅₀ were 22.406 µg/mL. The cytotoxicity is dosage-dependent, which is worth further developing and researching. on grow of tumor cells

3.2 The effect of saponins of asparagus on intracellular ROS of SGC-7901

After tumor cells had been acted on by saponins of asparagus of different concentrations for 24 h, FCM was used to measure the intensity of intracellular fluorescence, which reflects the corresponding yield of ROS. From Fig. 1, it can be seen that as the concentration of saponins of asparagus increases, the number of cells with relatively intense fluorescence gradually increases. Compared with the control group, ROS yield for the treated groups gradually increases.

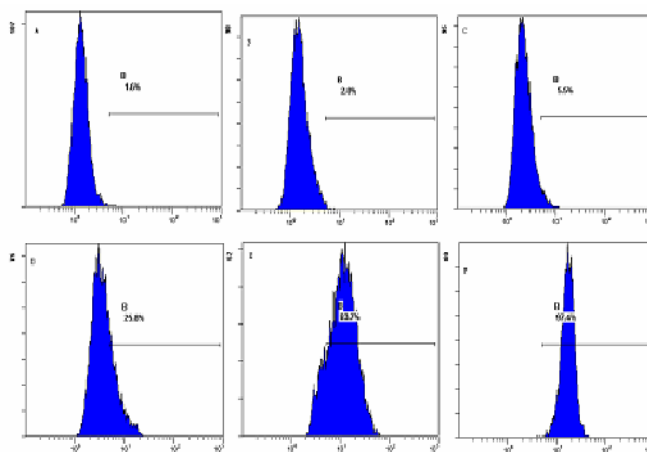


Fig. 1. Effects of saponins of asparagus on intracellular ROS levels of SGC-7901

The fluorescence intensity for the 120 and 240 $\mu\text{g/mL}$ groups saw marked increases. Thereinto, the intensity of SGC-7901 was increased by (83.7 \pm 1.2)%, (97.4 \pm 4.2)%, respectively.

3.3 The effect of saponins of asparagus on the intracellular $\Delta\psi_m$ of SGC-7901

After tumor cells had been acted on by saponins of asparagus of different concentrations for 24 h, changes in the intensity of intracellular fluorescence were measured using FCM. It was found that in tumor cells treated with saponins of asparagus, the percentage of cells with high fluorescence intensity gradually decreased, and that with the increase in drug concentration, the decrease in the percentage became more significant, showing a certain degree of dosage dependence, as shown in Fig. 2.

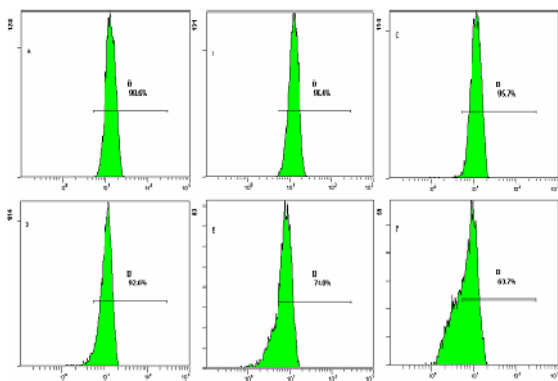


Fig. 2. Effects of saponins of asparagus on mitochondrial transmembrane potential of SGC-7901

3.3 The induction of apoptosis in SGC-7901 by saponins of asparagus

48 h after tumor cells had been acted on by 0, 60, 120, and 240 $\mu\text{g/mL}$ saponins of asparagus, it can be seen that the apoptotic rate of SGC-7901 was (4.3 \pm 1.6)%, (9.1 \pm 3.8)%, (20.1 \pm 4.2)% and (55.4 \pm 4.9)%, respectively. As shown in Fig. 3

IV. DISCUSSIONS

Epidemiological studies have shown that eating broccoli often can lower the risk of having lung and intestinal cancer. Saponins of asparagus can effectively prevent damage to DNA and cancer caused by many kinds of carcinogens such as polycyclic aromatic hydrocarbons, heterocyclic amines, and nitrosamines. At the same time, saponins of asparagus also have many kinds of biological activity such as bacteri-

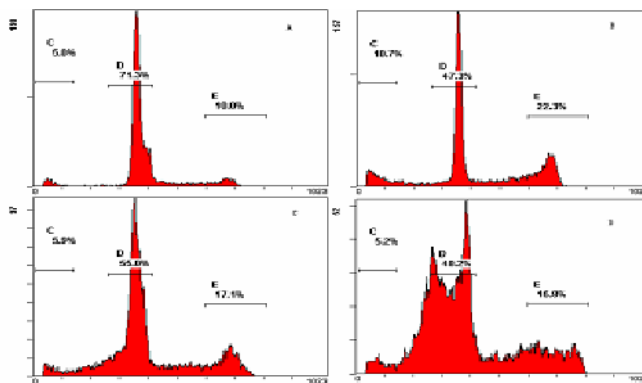


Fig. 3. Effects on apoptosis of SGC-7901 induced by saponins of asparagus

cidal activity and inhibition of platelet aggregation^[11]. Studies have shown that saponins of asparagus can exert their inhibitory effect at all the stages in the genesis and development of tumors, and can induce apoptosis of tumor cells through many different pathways. However, the specific mechanisms through which saponins of asparagus from broccoli induce apoptosis in tumor cells are yet unclear.

Research in recent years has shown that oxidative stress is involved – and indeed plays a crucial role – in the process of apoptosis. As a product of oxygen through single-electron reduction in the organism, ROS has been attracting an increasing amount of attention for its role in apoptosis. There is a great deal of evidence suggesting that ROS level rises, and that ROS may act as a secondary messenger that induces apoptosis by adjusting upward the expression of apoptosis-promoting proteins, promoting the opening of the permeability transition pores (PTPs) on mitochondria, activating aspartic acid-specific caspase, participating in Ca^{2+} pathways, etc. At the same time, the level of ROS may determine the specific response (apoptosis, necrosis, or tolerance) of cells to apoptosis-promoting signals by affecting the activity of caspase and ATP level^[12]. Results from our experiments show that when SGC-7901 is acted on by saponins of asparagus of different concentrations, their ROS level is raised significantly. Our results also suggest that the mechanism through which saponins of asparagus induces apoptosis in SGC-7901 is related to increase in ROS level and that oxidative stress is involved in the apoptotic process.

The mitochondrion is the power plant of the cell and has important physiological functions, such as oxidative phosphorylation, electron transfer, storage of Ca^{2+} , and energy metabolism. Its main function is to provide energy for the activities involved in various functions of the cell. Research has shown that changes in the functions of the mitochondrion are closely associated with apoptosis^[13], and it is known that the membrane potential of the mitochondrion directly reflects changes in its functions. Under the effect of

apoptosis-inducing factors, mitochondrial membrane potential in a cell begins to decrease before the nucleus shows characteristic apoptosis. Results from this experiment prove that mitochondrial membrane potential in SGC-7901 is decreased under the effect of saponins of asparagus, and that this change is associated with the rise in ROS level, showing that the mechanism by which isothiocyanates induce apoptosis is related to mitochondrial membrane potential.

To sum up, saponins of asparagus from *broccoli* have a rather strong inhibitory effect on human gastric adenoma cells. The mechanism by which saponins of asparagus induce apoptosis in SGC-7901 is related to its ability to increase the ROS level of the cells and thus lead to decrease in mitochondrial membrane potential.

REFERENCES

1. Zeng Yixin. Oncology[M]. Beijing: People's Health Press, 1999:329.
2. Li Zhimiao, Cao Jiashu. The anti-tumor properties of vegetables[J]. Northern Horticulture, 2001,4:4-6.
3. Wang Qiaomei, Steffen Abel. The anti-tumor mechanism of saponins of asparagus and related research[J]. Chinese Journal of Cell Biology, 2002,24(3):171-175.
4. E Zheng. Tissue Culture and Techniques for Molecular and Cell Biology[M]. Beijing: Beijing Press, 1995.
5. Situ Zhenqiang, Wu Junzheng. Cell Culture[M]. Xi'an: World Books Publishing Company, 1996.
6. Liu Wei, Lin Wenhao, Ji Yubin. Study on the acute toxicity experiment of mice and anti-tumor function *in vitro* of the qinglongyi[J]. China Journal of Chinese Materia Medica, 2004,29(9):887-890.
7. Armstrong J S, Steinauer K K, Hornung B, *et al.* Role of glutathione depletion and reactive oxygen species generation in apoptotic signaling in a human B lymphoma cell line[J]. Cell Death Differ, 2002,9(3): 252-263.
8. M. Concepción Serrano, Raffaella Pagani, Miguel Manzano, *et al.* Mitochondrial membrane potential and reactive oxygen species content of endothelial and smooth muscle cells cultured on poly(ϵ -caprolactone) films[J]. Biomaterials, 2006,27(27): 4706-4714.
9. Ying-Tang Huang, Yi-Hsuan Huang, Tzhy-Chyuan Hour, *et al.* Apoptosis-inducing active components from *Corbicula fluminea* through activation of caspase-2 and production of reactive oxygen species in human leukemia HL-60 cells[J]. Food and Chemical Toxicology, 2006,44(8):1261-1272.
10. Ji Yubin, Chi Wenjie, Zou Xiang, *et al.* Study on extraction, isolation and anticarcinogenic activity of sulforaphane in broccoli[J]. Journal of Harbin University of Commerce (science edition), 2005,21(3):270-273.
11. Zhang Qingfeng, Jiang Zitao, Li Rong. The biological activities of the hydrolytes (isothiocyanates) of glucosinolates in horseradish and cruciferous vegetables[J]. Research and Development in Food Products, 2005,26(3):83-88.
12. Yang Jie, Gao Fei, Yi Jing. Advances in research on reactive oxygen species and apoptosis[J]. Foreign Medical Sciences (cancer section), 2002,29(4):248-251.
13. Tong Tong, Zhan Qimin. The role of the mitochondrion in apoptosis and the molecular mechanism involved[J]. Foreign Medical Sciences (genetics section), 2004,27(5),263-289.

Effects of electric pulses on apoptosis induction and mitochondrial transmembrane potential of cancer cells

Fang-Yi¹ Jiang, Li-Ling Tang*¹, Chao Zeng¹, Huan Liu¹, Ke-Dao Liang², Yan Mi², Cai-Xin Sun²

¹ Bioengineering College, Chongqing University, Chongqing 400044, China

² State Key Laboratory of Power Transmission Equipment & System Security of Chongqing University, Chongqing 400044, China

Abstract — Application of electric pulses is becoming a promising strategy to killing cancer. In this study, the effects of different pulses on the apoptosis and mitochondrial transmembrane potential of human cancer cells SMMC7721 were studied. In our experiments, the apoptosis in cells was determined using Annexin-V-FITC. Results showed that 1.8 μ s, 200V/cm and 250 V/cm electric fields induced cells apoptosis while 120ns, 600V/cm pulses didn't have significant apoptotic effect on cells. Using confocal microscopy, changes of mitochondrial transmembrane potential ($\Delta\Phi_m$) were investigated when cells exposed to electric fields in real-time way. Results showed that the electric stimulation decreased mitochondrial transmembrane potential. Interestingly, the mitochondrial transmembrane potential decreased more significantly in cells that were exposed to the 120ns, 600V/cm electric fields (67.09%) compared to the cells in 1.8 μ s, 200V/cm and 250V/cm (23.71%,28.44%). In conclusion, electric pulses can induce cell apoptosis and decrease the mitochondrial transmembrane potential, depending on the duration and electric intensity of electric pulses. Moreover, shorter pulses have more effect on intracellular structure.

Keywords — cancer. electric pulses. apoptosis. mitochondrial transmembrane potential.

I. INTRODUCTION

Electric fields have been widely used in biology. The most advanced procedure is electrochemotherapy (ECT), in which electric pulse is used in cancer treatment by improving the effect of chemical medicine through the electroporation on cell membrane[1].

Responses of cells to electric pulses mainly depend on the parameters such as electric field intensity and pulse durations etc. Recent studies have shown that cell apoptosis could be induced by electric pulses in vitro and in vivo experiments [2-4]. Our previous study also claimed the apoptosis of cancer cells induced by electric pulses[5]. The observation of cell apoptosis which is induced by electrical pulses provides a bright future for cancer therapy without aids of drugs.

Apoptosis is the morphological manifestation of programmed cell death in cells. In most kinds of apoptosis, an early signal for the programmed cell death is a decrease of the mitochondrial transmembrane potential ($\Delta\Psi_m$)[6-8]. It is known that electric fields can induce cell apoptosis accompanied with changes of membrane, intracellular calcium, mitochondria, nucleus and so on [9]. The sequence and mechanistic details of these events are not yet clear. Therefore, the assessment of mitochondrial potential and apoptosis induced by electric pulses is of special interest.

This study focuses on the apoptosis induction and mitochondria transmembrane potential change of cells in response to electric pulses with different durations using real-time imaging methods, flowcytometry. The study is designed to specifically explore the effect of different electric duration on cells.

II. MATERIALS AND METHODS

A. Cell culture

SMMC-7721 cells, a human liver cancer cell line (Shanghai Biochemical Institution, Shanghai, China) were used in the experiments. Cells were cultured with RPMI-1640 medium containing 2% glutamine supplemented with 10% fetal bovine serum and 2% penicillin and streptomycin in a 37°C,5%CO₂ incubator. Before experiment, cells were digested with 0.25% trypsin and seeded in the chamber of the electric stimulation apparatus.

B. Pulse generator

The pulse generator is developed in State Key Laboratory of Power Transmission Equipment & System Security of Chongqing University [5]. It supplied the electric pulses of 100ns to 20 μ s duration. The values of the electric field for the experimental studies are shown in Table 1. The chamber is composed of two Pt electrodes and a slide where cells can be seeded on and cultured (Fig. 1).

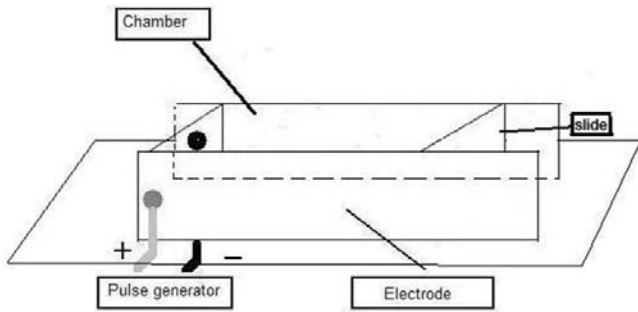


Fig. 1 The scheme of chamber in electric pulse generator

Table 1 The parameters of applied steep pulsed electric fields

Intensity(V/cm)	Frequency (Hz)	Duration	Time (min)
150	50	1.8 μ s	10
200	50	1.8 μ s	10
250	50	1.8 μ s	10
600	50	120ns	10

C. Cell apoptosis.

Annexin-V-FITC (Biosea Cop) was used as the fluorescent marker in the study. Annexin-V-FITC specifically binds to the cell membrane lipid phosphatidylserine. Cells were treated with different electric pulses for 10min and digested. Then cells in suspensions were incubated with Annexin-V-FITC for 10min prior to analysis by flow cytometry (FACSC alibur, Becton Dickinson Cop, USA).

D. Real-time change of mitochondrial transmembrane potential ($\Delta\Phi_m$)

After 24h culture in the chamber, cells were loaded with the Rhodamine123 (10 μ g/mL, Sigma) for 30min at 37 $^{\circ}$ C and washed with PBS. Laser Scanning Confocal Microscope (tcs-nt, Leica) was used to measure the real-time change of fluorescence when cells were treated with different electric pulses for 10min. And the changes of fluorescence intensity at the beginning and the end of the electric stimulations were calculated to evaluate the change of mitochondrial transmembrane potential.

E. Statistics

Data are expressed as mean \pm SEM. Statistical significance was determined using student's t-tests. A probability less than 0.05 was considered to be statistically significant.

III. RESULTS

A. Cells apoptosis induced by electric fields

Table 2 shows the results of apoptosis in cells that were exposed to different electric pulses. Compared to the control cells, 1.8 μ s, 200V/cm and 250 V/cm electric fields induced cells apoptosis while 120ns, 600V/cm pulses hadn't significant apoptotic effect on cells.

Table 2 The apoptosis of SMMC-7721 cells induced by different electric fields

Electric Pulses	Normal	Apoptotic	Necrosis
0V/cm	92.67 \pm 1.68	6.02 \pm 0.47	1.32 \pm 1.23
120ns, 600V/cm	89.26 \pm 7.20	9.40 \pm 6.55	1.35 \pm 0.73
1.8 μ s, 200V/cm	64.26 \pm 10.70*	30.97 \pm 6.57*	4.76 \pm 1.61*
1.8 μ s, 250V/cm	55.43 \pm 3.90*	39.01 \pm 2.26*	5.57 \pm 1.33*

*p<0.05 compared to the control cells (0v/cm)

**n=6, at least 10,000 cells were analyzed per experiment.

B. Real-time changes of mitochondrial transmembrane potential

Figure 2 showed the real-time change of mitochondrial transmembrane potential when cells exposed to different electric pulses. Results showed that the electric stimulation resulted in a decrease of mitochondrial transmembrane potential. Interestingly, the mitochondrial transmembrane

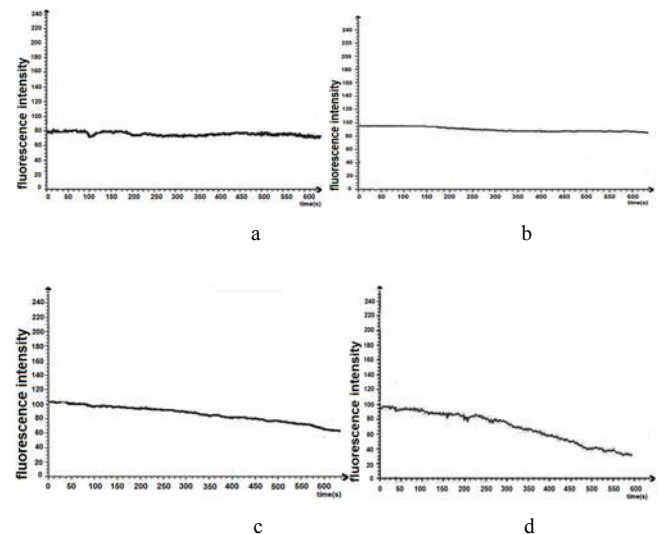


Fig. 2 The change of mitochondrial transmembrane potential in SMMC-7721 cells that were exposed to different electric pulses for 10min. a, untreated cells; b, cells were treated with 1.8 μ s, 200V/cm pulses; c, cells were treated with 1.8 μ s, 250V/cm pulses; d, cells were treated with 120ns, 600V/cm pulses

potential decreased more significantly in cells that were exposed to the 120ns, 600V/cm electric fields (67.09%) compared to the cells in 1.8 μ s, 200V/cm and 250V/cm (23.71%,28.44% respectively). That is to say, the short pulses has more effect on mitochondrial transmembrane potential.

DISCUSSION

Responses of cells to electric pulses depend on the parameters such as electric field intensity, pulse duration, frequency, etc. An amazing finding in the application of electric pulses is that apoptosis could be induced by electric pulses with certain parameters. Using the Annexin-V-FITC apoptotic marker, Beebe et al[2], Vernier et al[3] have reported that cell apoptosis could be induced by electric pulses in vitro experiments.

In our studies, electric pulses with different duration and electric intensity were applied to cancer cells in order to evaluate the effects of intensity and duration on cells behavior. Our results proved that electric pulses of 1.8 μ s, 200V/cm and 1.8 μ s, 250V/cm induced cell apoptosis. In contrast, there were no significant difference between control cells and cells that were exposed to the electric pulses of 120ns, 600V/cm.

In the initiation and accomplishment of the apoptotic process, mitochondria play an important and even decisive role. In most kinds of apoptosis, an early signal for the programmed cell death is a decrease of the mitochondrial transmembrane potential ($\Delta\Phi$) This may result from the opening of the so-called permeability transition pores in the inner mitochondrial transmembrane. Loss of the mitochondrial transmembrane potential causes the release of cytochrome c from mitochondria into the cytosol, where it then activates the pro-apoptotic caspases[7,10].

Our studies showed that electric pulses decreased the mitochondrial inner transmembrane potential ($\Delta\Phi_m$) in an intensity and duration-dependent manner. When cells were subjected to 1.8 μ s electric pulses, the $\Delta\Phi_m$ decreased with the increase of the electric intensity. However, the $\Delta\Phi_m$ decrease in stimulated cells weren't coincident with the degree of apoptosis when cells were treated with 120ns,600V/cm electric pulses. 120ns,600V/cm electric pulses resulted in the most significant $\Delta\Phi_m$ decrease (67.09%) in all electric stimulated groups, while the apoptosis degree was smallest(9.40). Therefore, we may conclude that the short pulse

has more effect on intracellular structure and the change of $\Delta\Phi_m$ was not directly related to cell apoptosis.

In summary, we have demonstrated that electric pulses can induce the apoptosis of cells and decrease the mitochondrial transmembrane potential depending on the duration and electric intensity of electric pulses. Moreover, shorter pulses have more effect on intracellular structure including the mitochondrial transmembrane. These results may provide an important support to the development of an independent application of electric pulses to cancer therapy.

ACKNOWLEDGMENT

This study is supported by the China Natural Science Foundation (No.50377046)

REFERENCES

- Hofmann GA, Dev SB, Dimmer S, et al. Electroporation therapy: a new approach for the treatment of head and neck cancer. *IEEE Biomed Eng* 1999; 46:752-759.
- Hair P S, Schoenbach K H, Buescher E S, Sub-microsecond, intense pulsed electric field applications to cells show specificity of effects. *Bioelectrochemistry*, 2003, 61(1-2): 65~72
- Vernier P T, Li A, Marcu L, et al. Ultrashort pulsed electric fields induce membrane phospholipid translocation and caspase activation: differential sensitivities of Jurkat T lymphoblasts and rat glioma C6 cells. *IEEE Trans Dielect Elect Insul*, 2003, 10(5): 795~809.
- R. Nuccitelli, U. Pliquett, X. Chen, W. Ford, R.J. Swanson, et al. Nanosecond pulsed electric fields cause melanomas to self-destruct. *Biochem Biophys Res Comm*. 2006,343:351-360
- LL Tang, C.X. Sun, H.Liu, Y. Mi, C.G. Yao, C.X. Li. Steep pulsed electric fields modulate cell apoptosis through the change of intracellular calcium concentration. *Colloids Surf B: Biointerfaces*, 2007, 57:209-214
- K. Piwocka, K. Zablocki, M.R. Wieckowski, J. Skierski, I. Feiga, J. Szopa et al. A novel apoptosis-like pathway, independent of mitochondria and caspases, induced by curcumin in human lymphoblastoid T (Jurkat) cells. *Experimental Cell Research*,249,299-307(1999)
- T. Hirsch, I.Marzo, and G. Kroemer. Role of the mitochondrial permeability transition pore in apoptosis. *Biosci. Rep.* 17,67-76 (1997)
- B.Mignotte, J.-L. Vayssiere. Mitochondria and apoptosis. *Eur J Biochem.* 252,1-15 (1998)
- Buescher E S, Schoenbach KH. Effects of submicrosecond, high intensity pulsed electric fields on living cells - intracellular electro-manipulation. *IEEE Trans Dielect Elect Insul*, 2003, 10(5): 788~794 *Science* 1997;275:1132-1136.
- M. Zoratte and I.Szabo. The mitochondrial permeability transition. *Biochim. Biophys. Acta* 1241,139-176,1995

*Corresponding author. Tel.:86-23-65102507; fax:85-23-63510225
E-mail address: lilingtang@yahoo.com.cn

Preparation and Release Efficiency of Poly (lactic-co-glycolic) Acid Nanoparticles for Drug Loaded Paclitaxel

You Ling, Yueshan Huang

School of Bioscience and Bioengineering, South China University of Technology, Guangzhou, China

Abstract — As a new drug delivery carrier, medical nanoparticles appears to be very promising and are widely studied. This work was to prepare poly (lactic-co-glycolic) acid (PLGA) nanoparticles for drug loaded paclitaxel using the emulsion solvent evaporation technique. Tocopheryl polyethylene glycol 1000 succinate (TPGS), as a new emulsifier, which has amphiphilic structure comprising lipophilic alkyl tail and hydrophilic polar head portion, played a key role in emulsion technique. The systems were characterized by light scattering analysis for their mean size and size distribution and by scanning electron microscopy for surface morphology. Nanoparticles drug loading efficiency and encapsulation efficiency and ability of *in vitro* drug release were assessed by ultraviolet spectroscopy. As a result, the nanoparticles were uniformly spherical with average diameter of 250 nm, drug loading efficiency of 4.84%, and encapsulation efficiency of 67.35%. The *in vitro* release curves of paclitaxel-loaded nanoparticles appeared to be two-staged. In the first day, the initial burst was observed. After that the release of paclitaxel was at a constant rate.

Keywords — Nanoparticles, PLGA, Paclitaxel, TPGS, Release Efficiency

I. INTRODUCTION

Paclitaxel is one of the best of anticancer drugs against a wide spectrum of cancers such as breast cancer, ovarian cancer, colon cancer, small and non-small cell lung cancer, and neck cancer [1-4]. It has been found that orally administrated paclitaxel would be eliminated from the first pass extraction by the cytochrome P450 and the drug transport protein P-glycoprotein, which are rich in the intestinal epithelium cell layer and other part of the digest system. However, the main limitation for its clinical application is its low solubility in water and most of the pharmaceutical solvents. The dosage form in its clinical application is Taxol, which is formulated in an adjuvant called Cremophor EL and dehydrated alcohol at a 50:50 (v/v) ratio, which is diluted 5–20 folds in normal saline or dextrose solution (5%). This adjuvant has been found associated with severe side effects including hypersensitivity reactions, nephrotoxicity, neurotoxicity and cardiotoxicity [5-6]. Alternative paclitaxel formulation strategies have been suggested to eliminate the Cremophor EL-based vehicle and to improve the therapeutic efficacy of the drug.

Polymeric nanoparticles show some advantages with respect to other drug delivery systems, such as more stability during storage. Moreover, these colloidal systems, after intravenous administration, may extravasate solid tumours and into inflamed or infected sites, where the capillary endothelium is defective, thus passively targeting drug-loaded nanoparticles to the tumour site. PLGA is a kind of polyester materials. PLGA has excellent biodegradable, biocompatible and controllable degradations [7]. In addition, PLGA nanoparticles can be degraded into glycolic acid and lactic acid that are non-toxic to the human body. PLGA appears to be an ideal new drug delivery carrier system.

A widely used emulsifier in the preparation of micro/nanoparticles is poly (vinyl alcohol). In this paper, we selected TPGS as a new emulsifier. TPGS is a water-soluble derivative of natural vitamin E, which has amphiphilic structure comprising lipophilic alkyl tail and hydrophilic polar head portion. Its bulky structure and large surface area make it to be an excellent emulsifier, solubilizer, bioavailability enhancer of hydrophobic drugs. TPGS can also enhance the oral bioavailability of anticancer drugs by improving the solubilization or emulsification of the drug in the finished dosage form and through formation of a self-emulsifying drug delivery system in the stomach. This is because TPGS can improve drug permeability across cell membranes by inhibiting P-glycoprotein, thus enhancing absorption of a drug through the intestinal wall and into the bloodstream. TPGS can be also a good emulsifier or additive in fabricating nanoparticles with high drug entrapment efficiency and high emulsification efficiency [8].

In this work, the paclitaxel-loaded PLGA nanoparticles were prepared by emulsion solvent evaporation technique, in which the macromolecular emulsifier TPGS plays an important role in determining the particle size and the drug encapsulation efficiency.

II. MATERIALS AND METHOD

A. Materials

Poly (lactic-co-glycolic) acid (PLGA; L/G=50/50, MW=15000) were purchased from Shandong Institute of Medical Devices, China. Tocopheryl polyethylene glycol

1000 succinate (TPGS) was purchased from Zhejiang Xinchang Pharmaceutical Factory (China). Paclitaxel of 99.5% purity was purchased from Yunnan Hande Biotechnology (China). The solvent methylene chloride (dichloromethane, DCM, analytical grade) was purchased from Fu Yu Fine Chemical Plant in Tianjin (China). Distilled water was used throughout the experiment. The in vitro release measurement was carried out at PH 7.4 in phosphate-buffered saline (PBS). All other chemical used were of analytical grade.

B. Nanoparticles preparation

The paclitaxel loaded nanoparticles were fabricated by emulsion solvent evaporation technique [9-10]. Typically, known amounts of mass of PLGA polymer and paclitaxel were added into DCM, which was suitably stirred to ensure that all material was dissolved. Then, the solution of organic phase was slowly poured into the stirred aqueous solution of TPGS and sonicated with energy output of 50 W in a continuous mode (Shanghai Kedao Ultrasonic Instrument Incorporated) for 10 minutes. The formed oil-in-water (O/W) emulsion was gently stirred at room temperature by a magnetic stirred (Jiangsu Honghua magnetic stirrer HJ-3) for not less than four hours to evaporate the organic solvent. The colloidal suspension was separated at low speed centrifugation (3000rpm, 5min) to remove aggregation. The resultant sample was collected by centrifugation (Anke of model TGL-16C, 12000-15000rpm, 15 min) and washed with distilled water at least four times to remove the emulsifier. The produced suspension was freeze-dried (FD-18S, Detianyou Incorporated, Beijing) to obtain the fine powder of nanoparticles, which was placed and kept in vacuum dessicator.

C. Nanoparticles characterization

The particle size and size distribution of the prepared nanospheres were measured by the laser light scattering (Mastersizer 2000, Malvern Instruments Corporation, UK). The dried power samples were suspended in distilled water and slightly sonicated before measurement. The obtained homogeneous suspension was determined for the volume mean diameter and size distribution.

The shape and surface morphology of the produced nanoparticles were investigated by the scanning electron microscopy (SEM, LEO 1530 VP, LEO Incorporated, Germany). Before observation, the nanoparticles sample was fix on a double-sided sticky tape that was stucked on the standard sample stand. And the sample required a previous coating with gold, which was performed in an Auto Fine Coater for seven minutes.

The drug entrapped in the nanoparticles and the drug loading efficiency was determined by the UV absorbance at 227 nm using a UV-visible spectrophotometer [11]. The entrapped paclitaxel content in the nanospheres cores was calculated from the mass of the incorporated drug using the following equation [12]:

$$\begin{aligned} & \text{Drug loading efficiency} \\ &= \frac{\text{Amount of paclitaxel in nanoparticles}}{\text{Amount of paclitaxel loaded nanoparticles}} \times 100 \quad (1) \\ &= \frac{\text{Paclitaxel}}{\text{Paclitaxel} + \text{Polymer}} \times 100 \end{aligned}$$

The drug encapsulation efficiency was defined as the ratio of the mass of the encapsulated drug to the mass of the drug used for nanoparticles preparation using the following equation:

$$\begin{aligned} & \text{Drug encapsulation efficiency} \\ &= \frac{\text{Amount of encapsulation paclitaxel}}{\text{Amount of paclitaxel used for nanoparticles preparation}} \times 100 \quad (2) \end{aligned}$$

In order to determine the exact drug content, rendering a determination of need before the linear correlation higher concentration - absorbance standard curve. A certain weight of pure paclitaxel was dissolved in DCM so that obtained standard paclitaxel solution which the concentration is 5, 10, 15, 20, 25, 30, 35 and 40ug/ml. UV spectrophotometer were used to determined the absorbance at 227nm. Then we can draw a map with concentration to the absorbance and obtain the linear equation. Further it could calculate the correlation coefficient.

D. In vitro release study

The release of paclitaxel from the nanoparticles was measured in triplicate in PBS (PH 7.4) [13]. Ten mg of paclitaxel-loaded nanoparticles were suspended in 10 ml of buffer solution in a screw-capped tube and placed in an orbital shaker, which was maintained at 37 centigrade degree and shaken horizontally at 120 min⁻¹. At particular time intervals, the tube was taken out of the shaker and centrifuged at 15000 rpm for 10 min. The precipitated nanoparticles were resuspended in 10 ml of fresh buffer before being put back in the shaker. The supernatant was taken for analysis of paclitaxel concentration.

III. RESULTS AND DISCUSSION

Most of the particle size was found in the range from 100 to 450nm. The size distribution illustrated in Fig. 1 was narrow. The average diameter of nanoparticles was 250 nm.

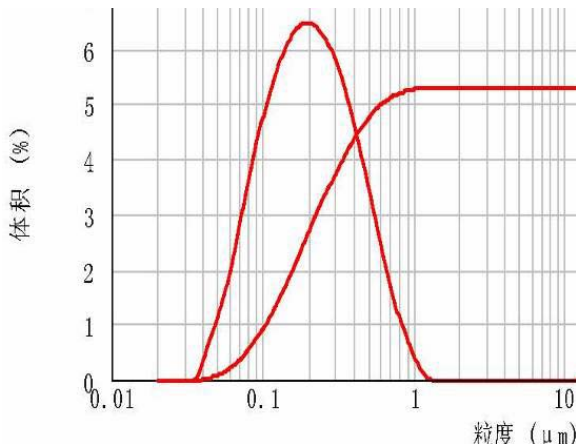


Fig. 1 Particle size distribution of PLGA nanoparticles

In fabrication of paclitaxel-loaded nanoparticles by applying the emulsion solvent evaporation technique, the use of surfactant stabilizer is necessary to stabilize the dispersed-phase droplets and inhibit coalescence. The amphipathic surfactants align themselves at the droplet surface, so promoting stability by lowering the free energy at the interface between the two phases and resisting coalescence and flocculation of the nanospheres [14]. The present research shows that TPGS could be a new excellent emulsifier which possesses all merits of traditional emulsifier poly (vinyl alcohol).

Under SEM observation (Fig.2), the nanoparticles all had a fine spherical shape with various degree of smooth surface. In the SEM photograph, we can see that there was somewhat adhesion between the nanoparticles. Two reasons for this phenomenon can be explained. One reason maybe was that the samples still had redundant emulsifier. The other prob-

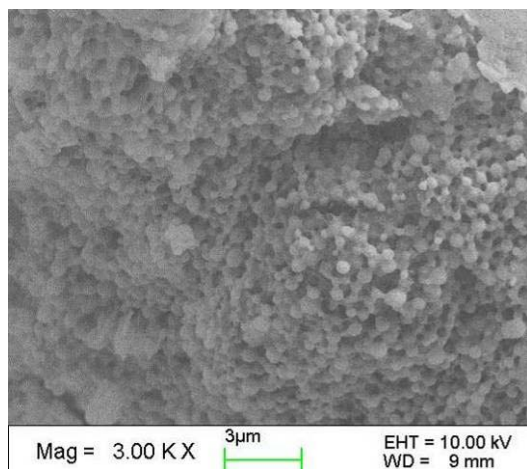


Fig. 2 SEM images of PLGA nanoparticles

Table 1 Absorbance values of standard paclitaxel concentration

Sample	Concentration	Absorbance
1#	5ug/ml	0.175
2#	10ug/ml	0.371
3#	15ug/ml	0.548
4#	20ug/ml	0.749
5#	25ug/ml	0.927
6#	30ug/ml	1.115
7#	35ug/ml	1.245
8#	40ug/ml	1.382

ably was the high temperature in the electron beam irradiation so that the PLGA nanospheres were slowly melted. However, a bit of adhesion was not a significant impact on nanoparticles in the dispersion of PBS. PLGA nanospheres could be suspended stably in buffer solution.

We could obtain the dates by determining the absorbance values of standard concentration paclitaxel solution (Table 1). It was calculated the following equation.

$$Y = 0.035X + 0.0266 \quad (3)$$

Where Y is the absorbance values, and X is the paclitaxel concentration. The calibration curve for the absorbance of paclitaxel was linear over the range of standard concentration paclitaxel at 5-40ug/ml with a correlation coefficient of $R^2 = 0.9958$.

The drug entrapped in the nanoparticles and the drug loading efficiency was calculated using the equation 1, 2 and 3. As a result, the encapsulation efficiency of drug loaded paclitaxel PLGA nanoparticles was 4.84% and the drug loading efficiency was 67.35%. There are many factors that can influence the encapsulation efficiency and loading efficiency. For example, modifying the dispersed or dispersing phase of the emulsion/stabilizer to reduce the leakage of the drug molecule from the droplets can thus make improvement of the encapsulation efficiency of the drug in the nanospheres [10].

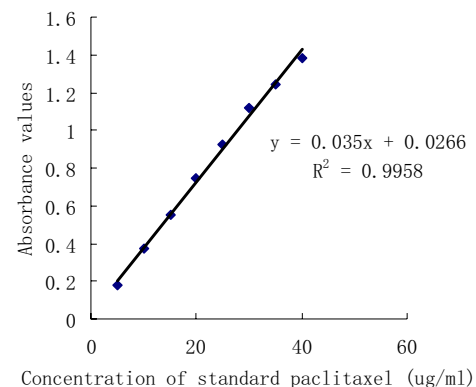


Fig. 3 Concentration - absorbance standard curve

The *in vitro* release mode of paclitaxel-loaded nanoparticles appeared to be two-staged. In the first day, the initial burst was observed. After that the release of paclitaxel was at a constant rate. The diffusion of the drug, the erosion and swelling of polymer matrix and the degradation of polymer are the main mechanisms for the drug release. Since the degradation of PLGA is slow, the release of paclitaxel from the nanoparticles would mainly depend on the drug diffusion and the matrix erosion. Thus, the porosity of the nanoparticles should have significant effects on the release property. The SEM examination indicated that the nanospheres had smooth surface, which supported the slow release of drug by diffusion and matrix erosion mechanism. Nevertheless, further investigations are needed to make a quantitative conclusion.

IV. CONCLUSIONS

To conclude, TPGS was applied for excellent emulsifier in the emulsion-solvent evaporation technique to fabricate paclitaxel-loaded nanospheres with achievement. PLGA nanoparticles could change the pharmacokinetics of paclitaxel, slower down drug release. Moreover, it could be prepared as intravenous injection and prolong the *in vivo* circulation time of paclitaxel, so as to play more efficient anti-tumor effects.

ACKNOWLEDGMENT

Authors are grateful to Mr. Zhang (Analytical and Testing Center of SCUT) for his technical on SEM studies and Ms Zhen for her helpful assistance on the laser light scattering operation.

REFERENCES

1. Wani MC, Taylor HL, Wall ME et al. Plant antitumor agents. VI. The isolation and structure of Taxol, a novel antileukemic and antitumor agent from *Taxus brevifolia*. *J Am Chem. Soc* 1971, 93:2325-2327
2. Thigpen JT. Chemotherapy for advanced ovarian cancer: overview of randomized trials. *Semin Oncol* 2000, 27: 11-16
3. Ishitobi M, Shin E, Kikkawa N. Metastatic breast cancer with resistance to both anthracycline and docetaxel successfully treated with weakly paclitaxel. *Int J Clin Oncol* 2001, 6: 55-58
4. Chang AY, Rubins J, Asbury R et al. Weekly paclitaxel in advanced non-small cell lung cancer. *Semin Oncol* 2001, 28: 10-13
5. Gelderblom H, Verweij J, Nooter K. Cremophor EL: the drawbacks and advantages of vehicle selection for drug formulation. *Eur J Cancer* 2001, 37: 1590-1598
6. Singla AK, Garg A, Aggarwal D. Paclitaxel and its formulation. *Int J Pharm* 2002, 235: 179-192
7. F. Tewes, E. Munniera, B. Antoona, et al. Comparative study of doxorubicin-loaded poly(lactide-co-glycolide) nanoparticles prepared by single and double emulsion methods. *Eur J Pharm* 2007, 66: 488-492
8. Zhiping Zhang, Sie Huey Lee, Si-Shen Feng. Folate-decorated poly(lactide-co-glycolide)-vitamin E TPGS nanoparticles for targeted drug delivery. *Biomaterials* 2007, 28: 1889-1899
9. Khin Yin Win, Si-Shen Feng. Effects of particle size and surface coating on cellular uptake of polymeric nanoparticles for oral delivery of anticancer drugs. *Biomaterials* 2005, 26: 2713-2722
10. L. Mu, S.S. Feng. Vitamin E TPGS used as emulsifier in the solvent evaporation/extraction technique for fabrication of polymeric nanospheres for controlled release of paclitaxel. *J Con Rel* 2002, 80: 129-144
11. Kai-Hong Huang, Zhao-Hua Zhu, Jian-Hua Liu, et al. preparation and release efficiency of polylactic acid nanoparticle. *Chin J Cancer* 2005, 24: 1023-1026
12. E. K. Park, S. B. Lee, Y. M. Lee. Preparation and characterization of methoxy poly (ethylene glycol)/poly (caprolactone) amphiphilic block copolymeric nanospheres for tumor-specific folate-mediated targeting of anticancer drugs. *Biomaterials* 2005, 26: 1053-1061
13. Musumeci T., C.A. Ventura, I. Giannone, et al. PLA/PLGA nanoparticles for sustained release of docetaxel. *Int J Pharm* 2006, 325: 172-179
14. L. Mu, S.S. Feng. A novel controlled release formulation for the anticancer drug paclitaxel: PLGA nanoparticles containing vitamin E TPGS. *J Con Rel* 2003, 86: 33-48

Author: You Ling, Yueshan Huang
 Institute: School of Bioscience and Bioengineering South China
 University of Technology
 Street: East Road of University City
 City: Guangzhou
 Country: China
 Email: lingyou8653@163.com.cn

Effects of Paclitaxel on human lung cancer cell lines *in vitro* and *in vivo*

Lihua Zeng¹, Changxu Zou², Xuejun Xie¹, S. Kizaka-Kondoh³, M. Hiraoka³, GuoZhen Guo¹

¹ Department of Radiation Medicine, Fourth Military Medical University, Xi'an, China

² Department of Neuroanatomy, Fourth Military Medical University, Xi'an, China

³ Department of Radiation Oncology and Image-applied Therapy, Kyoto University Graduate School of Medicine, Japan

Abstract — AIMS: Paclitaxel (PTX) is an inhibitor of microtubule function and is also known to have an antiangiogenic activity. In the present paper we investigated the effect of PTX on human lung cancer cell lines *in vivo* and *in vitro* to elucidate the correlation between the resistance to PTX under normoxic conditions. **METHODS AND RESULTS:** First, we established human lung adenocarcinoma cancer cell lines, PC14PE6 and H441 cells, which stably possess one of following reporter plasmids; pEF/Luc which constitutively expresses luciferase gene and p5HRE/CMVmp-Luc which expresses luciferase gene only under hypoxic conditions (PC14PE6/EF-Luc, PC14PE6/5HRE-Luc, H441/EF-Luc and H441/5HRE-Luc) for orthotopic lung cancer models and monitor the progression of lung cancer by *in vivo* bioluminescence imaging system, which enables us to monitor the growth and the hypoxic area of tumors growing in the body of mice non-invasively repeatedly. We have evaluated its effect with orthotopic lung cancer mouse model by using PC14PE6 and H441. We examined the effect of PTX with the tumor xenograft model and found that PC14PE6 cells were resistant to PTX and H441 cells were sensitive to PTX treatment. PTX significantly prolonged the survival of H441 lung cancer model, while it hardly influenced the survival of PC14PE6 lung cancer model. And then we also found that PTX didn't induce cell death to PC14PE6 cells *in vitro* under both hypoxic and normoxic conditions even at 100 nM PTX concentration (Fig. 4A). Contrast to PC14PE6, H441 cells showed significant sensitivity to PTX under normoxic conditions. In western blot analysis, the expression level of HIF-1 α protein was higher in PC14PE6 than in the H441. **CONCLUSION:** High level of HIF-1 α protein expression may have some relation with PTX resistant in PC14PE6 cell line.

Keywords — Paclitaxel (PTX); Human lung cancer cell line; nude mice; hypoxia inducible factor-1 (HIF-1)

I. INTRODUCTION

About 20-50% of the human cancers are sensitive at the first treatment of Paclitaxel (PTX) or other microtubule stability agents^[1]. PTX is one of the most important agents for the first-line chemotherapy in clinical cancer managements. It has shown promising response and improved the survival time in cancer patients with non-small cell lung cancer, breast cancer, ovarian cancer, head and neck cancer, and so on^[2]. PTX arrests the cell cycle in cancer cell via inhibition of microtubule dynamics, and PTX promotes the

assembly of stable microtubules from α -tubulin and β -tubulin^[3,4]. It has reported that microtubule-stabilizing and microtubule-destabilizing drugs inhibit Hypoxia-inducible Factor-1 (HIF-1) α accumulation, leading to suppression of HIF-1 activity and following tumor progression and angiogenesis^[5,6].

Hypoxia is one of the major resistant factors to conventional chemotherapy. Within solid tumors, hypoxic cell chemoresistance was originally attributed to poor drug delivery and to the contention that hypoxic tumor cells are predominantly quiescent^[7,8]. HIF-1 is a heterodimeric transcription factor composed of α and β subunits and activated in a wide range of cancer cells^[9]. Alpha subunit of HIF-1 (HIF-1 α) has been reported to be an important predictor of tumor progression for several types of solid tumors^[10,11] and associated with the resistance to chemotherapy^[12,13]. Although Huang L et al^[14] reported that the induced HIF-1 α expression by CoCl₂ could increase the resistance to PTX in an ovarian cell line, direct correlation between endogenous HIF-1 expression levels and PTX sensitivity has not been described.

In the present paper we investigated the effects of PTX on human lung cancer cell lines PC14PE6 and H441 and tried to explore the correlation between the resistance to PTX and HIF-1 α expression *in vitro* and *in vivo*.

II. MATERIALS AND METHODS

A. Cell cultures and Hypoxic treatment

H441 cell line was obtained from ATCC. PC14PE6 human adenocarcinoma cells were selected from the parental PC14 cell line for the ability to form pleural effusions in the nude mouse^[15]. PC14PE6 and H441 cell lines were maintained in RPMI 1640 (GIBCO, Invitrogen Corporation, CA) supplemented with 10% fetal bovine serum (Biosource, USA) supplemented with penicillin (100 units/ml) and streptomycin (100 μ g/ml). To create a hypoxic condition of <0.02% of oxygen tension, the cells were treated in an anoxia chamber, BACLITE-1 (Sheldon Manufacturing, Cornerlius, OR).

B. DNA transfection

Stable DNA transfection was carried out as described previously^[16]. Briefly, PC14PE6 and H441 cell (10^6 / 100-mm dish) were transfected with 20 μ g pEF/Luc or 5HRE-hCMVmp/luc plasmid, respectively. The cells were then trypsinized 24 h after transfection and cultured in the selection medium containing 5 μ g/ml Blasticidin-S or 500 μ g/ml G418 (Nacalai Tesque, Kyoto, Japan), respectively, for 10 days. The G418-resistant colonies were isolated and used for in vitro cell proliferation assays and mouse xenograft assays.

C. In vitro cell proliferation assay

Cells (200/100 μ l) were seeded in each well of 96-well plates and cultured under normoxic or hypoxic conditions on day 0. Cell count reagent SF (Nacalai tesque, Kyoto, Japan) was added to the culture medium (5 mg/well) at different time points and after exactly 24 h incubation with the reagents, the absorbance (540 nm) of the cultured cells was measured with a microplate reader (BIO-RAD, Benchmark, USA). Cell viability was calculated as the ratio of the absorbance value at each time point against the day 1.

D. Luciferase activity Assay

10^5 cells were seeded onto 24 wells plaques in 1ml 10%FBS RPMI 1640 medium, incubated at 37°C in 5% CO₂-95% air overnight, then cultured cells under the normoxic or hypoxic condition for 24h. The cells were then washed with PBS and lysed with 100 μ l Passive Lysis Buffer (Promega, Madison, USA) under normoxic or hypoxic conditions. Luciferase activity was measured using a luminometer (Lumat LB 9507, Berthold, Bad Wildbad, Germany) after the addition of 20 μ l of a substrate reagent (luciferin; Promega, Madison, USA) to 10 μ l of cell lysate.

E. Animals, orthotopic transplantation, in vivo imaging and PTX treatment

Cultured PC14pE6/EF-Luc cell and H441/pEF-Luc cell were harvested by exposure to 0.25% trypsin-0.02% EDTA solution. The cells were washed twice in PBS and resuspended in the growth factor reduced matrigel (0.5 mg/ml) in PBS. Cell viability was determined by the trypan blue exclusion test and only single-cell suspensions of >90% viability was used for in vivo studies. Seven to 8 weeks old male athymic nude mice (BALB/c nu/nu) were anesthetized by sodium pentobarbital (50 mg/kg body weight) and placed into the right lateral decubitus position. The skin over the

left chest wall was cut between the 4th and 5th intercostal spaces at the midaxillar line and lung cancer cells (PC14pE6/EF-Luc cell: 1×10^6 in 75 μ l; H441/EF-Luc cell: 5.0×10^4 in 50 μ l) were injected through the left chest wall using a 30 gauge needle following the method of Onn et al^[17]. After injection the skin was closed with wound clips.

For the *in vivo* imaging of bioluminescence, the tumor-bearing mice were intraperitoneally (i.p.) injected with 200 μ l of D-luciferin solution (10 mg/mL in PBS; -Xenogen Co., Alameda, CA) was intraperitoneally injected into the mice 20 min before imaging. The animals were then applied to IVIS™ 200 Imaging System (Xenogen Co., Alameda, CA) to monitor the cells in solid tumor. The luciferase activity was calculated as the externally detected photon count, using Living Image Software 2.20 (Xenogen Co., Alameda, CA). When tumor formation was confirmed by imaging, the mice were randomized into 4 groups ($n \geq 8$) as follows: saline treated control (PC14PE6 and H441 xenograft); PTX alone treatment. PTX (10 mg/kg) were given by i.p injection every 5 days for 3 or 4 times, beginning after the confirmation of tumor uptake by imaging. Body weights and photon counts were monitored every other day after the initial treatment. The ethical committee of the Kyoto University Institute of Laboratory Animals approved the study.

F. Western blotting analysis

Cells were harvested and lysed with 100 μ l of western lysis buffer (50 mM Tris (pH 7.5), 1% NP-40, 0.25% SOC, 150 mM NaCl, 1 mM EGTA). The cells cultured under hypoxic conditions were treated in an annormoxic chamber. The cell lysates were sonicated for 5min and then centrifuged at 10,000 g f or 30 min. The supernatant was assayed to determine protein concentration and 30 μ g per lane was applied to SDS-Polyacrylamde electrophoresis (10%). The protein was then transferred to a nitrocellulose filter (Hybond-ECL, Amersham Biosciences, Piscataway, NJ) and the resultant filter was blocked with 5% nonfat milk in PBS. For detection of HIF-1 and GAPDH, the filters were probed with monoclonal anti-HIF-1 α antibody (1:500, BD Bioscience Pharmingen, San Diego, CA) and polyclonal anti-GAPDH antibody (1:1000, Santa Cruz Biotechnology, Santa Cruz, CA, USA), respectively and incubated overnight at 4°C. Then horseradish-peroxidase linked 2nd antibodies against anti-mouse and anti-rabbit IgG (Amersham Biosciences), respectively were incubated 1h in the room temperature. Detection was carried out with a chemiluminescence-based method using the ECL Plus Western Blotting Detection System (Amersham Biosciences, Piscataway, NJ, USA).

G. FACS analysis of PTX sensitivity

in vitro. Cells (3×10^5 /300 μ l) were seeded into 24-well plates. The following day, various concentration of PTX (diluted with saline before adding to the cells) were added to the culture medium and incubated another 24h or 48h. In case of hypoxic conditions, the cells were preincubate in an anaerobic chamber for 6 h. Then the cells were harvested, gently suspended in PBS and mixed with equal volume of 2 \times hypotonic fluorochrome solution (100 μ g/ml propidium iodide in 0.2% sodium citrate–0.2% Triton X-100) immediately before the analysis with a flow cytometry using CELLQuest (BD Biosciences, Franklin Lakes, NJ). The population of the cells with degraded smaller genomic DNA (subG1 fraction) was determined by CELLQuest Analysis (Becton Dickinson) and indicated as % of dead cells.

H. Statistical analysis

All of the experiments were done in triplicate and each experiment was repeated at least three times. Data are expressed as means \pm SD. Statistical significance of differences was determined by the paired two-tailed Student t-test and logrank test for the survival curve. Differences were considered statistically significant for $P < 0.05$.

III. RESULTS

I. Stable Expression of Firefly Luciferase in the PC14pE6 and H441 Cell Lines

The firefly luciferase gene was transfected into PC14PE6 and H441 parental cells and stable constitutive luciferase expression clones was expanded and characterized *in vitro* to determine the level of bioluminescence.

Luciferase activity of PC14PE6/EF-luc, H441/EF-luc under aerobic conditions is higher than in the hypoxic, and luciferase activity of PC14pE6/5HRE-luc, H441/5HRE-luc increased significantly under the hypoxic condition as compared to the one under the aerobic condition (Fig 1 A,B).

These data showed these two kinds of report plasmid work well in the aerobic and hypoxic condition. So we can use pEF/Luc report plasmid to monitor the tumor growth *in vivo*, and 5HRE-hCMVmp/luc report plasmid to monitor the tumor fraction *in vivo*.

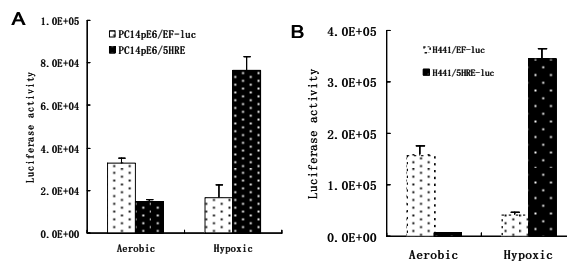


Fig. 1 Changes of luciferase activity of cell lines in the hypoxic or aerobic condition. A. Changes of luciferase activity of PC14pE6/EF-luc cells and PC14pE6/5HRE-luc cells in the aerobic or hypoxic condition; B: Changes of luciferase activity of H441pEF-luc cells and H441/5HRE-luc cells in the aerobic or hypoxic condition

J. *In vivo* imaging of PTX Effects on the PC14PE6 and H441 orthotopic lung cancer models

Using the cell lines stably expressing firefly luciferase we could non-invasively monitor the orthotopically transplanted xenografts by detecting bioluminescence from them with an *in vivo* imaging devise. The transfectants grew with a similar speed as their corresponding parental cell lines (data not shown). The cells were injected to the left lung through the left chest wall and bioluminescence externally detected from the xenografts was monitored daily. The typical time course of tumor progression in both H441 and PC14PE6 lung cancer was the following: the images were detected in the left lung in one week after transplantation; the image spreaded to the right lung during the second week; the mice died during the third week (Fig. 2, control groups). When photon counts of tumors were approximately 5×10^4 , the mice were randomized to start the PTX treatment. PTX were intraperitoneally (i.p.) injected every 5 days for 3 or 4 times. Body weights and photon counts of bioluminescence from the tumors were monitored every two days after the initial treatment. The image appearance and the photon counts during the experimental period were not significantly different between untreated and PTX-treated groups in PC14PE6 xenografts (Fig. 2 and Fig. 2A). On the other hand, the increases in images and photon counts were significantly delayed in the PTX-treated group compared to the untreated one in H441 xenografts (Fig. 2 and Fig. 2B). Furthermore, mean survival of PTX-treated H441-tumor bearing mice was prolonged to 22 days compared with 12 to 13 days in untreated H441-tumor bearing mice and in both untreated and PTX-treated PC14PE6-tumor bearing mice (Fig. 3C D and Table 1). There was no significant body weight loss associated with the treatments (data not shown). These data indicate that H441 cells are sensitive to PTX *in vivo* but PC14PE6 cells are not.

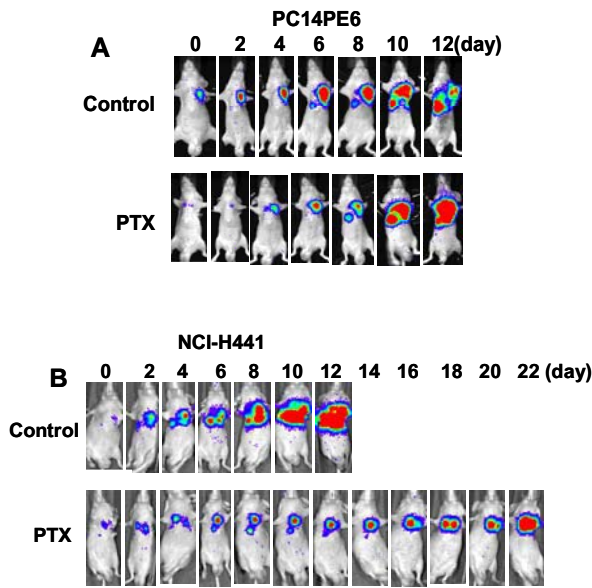


Fig. 2. The representative luciferase images of PTX on lung orthotopic tumor Xenografts model; A. The representative images of PTX on PC14pE6 cell Xenografts model; B. The representative images of PTX on H441 cell Xenografts model

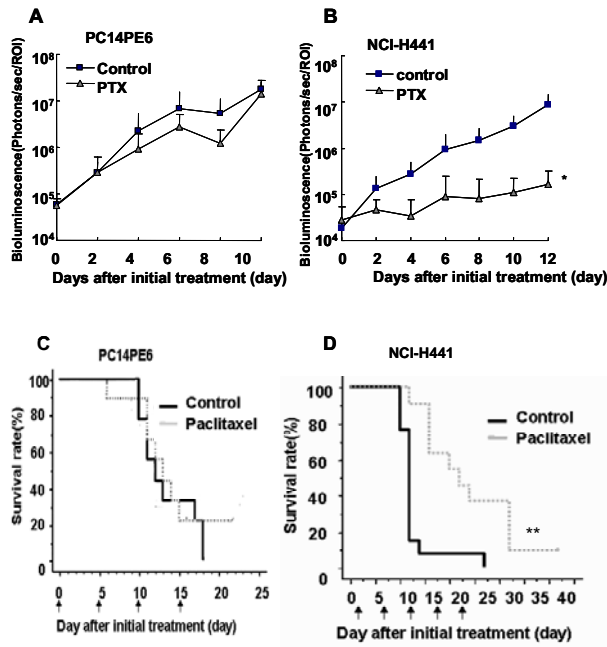


Fig. 3 Effects of PTX on PC14PE6 and H441 cell xenograft model. A. Changes of average bioluminescence count in the PC14pE6 cell Xenografts model; B. Changes of average bioluminescence count in the H441 cell Xenografts model; C. Survival Curve for PC14pE6 cell Xenografts model; D. Survival Curve for H441 cell Xenografts model.

Tab 1 Median survival time of PC14PE6/EF-Luc and H441/EF-Luc cell Xenografts model.

Cell type	Treatment group	Number of Mice	Median Survival Time (days ± SD)
PC14PE6/	Control (saline)	9	12± 1.49
EF-Luc	Paclitaxel	9	13± 1.49
H441/	Control (saline)	13	12± 4.39
EF-Luc	Paclitaxel	11	22±9.34*

(*p<0.05 vs. control group)

K. Effects of PTX on the PC14PE6 and H441 Cells in vitro

To investigate the effects of PTX on PC14PE6 and H441 cells in vitro, we treated them with various concentration of PTX. The effect of PTX on cell death was examined by FACS analysis, in which cells with degraded genome DNA corresponds to the sub-G1 fraction. PTX induces polymerization of tubulin and thus blocking cell cycle in the M phase^[19]. We found that PTX didn't induce cell death to PC14PE6 cells under both hypoxic and normoxic conditions even at 100 nM PTX concentration (Fig. 4A). Contrast to PC14PE6, H441 cells showed significant sensitivity to PTX under normoxic conditions. Even 0.01 nM PTX induced H441 to cell death under normoxic conditions (Fig. 4B). Under hypoxic conditions, however, both PC14PE6 and H441 cells showed significant resistance to PTX .

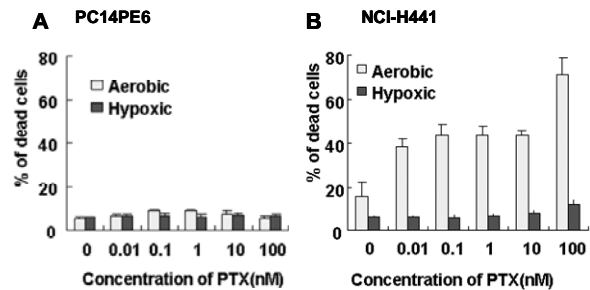


Fig. 4 Difference between PC14pE6 and H441 cell lines in vitro A. Effects of PTX on PC14pE6/EF-Luc cells in vitro by FACS; B. Effects of PTX on H441/EF-Luc cells in vitro by FACS

L. HIF-1α protein expression in the PC14pE6 and H441 Cells in vitro

We doubted whether HIF-1α activity contributes to resistance to PTX of human lung cancer cell lines. Then we investigated HIF-1α protein expression in the PC14pE6 and H441 Cells and found HIF-1α in PC14PE6 is higher than in

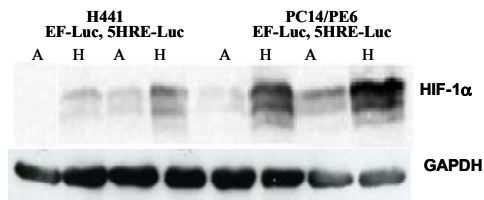


Fig. 5 HIF-1 α protein expression in the PC14PE6 and H441 cell with different report plasmids in the aerobic or hypoxic condition

H441 cells even in the aerobic condition (Fig. 5). We hypothesized the PTX sensitivities of the PC14pE6 and H441 Cells in vitro inversely maybe related to the HIF-1 α expression level.

IV. DISSCUSSION AND CONCLUSION

These results suggest that PTX sensitivity of these cells has some relationship with HIF-1 α protein expression, which induces many angiogenic factors and thus may suppress the effect of PTX on these cells lines. We found endogenous HIF-1 α protein level in PC14PE6 is significantly higher than H441 (Fig. 5), which is corresponding to their PTX sensitivity, that is, PC14PE6 is more resistant to PTX than H441 in vivo (Fig. 2) as well as in vitro (Fig. 4). These results suggest that HIF-1 is one of the regulators of PTX sensitivity.

Although we do not know how HIF-1 influences the assembly of tubulin right now, previous reports have been suggested some possible mechanisms for the association between HIF-1 α and PTX resistance. At present, the best-described mechanism of resistance to tubulin-binding agents is the multidrug resistance (MDR) pump model. In a number of cases^[20,21], development of cell lines resistant to paclitaxel has been shown to be associated with the expression of *mdr1*. But little is known concerning the significance of the MDR phenotype in the emergence of resistant tumors in patients treated with tubulin-binding agents. Clinical trials^[22] aiming to sensitize MDR-positive tumors to agents such as vinblastine with P-glycoprotein (P-gp) modulators have been disappointing. Comerford et al^[23] found HIF-1 induced *MDR1* gene expression and concomitant functional P-gp expression in both transformed epithelia and primary cultured endothelia and suggest that P-gp expression represent a pathway for resistance of some tumors to chemotherapeutics. Thus we examined the P-gp expression in PC14PE6 and H441 under both normoxic and hypoxic conditions. P-gp protein was, however, not detected in either cell lines under both conditions, although other cancer cell lines such as HepG2 expressed significant amount of P-gp protein under both conditions (data not shown). In these

human cancer cell lines, P-gp seems not to contribute to PTX resistance.

Another explanation includes the impacts of HIF-1 α induced downstream genes on the cell cycle and apoptosis associated pathways. HIF-1 α can influences the product of the tumour suppressor gene p53^[24], which can induce programmed cell death by regulating proteins such as Bax, or cause growth arrest that is mediated by p21. It was shown that HIF-1 α directly binds to the p53 ubiquitin ligase mdm2 both in vivo and in vitro, thereby stabilizing p53^[25]. However, there was also report that showed a direct binding of p53 to the oxygen-dependent degradation domain of HIF-1 α . HIF-1 α interacts with wild-type p53 but not with tumour-derived mutant p53^[26]. These reflect that the contribution of different p53 status of cells might impact their response to stress factors such as PTX treatment for cancer cells. Thus the status of p53 gene might play roles in the difference of PTX resistance in PC16 and H441 because PC16PE6 is wild-type p53 and H441 has a mutant-type p53^[27]. Whether the difference in p53 status in PC16 and H441 play roles or not for the association between PTX and HIF-1 α in our experiments have not been revealed. Further study should be done to clarify this issue.

The PTX resistance is also explained basing on the dynamics of microtubule^[28]. Cabral et al^[29] described a PTX resistance model of “hypostable” and “hyperstable” microtubule. Hypostable microtubules tend toward depolymerization spontaneously, and hyperstable microtubules are relatively resistant to depolymerization. Cells with hypostable microtubules are hypersensitive to the depolymerizing agents such as vinca alkaloids while resistant to the microtubule stabilizing agents such as PTX. Conversely, cells containing hyperstable microtubules are resistant to the vinca alkaloids but relatively sensitive to PTX. Jordan et al^[30] gave rise to another model. They analyzed the dynamic behavior of individual microtubules and found that paclitaxel at low concentrations reduces microtubule dynamics without significant alteration in microtubule length. According this explanation, the cells with highly dynamic microtubules is more sensitive to the microtubule stabilizing agents such as PTX than the cells with less dynamic microtubules.

Since there seems to be strong correlation between HIF-1 α expression levels and PTX resistance, HIF-1 signal may influence the assembly and dynamics of microtubules through a role of unknown factors whose expression is induced by HIF-1. Thus we expected that HIF-1 targeted approaches in combination with PTX may contribute to improve outcome of PTX treatment.

ACKNOWLEDGMENTS

We are grateful to Yumi Takahashi for skilled technical assistance. This work was supported in part by Grant-in-Aid for Scientific Research on Priority Areas, Cancer, from the Ministry of Education, Culture, Sports, Science and

Technology, and by a Grant-in-Aid for the 3rd Term Comprehensive 10-Year Strategy for Cancer Control from the Ministry of Health, Labor and Welfare, Japan.

REFERENCES

1. Yusuf RZ, Duan Z, Lamendola DE et al. Paclitaxel resistance: molecular mechanisms and pharmacologic manipulation. *Curr Cancer Drug Targets* 2003; **3**(1): 1-19.
2. Michael L. Miller, Iwao Ojima. Chemistry and chemical biology of Taxane anticancer agents. *The Chemical Record* 2001; **1**: 195-211
3. Schiff PB, Fant J, Horwitz SB. Promotion of microtubule assembly *in vitro* by Taxol. *Nature* 1979; **277**: 665-7.
4. Sangrajranga S., Fellousb A. Taxol resistance. *Chemotherapy* 2000; **46**: 327-34.
5. Escuin D, Kline ER, Giannakakou P. Both microtubule-stabilizing and microtubule-destabilizing drugs inhibit hypoxia-inducible factor-1alpha accumulation and activity by disrupting microtubule function. *Cancer Res* 2005; **65**(19): 9021-8.
6. Mabeesh NJ, Escuin D, LaVallee TM et al. Giannakakou P. 2ME2 inhibits tumor growth and angiogenesis by disrupting microtubules and dysregulating HIF. *Cancer Cell* 2003; **3**(4):363-75.
7. Unruh A, Ressel A, Mohamed HG et al. The hypoxia-inducible factor-1 α is a negative factor for tumor therapy. *Oncogene* 2003; **22**: 3213-20.
8. Erler JT, Cawthorne CJ, Williams KJ et al. Hypoxia-mediated down-regulation of Bid and Bax in tumors occurs via HIF-1-dependent and-independent mechanisms and contributes to drug resistance. *Mol Cell Biol* 2004; **24**: 2875-89.
9. Semanza GL. Targeting HIF-1 for cancer therapy. *Nat Rev Cancer* 2003; **3**: 721-32.
10. Brown JM, Wilson WR. Exploring tumor hypoxia in cancer treatment. *Nat Rev Cancer* 2004; **4**: 437-47.
11. Swinson DE, Jones JL, Cox G, Richardson D, Harris AL, O'Byrne KJ. Hypoxia-inducible factor-1 alpha in non small cell lung cancer: relation to growth factor, protease and apoptosis pathway. *Int J Cancer* 2004; **111**:43-50.
12. Brown LM, Cowen RL, Debray C et al. Reversing hypoxic cell chemoresistance in vitro using genetic and small molecule approaches targeting hypoxia inducible factor-1. *Mol Pharmacol* 2006; **69**: 411-18.
13. Unruh A, Ressel A, Mohamed HG et al. The hypoxia-inducible factor-1 alpha is a negative factor for tumor therapy. *Oncogene* 2003 ; **22**(21): 3213-20.
14. Huang L, Ao QL, Li F, Xing H, Lu YP. Impact of hypoxia on taxol-induced apoptosis in human ovarian cancer cell line A2780 and its mechanism. *Ai Zheng* 2005; **24**(4): 408-13.
15. Yano S, Herbst RS, Shinohara H et al. Treatment for malignant pleural effusion of human lung adenocarcinoma by inhibition of vascular endothelial growth factor receptor tyrosine kinase phosphorylation. *Clin Cancer Res* 2000; **6**(3): 957-65.
16. Harada H, Kondoh SK, Hiraoka M. Optical imaging of tumor hypoxia and evaluation of efficacy of a hypoxia-targeting drug in living animals. *Molecular Imaging* 2005; **4**(3): 182-93.
17. Onn A, Isobe T, Itasaka S et al. Development of an orthotopic model to study the biology and therapy of primary human lung cancer in nude mice. *Clin Cancer Res* 2003; **9**(15): 5532-9.
18. Louisa M. Brown, Rachel L. Cowen, Camille Debray et al. Reversing Hypoxic Cell Chemoresistance in Vitro Using Genetic and Small Molecule Approaches Targeting Hypoxia Inducible Factor-1. *Mol Pharmacol* 2006; **69**: 411-8.
19. Rahat MA, Marom B, Bitterman H, Weiss-Cerem L, Kinarty A, Lahat N. Hypoxia reduces the output of matrix metalloproteinase-9 (MMP-9) in monocytes by inhibiting its secretion and elevating membranal association. *J Leukoc Biol* 2006; **79**: 706-18
20. Horwitz SB, Liao LL, Greenberger L et al. Mode of action of Taxol and characterization of multidrug-resistant cell line resistant to Taxol. In: Kessel D, ed. Resistance to Antineoplastic Drugs. Boca Raton, FL: CRC Press, 1989;109-26.
21. Breier A, Barancik M, Sulova Z, Uhrík B. P-glycoprotein-implications of metabolism of neoplastic cells and cancer therapy. *Curr Cancer Drug Targets*.2005; **5**: 457-68.
22. Dumontet C, Sikic BI. Mechanisms of action of and resistance to antitubulin agents: microtubule dynamics, drug transport, and cell death. *J Clin Oncol* .1999; **17**: 1061-70.
23. Comerford KM, Wallace TJ, Karhausen J, Louis NA, Montalto MC, Colgan S. Hypoxia-inducible factor-1-dependent regulation of the multidrug resistance (MDR1) gene. *Cancer Res* 2002; **62**: 3387-94.
24. Hansson LO, Friedler A, Freund S et al. Two sequence motifs from HIF-1.alpha bind to the DNA-binding site of p53. *Proc Natl Acad Sci USA* 2002; **99**: 10 305-9..
25. Chen D, Li M, Luo J et al. Direct interactions between HIF-1 alpha and Mdm2 modulate p53 function. *J Biol Chem* 2003; **278**: 13 595-8.
26. An WG, Kanekal M, Simon MC et al. Stabilization of wild-type p53 by hypoxia-inducible factor 1 alpha. *Nature* 1998; **392**: 405-8.
27. Lai S-L, Perng R-P, Hwang J. p53 Gene status modulates the chemosensitivity of non-small cell lung cancer cells. *J Biomed Sci* 2000; **7**: 64-70.
28. Verdier-Pinard P, Wang F, Martello L, Burd B, Orr GA, Horwitz SB. Analysis of tubulin isotypes and mutations from taxol-resistant cells by combined isoelectrofocusing and mass spectrometry. *Biochemistry* 2003; **42**:5349-57..
29. Cabral F. Factors determining cellular mechanisms of resistance to antimetabolic drugs. *Drug Resist Updat* 2001; **4**: 3-8..
30. Jordan MA, Wilson L. Microtubules and actin filaments: Dynamic targets for cancer chemotherapy. *Curr Opin Cell Biol* 1998; **10**: 123-30

Author address

ZENG Lihua, Department of Radiation Medicine, Fourth Military Medical University, ChangLe west road 17, Xi'an, China, lzwei1998@gmail.com

corresponding author:

GUO Guozhen, Department of Radiation Medicine, Fourth Military Medical University, ChangLe west road 17, Xi'an, China, guozhen@fmmu.edu

Magnetoviscous Effect of Magnetic Fluid Targeting Drug Delivery System

Dong Cao¹, Jun Yi², Hui Cao³, Wei Liu¹, Shi Ying Yuan³

¹ Information Technology College, Guangzhou University of Chinese medicine, Guangzhou, Guangdong, 510006, China

² College of Medical Information Engineering, Guangdong Pharmaceutical University, Guangzhou, Guangdong, 510006, China

³ School of Electrical and electronic Engineering, East China Jiaotong University, Nanchang, Jiangxi, 330013, China

Abstract — The magnetic fluid (MF) viscosity in MF targeting drug delivery system isn't constant. With the change of magnetic field strength, MF viscosity will change due to MF magnetoviscous effect. The magnetoviscous effect mechanisms in low and high concentration MF are different and qualitatively analyzed respectively. Drop needle movement method under controlled temperature was adopted to measure magnetoviscous effect. Experiment results show the viscosity linearly increases by magnetic field strength under low magnetic field. The viscosity reaches max value when MF is magnetic saturation. Through curve fitting, the magnetoviscous effect formula is got. Based on this formula, the MF viscosity in changed magnetic field can be obtained. The MF drug movement behavior will be controlled by magnetic field and can be transferred accurately to target. This result also can be generalized to other MF viscosity research field.

Keywords — magnetic fluid, magnetoviscous effect, targeting drug delivery.

I. INTRODUCTION

Magnetic fluid (MF) is nano function material that combines magnetic and fluid properties and has significant application perspectives on magnetic targeting drug delivery [1-5]. MF targeting drug delivery is close correlative with MF viscosity. MF targeting drug movement navier-stokes formula includes MF viscosity parameter. General, the viscosity is considered as constant. In fact, due to the special constitute structure of MF, it has unique magnetoviscous effect—the viscosity will be changed under magnetic field [6]. There has variable magnetic field in the MF targeting drug delivery system. Due to magnetoviscous effect, it will arise the change of viscosity and the MF viscosity can't be consider as constant in targeting drug delivery system.

The MF magnetoviscous effect mechanism is very complex. In microcosmic, there has anfractuosity reciprocity between the magnetic particles, carrier liquid and surfactant in MF. This paper studies on the MF magnetoviscous effect mechanism and experiment is made to measure one type of MF magnetoviscous effect and the data is fitted to curve formula.

II. MF MAGNETOVISCOUS EFFECT MECHANISM

Due to MF special structure, it has different magnetoviscous effect under low concentration and high concentration. It's necessary to analyze the different mechanisms respectively.

A. Low concentration MF

Under low concentration magnetic particles, it is reasonable on the assumption that the magnetic particles are independency and can't interact.

In the fluid field, under the act of shear fluid, the magnetic particles will rotate and its rotation axis will align with vorticity direction. When acted by the magnetic field, the rotation of magnetic particles will lead to the disalignment of magnetic moment and magnetic field direction due to viscous friction. It results in the hindrance of magnetic particles' free rotation [7]. Thus, an increase of viscosity would be observed.

If the vorticity direction is align with magnetic field direction, there is no disalignment and won't hinder the magnetic particles' free rotation. The viscosity won't increase. When the vorticity direction is perpendicular to magnetic field direction, the hindrance effect is strongest. Its viscosity reaches maximum.

When taking into account the magnetic and mechanic torques as well as interaction between magnetic particles, the viscosity could be expressed by rotation viscosity.

Shlomis[8] introduce internal angular momentum S , $S=I\omega$, I is the unit volume and ω is average angular speed. Then under the magnetic field and fluid field, the MF Internal angular momentum equation can be expressed as

$$\frac{dS}{dt} = \mu_0(M \times H) - \frac{1}{\tau_s}(S - I\Omega) \quad (1)$$

Therein, μ_0 is vacuum magnetic permeability, M is magnetic particle susceptibility, H is magnetic field intensity, τ_s is magnetic particle relaxation time, and Ω is magnetic particle vorticity.

MF Navier-Stokes equation is

$$\rho \frac{dv}{dt} = -\nabla[p + \frac{1}{2}\mu_0(\mathbf{MH}) + \frac{\mathbf{S}}{I}(\mathbf{S} - I\boldsymbol{\Omega})] + \eta_0 \nabla^2 \mathbf{v} + \mu_0(\mathbf{M}\nabla)\mathbf{H} + \frac{1}{2\tau_s} \text{rot}(\mathbf{S} - I\boldsymbol{\Omega}) \quad (2)$$

Therein, ρ is MF density, v is velocity of flow, P is pressure, η_0 is viscosity without magnetic field.

MF drug movement in the blood vessel can be considered as laminar flow. Under laminar flow condition, it can get viscosity expression as

$$\eta_{H,a} = \frac{3}{2} \phi' \eta_0 \frac{\alpha - \tanh \alpha}{\alpha + \tanh \alpha} \langle \sin^2 \beta \rangle \quad (3)$$

Therein, ϕ' is magnetic particles and surfactant volume fraction, $\alpha = \mu_0 m H / (k_B T)$, m is magnetic moment, T is absolute temperature, k_B is Boltzmann constant, β is angle between magnetic filed direction and vorticity direction.

In order to describe the magnetoviscous effect clearly, introduce the relative viscosity ratio R . It can be expressed by

$$R = \frac{\eta_{(H)} - \eta_{(H=0)}}{\eta_{(H=0)}} = \frac{\eta_{H,a}}{\eta_0} = \frac{3}{2} \phi' \frac{\alpha - \tanh \alpha}{\alpha + \tanh \alpha} \langle \sin^2 \beta \rangle \quad (4)$$

From formula (4), the relationship curve can be gotten as Figure 1. It shows that the R increases when magnetic field intensity increases, and when the magnetic field intensity reaches infinite, α is very large, $\tanh \alpha$ is close to zero, R reaches max. In the right down corner of Figure 1, it is the enlarged view of low magnetic filed zone. It shows R is parabola curve under low magnetic filed intensity.

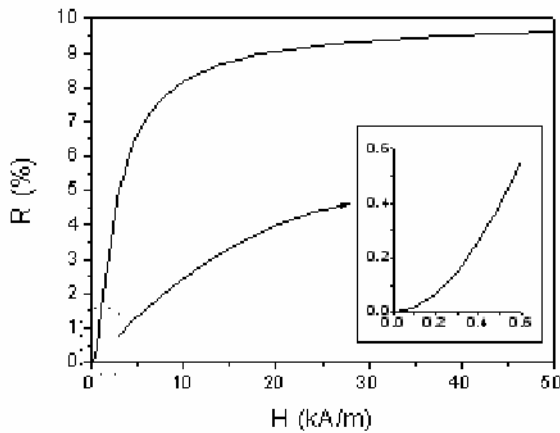


Fig. 1 Relative viscosity ratio R curve in low concentration MF

B. High concentration MF

On high concentration condition, the low concentration theory won't work, because in microstructure the anfractu-ous actions between the components of MF—magnetic particles, carrier liquid and surfactant must be taken into account. Under the magnetic filed, the components of MF will couple between magnetic field, fluid field, movement field and force field and make it difficultly express magne-toviscous effect formula quantitatively. Experimental and qualitative method is good means to find its mechanism. In many experiments, it found that the viscosity increases larger more than under low concentration. Rosensweig[9] and Zubarev A.Y. [10] considered that the magnetic parti-cles will interact, form chain structure under high concen-tration, and then its viscosity grandly increases. Some re-searcher used compute technology simulating the existence of chain structure. Pop L.M. used scatter technology prov-ing that theory [11].

This theory primarily explains the magnetoviscous effect mechanism under high concentration MF, but the quantita-tive relation between viscosity and magnetic field still can't be gotten.

Presently, the experimental method is the way to get this magnetoviscous effect data, and then adopt curve fitting technology to fit those data and find the quantitative relation.

III. EXPERIMENT

In order to measure the magnetoviscous effect in MF tar-geting drug delivery system, drop needle movement method under controlled temperature was adopted. This experiment equipment is rebuilt based on drop needle viscosity instru-ment. As shown in Figure 2, it includes main body, drop needle, Hall sensor, single-chip time counter, magnetic filed instrument and temperature control system. Main body is long hollow cylinder which is wrapped coil outside and filled with MF. The coil is used to produce uniformity magne-tic field in the centre of hollow cylinder. Drop needle represents the movement body vertical drop in liquid under gravity. Through measuring the ending speed of drop needle, the MF viscosity can be calculated. Since the magnetic field is acted on MF, magnetic field will produce heat and rise MF temperature. It will affect the MF viscosity, thus viscosity can't be measured accurately. Temperature control system is built to maintain the constant temperature in the experiment process. The long hollow cylinder composes two hollow concentric cylinders. Inner cylinder is filled with MF, and outer cylinder is filled with constant temperature water and keeps the temperature inside the MF constant.



Fig. 2 MF magnetoviscous effect experimental instrument

When the needle drops in the center of main body filled with MF, after some times, the needle gravity, viscosity resistance force and the up surface and bottom surface pressure difference will get balance. The needle move speed becomes constant. This speed V_∞ can be gotten by two sensors amount on main body. Then the MF viscosity η can be calculated by follow equation.

$$\eta = \frac{gR_2^2(\rho_s - \rho_L)}{2V_\infty} \frac{1 + \frac{2}{3}L_r}{1 + 3(\ln \frac{R_1}{R_2} - 1)/(2C_w L_r)} (\ln \frac{R_1}{R_2} - 1) \quad (5)$$

Therein, C_w is coefficient of correction of main body radius

$$C_w = 1 - 2.04k + 2.09k^3 - 0.95k^5 \quad (k=R_2/R_1) \quad (6)$$

L_r is coefficient of correction of needle length

$$L_r = (L - 2R_2) / 2R_2 \quad (7)$$

R_1 and ρ_s are radius and density of needle, R_2 is radius of inner hollow cylinder of main body, ρ_L is density of MF.

IV. RESULT

Experiment results show the viscosity linearly increases by magnetic field strength under low magnetic field (as shown in Figure 3). Along with the increasing of magnetic field strength, the viscosity increase rate becomes slow. The viscosity reaches max value when MF is magnetic saturation. The experiment data is fitted by polynomial curve and get the magnetoviscous effect formula as,

$$\eta = 2.14 * 10^{-9} H^3 - 2.5 * 10^{-5} H^2 + 5.3 * 10^{-2} H + 16.85 \quad (8)$$

Therein, η is viscosity and H is magnetic field strength.

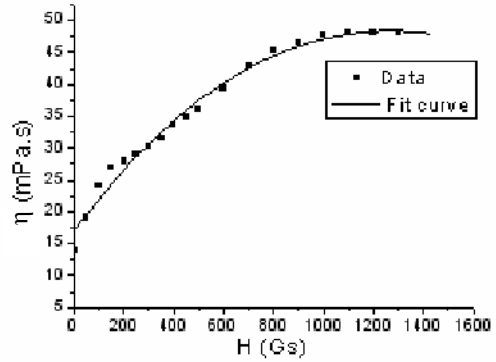


Fig. 3 Magnetoviscous effect curve in high concentration MF

V. CONCLUSIONS

In the process of MF targeting drug delivery, MF viscosity is a necessary parameter. The MF unique property correlative to viscosity – magnetoviscous effect make significantly important role in the targeting drug delivery. The magnetoviscous effect mechanisms in low and high concentration MF are different.

In low concentration, MF can be considered as individual magnetic particle model. The main reason is the disalignment of magnetic moment and magnetic field direction which results in the hindrance of magnetic particles' free rotation, then increases the viscosity. In high concentration, the magnetic particles in MF form chain structure under magnetic field and fluid field. Drop needle movement method under controlled temperature was used to measure magnetoviscous effect. Through curve fitting, the magnetoviscous effect formula is got. Based on this formula, the MF drug movement behave will be controlled by magnetic field and can be transferred accurately to target.

ACKNOWLEDGMENT

This work is supported by grant from National Natural Science Foundation of China (50775077), PhD. Programs Foundation of Ministry of Education of China (20060561003), and Guangdong Province Natural Science Foundation (06025670).

REFERENCES

1. Ganguly R, Gaid A P, Sen S, et al. (2005) Analyzing ferrofluid transport for magnetic drug targeting. *J Magn Magn Mater* 289: 331-334
2. Alexiou C, Jurgons R, Schmid R, et al. (2005) In vitro and in vivo investigations of targeted chemotherapy with magnetic nanoparticles. *J Magn Magn Mater* 293:389-393
3. Yoshida Y, Fukui S, Fujimoto S, et al. (2007) Ex vivo investigation of magnetically targeted drug delivery system. *J Magn Magn Mater* 310:2880-2882
4. Fuku S, Abe R, Ogawa J, et al. (2007) Study on optimization design of superconducting magnet for magnetic force assisted drug delivery system. *Physica C* 463-465:1315-1318
5. Aviles M O, Chen H T, Ebner A D, et al. (2007) In vitro study of ferromagnetic stents for implant assisted-magnetic drug targeting. *J Magn Magn Mater* 311:306-311
6. Cao D, Liu G X. (2006) Mechanism and simulation of intelligent magnetic fluidic acceleration sensor based on magnetoviscous effect. *SPIE*, 2006, Vol.6280: 62801D
7. Hall W. F., Busenberg S. N. (1969) Viscosity of Magnetic Suspensions. *J Chem Phys* 51: 137-144
8. Shliomis M. I., Pshenichnikov A. F., Morozov K. I. (1990) Magnetic properties of ferrocolloids. *J Magn Magn Mater* 85: 40-46
9. Rosensweig R.E. (1985) *Ferrohydrodynamics*. Cambridge, London
10. Zubarev A.Y., Iskaova L.Y. (2007) Rheological properties of ferrofluids with drop-like aggregates. *Physica A* 376(15): 38-50
11. Pop L.M., Hilljegerdes J., Odenbach S. (2004) The microstructure of ferrofluids and their rheological properties. *Appl Organomet Chem* 17: 523-528

Author: Cao Dong

Institute: Information Technology College, Guangzhou University of Chinese medicine

Street: Guangzhou Higher Education Mega Center, Pan Yu District
City: Guangzhou, Guangdong, 510006

Country: China

Email: caodong@gzhtcm.edu.cn

Effects of Asparagus Polysaccharide on GPA and Band 3 from Erythrocyte Membrane of S₁₈₀ Mice

Yubin Ji, Chenfeng Ji, Xuejun Chen

Postdoctoral Programme, Institute of Meteria Medica, Center of Research and Development on Life Sciences and Environment Sciences of Harbin University of Commerce, Harbin 150076, China
jyb@hrbcu.edu.cn; jichenfeng@hrbcu.edu.cn

Abstract — Objective To explore the influence of *Asparagus* polysaccharide on Band 3 proteins and glycoporphin A(GPA) of S₁₈₀ mice erythrocyte membrane by contrasting the groups treated with deferent ways. Methods The experiment was equipped with 5 groups: normal control group (physiological saline), negative control group (physiological saline), *Asparagus* polysaccharide group (25mg/kg), *Asparagus* polysaccharide group (50mg/kg) and *Asparagus* polysaccharide group (100mg/kg). The content of sialic acid(SA) was determined by spectrophotometric method; the negative charges were detected by high performance capillary electrophoresis(HPCE); the relative content of glycoporphin A and Band 3 were separated by sodium dodecyl sulfate polyacrylamide gel electrophoresis (SDS-PAGE; anion transportation function of Band 3 was examined by the fluorescence spectrophotometric method; Flow Cytometer(FCM) was needed to observe the potential of erythrocyte membrane. Results *Asparagus* polysaccharide increased the content of sialic acid; advanced the migration time; improved the relative content of GPA and Band 3; obviously enhanced the Cl⁻ transportation function of erythrocyte Band 3; and caused the membrane potential obviously to elevate, *Asparagus* polysaccharide has the simultaneously influence on the functions of glycoporphin A and Band 3 which are closely connected. Conclusion It is assumed that the anti-tumor function of *Asparagus* polysaccharide partly concerns function adjustments of glycoporphin A and Band 3 from S₁₈₀ mice erythrocyte membrane.

Keywords — *Asparagus* polysaccharide; Band 3 proteins; glycoporphin A

I. INTRODUCTION

Asparagus deserves to be paid more attention by the medicinal arena. Massive findings have confirmed that *Asparagus* has anti-tumor function and immunity control action. Then studying thoroughly the ingredient and the mechanism of anti-tumor function has the very vital significance. The experiment conducted the research to the influence of *Asparagus* polysaccharide on Band 3 and GPA from S₁₈₀ mice erythrocyte membrane^[1].

II. MATERIALS

A. Model and Cell Line

KM mouse (20±2.0)g, purchased from Harbin Medical University; sarcoma S₁₈₀, which has been maintained by the Institute of Cancer Studies of Heilongjiang Cancer Hospital. To form a mouse model with tumor, Cell line solution with a concentration of 2×10⁷个/mL was inoculated 0.2 mL a mice.

B. Biochemical reagents

Asparagus polysaccharide, provided by Institute of Meteria Medica, Center of Research and Development on Life Sciences and Environment Sciences of Harbin University of Commerce.

C. Groups and Dose

The experiment was designed with six groups: normal control group (not planted by S₁₈₀ cell line and treated by physiological saline), negative control group (S₁₈₀ mice, physiological saline), positive control group (S₁₈₀ mice, 5-fluorine uracil), *Asparagus* polysaccharide dose group (S₁₈₀ mice, 25mg/kg), *Asparagus* polysaccharide dose group (S₁₈₀ mice, 50mg/kg) and *Asparagus* polysaccharide dose group (S₁₈₀ mice, 100mg/kg).

III. METHODS

A. The content of SA from erythrocyte membrane

Erythrocytes were hemolysed in Tris-HCl (10 mmol/L, pH7.4), and the protein in cell membrane was separated by centrifuge (12000×g, 15 min, 4°C). During the hemolysis, PMSF was applied to inhibit the degradation of the protein. The content of protein in the membrane was quantified by CBBG₂₅₀. The content of SA was determined on spectrophotometer depending on a purple compound formed by oxidated SA and 5-Methylresorcinol.

B. The migration time of erythrocytes

The migration of erythrocytes was a process on HPCE. The sampling pressure was 0.5 psi; The sampling time was 10 seconds; The separation voltage was 20 kV; The separation temperature was 25°C; The detecting wavelength in ultraviolet radiation was 240 nm; The electrophoresis Buffer was phosphate with a concentration of 0.1 mol/L and pH 7.4[2].

C. The relative content of GPA and Band 3 from erythrocyte membrane

Erythrocytes were hemolysed in Tris-HCl (10 mmol/L, pH7.4), and the protein in cell membrane was separated by centrifuge (12000×g, 15 min, 4°C), and PMSF was applied to inhibit the degradation of the protein. The SDS-PAGE was applied to separate the protein. For GPA, the gel was dyed by PAS and for Band 3 by CBB_{R250}^[3].

D. Anion exchange of erythrocyte membrane

Methoxyquinolinium bromide(MQAE) with a final concentration of 2.5 mmol/L was added to the solution containing erythrocytes and buffer to react on Cl⁻. Then the solution was incubated under a condition of 37°C, 2h and observed on fluorescence spectrophotometer. Fluorescence was detected in absorption spectrum of 350nm and fluorescence spectrum of 460nm^[4].

E. The potential of erythrocyte membrane

Rhodamine 123 with a final concentration of 10 µg/mL was incubated with erythrocytes under a condition of 37°C, 30 min. Then the mixture was washed in PBS buffer(pH 7.4) three times and observed on FCM with absorption spectrum of 488nm and fluorescence spectrum of 530nm^[5].

IV. RESULTS

A. Effects of Asparagus polysaccharide on the content of SA from erythrocyte membrane of S₁₈₀ mice

Tab.1 Effects of *Asparagus* polysaccharide on the content of SA from erythrocyte membrane of S₁₈₀ mice

Group	SA Content (mmol/L)
Normal	1.06±0.29
Control	0.54±0.24 ^{△△}
Polysaccharide Low	0.57±0.15
Polysaccharide Mid	0.97±0.12**
Polysaccharide High	0.82±0.21*

^{△△} p<0.01 ; *p<0.05, ** p<0.01 compared with control

B. Effects of Asparagus polysaccharide on the migration time of erythrocytes of S₁₈₀ mice by HPCE

Tab.2 Effects of *Asparagus* polysaccharide on the migration time of erythrocytes of S₁₈₀ mice by HPCE

Group	migration time (minute)
Normal	11.42 ± 0.39
Control	17.20±0.48 ^{△△}
Polysaccharide Low	14.33±0.29**
Polysaccharide Mid	11.95±0.54**
Polysaccharide High	13.03±0.51**

^{△△} p<0.01 ; ** p<0.01 compared with control

C. Effects of Asparagus polysaccharide on the relative content of GPA and Band 3 from erythrocyte membrane of S₁₈₀ mice

Tab.3 Effects of *Asparagus* polysaccharide on the relative content of GPA from erythrocyte membrane of S₁₈₀ mice

Group	Relative Content (%)
Normal	84.07±3.08
Control	73.19±5.88 [△]
Polysaccharide Low	75.98±7.27
Polysaccharide Mid	82.12±4.62*
Polysaccharide High	80.51±4.28*

[△]p<0.05 ; *p<0.05 compared with control

Tab.4 Effects of *Asparagus* polysaccharide on the relative content of Band 3 from erythrocyte membrane of S₁₈₀ mice

Group	Relative Content(%)
Normal	23.12±2.93
Control	14.55±2.55 [△]
Polysaccharide Low	14.76±2.20
Polysaccharide Mid	19.20±3.20*
Polysaccharide High	21.38±3.75*

[△]p<0.05, ; *p<0.05 compared with control

D. Effects of *Asparagus polysaccharide* on anion exchange of erythrocyte membrane of *S₁₈₀* mice

Tab.5 Effects of *Asparagus polysaccharide* on anion exchange of erythrocyte membrane of *S₁₈₀* mice

Group	Flu-intensity		
	5 min	20 min	35 min
Normal	2.59±1.75	4.23±2.16	6.73±2.26
Control	1.39±0.67	1.68±0.68 ^Δ	2.15±0.61 ^{ΔΔ}
Polysaccharide Low	3.98±1.43**	6.35±1.06**	10.50±1.22**
Polysaccharide Mid	3.41±1.54*	4.45±1.87**	6.05±1.88**
Polysaccharide High	1.84±0.89	2.96±1.28	4.60±1.78*

^Δp<0.05, ^{ΔΔ}p<0.01 ; *p<0.05, ** p<0.01 compared with control

E. Effects of *Asparagus polysaccharide* on the potential of erythrocyte membrane of *S₁₈₀* mice

Tab.6 Effects of *Asparagus polysaccharide* on the potential of erythrocyte membrane of *S₁₈₀* mice

Group	Flu-intensity(%)
Normal	99.4±0.35
Control	45.0±3.28 ^{ΔΔ}
Polysaccharide Low	65.5±6.04**
Polysaccharide Mid	98.4±1.42**
Polysaccharide High	89.9±3.92**

^{ΔΔ}p<0.01 ; ** p<0.01 compared with control

V. DISCUSSION

The red cell immunity is one of the most effective systems in the anti-tumor immunity^[6]. As the components of erythrocytes membrane, GPA and Band 3 are vitally important for the function of erythrocyte. SA which mainly exists in the terminal of GPA is involved in the combination between erythrocyte and antigens; The negative charges which originate in SA on the surface of erythrocyte can prevent

erythrocytes from accumulation. Band 3 is a protein chiefly functioning as an anion transporter of erythrocyte membrane^[7]. Potential of the erythrocyte membrane is one of the factors which influence the action of anion transport of Band 3 by means of redistributing the binding points. Massive findings have confirmed that *Asparagus* has anti-tumor function and immunity control action. The experiment conducted the research to the anti-tumor function mechanism of *Asparagus polysaccharide* from the red blood cell immunity angle and initially explored its influence on Band 3 and glycophorin A of *S₁₈₀* mice erythrocyte membrane.

The results indicate that *Asparagus polysaccharide* in the varying range increased the content of SA, made the migration time of erythrocytes shorter which suggested that the quantity of negative charges on erythrocyte surface was promoted, heightened the relative content of GPA and Band 3, enhanced the activity of anion transport of Band 3, and elevated the potential of erythrocyte. It can be concluded that *Asparagus polysaccharide* has simultaneous effects on GPA and Band 3 which locate in the erythrocyte membrane. All of the results suggest that the anti-tumor function of *Asparagus polysaccharide* concerns its effects on GPA and Band 3 which is consequently related to the action of erythrocytes.

REFERENCES

1. Zhou LG, Wang CH, Wang JH. The effective component and biological function of *Asparagus*[J]. Auhui Agricultural Science Bulletin, 2006, pp.23-25
2. Wu LW, Liu ST. Separation of normal RBC and sick RBC by capillary electrophoresis[J]. Journal of Fuzhou University(Natural Science), 2005, pp.822-824
3. Ji YB, Ji CF, Zou X. Study on the effects of two kinds of cactus polysaccharide on erythrocyte membrane protein and fluidity of the lipid in *S₁₈₀* mice[J]. China Journal of Chinese Materia Medica, 2004, pp.967-970
4. Bai SZ, Liu XB, Fu GH. Expression of Band 3 Protein on Erythrocytes of Malignant Tumor Patients and Its Impact on Proliferation of K562 Cells[J]. Chinese journal of cancer, 2005, pp.543-547
5. R Grygorczyk, W Schwarz, H Passow. Potential dependence of the "electrically silent" anion exchange across the plasma membrane of *Xenopus oocytes* mediated by the band-3 protein of mouse red blood cells[J]. J Membr Biol, 1987, pp.127-136
6. Wei Y, Zheng Y, Ding YC. The function and position of the red cells in the tumor immunity[J]. Stockbreeding Market, 2006, pp.183-185
7. Lu YQ, Liu JF. Erythrocyte Membrane Proteins and Membrane Skeleton[J]. Life Science Research, 2005, pp. 283-291

Study on S180 Tumor Mice Erythrocyte Membrane Function of Sargassum Fusiform Polysaccharides

Yubin Ji, Chenfeng Ji, Chong Wang

Postdoctoral Programme, Institute of Materia Medica, Center of Research and Development on Life Sciences and Environment Sciences of Harbin University of Commerce, Harbin 150076, China
jyb@hrbcu.edu.cn; jichenfeng@hrbcu.edu.cn

Abstract — Objective To study the effect of *Sargassum fusiforme* polysaccharides (SFPS) on biochemistry function of erythrocyte membrane of S₁₈₀ mice. Methods A tumor mouse model was developed, and the mice were treated with high, medium, and low doses of SFPS through abdominal injection for 7 d. Erythrocytes were collected and erythrocyte suspensions were prepared. Changes in [Ca²⁺] in the erythrocytes in the tumor-bearing mice were measured using laser confocal scanning; changes in the content of sialic acid and the activities of Na⁺,K⁺-ATPase and Ca²⁺,Mg²⁺-ATPase were measured using relevant test kits; changes in the level of erythrocyte membrane potential were analyzed using flow cytometry; and changes in the complex mobility of erythrocytes were measured using high performance capillary electrophoresis (HPCE). Results SFPS lowered the intracellular [Ca²⁺] of erythrocytes in tumor-bearing mice, increased the content of sialic acid on surface of erythrocyte membrane, increased the activities of Na⁺,K⁺-ATPase and Ca²⁺, Mg²⁺-ATPase, and raised the level of erythrocyte membrane potential and the complex mobility of erythrocytes in electrophoresis. Conclusions *Sargassum fusiforme* polysaccharides (SFPS) can adjust or restore some biochemistry functions of erythrocyte membrane of S₁₈₀ mice.

Keywords — *Sargassum fusiforme* polysaccharides (SFPS); erythrocyte membrane; biochemistry

I. INTRODUCTION

Based on our earlier studies, this paper further explores the anti-tumor mechanisms of *Sargassum fusiforme* in terms of the functioning of erythrocyte membrane, with a focus on the study of changes in the intracellular [Ca²⁺] and membrane potential of erythrocytes, as well as changes in the complex mobility of the erythrocytes in electrophoresis. There is no report in China yet on this kind of research.

II. EXPERIMENTS

2.1 Materials, Apparatuses, and Reagents

2.1.1 Drugs and reagents

Sargassum fusiforme polysaccharides (SFPS), 5-FU; saline; Fluo-3/AM; PMSF; protein content test kit; sialic acid test kit; ATPase test kit; Rhodamine 123.

2.1.2 Apparatuses

Low-speed centrifuge; electrothermal constant temperature waterbath; laser confocal scanning system; low-temperature high-speed centrifuge; 752 light spectrophotometer

2.1.3 Laboratory animals and tumor cell line

Kunming strain mice, weight 20.0 ±2.0 g, half male and half female.

2.1.4 Developing a mouse tumor model

The abdominal dropsy was diluted with normal saline 1:4, and each mouse was inoculated with 0.2 ml of the dropsy through injection at the armpit of the right fore limb.

2.1.5 Grouping of the animals and dosage and route of drug administration

The mice were randomly divided into 6 groups of 10 animals each, including 3 experimental groups; a positive control group to be treated with 5-FU; a negative control group to be administered saline; and the normal group. The dosages were 40 mg/(kg•d), 20 mg/(kg•d), and 10 mg/(kg•d),

2.2 Method

2.2.1 The effect of SFPS on [Ca²⁺] in the erythrocytes of S₁₈₀ tumor-bearing mice

100 μl of the erythrocyte suspension was accurately drawn, and 500 μl calcium-free Tyrode's solution together with 200 μl of Fluo-3/AM was added. The solution was then kept away from light at 37°C and stained for 120 min, after which it was centrifuged for 10 min at 3,500 rpm. The supernatant was then discarded, 300 μl of calcium-free laser scanning microscope was used.

2.2.2 The effect of SFPS on the content of sialic acid on the erythrocyte membrane of S₁₈₀ tumor-bearing mice

Erythrocytes were hemolysed in Tris-HCl (10 mmol/L, pH7.4), and the protein in cell membrane was separated by centrifuge (12000×g, 15 min, 4°C). During the hemolysis. The content of protein in the membrane was quantified by CBB_{G250}. The content of SA was determined on spectrophotometer depending on a purple compound formed by oxidated SA and 5-Methylresorcinol.

2.2.3 The effect of SFPS on the activities of Na^+,K^+ -ATPase and Ca^{2+},Mg^{2+} -ATPase on the erythrocyte membrane of S_{180} tumor-bearing mice

The sample was examined using the relevant test kit following procedures given in literature. Enzyme activity is expressed in number of moles of inorganic phosphorus produced by a milligram of protein per hour. The unit is $\mu\text{mol Pi}/(\text{mg}\cdot\text{pr}\cdot\text{h})$.

2.2.4 The effect of SFPS on the membrane potential of erythrocytes in S_{180} tumor-bearing mice

100 μl of the blood solution was drawn and PBS was added to bring the volume to 2 ml to yield the needed erythrocyte suspension. 2 ml of PBS was added to the suspension, which was centrifuged for 6 min at 2,500 rpm, after which the supernatant was discarded. 0.5 ml of Rhodamine 123 with a final concentration of 10 $\mu\text{g}/\text{ml}$ was added to the residue, and the sample was incubated for 30 min at 37°C. An EPICS-XL flow cytometer was used, excitation wavelength:488 nm ,radiation wavelength:530 nm.

2.2.5 The effect of SFPS on the complex mobility of erythrocytes in S_{180} tumor-bearing mice

100 μl of the erythrocyte residue was accurately drawn and diluted with PBS to bring the volume to 3 ml. conditions Capillaries: 75 $\mu\text{m}\cdot 50$ cm; Voltage: 20 kV; buffer: 0.1 mol/l phosphate buffer solution with pH of 7.4.injection pressure: 3.448 kPa; injection time: 10 s; separation temperature: 25°C; detecting wavelength: 210 nm; cleansing liquid: 0.1 mol/l HCl and 0.1 mol/l NaOH in deionized water; marker: deionized water.

2.3 Data Processing

The data were processed using SPSS 11.5, with the results for the various groups expressed in the form $\bar{x} \pm s$. Variance test was used to compare the samples.

III. RESULTS

3.1 The effect of SFPS on $[Ca^{2+}]$ in the erythrocytes of S_{180} tumor-bearing mice

The result was shown in Table 1.

Table 1 The effect of SFPS on $[Ca^{2+}]$ in erythrocyte of S_{180} mice

Group	Fluorescence intensity
Normal	23.52±5.71
Control	61.73±6.29
5-FU	30.47±3.48**
SFPS High	39.85±3.61**
SFPS Mid	32.15±4.62**
SFPS Low	46.43±5.39*

*P<0.05 Compared with control; **P<0.01 Compared with control

3.2 The effect of SFPS on the content of sialic acid on the erythrocyte membrane of S_{180} tumor-bearing mice

The result was shown in Table 2.

Table 2 The effects of SFPS on sialic acid content in erythrocyte membrane of S_{180} mice

Group	SA Content (mmol/L)
Normal	1.06±0.29
Control	0.37±0.16
5-FU	0.54±0.24
SFPS High	0.82±0.21**
SFPS Mid	0.97±0.12**
SFPS Low	0.57±0.15*

*P<0.05 Compared with control; **P<0.01 Compared with control

3.3 The effect of SFPS on the activities of Na^+,K^+ -ATPase and Ca^{2+},Mg^{2+} -ATPase on the erythrocyte membrane of S_{180} tumor-bearing mice

The result was shown in Table 3.

Table 3 The effect of SFPS on Na^+,K^+ -ATPase and Ca^{2+},Mg^{2+} -ATPase activity in erythrocyte membrane of S_{180} mice

Group	Na^+,K^+ -ATPase	Ca^{2+},Mg^{2+} -ATPase
Normal	0.3042±0.0214	0.2461±0.0168
Control	0.1351±0.0179	0.1137±0.0302
5-FU	0.2516±0.0217**	0.2398±0.0226**
SFPS High	0.1863±0.0231*	0.2207±0.0167**
SFPS Mid	0.2324±0.0163**	0.1883±0.0249**
SFPS Low	0.1807±0.0194*	0.1475±0.0312*

*P<0.05 Compared with control; **P<0.01 Compared with control

3.4 The effect of SFPS on the membrane potential of erythrocytes in S_{180} tumor-bearing mice

The result was shown in Table 4.

Table 4 The effects of SFPS on the membrane potential of erythrocyte of S_{180} mice

Group	Rh123 flu-intensity (%)
Normal	99.1±4.2%
Control	88.0%±3.4%
5-FU	96.2%±4.4%**
SFPS High	89.8%±5.6%
SFPS Mid	97.8%±4.3%**
SFPS Low	93.4%±5.5%*

*P<0.05 Compared with control; **P<0.01 Compared with control

3.5 The effect of SFPS on the complex mobility of erythrocytes in S_{180} tumor-bearing mice

The result was shown in Table 5.

Table 5 The effects of SFPS on electrophoretic complex mobility of erythrocyte of S_{180} mice

Group	Electroosmotic mobility	Complex mobility
Normal		1.45×10^{-4}
Control		1.06×10^{-4}
5-FU	2.16×10^{-4}	1.17×10^{-4} *
SFPS High		1.23×10^{-4} **
SFPS Mid		1.29×10^{-4} **
SFPS Low		1.19×10^{-4} **

*P<0.05 Compared with control; **P<0.01 Compared with control

IV. DISCUSSION

The negative charges on the surface of erythrocytes mainly comes from the pantothenic acid or N-acetyl neuraminidase on the glycoproteins or glycolipids on the surface of the cells. Changes in the density and nature of the charges on cell surface are due to changes in the content of neuraminidase, ATP activity, and the functioning of the sodium pumps on the membrane caused by structural

changes in cell membrane. Such changes lead to a change in the transmembrane potential, which ultimately leads to changes in the electrophoretic mobility of the cell. From results from the experiment to determine the SA content on the surface of erythrocytes in tumor-bearing mice, it can be seen that in all the SFPS groups the content of SA on the surface of erythrocytes of tumor-bearing mice were increased compared with the negative control. Since SA is the main source for negative electric charge on cell surface, increase in its content means that the amount of negative charge has been increased. SA combines with Ca^{2+} to increase the activities of Na^+, K^+ -ATPase and Ca^{2+}, Mg^{2+} -ATPase. This raises the membrane potential and leads to an increase in the complex mobility of the cells in electrophoresis, which is completely consistent with the results from the experiment to measure complex mobility. Therefore, we believe that SFPS can increase the content of SA on the surface of erythrocytes by lowering the $[Ca^{2+}]$ in the erythrocytes of S_{180} mice. SA combines with Ca^{2+} to increase the activities of Na^+, K^+ -ATPase and Ca^{2+}, Mg^{2+} -ATPase, leading to a rise in membrane potential and an increase in the complex mobility of the cells in electrophoresis. In this way, SFPS restores many biological functions of the erythrocyte, such as cell division, migration of malignant cells, and cell recognition, so that the immunological functions of the erythrocyte are brought into play. This is probably one of the anti-tumor mechanisms of SFPS.

REFERENCES

1. WANG C, WU T. Extraction and determination of polysaccharide from Sargassum fusiforme [J]. Journal of Harbin University of Commerce(Natural Sciences Edition),2006,22(1):11-13.
2. JI Y B, GAO S Y. Effects of Haimiding on the functioning of red cell membrane of FC and H_{22} tumor-bearing mice [J]. Chinese Pharmaceutical Journal, 2004,39(12): 913-916.
3. ZHANG X L, XIE Y K. Theory of charge on membrane and the effect of sialic acid on Na^+, K^+ channel characteristics [J]. Progress In Physiological Sciences,2004, 35(2): 167-169.
4. ZUO M X. Yield and maintain of cell resting membrane potential [J]. Bulletin of Biology,2006,41(4):1-2.
5. Matiushichev V B, Shamratova V G, Ahunova A R. Correlation of erythrocyte electrophoretic mobility and the velocity of their sedimentation in the norm and renal pathology[J].Klin Lab Diagn, 2004, 4(4):22-24.

Enhancement of Liposome Delivery Efficiency Via Cell Membrane Permeability by ultrasound exposure

Fang Yang¹, Ning Gu^{1*}, Di Chen², Junru Wu², Xiaoyu Xi³, Dong Zhang³

¹Jiangsu Laboratory for Biomaterials and Devices, State Key Laboratory of Bioelectronics, School of Biological Science and Medical Engineering, Southeast University, Nanjing, 210096, China; ²Department of Physics, University of Vermont, Cook Building, UVM, Burlington, VT 05405, USA; ³Institute of Acoustics, Nanjing University, Nanjing, 210093, China

Abstract—Ultrasound has a number of attractive features as the diagnostic imaging modality and therapeutic modality. Under the clinical application ultrasound irradiation, sonication may be performed noninvasively or minimally invasively. In order to evaluate and characterize the performance of the designed liposome with tumor cell under the ultrasound irradiation, we prepared the FITC- inclusion liposome drug delivery model. The effect of different voltage at 1MHz frequency ultrasound transducer applied to MCF7 cells in the presence of the liposome was evaluated morphologically, using a scanning electron microscope. The delivery efficiency of FITC- inclusion liposome drug delivery model had been quantified using flow cytometry. The ultrasound voltages were 400mv, 600mv, 800mv and 1000mv at the frequency of 1MHZ respectively. Exposure of MCF7 cells to these voltages with liposome resulted in a different FITC absorption. Under the appropriate ultrasound energy guiding, liposome can efficiently delivery drug transiently and nonlethally with increase in cell membrane permeability. In this way, the noninvasively focused ultrasound could deliver drugs, protein and genes to targeted tissues, minimizing side effects, lowering drug dosages and improving efficacy.

Keywords—Ultrasound, Scanning electron microscopy, liposome, MCF7 cells, drug delivery

I. INTRODUCTION

Lipid- vesicles are one of the modern drug carrier systems to deliver the active agent to the desired site of action with little side effects at non- target organs. They are formed by self-assembly of natural or synthetic amphiphiles in aqueous environment [1, 2]. Considering the drug nature and the liposomal composition, both hydrophilic and hydrophobic compounds can interact with lipid-vesicles in different ways, incorporating into the bilayer membrane, adsorbing on the surface, anchoring at the polar head group region or entrapping in the aqueous core, which made them become reliable and efficient vesicles delivering exogenous drugs, proteins and genes into tumor cells. However, the main drawback of the application of lipid- vesicles is their active targeting and low transfection efficiency under the normal conditions, especially for gene therapy or protein

drug delivery [3, 4]. Tremendous efforts and new drug delivery methods are currently paid to elucidate these problems. One of the methods is that lipid-vesicles have been modified by specific tumor cell antibody on the surface. Other methods are external environment- induced enhancement using lipid- vesicles, such as temperature, ultrasound [5-7].

As the diagnostic imaging modality and therapeutic modality, the new clinical application of ultrasound has already extended beyond just for imaging and diagnostic towards for therapeutic applications [8, 9]. A number of experimental findings have demonstrated the evidence of increased cell membrane permeability through ultrasound sonoporation process, resulting in effective intracellular drug uptake by the tumor cells [10].

In order to evaluate and characterize the performance of the designed lipid- vesicles with the ultrasound irradiation, we have used a simple formulation of liposome consisting of DPPE-PEG2K and PC as the lipid layer encapsulated FITC in the core as the drug model. The delivery efficiency of liposome to a cell with and without insonation was assayed by flow cytometry.

II. MATERIALS AND METHODS

A. Materials

1, 2 - Dipalmitoyl - sn - Glycero - 3 - phosphoethanolamine - N - [Methoxy(Polyethylene glycol)-2000](ammonium salt) (DPPE-PEG2k) was purchased from AvantiPolar Lipids, Inc. The L- α -phosphatidylcholine(PC, lyophilized powder) and Fluorescein Isothiocyanate- Dextran(FITC- Dextran) were purchased from Sigma- Aldrich, Inc. All other reagents were analytical grade and were used as received.

B. The preparation of FITC- inclusion liposome

DPPE-PEG2k/ PC (95:5, molar ratio) dissolved in chloroform were added to the round bottom flask. Chloroform was removed under a vacuum evaporation until the thin film

formed. A phosphate buffer solution (PBS, pH=7.4±0.1) with 0.05mol/mL FITC contents was added to the dried lipids and then was mixed well above the phase transition temperature of the lipids (60 °C) to form a milky solution of multilamellar vesicles encapsulated FITC. The multilamellar liposomes suspension was sonicated using a bath sonicator (40 kHz, 100W, 5min). The micron-sized liposomes and redundant FITC in solution were removed by centrifugal separation. The mean diameter was obtained at 322nm. The concentration was 2-6×10⁶ liposomes per milliliter of solution.

C. Cell culture and pretreatment

MCF7 cells, a human breast cancer cell line, were cultured as monolayer in RPMI1640 and 10% fetal bovine serum (FBS) media. They were grown in a humidified 5% CO₂ atmosphere at 37°C. For ultrasound exposure experiments, cells were harvested and resuspended in fresh media. The concentration of the cell solution was diluted to about 10⁶ cells /mL. For each trial, 1 ml cells suspension and 0.5ml liposome solution were placed in a plastic tube.

D. Ultrasound apparatus and the ultrasound exposure

The sample tube was put into the chamber filled with deionized water. The ultrasound was generated by a function generator (Agilent 33250A, 80.0MHZ Function/ Arbitrary waveform Generator, Agilent Technologies, USA) and amplifier (ENI Model A150 RF Power Amplifier, USA) that controlled the transducer via a matching transformer. The single- element 1.0 MHZ frequency transducer, spherically focused at 8cm, was mounted in the water chamber and aligned confocally with the center of the sample. In order to study the best efficiency of the tumor cell using lipid- vesicles under ultrasound, different voltage at a frequency 1MHz was applied to the transducer for 40S. In our experiment, the 400mv, 600mv, 800mv and 1000mv voltage excited ultrasound energy were applied. The according acoustic pressure was 0.19MPa, 0.25MPa, 0.27MPa, 0.30MPa respectively measured by the calibrated hydrophone.

E. Flow cytometry assay

After ultrasound exposure of the mixed sample of cell and FITC- inclusion liposome, the sample was washed 2 times with PBS (pH=7.4±0.1) and resuspended in PBS. Samples were run on a BD FACSCalibur flow cytometry using CellQuest Pro software (BD Biosciences, Franklin Lakes, NJ, USA). The cell surface uptake level and the intracellular uptake level were qualified by converting to an

average number of molecules per cell. The samples included the different ultrasound exposure with 400mv, 600mv, 800mv and 1000mv voltage.

F. Scanning electron microscopy (SEM)

In order to observe the effects of ultrasound exposure on cell membranes, MCF7 cells with liposome after ultrasound exposure were imaged using the SEM. After ultrasound exposure, each sample was fixed with 2.5% glutaraldehyde solution for 1 hours at -4°C and then washed in 0.1M PBS (pH=7.2±0.1) twice. Alcohol dehydration followed in 33%, 50%, 80%, 90% and 100% ethanol for 20 min respectively, each stage being repeated twice. Critical point drying was then performed, after which the samples were gold sputter-coated. A field emission SEM (Field emission scanning electron microscope, FEI Sirion-200, USA) was used to scan. Each sample should be scanned at the different magnification.

III. RESULTS AND DISCUSSION

A. The flow cytometry results

Under the different ultrasound exposure, the mean fluorescence intensity (MFI) was all increased significantly. In contrast, samples not exposed to ultrasound showed minimal vesicle retention. Fig. 1 shows the result of different delivery efficiency under different voltage ultrasound exposure. These results clearly show that FITC fluorescence is not transferred to the cells without ultrasound exposure at the very short time. Different ultrasound energy can enhance the different uptake of the cells. Over high ultrasound energy failed to efficiently enhance the uptake of the cells. At 600mv ultrasound exposure, liposome has the highest delivery efficiency.

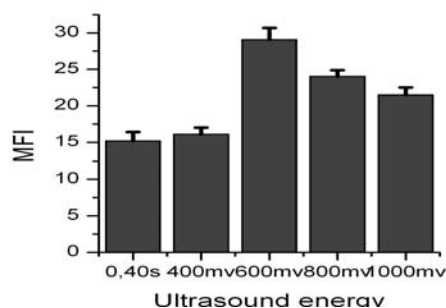


Fig. 1 Flow cytometric analysis of MCF7 cells absorbing the FITC fluorescence on the surface or into the plasma. Different absorbing efficiency under different ultrasound voltage exposure.

B. SEM morphology of MCF7 cells irradiated by ultrasound in the presence of liposomes

On the whole, the shape of the ultrasound irradiated cells was different from that of the control cells. Under the 400mv and 600mv ultrasound energy, conspicuous pits or pores were not identified. However, the existence of smaller pores or minute membrane ruptures existence after ultrasound exposure. Under the 800mv and 1000mv ultrasound energy, there are larger pores or pits observed. Especially under the 1000mv ultrasound, the surface membrane of some cells seemed to be not continuous and disruptions. So the appropriate ultrasound energy can enhance the uptake of the nano-carrier at the same time retaining the good morphology (Fig. 2).

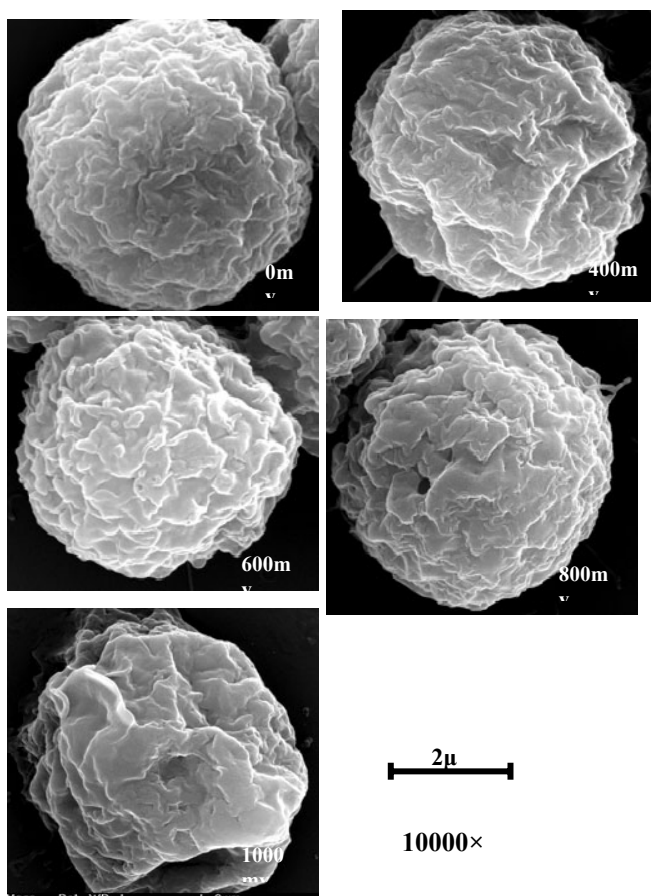


Fig. 2 SEM images of MCF7 cells in the presence of lipid-vesicles irradiated with 400mv, 600mv, 800mv and 1000mv ultrasound energy.

IV. CONCLUSIONS

This study presents the idea that the designed lipid-vesicles hold promise as an efficient therapeutic delivery after appropriate ultrasound exposure. Ultrasound may mediate the intracellular delivery of the active agents by the formation of small transient pores in cell membranes. Under the appropriate ultrasound energy guided drug delivery system, liposome can efficiently delivery drug transiently and nonlethally with increase in cell membrane permeability.

ACKNOWLEDGMENT

This work was funded in part by the National Important Science Research Program of China (Nos. 2006CB933206). Fang Yang is also thankful for the Scientific Research Foundation of Graduate School of Southeast University.

REFERENCE

1. Barbara R, Giovanni T, Eliana L et al. (2007) Application of atomic force microscopy to characterize liposomes as drug and gene carriers. *Talanta* 73: 12–22
2. Paraskevi Z, Maria H, Pavlos K et al. (2008) In vivo distribution of arsonoliposomes: Effect of vesicle lipid composition. *Int J Pharm.* 347(1-2): 86-92
3. Azadeh K, Katherine W. Ferrara (2007) Cholesterol transport from liposomal delivery vehicles. *Biomaterials* 28: 4311–4320
4. Marco Z, Spyridon M, Pavlos K et al. (2007) Liposomes for drug delivery to the lungs by nebulization. *Eur J Pharm Biopharm* 67: 655–666
5. Be' duneau A, Patrick S, Franc-ois H et al. (2007) Design of targeted lipid nanocapsules by conjugation of whole antibodies and antibody Fab' fragments. *Biomaterials* 28: 4978–4990
6. Robyn K, Harish R, Timothy P et al. (2006) Mechanism of Intracellular Delivery by Acoustic Cavitation. *Ultrasound in Med. & Biol.* 32: 915-924
7. Postema, Michiel; Gilja et al. (2007)Ultrasound-Directed Drug Delivery. *Curr Pharm Biotechno* 8: 355-361
8. Gail ter Haar (2007) Therapeutic applications of ultrasound. *Prog Biophys Mol Bio* 93:111–129
9. Bloch S. H., Dayton P. A, Ferrara K. W. (2004) Targeted Imaging Using Ultrasound Contrast Agents. *IEEE Eng Med Biol* 18-29
10. Manabu K, Kullervo H. (2007) Key factors that affect sonoporation efficiency in *in vitro* settings: The importance of standing wave in sonoporation. *Biochem Bioph Res Co* 359: 860–865

First author: Fang Yang Address: NO. 2 Si Pai Lou, Nanjing, China
210096 Tel: +86 25 82047266 Fax: +86 25 83272460
E-mail: yangfang2080@yahoo.com.cn

Corresponding author: Ning Gu Address: NO. 2 Si Pai Lou, Nanjing, China
210096 Tel: +86 25 83272460 Fax: +86 25 83272460E-mail: guning@seu.edu.cn

Numerical Analysis of a Deformable Model for Ultrasound Border Detection

Xiaoyan Liao and Dong C. Liu

School of Computer Science, Sichuan University, Chengdu, China

Abstract — This paper describes, mathematically, a two-dimensional deformable contour model for boundary detection of the left ventricular ultrasound images. To analyze the consistency, convergence and stability of the deformable contour model, this paper presents formal numerical analysis to prove that the deformable model for border detection itself is an ill-conditioned problem in the sense of perturbed input data always making converged result away from its true solution. With the help of mathematical analysis, we also present a fast numerical algorithm with controllable material coefficients and external forces terms. Selections of these coefficients are consistent with our theoretical works. Our algorithm has been implemented and applied to compute the inner border of a set of ultrasound left ventricular images. Test results show that this controllable algorithm always converges to a good enough final border starting from a reasonable initial contour.

Keywords — snakes, energy minimization, border detection, deformable model.

I. INTRODUCTION

Automatic border detection in ultrasound images has been a subject of considerable research. Classical segmentation techniques, such as edge detection and region classification have encountered difficulties due to ultrasound speckle noise and boundary gaps (due to ultrasound's inability to image interfaces that are parallel to the sound beam or hidden by acoustic shadowing). To address these difficulties, deformable models offer increased robustness by incorporating additional prior knowledge of the object shape to capture the boundary variability and provide more accurate results. The basic principle of the deformable model, also called snake algorithm [1], is starting from an elastic curve on the image, and let it evolve from an initial position under the action of both internal forces (smoothness and continuity constraints) and external forces (attraction towards local edges and weight forces) to converge to a final border which achieves the minimization of an energy function derived from internal and external energy terms.

This paper follows a mathematical formulation of an iterative version of a deformable contour model whose solution is equivalent to solving a static Euler-Lagrange equation associated with the original energy minimization problem, Section IIA. Then, to investigate the convergence of the finite difference approximation, Section IIB, we

prove that the eigenvalues of the leading matrix of the governed difference equation should be bounded by one which is equivalent to having the eigenvalues of the material matrix defined in the original energy minimization form be positive, Section IIC. At last, from the help of detailed numerical analysis, this paper also presents a fast numerical algorithm with controllable material coefficients and external forces terms, Section IID, followed by Conclusions, Section III.

II. A TWO-DIMENSIONAL DEFORMABLE CONTOUR MODEL

A. Formulation of deformable contour model [1]

The position vector of a contour in a 2D image plane can be represented in a parametric form,

$$V(s) = (x(s), y(s)) \quad (1)$$

With the energy defined in its domain $s \in \Omega = [0, 1]$,

$$E(v) = \int_{\Omega} \frac{1}{2} (\alpha(s) |v_s(s)|^2 + \beta(s) |v_{ss}(s)|^2) + P(v(s)) ds \quad (2)$$

where the subscript s denotes the derivative and P is the potential associated to the external forces.

Adjusting the weights $\alpha(s)$ and $\beta(s)$ in Eqn (2) controls the smoothness of the contour (called the internal spline energy). The potential P is a function of the image data. If we want the snakes to be attracted to edge points, the potential should depend on the gradient of the images. Moreover, the potential P can be extended to include other forces according to the desired goals, for example, the balloon force of [2] to enforce the expansion of the contour and the geometry energy to prefer a certain contour shape.

The expected boundary in a 2D image can be obtained by minimizing the functional of Eqn (2) which is equivalent to solve its associated Euler-Lagrange equation:

$$-(\alpha v_s)_s + (\beta v_{ss})_{ss} - F(v) = 0 \quad (3)$$

With the given boundary conditions at $v(0)$, $v_s(0)$, $v(1)$ and $v_s(1)$, where $F(v) \equiv -\nabla P$. The finite difference approximation of Eqn(3) is

$$\frac{1}{h^2}[\alpha_i(v_i - v_{i-1}) - \alpha_{i+1}(v_{i+1} - v_i)] + \frac{1}{h^4}[\beta_{i-1}(v_{i-2} - 2v_{i-1} + v_i) - 2\beta_i(v_{i-1} - 2v_i + v_{i+1}) + \beta_{i+1}(v_{i+2} - 2v_{i+1} + v_i)] - F(v_i) = 0 \quad (4)$$

where h is the difference interval. Eqn(4) can be written as system of linear equations in x and y coordinates:

$$\begin{aligned} Ax &= F_x(x, y) \\ Ay &= F_y(x, y) \end{aligned} \quad (5) \quad \text{where } F_x \text{ and } F_y \text{ denote the } x \text{ and } y$$

components of F . After moving coefficients of the boundary conditions (approximated by the previous iteration) to the right hand side of Eqn (5), the matrix A will become to a symmetric pentadiagonal matrix with the coefficients:

$$\begin{aligned} \alpha_{i,i} &= \frac{1}{h^2}(\alpha_i + \alpha_{i+1}) + \frac{1}{h^4}(\beta_{i-1} + 4\beta_i + \beta_{i+1}) \\ \alpha_{i,i+1} &= -\frac{1}{h^2}\alpha_{i+1} - \frac{2}{h^4}(\beta_i + \beta_{i+1}) \\ \alpha_{i,i} &= \frac{1}{h^4}\beta_{i+1} \end{aligned} \quad (6)$$

The boundary condition of Eqn (6) is computed as the vector:

$$b(v^{(p)}) = [b_1, b_2, 0, \dots, b_{n-1}, b_n]^T \quad (7)$$

where b_1, b_2, b_{n-1} and b_n defined by

$$\begin{aligned} b_1 &= -\frac{\beta_n}{4}v_{n-1}^{(p)} + \left[\frac{\alpha_1}{h^2} + \frac{2}{h^4}(\beta_n + \beta_1)\right]v_n^{(p)} \\ b_2 &= -\frac{\beta_1}{4}v_n^{(p)} \\ b_{n-1} &= -\frac{\beta_n}{4}v_1^{(p)} \\ b_n &= -\frac{\beta_1}{4}v_2^{(p)} + \left[\frac{\alpha_1}{h^2} + \frac{2}{h^4}(\beta_n + 2\beta_1)\right]v_1^{(p)} \end{aligned}$$

and the variable $v^{(p)}$ denotes the position vector at the previous iteration.

B. Deformable boundary detection algorithm

Instead of solving Eqn (3) (or its matrix form (5)) directly, one can solve its associated evolution equation [1],

$$\frac{\partial v}{\partial t} - (\alpha v_s)_s + (\beta v_{ss})_{ss} - F(v) = 0 \quad (8)$$

with the initial condition $v(0, s) = v_0(s)$. We, therefore, have a semi-implicit formulation of Eqn(8),

$$(I + kA)v^t = v^{t-1} + kF(v^{t-1}) + kb(v^{t-1}) \quad (9)$$

where k is a time interval. A solution of the static problem (5) is achieved when the solution of Eqn (9) stabilizes,

which means the time derivative vanishes and we end up a static solution.

Eqn (9) is implicit in terms of the internal energy (determined by matrix A) but explicit in the external forces. Because $(I+kA)$ is a symmetric pentadiagonal matrix, we can use LDL^T decomposition [3] to solve Eqn (9). Moreover, this decomposition need be computed only once if the material coefficients α and β are constant through time.

The LDL^T decomposition used in this paper is more efficient than LU decomposition of [1] and [2] because we utilize the special structure of the symmetric pentadiagonal matrix A . Its total computational complexity is $10n-14$ multipliers and total storage is $3n-3$ where n is the dimension of the position vector x .

The external force $F(v)$ in Eqn (9) can be written as the sum of the image force and other forces as desired:

$$F(v) = -\nabla P(v) + F_{other} \quad (10)$$

where P is the potential defined by the magnitude of the gradient image, $P = -\|\nabla I(v)\|^2$. The curve is then attracted by the local minima of the potential, which means the local maxima of the gradient, i.e., edges. The image force in the 2D plane is, then

$$F(v) = [\|\nabla I\|_x^2, \|\nabla I\|_y^2] \quad (11)$$

where we ignore F_{other} temporarily.

There are many ways to approximate the image force of Eqn (10). In this paper, we consider a 1D edge detector as

$$G_r^{1d} = \frac{1}{3}[I(r+2) + I(r+1) + I(r) - I(r-1) - I(r-2) - I(r-3)] \quad (12)$$

where r could be the x or y direction, and $I(r)$ represents the gray-level value at distance r .

The image force calculated by the 1D edge detector (12) is

$$\begin{aligned} F_{i_0, j_0}^{1d} &= [\|\nabla I\|_x^2, \|\nabla I\|_y^2] \\ &= [G_x^{1d}(\|\nabla I\|_{i,j}^2; S_x^{1d}(i_0, j_0, i, j)), G_y^{1d}(\|\nabla I\|_{i,j}^2; S_y^{1d}(i_0, j_0, i, j))] \end{aligned} \quad (13)$$

where G_x^{1d} and G_y^{1d} denote the 1D edge operator in x and y directions based on the index sets

$$S_x^{1d}(i_0, j_0, i, j) = \{(i, j) \mid i_0 - 3 \leq i \leq i_0 + 2, j = j_0\}$$

$$S_y^{1d}(i_0, j_0, i, j) = \{(i, j) \mid j_0 - 3 \leq j \leq j_0 + 2, i = i_0\}$$

respectively. The gradient image of $\|\nabla I(v)\|^2$ at the point (i, j) can be computed by the same operator again,

$$\begin{aligned} \|\nabla I\|_{i,j}^2 = & [G_x^{1d}(\|\nabla I\|_{i,j}^2; S_x^{1d}(i, j, i', j'))]^2 \\ & + G_y^{1d}(\|\nabla I\|_{i,j}^2; S_y^{1d}(i, j, i', j'))]^2 \end{aligned} \quad (14)$$

To enforce the expansion or contraction of the deformable contour in the region of no significant changes in amplitude, one may add a unit pressure force $B(v)$ with the direction normal to the tangent of the contour, [2],

$$(B_x, B_y) = \left(\frac{dy}{\sqrt{dx^2 + dy^2}}, \frac{-dx}{\sqrt{dx^2 + dy^2}} \right) \quad (15)$$

We, therefore, write the external force (see Eqn (11) and Eqn (15)) as

$$F(v) = -\gamma_1 \frac{\nabla P(v)}{\|\nabla P\|} + \gamma_2 B(v) \quad (16)$$

where γ_1 and γ_2 denote the amplitude of the image and pressure forces because we normalize the external forces for the sake of stabilities.

The convergence of the detection algorithm can be defined by measuring the distance of two contours,

$$Error_i = \max[|v_x^i - v_x^{i-1}|, |v_y^i - v_y^{i-1}|] \quad (17)$$

where i denotes the iteration number. When $Error_i$ is less than a predefined tolerance, the detection stops and writes a 2D position vectors to the file.

A. Numerical analysis of the deformable contour algorithm

In this section, we will analyze the consistency, convergence and stability of the deformable contour model, i.e., Eqn (9). To simplify our analysis, we assume the material coefficients α_i, β_i in matrix A are constant. Rewrite Eqn (10) for constant α and β , we have:

$$\begin{aligned} \frac{1}{k}(v_{i,j} - v_{i,j-1}) - \frac{\alpha}{h^2}(v_{i+1,j} - 2v_{i,j} + v_{i-1,j}) + \frac{\beta}{h^2}(v_{i+2,j} \\ - 4v_{i+1,j} + 6v_{i,j} - 4v_{i-1,j} + v_{i-2,j}) - F_{i,j-1} - b_{i,j-1} = 0 \end{aligned} \quad (18)$$

The difference equation of (18) is said to be consistent with the partial differential equation of (8) if the local truncation error tends to zero as the mesh lengths of k and h tend to zero [4]. The truncation error represents the error of the difference equation due to the Taylor's expansion. In the following, we define

$$v \equiv v_{i,j}, \quad v' \equiv \frac{\partial v_{i,j}}{\partial s}$$

for notational convenience where s is the spatial variable of x and y . From Taylor's expansion about the point (ih, jk) we have

$$\begin{aligned} v_{i\pm 1,j} &= v \pm hv' + \frac{h^2}{2}v'' \pm \frac{h^3}{6}v''' + \frac{h^4}{24}v^{(iv)} \\ v_{i\pm 2,j} &= v \pm 2hv' + 2h^2v'' \pm \frac{4}{3}h^3v''' + \frac{2}{3}h^4v^{(iv)} \\ v_{i,j-1} &= v - k \frac{\partial v}{\partial t} + \frac{1}{2}k^2 \frac{\partial^2 v}{\partial t^2} \end{aligned} \quad (19)$$

where we only consider the expansion up to the fourth-order derivative. Applying the above Taylor's expansion to Eqn (18) we obtain the truncation error T :

$$\begin{aligned} T &= \left(\frac{\partial v}{\partial t} - \alpha v' + \beta v^{(iv)} - F \right) - \alpha \frac{h^2}{12} v^{(iv)} - \frac{k}{2} \frac{\partial^2 v}{\partial t^2} \\ &= \frac{h^2}{12} v^{(iv)} - \frac{k}{2} \frac{\partial^2 v}{\partial t^2} \end{aligned} \quad (20)$$

It is clear that the difference equation of (18) is consistent to the original partial differential equation of (8) if the mesh length k and h tend to zero. However, there are two difficulties in the real implementation: (1) the mesh length h is not constant for each point (i.e., not even-spaced) and (2) derivatives in Eqn (8) are continuous which is not meaningful for intermediate results between the mesh points in a 2D image plane. We will investigate these issues in the computer simulations.

Before we investigate the convergence of Eqn (8) we want to see the positiveness of the matrices $(I+kA)$ and A . A matrix A is positive definite if and only if its eigenvalues are positive. From Brauer's theorem [4], each eigenvalue of A lies inside or on the boundary of at least one of the circles $|\lambda(A) - a_{s,s}| = P_s$, where $\lambda(A)$ is the eigenvalue of A and denotes the sum of the absolute values of s -th row, $P_s = |a_{s,1}| + |a_{s,2}| + \dots + |a_{s,n}|$. For the matrix $(I+kA)$ of Eqn (9), $a_{s,s} = 2k\alpha_0 + 6k\beta_0 + 1$ and $\max P_s = 10k\beta_0 + 2k\alpha_0$ where we have defined $\alpha_0 = h^2\alpha$ and $\beta_0 = h^4\beta$. So Brauer's theorem leads to

$$1 - 4k\beta_0 \leq \lambda(I+kA) \leq 16k\beta_0 + 4k\alpha_0 + 1 \quad (21)$$

From Eqn (21), the matrix $(I+kA)$ is positive definite if we enforce $1 - 4k\beta_0 > 0$, or equivalently, $\beta < 1/(4h^4k)$. In general, we always use a small value of β which maintains a positive definite matrix $(I+kA)$ in Eqn (9). Similarly, for matrix A we have

$$-4\beta_0 \leq \lambda(A) \leq 16\beta_0 + 4\alpha_0 \quad (22)$$

from which we can not enforce a positive definite A because the material coefficient β is always positive.

To analyze the convergence we rewrite the system equation of (9) to

$$v^t = (I + kA)^{-1} v^{t-1} + k(I + kA)^{-1} (F(v^{t-1}) + b(v^{t-1})) \quad (23)$$

The eigenvalue of the matrix $(I + kA)^{-1}$ is just $1/(I + k\lambda(A))$. If we assume that F of Eqn (23) and all its high order derivatives are continuous and uniformly bounded in the image plane, Eqn (23) is convergent if and only if the eigenvalues of $(I + kA)^{-1}$ are bounded by one [5], which induces to a one-side inequality $I + k\lambda(A) > 1$, or equivalently, $\lambda(A) > 0$. However, from Eqn (22), $\lambda(A)$ could be negative.

Therefore, convergence of the system equations (23) is necessary other than sufficient. It means that for a system equation of (23) it may not converge to the solution from a given initial curve, or equivalently, not stable in the sense of the error propagations.

B. A fast numerical algorithm with controllable material coefficients

There are four parameters in contour development, the time interval k of Eqn (9), the material coefficients α , β of Eqn (6), the image force γ_1 and γ_2 pressure force of Eqn (16). We use constant $\alpha = \alpha_i h^2$ and $\beta = \beta_i h^4$ of Eqn (6) because we will maintain all the coefficients in the same order.

In general, we use larger γ_1 and γ_2 in the beginning to converge to the real contour quickly. The value of γ_2 should be smaller than γ_1 such that the detected edge points not pass through the real border. After few iterations we will lower γ_1 and γ_2 but increase the material coefficients α and β so that we have a smooth boundary. In this paper, we use parameter set:

$$\gamma_1 = 3, k = 1, \alpha = 0.2, \beta = 0.2, \gamma_2 = 1$$

for the first two iterations and

$$\gamma_1 = 1, k = 1, \alpha = 0.5, \beta = 0.5, \gamma_2 = 0$$

for the rest of the iterations. Because the image and pressure forces have been normalized, the above parameter set is robotic for different image files.

In section II we have proved the current deformable model is not stable in terms of the error propagation. We, therefore, should have a good initial set of boundary points from which the deformable model can connect and interpolate those edge points to form a smooth and close contour.



Fig. 1 Test result of the ultrasound left ventricular border

Fig.1 shows the results of the current deformable boundary detection algorithm where we used a sequence of cardiac images as the test set. These *in vivo* images haven been acquired from a digital ultrasound scanner made in our lab. Test results show that starting from a good enough initial contour (derived from our 1D border detection), the proposed deformable boundary detection algorithm can always converge to right final border.

III. CONCLUSIONS

In this paper, we applied a deformable contour model to detect the inner border of a 2D digitized left ventricular echo images. From the computational viewpoint we have presented:

1. an efficient system equations solver by using the LDL^T decomposition to the given pentadiagonal matrix;
2. a fast 1D edge detector to calculate the image force only in the neighborhood of the detected edge points;
3. numerical analysis of the consistency, convergence and stability of the current model from which we proved that the convergence is necessary but not sufficient.

To improve the performance of the current model, we may need to investigate the following issues:

1. separate the system equations to four parts in four regions of the image plane to increase the effect of the local external forces
2. improve the current 1D edge detector by adding more information from ultrasound physics

REFERENCES

1. Kass M, Witkin A, Terzopoulos D. (1987) Snakes: Active contour models, *Int. J. Comput. Vision*, 1, 321-331.
2. Cohen L.D. (1991) On active contour models and balloons, *CVGIP: Image Understanding*, Vol.53, 2, 211-218.

3. Golub G., Van Loan C.F. (1983) Matrix Computation, the Johns Hopkins University Press.
4. Smith G.D., Numerical Solution of Partial Differential Equations: Finite Difference Methods, Clarendon Press, second edition, Chapter 3, 1978
5. Isaacson E. and Keller H.B., Analysis of Numerical Methods, John Wiley & Sons, New York, Chapter 9, 1966

Author: Xiaoyan Liao, Dong C. Liu
Institute: School of Computer Science, Sichuan University
Street: The First Ring Road
City: Chengdu
Country: China
Email: liao_923@163.com

Noninvasive Temperature Estimation Using B-Scan Image For Thermal Therapy

Wei Li, Tao Kan, Xiangling Xiao, Jinghai Niu*

College of Life Sciences and Technology, Shanghai Jiao tong University
Shanghai, 200240, China

Abstract — Noninvasive temperature estimation is a key and tough problem in hyperthermia. Here, we design a novel experiment to demonstrate the relationship between B-mode ultrasonic image grey scale and tissue temperature. In our experiment, negative effect of pixel shift caused by temperature change is avoided successfully. Experiments with animal tissue (chick heart, pig muscle and pig liver in vitro), indicate the average grey scale (AGS) of ultrasonic images is correlated with the temperature. This gives a potential method to estimation temperature from B-mode ultrasonic imaging, which will be more convenient, safe and economical than other methods.

Keywords — Temperature estimation, Ultrasound image, Hyperthermia, Noninvasive

I. INTRODUCTION

Noninvasive temperature estimation continues to attract attention as a means of monitoring and guidance for minimally invasive thermotherapy. High-intensity focused ultrasound (HIFU) and minimally-invasive RF ablation are the most commonly used form of thermal therapy. Successful implementation of noninvasive temperature estimation will be a benefit for thermal therapy [1]. Currently, magnetic resonance imaging (MRI) and ultrasound have both been proven to have the temperature sensitivity and spatial resolution necessary to provide noninvasive temperature feedback [2]. The main limitation for MRI is the cost and the potential complication of the heating protocol as the heating equipment must be MR compatible [3]. Ultrasound is relatively less expensive, portable, and can be used in conjunction with almost any heating protocol without adding any significant constraints. Therefore, noninvasive temperature estimation based on ultrasound echo data continues to be an important problem in the area of image-guided minimally invasive thermal therapy [4-5].

II. METHODOLOGY

There are more ultrasonic parameters of the tissue, correlated with temperature, which affect the reflected signal, e.g. speed of signal, reflection coefficient, scattering, attenuation, etc. The B-mode ultrasonic image is affected by

variations in the ultrasonic reflection echo from the tissue. All these ultrasonic parameters of tissue that correlated with temperature take part on the construction of a B-mode ultrasonic image. Thus some parameters of the B-mode ultrasonic image of tissue are correlated with tissue temperature. When the tissue ultrasonic parameters change due to tissue temperature variations, the B-mode image parameters change along with the echo signal change accordingly.

The Ultrasonic reflection coefficient is defined by

$$r = \left(\frac{Z_{a2} - Z_{a1}}{Z_{a2} + Z_{a1}} \right) \quad (1)$$

where r is reflection coefficient, Z_{a1} and Z_{a2} is an acoustic impedance of medium 1 and 2 representing the acoustic transition in medium. The acoustic impedance is defined by

$$Z_a = \rho \times c \quad (2)$$

Both c and ρ are temperature dependent. Several experiments have confirmed that temperature correlation of ultrasonic speed is a monotonic function of temperature in soft tissues.

So, reflection coefficient is correlated with temperature, which will be presented in grey scale of ultrasound image.

Average gray scales are obtained based on computation of a mean intensity value in a local region; it can be shown as average intensity of reflection:

$$\bar{f}(x, y) = \frac{\sum_{0 \leq x \leq M} \sum_{0 \leq y \leq N} f(x, y)}{M \times N} \quad (3)$$

Where M is the interesting area's width, N is the height.

The correlation analysis is processed using the first set of experimental data. As shown in Table 1, when the tissue temperature changes, the B-scan ultrasonic image gray also changes. In particular, the average correlation coefficient of AOIs is $r=0.8760 \pm 0.0765$, indicating that there is stronger correlation between image gray and temperature. The dependency of the correlation curve is a linear function approximately (Fig.5). The average slope of the correlation 2 function is 1.5786 ± 0.5270 (with $R = 0.7690 \pm 0.0932$).

III. EXPERIMENT AND RESULT

To demonstrate above analysis, we design a novel experiment scheme, which can exclude the negative effect of image shift caused by ultrasound speed change, which is correlated with temperature change. In heating process, image pixel will have a tiny shift up or down, because the ultrasound changes with temperature. This will have negative effect to our analysis, because it is difficult to keep pace with this tiny shift, and resulting AOI (area of interest) includes different imaging pixel. This is different from work of (X.Y. Ren 2007)^[6].

In our experiment, See Fig. 1 and Fig. 2, we hang the sample in the water with very thin line, whose diameter is less than 0.1 mm, and its ultrasound reflection can be ne-

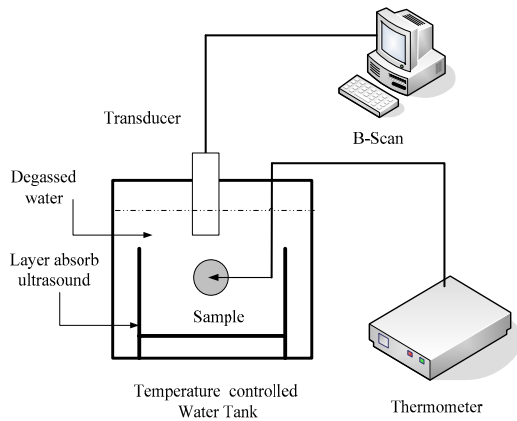


Fig.1 Experiment scheme



Fig.2 B-scan Ultrasound image with chicken heart

glect. We choose an AOI (area of interest), which surround the sample completely. No matter the image shift up or down, AOI contains image pixel all the time.

Water heating: The temperature range is starting at normal temperatures of the human body up to 45°C. The experimental system mainly consists of an electro-thermal water tank and a computerized B-mode ultrasonic diagnosis instrument. A block diagram was shown in Fig.1. The B-mode ultrasonic diagnosis instrument used in our experiment system is produced by Chinese Aerial Industrial Academe, and the B-mode ultrasonic images obtained from the instrument can be sampled and stored in diskette for analysis. The temperature fluctuation of the electro-thermal water tank (HH-W21-600C) is within 0.5°C. The mercury thermometer with a precision of 0.1°C is used to measure temperature in the water tank.

In order to eliminate the negative affection of pixel shift caused by temperature change, we should correct the AOI's position by image matching, so that the AOI of ultrasound image can be the same area during the water heating all the time. The result will be showed in Fig.3. The upper figure is the continuous AOI ultrasound images of chicken heart, which are saved with risen temperature during the equably water heating. The pixel shift caused by temperature change can be obviously found. The nether figure is the continuous AOI ultrasound images of chicken heart after image matching. The negative pixel shift is effectively avoided.

Pig muscle, pig liver and chicken heart are heated in our experiment. Fig.4 gives Pig muscle in vitro dependence curves of the Average Grey Scale with temperature. When the temperature rises from 26°C to 50°C, the Average Grey Scale of AOI rises from 53.1 to 71.2.

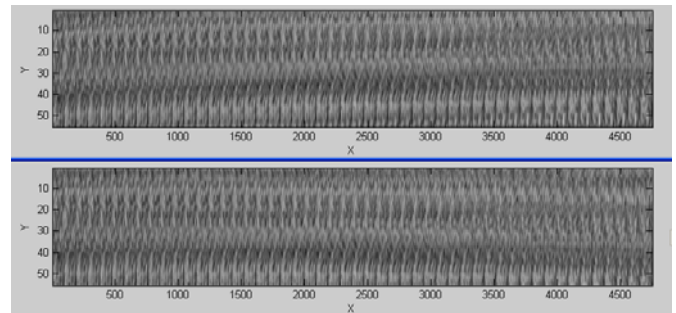


Fig.3 the continuous ultrasound images before and after image matching.

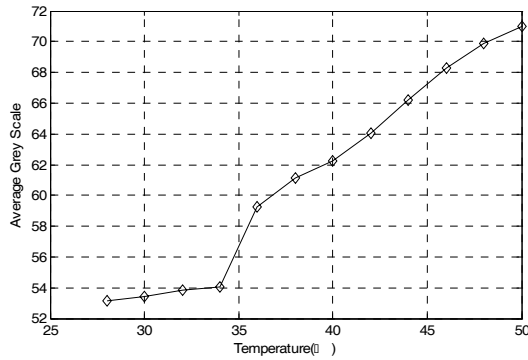


Fig.4 Pig muscle dependence of AGS with temperature

Fig.5 gives Pig liver in vitro dependence curves of the Average Grey Scale with temperature. When the temperature rises from 26°C to 50°C, the Average Grey Scale of AOI rises from 48.8 to 50.8.

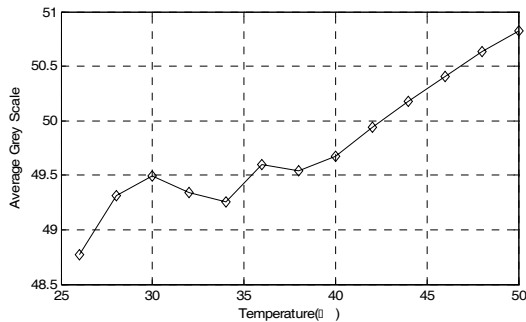


Fig.5 Pig liver dependence of AGS With temperature

Fig.6 gives chick heart in vitro dependence curves of the Average Grey Scale with temperature. When the temperature rises from 22°C to 58°C, the Average Grey Scale of AOI rises from 55 to 67.5.

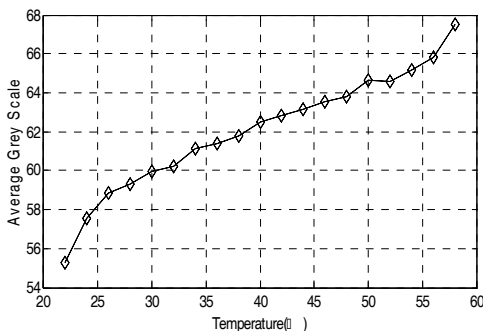


Fig.6 Chick Heart dependence of AGS With temperature

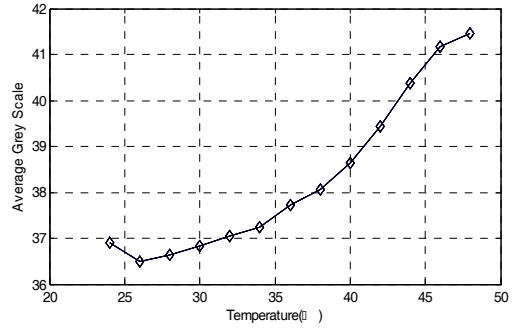


Fig.7 Chicken Heart with membrane tissue dependence of AGS with temperature

Fig.7 gives another experiment result of chick heart with membrane tissue in vitro dependence curves of the Average Grey Scale with temperature. When the temperature rises from 24°C to 48°C, the Average Grey Scale raises from 36.9 to 41.2.

It can be found that the AGS is almost linearly changed with temperature, the correlation coefficient of AGS and temperature is shown in Table 1 after more than ten experiments with each tissue sample.

So if we can find the correlation coefficient of different tissue in advance, the temperature will be calculated by the average grey scale change.

Table 1 Correlation coefficient of AGS and temperature

Tissue sample	Correlation coefficient
Pig muscle	0.752
Pig liver	0.833
Chicken heart	0.347
Chicken heart with membrane	0.179

IV. DISCUSSION

We have repeated about ten experiments; all of them have the same result. We conclude them as follow:

- 1) Average Grey Scale of Sample tissue has correlation with tissue temperature;
- 2) Average Grey scales of sample tissue increase, when temperature is arise. This result is suit for pig muscle, pig liver and chicken heart; tissue with rich fat is not confirmed;
- 3) Grads of Average Grey Scale with temperature are different in different samples, the correlation coefficient can be obtained in advance;
- 4) This result will give a potential method to estimate temperature in hypermeter.

REFERENCES

1. Seip R, Tavakkoli J, Carlson RF, et al. High-intensity focused ultrasound (HIFU) multiple lesion imaging: comparison of detection algorithms for real-time treatment control. 2002 IEEE Ultrasonics Symposium, 2002, 2:1427-1430
2. NIU Jinhai ZHANG Hongxuan WANG Hongzhang et al, Noninvasive temperature estimation in biotissue as a discrete random medium based on backscattered average ultrasonic power, ACTA ACUSTICA Vol. 26, No.3 May, 2001 page:247-251
3. Goldhaber DM, Deli M, Mineyev MI, et al. Measurement of tissue temperature by MRI. 1993 IEEE Nuclear Science Symposium and Medical Imaging Conference, 1993, 3: 1702-1705
4. NAOMI R. MILLER,* JEFFREY C. BAMBER and GAIL R. TER HAAR, IMAGING OF TEMPERATURE-INDUCED ECHO STRAIN: PRELIMINARY IN VITRO STUDY TO ASSESS FEASIBILITY FOR GUIDING FOCUSED ULTRASOUND SURGERY, *Ultrasound in Med. & Biol.*, Vol. 30, No. 3, pp. 345-356, 2004
5. Arthur RM, Straube WL, Starman JD, et al. Noninvasive temperature estimation based on the energy of backscattered ultrasound. *Medical Physics*, 2003, 30(6):1021-1029
6. X.Y. Ren, S.C. Wu, Y. Zeng, Noninvasive Estimation of Hyperthermia Based on B-mode Ultrasonic Tissue Characterization, 2007 IEEE/ICME International Conference on Complex Medical Engineering, p635-639

*Correspondence address: jhniu@sjtu.edu.cn

Author Wei Li
Institute College of Life Sciences and Technology,
Shanghai Jiao tong University
Street 800 Dong chuan Road, Min Hang, Shanghai
City Shanghai
Country China
Email liwei06@sjtu.edu.cn

The design of noninvasive temperature measure system and software

Kan Tao¹, Wei Li², Xianglin Xiao¹ and Jinghai Niu¹

¹ Department of Bio-medical Engineer In SJTU, Master, Shanghai, China

² Department of Bio-medical Engineer In SJTU, Master, Shanghai, China

Abstract — Ultrasound temperature measurement is one of the research emphases on noninvasive temperature measurement nowadays. This article introduces some methods about ultrasonic temperature measurement, especially focuses on B-mode ultrasound Image method. And the ultrasound noninvasive temperature measurement system with its software system. Besides, we discuss and analyze some results of the experiment.

Keywords — noninvasive temperature measure; B-mode ultrasound Image; system design; gray; area of interest

I. INTRODUCTION

The accurate measure of a temperature distribute in deep human body is one of the fields that has the most the clinical medical science meaning and the most challenge in biology hyperthermia physics therapy fields^[1]. At present, we really need to achieve the noninvasive temperature measure in human body in many aspects of medical treatment domains, such as WBPH (Whole Body Perfusion Hyperthermia), HIFU^[5-8] (High Intensity Focused Ultrasound), UTCTT^[9-10] (Ultra-low Temperature Cold Therapy of Tumor), and so on. These methods are used in common: EIT temperature measure, MW temperature measure, MRI temperature measure, X-CT temperature measure and Ultrasound temperature measurement, they can avoid the disadvantages that exist in invasive temperature measure.

II. NONINVASIVE TEMPERATURE MEASURE BASES ON ULTRASOUND

A. The advantage of ultrasound temperature measurement

Ultrasound temperature measurement uses ultrasound to scan the tissue in hyperthermia, based on the model of velocity of sound, non-linearity parameter, echo time-move characteristic, echo frequency-move characteristic, scatter energy, we can analyze ultrasound signal, pick up the information of temperature of tissue. It's more effective than other methods. Ultrasound has the advantage in real time speciality compares with MRI and X-CT, it's cheaper and can easily be popularized.

B. The methods of ultrasound temperature measurement

In 1989 He P and in 1986 Sehgal CM tried to get the information of tissue through researching the ultrasound attenuation coefficient and non-linearity parameter of tissue, but there is too much jam in the first, and the 2ed has weakly signal. These technique can hardly be used in clinic. In China, Wang Hongzhang in SJTU successfully developed some methods: (1) penetrate ultrasound ferry time^[15], (2) numerical figure out the equation of heat exchange in tissue^[16], (3)ultrasound CT^[17], (4) module of delamination medium measure temperature, and so on.

III. ABOUT THE SYSTEM

This picture shows the basic frame of the system. As we can see, the hardware of the system contains 4 parts: digital B-mode ultrasound, image grab card, temperature grab card and the PC. All the data submit to the software, and the get the result. The flow: 1st, heat up the experiment object (at this phase we used constant temperature water domain and simulate focused, aftertime we will use ultrasonic knife), at the same time, the B-mode monitor the object, and the image grab card grab the image in real-time, the image can show in the PC, we deal with it with arithmetic, the module of thermocouple collects temperature in real-time, and then show it in the intherface of software.

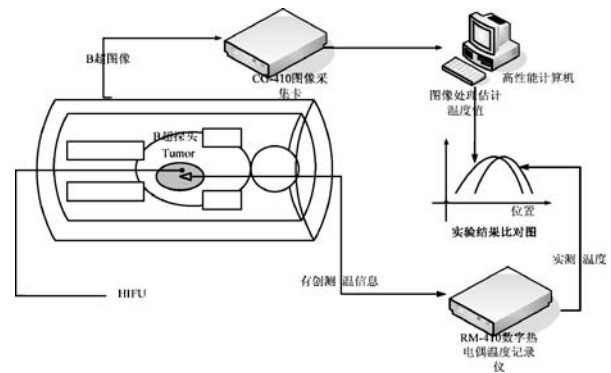


Fig.1

I. NONINVASIVE TEMPERATURE MEASUREMENT SOFTWARE SYSTEM BASE ON B-MODE ULTRASOUND

A. Function Introduction

Fig.3 shows the working of this software system. The whole frame consists of five parts: the top halves contain two modules and bottom half three modules. Each module has respectively clear work, which make up of a integrate software system with all aspects of data and real-time processing function.

Left top half module: Real-time display of the B-mode ultrasound image in computer

Right top half module: real-time display in the reference frame of the temperatures sampled by each thermocouple. The curves reflect the rules and the data show the detail values.

Left bottom half module: saving the B-mode ultrasound real-time images in the computer. The row of buttons in left top part control the starting and ending of system processing programmed.

Middle bottom module: computer the average gray of area and whole image and show the change.

The pop-up window: design the area of interest and divide it into several right small blocks for image processing. As the Fig.3, we customize the start coordinate position and the cut size, and then this area is divided into some small one with the area of 10×6 .

Right bottom half module: amply the area, which customized by the pop-up window by 3×3 times, as the Fig.4.

Other function: this software system not only real time process B-mode ultrasound image, also can selectively save them in the computer for the later experiment analyze.

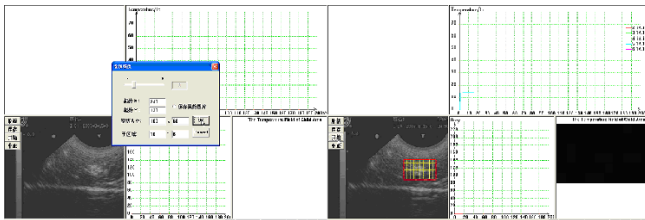


Fig.3 software frame one

Fig.4 software frame two

B. Method of processing the area of interest

During the experiment we cut an area of interest and divide it into several right small blocks. Meanwhile, the gray change of B-mode ultrasound image will be shown in different color in the right bottom module. We set the first image gray as the background of black and use the administrative levels red to show the gray change, which means that

the greater the gray changes, the deeper the red color of the block becomes.

C. Software realization of image processing

The image will bring some rules, which the origin image doesn't have after processing. The basic image processing technology provided by this software can be applied to B-mode ultrasound images and also some other possible methods for the trouble of processing origin image. Provided image processing software have realized:

Filter: average filter, Laplace filter etc.

Gray Algorithm: gray average, average histogram etc.

Others: Negative image, boundary monitor etc.

IV. EXPERIMENT DESIGN, PROCESS AND RESULT

A. Experiment designs and processes

First kind of experiment designs: constant temperature water domain

Experiment materials and equipment: besides the whole system which have been introduced above, there include one container, two pieces of rubber, one heater, several thermocouples, one shelf used to support and fix the B-mode ultrasound transducer, and one piece of pork with proper volume.

First, put some water of proper volume to the container. Because of the particularity of the B-mode ultrasound experiment, we should pay enough attention to the first step to reduce the content of air in the water, which can reduce the sound field noise and improve the accuracy of the experiment. The rubber, which is a sound absorption material, is also used for the same purpose, and it should be put into the container before putting the water.

Then, wash and clean the pork, and insert the pinheads of thermocouples to the pork. The needles must be at the same vertical plane, and keep consistent with the B-mode ultrasound transducer. So we can get accurate data, and reach effect conclusion through the analyze of the B-mode ultrasound images.

The fixation of the B-mode ultrasound transducer is also very important. We do our best to get better experiment results, but the noise still cannot be avoided because of the limits of our equipment. First, try to find out an angle, which can make the noise at the least, so we can get the clearest B-mode ultrasound images. As mentioned above, we also need to keep the thermocouples at the same plane.

Last, adjust the parameters of the B-mode ultrasound transducer, such as the frequency, the number of the focus points, the position of the focus points, and the measure

range of the transducer. Debug the software, set the parameters and define the frequency of saving images and temperatures, in order to get the best images.

Remaining works include recording experiment data, the parameters of the transducer, the size of the pork, and the distribution of the heater and thermocouples, and these are used for data management lately. During the experiment, we should pay attention to keeping consistency of the surroundings, and the position of the head of the transducer and the pork should not be changed, otherwise the images recorded are not consistent, and will make no sense.

Second kind of experiment designs: simulate focused

This design of experiment can analyze the impact of temperature on the gray grade of the experiment sample qualitatively to get better result.

Experiment materials and equipment: besides the things mentioned in the first kind of experiment, there include one rubber tube and one injector.

Experiment theory: make the rubber tube through the pork, and keep the head of the transducer vertical to the rubber tube, thus in the B-mode ultrasound image the rubber tube looks like a point. When filling the tube with hot water, it appears like one point heating, and this can simulate the situation of HIFU therapy more actually.

Experiment design: make the rubber tube through the pork, fill water into the tube with injector uninterruptedly, and observe the change of the image gray grade which is brought by the increase of the temperature.

Experiment purpose: try to prove that the temperature increase in some part of the pork induce by the filling of hot water can really lead the change of gray grade in the B-mode images, and affirm that the change of gray grade are really caused by the change of the temperature.

Experiment process: fix the head of the B-mode ultrasound transducer and the pork, affirm that the rubber tube are in the center of the B-mode ultrasound image; select interested area of appropriate size, divide it into some sub areas with reasonable number of sub areas; first fill cold water, observe if there is any change of gray grade in the area of image, in order to eliminate the effect of the non-temperature factors affecting gray grade change; fill water with the temperature of 70°C , observe the change of gray grade in the area, and record the magnitude of the change.

B. Parts of experiment results

First experiment design results

Fig.5 shows the change of gray grade in one experiment. The x-axis is temperature, the y-axis is gray grade and the

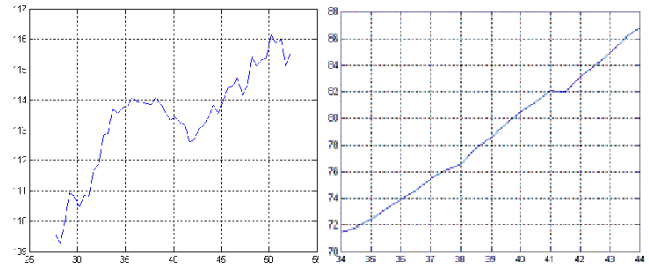


Fig.5

Fig.6

Fig.6 shows the change of gray grade in one experiment. The x-axis is temperature, the y-axis is gray grade and the experiment material is pork. The figure illustrates the change of gray grade in the process of temperature increase.

experiment material is liver of pig. The figure illustrates the change of gray grade in the process of temperature increase.

By observing the result of above two experiments, the gray grade of the B-mode ultrasound image obviously changes along with the temperature increase, and in addition, the slope is steady except for very few points with mutation.

Second experiment design result

The temperature of the surrounding is 12.000°C , and the temperature of the water is a litter higher. During this experiment, in the area near the rubber tube and with direction, which is vertical to the image, we insert 4 needles of thermocouples every 0.5CM paralleled. All the needles are in the interested area, which we define, from left to right the serial number of the needles are two, three, four, and five. In the right and up part of the figure, we have a module to watch the change of temperature in real time. We divide this area to 10×6 sub areas, and the position of the rubber tube is at the 4th grid of x-axis, and the 2.5th grids of y-axis in the interested area. The y-axis of the four needles is the same to the rubber tube, and the x-axis is: the number two needle in the 2nd grid, number 3 in the 4th grid, and so on.

The four figures above are the qualitative result of the second experiment, and the experiment material is pork. We can get the conclusion from fig.7 and fig.8 that when the condition doesn't change, or when fill the tube with water, which has the same temperature to the pork, the gray grade of the image has no obvious change. The temperatures of the four needles of thermocouples are consistent and steady. Our experiment model and condition are steady and credible.

When we fill hot water into the rubber tube, the color of the right interested area change obviously, and the change in

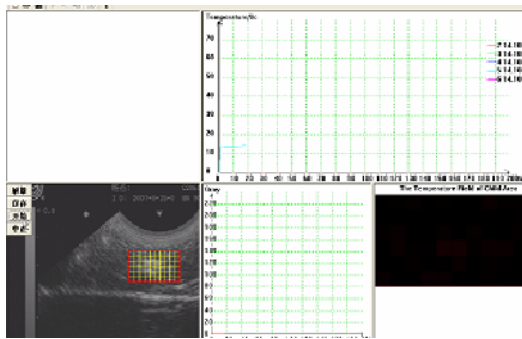


Fig.7 Condition with no change

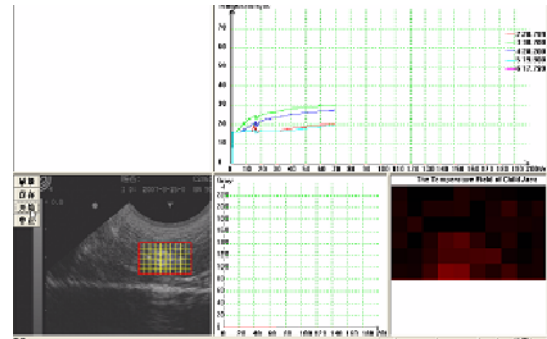


Fig.9 Filling hot water (1)

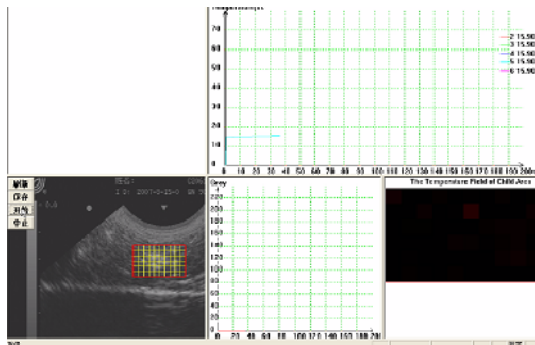


Fig.8 Filling cold water

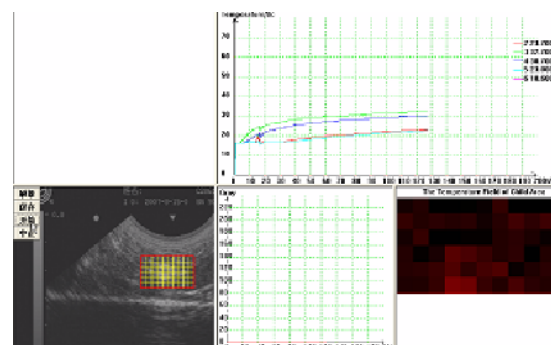


Fig.10 Filling hot water (2)

the position of the number three needle is especially obvious. Fig.9 and fig.10 have some difference, and at this time we can observe the temperature of needles and the curve of the temperature changes. In the fig.9, the temperatures of the four needles are: number two 20.799°C; number three 30.700°C; number four 28.200°C; number five 19.900°C. When compare the degrees of the change in the interested area and the positions of the tube and the needles, we can find that the gray grade changes in specific position are accord with our expectation. Experiment progress, and fig.10 shows: number two 23.799°C; number three 32.700°C; number four 30.700°C; number five 23.000°C. The temperatures are increasing, and then compare fig.9 and fig.10, we can find the degree of the color change grows on and the region of change extends. The change near the number three needle is the most obvious, and this is corresponding well to the temperature of the needle.

Experiment limitation: because of limit of the hot water temperature and experiment conditions, the final temperature can only stay at about 35.000°C.

V. CONCLUSION AND PROSPECT

Through abundance analyzes of experiment and therapy, we deem that the change of gray grade can reflect the temperature change in a certain extent. Especially in the second experiment design, when the change of the temperature are not great, but it can also make the change of the interested area obvious. Following, we will focus on inspecting mutations of biology tissues. After getting the new focus equipment, we will do a lot of experiment to achieve our goal—find the point of the biology tissue mutation effectively.

REFERENCES

1. Wang cuncheng, Chenhuaqing. Biomedical Medium Of Thermophysical Exploration . Beijing ; Society Press, 1994
2. Lin shiyin, Liruiying. Modern hyperthermic oncology: Principles, Methods and Clinics. Beijing: Academy Press, 1996
3. Zhangdongxu, Zhouzhaoying, Zhujunhua. Design of the Whole-Body Perfusion Hyperthermia System. Chinese Journal of Medical Instrumentation. 2003,27(6): 410-413
4. Vertrees RA, Tao W, Pencil SD, et al. Induction of whole body hyperthermia with venovenous perfusion. ASAIO Journal, 1996,42(4): 250-254

5. Lifaqi, Wangzhibiao, Duyonghong. INVESTIGATION ON TEMPERATURE FIELD OF BIOLOGICAL FOCAL REGION INDUCED BY HIGH INTENSISTY FOCUSED ULTRASOUND. Chinese Journal of Biomedical Engineering,2003,22(4) : 321-325
6. VanBaren P, Ebbini ES. Multipoint temperature control during hyperthermia : Theory and Simulation. 1995 IEEE Transactions on Bio-medical Engineering, 1995,42(8) : 818-827
7. Kaczkowski PJ, Keilman GW, Cunitz BW,etc al. High Intensive Focused Ultrasound (HIFU) array system for Image-guided ablative therapy (IGAT). 2003 Proceedings of SPIE – The International Society for Optical Engineering, 2003,4954:209-219
8. Seip R, Tavakkoli J, Carson RF, et al. High-Intensity focused ultrasound (HIFU) multiple lesion imaging; Comparison of detection algorithms for real-time treatment control. 2002 IEEE Ultrasonics Symposium, 2002,2:1427-1430
9. Hesheng,Wanghongwu,Zhangyunshan,etc. Ultrasonography Guiding Cryotherapy Using an Argon-Helium Based System for the Tumors. Chinese Journal of Medical Imaging Technology .2003,19(2); 216-218
10. [Qianguojun,Chenhan,Wushengpei,etc. percutaneous argon-helium cryoablation hepatoma 56 case clinical analysis of percutaneous puncture argon-helium cryoablation hepatocellular carcinoma 56 example clinical analysis . Journal of Abdominal Surgery,2003, 16(1) : 16-18
11. Xuhaidong,Zhouzhaoying,zhangdongxu. noninvasive temperature measure. Chinese Medical Equipment Journal. 2002; 2:25
12. Wang Hongzhang, Wu Xiangyu. Noninvasive monitoring of temperature in hyperthermia for cancer therapy.Proc.of IEEE, 9-th EMBS (Boston), 1987 : 1648
13. Wanghongzhang, Ding ying, Fan hua. A Modeling Study of the Temperature Field Induced by Ultrasonic Heating for Cancer Therapy. Journal of Shanghai Jiaotong University, 1995 ; 29(2) : 119
14. Yangyihong, Wanghongzhang. Ultrasound CT method noninvasive temperature measure. Journal of Shanghai Jiaotong University, 1993; 27(6): 39
15. Passechnik VI, Anosov AA, Isrefilov MG. Experimental reconstruction of temperature distribution at a depth through thermal acoustic radiation. Ultrasonics, 1999; 37 : 63

Author: Kan Tao
 Institute: Department of Bio-medical engineer. SJTU
 Street: 800.Dongchuang Road
 City: Shanghai
 Country: China
 Email: taokan_06@sjtu.edu.cn

Doppler US Nutrient Artery Waveform Change in Assessment of Non-pregnant Uterus Response to Oxytocin

Li-qun Sun, Jian-zhong Zou, Wen-zhi Chen, Zhi-biao Wang

Department of Biomedical Engineering
Institute of Ultrasound Engineering in Medicine
Chongqing Medical University, Chongqing, China

Abstract — Objective. Using Doppler Ultrasound to observe nutrient artery waveform change in uterine fibroids and focal adenomyosis before and after oxytocin, thereby assessing the response of non-pregnant uterus to oxytocin. **Methods.** 30 patients (mean age 39.77 ± 4.34 years) with uterine fibroids and 15 patients (mean age 36.27 ± 4.54 years) with focal adenomyosis were observed when ready for HIFU ablation. The nutrient artery waveform with Doppler US was observed for 30 minutes and compared before and after intravenous oxytocin (0.04u/min). **Results.** After oxytocin, abnormal waveforms were seen in 24 uterine fibroids patients (80%), as well as in 10 focal adenomyosis patients (66.7%), including monophasic-wedged, monophasic-domed, biphasic-wedged, or tropical fish. The difference was not statistically significant between uterine fibroids and focal adenomyosis ($p > 0.05$). Waveform change could be categorized into two types, i.e., bizarre waveform which included persistent change (19/30, 6/10) and alternative change (5/30, 4/10), and normal waveform which included velocity change (6/30, 5/15) and no change (0/30, 0/15). There was no significant difference in the waveform change between subserosal fibroids and intramural fibroids ($p > 0.05$). We did not observe any waveform change in uterine arcuate artery and bilateral uterine artery. **Conclusions.** Doppler US waveform change of uterine nutrient artery was useful in evaluating the response to oxytocin in non-pregnant uterus. Oxytocin could cause myometrium contraction, resulting in nutrient artery stenosis or spasm. There was no significant difference in the waveform change between subserosal fibroids and intramural fibroids, or between fibroids and focal adenomyosis, however, uterus responded quite individually to oxytocin.

Keywords — Doppler US; waveform; oxytocin; non-pregnant uterus

I. INTRODUCTION

Oxytocin, which is mainly used for labor and the prevention of postpartum hemorrhage^[1], can directly contract pregnant uterine myometrium, and the strength of contraction depends on the oxytocin dose and the physiological state of uterus. Oxytocin receptors are not only in the pregnant uterus but also in the extracorporeally-perfused non-pregnant isolated uterus^[2, 3]. Currently, oxytocin is generally used during myomectomy to reduce intraoperative hemostasis^[4,5].

Color Doppler ultrasonography (US) can demonstrate blood perfusion of uterine fibroids and focal adenomyosis, and reflect vascular hemodynamic information^[6]. To our knowledge, however, no study has been performed to assess the response of non-pregnant uterus to oxytocin by the means of uterine nutrient artery waveform change observed with Doppler US. Thus, the purpose of our study was to prospectively evaluate the reaction of non-pregnant uterus to oxytocin, through Doppler US waveform change before and after oxytocin in uterine fibroids and focal adenomyosis, and to further confirm that oxytocin has a crucial role on non-pregnant uterus.

II. MATERIALS AND METHODS

A. Materials

The subjects of our study were all ready for HIFU ablation at the First Affiliated Hospital of Chongqing Medical University. Related clinical examination and enhanced MRI examination were performed in all patients to confirm uterine fibroids or focal adenomyosis. Among all the cases, 30 patients (mean age 39.77 ± 4.34 years) were confirmed with single intramural fibroids, and 15 patients (mean age 36.27 ± 4.54 years) with focal adenomyosis. 3-7 days after the patients' menstrual periods, Doppler US was used to examine the uterine nutrient artery of uterine fibroids and focal adenomyosis in all the 45 eligible candidates of HIFU ablation. All subjects underwent US examination in the next morning after related preparations, such as overnight fasting, bladder filling 300ml with inverted indwelling urinary catheterization.

B. Methods

Before oxytocin administration, US was used to define the focus of the uterine fibroids or that of the focal adenomyosis. The nutrient artery was depicted by color Doppler energy imaging along transverse section of the defined foci, and then we acquired waveforms of the nutrient artery. The 3.5-MHz abdomen convex probe (HD3; PHILIPS, Ger-

many) was used. Doppler frequency was 2.8KHz, sampling volume 2 to 3 mm, acoustic beam angle with the blood flow was less than 60 °. Oxytocin 40u (Shanghai HEFENG Pharmaceutical Ltd; 10 u/ml) was added into 5% glucose solution 500ml, and the prepared oxytocin solution was injected persistently (about 0.04 u/min) via veins.

Immediately after oxytocin administration, the same method was used to observe waveform change of myometrium artery, fibroids peripheral and internal artery, and focal adenomyosis internal artery. We recorded the spectrum waveform change. waveform of all the patients was observed by the same ultrasound diagnostician (Li-qun Sun, with 6 years of experience with color Doppler US) . The observation lasted for 30 minutes after intravenous oxytocin administration. Waveform (monophasic-wedged, monophasic-domed, biphasic-wedged, or tropical fish)classification was based on the waveform amplitude and waveform dispersion in the cardiac cycle.

The results were expressed as mean±standard deviation. Statistical analysis was performed using χ^2 test for comparisons between measurements. Statistical significance was considered for $P < 0.05$.

III. RESULTS

Before administration, the waveforms of fibroids myometrium artery, fibroids peripheral and internal artery were similar to those of the normal myometrium artery. Peripheral and internal systolic flow velocity of fibroids was slightly lower than that of the normal myometrium, and diastolic notch disappeared or became fuzzy. Internal artery of adenomyosis showed peak systolic waveform, with clear diastolic notch (Figure 1).

After oxytocin, abnormal waveforms were seen in 24 uterine fibroids patients(80%), as well as in 10 focal adenomyosis patients(66.7%), including monophasic-wedged, monophasic-domed, biphasic-wedged, and tropical fish. Monophasic-wedged waveform refers to such waveforms as there is only a single one-way wave which was shaped like a wedge and the systolic and diastolic haziness can be seen in the entire cardiac cycle; Monophasic-domed waveform means there is only a single one-way dome-shaped wave and systolic and diastolic haziness can be seen in the entire cardiac cycle; Biphasic-wedged waveform refers to such waveforms as the wave is two-way, shaped like a wedge, and the systolic wave is upward and diastolic wave is downward, or vice versa, and waveform patterns can be either same or different; Tropical fish waveform is defined as such a waveform as there is a biphasic wave on both sides of the baseline, making the wave shape resemble tropical fish (Figure 2). The difference was no statistically

significant between uterine fibroids and focal adenomyosis ($p > 0.05$).

After oxytocin, the waveform change first appeared in the uterine radiate artery, and then in the periphery and internal artery of fibroids (in patients with uterine fibroids), or in the internal artery of focal adenomyosis (in patients with focal adenomyosis). Waveform change could be categorized into two types, i.e., bizarre waveform type which included persistent change (19/30,6/10) and alternative change (5/30,4/10), and normal waveform type which included velocity change (6/30,5/15) and no change (0/30,0/15). In bizarre waveform group, the persistent change means the waveform pattern is changed after oxytocin administration but afterwards it remains unchanged in the course of observation, while the alternative change means that the waveform pattern before oxytocin alternatives with that after oxytocin. In normal waveform group, velocity change means the systolic and diastolic waveform shapes are normal, but the change in flow rate are high or low. The difference was no statistically significant between uterine fibroids and focal adenomyosis ($p > 0.05$). (Figure 3 & Table 1). There were no waveform change in uterine arcuate artery and bilateral uterine artery during the observation time (30 minutes).

After oxytocin, different formwave change appeared in the periphery and internal artery of different types of uterine fibroids (subserosal, intramural, submucous, cervical fibroids) , including persistent change (5/7,14/20,1/2,0/1), alternative change (1/7,4/20,0/2,0/0) in the bizarre waveform, velocity change (1/7,2/20,1/2,0/0) in the normal waveform. There is no significant difference in the waveform change between subserosal fibroids and intramural fibroids ($p > 0.05$) (Table2).

In some of the lesions, the internal flow pattern height gradually reduced, and moreover, the artery waveform was not able to be detected, that is to say, the perfusion gradually reduced and even disappeared.

IV. DISCUSSION AND CONCLUSIONS

Oxytocin is the main hormone of the posterior lobe of pituitary. By the high affinity of oxytocin receptor mediated, it enters through the capillary blood circulation, reaches target organs, and has an effect^[7,8]. Whether the patients are pregnant or not, their myometrium, ovarian and endometrium may contain oxytocin receptor, but less content was in the ovary^[9,10,11]. Myometrium contraction of the human non-pregnant uterus is assumed to be receptor-mediated via the oxytocin receptor which can be modulated by steroid hormones and oxytocin respectively. Its sensitiv-

ity depends on the uterine oxytocin receptor density and the level of estrogen^[12,13,14].

Currently, many animal experiments and clinical research have been performed in examining the effects of oxytocin on pregnant uterus. However, for non-pregnant uterus, the research is mainly focused on oxytocin receptor expression as well as in vitro human intrauterine pressure change by extracorporeal perfusion test^[15,16,17,18]. Oxytocin receptors and gene expression in uterine fibroids are higher than in normal myometrium^[19]. Oxytocin receptor is highly expressed in myometrium, significantly expressed in the stroma epithelia in advanced proliferation stage or during ovulation, not expressed in endometrium stromal cells, and positively expressed in uterine fibroids (including cellular fibroids)^[20]. It has also been reported that endometriosis epithelial cells demonstrate higher oxytocin receptor expression while in the stromal cells the expression is negative. Oxytocin receptors in smooth muscle cells, endometrium of adenomyosis and ovarian cyst epithelial cells are expressed^[21].

By using Doppler to observe the artery waveform after oxytocin application, this study found that the artery waveform of myometrium, peripheral and internal fibroids, internal nutrient artery of adenomyosis were changed, which confirms the effects of oxytocin on the non-pregnant uterus. We found that there was no significant difference between uterine fibroids and adenomyosis in their response to oxytocin. Furthermore, it has been found that all the different types of fibroids could respond to oxytocin, indicating that the myometrium contraction effect of oxytocin on the uterus myoma is not closely related to the location of the myoma. At the same time, the bizarre waveform of different types of artery have been observed, which are different from the shapes of its normal artery waveforms. Different waveform patterns can reflect the greatest Doppler shift or the vascular maximum velocity as a function of time. In the case of vasospasm and vascular stenosis, a one-way waveform may be recorded, which shows an increased flow in the peak systolic velocity and a reduced flow in the end-diastolic velocity. Furthermore, in some cases, the peak waveform became dome-shaped, and diastolic reverse flow was detected. Biphasic-wedged waveform refers to high systolic blood flow and low diastolic reverse flow. Tropical fish waveform may be caused by two-way mirror artifacts. Emerson DS has reported that an one-way, two-way, such as the tropical fishes and the special-shaped peak dome-like spectrum have been found in trophoblast vascular ectopic pregnancy, which is of decisive significance in their diagnosis of ectopic pregnancy^[22]. Implanting the fertilized eggs into the myometrium will enable some forms of vascular wall limitations protruding through false similar small haemangioma. Therefore, when placing the sample volume at the entrance,

the spectrum of different types of two-way (To-and-fro Pattern)^[23] can be recorded.

The emergence of different types of waveforms may possibly be attributed for by myometrium contraction and mechanical compression on the vascular muscle fibers which causes deformation, stenosis, spasm and even occlusion of the blood vessel. In this study, the researchers have observed different waveform change after administration of the same dose of oxytocin. This phenomenon may be related with the strength of uterine muscle contraction, because the estrogen levels and the oxytocin receptor density in different individuals are different. The continuous strong contraction could lead to a significant decreased perfusion in the uterine fibroids and focal adenomyosis, and even the disappearance of the internal blood supply in uterine fibroids and focal adenomyosis, which is of important clinical significance. The oxytocin-induced waveform change may be used to identify uterine fibroids and endometrial stromal sarcoma, which needs further study. At the same time, the hemodynamics change of the nutrient artery after oxytocin application have yet to be further explored.

REFERENCES

1. Gerald Gimpl and Falk Fahrenholz. The Oxytocin Receptor System: Structure, Function, and Regulation. *Physiol. Rev* 2001; 81:629-683.
2. Bulletti C, Prefetto RA, Bazzocchi G et al. Electromechanical activities of human uteri during extra-corporeal perfusion with ovarian steroids. *Hum Reprod* 1993; 8:1558-1563.
3. Richter O, Wardelmann E, Schneider C, et al. Extracorporeal perfusion of the human uterus as an experimental model in gynaecology and reproductive medicine. *Hum Reprod* 2000; 15:1235-1240.
4. Wang CJ, Lee CL, Yuen LT, et al. Oxytocin infusion in laparoscopic myomectomy may decrease operative blood loss. *J Minim Invasive Gynecol* 2007; 14:184-188.
5. Agostini A, Ronda I, Franchi F et al. Oxytocin during myomectomy: a randomized study. *Eur J Obstet Gynecol Reprod Biol* 2005; 118:235-238.
6. Fleischer A. Color doppler sonography of uterine disorders. *UltrasoundQ* 2003;19:179-189.
7. Tadashi Kimura Osamu Tanizawa Kensaku Mori Michael. Structure and expression of a human oxytocin receptor. *J Brownstein & Hiroto Okayama Nature* 1992; 356:526 - 529.
8. Maggi M, Magini A, Fiscella A, et al. Modulation of neurohypophysial hormone receptors in human nonpregnant myometrium. *J Clin Endocrinol Metab* 1992; 74:385-392.
9. Bossmar T, Akerlund M, Szamatowicz J, et al. Br Receptor-mediated uterine effects of vasopressin and oxytocin in nonpregnant women. *J Obstet Gynaecol* 1995; 102:907-912.
10. Kimura T, Takemura M, Nomura S, et al. Expression of oxytocin receptor in human pregnant myometrium. *Endocrinology* 1996; 137:780-785.
11. Zeeman G, Khan-Dawood FS, Dawood MY. Oxytocin and its receptors in pregnancy and parturition: current concepts and clinical implications. *Obstet Gynecol* 1997; 89:873-883.
12. Zingg HH, Rozen F, Breton C, et al. Gonadal steroid regulation of oxytocin and oxytocin receptor gene expression. *Adv Exp Med Biol* 1995;395:395-404.

13. Lessl M, Klotzbuecher M, Schoen S, et al. Comparative messenger ribonucleic acid analysis of immediate early genes and sex steroid receptors in human leiomyoma and healthy myometrium. *J Clin Endocrinol Metab* 1997; 82:2596-2600.
14. Mueller A, Siemer J, Schreiner S, et al. Role of estrogen and progesterone in the regulation of uterine peristalsis: results from perfused non-pregnant swine uteri. *Human Reproduction* 2006; 21:1863-1868.
15. Richter O, Wardelmann E, Schneider C, et al. Extracorporeal perfusion of the human uterus as an experimental model in gynaecology and reproductive medicine. *Hum Reprod* 2000; 15:1235-1240.
16. Richter ON, Tschubel K, Schmolling J, et al. Immunohistochemical reactivity of myometrial oxytocin receptor in extracorporeally perfused nonpregnant human uteri. *Arch Gynecol Obstet* 2003; 269:16-24.
17. Richter ON, Kübler K, Schmolling J, et al. Oxytocin receptor gene expression of estrogen-stimulated human myometrium in extracorporeally perfused non-pregnant uteri. *Mol Hum Reprod* 2004; 10:339-346.
18. Richter ON, Bartz C, Dowaji J, et al. Contractile reactivity of human myometrium in isolated non-pregnant uteri. *Human Reproduction* 2006; 21:36-45.
19. Lee KH, Khan-Dawood FS, Dawood MY, et al. Oxytocin receptor and its messenger ribonucleic acid in human leiomyoma and myometrium. *Am J Obstet Gynecol* 1998; 179:620-627.
20. Mechsner S, Bartley J, Loddenkemper C, et al. Oxytocin receptor Expression in smooth muscle cells of peritoneal endometriotic Lesions and ovarian endometriotic cysts. *Fertility and Sterility* 2005; 34:1220-1231.
21. Loddenkemper C, Mechsner S, Foss HD, et al. Use of Oxytocin Receptor Expression in Distinguishing Between Uterine Smooth Muscle Tumors and Endometrial Stromal Sarcoma. *American Journal of Surgical Pathology* 2003; 27:1458-1462.
22. Emerson DS, Cartier MS, Altieri LA, et al. Diagnostic efficacy of endovaginal color Doppler flow imaging in an ectopic Pregnancy screening program. *Radiology* 1992; 183:413-420.
23. Polark JF. Peripheral arterial disease. Peripheral vascular sonography—a practical guide. In: Polark 1st ed. Baltimore, Maryland. Williams and Wilkins-A Weverly Co 1992; 7:247-302.

The Effects of Acoustic Interface Layer on Biological Focal Region By High Intensity Focused Ultrasound

Quanyi Li, Liyuan Fu, Faqi Li

(Department of biomedical engineering of Chongqing University of Medical Sciences
Institute of ultrasound engineering in medical of Chongqing University of Medical Sciences;
State Key laboratory of ultrasound engineering in medical co-founded by Chongqing and MOST, Chongqing, 400016)

Abstract — Interface layer was simulated by the magnetic nano-particles in the egg white phantom, and then the high intensity focused ultrasound (HIFU) was introduced to exposure egg white phantom in different depth blowing the acoustic interface by the same dosage using “point” exposure. The results show that the volumes of Biological Focal Region (BFR) enlarge. This means the magnetic nano-particles can enhance the therapeutic efficiency of HIFU when the Acoustic Focal Region (AFR) close with interface layer. When distance of the AFR from the interface layer was 10mm, the size and shape of the BFR were similar with control group, but there was a large lesion at the interface, this was harm for treatment. When distance of the AFR from the interface layer was 30mm, the size and shape of the BFR were similar with control group. When the thickness of the interface layer diminished, the utility of enhancement decreased.

Keywords — Magnetic nano-particles, interface layer, biological focal region, High Intensity Focused Ultrasound

I. INTRODUCTION

High intensity focused ultrasound (HIFU) has been used to treat solid tumor in clinical practice as a new method^[1-3]. Wang et al^[4] defined the punctiform coagulative necrosis region which was induced by HIFU as Biological Focal Region (BFR), and also considered that BFR was the basic unit of the ablation of tumor by HIFU. Because of the complexity of biological tissue, the acoustic interface layer was formed between the different tissue when ultrasound transmission in Multi-layer-tissue. Ultrasound will be reflected and refracted by this interface layer and the distribution of the energy was effected in target region, so it was very important to study the effects of acoustic interface layer on BFR.

II. MATERIALS AND METHODS

A. MATERIALS

Egg white phantom (storage time less than 24h); The magnetic nano-particles with diameter of 80-90nm(Beijing Zhongjianlong CO. LTD).

B. EXPERIMENTAL SYSTEM

A JC HIFU tumor therapy system (Chongqing Haifu Technology Co.Ltd, Chongqing, China). This system comprised an ultrasonic therapeutic unit and an ultrasonic diagnostic unit. The therapeutic transducer with a diameter of 110mm and the focal length of 150mm was amounted at the bottom of a tank filled with degassed water and beams of ultrasound pointed upwards. A diagnostic transducer was located in the centre of the therapeutic transducer in order that guide the HIFU treatment and to monitor the therapeutic effects in real-time. The ultrasound beam with a frequency of 1.60MHz was adopted in the present study (Figure 1).

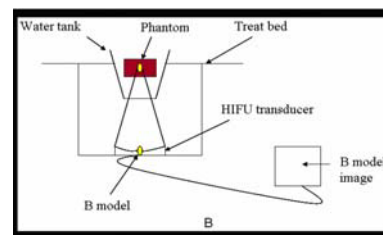


Fig. 1 Illustration of experimental system

C. METHODS

The egg white phantom was made. Interface layer was simulated by the magnetic nano-particles with the diameter of 80-90nm which was controlled by magnet according to our requirement (Fig. 2). In this experiment, HIFU was carried out as point exposure with power 175W, the exposure time was 10s and repeat exposure 6, exposure depth was 10mm, 30mm and 40mm respectively.

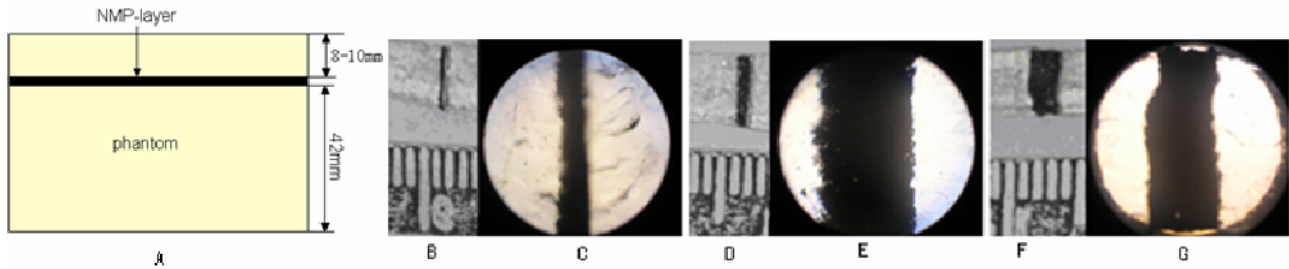


Fig. 2 the interface layer of magnetic nano-particles in the egg white phantom. A : the illustration of egg white phantom; B,D,F: the thickness of the interfaces are 0.27mm, 1.01mm and 1.67mm respectively. C , E , G: the thickness of the interfaces were seen at the microscope, the magnification were 100,100 and 40 respectively.

III. RESULTS AND DISCUSSION

The attenuation of acoustic energy is according to exponential when it is propagating in tissue. The volume of BFR which was induced by HIFU decreased with the increasing of exposure depth in the same dosage. The BFR reduced significantly when the exposure depth increased by 20mm. Fig. 3 shows the BFR in phantom (control group). Wang et al^[5] defined the acoustic environment in tissue (AET) as the biological structure, functional status and acoustic properties in tissue during HIFU; and pointed that the ideal AET are: firstly, there is a lot of energy can deposit in the target tissue; secondly, there is a reflecting interface behind the target region. Because reflection and transmission of ultrasound would be happened at the interface of two different media, and the energy allocation depended on the two media acoustic impedance characteristics, it claims that the characteristic impedance of biological tissue does not match, more easily temperature rise. When the reflected energy superimposed on the target tissue, the energy increased, thus enhancing the efficiency of HIFU treatment. At the interface thickness of 1.67 mm, 1.01mm and 0.27 mm, 40 mm depth of the treatment, including the direction of the sound source interface from the phantom surface length is 42 mm, the volume of the focal was about 1.1 mm × 2.1mm × 3.2mm, which focus on margin and the interfacial layer coincide with the surface. The results shows that the HIFU biological focal region increased significantly and the volume of the biological focal region decreased with the thickness of the interfacial layer decreased. The shape of the biological focal region changed from "labaxing" into "inverted triangle", showing in Figure 4, 5 and 6. The results were consistent with the viewpoint of Wang's: The existence of the interface can improve the efficiency of HIFU treatment.

When the exposure depth was 30 mm (The focal distance of interface about 10 mm), there were two injury in the phantom. The one was destroyed in the focal (Fig. 4, Fig. 5 and 6 in B ①), the another was necrotized out the focal, but in the interface (Figure 4, Figures 5 and 6 in B ②). The volume and the shape of the necrosis in the focal were similar with the control group. While the thickness of the interface layer decreased gradually, the volume of the necrosis in the interface became small. The protein gel phantom could not completely absorption ultrasonic sound, so the ultrasound transmission through the focal to nano-magnetic particles interface layer surface. Because the thermal conductivity of nano-magnetic particles was high, the energy could deposit in the interface, as a result, the damage occurred in the interface. The thicker the interface layer was, the more energy could deposit, and the large necrosis was in the interface. This was the negative impact on HIFU treatment. In order to improve the safety of HIFU, such a situation should be avoided.

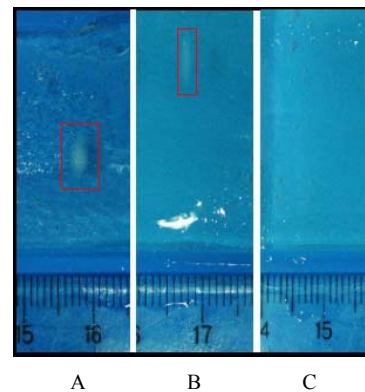


Fig. 3 Control group, the depth of exposure were 10mm, 30mm and 40mm respectively

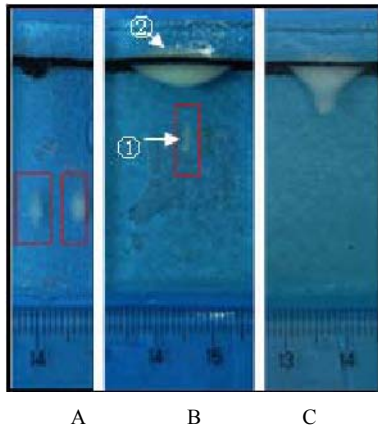


Fig. 4 the thickness of interface was 1.67mm, A, B, C: the depth of exposure were 10mm, 30mm and 40mm respectively

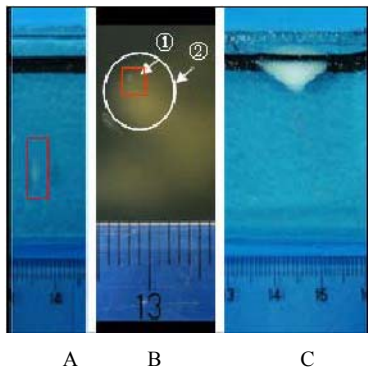


Fig. 5 the thickness of interface was 1.01mm, A, B (Vertical view), C: the depth of exposure were 10mm, 30mm and 40mm respectively

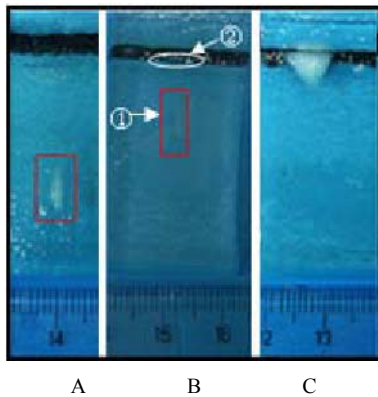


Fig. 6 the thickness of interface was 0.27mm, A,B,C: the depth of exposure were 10mm, 30mm and 40mm respectively

The size of BFR induced by HIFU were similar with control group when the exposure depth was 10mm, but the effect of interface layer reduced with the exposure depth, and there was no lesion at interface layer. The acoustic

wave transmission along the direction of convergence angle, the distance from focal to the interface layer was 30mm, so the acoustic energy deposition reduced in the interface layer (compare to treatment depth 30mm). The deposition of energy could not induce the egg white phantom lesion. It indicated that the safety treatment region enlarger with reducing the interface layer's thickness.

IV. CONCLUSION

It can enhance the efficiency of HIFU therapeutic when the focus nearby the interface layer, but when the acoustic focal at some region blow this layer, there would be negative impact on HIFU safety. The safety region below the interface was decided by the interface layer's thickness and therapeutic dosage. Experiment indicated that the safety therapy region was 30mm from the interface layer at the power of 175w. In a word, the middle interface layer has severely influence to the BFR. It was very important for the safety and efficiency of HIFU clinical practice.

ACKNOWLEDGMENT

We would like to thanks Zhang Dejun, Qinyan, Gong Xiaobo. The work was supported by NSFC: 30471653

REFERENCES

1. Feng Wu, Zhi-Biao Wang, Wen-Zhi Chen, *et al.*. Extracorporeal high intensity focused ultrasound ablation in the treatment of 1038 patients with solid carcinomas in China: an overview[J]. *Ultrasonics Sonochemistry*. 2004 11:149-154
2. Thüroff S, Chaussy C, Vallancien G, *et al.*. High-Intensity Focused Ultrasound and Localized Prostate Cancer: Efficacy Results from the European Multicentric Study[J]. *Journal of Endourology*, 2003,17:8
3. Stewart E, Gedroyc W, Tempany C, *et al.* Focused Ultrasound Treatment of Uterine Fibroids: Safety and Feasibility of a Noninvasive Thermoablative Technique[J]. *Am J Obstet Gynecol*, 2003 July; 48-54
4. Wang Zhibiao, Wu Feng, Wang Zhilong, *et al.* Concept of biological focal field and its importance in tissue resection with high intensity focused ultrasound.[J]*Acoust Soc Am*, 1998,103:2869
5. Wang Z, Li FQ, Bai J, *et al.* A study of acoustic Environment in tissue of high intensity focused ultrasound[M]. 3rd International Symposium on therapeutic ultrasound, 2003,68

Author: Li Quanyi, Fu Liyuan, Li Faqi
 Institute: Institute of ultrasound engineering in medical
 of Chongqing University of Medical Sciences
 City: Chongqing
 Country: China
 Email: liquanyi-007@163.com

Certification of Biomedical Engineering Technicians and Clinical Engineers: Important or Not

James O. Wear
PhD, CCE, CHSP, FASHE, FAIMBE

Scientific Enterprises, Inc, North Little Rock, AR, USA

Abstract — The clinical engineering staff including engineers and technicians is an important element in the use of medical technology in health care facilities. The clinical engineer is a member of the technology management team, which is involved in the selection of new technology and the design of facilities for the use of the technology. What is the impact on healthcare delivery as a result of certified Clinical Engineers and Biomedical Engineering Technicians (BMETs)? Can a certified clinical engineering staff improve accreditation of hospitals? Certification of staff is one measure of quality control for medical technology. However, no country requires that the BMETs and Clinical Engineers be certified in order to perform any functions with medical technology. The history of certification will be presented including how it differs in different countries. The recognition of certification of BMETs and Clinical Engineers by the healthcare community will be discussed. The first certification programs were initiated in 1972 in the United States. A clinical engineer may be called a biomedical engineer or medical engineer and different terminology is also used for the BMETs.

Keywords — Certification, BMET, Biomedical Engineering Technicians, Clinical Engineers, CAHTMA

I. INTRODUCTION

There is a lot said about certification and there are many different certification programs. So one might ask what certification means. Certification is not just a certificate for participating in a training program. At the same time, it is not a license, which is a legal document provided by a professional institution and recognized by a government. A certification is by some professional organization and requires experience, education and usually an exam. When one talks about a certified BMET, what are they really talking about? BMET can mean Biomedical Equipment Technician, Biomedical Electronics Technician, or Biomedical Engineering Technician, and there are degree programs with all these names. With a certification program, it is a Certified Biomedical Equipment Technician. When one talks about Clinical Engineering, this can have different names in the hospital setting. They are generally called Biomedical Engineer or Clinical Engineer. In some cases, they are a Medical Engineer or Medical Physicist, which is the more

common terminology used in Europe. According to the certification program, it is a Certified Clinical Engineer no matter what the degree or experience

II. HISTORY – CBET

The BMET education program in the U.S. started with the U.S. Army training of Medical Equipment Technicians in World War II. BMET positions did not occur in the medical centers until the late 1960s when medical equipment became prominent in healthcare delivery. Technical Education Research Center (TERC) was given a grant about 1967 by the U.S. government to develop a curriculum for the Biomedical Equipment Technician. As part of their grant, they funded a couple of pilot programs in community colleges. The program was designed to be a two-year associate degree program. After a few years, several associate degree programs were developed in vocational schools around the country. Unfortunately, most of these programs did not follow the curriculum developed by TERC. As a result, the quality of the programs and the type of training that individuals received varied greatly. They were from an electronics program with one course in biomedical instrumentation to programs that had several courses in instrumentation and internships at hospitals. The Association for the Advancement of Medical Instrumentation (AAMI) promoted the training of Biomedical Equipment Technicians, as well as, their hiring in hospitals. In order to assure some quality, with a standard set of skills for a Biomedical Equipment Technician, AAMI initiated the certification program for Biomedical Equipment Technicians or the CBET. The Board of Examiners included Lt. Col. Bert Dobson, who was in charge of the Air Force's medical equipment maintenance program, educators, clinical engineers, and other clinical staff. They developed an exam primarily based on skills required by the U.S. military training program and the curriculum developed by TERC. Over 5000 technicians have been certified under this program, with most of them in the United States.

In 1973, the Department of Veterans Affairs initiated its own certification program based on the AAMI certification

program. This was created because of the logistics of people being able to go to sites to take the AAMI exam. The exams continued in parallel with at times some of the same members on the Boards of Examiners. In 1985, the exams were merged and the AAMI/ICC program accepted all people certified by the Department of Veterans Affairs.

In the same timeframe, the Electronics Technicians Association (ETA International) developed a certification for Biomedical Electronic Technicians (CET-BMD). More recently, they have developed a certification for Certified Biomedical Imaging Equipment Technician (CET-BIET).

In the mid 1980s, the International Certification Commission was created as a result of certification programs being developed primarily for Clinical Engineers in other countries. The ICC is a coordinating commission that helps to maintain the quality of the various programs in different countries. The CBET exam was developed for the general Biomedical Equipment Technician. It was difficult for technicians that worked for vendors of specific products as well as technicians that worked in specific areas of the hospital, such as, radiological equipment and clinical lab equipment to pass the exam. In order to partially correct this situation, specialty certification exams were developed for technicians. For imaging equipment there is the certified radiological equipment specialists (CRES). This has been a popular certification and many technicians have been certified under this program including vendor technicians. For the clinical laboratory equipment there is the certified laboratory equipment specialist (CLES), which has not been a very popular certification program. This is primarily due to the fact that the change in the clinical laboratory equipment has reduced the number of technicians required to work on equipment in that area.

III. HISTORY – CCE

The term clinical engineer was coined by Dr. Caesar Caceres in 1970. The Clinical Engineer is an engineer that works in the hospital setting with the clinical staff as opposed to being a Biomedical Engineer that primarily does research. Very few training programs have been developed in the United States for Clinical Engineering and at the present time, there are only a handful of programs. Certification for the Clinical Engineer was developed initially by AAMI in 1975 to recognize the Engineers that were working in the clinical setting. Different engineering and physical science specialists were functioning as Clinical Engineers and this was one way to assure that engineers had the skill sets that were required to be a Clinical Engineer.

Also in 1975, the American Board of Clinical Engineering developed a certification for Clinical Engineers. This

was established as an independent group rather than any organization because they did not think that the acceptance of the initial group of Clinical Engineers based on experience was a way to certify people. As a result, they had five (5) people that self certified themselves and developed an exam for other people to take. The two Clinical Engineering programs continued until 1984 and at that time, the two programs were merged into one program under the International Certification Commission. In 1999, the International Certification Commission discontinued the certification program for Clinical Engineers in the United States. This was done from an economic standpoint since very few people were applying to take the certification exam, typically, one or two per year. At that time, about 400 clinical engineers had been certified. After some attempts to re-establish the certification program for Clinical Engineers, under the ICC, a new certification program was developed under the Health Technology Certification Commission (HTCC). HTCC gave the first new clinical engineering exam in 2003. This certification exam is based on the body of knowledge required for Clinical Engineers developed by the American College of Clinical Engineering.

IV. CERTIFICATION OUTSIDE THE US

There are a variety of certifications of Biomedical Technicians and Clinical Engineers in countries other than the United States. Most of them involve certification of engineers instead of technicians. Several are spin-offs of the American Clinical Engineering certification program and are members of the International Certification Commission. The Canadian program was originally part of the United States certification for both BMETs and Clinical Engineers. This program has some slightly different requirements. For instance, the Clinical Engineer has to be a Canadian Professional Engineer and the BMET program in Canada is a Bachelors Degree as opposed to the Associate Degree program in the United States. Approximately 50 Clinical Engineers are certified under the Canadian program.

Individuals that were certified under the United States certification program started the Clinical Engineer Certification program in Brazil. They have developed a program with an exam for Brazil in Portuguese and five engineers have been certified under this program. It has been discontinued, but there is an effort to restart the program. Mexico started a certification program and certified their first Clinical Engineers in 1991. Again, the initial engineers that made up their Board of Examiners were certified under the United States program. Mexico has also developed an exam in Spanish. This exam is available to other Latin American countries. In Latin America and the Caribbean only indi-

viduals with an engineering degree are eligible for certification.

Other countries have developed certification programs that are not affiliated with the International Certification Commission for Clinical Engineers and in some cases certification programs for technicians. Some of these programs have an exam and others have certified people based on their credentials including both experience and academic coursework.

South Africa has a voluntary registration program of Clinical Engineers, Clinical Engineering Technologists and Clinical Engineering Technicians, which is based on experience and academic requirements. All three of these groups are considered professionals and would have academic training. They also have medical equipment repair personnel.

Germany has developed a Certified Clinical Engineering program, but it does not require an exam. It is based on experience and academic background. They also are planning to develop a certified Biomedical Engineering Technician program. In most European countries, there are more engineers than technicians and so the certification of the engineer is more important. The United Kingdom initially developed a certification for Clinical Engineers in the 1990s but this program has been dropped due to lack of interest in it. They are now having a voluntary registration for Clinical Engineering Technologists, which includes Clinical Engineers, Medical Physics individuals and other scientific people that will be working in the clinical setting.

Sweden has a voluntary Clinical Engineering certification program. This program is based on academic credentials and experience. France does not have a certification program.

Uganda does not have a certification program, but are interested in starting one. Cameroon Association of Biomedical Professionals has as one of its objectives to establish a certification program.

Japan has a rather unique situation, in that they have Clinical Engineering Technologists. These must be certified by the government to operate equipment. These certified operators also do maintenance on some of the equipment.

Hong Kong engineers have been certified under the Health Technology Certification Commission in the United States, and technicians under the ICC program.

Certification of clinical engineers and practitioners was developed in China in 2005 with the help of Yadin David. The certifying body is China Medical Association – Clinical Engineering Society. The written and oral exams are given in English with a dictionary.

V. COMMISSION FOR THE ADVANCEMENT OF HEALTHCARE TECHNOLOGY MANAGEMENT IN ASIA (CAHTMA)

CAHTMA was initiated in 2005 with the endorsement of the Asian Hospital Federation at the Asian Hospital Management 2005 meeting in Kuala Lumpur, Malaysia. It was established to provide a platform for healthcare professionals to discuss and exchange ideas on healthcare technologies and practices. Central to these objectives are the promotion of best technology management practices, the certification of clinical engineering practitioners and healthcare professionals, and the dissemination of appropriate management tools through seminars and workshops.

CATHMA is registered in Singapore and is affiliated with IFMBE. The board of directors includes industrial, academic and ministry of health representation and a WHO advisor. The author is the current Co-chairman and Co-founder.

CAHTMA will certify technicians and engineers as clinical engineering practitioners (CEP). This certification is based on experience with an oral and written exam covering aspects of the clinical engineering field. These CEPs must have a basic knowledge in healthcare engineering standards such as IEC 60601, ANSI/AAMI EQ56, RD62, JCI, etc.

It will also certify training programs for clinical engineering practitioners in Asia. Workshops and seminars are conducted to aid clinical engineering practitioners to develop and advance their knowledge and skills in the field of healthcare technology.

In 2008, Malaysia is going to have a Medical Device Act, which will require people with credentials in clinical engineering for medical equipment maintenance. The CAHTMA certification of CEPs will meet this requirement.

The first exam will be given in the 2007 and 5 engineers were certified at the basic level. A second exam will be given in March, 2008. They are currently developing procedures to certify engineers with at least five years experience based on credentials for a one year period.

VI. CERTIFICATION REQUIREMENTS –UNITED STATES

In the United States program, the requirements for a CBET are the following: have a degree in Biomedical Equipment Technology; plus two years experience or an Electronics degree and three years experience or four years experience. The degree in both cases is an associate degree. They take a written exam of 150 questions for which the passing score is 70%. In order to maintain their certification, they have to demonstrate that they are continuing to maintain their skill level with continuing education every three years. The requirements for the Clinical Engineer in

the United States and for the programs that are under the ICC umbrella are as follows: they must have a bachelors degree in engineering or physical science; two years experience in the clinical setting; three references that demonstrate their work in the clinical setting as a Clinical Engineer. At least one of these references must be from a healthcare provider. They then take a 150 questions written exam. If they pass that exam they take the two-hour oral exam given by two members of the Board of Examiners.

VII. VALUE OF CERTIFICATION

How valuable is certification to the Clinical Engineering professional? No one appears to require certification for technicians or engineers. Certification should reduce the likelihood of equipment related accidents and misuse of medical devices, which would improve patient safety. It should lead to improved maintenance and repair of equipment and improved selection of technology, which would improve patient care in a cost effective manner.

There are increasing efforts in developing certification programs and perhaps even requiring it for some functions in some parts of the world. There has been some discussion of requiring certification of technicians to work on particular equipment, that is not to certify technicians in general but to certify them to work on a particular type of equipment and maybe even down to brand and model. This would really be a certificate program as opposed to certification. If this occurs anywhere, it would be a serious mistake because even manufacturers do not have their technicians fully trained on every piece of equipment that they make.

Certification can be a benefit in the hiring process. This is especially true as people are crossing country borders working in different parts of the world. Certification should indicate a minimum level of qualifications and skills. Certification in the hiring process is probably more important in the hiring of technicians than it would be in regard to engineers. There is a wide variety of training programs for technicians. At least with engineers, they do have a standard engineering background, though it may not be in the clinical setting.

Certification programs have provided some benefits to the profession of Clinical Engineering. For the BMET, it provides them with recognition as being a member of the healthcare team. Other members of the healthcare team have certification or licensing within their allied health profession. With the accreditation of hospitals, there is a

requirement for competency of the staff that maintain equipment. Certification of the technician is one way to demonstrate the level of competency. Certification has also helped hospitals in dealing with vendors, service contracts, and access to documentation. It is very difficult for a vendor to say that a Certified Radiological Equipment Specialist is not qualified whenever their own technician does not have that certification. Therefore, certification of the technicians can result in cost saving of the overall maintenance program for the hospital.

The certification of Clinical Engineers has provided the engineer with recognition in a clinical setting. This has aided them with acceptance to the clinical staff since it provides recognition of clinical knowledge and not just engineering expertise.

An important area for certification of the Clinical Engineer is when there is an accident in the hospital involving equipment. The Clinical Engineer is the one that should do the accident investigation and probably in the case of litigation will be called as an expert witness. The certification as a Clinical Engineer recognizes the engineer as an expert in the field and helps the hospital to establish that they have a good equipment evaluation and maintenance program.

VIII. CONCLUSION

The certification of Biomedical Engineering Technicians and Clinical Engineers is important as the world becomes smaller and engineers and technicians are working in both developed and developing countries. Certification is important to provide initial or at least a minimum level of qualifications for people. The interaction between certification programs in different countries will become more important as certification develops. Perhaps some time there can be a global certification of both engineers and technicians.

There should be some harmonization of the certification standards and terminology used while each certification body maintains its program.

Author:	James O. Wear, PhD, CCE
Company:	Scientific Enterprises, Inc
Street:	5104 Randolph Road
City:	North Little Rock, AR 72116
Country:	USA
Email:	wearjam@cswnet.com

The Computer Model in View of Hemodynamic Effects of Electro Ventilation Double Pump CPR

Xiaoming Wu¹, Yanru Zhang², Lin Xu², Hengxin Yuan³

¹ Biological Mechanics Institute, South China University of Technology, Guangzhou, China

² School of Computer Science and Engineering, South China University of Technology, Guangzhou, China

³ Sun Yat-Sen Medicine School, Sun Yat-Sen University, Guangzhou, China

Abstract — Electro ventilation double pump cardiopulmonary resuscitation (EDCPR) was a cardiopulmonary resuscitation (CPR) technique that chest compression was coupled with Lower limbs compression to improve the aortic pressure and myocardial perfusion pressure. The paper was to study the hemodynamic effects during human cardiac arrest and find the optimum value of lower limbs compression pressure (LLCP) when chest compression pressure was definite. First the computer model of human circulation was developed, second the effects of EDCPR to the model were performed, third the compression schemes were performed by computer simulation and the optimum value was found. The results were that EDCPR got the good hemodynamic effects. The proper value of the LLCP was found. And they were in accordance with the results of parallel animal experiments and the data published before. The developed model can successfully describe the effects of different CPR techniques and different compression schemes to the circulation system during cardiac arrest.

Keywords — circulation model, electro ventilation double pump cardiopulmonary resuscitation, systemic perfusion pressure, lower limbs compression pressure

I. INTRODUCTION

Standard cardiopulmonary resuscitation (CPR) was put forward by Kouwenhoven in 1960. However it can't generate enough forward flow to the heart and coronary perfusion pressure. Electro ventilation double pump CPR (EDCPR) was put forward by Yuan Hengxin in 1994 [1]. EDCPR was a new CPR technique that chest compression was combined with impedance threshold valve (ITV) [2] and enhanced external countpulsation (EECP). Lower limbs compression was coupled with the chest compression to improve the aortic pressure and myocardial perfusion pressure. However, whether the lower limbs compression pressure (LLCP) was put more the effects got better? Were there any proper values of LLCP or proper ratios between chest compression and lower limbs compressure? Studies in animals' experiments have demonstrated greater venous return and greater perfusion pressures when EDCPR was performed. But there's no experiments to find the value in the computer

model. According to the related researcher's work, the ratio between chest compression pressure and LLCP had a great impact on the effects of CPR. It was important to find the proper ratio to get better effects. Animal and clinical experiments had some disadvantages such as high cost, complexities, influence of external factors, man-made influence and time and space limitation.

Developing a mathematical model [3] was a different way to compare and find the proper value of LLCP when the chest compression pressure was determined. It can save resource, decrease the artificial interference. It was convenient to repeat the experiments. In medical science, mathematical modeling became increasingly important and would predict behavior of the human body as a response to internal or external changes [4].

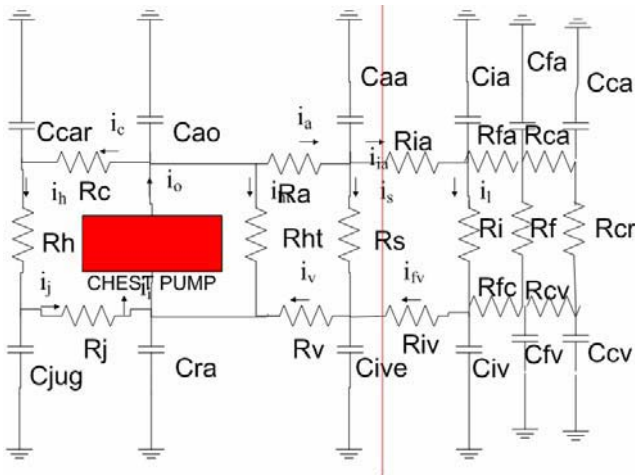
The present paper described a comprehensive study of the hemodynamic effects of EDCPR in a computer model [5]. External forces on the chest and iliac, femoral, tibial compartments were explicitly modeled. This circulatory model for CPR was from Babbs [2]. It was modified and extended with the influence of EDCPR by our group.

II. METHODS

The circulatory model was built before the effects of EDCPR added to it. To model the effects of EDCPR the pressure was considered not only to the chest but also to the iliac, femoral, tibial compartments. The different effects of different ratios between chest compression pressure and LLCP were presented, and the optimum ratio was found.

A. Circulatory system model

The circulatory system model (Fig. 1) had 18 vascular compartments; the related informations can be found in [6]. Every compartment had the similar simplified structure: a lumped blood resistance and a lumped compliance. However there are the different parameters in all the structures. The model was based upon normal human anatomy and physiology; the definition of resistances, compliances was deduced from Navier-Stokes equations, in the model the



C_{ia}: Compliance of both iliac arteries, C_{iv}: Compliance of both iliac veins, C_{fa}: Compliance of both femoral arteries, C_{fv}: Compliance of both femoral veins, C_{ca}: Compliance of both crural arteries, C_{cv}: Compliance of both crural veins, R_{ia}: Resistance of both iliac arteries, R_{iv}: Resistance of both iliac veins, R_i: Resistance of iliac vasculature, R_{fa}: Resistance of both femoral arteries, R_{fv}: Resistance of both femoral veins, R_f: Resistance of femoral vasculature, R_{ca}: Resistance of both crural arteries, R_{cv}: Resistance of both crural veins, R_c: Resistance of crural vasculature

Fig. 1 The model of human circulatory system

relations with all the compartments accorded with Ohm's Law. And it was solved using MAT LAB/Simulink, in which the fixed-step size was 0.0005s, the initial pressure of all organs' compartments was 5mmHg, the simulation time was 70s. The programme interface in simulink was showed in Fig. 2.

B. The model of effects of different ratios in EDCPR

How to describe the effects of EDCPR techniques to the circulatory system model was a key part to study the hemodynamics. For according with the clinical theory methods and 2005 International Consensus on CPR and ECC Science

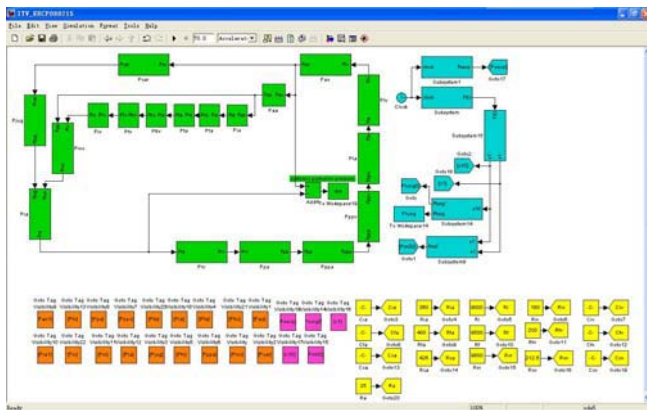


Fig. 2 The interface of simulation program

with Treatment Recommendations [7] there were two methods to describe them.

First, when the chest compression pressure F(t) was performed, it led to sternal and anterior chest wall x₁(cm), at the same time the cardiac chamber expanded x₂(cm) with the blood. Then x₁(cm) and x₂(cm) led to compression to the organs in the rib cage. The compression pressures to the organs in the rib cage were expressed by x₁ and x₂ directly. Second, when the LLCPR Peecp was performed, Peecp acted as a direct pressure source.

How to get the model of the chest and chest compression is described particularly in paper [3]. This paper showed how to get the parameters of lower limbs structures, and how to couple Peecp to the lower limbs model.

When the LLCPR Peecp of EDCPR was performed, in the model the pressure sources which equaled to Peecp were in series with C_{fa}, C_{fv} directly. F(t) and Peecp was opposite to each other, when the chest compression was performed, the lower limbs compression was relaxed or otherwise.

The lower limbs compression was represented as follows.

For the iliac arteries and vena

$$\begin{aligned} \Delta P_{ia} &= \Delta Peecp + \frac{1}{C_{ia}}(i_{ia} - i_i)\Delta t \\ &= \Delta Peecp + \frac{\Delta t}{C_{ia}} \left[\frac{P_{aa} - P_{ia}}{R_{ia}} - \frac{P_{ia} - P_{iv}}{R_i} \right] \end{aligned} \tag{1}$$

and

$$\begin{aligned} \Delta P_{iv} &= \Delta Peecp + \frac{1}{C_{iv}}(i_i - i_{iv})\Delta t \\ &= \Delta Peecp + \frac{\Delta t}{C_{iv}} \left[\frac{P_{ia} - P_{iv}}{R_i} - \max(0, \frac{P_{iv} - P_{ivc}}{R_{iv}}) \right] \end{aligned}$$

The max () functions indicated the one-way valve actions of venous valves in the iliac, femoral and crural veins that prevent retrograde flow.

For the femoral arteries and vena

$$\begin{aligned} \Delta P_{fa} &= \Delta Peecp + \frac{1}{C_{fa}}(i_{ia} - i_f)\Delta t \\ &= \Delta Peecp + \frac{\Delta t}{C_{fa}} \left[\frac{P_{ia} - P_{fa}}{R_{fa}} - \frac{P_{fa} - P_{fv}}{R_f} \right] \end{aligned} \tag{2}$$

and

$$\begin{aligned} \Delta P_{fv} &= \Delta Peecp + \frac{1}{C_{fv}}(i_f - i_{fv})\Delta t \\ &= \Delta Peecp + \frac{\Delta t}{C_{fv}} \left[\frac{P_{fa} - P_{fv}}{R_f} - \max(0, \frac{P_{fv} - P_{iv}}{R_{fv}}) \right] \end{aligned}$$

Similarly, for the crural arteries and vena,

$$\begin{aligned} \Delta P_{ca} &= \Delta P_{eecp} + \frac{1}{C_{ca}}(i_{ca} - i_{cr})\Delta t \\ &= \Delta P_{eecp} + \frac{\Delta t}{C_{ca}} \left[\frac{P_{fa} - P_{ca}}{R_{ca}} - \frac{P_{ca} - P_{cv}}{R_{cr}} \right] \end{aligned} \tag{3}$$

and

$$\begin{aligned} \Delta P_{cv} &= \Delta P_{eecp} + \frac{1}{C_{cv}}(i_{cr} - i_{cv})\Delta t \\ &= \Delta P_{eecp} + \frac{\Delta t}{C_{cv}} \left[\frac{P_{ca} - P_{cv}}{R_{cr}} - \max(0, \frac{P_{cv} - P_{fv}}{R_{cv}}) \right] \end{aligned}$$

The values of parameters (C_{ia} , C_{iv} , C_{fa} , C_{fv} , C_{ca} , $C_{v}\dots$) were deduced by the human physiology and the clinical experiments [6] by our group and they were verified by simulating the normal human physiology, The values of lower limbs' parameters were provided in Table 1.

Table 1 Model parameters

	Value(mmHg/L/s)	Definition
Rsistances(>0)		
Ria	360	Resistance of both iliac arteries
Riv	180	Resistance of both iliac veins
Ri	9120	Resistance of iliac vasculature
Rfa	400	Resistance of both femoral arteries
Rfv	200	Resistance of both femoral veins
Rf	9510	Resistance of femoral vasculature
Rca	426	Resistance of both crural arteries
Rev	213	Resistance of both crural veins
Rcr	9812	Resistance of crural vasculature

	Values(L/mmHg)	Definition
Compliance(>0)		
Cia	0.00035	Compliance of both iliac arteries
Civ	0.0078	Compliance of both iliac veins
Cfa	0.0003	Compliance of both arteries
Cfv	0.0063	Compliance of both femoral veins
Cca	0.00028	Compliance of both crural arteries
Ccv	0.00568	Compliance of both crural veins

In short, the organs in the rib cage including chamber of the heart and their associated large veins, thoracic aorta and central pulmonary arteries experienced the sum of the chest compression pressure and lung pressure (in this paper, the thoracic pump mechanisms were used. That meant the thoracic pump factor $f_{tp}=1$) [4, 6], besides, the peripheral pulmonary arteries and veins experienced lung pressure only [4, 6]. If EDCPR was performed, the lower limbs including iliac, femoral, tibial compartments experienced the lower limbs pressure P_{eecp} .

A. Simulation Results

The model was tested by establishing the normal adult circulatory model with $f_{tp}=0$. This model operated normally. Then the effects of different values of P_{eecp} were compared in Fig.3, Fig.4, Fig. 5, Fig.6, and Fig.7 respectively. The maximal chest compression force $F(t)$ was 400Nt, the maximal LLCP P_{eecp} was set to 125mmHg, 150mmHg, 200mmHg, 300mmHg, and 400mmHg respectively. They were both half sinusoidal waveforms. The proper value of lower limbs pressure was found when the chest compression force was set.

SPP (Systemic Perfusion Pressure) was an important indicator to evaluate the efficiency of CPR techniques. It was equal to the thoracic aortic minus right atrial pressure. In Fig.2 the top traces were LLCP; the middle traces were thracic aortic pressure, right atrial pressure and lung pres-

sure; the bottom traces were systemic perfusion pressure SPP. The traces arrange is the same in the following figures.

Obviously, with the Peecp increased from 125mmHg to 150 mmHg, the systolic pressure of SPP (the first wave crest) impaired from 25.31mmHg to 22.82mmHg, and diastolic pressure of SPP (the second wave crest) improved from 28.72mmHg to 30.8 mmHg (Fig.3 and Fig.4). The following figures had the same rules. However, according to the 2005 International Consensus on CPR and ECC Science with Treatment Recommendations, to implement the CPR is not only to improve the systolic pressure but also to improve the diastolic pressure to some level. However, there was an issue: how to find a proper value of Peecp which can make both systolic and diastolic pressures meet the qualification. Fig.5 and Fig.6 gave the changes of SPP with the Peecp changing. In Fig.5 the systolic pressure was 20 mmHg and the diastolic pressure was 34.67mmHg, in Fig.6 the two values were 10.5mmHg and 44.09mmHg. According to the criterions there should be one or several proper values around Peecp=200mmHg. However It was only calculated and measured by handwork now.

There was a difference from EDCPR to the existed CPR techniques. The LLCP can be increased greatly; for there weren't important organs in the iliac, femoral, crural compartments as in the chest and abdomen. The maximal lower limbs compression force can be up to 600mmHg. When Peecp was increased to 400mmHg, the diastolic pressure was improved greatly in Fig. 7, SPP got 55.37mmHg.

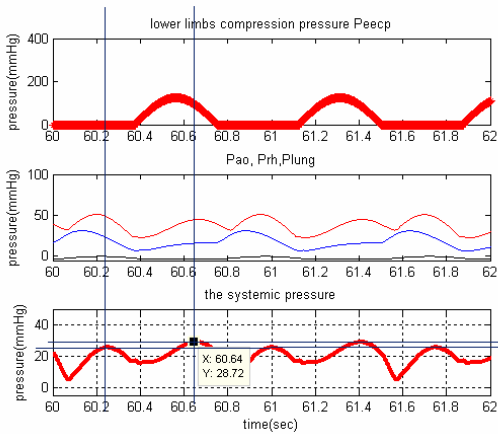


Fig. 3 Systemic perfusion pressure with the Peecp=125mmHg

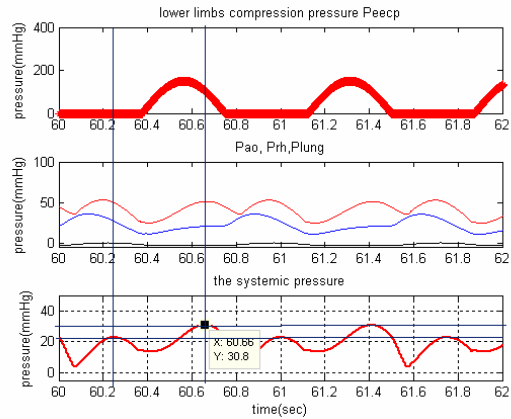


Fig. 4 Systemic perfusion pressure with the Peecp=150mmHg

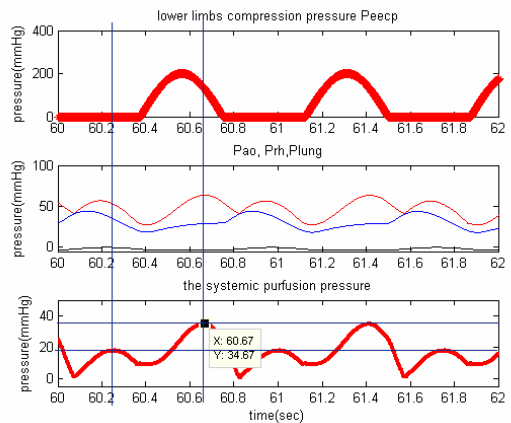


Fig. 5 Systemic perfusion pressure with the Peecp=150mmHg

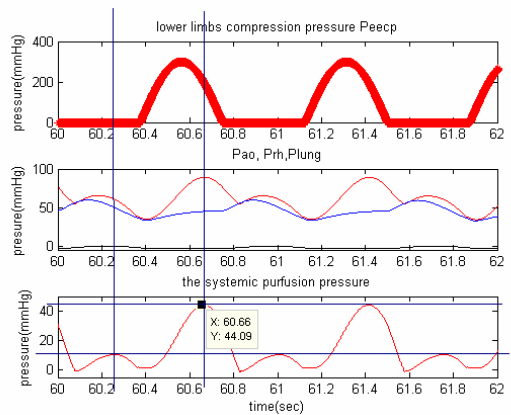


Fig. 6 Systemic perfusion pressure with the Peecp=150mmHg

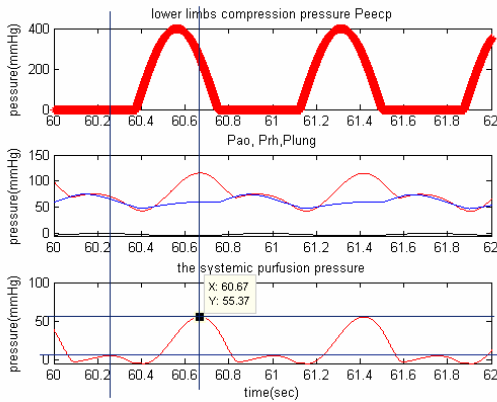


Fig. 7 Systemic perfusion pressure with the Peecp=150mmHg

III. CONCLUSIONS

By the computer modeling and simulating EDCPR can improve the systemic perfusion pressure. The results closely matched the animal experimental records. However, the utility of the model should not be limited to these [8]. In the future the model will be refined further and the simulated results will guide the animal experiments even clinical applications.

Moreover it might help diagnose or analyze other normal or disordered physiological responses [9, 10] such as the pulmonary effects of congestive heart failure and the adult respiratory distress syndrome. As far as know, this combination of the outcome of diagnostic measurements and results of mathematical modeling was a strategy known as model or simulation-based diagnostics [11].

ACKNOWLEDGMENT

The paper was supported by projects National Natural Science Foundation of China □30670538 □□Guangdong Natural Science Foundation (04020048).

REFERENCES

1. Yuan HX, Zheng ZS, Jiang SS et al. (1995) The Hemodynamic Study of the Chest Compression Assisted with Enhanced External Counterpulsation, *Emergency Medicine* (.4(3)):140-144
2. Charles F. Babbs (2005) Effects of an impedance threshold valve upon hemodynamics in Standard CPR: Studies in a refined computational model, *Resuscitation* (66):335-345
3. Lu K, Clark JW, Ghorbel FH, et al. (2001) A human cardiopulmonary system model applied to the analysis of the Valsalva maneuver, *Am J Physiol Heart Circ Physiol* (281):H2661-H2679
4. Charles F. Babbs(1999) CPR techniques that combine chest and abdominal compression and decompression hemodynamic insights from a spreadsheet model, *Circulation*(100):2146-2152
5. Athanasiades A, Ghorbel F, Clark JW(2000) Energy analysis of a nonlinear model of the normal human lung, *J Biol Sys*(8):115-139
6. Zhang Yanru,Xu lin,Wu Xiaoming et al(2008) The Hemodynamic Effects Analysis of the New CPR Technique-Electro Ventilation Double Pump CPR : Studies in the Computer Model (received),*ICBBE 2008. The 2nd International Conference on Bioinformatics and Biomedical Engineering* ,Shanghai,China
7. The 2005 International Consensus Conference on Cardiopulmonary Resuscitation and Emergency Cardiovascular Care Science With Treatment Recommendations (2005), hosted by the American Heart Association in Dallas, Texas,American
8. Yanru, Zhang; Xiaoming, Wu; Hengxin et al(2007) The Human Cardiovascular Model with the Baroreflex Control of Central Nervous System, *CME 2007. IEEE/ICME International Conference*, Beijing, China, 2007,pp.43 - 47
9. K.van Heusden, J.Gisolf, W.J.Stok, et al(2006) Mathematical modeling of gravitational effects on the circulation: importance of the time course of venous pooling and blood volume changes in the lung, *Am J Physiol Heart Circ Physiol*(291):2152-2165
10. Heldt Thomas, EunB.Shim, Roger D.Kamm,et al(2002) Computational modeling of cardiovascular response to orthostatic stress, *J Appl Physiol*(92):1239-1254
11. Michael Danielsen(1998) Modeling of Feedback Mechanisms which control the heart function in a view to an implementation in cardiovascular models (PhD thesis), Demark, Roskilde University, pp.79-90

Author: Zhang Yanru

Institute: School of Computer Science and Engineering, South China University of Technology

Street: Wushang Road, Tianhe

City: Guangzhou

Country: P.R.China

Email: bsp03studio@126.com

The research of the community healthcare network based on ZigBee technology

Jihong Chai¹, Hongli Yang¹

¹Electronic and Information Engineering Institute, Shenzhen Polytechnic, Xili Lake, Shenzhen, China

Abstract — With the increasing need for healthcare and relative shortage of medical resources, the establishment of wireless sensor networks for the healthcare of the family in the community will become a promising research direction recently. In this paper, the wireless solution of healthcare networks based on ZigBee technology is proposed for the real-time monitoring of the physiological parameter. The healthcare networks are composed of three primary modules.

In this paper, the physiological parameter sensor networks based on Zigbee technology and the overall network architecture are designed. And it also introduces a solution of the sensor network node by using CC2430, which is a kind of popular System on Chip (SoC). The wireless healthcare network based on ZigBee is efficient method for monitoring the health state of every family member especially for the elders by the community doctors. The future home healthcare system will apply the new technologies and it will become a good platform for the development of community medical care system.

Keywords — ZigBee, Wireless Sensor Network, Community Healthcare, Telemedicine, CC2430

I. INTRODUCTION

Currently, coronary heart disease, hypertension, etc. have widespread influence on the health of the people especially the elderly. These diseases are chronic and require long-term treatment, and it is best of carrying out continuous monitoring. This requires the continuous monitoring of heart rate, ECG, blood pressure, oxygen, and other physiological parameters for users at home instead of in hospital. It is advantageous for medication instruction and pharmacological treatment effect monitoring.

Some current studies use the cable transmission such as telephone, which causes the user to move inconveniently with the monitoring device. This paper introduces a solution that transmits the information between the monitoring sensor node and the control center node of the community station by using wireless data transmission. It's convenient for users to move freely, while doctors of the community station can access the physiological parameters and give health guidance. In this way, the establishment of the community healthcare network is much useful for easing some social problems such as large population and limited resources of hospital in China.

This paper will focus on the community healthcare network architecture based on ZigBee, discussing an platform for continuous monitoring of community health which is especially useful for patients with chronic heart disease, and also presenting a solution of the sensor network node by using CC2430, which is a kind of popular System on Chip (SoC).

II. METHODS

A. ZigBee protocol framework and application features

The monitoring terminal of the community healthcare network does not need high data transfer rate, but requiring low latency and low power consumption.

Fortunately, ZigBee is a new close, low complexity, low-power, low-data-rate, and low-cost wireless network technology, which is based on IEEE802.15.4. The core is the use of high-frequency multi-channel wireless data transmission methods in order to autonomously formed ZigBee network. Its transfer rate can also meet the ECG, blood pressure and other physiological parametric transmission requirements, and its low-cost, low-power, and notable features are very suitable for family healthcare applications.

ZigBee protocol framework is shown in Figure 1. IEEE802.15.4 definite two physical layer protocols, but ZigBee protocols led by the ZigBee Alliance made the definition of the network layer, security layer, application layer, and so on. It only uses the 2.4 GHz band with 16 channels because of the free use of the global unity ISM band, which

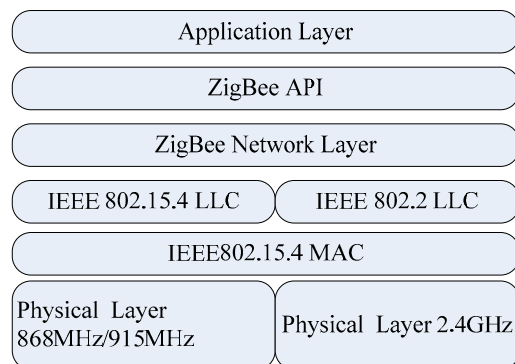


Fig. 1 ZigBee protocol framework

helps promote the ZigBee devices and the reduction of production costs.

ZigBee network topology as shown in Figure 2 has three kinds: Star Networks, Tree networks, and Mesh networks. The backbone network node is called coordinator, which is responsible for the establishment of the network. Moreover, ZigBee also defines the other two kinds of roles, the first is routing node, primarily responsible for the routing path of information packet; the second is terminal device node which can only choose to join the network already formed, and can send and receive information, but do not have routing capabilities either.

The above three kinds of roles correspond to three types of nodes otherwise correspond to two types of physical device, that is, full-function device (FFD) and reduced-function device (RFD). FFD has the controller functionality to provide two-way information transmission, and RFD can only send information or to receive information from the FFD. Thus, the center node must be posed by a FFD, and the routing node is also a FFD, but the terminal node in the network is the simplest node which can be a FFD or RFD.[1]

In addition, ZigBee protocol stack also uses a variety of strategies to effectively meet community health construction of the reliability of the network, real-time, security and other needs.

ZigBee network access using CSMA/CD and TDMA, effectively reduce the conflict between the transmission frames. The MAC layer using two strategies of the automatic re-transmission request (ARQ) and the frame buffer. The sender should receive the confirmation before sending the next frame, so as to ensure the reliability of communications. ZigBee devices have high real-time performance and low power consumption, the average power consumption is very low, the use of time can be maintained long up to 6 months to 2 years relying on two 5# battery.

ZigBee used many mechanisms to ensure the coexistence with other wireless standards, such as DSSS, idle channel

assessment (CCA), dynamic channel selection, to avoid interference with the same frequency. Some other method are used for the high security such as the data packet integrity checking based on Cyclic Redundancy Check (CRC), a security software based on 128-bit AES algorithm, and integrated 802.15.4 security element with security mechanisms of three levels, including non-secure manner, the use of access control list (ACL) authentication, Advanced Encryption mode. So it ensures ZigBee users the security of transmission their physiological parameters.

B. Community healthcare network architecture

Community healthcare monitoring network was designed based on the above ZigBee network topology and protocol. Mesh network is flexible, in that it can effectively avoid network fault caused by the routing node damage. The healthcare network is posed of Monitoring Center PC at community station, center node of base station, routing nodes and physiological parameter sensor nodes, which is shown in Figure 3.[2]

ZigBee terminal sensor node is essentially a kind of RFD in the family end. Each family can have one or more RFD, which is responsible for physiological signal acquisition and transmission. Physiological signals are acquired through sensors such as the electrode, the pressure sensor, etc. At the same time RFD is often in a state of sleep in order to allow the system power consumption greatly reduced.

ZigBee routing node, which is FFD equipment, is also in each family. FFD can optimize the shortest and most reliable path to complete transmission path selection.

The center node of FFD and the monitoring PC both are important. The center node is called coordinator, responsible for the construction of the network and node verification. And it receives health parameters and sends them to the connected PC to make unified database management and information display.

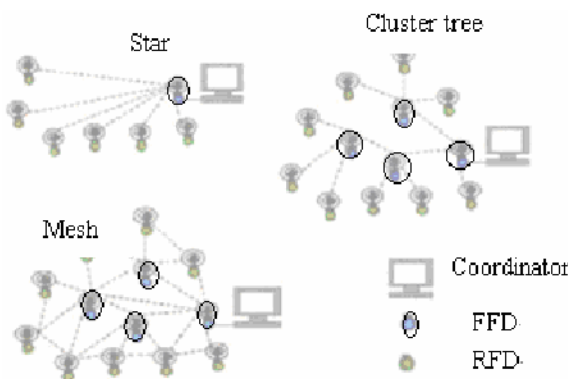


Fig. 2 ZigBee network topology

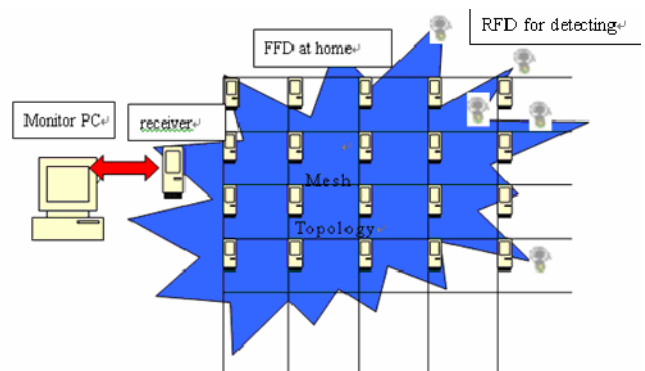


Fig. 3 Community healthcare network

By the community healthcare network, general diseases can be treated by the doctors of the community healthcare network. And it also can be connected to Internet so that the data is transmitted to a remote medical monitoring centre and the medical experts provide the necessary treatment.

C. Hardware block diagram of sensor node

Terminal sensor node is an important component of community healthcare network. The sensor node diagram is shown in Figure 4. The hardware of the network consists of data acquisition, data processing, data transmission and power supply modules. And the core of it is a kind of SoC, CC2430 of Chipcon company, which is the first SoC integrated with ZigBee communications module and MCU. The single chip integrated RF front-end ZigBee, microprocessors, memory, ADC, special Timer, verified ZigBee protocol stack, etc.

The solution using CC2430 requires only few external components, and its peripheral circuits including crystal clock circuits, RF input / output matching circuit. The chip can get vibration signal not only from the external active crystal, but also from the internal circuitry. If the crystal clock is provided by the internal circuitry, crystal oscillator and two load capacitors are needed and the capacitor depends on parameters of the size of the crystal frequency and input capacitance impedance. On the other hand, RF input and output matching circuit mainly used to match the input and output impedance.

D. ZigBee network protocol implementation

As shown in Figure 1, ZigBee protocol stack is divided into several layers. The code for implementation of each layer is in a separate source file, and services and application program interface (API) is defined in the header files. Thus the establishment of the ZigBee network and data transceiver is implemented by calling API the original language

for data transmission on the basis of the ZigBee protocol stack of CC2430.

1. Establishment of a ZigBee network

The wireless network is established on the hardware platform and the multi-level protocol stack should be defined called Z-Stack. The type information and PANID of each node in the network should be configured in IAR IDE software on PC. In additional PANID of each node must be consistent because the nodes with the same PANID can communicate with each other in the same.[3]

The center node as the coordinator of the network establishes the network. First of all, it detects and chooses an idle channel by channel scanning, and then determines its own 16-bit network address, the PANID of the wireless network, and the network topology parameter, and so on. When all the parameters are configured, the center node will be able to accept the other node as sub-node.

At this time, when a routing node wants to join the network, it then sends associated request. If the central node with the receipt of the request has capacity to accept node, then it assigns the exclusive 16-bit network address for the routing node, and issued related response. The routing node will be successful in joining the network after receiving the responses from the center node. The method of joining a number of the other sub-node is the same as above.

The adjacent table will be set up in the flash memory to store network node address and other related information node at the same time as the established of the network. To avoid that data is lost by damaged routing node, this network apply AODV algorithm to establish mesh network topology structure, in accordance with AD hoc network routing protocols to optimize the shortest and most reliable path.

If the terminal sensor node wants to join the network, it only need to send an original language of searching request in the network layer, after receiving the original language, the network layer should send scanning request to the MAC layer. Once the MAC layer scanning operation is completed, it will released original language of scan confirmed to the network layer. Then the network layer report the scanning result to the application layer and the application layer can understand all network information through the adjacent table, and chooses a suitable routing node with minimum depth from the network, and send connection request. The MAC layer then responds and returns connection state information and an exclusive 16-bit network address. The network layer in receiving confirmed information revise the adjacent table and the terminal node can work and transfer data in the wireless network.

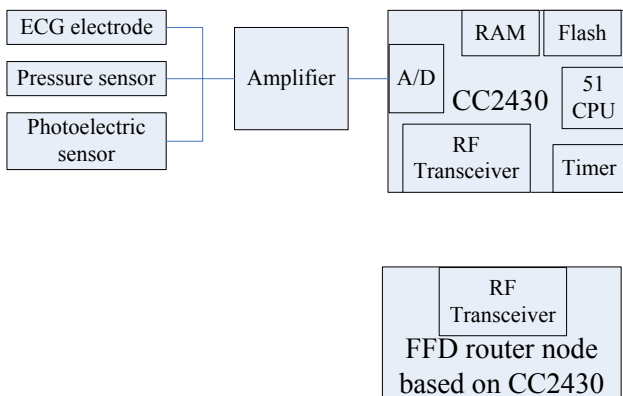


Fig. 4 Block diagram of the hardware

2. Data transmit model

There are two models of information transmission in the healthcare network. The one is that the doctors at the monitoring station give enquiry request for the physiological parameters. The orders are transmitted to the sensor node at home through ZigBee wireless network. The sensor node then completes signal acquisition immediately and then returns it to the center node.

The other is the mode that request of transmission is initiatively put forward by the user and then wait for the confirmation from center node. If the request is confirmed the other data transmission process is the same as model 1. In other words, the application layer in the development of communication protocol, the centre node is the host, and the sensor node is the Subordination. Sensor node data transmission software flow chart is shown in Figure 5.

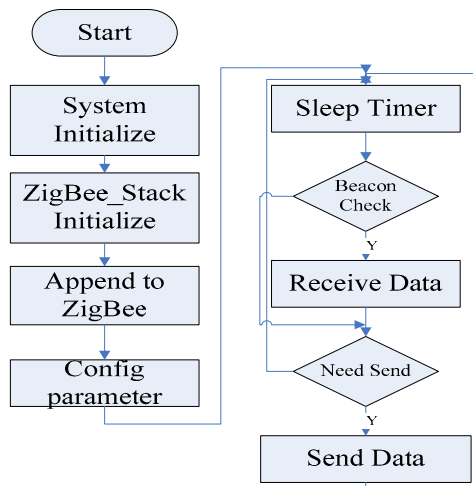


Fig. 5 Sensor node data transmission software flow chart

E. Result

Construct the ZigBee network hardware platform using CC2430 and download the relevant source node in each node. We made the test of sending and receiving between 4

nodes and achieved preliminary results. The data from the sensor node can be received through ZigBee wireless and then displayed on the connected PC.

III. CONCLUSIONS

In this paper, the community healthcare network based on ZigBee technology break the traditional medical model to promote the new concept of healthcare, and make full use of this popular ZigBee technology and the network for patients with chronic illnesses such as heart disease is useful for continuous monitoring. The paper also proposed a model for the future healthcare system that the hospital is at the core, and the communities, families and individuals connect to the internet through wireless LAN, leading to the formation of an organic system, to ensure that people both in the hospitals, and outside the hospital, and even in remote areas can receive timely, effective and professional medical diagnosis and treatment recommendations. It thereby greatly raises the level of healthcare, so that people's quality of life getting better and better.

REFERENCE

1. Li Jin, Cheng Shaoyan, Li Jialin et al. (2007) Wireless Sensor Network Based on ZigBee Technology. N Chin J Measure and Control Technology 26(8):63-65
2. David Geer. (2005) Users Make a Beeline for ZigBee Sensor Technology. N Engl J Computer 12(38):16-19.
3. Ang Zhimin, Jin Haihong, Fan Zhiguo et al. (2007) WSN Node Design and Communication Realization Based on ZigBee Protocol. N Chin J Modern Computer 249:47-49, 57

Author: Chai Jihong, Yang Hongli
 Institute: Electronic and Information Engineering Institute, Shenzhen Polytechnic
 Street: Xili Lake
 City: Shenzhen
 Country: China
 Email: chajih1979@163.com, szyhl@126.com

A Design of Mobile Monitoring System Based on Tradition Chinese Medicine

Zhicong Zhao, Qiong Liu, Xiaoming Wu, Shaojie Lin and Jumei Zhang

Department of Biomedical Engineering, South China University of Technology, Guangzhou, China

Abstract — Traditional Chinese medicine plays an important role in the medical realm of our country always for thousands of years. It is well thought by most of Chinese people and as much as world people. So in this paper we develop a mobile monitoring system with some skills of traditional Chinese medicine which are used for sickness preventive or diagnostic, e.g. taking stock of your color, hearing your sound, inquiring your feel, and taking your pulse. The scheme is set up by 5 sub-systems, namely a tele-video camera system, a tele-auscultating system, an IP-phone system, a tele-pulse taking system and Chinese Medicine assistant diagnosis system. The design is shown in Figure 1.

Keywords — Diagnostics of Chinese Medicine, tele-medicine, GPRS/3G, Mobile Monitoring System, the wearable technology.

I. INTRODUCTION

According to the investigation of Ministry of Public Health, in China, because of the high cost of the medical treatment, there are more than 50% people who haven't received proper treatment when should see a doctor.

Tele-medicine, benefited from the technology of tele-communication and information, is an activity, which serves patients medical help for a distance away from hospital [1]. The Tradition Chinese Medicine is an integrated knowledge, with tradition Chinese medical theory and practice as main body, studying the rules of the health and disease transformation about human being, with sickness prevention, diagnosis, and treatment, healing and health care. It is relative to modern medicine [2]. Therefore, it is an important subject of tele-medicine to research fulfilling long-distance Diagnostics of Chinese Medicine. With the function of cell phone and PDA diversification through the net of GPRS nowadays and 3G in future, we can achieve 24 hours mobile monitoring online about some human physiological parameters such as ECG and human pulse. Also, patients can receive mobile video consultation. We can exertion the advantages of Chinese Medicine in disease prevention and health care. The cost of medical treatment will be cut if this design succeeds.

II. THE DESIGN OF CHINESE MEDICINE MOBILE MONITORING SYSTEM

The Chinese Medicine mobile monitoring system is made by 5 sub-systems, namely a tele-video camera system, a tele-auscultating system, an IP-phone system, a tele-pulse taking system and Chinese Medicine assistant diagnosis system. The design is shown in Figure 1.

The tele-video camera system: Nowadays, cell phone has a camera. We can use this camera to take pictures of our face and tongue. Then, these pictures are sent to Chinese Medicine service center through GPRS or 3G network.

The tele-auscultating system: we can use the general electronic stethoscope to gain the user's heart sound and breathe sound. Then, these sounds are uploaded to Chinese Medicine service center.

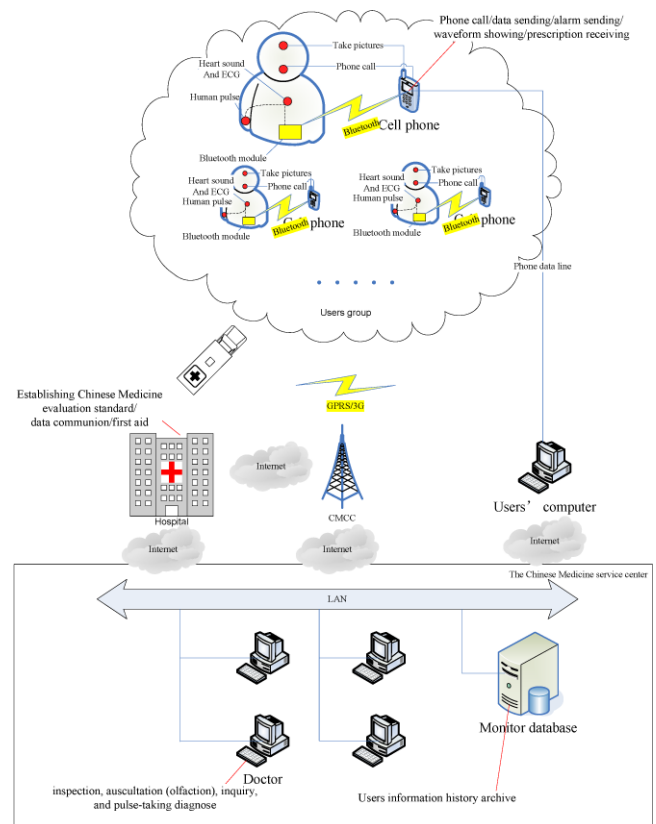


Fig. 1 The Chinese Medicine mobile monitoring system

The IP-phone system: there is an IP-phone in the Chinese medicine service center. Thus, users can receive the mobile long-distance video consultation.

The tele-pulse taking system: in this paper, a pulse taking device is cited [3]. The human pulse is obtained, and then sent to the center.

The Chinese Medicine assistant diagnosis system: in the Chinese Medicine service center, it receives data or IP-phone from users group. We can analyze these physiological data such as human pulse, ECG and heart sound in this system. Also, the pictures of users get division and analysis. Combining to the database of Chinese Medicine evaluation standard, it offers information about Chinese Medicine assistant diagnosis. In the system, it records the users' health care history.

III. THE SYSTEM FUNCTION DESIGN

A. The wearable pulse taking device

According to the Chinese medical literatures [4, 5], it is said that there are 29 wave patterns of the pulse, each having a specific name. The location-organ relationship, as shown in Figure 2, cannot be understood and needs to be substantiated by a scientific method. Therefore, a preferable pulse taking device is cited in this paper [3].

There are two types of PVDF (poly vinylidene fluoride) sensors cited in this paper. The first type of sensor can be used to measure the movement of Chun, Guan and Chy three parts of human pulse waveform. Each part has four measurement points, totally twelve points. This design offers a space concept about the human pulse analysis and eliminates the hap errors for single point measurement at the same time. The second type of sensor is used to measure the differences along the cross section of blood vessel in order to obtain its' change rules. There are nine measurement points juxtaposition in a column. The space between

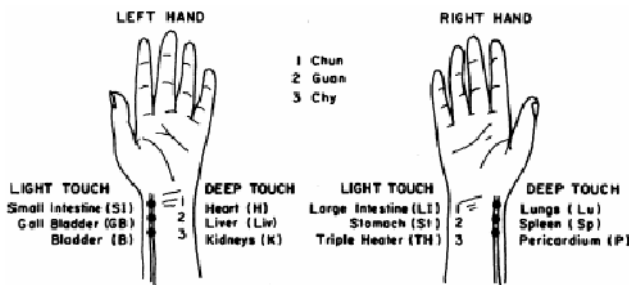


Fig. 2 Positions for pulse diagnosis used in traditional Chinese medicine. The relations of the positions with the organs are based on "Classic on Pulse" written by Wang Su Ho (265-317 A.D.).

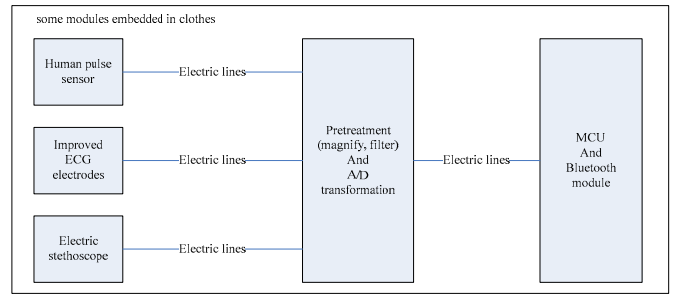


Fig. 3 Some modules and electric lines are embedded in clothes

each point is 1mm. The thickness of these sensors is both 35um. The area of single measurement point is 1.5mm by 1.5mm. Because of the thickness of PVDF sensor and multipoint detection, the method of down-lead becomes a big problem.

All electric lines are embedded in clothes. The principle is shown in Figure 3.

B. The wearable electrodes of ECG

According to the Einthoven's trigonometry, we can put the electrodes of ECG on three points, right arm (RA), left arm (LA) and left leg (LL). Then, we can get the standard conductance of ECG. In the improved Einthoven's trigonometry, these three points are instead by beneath right clavicle, beneath left clavicle and beneath left abdomen. All these electrodes and conductance lines are embedded in clothes as Figure 3.

C. The wearable electric stethoscope

The electric stethoscope module is set in the compositive clothes. Then, we can listen in heart sound and breathe sound.

D. The relay module in clothes

As a module of relay device, it is linked by others modules electric lines. After A/D transformation, it sends data to mobile phone. In this module, it includes the magnifying and filter circuit, A/D transformation, a MCU and Bluetooth module.

E. The multifunction GPRS/3G mobile phone

There are a camera, great capacity memory stick, Bluetooth module and GPRS/3G communication module in this mobile phone. It receives data from relay module. Then, we can carry out the simple characteristic pick-up, data long-

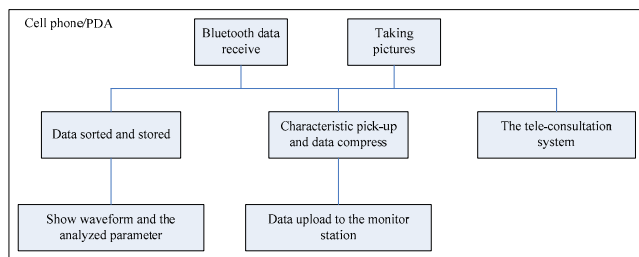


Fig. 4 GPRS/3G mobile phone monitoring system

time continuously storage, sending physiological parameter data and face and tongue pictures through GPRS/3G network to the Chinese Medicine service center. Also, users can have IP-phone video consultation. All these functions are shown in Figure 4.

Users can send data to the center according to different requirements. The following shows some requirements:

Sending data for a period: users can set up a sending period. Thus, the compressed data are sent to the center through GPRS/3G network.

Abnormity instance: when users' are abnormal, such as heart rate out of gear, this platform will send the alarm to the Chinese Medicine service center.

Sending manual: when having the long-distance consultation, user can send the data manually.

Sending 24 hours monitoring data through Internet: all these methods above are sending via GPRS/3G wireless network. Owing to the limited of wireless network transmission bandwidth and the charge, these data, which are compressed, are snippets. The 24 hours monitoring data are stored in the mobile phone memory stick. Thus, users can send these data to Chinese Medicine service center through Internet.

F. The Chinese Medicine service center

It receives the users' data. Then, data are archived and stored. After characteristic pick-up and combining to the database of Chinese Medicine evaluation standard, it offers information about Chinese Medicine assistant diagnosis. Users can accept doctor's health care prescription.

IV. RESULTS

In our scheme, the communication system and image display can work well now, including the Bluetooth module for stethoscope and pulse detector, which can communicate with a cell phone, the data transmitting and receiving well between cell phone and center server through GPRS, the

images taken by cell phone and shown on the screen of the center server and the information detected is archived. However, the techniques for the pulse detecting and analysis are still taken into account. The design of olfaction diagnosis system is now being built.

V. CONCLUSIONS

Our system developed the advantage of Chinese medicine in tele-medicine, from which a doctor can put up remote diagnosis with Chinese methods. The users can get daily health care properly with little incident, e.g. medicine diet, rest and exercise advice etc, and sometimes carry through Chinese therapy, such as acupuncture therapy. We advocate "treating before disease" and all we do can mitigate the pain of patient and the cost for care. This system will be improved continually, such as adding the olfaction diagnosis, virtual palpation diagnosis and being combined with Western medicine physiological survey, e.g. ECG, body temperature, breathing frequency etc.

ACKNOWLEDGMENT

This work is supported by Guangdong Province Science and Technology Plan (2007B031302003, 2007B010400055 and 2004B10401012). We are grateful to Guangdong Province Science and Technology Department.

REFERENCES

1. Perednia DA, ALLEN A. Telemedicine technology and clinical applications[J]. JAMA, 1995;273(6):483.
2. Zhou QH. Development limitation and future of traditional Chinese medicine [J]. Zhongyi Jiaoyu (Educa Chin Med), 1998;17(5):7.
3. JIN Guanchang, YU Miao, BAO Naikeng, Research of multi-point pulse wave computer measurement system using PVDF [J]. T singhua Univ (Sci & Tech), 1999;39(8):117~120.
4. Su Ho Wang (265-317AD) The classic of the Pulse(in Chinese) reprinted by Wen Kuan Publishing C O., Taipei Taiwan, ROC. 1972.
5. S. Y. Wang et al, Graphical Expression of pulse-wave pattern in Pulsology in orthodox Chinese medicine (in Chinese), National Science Council Monthly, Vol.5, No.8, P.688-697, Taiwan, ROC. Aug. 1977.

The address of the corresponding author:

Author: Xiaoming Wu
 Institute: Department of Biomedical Engineering
 Street: South China University of Technology (The South Campus)
 City: Guangzhou
 Country: China
 Email: bmxmwus@scut.edu.cn

A ZigBee-based wearable Cardio-Pulmonary Monitor for Mobile Health Care

Junnan Han, Yanhui Chen, Dongsheng Xiong, Xiaoming Wu

Department of Biomedical Engineering, South China University of Technology, Guangzhou, China

Abstract — A ZigBee-based wearable cardio-pulmonary monitor for mobile health care is introduced in the article. The monitor, which detects cardio-pulmonary parameters, exactly the heart rate, R wave and respiration rate, makes the mobile medical care available in the wireless communication way via ZigBee. Only three surface electrodes (Ag-AgCl) have been used in the device for cardio-pulmonary parameters detection. The acquired physical data are sent to the serve station via the ZigBee, where the data can receive the further analysis and the results can be stored properly. With the help of the wearable wireless monitor, both efficiency and quality of medical care will be greatly improved. In addition, not only the pain those patients suffered but also the death rate of the ICU patients will be significantly decreased. The device has the advantages of low cost, low power consumption, miniaturization and high comfortableness.

Keywords — ZigBee, cardio-pulmonary detection, mobile health care

I. INTRODUCTION

A. Background information

Medical monitoring devices, one kind of the most important medical devices in medical service system, have become an indispensable device in the area of monitoring, medical care and emergency [1]. Besides, Cardio-pulmonary diseases have become the most threatened killer to human lives. The most effective way to prevent patients from suffering from the diseases is to monitor the symptoms of the diseases as soon as possible. As the development of electronic technology and wearable sensor network, the change from the conventional method of cardio-pulmonary parameters detection to the wireless parameters measurement is available. The target of the study is to implement a wearable device with the feather of low cost, low power consumption, miniaturization and high comfortableness. High accuracy of collected data is available under the nature measurement condition.

B. Configuration of system

A ZigBee-based wearable cardio-pulmonary monitoring system is composed of five main parts: physical parameters detection module, wireless communication module, base

station, central server and terminals. The physical parameters detection module mainly takes charge of detecting cardio-pulmonary signals as well as preprocessing. The improved electrode system has been introduced so that the device has been dramatically simplified. A 2-Leads ECG detection system, consisting of all of three surface electrodes, is integrated with the respiration function detection system which consists of two of surface electrodes. The strategy that combines the simplest circuit and compound digital processing is accepted in our design. The wireless communication module, exactly the ZigBee module, composes the Intelligence Body Area Network (IBAN) and implements the data wireless communication in short distance. The data will be sent to the base station in wireless way and the data will receive further modification and analysis. The base station acquires the data from patients in the room where it is set. Then, the results will be delivered to the central server and displayed in the terminals of each department of the hospital through the network. In the meanwhile, the results will be stored properly in the database of the central server so that the doctor can easily find out the historical records of patients over the future. The cardio-pulmonary monitoring system structure is showed as Fig. 1.

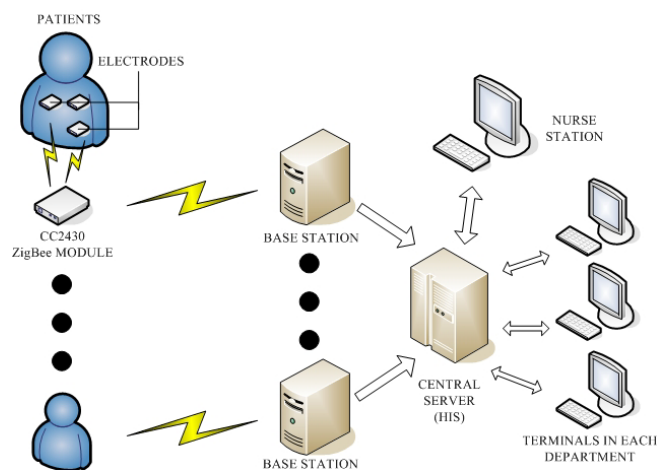


Fig. 1 The structure of the system

II. METHODS

A. ECG detection

ECG, served as the most significant physical parameter, not only reflects the cardiac function of human beings but also includes other information about human health conditions. For the ECG signals, its range is about 10uV~5mV and frequency range is between 0.05 Hz to 100Hz. In the detection course, the EEG, respiration signals and other noises will decrease the signal noise ratio (SNR) of the system, even worse the ECG will be submerged completely.

In order to solve the problem mentioned above and make the detection circuit as simple as possible, the improved electrode system, which only has three electrodes (Ag-AgCl), is introduced in the device [2]. The signals of lead I and II are available and can match the needs of monitoring, which pays much attention to the heart rate and R wave. The detection circuit of ECG, which should have the advantages of high input impedance and high CMRR, is mainly composed of four parts, including preamp, band pass filter, notch filter and main amp. Due to the frequency range of R wave, the four-order Butterworth filter with cut frequency of 35 Hz is used in the circuit and the gain of the whole circuit is about 800. The acquired signals will be transferred to digital signals in MCU after preprocessing and sent to the base station wirelessly via ZigBee. The structure of the circuit is showed in Fig. 2.

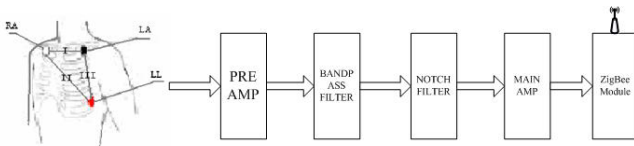


Fig. 2 Structure of circuit

B. Pulmonary signals detection [3]

Respiration system, regarded as the most important organ in the metabolism process, takes charge of inhaling fresh air, exchanging the air inside the alveolus and emitting CO₂. According to the physical structure, respiration system is susceptible to different pulmonary diseases.

Impedance method is introduced in the detection module. The MCU that integrated with CC2430 is used to produce the square wave with frequency of 62.5 KHz and amplitude of 5V. Then the square wave is used to stimulate the respiration signals via the electrodes of RA and LL. The acquired signals will be transferred to digital signals in MCU after preprocessing, such as preamp and filtering.

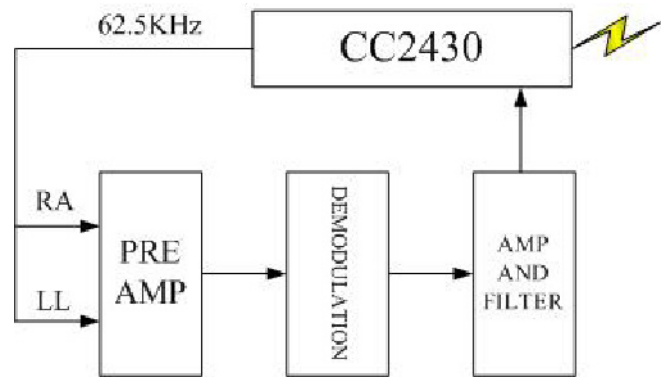


Fig. 3 Respiration detection flow chart

C. IBAN based on ZigBee

Intelligence Body Area Network (IBAN) [4], based on wireless sensor network, will become the indispensable part between wearable medical devices and abroad network for data exchanging. In our design, ZigBee (CC2430) has been used to make up the IBAN. The structure of the IBAN is showed as Fig. 4.



Fig. 4 IBAN

ZigBee [5], a novel short distance, low speed wireless communication technology, is suitable for medical service domain. It has the following advantages: ① low speed between 10 to 250 Kbps; ② low power consumption, AA battery is enough for up to 2 years use; ③ low cost and free protocol; ④ large capacity, up to 255 devices; ⑤ short time delay, usually between 15 to 30 ms; ⑥ security; ⑦ proper valid distance, usually between 10 to 75 meters, which meet the needs of indoor use; ⑧ high frequency compatibility.

D. Base station and processing technology

Base station, set in the patient room, is used to acquire the data from patients via ZigBee. In the data exchanging process, the ZigBee modules in the base station and on patients are performed as main devices and secondary de-

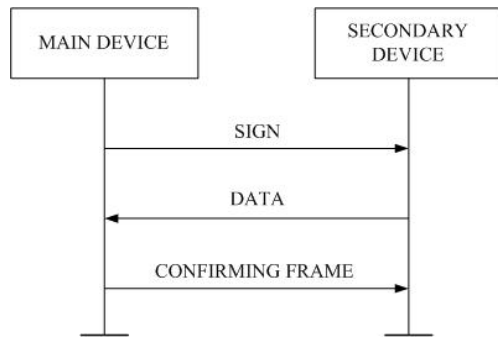


Fig. 5 Flow chart of data exchanging

vices respectively. When system works, first the secondary device sends the data to the main device in the preset format immediately when sign that the main device produced is detected; second the main device sends the confirming frame to the secondary device when all the data have been received successfully. The transmission process is showed as Fig. 5

Though the data that sent to the base station have been modified, the further processing in the base station is necessary for picking up characters of signals and calculating relevant value that reflect the index of health statue. In this stage, digital filtering^{[6][7]} is introduced in order to filter the noise signals that analog filter can not filter completely, such as 50 Hz signals. Wavelet is also used to help us find out the character points which are of significance in the calculating course.

III. RESULTS

With our novel monitoring device, the parameters of cardio-pulmonary can be measured respectively. Though small noise signals are still exist, original physical signals be can detected via the hardware circuit. The 50Hz signal and other noise signal can be increasingly restrained through the digital notch filter and the 4-order Butterworth filter. The characters of cardiogram and respiration wave can be easily distinguished in the signal sequence. The valid distance for the wireless data communication is nearly 100 meters in theory and more than 20 meters in practice, which has already meet application need in the sickroom. After the further processing in the base station, the heart rate and respiration rate is accessible. Other parameters that reflect the fitness index of cardio-pulmonary function also can be calculated for the further application.

IV. CONCLUSION AND SIGNIFICANCE

From the results above, we can easily see from the results above that the new wearable cardio-pulmonary monitor has already reached the goals we expect. The traditional physical parameter monitor will give way to the new generation monitor based on wireless communication technology. With the help of the wearable wireless monitor, both efficiency and quality of medical care has been greatly improved. In addition, not only the pain those patients suffered but also the death rate of the ICU patients has been significantly decreased. In the near future, the application is intend to expand from hospital to the community, even to the homecare.

ACKNOWLEDGMENT

This work is supported by Guangdong Province Science and Technology Plan (2007B031302003, 2007B010400055 and 2004B10401012). We are grateful to Guangdong Province Science and Technology Department.

REFERENCE

1. Shuhua Yue, Meihan Wang, Fei Guo, Zhaohui Meng, Jing Bai. Present status of the wearable wireless ECG. *BME & Clin Med*, July 2006, Vol. 10, No. 4
2. Thaddeus R. F. Fulford-Jones, Gu-Yeon Wei, Matt Welsh. A Portable, Low-Power, Wireless Two-Lead EKG System. *Proceedings of the 26th Annual International Conference of the IEEE EMBS*.
3. Jinsong Guo, Qinkai Deng. The Design of a Wearable ECG and Respiration Sensor Vest and its Monitoring System. *Chinese Journal of Medical Instrumentation*, 2006, Vol. 30, No. 5
4. Steve Warren, Jeffrey Lebak, Jianchu Yao, Jonathan Creekmore, Aleksandar Milenkovic, Emil Jovanov. Interoperability and Security in Wireless Body Area Network Infrastructures. *Engineering in Medicine and Biology 27th Annual Conference*. 2005.
5. ZigBeeover-iew [EB/OL]. <http://www.ZigBee.org/documents/Zig-BeeOverview4.pdf>.
6. Xingming Long, Jing Zhou. The Design of 50 Hz band stop Filter Based on MATLAB and Its Application in ECG Signal Preprocessing. *Journal of Chongqing Normal University (Natural Science Edition)*, Sep. 2003, Vol. 20, No. 3
7. Hansheng Yang, Ming Li, Chenwu Yang, Li Liu. A Design for the Digital Butterworth Filter. *Electrical Measurement & Instrumentation*, Apr. 2006, Vol. 43, No. 484

Development of telemonitoring system for PCG by telephone transmission

Dong Wang¹, Xingming Guo¹, Shouzhong Xiao² and Ming Ke²

¹College of Bioengineering, Chongqing University, Chongqing, China

²Bo-Jing Medical Informatics Institute, Chongqing, China

Abstract— The researcher development an telemedicine system for PCG based on telephone. The system mainly comprises of three modules: Portable PCG monitoring instrument, telephone communication network and hospital monitoring center.

The portable PCG monitoring instrument is used for heart sound signal capturing, processing and analyzing. This instrument is consist of five functional parts: piezoelectric heart sound sensor, heart sound signal pre-processing module, laptop computers, printer and heart sound signal processing software. The hospital monitoring center established a PCG database server. And the PCG database system is developed via SQL server 2000 software, applying VC++ 6.0 programming software to implement database access.

The remote PCG monitoring system is as safe as using a stethoscope, low-cost, and is able to combine with other cardiac function evaluation methods for synthetically analyzing the measured results.

Keywords— Heart sound, PCG, telephone, telemonitoring, database.

I. INTRODUCTION

Detecting and analyzing heart sounds is an important and economical method for determining the state of the heart and great vessels. Some of the lesions in the cardiovascular system firstly lead to heart sound changes and heart murmur generation is able to be found by heart auscultation before abnormal ECG signal generating.

In some circumstances, particularly in remote areas or developing countries, auscultation may be the only means available. Furthermore, when portability and clinical versatility are important considerations, the search for a new

portable and telemonitoring system device capable of robust and reliable analysis of heart sounds is not only justified but highly desirable. This paper, presented a remote PCG monitoring, which is not affected by the factors of times and places, working in a real-time mode, non-invasive, etc.

II. MATERIALS

The remote monitoring system based on telephone communication network is shown in Fig. 1. The telephone communication network is used to transmit the datas to monitor center, and then PCG displaying, recording and analysis are carried out in the monitoring center.

The portable PCG monitoring instrument is used for heart sound signal capturing, processing and analyzing. This instrument is consist of five functional parts: piezoelectric heart sound sensor, heart sound signal pre-processing module, laptop computers, printer and heart sound signal processing software. A piezoelectric heart sound sensor is applied to detect the acoustic vibration produced by the heart mechanical actions. The heart sound signal pre-processing module includes an adjustable amplifier, a bandpass filter circuit (30hz~1000hz) and a 12-bit A/D convertor. This module deals with biomedical signal capturing and conditioning. The signal processing software is programmed by Visual Basic.

The hospital monitoring center established a PCG database server. And the PCG database system is developed via SQL server 2000 software, applying VC++ 6.0 programming software to implement database access. The database server has achieved the functions of login authentication, heart sound signals reception, transmitting and analysis,

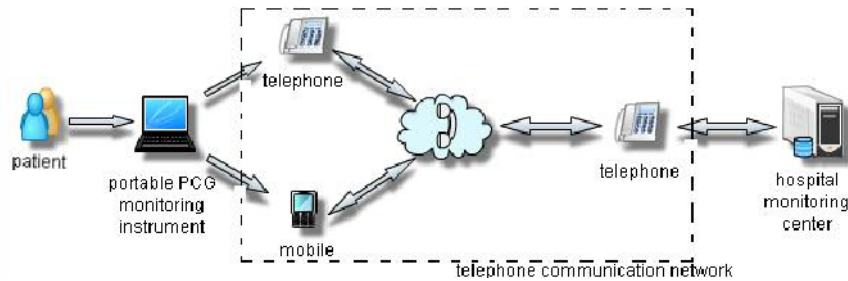


Fig. 1 The structural principle of whole system

PCG display and print out, and reviewing the previous recordings, heart sound data storage, and management of patient information, etc.

III. METHODS

A. Basis for the methods

Previous studies shown that there is a very close relationship between the amplitude of the S1 and the heart contractility. The animal study by Hansen showed that changes in the amplitude of S1 are found to correlate closely with changes in the maximum rate of rise of left ventricular pressure ($r = 0.9551, P < 0.001$) [1].

B. Relative value method

The absolute value of the first heart sound(S1) amplitude can not be used to evaluate cardiac contractility, as it is affected by some factors, such as the thickness of the chest wall,etc. However, some indicators of relative value can be used to evaluate cardiac contractility and cardiac reserve mobilization level:

1.The amplitude of S1 under different stress conditions, with respect to amplitude of S1 recorded at rest is defined as cardiac contractility change trend (CCCT), which is used to evaluate cardiac contractility and cardiac reserve mobilization level.

2. The maximum amplitude ratio of S1 and the second heart sound (S2) (S1/S2), as shown in Fig. 1, is used to evaluate the dynamically changing relation between cardiac contractility (CC) and peripheral pressure, including up-regulating condition of CC during stress.

3. The ratio of the amplitude of S1 at the tricuspid valve auscultation area to the amplitude of S1 at the cardiac apex (T1/M1), which is used to evaluate the relative change of cardiac contractility between the right and left heart.

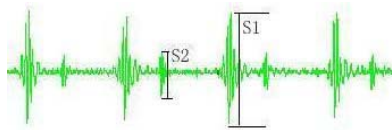


Fig. 1 Amplitude measurements of S1 and S2 of a record

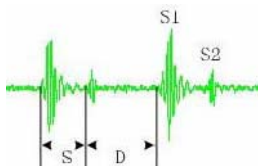


Fig. 2 Time domain measurements of diastolic and systolic

4. The ratio of diastolic to systolic duration (D/S) ,as showing in Fig. 2, is used to evaluate the time of blood flowing to the heart per se during diastole.

C. Evaluation of usability of this method

The correlation between this method and established methods was significant in Table 1.

The advantage of this method being :simultaneously observe CC and heart rate,giving new indicators for the heart (D/S, S1/S2, etc),simultaneously analyze cardiac contractility variability (CCV)[2] and heart rate variability (HRV)as well as their relation, simultaneously analyze CCCT[3] and heart rate change trend (HRCT) as well as their relation, simultaneously analyze cardiac contractility recovery trend (CCRT)[4] and heart rate recovery trend (HRRT)after a stress as well as their relation, etc[5].

Table 1 The correlation between indicator CCCT from this method and established ones

Established method	Indicator	Correlation
Oxygen uptake	Metabolic equivalent (MET)	$r=0.900, p<0.01$
Echocardiogram	Maximal elastance (Emax)	$r=0.702, p<0.05$
Echocardiogram	Ejection fraction reserve	$r=0.728, p<0.01$
Left ventricular x-ray contrast examination	Ejection fraction	$r=0.790, P<0.001$

IV. SYSTEM TEST RESULTS

The Fig.3 presents an example of heart sound recording displayed as a PCG.The heart sound in Fig. 3 was sampled at a rate of 11025 samples per second ($f_s = 11025 \text{ Hz}$).The researchers transmit the original heart sound signal (ORS) by two ways: mobile (M) to telephone (T) and T to T. The Fig. 4 is the received wave through M to T, Fig. 5 is the received wave through T to T. The test result is showed in Table 2.

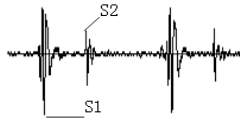


Fig. 3 The original heart sound signal



Fig. 4 The received wave through M to T



Fig. 5 The received wave through T to T

Table 2 The signal transmitting result

	ORS	M to T	T to T
HR	72	71	71
S1/S2	1.867	1.650	1.684
D/S	1.776	1.738	1.800

V. CONCLUSION

As long as there is an telephone communication network, the system can work. The remote PCG monitoring system is noninvasive, low-cost, and is able to combine with other cardiac function evaluation methods for synthetically analyzing the measured results. The monitoring instrument can be used in ward monitoring, in the daily heart health care for the patients at and as a portable phonocardiograph for doctor.

It is a practical system for remote and ward PCG monitoring, clinical diagnosis, in the daily heart health care for the patients at home and as a portable phonocardiograph for doctor, PCG research and teaching in medical colleges.

ACKNOWLEDGMENT

The authors would like to thank Professor Shouzhong Xiao and Professor Xingming Guo for their continued support of this research.

REFERENCE

1. Hansen PB, Luisada AA, David J, et al. Phonocardiography as a Monitor of Cardiac Performance During Anesthesia. *Anesth Analg*, 1989; 68(3):385-387.
2. Shouzhong Xiao, Cai Shaoxi, Liu Guochuan. Studying the Significance of Cardiac Contractility Variability. *IEEE Engineering in Medicine and Biology*, 2000; 19 (2):81-84.
3. Shouzhong Xiao, Zhigang Wang, Dayi Hu. Studying cardiac contractility change trend to evaluate cardiac reserve. *IEEE Engineering in Medicine and Biology*, 2002; 21 (1):74-76.
4. Chen L, Tian T, Xiao S, Peng C. Comparative study of cardiac contractility recovery trend and heart rate recovery trend based on simultaneously telemetering cardiac contractility and heart rate signals after exercise. *Acta Biophysica Sinica*. 2004; 20(5):403-407.
5. Xianglin Fang, Xingming Guo, Shouzhong Xiao. An exploration on the influence of exercise and respiration on heart rate and the amplitude of heart sound. *Beijing Biomedical Engineering*. 2002; 21(2): 126-129.

Author: Dong Wang
 Institute: College of Bioengineering Chongqing University
 Street: 174 shazheng street, Xiaoping district
 City: Chongqing
 Country: PR China
 Email: cqdong@hotmail.com
 Tel.: 023-62205190,

Research in Development on Wireless Health Care of Infants

Lili Zhang, Li Lao, Kai Wu, Qiong Liu and Xiaoming Wu

Department of Biomedical Engineering, South China University of Technology, 510006, Guangzhou, China

Abstract — The recent advances in physiological parameters monitoring, biosensor design, wireless communication and computer architecture have enabled the realization of integrated, miniature, low-power, intelligent wireless health care system for monitoring infants. Wireless health care system of infants improves monitoring conditions, community medical and health services not only by monitoring infants safely, reliably, continuously and dynamically, but also by achieving real-time transmission, display, analysis of the infants health information and alarm the crisis. This paper highlights the latest researches and achievements in this field and also gives a guide to pivotal techniques in wireless health care system of infants. At last, we give a lucid perspective of the development of wireless health care of infants in future.

Keywords — Wireless Health Care of Infants, Wearable Technique, Miniature and Low-power Wireless Sensor Technique, Adverse Biological Effects.

I. INTRODUCTION

Continuous monitoring of physiological parameters for infants is necessary because infants are very vulnerable and cannot feedback health complaints. The demand of physicians and parents for monitoring system which is more compact and easier to handle is the motivation for the development on wireless health care of infants. Another motivation is the concern frequently expressed by physicians or parents about the danger of apparently life threatening events (ALTE) or even the problems of Sudden Infant Death Syndrome (SIDS).

Due to infants' premature, vulnerable and tiny nature, there are several important techniques for monitoring infants safely and reliably. One is fully integrated, ultra-miniature physiological monitoring technique and biosensor design for the infants' special physiological status. It will allow the early detection of potential life threatening events more comfortable and easier for infants calling for rescue as well as the recognition of the development or progression of diseases at an early stage. The other is intelligent wireless sensor network and compact, mobile wireless communication for continuous, convenience monitoring of infants under clinical and home conditions. It imposes on the dynamic network topology design and wireless mobile station function prototype design to provide clinicians and parents reli-

able, in-time, ambulatory, convenience service of the infants physiological information.

On the base of the integrated, ultra-miniature biosensor design and wireless sensor network, we highlight portable physiological monitoring technique, especially the ultra-wearable wireless body sensor network, such as Sensory Baby Vest, Baby Sleep Safe, Baby Glove in this paper, including their functionality, safety and washability. In addition, this paper gives a comprehensive look at the challenge on reducing wireless radio frequency radiation which may cause the adverse biological effects of infants.

II. METHODOLOGY AND TECHNOLOGY

A. Monitoring technique

According to the different causes of ALTE and SIDS, there are a variety of monitoring techniques for health care of infants.

Direct monitoring technique: Monitoring physiological parameters of infants is the direct and regular monitoring method for evaluating health conditions and detecting life or health threatening events.

- Monitoring multiple physiological parameters will make a reliable, safe and accurate health care service of infants come true. For example, Carsten Linti et al developed a sensory baby vest [1] which including fully integrated sensors for continuous monitoring multiple physiological parameters of infants, such as respiration, heart rate, temperature, humidity(e.g. by sweating).
- Monitoring single, pivotal physiological parameter can lessen the operation of health care system and achieve an increase in the comfort of infants, when giving a reliable health care service of infants in a certain extent. With an increased risk of SIDS, these infants have an increased risk of cardiac arrest. A continuous measurement of the electrocardiogram(ECG) is necessary and important for these infants. Based on this, J.Coosemans et al developed a wireless ECG monitoring system [2] which integrated into textiles to measure the ECG of infants continuously.

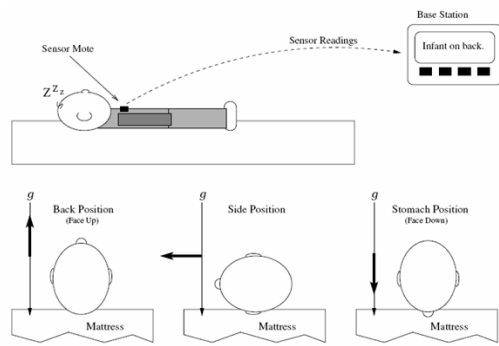


Fig. 1 SleepSafe baby monitor

Non-direct monitoring technique: The early detection of potential life threatening events and the recognition of the development of disease at an early stage can be realized not only by monitoring physiological parameters, but also by other forms of information, such as infants’ position, movement.

According to American SIDS Institute’s datum, infant sleeping on its stomach is up to 12.9 times more likely to die from SIDS [3]. Therefore, some wireless health care systems of infants utilized 3-axis accelerometer which is contained in the wireless mote to sense infants position relative to gravity, such as SleepSafe’s SHIMMER mote attached to infants’ clothing [4] and BBA bootee’s mote [5]. The principle of SleepSafe baby monitor detecting infant sleeping position is shown in Figure 1 [4].

Other researches show that SIDS may happen to healthy infants without any identifiable physiological preconditions and it usually happens during sleeping without any warning signs, such as crying, struggling [6]. Accordingly, HungCuo et al considered that an effective respiratory monitoring system may be a good way for early warning to reduce SIDS risk. So they used CO₂ sensors to non-invasively monitor the exhaled air from an infant. By monitoring the outputs of CO₂ sensors, it can detect if there is anything wrong with the infant’s respiration [7].

Mixed monitoring technique: Combining physiological parameters and other forms of information, Yves Rimet et al designed a special infant shoe named BBA bootee, integrating sensors, electronics and power supply. It is a newly developed system for wireless monitoring of pulse oximetry (SpO₂), actimetry and position in infants [5].

B. Wireless Sensing Application

Wireless sensing technologies play a key role in wireless health care system [8]. It shows great potential to significantly enhance the biometrics performance. The benefits of wireless sensing technology are already apparent: portabil-

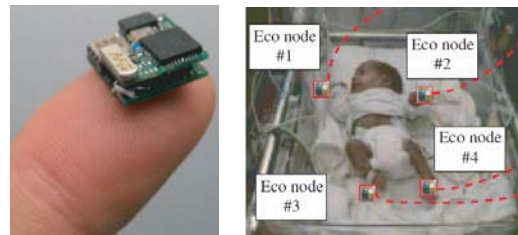


Fig. 2 Eco and its application

ity, convenience, ease of installation and low cost. Wireless health care system of infants, unlike other health care system, poses prominent characteristics to engineers. Typically, there are following several kinds of wireless sensing technologies that would augment the applications of health care system of infants.

Wearable wireless sensing: The advances in integrated, ultra-miniature biosensor design, wireless sensor network, textile materials and textile-compatible technologies have enabled the realization of ultra-wearable wireless sensing application.

To be wearable by a pre-term infants, such a wireless sensor node must occupy less than 1cm³ and weigh under 3 grams [9]. Therefore, ultra-miniature sensor is one of the pivotal techniques in wireless health care system of infants. Typically, Eco shown in Figure 2 (left) is a self-contained, ultra-wearable, expandable and low-power wireless sensor platform under 1cm³ [10]. Pai H.Chou et al used up to four Eco on pre-term infants arms and legs to monitor the spontaneous motion of them to assess infants growth in bones and muscle strength in response to assisted exercises as shown in Figure 2 (right) [11].

Integrating wireless monitoring sensors, antenna, interconnects, processing and transmission circuitry into textiles materials is another excellent application of wearable monitoring system. As an alternative to conventional electrodes, both knitted and woven stainless steel electrodes were developed [12]. They are less irritating than gel electrode. These dry electrodes are implemented on the inner surface of the garment consisting of a conductive silicone rubber printed on the textile substrate. In addition, stainless steel has a low toxicity. Conductivity is obtained by silver particles [1]. The yarns can be manipulated as a textile material and can be washed without losing their properties.

With the rapid development of wearable monitoring technology, the ultra-wearable health care system, such as Sensory Baby Vest, the Baby Suit, the Baby Glove and the BBA bootee have been made like ordinary baby clothes. They can be handled and worn practically as a common baby clothes while keeping the efforts for fixing wireless sensors at the infant’s body on a minimum level as shown in



Fig. 3 Baby Glove (left) and BBA bootee (right)

Figure 3 [4][5]. The perfect design of wearable monitoring system makes these textiles more suitable and convenient.

- The elasticity of the textiles assures a good contact between the baby and electrodes. For example, the adjustable straps in BBA bootee can ensure contact between the SpO₂ sensor and skin and permit to fit the bootee to the foot as the infant grows from one size to another. These textiles also can be designed in several sizes to suit the different age of infants, such as BBA bootee [5].
- All of the sensory baby vest, the baby suit, the Baby Glove and the BBA bootee can be washed when the circuit or the electronic sole be removed [1][2][4][5].

Non-wearable wireless sensing: Monitoring the infants' behavior, position and physiological parameters in the everyday life space will open the way to health care system of infants. Especially based on digital home environment [13] or telemonitoring system [14], wireless health care system of infants could make parents take care of infants more easily and safely in the future home. These following newly systems are recommend.

- Infant monitoring system using CO₂ sensors [6] around the crib on the bars can provide an effective respiratory monitoring of infants as shown in Figure 4 (left) [6]. The processing board connected to sensors is placed outside the crib including a wireless module for transmitting and receiving data. With RFID integration, this system also can be used to monitor a large number of infants in the nursery room.
- A set of instrumented toys equipped with a variety of sensors for behavioral analysis of infants in minimally environmental conditions have developed recently [15]. A sensorized ball shown in Figure 4 (right) [16] is small enough to be grasped with a single hand by a 1 year old child. It is able to sense both the orientation in 3D space and linear acceleration, as well as a force sensing unit, to detect grasping patterns during manipulation for ecological behavioral analysis of infants to diagnose neurodevelopmental disorder at an early stage.

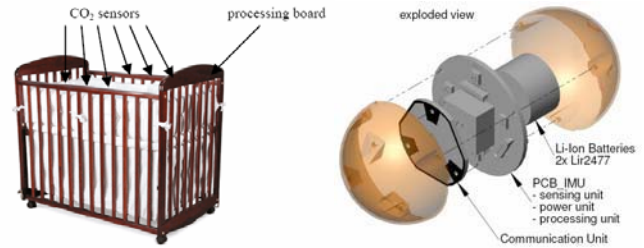


Fig. 4 Infant monitoring system using CO₂ sensors around the crib (left) and a sensorized ball (right)

- Infant drowning prevention system [17] can prevent infants from drowning injury by measuring the wave motion of water in bathtub at home.

III. DISCUSSION

Wireless technology has been enhanced health care system apparently. At the same time, wireless health care system faces a few problems and challenges. For example, the quality of wireless communication, such as security, credibility and coexistence between the different kinds of wireless communication technologies. Moreover, wireless health care system of infants poses prominent problems and challenges for infants' particular medical application. Of all these challenges, safety problems related to radio frequency radiation is the most important one. According to the equivalent Coefficient-of-Absorption-and-Bioeffects (CAB), transmission power, traffic load, data rate of wireless sensors are influence factors which we can control by software or hardware design. The following technologies and methods could be taken to ease parents and physicians' worry of wireless radio frequency radiation.

- A low-power, ultra-compact wireless sensor platform design plays an important part in reducing the adverse bioeffects and the bulk and cost of wireless sensor [9]. The low-power platform design mainly involves system architecture and radio communication. For system architecture, implementing runtime abstraction in software (e.g. Tiny OS) into all WSN nodes, a multi-core MCU architecture and larger flash memory components can lead to lower power at the system level. For radio communication, choosing high efficiency antennas (e.g. chip antennas) and developing suitable MAC protocols (e.g. Z-MAC) also is a practical method.
- Reducing the number of electrodes and placing the wireless sensors away from infants would be adoptable and useful, too. For example, the Baby Glove prototype

used the same electrodes to monitor the pulse rate and hydration with its own respective circuitry [4].

- According to CAB, relevant control algorithm should be developed to reduce the adverse biological effects caused by wireless radio frequency radiation. For instance, Hongliang Ren and Max Q.-H. Meng [18] have developed power control algorithm and a price-based rate control algorithm in wireless biomedical sensor network.

IV. CONCLUSIONS

Depending on the great development on the integrated, miniature, low-power, intelligent wireless health care system and the further research on the cause of the ALTE, SIDS and the adverse bioeffects effects when using wireless technology, there must will be an expansive application on monitoring of infants under clinical and home conditions for the evaluation of health conditions, diagnostic reasons and the detection of life or health threatening events. These techniques improve monitoring conditions, community medical and health services not only by monitoring infants safely, reliably, continuously and dynamically, but also by achieving real-time transmission, display, analysis of the infants health information and alarm the crisis. So it can reduce the happen of SIDS efficiently and accelerate the build and intelligence growth of infants. The integrated, miniature, low-power, intelligent wireless health care system will give a great promotion on the rapid development on the wireless health care system all over the world.

ACKNOWLEDGMENT

This work is supported by Guangdong Province Science and Technology Plan (2007B031302003 and 2007B010400055). We are grateful to Guangdong Province Science and Technology Department.

REFERENCES

1. Carsten Linti, Hansjürgen Horter, Peter Osterreicher, Heinrich Planck (2006) Sensory baby vest for the monitoring of infants, Proceedings of the International Workshop on Wearable and Implantable Body Sensor Networks (BSN'06)
2. J. Coosemans, B. Mermans, R. Puers (2005) INTEGRATING WIRELESS ECG MONITORING IN TEXTILES, The 13th International Conference on Solid-state Sensors, Actuators and Microsystems, Seoul, Korea, June 5-9, 2005, pp 228-232
3. American SIDS Institute Website at <http://www.sids.org>
4. Chris R. Baker, Kenneth Armijo, Simon Belka et al (2007) Wireless Sensor Networks for Home Health Care, 21st International Conference on Advanced Information Networking and Applications Workshops (AINAW'07)
5. Yves Rimet, Yves Brusquet et al (2007) Surveillance of infants at risk of apparent life threatening events (ALTE) with the BBA bootee: a wearable multiparameter monitor, Proceedings of the 29th Annual International Conference of the IEEE EMBS, Cité Internationale, Lyon, France, August 23-26, 2007, pp 4997-5000
6. Hung Cao, Lun-Chen Hsu et al (2007) An Infant Monitoring System Using CO₂ Sensors, 2007 IEEE International Conference on RFID, Gaylord Texan Resort, Grapevine, TX, USA, March 26-28, 2007, pp 134-140
7. Hung Cao, Lun-Chen Hsu et al (2007) A non-invasive and remote infant monitoring system using CO₂ sensors, IEEE SENSORS 2007 Conference, pp989-992
8. Hongliang Ren, Max Q.-H. Meng, Xijun Chen (2005) Physiological Information Acquisition through Wireless Biomedical Sensor Networks, Proceedings of the 2005 IEEE International Conference on Information Acquisition, Hong Kong and Macau, China, June 27 - July 3, 2005, pp483-488
9. Pai H. Chou (2006) Challenges on Low-Power Platform Design for Real-World Wireless Sensing Applications, pp1-4
10. Chulsung Park, Pai H. Chou (2006) Eco: Ultra-Wearable and Expandable Wireless Sensor Platform, Proceedings of the International Workshop on Wearable and Implantable Body Sensor Networks (BSN'06)
11. Chulsung Park, Jinfeng Liu, Pai H. Chou (2005) Eco: an Ultra-Compact Low-Power Wireless Sensor Node for Real-Time Motion Monitoring, pp398-403
12. M. Catrysse, R. Puers, C. Hertleer, L. Van Langenhove, H. Van Egmond, D. Matthys (2004) Towards the integration of textile sensors in a wireless monitoring suit, Sensors and Actuators A, 2004, 114, pp302-311
13. HyunJeong Lee, ShinYoung Lim, JaeDoo Huh. Design and Implementation of Baby-care Service based on Context-awareness for Digital Home, pp908-911
14. S. Singh, H. Hsiao (2003) Infant Telemonitoring System, Proceedings of the 25th Annual International Conference of the IEEE EMBS, Cancun, Mexico, September 17-21, 2003, pp1354-1357
15. Domenico Campolo, Massimo Molteni (2006) Towards Development of Biomechatronic Tools for Early Diagnosis of Neurodevelopmental Disorders, Proceedings of the 28th IEEE EMBS Annual International Conference, New York City, USA, Aug 30-Sept 3, 2006, pp3242-3245
16. D. Campolo, E. S. Maini et al (2007) Design of a Sensorized Ball for Ecological Behavioral Analysis of Infants, 2007 IEEE International Conference on Robotics and Automation, Roma, Italy, April 10-14, 2007, pp1529-1534
17. Yoshifumi NISHIDA, Keigo HIRATSUKA, Hiroshi MIZOGUCHI (2007) Prototype of Infant Drowning Prevention System at Home with Wireless Accelerometer, IEEE SENSORS 2007 Conference, pp1209-1212
18. Hongliang Ren, Max Q.-H. Meng (2006) Bioeffects Control in Wireless Biomedical Sensor Networks, 2006IEEE, pp896-904

The address of the corresponding author:

Author: Xiaoming Wu
 Institute: Department of Biomedical Engineering
 Street: South China University of Technology (The South Campus)
 City: Guangzhou
 Country: China
 Email: bmxmwus@scut.edu.cn

The research of medical services sharing platform base on semantic web services

Yuan Yao¹, Hai Wang¹, Qing-xi Hu¹, Gao-chun Xu¹, Di Wu¹

¹Rapid Manufacturing Engineering Center, Shanghai University,
Shanghai 200444, P. R. China

Abstract — with the people have higher demands for medical services, the medical information systems and related ancillary analysis and data services of base on medical information technology and network technology obtained the rapid development. Open public medical services platform faces the problem of the platform how to reduce semantic information deletion and conflict when different services interaction. This paper analyzes the semantic and construction of medical services sharing platform base on semantic web services. By uses the semantic web services technology construction the frame and data interface of medical services sharing platform. The purpose is solves the problem of semantic information deletion and conflict when different services interaction, realization the construction of medical services sharing platform base on semantic web services, thus provide a effective system platform that can publishing discovery and application medical services for medical mechanism.

Keywords — web services, ontology, medical services sharing platform, HL7RIM, medical information systems

I. INTRODUCTIONS

With the people have higher demands for medical services, the medical information systems related ancillary analysis and data services of base on medical information technology and network technology obtained the rapid development. Open public medical services platform faces the problem of the platform how to reduce semantic information deletion and conflict when different services interaction. There are several standardization efforts to digitally represent clinical data such as HL7 CDA, HER com and open EHR. These EHR standards, which are currently under development, aim to structure and markup the clinical content for the purpose of exchange. All of the EHR standards are based on reference information models. EN 13606 (EHRcom) is a five-part standard consisting of the Reference Model, Archetype Interchange Specification, Reference Archetypes and Term Lists, Security Features and Exchange Models. Currently, however, only the reference model (EN 13606-1) is stable, whereas parts 2 - 5 are still working drafts.

The HL7 Clinical Document Architecture (CDA) is a document markup standard. It specifies the structure and semantics of "clinical documents" for the purpose of ex-

change. CDA documents are encoded in Extensible Markup Language (XML) and derive their meaning from the HL7 Reference Information Model (RIM) and use the HL7 Version 3 Data Types. Document-level, section-level and entry level templates can be used to constrain the generic CDA specification.^[2]

However since there are more than one standard, it is still difficult to achieve interoperability and today the clinical data is mostly stored in proprietary formats. This paper researches the medical services sharing platform base on semantic web services. The purpose is solves the problem of semantic information deletion and conflict when different services interaction, realization the construction of medical services sharing platform base on semantic web services, thus provide a effective system platform that can publishing discovery and application medical services for medical mechanism.

II. ONTOLOGY

People are drawing increasingly attention to the research development and application of ontology since from the concept of ontology to be introduced by Niches. A ontology is an explicit, partial account of a conceptualization/ the intended models of a logical language. An abstract model of a phenomenon termed 'conceptualization', Ontology a precise mathematical description hints the word 'formal', the precision of concepts and their relationships clearly defined are expressed by the term 'explicit' and the existence of an agreement between ontology users is hinted by the term 'shared'.^[1]ontology is a semantic foundation communication in different subject (human machine software system etc) of domain internal^[1].it can promote the data sharing data exchange and knowledge reuse between human with heterogeneous system. It also promotes the automatic or semi-automatic reasoning of intellectual.

III. THE ONTOLOGY MODELING BASED ON THE EXTENDED HL7RIM VOCABULARY(WSO)

The integration of healthcare information system is difficult points of information integration domain. It involves many information systems (such as HIS PACS and RIS)

and application fields (such as Epidemiology and Gene Medical). It also uses many medical application protocols (such as HL7 Open EHR EHRcom and ENV13606) and industry standard (such as ICD SNOMED and LOINC UMLS). The many data sources make lack of effective sharing mechanism between different hospitals. [3]The WSO integrates the structure information integration method and semantic information integration method. It encapsulates the different medical system into unified service resources by the web services and middleware technology. It establishes semantic correlation of data model based on HL7RIM vocabulary. Meantime, the independence of the different medical field ontology is guaranteed. It supports the semantic mapping operation based on ontology^[4]. RMO using mixed ontology method and web service technology construction correlation ontology. Figure 1 show the frame of level. The prototype of father ontology (HL7RIM ontology) of all levels ontology is converted to OWL (ontology Web language) by HL7 modeling, then implementation it by introduction OWL to protégé 2000.

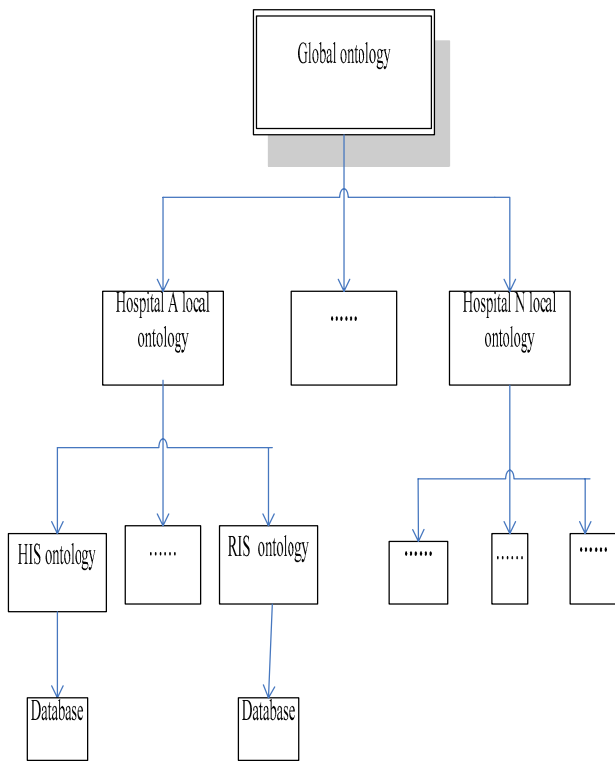


Fig. 1

IV. FRAMEWORK OF MEDICAL PLATFORM FOR SEMANTIC WEB SERVICES

THE ARCHITECTURE OF MEDICAL PLATFORM

As mentioned the framework of medical platform as the execution environment for Semantic Web Services has two operational aspects the registration and the execution of Semantic Web Services. Figure 2 presents the framework architecture and its most important components.

The Registration process (see Figure 3) is used to reregister descriptions of entities with the medical platform. The ontology Editor is used to create the description of the Web Services ontology and goals. These descriptions are passed to the Compiler for validation and for storing the compiled data in the repository.

The Execution process consists of two phases: the Discovery and the Invocation of Web Services. The first phase identifies those Web Services that suit the requester goal; the second phase makes the actual invocation of the selected Web Service.

In the Discovery phase, the Matchmaker matches the capability of Web Services in the Service Repository against the requester goal and returns a set of Web Services. The Selector component chooses one Web Service that best suits the requester preferences.

In the Invocation phase, the Communication Manager invokes the selected Web Services. As in the previous case, the help of the Data Mediator may be required, this time to transform the incoming data from one concept validation (used by the requester) into another concept validation (used by the provider). Also the Choreography Engine is used to link the communication patterns (choreographies) of the requester and of the Web Service. The framework Manager implements the execution semantics of the system and offers the underlying mechanisms for an event-based architecture. The Resource Manager offers an abstraction layer to the persistence layer.^[5]

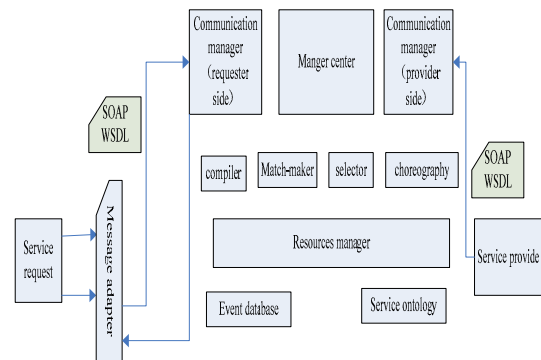


Fig. 2

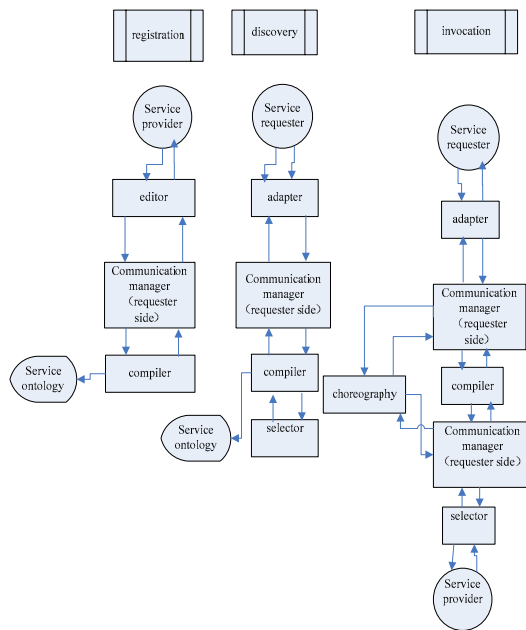


Fig. 3

THE COMPONENTS OF MEDICAL PLATFORM

This section describes in more detail the most important components of the medical platform architecture presented above. The medical platform offers default implementations for these components. These are connected to the architecture through a set of placeholders that have precisely defined interfaces; this allows external components to be easily plugged-in. Existing implementations of components can thus be replaced over time with alternative or more expressive implementations. In addition, using the same mechanism, the medical platform aims to offer dynamic discovery of Web Services having the same functionality as the default components, in order to achieve higher performance and accuracy^[6].

Adapters address a problem occurring even before the above mentioned interoperability becomes an issue, namely when trying to connect external systems to the medical platform. Although they are outside the medical platform architecture (see Figure1), we briefly describe them here to emphasize their role in overcoming data representation mismatches on the communication layer.

The Compiler component is responsible for checking the syntactical validity of WSMML documents and for storing the parsed information persistently. The Compiler is being used in both operational aspects of the medical platform (registration and execution). During the registration of services the Compiler reads a service description, validates and finally stores it. During execution of services the Compiler

reads a goal description, validates and stores it, after which the goal is passed to the management component in order to be resolved.

The matchmaking component is responsible for finding appropriate Web Services to achieve a goal. This component's input is a set of (existing) Web Services and a requester's goal; the output is a set of Web Services that can fulfill the goal. A different problem is finding the set of all existing Web Services (discovery); we have not yet addressed this (non-trivial) problem: the medical platform contains a local repository of known Web Services and can also use external (UDDI like) repositories.

The choreography of a Web Service defines its communication pattern, that is, the way a requester (which may as well be another Web Service) can interact with it. The requester of the service has its own communication pattern and only if the two of them match precisely, a direct communication between the requester and the provider of a service may take place.

The Communication Manager has two major tasks: first, to handle the various invocations that may come from requesters and second, to invoke Web Services and to retrieve the results of these invocations back to the medical platform (this could happen either as a consequence of a synchronous call or by a separate invocation of the medical platform in case of asynchronous calls)^[7]. Currently, even if a semantic description is provided for a certain Web Service capability (e.g. in order to register to the medical platform), the actual invocation still has to be made in a classical way, by representing all the data needed for the invocation in XML format. On the other hand, all the medical platform components and all its internal mechanisms operate using the semantic descriptions provided by WSO. In order to make the bridge between the semantic descriptions and the classical syntactic Web Service descriptions, the medical platform provides the necessary means for lifting non-semantic descriptions (e.g. XML messages and XML schemas) to a semantic level and to lower the elements semantically described (e.g. ontology instances and concepts) to the level required by the classical approaches. For accomplishing these tasks, additional, intermediary components need to be introduced to perform the lifting and lowering operations, the Adapters (addressed in a previous section). These two operations described above (i.e. lifting and lowering) may seem as burdensome and not very elegant from the Semantic Web Services point of view. But we believe that this is only an intermediary solution meant to compensate the current lack of fully semantically described Web Services (e.g. as WSO presents them) on the Internet. For Semantic Web Services described according to WSO specifications, the Communication Manager task is much simpler: no calls to Adapters are necessary, but only a simple invocation with

the proper data as the semantics of the service interface specifies.

V. CONCLUSIONS

This paper researches the medical services sharing platform base on semantic web services. Compare with traditional medical information sharing platform base on PACS (Pictures Archiving and Communication System) or HIS (Hospital Information System), the platform establish a unified formal medical resources ontology model and a clear description for service interface layer. It solves the problem of semantic information deletion and conflict when different platform interaction. On the basis of platform frame, this paper gives an example of the implementation of defect bone repair services. The experimental result shows, our medical sharing platform have greater improvement in flexibility maintainability and manageability. Thus the effectiveness of the frame of medical services sharing platform on reducing semantic information deletion and conflict is confirmed. I have done the useful attempt in medical services sharing platform base on semantic Web Service.

REFERENCE

1. Studer R, Benjamins VR, Fensel D(1998). Knowledge Engineering Principles and Methods. Data and Knowledge Engineer2ing, 1998, 25(122):161~197
2. QU Bin-Peng(2007) The system design and the technical discuss on telemedicine master paper for Shandong university 2007,5
3. Juha Myk,anena, Annamari Riekkinen, Marko Sormunena,Harri Karhunenb, Pertti Laitinenc(2007) Designing web services in health information systems:From process to application level international journal of medical informatics 76 (2 007) 89-95
4. PAN Lin, YU Lun, CHEN jin-xiong(2006) study on network architecture of a tele-medical information sharing platform.chinese journal of medical instrumentation 1671-7104(2006)-0293-03
5. ZHANG Kang—Kang LI Qing-Zhon(2004) Semantic-Based Information Interchange and Integration in Healthcare Application Integration computer science 2004V01. 31N9. 9
6. Tsai T-M. Yu Han-Kuan Liao Ping-Yao. Shih H-T(2003). Semantic modeling among Web services interfaces for services integration—SOTA (smart office task automation) platform. In: Proc. 14thIntl. Workshop on Database and Expert Systems Applications. Sept. 2003. 579~ 583
7. <http://www.dam1.org//services//owl-s//1.0//owl-s-wsd1.html>

Author: YAO Yuan
 Institute: shanghai University Rapid Manufacture Engineering Center
 Street: 99 Shangda Rd
 City: shanghai
 Country: china
 Email: wanghai4774@sohu.com

HealthED: An Opened Integrate Healthcare IT Architecture

Y. Yao¹, Q. Wang¹, Z. Sun² and Q.X. Hu¹

¹ Rapid Manufacturing Engineering Center, Shanghai University, 200444, Shanghai, P. R. China

² Department of Oral Medicine, Ninth People's Hospital, 200011, Shanghai, P. R. China

Abstract — New information technologies provide the technical possibility to solve problems of healthcare information sharing and process integration. This paper proposes an open architecture to support medical services registration and provide healthcare information solutions for the new requirements, from the view of both patients' and clinicians'. It can serve as a complementary part of the current clinical informatics system, which combines the provider-based integration approaches with patient-centered approaches and supports cross-institutional cooperation. Several demonstration healthcare applications are developed to test the usability and performance of this architecture.

Keywords — Enter up to five keywords and separate them by commas.

I. INTRODUCTION

Modern healthcare system is facing the ageing of population, the high medical expenses, burden of travel and many other issues. Now new needs proposed by patients and clinicians are more than any time in the past. For instance a correctly clinical decision often need to be made based on complete medical information and many cross-industry analyzing tools within several clicks, which brought new challenges to the current healthcare systems. Those requirements not only include the virtual integration of distributed patient health record but also the scientific medical analyzing service, the real-time monitoring of the health status and other cross-institutional medical cooperation. This indicates the needs for better health service architecture to improve health application integration.

Several related research projects have been already developed for healthcare information sharing and healthcare applications integration from 1992. GEHR projects[1] realized the first a federated healthcare record system. Followed by Synapses[2], Inter-Care[3], OpenEMed[4] and openEHR[5] projects. The objects of these works are all focused on record information sharing. With the development of service-oriented architectures (SOAs), new web technologies and wireless sensor technology provide the technical foundation to solve more complex application integration in healthcare system. PICNIC[6] project gave specification and deployment of a generic cross-institutional ICT architecture for regional healthcare networks. A peer-

to-peer architecture for decentralized, open healthcare networks, which uses information mediation and a sophisticated patient ID management method, is currently developed in the ARTEMIS project[7].

The projects mentioned above is far from complete, but indicates a trend towards provider-based integration approaches[8]. From the point of application patient-centred architecture[9] is a few easy to realize but more complex to control especially in large-scale commercial application. Azyxxi(Amalga)[10], using a special way, receives data from all the relevant hospital systems, stores the data in a real-time repository, and makes it available through a variety of tools to meet a variety of needs. The Microsoft's HealthVault[11] and the coming Google's Health project are typical provider orientated healthcare service. As dependant commercial provider the service content is limited by the capacity of the specific company.

Based on the analyzing of various published approach and projects we believe that integrated healthcare service hold by any dependant commercial corporation, government departments or healthcare facilities cannot satisfy the practical need. Healthcare information and applications integration is a large-scale project especially in countries like China. In this paper we propose an open provider oriented healthcare architecture HealthED. Following parts are discussed within it:

- A service description model is developed to define medical services.
- The most important components of the HealthED architecture are described in more detail.
- 3. It consists of a few simple building blocks

The healthED can serve as a complementary architecture for the current clinical informatics system, which combines the provider-based integration approaches with patient-centered approaches to support cross-institutional cooperation and health data sharing.

Three main objectives are achieved under this architecture: 1) providing a patient-centered health care information system for health information sharing between different hospitals; 2) providing an immediate ways to access the disease information or scientific analyzing tools for treatment process; 3) providing healthy situation awareness services for patient or the elderly people in need of care. Any inde-

pendent Internet Content Provider can carry out their own healthcare service under this framework, which serve as the supporting platform for patients, enterprises, research institutes and hospitals.

The remainder of this paper is organized as follows. In the second chapter, the three main parts of the architecture are discussed in detail. Based on this research, three different healthcare services are realized, which are currently evaluated in HealthED, a pre-research project, located in the website <http://www.healthevery.cn>. Finally, a conclusion and discussion of this architecture is presented.

II. ARCHITECTURE

A. Defect of Traditional Architecture

The core technology in conventional integrated healthcare IT system is the health records integration, which is called integrator-based strategy. The end user provider (hospitals, healthcare facilities) extracts health information from special provider systems using a jointly agreed information model. This approach simplifies application integration and patient data retrieval and allows for a smooth scalability for integrated system of different size. This approach applies in particular to small and medium-sized region. For instance, in Europe certain strategy may be applied locally, regionally, nationally, or may even be built as a cascade of several integrator components linking up from local to national level[8]. However, in countries like China with large population base and huge difference of medical conditions in different regions, the integrator model is not adaptable. In practice the concentration of a large amount of patient-related data cannot be guaranteed to synchronize immediately in such model. Because of the same reason the uniform authorization infrastructure is easy to design but it is hard to establish.

In the common integrate healthcare system data-oriented and process oriented integration models are the most common form. From a data oriented view, materialized integration is usually operated with a central repository on national or regional level. In contrast, a mediator-based approach[8] is capable of integrating various sources on demand. It can be defined as a middleware system, which translates global queries to the local resources and integrates local results to a virtual view on a comprehensive integrate healthcare service. Typical process-oriented approaches are service-oriented architectures[12]. Compare with materialized integration it split the integration task between information sources and consumers. A typical service-oriented model is the registry-repository integration pattern. The registry holds the location of service. The patient's health information,

that may be stored in various repositories, is retrieved by this service, which constructs a virtual integration model.

In an idealistic virtual integration model, patient record remains solely in digital archives and is accessed only on demand. However, some issues also constrain practicability of the virtual model:

- Responsibility for patient-centered information integration is shifted from the information provider to the healthcare provider. Depending on the registry-repository pattern, indexing and retrieval systems have to deal with locating various resources, integrating heterogeneous information models, and mapping different patient identifiers.
- The healthcare provider has to guarantee long-termed, permanent and liable availability of information, which may require outsourcing to an external service provider. This means a tremendous workload and a business model which is hard to achieve.
- Virtual sharing patient information is difficult because the decision about publication of these data is left to patient, healthcare facility and content service provider.

Speak from the source the reason that traditional architecture still not be widely used is its complicated structure can not form a complete business model.

B. Architecture

The HealthED is a useful architecture which is designed for both healthcare information sharing and healthcare process integration. By introducing an internal healthcare service model definition it allows dynamic discovery, invocation and composition of exist healthcare Web Services. In order to establish a viable business model HealthED provides an opened framework for both Health Service providers and requesters. As a healthcare service provider, one may register its service using HealthED in order to make it available to the consumers, as a healthcare service requester, one can find the healthcare service that suits their needs and then invoke them with HelathED API or HealthED customized service.

HelathED itself is made available as a Web Service, so either for finding a healthcare service or for actually invoking Web Services a requester has just to invoke HelathED itself. In the healthcare service finding process, a formal description of requester goal has to be provided, and in healthcare service invoking process request, the actual data the requester wants to process in the invocation should be provided. In this way, HealthED can take care of all the other required computations such as sub-service finding, composition, security or quotation. Any Internet Content

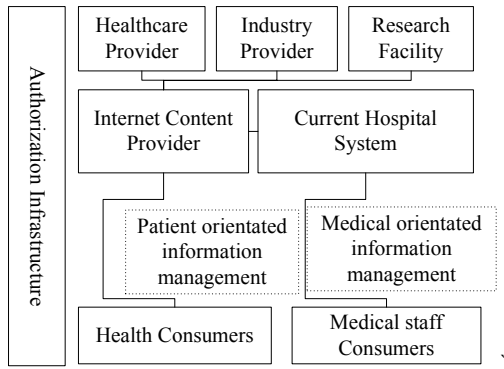


Fig. 1 Simple Function Component in HealthED architecture

Provider can use this architecture to establish their own commercial healthcare integration system.

Figure 1 shows the simple implementation component in HealthED architecture. The cooperation between Internet Content Provider(ICP) and Current hospital system(or others function provider) can be seen as a B2B operation. The ICP serves as a central point of a hub-and-spoke architecture which holds the user health information and healthcare service registry. In HealthED any healthcare service is published as a Web Service. If two partners want to communicate they only abstract their functionality to HealthED. HealthED itself is a Web Service, so if the applications offer their functionality as a WSDL interface no adapters need to be developed.

Figure 2 presents the HealthED architecture and its most important components, which is established with four layers: (1) User layer forming several groups of end users of the architecture, (2) Application layer building the application environment for user layer to access to the architecture, (3) Service Manager layer provides the intelligence searching, integration and interoperation of business services, and (4) Healthcare Service Providers layer exposing the functionality of back-end systems as Business Services.

User layer defines the various users groups which use the functionality of the architecture for various purposes. Two basic kinds of user groups are identified: users, and engineers. Users include patients, medical staff and so on, which interact with the architecture through specialized applications. For example, patient can query or update their own health records, to give certain doctor authority to view or to perform a kind of healthcare test. In general, the goal is to allow users to interact with business healthcare processes while reduce their physical interactions with back-office operations. On the other hand, the engineer users perform development and administrative tasks in the architecture. These tasks should support the whole SOA lifecycle including service modeling, creation, publishing, and manage-

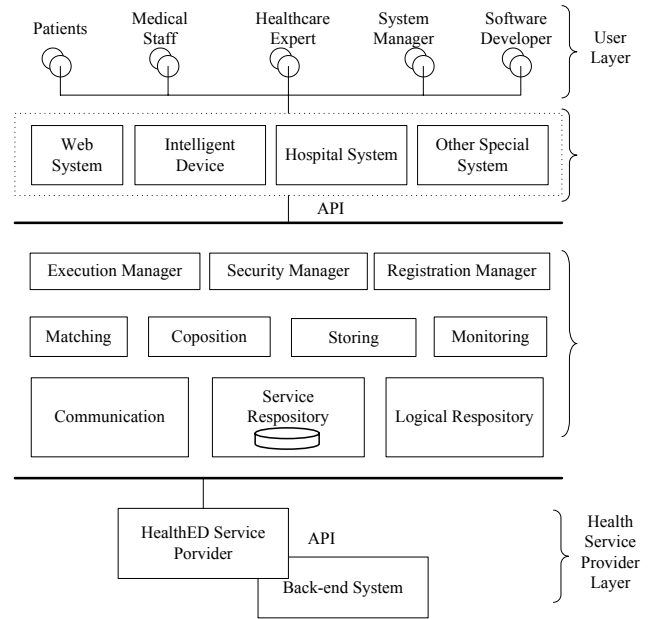


Fig. 2 HealthED architecture overview

ment. Different types of engineers could be involved in this process ranging from domain experts (modeling, creation), system administrators (deployment, management) and software engineers.

Application layer contains applications and devices which support the user layer by receiving of user requests and generates corresponding descriptions of such requests in the form of user goals. Through this layer, users can interact with the architecture in an intuitive way, i.e. the dental doctors want test the mechanical properties of ceramic crown the application layer will interact with the architecture during processing and get his/her desired results. Specialized applications built for specific purpose in a particular healthcare domain which also provides specific domain ontologies. The interaction between this layer and the service manager can be implemented depend on the HealthED API. In this project we develop a specialized ontology to describe the tissue engineering base skull repair process.

Service Management layer is the core of the architecture providing the main intelligence functions for the integration and interoperation of healthcare services. It consists of a number of services that can be further divided into the Manger group, Execution Component group and base group. In Manger group, the Service Execution Manager, Security Manager and Registration Manage are in charge of controlling specific service execution and secure communication and which are not visible to the Execution Components. The component of base group defines functionality

that is not directly required in a goal based invocation of healthcare services however they are required by the Service Management Layer for successful operation. Base group includes:

- **Communication:** Communication defines the message translation protocols of the architecture.
- **Service Repository:** Service Repository stores the entrance of the healthcare service.
- **Local Repository:** Local Repository stores the logic for service aggregation to satisfy certain goals or QoS requirements.

Healthcare Service Providers layer is a group of various special function systems which provide certain functionality for certain purpose. They can be exposed as a business web service to the architecture. However, they are not necessarily a complete medical services because of the HealthED can compose them depending on particular deployment and integration scenarios. They may originate from one organization (one service provider) or multiple organizations (more service providers) interconnected over the network (internet, intranet or extranet). The HealthED thus can serve various healthcare requests through Business to Business (B2B), Enterprise Application Integration (EAI) or Application to Application (A2A) integration. In all cases, functionality of special function systems is exposed as semantically described business services. (Because of the complexity of semantics, in the current implementation of healthED we are still using keyword matching method).

By providing client API and hiding the services integration detail. HealthED can establish a distributed healthcare provider network when such architecture is adopted by a number of independent business systems.

C. Execution Component

Execution component HealthED has given its default implementations for these components. These are connected to the architecture through a set of defined interfaces; this allows external components to be easily plugged-in. Existing implementations of components can thus be replaced over time with alternative or more expressive implementations. Using the same mechanism, HealthED can change the the implementation of default components, in order to achieve higher performance and accuracy(eg. Replace keyword matching with semantic recognition).

Matching component is responsible for finding appropriate web services to achieve a request. HealthED contains a local repository of known web services. This component's input is a requester's goal; the output is a set of web services that can fulfill the goal from the repository. A common situation is finding a set of all existing web services the

component will sort the list with matching degree and return the most suitable one. In the other hand, when there is no service matching the request's goal, the component can decompose the goal with certain logical(in Logical Repository) and return find corresponding service respectively then return a list of service. The current HealthED implementation use input and output of a service to decompose certain request. Quality of Service(QoS) parameters are still not considered.

The composition component is responsible for executing complex compositions of services in order to achieve a certain goal. The language for specifying these compositions is a complex task and still under consideration in healthED. We have considered two initial approaches, to use hard-coded format for composing goals and to embed the process flow in an external process language(like WS-BPEL). Given the component-based architecture of the HealthED we should change the implementation of this component if a more adapt method is found.

The Storing component is responsible for checking the syntactical validity of service description. The Storing component is being used in both operational aspects of HealthED (registration and execution). During the registration of services the Storing component reads a service description, validates and finally stores it. During execution of services it reads a goal description, validates and store, after which the goal is passed to the management component in order to be resolved.

Monitoring provides an independent repository for status query. It defines a monitoring of the execution of end point services, this monitoring may be used for gathering information on invoked services e.g. the processing status related or for identifying faults during execution, which allow the requester to monitor the state of request processing.

D. HealthED API

HealthED architecture exposes the service interface and of its functionality via an Application Programming Interface (API). It consists of a few simple building blocks to help developers build application. The API of mobile version is under developed.

Authentication: all HealthED service require authentication. Authentication API hide the relative authentication detail when invoke different services. For example, in the example application we developed in the next section a doctor can easily retrieve a patient's health records under his authentication.

Status: The Twitter API attempts to return appropriate status codes for every service invoking request. Here's what's going on with our various status codes. When the

HealthED API returns error messages, it will be encapsulated with a predefined XML format.

Request: Through pre-defined topologies and communications protocols, request API hiding the interact detail between application layer and the architecture that give an easy way for developing.

III. EXAMPLES

Based on the HealthED, the distributed healthcare process and patient record can be integrated in the same architecture. We use it to establish a serious of healthcare related services and client application to test the usability of the architecture, and to further improve the design of it. Three prototype system are shown as follows.

A. Health Monitor

The service providing long-term preservation of personal health record permits users to securely gather, store, manage and share their own and their family's health information anytime and anywhere, and with whom their choose. Preservation of the history of health records can help to realize the patient records sharing and promote a variety of new healthcare applications. For example, based on the health information an electronic private doctor service can be constructed. Our first demonstration HealthED application provides the similar function. Figure 3 shows the application design structure and user interface.

The designed of Health Monitor system follows a typical HealthED structure. Storage service and Health Expert service are published to HealthED independently. The Client service (running at Web Server and Call Center) is two part of one service. However, they use different register service and thus they can also be developed independently. There are two kinds of interface implemented in the Health

Monitor, through with users can update their health information and receive health tips by not only web browser but also mobile phone.

B. Patient Record Sharing

The aim of a traditional scalable electronic health records sharing system is providing the means to access all available clinical information, at a corporate, regional, national or even international level, and to meet challenges posed by patient mobility. Now, implementation of this demand is still very difficult because of the fact that an individual's health data may reside at many geographically dispersed information systems and not every hospital will preserve the history records. The provider-oriented and patient-centered method is a better way to solve this problem.

The other demand is security. The doctor cannot view a patient's record if not be authorized by the owner. In this demonstration application, we still use the storage service in Health Monitor to hold patient records. We add an Authentication service to deal with the process of one user give authentication to other client system.

Figure 5 shows the the Health Record Sharing system with authentication. Beside the Authentication service a Health Information(HI) application is deployed by a us (any ICP can deploy it) which is similar to the Web server in Figure 3. HI realizes an open business interface for public hospitals for patient health records query. Because of the complex of health information and inconsistent standards the Hospital System is implemented as part of ICP HI for hospital users.

The sharing procedure is simply with 2 steps: (1)the user uses mobile client(or web) choose the hospital he want to attendance and set it as an authentic unit; (2)the hospital users query and then get the results.

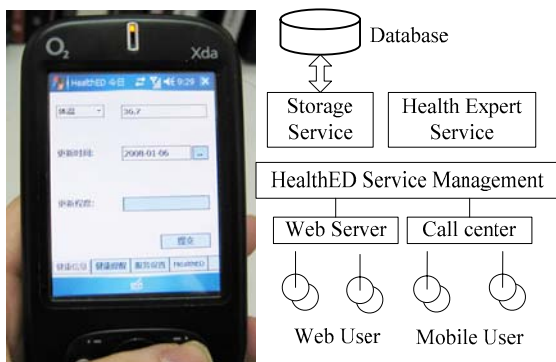


Fig. 3 Health Monitoring Design and Interface

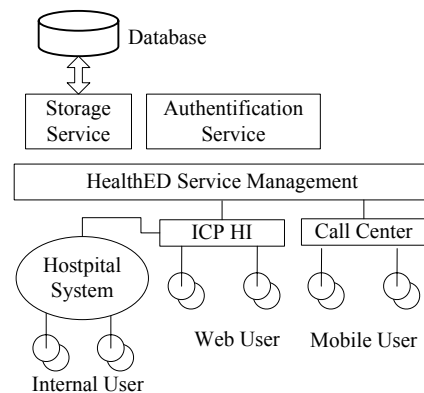


Fig. 4 Health Record Sharing Design

C. Root canal assisted analysis tools

The canal preparation is the most important step in dental therapy. Making finite element analysis in each preparation step is a complex task. The last demo application shows the service using multiple cross-industry processes.

As shown in Figure 5, under HealthED architecture this composition service is easy to design and implementation. However, its performance is poor. The reason is massive data streams unsuitable for transmission with message communication. This problem need to be further improved.

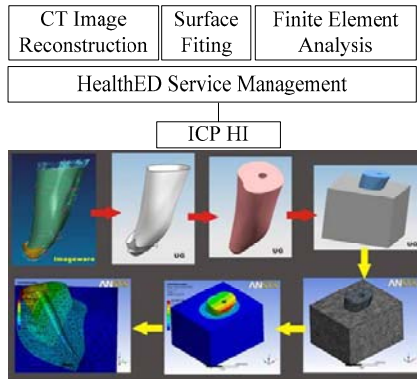


Fig. 5 Root canal analysis process

IV. CONCLUSIONS

Comparing with current healthcare systems, HealthED architecture presents independent and scalable medical services integration platform. Based on the architecture any services released by one provider may be integrated into different platform, which will promote more relevant enterprises to participate in the field of medical services and save the medical expenses while do not have large alterations to the existing health care information system. As a complementary part for current healthcare informatics system, the proposed architecture provides a cross-industrial solution and converts patient-centred system into provider-oriented architecture. It can help to deliver better care for less money within citizen-centred health delivery systems. In the cross-

field integration it still depend on too many "semantic bridges" defined for different source ontologies. Therefore the conversion mechanism in service management layer needs further evaluation.

ACKNOWLEDGMENT

This work is a pre-research project which is inspired by the tissue engineering base skull repair applications developed in National Natural Science Foundation of China (No. 60703029) and a Shanghai university doctoral project (Rapid Manufacturing Integration Platform). We would also like to thank to Shanghai ninth people's hospital for providing necessary medical data and test environment.

REFERENCES

1. J. Grimson, G. Stephens, B. Jung, W. Grimson, D. Berry, and S. Pardon, Sharing health-care records over the Internet, *Internet Computing*, vol. 5, no. 3, pp. 49-58, May2001.
2. J.Grimson, A CORBA-based integration using the synapses approach, *Biomedicine*, vol. 2, no. 3, pp. 124-138, 1998.
3. The InterCare Projects at <http://intercare.imsgrp.net/>
4. The OpenEMed Project at <http://openmed.sourceforge.net/>
5. The OpenEHR Project at <http://www.openehr.org/home.html>
6. The PICNIC Project at <http://www.medcom1-4.dk/picnic/>
7. The ARTEMIS Project at <http://www.srdc.metu.edu.tr/webpage/projects/artemis/index.html>
8. Joachim Bergmann, Oliver J.Bott, Dietrich P.Pretschner, and Reinhold Haux, An e-consent-based shared EHR system architecture for integrated healthcare networks, *International Journal of Medical Informatics*, vol. 76, no. 2-3, pp. 130-136, Mar.20070.
9. A.Shabo, A global socio-economic-medico-legal model for the sustainability of longitudinal electronic health records, Part 1. *Meth. Inf. Med.*, vol. 45, no. 3, pp. 240-245, 2006.
10. The Amalga Project at <http://www.microsoft.com/amalga/default.msp>
11. The HealthVault Service at [http:// and www.healthvault.com/](http://and www.healthvault.com/)
12. Thomas Erl, *Service-Oriented Architecture: A Field Guide to Integrating XML and Web Services* Prentice Hall PTR, 2004.

Author: Yao Yuan
 Institute: Shanghai University
 Street: Shangda Road
 City: Shanghai
 Country: China
 Email: yaoyuan@shu.edu.cn

Study of the Ballistocardiogram signal in non-contact life detection system based on radar

Jianqi Wang, Guohua Lu, Xijing Jing, Yang Zhang, Hao Lv

Faculty of Biomedical Engineering, Fourth Military Medical University, Xi'an 710032, China

Abstract — In this article, our study of non-contact method viaradar for monitoring the heart and respiratory rates of human subject is reported. The system is constructed which synchronously detects the lectrocardiogram signals by the electrocardiograph and the ballistocardiogram signals by the non-contact life parameter detecting technology. Also, the detected signals are analyzed respectively in the time and frequency domain. The results show that the cycle of the ballistocardiogram is obvious in time domain and that the rhythm of the two kinds of signals keeps consistent. And their characteristic points in frequency domain are also the same. The clinical medicine usefulness of ballistocardiogram detected by the non-contact technology is approved and the credible evidence for the succeeding signal analysis and the clinical application is provided. Furthermore, the characters of the heartbeat signal detected by our system and the reasons for that are also discussed in detail in our paper.

Keywords — Ballistocardiogram, non-contact, life detection, radar

I. INTRODUCTION

We have previously reported a non-contact method using microwave radar for monitoring the heart and respiratory rates of a human subject [1]. It's a new technology for detecting the Ballistocardiogram (BCG) signal, the carrier of which is the body jiggle signal caused by heartbeat in our detection system. Starr has reported that BCG can be used to predict disease of myocardial ischemia [2]. The succeeding research also proved that it could also be applied to the evaluation of medicine for circulation system and myocardial capability, the evaluation on the therapy effect, sleep monitoring, and also the physiological and psychology test. Because of its suitability for clinical application, the credible evidence for the succeeding signal analysis and the clinical application is needed to provide. In our previous study, we mainly resolved two problems existed in common: how to improve the SNR and how to restrain the strong randomness, time variability and sensitivity to the interferences produced by the moving objects [1]. To improve the SNR, the signal accumulation technique by FFT is used, which does not need the priori knowledge of signal and the period alignment [3]. In order to restrain the strong interferences produced by the moving objects, of which the

amplitude is much stronger than the body surface jiggle caused by their physiological activities[1], a dual filtering algorithm (DFA) is proposed, including two filters and one algorithm by tracing the interference spectral peaks [4]. The preliminary experimental results showed that the heartbeat signal could be well detected when the human subjects held their breath [5]-[6]. However the heartbeat can not be extracted effectively from the overlapped signals as the breath exists, since the minute chest movement caused by the respiration is stronger than the chest inching caused by the heartbeat, therefore, it is difficult to separate the latter from the overlapped signals. In order to make the detected signals easily visually analyzed by medical experts, the clearly display of heartbeat and breath signals is also required. Accordingly, the primary problem in processing signals received from the bio-radar is the separation of signals corresponding patient's heart activity from the signal mixture including, in addition to the desired signal, signals corresponding breath, body movement, interference and noise [7]. To effectively resolve the problems described above, the techniques of homomorphic filter, wavelet and narrow-band filter are used to extract the signal of breath and heartbeat. So the non-contact detection rate of life-parameters is promoted. The wavelet transform with Symmlet mother wavelet is applied. Experimental results demonstrated that the method integrating with the three signal processing techniques above is very promising in identifying the life-parameters via radar.

II. DESCRIPTION OF THE SYSTEM

The electromagnetic wave is generated by the oscillator via a directional coupler. Then it is radiated by the antenna via a circulator. The oscillator operates at 24 GHz, and the transmission power is 35mW. The output signal of the system contains both the respiration and heartbeat signals with serious noises. In our experiment it is sent to a pre-processor, where the 50Hz interference is removed by a band stop filter, and digitized by A/D converter. Finally, the signals are processed with the proposed techniques and displayed on the monitor (Fig.1.). ECG is one of the most widely applied clinical examination item. The body surface ECG is not only successfully applied to heart disease diag-

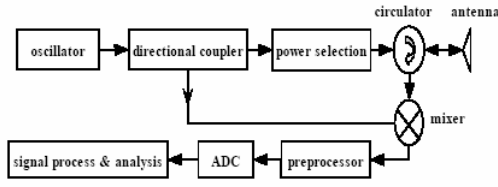


Fig. 1. The block scheme of the life-detection system.

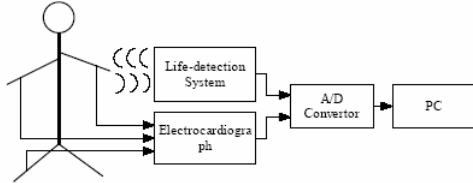


Fig. 2. The block scheme of the life-detection system.

nosis but also frequently acted as reference signal for various kinds of physiological measurement [8]. Our experiment was designed to synchronously gather the Ballistocardiogram and the ECG signal of the same subject and compare them in the time and frequency domain respectively (Fig.2).

A. Math

Though the SNR could be improved and the interferences produced by the moving human subjects around the system could be restrained, the principal component of the signal detected by the system is respiration. However, it is necessary to separate the heartbeat signal from the respiration signal when the system is used to monitor the patients in clinical application and so on. Since the minute chest movement is caused by both the respiration and the heartbeat, the possible biological ranges for heartbeat and respiratory frequencies are not well separated and higher-order harmonic components of the lower-frequency respiratory signal can overlap the heartbeat spectrum. Consequently, it's difficult to separate the heartbeat from respiration signal by using linear filters and the power spectrum estimation [9]. FIR digital filter and adaptive filter had been performed in our experiment, which could not produce the ideal results [1]- [10]. The frequency variation in the echo wave modulated by body surface jiggle caused by respiration and heartbeat is very low from 0.03Hz to 3.3Hz [10]. Because of the overlapped spectrum of the respiratory and the heartbeat signal, the signal processing methods used are expected to be very sensitive to the frequency variation with higher resolution in time domain. According to the requests of the signal processing described above, the wavelet transform may be used to separate the heartbeat from the respiration signal [11].

a. Principle

Wavelet transform is capable of providing the time and frequency information simultaneously, hence giving a time-frequency representation of the signal with a function of mother wavelet. The continuous wavelet transform can be defined as the inner product of the test signal $x(t)$ with the basis functions $\psi_{\tau,s}(t)$,

$$CWT_x^\psi(\tau, s) = \Psi_x^\psi(\tau, s) = \int x(t) \cdot \psi_{\tau,s}^*(t) dt \quad (1)$$

Where,

$$\psi_{\tau,s} = \frac{1}{\sqrt{s}} \psi\left(\frac{t-\tau}{s}\right) \quad (2)$$

It gives a variable resolution as follows: higher frequencies are better resolved in time, and lower frequencies are better resolved in frequency. With multi-scale decomposition of wavelet, the high-frequency noise and the low-frequency respiration signal could be removed, and the heartbeat signal can be extracted.

b. The type of wavelet

The similarity between the shape of the wavelet filter and the signal enhances the quality of the rectified signal. The Symmlets wavelet has been found to be optimal in terms of its general characteristics, such as compact support, orthogonal and symmetry. The preliminary experimental results also showed that the Symmlet mother wavelet of order 8 to be the optimal comparing to other wavelet basis functions such as Harr and Daubechies wavelet in our application.

c. The threshold selection rule

We use soft threshold method to eliminate noise from the wavelet coefficients by replacing the coefficients that are in the range of $[-\delta, \delta]$ with zero, while the others are shrunk in absolute value. The threshold δ proposed by Donoho is [12]:

$$\delta = \sqrt{2 \log(N) \sigma^{-2}} \quad (3)$$

the estimation of the respiration and noise variance, and N is the data length.

d. The algorithm

On basis of the frequency ranges of the heartbeat and the respiration signal, the algorithm of discrete wavelet transform is outlined below: 1). Apply wavelet transform to the signal with Symmlet mother wavelet. 2). Eliminate high frequency and low frequency noise by setting the corresponding wavelet coefficients to zero. 3). Threshold the coefficients depending on the breath signal variance and the number of samples of the data. 4). Perform inverse wavelet transformation to obtain the heartbeat signal.

B. Experiments

Fig.3 (a) is the original signal, where the respiration signal is dominant component and the heartbeat signal is difficult to identify. Fig.3 (b) is the profile of the respiration signal in time domain extracted by the digital filter proposed.

While Fig.4 (b) and Fig.5 (b) shows the profile of the heartbeat signal extracted by WT. Fig.4 (a) and Fig.5 (a) is the ECG signal collected by the physiological recorder. By comparison of Fig.4(c) with 4 (d) and Fig.5(c) with 5 (d) we can see that the rhythm of the heartbeat signal waveform detected by the life-detection system and that of ECG signal detected by the physiological recorder are quite identical. It suggests that heartbeat signal could be extracted effectively from the respiration signal detected by the life-detection system, even with strong background noise. The study was approved by an institutional review committee on human studies. After obtaining informed consent, the apparatus was tested on 11 healthy volunteers (ten 23~29 years old male, one 24 years old female) in order to testify the accuracy of the ballistocardiogram. The microwave antenna was located 2 m away from the chest wall of the volunteer in a sitting position. The data were got separately in breath-held and free breath conditions. As a reference, limb leads ECG was monitored along with the non-contact monitoring. On account of the frequency wideband of ECG signal (0.05~100Hz), the sampling frequency was set to 300 Hz. The power spectrum of BCG signal derived from the non-contact apparatus for 25s along with the power spectrum of ECG signal derived from electrocardiograph for the same period were calculated.

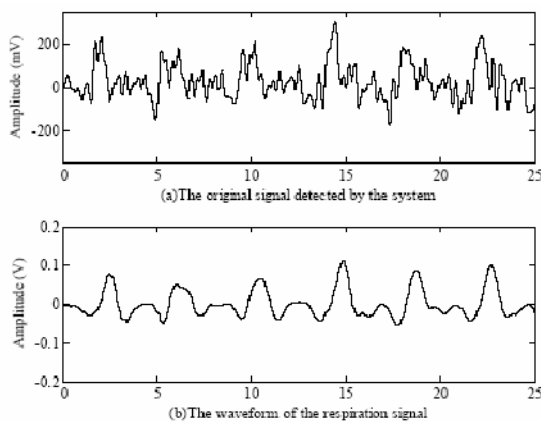


Fig. 3. The extraction of heartbeat signal by wavelet analysis

C. Results

The experimental results are shown in figure4 and figure5. Under the breath-held condition, the RR interval of ballistocardiogram and ECG is both 26 times in 25 s (Fig.4). While under the free breath condition they are both 24 times (Fig.5). Furthermore, the highest frequency peak points under the two conditions are both the same. We also record the pulse rate of the testing subject. The difference with the ballistocardiogram was in two times.

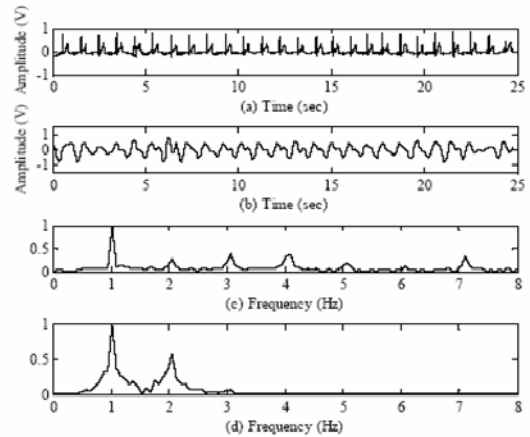


Fig.4. Contrast figure of ECG and BCG in time and frequency domain under breath-held condition

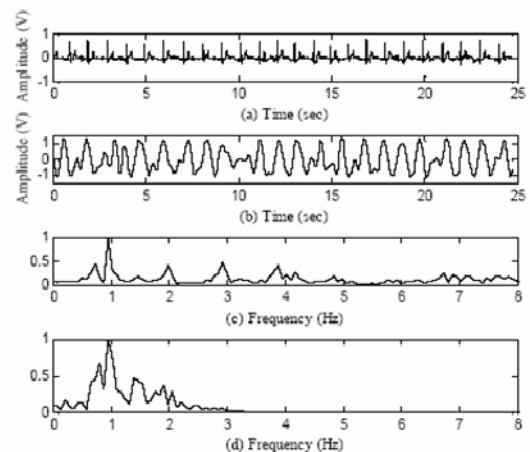


Fig.5. Contrast figure of ECG and BCG in time and frequency domain under free breath condition

III. CONCLUSIONS

The relativity of ECG and ballistocardiogram simultaneously are analyzed respectively in time and frequency domain. From the experimental results we can draw the conclusion that they can keep consistent rhythm in the same

time period. While in the time domain the waveform of the ballistocardiogram has an obvious periodicity. It also has a corresponding relationship with the ECG signal. It's feasible for the life parameter detection system via radar to be applied in clinical medicine, which showed a bright future in widely application. Furthermore, the heartbeat signals detected in our experiments are characterized with the following features:

1) Reiteration for the same object

If the test distance is unchanged, the heartbeat waveforms of the same object are approximately similar in different time.

2) Diversity for different objects

The heartbeat waveforms of different objects are quite unlike in different time, even if the test distance is unchanged.

3) Individual variety

The heartbeat waveforms of the same object vary with the test distance, even at the same period.

Generally speaking, in time domain, the signals are characterized by periodicity on the whole and unsteadiness in detail. In frequency domain, the highest peak existed in heartbeat frequency. There also exists two times and 3 times harmonics. The altered test condition has nonlinear influence on the frequency energy distribution. As to the reasons for individual difference, they are mainly the nonlinearity of the system, the instability of the heartbeat state, and also the diversity of the signal for different people. Meanwhile, we also find that the results were affected by some factors. For example, due to the time delay existed in both systems, the exact measurement synchronization can't be guaranteed. And what's more, the ballistocardiogram of free breathe is affected by breathe. So we are going to adopt relative algorithm to process the ballistocardiogram signal under free breathe condition to improve the SNR. Also, the experiment was done on the condition that the object was static and the algorithm for signal processing is post-processing Therefore to reduce the influence of the factors mentioned above and make the algorithm real-time is our working emphasis.

REFERENCES

1. WANG Jianqi, ZHENG Chongxun, et al, "Study on a non-contact life parameter detection system using millimeterwave", *Journal of Space Medicine and Medical Engineering of China*, vol.17, no.3, pp.157-161,2004.
2. Starr I, Karreman G, et al, "Blind study on the relations between the extent of coronary arteriosclerosis and the strength of the myocardial contraction as measured by invasive and noninvasive tests", *Am Heart J*, 96,pp.37-46, 1978.
3. NI Ansheng, WANG Jianqi, et al, "Non-contact life-parameters signal detecting of frequency domain signal integration based on FFT", *J Fourth Mil Med Univ*, vol.24, no. 2, pp. 172-175, 2003.
4. LU Guohua, Yang Guosheng, et al, "Study on Second Filtering Algorithm Based on Tracing the Interfering Spectral Peaks of Radar Non-contact Life-parameter Detection System", *J Biomed Eng*, vol23, no.4, pp.695-698, 2006.
5. Chuang HR, Chen YF, Chen KM, "Automatic clutter-canceller formicrowave life-detection systems", *IEEE Trans. Instru Measure Eng*, vol.40, no.4, pp. 747-750, 1991.
6. Chuang HR, Devedra M, Wang H, Postow E, "An X-band microwave life-detection systems", *IEEE Trans. Biomed Eng*, vol.33, no. 7, pp.697-701, 1986.
7. LU Guohua, WANG Jianqi, et al, " Experimental research on the technology for restraining self-dithering of the system for detecting life parameters in a non-contact way", *J Fourth Mil Med Univ*, vol.23, no. 4,pp. 376-378, 2002.
8. ZHANG Weizhen, *Biomedical Electronics* (Book style). Beijing: TsingHua University Press Hall, 1990, pp.11-16.
9. Chen KM, Huang Y, Zhang JP, Adam Norman, "Microwave life-detection systems for searching human subjects under earthquake rubble or behind barrier", *IEEE Trans. Biomed. Eng.*, vol.27, no.1, pp.105-114, 2000.
10. WANG Jianqi, Wang Haibin, JING Xijing, et al, "The study on non-contact detection of breathing and heartbeat based on radar principles", *Journal of Medical Instrumentation of China*, vol.25 no.3 pp.132-135, 2001.
11. LIU Xuehong, WU Aipin, WANG Liye, " Restraining the respiration interferences in ECG signal based on wavelet transform", *Journal of Biomedical Engineering and Clinical of China*,vol.6, no.7, pp. 78-82, 2003.
12. D.L.Donoho, "De-noising by soft-thresholding," *IEEETrans.Inform. Theory*, vol.41, pp.613-627, 1995.

Author: Wang Jianqi

Institute: Faculty of Biomedical Engineering, Fourth Military Medical University

Street: Changlexi Road 17#

City: Xi'an

Country: China

Email: fmmudzx@fmmu.edu.cn

Research and application of physical protection technology and equipment against biological contamination in mainland of China

Z. Wang, J.Q. Yang, J.C. Qi, Y.D. Wang, S.Q. Chen, S. Xia

National Biological Protective Equipment Engineering Research Center, Tianjin, China

Abstract — Biological contamination is considered to be great hazardous and related to national security, it is very important to strengthen physical protection against biological contamination accordingly. Key technologies of physical protection against biological contamination were described in terms of isolation, positive/negative pressure, air filtration, antibacterial material and disinfection. Present situation of research and development about Chinese physical protection equipment against biological contamination were presented involving individual protection, collective protection, disinfections, quality control and ergonomics. Finally, Chinese and overseas status about physical protection equipment against biological contamination were analyzed and compared in the areas of administration, research and market. It was concluded that Chinese physical protection equipment against biological contamination fell behind in administration, research and industrialization. As a result, some suggestions with Chinese characteristics were presented to promote development of Chinese physical protection equipment against biological contamination.

Keywords — biological contamination, physical protection, technology, equipment, China

I. INTRODUCTION

Biological contamination is closely related to human life and health. Accompanied by the variety of natural ecological environment, international military and political situation, biological contamination has performed as various forms, such as biological warfare agents, biological terrorist attacks, emergent natural epidemic and biological incidents, etc. Therefore, biological safety has become a hot issue in the world. As an example of SARS epidemic in the spring and summer of 2003, involving 32 countries and regions, there were total 8422 cases around the world, 919 cases of death, 11% of mortality rate. Mainland of China had total 5,327 cases, 349 cases of death, and 6.6% of mortality rate. In particular, there were up to 1,016 cases of infection, 31 cases of death for the medical staff in the rescue of SARS patients, which respectively covered 19% of total domestic infection cases and 8.9% of death cases^[1]. This high infection rate caused a great panic among the people, which seriously influenced the social stability and economic development. The worldwide economic losses caused by

SARS were up to about 59 billion US dollars (17.9 billion US dollars of China)^[2]. Since the end of 2003, the avian influenza spread in the world, involving 13 countries and regions, which had 348 cases of human infection, 215 cases of death with 62% of mortality as well as 3 billion US dollars of economic losses^[3]. After entering the 21st century, the importance of national biological safety is nothing less than any other form of national security. Hence, developing protection technology and equipment against biological contamination to minimize people infections and deaths has become an important task for all countries.

II. THE CONCEPT OF PHYSICAL PROTECTION TECHNOLOGY AND EQUIPMENT AGAINST BIOLOGICAL CONTAMINATION

Protection against biological contamination mainly covers medical protection and physical protection. Physical protection technology refers to technology utilizing the physical means to prevent human body from biological contamination attack. Physical protection equipment mainly refers to equipment being used for individuals or groups to prevent and treat biological contamination, which is the specialized equipment to effectively eliminate or control the source of contamination, block the channel of transmission as well as carry out the protection or isolation of individuals and groups. Compared with the medical protection measures, physical protection equipment is provided with the characteristics of easy to use, immediate effectiveness and reliable protection, which acts as a powerful supplement to medical protection measures. Physical protection equipment mainly covers individual protection equipment and collective protection equipment.

III. KEY TECHNOLOGY OF PHYSICAL PROTECTION AGAINST BIOLOGICAL CONTAMINATION AND APPLICATION

A. Isolation

Isolation is the basic technology of physical protection against biological contamination. Many protection equipments achieve the protection for humans through the barrier and obstruction function of materials, which isolate the skin or mucosa of human body from biological contamination,

such as protective respirator, protective clothing, protective masks, protective gloves / shoe covers, etc.

It usually adopts the independent building or regional construction for the sites with high-risk biological contamination, which use walls and sealed doors to isolate and protect the external environment. It can improve the protection performance in these sites by setting up sub-area to achieve regional isolation. For example, BSL-3 laboratory sets up clean area, buffer area and contaminated areas (core area).

B. Positive/negative pressure

Positive/negative pressure environment is generated by comprehensive utilization of technologies of the enclosed structure, ventilation, air distribution and air filtration. The application of positive pressure can protect the personnel within from outside contaminated environment; the application of negative pressure can protect the personnel outside from inner contaminated environment. The facilities and equipments applied with positive pressure technology include biological protection tents, biological reconnaissance vehicle, and positive pressure clothing, etc. And the facilities and equipments applied with negative pressure technology include biological safety laboratory, biological safety cabinet, negative pressure isolation wards, and negative pressure ambulances, etc.

C. Air filtration

Air filtration technology includes air filtering material and air filter. Fiber filtering materials is the primary air filtering medium. The filtration efficiency of fiber filtering material can achieve 99.97% (HEPA) and 99.999% (ULPA).

Air filtration technology must be combined with ventilation technology, and the relationship between the parameters of flow volume, flow resistance and clogging capacity, and the filtering effect is the focus of the research. Most of biological protection facilities and equipments related to the ventilation are applied with air filtration technology, such as protection mask, biological protection tents, and BSL-3 laboratory, etc.

D. Antibacterial protection material

Traditional air filtering material, which could only passively obstruct contamination, can not extermination microorganism. Therefore, it's significant to develop the protection materials with antibacterial function. At present, the main antibacterial protection materials include biological antibacterial materials, electret filtering material, and electrospinning materials, etc.

National Biological Protection Equipment Engineering Center (short as NPEC) had carried out the research of lysozyme filtering material, and found that sterilization efficiency could be up to 95%^[4]. NPEC had also carried out the research of polypeptide antibacterial filtering material, and found that it not only had a high sterilization rate up to 99%, but also had a good stability and long effectiveness^[5].

Electret air filtering materials achieve the filtration through mechanical effect and electrostatic adsorption effect. At the same time, electret materials play a role of restraining and killing the microorganisms. Currently, electret antibacterial air filtering material has applied to some air conditioner.

Electrospinning technology can produce fiber with fine diameter, large surface area, high porosity, and good gas and vapor permeability. Non-woven fabric produced by electrospinning has the low resistance of air, and the strong protection ability against microorganism aerosols.

E. Indoor air disinfection

Indoor air disinfection technology can limit the microorganism concentration of indoor air in a certain range. The indoor air disinfection technology mainly includes ultraviolet disinfection, chemical disinfection, ozone disinfection, and air-conditioning disinfection, etc.

F. Outdoor air decontamination

Outdoor air decontamination refers to utilizing disinfection agent and equipment to kill pathogenic microorganism and vector insect in the outdoor environment. And the decontamination equipments include sprayer, spraying machine and fog machine, etc. They can be divided into backpack type, hand-push type and vehicle-mounted type. At present, the decontamination agent with multi-function, low corrosion, pollution-free and fast efficiency is the R & D hot spots, such as biological enzyme-catalyzed disinfectant, metal complex catalysts disinfectant, nano-metal oxide disinfectant, polymer adsorption reaction disinfectant and self-catalysis sterilizing coating, etc. At the same time, high temperature, high pressure and jet technology are the characteristics for the new generation of decontamination equipment. In order to protect some sensitive equipment, the water-free decontamination technology is also under development.

G. Remote Monitoring of body signs

To decrease the contact with the infectious disease patients can effectively protect the medical personnel. NPEC developed the remote body temperature signs monitoring

technology. It has about 150 monitors, and 1,000m monitoring region. It can solve the problem of remote real-time non-contact multipoint temperature monitoring for infectious disease patients.

IV. DOMESTIC R&D PROGRESS OF PHYSICAL PROTECTION EQUIPMENT AGAINST BIOLOGICAL CONTAMINATION

A. Individual protection equipment

In recent years, Academy of Military Medical Science researched and developed some individual protection equipment against biological contamination such as the biological protection respirator, the positive pressure medical protection hood, the PTFE biological protection clothing, the TPU protection clothing and the negative pressure isolated cabin for infectious disease patient, etc. Hereinto, the biological protection respirator has a filtration efficiency great than 99.5% for bacteria and virus.

B. Collective protection equipment

China has developed some collective protection equipment against biological contamination these years such as the negative pressure isolation wards and the negative pressure ambulance for infectious disease patients, mobile biological safety level 3 laboratory, field hospital system with NBC protection function, etc. Hereinto, the mobile BSL-3 laboratory is the first one that China independently developed. When public health incidents occur suddenly, it can arrive at the designated locations quickly, and carry out the separation, cultivation, detection and identification operation on the suspicious pathogens.

C. Disinfection and decontamination equipment

At present, there are relatively abundant types of disinfection and decontamination equipment in the domestic market including ultraviolet disinfection devices, ozone disinfections devices, fumigation disinfection equipment, and spray decontamination equipment, etc. Such as the sanitation and anti-epidemic vehicle developed by Academy of Military Medical Science is used for exterminating the field large-area pathogenic microorganism and vector insect. The vehicle is provided with the field mobility and equipped with high efficiency spray equipments. Its decontamination capacity is not less than 100,000m² per hour.

D. Quality control and monitoring equipment

Quality control and monitoring equipment of biological protection equipment includes particle and microorganism

aerosol filtration efficiency testing equipment, air microorganism sampling equipment, synthesized blood penetration testing equipment, etc. Such as the microorganism aerosol filtration efficiency test system developed by NPEC, which is designed according to ASTM standard F2101-01, is provided with the characteristics of variable flow, negative pressure, precise measurement, and easy operation. It can test the microorganism aerosol filtration efficiency of air filtration material, protection material, and protection respirator.

E. Ergonomics evaluation equipment

Ergonomic and comfort evaluation equipment is applied in the research of biological protection equipment developed by NPEC. The influences of microenvironment parameters of the equipment such as oxygen, carbon dioxide, temperature and humidity on the physiological indexes of user such as heart rate, respiration, blood pressure, and oxygen saturation, etc. were researched. The ergonomics evaluation equipment mainly covers: microenvironment quality monitoring equipment, personnel physiological status monitoring equipment and evaluation test platform, etc.

V. R&D COMPARISON OF PHYSICAL PROTECTION EQUIPMENT AGAINST BIOLOGICAL CONTAMINATION AT HOME AND ABROAD

Biological contamination outbreak will trigger people's panic, and even impact on social stability, which may result in tremendous losses of the national public security and economic development. Therefore, the developed countries have attached great importance to the development and application of biological protection equipment.

A. Management

In mechanism of preventing and treating bio-terrorism incidents and urgent public health events, the United States and other developed countries have drawn up a series of national biosafety plans involving action plans and a wide range of emergency measures.

In the biological safety management, the World Health Organization (WHO) issued laboratory biosafety manual in 2004 (3rd Edition). For the standards: the United States and Europe have established a comparatively complete standards system for protection equipment. For example, standards for product and test method of protection clothing involve 42 ISO standards, 24 ASTM standards, 20 ANSI standards, and 51 EN standards.

After SARS, the bio-safety issue attracts great importance of Chinese Government that 2005-2020 state biological safety strategic countermeasures was studied and formulated. At present, more than tens of biological safety laws and regulations as well as standards have been issued in China.

B. R & D

R&D institutions of biological protection equipment at abroad are mainly divided into three types: the first type is national R&D institutions, such as the National Protection Center (NPC) of the United States, and the National Personnel Protection Technology Laboratory (NPPTL), etc.; the second type is military R&D institutions, such as the Biological and Chemical Protection Bureau of U.S. Army, the Army Medical Research Institute of Infectious Disease, and Walt Terry Army Medical Institute, etc.; the third type is enterprise R&D institutions, such as 3M company and DUPONT company in the USA, Elwyn E. Roberts Isolation Equipment Co., Ltd in the UK, and BACOU company in France, etc.

It also established various academic organizations at abroad, which played an important role to guide the development of biological protection technology and equipment. For example, Biological Terrorism Incidents Nursing Research Group under the Emergency Nursing Association (ENA) of the United States established in 1970, American Biological Safety Association (ABSA) established in 1984, European Biological Safety Association (EBSA) established in 1996, International Biosafety Working Group (IBWG) Established in Canada in 2001.

Biological protection equipment research and development in China was almost blank before SARS, In December 2003, National Biological Protection Equipment Engineering Center (NPEC) was established based on Academy of Military Medical Science approved by the Ministry of Science and Technology.

In October 2007, NPEC, Academy of Military Medical Science, and China Disease Prevention and Control Center co-established the Biological Safety and Protection Equipment Branch of Chinese Preventive Medicine Association.

C. Marketing

The foreign biological protection equipments have the advantages of various types, full functions, reliable performance and advanced technology, etc. For example, N95 series of respirator, Air-Mate protection hood, M40 protection mask from 3M, Tyvek series of protection clothing from Dupont, JSLIST of US Army, NBC protection casualty bags and NBC protection tents developed by Finland

EGO company, MPD100 multi-functional decontamination system from Germany Kach company. The products from the main foreign companies of biological protection equipment have almost dominated the global military and civilian market.

In comparison, the product of domestic biological protection equipment is relatively small in variety, quantity of production and sales, and is incomplete in function, which does not come up to its own well-known brand.

VI. GAPS AND SUGGESTIONS

Compared with developed countries, China fell behind in administration, research and industrialization in the filed of biological protection technology and equipment. It is very important to vigorously strengthen the management and construction of biological protection technology and equipment, and form a complete system of national biological protection equipment as soon as possible.

A. Management

Biohazard events relate to social public interests, it is the important responsibility for all levels of governments to cope with fast and properly. The government shall establish a full range of management systems, mechanisms, policies and regulations, such as early warning, response plans, prevention education, technical research, equipment reserves, materials supply, medical aid, and reconstruction after disaster, etc. and become the leading strength for dealing with biohazard events. Suggestions: First, strengthen the scientific research input. Second, strengthen strategic reserves input. Third, establish the technology standard systems, setup quality testing platform and certification institutions, as well as strengthen trade supervision and management. Fourth, combine reserves with rehearsals, and fully exert the performance of biological protection equipment.

B. R & D

At present, the R & D of biological protection technology and equipment in China has obvious gap with developed counties in establishment of professional institutions, the number of staff, research levels, platform construction and funds input. Suggestions: First, earnestly support the key project research, Second, improve the scientific research conditions, strengthen the research infrastructure investment, Third, establish levels of academic organizations, launch professional journals, build domestic and international academic communication platform.

C. Industrialization

At present, the number of domestic enterprise that specialized in biological protection equipment is rarely small, which could hardly satisfy the demands of domestic biological safety protection. Therefore, it urgently needs to speed up the cultivation of domestic professional manufacturing enterprises that owned famous brands, so as to improve the market shares of domestic biological protection equipment. Suggestions: Firstly, implement the positive fostering policy for domestic enterprises. Secondly, carry out the promoting technology innovation policy for domestic enterprises.

REFERENCES

1. http://news.xinhuanet.com/world/2003-08/16/content_1029860.htm
2. <http://news.sina.com.cn/c/2003-11-11/07161093996s.shtml>
3. http://www.who.int/csr/disease/avian_influenza/country/cases_table_2008_01_02/en/index.html
4. J.C. Qi, H.L. Duan. Preparation of Lysozyme-filter Material & Evaluation about its Bactericidal Action. Indoor Environment Quality-Problems, Research and Solutions, an international specialty conference, July 17-19, 2006, Research Triangle Park, NC, USA.
5. L.M. Hao, H.L. Duan. Research of antimicrobial activity of immobilized Polymyxin Sulfate. The 1st National Symposium on Biosafety & Bio-Protection Equipment, Oct. 2007, Beijing, China

PI3K-Mediated Epithelial Sodium Channel Activity by Regulating the Apical Membrane Morphology of Renal Epithelial Cells

Yanjun Zhang^{1,2}, Liying Ma², Bo Xu², J. Gorelik³, D. Klenerman⁴, M. Lab³, C. Edwards³, Y. Korchev³

¹ Tianjin Institute of Medical Equipment, Tianjin, China

² China National Academy of Nanotechnology & Engineering, Tianjin, China

³ Division of Medicine, Imperial College London, London, United Kingdom

⁴ Department of Chemistry, Cambridge University, Cambridge, United Kingdom

Abstract — Continuous high spatial resolution observations of living cells would greatly aid the elucidation of the relationship between structure and function and facilitate the study of major physiological processes such as the mechanism of action of aldosterone on the activity regulation of epithelial sodium channel (ENaC). Unfortunately, observing the micro-structural and functional changes in the membrane of living cells is still a big challenge in current nanomedicine. Scanning ion conductance microscopy (SICM) is such a kind of scanning probe microscopy, which is designed for continuous high-resolution topographic imaging of living cells. Under the help of SICM, we have found that aldosterone stimulates ATP release and the basolateral P2X₄-like receptors may be involved in the regulation of the activity of ENaC. However, the signaling components linking receptor binding to final ENaC channel regulation remain incompletely characterized. We have now further investigated using SICM and *Xenopus* A6 kidney epithelial cells that the involvement of the PI3K pathway during the aldosterone action.

Three hours continuous SICM observations showed how A6 cells changed their morphology in response to the aldosterone treatment. Patch clamping of individual cells enabled anatomy and function to be correlated, showed that the morphology changed cells with the ENaC channel activity. These morphology changes and ENaC activities were abolished by the specific Phosphoinositide 3-kinases (PI3K) inhibitor LY294002. SICM has the potential to become a powerful tool for research on living renal cells, and has been used to elucidate how PI3K pathway involved in the aldosterone action on renal epithelial sodium reabsorption.

Keywords — SICM, PI3K, ENaC, A6 cells, SPM

I. INTRODUCTION

It has been hypothesized that the renal epithelial sodium channel (ENaC) or channel regulatory components may be major factors in the development of essential hypertension. The intracellular signaling factors that regulate the ENaC activity may be key to understanding and better treating this devastating age-related disease. Such a challenge in current nanomedicine requires new methods to image a live renal cell on the nanoscale and study ENaC activity locally. The

scanning ion conductance microscopy (SICM) can be used to obtain high-resolution non-contact images of the surface of live cells under physiological conditions on the nanoscale, and hence allow the relationship between cell structure and function to be probed [1,2]. Under the help of SICM, we have found that aldosterone stimulates ATP release and the basolateral P2X₄-like receptors may be involved in the regulation of the activity of ENaC [3,4]. However, the signaling components linking receptor binding to final ENaC channel regulation remain incompletely characterized.

Phosphoinositide 3-kinases (PI3K) are a family of enzymes that phosphorylate phosphatidylinositol 4-phosphate (PtdIns-4-P) and phosphatidylinositol 4,5-bisphosphate (PtdIns(4,5)P₂) producing PtdIns(3,4)P₂ and PtdIns(3,4,5)P₃ (PIP₃) [5]. The production of these phospholipids activates a number of downstream kinases, which in turn propagate signaling cascades leading to a variety of intracellular biochemical processes, including membrane trafficking, signal transduction and Ca²⁺ signaling [5]. Although PI3K is not an aldosterone-induced protein, its activity is increased by both aldosterone and insulin in renal epithelial cells [6,7]. Moreover, aldosterone stimulation increases the formation of PIP₃, which has recently been shown to enhance ENaC activity directly [8]. However, the mechanisms of such PI3K and its activation pathways for ENaC are still unclear. We have now further investigated using SICM and A6 renal epithelial cells that the involvement of the PI3K pathway during the aldosterone action on ENaC activity.

II. MATERIALS AND METHODS

A. Cell preparations and solutions

A Single *Xenopus laevis* renal epithelia A6 cell line (kindly provided by Dr P. DeSmet, Karnolieke Universiteit, Belgium) was used in all the experiments, which carried out between 127-134 passages. Cells were cultured as described previously [9] on membrane filter inserts (23 mm diameter, 0.4 μm pore, 1.6×10⁶ pores/cm², Falcon, Becton Dickinson

Labware, Oxford, UK). Briefly, cells were grown and kept in a 1:1 mixture of modified Ham's F-12 medium and Leibovitz's L-15 medium (Gibco, Parsippany, NJ), modified to contain 105 mM NaCl and 25 mM NaHCO₃. The mature A6 cell monolayer was maintained in the growth medium together with 10% fetal calf serum, and supplemented with 1.5 μM aldosterone (Sigma, Dorset, UK). After 24 hours, the monolayer was incubated in a serum-free medium in the presence of aldosterone for another 24 hours. The cells were then grown in serum- and aldosterone-free culture medium and incubated at 28°C in an incubator with 1% CO₂ in air for a further 24-48 hours. Prior to being used in experiments, cell monolayers were bathed with a modified identical isosmotic Leibovitz's L-15 medium (Gibco), which contained (in mM): 114 NaCl, 4.5 KCl, 1 MgCl₂, 1 CaCl₂, and 10 HEPES at pH 7.4, with a final iso-osmolality as growth medium of 260 mosmol/kgH₂O. All experiments were performed at room temperature (26 ± 2 °C).

B. Scanning Ion Conductance Microscope (SICM)

The Scanning Ion Conductance Microscopy (SICM) setup, which has been previously described [1-4]. Nanopipettes of SICM were made from 1.00 mm outer diameter borosilicate glass capillaries (Intracel, Herts, UK) using a laser-based puller (P-2000, Sutter Instrument Co., CA,

USA). In all experiments, these nanopipettes and the bath were filled with the same modified L-15 medium (Gibco), so that salt concentration gradient potentials and liquid junction potentials were not generated. The SICM set-up was also adapted for "smart" patch clamping [10,11] by using an Axopatch 200B commercial patch-clamp amplifier (Axon Instruments, Inc.). The cell-attached configuration was selected for the current study of aldosterone regulated ENaC activity. The nanopipette when filled with the modified physiological L-15 medium had an average tip resistance of 150 MΩ. For patch-clamp recording currents were sampled at 10 kHz and filtered at 2 kHz (-3 dB, 4-pole Bessel) using an Axopatch 200B amplifier and pClamp 9.0 software (Axon Instruments, CA, USA), which was also used to generate pulse protocols

C. Effect of PI3K inhibitor LY294002

LY294002 is a inhibitor with a very high specificity for PI3K that acts as a competitive inhibitor for the ATP binding site of the enzyme in the micromolar concentration range [12]. To determine whether the effect of aldosterone on cell functions and structures could be blocked by the specific PI3K inhibitor, LY294002 (Sigma), both sides of the A6 cell monolayer were treated with 50 μM LY294002 [13] for 30 minutes before the aldosterone stimulation.

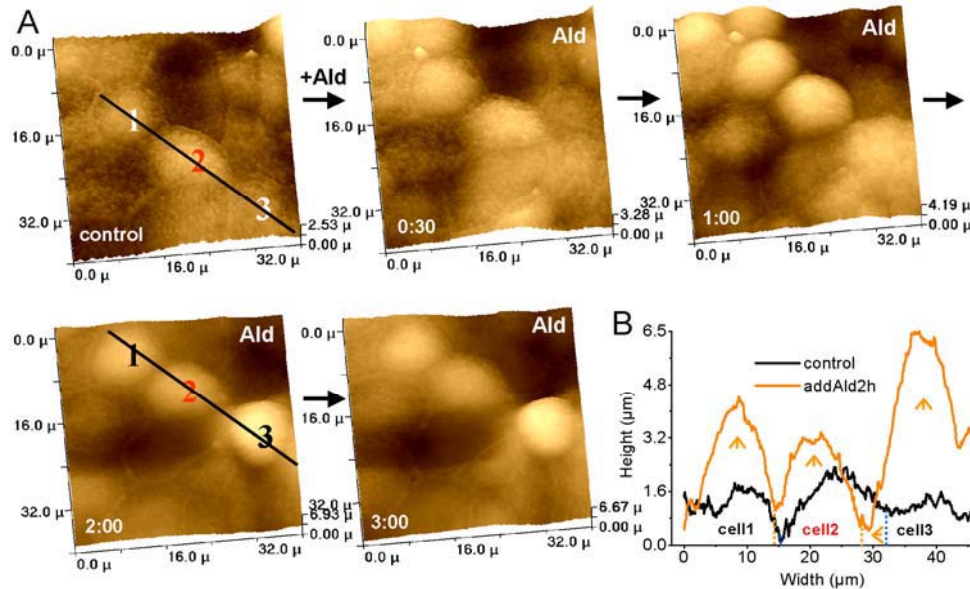


Fig. 1 Effects of aldosterone treatment on the topography of an A6 monolayer.

(A) Six images from a sequence of images of a 40 μm × 40 μm area of an A6 monolayer recorded every 15 minutes over a 3-hour period.

(B) Time-dependent profile changes in cells marked 1-3 in A. Bottom trace from control frame, top trace from frame 2:00.

The time marked on the frames represents hours: minutes.

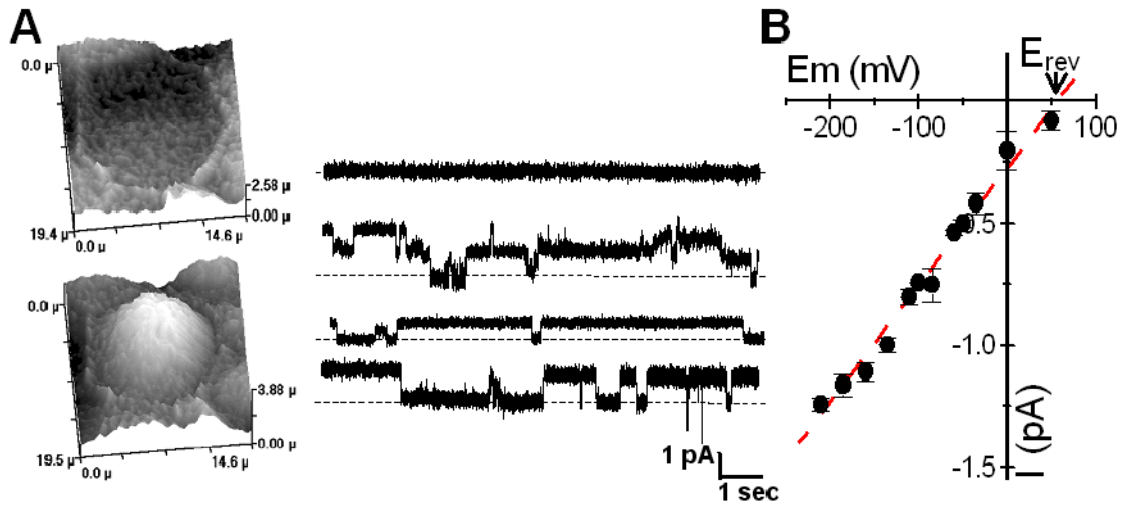


Fig. 2 Aldosterone-induced cell contraction and ENaC activity.

(A) “Smart” patch-clamp single-channel recordings of ENaC in the cell-attached configuration from a non-contracted A6 cell (upper panel) and a contracted A6 cell (lower panel), during aldosterone stimulation. The image on the left side of the recordings illustrates the morphology of the patched cell. (B) Current-voltage relationship of single-channel recordings from the contracted cells ($n=9$), derived from the experiments shown in figure A. Each point represents the mean current amplitude of nine individual current recording at corresponding membrane potential (E_m). The red-dashed line is drawn by linear fitting of these points and represents a unit conductance of 4.8 picoSiemens (pS) of the recorded single-channel. Its reversal potential (E_{rev}) is about 56.7mV.

III. RESULTS

SICM provides unique information about living cells that helps to understand the relationship between the microstructural and functional changes in the membrane of living cells. It provides high-resolution images of living renal A6 cells under physiological conditions (Fig. 1). Figure 1A presents five selected time-sequence images of the same area of an A6 monolayer taken over a three-hour period. The aldosterone effect on cell morphology was initially

more marked in a proportion of cells (note the changes in cells marked 1-3 on the figure). Aldosterone stimulation induced lateral cell contraction accompanied by apical membrane expansion (Fig. 1B). In Figure 1B, the bottom black color topographical profile drawing which represents the line across the three cells in the control frame of Figure 1A. The orange color profile line scanned two hours after aldosterone stimulation shows the dramatic morphology change.

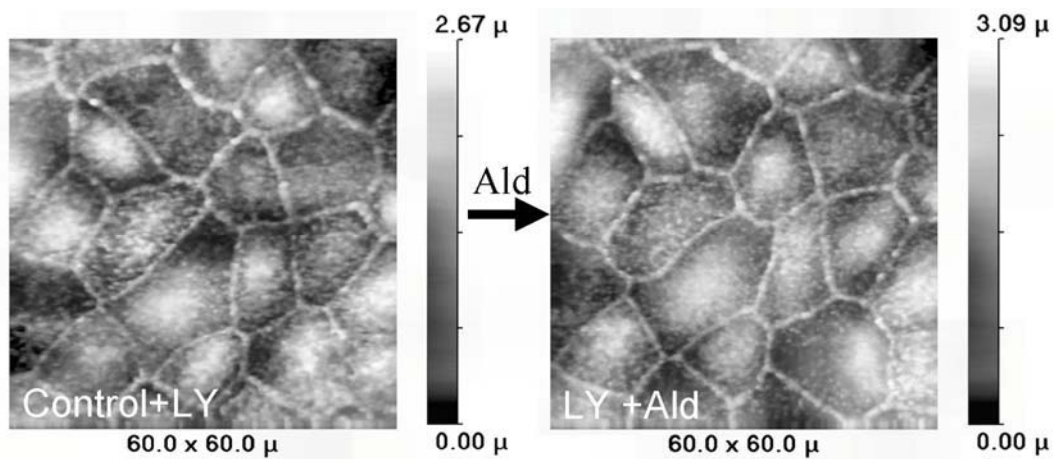


Fig. 3 Effect of the PI3K inhibitor LY294002 (LY) on the cell topography of an A6 cell monolayer during aldosterone (Ald) stimulation.

It is known that the amiloride-blockable ENaC can be expressed in the A6 cells when they cultured on membrane filter inserts [9]. To test whether the observed cell morphology change was directly associated with ENaC activity we used the “smart” patch-clamp technique to study individual lateral contracted and non-contracted cells (Fig. 2). A6 cells topography under aldosterone stimulation was studied using SICM to identify differences in cell morphotypes, non-contracted (Fig. 2A upper panel) or contracted cells (Fig. 2A lower panel). Then a total of 19 cell-attached patch-clamp recordings were performed on these two different morphotypes of cells: contracted ($n = 9$) and non-contracted ($n = 10$). The patch-clamp recordings of channel activity were actually obtained only on the contracted cells, whereas, no channel activity was recorded from any non-contracted cells (Fig. 2A). The current-voltage relation of these channel activities in such contracted A6 cells is presented in Figure 2B. Linear fitting of the current amplitude of nine individual current recording at corresponding membrane potential (E_m), a red dashed-line is obtained, and the gradient of this line represents a unit conductance of about 4.8 pS of the recorded ion channels (Fig. 2B). E_{Na} is calculated as 57.4 mV for the A6 cells in these experiments. This value is practically similar to the E_{rev} obtained (56.7 mV) in our experiments (Fig. 2B). These results and those previously published patch-clamp recordings of ENaC [9,14,15] demonstrated that this recorded ion channel activity is originated from ENaC.

Then we used SICM to examine the involvement of PI3K in the observed cell morphology changes (Fig. 3). SICM scans were performed over a 1-hour period of aldosterone action on a $60 \mu\text{m} \times 60 \mu\text{m}$ area of LY294002 pre-treated A6 monolayer. The control image was taken before the aldosterone stimulation and shows the expected features of a well-developed A6 monolayer with intact apical membrane. The scanning image (LY+Ald) after the aldosterone stimulation shows clearly that LY294002 pre-treatment inhibits all the previously noted cell morphology changes, including lateral contraction and apical membrane elevation.

IV. CONCLUSIONS

Continuous 3h observations showed how A6 kidney epithelial cells changed their morphology in response to the aldosterone treatment. Patch clamping of individual cells enabled anatomy and function to be correlated, showed that the morphology changed cells with the ENaC channel activity. These morphology changes and ENaC activities (data not shown) were abolished by the specific PI3K inhibitor LY294002. All these demonstrated that SICM has the potential to become a powerful tool for researching on living

renal cells, and has been used to elucidate how PI3K pathway involved in the aldosterone action on renal epithelial sodium reabsorption. To support our findings, the PI3K pathway has been shown to be an essential convergence point for aldosterone, insulin, and hypotonicity induced stimulation of Na^+ entry by ENaC in epithelial cells [6,7,13,16]. More evidence for the involvement of PI3K pathway in the transepithelial Na^+ transport comes from the fact that the PI3K-specific inhibitor LY294002 inhibits the ENaC activity in response to both aldosterone and hypotonic stress in amphibian renal tubular epithelial cells [6,13,17]. It is known that PI3K and its downstream lipid products, such as PIP3, not only regulate ENaC activity in aldosterone action, but also play critical roles in signaling to actin assembly and regulating actin cytoskeleton reorganization [18,19]. Thus PI3K pathway may be a focal point where aldosterone, other hormones, and osmotic stress signal transduction converge to activate a common cascade directed toward ENaC, and may serve as crucial physiological modulators for Na^+ transport.

REFERENCES

1. Korchev Y E, Bashford C L, Milovanovic M et al. (1997). Scanning ion conductance microscopy of living cells. *Biophys J* 73:653-658.
2. Korchev Y E, Milovanovic M, Bashford C L et al. (1997). Specialized scanning ion-conductance microscope for imaging of living cells. *J Microsc* 188:17-23.
3. Gorelik J, Zhang Y, Sanchez D et al. (2006). Aldosterone acts via an ATP autocrine/paracrine system: the Edelman ATP hypothesis revisited. *Proc Natl Acad Sci U S A*. 102(42):15000-15005.
4. Zhang Y, Gorelik J, Sanchez D et al. (2007). Basolateral P2X4-like receptors regulate the extracellular ATP-stimulated epithelial Na^+ channel activity in renal epithelia. *Am J Physiol Renal Physiol* 292:F1734-F1740.
5. Carpenter C L & Cantley L C (1996). Phosphoinositide kinases. *Curr Opin Cell Biol*. 8:153-158.
6. Blazer-Yost B L, Paunescu T G, Helman S I, et al. (1999). Phosphoinositide 3-kinase is required for aldosterone-regulated sodium reabsorption. *Am J Physiol* 277:C531-C536.
7. Shepherd P R, Withers D J, & Siddle K. (1998). Phosphoinositide 3-kinase: the key switch mechanism in insulin signalling. *Biochem J*. 333 (Pt 3):471-490.
8. Tong Q, Gamper N, Medina J L, et al. (2004). Direct activation of the epithelial Na^+ channel by phosphatidylinositol 3,4,5-trisphosphate and phosphatidylinositol 3,4-bisphosphate produced by phosphoinositide 3-OH kinase. *J Biol Chem*. 279:22654-22663.
9. Kemendy A E, Kleyman T R, & Eaton D C. (1992). Aldosterone alters the open probability of amiloride-blockable sodium channels in A6 epithelia. *Am J Physiol* 263:C825-C837.
10. Gu Y, Gorelik J, Spohr H A, et al. (2002). High-resolution scanning patch-clamp: new insights into cell function. *FASEB J* 16:748-750.
11. Gorelik J, Gu Y, Spohr H A, et al. (2002). Ion channels in small cells and subcellular structures can be studied with a smart patch-clamp system. *Biophys J*. 83:3296-3303.
12. Vlahos C J, Matter W F, Hui K Y, & Brown R F (1994). A specific inhibitor of phosphatidylinositol 3-kinase, 2-(4-morpholinyl)-8-phenyl-4H-1-benzopyran-4-one (LY294002). *J Biol Chem*. 269:5241-5248.

13. Rozansky D J, Wang J, Doan N, et al. (2002). Hypotonic induction of SGK1 and Na⁺ transport in A6 cells. *Am.J Physiol Renal Physiol* 283:F105-F113.
14. Alvarez d l R, Li H, & Canessa C M. (2002). Effects of aldosterone on biosynthesis, traffic, and functional expression of epithelial sodium channels in A6 cells. *J.Gen.Physiol* 119:427-442.
15. Palmer L G. (1992). Epithelial Na channels: function and diversity. *Annu.Rev.Physiol* 54:51-66.
16. Tong Q, Booth R E, Worrell R T, & Stockand J D. (2004). Regulation of Na⁺ transport by aldosterone: signaling convergence and cross talk between the PI3-K and MAPK1/2 cascades. *Am.J Physiol Renal Physiol* 286: F1232-F1238.
17. Paunescu T G, Blazer-Yost B L, Vlahos C J, & Helman S I. (2000). LY-294002-inhibitable PI 3-kinase and regulation of baseline rates of Na⁺ transport in A6 epithelia. *Am.J.Physiol Cell Physiol* 279:C236-C247.
18. Janmey P A. (1998). The cytoskeleton and cell signaling: component localization and mechanical coupling. *Physiol Rev.* 78:763-781.
19. Fenteany G, & Zhu S. (2003). Small-molecule inhibitors of actin dynamics and cell motility. *Curr.Top.Med.Chem.* 3:593-616.

The address of the corresponding author:

Author: Dr Yanjun Zhang
Institute: Tianjin Institute of Medical Equipment; China National Academy of Nanotechnology & Engineering
Street: Wandong Road
City: Tianjin
Country: China
Email: yanjun_zhang@cnane.com.cn

A Novel Method of Prokaryotic Promoter Regions Prediction with Feature Selection: Quadratic Discriminant Analysis Approach

Yaohua Du, Taihu Wu

Institute of Medical Equipment, Academy of Military Medical Sciences, Tianjin, People's Republic of China

Abstract — Promoter identification is an essential task in the research of transcription regulation, but the prediction accuracy of current methods is still far away from what it is expected. An effective and reliable prediction method for prokaryotic promoter regions would be very helpful. We have developed a quadratic discriminant analysis (QDA) method based on feature selection to predict prokaryotic promoter regions, which are classified according to their locations in genome. In order to utilize more characteristic information, we incorporate content features, signal features and structure features of the promoters in the candidate feature set and construct proper statistical models to calculate them. Especially for the main conserved signal features, a composite motif model is adopted, which achieves the optimal parameters by an iterative search algorithm OPSIA. Using the squared Mahalanobis distance as a measure, the discriminating features are selected out from the candidate features through a step-wise procedure and are combined as a multidimensional vector. Then the vector of combined features is further used by QDA to predict the potential promoter regions. The algorithm has been trained and tested on *E. coli* and *B. subtilis* promoter datasets by the jackknife method. For *E. coli* σ^{70} promoters located in the non-coding regions, the average prediction accuracy is 85.7%, and for the ones located in the coding regions and several other kinds of prokaryotic promoters, their prediction accuracies are also about 80%. The results indicate that our method is a universal algorithm that outperforms most of the existing approaches based on several performance measurements. Furthermore, the framework of the method is extendable, which can accept more new features to improve the prediction results efficiently. The OPSIA algorithm is also a useful tool to explore composite motifs in newly uncovered promoter sequences.

Keywords — Prokaryotic promoter prediction, Composite motif, Feature selection, Quadratic discriminant analysis (QDA), Jackknife method

I. INTRODUCTION

In prokaryotic genomes, a promoter region is often defined as the contiguous sequence stretch which determines where the transcription of a particular gene or an operon should be initiated and on what conditions. They usually occupy about 60 base pairs upstream of transcription start site (TSS) and a smaller area downstream of TSS. The pro-

moter regions are still undetermined in most sequenced prokaryotic genomes. Their correlative information of annotation is not yet available in many public databases. Therefore, a fully automatic and reliable computational approach for predicting prokaryotic promoter regions would be very helpful.

Experimental studies on prokaryotic promoter regions show that they usually have certain preference in base composition and contain a set of relatively short conserved motifs [1]. In *E. coli*, the σ^{70} promoter is the primary promoter and controls the majority housekeeping genes. Many prediction approaches have been developed for recognizing *E. coli* σ^{70} promoter because of its representative features. Most of them can be classified into two main groups: content-based methods [2] and signal-based methods [3]. Content-based methods only concern the global content property of the sequences and cannot provide exactly positional information of the signals. The quality of their predictions was quite low. Signal-based methods detect short conserved motifs as local signal features in the promoter regions. Because there is considerable variation in both the specific contents and the relative location of these motifs, they often achieve results with a large number of false positives. In order to model the motif signals more exactly, methods that use the motifs found by search algorithms as their input to some 'second level' recognizers were proposed, such as sequence alignment kernel + support vector machine (SVM) [4]. These hybrid strategies improved the prediction performance to some extent by incorporating different features of the promoter regions and then made the optimal decision under specific principle.

However, the performance of methods mentioned above is still far from satisfactory. In addition to the intrinsic degeneracy of the promoter motifs, the insufficient use of characteristic information is one of the important reasons that cause such situation. Subsequent experiments have described that there are some non-canonical elements in the promoter regions, such as the extended -10 motif [5] and the UP element [6]. They are less conserved than the canonical ones, but have important function for promoter activity. Most of current predicting methods have not concerned these motifs yet. Moreover, the double helices of promoter regions must form particular local conformations during the

initiation of transcription and must be easy to open. So the promoter regions are significantly more curved and less stable than other genomic regions [7]. The prediction methods utilizing these structure features have been proposed, but the results were still unsatisfactory [8]. Therefore, the content features, signal features and structure features cannot contain the whole characteristic information of the promoters when they are used separately. A preferable solution is to integrate the three kinds of features as many as possible.

This paper introduces a Quadratic Discriminant Analysis (QDA) based method for predicting prokaryotic promoters via feature selection from candidate features, which consist of content features, signal features and structure features. In signal features, the -10 motif, -35 motif and spacer between them are combined into a composite motif model, which achieves the optimal model parameters by an iterative search algorithm OPSIA. The squared Mahalanobis distance between classes is adopted as the measure for feature selection. Our method achieved a high prediction performance in jackknife tests on several real promoter datasets.

II. MATERIALS AND METHODS

A. Dataset preparation

The 676 *E. coli* σ^{70} promoter sequences with TSS positions were obtained from RegulonDB [9]. Each sequence had the format of [TSS - 60...TSS...TSS + 20]. According to the position information of coding regions in the genome sequences, the positive dataset was divided into two subsets: 607 promoters which locate in the non-coding regions and 69 promoters which locate in the coding regions.

Negative dataset should be taken from the non-promoter sequences. Genes in prokaryotic genomes often form operons and only the intergenic non-coding region upstream of the first gene in the operon may contain promoters. Based on the transcribed direction of proximal consecutive genes, the non-coding regions can be classified into three groups: divergent, convergent and tandem regions. Obviously, the divergent regions have the very high probability to contain promoters because they are guaranteed to be upstream regions of operons. On the contrary, the convergent regions usually do not contain promoters because they cannot be upstream regions of any genes. The tandem regions may contain promoters or not. For promoters located in non-coding regions, the negative dataset was taken from the convergent regions. While for promoters located in coding regions, the negative dataset was randomly taken from the coding regions which do not overlap with any known promoters.

Sample sequences in each negative dataset were extracted from the proper regions with the same number and length as the ones in corresponding positive dataset. That is to say, the negative sequences have the same format as the positive ones: [nonTSS - 60...nonTSS...nonTSS + 20]. The site which locates in the 61st position is a hypothetical false TSS (nonTSS).

B. Candidate feature calculation

Content feature calculation: Oligonucleotide frequency distribution is one of the main content features which reflect the global composition properties of promoter sequences. An oligonucleotide can also be called a word. For the DNA sequence composed of {A, C, G, T}, the number of possible words of length k is 4^k . Just like the PFD method [2], we first calculate the occurrence frequencies of 4^k possible words in the training set: f_i^P for the positive set and f_i^N for the negative set. The formula based on maximum likelihood estimation (MLE) is given by:

$$f_i = \frac{n_i}{\sum_{i=1}^{4^k} n_i} \quad (1)$$

where n_i is the number of every word found in the dataset. Then, for a test sequence, the k order cumulative score s_{wk} is obtained by using the following expression:

$$s_{wk} = \sum_j \log\left(\frac{f_j^P}{f_j^N}\right) \quad (2)$$

where the summing operation is to all the words found in the test sequence.

For promoters located in non-coding regions, the maximal value of k was calculated as 6. So the frequency distributions of words with length from 1 to 6 were all designated as candidate features. Their cumulative scores are denoted as s_{wk} where $k=1, \dots, 6$. In the same way, for promoters located in coding regions, the maximal value of k was 4 and the frequency distributions of words with length from 1 to 4 were designated as candidate features, whose cumulative scores were s_{wk} where $k=1, \dots, 4$.

Signal feature calculation: Signal features are generally short conserved motifs, which reflect the local properties of promoter sequences. Among such motifs, we first consider the -10 motif, -35 motif, TSS, extended -10 motif and UP element. As the spacing between -10 and -35 motifs is also fairly conserved, we combine the -10 motif, -35 motif and spacer into a composite motif. Then the composite motif, TSS, extended -10 motif and UP element were designated

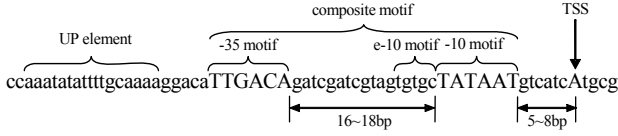


Fig.1 Conserved motifs in E. coli σ^{70} promoter sequences.

as candidate features finally. The relative locations of these motifs are shown in Fig. 1.

One of the most influential approaches to represent conserved motifs is position weight matrix (PWM) method. The PWM presents four lines, one for each kind of nucleotide, and as many columns as there are positions in the motif the matrix is modeling. Each cell $M(\alpha, i)$ of the matrix (where α is a line number and i a column) corresponds to the weight assigned to nucleotide α at position i of a putative motif. One of the convenient approaches to calculate the weight is the MLE method just like the word frequency calculation. Given a PWM of length L , the score s_j is calculated as follows:

$$s_j = \sum_{i=0}^{L-1} \left[\log \frac{M^P(\alpha_{j+i}, i)}{M^N(\alpha_{j+i}, i)} \right] \quad (3)$$

where j is the initiation position of the motif, P and N denotes the positive set and the negative set, respectively. Especially, there is no any motif in the negative sequences at all. So the $M^N(\alpha, i)$ should be substituted with the average occurrence frequency of the corresponding nucleotide for every column.

The composite motif model includes two PWMs for the -10/-35 motifs and an empirical distribution function for the spacer. Then the global motif score s_c is defined as the sum of the -10 motif score s_p and the -35 motif score s_x plus the score s_d of the spacer. Unfortunately, the training set did not provide any particular location information of the -10/-35 motifs. So we developed an iterative search algorithm, named PSIA, which is based on expectation maximization (EM) principle, to seek the optimal PWMs and the spacing distribution in each fixed search space. The PSIA is given below:

Input: W , the number of sequences in the training set; $[m, n]$, the alterable interval for the beginning position j of the -10 motif; $[p, q]$, the alterable interval for the length l of the spacer; T , the upper limit of the number of iteration; L , the length of PWM; σ , the lower limit of difference.

- (i) Initialization: build the initial PWMs E_0 and G_0 for the -10/-35 motifs, and set the initial distribution function $F_0(l)$ for the spacers.

- (ii) Optimization:

Loop1: for $t=1, 2, \dots, T$, do:

Loop2: for $k=1, 2, \dots, W$, do:

Calculate the score $s_c^t(k)$ of the composite motif:

$$s_c^t(k) = \max_{\substack{j \in [m, n] \\ l \in [p, q]}} [s_p^t(j, k) + s_d^t(l, k) + s_x^t(j-l-L, k)] \quad (4)$$

where:

$$s_p^t(j, k) = \sum_{i=0}^{L-1} \left[\log \frac{E_t^P(\alpha_{j+i}, i)}{E_t^N(\alpha_{j+i}, i)} \right] \quad (5-1)$$

$$s_d^t(l, k) = F_t(l) \quad (5-2)$$

$$s_x^t(j-l-L, k) = \sum_{i=0}^{L-1} \left[\log \frac{G_t^P(\alpha_{j-l-L+i}, i)}{G_t^N(\alpha_{j-l-L+i}, i)} \right] \quad (5-3)$$

Memorize the beginning position y_k^t of the -10 motif and the length $d^t(k)$ of the spacer in the $s_c^t(k)$.

Loop2 ends.

For each sequence, extract L bp consecutively from y_k^t and rebuild E_t ;

Extract L bp consecutively from $y_k^t - d^t(k) - L$ and rebuild G_t ;

Update $F_t(l)$ using all of the $d^t(k)$.

If $\|E_t - E_{t-1}\| < \sigma$ and $\|G_t - G_{t-1}\| < \sigma$, loop1 ends.

Loop1 ends.

- (iii) Output E_t , G_t and $F_t(l)$.

At the initialization step, we built E_0 and G_0 from the position $[TSS - 12 \dots TSS - 7]$ and $[TSS - 35 \dots TSS - 30]$, respectively. These positions are the typical locations for the -10/-35 motifs in the E. coli σ^{70} promoters. Establishing such initial models may accelerate the iteration to convergence. For simplicity, we set $F_0(l)$ as a uniform distribution function on the interval $[p, q]$.

In the PSIA, the interval pair $[m, n]$ and $[p, q]$ expand the search space of the composite motifs jointly. Obviously, the resulting pairs E_t and G_t may be different if the two intervals vary. In order to obtain the 'best' pair of the matrices, we devised the OPSIA (Optimal PSIA) algorithm on the basis of PSIA, which comprises two steps: the first estimates the approximate range of the locations according to the prior knowledge of motifs, and then calculate the total information content I_c ($I_c = I_E + I_G$) of the matrix pair on every possible interval:

$$I_E = \sum_{i=0}^{L-1} \left[H_{\max} - \left(- \sum_{\alpha} (E^P(\alpha, i) \log_2 \left(\frac{E^P(\alpha, i)}{E^N(\alpha, i)} \right)) \right) \right] \quad (6-1)$$

$$I_G = \sum_{i=0}^{L-1} \left[H_{\max} - \left(- \sum_{\alpha} (G^P(\alpha, i) \log_2 \left(\frac{G^P(\alpha, i)}{G^N(\alpha, i)} \right)) \right) \right] \quad (6-2)$$

In formulas above $H_{\max} = 2$, since the nucleotide alphabet contains 4 letters. The pair with the maximum value of I_c can provide the most sufficient information content, so we take it as the best recognition PWMs.

The extended -10 motif locates immediate upstream of the -10 motif. When the optimal E_i is obtained, the PWM of the extended -10 motif can be calculated from the positions $[y_k^i - 5 \dots y_k^i - 1]$ in each sequence, whose score is denoted as s_e . For the TSS and UP element, the locations of PWMs are fixed in the sequences, thus the PWMs can be calculated directly. The scores of TSS and UP element were denoted as s_i and s_u , respectively.

Structure feature calculation: The knowledge about structure features of promoters is still limited now. Several models for estimating DNA structure such as the local curvature and stability of the double helixes from the di- and trinucleotides have been devised, based on different kinds of experimental data.

Local curvature can be represented by three kinds of angles: roll, tilt and twist. We used the dinucleotide parameters given by Goodsell and Dickerson [10] to calculate these angles in the sample sequences. The scores of roll, tilt and twist are denoted as s_r , s_t and s_i , respectively.

Stability can be represented by the average free energy of the double helixes. We used the dinucleotide parameters given by SantaLucia [11] to calculate the free energy in the sample sequences. The score of average free energy is denoted as s_f .

The roll, tilt, twist and average free energy were designated as the candidate features. For more calculation details, please consult the original papers [10, 11].

Feature selection: In the preceding section, we screened 14 candidate features for promoters located in non-coding regions, and 12 candidate features for promoters located in coding regions totally. It is necessary to find out discriminating ones from the candidate features according to the significance. Naturally, the significance of given k features can be estimated by the squared Mahalanobis distance D^2 between two classes (i.e. promoter and non-promoter) [12]:

$$D_k^2 = (\bar{m}_1 - \bar{m}_2)' S^{-1} (\bar{m}_1 - \bar{m}_2) \quad (7)$$

where D_k^2 is the squared Mahalanobis distance of k features; \bar{m}_i is the sample mean vector of features for class i ; S is the pooled covariance matrix of features, which is given by:

$$S = \frac{n_1 S_1 + n_2 S_2}{n_1 + n_2 - 2} \quad (8)$$

where n_i is the sample size of class i ; S_i is the covariance matrix of class i .

We developed a step-wise procedure to choose features which significantly increase the squared Mahalanobis distance. Supposing D_k^2 is the squared Mahalanobis distance of k features, the algorithm is described as below:

- (i) Initialization: Calculate D_1^2 for each single candidate feature firstly, and sort them in descending order as the candidate queue. Then take the maximal one as the initial feature in the feature set.
- (ii) Adding features: Assuming that there are already p features in the feature set. For a pending feature, if the new distance D_{p+1}^2 increases significantly comparing to the former distance D_p^2 , we consider this feature can provide significant additional information and add it into the feature set, then go to step (iii). Else, for the next feature in the queue, repeat step (ii).
- (iii) Eliminating features: After a new feature is added, eliminate one of the former p features in turn for each time, if the distance D_p^2 of the remained p features does not decrease significantly comparing to the current distance D_{p+1}^2 , we consider the eliminated feature does not provide significant additional information any more after the addition of a new feature and eliminate it indeed from the feature set, then put it to the bottom of the candidate queue.
- (iv) For the features in the candidate queue, repeat step (ii) and (iii). If there is neither feature to be added nor feature to be eliminated, the selection procedure ends. The resulting set will be the optimal feature set.

The procedure to test the significance of the difference between D_p^2 and D_q^2 uses the fact that the quantity:

$$F = \frac{n_1 + n_2 - p - 1}{p - q} \frac{n_1 n_2 (D_p^2 - D_q^2)}{(n_1 + n_2)(n_1 + n_2 - 2) + n_1 n_2 D_q^2} \quad (9)$$

follows an $F(p - q, n_1 + n_2 - p - 1)$ distribution when testing hypothesis $H_0 : D_p^2 = D_q^2$ [12].

For promoters located in non-coding regions, the optimal feature set includes 4mers frequency, 6mers frequency, composite motif, TSS, extended -10 motif, UP element, rolls and average free energy, 8 features totally. Their scores can be combined into an 8D feature vector \bar{s}_n , given by:

$$\bar{s}_n = [s_{w4}, s_{w6}, s_c, s_i, s_e, s_u, s_r, s_f] \quad (10)$$

For promoters located in coding regions, the optimal feature set includes 4mers frequency, composite motif, TSS, UP element, rolls and twists, 6 features totally. Their scores can be combined into a 6D feature vector \bar{s}_o , given by:

$$\bar{s}_o = [s_{w4}, s_c, s_i, s_u, s_r, s_t] \quad (11)$$

Thus, each sample sequence in training set will be represented as a feature vector, and the task of promoter prediction can be redefined as the discrimination of vectors in the feature space.

QDA for feature vectors: Maximum discrimination between the two classes is achieved with the quadratic discriminant function (QDF):

$$QDF = \log \frac{p_1^0}{p_2^0} - \frac{1}{2}(D_1^2 - D_2^2) - \frac{1}{2} \log \frac{|S_1|}{|S_2|} \quad (12)$$

where p_i^0 is the prior probability of class i ; $|S_i|$ is the determinant of S_i and S_i is the covariance matrix of class i ; D_i^2 is the squared Mahalanobis distance from an object vector \bar{x} to the sample mean feature vector \bar{m}_i of class i , which is given by:

$$D_i^2 = (\bar{x} - \bar{m}_i)' S_i^{-1} (\bar{x} - \bar{m}_i) \quad (13)$$

According to formula (12), the \bar{x} will be classified into class 1 if $QDF > 0$ and into class 2 if $QDF \leq 0$.

III. RESULTS AND DISCUSSION

A. Prediction performance measures

The measures which are widely used to characterize the accuracy of predicting approaches often include sensitivity (Sn), specificity (Sp) and average accuracy (AC).

Define TP as the number of promoters which are predicted as promoters, TN as the number of non-promoters which are predicted as non-promoters, FP as the number of non-promoters which are predicted as promoters, FN as the number of promoters which are predicted as non-promoters, the measures are given by:

$$Sn = \frac{TP}{TP + FN} \quad (14)$$

$$Sp = \frac{TN}{TN + FP} \quad (15)$$

$$AC\% = \frac{TP + TN}{TP + FN + FP + TN} \times 100\% \quad (16)$$

B. Prediction results in the jackknife test

In our study, a jackknife test, one of the cross-validation methods, was performed. Each sample sequence in the dataset is singled out in turn as the test set, and the remaining sequence are used as the training set to distinguish if the sequence in test set is a promoter. The whole test result was achieved by counting all of the results in each single

Table 1 Prediction results based on jackknife test

Negative dataset	Promoters located in non-coding regions			Promoters located in coding regions		
	Sn	Sp	AC (%)	Sn	Sp	AC (%)
1	0.86	0.86	86.5	0.72	0.85	80.0
2	0.86	0.85	85.8	0.68	0.85	78.6
3	0.86	0.85	85.7	0.71	0.79	76.4
4	0.86	0.87	86.5	0.71	0.80	77.1
5	0.86	0.86	85.8	0.70	0.80	76.4
6	0.85	0.84	84.7	0.71	0.84	79.3
7	0.86	0.84	84.7	0.67	0.81	75.7
8	0.86	0.86	86.0	0.74	0.82	79.3
9	0.85	0.85	85.2	0.74	0.85	80.7
10	0.86	0.87	86.5	0.72	0.86	80.7
Average	0.86	0.86	85.7	0.71	0.83	78.4

test. Furthermore, our negative dataset was extracted from the background sequences randomly. To reduce the effect of randomness, we continuously generated 10 groups of negative datasets, and used the average result of the 10 tests as the final prediction results.

The prediction results for *E. coli* σ^{70} promoters located in non-coding and coding regions were shown in Table 1.

From the table we knew that the Sn , Sp and AC for promoters in the non-coding regions reached 0.86, 0.86 and 85.7%, respectively. And for promoters in the coding regions, they reached 0.71, 0.83 and 78.4%, respectively. These results indicate that the feature selection and strategy of ‘divide and conquer’ are effective.

C. Comparison with other prediction methods

In order to examine the performance of our method, we made some comparisons with the PFD [2] and sequence alignment kernel + SVM [4] methods. These two methods mainly focus on the prediction of *E. coli* σ^{70} promoters which locate in non-coding regions. Based on our datasets for non-coding regions, the comparisons were shown in Table 2.

Table 2 Prediction results for *E. coli* σ^{70} promoters in the non-coding regions based on different methods

Method	Sn	Sp	AC (%)
Penalized Frequency Distribution	0.73	0.71	71.3
Sequence Alignment Kernel + SVM	0.81	0.81	81.4
Our work	0.86	0.86	85.7

Obviously, our method performs better than other methods on all of the measures and significantly improves the prediction accuracy of the promoters in non-coding regions.

For promoters in the coding regions, as far as we know there is no other method which is available to compare with ours, whose average prediction accuracy was also about 78% on the small dataset. So we think it has reached a satisfactory performance in the current situation.

D. Application to other prokaryotic promoters

Relative research discovered that many prokaryotic promoters have the similar structure and features with the *E. coli* σ^{70} promoters. The main differences are the conserved contents and locations of the motifs [13]. So our method can be used to predict these promoters after adjusting the model parameters properly.

Using the same procedure of dataset preparation, we extracted several promoter datasets: the *B. subtilis* σ^{43} promoters from DBTBS [14]; the *E. coli* σ^{54} , σ^{38} , σ^{32} and σ^{24} promoters from RegulonDB. Because the sizes of these available datasets in databases were fairly small, we only considered the promoters in non-coding regions.

Just like the analysis of the *E. coli* σ^{70} promoters, we got the feature set which consisted of 4mers frequency, composite motif, TSS, rolls and average free energy after the feature selection. The prediction results in jackknife test were shown in Table 3.

From Table 3 we can see that, although our method was devised based on the *E. coli* σ^{70} promoters, it can also be applicable to other prokaryotic promoters and achieve the prediction accuracy of more than 80%. However, the prediction accuracy in Table 3 was lower than that of the *E. coli* σ^{70} promoters. One of the main reasons responsible for such situation is that the scarcity of annotated promoters makes the statistical models inexact to some extent. With the accumulation of the available data, this problem will be solved gradually.

Table 3 Prediction results for other kinds of prokaryotic promoters

Promoters	Dataset size	Sn	Sp	AC (%)
<i>B. subtilis</i> σ^{43} promoters	88	0.83	0.82	82.4
<i>E. coli</i> σ^{54} promoters	28	0.86	0.80	82.1
<i>E. coli</i> σ^{38} promoters	62	0.82	0.81	81.5
<i>E. coli</i> σ^{32} promoters	29	0.83	0.80	81.0
<i>E. coli</i> σ^{24} promoters	32	0.81	0.81	81.3

IV. CONCLUSION

In this paper, we classified the prokaryotic promoter regions into two groups according to their locations and introduced a QDA approach based on feature selection to predict them respectively. We considered content features, signal features and structure features of the promoters as the candidate features and calculated them using the proper models. For the composite motif model, an OPSIA algorithm was developed to optimize the parameters. Then we selected out the discriminating ones from the candidate features through a step-wise procedure and utilized them to make the prediction by the QDA. The jackknife test on the *E. coli* σ^{70} promoter dataset was performed and high prediction accuracy was achieved. For the promoters in non-coding regions, our method performed better in the comparison to other two methods. At last, we applied the method on other promoter datasets and also achieved the satisfying prediction accuracy.

The framework of our method is extendable, which can accept new discriminating features to improve the prediction accuracy. Without any major modification of the main structure, the incorporation can be achieved conveniently by adding new quantities in the combined feature vector. Besides for calculating the composite motifs, the OPSIA can also be used to explore the conserved elements of other promoters and retrieve their consensus sequences on information content maximization criteria.

REFERENCES

1. Galas D, Eggert M, Waterman M (1985) Rigorous pattern-recognition methods for DNA sequences. Analysis of promoter sequences from *Escherichia coli*. *J Mol Biol* 186:117–128
2. Oppon E (2000) Synergistic use of promoter prediction algorithms: a choice for small training dataset? PH.D. Thesis, Western Cape University, South Africa
3. Mulligan M, McClure W (1986) Analysis of the occurrence of promoter-sites in DNA. *Nucleic Acids Research* 14:109–126
4. Gordon L, Chervonenkis A, Gammerman A et al. (2003) Sequence alignment kernel for recognition of promoter regions. *Bioinformatics* 19:1964–1971
5. Mitchell J, Zheng D, Busby S et al. (2003) Identification and analysis of extended -10 promoters in *Escherichia coli*. *Nucleic Acids Research* 31:4689–4695
6. Meijer W, Salas M (2004) Relevance of UP elements for three strong *Bacillus subtilis* phage ϕ 29 promoters. *Nucleic Acids Research* 32:1166–1176
7. Kanhere A, Bansal M (2005) Structural properties of promoters: similarities and differences between prokaryotes and eukaryotes. *Nucleic Acids Research* 33:3165–3175
8. Kanhere A, Bansal M (2005) A novel method for prokaryotic promoter prediction based on DNA stability. *BMC Bioinformatics* 6:1–10
9. Salgado H, Gama-Castro S, Martínez-Antonio A et al. (2004) RegulonDB (version 4.0): transcriptional regulation, operon organization and growth conditions in *Escherichia coli* K-12. *Nucleic Acids Research* 32:D303–D306
10. Goodsell D, Dickerson R (1994) Bending and curvature calculations in B-DNA. *Nucleic Acids Research* 22:5497–5503
11. SantaLucia J (1998) A unified view of polymer, dumbbell and oligonucleotide DNA nearest-neighbor thermodynamics. *Proc Natl Acad Sci USA* 95:1460–1465
12. Afifi A, Aizen S (1979) *Statistical Analysis: A computer oriented approach*. Academic Press, New York
13. Lonetto M, Gribskov M, Gross C (1992) The σ 70 family: sequence conservation and evolutionary relationships. *Journal of Bacteriology* 174:3843–3849
14. Makita Y, Nakao M, Ogasawara N et al. (2004) DBTBS: database of transcriptional regulation in *Bacillus subtilis* and its contribution to comparative genomics. *Nucleic Acids Research* 32:D75–D77

The vitro and vivo study of Poly (3-hydroxybutyrate) microspheres

Feng Tian, Yong-Liang Zhao, Chang-Jun Liu, Fan Li, Nan Xing

Institute of Medical Equipment, Academy of Military Medical Science, Tianjin 300161, China

Abstract — Purpose: A controlled-release drug delivery of bovine serum albumin(BSA) has been developed by successful encapsulation of BSA in Poly (3-hydroxybutyrate) (PHB) microspheres. The vitro and vivo characteristics of the PHB microspheres have been investigated. Materials and Methods: BSA-loaded PHB microspheres with a mean size of 6.9 - 20.3 μ m were prepared by using the water/oil/water double-emulsion solvent evaporation method. Results : The diameter of the microspheres ranged from 6.9 to 20.3 μ m depending on the different preparation parameters. The maximum and minimum BSA encapsulation efficiency within the polymeric microspheres were 69.8 and 7.5%, respectively, varying with preparation conditions. The controlled release characteristics of the microspheres for BSA were investigated in pH 7.4 media. The initial BSA burst release from 8.9 to 63.1% followed by constant slow release for 28 days was observed for BSA from BSA-loaded microspheres and followed the Higuchi matrix model. The cytotoxicity degree was 1 score when the leaching liquor concentrations were 100% and 75%, and the cytotoxicity degree was 0 score when the leaching liquor concentrations were 50% and 25%. The inflammatory reaction was heavy on week 1 subcutaneous postimplantation, thereafter, the inflammatory reaction gradually reduced with time. CONCLUSION: The BSA controlled release from microsphere for 1 month could be obtained, demonstrating that the microsphere might be used as the carrier of drug controlled release. Both cellular compatibility and histological compatibility were considered to be excellent, implying that the microsphere was biocompatible with the body. Significance: The vitro and vivo characteristics of PHB microspheres showed the feasibility of BSA-loaded microspheres as controlled release devices.

Keywords — vitro cytotoxicity, histological examination, controlled release, Poly (3-hydroxybutyrate) microspheres, BSA

I. INTRODUCTION

Injectable microspheres which were prepared from biodegradable polymer containing proteins or peptides as controlled release devices have been widely used for the treatment of human diseases and animal health. Fundamental understanding of the relationship among the size of microspheres, encapsulation efficiency and protein release property is essential to design microspheres delivery systems. Double-emulsion solvent extraction/evaporation method is one of the most popular methods to encapsulate hydrophilic

drugs specially protein and peptide drugs into microspheres [1-3]. Both natural and synthetic biodegradable polymers have been investigated for controlled drug release [4-7]. Among these polymers, PHB (poly-3-hydroxybutyrate) is found to be remarkable for its application in drug delivery due to its excellent biocompatibility and biodegradability. Hydrolytic degradation of PHB in vitro proceed to the monomer, D-(-)-3-hydroxybutyric acid. This acid is a normal constituent of blood and, in common with acetoacetate and acetone, is one of the three ketone bodies which are produced endogenously by the process known as ketogenesis. It is therefore thought that PHB will be well tolerated in vivo. So PHB is considered to be a good candidate for drug delivery.

Some researcher has studied the effects of PHB weight on the characteristics of microspheres [8]. Decrease in average molecular weight of PHB tend to reduce drug release from compacts containing tetracycline hydrochloride and polyhydroxybutyric acid(PHB) as controlled release devices [9]. Progressively faster rates of drug release from P(HB-HV) copolymer matrices prepared by solvent casting and melt-processing are obtained on increasing HV content [10]. The crystallization kinetics and morphology of P(HB-HV) polyesters both with and without the incorporation of a model drug, Methyl Red, have been investigated to influence drug release characteristics [11]. The release rate of the drug can be controlled over a wide range by proper choice of the kind and amount of additive in the preparation of the PHB microspheres [12]. The effect of various PHB/Chitosan ratios on the morphology and crystal structure of the drug release microspheres is investigated [13]. However, there is few literatures focused on the effects of polymer concentration in oil phase, emulsification concentration in external water phase, volume ratio of inner water phase to oil phase and volume ratio of primary emulsion to external water phase on the characteristics of PHB microspheres containing protein. This is one aim of the present paper.

Studies have been conducted to use polyhydroxyalkanoates (PHA) as implant materials for various applications, and no toxicity has been reported for PHA and their degraded products [14]. PHB as one type of the PHA family should be no toxicity, however, the biocompatibility of BSA-loaded PHB microspheres which were prepared from our lab is whether good or not is a crucial problem for the PHB as drug delivery carrier. so, the other aim of this paper

is to evaluate the biocompatibility of the BSA-loaded PHB microspheres.

In this study, we attempted to examine the feasibility of formulating BSA with PHB microspheres as an injectable polymeric carrier system for long-term controlled drug delivery. We present the results of our study using this system, with a view of drug loading and encapsulation efficiency, size, *in vitro* release, cellular compatibility and histological compatibility of BSA-loaded PHB microspheres.

II. MATERIALS AND METHODS

A. Materials

Poly (3-hydroxybutyrate) (PHB) (Mw=437kDa) was purchased from Tianlu Food Co. Ltd (Tianjin, China). Poly (vinyl alcohol) (PVA) (98% hydrolyzed, Mw=25kDa) was purchased from Sinopharm Chemical Reagent Co. Ltd (Shanghai, China). Bovine serum albumin (BSA) (fraction V, 66kDa) was purchased from Sigma Chemical Company. Ethanol (AR grade) was from Tianbo chemical Co. Ltd (Tianjin, China). All other reagents were of reagent grade.

B. Microsphere preparation

Double-emulsion solvent evaporation method was used to prepare the microspheres. Briefly, certain volume of an aqueous solution of 30mg/ml BSA (W1 phase) was added into PHB dissolved in chloroform (O phase). The mixture was emulsified using a homogenizer (FJ 200, Shanghai, China) at 23000rpm for 1 min. The resultant W1/O emulsion was added to certain volume of an aqueous solution of PVA and 0.9% NaCl (W2 phase) and homogenized at 13000rpm for 4 min. The resultant W1/O/W2 emulsion was then stirred for up to 4 h at 500 ± 10 rpm on a magnetic stirrer to allow the solvent to evaporate. The particles were collected by centrifugation in 5000rpm for 20min, washed three times in solution of 0.9% NaCl and dried under vacuum at -40°C for 24 h. The particles were stored in a desiccator at 4°C prior to use.

C. Analyses of microspheres size

Freeze-dried microspheres were re-dispersed in distilled water and observed by microscopy (MicroStar, America).

D. Evaluation of the BSA loading and encapsulation efficiency

Ten milligram BSA-loaded microspheres were dissolved in chloroform with vigorous shaking at room temperature for 24 h. After dissolved completely, 10 ml physiological phosphate buffer (PBS) solution (pH7.4, 0.1mol/L) was added to dissolve the BSA in the microspheres. Then, the resultant solution was filtrated. After that, 5ml Coomassie brilliant blue was added into 0.5ml resultant solution to be detected at 595nm by UV/Vis spectrophotometer.

BSA loading and encapsulation efficiency were determined by Eqs. (1) and (2), respectively:

$$\text{BSA Loading} = \frac{\text{amount of BSA in microspheres}}{\text{amount of microspheres}} \quad (1)$$

$$\text{Encapsulation efficiency} = \frac{\text{retained BSA amount}}{\text{initially loaded BSA amount}} \quad (2)$$

E. *In vitro* BSA release

Microspheres (50mg) were placed in triplicate into Eppendorf tubes and incubated in 10 ml release medium (PBS buffer, pH=7.4 0.1mol/L) under agitation (100rpm) at $37 \pm 0.5^\circ\text{C}$. At desirable time intervals, the microspheres suspension was centrifuged at 5000 rpm for 20min. The supernatant (10ml) was withdrawn and replaced with 10ml fresh release medium. The amount of BSA released was determined by measuring the BSA content in the supernatant. To determine the BSA content in the supernatant, 5ml Coomassie brilliant blue was added into 0.5ml supernatant solution to be detected at 595nm by UV/Vis spectrophotometer.

F. Histological examination

Tissue samples were fixed in 10% phosphate-buffered formaldehyde solution and embedded in paraffin. The samples were then sectioned at a thickness of 7 μm using an automatic microtome, followed by staining with hematoxylin and eosin (H&E). The stained sections of each test sample were examined by light microscopy (MicroStar, America) for tissue inflammatory reaction and were photographed.

G. cell culture

The mouse fibroblast cell lines L929 were cultured in DMEM (Dubecco's Modified Eagle Medium, Invitrogen, California, USA) supplemented with 10% fetal calf serum (FCS), 100U/ml penicilin, and 100mg/ml streptomycin. Cells were incubated at 37°C in a 5%CO₂ incubator. Cyto-compatibility testing was performed as leaching liquor contact test. The leaching liquor concentration of PHB microspheres were diluted into 100%, 75%, 50%, 25%, respectively, sterilized in 75% ethanol for an hour and fixed in 24-well culture plate. 10,000 cells were seeded onto the different materials and incubated for 72h .

H. Mitochondrial metabolic activity studies

The metabolic activity of the cells was determined using a methylthiazol tetrazolium (MTT) assay. The cells were rinsed with phosphate-buffered saline (PBS) twice. Then 900µl of serum free medium and 100µl of MTT solution (5mg/ml in PBS) were added to each sample, followed by incubation at 37°C for 4 h. After incubation, the MTT solution was removed, and the insoluble formazan crystals formed were dissolved in 1000µl of dimethylsulfoxide (Sigma). The absorbance was measured at 550 nm using a 96-well plate spectrophotometer^[15]. The following equation

was utilized to calculate the relative growth rate (RGR) of mouse fibroblast cell, according to ^[16] to evaluate the cytotoxicity of the PHB microspheres.

$$RGR = \frac{OD \text{ value of experiment group}}{OD \text{ value of control group}} \quad (3)$$

III. RESULTS AND DISCUSSION

This study was carried out to explore the feasibility of preparing BSA microspheres using the double-emulsion evaporation method. Generally speaking, the characteristics of the microspheres such as their particle size, morphology, loading, encapsulation efficiency, and vitro release behavior were affected by the different experimental conditions. In the present study, several parameters such as PHB concentration in the oil phase, PVA concentration in the external water phase, volume ratio of inner water phase to oil phase(W1/O) and volume ratio of primary emulsion to external water phase((W1/O)/W2) were explored to confirm their effects on the characteristics of BSA-loaded microspheres. The preparation parameters used in this study are listed in Table 1. Biocompatibility is important for the PHB as drug delivery carrier, so the vitro cytotoxicity examination and histological examination were used to evaluate the biocompatibility of the BSA-loaded PHB microspheres.

Table 1 Preparation conditions for BSA microsphere

Formulation ID	PHB concentration(mg/ml)	BSA concentration(mg/ml)	PVA concentration(mg/ml)	W1/O	(W1/O)/W2
A	10	30	20	1:5	1:10
B	20	30	20	1:5	1:10
C	30	30	20	1:5	1:10
D	50	30	20	1:5	1:10
E	30	30	10	1:5	1:10
F	30	30	50	1:5	1:10
G	30	30	20	1:20	1:10
H	30	30	20	8:20	1:10
I	30	30	20	1:5	1:1
J	30	30	20	1:5	1:8
K	30	30	20	1:5	1:12

Table 2 Characteristics of BSA-loaded microspheres^a

Formulation ID	A	B	C	D	E	F	G	H	I	J	K
Particle size(μm)	7.8	10.2	11.9	15	12.5	11.5	16.3	6.9	20.3	14.9	9.2
BSA loading(%)	5.6	4.5	3.0	4.1	1.3	2.1	3.8	4.1	4.1	2.9	3.2
Encapsulation efficiency(%)	7.5	22.1	36.4	56	13.6	29.5	61.2	17.2	69.8	52.9	20.4
Initial BSA burst release(%)	63.1	49.5	39.3	8.9	57.0	49.6	12.4	57.1	20.1	22.2	47.0

^aFor sample characteristics in Table 1. Initial BSA burst (%): BSA released during the first 24h. All data are represented with the mean value (n=3)

A. Effect of preparation conditions on size, loading and encapsulation efficiency of the microspheres

Effect of the PHB concentration in the oil phase

Polymer concentration is a key factor to influence the characteristics of microspheres. As shown in Table 2 (formulation A, B, C and D), Generally, the viscosity of a polymer solution has a significant effect on the sizes of the resultant microspheres. The more viscous is the polymer solution, the more difficult it is to break it down into smaller droplets, leading to bigger microparticles [17]. Clearly, the PHB concentration had a greater impact on particle sizes. When the PHB concentration increased from 10 to 50 mg/ml, the average sizes of PHB microspheres increased from 7.8 to 15 μm due to the increase in viscosity of the polymer solution. Meanwhile, the solidification of microspheres was more rapid at a higher polymer concentration, which might result in a viscous polymer layer at the microsphere droplet. It hindered the diffusion of BSA to the external water phase. As a consequence, a higher polymer concentration yielded a higher encapsulation efficiency of BSA.

B. Effect of PVA concentration in the external water phase

It is well known that the particle size can be controlled by means of varying the emulsifier concentration in the external water phase [2, 18]. In the present work, 10, 20 and 50mg/ml PVA solutions are used as the external water phase to examine the effect of PVA concentration on the characteristics of the microspheres. The results are summarized in Table 2 (formulation E, C and F). The size of microspheres fabricated at 10, 20 and 50mg/ml PVA concentration is 12.5, 11.9 and 11.5 μm , respectively. Evidently, a decrease in particle size could be achieved by increasing the concentration of PVA in the external water phase. A higher PVA concentration could increase the stability of emulsion

droplets formed during homogenization because the increased viscosity of the external water phase would prevent emulsion droplets from coalescence, resulting in smaller emulsion droplets. These emulsion droplets gradually hardened to form microspheres as the solvent in the emulsion droplets continued to evaporate. Therefore, the size of the microparticles was relied on the size of the emulsion droplets formed during homogenization. It was observed that as its concentration increased, the encapsulation efficiency and the loading increased accordingly. But increase beyond an optimum value led to a gradual decrease. The maximum encapsulation efficiency and loading were obtained when 20mg/ml PVA was used. This may have been due to the role of emulsifier. Below a critical concentration, the amount of emulsifier in the medium was not enough to stabilize all the microspheres and thus some of the drug was dissolved in the aqueous phase and lost before the evaporation of the solvent. On the other hand, when the emulsifier used was more than the critical level it coated all the surfaces excessively and might interact with available free drug during microcapsule formation resulting in its leakage into the aqueous phase.

C. Effect of volume ratio of inner water phase to oil phase (W1/O)

The volume ratio (W1/O) of inner water phase / oil phase also plays a critical role in the characteristics of the microspheres. Table 2 lists the properties of microspheres prepared with different volume ratios of inner water phase to oil phase. It was observed that the average size of microspheres decreased from 16.3 to 6.9 μm on increasing the volume ratios of inner water phase to oil phase from 1:20 to 8:20. The change of size was perhaps due to the fact that the relatively higher viscous oil solution made the droplets break down into smaller droplets difficult. The decreased

BSA encapsulation efficiency with an increase at volume ratios of water phase/oil phase might be due to the fact that the higher viscous oil solution could hinder the BSA in inner water phase diffusion to the external water phase, so the encapsulation efficiency of microspheres prepared with lower water phase/ oil phase volume ratio was more than that of higher water phase / oil phase volume ratio.

D. Effect of volume ratio of primary emulsion to external water phase ((W1/O)/W2)

The effect of (W1/O)/W2 on the characteristics of the microspheres is shown in Table 2(formulation I,J,C and K). With the volume ratios increase of external water phase, the sizes of microspheres decrease from 20.3 to 9.2 μ m. The reason was perhaps that the viscous of double emulsion gradually decreased with the volume ratios increase of external water phase, then making the droplets more easily breaking down into small droplets. The encapsulation efficiency gradually decrease from 69.8% to 20.4% when the volume ratios of external water phase increases from 1:1 to 1:12. This might be that higher volume ratios of external water phase resulted in the higher osmotic pressure between inner water phase and external water phase, this could make the BSA in inner water phase largely leakage into the external water phase, so the encapsulation efficiency of microspheres prepared with higher volume ratios of external water phase was less than that of microspheres prepared with lower volume ratios of external water phase.

E. In vitro release studies

PHB, as a biodegradable polymer, is generally degraded very slowly in vitro^[19]. The rate of drug diffusion was substantially higher than that of polymer degradation, so the release profiles are more dependent on drug diffusion rather than on polymer degradation.

The diffusion of the drugs from spherical matrices can be expressed by the modified Higuchi equation as follows^[20]:

$$\frac{M_t}{M_\infty} = \sqrt{\frac{D \times t}{\pi \times r^2}} \quad (4)$$

Where M_t and M_∞ are the accumulative amounts of drug release at time t and infinity, respectively, D represents the diffusion coefficient of the drug, and r is related to the size of the microspheres. It indicates that the accumulative release amount is proportional to $t^{1/2}$.

F. Effect of the PHB concentration in the oil phase

Fig. 1 shows the accumulative release (%) vs. square root time curves of microspheres prepared at 10, 20, 30, and 50mg/ml PHB concentrations, which reveal the release plots from 1 to day 28 are nearly in line after an initial burst of first day. So the whole release rate, over the period of day 1 to day 28, is controlled by the diffusion rate of drugs.

As the PHB concentration is increased from 10 to 50mg/ml in the oil phase, the size of microspheres is increased from 7.8 to 15 μ m, and their slope of release curves is decreased correspondingly, the experiment results are in agreement with the Higuchi equation. This could be illuminated as follows. The higher polymer concentration led to the larger size of microspheres which had relatively smaller surface-to-volume ratio than that of smaller size of microspheres. So, it was more difficult for the drug to diffuse through a longer diffusion distance.

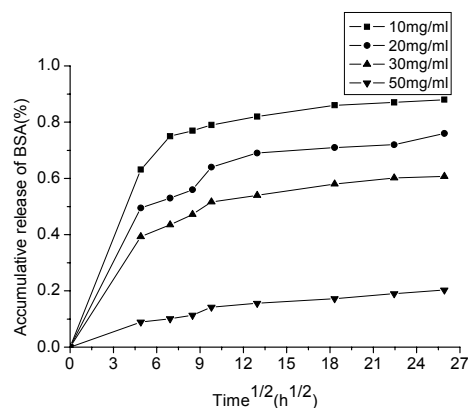


Fig. 1. Effect of PHB concentration on release profiles of BSA

G. Effect of PVA concentration in the external water phase

Release profiles of BSA-loaded microspheres prepared with PHB at 10, 20, and 50mg/ml of PVA concentrations are shown in Fig. 2. When the PVA concentration is increased from 10mg/ml to 50mg/ml, the size of microspheres is decreased from 12.5 to 11.5 μ m. According to the Higuchi equation, the slope of release curve of the microspheres prepared with 10mg/ml PVA in the external water phase should be lower than that of the microspheres prepared with 20mg/ml and 50mg/ml PVA in the external water phase. However, its slope was higher than that of them. This could account for the lower PVA concentration in the external water phase which could not stabilize the emulsion droplet enough, so the BSA distributed mainly toward the surface-associated area which led to a more rapid release.

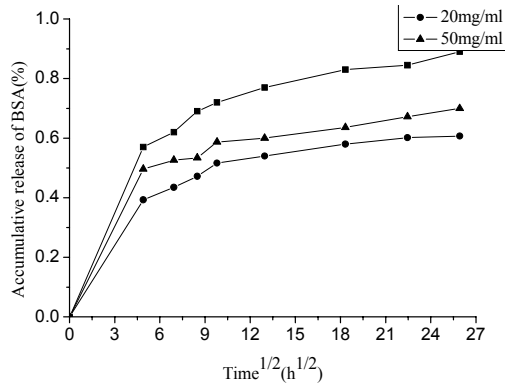


Fig. 2. Effect of PVA concentration on release profiles of BSA

H. Effect of volume ratio of inner water phase to oil phase (W1/O)

The microspheres are prepared using different W1/O. The BSA release profiles from these preparations are shown in Fig. 3. The slope of the release curves is increased when the size of the microspheres is decreased from 16.3 to 6.9 μm which are prepared with different W1/O. The Higuchi equation is fitted well by this results. It suggested that the relatively increased volume of inner water phase led to the formation of smaller emulsion droplets, followed by the formation of smaller microspheres. Consequently, smaller microspheres with a greater surface area were formed, resulting in microspheres having more surface-bound BSA. Therefore, the BSA release from the smaller microspheres would be faster than that of the larger microspheres.

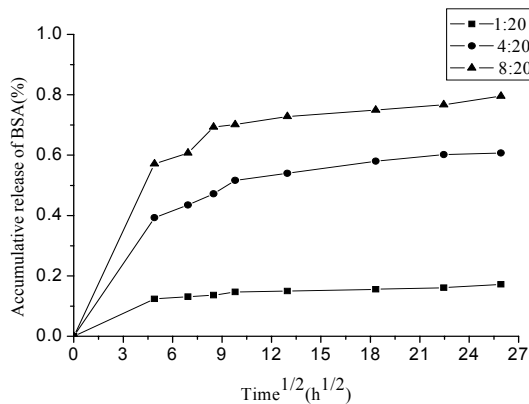


Fig. 3. Effect of water phase / oil phase volume ratios on release profiles of BSA

I. Effect of volume ratio of primary emulsion to external water phase ((W1/O)/W2)

Fig. 4 shows the effect of different (W1/O)/W2 on the accumulative release of microspheres made with PHB. It is obvious that the slope of the release curves is increased on decreasing (W1/O)/W2 followed by size of the decreasing from 20.3 to 9.2 μm . It is confirmed that the BSA release behavior from microspheres is complied with the Higuchi equation. The reason was considered to be that the diffusive distance of BSA from the microspheres would gradually become shorter on decreasing (W1/O)/W2.

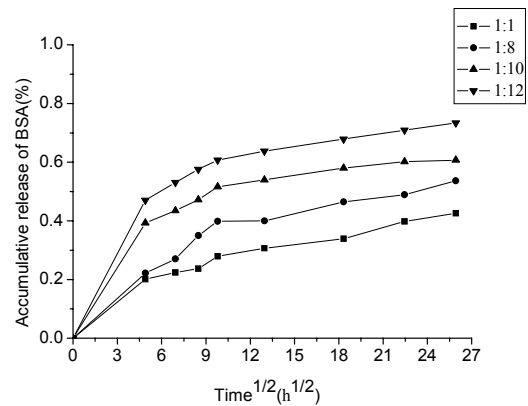


Fig. 4. Effect of volume ratio of primary emulsion to external water phase on release profiles of BSA

J. Histological examination

The levels of macrophage infiltration were studied histologically. The tissues implanted with BSA-loaded PHB microspheres stained with H&E and retrieved after weeks 1, 3, 5 showed differential macrophage response at different time intervals (Fig. 5). Histological analysis of the normal tissue showed the least macrophage infiltration (Fig. 5A), whereas the BSA-loaded PHB microspheres implanted after week 1 (Fig. 5B) showed heavy macrophage infiltration at the implanted site. These levels of macrophage infiltration gradually became reduced after week 3 (Fig. 5C) and week 5 (Fig. 5D). The volume of microspheres implanted into the subcutaneous tissue may be considered as an open porous implant, which induces an inflammatory response characterized by the infiltration of macrophage, neutrophils, fibroblasts and some lymphocytes and by the formation of fibrin, giant cells and new blood vessels^[21-24]. Tissue reaction to the PHB microsphere implanted site after week 1 showed heavy macrophage infiltration due to a systemic rise in the level of activated macrophages, which release cytokines, growth factors and other bioactive agents to modulate the function of other cell types in the inflammatory milieu^[25, 26]. The level

of macrophage infiltration gradually became reduced with time. This is due to polymer degradation as time progresses, with inflammatory reaction being mild at time points. This suggests that, during the early weeks when drug release from the polymers was in progress, there was decrease in the total volume of the microspheres, which attracted greater macrophage cell infiltration due to smaller particles of the microspheres.

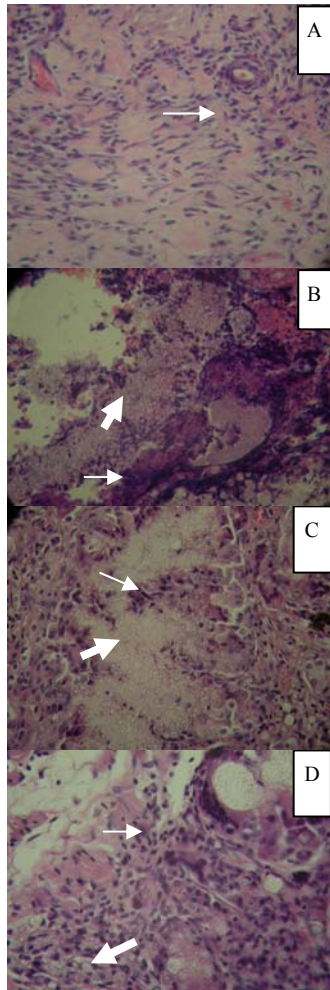


Fig.5. The histological observation of the microsphere ($\times 100$) BSA-loaded PHB microspheres preparation conditions: PHB concentration: 30mg/ml, PVA concentration: 20mg/ml, W1/O: 1:5, BSA concentration: 30mg/ml and (W1/O)/W2:1:10. (→) inflammatory cells surrounding the tissues.(→) microspheres

K. vitro cytotoxicity examination

A slight increase in cell growth was observed with the leaching liquor concentration decrease from 100 to 25%

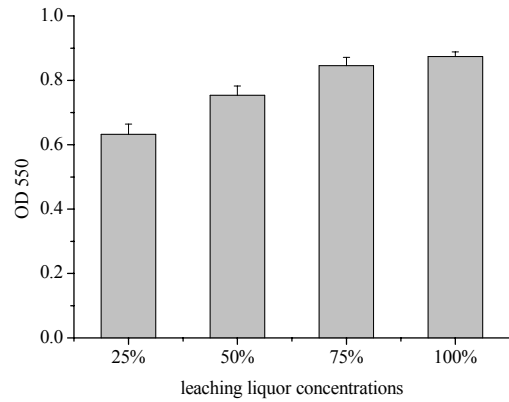


Fig.6. Fibroblasts cell line L929 proliferation analyzed by MTT assay on leaching liquor prepared from BSA-loaded PHB microspheres.reagent was used as control.

when fibroblast cell line L929 was inoculated on leaching liquor made from BSA-loaded PHB microspheres (Fig.6). The leaching liquor solution become more hydrophilic with decrease of leaching liquor concentrations from 100 to 25%, which can be more favorable for cell attachment and growth. This explains the increasing cell growth behavior on the leaching liquor prepared from the BSA-loaded PHB microspheres.

Table 3 showed that the cytotoxicity grade of 100% and 75% leaching liquor were 1 score,while the cytotoxicity grade of 50% and 25% leaching liquor were 0 score.This result indicated that the cytotoxicity grade was dependent on the concentrations of the leaching liquor made from the BSA-loaded PHB microspheres, which was consistent with the conclusion of the Lapp CA et al^[27].

Table 3 The relative growth rates and toxicity grades of L929 cells of mice

Leaching liquor concentration	RGR	Cytotoxicity grade
100%	80.7%	1
75%	89.2%	1
50%	100.1%	0
25%	103.4%	0
Control group	100%	0

IV. CONCLUSION

PHB microspheres containing BSA were prepared successfully by the double emulsion technique and characterized by optical microscopy, histological examination and *in vitro* cytotoxicity examination. The mean particle size of the microspheres ranged between 6.9 and 20.3 μm measured by optical microscopy, depending on the different preparation parameters. The maximum and minimum BSA encapsulation efficiency within the polymeric microspheres were 69.8 and 7.5%, respectively, varying with preparation conditions. The controlled release characteristics of the microspheres for BSA were investigated in pH 7.4 media. The initial BSA burst release from 8.9 to 63.1% followed by constant slow release for 28 days was observed for BSA from BSA-loaded microspheres and followed the Higuchi matrix model. Both cellular compatibility and histological compatibility were considered to be excellent, implying that the microsphere was biocompatible with the body. So, The *in vitro* and *in vivo* characteristics of PHB microspheres showed the feasibility of BSA-loaded microspheres as controlled release devices.

REFERENCES

- Jeffery, H., Davis, S.S., & O'Hagan, D.T. (1991) The preparation and characterization of poly(lactide-co-glycolide) microparticles. I. Oil-in-water emulsion solvent evaporation. *International Journal of Pharmacy* 77, 169-175.
- Jeffery, H., Davis, S.S., & O'Hagan, D.T. (1993) The preparation and characterization of poly(lactide-co-glycolide) microparticles. II. The entrapment of a model protein using a (water-in-oil)-in-water emulsion solvent evaporation technique. *Pharmacy Research* 10, 362-368.
- Metha, R.C., Thanoo, B.C., & Deluca, P.P. (1996) Peptide containing microspheres from low molecular weight and hydrophilic poly (DL-lactide-co-glycolide). *Journal of Controlled Release* 41, 249-257.
- Narayani R, Rao KP. (1996) Gelatin microsphere cocktails of different sizes for the controlled release of anticancer drugs. *Int J Pharm* 143, 255-8.
- Avgoustakis K, Beletsi A, Panagi Z, Klepetsanis P, Karydas AG, Ithakissios DS. (2002) PLGA-mPEG nanoparticles of cisplatin: *in vitro* nanoparticle degradation, *in vitro* drug release and *in vivo* drug residence in blood properties. *J Controlled Rel* 79, 123-35.
- Le Ray AM, Chiffolleau S, Iooss P, Grimandi G, Gouyette A, Daculsi G, Merle C. (2003) Vancomycin encapsulation in biodegradable poly (e-caprolactone) microparticles for bone implantation. Influence of the formulation process on size, drug loading, *in vitro* release and cytocompatibility. *Biomaterials* 24, 443-9.
- Carino GP, Jacob JS, Mathiowitz E. (2000) Nanosphere based oral insulin delivery. *J Controlled Rel* 65, 261-9.
- B.R. Conway, J.E. Eyles, H.O. Alpar. (1997) A comparative study on the immune responses to antigens in PLA and PHB microspheres. *Journal of Controlled Release* 49, 1-9.
- Augusta E. M. Collins, P. B. Deasy, Dense J. Maccarthy and D. B. Shanley. (1989) Evaluation of a controlled-release compact containing tetracycline hydrochloride bonded to tooth for the treatment of periodontal disease *International journal of pharmaceutics* 51, 103-114.
- Saghir Akhtar, Conlin. Pouton and Lidia (1992) Notaianni. Crystallization behaviour and drug release from bacterial polyhydroxyalkanoates. *J. polymer* 33, 117-126.
- Saghir Akhtar, Cofin W. Pouton and Lidia J. Notarianni. (1991) The influence of crystalline morphology and copolymer composition on drug release from solution cast and melt-processed P(HB-HV) copolymer matrices *Journal of controlled release* 17, 225-233.
- Kazuhiko Juni, Masahiro Nakano and Miho Kubota. (1986) Controlled release of aclarubicin, an anticancer antibiotic, from poly- β -hydroxybutyric acid microspheres *J. Control. Release* 4, 25-32.
- Wei Jen Shih, Yi-Hung Chen, Chi Jen ShIH, Min Hsiung Hon, Moo Chin Wang. (2007) Structural and morphological studies on poly(3-hydroxybutyrate acid)(PHB)/chitosan drug releasing microspheres prepared by both single and double emulsion processes *Journal of Alloys and Compounds* 434-435, 826-829.
- Chen GQ, Wu Q. Polyhydroxyalkanoates as tissue engineering materials. (2005) *Biomaterials* 26:6565-6578.
- Wang YW, Wu Q, Chen GQ. Reduced mouse fibroblast cell growth by increased hydrophilicity of microbial polyhydroxyalkanoates via hyaluronan coating. (2003) *Biomaterials* 24:4621-4629.
- GB/T16886.5-2003, Biological evaluation of medical devices-Part 5: Test for *in vitro* cytotoxicity.
- Y. Y. Yang, T.S. Chung, X.L. Bai, W.K. Chan. (2000) Effect of preparation conditions on morphology and release profiles of biodegradable polymeric microspheres containing protein prepared by double emulsion method *Chem. Eng. Sci.* 55, 2223-2236.
- M.K. Yeh, A.G.A. Coombes, P.G. Jenkins, S.S. Davis. (1995) A novel emulsification-solvent extraction technique for production of protein loaded biodegradable microparticles for vaccine and drug delivery, *J. Control. Release* 33, 437-445.
- G.T. Kose, H. Kenar, N. Hasirci, V. Hasirci, (2003) *Biomaterials* 24, 1949-1958.
- D. Sendil, I. Gursel, D. L. Wise, V. Hasirci, (1999) *J. Control. Release* 59, 207-217.
- Anderson JM. *In vivo* biocompatibility of implantation delivery systems and biomaterials. (1994) *Eur J Pharm Biopharm* 40:1-8.
- Anderson JM. Inflammation and the foreign body response. (1994) *Prob Gen Surgery* 11:147-160.
- Visscher GE, Pearsonn JE, Fong JW, Argenticri GJ, Robinson RL, Maulding HV. Effect of particle size on the *in vitro* and *in vivo* degradation rates of poly (DL-lactide-co-glycolide) microcapsules. [1988] *J Biomed Mater Res* 22:733-746.
- Visscher GE, Robinson RL, Maulding HV, Fong JW, Pearsonn JE, Argenticri GJ. Biodegradation of and tissue reaction to poly (DL-lactide-co-glycolide) microcapsules. (1986) *J Biomed Mater Res* 20:667-76.
- Ziats NP, Miller KM, Anderson JM. *In vivo* and *in vitro* interaction of cells with biomaterials. (1988) *Biomaterials* 9:5-13.
- Ward PA, Recruitment of inflammatory cells into lung: roles of cytokines, adhesion molecules, and complement. (1997) *J Lab Clin Med* 29:400-404.
- Lapp CA, Schuster GS. Effects of DMAEMA and 4-methoxyphenol on gingival fibroblast growth, metabolism, and response to interleukin21. (2002) *J Biomed Mater Res*, 60 (1): 30-35.

Address of the corresponding author:

Author: Fengtian
 Institute: Institute of Medical Equipment, Academy of Military Medical Science
 Street: WanDong Road 106, HeDong District
 City: Tianjin
 Country: China
 Email: tianfeng62037@yahoo.com.cn

Designing “Diagnostic ultrasound device” course in high-vocation education of BME

Hao Yu, Rong Song, Quan Su, Hongli Yang, Jun Han, Jihong Chai, Qingping Zhang

Biomedical Engineering department, Shenzhen Polytechnic, Shenzhen City, Guangdong province, China

Abstract — This article introduced the design of “Diagnostic ultrasound device” course in high-vocation education of biomedical engineering. The course is design as a constructing systemized course based on working process. The course objects analyzed deeply and contents designed in detail. The course achieved its teaching purpose.

Keywords — Course design, High-vocation education, Biomedical engineering, working process, constructing systemized course

I. INTRODUCTION

Biomedical Engineering (BME) as a scientific and professional discipline is increasingly known and spreading steadily in China. Experience to date shows that the career options for BME graduates are broad while with high threshold. Because the pre-requisite for a career in this field is the completion of a wide knowledge and a solid education in biomedical applications in electrical engineering, with an emphasis on biomedical electronics, instrumentation, signal analysis, and image analysis.

Education has been classified for three levels: vocational education level which train specialized workers, high-vocation education level which cultivate technicians, and professional education level which cultivate engineers^[1,2]. In China, the goal of high-vocation education is to educate students to be technicians who can be competent to corresponding work as soon as possible after graduate, and further more who can be competent to self-developed for much more advanced careers in this field for a long career life.

Chinese high-vocation education in BME was been initiated in 21 century 90’s, which adapted to Chinese medical device enterprises and hospitals rapid developing. Chinese high-vocation education in BME has characteristics of BME and high-vocation education, and the objects of high-vocation education in BME is to cultivate students to be technicians in medical device enterprises and hospitals, who have solid knowledge, technical competences and self-development competences. Accordingly, the graduate courses in Chinese high-vocation education of BME should be emphasis in on-the job training with solid knowledge tailored to suit them. Based on that, it is introduced and discussed in

this article that designing one graduate course “Diagnostic ultrasound devices” in high-vocation education of BME

II. COURSE DESIGN METHOD

In courses allocation of BME high-vocation education, the course is one of graduate elective courses after the compulsory course of “Medical devices principles”. Designing the “Diagnostic ultrasound devices” course has been designed as a constructing systemized course based on working process replacing comprehension course based on classified subjects^[3,4]. It means converting action field to learning field by analyzing working process and task, describing learning object as ability, and constructing systemized learning content represented by working tasks and subject knowledge tailor to suit them^[5-7].

III. DESIGN THE COURSE

Characteristics of the teachers: The course was developed by Biomedical engineering department of Shenzhen Polytechnic with the help of Shenzhen Association of Medical Devices, as well as a group of enterprises with solid knowledge and a great of experiences in medical devices especially diagnostic ultrasound devices. The teachers from colleges, enterprises, and hospital equipment sections are responsible for the course designing, lecturing and practicing with disassembly and maintainable diagnostic ultrasound devices as teaching equipments.

Characteristics of the learners: The course learners are the students at third year in high-vocation college, who are more adapt in perceptual thinking than in rational thinking. The students have learned basic knowledge of Analog Electrics, Digital Electrics, Micro Processing Unit, Physiology, Human Anatomy, and medical devices principles. In addition, they will take up occupations in medical device enterprises especially in diagnostic ultrasound device enterprises and hospitals after graduated.

Learning objects: The action field of “Diagnostic ultrasound devices” course is fixed on four working areas divided into occupation options after graduate and occupation options after self-education in the future career life:

1. After service and sales occupations in diagnostic ultrasound devices enterprises;
2. Inspection and maintenance occupations in hospital Equipment section;
3. Research engineer in diagnostic ultrasound devices manufacturing enterprises after self-education in future career life;
4. Clinical engineer on diagnostic ultrasound device in hospital equipment sections after self-education in future career life.

According to the action field orientation, the learning object of the course is described in five ability phases, which support action field as Figure 1 shown:

1. Basic understanding of clinical ultrasound physics;
2. Basic knowledge of advanced clinical ultrasound applications;
3. Basic ability of designing clinical ultrasound applications;
4. Solid education of operating and scanning technique;
5. Gain a mastery of diagnostic ultrasound device structure and maintenance approach.

Construct systemized learning content: Oriented by the course object of abilities, the “Diagnostic ultrasound devices” course content has contain five serial learning sectors.

1. The first sector is designing and exhibiting examples of the simplest ultrasound resonance signal detection and Doppler signal detection. The example exhibitions designed especially for the students who adapted at perceptual thinking to understand basic ultrasound physics principles and help them overcome their afraid of complex devices and inspire their confidence of the course.

2. The second sector is that students operate diagnostic

ultrasound devices in B mode, M mode, and Doppler mode. The students measure object samples in water according to the operation instructors, after that teacher import the basic principle of diagnose ultrasound principles via quizzes. Then the students diagnose each other of heart, liver, and bladder by themselves referring to the diagnose brochure. In this sector, the students are more inspired with their interesting in the course. They master basic principles of clinical ultrasound physics, basic knowledge of clinical ultrasound applications, and Solid education of operating and scanning technique. Especially in this sector, the students are trained to learn on their own initiative by using references.

3. The third sector is that teacher instruct students disassemble and maintenance the diagnostic ultrasound devices. By disassembling, the students recognize the diagnostic ultrasound device’s structure frame and every board. After that, the students detect the fault on circuit boards mainly focused on emitter, receiver, Doppler, display and record, and power supply. Teaching approach in this sector is that teacher give explain first, then student disassemble and maintenance under teacher instruction, and last teacher explain more deeply and summarize. In this sector, the students learn diagnostic ultrasound device structure and maintenance approach, and they are trained labor security.

4. The forth sector is an integrate practice in which the student are grouped to maintain diagnostic ultrasound devices on board level. They should work together using their knowledge and experiences to find out which board need to be replaced as an after service technician should do. The students integrate their knowledge and experiences, and cooperate with others. In this sector, they gain a mastery of diagnostic ultrasound device structure and maintenance approach, and are trained cooperate ability.

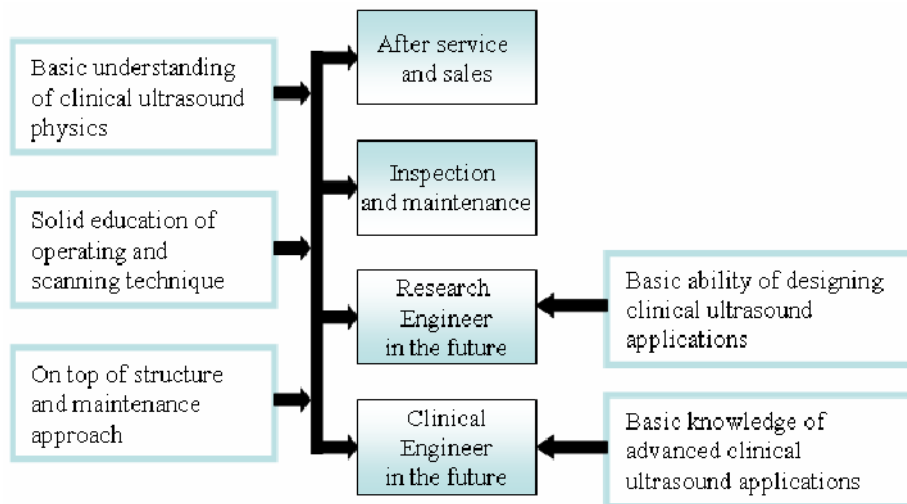


Fig. 1. Relationship between action field and learning field

5. The fifth sector can be put at the end of the course, or it can be carried out with the third sector and the forth sector simultaneously. In the sector, the students are required to design and manufacture a simple ultrasound detection system, which including emitter with drive circuit, receiver with amplifier, power supply circuit, and simple signal process unit. Their basic ability of designing clinical ultrasound applications is trained in this sector.

Learning assessment: In the “Diagnostic ultrasound device” course, the students are evaluated by two parts, which are process assessment and end-term paper examination. In process assessment, teacher mark every students in every sectors about operating, disassembling, maintaining, and designing practices fulfillment. End-term paper examination is mainly about principles, clinical applications, and designing knowledge. They are combined together to ensure the fruits of the course.

IV. CONCLUSION

The “Diagnostic ultrasound devices” course combines the characteristics of BME with the characteristics of high-vocational education. Orienting the course objects clearly, analyzing the contents of course deeply, and applying action-oriented teaching approach, the course is designed into five sectors to drive students learn and practice diagnostic ultrasound device initiatively under teacher instructions, and to train students working diathesis simultaneously about self-education, labor security, and cooperation.

BME department in Shenzhen Polytechnic has cultivated about 100 graduated students from 2004 autumn semester and they have entered the “Diagnostic ultrasound devices” courses at last academic year. Up to now, there are more than 30 students have practiced and taken up occupations in the Diagnostic ultrasound device enterprises and hospital equipment sectors. The students can be adapted to the occupations very quickly, and the enterprises and hospital equipment sectors have given higher estimates to the students. At

the same time, the students are self-developing for engineering occupations in future.

However, there is still much work to do in the course design especially in constructing resources library. The resources library should include operating brochure, maintenance brochure, system frame, schematic diagram of those typical diagnostic ultrasound devices, while by far the course just have resources and diagnostic ultrasound devices as teaching aid from Mindray Co., Ltd. and Landwind Co., Ltd. Other work should to be done is compiling of high-vocation teaching materials about “Diagnostic ultrasound device”, which has not been finished yet.

Therefore, the “Diagnostic ultrasound devices” course has achieved its teaching purpose, and it need to be developed more in constructing intact resources and teaching materials. It can popularize the course design to the other graduate elective courses in high-vocation education of BME.

REFERENCES

1. Akerlind, G.S. (2003). Growing and developing as a university teacher-variation in meaning. *Studies in higher education*. 28:375-390.
2. Marton, F. (1993) Conceptions of Learning. *International J. Educational Research*. 19: 277-300
3. Light G., Cox R. (2001) *Learning and Teaching in Higher Education: The Reflective Professional*. Sage, London.
4. Jiang Dayuan. (2003) “Learning Field” curriculum: Concep, Characters and Issues. *Studies in Foreign Education*. 30:26-31
5. Beard, R., Healey, F. and Holloway, P. (1974) *Society for Research into Higher Education*. Guildford, UK.
6. Foster, G. (1993) *Design of University Courses and Subjects: A Strategic Approach*. HERDSA Green Guide No 15. Campbelltown : HERDSA
7. Entwistle, N. (1997) *The Experience of Learning*. Scottish Academic Press, Edinburgh.

Author: Yu Hao
 Institute: Shenzhen Polytechnic
 City: Shenzhen
 Country: China
 Email: yuhao_zju@163.com

ECG-Analyzing Experimental System Based on Virtual Instrument

Jun Han, Hao Yu, Hongli Yang

Shenzhen Polytechnic, Shenzhen, China

Abstract — Introduces the concept and advantages of Virtual instrument (VI) and the graphical programming language LabVIEW, presents hardware and software design of the ECG-Analyzing experimental system and then briefly outlines its salient characteristics. The aim is to provide a new approach for training students to fully understand signal acquisition, data-saving process and some signal processing algorithms in biomedical research.

Keywords — virtual instrument, LabVIEW, ECG, DAQ

I. INTRODUCTION

An electrocardiogram (ECG) is a graphic tracing of the electric current generated by the heart muscle during a heart beat. It provides information on the condition and performance of the heart. It is one of the life signs monitored in many medical and intensive care procedure. It is also necessary for students to master ECG-detecting and analyzing knowledge during the study of biomedical engineering. Traditional ECG-detecting is depended on electrocardiographs which have the advantage of high integrated circuit, easy operation. It is very suitable for medical staffs to use. However, electrocardiograph has single function, lack of flexibility, not easy to extend its function in a laboratory environment.

In order to meet the requirement of providing flexibility in a laboratory style operation's environment, we develop an ECG-analyzing experimental system based on virtual instrument. This article introduces the concept and advantages of Virtual instrument (VI), presents hardware and software design of the system and briefly outlines its salient characteristics. The aim is to provide a new approach for training students to fully understand signal acquisition, data-saving process and some advanced signal processing algorithms in biomedical research.

II. VIRTUAL INSTRUMENT AND LABVIEW

Virtual instrument is defined as the combination of measurement and control hardware and application software with industry-standard computer technology to create user-defined instrumentation systems [1].

Virtual instrumentation provides an ideal platform for developing instructional curriculum and conducting scientific research. In an instructional laboratory course, students perform various experiments that combine measurement, automation, and control. Tools or systems used in these situations must be flexible and adaptable. In research environments, virtual instrumentation provides the flexibility that a researcher must have to modify the system to meet unpredictable needs. Research and instructional efforts also required that their systems be economical. Since we can reuse components in a virtual instrumentation system (without purchasing additional hardware or software), virtual instrumentation is an economical choice. Finally, measurement systems must be scalable to meet future expansion needs. The modular nature of virtual instrumentation makes it easy for us to add new functionality.

LabVIEW is a graphical programming language frequently used for creating test, measurement, and automation applications. LabVIEW uses icons instead of lines of text to create applications. Unlike text-based programming languages, LabVIEW use dataflow programming, where the flow of data determines execution. The flexibility, modular nature, and ease-of-use programming possible with LabVIEW makes it popular in top university laboratories.

III. SYSTEM HARDWARE DESIGN

The block diagram of the hardware construction is shown in Fig.1. ECG-signals picked up by three electrodes attached to an ECG-simulator are amplified by a high gain amplifier, such as Analog Devices AD623AN device, a specialized instrumentation amplifier offering precision balanced differential inputs and hence very high common mode signal rejection, combined with high gain. The isolation circuitry isolates DC component from the amplified

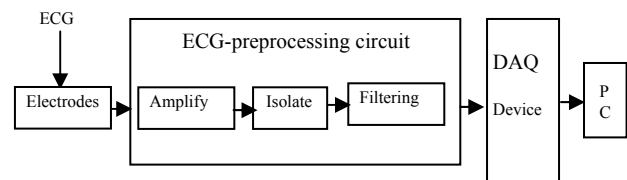


Fig. 1 The block diagram of Hardware Construction of the System

ECG signals. And an EMG noise which has a wide frequency range can be partially filtered by the RC low-pass filter circuitry.

We then use a multifunction NI-DAQ (data acquisition) Board PCI-MIO-16E-1 to sample the amplified signals and sending them back to the PC for display and analyzing. This NI-DAQ device has 16 analog input channels with 12-bit resolution each channel, its maximum sampling rate is up to 1.25MHz [2]. With NI-DAQ, the entire application development process is simplified, NI-DAQ features measurement-ready virtual channels and configuration services that reduce overall application development time by simplifying both hardware configuration and measurement troubleshooting.

IV. SYSTEM SOFTWARE DESIGN

With LabVIEW7.0, we complete the software design of the ECG-analyzing experimental system. The software is consists of main front panel module, data acquisition module, data-logging module, ECG-analyzing module and report generation & print module. Users can select a button on the main front panel to execute its appreciate function. The system front panel is shown in Fig.2.

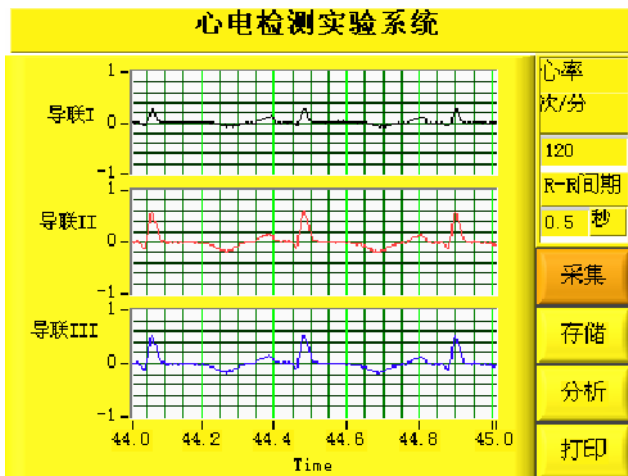


Fig. 2 The front panel of the system

A. Data acquisition module

LabVIEW installs Measurement & Automation Explorer (MAX), which establishes all device and channel configuration parameters. MAX saves the logical device number and the configuration parameters in the Windows automatically, detects and configures in the Windows Registry. NI-DAQmx is the NI-DAQ driver with the DAQ Assistant

which is convenient to configure parameters such as device number, channel number, sample frequency and timing.

B. Data logging module

It is often necessary to permanently store ECG-data acquired from the DAQ device. LabVIEW includes the ability to create a LabVIEW measurement file, an ASCII text file that can be read by a spreadsheet, or a text editor. The LabVIEW measurement file is easy to create. When you place the Write LabVIEW Measurement File Express VI on the block diagram, a configuration dialog box appears where we can specify how to store the file. For example, we can specify the format of the file, and how often you want the file to be saved to the hard drive.

C. ECG-analyzing module

This module can accomplish digital filtering, R-wave detecting, heart rate computation. The first processing unit is the digital filters, the raw signal and signal filtered are displayed and compared on the front panel, shown as Fig.2. Users can observe the performance of the filters.

We construct low-pass filter and band-pass filter using Butterworth Filter Express VI, the block diagram of the low-pass filter is shown as Fig.4. The low pass filter filters out the component with frequencies higher than a quarter of simple rate. This number can be adjusted according to ap-

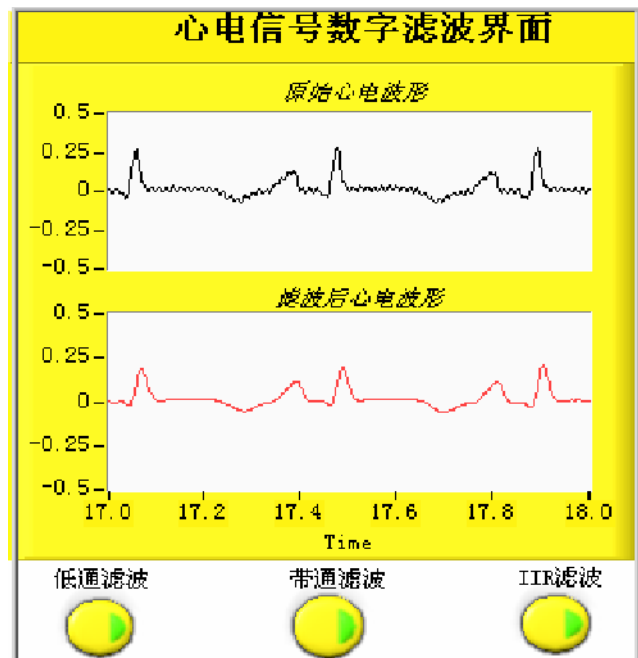


Fig. 3 The front panel of digital filters

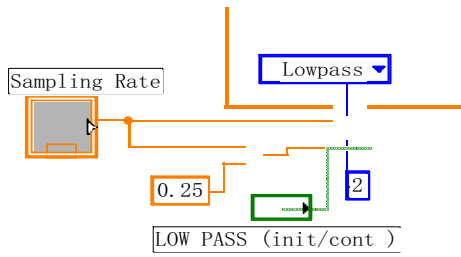


Fig. 4 Butterworth filter

plications. The band-pass filter further removes DC noise, and also removes the high frequency components. The bandwidth is from 0.01Hz to 100Hz. In order to remove 50Hz noise from AC power supply a band stop filter is needed. IIR Filter Express VI can be used as band-stop filter, the forward coefficients and reverse coefficient can be solved through a MATLAB program [3].

R-wave detection is a key process for the extracting ECG characters. There are several algorithms applied to detecting R-wave such as peak amplitude detection method, differential algorithm, wavelet transform algorithm [4], neural network algorithm [5] and so on. The differential algorithm executes fast and has better anti-jamming ability. We adopt two-order differential algorithm to detecting the position of P-wave. As Fig.5.shown, the P-wave position is labeled by red points.

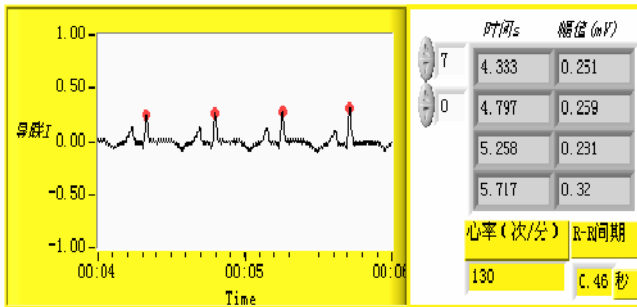


Fig. 5 The front panel of P-wave detection

V. CONCLUSIONS

The virtual instrumentation provides the flexibility for biomedical researchers. It can rapidly create applications using intuitive graphical language, it is easy to customize the instruments and add new functionality by modifying the LabVIEW code. This ECG-Analyzing experimental system based on virtual instrument is helpful to improve students' initiative and enhance the understanding of theoretic knowledge.

REFERENCES

1. National instruments Corporation. LabVIEW User Manual. April 2003 Edition
2. NI at <http://www.ni.com>
3. Chen Aiping, Hu Xiaodong. (2004) Design of IIR Digital Filter Based on MATLAB. Journal of Human Institute of Engineering Vol.14.No.3: 8-10
4. Yang Mingyao, Hu Weichi, Shuyu et al. (1997) ECG events detection and classification using wavelet and neural network. Proceedings 19th International Conference IEEE EMBS, Chicago, IL,USA.1997:280-282
5. Zumrury Dokur, Tamer Olmez, Ertugrul Yazgan et al. (1997) Detection of ECG wave forms by neural networks, Medical Engineering and Physics, Vol.9.No.8: 738-741

Author: HAN Jun, YU Hao , YANG Hongli
 Institute: Shenzhen Polytechnic/ Electrical Engineering Department
 Street: Xili
 City: Shenzhen
 Country: China
 Email: hanjun@szpt.net, vinyu@vip.163.com

Undergraduate Education on Biomedical Engineering of Comprehensive University in China

Xiaohong Weng

Chinese Society of Biomedical Engineering, Beijing 100005, China

Abstract—This paper mainly discussed undergraduate education on biomedical engineering (BME) in China. The history and development of BME education in China were reviewed. To sum up the undergraduate education of thirty years and explore the trends of future reform, the paper investigated five training programs on BME selected from top universities: Huazhong University of Science and Technology, Shanghai Jiaotong University, Tsinghua University, Xi'an Jiaotong University, Zhejiang University. They were divided into two groups according to their differences, and characteristics of each group were analyzed. Some suggestions about the training programs were brought forward.

Keywords—BME education, training program, undergraduate

I. INTRODUCTION: BME EDUCATION IN CHINA

Biomedical engineering (BME) education in China emerged in some comprehensive universities. It can be regarded as the first step that Zhejiang University (ZJU) in 1977 took the lead in establishing a specialty called Biomedical Engineering and Instrumentation. During the following two years, several famous universities like Xi'an Jiaotong University (XJU) in 1978, Tsinghua University (THU) in 1979 and Shanghai Jiaotong University (SJU) in 1979 etc., successively set foot in this field. Most of them at the beginning built BME discipline based on engineering departments or colleges. For instance, BME in THU was evolved from the department of electrical engineering, although it now belongs to Medical College. Compared with US although it has a later beginning, BME education in China was experiencing tremendous growth. Up to now, there are no less than 117 universities or colleges with BME discipline in China, including 92 undergraduate programs and 58 master programs.

Different from most traditional disciplines, due to its interdisciplinary characteristics, BME education in many universities began with training programs for postgraduate but not for undergraduate. Those postgraduate programs enrolled graduates from areas of both engineering and biomedicine at one time. When postgraduate educational programs were getting mature, undergraduate programs were just gained based on traditional engineering departments.

Among the earliest universities with BME disciplines in China, THU recruited undergraduate in 1982 after postgraduate in 1979; And Sichuan University even in 1999 began its undergraduate program on BME. From the first undergraduate program for bachelor's degree in 1977, to the Textbook Compiling Committee of BME and Instrumentation in the middle of the 1980's, and then evolving into current Teaching Instruction Committee of BME at the beginning of 1990's, undergraduate education on BME had been given more and more attention in China [1]. In 1987, a group of BME departments were set up in many Medical Colleges and Military Medical universities by Ministry of Health of PRC and General Logistics Department of PLA to train technicians competent for medical equipments maintenance in Hospital.

In China, BME educations are mainly involved in two kinds of universities, one is multiversity, and the other is medical university. A bachelor degree of BME in China can be conferred in three ways:

1) To confer a bachelor's degree of BME in BME department or specialty of either multiversity or medical university;

2) To confer a degree of BME in a multidisciplinary research center or institution in a university without a BME department;

3) To confer a degree of BME in a department or a specialty managed together by both multiversity and medical university, Such as the Second Military Medical University.

Two basic systems executed in China are academic year system and credit hour system [2]. The former mainly follows a four-year schedule in most universities, except few with a five-year one such as China Medical University and Chongqing Medical University; The latter has a flexible schedule for students to get a bachelor's degree if only pass regular credit hour.

It's quite necessary to review and sum up its growth when Chinese BME undergraduate education has gone across thirty years. The amount of universities with undergraduate training programs in China mainland has increased from the first one in 1977 to 68 in 2003 [3] and then to 91 in 2007. However, the strength and feature between them are different. Some universities launched a BME specialty only for drifting with the tide, which caused the good and bad

Table 1 Top universities on BME discipline in 2005, 2007 in China

University	Rank in BME in 2005	Rank in BME in 2007	Rank in Engineering In 2007
Southeast University	2	1	16
Shanghai Jiao Tong University	3	2	2
Sichuan University	6	3	18
Zhejiang University	1	4	3
Huazhong University of Science and Technology	5	5	6
Xi'an Jiao Tong University	4	6	7
Tsinghua University	7	7	1

intermingled. Among them the top ones are still those top comprehensive universities in engineering field (Table 1). Since their training programs are representative in certain extent in China, to investigate their curriculum systems for undergraduate will help to set good examples and explore the trends for the future reform on BME undergraduate education in China.

II. CHARACTERISTICS OF THE TRAINING PROGRAMS OF UNDERGRADUATE ON BME

There is no consensus among educators as to the best educational model of BME to be followed. Each university has its own feature and advantage, which causes diversity of training programs. Five universities, Huazhong University of Science and Technology (HUST), THU, ZJU, XJU and SJU, were involved in this paper. All samples are based on undergraduate teaching program schedule of each university. In general, curriculum structure for undergraduate on BME consists of six parts: basic courses in general education, basic courses in science discipline, common core courses in specialty, specialty-oriented courses, practice training and undergraduate project (Thesis). Commonness and differences between each training program were analyzed.

Manifest commonness can be seen: The curriculums of Engineering are core, complemented by Chemistry, life science and medicine. All programs have some practice courses, about eight percent to ten percent of whole credit hours, for students to develop hands-on engineering skills. Besides, some universities provide more abundant electives in general education part, such as economic management, human culture and social science. Specially, THU gives an emphasis on technical writing. ZJU and SJU provide an introductory course on BME for freshmen. On the other hand, the main differences in these training programs can be seen in specialty-oriented courses. Based on this, the five

training programs were divided into two groups. One has clear specific orientations, represented by HUST. The other hasn't, represented by other four. And the latter also can be subdivided by the differences in breadth and depth of curriculums.

Results of the comparison of differences in specialty-oriented courses:

A. Group one

As a typical kind of having clear specific orientations, HUST mainly focuses on four subspecialties with four groups of systematic curriculums:

- (1) Medical Electronics and Information Technology
- (2) Biomedical Photonics and Sensor Technology
- (3) Biomaterials and Tissue Engineering
- (4) Biomedical Analysis and Instruments

In each direction students must pass four or five required courses and one or two electives. The training program in HUST attaches importance to life science, and emphasizes specially on life science, optics and informatics application in engineering. And courses of Biomedical Photonics stand out as an educational feature based on its scientific research. This kind training program is helpful for future graduate to develop along a clear ladder in pursuing advanced study, and advantageous to students' employment in involved field.

B. Group two

In this group including four without systematic curriculums in specific orientations, XJU and ZJU have a quite broad range of subspecialties, while THU and SJU have a relative narrow but deep curriculum structure.

a. XJU provides more than twenty specialty-oriented elective courses in which about a dozen of subspecialties in BME will be touch upon by undergraduates. The list ranges from bioinformatics, medical image processing, Biomedical Imaging Equipment, telemedicine, biomedical photonics, molecular biology, biomaterial and tissue engineering, neural biology, Biomechanics, Rehab Engineering, electrophysiology, biomedical Ultrasound, biomedical instrument and device, Biomedical signal Processing to biosystem modeling, etc.. Students have to pass more than a dozen courses to get at least 28 credit hours, accounting for 15.4 percent of total credit hours.

Similarly, curriculums in ZJU are diverse as well as with more engineering feature. The program In ZJU focuses on electronic technique, information detection and processing, and computer science application in medicine. Based on its scientific research, the program has obvious correlation with

all kinds of basic knowledge on biomedical informatics and medical instrumentation.

Specially, an introductory course of BME is appeared in training programs of both ZJU and XJU.

The kind of a width knowledge structure of training program will give students a good platform to gain more opportunities in their advanced research or employment, especially offer them understanding and perspective abilities to the frontiers as an open-minded manager in a multidisciplinary area.

b. Also without a specific orientation in subspecialty, the training programs of BME in THU and SJU have differences from the former. THU, as a cradle of engineers, has more abundant and profound basic courses in engineering than others. It doesn't involve in so many subfields of BME, but concentrates on instructing students in fundamentals of engineering, particularly in innovation ability and application ability. In the same way, compared with others, the training program in SJU pays more attention to chemistry, life science and basic medicine, providing more than ten optional courses on life science and basic medicine. Otherwise the project for undergraduate thesis is strengthened, for 13 percent of credit hour is the highest in all five training programs in question.

This kind training program, with study of relative depth in certain basic field, mainly trains students to have concrete fundamental knowledge because they may be employed in many other fields out of BME.

Generally, in group two the following two aspects are very prominent. First is that the students have relatively flexible choices on the training programs. Second is that excellent training conditions and resources are provided to the students.

III. CONCLUSIONS AND DISCUSSION

According to the investigation, some characteristics can be concluded from top universities on BME.

1. There is no exception to emphasis on the training of breadth range and significant interdisciplinary characteristics between engineering and life science.

2. In the first group, the training program can make student a strong competitive power in employment or advanced study.

3. In the second group, the students have relatively flexible choices on the training programs. The training programs can provide broad spaces for students to develop their personalities and open their perspective.

Each training program has its own advantage. However, compared international mature training program of top

universities, some problems and suggestions are brought forward.

1. No matter what kind training programs, feature is important. It is not only beneficial for students' career, but also helpful to make good reputation for university. Usually the feature of training program depends on its strength of scientific research. A wide knowledge platform is good, but if students wish to get incommutable skill and ability they need to be more profound in fundamental.

2. A modular course may become a future trend.

Compared with mature training programs international, the lack of two aspects in China was exposed:

a. Training on ability to communicate effectively as biomedical engineers in oral, written, computer-based, and graphical forms.

b. Opportunities to interact with and gain real-world experience with local and national medical device and technology industries, health-care organizations, educational institutions, and constituent populations.

Recently, in ZJU and SJU an introductory course of BME was set up, and in THU a course of technique writing was listed in electives. For freshmen, to open an introductory course is necessary. A mature modular introductory course of Arizona State University (ASU) [4] may be a good example. It combined training on ability of communication by poster presentation, lab reports and technique writing, understanding of bioethics, and lab experience with modular designs together, to reach the goal of introduction of the breadth of studies under BME umbrella and focus on their interests. The feedback from students of ASU proved advantages of the course.

Universities in China with different features may have different modular designs, for its modular designs can complement the lack of specialty range in certain universities. Another important use is to enlighten freshmen to understand this highly intersectant discipline and then to find an interesting subspecialty for further development.

3. A win-win cooperation relationship between universities and industries should be established as soon as possible. In fact, as a part of undergraduate program, many universities of US have signed programs associated with industries [5]. In China some organizations have began to plan and work on that.

For education in universities, effective practice courses should depend on real-world experience. Attendance of senior students to research projects on the spot in industry would transform their passive acceptance from books into a voluntary participation in practice. On the other hand, real-world activities also can help modular introductory course of freshmen. With BME industry's abundant resources and experience adding to educational programs, a sharable platform will make students' eyes wide open. For instance,

more kinds of devices and instrumentation from industries would solve the problems of limited facility in lab.

For BME industry, through this win-win partnership, to find talents in advance and save training costs will be possible. It may absorb new energy from senior students who entered into its projects during practice period with passing trainings under industry standard.

4. An integrated teaching team is a guarantee of perfect curriculums. The survey of the programs in comprehensive universities showed that a wide-open training is one of current popular trends of BME undergraduate education. It means students will touch upon as more subfields in BME as possible, thus so-called all-powerful team are requested. All BME departments in universities mentioned above have teaching groups ranging from 10 teachers to no more than 30 teachers. So currently a relative small scale of persons qualified to teach is another limit for BME undergraduate education.

Undergraduate education on BME in China is facing a further reform. There is no doubt that top universities on BME would be the pioneers as well as mirrors in the reform. At the same time, they should also learn the advanced experience and perfect training programs continuously. All educators' are striving to promote BME educate career. It can be expected that undergraduate education on BME in China will have a bright future.

ACKNOWLEDGMENT

The author wishes to thank Professor Yi Peng and Dr. Xiaolin Yang in PUMC for their valuable suggestions.

REFERENCES

1. Jiarui Lin. (1993) Developing biomedical engineering education in China. The 2nd Fareastern Conference on Medical and Biological Engineering, Beijing, China, 1993, pp149
2. Xiaoxiang Zheng. (2006) The education of biomedical engineering in China. Chinese Health Pictorial (3):52-53
3. Xuelong Zhang. (2004) Training and requirement for profession staff in the field of biomedical engineering. Proceedings of the 6th Annual National Conference of Chinese Society of Biomedical Engineering, Wuhan, China, pp476
4. Whitaker at <http://www.bmes.org/WhitakerArchives/innovations/>
5. Anli Ju, Xin Yan, Xiuwen Cheng.(2005) Construction on the basic medical courses for biomedical engineering education. Medical Information 18(1):16-18

Author: Xiaohong Weng
 Institute: Chinese Society of Biomedical Engineering
 Street: 5 Dongdan Santiao
 City: Beijing
 Country: China
 Email: 21zryx@sina.com

Bioinformatics Education in Medical College

Xiaolin Yang, Zhengguo Zhang

Department of Biomedical Engineering, Institute of Basic Medical Sciences Chinese Academy of Medical Sciences, School of Basic Medicine, Peking Union Medical College, No.5 Dondan Santiao, Dongcheng District, Beijing, China

Abstract — After the completion of the draft of the human genome, researchers realized that bioinformatics was an important tool to analysis biological data. Bioinformatics as a university subject has established gradually since then. Because of the interdisciplinary nature of bioinformatics and the depth of knowledge teaching, teaching bioinformatics become a challenging task for most educators. Chinese bioinformatics education is still in its beginning period. This manuscript describes the attempt of carrying on bioinformatics education in graduate level in medical college. The main aim of this course is focused on improving hands-on skill in bioinformatics tools application. Our results show that proper application-oriented bioinformatics curriculum and student-centered instructional strategy stimulate students' activities in bioinformatics learning.

Keywords — bioinformatics education, Curriculum, student-centered teaching, medical college

I. INTRODUCTION

Since the end of the last century, many genomes including human species have been completely sequenced. Research and discovery activities in the life sciences were no longer limited to a single gene or protein, and began to shift to high-throughput screening and high-content detection systems[1]. In the transformation, the urgency to process and analyze the deluge of data created by proteomics and genomics studies has caused bioinformatics emerged as an independently scientific discipline. By now, bioinformatics became indispensable method in life science. But there is still disagreement over the definition of bioinformatics. According the most common used definition by NIH (National Institute of health), bioinformatics is "research, development, or application of computational tools and approaches for expanding the use of biological, medical, behavioral or health data, including those to acquire, store, organize, archive, analyze, or visualize such data" [2]. Apparently, bioinformatics is an interdisciplinary science with strong links between the life sciences and mathematics, statistics, and computer science.

The critical role in the development of biotechnology have impelled the formalization of bioinformatics education in 1998 from Russ Altman[3]. From then on, a handful of universities in some western country, such as USA, UK,

France and Germany commenced formal education in bioinformatics education. The Workshop on Education in Bioinformatics started as an annual satellite meeting to provide a forum for bioinformatics educators to meet, discuss and exchange ideas. Currently bioinformatics education has several features. Firstly, most educational opportunities in bioinformatics education are for graduates. The main reasons were bioinformatics is a new interdisciplinary field and it mainly focuses on research. However, some efforts are taking on to integrate bioinformatics throughout the undergraduate biology curriculum [4]. Secondly, the educational background of bioinformatics student is diverse, from biology, medicine, pharmacology to statistics and computer science. Thirdly, the emphasis of bioinformatics training can be divided into three levels, which is reaching the use of pre-existing tools, teaching basic programming with algorithm design and teaching in-depth theoretical foundations and principles behind bioinformatics [5]. Because of the depth and breadth of knowledge teaching bioinformatics requires, teaching bioinformatics become an interesting and challenging task. Lots of literature concern on bioinformatics education and often cover topics such as the desired contents of bioinformatics curricula [3,6], what resources should be devoted to bioinformatics education[7], and instructional methods in training[8,9].

Chinese university began to offer bioinformatics courses in the beginning of this century. However, most universities are key and comprehensive universities. The literature focused on bioinformatics education in China is limited. Additionally, there is no content standard in teaching bioinformatics in China by now. Peking Union Medical College (PUMC) began to open graduate level bioinformatics course in 2003. In the present paper, we discuss our strategies for teaching bioinformatics in the educational program.

II. WRITING THE PAPER

A. Methods

Our bioinformatics course is mainly for medical and biological students. Most of them lack adequate mathematical and statistical expertise. The aim of our course is that students will become extensively trained and develop hand-on skills in the use of bioinformatics technologies, and that

Table 1 Bioinformatics courses content in PUMC

Core Themes	Main topics
Basic computer skills and bioinformatics resource	Common used computer skills in bioinformatics training
	Introduction of bioinformatics resource in NCBI
	Introduction of bioinformatics resource in other important bioinformatics web sites
Sequence Analysis	Pairwise sequence alignment (dynamic programming, heuristic methods, similarity matrices)
	BLAST
	Multiple sequence alignment, motif and profiles
Protein structure and function	PDB database
	Visualization of protein 3D structure
	Protein structure comparison and classification
	2D and 3D protein structure prediction
Gene Expression and Genomes	EST and Unigene database
	Analysis the difference of gene expression
	Human Genome and mouse genome
	Application of UCLC, Ensembl and NCBI Genome Browser

they will understand and appreciate the enormous potential of bioinformatics in the contemporary life science.

Curriculum: The teaching contents were defined based on Altman's curriculum [3] and the bioinformatics course of Jonathan Pevsner at the Johns Hopkins School of Medicine [10] and modified according to the facts of Chinese students. Table 1 shows the basic themes of bioinformatics curriculum to be covered in 2007. Because the main aim of our curriculum is solving problems in research work, bioinformatics fundamental theories were introduced simply, and the application of genome analysis were emphasized, compare with the Altman's curriculum.

Instructional method: As our main purpose is to improve the students' skills in the use of bioinformatics technologies, student-centered teaching method is a good way to achieve the goal. In every class, teacher introduced the basic bioinformatics knowledge and the application of representative bioinformatics tools. Then the students began to use bioinformatics tools to practice and analyze pre-designed problems. Students were encouraged to try and challenge. According the characteristics of teaching content, problem solving learning and problem based learning methods were

used. Furthermore, we encouraged students self-teaching using online tutorials and education resource, such as NCBI and S*Star[11]. In such a learning setting, students acted as a problem solver and teachers take on the role as supporters and facilitators.

B. Results

After five years exploration, the number of the students enrolled bioinformatics increased significantly and have reached the maximum the computer lab can afford in recently three years. The acceptance and satisfaction also improved significantly. According student's feedback, 95% students felt "satisfactory" with the course and 82% students thought bioinformatics was interesting. The satisfaction and acceptance in 2007 improved significantly compare to 2003. Moreover, we found that there was positive correlation between the acceptance of bioinformatics course and the students' computer levels. And the acceptance was the highest in the student with mathematics and statistics background although the number of students with such educational background was limited.

C. Discussion

In this paper we reported the attempts to carry on bioinformatics education in Chinese medical college at graduate level. The result showed that an application-oriented bioinformatics curriculum and student-centered instructional strategy could stimulate students' activities in bioinformatics learning.

In the reformation of teaching contents, we reduced the introduction of basic theories. Such as Hidden Markov Model, which is an independent topic in Altman's curriculum, was only introduced its application in multiple sequence alignment. At the same time, we tried to use Problem Based Learning (PBL) pedagogy in bioinformatics teaching. For example, we demanded students to design a bioinformatics experiment to find a "new" gene from the NCBI nucleotide database at the end of bioinformatics course. Students could discuss relative problem in class and get the teacher's guidance individually. The students reflected that the ability of comprehensive using of bioinformatics tool improved and the understanding of bioinformatics application grew up from the exercise.

From our results, we got to know the computer level was close related with the effect of teaching. Indeed, inexperience in computer application and unfamiliarity with web culture in some students limited their exercise in class. Moreover, the weakness of basics of knowledge in mathematics and statistics in Chinese medical and biological student also baffled their understanding in bioinformatics train-

ing. For example, the matrix used in sequence alignment was the very difficult to understand for most medical and biological background students. Through explanation by teacher and discussion between students, there were still some students who did not really get the meaning of matrix and how it affects the alignment results. So we suggest the education about mathematical science in undergraduate school should be strengthened. There are some difficulties in bioinformatics education for teaching staff. Because of the rapid development in bioinformatics researching, new methods and tools emerge in endlessly. The teachers should follow the “hot spot” closely. However, the training courses for the teaching staff are still very limited in China.

The reformation of our bioinformatics education will be keeping with the development of bioinformatics. We are building an online PUMC bioinformatics center[12]. Services such as EMBOSS[13,14], BLAST, protein 3D structure prediction tools, the mirror of R archive, and some Chinese bioinformatics tutorials are offered on the center. A higher level bioinformatics curriculum is planning and preparing, which mainly focus on senior application of bioinformatics technologies and in-depth theoretical foundations and principles. The basic and higher bioinformatics education can form a course series, which offer more education chance to difference background graduate students.

III. CONCLUSIONS

We have outlined some of the strategies that we have used in teaching interdisciplinary science—bioinformatics in graduate level in Chinese medical college. The main aim of the course is focused on improving hands-on skill in bioinformatics tools application. Selecting proper application-oriented bioinformatics education content and using student-centered instructional strategy promote students’ activities in bioinformatics learning.

REFERENCES

1. Kane MD, Brewer JL (2007) An information technology emphasis in biomedical informatics education. *J Biomed Inform* 40:67-72.
2. NIH working definition of bioinformatics and computational biology at <http://www.bisti.nih.gov/CompuBioDef.pdf>
3. Itman RB (1998) A curriculum for bioinformatics: the time is ripe. *Bioinformatics* 14:549-550.
4. BEDROCK: Bioinformatics Dissemination Education - Reaching Out, Connecting and Knitting Together at <http://bioquest.org/bedrock/>.
5. Counsell D (2003) A review of bioinformatics education in the UK. *Brief Bioinform* 4:7-21.
6. Feig AL, Jabri E (2002) Incorporation of Bioinformatics Exercises into the Undergraduate Biochemistry Curriculum. *Biochemistry and Molecular Biology Education* 30:224-231.
7. Assessing bioengineering and bioinformatics research training, education and career development: opportunities for nih and nsf collaboration. at <http://www.bisti.nih.gov/NSFNIHFinalReport824.pdf>
8. Shachak A, Ophir R, Rubin E (2005) Applying instructional design theories to bioinformatics education in microarray analysis and primer design workshops. *Cell Biol Educ* 4:199-206.
9. Choo KH, Tong JC, Tan TW et al. (2004) Application of problem based learning pedagogy in global online bioinformatics education. *Workshop on Education in Bioinformatics* 3.
10. Pevsner J. Bioinformatics and Functional Genomics. at <http://pevsnerlab.kennedykrieger.org/wiley/index.html>
11. S*Star.org Alliance Bioinformatics Education at <http://www.star.org>
12. PUMC Data Mining center. at <http://bme.imicams.ac.cn/>
13. Rice P, Longden I, Bleasby A (2000) EMBOSS: the European Molecular Biology Open Software Suite. *Trends Genet* 16:276-277.
14. Sarachu M, Colet M (2005) wEMBOSS: a web interface for EMBOSS. *Bioinformatics* 21:540-541.

Author: Xiaolin Yang, Zhengguo Zhang
 Institute: Department of Biomedical Engineering, Institute of Basic Medical Sciences Chinese Academy of Medical Sciences, School of Basic Medicine, Peking Union Medical College
 Street: No 5, Dngdan Santiao
 City: Beijing
 Country: China
 Email: yangxl@pumc.edu.cn

Exploring Teaching Methods on Biomedical Courses in Engineering Universities

Zhuowei Guo, Jin Li, Hong Liang, Guang Tang, Keshen Li, Liwei Zhang, Kuan Luan, Liang Guo

Automation College, Harbin Engineering University, Harbin, China

Abstract—Biomedical engineering plays an important role in the development of current medicine and biology. The education of biomedical engineering has made great improvements due to huge market potential today. As most biomedical engineering emphasizes on Biomedical Electronics in china, how to teach engineering students biomedical courses effectively is a new topic. Through the teaching reform, we explore a set of teaching methods. First of all, we break the teaching of traditional education model, and fully carry out research style teaching by selecting interesting topics. Accompanied with problem solving, learning and teaching could be finished. Considering weak biological knowledge background of engineering students, the simple words are used to elucidate the profound truth. Moreover, current multimedia technology is used to provide students an open teaching system. Due to biomedical engineering require a strong foundation in integrated capacity particularly, a series of research-oriented experiments for the scientific interest groups have been designed to train the students to develop their innovative thinking ability and practical skills. Finally in order to promote biomedical study, a variety of assessment methods is employed rather than rely on the single theory examination.

Keywords—Biomedical engineering, biomedical course, research teaching style, multimedia, research-oriented experiments

I. INTRODUCTION

Biomedical engineering is an edging course integrated by the theories and principles of biology, medicine and engineering whose basic task is to use the engineering methods to develop solutions for health-related products and techniques that improve the quality of life. Biomedical engineering plays an important role in the development of current medicine. The education of biomedical engineering has made great improvements universally due to its quick development and huge market potential. In America, the universities ranking before 10 have launched this specialty, at the same time, biomedical engineering is the most popular professional in Graduate School [1]. The same situation has been found in most of the universities in China. As most biomedical engineering emphasizes on biomedical electronics, how to teach engineering students biomedical courses effectively, such as physiology, molecular biology, biochemistry, et al, is a new topic. In this paper, ideas as fol-

lows are presented for the innovative teaching methods in biomedical courses for engineering students [2].

II. ACTIVATING THE STUDENTS' INTERESTS

Generally speaking, students from engineering universities are good at reasoning and calculating but lack of accumulation of memorized knowledge, which makes them feel difficult even not willing to study biomedical courses. So how to stimulate the interests of students to make them concentrate on the basic biomedical knowledge appears to be particularly important.

The traditional teaching method may lead students learning passively. In our teaching process, we tried to break the traditional education model and fully carry out research style. Before students' learning, some topics and problems should be presented in the form of cases. Accompanied with problem resolution, learning and teaching could be finished. Problems solving could be run through the whole process of teaching. All in all, the research style teaching and learning can not only inspire the students thirst for knowledge and create impulse, but also make students study independently and train their thinking ability. Feedbacks to students are provided by excellent topics in the process of problem solving, which enables them to master the concepts, principles and techniques. For instance, the case of AIDS is chosen when we give the lecture on virology. HIV and pictures of infected person as well as relevant stories will be firstly used to inspire the curiosity of students, then the duplication process of HIV virus will be shown by animated cartoon, at the same time discussions will be created to help students design the research scheme on preventing HIV virus from infecting people's cells. Through this process, not only the newest international research results but also the principles of outbreak of HIV can be widespread among students. Besides, not only the research interests of students can be stimulated but also their ability to resolve practical problems with biological principles can be cultured. Various teaching plans equipped with animated pictures and videos have been designed according to different teaching contents during the years of teaching. For instance, the most popular research of developmental biology has been introduced by watching the growth process of babies in the uterus with help of films; the research teaching plan on the druggers in

the emergency room has been designed according to the morphine problems, which won excellent effect [3].

Biomedical courses are generally regarded as boring and complicated courses by biomedical engineering students which make them lose interest in it. Efforts should also be made by teachers who require rich knowledge in major as well as wide horizon in order to make the students study actively. Immense results could be achieved by adding common and new events in relation to textbooks when giving lessons. For example, when we learn principles of human respiratory system, the operating principles of respiratory system can be better introduced by reviewing knowledge of structure about respiratory system and emergency treatment regarding choke in air passage.

III. INTEGRATING ENGINEERING SCIENCE TO LECTURES

Biomedical courses request learners own the biological knowledge background, which is relatively weak for engineering students. The sophisticated terminologies may intimidate students, therefore, the simplest language should be used to elucidate the profoundest truth. Special cases and the change from hard-understood written language to easily-understood oral language should be paid attention to when explaining some concepts in order to make students understand.

Besides, some background knowledge of biology should be engrafted to students and relevant reference books should be provided for reading after class in order to save class time. For instance, when giving a lesson on the structure and function of a cell, it is better to help students review the knowledge on protein; otherwise the process of protein synthesis won't be well accepted. Therefore, class time could be better utilized by explaining the basic concepts first then directing students adjust to the study of the course.

On one side, due to the limitation of the hours of professional instruction, it is difficult for the students to master a great deal knowledge in a short period. So the basic medical knowledge should be focused on making students grasp the most important content first in order to avoid themselves losing in the biomedical ocean. The teaching aim of biomedical engineering course should be given prominence to the content of biomedical courses. Consequently the medical theory could be digested by the students thoroughly according to the teaching aim of biomedical engineering in our school. On the contrary, less important contents could be left to students.

On the other side, the importance of the study on biomedical engineering courses and the basic medical knowledge will be easily neglected by engineering students. Therefore, the relationship in-between courses should be

paid special attention to in order to make the study adjust to the training objectives. This not only deeps the comprehensions of why they should learn biomedical courses but also make them use what they have learned during the courses. For instance, when giving the bioelectricity lessons, the formation of bioelectricity and the conducting mechanism should be explained by connecting to the cytology. Besides, the measurement of bioelectricity such as heart electricity and brain electricity should be added. In conclusion, all of this will make students fully master the knowledge from theory to application in practical situation.

IV. CREATING AN OPEN TEACHING ENVIRONMENT

The most effective and convenient way to learn biomedical courses has been provided for students of engineering university by current multimedia technology with its unique visual and interesting character. At the same time, multimedia courseware can run through the campus network so that students can study the class repeatedly at different time and different locations. Such teaching mode makes the teaching extremely interesting. For instance, brain and relevant knowledge could be one of the most complicated teaching contents. However, it is easier to make students understood why the bleeding of left hemisphere brain could lead to the hemi paralysis of the right side of the body and why the brain damage could lead to the speech disorder by making the shape and the internal structure of the brain presented lively in front of the students with the help of multimedia. All in all, problems on teaching have been easily resolved [4].

V. STRENGTHENING EXPERIMENTAL TEACHING

It is an important link to emphasize the cultivation of the comprehensive ability and strengthen the experimental teaching in order to culture the professional talents in the field of biomedical engineering. The aim of biomedical engineering is to cultivate the compound talents with not only the strong basic knowledge of science and medicine but also the ability of thinking logically, resolving questions, working independently and cooperating with people. Therefore, the experimental teaching and the cultivation of students' comprehensive ability should be highly emphasized.

Therefore, on the base of traditional teaching, we promote the developing-style experimental teaching which focuses on the culture of ability in study and research. The contents of research subjects will be changed into several experimental subjects, which can help to build the develop-

ing-style experimental teaching system to realize the share of resources and improve teaching quality by full use of research fees and experimental fees.

Besides, the designing experiments are planned to open to the research-oriented scientific interest groups. First of all, the students are asked to learn from high-grade students to master basic skills, at the same time, access to information on the progress in related fields, and design experimental routes in a submitted report. With the teacher's help, work will be done. Through the design of the experimental system, students can be trained to develop innovative thinking ability and practical skills in particular the habits of referring to materials [5].

VI. MULTI-EXAMINE FORMS AND EVALUATION IMPERSONALLY

In order to promote biomedical study, a variety of assessment methods should be employed rather than relying on the single theory examination. Operating extracurricular achievements should be combined in the assessment of student learning. In addition to the theory examination, the classroom discipline, classroom speaking activities, the after-school assignment also should be given to students aiming at helping students to learn the courses. Practice has been proven that after-school exercises won't become a burden on students, but will make it easy for students to save more time and energy to learn other extra-curricular knowledge [6].

In the teaching process, we not only learn from our students and feel the happiness of communicating with students but also feel proud of our students. No doubt that there still is some weakness existing in our teaching proc-

ess. For instance, the attention should be drawn on the improvement of the excellent textbooks in connection to the practical situation of this specialty and the match between the teaching of biomedical engineering courses provided for students and the practical demands of students. Anyway, efforts will continue to be strived for the best teaching effect.

REFERENCES

1. Haiyun Li et al. Practice and research on education mode of biomedical engineering [J]. Chinese Medical Equipment Journal, 2006, 27, pp 59-60
2. Dongsheng Xiong et al. Discussion on teaching mode of basic medical knowledge for Biomedical Engineering students in science and technology college [J]. Chinese Medical Equipment Journal, 2006, 27, pp 72-73
3. Shaoxian Cai, Weiyong Chen et al. The Application and Exploration of Discussion Method Applied to New Medical Teaching Mode [J]. Researches in Medical Education, 2006, 5, pp 116-117
4. Yan Tang et al. Developing of Courseware about Biomedical Engineering [J]. Chinese Journal of Medical Physics, 2005, 22, pp 431-434
5. Jiaxue QI et al. Cultivating students' comprehensive ability through the experimental course of Biomedical Signaling Tracing and Operating [J]. China Higher Medical Education, 2004, 5, pp 47-48
6. Xiuzhen Dong et al. The exploration of the concerned problems of education in biological medical engineering [J]. China Higher Medical Education, 2002, 5, pp 6-9

Author: Li Jin
 Institute: Harbin Engineering University
 Street 45, Nantong Street, Nangang District, 150001
 City: Harbin
 Country: China
 Email: lijn999@hotmail.com

Build a Characteristic Specialty to Cultivate Persons with Ability in Biomedical Engineering

Ling Li, Huafu Chen and Nini Rao

School of Life Science and Technology, University of Electronic Science and Technology of China, Chengdu, China

Abstract — For the purpose of building a characteristic specialty to cultivate persons with ability in biomedical engineering, which is combined by the life science and information science, and to adapt the development of future discipline, the three guidelines in our education system are exhibited in this paper. The three guidelines include attaching importance to the integrating with information technology, paying attention to the education of fundamental theory, and emphasizing education of individuation. The education fruits show that these three guidelines play an important role in building our characteristic specialty.

Keywords — characteristic specialty, biomedical engineering, education of individuation

I. INTRODUCTION

As a university of gaining "211 Project" and "985 Project", University of Electronic Science and Technology of China (UESTC) has developed into a multidisciplinary university, which has electronic information science and technology as its nucleus, engineering as its major field. Based on the advantages of electronic information science and technology, the purpose of our biomedical engineering is to cultivate persons with ability in combining of life science and electronic information technology.

For the purpose of building a characteristic specialty to adapt the development of future discipline, the three guidelines in our education system are exhibited in this paper. The three guidelines are attaching importance to the integrating with information technology, paying attention to the education of fundamental theory, and emphasizing education of individuation. In 2007 our BME was selected as one of the characteristic specialties in Sichuan province, which showed that these three guidelines played an important role in building our specialty.

II. INTEGRATING WITH INFORMATION TECHNOLOGY

In order to embody the advantages of information technology, our first educational guideline is integrating life science with information technology as much as possible. Our BME department was developed from radio engineer-

ing and automation engineering, now it has about 350 undergraduate, Master, Ph.D. students and post-doctor candidates, and more than twenty professional teachers, whose research backgrounds almost are electronic information technology.

A. Curriculum arrangement

In current curricula, twenty-seven percent courses are the field of electronic information technology, including Fundamental Electrical Engineering, Signal and System, Digital Signal Processing, Information Theory and so on.

Along with the development of BME, our curricula are adjusted every year. We usually revise arrangement of courses after it runs four years. In this period, suggestions from teachers and students are collected, and slight changes are accepted each year, at the same time, teaching effects are also evaluated. After four years' running, according to the integrative report in this period, a revised curriculum arrangement is determined.

B. Building teaching groups

According to the research areas of teachers, three teaching groups were organized in our department, including medical signal and image processing group, medical instrument group and medical computing group. The tasks of each group include mutual checking teaching plan, listening to the classes inter-group, discussing the teaching methods within groups, communicating with students, directing students in project research, etc. In a word, teaching groups must be responsible for not only the teaching quality in classes but also the ability in actual experiments.

It is difficult for us to get a reasonable evaluation after listening to an unfamiliar course. But mutual listening courses within group, who are close research areas, can propose more acceptable, actual suggestions for teachers especially for new teachers, and also can find own existing problems. For example, Signal and System, Digital Signal Processing and Biomedical Signal Processing are the courses in medical signal and image processing group, and are taught by different teachers. How the fundamental course and professional course connect effectively depends to a certain extent on the understanding degree among these

teachers within group. Hence, it makes teachers clear that in future classes which content needs to be reviewed, which content needs to spend more time to explain and they can know students in advance.

Due to study tasks heavy, mostly students are short of the ability in understanding the whole course system. Communicating between teachers and students will enhance the cognition of students to study system and improve teaching effect by the method of accepting suggestions each other.

C. Constructing core courses

The core courses are Biomedical Signal Processing, Medical Imaging and Medical Instrument Theory. The building contents include reformation of teaching method, the arrangement of the contents, selection of multi-teaching methods, reformation of examination methods, the way of communication with students and the design of experiments, etc. In which Biomedical Signal Processing was selected as one of the provincial excellent courses, and Medical Imaging was available as a candidate.

In the process of constructing our core courses, fruits were acquired in recent years, including the second prize of teaching achievement of Sichuan province and about twenty teaching research theses and seven textbooks published.

III. THE EDUCATION OF FUNDAMENTAL THEORY

The education of fundamental theory is a very important part in undergraduate students. In current curricula, thirty-one percent courses are fundamental courses. Program of "3+6" are implemented in our university, which means the very importantly fundamental courses constructed by university. Three means University Physics, University English, Higher Mathematics and six indicates Fundamental circuit analysis, Analogous Circuit, Digital Circuit, Microprocessors Theory and Interfacing Technology, Signal and System and Electromagnetic Field and Wave.

University puts much resources and people in developing "3+6" program. Electromagnetic Field and Wave was selected as one of the national excellent courses and the others are provincial excellent courses. Till now there are a national representative center of laboratory education (electronic field) and a national mathematic base of engineering.

All the resources are shared in university, so that our students have good conditions to study the fundamental courses. A lot of productions were obtained in our department. For example, the mean passing ratio of College English Test Brand 4 in recent three years is 93.3%, and one student obtained the first prize of National English Contest for College Students in 2006.

IV. THE EDUCATION OF INDIVIDUATION

In educational system, the differences among students impel us to emphasize education of individuation. Except the education in classroom and laboratory, we adopt Open Experimental Training and Project Research Program to develop individual creativity.

Open Experimental Training is short term training, about one month, which opens to all students. Students propose the idea for a project, and then corresponding teachers direct them to finish the design. For example, medical instrument group ask students teamwork to report the title and accomplishing possibility of project. And teaching group selects several excellent teams to support and direct, such as "baby body-heat alarm", "amplified-filter circuit of ECG detection" and "ultrasonic parking radar", etc. This training can improve the actually experimental ability of students.

Project Research Program is long term training preparing for the future study, which opens to juniors and seniors. Each year about 10% students can enter scientific research lab for their training. According to the result of past semester, some students may be washed out so that new students are likely to be selected to replace them. For example, in last semester, there were thirty-two students entering six labs to accept basic scientific research training, including "EEG signal processing" and "functional brain imaging technology" of medical signal and image processing group, "A type ultrasonic instrument design" and "design of virtual instrument" of medical instrument group, and "particle swarm optimization algorithm" and "clustering algorithm" of medical computing group.

Students reflected that they could study knowledge and their views were broadened after training and they had published sixteen journal papers and five conference papers.

V. CONCLUSIONS

Facts showed that attaching importance to the integrating with information technology, paying attention to the education of fundamental theory, and emphasizing education of individuation play a key role in building our characteristic specialty.

Author: Ling Li
 Institute: School of Life Science and Technology, University of Electronic Science and Technology of China
 Street: NO.4, Section 2, North Jianshe Road
 City: Chengdu
 Country: China
 Email: liling@uestc.edu.cn

Integrated Training Model on Biomedical Engineering Undergraduates' Innovation Ability

Ting Liu¹, Xin Tian^{1*}

¹ Department of Biomedical Engineering, Tianjin Medical University, Tianjin, China

Abstract — Biomedical engineering is one of the most important cross discipline fields in the 21st century. The cultivation of cross discipline talents with creative minds is vital to the construction of an innovative nation. Qualified graduates from the college should possess the capabilities of adopting appropriate methodology to resolve practical problems and be self-motivated to learn, which is mainly reflected in the abilities to question what it is and resolve problems. They should be able to identify problems in the conventions, question them and put forward feasible solutions to the problems. From this aspect, we have proposed an integrated training model on biomedical engineering undergraduates in order to develop the undergraduates' innovation ability.

We take “Biological Modeling and Simulation” course as a starting point, implemented integrated training model which includes research-oriented study and exercise training mode, class discussion and defense mode and literature retrieval and scientific writing training mode. Integrated training of innovative ability on different levels has led students to combine theories with scientific practice, develop undergraduate students' ability of scientific thinking, analyzing and solving problems in practice. With regard to the cultivation mode of innovative talents, integrated training model has changed the traditional teacher-centered mode, stimulated the students' motivation to learn and make innovations, it has become one of the most important ways in developing cross discipline innovative talents.

Keywords — biomedical engineering, innovative undergraduate talents, integrate training.

I. INTRODUCTION

Biomedical engineering is one of the most important cross discipline fields in the 21st century which involves life science, science and engineering. The cultivation of cross discipline talents with creative minds is vital to the construction of an innovative nation. Qualified graduates from the college should possess the capabilities of adopting appropriate methodology to resolve practical problems and be self-motivated to learn, which is mainly reflected in the abilities to question what it is and resolve the problems. They should be able to identify problems in the conventions, question them and put forward feasible solutions to the problems. With the regard to the cultivation of innovative talents, teachers should guide the students to make innovation in

active practice. A comparison between the undergraduates in China and their peers in the developed countries clearly indicates that Chinese students lag behind their foreign peers in the capabilities of solving practical problems and making innovations[1]. Such a regretful state is caused by that traditional education is teaching centered or teacher centered while the education encouraging innovation is student-centered. To reverse such a situation, we have proposed an integrated training model on biomedical engineering undergraduates in order to develop their innovation ability.

II. INTEGRATED TRAINING MODEL ON BIOMEDICAL ENGINEERING UNDERGRADUATES

The key point in teaching undergraduate students is to develop the ability of investigation, analyzing and solving problems occurring in practice, and provide all round systemic and comprehensive framework of knowledge as well. In the recent years, we have established integrated training model (Fig. 1) for biomedical engineering undergraduate students, including: research-oriented study[2] and exercise

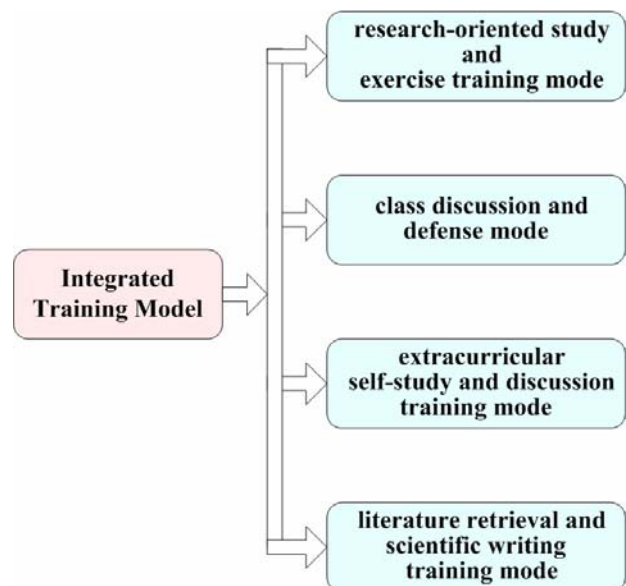


Fig. 1 Integrated training model on biomedical engineering undergraduates' innovation ability

training mode; class discussion and defense mode; extracurricular self-study and discussion training mode; literature retrieval and scientific writing training mode [3], etc. Systemic training is one of the most important means of fostering undergraduate innovative talents[4,5].

A. Research-oriented study and exercise training mode

In the traditional teaching, passive practice stands out prominently. Having the students follow the way pre-designed by the teacher, students come out with unitary result. This stifles students' innovation ability as the practice engaged in can not leave a deep impression upon the students and accordingly cannot promote students' capabilities of dealing with practical problems. To reverse such a situation, the exercises we assigned to the students have no standard answer. Students are required to construct their own ideas on the solving and analyzing of the problem. In this way, students will obtain different answers based on their own idea and may further compare the merit and drawbacks of different methods. This mode also enhances the students' motivation during self-study.

B. Class discussion and defense mode

Discussion in class plays an important motivational role in stimulating students' engagement in learning process. In the class, we have raised discussion topics on the key knowledge points and difficulties met in theoretical teaching. The discussion will improve the students' ability of finding problems, analyzing problems and finally solving problems confronted in the study, provide students with opportunities for explaining own ideas, facing other points of view, enriching understanding of a problem, and constructing knowledge networks.

C. Extracurricular self-study and discussion training mode

Extracurricular self-study involves the knowledge beyond that in the textbooks. Student will be recommended with English original textbooks, periodicals involve the application of modeling and simulation in life science, as well as the most pioneer research references related to textbooks. The self-study mode encourages students to seek relevant knowledge in various ways when facing problems and construct scientific thinking structure to solve the problem.

D. Literature retrieval and scientific writing training mode

Students are expected to play an active role in the *literature retrieval and scientific writing training mode*. A main educational principle in this mode is self-directedness in generation of the study aim, selection of the method, analy-

sis of the results and further discussion. Students will be introduced to the basic structure and writing skills of scientific paper. According to the content of the knowledge taught in class, students first choose a topic for further research. After literature retrieval and extracurricular self-study, students will conceive the outline of their paper in the aspects of study purpose, methods, possible results and key procedure in analyzing the problem. In the course of writing, students are encouraged to interact with each other and bring up discussions, helping students reconsidering a topic in richer and wider way. Finally, students will make a presentation based on their paper, defense themselves facing other points of view, enhancing understanding of the knowledge points and difficulties.

III. APPLICATION OF THE INTEGRATED TRAINING MODEL

'Biological Modeling and Simulation' is one of the main curricula in biomedical engineering major. It is a cross disciplinary course of modern medical education. The course involves life science, medicine and engineering. The aim of the course is to solve complex problems in the life system modeling and simulation with information technology and computer theory. We take "Biological Modeling and Simulation" course as a starting point, implemented integrated training model which includes research-oriented study and exercise training mode, class discussion and defense mode and literature retrieval and scientific writing training mode.

In the course, we have introduced four classical life system models helping to understand the process of modeling and simulation, they are:

- single specie ecological differential equation;
- Hodgkin and Huxley model of action potential;
- compartmental model ;
- system identification

In this paper, we will take these models as example and show how the integrated training model is implemented.

A. Research-oriented study and exercise training mode

Life system is a complex dynamic system, modeling of life system is a simplification of the reality, and a model is thought to be appropriate so long as it reflects the essence of the system studied. Same system may be simulated with different models, and same models may be used to simulate different systems. In addition, the algorithms used to solve the model vary.

For example, in the exercise of solving Hodgkin and Huxley model, students may choose different algorithms.

Since the system of equations is nonlinear due to the conductance terms, an analytic solution is not possible. To solve for membrane potential, it is therefore necessary to simulate the solution. Numerical solutions including Euler method, Gear method, Adams method, Runge Kutta methods, etc. may be used on Matlab. With different algorithm, students surely will come out with different results; they then may analyze why the results are different and decide which model is the most accurate.

B. Research-oriented discussion training mode

Research-oriented discussion training mode involves class discussion, oral defense and extracurricular discussion. In the class, teacher will propose discussions on difficulties and knowledge points so as to improve students' ability of accurate comprehension and knowledge point's refinement.

For example, when teaching Hodgkin and Huxley model and compartmental model, students are asked to analyze the errors of the model. In answering the question, they first have to go over the previously learned knowledge of *Verification, Validation and Accreditation in Modeling and Simulation*, analyze it from both mathematical model and mathematic simulation points of view. The discussion mode enhances the students' ability of analyzing problems systematically.

C. Scientific writing training mode

In this part, students will be acquainted with the process of carrying out a research, the basic structure of scientific paper and the key points in writing each section of the scientific paper.

The course not only provides students with latest domestic and foreign research in the class, but also makes recommendations of frontier literatures in the field of modeling and simulation in life system for after class reading. At the end of the class, students are asked to write a scientific paper which will be accounted into the final grade based on one of the four classical models. Students will elaborate the research in the sequence of literature retrieval, determine the aim of the study, and select methods and strategies that may be used solving the problem. In their minds, they should conceive a clear outline of the process of the research.

For example, a student comes up with a paper titled 'Prediction United States Population from 1780 to 1980 using Logistic Equation'. The paper first briefly introduced the history of studies on single specie differential equation and the advance of Logistic equation. In the methods section, the student predicted the population with: the Malthus equation and Logistic equation respectively (Fig. 2). The models are solved on Matlab. Results show that from year

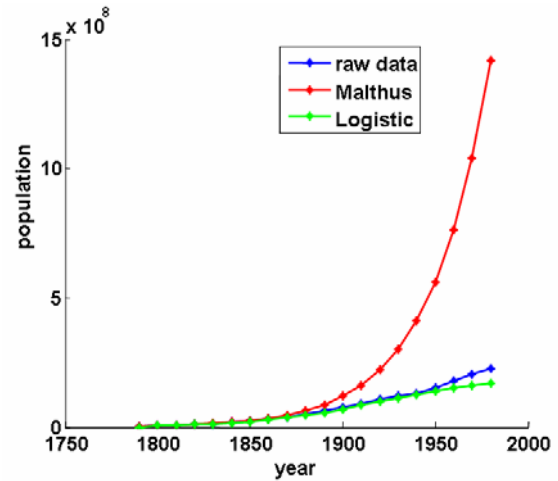


Fig. 2 Comparison of Malthus model and Logistic model in prediction of United States' population from 1780 to 1980

1780 to 1980, population predicted with Malthus equation increases unlimitedly; whereas Logistic equation may well predict the population from year 1780 to 1940. From 1950, the prediction is not so accurate. In the Discussion, the student analyzed the reason for different result of the prediction. Finally he came to the conclusion that Malthus' model predicts either population growth without bound or inevitable extinction; Logistic equation adds a carrying capacity of the system, which is the population level at which the birth and death rates of a species precisely match, resulting in a stable population over time. For the decrease of accuracy with Logistic equation after 1950 is because that 1930~1940 is the time that World War II broke out. To acquire better results, he proposed using Leslie model and models with multi influence factors.

IV. CONSLUSIONS

Integrated training of innovative ability on different levels has led students to combine theories with scientific practice, develop undergraduate students' ability of scientific thinking, analyzing problems encountered, and solving problems in practice. With regard to the cultivation mode of innovative talents, integrated training model has changed the traditional teacher-centered to student-centered mode, which stimulates the students to learn from the real practice and make further innovations, this is surely to become one of the most important ways in developing cross disciplinary course.

ACKNOWLEDGMENT

This research is supported by Tianjin Higher Institution Undergraduate Reform and Quality Development Key Program (2008).

REFERENCES

1. Fu WL, Chen JJ, (2005). A Study on the Patterns of the Development of Students' Practical Intelligence on Foreign Institution, *Education Science*, 1:52-56.
2. Zhou WS. (2006) Discussion on the Research-Type Teaching Mode. *Higher Education Forum*, 2: 55-56
3. Tian X, Zheng XY, Liu T, et al. (2007) Exploration and Practice of Research-Oriented Teaching Mode in Biomedical Engineering, *Northwest Medical Education*, 15(5):899, 931.
4. Silvia M, Henk GS, Geoffrey RN. (2006) Innovations in Problem-based Learning: What can we Learn from Recent Studies? *Advances in Health Sciences Education*, 11:403-422.
5. Loyens SMM, Rikers RMJP, Schmidt HG. (2006) Students' conceptions of constructivist learning: a comparison between a traditional and a problem based-learning curriculum. *Advances in Health Science Education*, 11(4): 365-379

Author: Tian Xin (Corresponding Author)

Institute: Tianjin Medical University

Street: #22 Qixiangtai Road

City: Tianjin

Country: China

Email: tianx@tjmu.edu.cn

Author: Liu Ting

Institute: Tianjin Medical University

Street: #22 Qixiangtai Road

City: Tianjin

Country: China

Email: liuting@tjmu.edu.cn

Biomedical Engineering Characteristics of Training Model of Education and Training Programme of Reform and Practice

Xu Zhang, Zhicheng Liu, Yalin Ye, Xiaopeng Han, Anyu Chen

School of Biomedical Engineering, Capital Medical University, Beijing, China

Abstract — he analysis of biomedical engineering education abroad on the basis of characteristics, with the domestic development of the field of biomedical engineering features on how medical schools under the school advantages, biomedical engineering in the reform of professional education and practice.

Keywords — biomedical engineering, characteristics, training mode, curriculum

I. INTRODUCTION

Biomedical engineering, rise in the United States in the 1960s, has developed rapidly in recent years. By integrating life sciences and engineering, it has made progress in methodological innovation and the establishment of technology platforms, etc., while also promoted social and economic development (formation of many new industries and industrial sectors), and created a substantial social benefits. And thus biomedical engineering has attracted widespread attention to the developed countries, and even into their national objectives [1]. China founded biomedical engineering undergraduate professional in 1977. As at the end of 2007, more than 90 colleges and universities have opened from the undergraduate level to Dr. Biomedical Engineering [2]. Concentrated in the engineering and medical schools, this professional is an interdisciplinary, cross-disciplinary particularity in the training mode. There has been emphasis on engineering or medical phenomenon, not really reflect the multidisciplinary medical engineering crossover characteristics. Along with the development of their disciplines, education industry needs to constantly explore the issue such as how to better integrate science, engineering and medicine to the organic combination; making the students nurtured in the knowledge structure and the basic quality; cultivating the types of people who can better apply what they have learned.

Capital Medical University is one of the earlier schools in biomedical engineering professional education in China. In 1978 it began biomedical engineering undergraduate education pilot. In 1987 the school set up a biomedical engineering and began the formal admission. Running in the early light of prevailing in the health sector in biomedical engineering and technical personnel in extremely short, the major consideration of school is the combination of medical

and engineering disciplines, and set up a sophisticated, the new interdisciplinary. At that time, according to the biomedical engineering understanding of the school and foreign experience, training objectives, both for training and know how to understand the engineering disciplines of the medical knowledge of senior personnel. Education position is: biomedical engineering senior professional and technical personnel training entities. March 2001 Capital Medical University established the Institute of Biomedical Engineering on the basis of the original biomedical engineering. According to the school's own advantages and social development needs, the Institute of Biomedical Engineering has gradually developed to two professional (biomedical engineering, prosthetics and Orthopaedic Engineering), three professional direction (of the hearing, medical imaging equipment and technology, quality supervision and medical equipment technology). Training direction from the biomedical engineering personnel training extended to the relevant biomedical engineering and technical personnel training, and gradually meets the needs of society and academic development. After more than 20 years of development, in education mode continuously optimize educational resources, the school has made full use of regional advantages and taking advantage of the medical school, and gradually formed its own characteristics education.

II. ADAPT TO THE NEEDS OF SOCIETY TRAINING OBJECTIVES

With the 21st century of life science, as well as the increasing importance of the continuous development of high-tech needs, modern medicine is increasingly inseparable from the development of modern science and engineering and technical support. In the medical and life sciences fields, the urgent need to science, engineering and medical personnel will be cross-disciplinary approach to introduce modern technology work in the field of medicine. Biomedical engineering and technical personnel needs widely distributed in hospitals, medical equipment and medical research institutions. Take the social demand as the specialized raise goal is when internationally approves criterion, therefore we will raise the localization of target in: Raise both rational, labor, medical interdisciplinary studies knowledge, and has the strong synthesis application ability, has

research application ability which the life sciences, the electronic technology, the computer technology and the information science related basic theory knowledge as well as the medicine and the engineering technology unify, can high-level engineering technology talented person who for the foundation medicine correlation technique research, the clinical medicine correlation technique research serves. The institute raises the student has the foundation to be solid, the aspect of knowledge is broad, medicine and project union close and so on characteristics.

III. ESTABLISHMENT OF COMPREHENSIVE TRAINING OF PERSONNEL TRAINING MODE

Biomedical engineering is a highly integrated cross disciplines. From the development of academic history, the new disciplines have a big traditional disciplines intersect or mature role of the results. Moreover, the meaning of biomedical engineering interdisciplinary, which is not the same biomedical engineering branch of a combination of simple, but multidisciplinary, wide-ranging, high-level integration. In addition, the biomedical engineering disciplines are involved in a very wide area. It can be said that the number of science and engineering branch, it will have a number of biomedical engineering fields, such multidisciplinary related to the intersections of all science, engineering disciplines and all branches of biology and medicine. As a result, any breakthrough progress of the subject can be made to affect the development of biomedical engineering, to the speed of development very rapidly.

A. Training Curriculum

Training Curriculum decided the basic pattern at the same time, on the subject of micro and macro aspects of the development of response, reflected the changing pattern of traditional education, the establishment of - psychological - Social curriculum system [3]. According to the disciplines, we will be subject to the original type-based curriculum, changes for the modular core curriculum. The basic curriculum in accordance with the guiding ideology of "re-base, Broad - range" ideas of education. Refers to raise plan which the domestic and foreign biomedical engineering specialized educational expert formulates, our curriculum mainly includes: public infrastructure programmes, the medical foundation courses, the basic courses, professional courses, elective courses, and practice on graduation design (thesis) 7 a module [4]. Application of capacity-building to the main line, teaching the theory and practice of combining teaching, medicine and engineering that is closely integrated prominent professional skills training to reduce compulsory,

additional elective courses; optimize the structure of courses, reduce repetitive.

Specific curriculum in the process of public infrastructure in addition to state provisions of the humanities and social science courses, according to today's development needs, we have provided medical ethics and medical psychology courses. Medical foundation courses include anatomy, physiology, and biochemistry, in the science, diagnosis and surgery. Major projects including basic courses based circuit analysis, analog electronics, digital electronics, signals and systems, medical sensors. Professional courses main tenets of the medical equipment, computer interface technology, medical signal processing, medical image processing, and biomechanics. Elective courses under the direction of different professional disciplines characteristics and colleges were set up in audiology, hospital equipment management, imaging equipment and apparatus, the quality of supervision and management of medical equipment, biomedical information, biological control, the theory of medical laser. And in accordance with the objective of fostering the knowledge and skills needed structure, we must strengthen basic education, infiltration between arts and science, combination of science and engineering, and knowledge and ability to unify. In the end, a unique knowledge of the framework is gradually formed.

B. Practical Teaching

Teaching in practice, we stressed that the students practical ability and the cultivation of creative thinking ability. We integrated the basis of the original laboratory for functional of diverse, open laboratory. At the same time, we have a comprehensive reform of the experimental curriculum, reduce verification experiment to increase design experiment. Students in the second grade, we set up a second classroom and Technology group activities for students, so that they could understand the subject's developments, preliminary study scientific research methods. The teachers of second classroom and scientific and technological activities group are all chaired national or provincial-level research projects of professors and/or associate professors. At the event, teachers not only take the quality of training of research, but also serving as mentors to guide students in accordance with their interest in establishing professional direction and the next phase of study, employment objectives. Practice has proved that this approach has yielded good results. Through the second classroom or technology group activities, many students have tempered the research capacity. Some students also issued high-level papers.

IV. FULL USE OF RESOURCES BUILDING CHARACTERISTICS EDUCATION

Capital Medical University has 14 affiliated hospitals, is the most abundant medical resources comprehensive medical university, providing the best medical environment for the biomedical engineering education. By Board of Education in Beijing encourage and support, aiming at the medical related technology talent market, we developed our program closely integrated with the advantage in biomedical engineering technology to more deep-seated clinical actual education. In 1999 we launched a biomedical engineering undergraduate education to expand. According to our school and Beijing geographical advantages, we established three professional interests in biomedical engineering: audiological professional direction of medical, imaging equipment and technology professional direction, supervision of the quality of medical equipment and technological expertise direction.

Relying on key national disciplines of otorhinolaryngology, audiological professional program is in order to raising senior technical staff who will engage in language training and rehabilitation of hearing and hearing language-related R & D, design, production, assembly and after-sales services. Taking full advantage of the school's localization in the capital, higher hospitals technical level, fully-equipped medical imaging, medical imaging equipment and technical personnel training play a important role in enhancing the large and medium-sized medical imaging equipment utilization and clinics in country's hospitals, improvement in medical imaging equipment and technology work of the professional staff level. Medical Device Quality Supervision technical training professional people to fill China's

quality supervision and medical equipment gaps in training technical personnel, changes in the quality of our medical equipment and technical personnel serious lack of supervision of the status quo.

After years of practice and exploration, our biomedical engineering undergraduate education gradually formed its own school characteristics: play works advantages, and promote the development of medicine, medical and engineering prominent characteristics combined with the focus on medical technology development related projects, in biomedical engineering technology to the more deep-seated actual clinical services, and promote the level of clinical medicine and rehabilitation clinics increased.

REFERENCES

1. Yuan Li, medical schools of higher education in biomedical engineering education and management of innovation and integration of personnel training, electrical and electronic teaching Journal, 2005, vol.27 (2). pp.17-21
2. [Http://gkcx.eol.cn/zyxxcx_searchpro_post.jsp](http://gkcx.eol.cn/zyxxcx_searchpro_post.jsp)
3. To Xiao, Juhailing, Lu Jing-hua, foreign biomedical engineering characteristics of higher education, medical and health equipment, 2003, No.10.pp.328
4. Li Haiyun, Liu Zhicheng, Ye Yalin, biomedical engineering education mode of practice and exploration, medical equipment, 2006, vol.27 (5). Pp.59-60

Author: zhangxu
 Institute: Capital Medical University
 Street: 10# Xitoutiao ,You An Men,
 City: Beijing
 Country: China
 E-mail: zhangxu@ccmu.edu.cn

Prosthetics and Orthotics Engineering Professionals Training Mode and Curriculum Research and Development

Zhicheng Liu, Xu Zhang, Yalin Ye, Anyu Chen, Xueqian Guo

School of Biomedical Engineering, Capital Medical University, Beijing, China

Abstract — Research on the current domestic and foreign prosthetics and orthotics engineering education status and characteristics, this paper introduced the Capital Medical University carries out the prosthetics and orthotics engineering professional education and the educational pattern and the curriculum system's exploration and the development.

Keywords — prosthetics and orthotics engineering, education, curriculum, educational pattern

I. INTRODUCTION

Prosthetics and orthotics engineering is the application of modern engineering principles and methods, compensation, correction or deletion has been the empowerment of persons with disabilities, deformity or weakened part of the body or organs to enable persons with disabilities to the extent possible, minimize or restore function compensatory function and the application of independent living. Rehabilitation project is one of the main elements. It is a marginal subject, involving a number of professional disciplines in medical and engineering. It covers the anatomy, biomechanics of human, mechanical, electronics, and polymer materials science disciplines. Modern prosthetics orthosis has tended to biological information and intelligent development. Many high tech ,such as Atmospheric pressure (or hydraulic) knee, computer-controlled artificial limbs, brain control, the dynamic electromyography prosthetic hand, intelligent bionic leg, CAD / CAM in prosthetics orthosis engineering applications, require held higher education, cultivate a high-level applications and composite talents.

China is a country with a large population, but also a disabled power. A total of 82.96 million different types of disabilities, including physical disabilities accounted for 30 percent, about 75 million people are in need of prosthetics orthosis assembly. But 74.4 percent still has not been installed. There are many reasons. First, the number of job holders in the assembly of prosthetic and orthopaedic is very small(less than 5,000). Secondly, there are the serious shortage of professional and technical personnel (less than 1,000 people) and senior personnel professionals. The majority technical personnel have apprentice's way by skilled worker to rise. In recent years, China has increased prosthetic orthotic training professionals, and has developed a

number of craftsmen, secondary and tertiary-level technical staff. Along with economic and technological progress and welfare and the protection of people development, it has been growing demand for qualified personnel. As the existing craft, and the secondary level of professional technical personnel narrow, poor foundation exposed the shortcomings in the practical work have been unable to meet the higher level needs. For the physically disabled in the research, development, and service areas, high-level talent is very scarce.

Therefore, in our higher education project organized prosthetics and orthotic profession is to meet the needs of the development of the cause of the handicapped, social civilization and progress of signs. Established prosthetic and orthotic engineering status is the most important measures, which would change our long-term prosthetics and orthosis industry lags behind the world's advanced level, low production efficiency, product quality poor conditions, and promote prosthetic and orthotic engineering high-tech industries, development of new technologies and materials technology.

At present many of the world's countries and regions regardless of the number of the population has a corresponding basic rehabilitation works (prosthetic and orthotic technology) professional higher education. The establishment of prosthetic and orthotic schools in the United States is a total of 15. While Asian countries and regions are 11. Britain, Germany and other European countries generally have 12. Rehabilitation engineering professionals abroad are graduate students, undergraduates, specialist, short courses, and other levels of the training of personnel, the following undergraduate professional levels of education are p prosthetics and orthosis technology at the core.

Capital Medical University began offering prosthetic and orthotic professional education in 2003. It is the first and only one in prosthetic and orthotic engineering undergraduate education in China. Training aim at the systematic training of prosthetic and orthotic, master the basic theory, knowledge and skills, getting a sense of innovation and practical ability, and, to provide engineering and technical services of senior engineering and technical personnel for the physically disabled and special populations.

II. PROFESSIONAL TRAINING OBJECTIVES

Training Objectives must adapt to the needs of society. According to the domestic industry demand and the detailed investigation of the relevant foreign professional education, we established the prosthetic and orthotic engineering training and operational objectives.

A. Specialized raise goal

The professional training will let the students gain the basic skill which can unify the rehabilitative medicine, the mechanical and electrical technology and the materials science, prosthetic and orthotic design and the manufacture related elementary theory as well as the rehabilitative medicine and the engineering technology. It also provides high-level application talented person in the clinical recovery and the prosthetic and orthotic project domain technical service.

B. Operational Training

The main requirements of students learning is about basic medicine, bio-mechanics, prosthetic and orthotic design and manufacture of basic knowledge of the basic theory study, accept electronic technology, mechanical design, materials science, computer technology and other basic training through the combination of theory and practice of teaching bear mode, enable students engaged in clinical rehabilitation, prosthetics and orthosis design and manufacture of quality and competence.

III. TRAINING MODE

Established under the premise of training objectives, we developed a prosthetic and orthotic engineering professionals and training model curriculum.

All school-four years, is divided into three stages:

Stage 1: 3 years, based on the learning phase. Mainly in the schools to carry out ideological and moral training, humanities and social sciences, natural sciences, basic medical sciences, electronics and computer technology, materials science and mechanics, prosthetics and orthosis mechanical design engineering professional courses of study. This phase mainly focus on the humanities quality of medical knowledge and scientific engineering and technical training, while stressing student's prosthetics and orthosis professional capacity-building projects, to closely combine theory and practice of the teaching model and train the students to the professional qualities.

Stage 2: 0.5 years, for clinical training and internship graduation stage. This phase is primarily in clinical hospi-

tals, prosthetics and orthotics for the production and assembly units for training and internships. This phase oriented students practical work capability training, and further training of students and orthopaedic prosthetic design, production, use and maintenance capabilities and clinical assessment reception capabilities

Stage 3: 0.5, in order to graduate thesis and design stage. This phase instructors take responsibility. Students under the guidance of instructors completed the corresponding graduation design issues and thesis writing or design report and participate in graduation reply. This stage clinical practice focus on the ability of students to solve practical problems and the ability to train, strengthen students to the integrated use of expertise.

In four years of undergraduate study, students focus on rehabilitation medicine, electrical and mechanical technology and material science, prosthetics and orthosis design and manufacture of basic theories of learning, the student in rehabilitation medicine and engineering technology, the basic skills of combining prosthetics and orthosis design and the practice of the production capacity of the training, ideological and moral, professional, well-practical ability to improve their innovation, adaptability and overall quality.

IV. CURRICULUM

According training model, the establishment of modular core curriculum, in the light of foreign professional education experts developed the training programme, our courses mainly include: humanistic quality training system, a system based on the teaching theory, experiment and practical teaching system. Through public foundation courses, the medical foundation courses, the basic courses, professional courses, elective courses, and practice on graduation design (thesis) 7 knowledge modules. Application of capacity-building to the main line, stressed that teaching the theory and practice of combining teaching, outstanding professional skills training.

A. The quality of the humanities building:

Through compulsory courses (philosophy, History of Modern China, ideological and moral cultivation, the legal basis, medical psychology, and the basic tenets of Marxism, etc.) and more humanities and social sciences Gate elective courses, multi-angle, and raise the quality of the humanities students, through lectures, and other forms of social practice and enhance the quality of humanities students training, and focus on the quality of students in the humanities and professional qualities and promote each other organic integration, improve their overall quality.

B. Basic theory teaching:

Teaching basic theory of natural sciences, rehabilitation medicine, materials science and mechanical, electronic and computer technology, mechanical design, prosthetics and orthosis and other knowledge modules for students of professional courses, graduate internships and lay graduate design comparatively solid theoretical foundation, further expansion of elective courses students the field of vision, increase their knowledge, a multi-angle display research in the field of professional direction.

C. Experiments and practice teaching:

The class hours of professional courses in the experimental or design are 2-3 times of theoretical lessons, the students hands-on training capacity, particularly the eight weeks of training, graduated from 17 weeks of the 14-week internship and graduate design, with particular emphasis on the students clinical practice ability, and ability to solve practical problems and comprehensive design capabilities, the initial research capacity training.

After a few years of teaching practice, the first session students have completed all courses of study and professional training, and adapt to the needs of the community as a sound professional ethics and professional standards for the production of prosthetic and orthotics division and corporate management, graduated in 2007 and embark on the job. And they were unanimously praised by the industry and welcome.

Summarizing several year school experiences, we believed that the prosthetic and orthotics project specialty is a practical very strong professional, must raise student's beginning ability emphatically. This requests the practice class occupies the proportion is very big when the student in school period, and needs huge amounts internships, laboratory equipment. In accordance with international prosthetics and orthosis association requirements, such professional practice course requires each student has a work-or console, the hardware configuration demands. And it also needs the massive practices, the test installation. The prosthetics and orthosis specialized disciplinarily decided the student in the school period teaching, the practice class not only to by school own solution, but must rely on the technical support and industry training graduates, the employment combination.

Author: Liu Zhicheng
Institute: Capital Medical University
Street: 10# Xitoutiao ,You An Men,
City: Beijing
Country: China
E-mail: zcliu@ccmu.edu.cn

Corresponding Author: zhangxu
Institute: Capital Medical University
Street: 10# Xitoutiao , You An Men,
City: Beijing
Country: China
E-mail: zhangxu@ccmu.edu.cn

The Effect of Acupuncture at Point Neiguan on the Pulse Picture for Patients with Arrhythmia

Jialiang Chen¹, Tao Wang¹ and Yuebo Wu¹

¹ Department of Mechanics and Engineering Science, University of fudan, Shanghai ,China

Abstract — **Objective:** This project mainly aims at quantify the pulse and acupuncture signal and investigates the effect of acupuncture at point Neiguan (PC6) on the pulse picture for patients with arrhythmia by using different signal analysis method. **Methods:** We choose 15 patients with arrhythmia which are led from different sickness in our project. For the practical data collection, the data of the pulse for each patient are recorded three minutes before acupuncture and after acupuncture. In order to compare results, for all the patients, we use the same acupuncture tact ('bu') applied on 'neiguan' and collect 'guan' pulse. Self-designed Pulse picture instrument and acupuncture instrument are used to detect the pulse picture. For these pulse signals, firstly we use one dimension wavelet to reduce the effect of noise on pulse, which includes three steps: 1, separate original signal to approximations and details in proper level; 2, select threshold method to eliminate details coefficients between thresholds; 3, reconstruct pulse signals. In the following, we use auto-relativity function method to determine time delay in the process of reconstructing phase portrait for each patient's pulse signal. The phase portrait of pulse signal supports a qualitative tool to find out the differences before and after acupuncture. In order to get quantitative results, coarse grained method is used for frequency analysis to obtain the power spectrum density. The ratio of the magnitude of the vice frequency to that of the main frequency is taken as a characteristic parameter. The parameter before acupuncture is compared with that after acupuncture. **Results:** From the qualitative prospect, we can find the shape of phase portrait curve changes dramatically after acupuncture. From the quantitative prospect, we find that the characteristic parameter increases remarkably ($P < 0.05$). **Conclusion:** Our project describes the effect of acupuncture on pulse from the qualitative prospect and the quantitative prospect respectively. These results have positive effects on the application of acupuncture in clinic.

Keywords — Acupuncture, Pulse picture, Arrhythmia, Coarse grained method, Phase portrait

I. INTRODUCTION

Pulse movement and acupuncture are considered as two essential parts of the traditional Chinese medicine. These two methods have close relationship and supplement each other in clinic treatment. According to Chinese traditional medicine, pulse must be detected before acupuncture and

then acupuncturist determines which kind of acupuncture tact should be applied on the patient. In addition, several scientific research results have showed that pulse can reveal some information about body system. In the recent years, the therapy of acupuncture with pulse detection has aroused the broad attention from physicians, and has been acknowledged by both domestic and foreign medical institution. In 1999, the <times> issue ranked acupuncture as the top ten projects in the 21st century. Above all, the acupuncture therapy has already become an international focused project [1]. The purpose of our project is to quantify the pulse & acupuncture signal and find out the difference between pulse movement before and after acupuncture. We think this process will make more and more people accept and understand acupuncture very well

II. METHOD

A. The detailed information of patients

We choose 15 patients (40% male, mean age 48 and 60% female, mean age 57) with heart disorders which are led from different sickness. For the practical data collection, the data of the pulse for three minutes are recorded before acupuncture and after acupuncture. In order to compare results, for all the people, we choose 'bu' (one kind of acupuncture tact) applied on 'neiguan' and collect 'guan' pulse.[2] All these patients are made experiments in the herbalist 'Guohua' hospital in Chenghuang Temple in Shanghai.

B. Pulse movement detector

The pulse detector is shown in the Fig.1. The antennae of the pulse detector have three sections and each section has six sensors. The electric signals are amplified by the inner circuit and then are demonstrated by the volt meter. Then the signals are finally recorded by special software. So each section of signals has six aisles. According to the data and pulse graphics displayed on the screen, the best aisle can be chosen to be analyzed.



Fig. 1 Pulse movement detector

C. Coarse graining spectral analysis

Considering $X(i)$ as discrete time series, it satisfies

$$X_h(i, i_0) = X(hi + i_0) = h^H X_1(i, i_0) \tag{1}$$

where d implies that both hands of d have the same distribution function, is characterized by determining the Hurst exponent $H(0 < H < 1)$ and the new time series $X_h(i, i_0)$ is called the “coarse grained” subset as it is constructed by taking every h samples from a part of the original time series $X(i)$. It is evident that pulse signals can satisfy relationship (1). Therefore, an auto-power spectrum of the original series is calculated from the discrete Fourier transform of $X_1(i, i_0)$ as [3]

$$S_{XX}(n) = \frac{1}{N_{subset}} \sum_{i_0}^{N_{subset}} \left\| \frac{1}{N_{data}} \sum_{k=0}^{N_{data}-1} X_1(k, i_0) e^{-j2\pi kn / N_{data}} \right\|^2 \tag{2}$$

D. Phase portrait analysis

For N dimension dynamic system

$$\overset{\bullet}{X}_1^{(n)} = f(\overset{\bullet}{X}_1, \overset{\bullet}{X}_1, \overset{\bullet}{X}_1, \dots, X_1^{n-1}) \tag{3}$$

We can use $(\overset{\bullet}{X}_1, \overset{\bullet}{X}_1, \dots, X_1^{n-1})$ to reconstruct phase portrait. In addition, derivative is computed from time series of system $X(t), X(t+\tau), \dots, X(t+(n-1)\tau)$ in order to reconstruct phase portrait.

In our project, we describe dynamic behavior of pulse in two dimension's phase portrait. It means that n is equal to 2. In the following, we must determine the value of τ . There are many methods used to fix on the value of τ . I choose auto-relativity function method. It is more adapted to low dimension system.

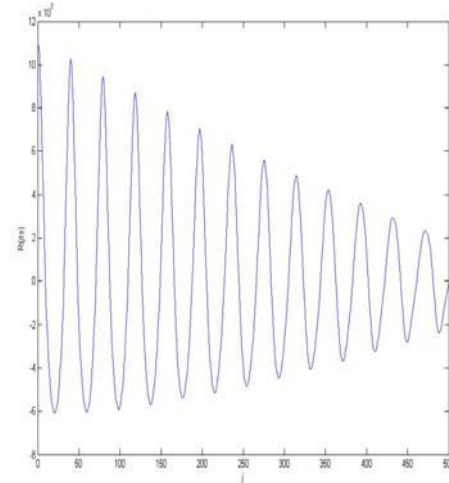


Fig. 2 $R_{xx}(jt_s) \sim j$

For our cases, auto-relativity function method [4] is

$$R_{xx}(jt_s) = \frac{1}{N} \sum_{i=0}^{N-j} X_i X_{i+jt_s} \quad 0 \leq j \leq N$$

t_s is the sampling period. First, we consider $R_{xx}(0)$ as initialization, then make j vary from 1 to N until $R_{xx}(jt_s)$ is smaller than $(1 - \frac{1}{e})R_{xx}(0)$ in the first time, then make $\tau = jt_s$.

From fig2 the increase of j will make attenuation of R_{xx} . For this case, I choose $j=5$, and $\tau = 5t_s$.

E. Eliminating noise with Wavelet method

For pulse signal, most energy should be concentrated on 1HZ, because the interval between heart beat is about 1 second. Therefore I use one dimension wavelet to reduce the energy in high frequency. The whole process includes three steps: 1 Separate original signal to approximations and details in proper level; 2 Select threshold method to eliminate details coefficients between thresholds and assume noise structure to be unscaled white noise; 3 save de-noised signal.

From fig3, the process of eliminating some high frequency in the pulse signal could make phase portrait curve seem more smooth which is beneficial to get some useful information from phase portrait.

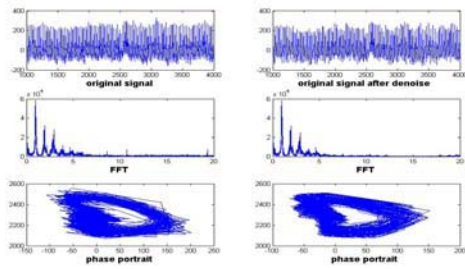


Fig. 3 the effect of de-noise on phase portrait and FFT

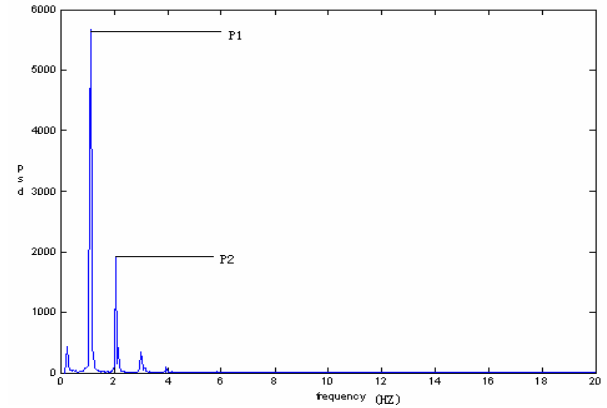


Fig. 5 frequency spectrum of pulse after acupuncture

III. RESULT

A. Frequency spectrum results

For all patients, time series of ‘guan’ pulse are transformed into frequency spectrum by auto-power spectrum. In the Fig4 and Fig5, we will show frequency spectrum of pulse for the same person before and after acupuncture.

From these two figure, we can find the ratio of the main frequency and the vice frequency (P2/P1) of guan becomes bigger after acupuncture. Therefore, we choose the ratio of the main frequency and the vice frequency (P2/P1) as statistical parameter, and make t-test for these statistical variables. The parameter before acupuncture was compared with that after acupuncture. The result is shown in the table1, which means that characteristic parameter increases remarkably ($P < 0.05$).

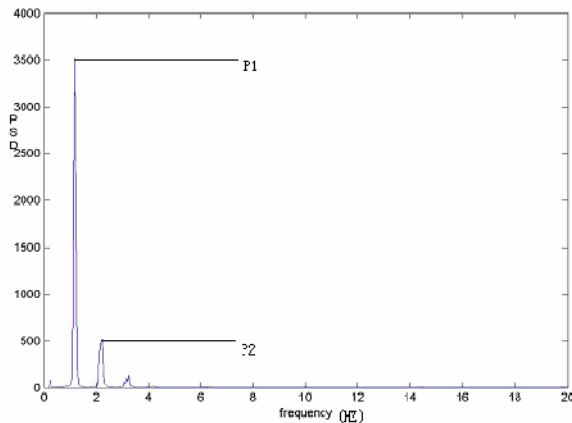


Fig. 4 frequency spectrum of pulse before acupuncture

Table 1 P2/P1

Item	P2/P1(before acupuncture)	P2/P1(after acupuncture)
1	0.14	0.34
2	0.16	0.25
3	0.17	0.21
4	0.11	0.15
5	0.24	0.26
6	0.49	0.65
7	0.17	0.35
8	0.16	0.2
9	0.15	0.17
10	0.25	0.61
11	0.19	0.24
12	0.19	0.22
13	0.16	0.15
14	0.2	0.2
15	0.67	0.62

$$T=2.877 \quad V=14 \quad P<0.05$$

B. Phase portrait results

For all patients, firstly we use one dimension wavelet to reduce the effect of noise on pulse, and then we use auto-relativity function method to determine time delay in the process of reconstructing phase portrait for each patient’s pulse signal. In the following, we will show one patient’s phase portrait before and after acupuncture.

From the qualitative prospect, we can find the shape of phase portrait curve changes dramatically after acupuncture.

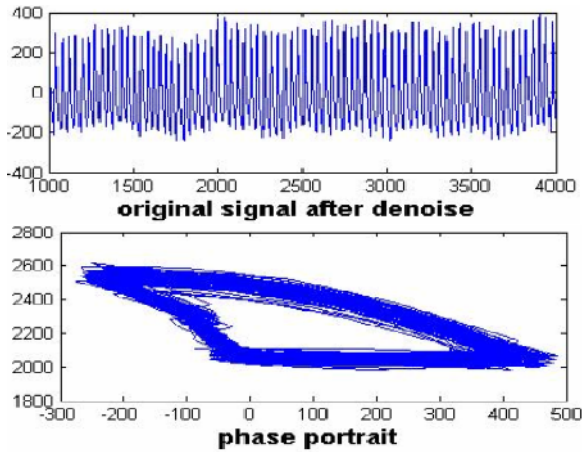


Fig. 6 phase portrait of pulse before acupuncture

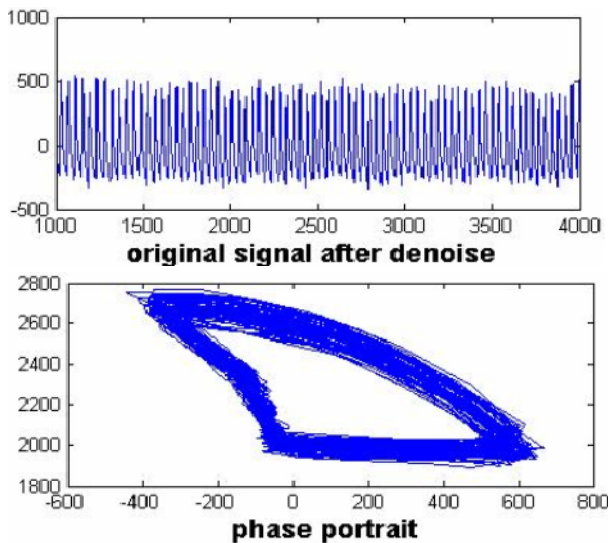


Fig. 7 phase portrait of pulse after acupuncture

IV. CONCLUSION

According to the above results, we can make an important conclusion that acupuncture does play a significant effect on pulse picture. Especially from the phase portrait of

pulse signal, we can easily find that pulse signal becomes more regular after acupuncture, which should be positive representation for patient's pulse. In addition, based on physiological definition of pulse, we believe P1 relates to main wave which corresponds to the blood ejection of the left ventricle and P2 relates to re-pulsation front wave which corresponds to blood's bouncing back from the blood vessel [5,6]. Therefore, the variety of (P2/P1) is possible to have relationship with some physiological change which results from acupuncture's positive effect on body system. Our project describes the effect of acupuncture on pulse from the qualitative prospect and the quantitative prospect respectively. These results have positive effects on the application of acupuncture in clinic.

ACKNOWLEDGMENT

This work was supported by Shanghai Leading Academic Discipline Project, Project Number: B112

REFERENCES

1. WHO Report.(2000).Consultation meeting on traditional and modern medicine: harmonizing the two approaches, Report series number: RS/99/GE/32(CHN), WHO Regional office for western pacific, Manila, Philippines,
2. Gusheng Huang (1995) Acupuncture after taking pulse. Anhui science& technology press
3. Yoshiharu Yamamoto, Richard L. Hughson.(1993) Extracting fractal components from time series. Physica D 68:250-264
4. Runsheng Huang. Chaos and non-linear dynamics. Wuhan University press.
5. Caro,C.G.,et.al.,(1978) The Mechanics of the Circulation, Oxford University Press.
6. Lim K O. Boughner D R.(1976) The low frequency dynamic viscoelastic properties of human aortic valve tissue. Circulation Res. Vol.39,(2),209-214.:

Author: Chen Jialiang

Institute: Department of Mechanics and Engineering Science, University of fudan

Street: No 220, Handan road,Shanghai,P.R.China

City: Shanghai

Country: China

Email: 051029010@fudan.edu.cn

Primary Study on the Parameters and Methods to Evaluate Needling Sensation and Maneuvers in Acupuncture

Ying Li, Yu Zhang, Zhipeng Liu, Tao Yin*

Institute of Biomedical Engineering Chinese Academy of Medical Sciences
Peking Union Medical College, Tianjin, China

Abstract — Aim To search the external method of Acupuncture Deqi and Manipulation Methods. Methods develop the experimental equipment to pick up the local myoelectricity signal on the point and volume pulse wave of the tiny artery in the finger-end. By which we can carry out acupuncture on the tested point, and pick up the local myoelectricity signal and volume pulse wave on the point before and after the condition of Deqi and under different manipulation methods. Results primarily deduce the relationship between the two coefficients and the extent of acupuncture Deqi and the reinforcing method and reducing method, that is, when the acupuncture point is under the state of Deqi, the myoelectricity signal of the point occurs, besides the extent of Deqi has a positive direct ratio relation with the intensity and number of the times of the myoelectricity; When carrying out the reinforcing method in acupuncture, the amplitude and frequency of the volume pulse wave decreases; when carrying out the reducing method, it increases. Conclusion the changes of Manipulation Methods and the difference of Acupuncture Deqi can be external evaluated by the local myoelectricity signal and volume pulse wave on the point.

Keywords — sensation of acupuncture, manipulation methods, myoelectricity signal records, volume pulse

I. INTRODUCTION

Chinese traditional acupuncture therapy as an excellent therapeutic method in Chinese traditional medicine features unique maneuver and outstanding effect, it is widely used and accepted. In acupuncture therapy, the arrival of Qi (needling sensation) and accurate application of reinforcing and reducing manipulations are two key factors that therapeutic effect relies on except the factors corresponding of prescriptions according to different conditions and accurate selection of the acupoints. In the chapter Jiu Zhen Shi Er Yuan of the book Ling Jiu, it is written that the key point of the acupuncture is that there is needling sensation, and there is effect, that is, the effect of acupuncture therapy mainly depends on the condition of needling sensation.

In practical therapy, however, the condition is usually judged by patients' and doctor's feelings of the needle. The patients have the feelings of ache, tingle, tightness and tumidness around the acupoints while the doctor feels tense

and dragging sensation when inserting deep and turning the needle. The accurate application of reinforcing and reducing manipulations is mainly based on the doctor's knowledge and clinical experience, and therefore the judgment whether the application are right can only be verified by the effect after the treatment. In addition, acupuncture manipulations are taught and trained by trainers according to their own understanding and experience without an external standard.

Therefore, a simple practical method that can reflect the degree of needling sensation and the maneuver of acupuncture manipulations with precise external standard is needed to improve and further develop the Chinese traditional acupuncture therapy as a part of the medical sciences of the world in modern times.

II. METHOD

Practical methods of external estimate on needling sensation and maneuver are merely reported in articles. Or there is but not practical. We notice that patients treated have the feelings of ache, tingle, tightness and tumidness around the acupoints, while doctors have the feelings of tenseness and dragging sensation from the needle. It demonstrates that acupuncture on the acupoints causes reflexible tensions of the muscles around the acupoints to various extents that transfer through main and collateral channels. We infer that there must be corresponding myoelectricity released around the acupoints, which causes reflexible changes of the volume pulse wave in the tiny artery through nervous networks, and it can be observed by measuring the wave in the fingertip. The wave varies with different manipulations and degrees of needling sensation.

At the beginning, the potential of palmer skin was chosen as the parameter observed in the experiment, the change of the potential is in disorder and varies greatly with environmental noise so that it can not be a real-time and practical parameter. As a result, the myoelectricity around the acupoints and the volume pulse wave of the tiny artery in the fingertip were adopted as the external parameters to evaluate the maneuver and degree of needling sensation. Furthermore, we studied the relationship between the degree of

needling sensation and the maneuver of reinforcing and reducing manipulations and set up a practical method to evaluate the acupuncture maneuver with external standard.

III. EXPERIMENTAL DEVICES

The experimental devices include two parts, that is, one is for the measurement of myoelectricity and another is for volume pulse wave.

Circuit for the measurement of myoelectricity signal

The circuit for measuring myoelectricity is shown in Figure 1. Surface electrodes were used to pick up the myoelectricity signal invasively. We noticed that the myoelectricity signal around the acupoints is very small when picked up on the skin, that the surface resistance of skin is rather large and myoelectricity has a wide frequency bandwidth. Hence, there are problems related to the noise of power frequency and the shift of baseline.

So the circuit system should have high Common Mode Rejection Ratio (CMRR), high input impedance, high gain, excellent noise feature and wide range of frequency response. And it is more external and precise on reflecting the maneuver and the degree of needling sensation than invasive methods such as using concentric or acupuncture needles as electrodes.

Measures were taken to effectively pick up the myoelectricity signal such as using differential inputs to amplifier, active data-proof circuit connection and providing a proper driver for two input shield lines in order to reduce the common mode rejection errors induced by line resistance of different lengths, various diffusion capacitance and wiring capacitance. Design principle of low noise was followed to reduce the influence of noise on myoelectricity signal when gain was to be assigned to all levels.

Therefore, the gain of the pre-amplifier should be as high as possible, but there are three points we should consider: first, the voltage gain of the amplifier A1 is restricted within the operation limits; second, the dynamic range of the pre-amplifier is limited by the polarized voltage before the voltage is removed from the electrode; third, the myoelectricity signal picked up is of microvolt level. The gain of A1 is

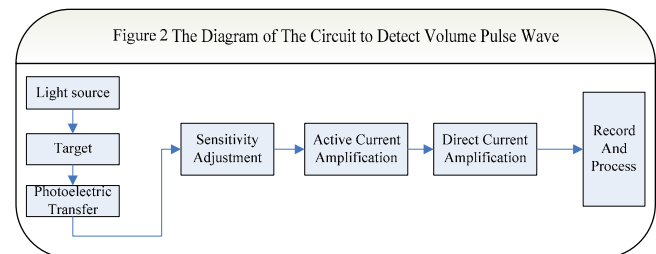
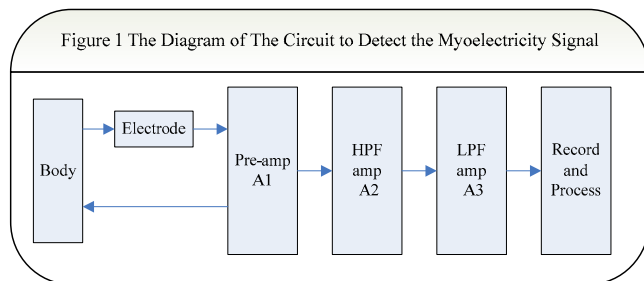
designed to have three adjustable levels: 40dB, 46dB and 54dB; A2, two: 34dB and 40dB; A3, two: 0dB and 20dB. The amplitude of myoelectricity signal is amplified to volt level after A1, A2 and A3. Besides, A2 and A3 are filter circuits designed to eliminate the high frequency and DC noise. A2 is one-stage high pass filter with cutoff frequency of 1.59Hz. A3 is one-stage low pass filter with cutoff frequency of 10kHz.

The gain of the whole circuit is 110dB at most, the CMRR is 115dB at most, the input impedance is more than 500 MΩ, the range of frequency response is from 1.59Hz to 10kHz, and the equivalent input noise is less than 10μF. In the experiment, using the device, the myoelectricity signal was successfully picked up on the acupoints on the condition of needling sensation.

IV. CIRCUIT FOR DETECTING VOLUME PULSE WAVE

The circuit to detect the volume pulse wave is shown in Figure 2. The photoelectric transfer method was adopted in the circuit to measure the volume pulse wave. There are three steps of process. 1) The red light reflected by oxygenic RBC by the blood of artery was used to irradiate the fingertip. 2) The reflexible light was received by the photoelectric transfer component. 3) The electrical signal was amplified in the electrical circuit.

A GaAsP red-light emitting diode with the wave-length of 660nm was adopted as light source, and silicon photo-voltaic sensor with acceptance range from 0.4μm to 1.1μm and high response to the light of wave length of 660nm was adopted as photoelectric transfer device. The sensor to detect volume pulse wave of the circuit was fixed in a plastic finger clip to shield the light outside and keep proper and stable pressure between the photosensitive surface and skin to prevent the wave from aberration and instability.



V. EXTERNAL PARAMETERS OF ESTIMATE AND RESULT ANALYSIS

Healthy volunteers of various ages were acupunctured on the acupoints of Shousanli and Zusanli in the experiment.

The myoelectricity signal around the acupoints and the volume pulse wave in the fingertip of the same side were measured on the conditions of before acupuncture and after acupuncture with and without needling sensation. Comparisons of the parameters on those conditions were made to ascertain the relationships between the parameters and the conditions of Qi arrived and the maneuver of reinforcing and reducing manipulations. And an external estimate method of acupuncture maneuver was primarily established and discussed.

VI. MEASUREMENT OF MYOELECTRICITY SIGNAL AROUND TREATED ACUPOINTS

To prepare the acupuncture experiment, first, we sterilized the skin around the acupoints of the volunteer with medical alcohol; second, applied the electro-conductive paste uniformly to the surface of the annular electrodes, fixed an electrode on the treated acupoint and the other 2cm away from the former; third, fixed the driver ends of the myoelectricity circuit on the other arm of the volunteer and connected the electrodes and the driver ends through shield line.

Volunteer was asked to lie calmly on a bed and relax to avoid pseudo signal of myoelectricity caused by tension of muscles. Then connected the output to oscilloscope to observe and memorize the signal. After that, the acupuncture doctor insert a needle into the acupoint.

VII. ANALYSIS OF EXPERIMENTAL RESULT

As a result of the experiment, there was no Qi arrived, the doctor felt loose from the needle and the volunteer didn't feel the feelings of ache, tingle, tightness, and tumidness, and that there was no evidence of myoelectricity releasing caused by acupuncture since there was almost no difference between the signal before and after acupuncture. However, when there was Qi arrived, the volunteer had the feelings of ache, tingle, tightness, and tumidness, the doctor felt tense, and myoelectricity releasing caused by acupuncture could be observed as in Figure 3. The signal R1 in the figure is the myoelectricity signal after acupuncture without needling sensation, and R2 is the one with needling sensation. We concluded that the phenomenon that the volunteer had the feelings of ache, tingle, tightness, and tumidness, and that the doctor felt tense is the result of shrink of muscles under the acupoint. Furthermore, the myoelectricity caused by acupuncture that is different from the one caused by active movements features low amplitude and frequency and lasts until the end of the course of acupuncture. We also observed that the myoelectricity signal has a certain relationship with the degree of needling sensation: When there

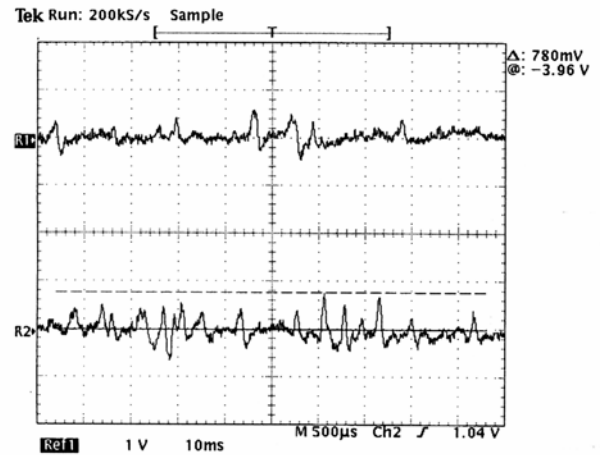


Figure 3 The Myoelectricity Signal With and Without Needling sensation

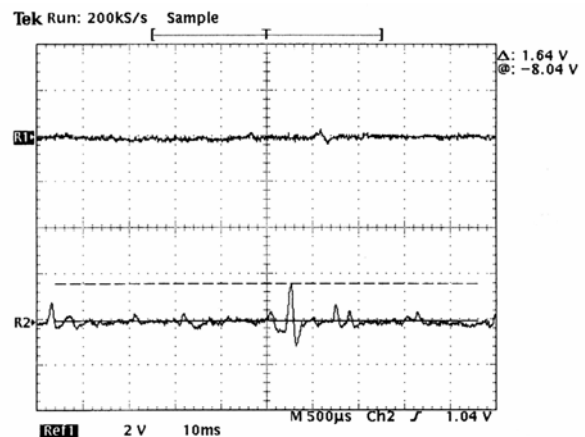


Figure 4 The Myoelectricity Signal with Weak and Strong Needling Sensation

is strong needling sensation, the amplitude and frequency of the signal is higher, and vice versa as shown in Figure 4. R1 is the myoelectricity signal with weak needling sensation and R2 is with strong needling sensation.

VIII. ACQUISITION OF THE VOLUME PULSE WAVE IN THE FINGERTIP

The volunteer was asked to lie down calmly and relax as well before the acquisition of the volume pulse wave in the fingertip. The finger clip that had a photoelectric sensor inside was applied to the index finger of the volunteer. Then the acupuncture doctor carried out acupuncture of different manipulations on the acupoints and recorded all the signals. Marks were not set on the figure because what we concerned was the relative changes of the amplitude and frequency of the volume pulse wave.

IX. ANALYSIS OF EXPERIMENTAL RESULT

We noticed that there was no essential difference between the volume pulse signals in the fingertip before acupuncture and after that without needling sensation. When acupuncture of reinforcing manipulation was applied to the acupoint with needling sensation, there was an apparent decrease in the amplitude and frequency of the signal as shown in Figure 5. The upper part of the figure is the signal when reinforcing manipulation was applied without needling sensation, and the lower one is the signal when reinforcing manipulation was applied with needling sensation. On the other hand, when acupuncture of reducing manipulation was applied with needling sensation, there was increased in the amplitude and frequency of the signal as shown in Figure 6. The upper part is the signal when reducing manipulation was applied without needling sensation, and the lower one is the signal when reducing manipulation was applied with needling sensation. Besides, we noticed that when needle was left on the acupoint, the amplitude and frequency of the volume pulse wave in the fingertip had the tendency of recovery along with the relief of the volunteer's feelings of ache, tingle, tightness and tumidness.

When excitability of sympathetic nerve increases, the heart beat will become fast, the blood vessels of skin and internal organs in abdominal cavity will contract, and the amplitude and frequency of the volume pulse wave will increase. On the other hand, when excitability of parasympathetic nerve increases, the heart beat will slow down, the contraction of atria will decrease and the blood vessels will expand. When acupuncture of reinforcing manipulation was applied to the acupoint, the excitability of parasympathetic nerve increased. Therefore, the pulse rate slowed down and the tensivity of blood vessels decreased so that the amplitude

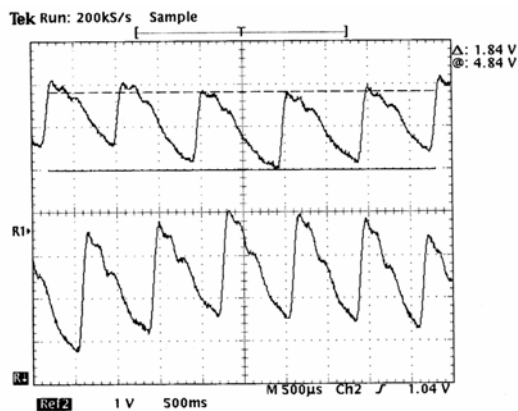


Figure 5 The Signal of Volume Pulse When Apply Reinforcing Manipulation With and Without Needling sensation

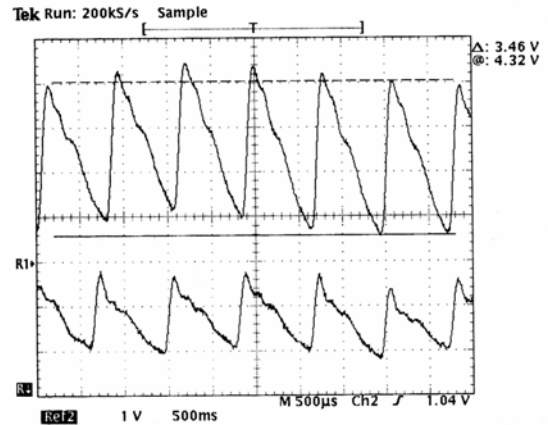


Figure 6 The Signal of Volume Pulse When Apply Reducing Manipulation With and Without Needling sensation

and frequency of volume pulse wave decreased as shown in Figure 5. On the contrary, when reducing manipulation was applied, the excitability of sympathetic nerve increased. As a result, the pulse rate speeded up and the tensivity of blood vessels increased so that the amplitude and frequency of volume pulse wave increased as shown in Figure 6.

X. DISCUSSION

We studied the experimental device that can pick up the myoelectricity signal around the acupoint and the volume pulse wave of tiny artery in the fingertip. When the acupoint was acupunctured with needling sensation, we successfully obtained the myoelectricity signal around the acupoint and the volume pulse wave in the fingertip of the same side before and after there was needling sensation in both manipulations, and made a further comparison. We primarily established the relationship between the degree of needling sensation, the two manipulations and the two parameters: The first parameter is myoelectricity signal. When acupuncture applied without needling sensation, there was no corresponding myoelectricity released. When acupuncture applied with needling sensation, there was corresponding myoelectricity released and the amplitude and frequency of myoelectricity was in positive proportion to the degree of needling sensation. The stronger the degree was, the higher the amplitude and frequency were.

The second is volume pulse wave. When acupuncture applied without needling sensation, the amplitude and frequency of the wave made no difference. When acupuncture of reinforcing manipulation applied, the amplitude and frequency of the wave decreased. While acupuncture of reducing manipulation applied, the amplitude and frequency

increased. Finally, we established an external method with two parameters to accurately evaluate the degree of needling sensation and the maneuver of acupuncture manipulation. With this method, we can make further study on the principle of acupuncture and theory of main and collateral channels, improve the clinical effects of acupuncture, enhance the teaching and training of acupuncture, develop practical Chinese traditional medical devices, and broaden the acceptance of the Chinese traditional therapeutics.

REFERENCES

1. Zhongchao Wu, Decheng Chen. Essence of Professor Qiu Maoliang's Acupuncture Manipulation Methods and Deqi. *Chinese Acupuncture & Moxibustion*, 2001, 21 (5):297-299
2. Yanjun Wang, Hui Cai, Jinyang Hu. The Different Manipulations' Effects to the Temperature of the Points Tested in Healthy People. *Journal of Hebei Traditional. Chinese Medicine and Pharmacology*, 2001, 16 (1):42-44
3. Ling Wang, Mingde Tao, Guanghong Ding. The Calculation of Energy Distribution Based on Two Respective Techniques of Acupuncture Therapy. *Journal of Medical Biomechanics*, 2003, 18 (4):195-201
4. Xing Gu. Development of Teaching Test Apparatus for Acupuncture Manipulations in TCM. *Chinese Acupuncture & Moxibustion*, 2001, 21 (4):220-230
5. Tangyi Liu, Huayuan Yang, Xunjie Gu, et al. Development of ATP-Instrument to measure the parameters of manipulation methods. *Chinese Acupuncture & Moxibustion*, 2003, 23 (11):668-679

Development of Implantable stimulating system used for electroacupuncture

C.S. Niu¹, Y. Yu², H.W. Hao² and L.M. Li²

¹ Department of Mechanical Engineering, Tsinghua University, Beijing, China

² School of Aerospace, Tsinghua University, Beijing, China

Abstract — Electroacupuncture (EA) has been proved effective for treatment of various diseases, such as pain, depression and drug abuse in animal experiment and clinical applications. However, professional operations, including acupoints selection and needles insertion, are needed for needle EA and painful sensation may be generated in surface electrode EA because the non-selective stimulation of the flat electrode activates the cutaneous pain receptor. These disadvantages impede their expansion and design of new EA system is motivated. We present an implantable EA system based on a single acupoint, which consists of stimulator implanted into the acupoint and signal transmitter used out of body. The circuit of the internal stimulator is packaged in silicon rubber and only the stimulating electrodes are left out. The internal stimulator is about 1g and its principal size is $\Phi 14\text{mm} \times 4.2\text{mm}$. The external transmitter is $39\text{mm} \times 43\text{mm} \times 12\text{mm}$ in size and 20 g in weight. Monomial square pulse is gained and its amplitude is 5mA while the testing load is 500Ω . The implantable EA system presented in this paper offers a new method of EA stimulation. It can be used for diseases which need long-term, even coercive treatment, such as chronic pain, depression and drug abuse. Because the EA stimulation is applied at a single acupoint and no other acupoints and meridians are activated, so it also provides a feasible way for the study of acupoint specificity.

Keywords — Single acupoint, Implanted, Electroacupuncture.

I. INTRODUCTION

Electroacupuncture (EA) is the application of electrical current to excite the acupoints in human body for treatment of various diseases, such as pain, depression and drug abuse [1][2][3]. Two electrodes are required to form current-loop in electrical stimulation. For regular EA stimulation, they are always provide by needles inserted into acupoints or self-adhesive electrodes placed on the skin above the acupoint, which is also called transcutaneous electroacupuncture stimulation (TEAS). Both of them have been proved effective in animal experiment and clinical applications.

However, professional operations, including acupoints selection and needles insertion, are needed for needle EA and painful sensation may be generated in surface electrode EA because the non-selective stimulation of the flat electrode activates the cutaneous pain receptor. Otherwise, an EA treatment typically takes weeks or even months. These

disadvantages, including high dependence on physicians and tedious operations, especially in long-term and imperative treatment, impede their expansion and design of new EA system is motivated. In this paper, we present an implantable EA system, which is based on a single acupoint and has great potential in treatment of chronic pain, depression and other long-term diseases.

II. METHOD AND SYSTEM

A. Uni-acupoint EA method

The regular EA is carried out in the way of bi-acupoint and two acupoints are needed to form the current loop [4][5], e.g. left Zusanli (ST 36) and left Sanyinjiao (SP 6) act as anode and cathode respectively. The electrodes can be provided by needles inserted into the acupoints or self-adhesive electrodes placed on the skin above the acupoints.

Differently, uni-acupoint, a novel EA method, is applied based only a single acupoint. A thin ring electrode (about 8mm of external diameter, 2mm of internal diameter and 0.05mm of thickness) used as positive electrode is placed above the selected acupoint area. An ordinary acupuncture needle ($\Phi 0.25\text{mm} \times 13\text{mm}$), which is treated by isolation process and only the handle and 4mm of the point are conductive, is inserted into the selected acupoint through the central hole of the ring and used as negative electrode.

Adult female Wistar rats were used to validate the effectiveness of uni-acupoint EA method for pain relief. Bilateral symmetrical current pulse was exerted at left Zusanli (ST 36) and its effect was evaluated by tail flick latency (TFL) elicited by radiant heat. Our experiments have shown that: 1) average analgesic effect of EA stimulation is significantly higher than control group ($p < 0.01$); 2) analgesic effect of uni-acupoint EA method is lower than the bi-acupoint EA method but there is no statistical significant difference between them. These results suggest that uni-acupoint EA stimulation is a valid EA method for pain relief.

B. Implanted EA system

As shown in Fig. 1, the implanted system for EA acupuncture consists of internal stimulator implanted into the acupoint and signal transmitter used out of body.

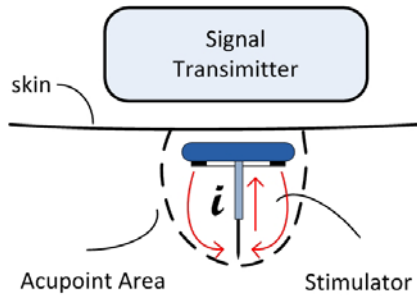


Fig. 1 Schematic of the implanted EA system

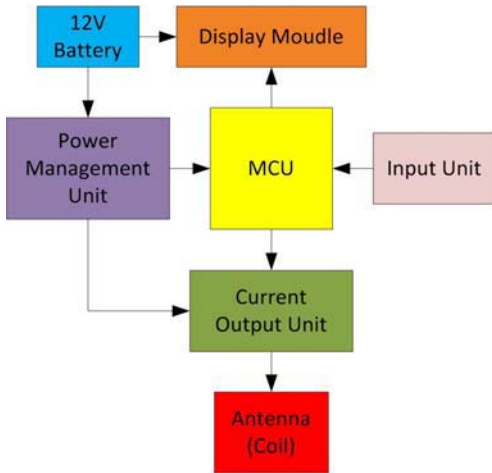


Fig. 2 Circuit diagram of the signal transmitter

The signal transmitter is mainly made up of Power management unit, MCU, current output unit, display module, input unit and transmit coil (antenna).

The power management unit transforms the supply voltage to 3.3V by a buck DC-DC converter for the other parts of the system. The C8051F020 microcontroller is used for the logic control of the system, treatment of the input command for the input unit and status management of the display module.

The current output unit is controlled by MCU to generate modulated carrier waves of the simulating wave, and the carrier frequency is about 100k Hz. The modulated carrier wave generated by the current output unit is shown in Fig. 3.

The parameters (see Table 1), including frequency, wave form and amplitude, can be programmed through the input unit and shown on the OLED screen.

The current output unit mainly consists of a numeric control source and a NPN transistor is the core part of them. The microcontroller controls the Digital-to-Analog Converter (DAC) output voltage which can be used as base voltage to control the current out of the transistor. Antenna

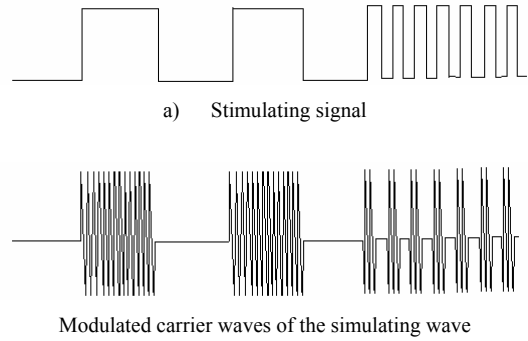


Fig.3. Schematic of the modulated carrier wave generated by the current output unit

excited by the output current transmits the stimulating signal by electromagnetic coupling to the internal stimulator.

The internal stimulator is made up of receiver coil, voltage rectifier and filter and charge balance unit. The stimulating signal transmitted by the antenna of the external signal transmitter is received by the receiver coil, and rectified and filtered by the next unit. A capacitor is used for the charge balance to make sure the net charge flow into the body is zero. So, the damage of tissues and erosion of electrodes induced by the net current will be avoided [6][7][8]. The stimulating signal acted to the acupoint is shown in Fig. 5.

In order to satisfied the requirement of the implant, the internal stimulator is totally packaged in biologic consistent silicon rubber and only the stimulating electrodes are left

Table 1 Parameters of the stimulating signal

Parameter	Value
Waveform	square, sine, saw-tooth, triangular, exponential
Amplitude	0~6mA, 12 step (testing load, 500Ω)
Frequency	0~150Hz, 10Hz per step, or 2/100Hz distant-dense wave
Pulse Width	0~600us, 50us per step

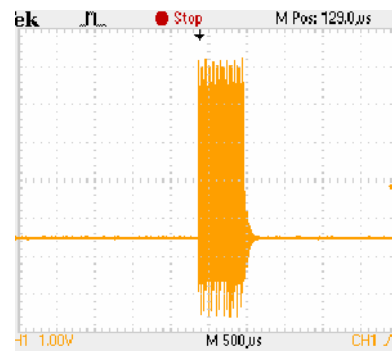


Fig. 4 Transmitting wave of the antenna

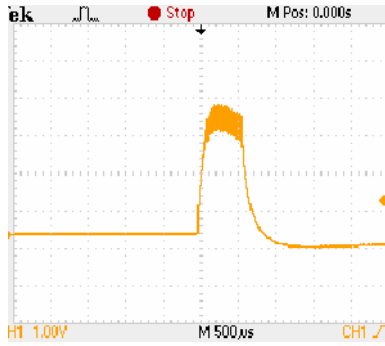


Fig. 5 Stimulating signal acted on the acupoint



Fig. 6 Integrate implanted EA system

out. Two layout methods of electrodes are also considered to fit the implantation in acupoints.

The integrated implanted EA system is shown in Fig. 6. The internal stimulator is about 1g and its principal size is $\Phi 14\text{mm} \times 4.2\text{mm}$. And the external signal transmitter is $39\text{mm} \times 43\text{mm} \times 12\text{mm}$ in size and 20 g in weight. Monomial square pulse is gained and its amplitude is 5mA, which is enough for animal EA stimulation, while the testing load is 500Ω .

We selected Zusanli (ST36) of rabbit as the acupoint to verify its security and usefulness for pain relief of the implantable system and these experiments is in process.

I. CONCLUSIONS

The implanted EA system presented in this paper is made up of external signal transmitter and internal stimulator. The internal stimulator is small, light, and fit for implant. The

stimulating signal is powerful enough for experimental use, while the testing load is 500Ω . The system offers a new method of EA stimulation. It can be used for diseases which need long-term, even coercive treatment, such as chronic pain, depression and drug abuse. Because the EA stimulation is applied at a single acupoint and no other acupoints and meridians are activated, so it also provides a feasible way for the study of acupoint specificity.

ACKNOWLEDGMENT

This study has been supported by National High Technology R&D Program of China (863 program) (Grant No.2006AA02Z4E9) and National Key Technology R&D Program of China (Grant No.2006BAI03A18).

REFERENCES

1. G.A. Ulett, S.P. Han, J.S. Han, (1998) Electroacupuncture: Mechanisms and clinical application, *Biol. Psychiatry* 44:129-138.
2. Y. Wang, Y. Zhang, W. Wang, et al. (2005) Effects of synchronous or asynchronous electroacupuncture stimulation with low versus high frequency on spinal opioid release and tail flick nociception, *Exp. Neurol.* 192:156-162.
3. J.S. Han. (2003) Acupuncture: neuropeptide release produced by electrical stimulation of different frequencies, *Trends Neurosci.* 26:17-22.
4. S.J. Yun, H.J. Park, M.J. Yeom. (2002) Effect of electroacupuncture on the stress-induced changes in brain-derived neurotrophic factor expression in rat hippocampus, *Neurosci. Lett.* 318:85-88.
5. W.T. Zhang, Z. Jin, F. Luo. (2004) Evidence from brain imaging with fMRI supporting functional specificity of acupoints in humans, *Neurosci. Lett.* 354:50-53.
6. Donaldson NDN, Donaldson PEK. (1986) When are actively balanced biphasic ('Lilly') stimulating pulses necessary in a neurological prosthesis? *Medical & Biological Engineering & Computing* 24:50-56.
7. Scheiner A, Mortimer JT, Roessmann U. (1990) Imbalanced biphasic electrical-stimulation - muscle-tissue damage. *Annals of Biomedical Engineering* 18(4):407-425.
8. Dennis R G, Dow D E, Faulkner J A. (2003) An implantable device for stimulation of denervated muscles in rats. *Medical Engineering & Physics* 25:239-253.

Author: Luming Li
 Institute: School of Aerospace, Tsinghua University
 Street: Room 803, main building, Tsinghua University
 City: Beijing
 Country: China
 Email: lilum@tsinghua.edu.cn

Study of Acupuncture Manipulation Parameter Based on Data Mining Technique

Yin-e Hu, Hua-yuan Yang

Department of TCM Engineering, Shanghai University of TCM, Shanghai, China

Abstract— Currently the scholars study acupuncture manipulation parameter from the two aspect mainly, firstly, they quantify the acupuncture manipulation parameter through clinical work and science experiment method; secondly, acquire the acupuncture manipulation parameter through the crossing of multiply subject, then analyze and deal with the parameters. Due to the analysis and research on acupuncture manipulation parameter is not enough in the earlier work ,At the same time, Data Mining has good applications in TCM field. The study explained the science intension of the TCM in modern science knowledge and widened the research idea. The article proposes to acquire with the laboratory apparatus, and mine the rule information from the plenty of the collected acupuncture manipulation parameters with the Data Mining technique. Then find the relation between the acupuncture manipulation parameters and acupuncture curative effect. Consequently it will be make a theory base for the standard, normalization and quantification study of the acupuncture manipulation parameter.

Keywords— Acupuncture manipulation parameter; Data Mining; Stimulation amount; Manipulation waveform; Sensor; Quantification.

I. INTRODUCTION

Acupuncture and moxibustion as a kind of physical stimulation, has to exist the topic about the stimulation quantity parameter. A large number of experiments and clinical practice prove that the curative effect of acupuncture and moxibustion is obviously influenced by the quantity of stimulation, the different stimulation quantity should cause the different physiological effects, so while operating acupuncture and moxibustion, it is not only simple choice of acupuncture manipulation, but also the more important thing is how to choose stimulation size of acupuncture manipulation parameter.

At present, the research of the acupuncture manipulation parameter is being paid attention to. The scholars utilize technology of crossing multi-disciplinarily to develop the instrument that can gather the acupuncture manipulation parameter while handling the needle in real time, which concretes research and establishes the foundation to the acupuncture manipulation parameter in order to utilize computer technology to carry on deeper. This article analyzes acupuncture manipulation parameter quantification and

acupuncture manipulation parameter collecting on current study, and points out their insufficient and provide the way to solve. Propose to apply dataming technique to the acupuncture manipulation parameter studying, expect for being intuitionistic, concrete , qualitative and quantitative understanding the essential law of stimulation quantity, discovering the relation between the acupuncture manipulation parameter and acupuncture curative effect, which instructs the clinical acupuncture manipulation to operate.

II. CURRENT RESEARCH ON ACUPUNCTURE MANIPULATION PARAMETER DETERMINING

In order to make use of change characteristic of the acupuncture manipulation parameter to discuss and study acupuncture essence, acupuncture mechanism and acupuncture effect, etc., scholar use modern science and technology to develop the instrument that can gather manipulation of parameter in real time and carry on the objectified research to the stimulus amount of the acupuncture manipulation.

A. Development of acupuncture manipulation parameter's collecting equipment

At the beginning 1990s, Yang Huayuan ,etc. [1] carried on the development of acupuncture manipulation simulation operation, and developed the acupuncture manipulation parameter measure apparatus which adopts the sensor technology of the resistance to gather the acupuncture manipulation parameter and outputs the manipulation wave form through two physiological recording instruments , there are number value marks on the wave form. Gu Xin [2] also developed the acupuncture manipulation teaching tester which mainly gathers the signal of lifting and thrusting, twiddle through little electrical machinery sensing technology and can reflect the changes of the speed , force of the acupuncture manipulation through two physiological recording instruments. These two kinds of manipulation measure apparatuses just show the acupuncture manipulation wave form on the LCD, carry on relevant analysis and study about the acupuncture manipulation parameter according to the manipulation wave form characteristic.

Other scholars do certain research on gathering force of the needle body and manipulation wave form. For instance

Ding Guanghong [3], etc. develop one measure system in modern integrated sensing technology and biomechanics principle, which can test various kinds of acupuncture manipulation at the living person body and receive the mutual power between person who constructs needle and person who receives needle, this system can be written down the force wave form and number of even lifting and thrusting / twiddle manipulation. Li Qinghua [4], etc. also developed "acupuncture manipulation sensing needle" in micro-force sensing technology and biomechanics principle, which can show the force wave form of the sensor needle in the computer directly, then can write down the detail of handling the needle objectively. The research of the two haven't made breakthrough progress, still mainly study the acupuncture manipulation parameter and relation with acupuncture effect through analysing the law of the manipulation wave form. It is extremely urgent that can develop writing down the acupuncture manipulation parameter and system that can be analysed and dealt with to the manipulation parameter objectively in real time. For this reason, Yang Huayuan [5], etc. improve the craft on the basis of original acupuncture manipulation parameter measure apparatus, and use modern communication technology and computer technology, gather and observe the change the acupuncture manipulation parameter in real time, and then analysis and study relationship between the acupuncture of parameter change and acupuncture effect, have offered the new means for quantization research and teaching of the acupuncture manipulation. The acupuncture manipulation test system can carry on gathering, storing a large amount of acupuncture manipulation for the single polymorphous acupuncture manipulation (every great school), and setting up acupuncture manipulation point scale and expert's acupuncture manipulation database. It has offered a large number of data sources for the thing that utilize technology of the computer and carry on deeper treatment, analysis and study to the acupuncture manipulation parameter, and it has offered a kind of new thinking of scientific research for the thing that study the law between the acupuncture manipulation parameter and acupuncture effect.

B. Study on acupuncture manipulation parameters analyzing

Through the analysis of the above thesis, it is discovered that researchers have utilized modern science and technology to gather acupuncture manipulation in real time. They also utilize physics, statistics and computer technology to carry on corresponding analysis and treatment to the acupuncture manipulation parameter, and then discover the acupuncture manipulation law and relation with acupuncture effect.

At the beginning of 1990s, Yang Huayuan [6], etc. not only developed the acupuncture manipulation parameter measure apparatus but also utilized the the knowledge and principle of physics to analyze the force of lifting and thrusting, twiddle operation and the manipulation parameter. The research acupuncture manipulation can be done better according to analysis result. He proposes the following conclusion through analyzing the force of lifting and thrusting, the different the level of the human body and changes of obstruction make the needle body do the uniform motion and change the acceleration of lifting and thrusting, thus caused the change of the operator feeling, when obstruction is big enough, displacement hardly takes place in the needle body, but the effort still exists; it get the conclusion to Analyze effect power of twiddle process: as human body's organizational form and the change of twiddle's times, cause the change of the obstruction square, the same obstruction square changes with twiddle different the corner speed changing and the response of human body. Yang Huayuan, etc. have elucidated the scientific intension of the traditional acupuncture and moxibustion theory through observing the acupuncture manipulation wave form gathered. The wave form of the simple lifting and thrusting manipulation is similar to straight wave curve, which proves that frequency is more steady and depth changes nearly consistently. Through analysing the wave form, it can be better that discussion and studying acupuncture mechanism, the essence of acupuncture and acupuncture effect, etc.

Ding GuangHong, etc. [7] have carried on the statistics and analysis on the land frequently to various kinds of force effected on needle body and measured manipulation wave form while developing and monitoring the needle body and receiving the force system dynamically, filtered the regular desired sensation index and parameter. He analyses about the data of measuring from two respects mainly. First, wave form of force on needle body indicates that it is identical between needle receiving change law of force and traditional acupuncture description of manipulation; Second, do the experiment study to even twist, even lift and thrust, twist reinforcing method, twist purgation method, lift and thrust reinforcing method, lift and thrust purgation method, the six kinds of manipulation, the needle's wave form and number value on the body have significance differences to different manipulation, and different persons who constructs needle all have surprising similar wave form and number value to implement the same acupuncture manipulation examined and got on the human body. So propose adopting the size of needle's receiving force and wave form as the objective quantitative parameter of acupuncture manipulation.

With the computer technologies' rapid development and its function and advance on processing and storing a huge data, Yang Huayuan, etc. [8] utilize the knowledge of phys-

ics combining the modern computer technique to analyze and process the acupuncture manipulation parameters, take the change value of the force on the three axis of coordinate as an important parameter, the parameter is expressed as

$$k^i = c^k \cdot s^k \cdot f^k \quad (1)$$

Here, compute the effect power according to the corresponding physical amount. In teaching, mainly pass and gather students' acupuncture manipulation parameter, and set up acupuncture manipulation point scale through establishing corresponding weight value, thus there is a objectified quantization index in the appraisal on the acupuncture manipulation.

II. THE DEFICIENCY OF ANALYSE AND STUDY IN EXISTING ACUPUNCTURE MANIPULATION PARAMETER

Through reviewing these documents about study of acupuncture manipulation parameter, we can find that it has already made the progress attracting people's attention in study on acupuncture manipulation parameter. Still there were some unperfected places. First, though some scholars summarize the choice law of the acupuncture manipulation parameter according to a large number of clinical experience and scientific experiment, but has not utilized technology of the computer to carry on further analysis and treatment to these data, thus inherit and develop Chinese medicine culture with the method of crossing multidisciplinary. Second, with the development of technology of the sensor, develop the instrument that can gather to the acupuncture manipulation parameter one after another. But the analysis and study to the gathered acupuncture parameter is not very abundant at present, mainly summarize the law through observing the manipulation wave form in vision directly, though and analyse the acupuncture manipulation parameter through statistics and computer technical treatment, but has not fully utilized computer technical to treat a large amount of data information, and explore out the rule from a large amount of data information. Third, it is usually to proceed from clinical curative effect about research of acupuncture manipulation quantification, and summarize the choice of the acupuncture manipulation parameter, but has not provided the concrete acupuncture manipulation parameter, and then verifies the thinking of research of the curative effect of this group of parameters. So the research about the quantification still mainly summarizes experience according to the clinical practice, but don't work out the acupuncture manipulation parameter at first, then apply to clinic through the thinking of clinical examines.

III. DATA MINING'S APPLICATION IN THE FIELD OF TRADITIONAL CHINESE MEDICINE

Professor Shi Xuemin[9] has pointed out that only if we use modern scientific and technical knowledge, we could promote the development of medical science of acupuncture and moxibustion, though the past dynasties Chinese medicine classic emerges in an endless stream, only form supplementing each other academy, there is no great breakthrough. In the ranges from negative and positive philosophy, many doctors only draw the conclusion from the personal observation and extended duplicated experience, not able to deep the reach in field of the medical essence that can't be observed in naked eye but can be probed into by the scientific method. Acupuncture and moxibustion as the clinical medical science, if it isn't followed up by the basic research, it is difficult to progress and enter mankind's scientific palace, one kind forever effective but unidentified treatment which isn't explained clearly.

Data mining is a frontier branch of science with artificial intelligence and database technology in recent years, it is devoted to find the knowledge or law about thing's essence and development trend implied in the data, and offer the support [10] for the expert's decision. In some research fields of traditional Chinese medicine at present, it already demonstrates the good application prospect. Traditional Chinese medicine is the treasure of Chinese nation, it is important components [11] of the traditional Chinese medicine modernization to mine the traditional Chinese medicine information. The data mining technology already has a good application trend in some fields of traditional Chinese medicine.

To research in medicine made of two or more ingredients of traditional Chinese medicine, it was that the clinician utilized one's own knowledge and experience to develop a new medicine basically in the past, and it is used for proving clinically. After obtaining better curative effect, carry on the research in pharmacology, traditional Chinese medicine chemistry, etc., this is a kind of experience development mode [12]. In recent years, on the basis of abundant experience that the Chinese medicine field accumulates, utilize the data mining technique to make up the new medicine then explain with the relevant theory, which has already been paid attention to. For example, He Qianfeng [13], etc. utilize high frequency pattern mining to analyse the composition data of the traditional Chinese medicine prescription, in Chinese Recipe Database, New Medicine of TCM Database and TCM Set Prescription Pharmaceuticals Standardization Database, get some high frequency medicine combination, and put forward to use the relevant nature theory to be explained, put in order, make the traditional Chinese medicine medicine drug develop. Yao Chunmei, etc. [14] use the

association rules(a kind of data mining technique) to analyse the scientific intension of compatibility of medicine made of two or more ingredients of traditional Chinese medicine of the disease carries on exploratory analysis and research to treating and quenching thirst. Song Yaoping, etc.[15] utilize data mining technology to carry on relative analyse Chinese traditional medicine dosage of treating spleen and stomach disease, and seek the medicine difference to dependence of the same and different medicine's related degree.

They have applied data mining to Chinese traditional medicine diagnoses to find out the relationship between the syndrome and the symptom through a large number of clinical data, thus simulate the diagnosis reasoning process of the expert. Such as Wang XueWei [16],etc. use the Bayesian Network method to analyse diagnosis clinical data of 474 cases of blood stasis and carry on the quantificational diagnose, find blood stasis disease's 7 key symptom , calculate their diagnosis contribution degree quantificationally. Liu Baoyan, etc. [17] choose autoregressive model modeling method confirm the final return equation, thus get the discrimination equation of the sub-healthy state and its clinical characteristic.

The data mining technology has played a certain role in study of syndrome standardization and normalization. Setting-up of the traditional Chinese medicine standardization and objectivity study and curative effect appraisal system, research that objectifies, can't do without the standardized research on symptom. Liang WeiXiong, etc. [18] apply index clustering on 221 cases of paralytic patient in the acute stage, analyse the relation of their syndrome character and the relative symptom, tongue picture, pulse condition, propose that the syndrome of paralytic patient in the acute stage can be divided into wind fire, phlegm stasis, deficiency of the vital energy, deficiency of yin with excess of yang. Zhang ShiJun, etc. [19] utilize epidemiology and variable clustering analysis mathematical statistics method, analyse and study about the liver syndrome of Chinese medicine, finally, divide its main syndrome into substantial syndrome , wind syndrome and deficiency syndrome. Yuan Shihong, etc.[20] symptom look for natural group that suffer from a deficiency of the kidney with clustering analysis method, probe into the relation between the structure of syndrome and symptom of the deficiency of the kidneying, offer the scientific explanation for relevant symptom structure of the deficiency of the kidney in Chinese medicine diagnostics.

IV. THINKING OF THE STUDYING ACUPUNCTURE MANIPULATION PARAMETER WITH DATA MINING TECHNOLOGIES

There is certain progress in acupuncture manipulation parameter quantification research, gather the acupuncture manipulation parameter through the developed modern instrument, and thus stride greatly in the quantification of acupuncture manipulation parameter. But there is not yet any report about data mining technology applied on analysing and studying acupuncture manipulation parameter at present. On the basis of previous research work, this article puts forward the thinking of analysing acupuncture manipulation parameter based on data mining technology.

A. Research approach

According to the thinking of research in other traditional Chinese medicine applying data mining technologies, apply data mining technique to the study of acupuncture manipulation parameter, and exploit a thinking of scientific research on the acupuncture manipulation parameter.

At first, gather a large number of acupuncture manipulation parameters through the modern scientific instrument, set up acupuncture manipulation parameter database; Then by the advantage of the data mining which can fully deal with and analyse a large number of data, explore out regular information from a large number of acupuncture manipulation parameter, combine the acupuncture and moxibustion expert with abundant clinical practical experience and explain that the data mining result, explore to set up standardized acupuncture manipulation parameter; Finally revised by the senior acupuncture and moxibustion expert and a large amount of clinical examination. Figure 1 shows the main following of the thinking.

B. Meaning of the Study

Analyse and study about the acupuncture manipulation parameter through the data mining, on one hand, can find out the combination of the acupuncture manipulation parameter and the consistency of acupuncture and moxibustion curative effect and existing acupuncture and moxibustion theory, and then explain the scientific intension of acupuncture and moxibustion with modern science. On the other hand, can explore some new acupuncture manipulation parameter associations, The senior acupuncture expert and the scientific experiment summarize these acupuncture and moxibustion curative effect with corresponding parameter. The study will provide a theoretical foundation for the standardization and quantification of acupuncture manipulation parameter, and there is important directive significance to the clinical practical operation of acupuncture and moxibustion.

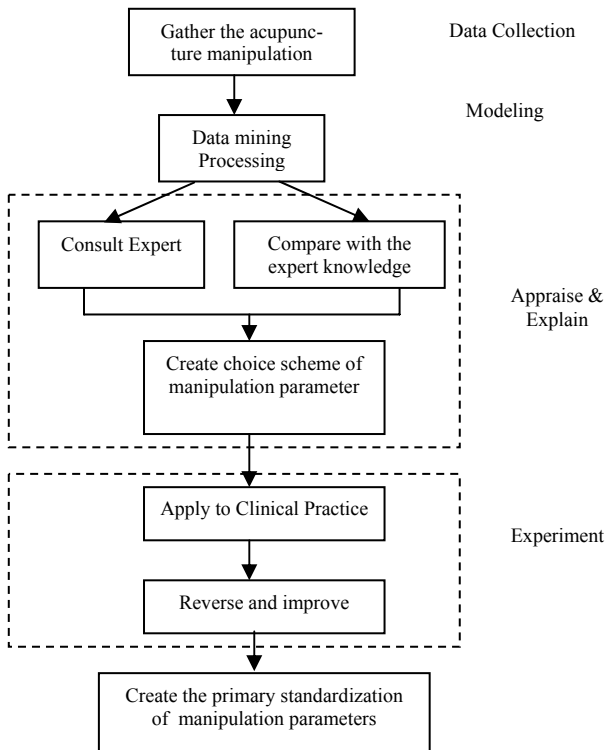


Fig. 1 The thinking of study acupuncture manipulation parameter based on data mining

REFERENCES

1. Yang huayuan, Gu Xunjie, Xia Jinshan. Development of acupuncture manipulation parameter determination apparatus and analysis of the force of manipulation. *Journal of Clinical Acupuncture and Moxibustion*. 1995, 11 (6) :51
2. Guxing. Development of Teaching Test Apparatus for Acupuncture Manipulations in TCM. *Chinese acupuncture & Moxibustion*. 2001; 21 (4) :229
3. Ding Guanghong, Shen Xueyong, Dai Jianhua, etc. Research and Development on the Dynamic System for Detecting the Force of Acupuncture Needle during the Acupuncture Process in the Clinical Practice of Traditional Chinese Medicine. *Journal of Biomedical Engineering*. 2003, 20 (1):121- 124
4. Li Qinghua, Li Fuguo, Ai Bingwei. Research of Detecting Acupuncture Needle for Acupuncture Manipulation. *Chinese Journal of Sensors and Actuators*. 2006,19(2) 285-288.
5. Liu Tangyi, Yang Huayuan, Gu Xunjie, Xia Jinshan. Development of model ATP-I acupuncture manipulation parameter determination apparatus. *Chinese Acupuncture & Moxibustion*. 2003,23 (11) :668-670
6. Yang Huayuan, Gu Xunjie, Xia Jinshan. Development and application of acupuncture manipulation parameter analysis apparatus. *Shanghai Journal of Acupuncture and Moxibustion*. 1991, 3 :35-36
7. Ding Guanghong, Shen Xueyong, etc. THE CONTRAST RESEARCH BETWEEN ACUPUNCTURE MANIPULATIONS AND THE PARAMETERS OF FORCE ACTING ON NEEDLE. *Chinese Journal of Biomedical Engineering*. 2004, 23(4):254-256
8. Hua-Yuan YANG, Tang-Yi LIU, Le KUAI, Ming GAO, Zhui-Cheng HU. Research on real-time data collection and demonstration system for acupuncture manipulation. *Journal of Chinese Integrative Medicine*. 2006, 5(4):311-314.
9. Shi Xuemin. Issues and Countermeasure Lie Ahead of Acupuncture and Moxibustion in the New Century. *Traditional Chinese Medicine Journal*. 2002,1(3):1-4.
10. Fayyad U , Shapiro GP ,Smyth P. From Data Mining to Knowledge Discovery : An Overview. In : Fayyad (Eds) . *Advances in Knowledge Discovery and Data Mining*. Cambridge , MA:MIT Press , 1996:1-3
11. Qiao Yanjiang, Li Pengtao, Su Ganqiang. The meaning of KDD study on traditional Chinese compound prescription. *Journal of Beijing University of Traditional Chinese Medicine*. 1998,21(3):15-17.
12. Qin Xue-jun,SHI Cheng. The application of data mining in the area of traditional Chinese Medicine. *Medical Information*. 2006,19(5):945-947
13. He Qianfeng, Cui Meng, Wu Chaohui. The Knowledge Discovery of Formula Construction. *Journal of the China Society for Scientific and Technical Information*. 2004,11(7):655-658.
14. Yao Meicun,Ai Lu, Yuan Yuemei. Analysis of the Association Rule in the Composition of the TCM Formulas for Diabetes. *Journal of Beijing University of Traditional Chinese Medicine*. 2002,25(6):48-50.
15. Song Yaoping, Li Kun, Wu Mengxu. Research to Association of Couplet Medicines Dosage. *Liaoning Journal of Traditional Chinese Medicine*. 2006,33(9):1095-1096
16. Wang Xuewei, quhaibin, Wang Jie. A quantitative diagnostic method based on data-mining approach in TCM. *Journal of Beijing University of Traditional Chinese Medicine*. 2005,28(1): 4-7
17. Liu Baoyan, He Liyun, Xie YanMing. The logistic regression method based on the data mining process-The application of the sub-health classification and the analysis of effect factors. *World Science and Technology-Modernization of Traditional Chinese Medicine*. 2006,8 (2):48-52
18. Liang Weixiong, Wen Zhehuai, Ou Aihua, etc. Multivariate Analysis of TCM Syndromes of Apoplex at Acute Stage. *Journal of GuangZhou University of Traditional Chinese Medicine*. 1998 ,15 (4):293
19. Zhang Shijun, Shen Mingxiu, Wang Xianchun, etc. Cluster Analysis of Variables in Liver Syndrome of TCM. *Chinese Journal of Integrated Traditional and Western Medicine*. 2004,24(1):75-76
20. Yuan Shi-hong, Wang Mi-qu, Wang Tian-fang, etc. Study on kidney-deficiency symptoms with cluster analysis. *Journal of Beijing University of Traditional Chinese Medicine*. 2006,29(4):254-257.

Author: Hu Yin-e, Yang Hua-yuan
 Institute: Shanghai University of TCM
 Street: No. 1200, Cailun Road
 City: Shanghai
 Country: China
 Email: huyine@sina.com, yhy5921@126.com

A fMRI Study on Electroacupuncture Intervening Heroin Abstiners' Cognitive Attention

Ping Xu¹, Yingping Jiang¹, Daoying Geng², Yan Wang³, Guanghua Lu⁴

¹Acumox-Tuina College of Shanghai University of T.C.M., Shanghai, China

²Department of Radiology, Huashan Hospital affiliated to Fudan University, Shanghai, China

³Department of Psychology, East China Normal University, Shanghai, China

⁴Shanghai Drug Abuse Treatment Center, Shanghai, China

Abstract — **Objective:** To observe heroin abstiners' cerebral functional changes of cognitive attention on the heroin-related cue, positive and negative emotional cues before and after electroacupuncture intervention, and to explore the possibly involved neural mechanism in relapse and central principles of electroacupuncture intervention. **Methods:** Magnetic resonance imaging technique as well as Block and Dot-probe event-related stimulating modes were used to compare and analyze images obtained from fMRI-BOLD technique before and after electroacupuncture intervention. **Results:** In the attention shift task, significantly stronger activation intensity was shown in the dorsolateral frontal cortexes, inferior frontal gyri, anterior cingulate cortexes and left corpus striatum after electroacupuncture treatment. In the attentional bias task, after electroacupuncture treatment, the activation volume of the dorsolateral areas of the left frontal lobe decreased significantly, and the activation intensity of the right superior parietal lobule increased. **Conclusions:** Heroin abstiners showed significantly higher attentional bias to visual drug-related cue than to positive and negative emotional cues, and they had higher attentional bias to the processing of negative emotion than to the positive emotional cue. Electroacupuncture intervention could obviously lower the attention level of heroin abstiners to the drug-related cue, inhibit the susceptibility of heroin abstiners to negative emotion and promote the rehabilitation of cognitive function of emotion of the brain.

Keywords — Heroin abstinence, Electroacupuncture, functional Magnetic Resonance Imaging (fMRI), cognitive attention, Drug-related cue

I. INTRODUCTION

Drug addiction is a chronic refractory and recurrent brain disease. It has been doing enormous harm to national economy, quality of population and social stability because it results in not only the consumption of capitals, but also loss of labour force, increase of crime and transmission of venereal diseases. The most difficult problem to handle in the abstinence of drug is to inhibit irresistible psychological urges, of which the memory of euphoria is the main reason. More and more research shows that there's significant correlation between attentional bias and drug addiction due to

urges^[1]. Hence the intervention of urges in drug addiction is the key to solve the problem of relapse, and it's an important part to correct abnormal cognitive processing in the intervention of urges. Previous clinical experiment "Influence of acupuncture on heroin addicts' attentional bias" by our research group showed that, the intervention of acupuncture could obviously correct the attentional bias of heroin addicts to drug-related pictures, which indicated that acupuncture could be used as a treating method to improve the cognition of heroin addicts, and it had good potential of preventing relapse.

In this research, magnetic resonance imaging technique, Block stimulating mode based on attention shift and dot-probe event-related stimulating mode based on attentional bias were used to compare and analyze images obtained from fMRI-BOLD technique on the execution of cognitive tasks under three kinds of attention cues of positive emotion, negative emotion and heroin-related before and after electroacupuncture intervention, and rewarding results were found. Now the research is reported as follows.

II. MATERIALS AND METHODS

A. Research Subject

7 cases of heroin abstiners that accorded with inclusive criteria as well as 8 normal and healthy cases were collected, and informed consent forms were signed.

7 cases in the heroin abstainer group came from Shanghai Drug Abuse Treatment Center. Male, aging from 22 to 37 years old with an average of 26.1 ± 5.3 years, continuous heroin abuse for 4-8 years with an average of 6.6 ± 1.5 years; the average dose was 1.1 ± 0.8 gram per day; detoxification time for 35-79 days with an average of 52.4 ± 14.6 days; according with the 4th version of Heroin Dependence Standards of American Diagnostic & Statistical Manual (DSM) of Mental Disorder (DSM-IV), all were right-handed with normal vision or corrected vision of 1.0, none had color blindness.

8 cases in the control group, male, healthy volunteers, aging from 24 to 31 years old with an average of 25.9 ± 2.3 years, with roughly matched age and educational level to those of the experimental group. No serious heart or brain diseases (such as hypertension, diabetes, organic diseases of the brain, etc.), no application of addictive drugs or psychotropic drugs, no drug withdrawal history, no claustrophobia; all were right-handed with normal vision or corrected vision of 1.0, none had color blindness.

Group t-test showed that there's no significant difference in age between the two groups ($P > 0.05$).

B. Materials and Apparatuses

1. Experimental materials

36 pictures of drug-related cue and emotional cue were used, among them there're 12 pictures of drug-related cue-heroin taking scene, positive and negative emotional cue respectively. The complexity of the picture contents was basically matched. The resolution was 72 pixels per inch, and the size was 240×180 mm. The resolution, brightness and contrast were basically accordant with each other after the procession of Photoshop 7.0

Before the experiment, emotion evaluation was did for the two kinds of emotional cue pictures. -10 to 10 scoring method was used in the evaluation. 50 copies of questionnaire were distributed, and 43 were effective. The scores of two kinds of emotional cue pictures were: $M=0.8$, $SD=1.6$, $M=9.3$, $SD=2.1$, $M=-8.6$, $SD=2.8$.

2. Main apparatuses and equipments

Electroacupuncture apparatus: G6805-II low frequency electric pulse therapeutic apparatus (Manufactured by Shanghai Medical Electric Apparatus Factory, Product Registration No. HSYJX(Z) 2005-2261154, Product Standard No. Q/CYBV24-2000, Product License No. HSYJXSCX 20000108).

Needles: Because of high magnetic field intensity of fMRI equipment, non-magnetic silver acupuncture needles were used in the experiment. 0.30mm in diameter, 40mm in length (Manufactured by Suzhou Shen Long Medical Apparatus Factory, Product Registration No. SYGX(Z) 2001-2150231, Product License No. SYGXSCX20010026).

fMRI apparatus: 3.0T signa Horizon LX superconduct magnetic resonance imaging system by American General Electric Company (GE), with the maximum gradient strength of 40mT/m and slew rate of 120T/m/s. Quadrature head coil matched with the machine was used to stimulate and collect signals, and the task presentation equipments included Legeng LCD computer as well as projector and

screen manufactured by Sony company, the presentation software was Eprime 1.1. Subjects responded with the key-stroke in hand. This stimulation presentation system could record the reaction time and accuracy of the subjects simultaneously.

C. Experimental procedure

Before the experiment, the subjects were trained with cognition task so as to guarantee the accuracy of task response.

1. Experiment task 1

Emotional and drug-related pictures were used to observe the difference of attention shift between heroin abstainers and normal subjects.

Block design was used, that is, positive emotional, negative emotional and drug-related pictures were grouped into 3 blocks, each block contained 24 trials consisting of stimulating pictures of the same type. In each trial, stimulating pictures were presented randomly on any of the 4 positions of the upper, lower, left and right of the screen. Each picture was presented for 1 second, and the response time for the subject was 2 second, then the next picture was presented. Subjects were required to respond with keystroke to the presented position of the pictures. There's an interval of 30 seconds between blocks, and totally 72 trials were presented. The experiment flow was shown in Fig. 1.

2. Experiment task 2

Emotional and drug-related pictures were used to observe the difference of attention bias between heroin abstainers and normal subjects.

Dot-Probe design was selected, that is, 1. The three types of positive emotional, negative emotional and drug-related pictures were paired randomly and thus composed 3 kinds of pairs, i.e., positive-negative, positive-drug-related, and negative-drug-related; 2. The three pairs mentioned above were paired upside-down to form 6 combining ways, i.e., positive-negative, negative-positive, positive-drug-related, drug-related-positive, negative-drug-related, and drug-related-negative, and thus there're 36 trials. First, Fixed focus "+" was presented for 1 second, then on the upper and lower position of the screen, a pair of paired stimulating pictures was presented randomly. After that, the mark of "*" was randomly presented on the upper or lower position where the paired stimulating pictures were presented, and the subjects were required to respond to the position of "*" as quick as possible. Then the next trial was presented. The intervals between two trials were randomly selected from 4, 6 or 8 seconds. The experiment flow was shown in Fig. 2.

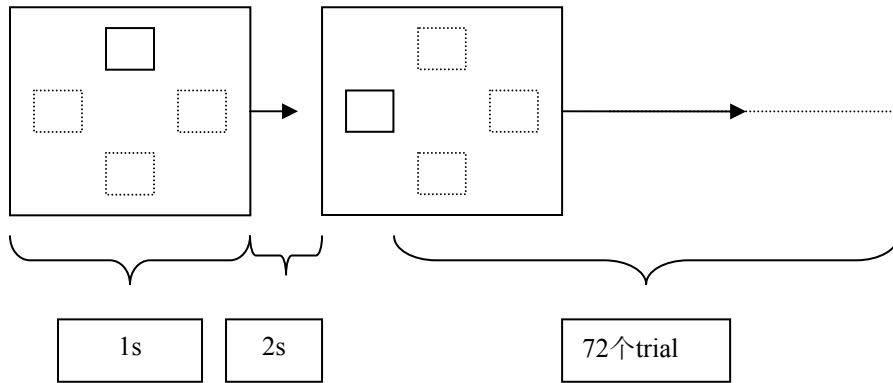


Fig. 1 Experiment Task 1

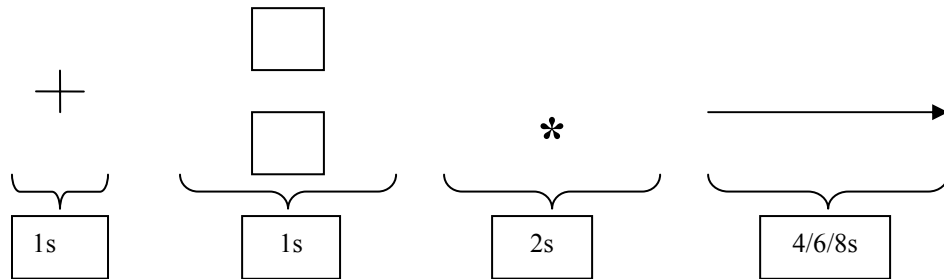


Fig. 2 Experiment Task 2

3. Electroacupuncture method

Acupoints: Neiguan (PC6), Zusanli (ST36). The points were located according to the National Standard of “Location of Points”.

Methods: The needles were inserted in the order of left Neiguan, Zusanli, right Neiguan and Zusanqi. After the acupoint stimulation was obtained, G6805-II low frequency electric pulse therapeutic apparatus was applied, with two groups of electrodes connecting points on the left or right side respectively, the anodes connecting Neiguan on the upper limbs, and cathodes connecting Zusanli on the lower limbs, continuous pulse wave, 2 HZ of stimulating frequency, and the stimulating intensity was decided based on the principle that that no discomfort should be aroused.

To avoid the interference of magnetic field with the electroacupuncture apparatus, copper extension lead was used to connect silver needles, and the electroacupuncture apparatus was placed far away from the magnet of magnetic resonance machine.

4. fMRI scanning

After the collection of routine anatomic structure images, visual stimulating materials were played, and experiment

task 1 and 2 were presented in turn; while functional images were scanned simultaneously. After the two cognition tasks mentioned above, the subjects were applied with electroacupuncture intervention. During the continuous process of electroacupuncture intervention, the experiment task 1 and 2 before electroacupuncture were repeated, and functional images were scanned again.

Research areas: Dorsolateral/ventromedial area of the prefrontal cortexes, anterior cingulate cortexes, temporal lobes, fusiform gyri, superior parietal lobule, inferior parietal lobule, corpora striata, dorsal thalamus and amygdaloid nucleus belonging to the attention circuit, emotion circuit and brain areas relatively specifically activated by acupoints were selected. According to the experiment objective, observe and compare the changes of activation volume and activation intensity of above related brains areas of the experimental group and control group on executing the cognitive tasks of attention shift and attentional bias before and after electroacupuncture. All parts of the left and right brain areas mentioned above were studied.

The software of AFNI (Analysis of Function NeuroImage, Robert W Cox, Medical College of Wisconsin) was used to process the image data.

D. Statistical methods

The statistical software of SPSS 12.0 for windows was used to carry through non-parametric test (Kruskal-Wallis Test) for the activation range and intensity of brain functional areas of the two groups on three cues before and after electroacupuncture intervention. For multiple comparison for intergroup differences, bonferroni method after rank transformation was used to make paired comparison; for the activation areas of the two groups before and after electroacupuncture, paired non-parametric test (Wilcoxon Signed Ranks Test) was used. The test criterion $\alpha=0.05$, $P<0.05$ showed difference and indicated statistical significance.

III. RESULTS

A. Behaviour Results

1. Block task

Before the electroacupuncture therapy, the response accuracy of the control group was $95.1\pm 1.9\%$, while that of the heroin abstiners group was $94.4\pm 3.0\%$. Group t test showed that $P>0.05$ and there's no significant difference in the response accuracy between the subjects of two groups. After the electroacupuncture therapy, the response accuracy of the control group was $95.6\pm 2.3\%$, while that of the heroin abstiners group was $93.6\pm 2.3\%$. Group t test of the two groups before and after the electroacupuncture showed that $P>0.05$, and there's no significant difference in the response accuracy between the subjects of the two groups before and after the electroacupuncture therapy.

2. Dot-probe task

Before the electroacupuncture therapy, the response accuracy of the control group was $96.1\pm 3.0\%$, while that of the heroin abstiners group was $94.8\pm 3.0\%$. Group t test showed that $P>0.05$ and there's no significant difference in the response accuracy between the subjects of two groups. After the electroacupuncture therapy, the response accuracy of the control group was $97.2\pm 2.1\%$, while that of the heroin abstiners group was $95.2\pm 2.7\%$. Group t test of the two groups before and after the electroacupuncture showed that $P>0.05$, and there's no significant difference in the response accuracy between the subjects of the two groups before and after the electroacupuncture therapy.

B. Comparison of brains areas on attention to different cues in different tasks

1. Task results of "attention shift" based on block design

1) Comparison of the brain areas activated by the attention shift to drug-related cue before electroacupuncture

The following brain areas were activated in both the experimental group and control group: ventromedial area of the left frontal lobe, dorsolateral areas of the frontal lobes, superior/inferior parietal lobule, fusiform gyri, anterior cingulate cortexes and temporal lobes; there's no significant difference in the activation volume and intensity of the brain areas between the two groups ($P>0.05$).

2) Comparison of the brain areas activated by the attention shift to positive cue before electroacupuncture

The following brain areas were activated in both the experimental group and control group: dorsolateral area of the left frontal lobe, left superior parietal lobule and anterior cingulate cortexes; there's no significant difference in the activation volume and intensity of the brain areas between the two groups ($P>0.05$).

3) Comparison of the brain areas activated by the attention shift to negative cue before electroacupuncture

The following brain areas were activated in both the experimental group and control group: dorsolateral areas of the frontal lobes, superior/inferior parietal lobule, fusiform gyri and temporal lobes; there's no significant difference in the activation volume and intensity of the brain areas between the two groups ($P>0.05$).

4) Comparison of the brain areas activated by the attention shift to positive, negative and drug-related cues before and after electroacupuncture

In the experimental group, there's no significant difference in the brain functional response to negative cue before and after electroacupuncture ($P>0.05$), and no significant difference in the brain functional response to drug-related cue before and after electroacupuncture ($P>0.05$); in the control group, there's no significant difference in the brain functional response to drug-related cue before and after electroacupuncture ($P>0.05$), no significant difference in the brain functional response to positive cue before and after electroacupuncture ($P>0.05$), and also no significant difference in the brain functional response to negative cue before and after electroacupuncture ($P>0.05$). Changes were only seen in the experiment group to the positive cue before and after electroacupuncture. In the experimental group before electroacupuncture, basically the following brain areas were activated by positive cue: dorsolateral areas of the frontal lobes, inferior frontal gyri, left superior parietal lobule, anterior cingulate cortexes and left corpus striatum; after the electroacupuncture intervention, all brain areas mentioned above showed enlarged activation volume and increased

activation intensity except the dorsolateral area of the right frontal lobe, right inferior frontal gyrus and anterior cingulate cortexes. In addition, the activation intensity of the dorsolateral area of the frontal lobes, inferior frontal gyri, anterior cingulate cortexes and left corpus striatum was obviously increased than that before electroacupuncture, and the difference was statistically significant ($P < 0.05$), which indicated that electroacupuncture improved the susceptibility of heroin abstiners to positive emotion.

2. Task results of "attentional bias" based on dot-probe design

1) Comparison of the brain areas activated by drug-related cue before and after electroacupuncture in the experimental group

In the experimental group, basically the dorsolateral areas of the frontal lobes, anterior cingulate cortexes, superior/inferior parietal lobule, fusiform gyri and right temporal lobe were activated by the drug-related cue; after the electroacupuncture intervention, the main manifestations of the areas mentioned above were decreased activation volume and intensity. Among which, the activation volumes of the dorsolateral area of the left frontal lobe and left superior parietal lobule decreased obviously, and the activation intensity of the right temporal lobe decreased, both differences were statistically significant ($P < 0.05$).

2) Comparison of the brain areas activated by positive cue before and after electroacupuncture in the experimental group

In the experimental group, basically the dorsolateral areas of the frontal lobes, inferior frontal gyri, superior/inferior parietal lobule, temporal lobes, fusiform gyri and dorsal thalamus were activated by the positive cue; after the electroacupuncture intervention, the main manifestations of the areas mentioned above were decreased activation volume and intensity. Among which, the activation volumes of the dorsal thalamus, left temporal lobe and inferior frontal gyri decreased obviously, and the difference was statistically significant ($P < 0.05$).

3) Comparison of the brain areas activated by negative cue before and after electroacupuncture in the experimental group

In the experimental group, basically the dorsolateral areas of the frontal lobes, anterior cingulate cortexes, superior/inferior parietal lobule and fusiform gyri were activated by the negative cue; after the electroacupuncture intervention, the main manifestations of the areas mentioned above were decreased activation volume and intensity. Among which, the activation volumes of the dorsolateral area of the

left frontal lobe decreased obviously, and the activation intensity of the right inferior parietal lobule increased, and the differences were statistically significant ($P < 0.05$).

4) Comparison of the brain areas activated by drug-related cue before and after electroacupuncture in the control group

In the control group, basically the dorsolateral areas of the frontal lobes, ventromedial area of the left frontal lobe, anterior cingulate cortexes, superior/inferior parietal lobule, fusiform gyri, right corpus striatum, left dorsal thalamus and temporal lobes were activated by the drug-related cue; after the electroacupuncture intervention, the main manifestations of the areas mentioned above were decreased activation volume and intensity. Among which, the decrease of the activation intensity in the dorsolateral areas of the frontal lobes was statistically significant ($P < 0.05$).

5) Comparison of the brain areas activated by positive cue before and after electroacupuncture in the control group

In the control group, basically the dorsolateral areas of the frontal lobes, ventromedial area of the left frontal lobe, anterior cingulate cortexes, superior/inferior parietal lobule, fusiform gyri, left dorsal thalamus and temporal lobes were activated by the positive cue; after the electroacupuncture intervention, the main manifestations of the areas mentioned above were decreased activation volume and intensity. Among which, the activation intensity of the left dorsal thalamus and dorsolateral area of the right frontal lobe decreased obviously, and the difference was statistically significant ($P < 0.05$).

6) Comparison of the brain areas activated by negative cue before and after electroacupuncture in the control group

In the control group, basically the dorsolateral areas of the frontal lobes, ventromedial area of the left frontal lobe, inferior frontal gyri, anterior cingulate cortexes, superior/inferior parietal lobule, fusiform gyri, dorsal thalamus and temporal lobes were activated by the negative cue; after the electroacupuncture intervention, the main manifestations of the areas mentioned above were decreased activation volume and intensity. Among which, the activation volumes of the right inferior frontal gyrus and right inferior parietal lobule decreased, the activation intensity of the dorsolateral areas of the right frontal lobes and inferior frontal gyri decreased obviously, and the differences were statistically significant ($P < 0.05$).

3. Images of brain area activation to different cues in different tasks

See Fig. 3, 4, 5 and 6.

1. Activated functional areas of brain of the two groups before electroacupuncture by drug-related cue in block task (The red color indicates the activated areas)

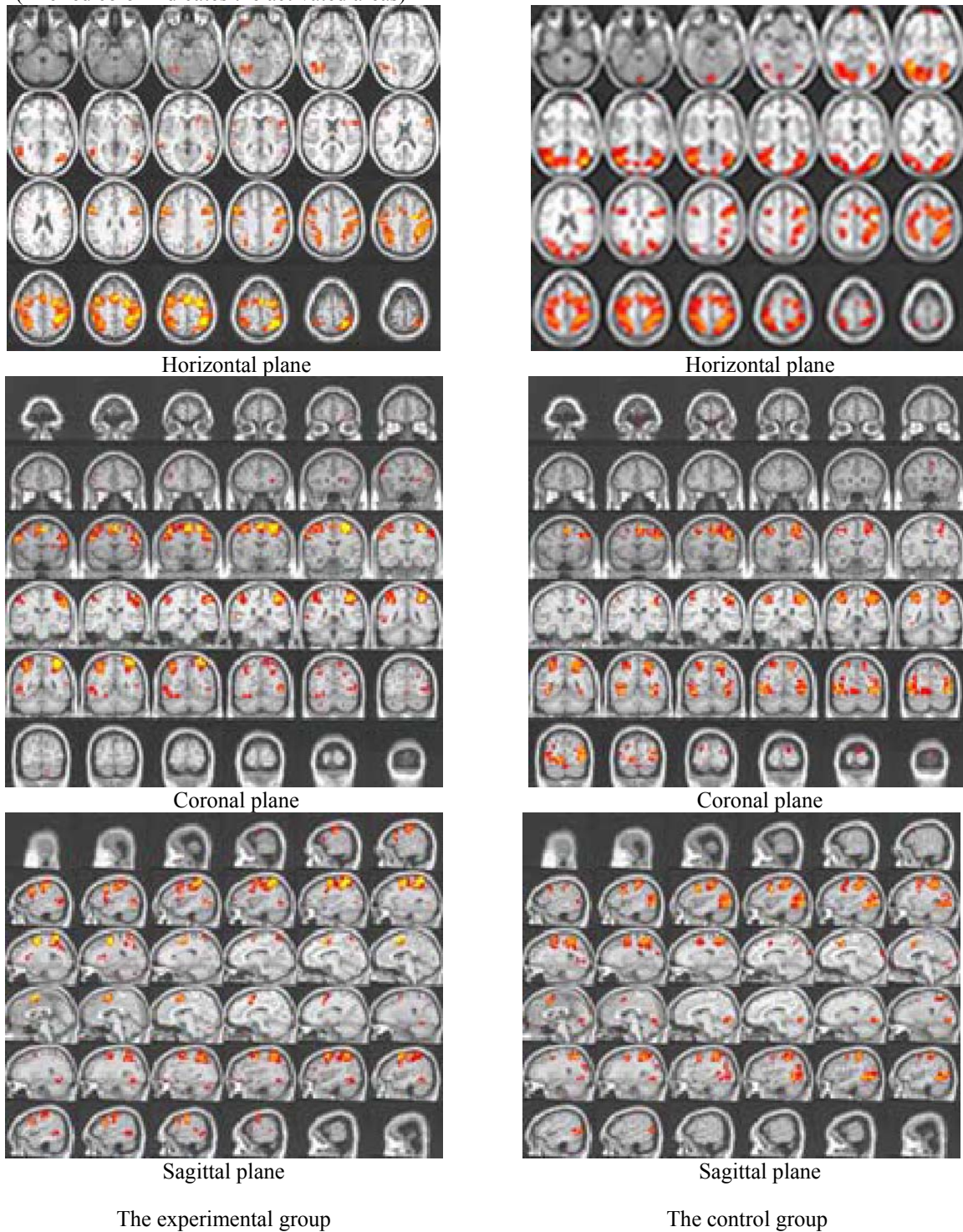


Fig. 3 Images of brain area activation 1

2. Activated functional areas of brain of the experimental group before and after electroacupuncture by positive cue in block task (The red color indicates the activated areas)

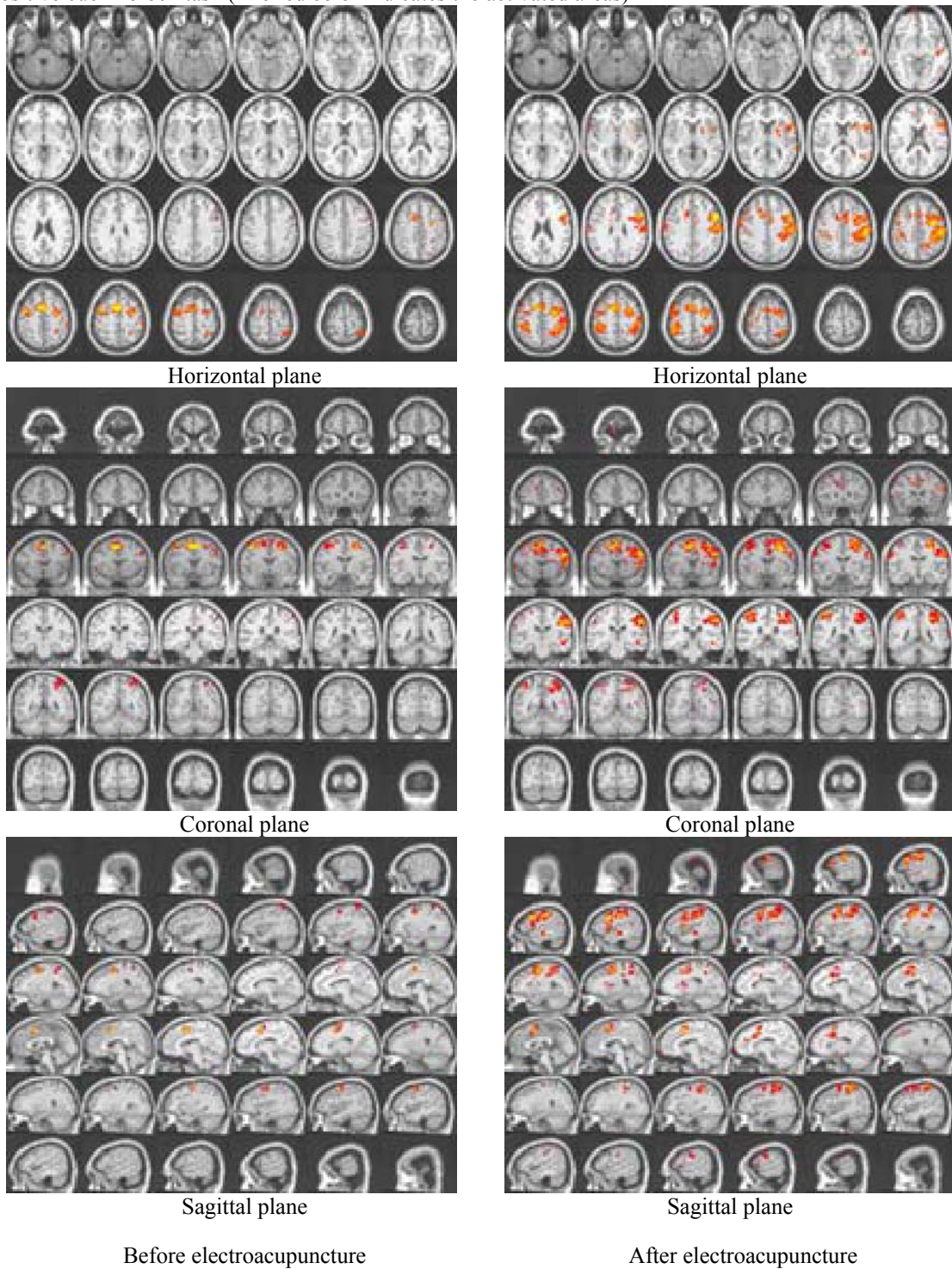


Fig. 4 Images of brain area activation 2

3. Activated functional areas of brain of the experimental group before and after electroacupuncture by drug-related cue in dot-probe task (The red color indicates the activated areas)

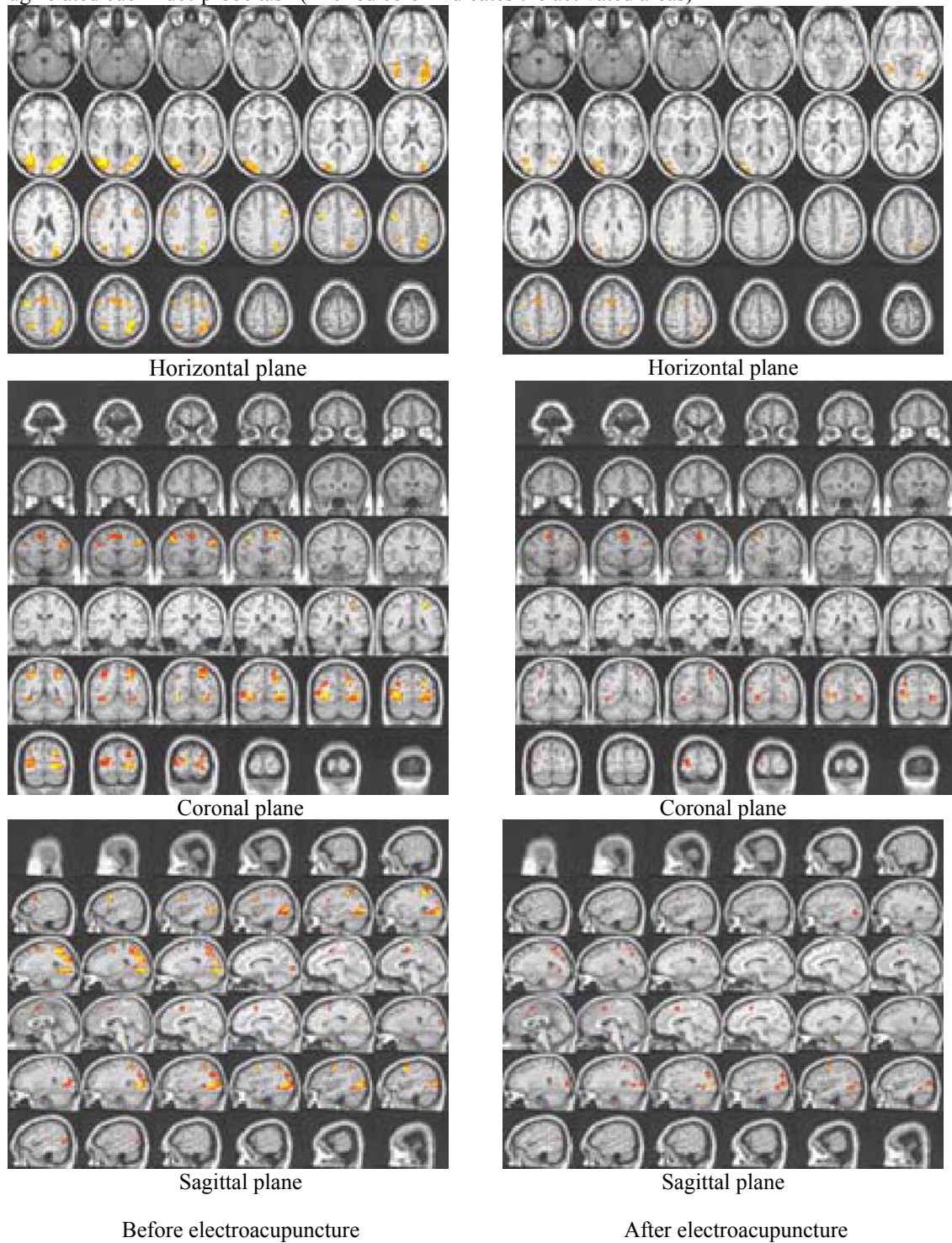


Fig. 5 Images of brain area activation 3

4. Activated functional areas of brain of the control group before and after electroacupuncture by drug-related cue in dot-probe task (The red color indicates the activated areas)

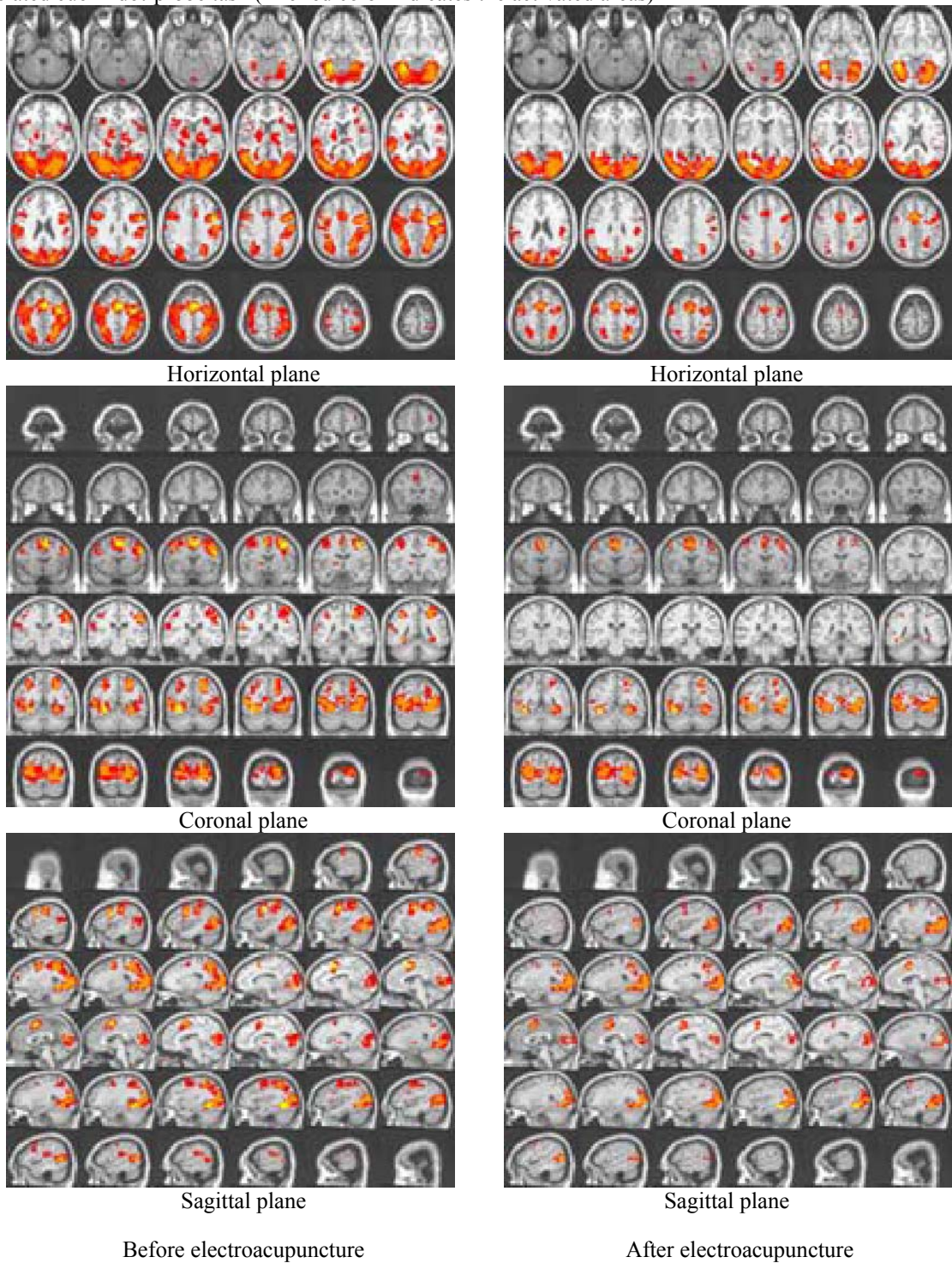


Fig. 6 Images of brain area activation 4

IV. CONCLUSIONS

1. Heroin abstainers showed significantly higher attentional bias to visual drug-related cue than to positive and negative emotional cues, and had more emotion processing on the drug-related cue, which indicated that the drug-related environment had close relation with the relapse resulted from elicited urges.

2. Heroin abstainers showed obviously higher attentional bias to the processing of negative emotion than to the positive emotional cue and had higher emotion evaluation on negative emotional cue, which may possibly be the intrinsic mechanism of relapse after drug withdrawal.

3. Results of the study supported the attentional bias and emotion processing model for relapse.

4. Electroacupuncture intervention could obviously lower the attention level of heroin abstainers to the drug-related cue, which indicated that electroacupuncture could effec-

tively inhibit the attentional bias of abstainers to the drug-related cue and had the potentiality of lowering relapse rate.

5. Electroacupuncture intervention could significantly inhibit the susceptibility of heroin abstainers to negative emotion while increasing the susceptibility to positive emotion, which indicated that electroacupuncture could improve persistent depressed emotion after heroin withdrawal, and promote the rehabilitation of cognitive function of emotion of the brain.

REFERENCES

1. DeRubeis, R.J., Crits-Christoph. Empirically supported individual and group psychological treatments for adult mental disorders. *Consult Clinical Psychology*, 1998, 66: 37-52
2. Xu Ping, Jiang Yingping, Wang Yan, et al.. Influence of acupuncture on heroin addicts' attentional bias. *Shanghai Journal of Traditional Chinese Medicine*, 2006, 40(3): 40-41
3. Bolla K, et al. Prefrontal cortical dysfunction in abstinent cocaine abusers. *Neuropsychiatry Clin Neurosis*. 2004, 16(4): 456

Effects of Acupuncture On Mitochondria of Muscle Cell In Rats of Acute Swimming Exercise

Ming Gao, Huayuan Yang, Tangyi Liu, Le Kuai

Shanghai University of Traditional Chinese Medicine, Shanghai 201203, China

Abstract— **Objective** To research on the effects of acupuncture and electroacupuncture on antioxidant enzymes activity, Ca^{2+} content and Ca^{2+} -ATPase regulation in rat muscle mitochondria after acute swimming exercise. **Method** Forty male SD rats were divided randomly to 4 groups. The rats in the acupuncture group and electroacupuncture group were respectively treated by the two different methods of acupuncture and electroacupuncture before acute swimming exercise. After the swimming exercise, the rats were executed and the needed materials were taken. Then the relational indexes were determined. **Result** After acute swimming exercise, the values of GSH-Px activity and Ca^{2+} -ATPase in rat muscle mitochondria in the swimming groups decreased obviously than those in the control group ($P < 0.05$), and the values of Ca^{2+} content increased obviously ($P < 0.01$). In acupuncture group, SOD activity increased obviously ($P < 0.05$). Compared with swimming team, GSH-Px activity and Ca^{2+} -ATPase in acupuncture group increased obviously ($P < 0.05$). Ca^{2+} content in swimming group and electroacupuncture group obviously increased than that in control group ($P < 0.01$). **Conclusions** Acupuncture can protect cells to avoid the acute sports injury, maintain the functions of mitochondria so as to postpone fatigue, extend muscle working time and prevent muscle injury.

Keywords — Acupuncture; Electroacupuncture; Acute swimming exercise; Mitochondria; Antioxidant enzymes; Ca^{2+} ; Ca^{2+} -ATPase;

I. INTRODUCTION

Mitochondrion is a main place in the process of biological oxidation, citric acid cycle and oxidative phosphorylation in cells. Activities of various enzymes in the mitochondrion immediately reflect the function of the mitochondrion. After acute or long exercise, great amount of free radicals, peroxides will be produced inside the mitochondrion. If the accumulation of Ca^{2+} in the mitochondrion after the exercise exceeds its buffer capacity, it will result in the injury of the mitochondrion, decrease in its function, inhibition of oxidative phosphorylation, disorder of the ATP supply, etc. As a method to improve the exercise capacity, acupuncture has been gradually valued in recent years. Our experiment indicates^[1-3] that acupuncture can not only prolong the swimming time of the mouse and enhance endurance, but also increase the activities of several enzymes concerning energy metabolism and has some effects on the improve-

ment of the athletics. The experiment aims at studying the therapeutic mechanism of acupuncture to provide evidence for extensive use of acupuncture in athletic sports.

II. MATERIALS AND METHODS

2.1 experimental animals and grouping:

40 healthy SD male rats are provided by experimental animal center in Shanghai University of TCM, weighting from 170-190g. The animals are grouped into 4 in random: 10 in controlled group, 10 in swimming group, 10 in acupuncture group and 10 in electropuncture group.

2.2 Methods:

(1) Acupoints:

“Dazhui”, “Mingmen”, “Huangtiao” and “Zusanli”

(2) Stimulation parameter:

Acupuncture group: used 0.30×25mm needles, directly insert into 2-6mm with twist manipulation. The needles are manipulated once per 3min with a lasting time of 30-60s. retain the needles for 20min.

Electropuncture group: 30×25mm needles, directly insert into 2-6mm, connect with BX electronic acupunctoscope. Parameter is the acoustic-pulse modulating wave with a frequency of 500-800Hz. The current is 0.20-0.25mA. The stimulation time is 20min.

(3) Experimental procedure:

The controlled group is fed as usual. The swimming group, acupuncture group and electropuncture group are all trained for the adaptation to swim^[4-5]. After the exercise, the rats are executed and skeletal muscles are taken off from the hind leg.

Needle the acupoint of “Dazhui”, “Mingmen”, “Huantiao”(both sides), “Zhusanli”(both sides) of the acupuncture group and electropuncture group respectively for 20min before the train. Use BX electronic acupunctoscope for the electropuncture group, “Zhusanli” and “Huantiao” are connected with positive pole and negative pole respectively on the same side, Acupoints on both sides are connected. Then acute swimming exercise is conducted after a 15-minute rest when stimulation is completed.

(4) Method of extracting tissue from the experimental animals and preparation of skeletal muscle mitochondrion

Rats are executed right after the swimming.4g skeletal muscle is taken off from the hind legs.

The skeletal muscles are rapidly put into the icy homogenate medium to wash out the blood and cut into pieces in the beaker among icebath. 20mL extraction homogenate medium (0.25mol/L accharose, 10mmol/LTris, pH=7.4) is added for 30-second homogenate under 4°C, in which the homogenate liquid is used for 10-minute centrifugation of 2000r/min. Then the supernatant is used for 15-minute centrifugation of 10000r/min.Sediment acquired after pouring away the supernatant is the mitochondrion. Put the mitochondrion into the preservation medium (0.25mol/L accharose, 10mmol/LTris-HCL, pH=7.4) for use under minus 20°C

(5)Measurement of indicators:

1) Measurement of protein content.

Measured by Bradford method

2) Measurement of SOD activity.

Measured by xanthine oxidase methods

3) Measurement of GSH-Px activity. Use GSH-Px activity testing box.

4) Measurement of mitochondrion calcium content.

Measured by MTB method.

5) Measurement of Ca²⁺-ATP activity.

Use reagent box for ATPase measurement.

2.3 Statistical methods.

Database is processed with SPSS11.0 software and analysis of variance is conducted.

III. RESULTS

3.1 SOD activity and GSH-Px activity (referring to Table 1)

Compare with the controlled group ** P<0.01 □

From Table 1 we see that SOD activity value of the acupuncture group is greatly higher than those of other three groups. The statistic differences are obvious or very obvious (P<0.05, P<0.01). Differences between the swimming group and the controlled group have no statistic meanings, and so is the difference between the electropuncture group and the controlled group. SOD activity value of the swimming group is lower than those of the acupuncture group and controlled group, and the differences are obvious or very obvious (P<0.05) .During the training,2 rats in the swimming group and 1 in the electropuncture group are accidentally dead.

3.2 Mitochondrion calcium content and Ca²⁺-ATPase activity (referring to Table 2)

From Table 1 we learn that mitochondrion calcium contents of swimming group and electropuncture group are obviously higher than those of the controlled group and acu-

Table 1 Effects of Acupuncture on SOD activity and GSH-Px activity ($\bar{X} \pm S$)

Group	n	SOD activity (U/mgprot)	GSH-Px activity (U/mgprot)
Controlled Group	10	30.667±4.630 ▲	13.923±1.664 ●
Swimming Group	8	28.883±6.022 ▲▲	11.924±1.937
Acupuncture Group	10	40.696±7.982	14.001±2.469 ●
Electropuncture Group	9	31.780±4.631 ▲	12.722±1.936

Compare with the acupuncture group ▲ P<0.05; ▲▲ P<0.01 ; Compare with the swimming group *P<0.05; ** P<0.01

Table 2 Effects of Acupuncture on calcium content and Ca²⁺-ATPase activity ($\bar{X} \pm S$)

Group	n	Ca ²⁺ content (mmol/gprot)	Ca ²⁺ -ATPase activity (U/mgprot)
Controlled Group	10	0.0696±0.0140	9.989±1.459*
Swimming Group	8	0.0911±0.0168***▲▲	7.578±2.051
Acupuncture Group	10	0.0679±0.0149	10.950±1.789**
Electropuncture Group	9	0.0897±0.0116***▲▲	9.685±2.350*

puncture group. Ca^{2+} -ATPase activity value is considerably lower than those of other three groups, and the differences are obvious or very obvious.

IV. DISCUSSION

4.1 Effects of acupuncture and electroacupuncture on SOD activity and GSH-Px activity.

In normal condition, production and removal of free radical keep the balance. There will be an obvious increase in free radical content and decrease in antioxidant enzymes activity of the body during the process of acute or active sports^[6].

The experiment indicates that SOD activity of mitochondrion in skeletal muscle has been evidently raised in the acupuncture group. Compared with the controlled group, electropuncture group and swimming group, the differences are obvious. GSH-Px activity of the acupuncture group is higher than the swimming group, and the differences are obvious. There is no difference between the electropuncture group, swimming group and controlled group. It can be induced from the experiment that acupuncture can raise the antioxidant enzymes activity in skeletal muscle mitochondrion of rats after exercise. Zhangjun^[7] and other researchers used the rats after exhaustive exercise as models to study changes of SOD activity in cardiac muscle. They found that SOD activity value immediately decreases right after exhaustive exercise. Needling points can create favorable condition for local metabolism by exciting nerve and muscle, increasing angiogenesis. This is one of the mechanisms through which acupuncture ease fatigue, prolong working time of skeletal muscle and increase exercise capacity.

4.2 Effects of acupuncture and electropuncture on Ca^{2+} and Ca^{2+} -ATPase

After long-term exhaustive or acute exercise, there will be a considerable increase in calcium content of mitochondrion which can inhibit the process of oxidative phosphorylation, hamper energetic metabolism inside mitochondrion. The change is an important reason resulting in decrease in body's movement ability. Calcium concentration of cell and mitochondrion is closely related to cell injury. Our research found that calcium content of mitochondrion evidently increases and Ca^{2+} -ATPase activity value considerably

decreases right after acute exercise. But compared with the controlled group, the calcium content of mitochondrion of the electropuncture group is higher; differences of the Ca^{2+} -ATPase activity between the electropuncture group and the swimming group are not obvious; differences of the calcium content of mitochondrion and Ca^{2+} -ATPase activity between the acupuncture group and the controlled group are not obvious, however differences between the acupuncture group and the swimming group are obvious. This shows that although both acupuncture and electropuncture can improve Ca^{2+} -ATPase activity, acupuncture is better than electropuncture as to regulating calcium content of mitochondrion, thus helping maintain steady state of calcium circulation to prevent its massive concentration.

Acupuncture methods provide a new way to study the mechanism of enhancing athletic capacity and easing fatigue in TCM sector. Acupuncture methods should be appropriately adopted according to different athletics (such as variance of genre and age), different sports (such as speed, strength and endurance). In addition, training methods, different phrase of match and after-match recovery should also be considered. We should also pay attention to the adoption of points, manipulation method and stimulation parameter.

REFERENCES

1. Gu Xunjie, Observation On Enhancing Strength Of Mouse Through Electropuncture. *Clinical Journal Of Acupuncture*, 1998, 14 (12):9-10
2. Yang Huayuan, Xie Jiaying, Gu Xunjie etc. Effect of Electric Stimulation Of Acupoint On Energy Metabolism of Skeletal Muscles in Rats. *Chinese Acupuncture And Moxibustion*, 2001, 21(4):239
3. Wuying, Zhen Yuchun, Yang Huayuan etc. Effective Research On The Improvement Of Rapid Strength Of Track-And-Field Athletics Through Acupoint Stimulation. *Journal of Shanghai Institute of Physical Education*, 2000, 24(4):55
4. Zhuquan, Pu Junzong. Application Method On Swimming Train Of Rats In Movement Experiment. *Journal Of Chinese Medical Sports*, 1996, 15 (2):125
5. Han Chunhua, Wang Qi'en, Wangsheng, etc. Functional Changes In Mitochondrion After Acute Exercise And Protective Effect Of Bilirubin. *China J Appl Physiol*, 2001, 17(1): 72
6. Han Chunhua, Wangsheng, Wang Yunxun. The Protective Effect Of Bilirubin On The Oxidative Stress In Mitochondria Of Skeletal Muscle Induced By Acute Exercise, *Journal Of Chinese Medical Sports*, 2001, 20 (1):27
7. Zhangjun, Guo Yongli. Effects Of Taurine On Myocardial Mitochondrion In Rats After Exhaustive Exercise. *Journal Of Chinese Medical Sports*, 1998 ; 17(3) : 206

Determination of Indirect Moxibustion's Temperature and Research on Thermal Conduction Model

Huayuan Yang¹, Hu Yine, Zhuicheng Hu¹

Shanghai University of Traditional Chinese Medicine, Shanghai, China

Abstract — Apply Ti30 High Performance Thermograph with to determine the temperature variation of ginger moxibustion, garlic moxibustion, aconite root moxibustion and salt moxibustion. In this experiment, the temperature of aconite root moxibustion is relatively stable with a longer lasting time, while those of ginger moxibustion, garlic moxibustion and salt moxibustion are unstable. The result indicates that temperature conduction of indirect moxibustion is a kind of energy transmission generated by body temperature difference. Such kind of temperature conduction can relatively produce physical and biochemical effects on human body. By studying the essential characteristics of indirect moxibustion, we try to establish a temperature model for research of this kind.

Keywords — Indirect moxibustion; Temperature determination; Temperature conduction model.

As an important component of Acupuncture and Moxibustion Science, moxibustion therapy is very popular in ancient China. Moxibustion possesses a special therapeutic effect and its origin may be earlier than acupuncture and herbs. There is a record in «Ling Shu Guan Neng» saying: “When the disease can't be cured by acupuncture, referring it to moxibustion”. «Elementary Medicine» also indicates “If the disease can be cured by acupuncture and medicine, moxibustion is a must”. The conception of acupuncture more important than moxibustion has somewhat been changed. Researchers both at home and abroad have done many explorations of its therapeutic mechanism. The effect of moxibustion includes the medical action and non-medical action. The non-medical action includes warming effect, spectrum effect, columns and time. Understanding the physical properties of moxibustion is helpful for studying the therapeutic mechanism of moxibustion in order to improve its clinical effects.

I. MATERIAL AND METHOD

1.1 Material

1.1.1 Instrument Ti30 High Performance Thermograph

1.1.2 Instrument performance

Temperature measuring range: 0° to 250°C(32°to 482°F)

Temperature indicating resolution: 0.1 (°F or °C)

Spectrum range: 7-14μm

Object aiming: single wavelength laser point (meeting the standards of IEC 2 and FDA II)

1.1.3 Material for moxibustion: fresh ginger slice, fresh garlic slice, salt, wet aconite root slice (self-made, thick : 1 mm, diameter: 1.5cm)

1.1.4 Moxa stick (Made by Suzhou Medical Instrument Factory, diameter: 8mm, length: 3cm)

1.2 Method

1.2.1 Measuring the temperature of fresh ginger slice, fresh garlic slice, salt and wet aconite root slice when they are heated by moxa. The Ti 30 High Performance Thermograph is fixed on support. There is a support for the placement of moxa material above the sensor. In the process of measuring the temperature, fresh ginger slice, fresh garlic slice, salt and wet aconite root slice are placed on the support. Temperature and thermal image are determined by Ti 30 High Performance Thermograph and then printed after data processing and analysis through software. Figure 1 is the experimental apparatus for the determination of indirect moxibustion temperature.

1.2.2 In the process of determining the indirect moxibustion temperature, the burning time of moxa is 2min, i.e. the average scan time(AUR) is 2min.

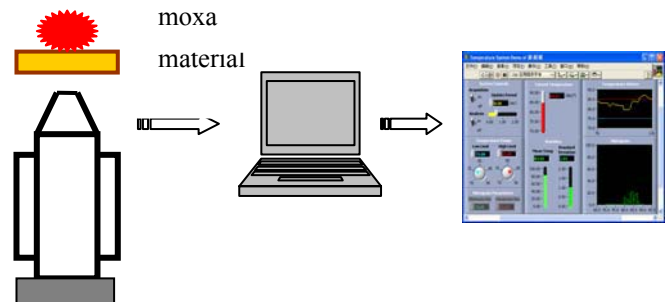


Figure 1 experimental apparatus for the determination of indirect moxibustion temperature.

II. ESTABLISHMENT OF THERMAL CONDUCTION MODEL FOR INDIRECT MOXIBUSTION

Thermal conduction is a energy conduction due to temperature difference between environment and system. The direction is always from the higher place to the lower one. Energetic conduction of indirect moxibustion has the basic characteristic of Thermal conduction. Data obtained from our experimental instrument is processed and analyzed by software to established the thermal conduction model of indirection moxibustion.

In the biological system, conducting speed of inner energy is fairly higher than that of any other thermal phenomenon. So according to fourier law, the temperature of X direction in rectangular coordinate system can be calculated through the following formation.

$$q_x = -A_x (k_{xx} \frac{\partial T}{\partial x} + k_{xy} \frac{\partial T}{\partial y} + k_{xz} \frac{\partial T}{\partial z}) \quad (1)$$

The minus sign represents that thermal conduction is opposite to temperature gradient. Proportionality constant “k” represents thermal conduction coefficient component. There are three components in each direction and components k^{xx} , k^{xy} and k^{xz} only exist in three major directions. Thermal conduction is only determined by temperature gradients but not interactive in major directions.

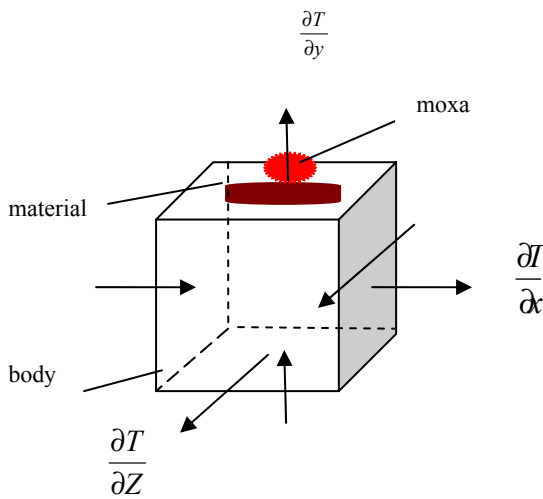


Figure 2 Sketch map of energetic conduction in rectangular coordinate system.

2.1 Thermal conduction of indirect moxibustion

Comprehensive biothermal conduction equation is used to analyze thermal conduction in thermal conduction model of indirect moxibustion[1]. Heat is conducted to skin through moxibustion material in the process of indirect moxibustion. It can be calculated by equation (2). Equation (3) can be used to calculated the heat conducted from skin to surrounding tissues and vessels[2].

$$\rho_b C_b \frac{\partial T}{\partial t} = k_b \cdot \nabla^2 T - \rho_b C_b u \nabla T + Q_b \quad (2)$$

$$\rho_t C_t \frac{\partial T}{\partial t} = k_t \cdot \nabla^2 T - \omega_t C_b (T - T_\omega) + Q_t \quad (3)$$

In the equations, ρ , C , k respectively represent density, specific heat and conduction coefficient. The subscript b , t respectively represents skin and blood. Others like ω is the symbol of blood perfusion ratio, U blood flow speed and Q unit volume heat-generating ratio of indirect moxibustion. Reference conduction coefficient is indicated in the following table[3][4].

Table 1 Material conduction coefficient

Tissues	Heat conduction coefficient k[w/(m·°C)]	Diffusivity $a \cdot 10^7$ [m ² /s]	Thermal lag $k_p \cdot 10^{-6}$ [w ² s/(m ⁴ °C)]
skin	0,21-0,41	0,82-1,2	1,2-2,2
muscle	0,34-0,68	1,2-2,3	0,94-2,0
fat	0,094-0,37	0,32-2,7	0,28-0,51
blood	0,48-0,60		

2.2 Heat of indirect moxibstion and temperature variation of tissues

When the body is receiving indirect moxibustion, heat quantity can be evaluated through quantitative relation between tissue heating time and temperature. The temperature is often 40 Celsius in indirect moxibustion. So heat quantity T can be calculated by the following equation[5]:

$$T_{FU} = \sum_{t=0}^{end} 2^{(T(t)-30)} \Delta_t \quad (4)$$

$T(t)$ is the tissue temperature related to time changes.

2.3 Thermal conduction between tissues

Thermal conduction model between tissues is composed of the following three equations[6]:

Artery

$$\rho_b C_b \frac{\partial \theta_a}{\partial t} = \rho_b C_b u_a \left(\frac{\partial \theta_a}{\partial x} + \frac{\partial \theta_a}{\partial y} + \frac{\partial \theta_a}{\partial z} \right) - q_{av} + q_{ta} + Q_{hlf.a} \quad (5)$$

Vein

$$\rho_b C_b \frac{\partial \theta_v}{\partial t} = \rho_b C_b u_v \left(\frac{\partial \theta_v}{\partial x} + \frac{\partial \theta_v}{\partial y} + \frac{\partial \theta_v}{\partial z} \right) + q_{av} + q_{tv} + \rho_b W_b C_b (\theta_t - \theta_v) + Q_{hlf.v} \quad (6)$$

Tissue

$$\rho_t C_t \frac{\partial \theta_t}{\partial t} = k_t \left(\frac{\partial^2 \theta_t}{\partial x^2} + \frac{\partial^2 \theta_t}{\partial y^2} + \frac{\partial^2 \theta_t}{\partial z^2} \right) - q_{ta} - q_{tv} + \rho_b W_b C_b (\theta_a - \theta_t) + Q_{met} + Q_{hlf.t} \quad (7)$$

In the equations above, ρ , C, k respectively represent density, specific heat and thermal conduction coefficient. The subscript b and t respectively represents skin and blood. Others like W^b is the symbol of blood perfusion ratio and u blood flow speed. The subscript a and v respectively represent artery and vein. q^{av} represents heat quantity between artery and tissue q^{tv} represents heat quantity between vein and tissue. Q^{hlf} represents extra volume heat resource of indirect moxibustion and Q^{met} represents biometabolic heat-generating ratio.

Extra volume heat resource Q^{hlf} is tens of times of biometabolic heat-generating ratio Q^{met} . So Q^{met} can be neglected in calculation. The fourth item in equation (6) represents the heat when heat balance between tissue and capillary transferred to vein. The fourth item in equation (7) represents heat loss from tissue to artery caused by capillary perfusion.

Heat flow rate between tissue and its surrounding vessels is[6]:

$$q_{av} = k_b \sigma_b (\theta_b - \theta_v) \quad (8)$$

$$q_{ta} = k_t \sigma_a (\theta_t - \theta_a) \quad (9)$$

$$q_{tv} = k_t \sigma_v (\theta_t - \theta_v) \quad (10)$$

σ_b , σ_a and σ_v are form factor, respectively represents vessel distance and semidiameter as well as function of thermal conduction between blood and surrounding tissues.

III. RESULT AND DISCUSSION

Temperature and warming stimulation, parameters mainly affected by different moxibustion material, moxibustion volumes and moxibustion methods, are the major physical property of moxibustion. We apply Ti30 High Performance Thermograph to measure the temperature on skin surface to study the characteristics of skin and tissue temperature variation after indirect moxibustion. We find that in indirect moxibustion, skin injury is smaller and recovery is faster than direct moxibustion. This kind of therapy can make appropriate heat stimulation permeate into tissue to generate some therapeutic effects. The experiment indicate that heat peak is different in each moxibustion and temperature variation has its own property according to specific locations. Constant moxibustion can increase the temperature beneath skin and muscles, indicating that moxibustion stimulation not only affects superficial area, but also the deeper one. Moxibustion stimulation may be cumulative and has a limited thermal conduction deep. Comparing to direct moxibus-

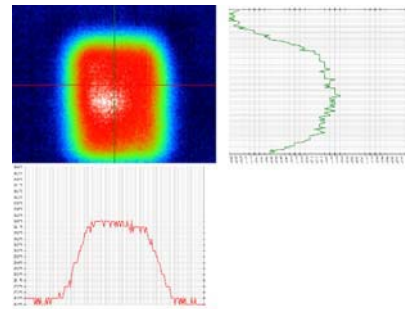


Figure (3) thermograph of aconite root moxibustion

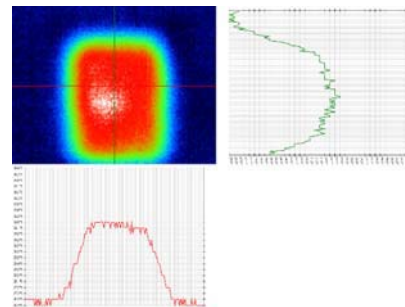


Figure (4)

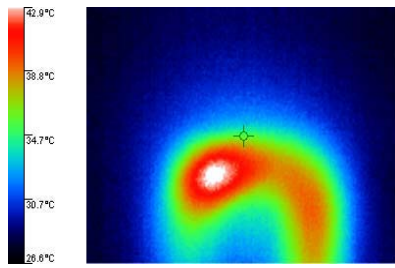


Figure (5) thermograph of garlic moxibustion

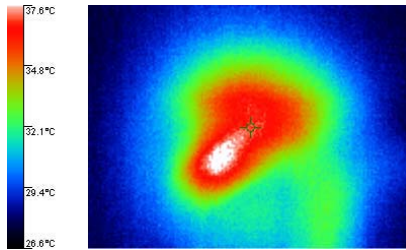


Figure (6) thermograph of salt moxibustion

tion, indirect moxibustion's thermal curve rises and descends slower. Ginger, garlic and salt moxibustion have their own specific properties, just as figures 3,4,5,6 indicated. Among the moxibustion material, salt has the fastest heat permeation with the highest heat peak, next is aconite root, ginger has the slowest heat permeation with the lowest heat peak. Generally speaking, faster heat permeation, easier recovery.

Thermal transmission in biological tissue includes conduction according to thermal conductivity and convection

caused by body fluid flow. Thermal effect in liquid tissue is due to the temperature oscillation generated by convective whirl of body fluid. If the radiation continues, there will be a so-called "non-thermal effect" to keep the tissue temperature stable. From the tables, we can see that the temperature is gradually rose and fairly unilateral which is different from neovascular reaction. This is quite coincident with the assumption introduced by a Japanese researcher who holds the idea that body fluid flow outside vessels is related to meridians. In the experiment, we try to establish a preliminarily thermal conduction model between

artery, vein and tissue by measuring the temperature variation of ginger moxibustion, garlic moxibustion and salt moxibustion. This will help us to understand the basic characteristic of thermal conduction in indirect moxibustion and provide a experimental method for such kind of research. Also it will represent us with a new way to study the therapeutic effect of moxibustion.

REFERENCES

1. Penns H H. Analysis of tissue and arterial blood temperatures in the resting human forearm .J Applied Physiology, 1948, 1(1) :93-122 .
2. Kolios MC, Sherar MD, Hunt JW. Blood flow cooling and ultrasonic lesion formation. Med Phys, 1996, 23: 1287-1298
3. Duck FA. Physical properties of tissue. A Comprehensive Reference Book, London: Academic Press, 1990, 13-37
4. Weinbaum S, Jiji L M. A new simplified bioheat equation for the effect of blood flow on local average tissue temperature .ASME J Biomech Eng, 1985, 107(2) :131-139. [5] Chato J C. Heat transfer to blood vessels .ASME J Biomech Eng, 1980, 102(1) :110-118 .
5. CH EN Qi, BAI Jing—ng, CH EN Ya—zhu. Effect of Unequal COuntercurrent Blood Vessel on the Temperature Distribution Due to HIFU 2004, 38 (1): 130-134

Quantitative Analysis of Different Consciousness Process Based on Multi-index Dynamic BEAM Technology

Yihe Zhang¹, Chi Chen¹, Yafei Liu² and Jianfen Xu¹

¹Qigong Institute Shanghai University of TCM, Shanghai, China

²Hebei Medical Qigong Hospital, Beidaihe, China

Abstract — EEG is produced by the non-linear regularity system made up of many cerebral nerve cells. It is the only source from which we can know the electric activities of the brain based on non-invasion condition. BEAM is an imaging technology about brain function. It can be formed via interpolation calculation after converting EEG into an eigenvalue (index). This transformation is the core of BEAM, reflecting the reading ability on the EEG information. The majority of the existing BEAM adopts the analysis of power spectrum - a linear analysis technology which can only read the linear characteristics incompletely. Moreover, the method which only captures any part of EEG can not reflect the unstable dynamic characteristics of EEG. In considering of that, we have developed a new BEAM system for EEG detecting with wireless communication and EEG analysis based on multi-index. Have used this system, we studied 50 cases for different brain conscious activities, such as practicing Qigong and mental arithmetic. It had been said that this new BEAM technology was appropriate to the research of brain conscious activities. At one time we had got several experimental conclusions about practicing Qigong and mental arithmetic by quantitative analysis of experiment result.

Keywords — EEG, BEAM, Nonlinear, Consciousness, Qigong

I. INTRODUCTION

People's conscious actions come from the electric-physical actions of many brain nerve cells. In the today's technology, EEG is the only one source for directly obtaining this sort of electric activities under the non-invasive condition. Since in EEG, the information observed by naked eyes is greatly limited, people transfer the EEG wave to the digital signals via A/D transform, and then deal with the digital signals in a bit time, in order to create some kinds of EEG index that have the definite sense in physics. In a bit time period, after synchronous inspections on EEG of multi-channels, EEG index distributed over the whole brain could be obtained by data processing. And also, BEAM in this time period could be created by interpolation calculating in the space. Therefore, BEAM is a kind of brain scalp imagery technology based on the EEG index. Actually, it shows intuitively the strength and distribution situation of

the nerve cell electrical activities, which were projected over the scalp in a form of both EEG index and limitless montage. Compared with the existing slice imaging of brain function like PET, FMRI and etc., BEAM directly makes image for characteristic of this kind of electrical activities, rather than make an indirect image of chemical changes with these electrical activities. So, direct source of information, higher time resolving power and lower inspection cost are the main advantages of BEAM.

The core technology of BEAM depends on the second-time treatment for EEG, that expressing the sort of EEG index. In the existing BEAM, generally, analysis of power spectrum was only adopted and four kinds of frequencies of EEG were selected as the EEG index. The provided analysis method is to let the end-users make a willful selection for seconds in the EEG backward played screen, so that creating the power spectrum of each montage or BEAM of one frequency [1]. Such BEAM technology used for studying the conscious process causes at least two big faults, reasons:

The recent years' research has proved that the EEG is a kind of random and non-stable signal coming from the non-linearity's system, its nature is non-linearity [2]. Analysis of power spectrum is the linear analysis technology. As principle, foundation for EEG analysis is to look it as the quasi-linear stable signal in a short time. Therefore, analysis of the power spectrum for the EEG is only an incomplete linear pattern expression.

Due to the non-stability of EEG, power spectrum index of EEG changes greatly with time passes, the BEAM in static state couldn't reflect the change characteristic of time in the conscious activities. If selection for EEG analysis takes too shorter time, the EEG index got couldn't represent the whole conscious process; if selection made taken longer time, it couldn't meet the requirement of the quasi-linear stable signal. Further, this kind of willful selection is made with an obvious subjectivity by itself.

II. MULTI-INDEX DYNAMIC BEAM TECHNOLOGY

Hardware: use 24-channel EEG instrument with wireless communication, manufactured by Shanghai Nuochen Co. in China. Since man and equipment are separated, there should

be no 50HZ frequency interference, and with an ideal ability of resisting fake-signal.

Software: it is researched and developed by ourselves, including the data interface with this said EEG instrument, second-time treatment for these data, creation of three dimensional dynamic BEAM, quantification of consciousness process, group statistic treatment and so on.

A. Varieties of EEG index:

Use 2 kinds of non-linear index based on the statistic sense, approximate-entropy (AP) [3-5] and LZ complexity (LZ) [6-8]; use 2 kinds of relativity index, relative coefficient of right and left symmetry brain area and relative coefficient of relative to neutral montage; keep the existing power spectrum index, such as frequency pattern like δ , θ , α , β . The original EEG could be read from each different physical sense via eight EEG index.

B. Realization of Dynamic BEAM

Since EEG index changes with the time passes, dynamic BEAM is an essential technology for studying the consciousness process. And also, as it needs enough time for the second-time treatment for EEG (to calculate the EEG index), if such treatment is done on line, refreshing the dynamic BEAM is too slow and couldn't be showed in time; if creating the picture ahead of time, memory space in the PC will be occupied too much. Therefore, we adopt a method of establishing a EEG index file for transition, i.e. after completing the inspection of EEG, the second-time treatment for the data will be pre-made, then create the EEG index file for storing, when playing back the dynamic BEAM, read the EEG index of the next BEAM, and done both the interpolation calculation and the pictures creating. If so, time of refreshing BEAM could be controlled in 1 second, but the memory space could be saved about hundreds times.

C. Connection of OLE with Matlab

Matlab is a kind of famous international software used for matrix calculation. Through connection of Matlab and partial Matlab language programming, our software could share with some rape data and picture treatment technology, such as FIR digital filter, Wavelet transform, AR spectrum estimation, Map creating. It not only could raise the working efficiency, but also authority will be improved.

D. Quantitative analysis in the consciousness process

In the experiment, set several conscious tasks, such as: before Qigong, in Qigong, after Qigong, mental arithmetic, mental relaxing and etc. Make a quantitative study of the process characteristic in the relative conscious activities through the Tracking curve and Process BEAM.

Tracking curve: reflect the time characteristic of EEG index. Take the time as an independent variable drawing EEG index curve for each montage, to calculate some parameters such as the mean and variance of EEG index in each consciousness process, and relative coefficient of EEG index between symmetrical montages.

Process BEAM: reflects the space distribution of EEG index in the process. Process BEAM is the accumulated hundreds of dynamic BEAM in each consciousness process, which is divided into eight brain area, such as: right and left Forehead, Peak, Occiput, Temporal, calculate the Means and Variance of the whole brain for each index, and Percentage of each brain area relative to the whole brain.

Variance analysis of two factors: get rid of the effect of individual difference on the group's statistics. Since people's EEG has a large individual difference, not only the experiment in group form is required for studying the conscious activities, but also a suitable statistics treatment is needed. Here, the variance analysis of two factors in F test was used. The purpose is to get rid of the effect of the in-group factor (individual difference) on the between-group factor (process difference). Q test based on the Studentized range is used for the comparison between two processes. F value sheet and Q value sheet are set up in this said system. All of the statistics were finished via auto search and calculation in the PC.

III. EXPERIMENT METHOD

Experimental object are 17 Inner-nourishing Qigong exercisers in Beidaihe, with 5 years of practicing qigong, against a contrasting group of 5 persons. With 5 minutes of keeping quite before making experiment, close eyes and sitting pose in the experiment, orders for each conscious task are issued out from speak of PC, such as before-Qigong, in-Qigong, after-Qigong and etc. Samples are taken continuously in the experiment.

Experimental Scheme 1: "Qigong and mental arithmetic".

5 conscious tasks: 5 minutes for before-Qigong/ 10 minutes for in-Qigong/ 5 minutes for after-Qigong/5 minutes for mental arithmetic/5 minutes for relaxing (listen to prose). Mental arithmetic is made randomly via the PC and that give out the answer as like correct or incorrect. Scores over 80 is looked as the qualified sample. Experiment was

carried out by a group of 17 Qigong exercisers two times every one day at the same time, got 34 cases. Experiment on the contrasting group of 5 persons was once for each one, got 5 cases.

Experimental Scheme 2: “Yishou and Rujing”.

4 conscious tasks: 5 minutes for before-Qigong/10 minutes for Yishou/10 minutes for Rujing/5 minutes for after-Qigong. Experiment on 7 senior Qigong coaches one time separately, among it, 4 persons repeated the experiment for one time, got 11 cases.

After finishing the sample detection, data of the whole process in the original EEG has to be dealt with; i.e. create 8 EEG index files, data file in the process BEAM of each task, and EEG index of each montage are automatically recorded in the database.

The dynamic BEAM is created while playing backward the EEG, and displayed in the original EEG at the same time. Tracking curve in each montage and Process BEAM in each process could be showed respectively in the same

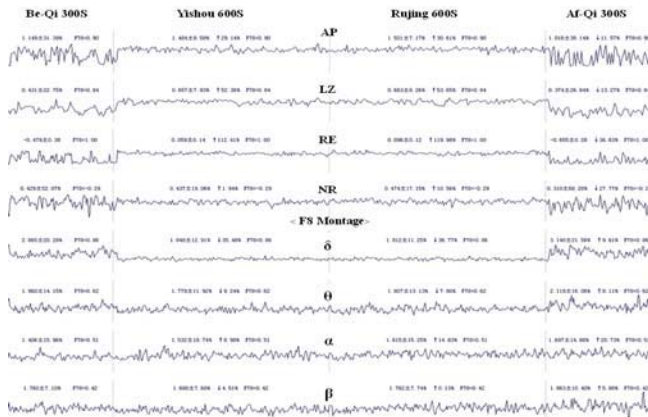


Fig. 1 the Qigong coach’s tracking curve at F8 montage in Scheme 2

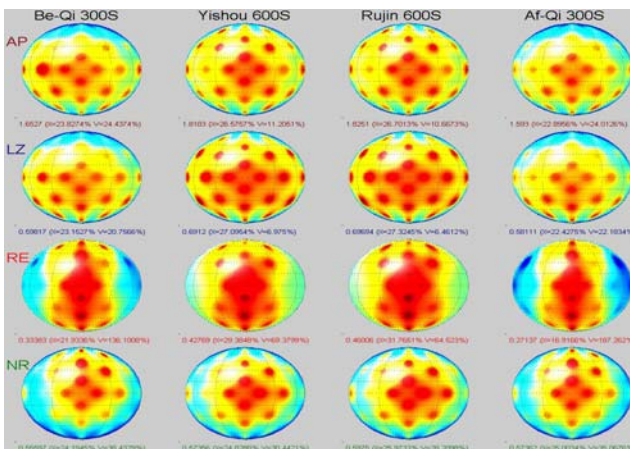


Fig. 2 the same coach’s 1st process BEAM in Scheme 2

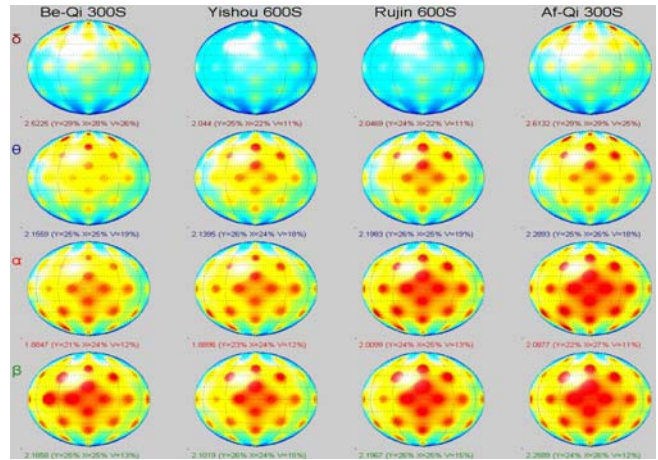


Fig. 3 the same coach’s 2nd process BEAM in Scheme 2

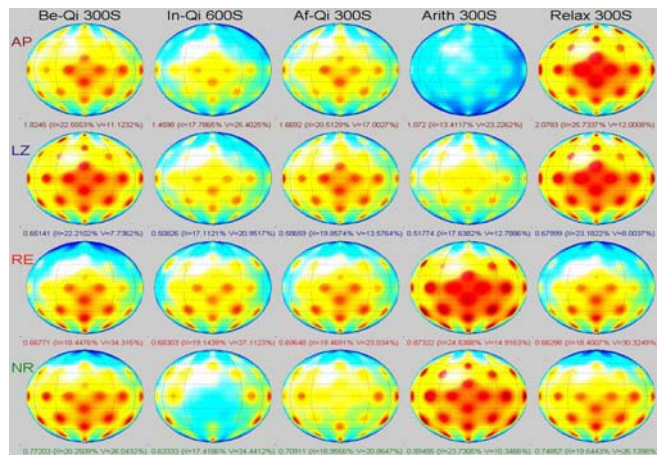


Fig. 4 the Qigong exerciser’s 1st process BEAM in Scheme 1

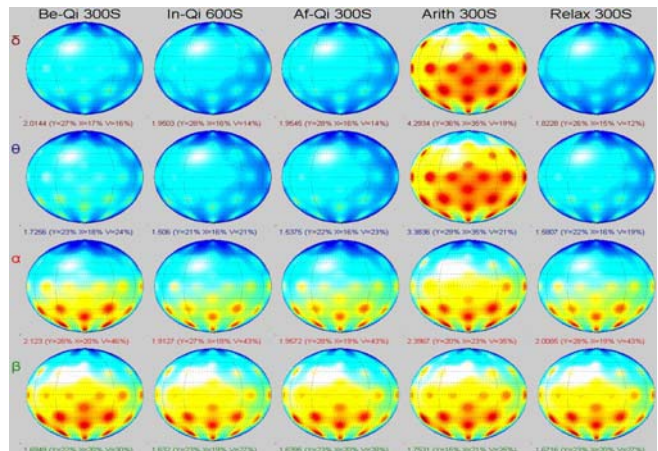


Fig. 5 the same exerciser’s 2nd process BEAM in Scheme 1

screen for comparison purpose. After completing the whole samples detection, choose the experimental scheme and 2 conscious tasks, which could create the group statistic result of each index in each montage.

In process BEAM, the top is forehead, the bottom is occiput.

IV. EXPERIMENTAL RESULT

Below is the result of two factors variance analysis for 17 Qigong exercisers (34 cases) in Scheme 1.

Table 1 mental arithmetic Vs relaxing by Q value of EEG index

	AP	LZ	RE	NR	δ	θ	α	β
Mean	<u>5.78#</u>	<u>7.03#</u>	6.51#	3.05*	8.48#	5.49#	<u>3.77*</u>	2.11~
CV%	7.20#	7.11#	<u>5.53#</u>	<u>0.80~</u>	6.75#	5.62#	<u>0.07~</u>	1.94~
Fp1	<u>7.81#</u>	<u>7.74#</u>	5.17#	1.66~	8.68#	8.08#	<u>1.03~</u>	2.43~
Fpz	<u>8.17#</u>	<u>8.03#</u>	<u>1.72~</u>	1.00~	8.93#	7.42#	<u>1.86~</u>	2.53~
Fp2	<u>7.79#</u>	<u>7.40#</u>	5.17#	0.83~	8.71#	7.93#	<u>1.18~</u>	2.65~
F7	<u>4.77#</u>	<u>7.00#</u>	7.26#	6.29#	7.92#	5.33#	<u>2.33~</u>	1.55~
F3	<u>4.87#</u>	<u>7.42#</u>	2.49~	4.64#	7.44#	4.32*	<u>4.39*</u>	0.04~
Fz	<u>4.69#</u>	<u>6.45#</u>	<u>1.72~</u>	3.87#	7.35#	4.20*	<u>4.62#</u>	1.31~
F4	<u>5.76#</u>	<u>6.63#</u>	2.49~	2.06~	8.85#	3.78#	<u>5.01#</u>	0.21~
F8	<u>5.79#</u>	<u>7.55#</u>	7.26#	6.21#	8.53#	4.83#	<u>3.25~</u>	0.67~
C3	<u>4.26*</u>	<u>5.43#</u>	4.95#	3.75*	7.07#	4.73#	<u>3.58~</u>	0.77~
C1	<u>5.98#</u>	<u>7.13#</u>	0.84~	<u>2.14~</u>	6.82#	4.08#	<u>4.79#</u>	<u>1.08~</u>
Cz1	<u>6.55#</u>	<u>7.34#</u>	<u>1.93~</u>	<u>2.05~</u>	7.94#	4.16#	<u>5.50#</u>	<u>0.20~</u>
Cz2	<u>5.38#</u>	<u>6.47#</u>	<u>1.93~</u>	<u>4.25*</u>	6.08#	4.00*	<u>4.53#</u>	<u>0.05~</u>
C2	<u>5.88#</u>	<u>7.02#</u>	0.84~	<u>2.08~</u>	7.33#	4.05#	<u>4.63#</u>	<u>0.31~</u>
C4	<u>4.06*</u>	<u>6.52#</u>	4.95#	0.09~	6.15#	3.90*	<u>3.32*</u>	0.16~
T3	<u>1.42~</u>	<u>3.28~</u>	5.83#	2.74~	5.15#	3.84~	<u>3.57~</u>	2.83*
T5	<u>5.10#</u>	<u>5.95#</u>	4.65#	3.37~	6.16#	3.29~	<u>4.88#</u>	1.07~

T6	<u>1.82~</u>	<u>3.59~</u>	4.65#	5.86#	6.30#	3.96*	<u>3.14~</u>	3.94#
T4	<u>1.65~</u>	<u>3.70*</u>	5.83#	4.59*	6.75#	4.23*	<u>2.79~</u>	3.91#
P3	<u>2.30~</u>	<u>4.24*</u>	3.99#	3.03~	6.24#	3.41~	<u>3.12~</u>	2.50~
Pz	<u>4.57*</u>	<u>6.07#</u>	0.17~	<u>2.87~</u>	5.91#	3.80~	<u>3.92*</u>	0.30~
P4	<u>3.45~</u>	<u>4.91#</u>	3.99#	<u>1.62~</u>	6.31#	3.80*	<u>3.08~</u>	1.80~
O1	<u>3.97*</u>	<u>4.87#</u>	4.19#	0.80~	6.61#	3.48~	<u>2.33~</u>	3.02*
Oz	<u>3.48~</u>	<u>5.07#</u>	0.17~	0.24~	6.39#	3.78~	<u>2.38~</u>	2.66~
O2	<u>3.33~</u>	<u>4.01*</u>	4.19#	1.64~	6.17#	3.66~	<u>2.25~</u>	2.56~

Remarks: “#” means P<0.01, “*” means P<0.05, “~” means P>0.05, have underline means decrease, have no underline means increase.

Table 2 practicing Qigong Vs relaxing by Q value of EEG index

	AP	LZ	RE	NR	δ	θ	α	β
Mean	<u>2.59~</u>	<u>4.13*</u>	<u>3.37~</u>	<u>0.76~</u>	<u>1.73~</u>	<u>0.57~</u>	<u>7.36#</u>	<u>7.43#</u>
Cv%	<u>1.56~</u>	<u>0.13~</u>	<u>0.36~</u>	<u>3.75~</u>	<u>3.44~</u>	<u>0.85~</u>	<u>5.97#</u>	<u>3.35~</u>
Fp1	2.04~	<u>0.35~</u>	<u>8.79#</u>	2.18~	<u>6.13#</u>	<u>4.63*</u>	<u>6.51#</u>	<u>4.05*</u>
Fpz	1.58~	<u>1.22~</u>	0.63~	2.55~	<u>5.23#</u>	<u>3.03~</u>	<u>5.83#</u>	<u>3.90~</u>
Fp2	0.04~	<u>2.07~</u>	<u>8.79#</u>	2.49~	<u>4.98#</u>	<u>3.77~</u>	<u>5.65#</u>	<u>5.62#</u>
F7	<u>3.01~</u>	<u>4.71#</u>	<u>0.22~</u>	<u>1.49~</u>	<u>1.16~</u>	0.16~	<u>1.75~</u>	<u>3.38~</u>
F3	<u>3.38~</u>	<u>4.53*</u>	<u>2.01~</u>	<u>1.71~</u>	<u>0.52~</u>	<u>0.22~</u>	<u>5.61#</u>	<u>4.83#</u>
Fz	<u>3.32~</u>	<u>3.85~</u>	0.63~	<u>1.34~</u>	<u>0.85~</u>	0.56~	<u>4.39*</u>	<u>5.07#</u>
F4	<u>1.96~</u>	<u>4.05*</u>	<u>2.01~</u>	<u>0.93~</u>	<u>1.97~</u>	<u>0.42~</u>	<u>6.43#</u>	<u>7.56#</u>
F8	<u>4.16*</u>	<u>5.19#</u>	<u>0.22~</u>	<u>1.19~</u>	<u>0.60~</u>	<u>0.01~</u>	<u>3.74~</u>	<u>4.00~</u>
C3	<u>2.70~</u>	<u>4.31*</u>	<u>3.06~</u>	<u>1.29~</u>	<u>0.49~</u>	0.31~	<u>3.95~</u>	<u>4.06*</u>
C1	<u>1.27~</u>	<u>3.37~</u>	<u>5.92#</u>	<u>4.35*</u>	<u>1.01~</u>	<u>0.68~</u>	<u>8.17#</u>	<u>8.71#</u>
Cz1	<u>2.27~</u>	<u>3.73~</u>	<u>3.72*</u>	<u>3.22~</u>	<u>1.18~</u>	<u>0.06~</u>	<u>6.95#</u>	<u>9.37#</u>
Cz2	<u>1.36~</u>	<u>3.55~</u>	<u>3.72*</u>	<u>4.60*</u>	<u>0.65~</u>	0.28~	<u>7.99#</u>	<u>9.96#</u>

C2	<u>1.91~</u>	<u>3.62~</u>	<u>5.92#</u>	<u>3.21~</u>	<u>1.17~</u>	<u>0.85~</u>	<u>8.15#</u>	<u>9.14#</u>
C4	<u>2.50~</u>	<u>3.71~</u>	<u>3.06~</u>	<u>3.58*</u>	<u>1.42~</u>	<u>0.99~</u>	<u>6.09#</u>	<u>5.99#</u>
T3	<u>3.54~</u>	<u>4.32*</u>	<u>0.28~</u>	<u>1.33~</u>	<u>0.26~</u>	<u>0.54~</u>	<u>3.00~</u>	<u>4.26*</u>
T5	<u>2.54~</u>	<u>3.56~</u>	<u>0.16~</u>	<u>2.01~</u>	<u>0.59~</u>	<u>0.24~</u>	<u>8.23#</u>	<u>7.59#</u>
T6	<u>2.50~</u>	<u>3.36~</u>	<u>0.16~</u>	<u>2.63~</u>	<u>0.55~</u>	<u>0.40~</u>	<u>5.98#</u>	<u>5.32#</u>
T4	<u>4.42*</u>	<u>5.55#</u>	<u>0.28~</u>	<u>1.10~</u>	<u>0.25~</u>	<u>0.79~</u>	<u>1.56~</u>	<u>4.59*</u>
P3	<u>3.06~</u>	<u>3.90~</u>	<u>1.59~</u>	<u>0.92~</u>	<u>0.26~</u>	<u>0.30~</u>	<u>7.09#</u>	<u>4.54*</u>
Pz	<u>1.93~</u>	<u>3.82~</u>	<u>1.65~</u>	<u>2.54~</u>	<u>0.68~</u>	<u>0.86~</u>	<u>8.37#</u>	<u>12.5#</u>
P4	<u>1.79~</u>	<u>2.93~</u>	<u>1.59~</u>	<u>3.60~</u>	<u>0.84~</u>	<u>0.13~</u>	<u>7.94#</u>	<u>10.4#</u>
O1	<u>1.54~</u>	<u>2.68~</u>	<u>3.12~</u>	<u>1.17~</u>	<u>0.23~</u>	<u>1.23~</u>	<u>8.89#</u>	<u>9.06#</u>
Oz	<u>0.85~</u>	<u>2.95~</u>	<u>1.65~</u>	<u>1.09~</u>	<u>0.01~</u>	<u>1.48~</u>	<u>8.79#</u>	<u>8.21#</u>
O2	<u>0.20~</u>	<u>1.86~</u>	<u>3.12~</u>	<u>1.12~</u>	<u>0.21~</u>	<u>1.02~</u>	<u>9.13#</u>	<u>8.00#</u>

Remarks: “#” means $P < 0.01$, “*” means $P < 0.05$, “~” means $P > 0.05$, have underline means decrease, have no underline means increase.

V. EXPERIMENTAL CONCLUSION

Complexity index is a statistic value about the attribute of new mode in EEG, both of AP and LZ reflect the probability and speed rate occurred in this new mode respectively, and take a negative relativity with regularity of EEG. The relativity index reflects the synchronism of EEG in the right and left part of brain. In the Mental arithmetic task, the two kinds of complexity index declined obviously, which reflects the increased strength of the structure regularity in EEG, especially in the forehead; the two kinds of relativity index going up obviously reflects the coordination of the symmetrical brain is strengthened, especially in the temple. This great obvious difference shows that these new index could better reflect the characteristic of the brain's conscious activities.

Besides the above-mentioned points, the regularity of mental arithmetic also has α wave weakened and other three waves strengthened. Total energy of the brain wave increased reflects that the effect of brain ERS is strengthened. Its physiological function is to have concentration and positive thinking for excitability of the diencephalon net nerve cell to be bated, strengthen the free oscillation of the thalamus nerve cell loop. Both of the experimental group and the

contrasting group have this regularity. Compared with the contrasting group, complexity of the Qigong group declined in a large part, spread to the whole brain. Strengthening of the relativity in the symmetrical EEG is obvious, especially in the forehead.

In Qigong task, since the index of complexity and relativity present in a multi-state, the group statistic has not the obvious difference; but in the power spectrum index, energy of the four waves are weakened obviously, which refers that the effect of brain ERD is strengthened; further the relativity index is weakened. All of these are definitely different from the regularity of the mental arithmetic.

Yishou is a kind of conscious action, Rujing is a kind of target, refers to this action is to be stopped. In the general understanding, these two are different conscious actions, but the experimental result is not so. What happened is that the trend goes to the same maintaining and strengthening with a good repeated result. It reflects that for those Qigong masters, Yishou and Rujing is the same unit, which made these two actions present a characteristic of heritage while practicing Qigong.

No matter in the distribution of normal state or changes in various kinds of conscious tasks, generally, EEG index in the right and left part is balance, which reflects that the brain action is based on the coordination of right and left brain. Although, we didn't find the advantage of one side of brain, there is an obvious index difference in the different brain part. For instance, under the condition of the normal state, AP value is the highest, RE value is the lowest, α and β index is raised higher along the forehead to the occiput. In practicing Qigong, these differences are weakened with various degrees and make the variation rate in the whole brain declined. It reflects that advantage of the brain index could be weakened or widened in practicing Qigong. Remind: Widening degree of the EEG index in the whole brain maybe become a very important evidence for the Qigong state and efficiency of practicing Qigong.

In EEG, α wave appears while closing eyes, disappears while opening eyes, which normally refers to the quite state. Although reason of this function couldn't be found out, much attention has been paid in Qigong research. In this experiment, practicing Qigong and mental arithmetic present the same characteristic of α wave decline, therefore, α wave only could play an instruction role for disconnecting the quite state, saying of increment of α wave in practicing Qigong is not general. Also, for reminding, in practicing Qigong, no matter Yishou or Rujing, both of them has an obvious direction in the conscious actions.

Multi-state of practicing Qigong mainly is showed in the index of complexity and relativity, maybe, these indexes are more close to internal structure characteristic in EEG. However, the experimental objects couldn't get the basic consis-

tence in understanding and practicing Qigong. Regularity of the mental arithmetic is integrated, as it is guaranteed because of the random questions and correction rate from the mental arithmetic. Such experiment could be controlled better. Therefore, how to improve controlling in the Qigong experiment is an important work.

VI. SUMMARY

In the previous Qigong researches, many are focuses on the individual, experimental conclusions always come from the power spectrum analysis. The representative conclusion is that α wave in practicing Qigong is strengthened, advantage transfers from the occiput to the forehead with the declining of peak value of α frequency. Such indication hasn't been found in this present research from the dynamic BEAM continuous playing backward and the quantitative analysis of the process BEAM.

EEG is a non-linear signal with random and non-stable characteristic, analysis of power spectrum is just only a reading for the linear part in EEG. From continuous playing of the dynamic BEAM, compared with other index, power spectrum index always present a violent variety in any conscious activity process. The reason lies in the second-time treatment for EEG which didn't improve the original non-stability. Besides, it is unacceptable to capture a bit EEG by naked eye in study of the conscious actions.

In principle, analysis of non-linear is more suitable for reading EEG. Its calculation method nowadays has become ripe in recent years. For example: AP is tolerant to EEG

with a very strong ability of anti-jamming. These said work is just a preliminary research. We believe that with the depth of it, in view of the dynamic BEAM technology with multi-index, it is expected that a good result could be achieved in Qigong research and the known scientific area.

REFERENCES

1. Tan Yulin. (2001) Theory of EEG and BEAM on clinic. People's Medical Publishing House, Beijing, pp 298-300
2. Sarbadhikari S N, Chakrabarty K (2001) Chose in the brain: a short review alluding to epilepsy, depression, exercise and lateralization. Medical Engineering Physics, 23:445-455
3. Li M, Vitanyi P (1993) An introduction to Kolmogorov Complexity and its Applications. Springer Publ. Co, Berlin
4. Lempel A, Ziv J (1976) On the Complexity of Finite Sequence. IEEE Trans On Information Theory, IT-22(1):75-81
5. Keller G (1991) Lyapunov exponents and complexity for interval maps. In Lecture Notes in Math, Springer Publ. Co, Berlin, pp 216-226
6. Steven M Pincus, Burton H Singer (1996) Randomness and degrees of irregularity. Proc Natl Acad Sci USA, val.93:2083-2088
7. Steven M Pincus (1991) Approximate Entropy as a measure of system complexity. Proc Natl Acad Sci USA, vol.88:2297-2301
8. Steven M Pincus (1991) A regularity statistic for medical data analysis. Journal of Clinical Monitoring, 7:335-345

Author: Zhang Yihe
 Institute: Qigong Institute Shanghai University of TCM
 Street: 650 Wan Ping Road (South), 200030
 City: Shanghai
 Country: China
 Email: shqigong@shqigong.com

Study of the urinary metabolite profile associated with osteoarthritis and the correlation with its TCM syndromes

Li-Xi Chu¹, Song-Bin Yang¹, Wei Jia², Yun-Ping Qiu², Ming-Ming Su²

¹College of Acupuncture and Manipulation, Shanghai University of Traditional Chinese Medicine, Shanghai 201203, China;

²school of Pharmacy, Shanghai Jiao Tong University, Shanghai 200240, China

Abstract — To compare the distinction of endogenous small molecular metabolites in urine samples from the patients suffering from osteoarthritis(OA) and the healthy people. To contrast the variance of metabolic phenotypes belong to the two different TCM syndromes of OA. **Methods:** Urine samples of 85 participants (43 non-OA controls and 42 individuals with the disturbance of OA which include two different classes in TCM theory) were selected. Utilizing the combined gas chromatography and mass spectrometry (GC-MS) method for the detection of such urine samples. Pattern recognition was applied to analyze the raw data. Some potential biomarkers of OA were identified by means of retrieval of mass spectral database. By the same means, comparative study was carried out between the two groups of TCM syndromes. **Results:** Obvious differences were found in the total ion chromatograms (TIC) of urine samples between the OA and control subjects. When compared the insufficiency of liver and kidney with tendon and vessel stagnation syndrome group with the control, the plot of PCA scores showed that satisfactory separation was made. Better division was realized when the more sophisticated model PLSDA and OPLSDA were utilized. Well-pleasing separation was achieved when the comparison between of the asthenia of both spleen and kidney with dampness invading joints syndrome group and the control one as well as between of the two TCM syndromes. **Conclusion:** There are differences in the urine metabolite profiles among different types of syndrome of OA and the control group. The metabolic regulatory network in organism probably is perturbed in the progress of OA. The nature of types of syndrome of TCM maybe base on the variation of metabolites in vivo and the technique of metabonomics could facilitate the research of the nature of TCM theory.

Keyword — Osteoarthritis(OA); metabonomics; gas chromatography and mass spectrometry (GC-MS); urinary metabolite profile; pattern recognition; study of the nature of TCM syndromes

Osteoarthritis (OA), a chronic joint disease common to the middle-aged and senile people, may result in pain and functional disability in the joints, or even cause one disabled, hence affecting considerably the life quality of patients. Via such metabonomics techniques as gas chromatography-mass spectrometry (GC-MS) and data mining, our

study aims to observe the influence of OA on endogenous metabolites of the body by detection and analysis of urine from knee OA patients with different syndromes in TCM, and by comparison with the normal population; through comparison of metabolic phenotypes from different TCM syndromes, we aim to provide grounds for exploring the essence of “syndrome” in TCM from systems biology level.

I. MATERIALS AND METHODS

1.1 Selection of cases

1.1.1 Diagnostic criteria in western medicine: please refer to the diagnostic criteria of knee osteoarthritis revised by American Rheumatology Association (ASA) in 1995.

1.1.2 Diagnostic criteria in TCM differentiation: please refer to the diagnostic criteria of TCM symptoms and signs of knee osteoarthritis in Clinical Research Guidelines for New Traditional Chinese Medicines (trial) revised by Drug Administration Bureau of the People's Republic of China in 2002.

1.1.3 Including criteria: (1) comply with clinical criteria of knee osteoarthritis in western medicine; (2) comply with the clinical criteria of knee osteoarthritis with the syndrome of deficiency in the liver and kidney and stagnation in the tendons and vessels and the syndrome of deficiency in the spleen and kidney and dampness in the joints in TCM; (3) informed consent was signed by patients or their families.

1.1.4 Excluding criteria: (1) complicated with severe diseases in heart, lung, liver, kidney, hematopoietic and endocrine systems (2) complications affecting the joints, such as psoriasis, syphilitic neurosis, metabolic bone disease, rheumatoid arthritis and acute trauma; (3) patients who still use glucocorticoids within half a month during this study, or without stopping application of non-steroidal anti-inflammatory analgesic drugs within a week during the study; (4) Patients with such metabolic or endocrine diseases as thyroopathy, diabetes and hyperlipemia or other diseases significantly affecting the biochemical metabolism of the body.

1.2 Source of study subjects

Disease group 2 cases of patients with final diagnosis as knee osteoarthritis and treated in outpatient department of fracture and wounds in Yueyang Integrated Chinese and Western Medicine Hospital affiliated to Shanghai University of TCM from September, 2006–November 2006; Normal group: 43 cases of healthy people received medical examination in medical examination center of Yueyang Integrated Chinese and Western Medicine Hospital affiliated to Shanghai University of TCM in December 2006.

1.3 Laboratory apparatuses and reagents

Main apparatuses: gas chromatography- mass spectrometry (American Perkin Elmer company AutoSystem XL Gas Chromatogram/ TurboMass Mass Spectrometer). Required reagents: ethyl chlorformate (ECF), chloroform, absolute alcohol, pyridine, sodium hydroxide and natrii sulfas exsiccatus, all of which are analytical reagents, and purchased from Shanghai Runjie Chemical Agent Limited Company. Internal label: L-2-chlorophenylalanine, purchased from American SIGMA Company.

1.4 The collection and pretreatment of urine samples

About 10–15ml of urina sanguinis was collected on an empty stomach from patients with knee OA and healthy people in the control group included in this study. After antiseptic treatment by 0.5ml of toluene, the sample was put in -20°C deep freezer for cryopreservation. 30min prior to the experiment, the urine sample was taken out to thaw in common temperature. Derivatization by ethyl chlorformate (ECF) was performed before GC-MS analysis.

1.5 GC-MS analysis

A 1- μL extract aliquot of the extracts was injected into a DB-5MS capillary column coated with 5% diphenyl cross-linked 95% dimethylpolysiloxane (30m \times 250m i.d., 0.25 μm thickness) in the split mode (3:1). Either the injection temperature or the interface temperature was set to 260°C ; and the ion source temperature was adjusted to 200°C . Initial GC oven temperature was 80°C . 2 min after injection, the GC oven temperature was raised to 140°C with $10^{\circ}\text{C min}^{-1}$, to 240°C at a rate of $4^{\circ}\text{C min}^{-1}$, to 280°C with $10^{\circ}\text{C min}^{-1}$ again, and finally held at 280°C for 3min. Helium was the carrier gas with a flow rate set at 1mL min^{-1} . The measurements were made with electron impact ionization (70eV) in the full scan mode (m/z30-550).

1.6 Data analysis

All the GC-MS raw fills were converted to CDF format via DataBridge (PerkinElmer Inc., USA), subsequently processed by the XCMS toolbox. The resulting table (TSV file) was exported into Matlab software 7.0, where normalization was performed prior to multivariate analyses. Then principal components analysis (PCA) was utilized with Simca-P11.0 Software package. Additionally, the majority of the metabolites detected were identified by Turbomass 4.1.1 software (PerkinElmer Inc., USA) coupled NIST mass spectra database.

II. RESULTS

2.1 Comparison of general conditions

There were 42 cases included into the disease group in all (including 20 cases of deficiency in the liver and kidney and stagnation in the tendons and vessels and 22 cases of deficiency in the spleen and kidney and dampness in the joints), and among them, there 9 males and 33 females, with the youngest as 42 years old, the oldest as 74 years old, the average age as 56.8 ± 7.1 years old, and the average body weight index (BMI) as 25.13 ± 3.25 ; There were 43 cases in the normal group, and among them, there were 12 males, 31 females, with the youngest as 40, the oldest as 73, the average age as 56.0 ± 7.4 years old, and average BMI as 4.06 ± 2.11 . There was no statistical significance between the two groups in the differences of age distribution, sex constitution and body weight index.

2.2 The acquisition of GC-MS data and the expression of chromatographic peak

After GC-MS analysis of urine sample in each group, the corresponding chromatograms were obtained, which were showed in graph 1. From the graph, it was observed that there were obvious differences in the expression of chromatographic peak between the two varied syndrome groups regarding OA and the normal group, indicating that endogenous metabolites level in the OA patient had changed.

A: Normal control B: OA patients with deficiency in the liver and kidney and stagnation in the tendons and vessels C: OA patients with deficiency in the spleen and kidney and dampness in the joints

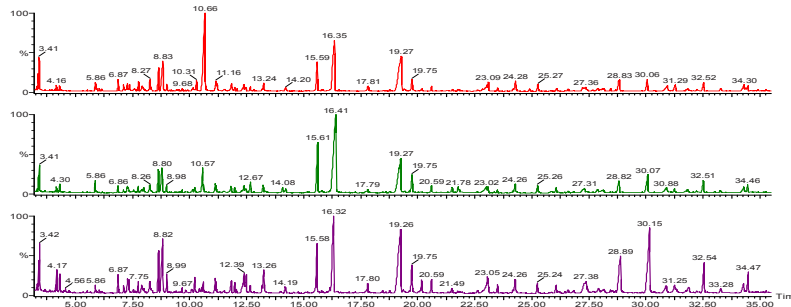


Fig. 1 Chromatogram of urine sample

A. 2.3 The comparison between metabolite spectra from the group of OA patients with deficiency in the liver and kidney and stagnation in the tendons and vessels and the group of normal people

Principal component analysis (PCA) was performed on the two groups of data, and a principal component integrogram with PC2 and PC3 as coordinate axes was drawn. As indicated in graph 2, the black square marks represent samples from the normal (control) group, and the red round marks represent the samples from the group of OA patients with deficiency in the liver and kidney and stagnation in the tendons and vessels (OA1). From this graph, it can be seen that the two groups of samples were well differentiated in PC2 dimension.

In order to make the maximum reflection of the separation trend of the two groups, the partial least-squares discriminant analysis (PLSDA) and orthogonal partial least-squares-discriminant analysis (OPLSDA) were employed to construct the model and explore the mode relationship between the high-dimensional variable data concentration samples. The integrated model of PLSDA was shown in graph 3. In the three-dimensional space constructed by PC1, PC2 and PC3, the samples from the OA1 group and the normal group were clearly differentiated. To further evaluate the construction effect of the model, the SIMCA-P 11.0 software was utilized to calculate the values of R2Y (to evaluate the reliability of the model) and Q2Y (to evaluated the predictability of the model). The calculation showed that R2Y=0.986 and Q2Y=0.679, indicating that the model has good differentiation and predictability. Graph 4 is the integrated diagrammatic figure of OPLSDA, and further calculation showed that R2Y=0.871 and Q2Y=0.498.

On the basis of model construction, variable importance projection (VIP) analysis was used to determine the variables (chromatographic peaks) accountable for the differential expressions of metabolite spectra in the two groups, and the NIST database was also employed to qualitatively ana-

lyze the chromatographic peaks (part of them could not be determined due to the limited resources in the chromatographic database). Many metabolite levels changed in different degrees in the urine of OA1 patients, as compared to those in the urine of normal people. The metabolites with increased levels were mainly glycine, indoleacetic acid, tyrosine, aconitate, acetyl-citrate, citrate, hippurate, isocitrate, benzeneacetate, 4-hydroxy and tyrosine, etc. The metabolites with decreased levels were mainly alanine, threonine, glutamine, dopamine and histidine, etc.

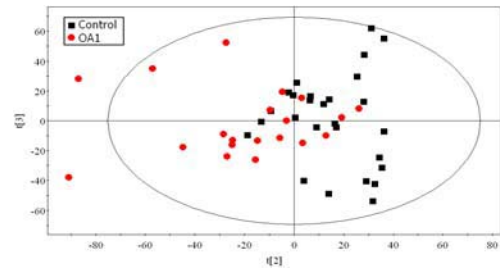


Fig. 2 the PCA integrogram of the OA1 group and the normal group

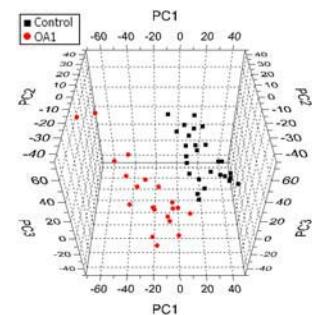


Fig. 3 the PLSDA diagrammatic figure of the OA1 group and the normal group

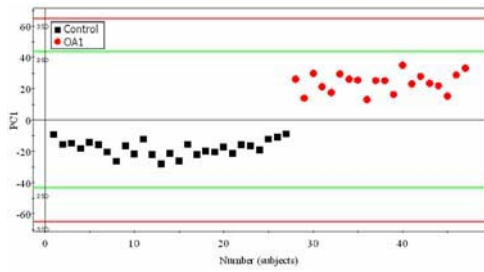


Fig. 4 the OPLSDA diagrammatic figure of the OA1 group and the normal group

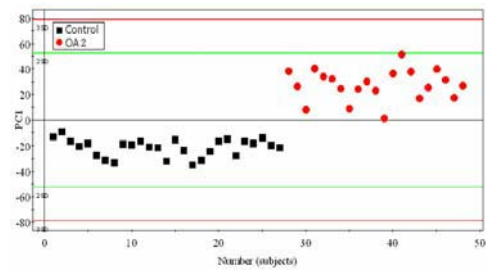


Fig. 7 the OPLSDA diagrammatic figure of the OA2 group and the normal group

2.4 The comparison between metabolite spectra from the group of OA patients with deficiency in the spleen and kidney and dampness in the joints and the group of normal people

PCA result was shown in graph 5, the back square marks represent samples from the normal (control) group, and the red round marks represent the samples from the group of OA patients with deficiency in the spleen and kidney and dampness in the joints (OA2). From this graph, it can be seen that the two groups of samples were well differentiated in PC2 dimension, and obvious intra-group clustering trend existed. The model indicated in graph 6 was constructed by

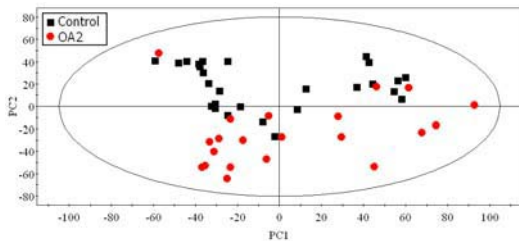


Fig. 5 the PCA integrogram of the OA2 group and the normal group

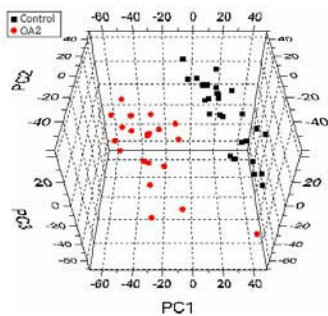


Fig. 6 the PLSDA diagrammatic figure of the OA2 group and the normal group

means of PLSDA. In the three-dimensional space constructed by PC1, PC2 and PC3, the samples from the OA2 group and the normal group were clearly differentiated, and there was clear clustering trend and no inter-group confounding in the samples. The calculation showed that $R^2Y=0.872$ and $Q^2Y=0.537$, indicating that the model has good differentiation and predictability. The integrated diagrammatic figure of OPLSDA is shown in graph 7. The two groups were well differentiated in PC1 dimension. The calculation showed that $R^2Y=0.872$ and $Q^2Y=0.576$.

2.5 The comparison between metabolite spectra from the OA1 group and the OA2 group

PCA result was shown in graph 8. From this graph, it can be seen that the two groups of samples were well differentiated in the PC2 dimension. The model constructing result of PLSDA was shown in graph 9. In the three-dimensional space constructed by PC1, PC2 and PC3, there was clear intra-group clustering trend and inter-group mutual separation in the samples from the OA1 group and OA2 group, indicating that there were different expression phenotypes in the two groups. The calculation showed that $R^2Y=0.863$ and $Q^2Y=0.705$, indicating that the model had been well constructed. The model constructed by means of OPLSDA is shown in graph 10. The two groups were well differenti-

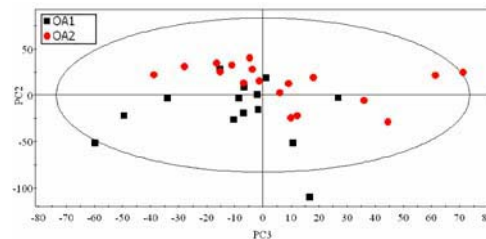


Fig. 8 the PCA integrogram of the OA1 group and the OA2 group

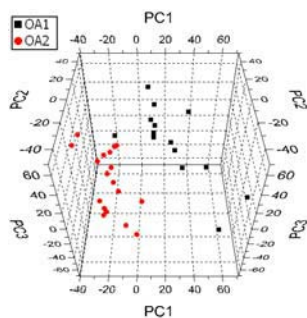


Fig. 9 the PLSDA diagrammatic figure of the OA1 group and the OA2 group

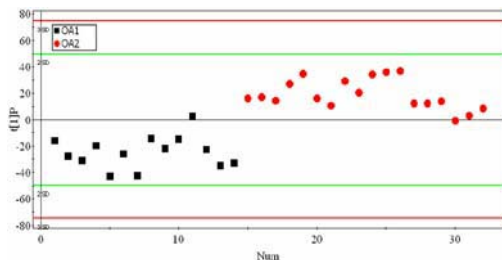


Fig. 10 the OPLSDA diagrammatic figure of the OA1 group and the OA2 group

ated in PC1 (t1) dimension. The calculation showed that $R^2Y=0.782$ and $Q^2Y=0.637$, indicating good reliability and predictability of the model.

III. DISCUSSION

In recent years, with the rapid development of various spectroscopy and bioinformatics techniques, metabonomics has displayed huge potential in disease prediction and diagnosis. Life is an integral system, in which the biological molecular tissues and its manipulation level are interrelated and interdependent, meanwhile, they are also influenced by various physiological and environmental factors. All chemical reactions directly caused by physio-pathological disorder, or disturbance in terms of the proportion, concentration, metabolic flux of endogenous biochemical material by binding with enzyme or nucleic acid which control the metabolism can be reflected in the components of metabolites[2]. At present, studies showed that compared with normal person, the neutral hormone of body fluid, amino acid, cytokine, as well as the metabolite of collagen of articular cartilage and proteoglycan in OA patients witnessed changes.

OA is mainly caused by the degeneration of articular cartilage, featuring the damaged and degenerative of articular cartilage. Besides the change of cartilage, its metabolites also flow into the body fluid through the lymph system, causing a series of meaningful changes [5] and our early study also proved this point [6]. In this study, GC-MS and pattern recognition were applied to test and analyze endogenous metabolites as well as their concentration in the urine of testees. Findings show that there is a desirable recognition between OA patient and controlled testees according to those minute changes. It also showed that OA can disturb the metabolic system, causing the change of internal metabolic phenotype. The techniques of metabonomics can be a novel diagnostic method of OA, and need further development.

The research made a comparison and analysis over the metabolites in urinary samples of OA patient with different TCM syndromes. The findings showed that there is significant difference between the two OA groups in terms of urinary metabolites. By applying PCA, and model construction of PLSDA, OPLSDA, we finely differentiated these two groups of patients, indicating a substantial material basis of the “syndrome differentiation”, and the change of disease disturbed metabolic phenotype is closely related with the nature of “syndrome”. “syndrome” in TCM is the pathological generalization of a disease at certain developmental stage, featured by holism and dynamics. By using microscopic way, metabonomics makes a systematic research over the rule of change of the metabolite during the dynamic process of the metabolism. There is similarity between the metabonomics and TCM syndrome in terms of way of thinking and research method.

A disease covers different syndromes, on the other hand, a syndrome may be shared by different diseases, and the application of metabonomics techniques & methods to make qualitative and quantitative analysis over their metabolite is of vital importance to grasp the nature of TCM syndrome and to standardize the clinical syndrome differentiation.

REFERENCES

1. Brindle J T, Nicholson J K, Schofield P M, et al. Application of chemometrics to ^1H NMR spectroscopic data to investigate a relationship between human serum metabolic profiles and hypertension[J]. *Analyst*. 2003, 128(1):32-36.
2. Yan Xianzhong, Zhao Jianyu, Pengshuanqing. The role of metabonomics in post-gene era, *Journal of spectroscopy*, 2004, 21 (6):267.
3. Garnerio P, Conrozier T, Chrislgau S, et al. Urinary type II collagen C-telopeptide levels are increased in patients with rapidly destructive hip osteoarthritis. *Ann Rheum Dis*, 2003;62(10):939-943.

4. Wei Xiaoen, Yang Qingmin, Deng Lianfu, etc. Experimental study on metabolic change of proteoglycan in body fluid of osteoarthritis [J]. Chinese Journal of rheumatology, 2002, 6 (6): 445–446.
5. Ishiguro N, Ito T, Ito H, et al. Relationship of matrix metalloproteinases and their inhibitors to cartilage proteoglycan and collagen turnover: analyses of synovial fluid from patients with osteoarthritis. Arthritis Rheum, 1999, 42: 129-136.
6. Zhu Lixi, Xie Dianhong. Correlation of biochemical metabolism of knee osteoarthritis fingerprint spectrum and sign & symptom. Shanghai: Shanghai University of TCM, 2005.

Author: CHU Li-Xi
Institute: College of Acumox and Tuina, Shanghai University
of TCM
Street: 1200 Cailun Road
City: Shanghai
Country: China
Email: chulixi@163.com

Research on the Cun-Guan-Chi Pulse Detecting System

Wei-chang Tang¹, Cong-ying Liu¹, Yu-ping Zhao¹

¹ Shanghai University of Traditional Chinese Medicine, Shanghai, China

Abstract — The paper introduces the designing concept of the Cun-Guan-Chi Pulse Detecting System and its basic principles, and structural features. The system comprises 3 independent pressure sensors with same design parameters. It provides a scientific and quantitative method of detecting the pulses, which tallies well with the diagnostic method of the traditional Chinese medicine.

Keywords — pulse, sensor, detecting system

I. PREFACE

With the development of medical level both domestic and abroad, demands on medical service and health preservation have been increasingly rising. At the same time with the improvement of medical level, people are stepping forward to prevention of sub-health and prevention. Chinese medicine has its unique advantages in treatment and prevention. With “four diagnostics” which include inspection, auscultation, interrogation and pulse-feeling as the basis, “treatment based on syndrome differentiation” is the essence of diagnostics of Chinese medicine. On the principle of combination of the four diagnostics, clinical information is analyzed and synthesized to achieve the aims of identification of etiology according to differentiation of symptoms and signs, selecting therapeutic principle, appreciation of therapeutic effect, and presumption of prognosis. Traditional diagnostic methods are short of standards of objective evaluation. Without modern diagnostic techniques, its diagnostic result may be affected by many subjective and outside conditions. The truth and repetitiveness are not good, so there are many difficulties in pervasion and generalization. Accordingly, research collecting information of the “four diagnostics” is the prerequisite of modernization of Chinese medicine.

There is a long history of the standardization of pulse in Chinese medicine. Since the 1970's, multi-disciplinary technicians in China have cooperated to make considerable research on the principles, detecting method, instrument, pulse information and clinical application of pulse diagnosis. The current research condition mainly focuses on pulse detection on Guan with single-headed electropulesograph. However, the pulse taking method known as “three portions and nine pulse takings” contains various information, including more comprehensive observation of the

active physiological and pathological process. So, the research about the Cun-Guan-Chi pulse detection is an essential part of the objectification and qualification of the research of the “four diagnostics” in Chinese medicine. This article is a preliminary introduction of the Cun-Guan-Chi pulse detecting system developed by us.

The pulse information in Chinese medicine contains various information, involving in pressure, creep, fluid mechanics, degree of hardness, etc. From the course of pulse taking, the information involves the pressure of finger on the blood vessel, and the eating force that the finger feels. With mechanics as the main characteristic, pressure-transducer is adopted in our Cun-Guan-Chi pulse detecting system.

II. CUN-GUAN-CHI PULSE DETECTING SYSTEM

A. Fundamental principles of the sensor

Physical Model: The Cun-Guan-Chi pulse sensor comprises 3 independent pressure sensors with same design parameters. The physical model of the sensor is as follow:

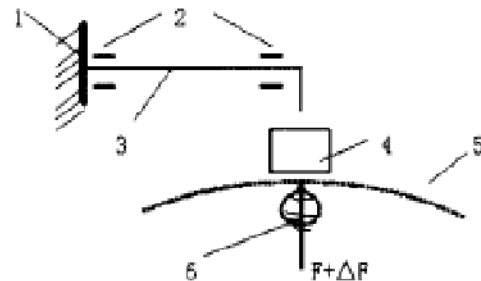


Fig. 1 Physical model of the sensor

1—Fixture 2—Strain gages 3—Springy beam
4—Sense stub 5—Skin 6—Blood vessel

When sense stub 4 applies pressure onto “skin 5, blood vessel 6” system round the radial artery (equal to the floating, medium and sinking pulse taking pressure with fingers), the stub 4 is affected by counterpressure F and pulse force ΔF . These two forces are transferred to springy beam 3, which is strained and therefore resistance quantity of the strain gage 2 on the springy beam changes accordingly. The

measuring circuit, attached by the strain gage, outputs signals in different levels with the changes of $F+\Delta F$, so we can distinguish different pulse taking pressures and different pulses according to different signals so as to realize qualified detection of pulse.

Structure of the sensor: On the surfaces of the three sense stubs, Cun, Guan and Chi, mini-sensors are compounded to detect the information of multi-dimensional pulse. The main body of the sensor is made of aluminium alloy. The forcing part is mini-stepping generator. With the energizing circuit, automatic forcing pattern has been realized.

The structure of the core part of the sensor is designed in view of the compound cantilever construction with secondary beam in ZMH-I Single Headed Pulse Transducer^[1], and the technical difficulties of transducer such as repeatability and stability are resolved.

Besides the fact that the pulse sensor is 3D adjustable, in order to simulate the flexible Cun-Guan-Chi pulse taking method with fingers, relative distance regulator of Cun-Guan-Chi contacts and the regulator which enables the three contacts to freely move along the blood vessel are added.

Main technical targets of the Cun-Guan-Chi pulse sensor: Detection shows the main static technical targets as follow:

- ① sensitivity: 0.5mV/gram force;
- ② linear range: 0 ~ 300 g;
- ③ nonlinear error: <1%F.S(0 ~ 300g);
- ④ harmonic frequency: > 1 kHz;
- ⑤ temperature error: < 2%F.S (5°C ~ 40°C);
- ⑥ lag error: < 1%F.S.

B. The multi-channel pulse signal-amplifier

The multi-channel pulse signal-amplifier is composed of low-noise, low-power consumption, strong antiturbulence computer amplifiers, including stabilized voltage supply, AC&DC mixed amplifier, DC amplifier, AC amplifier, etc. Besides the public stabilized voltage supply, the multi-channel pulse signal-amplifier is composed of many independent units with same design parameters. Fig.2 is the schematic diagram of pulse amplifying principle of single channel.

The stabilized voltage supply, comprising voltage changer, rectifier circuit, filter circuit, and three terminal integrated regulation tubes, outputs corresponding power for the sensor and amplifiers. During designing course, enough output power and good voltage-regulation coefficient should be guaranteed. Meanwhile, heat dissipation, earth connection and some other factors need to be considered.

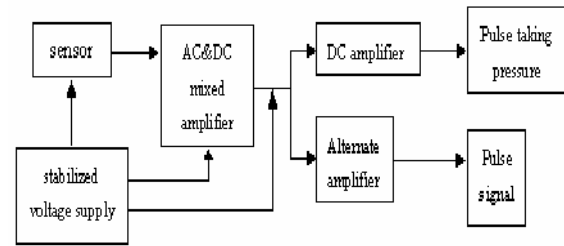


Fig. 2 The pulse amplifying principle of a single channel

The AC & DC mixed amplifier functions to mix and amplify the pulse taking pressure output by the sensor and the pulse force. SD system with high input impedance, low power consumption and noise is adopted to operate the amplifier.

The DC mixed amplifier is common, which comprises of general operational amplifier. It magnifies and outputs the pulse-taking pressure.

The AC amplifier is also composed of common general operational amplifier. Analog voltage signal of pulse is output after being magnified. If it is input to computer through A/D conversion, automatic analysis of pulse atlases can be processed by computer.

C. classification and management of multi-channel signals

The pulse-taking technology discussed here can get multi-directional and multi-dimensional pulse information. So, according to the pulse theory of TCM, the information need to be managed and classified, such as pressure, frequency, breadth, length, excess or deficiency, change tendency, relations among pressures on Cun, Guan and Chi region. The information of breadth, length, relations among pressures on Cun, Guan and Chi region were not involved in the techniques of research on pulse detecting instrument on single channel. And related report has not retrieved either. Through large amount of clinical test, combining with basic theory of Chinese medicine, creative research needs to be done.

III. PROSPECTS

According to literatures domestic and abroad, there is certain research on single-headed pulse detecting device in style, magnitude or depth, while the research on the detecting device of Cun-Guan-Chi pulse is seldom seen. So, further research on objectification and quantification of the Cun-Guan-Chi pulse is necessary. Clinical data needs to be steadily gained. The author holds that there are some works in urgent need:

A. Research on automatic regulating device of the sensor

At present, research is all carried in laboratory. Development and application need to be done to meet social demand.

B. Research on processing unit of pulse information

Through computer software, pulse information of Cun, Guan and Chi can be distinguished, recognized and read. Combining with the pulse taking principle of “three portions and nine pulse takings”, distinguishing conclusion in accordance with TCM theory was made.

C. Research on normalization and standardization of detection of the Cun-Guan-Chi pulse sensor

For the requirement of standardization of Chinese medicine, research on pulse instruments should step to normalization and standardization, such as standardization of instrument, standardization of parameters of pulse atlas, etc.

D. Clinical research

Nowadays, materials and literature about detection of Cun-Guan-Chi pulse sensor are limited, so collection and research of clinical data on correlations between Cun-Guan-Chi pulse and clinical diseases are in need.

REFERENCES

1. Tang Weichang. et al. (1990) Designing Techniques of ZMH—I Pulse Sensor in Traditional Chinese Medicine
2. Fei Zhaofu. et al. (1991) Research on Pulse Diagnosis in Traditional Chinese Medicine. Publishing House of Shanghai College of TCM
3. Zhang Fuxue. (1991) Application of Sensor and Selection of Circuits. Publishing House of Electronics Industry

Traditional Chinese Medical Informatics and Virtual Body

Shi Cheng¹, ChangYue Li², Shiqi Fang¹

¹ Nanjing university of Traditional Chinese medicine, Nanjing, China

² Heilongjiang University of Chinese Medicine, Haerbin, China

Abstract—This paper Reviews the history of computer technique application in Traditional Chinese Medicine (TCM), along with applied in depth, “Traditional Chinese Medical Informatics(TCMDI)”, a new interdisciplinary appeared from medicine and computer. Traditional Chinese medicine is a subject with dynamic human body for research object, for long time because of can't be in true human body ascend start experiment, therefore the aspects of experimenting research always was placed in passive situation. In recent years along with the present of the crossing subject in the modern technique of computer information and modern medicine, gave the computer technique to expand the more wide investigate foreground in TCM realm. This paper introduces some conveys for the foreground of Virtual Body application in TCM.

Keyword— Traditional Chinese Medical Informatics, Virtual Body, TCM Research

I. HISTORICAL REVIEW

As early as the beginning of 70's, that is the Cultural Revolution in our country period, because of investigating the mechanism of acupuncture anesthesia, meet a lot of experimental data in biosignal, for solving this problem, the researcher beginning applied computer to process millions biosignal data.

In the beginning of the 80's, along with the software on the diagnosis and treatment of hepatitis by Guan Youbo , a famous TCM expert, thereafter, about hundreds software on the experts' consultation about diseases were produced. The Computer Diagnosis and Treatment System Research Association was established on this foundation which is the precursor for China Medical Informatics Association(CMIA). CMIA was established on 1980 in ChangSha of Hunan province. It is a profession set in Chinese Artificial Intelligence Academic Association. The first author of this paper is one of initiator for CMIA. Because the majority of engineers that attended CMIA are members of Chinese Institute of Electronics which is a branch of International Federation for Information Processing (IFIP), in order to manage the agreeable relation, the CMIA changes its relation belong to Chinese Electronics Academic Association in March 1983. Along with the further research of TCM clinical information, it was found that the four-diagnosis information, which is the foundation of TCM decision and lacks quantitative

basis. This is inconvenient for the teaching and repetitious experiments. In order to solve this problem, many engineering technicians and TCM doctor devoted to the research of the objectivity of TCM four diagnostic methods, for example manufacture of electron pulse-graphics, apparatus to the tongue inspection and instrument of detecting channels and points. With the improvement of computers' performance and the emergence of CD-ROM and disks with high capacity, the Retrieval System of TCM has been put into practice. During the progress, researchers discovered that National standard Chinese word data GB2312 cannot satisfy the investigative demand in TCM literature, and the research work of With the decrease of the computer price and the improvement of the network, the information management of TCM hospital information system are becoming mature. Along with the emergence of the information superhighway and Internet applied universality in view, E-mail ... etc, all these urge the net of the TCM tele-education, TCM remote consulting, TCM remote access and processing became the realistic.

China is one of the countries which have ancient civilizations in the world. Chinese medicine has a history of several thousand years. The TCM is the crystallization of the Chinese people's experience in medical practice. The ancient Chinese medicine and modern computer information processing technologies for distant hybridization will definitely bear abundant fruit.

At present, the Traditional Chinese Medical Informatics (TCMI) is taking its place in the world as a new interdisciplinary science about how the computer information processing technology will be applied to TCM

II. VIRTUAL BODY AND TCM

In recent years, along with the present of the Virtual body in the modern technique of computer information and modern medicine, gave the computer technique to expand the more wide investigate foreground in TCM realm. The data of the Virtual body is a digital image from the real human body.

In real life, since mankind are communities which have wise brain, walk erectly, and live in highly civilized society, the human body is greatly difference from the animals.

Traditional Chinese medicine is a subject use dynamic human body as research object. Because of this reason, for long time the study of TCM cannot experiment on real human body for long, and the aspects of experimenting research remained in passive situation.

The Virtual body is made by the computer imitating technique based on the data from real human body. It can complete the TCM laboratory research which can not make experiments on human body. Therefore the emergence of the Virtual body expanded a new path for the TCM experimental medical science .

The key of the problem is how to establish the inside environment model of the Virtual body, therefore establishing the mathematics model is the key of the item's research work.

In the aspects of setting up the mold, there are two kinds of models on the whole, one is regard the physiology pathology of the modern medical science as the foundation, another is with the TCM theories and TCM clinical.

The first one demand the extensive cooperation of many subjects, for example, cardiovascular physiology, cardiovascular pathology, nerve physiology, biomechanics, and hemorheology etc. Based on this, the inside environment model of Virtual Body can be established by mathematical modeling for medical research. The latter demand extensive cooperation for example, computer and information researcher, TCM foundation theories researcher, TCM doctor and the researcher of combining traditional Chinese and Western medicine etc.

Because the medical theories system of TCM is different from modern medicine, so it needs the Researchers of Interdiscipline to build up the bridge between mathematical modeling and TCM. In this respect, there's much method in past TCM expert system that we can make use of .

Three investigate directions will be introduced in TCM and Virtual Body below.

A. TCM Expert Consults System:

In the early 1980's, people began to investigate TCM expert system. Researchers did much work in mathematics model that imitated the well-known TCM doctor thought characteristics. However, because of the problems in the objectivity of TCM four diagnostic methods, the research of TCM expert system is aground slowly. Along with the Virtual Body environmental emergence, the TCM expert system will acquire the freshman again, and it could be used for the clinical teaching and clinical consult in TCM in the future. Moreover along with the development of the hospital information system (HIS), some researchers has showed their interests in the research of the TCM Electronic Patient Record. This research will involve the natural language in

the artificial intelligence realm, this is also a hard problem in the world.

To give the Virtual Body a wise brain which can understand natural language is a ideal belong to the remote future. Now someone interested in Knowledge Discovery of Database(KDD) for the worthy information of TCM literature and TCM clinical. This will need to establish TCM Data Warehouse(DW) for discovering more valuable knowledge. If the discovered worthy knowledge is combined with the Virtual Body to form TCM symptoms and signs, then TCM clinic phenomenon can be kept the view an emersion. In short, these research directions all belong to TCM realm. Their workload and difficulty is bigger.

B. The Research of the Objectivity of the Four-diagnosis Information

The techniques of TCM diagnosis includes the Four Diagnostic Methods and Differential Diagnosis. The former use of the Inspection, Auscultation and Olfaction, Interrogation, Feeling Pulse and Palpation, in order to obtain objective evidences and indications of the clinical status. The Inspection includes to evaluate the facial expression, complexion, general appearance, characteristics of the tongue, excreta, the distribution of superficial venules of the infant's fingers, etc. The latter is the procedure to analyse and synthesize such evidences and indications. The two techniques are correlated to arrive at to correct diagnosis.

In the research of the objectivity of TCM four diagnostic methods The more is lingual diagnosis and pulse diagnosis. The research of the objectivity of lingual diagnosis belongs to the category of image processing. The research of the objectivity of pulse diagnosis belongs to the work of the aspect signal processing.

Use the TCM pulse as an example, in the beginning of 1990's professor Xi Baoshu of Qinghua University established a model dealing with the dynamic simulated test on pulse under the similar conditions of physiology, geometry, movement and dynamics. The result of the primary research has proved that this equipment is capable of imitating human physiological condition. At the same time in Shanghai, professor Liu Zaorong of Fudan University mathematics department researched TCM pulse with the biomechanical line theories by computer numerical imitate to proof the mechanism in the TCM slippery pulse of pregnant woman and stringy pulse of hypertension. Along with the emergence of Virtual Body, people can research TCM pulse in a digital image from the true person's body by mathematics model to realize their dream of TCM pulse research.

C. The Research of the acupuncture

Recalling the history of computer application in TCM field of our country, the computer application in acupuncture is the earliest.

As early as the beginning of 1970's, along with research of acupuncture anesthesia, for investigating the inside relation in TCM channels and bioelectronic signal, researchers began to applied computer to process millions biosignal data. After this, along with the climax of TCM expert system many researchers as started the work for acupuncture expert system to produce a lot of acupuncture expert system.

At the same time, the information processing technology is applied by computer to the aspect of acupuncture clinical, teaching, science research and image processing of acupuncture point etc broadly. Along with the present of the Virtual Body, the new opportunity for acupuncture simulated teaching appeared. In Song Dynasty (960-1279D.C.), doctors use the bronze statue with acupuncture points to imitate the human body. On the Virtual Body, people can proceed fixed position of acupuncture points and teachings accurately, investigate the level of structure construction, cross section construction, CT cross section construction of the acupuncture points, and investigate the characteristic of gross anatomy in acupuncture points etc. If it can be combined with time medical science and expert system in acupuncture, researchers can get more achievement. On the other hand, if the model of normal human body physiology, neurophysiology, electricity physiology etc. can be established in the Virtual Body, people can get More thorough research of TCM channels and theories.

III. CONCLUSIONS

This paper Reviews the history of computer technique application in Traditional Chinese Medicine(TCM). And it tells us the birth of a new interdisciplinary of Traditional Chinese Medical Informatics(TCMI) which is to study how computer information processing technology will be applied to TCM.

Virtual body is make use of the true human body data by the computer imitating technique. It can complete the TCM laboratory research which can not make experiments on human body. Therefor the emergence of the Virtual body expanded a new path for the TCM experiment medical science.

In short there is plenty space for development in Traditional Chinese Medical Informatics(TCMI) and Virtual Body.

REFERENCES

1. Shi Cheng et al. Chinese Character Operating System of Traditional Chinese Medicine and Pharmacology(TCMP) MEDINFO 95. North-Holland 1995 pp1123-1124
2. Shi Cheng et al. Present Situation and Characteristics of Traditional Chinese Medical Informatics (TCMI) MEDINFO 98 pp.841-844

Study on Brain FMRI of the Mechanism of Tuina Analgesia

Zhengyu Li¹, Xiwen Sun² and Juntao Yan³

¹College of Acupuncture and Tuina, Shanghai University of T.C. M., Shanghai, China

²Radiology Dept. Shanghai Huadong Hospital, Shanghai, China

³Yueyang Hospital, Shanghai University of T.C. M., Shanghai, China

Abstract — According to clinical data, a lot of patients suffering from chronic pain like to be pressed on the tenderness point, and after Tuina they feel apparently better. Some patients even come back frequently to receive further Tuina treatment after their pain has relieved. So to research on the intervention of the therapy of pressing and kneading on the tenderness point in chronic pain and the mechanism of Tuina analgesia by using functional magnetic resonance imaging. Five patients with one-sided fits of lumbar disc herniation (LDH) were selected according to single-blind randomized experimental method. FMRI was applied to observe the activation and inhibition of brain-functioning area in five cases of patients with lumbar disc herniation after pressing and kneading on their Weizhong (B40) point. Every patient must finish 11 trials in the experiment. Functional MRI data were obtained from scanning the whole brain, but focusing on ACG, hypothalamus, NAC, amygdaloid body GOB etc. T-test was performed to analyze the data in SPSS software package. The data sets from 5 subjects were all used in the study. Signal increases and signal decreases elicited by Tuina stimulation were demonstrated in multiple brain regions. After pressing and kneading on the patient's Weizhong (B40) acupoint, the patient's hypothalamus, left nucleus accumbens and left amygdaloid body were excited ($P < 0.05$) and his left anterior cingulate gyrus was inhibited ($P < 0.05$). By pressing and kneading on the pain point (B40), both the pain circuitry and the reward circuitry are affected which indicates that there might be a close correlation between the effects of analgesia and pleasure through Tuina. And this might also be one of the reasons why clinical Tuina patients with chronic pain like to be pressed on their pain points.

Keywords — Tuina, analgesia, lumbar disc herniation, fMRI, central nucleus

I. INTRODUCTION

Previous clinical studies have shown that a lot of patients suffering from chronic pain like to be pressed on the tenderness point, and after Tuina they feel apparently better [1]. It demonstrates that Tuina therapy plays a good analgesic role in treating many diseases. But the central mechanism of Tuina analgesia is still unknown. And this work also can not be done on live human body. FMRI techniques can help solve this problem [2,3]. It has a great value in observing the change of the brain in the physical state of the human body

and illustrating Tuina analgesia modulating within the human brain. This study based on the principle of "treating on the tenderness point" in traditional Chinese medicine, pressing and kneading on the Weizhong (B40) point of patients with lumbar disc herniation to explore the central mechanism of Tuina analgesia through functional magnetic resonance imaging.

II. MATERIALS AND METHODS

A. Case selection

Five patients with one-sided fits of lumbar disc herniation (LDH) were selected according to single-blind randomized experimental method. 4 are male, 1 female, all right-handed, with a disease course over 6 months. Their age was between 27-48, and the average age was 36. Diagnosis of LDH was confirmed by CT or MRI. None of them had nerve or mental problems and other body diseases. No patient had taken any sedatives or felt any discomfort 3 days before testing.

B. Equipments

MRI was performed on a 1.5-Tesla system (GE Medical Systems) with a whole-body gradient coil (switching capacity, 40 mTm⁻¹ within 268 μ s). Force of Tuina manipulation was tested by the real time processing Tuina manipulation testing device.

C. Tuina Method

Using the pressing and kneading manipulation, its force measured by real time processing Tuina manipulation testing device was 5-6Kg, with a frequency of 60 time/min.

D. Acupoint

Weizhong point (B40).

E. Procedures

Before every experiment, let the patient lie on the testing table with their eyes closed for 10 mins, then scan the whole

brain for 120 sec., pause for 40 sec. in its resting state; then carry out 11 trials, including 5 intervening manipulations and 6 breaks. Each trial needs 40 sec. The signal is collected every 2 sec. The total scan time is 560 sec. The Tuina manipulation is performed by a sophisticated and licensed Tuina doctor.

F. Observation areas

FMRI was applied to observe the activation and inhibition of the brain-functioning area^[4] hypothalamus, nucleus accumbens (NAC), amygdaloid body, orbital gyrus (GOB), insula (INS) and anterior cingulated gyrus(aCG), in five cases of patients with lumbar disc herniation after pressing and kneading on their Weizhong (B40) point.

G. Imaging Sequences

The functional images acquired by using gradient echo-planar imaging (EPI) (ep2d-fid-60b2080-62-16.ekc, TR=2s, TE=67ms, Flip Angle=90,FOV=24cm, No. Acq=1, slice thickness =5mm, slices =16, TD1=0ms, TD2=0ms, Dist factor=0.25, Number of measurement=243, Freq=64, Phase=64, Excit order=Ascending.) were obtained for anatomic reference. 3D T1-weighted anatomic images were acquired with a spoiled gradient-recalled sequence (mprestnst1-4b195.wkc,TR=9.7ms,TE=4ms,Flip Angle=15, FOV=24cm, slice thickness=170mm, slices=170). The anatomic T1-weighted spin-echo images were acquired with the number of sections and orientation as with the axial plane for coregistration of fMRI signal intensity on the anatomic images.(se-14b89-a.ykc,TR=420ms, TE=14ms, No.Acq=1, No.Meas=1, Freq=256, Phase=256).

H. Image Processing and Analysis

Images were transferred to a workstation (Advantage Windows, GE Medical systems).The fMRI data were analyzed by using Analysis of Functional NeuroImaging (AFNI, ilwaukee, WI) software^[5]. 3D rigid-body registration was used to align the reconstructed fMRI data against a reference image, and spatial smoothing (Gaussian filtering: full width of half maximum = 5 mm) was applied^[6]. The volume of activation of the PMC was determined by using a cross-correlation technique.

I. Statistical Evaluation

T-tests were used to test for differences between the mean volume of change in the hypothalamus, nucleus accumbens , amygdaloid body ,GOB,INS and anterior cingulated gyrus after pressing and kneading on the Weizhong (B40) point.

The statistical tests were 2-sided, with a *P* value ≤ 05 considered significant. Analyses were performed in SPSS software package (version 13.0 for Windows, SPSS Inc).

III. RESULTS

A. Signal increase area (Table1)

Signal increases elicited by pressing and kneading on the patient's left Weizhong (B40) acupoint were demonstrated in multiple brain regions, such as hypothalamus, GOB, nucleus accumbens and amygdaloid body, but only hypothalamus, left nucleus accumbens and left amygdaloid body (Figure 1) have significant statistical difference before and after treatment. (P<0.05)

Table 1 Signal increase brain area (mm³) ($\bar{X} \pm SD$)

Region	Brodmann area	Talairach coordinate			Volume	
		X axis	Y axis	Z axis	Before	After
left hypothalamus	-	4	5	-8	13.0±8.7	40.6±3.8*
right hypothalamus	-	-3	4	-10	18.8±7.9	54.6±7.8*
left amygdaloid body	-	24	6	-20	18.6±9.5	322.2±96.1*
right amygdaloid body	-	-20	5	-13	36.8±22.6	176.8±59.5
left NAc	-	13	-9	-9	3.8±3.8	47.6±11.9*
right NAc	-	-13	-9	-8	3.6±3.6	49.8±20.5
left GOB	-	4	48	20	37.2±37.2	70.0±44.8
right GOB	-	4	48	20	23.4±23.4	30.0±19.3

* P<0.05

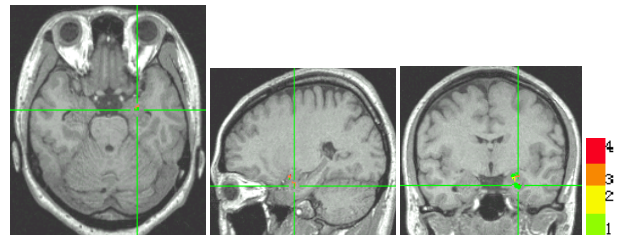


Fig1-1 Left amygdaloid body before Tuina therapy

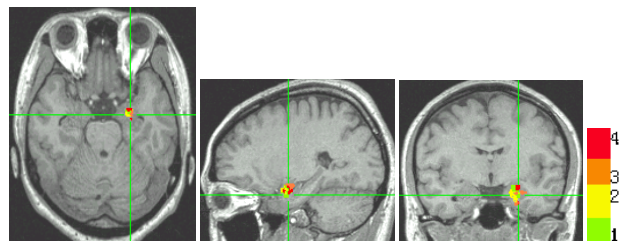


Fig1-2 Left amygdaloid body after Tuina therapy

B. Signal decrease area (Table2)

Signal decreases induced by pressing and kneading on the patient’s left Weizhong (B40) acupoint were demonstrated in INS, anterior cingulated gyrus ares, but only the left anterior cingulated gyrus (Figure 2) has significant statistical difference before and after treatment ($P<0.05$).

Table2 Signal decrease brain area (mm^3) ($\bar{X} \pm \text{SD}$)

Region	Brodmann areas	Talairach coordinate			Volume	
		X axis	Y axis	Z axis	Before	After
left aCG	24	6	-26	19	2921.2±929.2	136±32.9*
right aCG	32	-6	-28	21	3301.4±1023.8	418±81.4
left INS	-	11	21	8	1376.8±771.3	245.8±51.3
right INS	-	9	12	-15	1448.4±502.6	389.4±93.3

* $P<0.05$

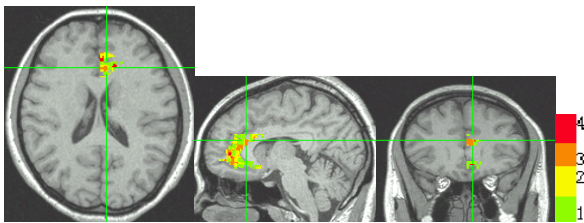


Fig2-1 Left anterior cingulated gyrus before Tuina therapy

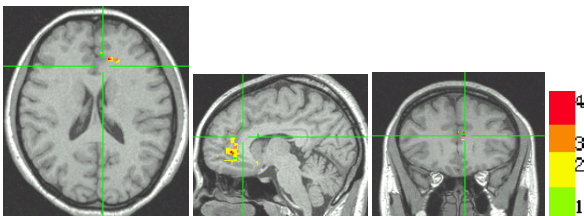


Fig2-2 Left anterior cingulated gyrus after Tuina therapy

IV. DISCUSSION

Functional magnetic resonance imaging (fMRI) is used to visualize brain function, by visualizing changes in the chemical composition of brain areas or changes in the flow of fluids that occur over timespans of seconds to minutes^[7]. In the brain, blood perfusion is presumably related to neural activity, so fMRI can be used to find out what the brain is doing when the subjects perform specific tasks or are exposed to specific stimuli.

Blood oxygen level-dependent (BOLD) MRI method is very commonly used in clinic. It reflects tissue oxygenation and may be useful for the detection of change of brain areas^[8]. The principle of (BOLD) MRI I imaging is to take a series of images of the brain in quick succession and to statistically analyze the images for differences among them. BOLD fMRI constructs functional images by exploiting the susceptibility produced by the paramagnetic nature of deoxyhemoglobin (deoxy-Hb). Neuronal activation corresponding to specific functional tasks increases local blood flow to the eloquent cortices, which reduces deoxy-Hb concentration and susceptibility and increases signal intensity in a susceptibility sensitive image such as T2. This signal intensity change is referred to as the BOLD effect. In fact, hemoglobin shows up better on MRI images than deoxyhemoglobin; thus, oxygenated blood shows up better. Brain areas with more blood flow have been shown to have better visibility on MRI images. Therefore, better visibility is thought to be correlated with brain activation by specific stimuli.

Modern medicine considered that varied function of the body was controlled by related brain-functioning area^[9]. According to recent reports of fMRI, puncture acupoint may first activate the related brain-functioning area, then make certain chemical material or hormone release to the target and get effect^[10,11]. This study based on the principle of (BOLD) MRI, compared the fMRI data both before and after stimulating the acupoint Weizhong (B40). Signal increases and signal decreases elicited by Tuina stimulation were demonstrated in multiple brain regions. After pressing and kneading on the patient’s Weizhong (B40) acupoint, the patient’s hypothalamus, GOB, nucleus accumbens and amygdaloid body were excited, but only hypothalamus, left nucleus accumbens and left amygdaloid body had significant statistical difference ($P<0.05$). And INS, anterior cingulated gyrus were inhibited, in which only the left anterior cingulated gyrus had significant statistical difference ($P<0.05$). According to neurobiology, nucleus accumbens (NAc), hypothalamus, amygdaloid body and the orbital gyrus (GOB) belong to the reward circuitry^[12] which have been shown to be activated in studies of drug-associated reward. Especially, amygdaloid body is thought to be important for information processing in the service of emotional and motivational states. So after pressing and kneading on the patient’s Weizhong (B40) acupoint, the patient’s hypothalamus, nucleus accumbens and amygdaloid body are excited, which can induce pleasure effect of human beings to soothe pain.

The anterior cingulated gyrus (aCG) and INS may be considered to be a classic formulation of circuitry involved with the processing of pain^[13]. Reserch shows that pain will induce the blood flow in the aCG and cause pain. After pressing and kneading on the patient’s Weizhong (B40)

acupoint, the patient's anterior cingulate gyrus is inhibited, which indicates that Tuina analgesic effects are related with the regulation of aCG.

V. CONCLUSION

Through this study we know that by pressing and kneading on the pain point (B40), both the pain circuitry and the reward circuitry are affected which indicates that there might be a close correlation between the effects of analgesia and pleasure through Tuina. And this might also be one of the reasons why clinical Tuina patients with chronic pain like to be pressed on their pain points. In addition, real time fMRI was very useful in exploring Tuina mechanisms.

ACKNOWLEDGMENT

This Project was done with the assistance of Prof. Shen Xueyong from the College of Acupuncture and Tuina, Shanghai University of T.C. M., Shanghai, China, Prof Ji Ming from the Radiology Dept. of Shanghai Huadong Hospital, Shanghai, China and Mr. Zhang Xiaochu from the China University of Science and Technology, Hefei, China. Here I'd like to extend my hearty thanks for them.

REFERENCES

1. Wang Yong, Zheng Lan (2001) Probe into the mechanism of Tuina analgesia. *Sandong Journal of Traditional Chinese Medicine* (11):678-679
2. Shu-Ming Wang, Zeev N Kain, Paul White (2008) Acupuncture analgesia: I. The scientific basis. *Anesth Analg* 106 (2):602-10
3. Sridhar S. Kannurpatti and Bharat B. Biswal (2004) Effect of anesthesia on CBF, MAP and fMRI-BOLD signal in response to apnea *Brain Research*, Volume 1011, Issue 2: 141-147
4. Gear, R.W., Aley, K.O., and Levine, J.D. (1999) Pain-induced analgesia mediated by mesolimbic reward circuits. *Neurosci.* 19: 7175-7181
5. Lancaster JI, Liu J et al. (1999) Global spatial normalization of human brain using convex hulls. *Nucl Med* 40:942-955.
6. GaJiy, Bower JM, et al. (1996) Cerebellum implicated in sensory acquisition and discrimination rather than motor control. *Science* 271:545-547.
7. Edehnan RR, Siewer B, Darby IX, et al. (1994) Qualitative mapping of cerebral blood flow and functional localization with echo-planar MR imaging and signal targeting with alternating radio frequency. *Radiology* 192:513-59.
8. RaicMe ME, Grall RL, et al. (1976) Correlation between regional cerebral blood flow and oxidative metabolism: in vivo studies in man. *Arch Neural* 33:523-526.
9. Xu Shaofen *Neurobiology* (1999, Second Edition). China: Shanghai Medical University Publishing House 311-327.
10. Mark W Strudwick, Stephen J Wilson (2007) Automated syringe driver for acupoint injection in functional MRI studies: a case for quantified point injection in neuroimaging studies of acupuncture. *Expert Rev Med Devices* 4 (6):815-819
11. Chae, Younbyoung; Park, Hi-Joon; Hahm, Dae-Hyun; Hong, Mee-Suk; Ha, Eunyoung; Park, Hun-Kuk; Lee, Hyejung (2007) fMRI review on brain responses to acupuncture: the limitations and possibilities in traditional Korean acupuncture *Neurological Research*, Volume 29, Supplement 1, February (7): 42-48
12. Lino, Becerra, Homs c. Breiter, Roy Wise, R. Gilberto Gonzalez, and David Borsook (2001) Reward circuitry activation by noxious thermal stimuli. *Neuron* 32:927-946
13. Backes WH, Mess WH, Kranen-Mastenbroek V, Reulen JP. (2000) Somatosensory cortex responses to median nerve stimulation: fMRI effects of current amplitude and selective attention. *Clin Neurophysiol.* 111:1738-1744

Qualitative Frequency Response Calibration of Sonocardiography System to Sense Wrist Pulse

Yih-Nen Jeng¹ and Shang-Yin Lee²

¹ Professor, Dept. Aeronautics and Astronautics, National Cheng-Kung University, Tainan, Taiwan

² Graduate student, Dept. Aeronautics and Astronautics, National Cheng-Kung University, Tainan, Taiwan

Abstract—The frequency response of the microphone of the Yu and Wang sonocardiography system is qualitatively proven to cover the 0.5 to 10 Hz zone which is in the traditional Chinese medicine's interesting range of the wrist pulse data and is beyond the announced range of most commercial product. The calibration system employs a small speaker and a small capacity type microphone to construct a small air cell to service as an acoustic wave transfer zone where the speaker is employed to simulate the wrist pulse input. In order to simulate the small air column enclosed by the microphone's membrane cell and a patient's skin, the air cell bounded by the speaker and microphone has tiny and/or small leakage through the bounding interface. The air leakage is employed to simulate the patient's soft tissue around the measuring point. The data picked by the microphone is treated by a Fourier sine spectrum/spectrogram generator. Experimental results show that both cases with tiny and small air leakages have apparent responses in the interested frequency range. Two test cases were included to demonstrate the system performance: one had the spleen disease and the other had heart problem. According to the Wang frequency resonance theory of arterial and vascular system, their spectrograms show that every corresponding harmonic mode has unstable amplitude variation with respect to time. In other words, the data acquisition system together with time-frequency analysis accurately reflects the connection between the abnormal harmonic mode and corresponding organ.

Keywords—Frequency Response, Identification, microphone, wrist pulse, organ-meridians.

I. INTRODUCTION

The development of the technique in the traditional Chinese medicine has achieved a giant progress in recent decades. The study of the organ-meridians of human body has obtained more attention. Wang et. al. developed the resonance theory that each arterial bed in the vascular system is oscillated by the pressure waves at its own resonant frequency [1-3]. They came to two important conclusions. First, the organ spectra can be used as parameters to elucidate the physical status of the specific vascular beds. Specifically, the magnitude of a harmonic mode reflects the amount of blood spent by the corresponding organ. Second, as physical properties of a specific arterial bed change, the

amplitude of the corresponding resonant mode changes more than that of the others. However, the corresponding resonant frequency will be approximately maintained by the heart rate control system to minimize the energy loss. Based on this theory, Yu and Wang developed an artery blood pressure pulse acquisition system to take the wrist arterial blood pulse pressure impulse data via a commercial microphone [4]. However, the interested frequency range of the wrist pulse data of the traditional Chinese medicine is lower than the announced range of most commercial microphone. The main concerning of this study is to qualitatively justify that the specific design of the Yu and Wang system [4] shift a microphone's frequency response to the range of human organ-meridians.

II. THEORETICAL DEVELOPMENT AND EXPERIMENTAL SETUP

A. Spectrum and Spectrogram Generator

Consider a data string, y_0, y_1, \dots, y_N . After applying the Gaussian smoothing, a smooth response is always available. It can be shown numerically that it is a diffusive smoothing in the interior point remote from the two ends [5,6]. If the remaining high frequency part is repeatedly smoothed m -steps, the difference between the original data string and final high frequency part is the desired smooth part. Note that this iterative filter is also diffusive in the interior points. Suppose that the original data string involves sinusoidal and non-sinusoidal parts where the latter can be properly approximated by a polynomial with finite degree M . In Ref.[7], it is further proven that, the non-sinusoidal part will be effectively removed from the high frequency part after applying the iterative Gaussian smoothing method m -steps provided that $m > M/2$. In a practical application, one can only provide a data string with finite length. The missing data beyond two ends will induced a result deviates from that without the missing data there. In Ref.[6], it was shown that, the significant error is about $\sigma/[1+0.8\log_{10}(m)]$ for that applying the iterative Gaussian smoothing method, where σ is the Gaussian smoothing factor. It is recommended to remove these segments around the two ends.

In Ref.[8,9], the above mentioned iterative filter is employed to remove the non-sinusoidal and low frequency parts. The Fourier sine spectrum of the remaining high frequency part will then have a small direct current error.

The time-frequency transform imposes a finite bandwidth window (centered on a given frequency) on the Fourier sine spectrum. The corresponding inverse Fourier transform of the band-pass limited spectrum is the real part of the spectrogram associated to the given frequency. Subsequently, the corresponding amplitude is obtained in terms of the Hilbert transform. After sweeping all the desired frequencies, the desired spectrogram is obtained.

B. Experimental Setup and Procedures

In order to achieve stable sensitivity in response to the tiny wrist arterial pressure pulse data, a commercial capacity type microphone is employed, whose instructions are 20-20,000 Hz, 100mw, 32 Ω 105db sound pressure level sensitivity at 1kHz \pm 2% and uses jack 3.5mm stereo plug for connection. The experimental facilities include a function generator (Iwatsu Inc. FG-350), two UNO speakers (10 mm and 21.85 mm diameters, 20-20,000Hz), a digital audio board (Onkyo Inc. SE-150PCI, SN ratio 100dB, 0.3-44KHz, sampling rate 32-192KHz).

Procedures of the experiment and data analytic involve the following steps. At first, a function generator sends a sine function with prescribed frequency (ranging from 0.5 to 10Hz) to the speaker to produce acoustic wave. After propagating through the confined air cell, the tiny pressure wave is then picked up by the microphone voltage output. The air cell is constructed by the speaker, microphone and a flat plate with a hole larger than the microphone membrane camber and smaller than the cone of speaker. The air leakage exists whenever the bonding plate was not sealed up firmly. The analogy signal is then converted to be a digital signal through a digital audio board. Finally, the digital data is saved in a personal computer via the Microsoft XP window system.

Note that, if the air cell is airtight, the microphone would not receive obvious signal because the speaker does not have enough energy to push the air cell in the frequency range less than 5Hz. In this study, a tiny and a small air leakages are examined for both speakers.

For the wrist pulse data measurement, the microphone is embedded into a belt so that the opening of the microphone membrane camber can be attached to a human skin around the wrist vessel without any air leakage. Note that air pressure variation is induced by the composite effect of the blood vessel expansion and contraction together with nearby soft tissue. As a consequence, it can not be properly picked up by most microphones except the capacity type

with a small membrane camber. After a searching procedure via the finger, the measuring point is approximately located at the maximum response point among the three attach points of the classical feel pulse technique.

C. Data Analysis

Since the capacity type microphone principally senses the pressure wave's derivative, all the raw data are integrated once to become the pressure data. The non-sinusoidal part of the digital data string is then removed by the iterative Gaussian smoothing method. In order to ensure the periodic condition, the following steps are employed: zero values of the sinusoidal part around the two ends were located by searching and interpolation; redistribute the data via a monotonic cubic interpolation; and perform the odd function with respect to an end. Subsequently, the Fourier sine spectrum of the remaining sinusoidal part is generated by the fast Fourier transform. Finally, the time-frequency plot is obtained by the Fourier sine spectrogram generator. In order to obtain a meaningful result, the experiment is repeated three times at every frequency input.

III. RESULTS AND DISCUSSIONS

A. Frequency Response Identification

At first, the arrangement employing the 10mm speaker with tiny air leakage is tested. Resulting spectrograms of the sinusoidal part for cases of 0.5 and 5 Hz are shown in Figs.1a and 1b, respectively. The 0.5Hz case has three dominate modes and many minor modes which have amplitude and frequency variations. These modes and variation of frequency and amplitude are caused by the tiny air leakage of the air cell and cannot be reflected from the spectrum. The spectrogram of the 5Hz case does not have significant variation of amplitude and frequency. This means that the air leakage does provide regular air stream almost in the in-phase manner with respect to the speaker membrane. The frequency response of the case is shown in Fig.2. In the low frequency part, the captured amplitude increases up to 1.5Hz and then rapidly decreases after 2Hz. The fast attenuation reflects that the tiny air leakage is apt to become airtight in the high frequency part. It means that the speaker does not have enough energy to produce pressure fluctuation.

As to the small air leakage plus 10mm speaker arrangement, the resulting spectrograms are shown in Figs.3a and 3b which are corresponding to Figs.1a and 1b, respectively. A careful inspection upon these figures reveals that, in addition to the interested modes, many other modes exist too.

These extra-modes reflect the complicated flow field induced by the oscillatory air stream flowing through the air leakage. Nevertheless, both the 0.5Hz and 5Hz modes are captured as shown. Figure 4 shows the resulting frequency response where the test results obviously scatter one from another especially in the extreme low frequency zone. Again, this scattering is induced by the complicated flow field within the test air cell. Unlike that shown in Fig.2, in the high frequency part, the response amplitudes do not decay because the airtight is not a problem.

For the arrangement employing the 28.5 mm speaker, the corresponding frequency responses for the tiny and small air leakages are shown in Figs.5 and 6, respectively. Since a large speaker is more difficult to send energy to the microphone membrane chamber (in the central part of the speaker) than that of a small speaker, the amplitude responses in the extreme low frequency zone of these figures are smaller than that shown in Figs.2 and 4, respectively. In other words, their response curves shift to the right. Moreover, degrees of scattering of the 28.5mm speaker cases are larger than those of 10mm speaker.

Although there are some discrepancies, these tests show that the frequency response of the examined microphone is active in the range of 0.5-10Hz. This is quite different from the announced range of 20-20,000Hz. A reasonable explanation comes from the energy density reaching the microphone. In the open space, only a small amount of acoustic energy is received by the microphone. Therefore, if the frequency is lower than 20Hz, the acoustic pressure variation can not actuate the microphone. On the other hand, when the acoustic wave is confined within a small air-cell, most acoustic energy emitted from the speaker reaches the microphone. Therefore, the active frequency response range becomes 0.5-20,000Hz in such a special environment. As a consequence, the frequency response of the microphone of the Yu and Wang sonocardiography system covers the range of the wrist vessel pulse data whose fundamental frequency is corresponding to a human heart beating rate.

Finally, two tests are employed to demonstrate the performance of the whole data analysis system: one has the spleen disease and the other had heart problem. Figure 7 shows the resulting spectrogram of the wrist vessel pulse data of the former patient where the first seven modes are clearly shown. According to the Wang frequency resonance theory [1-3], the first 12 modes are the heart, liver, kidney, spleen, lung, stomach, Gall bladder, bladder, large intestine, sanjiao, small intestine, and pericardium meridians, respectively. The fourth mode shows abnormal amplitude variation which reflects the disease of the spleen. In Fig.8, the resulting spectrogram of the patient with heart problem shows that the first mode has an abnormal amplitude decrease in the interval of 4 to 6 seconds. It means that his heart has problem. These

two tests obviously confirm that the sonocardiography data collecting system, Wang resonant theory and present data analysis system have the potential to help the traditional Chinese diagnosis of the wrist feel pulse technique.

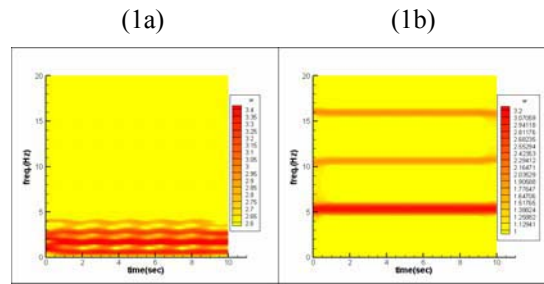


Fig.1 Spectrograms of the sinusoidal part of the 10mm speaker with tiny air leakage: (a) 0.5Hz case and (b) 5Hz case..

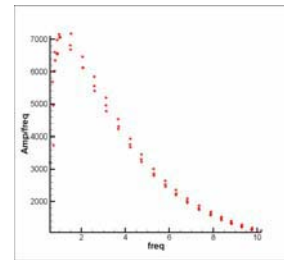


Fig.2 The overall frequency response plot of the 5Hz case of the 10mm speaker with tiny air leakage.

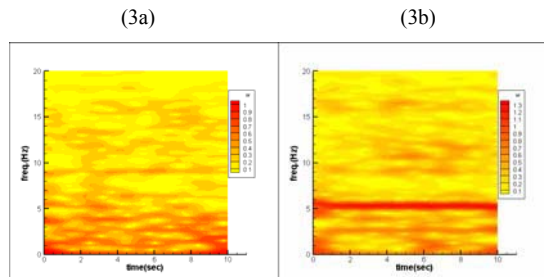


Fig.3 Spectrograms of the 10mm speaker with small air leakage: (a) 0.5Hz case and (b) 5 Hz case.

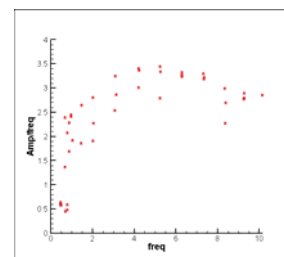


Fig.4 The overall frequency response plot of the 5Hz case of the 10mm speaker with small air leakage.

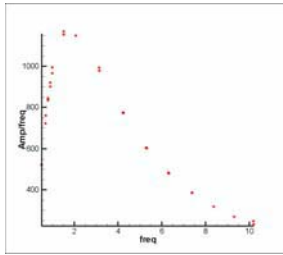


Fig.5 The overall frequency response plot of the 5Hz case of the 28.5mm speaker with tiny air leakage.

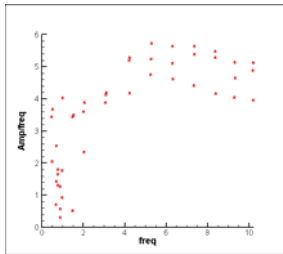


Fig.6 The overall frequency response plot of the 5Hz case of the 28.5mm speaker with small air leakage.

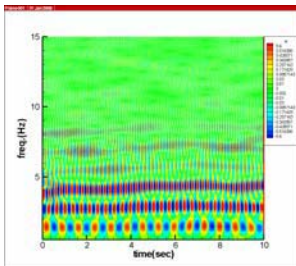


Fig.7 The real part spectrogram of the test case with spleen disease.

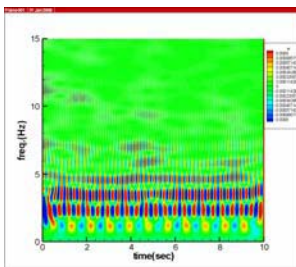


Fig.8 The real part spectrogram of the test case with heart disease.

IV. CONCLUSIONS

An experimental set up was employed to simulate the operation conditions of a small commercial microphone to measure a human wrist vessel pulse data. Experimental results qualitatively show that the frequency response range

of the microphone covers the range of 0.5-10Hz which is just the range of traditional Chinese wrist pulse diagnosis. Two tests cases confirm that the overall system has the potential to modernize the traditional Chinese wrist pulse diagnosis.

ACKNOWLEDGEMENT

This work is supported by the National Science Council of Taiwan under the grant number NSC-96 -2221-E006-186-MY3. The authors are grateful to professor Yu, who helps us to build the sonocardiography system.

REFERENCES

1. S. T. Young, W. K. Wang, L. S. Chang, and T. S. Kuo, "Specific Frequency Properties of the Renal and the Superior Mesenteric Arterial Beds in Rats," *Cardiovas Res.* Vol. 23, pp.265-467, 1989.
2. Y. Y. Wang Lin, M. Y. Jan, C. S. Shyu, C. A. Jiang, and W. K. Wang, "The Natural Frequencies of the Arterial System and Their Relation to the Heart Rate," *IEEE Trans. Biomed. Eng.*, vol. 51. no.1, Jan. 2004, pp. 193-195.
3. T. L. Hsu, P. T. Chao, H. Hsiu, W. K. Wang, S. P. Li and Y. Y. Lin Wang, "Organ-Specific Ligation-Induced Changes in Harmonic Components of the Pulse Spectrum and Regional Vasoconstrictor Selectivity in Wistar Rats," *Experimental Physiology*, vol. 91, no.1, pp.163-170, 2006.
4. Yu, F. M. and Wang, S. C., "Design of a Sonocardiography System and Its Application in the Diagnostic of the Cardiovascular Disease," to appeared in the Proceedings of 2006 TSB conference, Taiwan, Dec. 2006.
5. Y. N. Jeng, P. G. Huang, and H. Chen, "Filtering and Decomposition of Waveform in Physical Space Using Iterative Moving Least Squares Methods," *AIAA paper no.2005-1303*, Reno Jan. 2005.
6. Y.N. Jeng, P. G. Huang, and Y. C. Cheng, "", to appeared in *Proc. Royal Soc. A*, 2008.
7. Y. N. Jeng and P. G. Huang, "Decomposition of One-Dimensional Waveform with Finite Data length Using Iterative Gaussian Smoothing Method," *Proc. 31th National Conference on Theoretical and Applied Mechanics, DYU, Changhwa, Taiwan*, paper no. ctam 30-389, Dec. 15-16, 2006.
8. Y. N. Jeng and Y. C. Cheng, "Fourier Sine/Cosine Spectrums and Errors of Derivatives Estimated by Spectrums," *Proc. 17th Combustion Conf.*, paper I07, March, 2007, Taiwan.
9. Y. N. Jeng and Y. C. Cheng, "A Time-Series Data Analyzing System Using a New Time-Frequency Transform", *Proc. 2006 Internat. Conf. Innovative Comput., Inform. Control*, paper no. 0190, Sept. 30, 2006.

Author: Yih-Nen Jeng
 Institute: Department of Aeronautics and Astronautics, National Cheng-Kung University
 Street: No.1, University Road
 City: Tainan
 Country: Taiwan
 Email: z6208016@email.ncku.edu.tw

The Effect of Electric Acupuncture on the Retinal Ganglion Cells in Rabbits with Acute High Intraocular Pressure

Wenxin Zhou¹, Jingying Yang², Yong Xia¹, Hongwei Wang², Genying Guo², Jing Zhang¹

¹ College of Acumox and Tuina, Shanghai University of TCM, Shanghai, China

² Department of Electron Microscope, Shanghai University of TCM, Shanghai, China

Abstract — Purpose: To assess the effect of electric acupuncture on the retinal ganglion cells (RGCs) in rabbits with acute high intraocular pressure (IOP). **Methods:** This comparative experimental study included 32 rabbits assigned into 3 groups: group 1 (n=5), group 2 (n=10) and group 3 (n=17). The rabbits in groups 2 and 3, which were anesthetized with an intravenous injection of 30% sodium urethane, were subjected to high pressure perfusion to anterior chambers by increasing the IOP to 30, 50 and 70 mmHg for 2 hours. After 2 weeks of electric acupuncture treatment with G6805-2 electron treatment device on acupoints Housanli and Jingming of rabbits in group 3, the rabbit's eyes of all three groups were enucleated and its RGCs were observed with transmission electron microscope. **Results:** In group 1, that's the normal control, its ultrastructures appeared normally while different changes of RGCs were happened in the other two groups. Ultrastructurally, in group 2, under different degrees of high pressure perfusion, its RGCs showed the light colour of cytoplasm, less organelles, irregular rough endoplasmic reticulum (RER) and Golgi apparatus, and vacuolated mitochondria with broken cristae etc. And in group 3, a few relatively intact RGCs were noticed especially under 30 mmHg and 50 mmHg perfusion but no obviously improved under 70 mmHg perfusion. **Conclusion:** Electric acupuncture is more helpful to RGCs with high pressure perfusion from 30 mmHg to 50 mmHg. Electric acupuncture might be used for vision injury of glaucoma with moderate high IOP.

Keywords — High intraocular pressure (IOP), retinal ganglion cells (RGCs), electric acupuncture, electron microscope

I. INTRODUCTION

Primary glaucoma is a common and complex ophthalmic disease, which is often associated with increase in intraocular pressure (IOP), discus opticus change, defect of visual field and visual disorder. In experimental researches about glaucoma, the effect of high IOP on the retina was emphasized and the most important is the changes of the retinal ganglion cells (RGCs)[1, 2].

Acupuncture can play some role in treatment of primary glaucoma especially for its visual disorder [3, 4].

This comparative experimental study tried to assess the effect of electric acupuncture on the RGCs in rabbits with acute high IOP and find out the suitable condition for electric acupuncture treatment.

II. MATERIALS AND METHODS

A. Experimental animal

32 white healthy male rabbits, weighting from 2~3kg, were provided by the experimental animal center in Shanghai University of Traditional Chinese Medicine (TCM). Their eyes, pupils and IOP were normal and they were assigned into 3 groups by randomization: group 1 (normal group, n=5) received neither perfusion to anterior chambers of the eyes nor electric acupuncture treatment; group 2 (control group, n=10), merely received perfusion to anterior chambers of the eyes as animal models; group 3 (acupuncture group, n=17) first received perfusion to anterior chamber of the eyes and then electric acupuncture treatment.

B. Method for rabbit model with acute high IOP

The animals in control group and acupuncture group were anesthetized with an intravenous injection of 30% sodium urethane (1g/kg body weight), and their cornea with topical anesthesia of 1% dicaine. Then the anterior chambers of the eyes were punctured with an infusion needle (0.5×20 mm) connected to a bottle containing normal saline [5]. The perfusions were kept for 2 hours by elevation of the saline bottle to certain altitude, which was equal to 30 mmHg or 50 mmHg or 70 mmHg. After that, the eyes were applied with acronize ointment to prevent infection.

C. Electric acupuncture treatment

The rabbits in acupuncture group, after high pressure perfusion, were punctured 2 pairs of acupoints, Jingming and Housanli with the filiform needles (0.28×25 mm, Suzhou Medical Appliance Factory, Suzhou, China). The location of Jingming is a little bit mediate to the inner canthus of the eye, while Housanli is about 1.2 cm inferior to the head of fibula and 1 cm posterior to the crista of tibia [6]. After the needles were inserted to the above points and rotated for a while to get Qi arrived, they were connected to the G6805-2 electron treatment device (Shanghai Medical Electron Equipment Company, Shanghai, China). Sparse-

dense waves were out to stimulate the points for 20 minutes with the intensity that was the maximum for animals to tolerate. The treatment was done on alternate days with total 6 times.

D. Tissue preparation

2 weeks later, all the 32 rabbits were anesthetized with the same methods, an intravenous injection of 30% sodium urethane and topical anesthesia of 1% dicaine on eyes. Then the eyes were enucleated and transversely cut through its equator. The posterior poles of the eyes were rapidly fixed in 2% glutaraldehyde. 2 hours later, the side inferior-temporal to the head of optic nerve was divided into small sections (about 1×6 mm) and left in the same fixative. The specimens were washed in buffer, post fixed in 1% osmium tetroxide, dehydrated in ascending grades of alcohol, immersed in propylene oxide and embedded in 618 epon. While ultrathin sections (70 nm, cut by Leica A-1170, Germany) were mounted on copper grids and stained with uranyl acetate and lead citrate, they were examined under transmission electron microscope (Philips Tecnai-12, Holland)[7].

III. RESULT

A. Normal group

The eyes of 5 normal rabbits have been observed ultra-structurally. The intracellular structures of RGCs were noticed clearly. The nuclei and its membranes of RGCs appeared normal. The color of cytoplasm was dark and abundant organelles were seen, such as mitochondria, rough endoplasmic reticulum (RER), Golgi's apparatus etc. But a small amount of cytolysosomes could also be seen (Fig. 1).

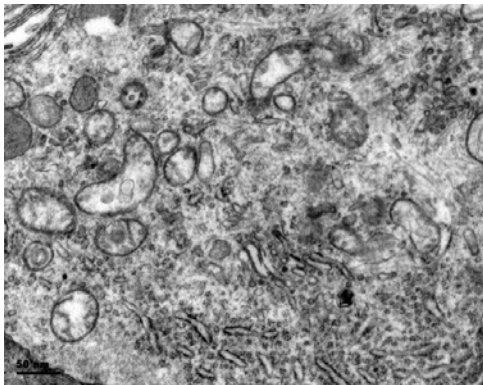


Fig. 1 Normal group (at 11500× magnification) showing mitochondria, rough endoplasmic reticulum, Golgi's apparatus and cytolysosomes

B. Control group

This group was divided into three subgroups according to their different pressures of perfusion. The eyes of 3 rabbits were perfused under 70 mmHg of normal saline, 3 rabbits under 50 mmHg of normal saline and 4 rabbits under 30 mmHg normal saline.

In eyes under 70 mmHg perfusion of normal saline, ultra-structurally, the color of cytoplasm in some RGCs was light. Some of its RER showed degranulation. Swollen Golgi's apparatus, vacuolated mitochondria with severe broken cristae and a large amount of cytolysosomes were noticed (Fig. 2).

In eyes under 50 mmHg perfusion of normal saline, ultra-structurally, some of its RER showed degranulation, mildly swollen Golgi's apparatus and vacuolated mitochondria with broken cristae were present and a large amount of cytolysosomes were also noticed (Fig. 3).

In eyes under 30 mmHg perfusion of normal saline, ultra-

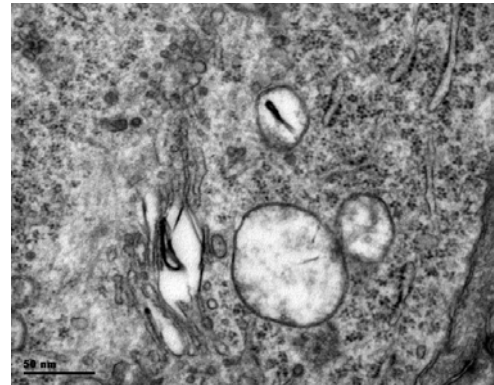


Fig. 2 Control group 70 mmHg perfusion (at×26500 magnification) showing swollen Golgi's apparatus and vacuolated mitochondria with severe broken cristae

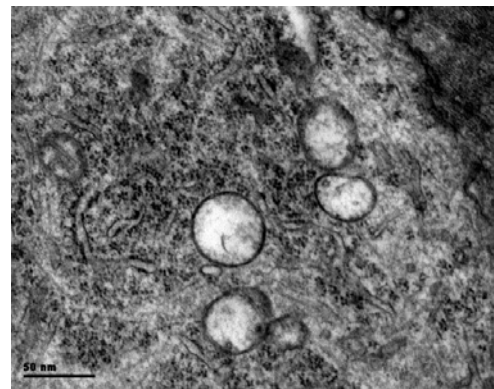


Fig. 3 Control group 50 mmHg perfusion (at×26500 magnification) showing vacuolated mitochondria with broken cristae

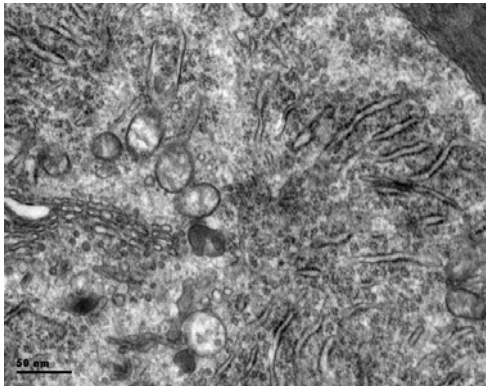


Fig. 4 Control group 30 mmHg perfusion (at $\times 20500$ magnification) showing some vacuolated mitochondria and a small amount of cytolysosomes

structurally, organelles of RGCs were more abundant than the ones under 50 mmHg or 70 mmHg perfusion of normal saline. Its RER and Golgi's apparatus were in almost normal performance. Still some vacuolated mitochondria could be found in RGCs and there were a small amount of cytolysosomes (Fig. 4).

C. Acupuncture group

This group was also divided into 3 subgroups as in control group, but the rabbits were received electric acupuncture treatment. The eyes of 5 rabbits were perfused under 70 mmHg normal saline, 6 rabbits under 50 mmHg normal saline and 6 rabbits under 30 mmHg normal saline.

In eyes under 70 mmHg perfusion of normal saline, transmission electron microscopy appeared that the intracellular appearances were as same as the control group under 70 mmHg perfusion, such as light color of cytoplasm in some RGCs, some RER with degranulation, swollen Golgi's apparatus, vacuolated mitochondria with severe broken cristae and a large amount of cytolysosomes (Fig. 5).

In eyes under 50 mmHg perfusion of normal saline, ultrastructurally, the color of cytoplasm in some RGCs was light, its RER and Golgi's apparatus were present well, and still some vacuolated mitochondria with mildly broken cristae could be found in RGCs but it was better than the control group under 50 mmHg perfusion (Fig. 6).

In eyes under 30 mmHg perfusion of normal saline, transmission electron microscopy showed relatively intact RGCs. The color of cytoplasm in many RGCs was dark and its RER and Golgi's apparatus were present well. However, a little mildly vacuolated mitochondria as well as a small amount of cytolysosomes in RGCs could be found (Fig. 7).

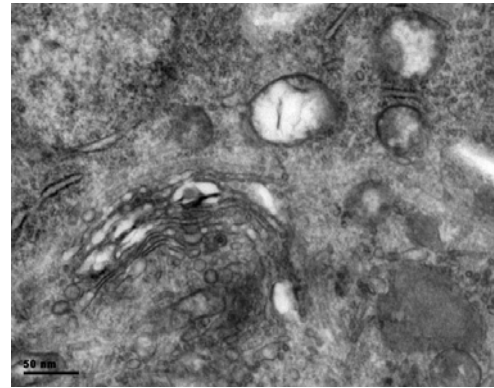


Fig. 5 Acupuncture group 70 mmHg perfusion (at $\times 20500$ magnification) showing swollen Golgi's apparatus, vacuolated mitochondria with severe broken cristae and a large amount of cytolysosomes

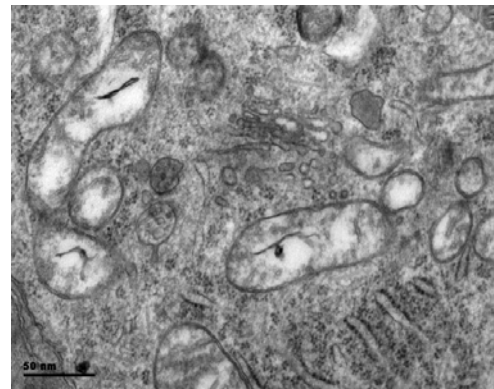


Fig. 6 Acupuncture group 50 mmHg perfusion (at $\times 26500$ magnification) showing mitochondria with some cristae, rough endoplasmic reticulum and Golgi's apparatus

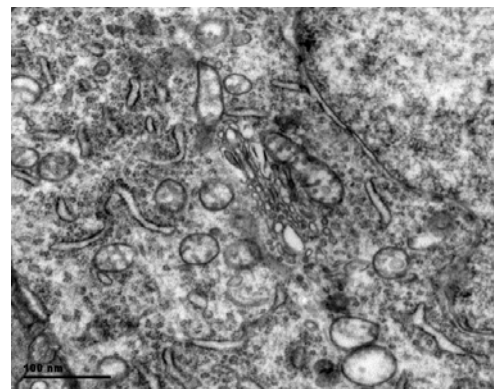


Fig. 7 Acupuncture group 30 mmHg perfusion (at $\times 16000$ magnification) showing rough endoplasmic reticulum and Golgi's apparatus presented well, mitochondria with some cristae noticed

IV. DISCUSSION

The models used in this experiment were shown successfully. The ultrastructural intracellular structures of RGCs were changed relatively under 70 mmHg, 50 mmHg and 30 mmHg perfusion of normal saline in rabbits for 2 hours. Transmission electron microscopy showed, for example, that the color of cytoplasm in some RGCs was light, some of its RER showed degranulation, and swollen Golgi's apparatus and vacuolated mitochondria with broken cristae and a large amount of cytolysosomes were noticed. The intracellular structure changes were obviously different comparing with the ones in normal rabbits. The perfusion injury model of rabbit, which could result in experimental acute high IOP, is an easy and useful way in research of experimental glaucoma. Generally speaking, the transmission electron microscopy in this study discovered what was usually difficult to discover under light microscopic examination. These changes, however, were similar to reports from someone else's [2].

The study showed that the electric acupuncture had a relatively beneficial effect on the lesion of RGCs in rabbits under high pressure perfusion. In electric acupuncture treatment group, especially for rabbits models under 30 mmHg perfusion, this effect was significantly obvious because the ultrastructural results appealed relatively intact RGCs. And for rabbits models under 50 mmHg perfusion, electric acupuncture treatment still performed some effect on the injured RGCs. So these might be ascribed to acupuncture's modifications to the effected neurons. By deduction, electric acupuncture might be used for vision injury of glaucoma with moderate high IOP. Acupuncture can be an assistant therapy for glaucoma.

The study had put in use of G6805-2 electron treatment device, as it's one of the most commonly used devices in acupuncture clinics. The output wave was sparse-dense as its frequency was changing alternatively and regularly, thus the animals were not easy to get used to the electric current. The intensity of electric current was based on the endurance of rabbits according to the routine in acupuncture clinics.

The first acupoint used in this study was Jingming (BL1), which is pertaining to Gallbladder Meridian of Foot Shaoyang. Because it locates near the eye, it's one of the most important acupoints for eyes diseases. Clinically, this acu-

point should be cared for preventing bleeding from needling and not hurting the eyes. The second one was Housanli, which is similar to the famous acupoint, Zusanli (ST36). Zusanli (ST36) is pertaining to Stomach Meridian of Foot Yangming. Although it is on leg, it is usable in strengthening the function of spleen and stomach and benefiting to Qi and blood [8]. According to TCM theory, Qi and blood are helpful to vision, with an old saying that the bright vision would be if Qi and blood were enough.

ACKNOWLEDGMENT

Supported by a grant from Shanghai Natural Science Foundation, Shanghai, China, 04ZR14129

REFERENCES

1. Quigley HA, Nichells RW, Kerrigan LA et al. (1995) Retinal ganglion cell death in experimental glaucoma and after axotomy occurs by apoptosis. *Invest Ophthalmol & Vis Sci* 36: 774-786
2. YUAN Huiping, CHU Liqun, WANG Lina et al. (2004) Apoptosis of retinal ganglion cells in experimental high intraocular pressure of rabbits. *China Ophthal Res.* 22(2):180-182
3. JIANG Jun, YAN Zhenguo, TAI Haoqing et al. (1999) A study on the acupuncture treatment of primary glaucoma. *Acupuncture Research.* 24(2): 95-97
4. Zhao Junjing, Li Zhiyong. (1999) A review of literature on present situation of glaucoma in the clinical study and experimental research. *Journal of Traditional Chinese Ophthalmology* 9(3): 189-191.
5. ZHOU Yifeng, TAO Lirming, ZHANG Jiwen et al. (2002) Influence on cat retinal ganglion cells by acute intraocular pressure elevation. *Basic Medical Sciences and Clinic* 22(5):469-472
6. LIN Wenzhu. The guideline for experimental acupuncture (1989) Publishing House of Shanghai College of TCM, Shanghai
7. Kanji Takahashi, Tim T. Lam, Jun Fu et al. (1997) The effect of high-dose methylprednisolone on laser-induced retinal injury in primates: an electron microscopic study. *Graefes Arch Clin Exp Ophthalmol* 235:723-732
8. CHEN Xinnong. *Chinese Acupuncture and Moxibustion*. (2003) Foreign Languages Press, revised edn, Beijing

Author: Zhou Wenxin

Institute: College of Acumox and Tuina, Shanghai University of TCM

Street: 1200 Cailun Road

City: Shanghai

Country: China

Email: zhouwenxin@citiz.net

Quantitative Research on Analgesic Effects of Electroacupuncture at Multiple Factors Parameters in Rats of Adjuvant-Induced Arthritis

Le Kuai, Huayuan Yang, Jie Jiang

Lab of TCM Engineering, College of Acupuncture-Moxibustion and Tuina, Shanghai University of TCM, Shanghai 201203, China

Abstract — **Objective** To research into the best parameters plan of electroacupuncture for treating pain in rats of adjuvant-induced arthritis (AA). **Methods** One hundred and twenty Wistar rats were randomly divided into 12 groups. Rats of AA arthritis were treated by electroacupuncture at different frequencies, waveforms and current. The analgesia effects of these groups were compared by orthogonal experiment and so on. Pain threshold and the contents of β -EP in local tissues of inflammation were observed. Parameters of electroacupuncture were measured. **Results** Optimized parameters plan of raising pain thresholds was: 100Hz, 0.1mA, intermittent wave. Electroacupuncture at 100Hz was prior to that at 2 Hz in increasing the contents of β -EP. Difference of analgesic effects of electroacupuncture between 4/20Hz, 0.1mA, dense-disperse wave and 100Hz, 0.1mA, intermittent wave on inflammatory pain in rats had no statistics significance ($P > 0.05$). **Conclusions** Optimized parameters plan of electroacupuncture should be selected in treating pain in rats of AA. Quantization and standardization of electroacupuncture should be further enhanced.

Keywords — Electroacupuncture; Stimulating Parameters/acup eff; Acupuncture Analgesia

I. INTRODUCTION

Analgesic effect of electroacupuncture is definite. There are some researches of electroacupuncture parameters that indicate electroacupuncture at different parameters has different central and peripheral effects and analgesic mechanism^[1,2]. But the former researches of electroacupuncture parameters often used the single factor analysis, the results was relatively isolated and limited, and seldom selected multi-factors and multi-levels analysis. Among parameters of electroacupuncture, frequency, waveform and current intensity are main parameters, which can be regulated. This experiment compared the analgesic effects of electroacupuncture at the above factors parameters in rats of adjuvant-induced arthritis (AA), to probe into the best parameters plan of electroacupuncture for treating inflammatory pain. It was reported as follows.

II. MATERIALS AND METHODS

A. Experimental animal and grouping

One hundred and twenty female Wistar rats, weighing between 170 and 200g, supplied by animal department of Shanghai University of TCM, were randomly divided into 12 groups by randomized grouping plan formed by SPSS software, 1 normal control group, 1 model group and 10 electroacupuncture treatment groups, 10 rats in each group. Eight electroacupuncture groups accorded with orthogonal design, orthogonal table $L_8(2^7)$ was selected to observe the analgesic effects of parameters at three factors (A frequency, B waveform, C current), two levels (A1: 2Hz, A2: 100Hz; B1: successive wave, B2: intermittent wave; C1: 0.1mA, C2: 0.2mA), and the reciprocal effects of $A \times B$, $A \times C$ and $B \times C$. Eight groups are $A_1B_1C_1$, $A_1B_1C_2$, $A_1B_2C_1$, $A_1B_2C_2$, $A_2B_1C_1$, $A_2B_1C_2$, $A_2B_2C_1$ and $A_2B_2C_2$ electroacupuncture groups. The other 2 groups are $A_3B_3C_1$ (4Hz/20Hz, dense-disperse wave, 0.1mA) and $A_3B_3C_2$ (4Hz/20Hz, dense-disperse wave, 0.2mA) electroacupuncture groups.

Normal control group: The rats were fixed for 20 min once everyday since the 2nd day of the experiment as the same method of the rats in treatment groups for successive 6 d.

Model group: On the 1st day, Freund's complete adjuvant 0.1 ml was injected into right postpotes of rat through foot pad to lateral malleolus. The rats were disposed as the rats in normal control group since the 2nd day.

Electroacupuncture group: On the 1st day, the model was made as the method of model group. Since the 2nd day, the rat was treated by electroacupuncture once everyday. The rat was fixed by the rat clamp. The filiform needles of 25 mm in length and 0.30 mm in diameter were punctured perpendicularly 0.3~0.5 mm into Kunlun (BL60, in the depression between the external malleolus and tendo calcaneus of hind limb) and Xuanzhong (GB39, 10 mm directly above the tip of the external malleolus). G6805 electrotherapy instrument was determined the unloaded current intensity by UT50A digital multimeter. Then the needles were connected to G6805 electrotherapy instrument with the different parameters for 20 min. The treatment was given for the successive 6 days.

Pain thresholds and swelling degrees of joints of all the rats in the 5 groups were determined before making the model on the 1st day and the electroacupuncture treatment on the 2nd day, and after the electroacupuncture treatment on the 4th day and the 7th day.

B. Method of determination

Pain thresholds of joints of all the rats in the 12 groups were determined before making the model on the 1st day and the electroacupuncture treatment on the 2nd day, and after the electroacupuncture treatment on the 7th day. After the determination of pain thresholds on the 7th day, the rats were put to death and the tissue of right postpapes was got for determination of β -EP.

Determination of pain threshold: It was determined by the latent period of withdrawing leg reaction for heat pain induced by the irradiation of radiant heat lamp with YLS-12A illumination pain threshold detector. The interval was 5 min between the twice determinations. The average value of three times was the value of pain threshold. The irradiation was stopped when the value of pain threshold exceeded 10 s to prevent the injury of skin. Pain threshold before treatment on d 2 was the basic pain threshold. Change rate of pain threshold = [(post-treatment pain threshold - basic pain threshold) / basic pain threshold] \times 100%.

Determination of β -EP: On the 7th day, skin and hypoderma 100mg of foot pad and external malleolus of right postpapes were got to cook in boiled normal saline for 5 min immediately. They were taken out and added 1mol/L HCL 1ml to homogenate. After they were placed in homogenate for 2 h, 1mol/L NaOH 1ml was added, 4°C 4000r/min centrifugalization was done for 120min, then supernatant was got to conserve below -20 °C. Radio immunoassay was used and the method accorded with directions of kit.

Measure of electroacupuncture parameters: The loaded and unloaded electroacupuncture parameters, such as waveform, amplitude, current intensity and voltage, were measured by Tektronix TDS2002 Digital Storage Oscilloscope and UT50A digital multimeter.

C. Statistical methods

SPSS 12.0 statistical software was used. Multifactorial orthogonal ANOVA and one-way AVOVA were done.

III. RESULTS

A. Comparison of pain threshold in AA rats in various groups

There was no significant difference in pain threshold among the 12 groups before making the model on the 1st day ($P > 0.05$). The pain thresholds in the model group and 10 treatment groups wave group were lower than those in the control group before the electroacupuncture treatment on the 2nd day ($P < 0.01$), which indicated the existence of states of hyperalagia in AA rats. After the electroacupuncture treatment on 7th day, the pain thresholds in the model group were still lower obviously than those in the control group ($P < 0.01$), the pain thresholds in treatment groups wave group were higher than those in the model group ($P < 0.05$, $P < 0.01$), which indicated all the electroacupuncture at different parameters had the analgesic effect in AA rats. Seen in Table 1.

Eight treatment groups in orthogonal design, the order of factors of electroacupuncture parameters arranged by range R value of post-treatment pain threshold and change rate of pain threshold was: frequency, current and waveform. Seen in Table 2. Multifactorial orthogonal ANOVA of pain threshold showed that there was significant difference in A, C and $A \times B$ ($P < 0.01$, $P < 0.05$), B and the rest reciprocal effect were unobvious. Then according to binary table, the better configuration of reciprocal effect was got, level B2 was good when A2. The optimum parameters plan of post-treatment pain threshold was A2 (100Hz), C1 (0.1ma) and B2 (intermittent wave). Multifactorial orthogonal ANOVA of change rate of pain threshold showed that there was significant difference in A and C ($P < 0.01$), B and the reciprocal effect were unobvious. The optimum parameters plan of post-treatment pain threshold was A2 (100Hz), C1 (0.1ma). Wave could be selected freely.

Comparing $A_3B_3C_1$, $A_3B_3C_2$, $A_2B_1C_1$ with $A_2B_2C_1$ treatment groups, one-way AVOVA showed that post-treatment pain threshold in $A_3B_3C_2$ treatment group was lower than that in $A_2B_2C_1$ treatment group ($P < 0.05$), and there was no significant difference between the other groups ($P > 0.05$). Change rate of pain threshold in $A_3B_3C_2$ treatment group was lower than that in $A_2B_2C_1$ and $A_2B_2C_1$ treatment groups ($P < 0.05$). There was no significant difference between $A_3B_3C_1$ and $A_2B_1C_1$, $A_2B_2C_1$ treatment groups ($P > 0.05$).

B. Comparison of β -EP content of local tissue in AA rats in various groups

β -EP contents in the model group were higher obviously than those in the control group ($P < 0.01$). β -EP contents in

A₂B₁C₁, A₂B₂C₁, A₂B₂C₂, A₃B₃C₁ and A₃B₃C₁ treatment groups were lower than that in model group (P<0.05, P<0.01). Seen in Table 1.

Eight treatment groups in orthogonal design, the order of factors of electroacupuncture parameters arranged by range R value of β-EP contents was: frequency, waveform and current. Seen in Table 2. Multifactorial orthogonal ANOVA of pain threshold showed that there was significant difference in A (P<0.05), B, C and the reciprocal effect were unobvious. The optimum parameters plan of β-EP contents was A₂(100Hz). Combined with the comparison result in Table 1, A₂B₁C₁, A₂B₂C₁ and A₂B₂C₂ treatment groups had the effect of reducing β-EP content.

Comparing A₃B₃C₁, A₃B₃C₂, A₂B₁C₁ with A₂B₂C₁ treatment groups, one-way AVOVA showed that there was no significant difference between the groups (P>0.05).

C. Measure results of the electroacupuncture parameters

Electroacupuncture parameters of electroacupuncture at 100Hz and successive wave were seen in Table 3. Loaded (when electrode of electroacupuncture instrument was connected with the acupuncture needle inserting acupoints of rats) current, voltage and peak-to-peak value were lower than unloaded. Waveform, frequency and pulse width were unchanged. At the same frequency, frequency, current,

Table 1 Comparison of post-treatment pain threshold, change rate of pain threshold and content of β-EP in 12 groups ($\bar{x} \pm s$)

Group	N	Post-treatment pain threshold (s)	Change rate of pain threshold (%)	β-EP (ng/g)
Control	10	7.57±0.85	-1.31±4.27	0.82±0.48
Model	10	4.08±0.80★★	-7.52±7.25	4.10±2.62★
A ₁ B ₁ C ₁ treatment	10	6.15±0.92★★▲▲	48.37±36.55▲▲	6.04±3.36★★
A ₁ B ₁ C ₂ treatment	10	5.46±1.20★★▲▲	14.42±11.46	5.37±2.65★★
A ₁ B ₂ C ₁ treatment	10	5.64±0.89★★▲▲	27.08±21.87▲▲	7.40±3.83★★
A ₁ B ₂ C ₂ treatment	10	4.96±0.49★★▲	18.60±15.34▲	6.03±2.31★★
A ₂ B ₁ C ₁ treatment	10	6.33±0.64★★▲▲	48.67±27.57▲▲	7.87±5.21★★▲
A ₂ B ₁ C ₂ treatment	10	6.00±0.59★★▲▲	41.34±19.71▲▲	6.95±3.99★★
A ₂ B ₂ C ₁ treatment	10	6.67±0.63★★▲▲	45.96±21.05▲▲	8.81±4.99★★▲▲
A ₂ B ₂ C ₂ treatment	10	6.21±0.83★★▲▲	42.80±20.08▲▲	8.31±3.47★★▲
A ₃ B ₃ C ₁ treatment	10	6.29±0.91★★▲▲	53.79±23.93▲▲	9.34±4.39★★▲▲
A ₃ B ₃ C ₂ treatment	10	5.81±0.92★★▲▲	27.28±18.93▲▲	8.82±4.20★★▲

Compared with control group, ★ P<0.05, ★★ P<0.01 ; compared with model group, ▲ P<0.05, ▲▲ P<0.01.

Table 2 Range R value of post-treatment pain threshold, change rate of pain threshold and content of β-EP influenced by the factors in orthogonal design

Index	A (Frequency)	B (Waveform)	C (Intensity)	Primary and secondary order		
Post-treatment pain threshold	0.763	0.115	0.540	A	C	B
Change rate of pain threshold	17.575	4.583	13.233	A	C	B
β-EP	1.775	1.080	0.865	A	B	C

Table 3 Electroacupuncture parameters of electroacupuncture at 1 00Hz and Successive wave

Group	Current (mA)		Voltage (V)		Peak-to-peak value (V)	
	Unloaded	Loaded	Unloaded	Loaded	Unloaded	Loaded
A ₂ B ₁ C ₁ treatment	0.1	0.025	0.046	0.040	3.36	2.56
A ₂ B ₁ C ₂ treatment	0.2	0.075	0.156	0.103	12.2	6.60

voltage, peak-to-peak value and pulse width were same between the successive and intermittent wave and the stimulating time in unit time of intermittent wave was reduced than that of successive wave. At the same scale of intensity knob, peak-to-peak value of voltage was same when different waveform and frequency was selected.

IV. DISCUSSION

The electroacupuncture therapy has the virtues of simple and convenient manipulation, credible therapeutic effect, safe use, is easy to control the factors of stimulation compared with acupuncture, and is applied increasingly extensively at home and abroad at present. G6805 electroacupuncture apparatus is the most commonly used in acupuncture clinic and scientific research. Electroacupuncture parameter is one of the important factors in influencing the therapeutic effect of acupuncture. Frequency of output impulse of G6805 electroacupuncture apparatus can be selected from 0.6 to 100 Hz. Our experiment selected the frequently used 2Hz (low frequency) and 100Hz (high frequency) in the former researches of analgesic effect of electroacupuncture at different frequency^[3]. Its output waveforms are successive wave, intermittent wave and dense-disperse wave and the frequency of dense-disperse wave is fixed at 4Hz/20Hz. Current or voltage is controlled by intensity knob. According to our former research, the higher 0.2mA and the lower 0.1mA that the rats could be tolerated were selected^[4]. Orthogonal design is the most effective design method in the experiment of multi-factors and multi-levels and can identify primary or secondary rank of various factors, high or low grade of various levels, and which factors has reciprocal effect, to find out the optimum plan of various factors. The research of electroacupuncture parameters also fit to use this method to save considerable number of experimental samples and achieve the abundant effective information. So we used this method in this experiment.

AA model of rat is the received experimental arthritis model and good clinical pain model with the symptoms of red, swelling, heat and pain in acute period, like the "Heat Bi" in TCM. It was used widely in empirical study^[5]. Pain threshold is the index of estimating the analgesic effect, which is adopted abroad at present. β -EP is the main analgesic material in the system of endogenous opioid peptides. Endogenous opioid peptides participates mechanism of peripheral analgesia in treating inflammatory pain by electroacupuncture.

This experiment's result showed that optimized parameters plan of raising pain thresholds was: 100Hz, 0.1mA and intermittent wave. Electroacupuncture at 100Hz was prior to that at 2 Hz in increasing the content of β -EP. The increase of local analgesic material, β -EP content, is one of mechanism of peripheral analgesia. The central mechanism should be research in the future. Difference of analgesic effects of electroacupuncture between 4/20Hz, 0.1mA, dense-disperse wave and 100Hz, 0.1mA, intermittent wave on inflammatory pain in rats had no statistics significance. The methods of isoeffect test or increase of sample size can be done to further compare. So optimized parameters plan of electroacupuncture should be selected in treating inflammatory pain.

At the same time, the selected electroacupuncture parameters were measured by technologies such as frequency spectrum analysis and the different influences of changes of these parameters were discussed. We found it was difficult in adjusting accurately to the needed current by intensity knob. The current value was changed by a little turning of knob. So every time before electroacupuncture therapy, the current should be measured by digital avometer. G6805 electroacupuncture apparatus is used from 1970 to now. Though it is improved, the problems such as inadequate adjusting precision of stimulus intensity and electromagnetic interference still exist. Development of acupuncture science needs the advancement of acupuncture instrument. In the period of fast development of high science and technology, the research and exploitation of acupuncture instrument also should combine the acupuncture and multi-subjects of modern science and technology. In the future, the new acupuncture instruments which apply advanced technology should be further exploited and spread, and technology platform of crossed multi-subjects should be organized to enhance the quantification, objectivity and standardization of acupuncture, so as to promote the development of acupuncture science and contribute much more to human health.

V. CONCLUSIONS

Optimized parameters plan of electroacupuncture should be selected in treating pain in rats of AA arthritis. Quantization and standardization of electroacupuncture should be further enhanced.

REFERENCES

1. Taguchi T, Taguchi R. Effect of varying frequency and duration of electroacupuncture stimulation on carrageenan-induced hyperalgesia. *Acupunct Med*, 2007;25(3):80
2. Kuai L, Yang HY. Advance Clinical and Experimental Research on the Quantification of Electroacupuncture Parameter. *Journal of Clinical Rehabilitation*, 2002;6(15):2224-2226
3. Jiang YX, Wang Y, Liu HX, et al. Comparison between Therapeutic Effects of Transcutaneous Electrical Nerve Stimulation with the Frequency of 2 Hz and 100 Hz on Chronic Inflammatory Pain in Rats. *Chinese Journal of Integrated TCM and Western Medicine*, 2001;21(12):923-926
4. Kuai L, Yang HY, Liu Tangyi. Quantificational Research on Effects of Electroacupuncture at Different Parameters on Analgesia in Rats of Adjuvant-Induced Arthritis. *Journal of Biomedical Engineering*, 2007;24(1):186-190
5. Takahashi K, Okumura S, Sato J, et al. Adjuvant-induced arthritis. *Nippon Rinsho*. 2005 Jan;63 Suppl 1:51-54

Computer-Aided analyzing system in root canal therapy

Hu Qingxi, Song Chenxia, Yao Yuan, Lu Qi

Rapid Manufacturing Engineering Center, Shanghai University,
Shanghai 200444, P. R. China

Abstract—To develop a new system that can evaluate the relative performance of the root canal shaping instruments via accurately measuring root canal geometric centerline, root canal ‘thickness’ (diameter), root canal sectional profile area, and root canal volume before and after the root canal preparation.

Extracted human maxillary molars were scanned before and after root canal shaping employing micro-computed tomography at an isotropic resolution of 34 μm . Three-dimensional root canal models were reconstructed. The C# language was adopted to compile the: “Computer-aided analyzing system in root canal therapy”, which could quantitatively evaluate the root canal shaping ability by accurate measuring root canal geometric parameters mentioned in above. Preparation errors such as apical zips, perforations and fractured instruments were visually determined from those models.

Volume and surface area increased significantly and similarly in root canals after preparation. Mean root canal sectional diameter (which is 12mm coronal to the apex) increased from 0.31mm to 0.52mm. Mean volume, increased from 7mm³ to 10mm³. From the root canals centerline graph, the root canals were significantly straightened during preparation. After the testing in the actual root canal treatment, the evaluation of the root canal geometry changes before and after the preparation can be made by the Computer- Aided analyzing system.

Keywords—micro-computed tomography, root canal preparation, centerline, volume, sectional area

I. INTRODUCTION

Endodontic therapy involves cleaning and shaping the root canal so that patients can retain their natural teeth in function and esthetics [1]. Although successful root canal therapy depends on many factors, the key step in any root canal treatment is canal preparation. This is essential because preparation determines the efficacy of all subsequent procedures and includes mechanical debridement, creation of space for medicament delivery, and optimized canal geometries for adequate obturation [1] [2]. So evaluating the changes of root canal geometry before or after preparation in more detail becomes more and more important. This study introduces a new system permitting root canal geometric centerline, canal sectional profile diameter, sectional

area and volume before or after preparation as evaluate indicators to evaluate the outcome of the root canal preparation.

II. PRINCIPLES AND METHODS

A. System flow chart

The system flow^[3] mainly contains two parts: reconstructing the three-dimensional images by the μCT data; calculating the root canal evaluating geometric parameters : geometric centerline, root canal ‘thickness’ (diameter), root canal sectional profile area, and root canal volume. Fig.1

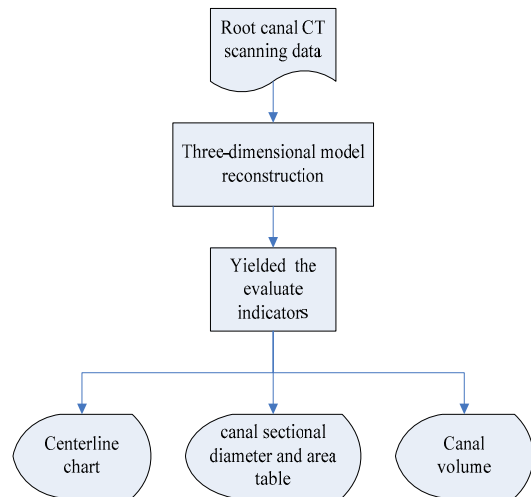


Fig. 1 System flow chart

B. Three-dimensional reconstruction

Extracted human maxillary molars canals were scanned before or after shaping employing micro-computed tomography at an isotropic resolution of 34 μm [4]. Then the rapid contrary engineering software Mimics10.01 of the Materialise Company was adopted to complete the three-dimensional images of the root canals reconstruction.

Finally three-dimensional images of the root canals were directly converted into STL file format and got the best accuracy. The main steps are as follows:

Step1: Input the Dicom format image data into Mimics8.1.

Step2: Determine the spatial position of the root canal.

Step3: Regulate the reshould value of the root canal to eliminate noise of the root canal images .The reshould value of the root canal is 226~3071.

Step4: Reconstruct three-dimensional root canal and converted the 3D images into the STL documents.

Furthermore the software Magics11 also produced by Materialise Company was adopted to revise the surface of the root canal and complete three-dimensional root canal reconstruction [5].Steps are as follows:

Step1: Import the STL document of root canal into Magics11.

Step2: Modify the 3D model of the root canal: Deleting excrescent points, filling loophole, smoothing 3D model surface.

Finally the three-dimensional images of the root canals were reconstructed. And the canals were again scanned, as above, after shaping so that each canal served as its own control.

Subsequently, the C# language[6] was adopted to compile the Computer-added analyzing system, which can quantitatively calculate the root canal geometric centerlines, root canal diameter profile areas and root canal volume.

This system uses overall data interface settlement scheme: 1) Supporting the network environment.2) Supporting the method of DICOM [7] communication network pass to procure data and can directly read standard DICOM's 3.0 format files from the network.3) directly reading the data file ACR-NEMA2.0's format.4) Supporting the various general image format like BMP/JPEG/TIFF etc, which makes it can be easily integrated into a service oriented medical analyzing architecture due to above features.

C. Calculate the evaluating parameters

Adopting the C# language to obtain the profiles points of the root canal. Series parallel planes which parallel the XOY plane were used to intercept the root canal. And then the loop points on the profiles were acquired.

- .Calculating the centerline

The center point of the section was calculated according the loop points on the profile. The needed center point for evaluating the root canal was the largest inscribed circle of the profile. The main calculate process of the centerline is described as follows:

Step1: Read the information of each section profile from the STL model of the root canal. Slicing the STL model, let N denote the total amount of profiles. The profiles are described by a set of loop points X, Y and Z coordinates (x_i, y_i, z_i). Let n denote the total amount of points on the profile. The average value point O of the loop points on the jth profile is defined as follows (fig.2).

$$x_c = \frac{\sum_{i=1}^n x_i}{n} \tag{1}$$

$$y_c = \frac{\sum_{i=1}^n y_i}{n} \tag{2}$$

$$z_c = z_i \tag{3}$$

Step2 : As show in fig.2 the average value of the loop points wasn't the needed evaluating center point of the jth profile. The center point can be estimated by the following method. Find the point P on the profile which was nearest point to the average point and the center point was on the PO line. (fig.3)

Step3 : Offset the point O (x_c, y_c) Δd step each time along the line PO to find the maximum inscribed circle and the center point O1 .(fig.4)

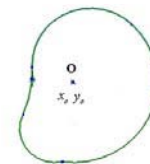


Fig. 2 the average value point

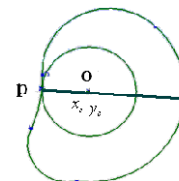


Fig. 3 the nearest point p

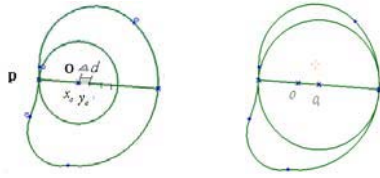


Fig. 4 find the center point

Step3 : Then, center points of the canals, calculated for each slice, were connected along the z-axis by a fitted line.

- Calculating the root canal sectional area and root canal volume

Read the loop points(x1, y1), (x2, y2)... on the jth sectional profile and the calculated center point (x0, y0) of the jth section. So the sectional area s_j denotes as follow.

$$s_j = \frac{1}{2} \begin{vmatrix} x_0 & y_0 & 1 \\ x_1 & y_1 & 1 \\ x_2 & y_2 & 1 \end{vmatrix} \quad (4)$$

- Calculating the root canal volume

The method of calculating the root canal's volume is described as follows.

Step 1: Read the information of each triangular facet from the STL model of the root canal, and store it in the buffer. In a STL file, triangular facets are described by a set of X, Y and Z coordinates for each of the three vertices and a unit normal vector with X, Y and Z to indicate which side of facet is an object. Let N denote the total amount of triangular facets which can be obtained directly from the STL file.

Step 2: Let $P_{i1} (X_{i1}, Y_{i1}, Z_{i1})$, $P_{i2} (X_{i2}, Y_{i2}, Z_{i2})$ and $P_{i3} (X_{i3}, Y_{i3}, Z_{i3})$ be the X, Y and Z coordinates of the three vertices for the ith triangular facet respectively. Let $F_{Ni} (n_iX, n_iY, n_iZ)$ represent its unit normal vector. Therefore, the surface of the ith triangular facet is defined asEqu.3

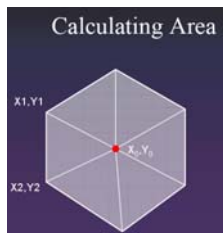


Fig. 5 calculate the area

$$s_i = \frac{1}{2} \left| \overrightarrow{p_{i1}p_{i2}} \times \overrightarrow{p_{i1}p_{i3}} \right| \quad (5)$$

Step 3: Let Z_i be the height along Z-axis for the ith triangular facet, and $Z_i = 1/3 (Z_{i1} + Z_{i2} + Z_{i3})$. The volume of the prism which is enveloped by the ith triangular facet along Z-axis is given by

$$v_i = s_i \times z_i \quad (6)$$

Step 4: Judge the normal vector along Z-axis of the ith triangular facet. If $Z_{ni} > 0$, $v_i > 0$, then the value of v_i is positive, otherwise negative.

Step 5: Calculate the volume of the STL model by Eq. (7)

$$V = \sum_{i=1}^n v_i \quad (7)$$

III. RESULTS

Briefly, specimens were scanned at anisotropic resolution of 34 μm using a micro-computed tomography system. Scanning of unprepared (Fig.6a) and instrumented canals (Fig.6b) yielded detailed three-dimensional canal images. Three-dimensional image of the root canal models before or after preparation can be shown on the computer screen. Three-dimensional data acquisition became available for the description of canal geometry and possible changes during shaping procedures.

Figure 7 illustrates diameters of canals, evaluated as 'thickness', by plotting means against canal lengths and yielding canal dimension estimates, before and after preparation. Overall, 'thickness' increased significantly while canals were prepared.

Root canal centerlines were used concerning root canal transportation and indicating the ability of a specific instrument to remain centered within the canal.

Root canal centerlines can be displayed in the Computer-Aided analyzing system. (Figure 8)

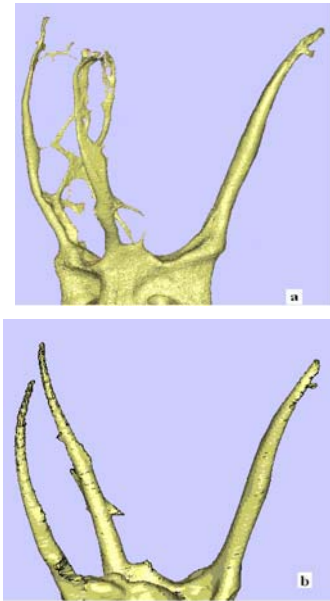


Fig. 6 Images of unshaped (a) and prepared (b) root canal systems reconstructed from μ CT data.

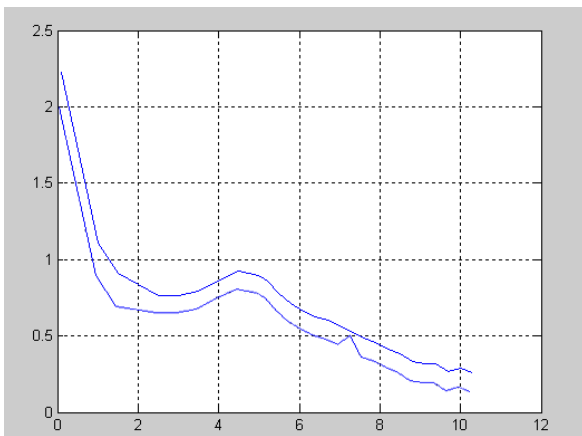


Fig. 7 Canal ‘thickness’ profiles detailing clinical diameters along canal length (mean scores from mesiobuccal canals before or after preparation).



Fig. 8 root canal centerlines

Preparation significantly increased root canals’ volumes.

Table 1 root canal volume unprepared

	Mesiobuccal	Distobuccal	Palatal
volume (mm ³)	5	3	2

Table 2 root canal volume prepared

	Mesiobuccal	Distobuccal	Palatal
volume (mm ³)	7	4	3

IV. CONCLUSION

This study using self-made “Computer-Aided analyzing system” permits three-dimensional evaluation of root canal geometry before and after preparation, by measuring changes in root canal diameter profile area, ‘thickness’ (diameter), and root canal bending angle, the movements of root canal geometry of the centerline before and after the root canal preparation, and quantitatively analyzing the changes and movement. The accurate measurement of root canal bending angle, the location of the centerline, ‘thickness’ (diameter) and canal diameter profile area are more precise and objective than the qualitative descriptions. In addition, the technique yields a mass of exact metric data. After the testing in the actual root canal treatment; the evaluation of the root canal geometry changes before and after the preparation can be made.

ACKNOWLEDGMENT

The authors wish to express their gratitude to Dr Sun zhe for performing the root canal preparations with the Endo-Eze AET system.

REFERENCES

1. Weine F. Endodontic therapy (1982). 3 rd ed. St Louis: C. V. Mosby. 256~340.
2. Vertucci FJ. Root canal anatomy of the human permanent teeth (1984). Oral Surg Oral Med Oral Pathol. 58 (5):589~599.
3. Sun W, Lal P. (2002) Recent development on computer aided tissue engineering-a review. Computer Methods and Program in Biomedicine. 67(2):85~103
4. Morfis A, Sylaras SN, Georgopoulou M, et al. (1994) Study of the apices of human permanent teeth with the use of a scanning electron microscope [J]. Oral Surg Oral Med Oral Pathol.77 (2):172~176.
5. Zhu jianwei .The Computer Assisted Design of the Custom Femur Prosthesis and Relative Research (2006).SuZhou: Suzhou University.
6. Karli Watson, Christian Nagel.Beginning C #language (2006) .Qinghua University.
7. Cox RD, Henri CJ, Rubin K.On-demand server-side image processing for web-based DICOM image display (2000). SPIEPACS: Design and valuation.2435:302~309

Author: HU Qing-xi
 Institute: Shanghai University Rapid Manufacture Engineering Center
 Street: 99 Shangda Rd
 City: shanghai
 Country: China

The Research of an Optimized Boolean Operation Algorithm for Skull Defect Mending

Yuan Yao¹, Fu Wu¹, Qing-xi Hu¹, Gao-chun Xu¹, Fei You¹

¹ Rapid Manufacturing Engineering Center, Shanghai University,
Shanghai 200444, P. R. China

Abstract— An optimized three-dimensional Boolean operation algorithm based on STL model for skull defect mending is given in this paper. Triangulation is a very important step in arithmetic of Boolean. Delaunay Triangulation is a usual method, but its computational efficiency is not high. The STL model of skull is very complicated, so the computational efficiency of algorithm is crucial. This text proposes a new triangulation algorithm to this. It improves the computational efficiency greatly and can be implemented easily. Also, de-noising algorithms are given to the burr error and noises. This algorithm is implemented and applied to skull defect mending in arbitrary condition and it also obtains the model of the defect. It solves the problem that the defect model cannot anastomose the border and optimizes the result.

Keywords— Boolean operation, skull defect mending, triangulation, detaching mesh, STL model.

I. INTRODUCTION

For various reasons, many people suffer from the skull defect, and skull tissue repair with the tissue engineering method has become a hot topic [1, 2]. The structure of the bone scaffold, as cell culture carrier, is very important of the process of cells growth and degradation, so modeling technology of bone repair bionic scaffold plays a key role in the process of repairing defective bone based on tissue engineering. Bone tissue engineering scaffold is fabricated by rapid prototyping quite popularly at present. Therefore, we represent the exported model of the defect by STL file that is widely used in rapid prototyping (RP) system.

Now, the 3-D image reconstruction for the skull has been already riper technically. The all-important problem is how to construct the model of the defect. The initial model of the defect can be obtained by some method in computer graphics. However, there is unavoidable deviation between the initial model of the defect and the original model of the skull. Boolean operations are used to obtain the precise model of the defect.

When the current Boolean operation algorithm applied to the skull with complex configuration, there will be burr problem and some useless noises, which affect that defect model cannot anastomose defect border because of the

deviation to thickness and radian between the initial model of the defect model and the original model of the skull.

An optimized Boolean operation algorithm for skull defect mending based on STL model is given in this paper. Triangulation is a very important step in arithmetic of Boolean. Delaunay Triangulation is a usual method [3], but its computational efficiency is not high [4]. The STL model of skull is very complicated, so the computational efficiency of algorithm is crucial. This text proposes a new triangulation algorithm to this. It improves the computational efficiency greatly and can be implemented easily. Also, de-noising algorithms is given to above-mentioned burr and noises.

The rest of the paper is organized as follows: Section 2 is dedicated to an optimized 3D Boolean Operation algorithm based on STL. Section 3 deals with constructing the model of the defect in this paper. The last section presents experimental results and conclusions.

II. ALGORITHM

A. Topology reconstruction

In light of the characteristics of practical applications, the half-edged structure is used to reconstruct the topology of STL models.

B. Obtaining the intersection loop

Every entity is composed of one or many surfaces. According to geometric continuity of the surfaces, the intersection lines should be loops. From the viewpoint of geometry, the intersection loops should be the critical planes of the intersection surfaces, which is of great importance for detaching the intersection surfaces at latter procedure.

Firstly, we traversed the every triangle of the STL model; we can get the intersection lines between every triangle and all triangles of the other STL model. The intersection lines between the triangles can be got by the method that was proposed by Tomas Möller [5]. Secondly, we can get the adjacent line segments by coincident relation between the vertexes of the two intersection lines. Then we can obtain the loop lines by linking the intersection lines (e.g. Fig.1).



Fig. 1

C. Triangulating the intersection triangles

The intersection surfaces are divided into several surface regions by the loop lines. Because the positional attribute between each region and another STL model is different and when we do Boolean operation, we must keep some regions and discard the other, the intersection surface should be detached according to the loop line. The intersection triangles should be triangulated again for detaching the surfaces reasonably.

The intersection situation between the loop line and the intersection triangles can be divided into three types (e.g. Fig.2).

- (1) Intersect two edges.
- (2) Intersect three edges.
- (3) Intersect one edge.

Two latter cases can transform into the first case. The procedure is as follows. Firstly, find the edge on which have two intersection points and get the middle point of the two points. Then connect the middle point and the diagonal apex and divide the original triangle into the two triangles in first case (e.g. Fig.3).

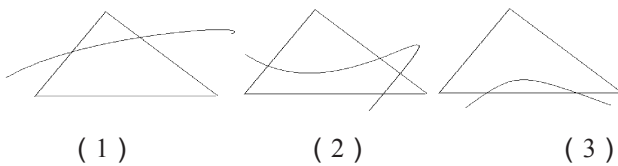


Fig. 2

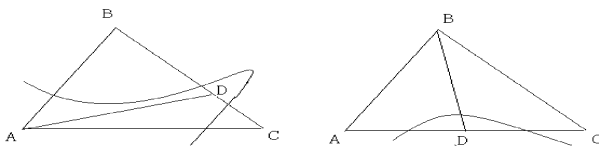


Fig. 3

The triangulating algorithm for each triangle is as follows.

1. Get the set of intersection points (e.g. Fig.4 (a)).
2. Put the set of intersection points in order, find the two edges which have the intersection point, such as edge AB and AC (e.g. Fig.4 (a)), get the intersection points on the edge, such as point O on AB and point P on AC. Project the set of the intersection points on the line OP. Then put the set in order according to the distance from the point in the set to point O.
3. Triangulate the triangle according to the order.

The specific procedure is as follows:

- a) Triangulate the region include vertex A according to the order (e.g. Fig.4 (b)).
- b) Triangulate the region include vertex B and C, The specific procedure is as follows.
 - i. Assume that from the vertex C, judge whether $\angle PCY > \angle PCZ$, if $\angle PCY > \angle PCZ$, go to step ii. Otherwise go to step iii. This step ensures that there is no wrong triangulation. (e.g. Fig.4 (d))
 - ii. Triangulate the region according to the order (e.g. Fig.4 (c)), let next point be P, repeat step i until next point is O.
 - iii. Get the middle point of the line segment BC, let it be Q. Then, divide the region CPOB into the region CPZQ and the region QZOB (e.g. Fig.4 (e)), go to step i.

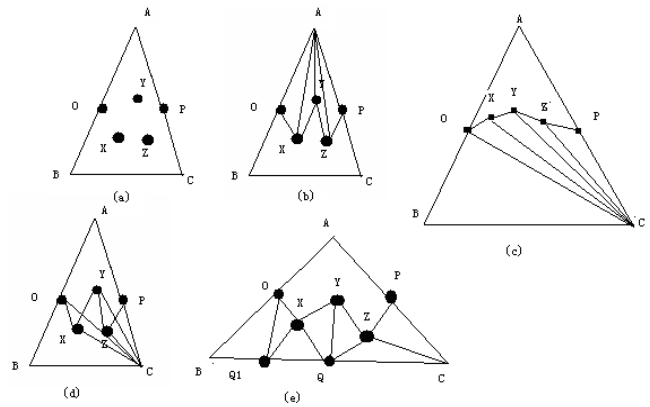


Fig. 4

D. Detaching the patch

The original triangles are replaced by the triangulated triangles. We should detach the surface patches for each STL model, which has different relations to another STL model, according to the loop lines.

In reality, there may be many loops when both STL model are intersecting. Here we assume there is only one loop and the procedure is as follows.

1. Find an edge on the triangle belong to the intersection loop, denoted by $\triangle x$, push it into a vector set, denoted by $v0$.
2. Traversal the all triangles, obtain the adjacent triangle, and get the intersection line. Determine whether the intersection line belongs to the intersection loop. If it is not in the intersection loop, the two adjacent triangles are on the same side and push the adjacent triangles into $v0$. Otherwise push them into another vector set, denoted by $v1$.
3. Let another triangle in $v0$ be $\triangle x$, repeat step 2 until the all triangles in $v0$ are traversed.
4. Let another triangle in $v1$ be $\triangle x$, repeat step 2 until the all triangles in $v1$ are traversed.
5. Exit while the sum of $v0$ and $v1$ equals the number of the all triangles of the STL model.

E. Testing the positional relationship

If a point in a polyhedron X is in another polyhedron B, X is in B. we can judge whether a point in a polyhedron X is in another polyhedron B by ray method. The algorithm of testing the positional relationship is as follows. Use the point as the original point, generate a ray, and judge the times of the ray through the polyhedron. If the times are even, the point is not in the polyhedron. Otherwise, it is in the polyhedron.

Then, we can test the position of every patch. For example, the patches of the polyhedron A and B can be classified into A_in_B , A_out_B , B_in_A , B_out_A (e.g. Fig. 5)

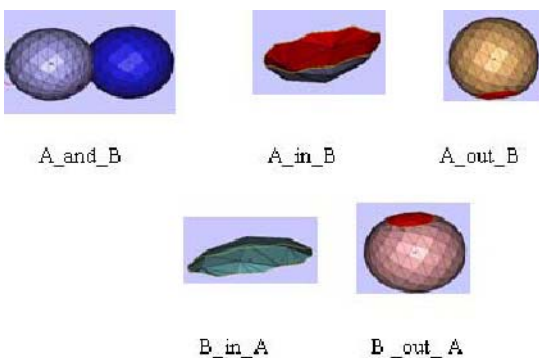


Fig. 5

F. Processing the burr errors and noises

1. Processing the noises

The noises are the isolated sets of triangular faces here. The algorithm of processing the noises is as follows.

- i Traversal all triangles and classify the sets of triangular faces according to topological connection among triangular faces.
- ii Get the maximal set of triangular faces, remove the other.

2. Processing the burr errors

The burr errors distribute on the edge of the model, and have a character of very acute angle. The algorithm of processing the burr errors is as follows. Traverse the triangles at boundary, judge the minimal angle of each triangle, set a parameter to judge if the triangle is the burr error.

III. CONSTRUCT THE MODEL OF THE DEFECT

The position of skull defect has mainly two cases, one is on symmetric region of the skull (e.g. Fig. 6 left) and the other is in unsymmetrical condition (e.g. Fig. 6 right).

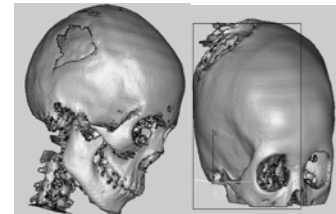


Fig. 6 the left is on symmetric region of the skull, the right is in unsymmetrical condition.

In this section, a method for mending skull defect in arbitrary condition is given.

A. Mending the skull defect in symmetric condition

i Get the minimum bounding box of the defect to simplify subsequent operations. Firstly, search the boundary coordinate and find the maximal and the minimal coordinates on xy plane. Then generate a rectangular parallelepiped according to the coordinates, do Boolean intersection with the original STL model to get the model that include defect and its symmetric body only (e.g. Fig. 7).

ii Let the defect and its symmetric body is on the same position by computer graphics technology like rotation and

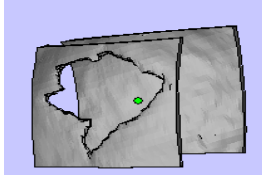


Fig. 7

translation and so on. Then, apply our algorithm to do Boolean intersection to get the model of the defect.

B. Mending the skull defect in asymmetric condition

In the first instance, we can get the initial model of the defect using the algorithm of three-dimensional hole repairing in mesh surfaces [6]. In the second instance, completely anastomosed defect model can be obtained through Boolean subtraction operation of the initial model of the defect and the original model of the skull.

IV. EXPERIMENT RESULT AND CONCLUSION

This algorithm is implemented in visual c++ 7.0. It is applied to skull defect mending in arbitrary condition and obtains the model of the defect. It solves the problem that the defect model cannot anastomose the border and optimize the result.

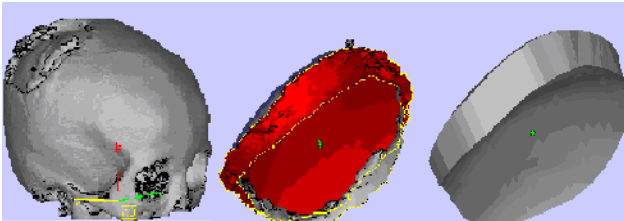


Fig. 8 the left is the model of skull in asymmetric condition, the center is the initial defect model, the right is the defect model by our algorithm.

ACKNOWLEDGMENT

This project is supported by NSFC (NO. 50775134) and SEDF (NO. 06AZ029).

REFERENCES

1. GUO Guifang, LI Limin, HU Qingxi. (2003) Tissue Engineering Oriented Reconstruction Technology of Bone Defects. Journal of Shanghai University (English Edition).)2003, 8(Supp1.) : 37-4.
2. Scott J. Hollister, Cheng Yu Lin. (2006) Computational design of tissue engineering scaffolds. Computer method in applied mechanics and engineering.
3. Guo Kaibo Zhang Lichao et al. (2005) Implementation of Boolean operations on STL models. J. Huazhong Univ. of Sci. & Tech. (Nature Science Edition) Vol. 34 No. 7.
4. Qiang Du, Dsheng Wang. (2006) Recent progress in robust and quality Delaunay mesh generation. Journal of Computational and Applied Mathematics 195 (2006) 8-23
5. Tomas Möller (1997). A Fast Triangle-Triangle Intersection Test. Journal of Graphic tools. issue Volume 2, Number 2
6. Qingxi Hu, Hongfei Yang, and Yuan Yao. (2007) A Software Method to Model and Fabricate the Defective Bone Repair Bioscaffold Using in Tissue Engineering. Life System Modeling and Simulation. DOI 10.1007/978-3-540-74771-0_51
7. Yohan D. Fougerolle, Andrei Gribok, Sebti Fougou, (2005). Boolean Operations with Implicit and Parametric Representation of Primitives Using R-Functions. VISUALIZATION AND COMPUTER GRAPHICS, VOL. 11, NO. 5.

Author: YAO Yuan
 Institute: Shanghai University Rapid Manufacture Engineering Center
 Street: 99 Shangda Rd.
 City: Shanghai
 Country: China
 Email: wufu304@163.com

Study on the Application of Rapid Prototyping in Assistant Surgical Planning

Di Wu^{1,2}, Qingxi Hu¹, Qi Lu¹, Gaochun Xu¹

¹ Rapid Manufacture Engineering Center, Shanghai University, Shanghai, China

² College of Mechanical and Electrical Engineering, Jiaozuo University, Jiaozuo, China

Abstract — Rapid Prototyping (RP) technology has been widely applied in medicine for its fast development. The paper adopt a method which reconstruct twice, construct a combined model which contains simulative brain profile and try to put forward a new concept which call “Touch To Simulate”. Surgeons can practise on the 3D models pre-operation, carry through surgical planning, not only to know fairly well, but also to decreases operating time, reduce the risk of surgery and complications during the surgery and help surgeons to make complex surgical planning rapidly.

Keywords — RP, medical model, surgical planning

I. INTRODUCTION

Rapid Prototyping (RP) is a kind of high technology developed at the end of the 1980s, which integrate latest results in the fields of mechanical engineering, CAD/CAM, laser, material science, automatic control, etc. Compared with the traditional cutting methods, the method of layers dumped was used for processing. The basic principle of RP is: According to the part’s shape, first, make 3D model by CAD system, then turn it to discrete, 3D model is cut into series of 2D planes by data processing, forming materials are placed in the container. Using RP equipments to scan according to the synusia profile shape and make material form layer by layer, 3D solid will be formed through sequential stacking finally.

RP technology has been widely used in medicine for such merits as high automation of operation and forming precision, widely applied material, very complex parts can be easy to made, which solve the problem successfully that 3D model can not be touched in CAD software [1]. By means of data information of CT (MRI), RP can process the skeleton or tissue models of patients in a shorter time, it provides a useful reference for surgeons, research personnel and prosthesis designers who want observe patients traumatic position without operation. For example, the anatomical structure of person’s maxillo–cranio–facial (CMF) is very complex, quite irregular shape and high spatial structure change, vitals and innervation concentrated etc, the advantages of RP model application is more obvious. It can help surgeon effectively to surgical planning. Recently, it has become hotspot in this research field.

Many complex diseases and trauma need to be performed operations in clinical surgery, X-ray Film, CT and MRI are often adopted before the operation. But, 2D image representation can not achieve actual clinical demands because much information can not be obtained by classical anatomy atlas for individual differences. The key of success or failure for many complex surgical operations depends on the doctor who grasp the trauma regions and relative position of vascular, nerve around them[1].Consequently, surgeon often rehearse rely on the 3D model to ensure the operation success. The medicine models made by RP are helpful for medical workers to understand profoundly the body, azimuth, comparative position and internal structure of anatomy models. They are also used in diagnosis, surgical planning, design of prosthesis implantation, surgical repairing, surgical template, auxiliary communication and teaching, etc. Most medicine anatomy model come from bones model of CT scan data and structural model of soft tissue from MRI [2]. Models can be used various color to represent different tissue structure, RP models facilitate communication effectively between medical doctors and patients, thus make patients has preliminary cognition to their diseases and cooperate treatment actively. In addition, RP models (nontoxic materials) can be brought in operating room after lusterized and as direct visualization models for surgical guidance.

This paper presents a method to build solid models which produced by RP technology. Taking a skull defect patient as an example, we get a combined model which contains simulative brain profile and try to put forward a new concept which call “Touch To Simulate”. Surgeons can practise on the 3D models pre-operation, carry through surgical planning, not only to know fairly well, but also to decreases operating time, reduce the risk of surgery and complications during the surgery, this study are to be expected [3].

II. RP MEDICAL MODEL CONSTRUCTION

CT (MRI) is one of the very important tools in modern image diagnostics and the most universal method to acquire particular anatomy information. Its working principle accord with the that of RP.

A. Construct method and process of medical model

Firstly, collecting CT data, then 3D data model is generated by special software Mimics (Materialise Interactive Medical Image System Software, Materialise, Belgium). It is transformed to STL file format and be processed by imported in Magics (Materialise, Belgium). Finally, it is output to RP equipments to machining entity model which is used to assist surgical planning and simulation for surgeons (Fig.1).

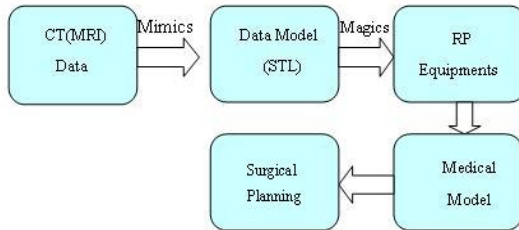


Fig. 1 Medical model construction flow chart

The CT (MRI) scan data include interested region and neighboring tissue information. As a result, need to extract useful information from such data. Mimics is a general purpose segmentation program for gray images, so it can interface with all common scanner formats. In Mimics, threshold segmentation method is usually used to establish primary definition of segmentation object. The interested segmentation regions can be completed by complex 3D selection and editing tool. The method adopted for visualization is through the conversion of 2D image slice data with 256×256 up to 512×512 as gray value images (a density threshold)[4]. When use alternation selection window to accomplish contrast enhancing, segmentation mask is showed with different color in the image.

B. RP system choosing

Generally, accurate surgical planning and the shortened operating time can reduce the risk to the patients and decrease cost. Accordingly, the model should have the following characteristics [4]:

1. Possess clear visualization and pre-surgical planning, with reduced cost and operating room time.
2. Improved patient outcome, such as fewer complications and faster rehabilitation.
3. Increased surgical precision, reduce possible damage to healthy tissue.
4. Possibility of performing new, or previously impossible, minimally invasive procedures.

5. Better communication between the surgeon and the patients.
6. Predictable surgical results.

The common RP technology include SLA (Stereo Lithography Apparatus), SLS (Selected Laser Sintering), LOM (Laminated Object Manufacturing), FDM (Fuse Deposition Modeling) etc, every RP system has its strengths and limitations. SLA is one of the earliest and the most widely used techniques.

SLA is mainly composed of a container which full of liquid resin. The container is regarded as forming chamber and storing room. It has fixed molding platform which can move along Z axis and a laser scanning element. When the current section contour information are projected or written by laser parts into the resin surface of forming chamber, one product layer hardened. Then the layer fall a layer thickness after it solidifies along with molding platform. Subsequently, begin to form a new layer and be solidified by exposing. The process cycles layer by layer until the whole model is completed from bottom to top [5].

Owing to the advantages of SLA are high precision and good surface finishes, so most medical models using this. We fabricate a combined model which contains brain profile as well as by SLA.

III. APPLICATION IN SURGICAL PLANNING

The medical model usually includes special important parts and also has many others. It not only deals with the local problem, but also whole aesthetic result. SLA model is translucent generally, so the inside fabric of brain model which we use is clear in visualization and benefit to doctor's decision. In RP processing, acrylate that used in all SLA models is considered as the only materials with biological compatibility. Therefore, medical staffs can do surgical experiments with real operation instruments. After actual practice, they know the case, design and control the surgical processes and make planning preoperative [6]. Summarizing evaluation after testing is favorable to improve the success rate of operation all the more.

A patient with skull broken on the front-left for contingency demands repairing surgery. It is necessary to fabricate a RP model to simulate in surgical planning.

Vide ut supra, according to his CT image data, a skull model is reconstructed firstly by Mimics (Fig.2), export STL files. After that, built the contour of patient's cerebral cortex in the second reconstruction by same way, export and saved as STL files (Fig.3).

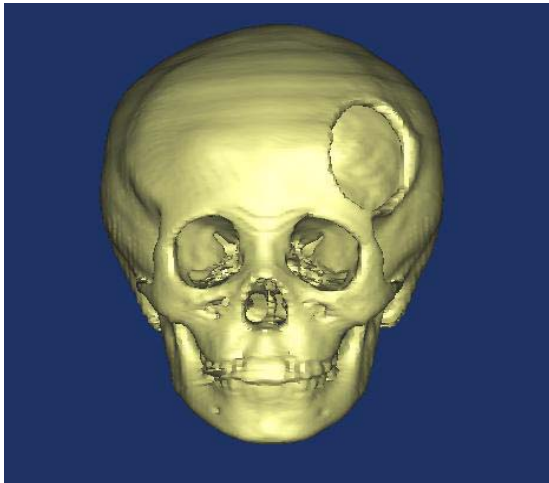


Fig. 2 Reconstructed skull model in Mimics

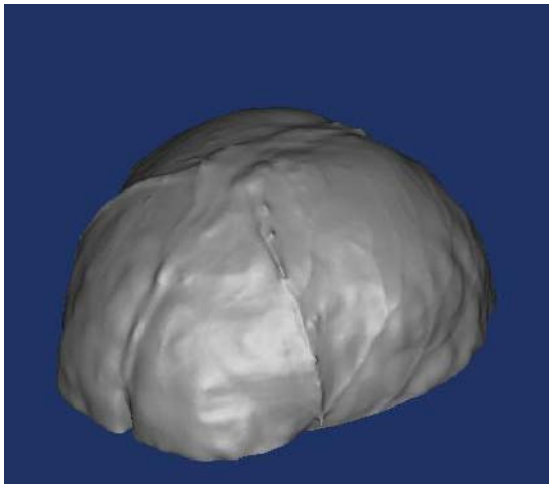


Fig. 3 Reconstructed cerebral cortex profile (Part)

Then open STL files output in Magics and build combined model of brain (Fig.4). In order to explain and need of manufacturing, we just extract upper half part of contour of cerebral cortex in the case. We can see clearly the cross-section part of brain contour. After processing, we can output STL files and manufacture the medical model by the SLA equipment. It is a personalized and accurate model because of using real data from patients.

Using the idea R.Petzold for reference [7], we put forward the concept of "Touch to simulate", namely the doctors can get a real sense of touch through the model. The doctor can get effect of vision and sense of touch by the scalpel touching the model. It is obvious to improve surgical schemes and renovate operation skills. The doctors can make out specific judgments through the combined model

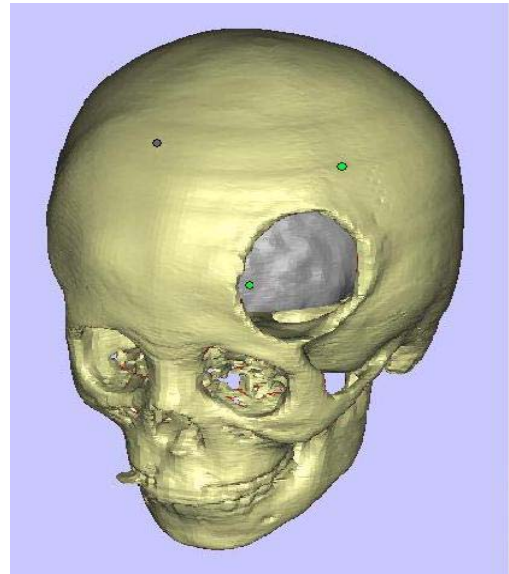


Fig. 4 Combined model of brain fabricated in Magics

of brain. The doctors can analyze aiming at the injury parts and avoid damaging the brain tissues during the operation because the appearance of brain model and contour model can display clearly. Especially for the patients with brain tumor, the combined model of brain can accurately show the corresponding orientation of focus.

IV. CONCLUSIONS

We can fabricate the medical model conveniently by RP technology and simulate different tissues or detailed structure with various colors. Owing to the high requests of skull defect repairing operation, the combined model is helpful for surgeons to have better understanding according to individual patient.

In a word, the utilization of RP medical model assist surgeons to make complex surgical planning rapidly, such as complex skull defect repair operation. The simulation of pre-operation can allow surgeons to develop the optimal surgical approach and improve foresee abilities of problem possible happen, also enhance confidence of medical and nursing staffs, reduce surgical time greatly, so the patient's pains are alleviated in the same. The use of RP has been shown in this study, the technology has obtained obvious effects as a tool in complex traumatic surgery and orthopedics operation presently. Of course, we do not believe that these models are necessary in all cases, they need continuously evaluating and improving in clinic [8]. With the deeply study on the application, It brings evangel to the faster patient's recovery and has prospect infinitely.

ACKNOWLEDGMENT

This project was supported by NSFC 50775134 and Rapid Manufacture Engineering Center, Shanghai University.

REFERENCES

1. Weibing Wan. (2007) Research of rapid prototyping in tissue engineering bone repair. Shanghai Jiao Tong University, Shanghai
2. Guangfu Liu, Shu Zhang, Zhongming Huang (2001) Using rapid prototyping to build medical models. *Manufacturing Automation* 23(2):5-7
3. Delin Xia, Lai Gui. (2005) Fabrication of 3-dimensional skull model with rapid prototyping technique and its primary application in repairing one case of craniomaxillofacial trauma. *Chinese J Reparative and Reconstructive Surgery* 19 (10):811-814
4. Qingbin Liu, Ming C.Leu, Stephen M.Schmitt. (2006) Rapid prototyping in dentistry: technology and application. *Int J Adv Manuf Technol* 29:317-335 DOI 10.10007/s00170-005-2523-2
5. Andreas Gebhardt, Zhiqing Cao et al. (2005) Rapid prototyping. Chemical Industry Press, Beijing
6. C.Hurson, A.Tansey, B.O'Donnchadha et al. (2007) Rapid prototyping in the assessment, classification and preoperative of acetabular fractures. *Injury, Int. J. Care Injured* 38:1158-1162
7. R.Petzold, H.F.Zeilhofer, W.A. Kalender. (1999) Rapid prototyping technology in medicine-basics and applications. *Computerized Medical Imaging and Graphics* 23:277-284
8. S.Weber, R.Sodian, M.Markert (2007) 3D printing of anatomical heart models for surgical planning in cardiac. *Int. J. CARS* 2(Suppl 1):S160-S180

Author: Di Wu
 Institute: Rapid Manufacture Engineering Center
 Street: 99 Shangda Rd.
 City: Shanghai
 Country: China
 Email: wudy@shu.edu.cn

Augmented Reality Interactive Interface for Defective Bone Repair System

Yuan Yao¹, Xiu-xiang Pang¹, Qi Lu¹, Qing-xi Hu¹

¹Rapid Manufacturing Engineering Center, Shanghai University, Shanghai 200444, China

Abstract — Computer Aided Surgery as a new technology has developed rapidly in recent years, which applies computer technology and computer graphics technique to simulate the different processes of the medical surgery. This paper presents an aided planning and test interactive interface based on Augmented Reality technology for defective bone repair surgery. Experimental results test the feasibility of applying the Augmented Reality technology to the defective bone repair system. A detailed introduction is given to the design of visual augmentation and interactive interface.

Keywords — Interactive Interface; Augmented Reality; Defective Bone Repair.

I. INTRODUCTION

Computer Aided Surgery has developed rapidly in recent years. Nowadays computer based tools for preoperative planning and simulation are widely spread. With technology support provided by computer-aided tool, it is possible to make operation process safer and more accurate.

Repairing the defective bone is a common neurosurgery and plastic surgery. Research shows the main reasons for the failure of operation are the design of defective bone scaffold, material and the accuracy of the operation. Furthermore, the communication between the doctors and the patients has a lot of problems. It is hard to express patient's idea and will only through languish and flat image, so the surgical effect is difficult to be guaranteed. As a result, surgical effect even more depends on the doctor's aesthetic conceptions, experiences and technology level. The patient is fully placed in a passive position, so how to recover the original appearance and arrive to the requirement of beauty is a problem anxious to be solved in the defective bone repair operation.

Augmented Reality (AR) technology makes it possible to solve the above problems. Augmented Reality is a new technology developed from Virtual Reality (VR) technology. VR technologies completely immerse a user inside a synthetic environment. While immersed, the user cannot see the real world around him. In contrast, AR allows the user to see the real world, with virtual objects superimposed upon or integrated with the real world. Therefore, AR supplements reality, rather than completely replacing it. Ideally,

it would appear to the user that the virtual and real objects coexisted in the same space^[1].

The use of interactive interfaces allows users to naturally interact with the computer-generated information. In this paper, a user-focused interactive interface based on computer display is proposed. The architecture of the system is designed to be as general as possible so that it can be easily adapted to many application domains. Different graphics algorithms for presenting a realistic augmentation of computer-generated information have been applied.

II. SYSTEM DESIGN

The main system components and software modules with data flow in our system are shown in Fig.1. The system consists of a video camera and a computer. A marker is used for tracking the defective bone and registering its location. Frames from video camera are analyzed using ARToolkit^[3] (2.7.2) software.

A visualization software module creates the defective bone model and cross-section image and makes their proper superposition with video produced by the camera. The result is real-time AR visualization of 3D model projected on the patient's skull.

The AR interactive interface uses API libraries for video operations tracking based on maker drawn from ARToolKit. In addition, computer graphics and render functions are coded in OpenGL APIs respectively. The above technologies are integrated into a high level C++ framework. Finally, an MFC windows application was designed in order to connect the various components and to produce the final AR interactive interface software environment^[2].

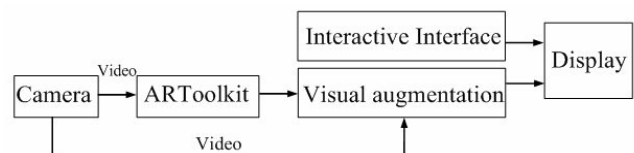


Fig. 1 system design

III. VISUAL AUGMENTATION

Visualizing the constructed 3D model of patient's skull and defective bone is the most important during the operation planning and simulation. The visualization method should provide sufficient details of the defective bone model for doctors to validate and simulate the defective bone model. Simulation results must be presented on the display devices really. The model implements model augmentation and image augmentation to aided-check the bone scaffold model.

A. Model augmentation

The defective bone model (Fig.2) is represented by importing the STL file. Also, 3D representation of the virtual model can be rendered in the aspect of lighting, material, scene and color, fast realistic effect can be generated in real-time. The generation of model augmented visualization plays a crucial factor for the simulation, which give the fused visualization of virtual defective bone model and real patient's skull. By rendering, the doctor can observe several vision effects. Simulation results are shown in Fig.3, the visualization effect is different from the color and light setting.



Fig. 2 the defective bone model

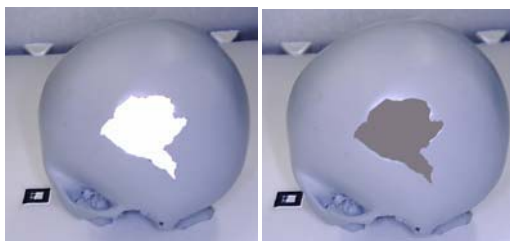


Fig. 3 simulation results of model augmentation

B. Image Augmentation

The image format is JPG or BMP format. Texture Mapping is a relatively efficient means to create the appearance of complexity without the tedium of modeling and rendering the image.



Fig. 4 simulation result of image augmentation

To use texture mapping in OpenGL, you perform the following steps:

1. Create a texture object and specify a texture for that object.
1. Indicate how the texture is to be applied to each pixel.
2. Enable texture mapping.
3. Draw the scene, supplying both texture and geometric coordinates.

Following the above steps, users can render image using Texture Mapping technology. But a problem appears during the presentation. The faces which should be hidden are also be visualized. As a result, computer-generated scene is not clear and real. The problem of computing only the visible surfaces has been well-studied. One approach that has gained popularity is the Z-buffer algorithm. With a z buffer the depth-sort required of a visible surface algorithm is accomplished by maintaining, for each pixel, a record of the Z-depth of the object whose intensity (color) is stored at that pixel. As subsequent objects are scan converted into the frame buffer, their z-depths are compared and used to decide whether the new object is in front of or behind the object currently displayed at each pixel.

In conclusion, rendering the image with Texture Mapping is fast and flexible. The Z-buffer algorithm is simple and reliable. But big memory capacity is needed, algorithm is complicated and time-consuming. simulation result is shown as Fig.4, the hidden and representation effects are perfect.

IV. HUMAN-COMPUTER INTERACTIVE INTERFACE

Human-computer interactions are one of the most important issues when designing any visualization system and especially when developing a generic AR interface. Therefore, interactive interface in this system have to be performed in a natural way so that inexperienced users can become familiar quickly with the augmented reality system^[2].

This system provides two kinds of interactive interface, including graph user interactive interface and hardware interactive interface.

C. Graph User Interaction interface

The graph user interactive interface is shown in Figure.5. The toolbar menu allows the user to have full control of the visualization. To register computer generated information into a marker, the user has to select from the toolbar menu which type of digital information (STL) wants to visualize and then click on it. The corresponding information will be correctly aligned to the marker^[2].

Other functionality available to the user includes major graphics operations such as render setting and manipulation setting. The two operations are commonly used. As shown in Fig.6, the users can set in the aspects of light, color, material in order to satisfy users' visual requirement of augmented visualization. Using the manipulation interface (Fig.7), the users can transfer or rotate the virtual model.

This interface gives full power to the doctors to control the location of virtual information. By transferring, rotating or scaling the defective bone model, the doctors can detect whether the results of computer simulation are in concor-

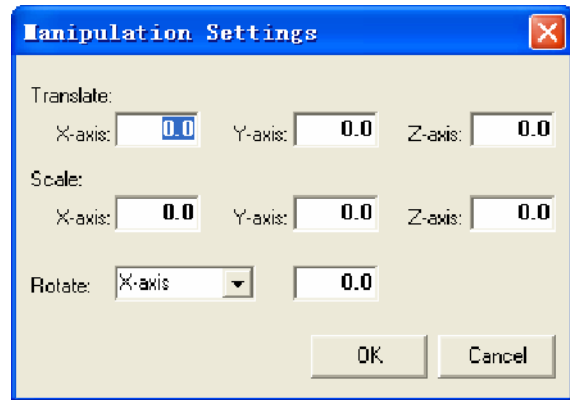


Fig. 7 manipulation setting interface



Fig. 8 simulation results



Fig. 5 graph user interactive interface

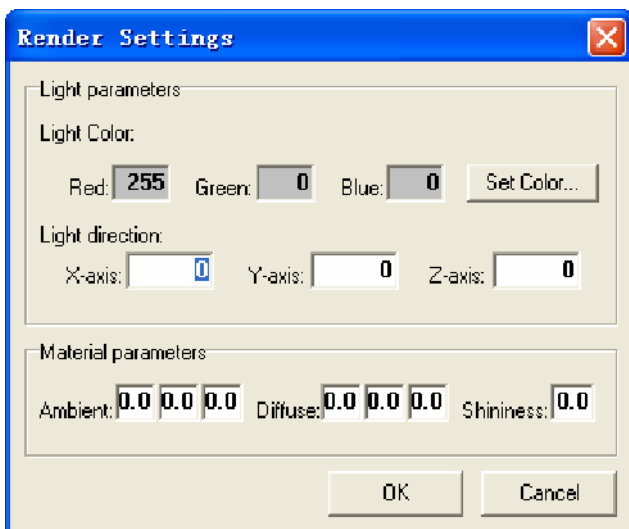


Fig. 6 render setting interface

dance with the theoretical analysis. And the rendering results are used to help to observe different scenes. The simulation results are shown as Fig.8.

D. Hardware interactive interface

Hardware interactive interface based on popular interaction input devices like the keyboard and the mouse. Through responding the operation of mouse and keyboard real-time, users can interact with interface dynamically. Furthermore, predefined keyboard controls (hot keys) offer the same functionality as with the toolbar menu. This has the advantage of changing the parameters of the virtual objects faster, i.e. change lighting setting; material setting.^[2].

It is important for users to operate the 2D cross-section image, so this system provides the relative interactive interface. With the mouse pointing to the edge of the defective bone model (Fig.9), the 2D cross-section image manipulation interactive interface appears. The users can select the direction axis from Drop Down List Box and adjust the location drag the track bar, then the relative cross-section image is visualized in the screen, simulation result is shown as Fig.10.

Lastly, by using immersive AR interactive interface, the doctor can feel as if he is in the real environment. With the developed system, the doctors can detect not only the augmented visualization between the real skull and the virtual defective bone scaffold model, but also the presentation of



Fig. 9 point the model with mouse

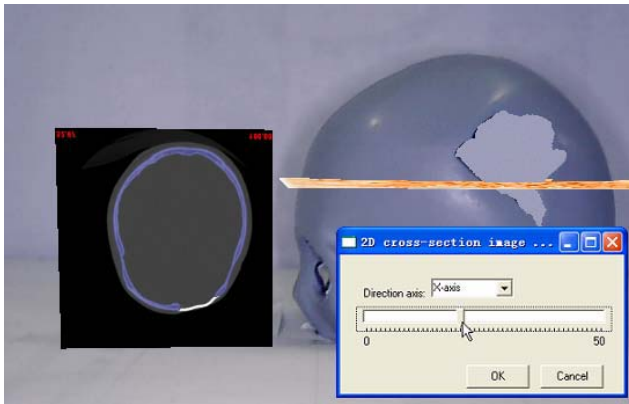


Fig. 10 simulation result

all cross-section images. Therefore, this makes it possible to compare simulation results from several aspects and validate and modify the bone scaffold model. So surgical quality and clinical cure rate are improved, surgical risk is reduced, and surgical injury from multiple operations is alleviated.

V. SYSTEM EVALUATION

Compared with the other system, the main feature of this system is using the AR technology. So two advantages are illustrated as follows:

1. The information in the system comes from the image of the real world, and the virtual model only play a assistant role. Furthermore, the system is of low hardware configuration requirement, good rendering effect, and strong real-time character.
2. The method of interaction is intuitive and natural. The traditional input devices such as mouse and keyboard provide an intuitive and natural interaction, which en-

ables users to interact with computer-generated information in a natural way. So the usability of the system is greatly enhanced.

Because this system has adopted the virtual-real registration algorithm based on marker, the virtual information can not be displayed, once the marker is hidden. This is a significant drawback in this system. Besides, the accuracy of the registration is not high. How to solve these problems is our work in the future.

VI. CONCLUSIONS

This system with good expansibility and portability is advanced in technology, strongly interactive, and easy to use. It meets the requirements of the characteristics of reality-virtual fusion and human-computer interactive in the surgical planning and simulation process, and fully embodies Augmented Reality technology's advantage in the defective bone repair surgical application. It has great practical significance in improving defective bone repair surgical.

ACKNOWLEDGMENT

This project is supported by NSFC (NO.50775134, NO.60703029) and fund of SEDF (NO.06AZ029).

REFERENCES

1. Azuma, R. T. (1997) A survey of augmented reality. Presence: Teleoperators and virtual environments, Vol. 6, No. 4, MIT Press, Cambridge, Mass., 355-385
2. Fotis Liarokapis, Martin White, Paul Lister (2004) Augmented Reality Interface Toolkit, Proc. International Symposium on Augmented and Virtual Reality, IV04-AVR, IEEE Computer Society, London, 761-767, (2004). ISBN: 0-7695-2177-0
3. ARtoolkit at <http://www.hitl.washington.edu>
4. H. Siegl, M. Hanheide, S. Wrede, A. Pinz (2007) An augmented reality human-computer interface for object localization in a cognitive vision system. Image and Vision Computing, 25 (2007) 1895-1903

Author: YAO Yuan
 Institute: Shanghai University Rapid Manufacture Engineering Center
 Street: 99 Shangda Rd
 City: Shanghai
 Country: China
 Email: yaoyuan@shu.edu.cn

Computer Aided Analysis in Maxillary Sinus Surgery

Qing-xi Hu¹, Qin Xu¹, Yuan Yao¹, Qi Lu¹, Yuan-zhi Xu², Jiao-jiao Wang², Qi-xiang Yang²

¹Rapid Manufacturing Engineering Center, Shanghai University,
Shanghai 200444, P. R. China

²Department of stomatology Shanghai Tenth People's Hospital, Affiliated to Tongji University
Shanghai 200072, P. R. China

Abstract — the focus of this paper is methods of computer simulation of surgery process. Firstly, CT scan digitized images were obtained by using 16-slice CT (GE Light Speed, USA) to scan from the bottom of mandible to the top of skull along the transverse axis. Secondly, maxillary sinus was reconstructed by using Mimics 10.01 (Materialise, Belgium) which is professional software of 3D Reconstruction for Medical Images. Then the 3D model in STL format will be inputted into imageware11.1 (Siemens PLM, USA). Using this software, the outer contour of maxillary sinus will be reconstructed into sheet body. Third, the sheet body will be input into UG NX4.0 (Siemens PLM, USA). Mucosa, Trabecular and Cortical Bone will be reconstructed by Means of UG NX4.0 Software. The 3D model of bone condenser was built by the same ways. Finally, by using Ansys Workbench program nonlinear finite element analysis is carried out.

Keywords — OSFE, maxillary sinus, finite element analysis, FEM

I. INTRODUCTION

Implant therapy should be based on simple and safe principle, so too complex surgery and Large-scale bone graft should be avoided.[1,2] Summers put forward OSFE (Osteotome sinus floor elevation) [3,4] which named maxillary sinus lifting. Due to less surgery trauma and less postoperative reaction, maxillary sinus lifting has been used clinically in recent years. [5] The damage of floor mucosa of the maxillary sinus is the main complication of maxillary sinus lifting.[6] Most surgery is made under blind area, so it's hard to judge the integrity of the floor mucosa of the maxillary sinus especially micro hole which will influence the bone healing of hydroxyapatite around implants. When the Osteotome sinus floor elevation is done, it difficult to know the state of maxillary sinus mucosa using conventional methods such as CT, MRI, etc. though some date can be obtained by animal experiment, there are some difference among clinical symptoms and experimental data. Animal experiments are not reliable because of their randomness.

II. WRITING THE PAPER

A. CT data processing

Mimics10.01 is software of reverse engineering based on medical imaging and computer-aided design. The scope of image recognition, pixel interval and distance of image will be adjusted automatic by using this software. The software also has a good image editing functions. first, the data it get from CT will be imported into Mimics by the means of DICOM. Meanwhile, designated top and the bottom plane, establishing three-dimensional coordinate system.(Fig.1)

The image is divided into regions of different materials by setting division threshold appropriately, and the boundary of interested region was extracted. Bone was extracted by contour extraction and threshold segmentation.

Using regional growth, the 3D model of skull was reconstructed and output with STL format, and then stored in the computer. After that, maxillary sinus and surrounding bone tissues is separated from 3D model of skull by using Magics 11(Materialise, Belgium) and saved as STL. (Fig.2)



Fig. 1 CT data

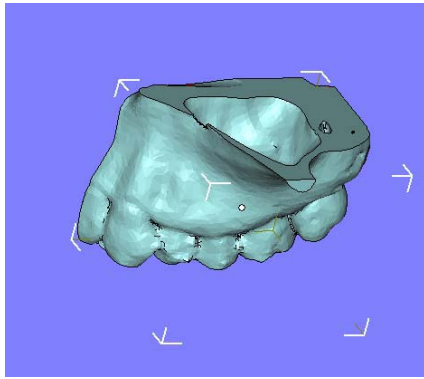


Fig. 2 STL data

B. surface reconstruction

Magics 11 can reconstruct the 3D model in STL format only, which can't be used for finite element analysis directly. Then the 3D model in STL format will be inputted into imageware11.1 (Siemens PLM, USA). In Imageware, STL data is described through point cloud which including the vertexes of the triangles.(Fig.3)



Fig. 3 point cloud

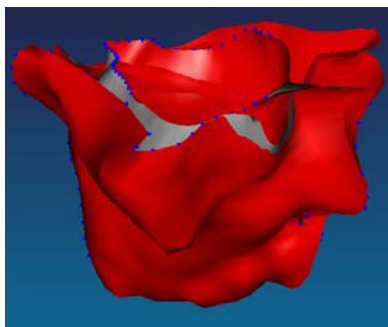


Fig. 4 surface

First, the cloud data are preprocessed for simplification, needless point is removed. Second, the point cloud will be divided into three parts, and it will be reconstructed into three surfaces. Third, the distance error between surface and point cloud could be within 0.5mm by using control point of surface, and saved as IGES format.(Fig.4)

C. Three-dimensional reconstruction

If we use CT data to reconstruct maxillary sinus mucosa, trabecular and cortical bone directly, the model will be too complex and hard to be edited.. If the model is too complex, it's hard to analysis by finite element analysis method. [7] In this paper, maxillary sinus mucosa, trabecular and cortical bone is reconstructed by UG NX4.0. By this way, the model will be simple and easy to edit.

Three surfaces which are reconstructed by Imageware 11 are imported into UG NX4 as format of IGES. The STL data is imported into UG NX4, at the same time, STL data can't be edited by UG NX4.0, so the STL data of maxillary sinus is only used to be a reference for reconstruction.

First, using "scale" order to make scaling operations to the bottom surface of maxillary sinus. the distance between new surface and the bottom surface of maxillary sinus should be at 1mm by method of surface editing. By this way, we will get a model of maxillary sinus mucosa which thickness is about 1mm. Second, three surface will be processed by above mentioned method, respectively. This step is used to reconstruct cortical bone which thickness is about 1mm. Third, trim excess parts of surface and use "sew", "Boolean" order to get the 3D model of maxillary sinus.(Fig.5)

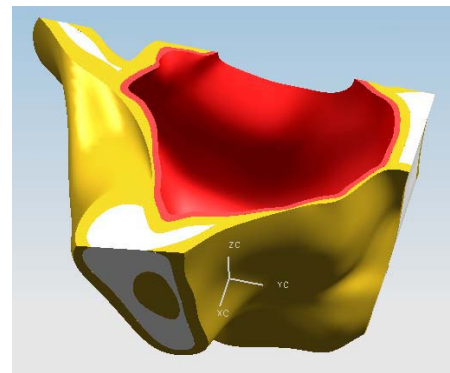


Fig. 5 3D model

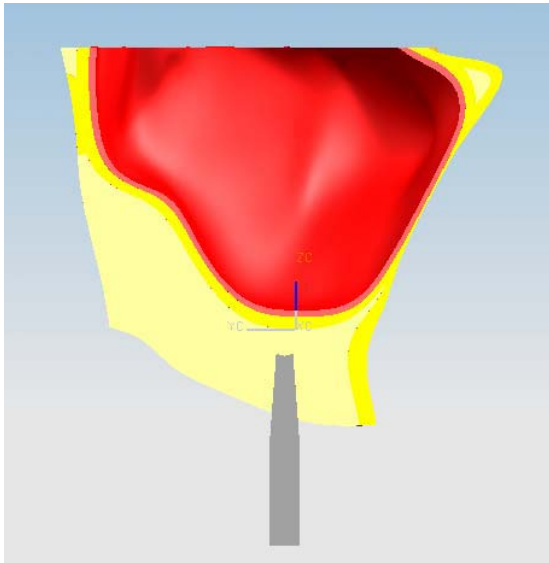


Fig. 6 90 degree

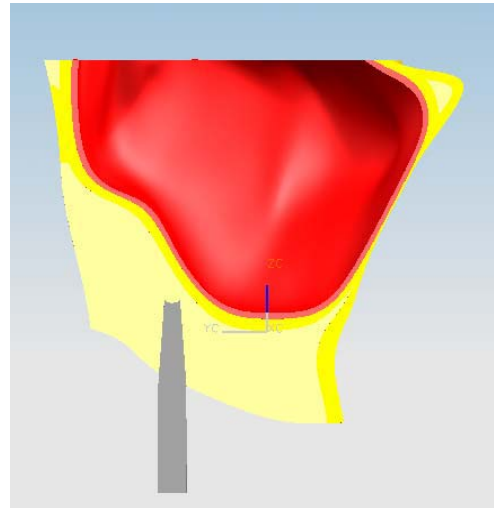


Fig. 8 30 degree

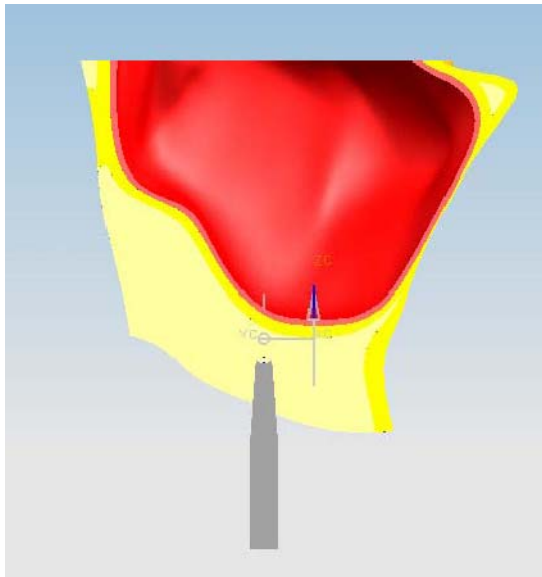


Fig. 7 45 degree

Finally, bone condenser will be import into this model. The angles between bone condenser and maxillary sinus are 90(Fig.6), 45 (Fig.7) and 30 (Fig.8) degrees.

A. finite element analysis

Call Ansys Workbench from UG NX4, and import three maxillary sinus model into Ansys. first, define material parameters of maxillary sinus mucosa, bone condenser, trabecular and cortical bone.(Table.1)

Second, tetrahedron element was used for intellectual finite element mesh division. The size of element used in maxillary sinus mucosa and cortical bone is 2mm. The size of element used in trabecular bone and bone condenser is 1mm.(Fig.9)

Third, define boundary condition of model. Define fix support to the top surface of model and apply 4800N vertical force to the bottom surface of bone condenser to simulate the condition of osteotome sinus floor elevation. As a large force was effect on the maxillary sinus, large deformation will be happened. Stresses and displacements are calculated by means of initial-stress method—one of nonlinear iterative approaches.

Table 1 material parameters

material	Young's Modulus(Mpa)	Poisson's Ratio
maxillary sinus mucosa	70.3	0.45
bone condenser	2e5	0.3
Trabecular bone	1370	0.3
cortical bone	13700	0.3

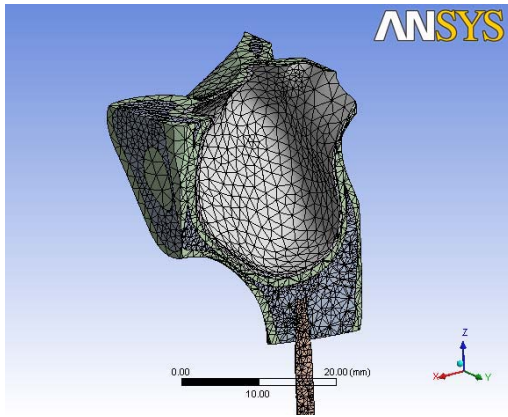


Fig. 10 Mesh

III. CONCLUSIONS

The damage of floor mucosa of the maxillary sinus is the main complication of maxillary sinus lifting. Most surgeries are made under blind area, so it's hard to judge the integrity of the floor mucosa of the maxillary sinus especially micro hole which will influence the bone healing of hydroxyapatite around implants. In this paper, we discuss the stress status of maxillary sinus mucosa mainly.(Fig.10)(Table.2)

It is shown by the results that when the angle between maxillary sinus floor and bone condenser is 90 degree, the equivalent (von-Mises) stress of maxillary sinus mucosa is the minimum and the deformation of it is the largest. when the angle between maxillary sinus floor and bone condenser is 30 degree, the equivalent(von-Mises) stress of maxillary sinus mucosa is the maximum and the deformation of it is the smallest. When this angle is too small, the damage

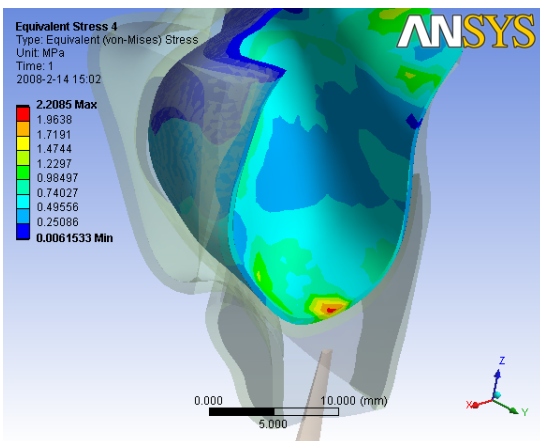


Fig. 9 equivalent (von-Mises) stress

Table 2 analysis result

Angle(Degree)	deformation(mm)	equivalent(von-Mises) stress(Mpa)
90	0.38868	2.2085
45	0.3972	2.254
30	0.35303	2.4916

of floor mucosa of the maxillary sinus is more easily to happen.

This method can be used for predicting the treatment outcome, which will reduce the time spent by the treatment process and improve the success rate of surgery.

REFERENCES

1. Kent JN,Block MS. (1989)Simultaneous maxillary sinus floor bone grafting and placement of hydroxylapatite-coated implants[J].J Oral Maxillofac Surg,47:238-242.
2. Lazzara RJ, Poaer SS. (2006)Platform switching: a new concept in implant dentistry for controlling postrestorative crestal bone levels[J]. Int J Periodontics Restorative Dent 26(1): 9-17.
3. Summers R B.(1998) Sinus floor elevation with osteotomes.J Esthet Dent; 10: 164-171
4. Summers R B.(1994) A new concept in maxillary impant surgery: the osteotome technique[J].Compend Contin Euuc Dent, 15:152-162.
5. Attard NJ, Zarb GA. (2004)Long-term treatment outcomes in edentulous patients with implant-fixed prostheses: the Toronto study[J]. Int J Prosthodont, 17(4): 417-424.
6. John Jensen, Steen Sindet-pedersen, Anthony JO. (1994)Varying treatment strategies for reconstruction of maxillary atrophy with implants: results in 98 patients[J]. J Oral Maxillofac Surg, 52(2): 210-216
7. Pascal Magne.(2006) Efficient 3D finite element analysis of dental restorative procedures using micro-CT data. dental materials[J]. 958:xxx-xxx

Author: HU Qing-xi
 Institute: shanghai University Rapid Manufacture Engineering Center
 Street: 99 Shangda Rd
 City: shanghai
 Country: China
 Email: redbreeze@163.com

MRI Compatible Rigid-flexible Outer Sheath Device Using Pneumatic Locking Mechanism for Endoscopic Treatment

Siyang Zuo¹, N. Ymanaka¹, K. Masamune¹, H. Liao², K. Matsumiya¹, T. Dohi¹

¹ Graduate School of Information Science and Technology, the University of Tokyo, Japan

² Graduate School of Technology, the University of Tokyo, Japan

Abstract— To reduce the invasiveness of surgery, we developed an outer sheath device using flexible toothed link and vacuum pressure locking mechanism for flexible devices in endoscopic surgery. The outer sheath can be switched to flexible mode and rigid mode. Furthermore, the angle of its forward part can be controlled using nylon wire. All of the parts of this device are made by plastic so that it has excellent compatibility with MRI. We manufacture a prototype of sheath with 20mm in the outer diameter, 8mm in the inner diameter and 300mm long. The experiment showed that our mechanism could switch flexible mode and rigid mode, and the outer sheath was sufficient to fix its shape by our mechanism.

Keywords— Outer sheath, Pneumatic locking mechanism, flexible manipulator, Endoscopy, Minimally Invasive Surgery.

I. INTRODUCTION

Endoscopy is a surgical technique that involves the use of an endoscope, a special viewing instrument that allows a surgeon to see images of the body's internal structures through very small incisions, including laparoscopic surgery, arthroscopic surgery and thoracoscopic surgery. Because of the advantage of minimal invasion, endoscopic surgery has been widely performed in modern surgery. Moreover, we considered that the endoscopic surgery with MRI guidance is useful. Therefore, the MRI compatible device is necessary.

Many groups developed various instruments to improve performance, and reduce risks and difficulties of performing endoscopic surgery. For instance, dexterous robotic manipulator adds multiple degrees-of-freedom (DOFs) [1]-[3] motion to the instruments and thus improved performance of surgery. Master-Slave type robotic manipulators [4], such as da Vinci, enable to help perform surgery with precise motion. However, some problems remain unsolved. First, laparoscopic surgery requires wide space below the abdominal wall. Pneumoperitoneum is commonly used to secure the space, but some complications caused by this method are reported. Second, laparoscopic surgery is useful to approach the target on anterior area in the body. However it is difficult to approach the target in deep, narrow area.

Several groups developed different flexible manipulators with wide curve. Ikuta et al. developed a micromanipulator to reach difficult area [5]. Moreover, other flexible manipulators using shape memory alloy (SMA) [6], or wire-driven mechanism were also developed [7]. However, flexible instruments can not be inserted easily in narrow space between the tissues or organs, and can not be stabilized completely when approaching target.

To insert the instrument into the required area without injury other tissues, surgical instrument with flexible mode for inserting and rigid mode for fixing the outer sheath is required. In this study, we developed a rigid-flexible outer sheath device using flexible toothed link and vacuum pressure locking mechanism for endoscopic surgery. The outer sheath is developed to enable an instrumental path in human body. This sheath is able to be distorted to any required shape, and the shape is able to be hold against of the external force. Before inserting flexible instruments, the surgeon inserts the outer sheath through the narrow gap between the safety areas. After approaching the target, the surgeon locks the shape, and then the surgeon is able to insert flexible instruments easily through the planned path.

This paper reports a mechanism that enables to switch flexible mode and rigid mode, a prototype of outer sheath, and evaluation experimental results about the stiffness.

II. OUTER SHEATH DESIGN

A. Minimally Invasive Endoscope Surgery

We adopt laparoscopic surgery as our focal application. One major problem is that when there is an affected part in the rear of the abdomen such as the back side of the liver and stomach, it becomes difficult to perform local approach for the affected part because the field of vision of the laparoscope and the surgical instrument do not reach by the internal organs in the front. To address these problems, instruments are required to be flexible to go into the body avoiding the critical areas. In order to solve problem of flexible instruments, it is required to manage rigid path to insert flexible instruments in advance.

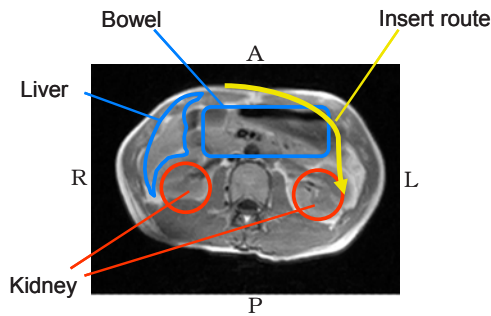


Fig. 1 The insert route: approach of kidney

The insert route, depicted in Fig. 1, is thought of as one ideal path of entry for laparoscopic surgery for its use avoids the need for a large abdominal incision.

B. Design concept

With the mechanism described below, the outer sheath can be switched between flexible mode and rigid mode. The outer sheath design consists of flexible toothed links and bellows tube.

We use vacuum pressure to rigid outer sheath. The toothed link is pushed to the bellows tube by vacuum pressure, and the outer sheath is locked by pushing tooth of the link into the chase of the bellows tube (Fig. 2). By the mechanism mentioned above, the outer sheath is rigid with arbitrary shape by control of the vacuum pressure.

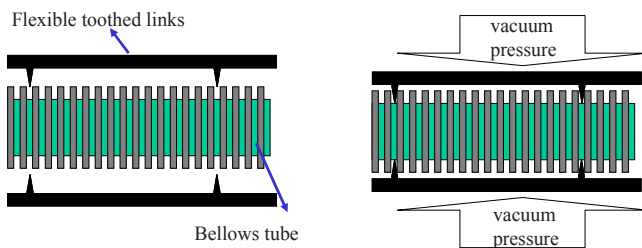


Fig. 2 Design concept

C. Prototype

A prototype of outer sheath device has been built and tested in our lab. The current prototype is 20 mm in the outer diameter, 8 mm in the inner diameter and 300 mm in length, and can achieve an 8.5 cm radius of curvature (Fig. 3). The outer sheath consists of three long flexible toothed links, three nylon wires, a bellows tube, and a polyethylene sheath (Fig. 4). The links and bellows tube are flexible and the shape is free and changeable. The three toothed links are 120° apart, making it possible to lock in

any direction. Furthermore, the angle of its forward part can be controlled using three nylon wire. The nylon wires are also 120° apart. The outer sheath follows an arbitrary curve in three-dimensional space. All of the parts of this device are made by plastic so that it has excellent compatibility with MRI.

The outer sheath can be switched to two modes, flexible mode and rigid mode. In flexible mode, the sheath can be inserted into the tissues or organs from a narrow gap. When the devices reach the target of the deep area, the flexible sheath switches to the rigid mode by vacuum pressure using the polyethylene sheath. By the above-mentioned mechanism, the outer sheath is rigid with arbitrary shape by control of the vacuum pressure. The shape of developed outer sheath is possible to be changed, even complex shape such as the letter 'S'. In rigid mode, flexible toothed links are engaged with bellows tube and locked by vacuum pressure, so the sheath can be switched to rigid mode. When the vacuum pressure is off, the bending bellows tube return straight, then the sheath can be switched to flexible mode. Using the mechanism mentioned above, the outer sheath keeps its shape when the vacuum pressure is added.

This system consists of the outer sheath device and vacuum pump (Fig. 5). Our future works include the evaluation of the wire tension form motors and motor drivers. All of the outer sheath will be controlled with PC base program.



Fig. 3 The outer sheath prototype

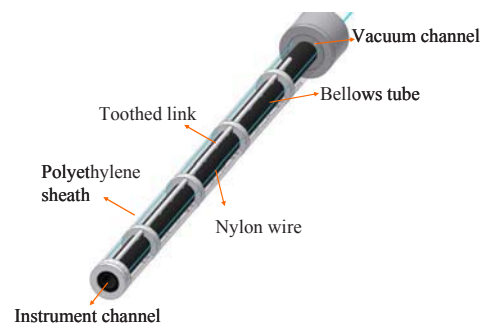


Fig. 4 The outer sheath mechanism assembly

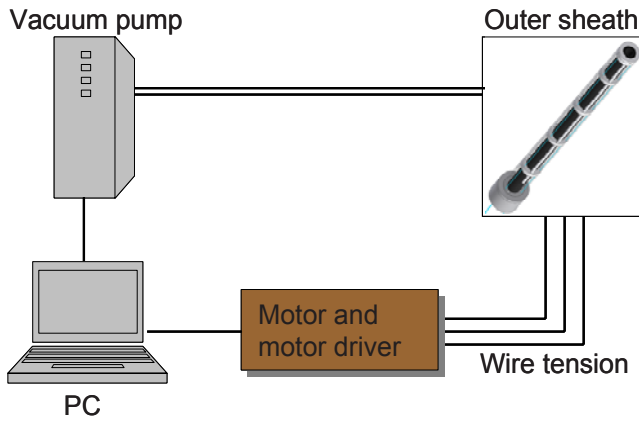


Fig. 5 The system of the outer sheath

III. VALIDATION

We evaluated the performance of switching between the two modes and the stiffness with a set of experiments.

We fixed the outer sheath at the fourth unit from the tip, load vertically from the straight line state on the tip, and measure the load on the tip and the bending angle from the straight line state (Fig. 6).

The relationship between load and the bending angle, in the state that does not increase vacuum pressure, is showed in Fig.7, and the relationship of increase vacuum pressure is show in Fig. 8.

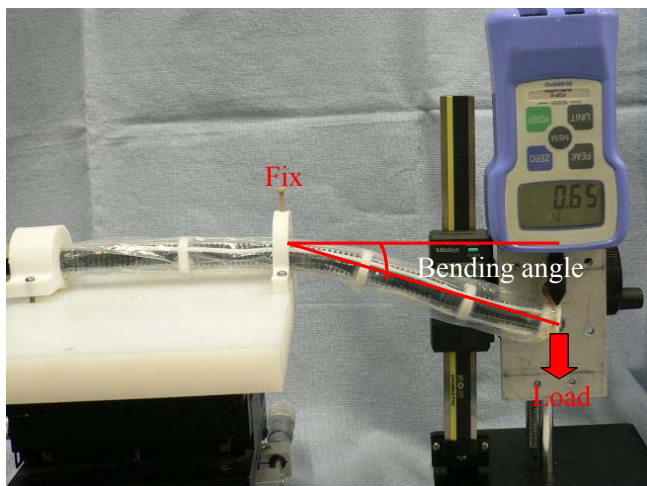


Fig. 6 Experiment condition and parameter

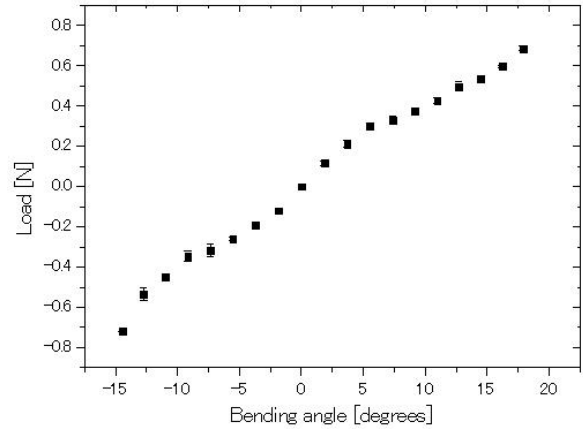


Fig. 7 The relation between bending angle and load in flexible mode

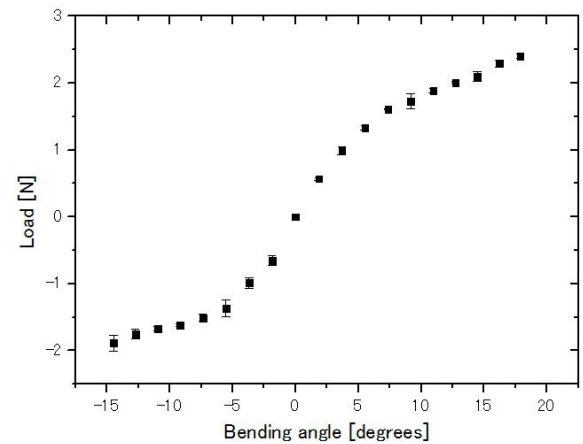


Fig. 8 The relation between bending angle and load in rigid mode

The flexible mode, bending angle can be changed by small external force. The rigid mode is able to show a property similar to a rigid-body. The allowance between toothed link and bellows is thought about as a cause of the curve in rigid mode. However, it is thought that the influence of the allowance at the tip shrinks in a bent state, and there is little influence when inserting and operate a surgical instrument in the outer sheath.

IV. DISCUSSION

The experiment result showed that our mechanism could switch flexible mode and rigid mode, and the outer sheath was sufficient to fix its shape by our mechanism. This outer sheath is helpful for the manipulator, such as fiber scope and laser knife. We don't take the situation that flexible manipulators move heavy organs into consideration because

manipulator enters the narrow space between organs. Then, our outer sheath doesn't need to generate sufficient stiffness to keep the shape from overlarge force.

V. CONCLUSION

To perform the minimally invasive endoscopic surgery with MRI guidance, we have developed the MRI compatible rigid-flexible outer sheath that secures instrumental path for flexible device. The outer sheath is possible to be inserted into the narrow and deep area where conventional laparoscopic tools were difficult to approach. Our research to develop outer sheath which can become flexible and keep its own shape is important to minimize the invasive of surgery.

ACKNOWLEDGMENT

A part of this work is supported by Research Program for development of analysis, help, and alternation of human function "Research for the development of new surgical robot", administrated by Ministry of Health, Labour and Welfare of Japan.

This work is partly supported by Research on medical devices for analyzing, supporting, and substituting the function of human body (H15-physi-002), Health and Labor Sciences Research Grants of Ministry of Health, Labor and Welfare in Japan, Grant-in-aid for Scientific Research (18680042, 1710008) of Ministry of Education, Culture, Sports, Science and Technology (MEXT) in Japan. H. Liao was also supported in part by Grant-in-Aid for Scientific Research (17680037) of the MEXT in Japan and Grant for Industrial Technology Research (07C46050), New Energy and Industrial Technology Development Organization, Japan.

REFERENCES

1. Peirs, J., Reynaerts, D., Van Brussel, H.: A miniature manipulator for integration in a self-propelling endoscope. *Sensors and Actuators A*. 92 (2001) 343–349
2. Nakamura, R., Oura, T., Kobayashi, E., Sakuma, I., Dohi, T., Yahagi, N., Tsuji, T., Hashimoto, D., Shimada, M., Hashizume, M.: Multi-DOF Forceps Manipulator System for Laparoscopic Surgery - Mechanism miniaturized & Evaluation of New Interface -. Proc. of 4th International Conference on Medical Image Computing and Computer-Assisted Intervention. (2001) 606–613
3. Yamashita, H., Hata, N., Kim, D., Hashizume, M., Dohi, T.: Hand-held Laparoscopic Forceps Manipulator Using Multi-slider Linkage Mechanisms. Proc. of 7th International Conference on Medical Image Computing and Computer-Assisted Intervention. 2 (2004) 121–128
4. Abbou, C.C., Hoznek, A., Salomon, L., Olsson, L.E., Lobontiu, A., Saint, F., Cicco, A., Antiphon, P., Chopin, D.: Laparoscopic radical prostatectomy with a remote controlled robot. *JOURNAL OF UROLOGY*. 165 (2001) 1964–1966
5. Ikuta, K., Sasaki, K., Yamamoto, K., Shimada, T.: Remote Microsurgery System for Deep and Narrow Space - Development of New Surgical Procedure and Microrobotic Tool. Proc. of 5th International Conference on Medical Image Computing and Computer-Assisted Intervention. (2002) 163–172
6. Nakamura, Y., Matsui, A., Saito, T.: Shape Memory-Alloy Active Forceps for Laparoscopic Surgery. Proc. of the 1995 IEEE International Conference on Robot and Automation. (1995) 2320–2327
7. Simaan, N., Taylor, R., Flint, P.: High Dexterity Snake-Like Robotic Slaves for Minimally Invasive Telesurgery of the Upper Airway. Proc. of 7th International Conference on Medical Image Computing and Computer-Assisted Intervention. 2 (2004) 17–24

Author: Siyang Zuo
 Institute: the University of Tokyo
 Street: 7-3-1, Hongo, Bunkyo-ku
 City: Tokyo
 Country: Japan
 Email: sa.siyang@atre.t.u-tokyo.ac.jp

Development of interactive three-dimensional autostereoscopic image for surgical navigation system using Integral Videography

Tran Huy Hoang¹, Hongen Liao², K. Matsumiya¹, K. Masamune¹, T. Dohi¹

¹Graduate School of Information Science and Technology, The University of Tokyo, Japan

²Graduate School of Technology, The University of Tokyo, Japan

Abstract — 3D auto stereoscopic Integral Videography (IV) has been proved ideal for use in biomedical applications such as image guided surgery and computer aided diagnostics. The purpose of this study is to develop a high-speed IV-based medical imaging system for intra-operative navigation and pre-operative diagnostics. The system consists of image acquisition, 3D rendering and displaying, real-time positioning and other functions. Current IV rendering algorithm that takes advantage of Computer Graphics can visualize IV with high quality but low speed and is not suitable for clinical use. In this paper, we introduce a new IV rendering technique based on Light Field Rendering in which part of the computation is preprocessed and computational time is significantly reduced. This technique enables us to visualize high-speed, high-quality IV images that can be used in real-time tracking as well as user-interaction and should be of practical use in the biomedical field.

Keywords — Integral Videography, Light Field, real-time rendering

I. INTRODUCTION

Integral Videography (IV) [1, 2] is an ideal method for displaying three-dimensional medical images because it eliminates the need of wearing special devices, provides full-parallax, full colored 3D still as well as animated images and enables simultaneous observation. The hardware of IV consists of a micro convex lens array and 2D elemental images displayed on a high-resolution high-density monitor. When the elemental images is placed in the focal plane of the lens array, only one pixel of the elemental image covered by corresponding micro lens can be observed from one viewpoint. By taking photos of an object from many viewpoints (which is actually to render 2D images of the object using CG) and integrating them back to the elemental images using pixel distribution method [3], full parallax 3D images are observed.

Supposed each micro lens covers $P_x \times P_y$ pixels, we will then need images from $P_x \times P_y$ viewpoints. Pixel distribution is described in Fig. 1. For each set of $P_x \times P_y$ pixels, the lowest pixel is from the highest viewpoint, the highest pixel is from the lowest viewpoint and so on.

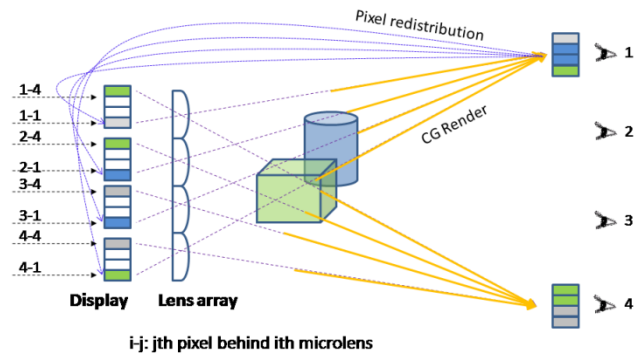


Fig. 1 Principle of IV using pixel distribution

These $P_x \times P_y$ images are basically rendered using conventional geometric data based computer graphics (CG), in which large computational resource is required and performance significantly depends on the scene complexity. In most case when number of pixels covered by one lens is large (from 50 to 2000) this method is not suitable for interactive viewing, which is important in surgical navigation and other biomedical applications.

In this paper we propose a fast IV rendering method based on pixel distribution using Light Field Rendering and integrated it into a surgical imaging system, which provides surgeons with full parallax, interactive 3D IV images.

II. HIGH SPEED MEDICAL IV IMAGING SYSTEM

A. System configuration

The system configuration is described in Fig. 2. 3D image data is acquired using scanning devices (MRI, CT scanner). Segmentation and model reconstruction will then be processed on PC. The acquired data is input to IV rendering module, which visualize IV directly or overlay it onto the patient's body using half mirror.

We employ an image based rendering method-Light Field Rendering (LFR) [4, 5, 6, 7] for visualization of IV in the system. LFR is a technique that renders image from a viewpoint using images from other pre-rendered viewpoints

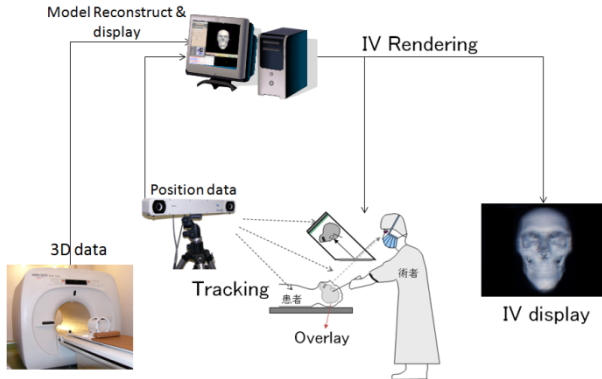


Fig. 2 System configuration

(sampled images). Conventional CG is still needed to acquire sampled images but once these are acquired, no geometric data is needed and render speed is completely independent of scene's complexity. We will discuss about LFR in the next section.

B. Light Field Rendering

Each pixel in a sampled image is considered a light ray with source positioned at the viewpoint where the image is rendered in world space and direction toward the pixel. It is represented by 5 coordinates (u, v, w, s, t) where (u, v, w) is the geometric position of the viewpoint which, in space free of occlusion, can be reduced to (u, v) and (s, t) is the position of the pixel in the image plane (focal plane). (Fig. 3)

This representation forms a light space in which each image is a slice. To render an image is just to extract a 2D array of pixels from the light space.

Using LFR, the region from which an image can be rendered is restricted to the region where images are sampled. If we capture images only from the front of the object we cannot render image from a viewpoint behind it.

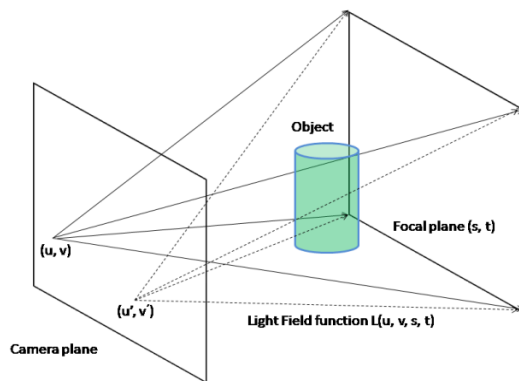


Fig. 3 Representation of 4D light field

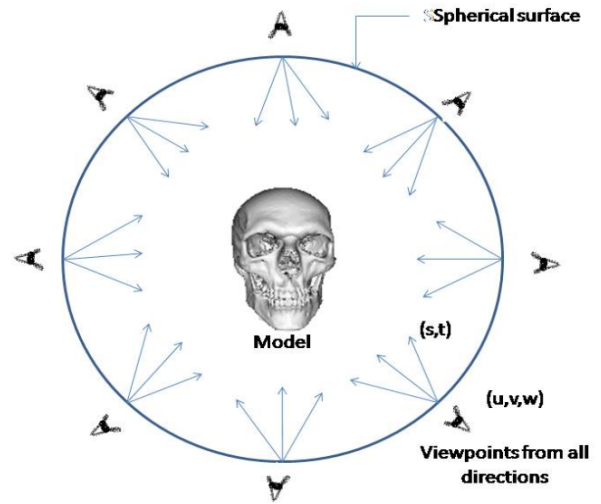


Fig. 4 All viewed Light Field Rendering

To enable user interaction such as rotating, scaling with the IV image, sample images from all direction are required. For that reason the sample viewpoints need to be distributed from all direction (Fig 4).

Quality of the extracted image basically depends on how densely the light space is sampled (how many images are inserted into that space). Therefore, to archived uniform quality from all directions, viewpoints use to sample the light space need to be distributed uniformly around the scene. This is done by recursively dividing each of the 20 faces of an Icosahedrons into small equal triangles. Fig. 5 shows an Icosahedrons and the distribution of sample viewpoints after dividing each face.

We denote each viewpoint using its coordinates (u, v, w) and form a 5D Light Space (u, v, w, s, t) . For each image is captured (rendered) in different focal plane (s, t) , projective transformation is performed before other computations are processed.

We use the CG library VTK (Visualization Tool Kit) and 3D Slicer for segmentation, model reconstruction as well as rendering sample images.

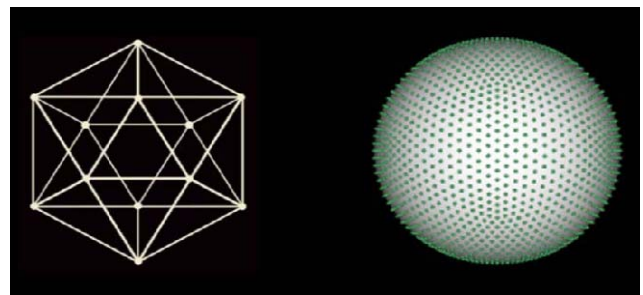


Fig. 5 Icosahedrons and distribution of sample viewpoints

C. Extracting image from a single viewpoint

This section describes how an image from a given viewpoint is rendered using Light Field Rendering. For a given viewpoint $V_0(u_0, v_0, w_0)$, the image observed from this viewpoint can be thought of as the set of light ray from each lens of the lens array that converge at the viewpoint. The whole image is rendered by extracting single light ray from the light space. To simplify the computation, we use only data from the 3 closest sample viewpoints in the extraction.

Let V_1, V_2, V_3 be the 3 closest sample viewpoint to V_0 and d_1, d_2, d_3 be the distance from them to V_0 respectively. We define the Light Field function $L(V, s, t)$ as the value of the light ray connecting the viewpoint V and pixel (s, t) in the corresponding focal plane. This function in fact is a mapping from a 5D space (u, v, w, s, t) to a 3D color space (R, G, B) . Light Field function at V_0 is computed as follow.

$$L(V_{0,s,t}) = L(V_{1,s,t})/d_1 + L(V_{2,s,t})/d_2 + L(V_{3,s,t})/d_3 \tag{1}$$

For this image will be viewed through the lens array, the (s, t) plane is in fact the lens array plane and each pixel actually corresponds to one lens. Therefore, extracting image from a single viewpoint is identical to compute the value of the Light Field function at every micro lens.

D. Synthesizing IV image

IV image is synthesized by rendering multiple 2D images from equally spaced viewpoints around a given direction. (Fig. 6). These viewpoints are computed so that each is the convergence point of light rays from corresponding pixel behind every micro lens. The convergence of these light rays is guaranteed because the total size of pixels behind

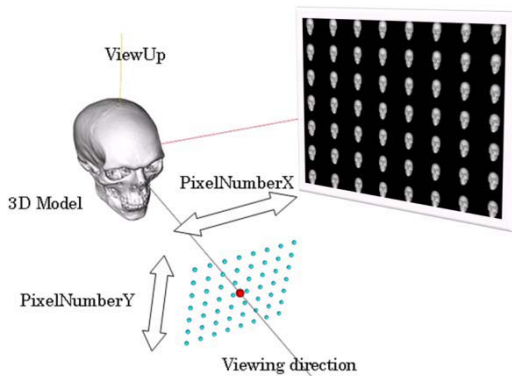


Fig. 6 Viewpoints for rendering IV images

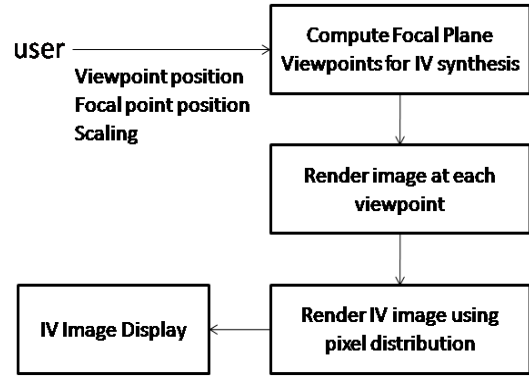


Fig. 7 IV rendering algorithm

one lens is slightly larger than the lens pitch in both directions.

Fig. 7 described the algorithm of synthesizing one IV image. The focal plane and viewpoints for synthesizing IV image are compute based on user’s input parameters such as rotation, scaling. Then at each viewpoint, the corresponding image is extracted as described in the previous section. The final IV image is synthesized using pixel distribution method.

III. RESULT

We use two different models to evaluate our method. Both of the models is reconstructed from CT data. The human head model is rather simple with only 55424 vertices while the human heart model has 401587 vertices (Fig. 8). The PC used in experiment is a Pentium PC with Core 2 Duo, 2.4 GHz CPU, Nvidia Geforce 8800 GTX graphics card and running on Linux Fedora.

Specifications of display and lens array are described in table 1.

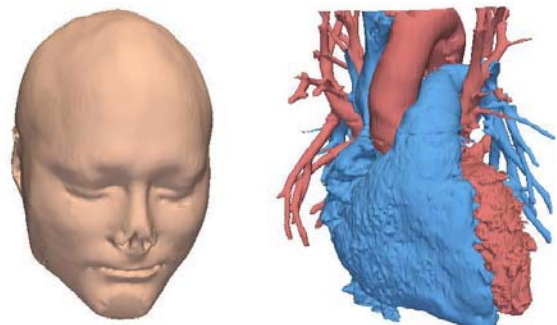


Fig. 8 Models used in experiment

Table 1 Display and lens' specifications

Display	XGA (1024x768), 203 dpi
Pixel pitch	0.125 mm
Lens array type	Fly's eye
Lens pitch	1.001x0.876

The result is shown in table 2, in conventional method, the rendering time significantly depends on the complexity of the models while in the proposed method, rendering time is around 90 ms for one frame and does not increase as the model becomes more complex.

Table 2 Rendering time for one frame

Model	Old method	Proposed method
Head	346.8 \pm 2.4 ms	92.1 \pm 2.4 ms
Heart	625.3 \pm 3.9 ms	95.4 \pm 3.7 ms

Fig. 9 shows the IV images of the human head model with vessels and ventricles included, the images are taken by normal camera from left and right direction. As we can tell from the pictures, shape, color of the object are properly visualized with full motion parallax.

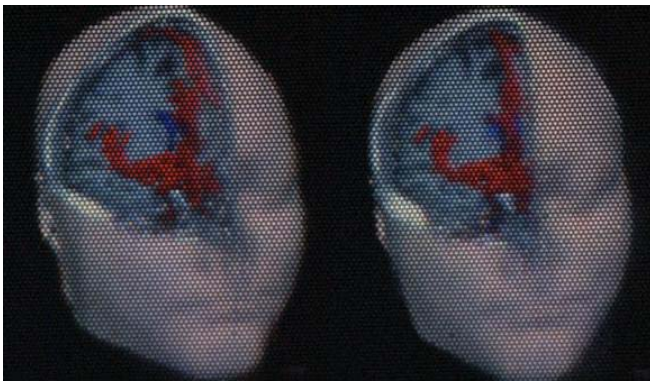
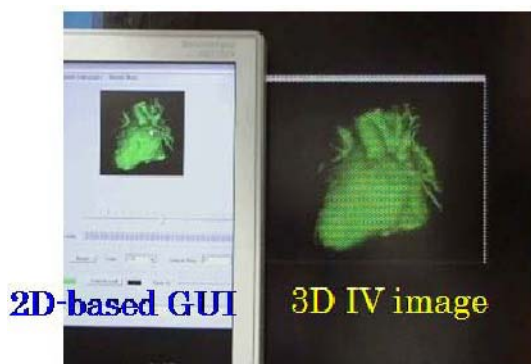


Fig. 9 Motion parallax of IV image



Zoom, Rotate, ...

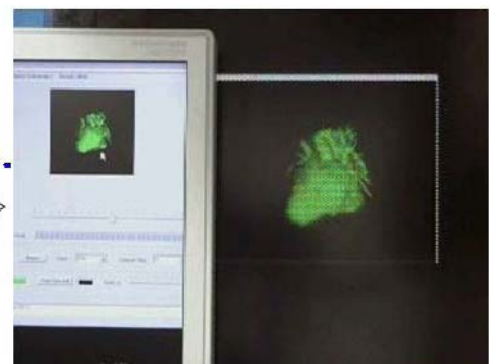


Fig. 10 2D based user interface

IV. DISCUSSION

The resolution of IV image is rather lower compared to the original image. This is because the number of micro lens is lower than the number of pixel in the original image. Using smaller micro lens would improve the resolution of IV, but as the number of pixels behind each lens becomes smaller, the region in which proper IV can be observed (the region contains green dots in Fig. 6) is smaller.

Due to the sampling theorem, distance between 2 sample viewpoints in Fig. 5 must at least be one half of the distance between 2 adjacent viewpoints in Fig. 6. Using less sample point would speed up the computation but deteriorate the quality of IV. In the experiment, 2562 sample viewpoints are used, consuming about 500MB of memory.

V. USER INTERFACE

We developed a 2D based user interface which enables user to interact with 3D IV image through the model on normal screen. Each time the model is updated, parameters of current viewing position is passed to the IV rendering module, IV image is rendered with the same parameters in high speed so that user would feel no gap between 2D and 3D image (Fig. 10).

VI. CONCLUSION

By using Light Field Rendering, part of the computation can be preprocessed so render speed of IV image is significantly improved. For image of size 1024x768 pixels it takes only 90 ms to render one frame, which is several times faster than the conventional method. Therefore, our system can provide surgeons with full parallax, interactive 3D autostereoscopic image and would be useful in medical solutions such as minimally invasive fetal surgery, mini-

mally invasive orthopedic surgery where precise, interactive 3D information of the instrument and patient anatomy is needed.

In the future, by implementing our algorithm on special hardware, we hope to improve the render speed to 20-30 fps so that smooth animation of IV can be visualized.

ACKNOWLEDGMENT

This work was supported in part by Communications R & D Promotion Programme (062103006) of the Ministry of Internal Affairs and Communications in Japan, Grant-in-Aid for Scientific Research (1710008, 17680037) of the Ministry of Education, Culture, Sports, Science and Technology in Japan and Grant for Industrial Technology Research (07C46050) of New Energy and Industrial Technology Development Organization, Japan.

REFERENCES

- [1] P. Lippman, "Epreuves reversibles donnant la sensation du relief," *Journal de Physique*, 7, 821-825, 1908
- [2] H. Liao, N. Nakajima, et al. "Intra-operative Real-Time 3-D Information Display System based on Integral Videography," *MICCAI 2001*:392-400
- [3] H. Liao, K. Nomura, et al. "Autostereoscopic integral photography imaging using pixel distribution of computer graphics generated image," *ACM SIGGRAPH 2005 poster*, No. 73, 2005
- [4] M. Levoy, P. Hanrahan, "Light field rendering," *Proceedings of the 23rd annual conference on Computer graphics and interactive techniques*, p.31-42, 1996.
- [5] W.C. Chen, et al., "Light field mapping: efficient representation and hardware rendering of surface light fields," *ACM Transactions on Graphics (TOG)*, v.21 n.3, July 2002.
- [6] T. Naemura, T. Yoshida and H. Harashima, "3-D Computer graphics Based on Integral Photography," *Opt. Exp.* 2001 Vol.8 No.4
- [7] Takeshi Naemura, Junji Tago, Hiroshi Harashima, "Real-Time Video-Based Modeling and Rendering of 3D Scenes," *IEEE Computer Graphics and Applications*, v.22 n.2, p.66-73, March 2002

Author: Hoang Tran Huy
Institute: The University Of Tokyo
Street: Hongo, Bunkyo-ku, Tokyo 113-8656
City: Tokyo
Country: Japan
Email: tran@atre.t.u-tokyo.ac.jp

Distortion Correction of Wedge Prism 3D Endoscopic Images

Y. Takata¹, T. Torigoe¹, E. Kobayashi², I. Sakuma²

¹ Graduate School of Frontier Sciences, The University of Tokyo, Tokyo, Japan

² Department of Precision Engineering, The University of Tokyo, Tokyo, Japan

Abstract— We have developed a wedge prism 3D endoscope moving its FOV with the rotation of the prisms to realize safe and precise robotic assisted laparoscopic surgery. However, it is difficult to perform image registration between preoperative MRI data and endoscopic images for image guidance surgery because our endoscopic images have prism-specific distortion. In this study, we propose the algorithms of distortion correction of the endoscopic images. Wedge prism distortion separated from lens distortion was corrected by tracking optical rays. The linearity of image distortion correction was 0.83 in a front of view and 0.94 in a right side view. By our developed method of image distortion correction, the disadvantage of wedge prism endoscope was improved. The wedge prism 3D endoscope is useful for the image guidance system in robotic assisted minimally invasive surgery.

Keywords—Endoscopic image, Robotic assisted surgery, Surgical navigation.

I. INTRODUCTION

Recently, minimally invasive surgery is widely performed in various fields of surgery. Robotic-assisted systems for them have been developed. To assist laparoscopic surgery, we have developed a wedge prism 3D endoscope that optically controls the FOV to avoid a risk of hitting internal organs due to manipulating its body [1-3].

For abdominal surgery such as hemihepatectomy, image registration between preoperative MRI volume data and intraoperative endoscopic images is useful to resect a partial liver around important vessels in safety. Therefore, several navigation systems for image guidance surgery combining pre-operative 3D image and endoscopic image have been studied [4-7].

However, our developed endoscope has a problem of image distortion caused by wedge prism. It has not only radial distortion derived from an endoscopic lens but also peculiar distortion derived from wedge prism. It is difficult to perform image registration between MRI volumes and endoscopic images because of its image distortion.

Wedge prisms distort endoscopic images. Rays from an focal point spread outward. They are not parallel. The incident and refraction angles vary depending on the position of rays. The rays through the outside of prisms bend sharper than those through the central of prisms. The outer of an

image captured by a wedge prism 3D endoscope is more distorted than the center of the image. The image distortion by wedge prisms varies depending on the direction of a viewpoint. Two CCDs face inward and a 3D endoscope has left image distortion and right image distortion. To correct image distortion through wedge prisms, the development of distortion correction based on optical tracking in wedge prisms is needed.

In this study, we propose a method to correct peculiar image distortion with wedge prisms to realize image navigation system for the wedge prism 3D endoscope in minimally invasive abdominal surgery.

II. METHODS

A. Wedge prism 3D endoscope

The wedge prism 3D endoscope (Fig 1) consisted of a 3D endoscope (LS-501D, Shinko Optical Co. Ltd, Tokyo, Japan), double wedge prisms and double motors. The diameter of the 3D endoscope was 5.4 mm. Two 1/10 inch CCD (270,000 pixels) and two wedge prisms (LAL18) mounted at the tip on it. Each prism was attached to a sleeve and independently rotated with a motor. It had a lens tube with a diameter of 14 mm excluding an optical fiber guide tube to insert into a trocar (ENDOPATH Large-Port Trocar, Ethicon) with a diameter of 18 mm. The endoscope has the angle of view of 76 degree and the maximum bending angle of 14.5 degree (Fig 2).



Fig 1 Wedge prism 3D endoscope

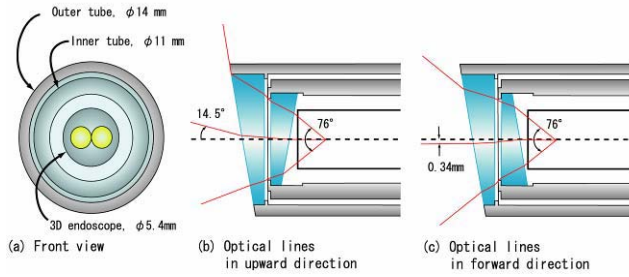


Fig 2 The assembly of double wedge prisms

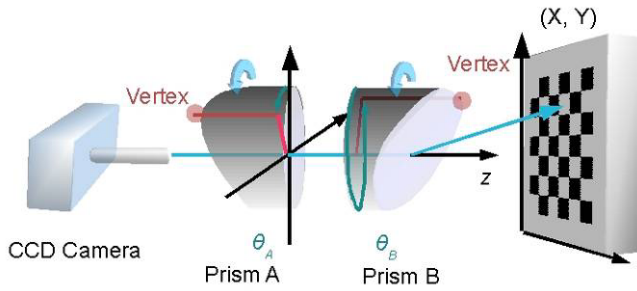


Fig 3 the rotation of prisms and the viewpoint of a wedge prism endoscope

The viewpoint of the endoscope was determined by the rotation angles of wedge prisms (Fig 3). The rotation of one prism rotates endoscopic views. The rotation of double prisms moves the views on 2D plane. The rotation angles of prism A and B are θ_A and θ_B . A viewpoint (X, Y) on a projected screen was determined by θ_A and θ_B . A viewpoint movement of wedge prisms 3D endoscope is controlled by the control of the rotation of prisms.

B. Image distortion correction

The distortion correction of wedge prism 3D endoscopic images was performed in three steps. The first step is to estimate the camera intrinsic parameter with camera calibration [8]. In a front view, the model plane containing a pattern of squares is captured by the endoscope at several times and the camera intrinsic parameter was estimated. The optical center line of wedge prisms is on the almost same line of endoscope in a front view, camera calibration can be done without the optical effects of wedge prisms. The second step is to correct distorted images derived from the endoscopic lens with the camera intrinsic parameter in the first step. The third step is to remove a distortion with wedge prisms from the corrected image in the second step. The distorted image was projected onto a virtual screen through a pinhole of the camera and the wedge prisms

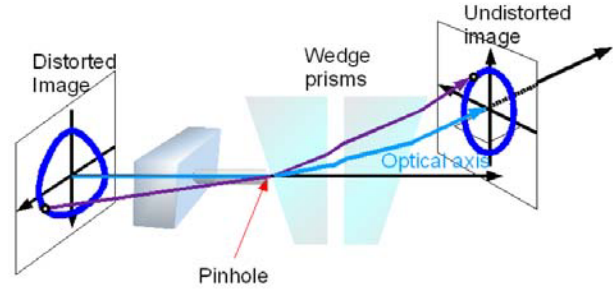


Fig 4 Projection of distorted image through wedge prisms

(Fig 4). The image distortion with wedge prisms was corrected by a ray trace through double wedge prisms at each pixel of the image.

C. Optical tracking in wedge prisms

To correct the image distortion with wedge prisms, we used the optical tracking in wedge prisms. The theory of the optical tracking with double wedge prisms is as follow. The refraction of a ray in wedge prisms is considered as 3D snell's law. In Fig 5, A ray refracts at plane Π_k ($k=1,2,3,4$). The vector v_k in wedge prisms was calculated with 3D snell's law (1)

$$n_k \frac{\mathbf{p}_k \times \mathbf{v}_k}{|\mathbf{p}_k| |\mathbf{v}_k|} = n_{k+1} \frac{\mathbf{p}_{k+1} \times \mathbf{v}_{k+1}}{|\mathbf{p}_{k+1}| |\mathbf{v}_{k+1}|} \quad (1)$$

where n_k is refractive index before Π_k , \mathbf{p}_k is normal vector of plane Π_k . Fig 5 shows the path of a refracted ray. The normal vector \mathbf{p}_k is determined by the angle of the wedge prism (2).

$$\begin{aligned} \mathbf{p}_1 &= {}^T [\sin w \cos \theta_A \quad \sin w \sin \theta_A \quad \cos w] \\ \mathbf{p}_2 &= \mathbf{p}_3 = {}^T [0 \quad 0 \quad 1] \\ \mathbf{p}_4 &= {}^T [-\sin w \cos \theta_A \quad -\sin w \sin \theta_A \quad \cos w] \end{aligned} \quad (2)$$

A refracted ray is represented as a recurrence equation (3) by 3D snell's law

$$\mathbf{v}_{k+1} = \left(\frac{n_k}{n_{k+1}} \right) \mathbf{v}_k + \left\{ \left(\sqrt{1 - \left(\frac{n_k}{n_{k+1}} \right)^2 (1 - (\mathbf{v}_k \cdot \mathbf{p}_k)^2)} \right) - \frac{n_k}{n_{k+1}} (\mathbf{v}_k \cdot \mathbf{p}_k) \right\} \mathbf{p}_k \quad (3)$$

and also the cross point on the plane of wedge prisms is represented as a recurrence equation (4)

$$\mathbf{C}_{k+1} = \mathbf{C}_k - \frac{(\mathbf{C}_k - \mathbf{d}_{k+1}) \cdot \mathbf{p}_{k+1}}{\mathbf{v}_k \cdot \mathbf{p}_{k+1}} \mathbf{v}_k \quad (4)$$

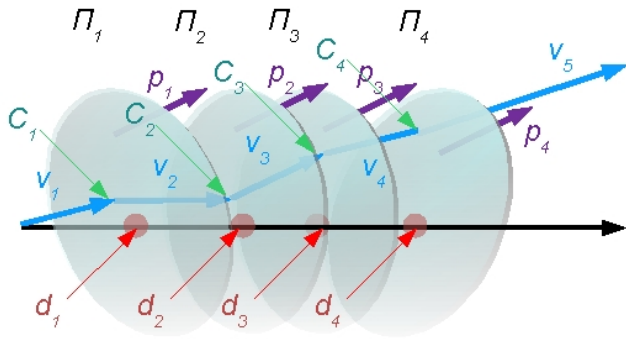


Fig 5 Optical tracking in wedge prisms

By using previous equations, any ray in a radial pattern from the endoscopic tip can be calculated. The image distortion is able to be estimated with the optical tracking.

III. RESULTS

Image distortion derived from wedge prisms was corrected by our method. The accuracy of image distortion correction was evaluated in a front-view image and a right-view image (Fig 6). In a front view, the model plane containing a pattern of squares was put at the front of the endoscope and images were captured. In a right-side view, the plane was put at right angles to the optical axis of a lens of the endoscope and images were captured. The distance between the endoscope and the board was 70 mm. Fig 7 shows the results. The endoscopic images in the front view and the right view were undistorted by our method. In a right view, the right side of endoscopic image was distorted by the refraction effects of wedge prisms.

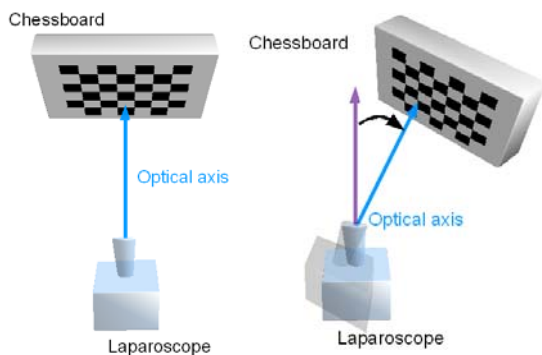


Fig 6 The evaluation of image distortion correction

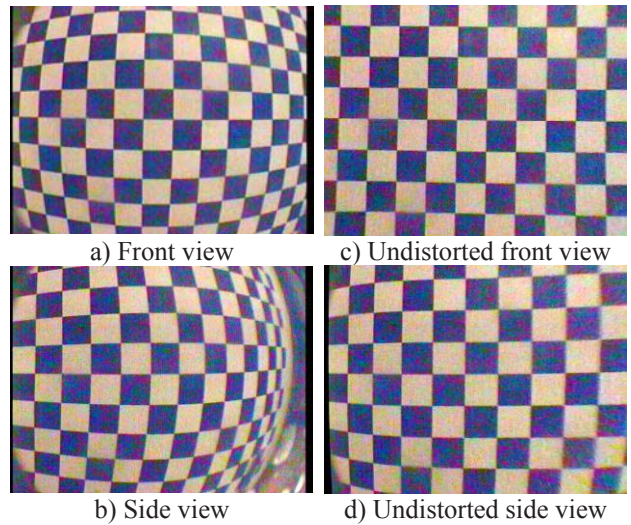


Fig 7 Original images and undistorted images

Table 1 The evaluation of image distortion correction

View angle	Mean value of R square	
	Original image	Undistorted image
Front	0.31	0.83
Side	0.48	0.94

The linearity of chess patterns of endoscopic images was measured to evaluate the accuracy of the image distortion correction. The corners of the squares were extracted from images. R-squared value of collinear approximation was calculated as linearity. As R-squared value approaches 1, a plotted line is close to linear.

In the front view, the average of R-squared value of a pre-corrected image was 0.31 and that of a post-corrected image was 0.83. In the right-side view, the average of R-squared value of pre-corrected image was 0.48 and that of post-corrected image was 0.94. With our method, the image distortions were remarkably improved in both cases (Table 1).

IV. CONCLUSIONS

An image distortion correction by using optical tracing in wedge prisms is able to correct wedge prisms endoscopic images. The same algorithm is useful for 3D endoscope with left and right images. The method has a difficulty of calculation in real-time because of amount of calculation.

We proposed a method to correct the distortion of wedge prism 3D endoscopic images. Compared to other robotic assisted endoscopes, our endoscope with optically move-

ment of viewpoint avoids a risk of hitting internal organs and has accuracy of moving its viewpoint. In addition, image distortion correction of wedge prisms enables to perform the accurate registration of preoperative MRI images and intraoperative endoscopic images.

Future work is to perform image registration with 3D endoscopic image. For abdominal surgery, it remains problems of intraoperative organ distortion and respiratory organ movement. The endoscopic navigation system is useful in a minimally invasive abdominal surgery and realizes a safe and accurate procedure.

ACKNOWLEDGMENT

This research is partly supported by JSPS(#18680041)

REFERENCES

1. Kobayashi, E., Masamune, K., Sakuma, I. & Dohi, T. A wide-angle view endoscope system using wedge prisms Medical Image Computing and Computer-Assisted Intervention - MICCAI 2000. Third International Conference. Proceedings (Lecture Notes in Computer Science Vol.1935), 2000, 661 – 8
2. Kobayashi, E., Sakuma, I., Konishi, K., Hashizume, M. & Dohi, T. A robotic wide-angle view endoscope using wedge prisms Surgical Endoscopy And Other Interventional Techniques, 2004, 18, 1396-1398
3. Kobayashi E et. al. (2007) Development of wide-angle view 3D endoscope using wedge prisms. Int J CARS 2(Suppl 1):S505
4. Dey, D., Gobbi, D., Slomka, P., Surry, K. & Peters, T. Automatic fusion of freehand endoscopic brain images to three-dimensional surfaces: creating stereoscopic panoramas IEEE Transactions on Medical Imaging, 2002, 21, 23 – 30
5. Wierzbicki, M. & Peters, T. M. Determining epicardial surface motion using elastic registration: Towards virtual reality guidance of minimally invasive cardiac interventions MEDICAL IMAGE COMPUTING AND COMPUTER-ASSISTED INTERVENTION - MICCAI 2003, PT 1, 2003, 2878, 722-729
6. Nakamoto M, Nakada K, Sato Y, Konishi K, Hashizume M and Tramura S. Intraoperative magnetic tracker calibration using a magneto-optic hybrid tracker for 3D ultrasound-based navigation in laparoscopic surgery. IEEE Transactions on Medical Imaging, in press.
7. Nakamoto M, Hirayama H, Sato Y, Konishi K, Kakeji Y, Hashizume M and Tramura S. (2007) Recovery of respiratory motion and deformation of the liver using laparoscopic freehand 3D ultrasound system. Medical Image Analysis 11(5):429-442
8. Zhang Z. (2000) A flexible new technique for camera calibration. IEEE Transactions on Pattern Analysis and Machine Intelligence 22(11):1330-1334

Author: Yuhei Takata

Institute: Graduate School of Frontier Sciences, The University of Tokyo, Tokyo, Japan

Street: Hongo 7-3-1

City: Bunkyo-ku, Tokyo

Country: Japan

Email: takata@bmpe.t.u-tokyo.ac.jp

Intraoperative Local Demarcation System of Brain Tumor Based on 5-Aminolaevulinic Acid Induced Porphyrin Fluorescence

T. Ando¹, M. Noguch², K. Shimaya², K. Wang², E. Kobayashi¹, H. Liao¹, T. Maruyama³, Y. Mulagaki³, H. Iseki^{3,4} and I. Sakuma¹

¹ Graduate School of Engineering, The University of Tokyo, Japan

² Graduate School of Frontier Sciences, The University of Tokyo, Japan

³ Department of Neurosurgery, Neurological Institute, Tokyo Women's Medical University, Japan

⁴ Institute of Advanced Biomedical Engineering and Science, Tokyo Women's Medical University, Japan

Abstract— A lightweight intraoperative spectrum measurement system for 5-ALA induced PpIX fluorescence was developed. The developed system includes a semiconductor LASER for excitation light (output light wavelength: 405nm), a CCD spectrometer, optical fiber coupled on lens system and PC. The first prototype device has a bundled fiber which contains 6 excitation fibers around one measurement fiber. The second one uses a dichroic mirror which reflects blue light ($\lambda \leq 550\text{nm}$) and transmits other wavelength. The third one contains not only a dichroic mirror but also a long path filter (cut on: $\lambda = 570\text{nm}$) and has improved mechanical strength. The weight of the first and the prototype probe is 45g, and the external diameter is 11mm. The weight of this probe is 25g and the external diameter is 18mm. The probes can be positioned manually and measure 5-ALA induced PpIX fluorescence.

Keywords— 5-ALA, Protoporphyrin IX, Brain tumor, Fluorescence measurement, Handheld device

I. INTRODUCTION

Glioma, originates in the glia cells, occurs with the highest frequency in primary brain tumors. Especially, malignant glioma such as glioblastoma has a poor prognosis because of their growing speed. In addition, there is high relationship between resection rates of malignant glioma and patient prognosis [1]. Recently, surgical navigation system using magnetic resonance images (MRI) and 3-D optical tracking system has been used to improve resection rates. Although they achieved more precise tumor resection, there are several registration errors affected by brain shift [2].

5-Aminolevulinic Acid (5-ALA) is a metabolic precursor of protoporphyrin IX (PpIX) that emits fluorescence with peak wavelength of 636nm with 405nm excitation light. Because 5-ALA specifically accumulates at malignant glioma tissues, it has recently been used for intraoperative demarcation and visualization of glioma tissues [3][4]. However, it is difficult to discriminate infiltrating tumor margin because of low sensitivity of naked eye detection. It is necessary to improve the fluorescence detection system

that has high sensitivity and high-resolution ability. Moreover, the quantitative spectroscopy is required for objective discrimination between tumor and normal brain tissues. In our previous study, we developed an intraoperative spectrum measurement system for PpIX fluorescence and a handheld spectroscopic device for localized identification of brain tumor with the measurement resolution 0.6mm. The device should be positioned at appropriate distance from the target point during measurement. However, the device is not light enough for handling. As a result, it was difficult to measure spectrum stably hold by hands. We developed a new pen-like lightweight fluorescence measurement probe. It is equipped with a coaxial light guide. It has high fluorescence signal collection efficiency and high spatial resolution. Specification of the probe was determined from the following clinical requirements: measurement time is no longer 1s, probe weight is lighter than 100g, and spatial resolution is smaller than 1mm

II. SYSTEM DESCRIPTION

A. Overview

An Intraoperative spectrum measurement system is constructed of a semiconductor LASER for excitation light source (output wavelength: 405nm, Digital Stream, Yokohama Japan), a CCD spectrometer (BTC111E, B&W Tek Inc., Delaware, USA), optical fibers coupled on lens system (fluorescence detection probe) and PC for controlling a LASER and a spectrometer. A collimation lens and an adjustable FC-type coupler are mounted to a LASER outlet port in order to put in the light beam to the optical fiber efficiently. Output power is variable by changing applied direct voltage (0 to 4V). A diode array spectrophotometer with 2048 channels CCD image sensor was used for spectrum measurement. Its wavelength resolution is 0.3nm.

B. Fluorescence measurement probe

We developed three prototype probes.

The first prototype probe has a bundled fiber that contains 6 excitation fibers around one measurement fiber (Fig.1). The excitation fibers are connected to a semiconductor LASER and the measurement fiber is connected to a spectrometer. The core diameter of each fiber is 400µm and numerical aperture (N.A.) is 0.22. At the top of the probe, there are two achromatic lenses for both excitation light collection and fluorescence measurement. The focal length of both an object side and a fiber side one are $f=18\text{mm}$ and the diameters of two lenses are $d=9\text{mm}$. The working distance of this probe is about 13mm. The weight of this probe is 45g, and the external diameter is 11mm. The bundled fiber is located at focal point of fiber side lens, whence it can estimate from the lens magnification that the measurement spot diameter is about 400µm.

The second prototype probe uses a coaxial optical system. A dichroic mirror is used for separation of excitation light and fluorescence. To insert a dichroic mirror on the light path, three collimator lenses are mounted to a cubic box. Fig.2 shows schematic diagrams. Angles and Positions of all collimator lens and a dichroic mirror can be adjusted to improve coupling efficiency of the light.

The excitation light from a semiconductor LASER is reflected by a dichroic mirror (cut off: $\lambda \leq 550\text{nm}$) and enters

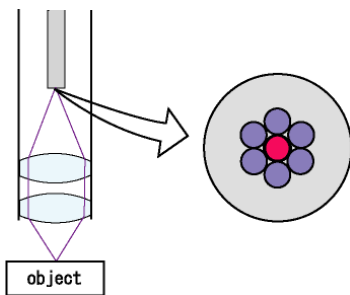


Fig. 1 The first experimental probe

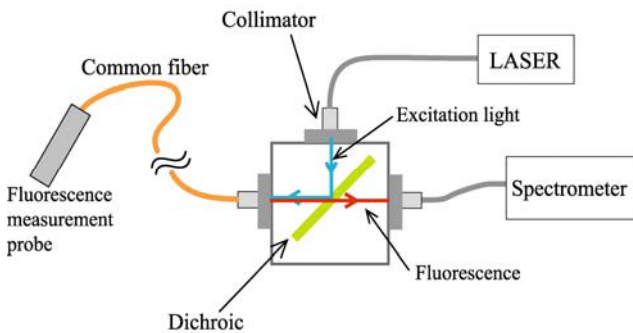


Fig. 2 The second experimental probe

the common fiber. Excited fluorescence light re-enters to the common fiber from opposite side. The dichroic mirror only transmits only fluorescence light, therefore it is possible to measure spectrum of PpIX fluorescence.

A core diameter of the common fiber is 365µm and the lens unit is the same to the first probe. It can also estimate that the spot diameter is almost the same to a core diameter of the fiber.

The third prototype probe is the same mechanism as the second one. However, it has improved mechanical strength and optical stability. It is also equipped with a long pass filter to remove the reflected excitation light from fluorescence signal. Specification of the optical lens system changed as follows: focal length of a fiber side lens is 19mm, that of an object side is 30mm, the working distance is 22mm and lens diameter is 12.5mm. The weight of this probe is 25g and the external diameter is 18mm. Other fibers are the same to the second prototype probe. The measurement spot diameter is estimated as about 580µm from lens magnification.

At the third experimental probe, the spectrum measurement software was also improved in order to prevent from influence of the room light. The procedure of the spectrum measurement is as follows: one sets the probe manually to appropriate distance from object leaving an excitation light on. After positioning the probe at a proper location, scanning is started by click a "Scan" button. Dark current is measured while the excitation light is turned off (dark scan). Then, the excitation light is turned on and spectrum measurement is conducted (normal scan). Background noise such as signals from ambient light is eliminated from the measured data by subtracting dark scan data from normal scan data.

III. PERFORMANCE EVALUATION

All experimental probes were evaluated their optical properties such as output light power, light collection efficiency and the optimal distance between the probe and objects. Fluorescence measurement ability was also examined in vitro and in vivo.

A. Optical properties

A light power meter (ADVANTEST TQ8210) was used to measure output light power quantitatively. The output power efficiency was evaluated from comparing an intensity at the edge of the probe with the intensity of the LASER output.

The light collection efficiency was evaluated by measuring an intensity of light reflected from a white board under

constant illumination using a spectrometer. During measurement, the probe was stably fixed in front of a white board. Then, the intensity at wavelength of 635nm was compared with that collected with an optical fiber (Core diameter: 365 μ m, N.A: 0.22, Length: 1m) placed at the same position as the probe. The light collection efficiency was defined as the ratio of the intensities acquired by the probe and an optical fiber.

A relationship between a distance from the probe edge and acquired intensity was measured using a mechanical stage. A white board fixed to the stage was stepped away from the edge of the probe measuring spectrums at each 0.1mm.

B. *In vitro* and *In vivo* experiments

Agar gel with PpIX and Intra Lipid-10% (scattering matter) was used to confirm the device's spectrophotometric measurement function. The optical phantom of agar gel was made as follows: 1.5g of agar powder were dissolved in 47.85ml of boiled pure water. After agar was dissolved completely, 1.15ml of Intra Lipid was pored to the agar solution. 1ml PpIX solution was added to the agar solution after it was cooled slightly. Then, the solution was well stirred. PpIX concentration used in this experiment was 200 μ g/ml. Concentration of Intra Lipid was controlled so that the optical phantom had the same scattering coefficient with brain tumor [5][6].

The reproducibility of measurement was examined as follows: 25 holes were filled with agar gel with PpIX and then spectrum was measured by manual. Sample in each hole was measured only once in order that the data were not influenced by bleaching of PpIX.

The first prototype probe is also tested *In vivo* experiments. A pig normal brain is used. The experiment was conducted with protocol approved by the in-house ethics committee. Before craniotomy, 50ml/kg of PpIX was administered by intravenous injection. 5-ALA accumulates even at a normal porcine brain tissue if excessive amount is administrated. A neurosurgeon evaluated usability of the system.

IV. RESULTS AND DISCUSSION

The output light powers measured by a light power meter are as follows: the output light power of the first experimental probe was about 11.2mW, the second one was 9.5mW, and the third one was 7.8mW. Since the input light power was set at the power of 14.5mW, 77%, 68%, and 54% of the input light power was transmitted respectively.

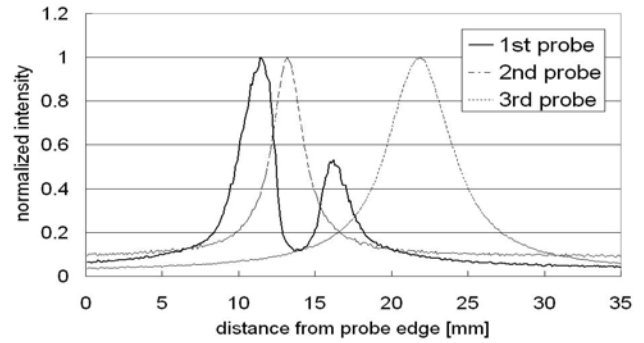


Fig. 3 Relationship between acquired intensity and probe edge

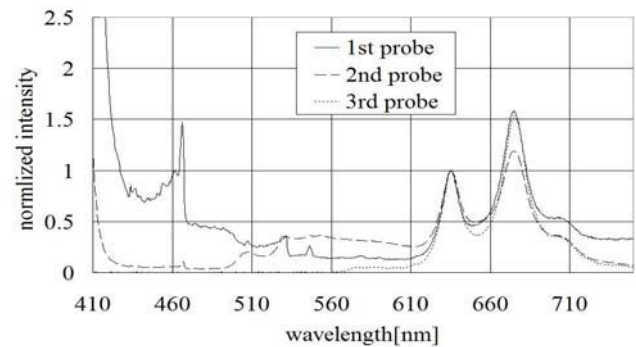


Fig. 4 The acquired spectrum using optical phantom

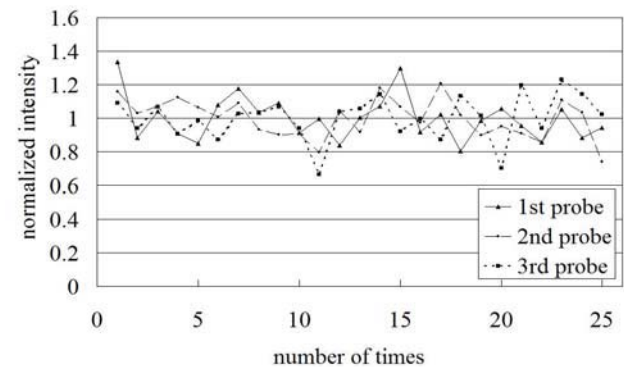


Fig. 5 The stability of spectrum measurement using phantom

The light collection efficiency of the first probe was 91%, the second one was 67% and the third one was 69%.

Since the excitation and the measurement fiber of the first probe are directly connected to a LASER, coupling efficiency was the largest. In the second and the third one, a dichroic mirror and collimator lenses lowered efficiency. Especially, the collimator lenses of the third experimental probe could not be adjusted adequately because of their adjusting mechanism.

A relationship between a distance from the probe edge and obtained signal intensity is shown as Fig.3. Each graph was normalized by maximal intensity.

The first probe has two peaks because it uses a bundled fiber. Since the edge of the bundled fiber is completely projected to objects at its focal point, an excitation light cannot be superimposed onto measurement spot. In fact, there is a "valley" at the point where the second probe (completely coaxial light path) acquires maximal intensity. If the measurement object is a brain tissue, this valley will become smaller since an excitation light infiltrates several hundred micro meter in tissue.

The second and the third probe have single peak around their focal point. The peak of the third probe is wider than the second one because N.A. of lens system is smaller.

Measured spectra of optical phantom using each probe are shown in Fig.4. The spectrum was normalized by the intensity at the wavelength of 635nm in order to compare spectra shapes. Fig.5 shows the result of the evaluation of measurement stability. The abscissa axis is the number of measurement times and the vertical axis is the acquired intensity at 635nm. The intensity was also normalized by the average intensity over 25 time measurements.

These results show that each probe can measure PpIX peak at 635nm. Since the first probe has no filter, strong reflected light of the excitation light appears at 400~500nm. Furthermore, a baseline of the spectrum is elevated compared with those obtained by the other two probes because photo electrons leaks from one photodiode array channel to the neighboring channels in the CCD image sensor under strong input light. Although the second probe has a dichroic mirror, the reflected light was observed. In the third probe, almost no reflectance was observed as a result of inserting a long path filter.

The spectrum measurement stabilities of each probe were almost the same performances. There were about 20% fluctuations attributed to difficulty of manual adjustment of the distance to the object. This result implies use of a raw intensity data might leads to errors in demarcation of tumor. Normalized intensity data or the shape of the observed fluorescence spectra should be used.

At In vivo experiments, a similar spectrum to optical phantom was acquired. However, it was impossible to measure the PpIX peak if there was much blood over a brain surface. It is need to rinse blood as much as possible

in clinical practice. It was also required that the working distance should be longer, like 20~30mm.

V. CONCLUSION

The intraoperative spectrum measurement system was developed. The first prototype probe has a bundled fiber, the second and third one are completely coaxial using a dichroic mirror. A relationship between a distance from the probe edge and acquired intensity was evaluated. In vitro and In vivo experiments were also performed. The weight of the first and the prototype probe is 45g, and the external diameter is 11mm.. The weight of this probe is 25g and the external diameter is 18mm.Each probe could measure a spectrum of protoporphyrin IX fluorescence with a high resolution.

REFERENCES

1. The Committee of Brain Tumor Registry of Japan. (2000) Report of brain tumor registry of Japan (1969-1993). 10th ed. Neuro Med Chir (Tokyo); 40(Supply)
2. Nabavi A, Black PM, Gering DT, Westin CF, Mehta V, Pergolizzi RS Jr., Ferrant M, Warfield SK, Hata N, Schwartz RB, Wells WM 3rd, Kikinis R, Jolesz FA. (2001) Serial intraoperative magnetic resonance imaging of brain shift. *Neurosurgery* 48:787-797
3. Stummer W, Novotny A, Stepp H, Goetz C, Bise K, Reulen HJ. (2000) Fluorescence-guided resection of glioblastoma multiforme by using 5-aminolevulinic acid-induced porphyrins: a prospective study in 52 consecutive patients. *J Neurosurg* 93:1003-1013
4. Stummer W, Pichlmeier U, Meinel T, Wiestler OD, Zanella Friedhelm Z, Reulen HJ. (2006) Fluorescence-guided surgery with 5-aminolevulinic acid for resection of malignant glioma: a randomized controlled multicentre phase III trial" *Lancet Oncol* 7:392-401
5. Tuan Vo-Dinh (2003) *Biochemical Photonics HANDBOOK*. CRC Press
6. H. J. van Staveren, C. J. M. Moes, J. van Marle, S. A. Prahl, and M. J. C. van Gemert. (1991) Light scattering in Intralipid-10% in the wavelength range of 400-1100 nm *Appl. Opt.* 30:4507

Author: Takehiro Ando

Institute: The graduate school of engineering, The University of Tokyo

Street: Hongo 7-3-1

City: Bunkyo-ku, Tokyo

Country: Japan

Email: take_and_o@bmqpe.t.u-tokyo.ac.jp

Author Index

A

Abbaspour A. 269
Abe Y. 62, 66
Akhlaghpour S.H. 269
Ando T. 754
Arafune T. 484

B

Babapour F. 269
Bai Dongting 290
Bai Yanping 210, 213
Bo Xuefeng 117

C

Cai Changsi 54
Cai Hua 385
Cai R. 333
Cai Xiang 29
Cao Dong 524
Cao Hui 524
Cao Lei 58
Cao Pengjia 54
Cen Lian 88
Chai Jihong 567, 623
Chai Xinyu 54, 399, 492
Chang Yu 44, 47, 50
Chen Anyu 645, 648, 685
Chen C.H. 190
Chen Di 534
Chen Guoshao 404
Chen Hong-Li 13
Chen Huafu 639
Chen Jialiang 651
Chen Jianping 73, 76
Chen Lian-feng 92
Chen Lingling 155, 488
Chen Min-Mao 13
Chen Ningning 47, 44
Chen Panpan 54
Chen Rufu 29
Chen S. Q. 598
Chen S.C. 202
Chen Wei 317
Chen Wen-zhi 551
Chen Xuejun 528

Chen Xuemei 4
Chen Y.T. 190
Chen Yanhui 574, 344
Chen Yongbin 466
Chen Yong-Jin 99
Chen Yongpeng 70
Chen Yu 255
Chen Z. 381
Chen Zhili 404
Chen Zikuan 237, 434, 206
Cheng Qiuju 151
Chinzei T. 62, 66
Chu Li-Xi 691
Chua Y.L. 159
Cong Y. 500
Cuong N.V. 190

D

Dai Xiangkun 447
Deng Xiaowu 447
Ding Fei 4
Ding G.R. 458, 469
Ding Zuquan 133, 103
Dohi T. 741
Dohi Takeyoshi 745
Du Qian 58
Du Yaohua 608
Duan J.H. 202

E

Edwards Christopher 603

F

Fan Y.B. 133, 182, 329
Fang Liu 420
Fang Quan 92
Fang Yang 534
Fang Ying 164, 167, 171
Fu Liyuan 555

G

Gao Bin 44, 47, 50
Gao Fu-Ping 13
Gao H.T. 497

Gao Hongjian 213, 210
Gao Ming 678
Gao Shiyong 36
Ge Ruigang 447
Geng Daoying 668
Goetz W.A. 159
Gong H. 182
Gong Hanshun 447
Gong Hanyan 58
Gong Siyuan 155
Gorelik Julia 603
Gu Huiru 480
Gu Ning 534
Gu Xiaosong 4
Guo G.Z. 458
Guo Genying 711
Guo Guanghua 80
Guo Guo-Zhen 455, 461,
518, 466, 469, 473
Guo Liang 636
Guo Qiyong 225
Guo Shengwen 260
Guo Xia 103
Guo Xin 417
Guo Xingming 577
Guo Xueqian 648
Guo Yanhai 404
Guo Yao 455
Guo Zhuowei 151, 636

H

Han Feng 221
Han Jun 623, 626
Han Junnan 574, 344
Han Xiaopeng 645
Han Z. Z. 194
Han Zheng 206
Hao An 366
Hao H.W. 430, 660
Hao Hongwei 179, 392
He F. 113, 143
Heng P. 381
Hoang Tran Huy 745
Hong Haifa 139
Hsieh M.F. 190
Hu C.H. 430
Hu Chunhua 179

Hu Peng 1
 Hu Q. 381
 Hu Q.X. 588
 Hu Qing-xi 584, 720, 725, 733,
 737, 84, 88, 250, 729
 Hu Xiaogang 352
 Hu Y. 202
 Hu Yin-e 663, 681
 Hu Zhaoying 385
 Hu Zhuicheng 681
 Huang Anhu 341
 Huang Peixin 73, 76
 Huang Qingsheng 167
 Huang X.L. 326
 Huang Yifu 29
 Huang Yu 420
 Huang Yueshan 514

I

Inoue Y. 62, 66
 Iseki H. 754
 Isomura T. 484, 62, 66

J

Jeng Yih-Nen 707
 Ji Chenfeng 36, 507, 528, 531
 Ji ChengFeng 503
 Ji Yubin 36, 503, 507, 528, 531
 Jia Wei 691
 Jiang Fang-Yi 511, 408
 Jiang Jie 715
 Jiang Yingping 668
 Jiang Zhiqiang 293
 Jimbo Y. 484
 Jin Xianchun 70
 Jing Xijing 594
 Ju Shaohua 88

K

Kang Tianliang 361
 Kang Yan 206
 Ke Ming. 577
 Kishi A. 62, 66
 Kizaka-Kondoh S. 518
 Klenerman David 603
 Kobayashi E. 484, 754
 Kobayashi Etsuko 750
 Kong H. 194

Korchev Yuri 603
 Kouno A. 62, 66
 Kuai Le 678, 715

L

Lab Max 603
 Lan Qi 32
 Lan Wei 73, 76
 Lang Lang 507
 Lao Yonghua 164, 171
 Lee Shang-Yin 707
 Li C.S. 363
 Li C.Y. 497
 Li Deyu 329
 Li Fan 615
 Li Faqi 555
 Li Gang 317
 Li Gui 451
 Li Hong 245
 Li J.Z. 129
 Li Jiandong 442
 Li Jin 151, 636
 Li K.C. 458
 Li Keshen 636
 Li L.M. 430, 660
 Li Lao 580
 Li Liming 54
 Li Ling 44, 47, 639
 Li Luming 392, 179
 Li Quanyi 555
 Li Quhuan 164
 Li Quhuang 171
 Li Ran 329
 Li Shanglin 357
 Li Wei 542, 546
 Li X.Y. 113, 143
 Li Xia 361
 Li Xiaoliang 54, 80
 Li Xue-Ming 13
 Li Y. 333
 Li Ying 655
 Li Yinghui 317
 Li YueChang 700
 LI Yu-Rong 461
 Li Z. 333
 Li Zhao 84
 Li Zhengyu 703
 Liang Dong 399
 Liang Hong 151, 636
 Liang Ke-Dao 511
 Liang Song 155
 Liang Ting 317
 Liao H. 754
 Liao Hongen 741, 745
 Liao Xiaoyan 537
 Lim K.H. 159
 Lin Hui 451
 Lin Jianguo 171
 Lin Liulan 84, 88
 Lin Shaojie 571, 357
 Lin Wei 216, 26
 Lin Xue 92
 Liu Aizhen 290
 Liu Bo-jiang 92
 Liu C. 497
 Liu Chang-Jun 615
 Liu Chao 233
 Liu Cong-ying 697
 Liu D.C. 264, 273, 278, 282,
 286, 293, 408, 537
 Liu Dewu 73, 76, 80
 Liu F.J. 430
 Liu Fangjun 179
 Liu Guanglei 329
 Liu H. 123
 Liu Hongzhi 216
 Liu Huan 511
 Liu Huwei 492
 Liu J. 381
 Liu Jie 4, 488
 Liu Jinfen 139
 Liu Jinghua 361
 Liu Jiren 206
 Liu Kai-Dong 473
 Liu Li 167
 Liu Qidong 480, 488
 Liu Qingjun 306, 309
 Liu Qiong 260, 357, 571, 580
 Liu R. 377
 Liu Shengping 302
 Liu Tangyi 678
 Liu Tianjun 558
 Liu Tie-bing 426
 Liu Ting 641
 Liu Wei 524
 Liu X. 377
 Liu Y.H. 123
 Liu Yafei 685
 Liu Yingzheng 139
 Liu Yuangang 26, 32
 Liu Yuhong 245
 Liu Zhicheng 645, 648, 117
 Liu Zhipeng 655

Liu Zhipeng 366
 Liu Zongbin 306
 Lu Cheng 352
 Lu Guanghua 668
 Lu Guohua 594
 Lu Huihai 233, 241
 Lu Laichun 70
 Lu Lu 22
 Lu Qi 250, 720, 729, 733, 737
 Lu Yiliang 317
 Luan Kuan 636
 Luo Chong 373
 Luo Fei 273
 Luo Lailong 70
 Luo Xin 9, 18
 Luximon Y. 500
 Lv Feng 558
 Lv Hao 594
 Lv Xin 99

M

Ma B. 107
 Ma B.Z. 430
 Ma Bozhi 179, 392
 Ma Liying 603
 Ma Xin 389
 Ma Xinrui 44, 47
 Ma Y.B. 497
 Mao Yuanguai 73, 76
 Maruyama T. 754
 Masahiro Hiraoka 518
 Masamune Ken 741, 745
 Matsuda Y. 484
 Matsumiya Kiyoshi 741, 745
 Meng J. 194, 198
 Miura H. 62, 66
 Miyakoshi J. 458
 Mulagaki Y. 754

N

Nakagawa H. 62, 66
 Ning X.B. 326
 Niu C.S. 660
 Niu Haijun 329, 58
 Niu Jinghai 542, 546
 Niu Wenxin 103, 133
 Noguch M. 754

O

Ono T. 62, 66

P

Pan Qiaoling 167
 Pan Shi-rong 9, 18
 Pan Xiaochuan 221
 Pang Xiu-xiang 733
 Peng Ningfu 29
 Ping Ziliang 290
 Pu Fang 329
 Pu Lina 366

Q

Qi J. C. 598
 Qi Yu-Hong 473
 Qi Yusha 22
 Qian Jiang 13
 Qian YueHong 255
 Qiao A. 107
 Qiu Juhui 40
 Qiu Y. 333
 Qiu Yun-Ping 691
 Quan Haiying 117

R

Rao Nini 639
 Ren Dong-Qin 461
 Ren Dong-Qing 455, 473
 Ren Haiping 290
 Ren Qiushi 54, 58, 317, 399, 492
 Rolfé P. 377, 413

S

Saito I. 62, 66
 Sakhaeimanesh A.A. 95
 Sakuma I. 484, 750, 754
 Scopesi F. 377, 413
 Serra G. 413, 377
 Shan Lian-gang 323
 Shen Guang-si 103
 Shi Chang-Hong 469
 Shi Cheng 700
 Shi Linxi 44, 47, 50
 Shi Li-yi 323
 Shi Qi Fang 700
 Shi W. 62, 66
 Shi Zengguang 155
 Shimaya K. 754
 Song Chenxia 720
 Song L. 198

Song Li 366
 Song Lifeng 237
 Song Rong 623
 Su Ming-Ming 691
 Su Quan 623
 Su Xiao-Ming 473
 Sui Xiaohong 317
 Sui Y. 107
 Sun B. 326
 Sun Cai-Xin 511
 Sun J.W. 377, 413
 Sun Jian 84
 Sun Li-qun 551
 Sun Mingjie 54
 Sun Qi 139
 Sun Xiwen 703
 Sun Yu-bao 426
 Sun Z. 202, 588

T

Takeshi T. 750
 Tan H.N. Serena 129
 Tan Haimin 313
 Tang Guang 636
 Tang Li-Ling 511
 Tang Li-ming 426
 Tang Mingwang 282
 Tang Nan 58
 Tang Wei-chang 697
 Tao Chunjing 476, 480
 Tao Jiang 40
 Tao Kan 542, 546
 Tao Yin 366
 Teo E.C. 119
 Tian Aiying 417
 Tian Feng 615
 Tian Jinhuan 22
 Tian Xin 361, 641
 Tian Yukun 492
 Tong Aili 84
 Tong S. 333

W

Wan Dawei 139
 Wang C. Y. 194, 198
 Wang C. 198
 Wang Chong 531
 Wang Chunyan 260
 Wang Dong 577
 Wang Guixue 40, 70

Wang H. 363, 497
 Wang Hai 584
 Wang Han-Guo 99
 Wang Hong 298
 Wang Hongwei 711
 Wang Jianqi 594
 Wang Jianyu 352
 Wang Jiao-jiao 737
 Wang Jing-Jie 99
 Wang Yunlai 447
 Wang K. 754
 Wang Kai 317
 Wang Lianqun 73, 76
 Wang Lianyuan 447
 Wang Ping 313, 385, 396, 329
 Wang Q. 588
 Wang Qian 139
 Wang Qiang 278
 Wang R. 198
 Wang Shengzhang 147
 Wang Shibin 26, 32
 Wang Shuo 352
 Wang Tao 651
 Wang W. 202
 Wang Weiming 392
 Wang X.W. 458
 Wang Xiaoning 174
 Wang Xiao-Wu 461, 469
 Wang Xitai 155, 476
 Wang Y. D. 598
 Wang Y. 123
 Wang Yan 668
 Wang Ying 245, 32
 Wang Yongli 241
 Wang Z. 598
 Wang Z.F. 123
 Wang Zhanping 373
 Wang Zhi-biao 551
 Wang Zhifang 245
 Wear James O. 558
 Wei Xing 237
 Wei Yunlong 302
 Wei Zhi-hui 426
 Wen X.W. 430
 Wen Yuting 9, 18
 Weng Xiaohong 629
 Wu Aidong 451
 Wu Baoming 298
 Wu Chunsheng 313
 Wu Di 729, 584
 Wu Fu 725
 Wu Jian 4

Wu Jianbo 260, 348
 Wu Jianhua 164, 167, 171
 Wu Junru 534
 Wu Kai 580, 344, 348
 Wu Li 558
 Wu Min 426
 Wu Qing 29
 Wu Shuicai 213, 210
 Wu Taihu 608
 Wu Wenguo 26
 Wu Xiaoming 344, 348, 357,
 260, 562, 571, 574, 580
 Wu Yican 451
 Wu Yongbo 302
 Wu Yuebo 651

X

Xi Xiaoyu 534
 Xia S. 598
 Xia Yang 373
 Xia Yong 711
 Xiao Feng 503
 Xiao Lidan 309, 385
 Xiao Shouzhong 577
 Xiao Xianglin 542, 546
 Xie Chuanbin 447
 Xie Lingli 420
 Xie S.S. 194, 198
 Xie Xue-Jun 455, 469, 518
 Xie Yijing 317
 Xie Z.X. 123
 Xie Zhengxiang 245
 Xing Nan 615
 Xiong Dongsheng 574
 Xiong F. 159
 Xu Bo 603
 Xu Gao-chun 584, 725, 729
 Xu H.Y. 194, 198
 Xu Jianfen 685
 Xu Lin 562
 Xu Mantao 216, 225, 241
 Xu Ping 668
 Xu Qin 737
 Xu Shouping 447
 Xu You-jia 103
 Xu Yuan-zhi 737

Y

Yamaguchi-Sekine S. 62, 66
 Yan Juntao 703

Yan Mi 511
 Yan Xi 58
 Yan Zhuangzhi 255
 Yang Chun-lan 210, 213
 Yang Hongli 567, 623, 626
 Yang Huayuan 663, 678, 681,
 711, 715
 Yang J. Q. 598
 Yang Le 417
 Yang Lihong 404
 Yang Liqun 29
 Yang Lu 229
 Yang M. 198
 Yang Mo 306, 309
 Yang Peng 306, 309, 417, 488
 Yang Qi-xiang 737
 Yang Song-Bin 691
 Yang Wen-Zhi 13
 Yang X.D. 202
 Yang Xiaolin 633
 Yang Yumin 4
 Yang Yunfeng 133
 Yao Y. 588
 Yao Yuan 720, 725, 733, 737,
 584, 250
 Ye Yalin 645, 648
 Yeo J.H. 159
 Yi Jun 524
 Yin Ming 103
 Yin Tao 655
 Ymanaka Noriaki 741
 You Fei 725, 250
 You Ling 514
 Yu Gaohang 420
 Yu Guangrong 133
 Yu Hao 396, 623, 626
 Yu Hui 309, 313, 385
 Yu Jinjiang 306, 309
 Yu Lei 507
 Yu Mengsun 174
 Yu Y. 660
 Yuan Hengxin 562
 Yuan Ni 404
 Yuan Shi Ying 524
 Yuan Yuan 179
 Yuhei T. 750

Z

Zeng Chao 511
 Zeng Gui-Ying 455
 Zeng Li-Hua 455, 469, 461, 518

- Zhang Chunpeng 373
Zhang Dong 534
Zhang Gang 70
Zhang Huicun 88, 13
Zhang Jiafeng 84
Zhang Jie 461, 469
Zhang Jing 711
Zhang Jiwu 216, 221, 225, 233, 241
Zhang Ju 404
Zhang Jumei 571
Zhang Li 473
Zhang Lili 580
Zhang Li-Ming 29
Zhang Liwei 636
Zhang M. 500, 182, 326
Zhang Min 99
Zhang P. 159
Zhang Q.H. 119, 129
Zhang Qingping 623
Zhang Qi-Qing 13
Zhang Shu-ping 323
Zhang Tengyu 488
Zhang Tie 442
Zhang Wei 18, 9, 306, 385, 434
Zhang X.J. 113
Zhang Xi 352
Zhang Xiangrong 80
Zhang Xiaoyu 476, 480
Zhang Xu 645, 648
Zhang Xuan 18
Zhang Xuefeng 434
Zhang Yang 594
Zhang Yanjun 603
Zhang Yanru 562
Zhang Yihe 685
Zhang Yu 655
Zhang Zhengguo 633
Zhang Zhian 80
Zhao Jun 229
Zhao Luhang 313
Zhao Qi 348
Zhao Tao 469
Zhao Yi 420
Zhao Ying 399, 492
Zhao Yong-Liang 615
Zhao Yu-ping 697
Zhao Zhicong 571, 357
Zhen Minghui 264
Zheng Yi 323
Zhou Changren 22
Zhou Hai-bin 103
Zhou Jing 344
Zhou Weidong 341, 337, 389
Zhou Wenxin 711
Zhou Xiaoming 286
Zhou Yi 420
Zhu Cheng 164, 171
Zhu Ming 139
Zhu Shi 385
Zhu Y. 333
Zhuang J.J. 326
Zoroofi R. 269
Zou Chang-xu 461, 518
Zou Jian-zhong 551
Zou M. 326
Zou Xiang 36
Zuo Nianming 221
Zuo Siyang 741

Subject Index

- 2**
2N+1 sources 229
- 3**
3-D visualization 210
- 5**
5-ALA 754
- A**
A6 cells 603
AAA-ICT 123
ABM 50
Absolute pressure sensor 66
Acetylcholinesterase 323
Active knee joint 155
Acupuncture Analgesia 715
Acupuncture manipulation parameter 663
Acupuncture 651, 678
Acute swimming exercise 678
ADAMS 151
Adaptive interference cancellation 245
Adaptive method 381
Adverse Biological Effects 580
AK prosthesis 488
Alginate 22, 26
Aliasing 278
Alkanes and aromatic hydrocarbons 396
Amputation 480
AMS 389
Amylose 29
Analgesia 703
Anechoic 282
Animal experiment 430
Anisotropic equation 255
Antegrade pulmonary blood flow 139
Anterior cruciate ligament reconstruction 103
Anti-cancer drugs 309, 32
Antimicrobial peptide 167
Antioxidant enzymes 678
Anti-tumor 202
- Apoptosis 198
Apoptosis 507, 511
Approximate algorithm 229
Area of interest 546
ARM 417
Arrhythmia 651
Artifact 337
Artificial heart valve detector (AHVD) 352
Artificial vision 58
Asparagus polysaccharide 528
Astronauts 179
Auditory intensity perception 333
Augmented Reality 733
Auto-correlation 245, 278
Automatic calibration method 66
Auto-reference 245
- B**
Ballistocardiogram 594
Band 3 proteins 528
Basic fibroblast growth factor 80
Basic multicellular unit 182
BEAM 685
Behavior 473
Bidirectional cavopulmonary anastomosis 139
Biochemical function 503
Biochemistry 531
Biocompatibility 40, 317, 4
Biodegradable 22
Bioinformatics education 633
Biological contamination 598
Biological effect 198
Biological focal region 555
Biomechanical properties of iris 117
Biomechanics 155
Biomedical course 636
Biomedical engineering technicians 558
Biomedical engineering 623, 636, 639, 641, 645
Biomembranes 302
Biosensor 313, 302
Bipolar current 58
Blind men 213
Blood gas and pH 413
- Blood Pump 50
Blood vessel segmentation 233, 241
BME education 629
BMET 558
B-mode ultrasound Image 546
Body temperature 344
Bone tissue engineering 84
Bone tunnel enlargement 103
Boolean operation 725
Border detection 537
Brain tumor 754
Brain-computer interface (BCI) 341, 363
Broccoli 507
BSA 615
- C**
C0 Complexity 420
Ca²⁺ in the cell 36
Ca²⁺ 678
Ca²⁺-ATPase 678
CABG 107
CAHTMA 558
CAN 417
Cancer 309, 511
Carbamate pesticides 323
Carbon nanotubes 194, 198
Carbon nanotubes 323
Cardio-pulmonary detection 574
Cationic polymer 18
CC2430 567
Cell adhesion 164, 171
Cell cycle 198
Cell physiological analysis 385
Cell uptake 186
Cell 290
Cell-based biosensor 309
Cellular on-rate 164
Centerline 720
Central nucleus 703
Cerebral aneurysm 113
Cerebral circulation 147
Certification 558
Cervical vertebra disease 497
CFM 264
Characteristic specialty 639
Characteristics 645

Characterization 198
 Chemiluminescent 466
 Chemosensitivity 309
 Chest radiographs 260
 Children Healthcare 344
 Children 44
 China 598
 Chitosan 9
 Cholesterol succinate modified
 pullulan 13
 Circulation model 562
 CKD 399
 Clinical Engineers 558
 Coarse grained method 651
 Cognitive attention 668
 Color transparency 273
 Community healthcare 567
 Compact flash (CF) interface 426
 Comparing coefficient 366
 Composite motif 608
 Compression 119
 Computational fluid dynamics 139
 Computed tomography 229
 Cone beam computed tomography
 (CBCT) 206
 Confidence Interval, 389
 Consciousness 685
 Constructing systemized course 623
 Control method 62
 Control process 352
 Controlled release 26, 615
 Convolution/superposition 442
 Cortical bone 182
 Coupled coils 392
 Course design 623
 Crank-rocker Mechanism 497
 Cross-correlation 278
 Curriculum 633, 645, 648
 Curvature 233
 Cytotoxicity 18

D

DAQ 626
 Data acquisition 348, 352
 Data mining 663
 Database 577
 DBS 430
 Deafblind 484
 Decision trees 413
 Defective bone repair 733
 Defective bone 250

Deformable mesh 293
 Deformable model 537
 Deformation based morphometry 213
 Delaunay triangulation 250
 Density drop artifact 206
 Detaching mesh 725
 Detecting system 697
 Detection analysis systems 404
 Dexamethasone 70
 Diabetic retinopathy 216
 Diagnostics of Chinese Medicine 571
 Different control technologies 476
 Differential coefficient arithmetic 174
 Diffuse reflectance 377
 Diffusion tensor imaging (DTI) 237
 Dipole model 337
 Disabled people 476
 Disc 119
 Display techniques 273
 DNP 202
 Doppler color flow mapping 278
 Doppler power spectrum 264
 Doppler signal 408
 Doppler ultrasound 264
 Doppler US 551
 Dose calculation 442
 Dose verification 447
 Drug delivery 534
 Drug discovery 313
 Drug-related cue 668
 Dual-loop speed control 50
 Dynamic model 147
 Dynamic stabilization 119

E

Electroacupuncture 715
 ECG 626
 Echocontrol 155
 ECIS 385
 Education of individuation 639
 Education 648
 Educational pattern 648
 EEG (electroencephalography) 420,
 337, 685, 363, 373
 EGSnrc 442
 Elastography 293
 Electric acupuncture 711
 Electric pulses 511
 Electrically evoked potentials 54
 Electro ventilation double pump
 cardiopulmonary resuscitation 562

Electroacupuncture 660, 668, 678
 Electromagnetic pulse (EMP) 455,
 461, 473, 469, 466
 Electromyography (EMG) 329
 Electron microscope 711
 Electron spectrum 451
 Electronic tongue 306
 Electrospun scaffold 194
 EMG signal 488
 Emotion recognition 484
 Emotional expression 484
 Emulsification 26
 ENaC 603
 Endoscopic image 750
 Endoscopy 741
 Endothelial cells 194
 Energy loss 159
 Energy minimization 537
 Environmental control system 476
 Enzyme immobilization 323
 Epidermal stem cell 73, 76
 Epilepsy characteristic wave 426
 Epileptic absence seizure 420
 Equipment 598
 ERP signal 333
 Erythrocyte membrane 531
 Erythrocyte 503
 Euclidean reconstruction 434
 Evolution equation 255
 Exercise heart rate variability 361
 Experimental model 133
 Experimental system 117
 Exudates 216
 Eye Closure 363

F

Fast marching 225, 233
 FastICA-CKD 399
 FDK 206
 FDM 88
 Feature selection 608
 FEM 737
 Fiber tracking 237
 Finger braille 484
 Finite element analysis, 737
 Finite element method 103
 Finite element 119, 129
 Flatfoot 133
 Flexibility 167
 Flexible manipulator 741
 Flow chamber 164, 171

- Fluid-wall interaction 143
 Fluorescence measurement 754
 Fluorescence probe 186
 fMRI 703
 Focus 366
 Foot-ankle biomechanics 133
 FPIA 404
 Fractional anisotropy 237
 Free radical 455
 Freeze drying 88
 Frequency compounding 286
 Frequency-domain 326
 Frequency response 707
 Functional magnetic resonance imaging (fMRI) 668
- G**
- Gait 488
 Gas chromatography 396
 Gas chromatography and mass spectrometry (GC-MS) 691
 Gas press 174
 Gastric cancer cell 466
 Gaussian interpolation 286
 Gene and protein 404
 Gene delivery 9, 18
 Gene vector 9
 Glioma cells 458
 Glucose monitoring 298
 Glycophorin A 528
 Gold nanoparticle 186
 G-protein-coupled receptors 313
 GPRS 344
 GPRS/3G Mobile Monitoring System 571
 Gray 546
- H**
- Handheld device 754
 Heart sound 577
 Heart valves 95
 Helical tomotherapy 447
 Hemodynamics 107, 113, 143, 159
 Hepatocarcinomatous cell 36
 Heroin abstinence 668
 Heuristic weighting function 206
 High intensity focused ultrasound 555
 High intraocular pressure (IOP) 711
 High-heeled shoes 500
 High-vocation education 623
- Histological examination 615
 HL7RIM 584
 Hsp27, 458
 Hsp70, 458
 Human amniotic mesenchymal stem cell 92
 Human lung cancer cell line 518
 Hydrodynamic interaction of cells 164
 Hydrogel 22
 Hydroxyapatite 22
 Hypertensive 361
 Hyper-gravity 179
 Hyperthermia 210, 542
 Hypoxia inducible factor-1(HIF-1) 518
- I**
- ICA 399
 ICU 357
 Identification 707
 Illusion 333
 Image processing 210
 Image smoothing 255
 Image uniformity 282
 Immunotherapy 202
 Impedance spectroscopy 309
 Implantable neuro-stimulator 430
 Implantable pressure sensor 62
 Implantable 392
 Implanted 660
 IMRT 447
In vitro 70, 73
 Independent component analysis (ICA) 337
 Indirect moxibustion 681
 Indomethacin 29
 Induced electrical field 366
 Induced signal 426
 Inertial measurement unit 155
 Initial placement 260
 Injectable 22
 Innovative undergraduate talents 641
 Integral videography 745
 Integrate training 641
 Integrated chip 385
 Interactive interface 733
 Interface layer 555
 Interface 302
 Interpolation 221
 Intracarotid amobarbital procedure (IAP) 337
- Invasive blood pressure sensor 47
 Ion channel 306, 92
 Jackknife method 608
- K**
- K562 455
 k-nearest neighbor graph 216
 k-nearest neighbor 250
 Knee biomechanics 103
- L**
- LabView 626
 Largest Lyapunov index 361
 Laser confocal scanning microscopy (LCSM) 36
 Lattice Boltzmann method 255, 113
 Layer-by-layer self-assembly 323
 LDA technique 95
 Life detection 594
 Ligament resection 133
 Light Field 745
 Linear discriminant analysis (LDA) 341
 Linux 417
 Lipid bilayer membranes 306
 Liposome 534
 Liver 210
 Local deformable spherical map 250
 Local threshold 241
 Low power consumption 392
 Low resolution 492
 Lower extremity 151
 Lower limbs compression pressure 562
 Lumbar disc herniation 703
 Lumped Parameters 147
 Lung cancer 396
 Lung region segmentation 260
- M**
- M-AFP 44
 Magnetic fluid 524
 Magnetic nano-particles 555
 Magnetic stimulating coil 366
 Magnetoviscous effect 524
 Malondialdehyde (MDA) 455
 Mandibular condylar chondrocytes 99
 Manipulation methods 655
 Manipulation waveform 663

- Matched filter 233, 241
 Matching pursuit 426
 Maxillary sinus 737
 MCF7 cells 534
 MEA 385
 Measured percent depth dose 451
 Measurement system 47
 Mechanical ventilation 413
 Mechanotransduction 99
 Medical college 633
 Medical information systems 584
 Medical model 729
 Medical services sharing platform 584
 Membrane potential 36
 MEMS 317
 Mesenchymal stem cells 80
 Metabonomics 691
 Method of phase difference 174
 Mice 469
 Micro current 58
 Micro-adjusting algorithm 451
 Microcapsule 26, 32
 Micro-computed tomography 720
 Micro-electrode arrays 309
 Microelectrode 317
 Micro-morphology 302
 Microphone 707
 Microphysiometer 385
 Mine 129
 Miniature and low-power wireless sensor technique 580
 Minimally invasive surgery 741
 MITK 210
 Mitochondria 678
 Mitochondrial transmembrane potential 507, 511
 Mitral valve 159
 MKN28 cell 466
 ML4428 chip 50
 Mobile health care 574
 Modified electrode 323
 Moment 290
 Monitor 417
 Monitoring 357
 Monomethoxy poly(ethylene glycol) 190
 Motion compensation 273
 Motion simulation 151
 Motion tracking 293
 MPF 329
 MTF 221
 Multi-ASM 260
 Multifunctional instrument 385
 Multi-media sound technique 245
 Multimedia 636
 Muscular fatigue 329
 Muscular model 151
 Myoelectricity signal records 655
- N**
- Nanoparticles 514
 Nanopores 306
 Natural heartbeat synchronization 62
 NDV Ulster 202
 Neonatal monitoring 413
 Nerve conduit 4
 Nerve regeneration 4
 Network 357
 Neural stimulator 58
 NIRS 377
 Nodule segmentation 225
 Non-contact 594
 Noninvasive temperature measure 546
 Noninvasive 542
 Nonlinear programming model 451
 Nonlinear 685
 Non-pregnant uterus 551
 Non-rigid registration 213
 nRF24E1 373
 Nude mice 518
 Numerical simulation 107, 159, 139
 Numerical simulation 171
- O**
- Olfactory receptor 313
 Ontology 584
 Open-field 473
 Optic nerve 54
 Optical polarimetric sensing 298
 Optical System 404
 Optimization 107
 Organ-meridians 707
 Orthogonal twin polarized light 298
 Oscillation 95
 OSFE 737
 Osteoarthritis (OA) 691
 Osteoporosis 182
 Outer sheath 741
 Oxygen free radical 466
 Oxytocin 551
- P**
- P300, 341
 Paclitaxel 514
 Paclitex (PTX) 518
 Parasympathetic nerve 326
 Patch clamp 92
 Pattern recognition 691
 PCG 577
 Pedorthic care arthritic foot save 1
 PEG 9
 PEI 9
 Penetrating electrodes 54
 Performance 44
 Personal digital assistant (PDA) 426
 Phase portrait 651
 Photon beam 442
 Photosensitizers 186
 Physical protection 598
 Physiological parameter 417
 PI3K 603
 Pixelized image 492
 Plantar pressure 488, 500
 PLGA 514
 Pneumatic locking mechanism 741
 Point correspondence 434
 Point Distribution Model 260
 Point-point force 151
 Poly (3-hydroxybutyrate) microspheres 615
 Poly (ethylene glycol) 18
 Poly(ϵ -caprolactone) 190
 Polyethylenimine 18
 Poly-L-arginine 26, 32
 Polysaccharide 503
 Porous scaffold 84
 Porphyrin 186
 Post-operative 480
 Posture 129
 Power density spectra 95
 PPM 392
 Preference direction 237
 Pressure waveform 143
 Pressure 99
 Previous propagation directions 237
 PRF 264
 Processing strategies 492
 Prodrug 29
 Projection reconstruction 434
 Prokaryotic promoter prediction 608
 Prosody 484

- Prosthetics and orthotics engineering 648
 Protein expression 458
 Protein 32
 Protoporphyrin IX 754
 Psychological stressor 326
 Pulse picture 651
 Pulse wave 344
 Pulse 697
 Pump 44
 Pupil-blocking phenomenon 117
 PWM 50
- Q**
- Qigong 685
 Qinglongyi 503
 Quadratic discriminant analysis (QDA) 608
 Quality Assurance 447
 Quantification 663
 Quartz crystal microbalance 313
- R**
- Radar 594
 Radio-frequency field 458
 Radiotherapy 451
 Rat 373
 Rationalized gain compensation 282
 Reactive oxygen species 507
 Real-time rendering 745
 Rebin projection data 221
 Recognition 290, 492
 Reconstruction 206
 Reference 480
 Region merging 216
 Registration 269
 Rehabilitation horse 497
 Release efficiency 514
 Release 29
 Remodeling 182
 Research teaching style 636
 Research-oriented experiments 636
 Residual limb 480
 Respiratory training 179
 Response surface methodology 107
 Retinal ganglion cells (RGCs) 711
 Retinal image 216, 233, 241
 RF Beamline 264
 RMS 329
 Robotic assisted surgery 750
- Root canal preparation 720
 Rotational C-arm system 434
 RP 729
- S**
- Saddle trajectory 229
 Saponins of asparagus 507
 Sargassum fusiforme polysaccharides (SFPS) 531
 Scaffold 40, 88
 Scanning electron microscopy 534
 Schwann cell 4
 Screen 396
 SD rat 461, 473
 Sectional area 720
 Segmentation methods 273
 Segmentation 381
 Selective laser sintering 84
 Self-assembled nanoparticle 13
 Sensation of acupuncture 655
 Sensor 413, 663, 697,
 SEP 123
 Shank curve 500
 Shaping figure 497
 Shear stresses 95
 Shooting 326
 SICM 603
 Signal molecules 99
 Silk fibroin 4
 Simulated prosthetic vision 492
 Simulative circulation apparatus 44
 Single acupoint 660
 Single trial 123, 245
 Skin 76
 Skull defect mending 725
 Slow cortical auditory EPs 245
 Slow-release 32
 Slow-release 70
 Small intestine submucosa 40
 Snakes 537
 SNR 286
 Solanine 36
 Solid phase microextraction 396
 Sparse Representation 426
 Spatial averaging 278
 Speckle noise 286
 Spectrum 286
 Speech recognition 389
 Speed 488
 Speed-modulate design 50
 SPM 603
- Sponge 40
 Stay chords 159
 Stent 113, 70
 Stereo reconstruction 434
 Stimulating parameters 715
 Stimulation amount 663
 STL model 725
 Strain image 273
 Strain imaging 293
 Structure-activity relationship 167
 Student-centered teaching 633
 Study of the nature of TCM syndromes 691
 Superoxide dismutase (SOD) 455, 461
 Support vector machine (SVM) 225, 381
 Supramodal interaction 333
 Surface reconstruction 250
 Surface roughness 302
 Surgical navigation 750
 Surgical planning 729
 Sympathetic nerve 326
 System design 546
 Systemic perfusion pressure 562
- T**
- Targeting drug delivery 524
 Taste sensor 306
 TCM Research 700
 Technology 598
 Telemedicine 567, 571
 Telemetric system 373
 Telemonitoring 577
 Telephone 577
 Telomerase reverse transcriptase 73
 Telomerase 76
 Temperature conduction model 681
 Temperature determination 681
 Temperature estimation 542
 Tent-FDK algorithm 221
 TEOAEs 399
 Testicle 469
 Testis 461
 Texture analysis 381
 The law of horse movement 497
 Therapy 480
 Thin-plate spline 269
 Thoracolumbar spine 129
 Threshold probing 241
 Threshold shrinkage denoising 408
 Thresholding 381

Time gain control 282
 Time-frequency analysis 399
 Tissue blood oxygen content 377
 Tissue engineering 73, 76, 88
 TPGS 514
 TPS 442
 Trabecular bone 182
 Traditional Chinese medical informatics 700
 Training mode 645
 Training program 629
 Transcutaneous wireless communication 392
 Tri-angulation 725
 Triblock copolymers 190
 Tuina 703
 Tumor Vaccine 202
 Tumor 290
 Tunnel angle 103

U

Ultrasonic 174
 Ultrasound image 293, 542

Ultrasound imaging 282
 Ultrasound 534
 Undergraduate 629
 Undulation pump 62, 66
 UPVAD 62, 66
 Urinary metabolite profile 691

V

Vascular endothelial growth factor 80
 Vascular endothelial-like cells 80
 Velocity of sound 174
 Vi-bration 129
 Vimentin 469
 Virtual body 700
 Virtual instrument 626
 Visual cortex 54
 Visual display terminal (VDT) 329
 Visual prosthesis 54, 317
 Visual spatial sensory 333
 Vitro cytotoxicity 615
 VNS 430
 Volume pulse 655
 Volume 720

W

Warping 269
 Waveform 551
 Wavelet packet analysis 408
 Wavelet transform 363
 Wearable detection 344
 Wearable technique 571, 580
 Web services 584
 Wireless health care of infants 580
 Wireless sensor network 567
 Wireless transmission 348
 Wireless 373
 Working process 623
 Wrist pulse 707

Z

ZigBee 348, 357, 567, 574

β

β-tricalcium phosphate 84
 β-TCP 88